IBIC 2015

International Beam Instrumentation Conference

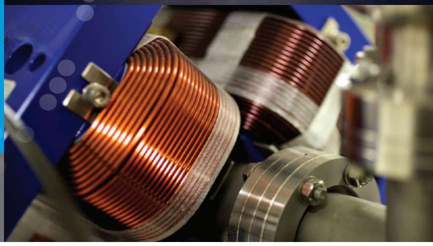

13-17 SEPTEMBER 2015 MELBOURNE **AUSTRALIA**

IBIC 2015, hosted by the Australian Synchrotron, will bring together beam instrumentation specialists from international accelerator facilities, in the major research hub of Melbourne, Australia.

IBIC is dedicated to exploring the physics and engineering challenges of beam diagnostic and measurement techniques for charged particle accelerators worldwide.

The conference program will include the latest developments in:

- Overview and Commissioning
- BPMs and Beam Stability
- Time Resolved Diagnostics and Synchronization
- Beam Loss Detection
- Beam Profile Monitors
- Beam Charge Monitors and General Diagnostics
- Collider Specific Instrumentation

IBIC2015

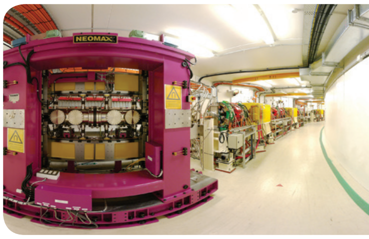

www.ibic2015.org

Hosted by:

State Government Victoria · Australian Government · ansto · Australian Synchrotron

Dear Colleagues,

On behalf of the program committee, I am pleased to welcome you to Melbourne, Australia, for the 2015 International Beam Instrumentation Conference ***IBIC 2015.*** IBIC is a fruitful and successful gathering of the world's beam instrumentation community and it reflects the maturity of international collaboration in the field of beam instrumentation for accelerators.

IBIC is dedicated to exploring the physics and engineering challenges of beam diagnostic and measurement techniques for charged particle accelerators worldwide. The conference program will include tutorials on selected topics, invited and selected talks, as well as poster sessions. An industrial exhibition and a tour of the accelerator facilities at the Australian Synchrotron will also be included.

Melbourne is located in the southern state of Victoria, Australia, with a population of 4.2 million people. It is a major research hub with 9 universities, 7 teaching hospitals and 263 biotech companies. The venue of IBIC 2015 is the Melbourne Convention and Exhibition Centre, located on the Yarra River in the heart of the city - the same location the discovery of the Higgs particle was announced at ICHEP 2012.

We look forward to welcoming you to Melbourne.

Mark Boland, Chair
IBIC 2015 Program Committee

Conference Chair

Mark Boland	Australian Synchrotron

Program Committee

Mark Boland	Australian Synchrotron	Asia 1
Toshiyuki Mitsuhashi	KEK	Asia 2
Prapong Klysubun	SLRI	Asia 3
Yongbin Leng	SINAP	Asia 4
Hitoshi Tanaka	SPring-8	Asia 5
Kuotung Hsu	NSRRC	Asia 6
Junhui Yue	IHEP	Asia 7
Bagrat Grigoryan	CANDLE	Asia 8
Sung-Ju Park	PAL	Asia 9
Dinakar Kanjilal	IUAC	Asia 10
Nikolai Lobanov	ANU	Asia 11
Seadat Varnasseri	ESS-Bilbao	Asia 12
Guenther Rehm	Diamond	Europe 1
Francis Perez	ALBA	Europe 2
Hermann Schmickler	CERN	Europe 3
Kay Wittenburg	DESY	Europe 4
Andreas Jansson	ESS	Europe 5
Mario Ferianis	ELETTRA	Europe 6
Steve Smith	SLAC	Americas 1
Rafel Baron	LNLS	Americas 2
Kevin Jordan	JLAB	Americas 3
James Sedillo	LANL	Americas 4
Glenn Decker	APS	Americas 5
Steven Lidia	FRIB & IBIC17 chair	Americas 6

Local Organizing Committee

Mark Boland	Australian Synchrotron
David Button	ANSTO
David Krenus	Cyclotek
Greg LeBlanc	Australian Synchrotron
Dean Morris	Australian Synchrotron
Natalia Ferreira	Australian Synchrotron
Roger Rassool	UoM
Dimitrios Tsifakis	ANU
Rohan Dowd	Australian Synchrotron

Contents

THE ROLE OF BEAM DIAGNOSTICS IN THE RAPID COMMISSIONING OF THE TPS BOOSTER AND STORAGE RING

P. C. Chiu, C.Y. Liao, C. Y. Wu, K. H. Hu, Y.S. Cheng, C. H. Huang, Demi Lee, Jenny Chen, C. H. Kuo, K.T. Hsu
NSRRC, Hsinchu 30076, Taiwan

Abstract

The TPS is a newly constructed 3-GeV third-generation synchrotron light source featuring ultra-high photon brightness with extremely low emittance. After some hardware improvement especially demagnetization of chamber are completed, the commissioning of the beam in the booster ring began on December 12 and attained 3-GeV energy on December 16. The storage ring obtained its first stored beam and delivered synchrotron light on December 31[1][2]. This report summarizes the role of beam diagnostic for hardware improvement and parameter tuning during TPS successful commissioning.

INTRODUCTION

The TPS accelerator complex consists of a 150 MeV S-band linac, linac to booster transfer line (LTB), 0.15–3 GeV booster synchrotron, booster to storage ring transfer line (BTS), and 3 GeV storage ring. The linac was a turn-key system delivery by RI GmbH. The booster and the storage ring share the same tunnel in a concentric fashion. The booster has 6 FODO cells and its circumference is 496.8 meters. The Storage Ring's circumference is 518.4 meters with 24 DBA lattice and 6-fold symmetry [3].

To catch up the delayed schedule due to construction delay, it was decided to perform system test and beam commissioning in parallel just after get operation permission from government authority in mid August. After solved overheating problem of the booster dipole power supply and optimize post-pulse residual field of the booster injection kickers, multi-turn circulating beam was observed in the booster synchrotron in beginning of September. These hardware problems are mostly due to the limited rush time before operation. However, the captured and stored beam intensity is decay exponentially even any kind of efforts were did such as orbit optimization, add extra correctors, chamber and magnet re-alignment and etc. Finally, it was recognized the relative permeability (ranging from 1.2 to 2.0) of the pipes arising from the cold-drawn process of the booster vacuum pipe was too large on November 12. After dismantle vacuum pipe, heat treatment, and re-install again, beam was stored successfully on December 12, energy ramp to 3 GeV on December 16. Later, after improving field leakage of booster extraction DC septum, we had a 5-mA stored beam on Dec. 31 2014. Diagnostic system played a helpful rule to provide beam profile and information to improve or tune subsystem to make progress quickly during beam commissioning. This report will brief about diagnostics for TPS.

SCREEN MONITOR

The screen monitor system is the most import destructive monitor during the TPS beam commissioning. There are 33 screen monitor systems distributed around Linac (5), LTB (5), booster synchrotron (7) , BTS (5), storage ring (4), and frontend (7). The screen monitor is responsible for the beam profile acquisition from fluorescent screen and used to analysis to find the beam characteristic data. The beam profile image has extensive information on beam parameters, including beam center, sigma, tilt angle and etc. The system contains YAG:Ce screen, lens, lighting system, LEDs illuminator, and GigE Vision CCD camera. A pneumatic device is used to move the whole assembly in or out. All of these devices are controlled remotely including the CCD power control, screen in/out control and LED lighting system. The camera timing trigger clock is locked with TPS injection system, which is produced from a local timing IOC (EVR). Based on the area Detector module which provides a general-purpose interface for area (2-D) detectors in EPICS, it is easy to construct a camera control panel by using the EDM, and analysis tool by using the Matlab tool. Figure 1 shows the beam profile observed at booster 1st screen monitor.

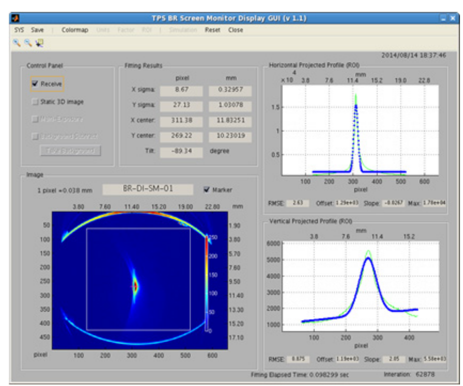

Figure 1: Beam profile at booster 1st screen monitor.

INTENSITY MONITOR

Linac contracted to RI GmbH is provided two Faraday cups and two warm current monitors. Figure 2 shows bunch waveform observed by the wall current monitor just after electron gun. There are two ICTs and two FCTs for LTB, two ICTs and one FCT at BTS where Figure 3 shows ICT waveform at LTB for single bunch beam and

ISBN 978-3-95450-176-2

Figure 4 shows the booster current via FCT VNC display. The beam trips when ramping down to 2 GeV due to tune cross resonance line. The booster equipped with one DCCT and one FCT.

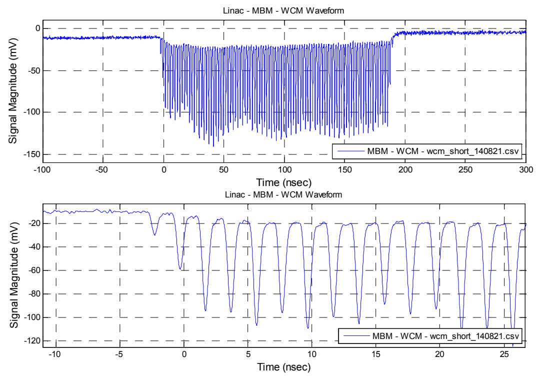

Figure 2: Bunch waveform observed by the wall current monitor just after electron gun.

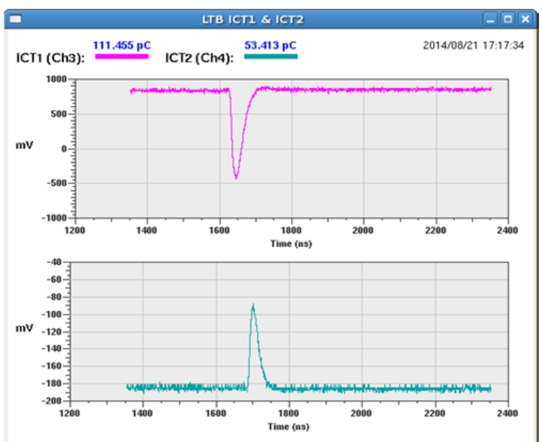

Figure 3: ICT waveform at LTB for single bunch beam.

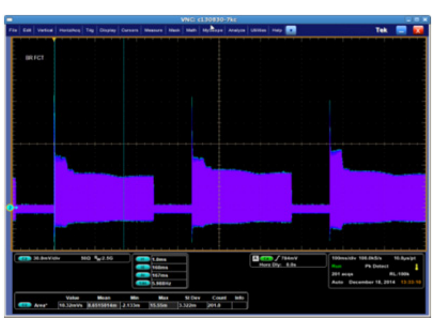

Figure 4: FCT display for booster ramping.

Data acquisition of the storage ring DCCT is via with high precision ADC and digital multi-meter used to measure beam current from DCCT. Lifetime is calculated by regression from measured beam current. Injection efficiency estimation and injection sequence control is to use information of the measured beam current as well. Only single NPCT was installed at the storage ring, to prevent possible fault resulting in another problem, a tone loop winded on NPCT is to detect correction of the devices and connected to machine protection system.

Signal from BPM pickup and synchrotron light are both used to measure filling pattern. Figure 5 shows the filling pattern measured from pickup and TSCPC respectively. High resolution oscilloscope to observed signal from FCT at the booster synchrotron and BPM buttons at storage ring are used to provide information of filling pattern. Time-correlated single proton counter is also available at the storage ring synchrotron light diagnostics port. There monitors can provide bunch current information and also measure single bunch purity with high dynamic range as Figure 6 shown.

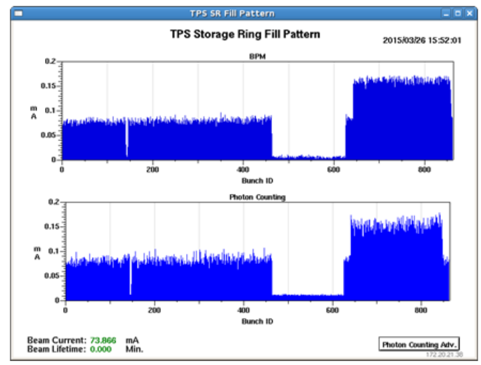

Figure 5: Filling patterns of the storage ring are measured from BPM button (upper) and TCSPC (lower).

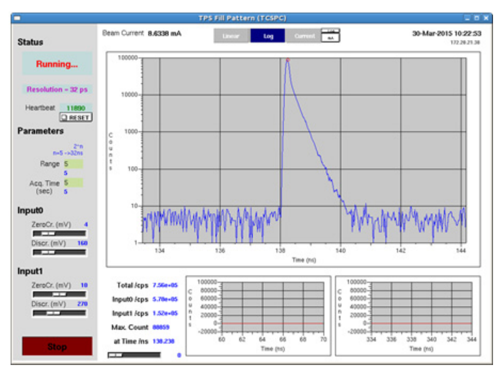

Figure 6: Single bunch impurity is achieved 10^{-5} by using bunch cleaning observed by TSCPC.

BEAM POSITION MONITOR

BPM is the major diagnostic device for beam commissioning. The electronics adopt commercial product Libera Single Pass Brilliance and Libera Brilliance Plus [4]. Linac optimization had much depended on BPM and the first turn of the booster beam had achieved and observed by BPM soon after correctors steering. There are only few buttons of booster BPM found to have contact problems quickly by observing ADC data with extremely low count compared to other buttons. The real BPM calibration factor was agreed with the designed values by measuring and comparing the optical function of machine model. Beam transport efficiency at BTS achieved up 90% estimated by BPM. The first turn and accumulated beam of the storage ring

ISBN 978-3-95450-176-2

soon obtained without correctors after injection started. It was also found that there are some cabling problems during measure and optimize machine. Button B and C of two BPMs are cross connected. The cables of BPM 24_4 and 24_6 are also connected in wrong order. Besides, the LOCO fitting for BPM calibration factor showed that there are three primary BPM located near RF cavity which the fitting factors Kx/Ky are almost only one half of the expected value. It was caused by incorrect set to the configuration of the primary type BPM while they should have configurations of the standard type [5].

LTB & BTS

There are seven and six BPM installed at LTB and BTS transport line. Both are elliptical shape with chamber dimensions of 56x28 and 35x20 mm and button diameter of 10.2 and 10.7 mm for LTB and BTS respectively. The commercial product – Libera Brilliance Single Pass are adopted to provide measured data with EPICS support. Figure 7 shows the GUI main page for BTS transport line. BPM ADC data and detail configuration could be also accessed in the below pages.

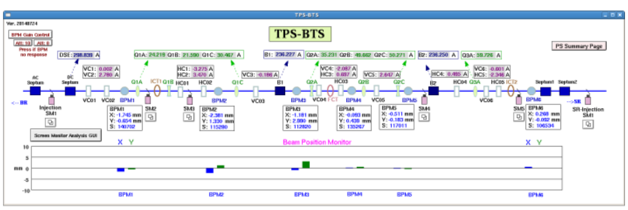

Figure 7: BTS GUI main page. BPM ADC data and detail configuration could be also accessed in the below pages.

Booster Synchrotron

The TPS booster ring has six cells where each cell is equipped with 10 BPMs which can be used to measure beam position and rough beam intensity along the longitudinal position and tune measurement. The mechanical dimension of booster BPM shapes 35x20 mm elliptical and button diameter 10.7 mm. For TPS booster BPM, there are 60 sets of phase-trimmed 0.240" form polyethylene coaxial cables connected between the buttons and BPM electronics. The BPM electronics Libera Brilliance+ are adopted for both booster and storage ring of TPS and provides various BPM data flow for diverse functionalities and purposes. In this section, different BPM data flow will be demonstrated for different applications.

The ADC raw data is useful for checking the timing of the beam and beam property especially in the first turn. The phase delay due to time difference when beam travel pass the buttons along the ring could be aligned by ADC clock offset. The timing of kicker and septum trigger are also adjusted by compared to BPM ADC signal as Figure 8 shows which the first turn of BPM should be located between the pulse of the kicker waveform.

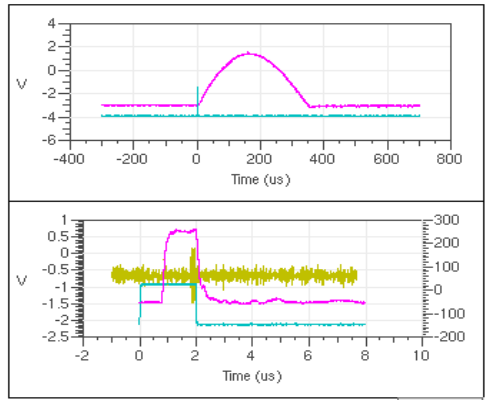

Figure 8: The upper plot is septum waveform (pink) and its trigger (blue). The below plot is kicker waveform, its trigger and ADC data of booster 1st BPM button D (yellow) located between the pulse of kicker waveform.

BPM electronics provides single pass mode for calculating first turn trajectory from ADC data. However, vast beam losses and ADC DC offset up to 100 count will result in worsen signal to noise ratio and position calculation offset error. Therefore, a soft IOC would be applied to acquire more precise first turn trajectory from ADC raw minus DC offset. Figure 9 shows the first turn orbit trajectory and sum along 60 BPMs. Horizontal trajectory shapes like dispersion function due to energy drift from Linac modulator.

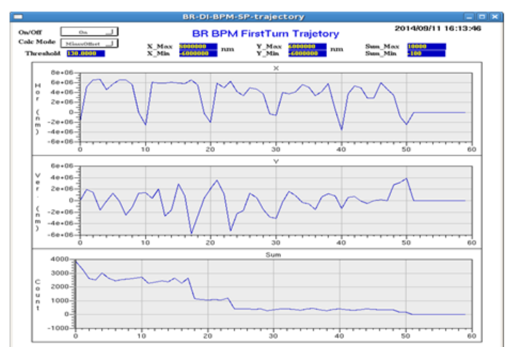

Figure 9: First turn horizontal, vertical trajectory and sum along 60 BPMs of booster. Horizontal trajectory shape like dispersion and it indicates the injection beam energy is higher that dipole current settings.

DDC (Digital Down Converter) and TDP (Time Domain Processing) Turn-by-turn data are both provided by BPM electronics and the resolution could achieve around 150 um at 0.5 mA. The BPM TBT data could be applied to extract tune as well as calculate optical function more efficiently. To use TDP properly, phase offset should be adjusted by beam according ADC data and mask window also should be set correctly according bunch length. Compared to DDC, TDP could well resolve beam loss status and tune extraction due to clear and no smear TBT data [5].

The BPM electronics also provide 10 kHz fast position

ISBN 978-3-95450-176-2

data to measure average stored beam orbit. It shows orbit variation during ramping could be around 6 mm in horizontal and 2 mm in vertical. The low frequency synchrotron motion around 1.5 kHz is contributed for the injection initial variation [5]. The related applications including GUI and acquiring scripts are developed and provided for studying and helping commissioning.

Storage Ring

The TPS storage ring is divided into 24 cells and there are 7 BPMs per cell. Another six BPM are also installed at three straight lines located with double minimum betay quadrupels for local measurement. There are two kinds of BPM for storage ring: one is standard button BPM shapes 68x30 mm elliptical and diameter 7.4 mm at arc section; the other is primary BPM shapes 64x16 mm racetrack and diameter 7.4 mm at straight line. The calibration factor Kx/Ky is 13.8/12.73 and 6.58/8.89 mm for standard and primary BPM respectively.

BPM electronics also provides several data type for different application. ADC and TBT data is acquired on demand by trigger; 10 Hz slow data is for DC average orbit and 10 kHz fast data could be applied for stability analysis and fast orbit feedback application.

After beam stored, the beam current had achieved 50 mA in March 2015 with vacuum pressure dropped. However, it was hardly continuously accumulated and beam trip happened. It was later verified that synchrotron motion is the major reason due to RF feedback loop resonance. The BPM turn-by-turn data observed that the synchrotron motion make horizontal position vibration at same phase as Figure 10 shown and it became stronger as beam current increased.

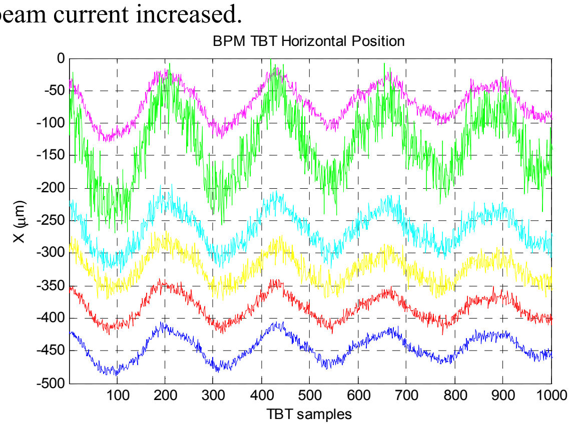

Figure 10: Horizontal TBT data. The synchrotron motion’s amplitude for each BPM is proportional to its dispersion and also increased as beam current increased.

TBT data is also applied to extract tune in the storage ring. Besides injection kickers, the horizontal and vertical pingers are used to excite beam motion in two planes respectively. Timing for trigger of BPM, kickers and pingers are controlled by event system. Figure 11 shows the real time tune display page. The chosen BPM, average number, FFT length and etc. could be selected according to different condition and requirement.

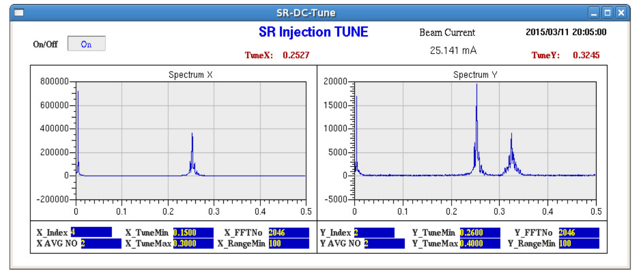

Figure 11: Storage ring tune extracted from BPM TBT data where beam are excited by pingers.

10 kHz FA data could be provided to analyse transient motion, orbit stability as well as applied for fast orbit feedback. The synchrotron motion around 2 kHz could be also observed. According to BPM spectrum from FA data, 29 Hz noise was found the dominant noise source induced from turbo-pump motor. Booster extraction at 3 Hz repetition rate also makes 3 Hz noise observed. Besides, water flow also causes wide band vibration from 30 to 70 Hz. Figure 12 shows the integrated PSD for the horizontal and vertical planes. Efforts to eliminate the noise source will be undertaken in the future.

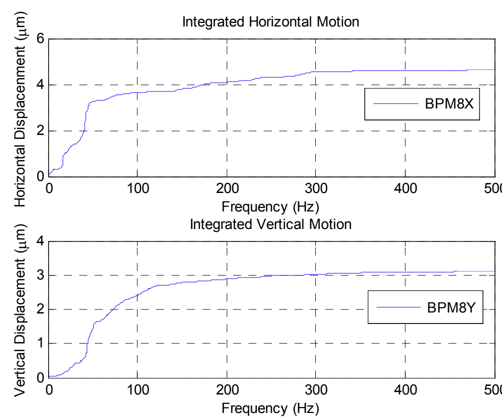

Figure 12: Horizontal and vertical integrated PSD.

Moreover, BPM FA data of the storage ring are also used for interlock safety of position and angle. BPM electronics itself provide position interlock functionalities. Another dedicated IOC is adopted to calculate all angles between different BPM from streaming in FA data through Gigabit Ethernet and activates interlock.

TUNE MONITOR

Booster Synchrotron

Originally during booster commissioning beginning in Sep. 2014, the magnetic shakers where two multi-turn coils are mounted on vacuum chamber in horizontal and vertical plane are applied to excite beam. The kickers with 50Ω terminated load have calibration factor of 3 mG/A and are driven by a 50W amplifiers. Later, the stripline electrodes are adopted to replace magnet shakers

ISBN 978-3-95450-176-2

on the booster synchrotron considering more power strength to excite beam. The TBT data provided by BPM electronics would be acquired to extract tune by FFT. Agilent arbitrary signal generator would provide band-limited, strength-adjustable excite signal. The functional block diagram of this new tune monitor system is shown in Figure 13. Figure 14 shows the tune measurement GUI. The tune variation was as large as 0.25 for horizontal and 0.2 for vertical before tune compensation. It could be inferred that reference waveform generated from the measured I-B table provide by the magnet lab could be deviated from the actual machine.

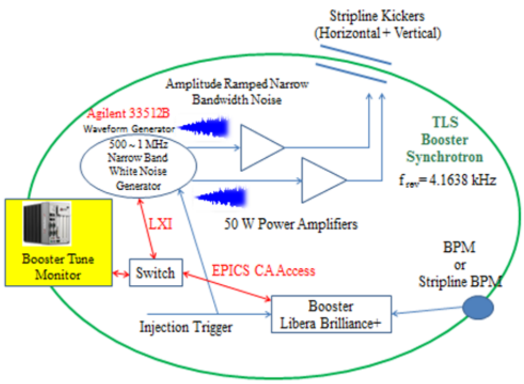

Figure 13: Functional block diagram of the tune monitor for TPS booster.

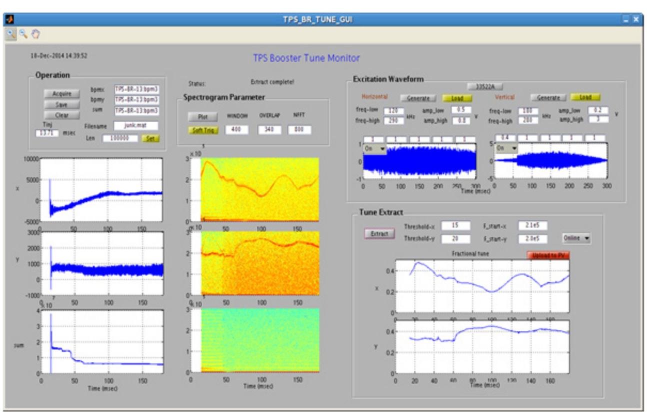

Figure 14: Tune monitor during Booster ramping before tune compensation. Vertical tune variation was as large as 0.25.

Storage Ring

Residue beam motion during injection caused by injection kickers, or shaking beam by dedicated horizontal and vertical pingers are used to excite beam motion in two planes respectively. Timing for trigger of BPM, kickers and pingers are controlled by event system. The TBT data provided by BPM electronics would be acquired to extract tune by FFT. The chosen BPM, average number, FFT length and etc. could be selected according to different condition and requirement. Figure 15 shows the real time tune display page.

Tune can also be measured by the bunch-by-bunch feedback system. Notch in the averaged spectrum after close feedback loop can use to indicate working tune. Single bunch excitation and perform FFT can also extract tune. Single bunch excitation will not deteriorate stored beam quality.

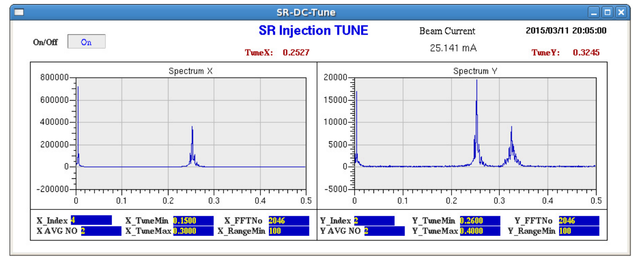

Figure 15: Storage ring tune extracted from BPM TBT data where beam are excited by pingers.

SYNCHROTRON RADIATION MONITOR

Booster Synchrotron

The synchrotron light monitor was designed. The light leads to the wall via a four-piece adjustable mirror, focusing through a lens and band-pass filter to GigE Vision camera. The camera trigger is synchronized with the machine cycle; change the delay time will change the energy point of observation. A 1-inch size CCD is used to quickly and easily to find a first-time beam spot. This synchrotron light monitoring port was used for streak camera measurement for linac beam and booster stored beam also.

The shape and size of the electron beam profile vary during the energy ramping from 150 MeV to 3 GeV, as shown in Figure 16. The beam size in both axes decreases when the energy increases due to radiation damping clearly (see Figure 17). This result is consistent with the design [3][6].

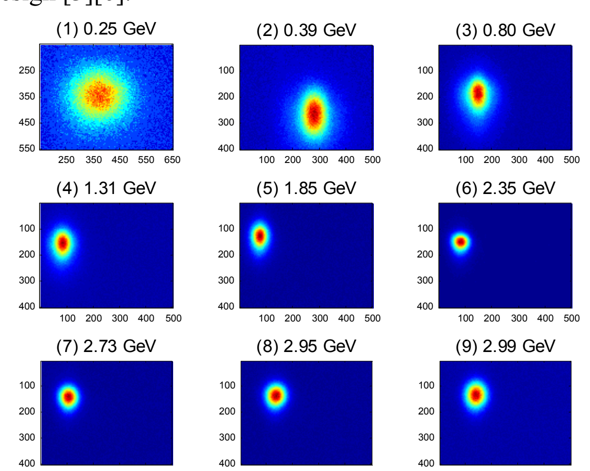

Figure 16: TPS booster synchrotron radiation profiles at varied energy ramping point, 1 pixel is around 9 μm.

ISBN 978-3-95450-176-2

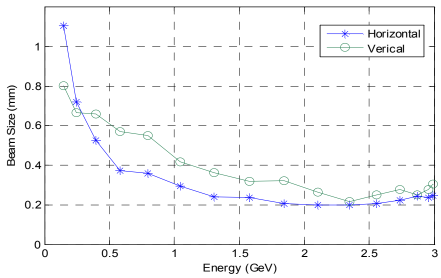

Figure 17: Measured variation of beam size with energy ramping of booster synchrotron.

Storage Ring

The photon diagnostics beamline utilized visible light and X-ray of the synchrotron radiation which generated in a bending magnet. The X-ray pinhole camera design for imaging the electron beam from bending magnet for the beam size and emittance measurements. They offer the required resolution and the dynamic range to measure the electron beam size accurately at all currents. The visible light of synchrotron radiation was design for streak camera, interferometer and fill pattern measurements.

The beam size of single bunch measured via X-ray pinhole camera in low current (~2 mA) is 39.1±0.6 µm in horizontal and 15.7±1.5 µm in vertical. When the storage beam current increases, the beam size of the horizontal axis also increases, but the vertical axis is no significant change. The CCD exposure time is reduced (~10 ms) to avoid the measurement error caused by the beam oscillation due to mechanical vibration. The calculated emittance and coupling are $\varepsilon_x \approx 1.64$ nm·rad, $\varepsilon_y \approx 15.7\pm3$ pm·rad, and $k \approx 0.96\%$ [6]. The TPS design natural emittance (ε_{x0}) is 1.6 nm·rad.

Streak Camera Measurement

For the bunch length measurement, the synchroscan unit of 250 MHz is used. The result shows that the bunch length of the TPS storage ring is around 11.4 psec (sigma) in low current (~0.2 mA) single bunch mode as Figure 18. When the current is increased, the bunch length is also significantly increased.

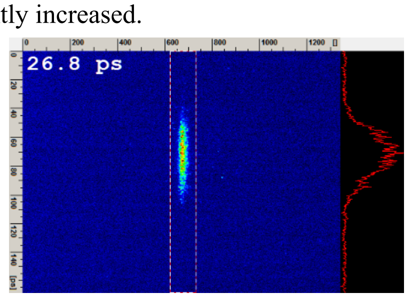

Figure 18: Typical streak image of bunch length measurement at TPS storage ring under single bunch mode.

BEAM LOSS MONITOR

In the booster ring, the radiation-sensing field-effect transistor (RadFET) is installed before the fifty-four bending magnets of the booster synchrotron in six cells to monitor the beam loss during beam commissioning [7]. Nine RadFETs in each cell are collected by a reader. Six readers and the controlling IOC is linked with a private virtual LAN [8]. The accumulated dose, dose rate and beam loss distribution are published and shown in the control system online. The typically beam loss distribution during booster commissioning is shown in Figure 19. The six RadFETs are installed in the inside-wall chamber of the storage ring in each cell. One reader is setup in the cable tray of the tunnel to minimize the cable length from RadFETs to the reader.

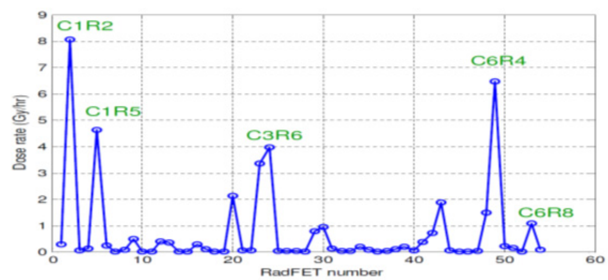

Figure 19: Beam loss distribution of booster ring during beam commissioning.

Several kinds of beam loss monitor were installed. Bergoz's PIN diodes beam loss monitor (BLM) was installed at the storage ring in June. The six Bergoz PIN diodes are installed in the inside-wall chamber of the storage ring in each cell Multichannel scaler data acquisition system were sat up a tested in July. The output pulse of PIN diodes is coupled via pulse transformer and send by twisted pairs cable (UTP/STP) to a differential receiver to convert to LVTTL pulse to compatible with input of the data acquisition system. The data acquisition consists of a 16 channel multichannel scaler in Industry Pack form factor installed on cPCI carrier board of a cPCI EPICS IOC on the equipment area. All scalers which distributed at 24 IOCs are synchronized by the timing system of the accelerator. Commissioning of this system is scheduled in September.

Several high counting rate BLMs such as scintillation detectors and Cerenkov detectors are also installed in the first cell below the injection straight for preliminary studying.

ORBIT FEEDBACKS

Fast correctors just installed June 2015. The firmware modification of fast orbit feedback is still underway. TPS will first provide a simple slow orbit feedback system which is implemented by Matlab script to support insertion devices commissioning with 10 Hz updating rate during 4th quarter 2015. All components for fast orbit feedback system would be installed in last several months as well. Testing is on going to ensure every component is working properly. Fast orbit feedback will commission in adequate window in late of 2015.

ISBN 978-3-95450-176-2

BUNCH-BY-BUNCH FEEDBACKS

A simple two parallel stripline prototype vertical kicker was installed at the storage ring rather than real kickers will used due to implementation schedule cannot be met. Preliminary test of the vertical bunch-by-bunch feedback was performed. Commercial feedback processor (iGp12) was used for TPS. The feedback loop was closed in mid-January [9]. Preliminary test were performed despite very strong energy oscillation existed. Various functionalities of the bunch-by-bunch system were examined. Figure 20 shows the typical grow/damp experiment of the 90 mA stored beam. Resistive wall instability is the major cause. Adequate damping is achieved. Single bunch purity is bad during several shift for parameter measurement, bunch clean is performed to keep bunch purity better than 10^{-5}.[6]. Two vertical kickers and one horizontal kicker which are derived from the design of SLS/ELETTA were implemented and installed for the preparing next phase commissioning. Co of bunch-by-bunch feedback by using new kickers is schedule after beam stored in September.

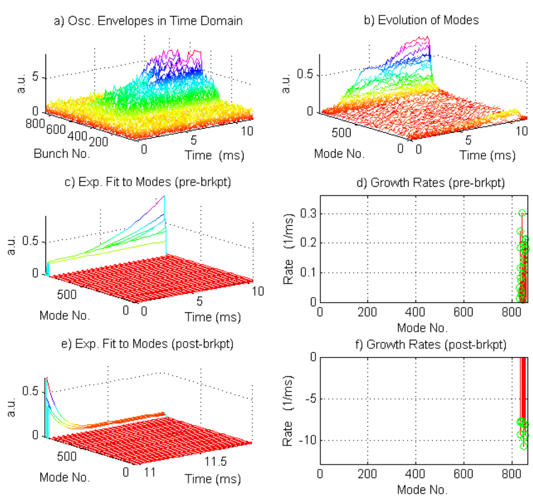

Figure 20: Grow/damp data shown that the adequate damping is achieved for 100 mA beam current.

MACHINE PROTECTION SYSTEM

To protect accelerator from damage for miss-steering of the beam, beam position as well as angle interlock are implemented. The beam position interlock is implemented at the BPM platform. Beam angle are calculated at a dedicated PC running Linux to receive BPM grouping data, then calculated beam angle at 10 kHz rate. The PC also are installed EPICS IOC to serve as interface of the 10 kHz loop as man-machine interface. Configuration of the operation can be set via EPICS channel access.

CURRENT STATUS

Phase I commissioning was proceeded with two Petra cavities and without insertion devices during December 2014 until March 2015 to examine feasibility and validity of the design of accelerator system. Beam was stored up to 100 mA very soon. Various measurements were performed. Diagnostics play an important role during commissioning in all-round aspects. Two KEK-B superconducting RF cavities and the 7 sets of in-vacuum undulators and three sets of elliptically polarized undulators had been installed during shutdown from April to late August 2015. Phase II commissioning is started from 2015 September. Diagnostic provide quite a lot of beam information during commissioning as well as future optimization.

ACKNOWLEDGEMENT

Thanks for the helps from diagnostics communities, especially Jean-Claude Denald of Soleil, G. Rhem of DLS, Bob Hettel of SSRL/SLAC, Ubado of ALBA, H, Nakamura of Spring-8 are highly appreciated. The authors also appreciate help from people of I-Tech and Dimtel for brainstorming and discussion. Help from colleagues of vacuum group, precision mechanical group, beam dynamics group.

REFERENCES

[1] H. J. Tsai et al., “Hardware Improvements and Beam Commissioning of the Booster Ring in Taiwan Photon Source”, IPAC2015, Richmond, VA, USA, May 2015.
[2] C. C. Kuo et al., “Commissioning Results of Taiwan Photon Source”, IPAC2015, Richmond, VA, USA, May 2015.
[3] TPS Design Handbook, version 16, June 2009.
[4] P. C. Chiu, et. al., “TPS BPM electronics performance measurement and statistics”, IBIC 2012, Tsukuba, Japan.
[5] P. C. Chiu, et al., “Commissioning of BPM system for the TPS project”, these proceedings.
[6] C. Y. Liao, “Synchrotron Radiation Measurement at Taiwan Photon Source”, these proceedings
[7] Demi Lee, et al., “Online RadFET Reader for Beam Loss Monitoring System”, IPAC 2015, Richmond, USA.
[8] C. H. Huang, et al., “Beam loss monitoring system in Taiwan photon source”, these proceedings.
[9] Y. S. Cheng, et al., “Preliminary Commissioning of the Bunch-by-Bunch Transverse Feedback System for TPS Storage Ring”, these proceedings.

ISBN 978-3-95450-176-2

SNS BEAM DIAGNOSTICS: TEN YEARS AFTER COMMISSIONING

A. Aleksandrov
Oak Ridge National Laboratory, Oak Ridge, TN 37830 USA

Abstract

The Spallation Neutron Source, a neutron scattering user facility based on a 1.4 MW proton accelerator, has been in operation since 2006. The accelerator beam diagnostics were designed, in large degree, with commissioning unknowns in mind. Today we face new challenges to support stable 1 MW beam power operations and an accelerator upgrade for even higher power. The beam instrumentation problems span a range from mitigating obsolescence of many electronics to developing new techniques for measuring beam parameters important for high power operation. This report describes several examples of the ongoing work: development of new electronics for the Beam Position Monitor (BPM) and Beam Loss Monitor (BLM) systems to replace the aging designs; and development of large dynamic range and high precision beam phase space characterization tools to facilitate model based accelerator tuning.

INTRODUCTION

The SNS accelerator complex consists of an H^- injector, capable of producing one-ms-long pulses with 38 mA peak current, chopped with about 70% beam-on duty factor and a repetition rate of 60 Hz to produce 1.6 mA average current; an 87 MeV Drift Tube Linac (DTL); a 186 MeV Coupled Cavity Linac (CCL); a 1 GeV Super Conducting Linac (SCL); a 1 GeV Accumulator Ring (AR); and associated transport lines. A diverse set of diagnostics is used to monitor various parameters of the beam [1] in the accelerator. Results of the initial beam instrumentation commissioning and operation experience can be found in [2]. The Second Target Station Project (STS) [3] aims at doubling the beam power. This will be achieved by increasing the SCL and AR beam energy to 1.3 GeV and the peak current in the linac to 59 mA.

After completion of the initial beam commissioning and gradual power ramp up, the SNS accelerator complex has been delivering proton beam to the neutron target for about 4500 hours per year with availability exceeding 80%. As shown by a historical plot of the beam power on the target in Fig. 1, the beam power has been mostly above 1 MW since 2010 and close to the design level of 1.4 MW lately.

With the SNS entering routine neutron production operations, the roles and requirements for the beam diagnostics are changing as well. Only a limited subset of diagnostics is absolutely required during steady neutron production: the Beam Loss Monitors to ensure accelerator safety, the Beam Current Monitors for beam accounting, and a multi-wire monitor (the Harp) to validate the beam size on the target. Reliability and maintainability are the most important qualities for these systems. Additional diagnostics are needed to tune the machine after long maintenance periods or significant configuration changes (e.g. taking out of service failed superconducting RF cavities): the Beam Position and Phase Monitors (BPM) and some Wire Scanners. The rest of the diagnostics systems provide convenience for operators (e.g. the Target Imaging System) or are used for machine studies. The main thrust of the machine studies is to create a realistic beam dynamics simulation tool to facilitate machine tuning and improve beam transport.

This paper describes the ongoing development work for selected systems from each category.

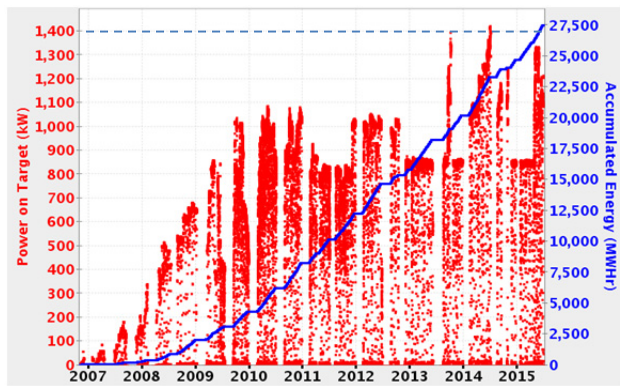

Figure 1: A history of beam power on the target (red points) and accumulated beam energy (blue line). The dashed line shows the design beam power level.

OBSOLESCENCE MITIGATION EFFORTS

The original set of SNS diagnostics was designed about 15 years ago, which is quite a significant time in the electronic components industry. Many of the parts became or are becoming obsolete and many of them do not have a direct replacement suitable for drop in replacement. We have a sufficient amount of spare parts for supporting operations in the short term but replacement electronics need to be developed for long term sustainability. This task is easier in some regards compared to developing the original diagnostics: we know precisely what is needed for operation as all uncertainties of the machine commissioning already have been resolved; there is less schedule pressure; and there is less equipment to install at once. On the other hand, there are additional constraints: the available operational budget and manpower is significantly smaller compared to the construction project. Therefore, we use the following approach to all new electronics design:

ISBN 978-3-95450-176-2

1. New systems are a drop-in replacement for the existing system in size, power requirements, controls system interface, pick-ups, cable plant, etc. This allows staged replacement of the electronics one-by-one or in groups.
2. New designs are optimized for easier maintenance with all unnecessary functions or future development options removed unless they will be required for the power upgrade. In practice, this usually simplifies designs because the original electronics had various options for commissioning uncertainness e.g. switchable gains etc.
3. Non-interceptive diagnostics have a 60 Hz data acquisition rate. This became feasible for many diagnostics with the latest advances in digital electronics.
4. New electronics have no custom designed digital boards, only commercial-off-the-shelf solutions should be used. This requirement is dictated by the available expertise in the Beam Instrumentation Group. A typical configuration following this principle is shown in Fig. 2.

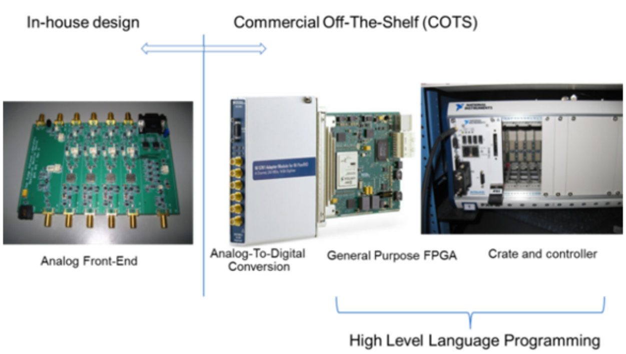

Figure 2: A typical system configuration for new BI electronics designs.

Short descriptions of the new electronics designs for the two largest beam diagnostics systems are given below.

Beam Loss Monitors

The SNS BLM system consists of 362 detectors measuring the secondary radiation due to beam loss. The BLMs are used as sensors in the machine protection system for shutting off the beam if the integral loss is above a certain threshold. The ionization chamber (IC) is the main detector type in the BLM system due to its simple design and immunity to radiation damage. In addition to the ICs we use several types of photo-multiplier tube based detectors (PMTs). The old BLM multichannel electronics are based on VME chassis and use custom designed and obsolete commercial cards. The electronics are programmable for use with different types of detectors in different locations. One VME IOC serves 32 channels of BLMs [1]. The new design is based on NI cRIO technology [3]. The only custom design piece of electronics is analog front-end preamplifier (AFE). The two flavors of the AFE and four flavors of chassis listed in Tables 1 and 2 cover all the SNS needs. An assembled AFE PCB is shown in Fig. 3. A complete BLM chassis is shown in Fig. 4.

Table 1: Parameters of the Four Different Flavors of the New BLM Chassis

Flavor	Number of signals	Number of HV	Number of MPS	AFE
ITSF	8	8	1	none
IC	16	4	16	LG amp
Target	8	8	0	HG amp
ND	8	8	8	LG amp

Table 2: Parameters of the Low (LG) and High (HG) Gain AFE Preamplifiers of the New BLM Electronics

AFE	Gain (Ohm)	Min current (nA)	BW (Hz)	Sampling rate (kS/s)
LG	600k	2	200k	1000
HG	100M	0.01	1	100

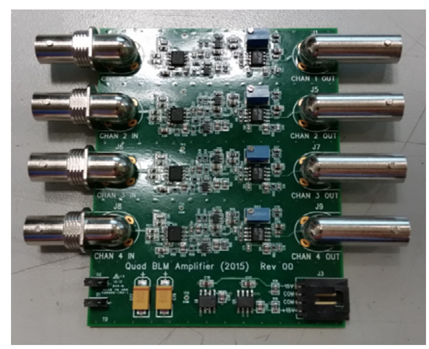

Figure 3: Assembled BLM AFE board.

Figure 4: New BLM electronics chassis in the rack.

Beam Position and Phase Monitors (BPM)

Beam phase monitors are the main tools for the linac tune up which utilizes time-of-flight algorithms. Position measurements are used for trajectory correction, ring

ISBN 978-3-95450-176-2

injection set up and centering the beam on the dumps and target. Both the phase and the position are measured by the BPM system, using 160 4-lobe strip-line pick-ups installed along the beam path. Narrow-band RF front-end electronics is used in the linac and the HEBT. Base-band front-end electronics is used in the ring and the RTBT. The existing BPM electronics consist of custom designed PCI boards installed in a rack-mounted PC running the LabView program under the Windows XPe operating system. One chassis per BPM is used for both linac and ring systems [1].

The new BPM electronics, both linac and ring style, use NI PXIe chassis and FlexRIO FPGA technology [4]. The only custom designed piece of electronics is the Analog Front End (AFE) board. The linac BPM AFE design is based on the SNS LLRF input card design [5]. The 402.5 MHz or 805 MHz signal from the pick is down-converted to 50 MHZ in the AFE. The 50 MHZ IF is digitized by an ADC, processed in an FPGA and transferred to an EPICS IOC. One PXIe crate can support up to six linac style BPMs. A set of six BPM electronics in the SNS MEBT is shown in Fig. 5.

Figure 5: The new BPM electronics for the SNS MEBT in the rack.

The new linac BPM electronics demonstrated good performance during beam tests as demonstrated by Fig. 6 which shows beam phase measurements during several hours using the old (blue) and the new (green, red and white) electronics. The new system shows less noise because it can take advantage of its 60 Hz acquisition capability for signal averaging.

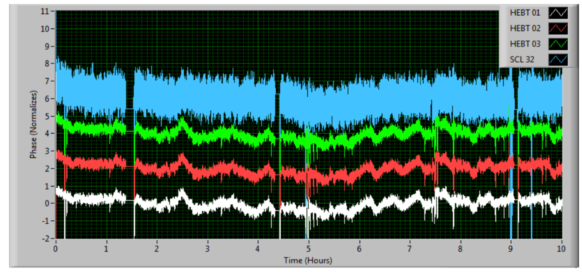

Figure 6: A comparison of the beam phase measured by the old (blue) and the new (green, red, and white) linac BPMs. The old BPM data were acquired and plotted at 1 Hz trigger rate, and the new BPM data were acquired at 60 Hz, averaged, and then plotted at 1 Hz.

The ring BPM electronics operate in base band with 5 MHz bandwidth. The main challenge is the required dynamic range of about 60 dB. The old system used a fast gain switching during the 200 ns gaps in the beam pulse. The new electronics will have two separate channels with low and high gain. The two signals will be independently digitized by multi-channel ADCs, combined in an FPGA processor and transferred to an EPICS IOC. One PXIe crate can support up to eight ring style BPMs. A diagram of the ring BPM prototype AFE is shown in Fig. 7.

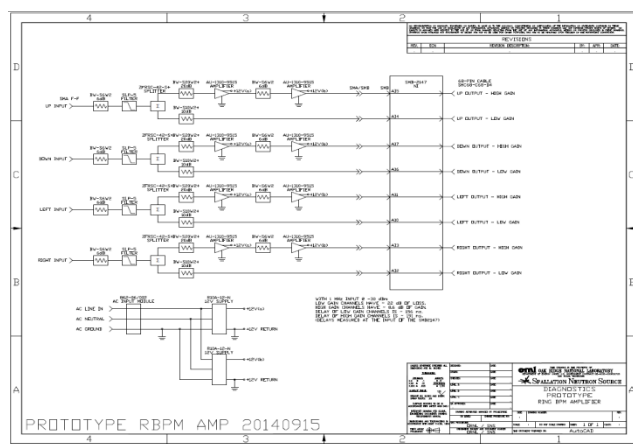

Figure 7: A block diagram of the prototype ring BPM AFE.

MACHINE STUDY DIAGNOSTICS

Significant machine study efforts are devoted to creating a reliable beam dynamics simulation model, which would allow model based tuning of the accelerator. This development is evolving from the center of mass motion model to the RMS envelope model, and finally, to the large dynamic range particle-in-cell model. The single particle model uses only BPM data. Its deployment shortened the linac tuning time from 10-20 hours to 2-3 hours. The RMS envelope model requires transverse and longitudinal profile data provided by the wire scanners (WS), the laser wire (LW) and the beam shape monitors (BSM). These diagnostics perform sufficiently well to allow finishing the model development in the next 1 or 2 years. The longitudinal profile measurements are on the

ISBN 978-3-95450-176-2

edge of the required resolution and we are actively searching for improvements [6]. The most difficult part is to develop a high resolution PIC model capable of predicting beam loss at the 10^{-4} level and below. This requires measuring as many parameters of the beam 6D distribution with large dynamic range as possible in as many places as possible. The minimum useful dimensionality of data for a PIC model is 2D emittance. We have developed a high resolution emittance measurement system in the 2.5 MeV MEBT [7]. We also have a large number of wire scanners throughout the machine. The dynamic range of the current wire scanner system reaches 10^5 as shown in Fig. 8 and we expect it to increase further with multiple pulses data averaging, if needed.

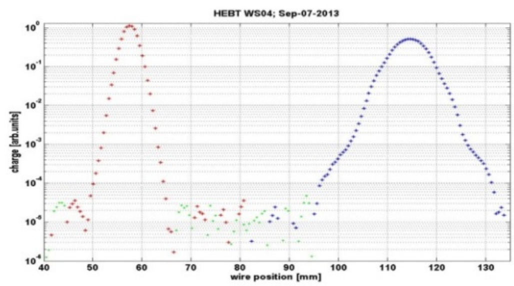

Figure 8: Transverse beam profiles (vertical - red, horizontal - blue) measured with an SNS wire scanner.

A method is required to reconstruct 2D emittances from the 1D profiles without loss of dynamic range. The MENT tomographic reconstruction [8] has shown the most promising results thus far. A reconstructed emittance with 10^3 dynamic range is shown in Fig. 9. A direct emittance measurement using a laser emittance scanner at the 1 GeV end of the SNS linac [9] is used to validate the reconstruction accuracy.

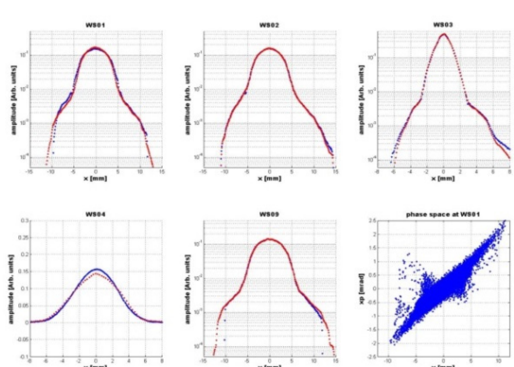

Figure 9: A comparison of measured (red) and calculated from reconstructed emittance (blue) beam profiles. The beam phase space footprint reconstructed using the MENT algorithm is shown in the bottom left plot.

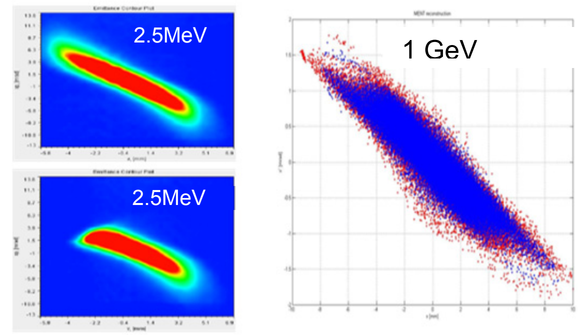

Figure 10: An example of measurements used for beam dynamics studies in the SNS linac.

An example of measurements used for beam dynamics studies in the SNS linac is shown in Fig. 10. The upper left plot shows the beam emittance in the MEBT with the MEBT horizontal scraper retracted. The bottom left plot shows the beam emittance with the scraper inserted to remove a few percent of the beam charge. As the scraper is just a few meters upstream of the emittance scanner its shadow is clearly seen on the image. The right plot shows the measured beam emittance at the end of the linac, in red with the scraper retracted and in blue with the scraper inserted. It is easy to see that the scraper insertion results in emittance reduction but there is no discernable scraper shadow on the image because particles mix up in transport from the MEBT to the end of the linac. This kind of measurement is a sensitive tool for a PIC model set up and validation.

ACKNOWLEDGEMENT

Material for this presentation was provided by SNS Beam Instrumentation Team members: Wim Blokland, Richard Dickson, Cary Long and Sasha Zhukov.

SNS is managed by UT-Battelle, LLC, under contract DE-AC05-00OR22725 for the U.S. Department of Energy.

REFERENCES

[1] S. Henderson et al., Nuclear Instruments and Methods in Physics Research A 763 (2014) 610-673.
[2] A. Aleksandrov, in Proc. BIW 2010, Santa Fe, USA, 2010.
[3] www.ni.com/compactrio/.
[4] www.ni.com/flexrio/.
[5] M. Crofford et al. In Proc. LINAC 2010, Tsukuba, Japan, 2010.
[6] A. Aleksandrov, et al. In Proc. BIW2012, Newport News, USA, 2012.
[7] A. Aleksandrov, et al. In Proc. LINAC2012, Tel Aviv, Israel, 2012.
[8] G. Minerbo, in *Comput. Graph. Image Processing,* vol. 10, pp. 48-68, 1979.
[9] Y. Liu et al. / Nuclear Instruments and Methods in Physics Research A 675 (2012) 97–102.

ISBN 978-3-95450-176-2

OVERVIEW AND STATUS OF SWISSFEL DIAGNOSTICS

V. Schlott, V. Arsov, M. Baldinger, R. Baldinger, G. Bonderer, M. Dehler, R. Ditter, D. Engeler, F. Frei, S. Hunziker, R. Ischebeck, M. Kaiser, B. Keil, W. Koprek, R. Kramert, F. Marcellini, G. Marinkovic, G.-L. Orlandi, C. Ozkan Loch, P. Pollet, M. Roggli, M. Rohrer, A. Romann, S. Schnabel, M. Stadler, D. Treyer, PSI, Villigen, Switzerland

Abstract

SwissFEL is an X-ray free electron laser user facility presently under construction at the Paul Scherrer Institut (PSI) in Villigen, Switzerland. All diagnostics systems have been developed and successfully tested within the baseline SwissFEL parameters, including a low charge, ultra-short pulse operation mode. The monitor designs have been finished, production is ongoing and most of the components are ready for installation. The paper will give an overview of the SwissFEL diagnostics systems, highlight some of the instrumentation developments, summarize the latest results and report on the installation and commissioning schedule.

SWISSFEL

SwissFEL is a compact free electron laser user facility presently under construction at the Paul Scherrer Institut in Villigen, Switzerland [1]. In its first project stage, which lasts from 2012 – 2017, it will provide hard X-rays with photon energies ranging from 4 to 12 keV to the three ARAMIS user end-stations [2]. In a second project stage, which is scheduled for 2018 – 2020 soft X-ray users will be served by an additional FEL line, called ATHOS [3].

Most of the SwissFEL key accelerator components (e.g. solid state modulators, C-band accelerator structures, in-vacuum undulators, as well as the optical synchronization system and also the beam instrumentation devices) have been developed and successfully tested at the SwissFEL Injector Test Facility (SITF) during the past years. The SwissFEL building is almost ready for occupation and the technical infrastructure is presently being built up, so that installation of accelerator components can start by the end of 2015 and commissioning of the accelerator complex has been scheduled for spring 2016.

The SwissFEL electron beam is generated in a 2½ cell S-band photo-injector RF gun, which provides a 7 MeV, low emittance beam with bunch charges of 10 to 200 pC at a bunch repetition rate of 100 Hz. The S-band injector LINAC, which boosts the beam energy up to 450 MeV, contains a laser heater and two X-band RF structures, located in front of the first magnetic bunch compression stage (BC-1) for linearizing the longitudinal phase space. Further acceleration to 2.1 GeV is achieved by the C-band LINAC-1, before the electron bunches are fully compressed in the second bunch compressor (BC-2) to 2.5 fs (at 10 pC) respectively 20 fs (at 200 pC). The C-band LINAC-2 and LINAC-3 are ramping the beam energy up to its final value of 5.8 GeV before the electron bunches are transferred to the hard X-ray ARAMIS FEL line. For the future ATHOS soft X-ray FEL line, a second bunch will be accelerated at a distance of 28 ns and extracted in a magnetic switchyard at beam energies of 2.4 GeV. All diagnostics components have accounted for this two-bunch option already during their design stage and beam tests have been executed at the SITF [5, 6] in

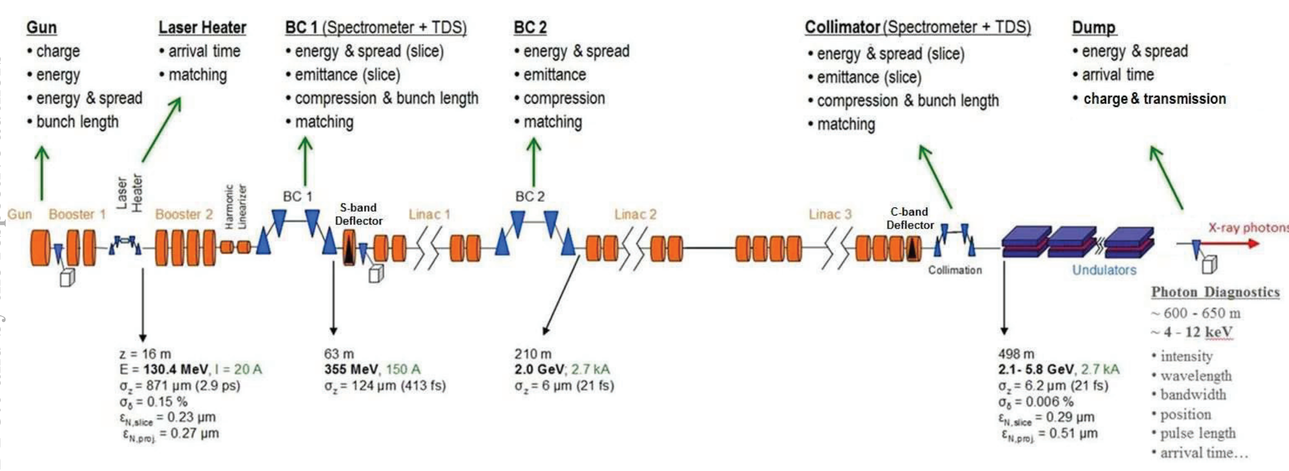

Figure 1: Schematic overview of the SwissFEL hard X-ray ARAMIS line, which will be set-up in the first project phase. Locations are indicated, where the most important beam parameters will be measured during set-up and commissioning and monitored during operation. In addition (not shown here), beam position monitors, loss and charge monitors as well as wire scanners and screens are distributed along the machine to measure transverse beam positions and profiles as well as transmission and losses. Photon diagnostics is set-up in the ARAMIS front end.

ISBN 978-3-95450-176-2

order to resolve the SwissFEL beam parameters as listed in table 1.

Table 1: SwissFEL Key Parameters

SwissFEL Key Parameters	Operation Modes	
	Long Bunch	Short Bunch
photon energy	0.2 – 12 keV	0.2 – 12 keV
power / energy	60 µJ / 2 GW	3 µJ / 0.6 GW
electron energy	5.8 GeV (1 Å)	5.8 GeV (1 Å)
bunch charge	200 pC	10 pC
rep. rate	100 Hz	100 Hz
bunch distance	28 ns	28 ns
bunch length	20 fs (rms)	2.5 fs (rms)
comp. factors	125	240
norm. emittances	430 nmrad	180 nmrad
timing stability	jitter	drift
sync. system	< 10 fs (rms)	< 20 fs_{pp} / day
bunch arrival time	< 10 fs (rms)	< 10 fs_{pp} / day

Figure 1 provides a schematic overview of the SwissFEL facility, indicating the different locations along the accelerator where a full phase-space characterization can be performed (sliced and projected transverse emittances and energy spreads) and the longitudinal beam parameters can be measured (compression, bunch length and bunch arrival time). In addition to these dedicated measurement stations, a large number of beam position (BPM), profile (screens and wire scanners), beam loss (BPM) and charge monitors (BCM) are distributed along the accelerator to observe and control the orbit, transmission and matching. The hard X-ray ARAMIS FEL line will also be equipped with a full suite of photon beam diagnostic monitors, which provide intensity, wavelength and bandwidth, position, length and arrival time of the hard X-ray (4 - 12 keV) pulses.

DIAGNOSTICS REQUIREMENTS

Table 2 summarizes the type and number of electron beam diagnostics devices for the first stage (ARAMIS) of the SwissFEL project.

Table 2: SwissFEL Electron Beam Diagnostics Devices

Diagnostics Device	Type	Number
beam position	cavity BPMs	145
transverse profile monitors	scintillator screens	24
	wire scanners	23
	SR-monitors	3
charge monitors	Turbo ICT	4
loss monitors	scintillating (local)	38
	Cerenkov (dist.)	8
dose rate monitors	Rad-FET	32
beam arrival time	electro-optical	4
compression	THz / FIR-vis	1 / 2
laser arrival time	electro-optical	1
transverse deflector	S-band / C-band	1 / 1

The main challenges for the SwissFEL beam instrumentation are posed by the “low charge (10 pC) / short bunch” operation mode, where the diagnostics systems have to cope with low signal levels, small beam sizes, high compression factors, short bunches and stringent temporal jitter and drift tolerances. In addition, fast detection schemes and high bandwidth data acquisition systems are required for the future “two-bunch option”, which is realized in the 2nd project stage, where two bunches at a distance of 28 ns will be accelerated in a single RF pulse allowing the operation of both, the ARAMIS hard X-ray and ATHOS soft X-ray FEL lines at the full repetition rate of 100 Hz. The specific demands to the particular diagnostics systems are described below. In some cases the selected solution is shorty described and more detailed information and results are referenced, while in other cases, the latest achievements are presented in more detail in the following paragraph on diagnostics performance.

- For controlling the beam orbit and thus preserving the low emittance of the SwissFEL electron beam, the beam position monitors (BPM) should provide rms position noise of < 5 µm along the whole SwissFEL accelerator. In the undulators < 1 µm rms position noise is required in order to ensure sufficient overlap between electron and photon beam for stable SASE operation. In addition, the BPMs should provide a beam charge related signal with sufficient resolution (< 1% of the bunch charge) to monitor the overall transmission through the accelerator, serving as an input for the SwissFEL machine protection system.
- Transverse profile monitors have to provide high spatial resolution (< 10 µm rms) to allow the determination of projected and sliced emittances, the measurement of beam optics and the matching of the highly brilliant SwissFEL electron beam. Coherent optical transition radiation has to be supressed for the preferred solution of two-dimensional profile imaging with screen monitors (SCM), while one-dimensional profile information is obtained by wire scanners (WSC), which serve as a “SCM back-up solution” and which will be used for online and quasi non-destructive monitoring of transverse beam profiles and emittances (with four WSCs at 90° betatron phase advance) in the C-band LINACs. In addition, synchrotron radiation monitors (SRM) are installed in the centre of the bunch compressor chicanes to measure the transverse beam profile and thus to monitor the energy spread (and chirp) of the electron beam during compression.
- Bunch charge and transmission through the SwissFEL accelerator has to be determined with < 5% absolute accuracy and 1% resolution. Thus, one Turbo-ICT [7] per accelerator section (injector, LINAC-1, LINAC-2 and undulator region) has been installed to allow the calibration of the high(er) resolution BPM charge measurement.

ISBN 978-3-95450-176-2

- As an input to the machine protection system, beam loss needs to be monitored along the SwissFEL accelerator, which is achieved by installing Cerenkov fibres parallel to the accelerator. In addition, local hot-spots will be surveyed with scintillating fibres, which are wrapped around the accelerator beam pipe. These very sensitive scintillating fibres are also serving as detectors for the WSC profile measurements [8]. A set of dose rate monitors (rad-FET types) [9] are installed in the undulator sections to monitor the absolute acquired dose and to make sure that radiation-induced demagnetization of insertion devices is avoided.
- Beam arrival time (BAM) information with < 10 fs rms accuracy in reference to the SwissFEL optical synchronization system is required at the bunch compressors to determine the longitudinal stability of the accelerator and to provide an input signal for a possible beam-based feedback of the previous RF stations. Behind the ARAMIS undulator, the BAM information will be given to the users for monitoring the longitudinal stability of the electron beam and for possible sorting of their experimental data. Since the temporal stability of the photo-injector (gun) laser is important to retain the injector beam parameters for stable SASE operation, an additional arrival time monitor for the gun laser (LAM) following the principle of the electro-optical BAM is presently under development. The LAM output signal will be used to monitor and improve the gun laser to accelerator RF temporal stability by providing active common mode jitter and drift suppression.
- In addition to the beam arrival time, the bunch compression needs to be monitored (preferably non-invasively) in BC-1 and BC-2 as well as in the ARAMIS collimator section, which can also be operated as an additional bunch compressor in case of the SwissFEL ultra-short pulse (sub-fs) operation mode. Different types of compression monitors (BCM) have been developed, covering the spectral ranges of coherently emitted edge (or diffraction) radiation, ranging from THz (BC-1) to NIR (BC-2 and collimator). In a possible compression feedback, the BCM outputs are used as input signals for the phase regulation of the previous RF stations to adjust and stabilize the energy chirp of the electron bunches.
- Bunch length respectively the longitudinal distribution of the SwissFEL electron bunches and the sliced beam parameters such as transverse emittance and energy spread will be measured with two different transverse deflectors (TDS). Behind BC-1, a S-band standing wave deflector will be used at beam energies of 450 MeV to control the SwissFEL injector set-up, while two C-band deflecting structures (of the SACLA RAIDEN [10, 11] type) will be installed behind LINAC-3 at full energy and compression to provide time-resolved phase space information before transporting the electron beam to the ARAMIS undulator. With an anticipated deflecting voltage of 70 MV, a temporal resolution of 2.5 fs (rms) should be achievable at full SwissFEl energy of 5.8 GeV. This is adequate to set-up the SwissFEL electron beam in the 200 pC operation mode, but may not be sufficient for the low charge / short bunch operation mode at 10 pC.

All SwissFEL diagnostics devices will be pre-calibrated such that they are able to support accelerator commissioning with slightly reduced resolution, accuracy and dynamic ranges. Beam-based alignment (e.g. of BPMs) and cross-calibration of monitors (e.g. relative charge measurement of BPMs against absolutely calibrated Turbo-ICTs or compression monitors against TDS bunch length measurements) will lead to the ultimate performance level of the diagnostics systems. For active stabilization of the SwissFEL accelerator, all monitors will finally provide signals, which will be / can be used in beam-based real-time feedbacks.

DIAGNOSTICS PERFORMANCE

The SwissFEL diagnostics systems follow a modular topology, which is divided in three blocks: optimized pick-up and detector types followed by customized and well matched (RF) front ends and a generic digital back end. Figure 2 illustrates this approach for some selected monitors.

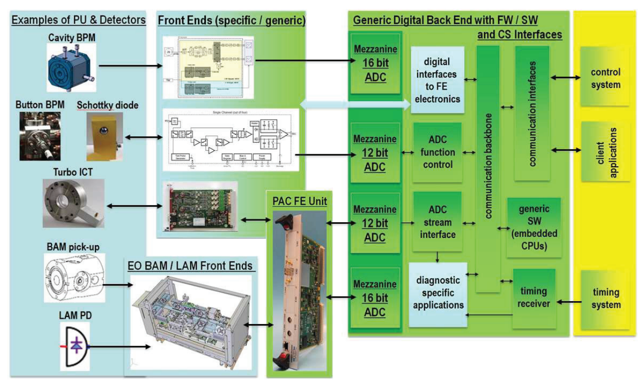

Figure 2: Schematic illustration of the modular topology of the SwissFEL diagnostics systems with specific pick-ups, detectors and customized front ends (blue) and the generic digitization and signal processing part.

The selected measurement method (e.g. electrical or optical) defines the pick-up or detector type, which is optimized to the required sensitivity and dynamic range of the detection system. The (RF) front ends provide signal conditioning for best signal-to-noise performance and adjustment of dynamic ranges. They are customized to the pick-up / detector signal type, allow (online) calibration and adjust the output levels to the optimum input of the digitizing and signal processing part of the detection system. The control of (RF) front end parameters is usually achieved by a single, generic interface (electronics board and firmware). For some of the SwissFEL diagnostics monitors with similar signal types (e.g. BAM and LAM, compression monitor and (button-type) BPMs), it was possible to make use of the same front end electronics. All SwissFEL diagnostics

ISBN 978-3-95450-176-2

components are connected to the generic FPGA-based electronics platform (GPAC) with its fast (12 bit, 500 MS/s) and high resolution (16 bit, 160 MS/s) digitizers as well as its generic communication interfaces to the timing, control and feedback systems. In this way most of the (generic) firmware and software of the GPAC platform is re-used by every diagnostics system, while only the monitor-specific interfaces and applications have to be adapted to the particular pick-up / detector and (RF) front end combination. A more detailed overview of this signal processing concept for SwissFEL diagnostics is given in [12] and a specific example for the loss and charge monitors is introduced in [8].

A more detailed description of the design approach and the latest results and achievements of some SwissFEL diagnostics systems are given in the following sections.

Beam Position Monitors

In order to satisfy the high demands on orbit stability at low bunch charges, cavity-type BPM pick-ups have been selected for the entire SwissFEL accelerator. The pick-ups have three different apertures: 38 mm diameter behind the gun, in the bunch compressors and the beam switchyard to the soft X-ray FEL line (ATHOS), 16 mm diameter in the injector, LINACs and transfer lines and 8 mm in the ARAMIS and (future) ATHOS undulators. While the BPM-38 and BPM16 pick-ups are a low-Q (40) stainless steel design with a resonant frequency of 3.3 GHz to accommodate for the SwissFEL "two-bunch operation mode", the undulator BPM-8 pick-ups have been designed in a special stainless steel / copper sandwich structure to provide a high quality factor (1000) at 4.9 GHz. This design approach has been chosen to achieve the best performance for single bunches in the SwissFEL FEL lines. The rms position resolution of the BPM-38 has been measured to be < 10 µm over a measurement range of ± 10 mm. The BPM-16 provides < 5 µm rms position noise over a measurement range of ± 5 mm and the first (not yet optimized) prototypes of the undulator BPMs (BPM-8) have achieved < 1 µm rms position noise over a limited measurement range of ± 500 µm. All BPMs provide excellent charge noise of about 10 fC, which is extracted from the monopole cavity signal. The BPM electronics is based on the PSI design for the European XFEL using the latest FPGA technology (Kintex-7/Artix-7). While the LINAC BPM electronics makes an IQ down-conversion of the BPM pick-up signal to base-band followed by digital post-processing and local oscillator (LO) feedback, the higher frequency undulator BPM signals are first down-converted to an intermediate frequency (IF) followed by a digital down-conversion stage to base-band. A more detailed description of the SwissFEL BPM system with its latest achievements can be taken from [13].

Transverse Profile Monitors

Scintillating screen monitors and wire scanners are used for transverse profile measurements along the SwissFEL accelerator. While the SCMs provide two-dimensional profile information in a single-shot, the WSCs can be used during accelerator (possibly also SASE) operation to monitor one-dimensional profiles and transverse beam emittances in the background. Both monitor types can be used at low charges (10 pC) and have achieved < 10 µm spatial resolution. The SCM design follows the Scheimpflug imaging principle so that a large region of interest (RoI) can be observed without depth-of-field issues. The tilted CMOS sensor (15°) of the camera provides 1:1 imaging and avoids astigmatism. YAG (or LuAG) scintillator crystals are used instead of optical transition radiators (e.g. Al or metallized Si) and the beam profiles are observed according to Snell's law of refraction so that electron beam sizes can be imaged, which are much smaller than the scintillator thickness. A more detailed description of the SwissFEL SCM design and results of test measurements from LCLS proofing their COTR immunity have been presented in [14].

The SwissFEL wire scanners have been tested and optimized in a series of measurements at the FERMI FEL facility in Trieste. Profile measurements with the required spatial resolution and sufficient sensitivity have recently been made by using Al:Si wires of 12.5 µm thickness. It is planned to move the wires continuously through the beam while applying a beam-synchronized readout of the wire position (encoder) to retrieve the profiles. The WSC detection system is identical to the SwissFEL beam loss monitors and described in more detail in [8].

Compression Monitors

Coherent edge radiation (CER) from the 4th bending magnet of both bunch compressors BC-1 and BC-2 will be used to obtain a signal, which is related to the compression of the electron bunches. For nominal bunch lengths of a few hundred femto-seconds in BC-1 (250 to 500 fs rms), the detected CER spectrum falls into the THz range. Two signal paths are equipped with THz high-pass filters and broadband Schottky diodes to obtain the best sensitivity for the different bunch lengths and to allow for the SwissFEL "two bunch operation" at bunch distances of 28 ns. The signals from the highly sensitive Schottky detectors are processed in a button-type BPM electronics (as also used for the European XFEL button BPMs), which provides sufficient signal-to-noise (in the order of 0.5%) for bunch charges as low as 10 pC, thus fulfilling the stability requirement for a phase feedback of the upstream S-band or X-band RF stations. The CER emission in the bunch length range behind BC-2 (2 to 20 fs rms) falls in the FIR to NIR spectral range (30 to 1 µm) so that liquid nitrogen cooled MCT detectors have to be used. For the SwissFEL BC-2 compression monitor, a KBr prism spectrometer with a 32-channel MCT detector array is presently under design. It will be set-up in the technical gallery, where the CER will be transported through an optical transfer line.

Beam and Laser Arrival Time Monitors

SwissFEL is following the design of an electro-optical beam arrival time monitor, which was originally

ISBN 978-3-95450-176-2

developed at DESY [15]. It correlates the signal of a high bandwidth pick-up with the laser pulses of the highly stable optical reference distribution (< 10 fs jitter and drift) in an electro-optical modulator. In order to accommodate for the low charge SwissFEL beam (10 pC) a high-bandwidth (40 GHz) pick-up has been developed in collaboration with DESY and TU-Darmstadt. In addition, further improvements and optimizations on several critical BAM components such as EO modulator, RF cables etc. as well as in the BAM front end box and data acquisition system (using the GPAC-based digital back end) could be implemented in the latest SwissFEL BAM design, so that the required time resolution of < 10 fs over the whole dynamic range (200 to 20 pC) can be expected for SwissFEL (7 to 13 fs resolution have already been shown at the SwissFEL Test injector Facility from bunch charges between 30 and 200 pC) [16].

A laser arrival time monitor (LAM) for the SwissFEL gun laser following the BAM principle is presently under design. It uses a high speed UV photo-diode, which has been optimized for minimal AM/PM conversion to detect the UV gun laser pulses. Its signal is then correlated with the pulses from the highly stable optical reference distribution system in an electro-optical modulator. This approach has been selected, since it is expected to be much more robust than a spectrally resolved auto- or cross-correlator but promises to provide the required high resolution (10 fs) and covers at the same time a large measurement range of several tens of pico-seconds. All LAM components have been tested, a demonstrator is expected by the end of 2015 and a first operational prototype will be installed in Q2/2016 to support the SwissFEL injector commissioning.

STATUS AND OUTLOOK

All SwissFEL diagnostics monitors have achieved the performance requirements and will be ready for commissioning of the first project stage (ARAMIS) starting in spring 2016. Full integration in the new SwissFEL control system is still ongoing and integration of the monitor signals in beam-based feedbacks will be realized in the first stage of the SwissFEL user operation. Presently, new ideas for measurement of ultra-short electron bunches are under considerations, such as THz streaking of the X-ray pulses [17] and electron bunches [18] as well as the development of a "plasma peak current" monitor [19].

ACKNOWLEDGEMENTS

Apart from the SwissFEL project team and the beam dynamics, controls, operation groups at PSI, I would also like to thank all support and infrastructure groups at PSI, who helped realizing the SwissFEL diagnostics systems. In the same way, the Diagnostics Section has profited immensely by close collaborations with external partners such as our colleagues at DESY, SLAC, FERMI, KIT and the University of Berne.

REFERENCES

[1] SwissFEL Conceptual Design Report is available under: ftp://ftp.psi.ch/PSI_outgoing/SwissFEL_CDR/SwissFEL_CDR_V20_23.04.12.pdf
[2] SwissFEL CDR ARAMIS Beamline is available under: https://www.psi.ch/swissfel/CurrentSwissFELPublications EN/CDR_ARAMIS_Beamline_V2_2013-06-21_VM16-S.pdf
[3] SwissFEL ATHOS Science Case is available under: https://www.psi.ch/swissfel/CurrentSwissFELPublications EN/ATHOS%20V14.pdf
[4] SwissFEL Injector Test Facility CDR is available under: https://www.psi.ch/swissfel/CurrentSwissFELPublications EN/SwissFEL_Injector_CDR_310810.pdf
[5] R. Ischebeck et al., "Instrumentation Activities at the SwissFEL Injector Test Facility", Proc. IBIC'13, Oxford, UK (2013), 12, MOBL1.
[6] R. Ischebeck et al., "Overview of Beam Instrumentation Activities for SwissFEL", Proc. IBIC'14, Monterey, USA (2014), 119, MOPF31.
[7] S. Artinian et al., "Goubau Line and Beam Characterization of Turobo-ICT for SwissFEL", Proc. IPAC'13, Shanghai, China (2013), 476, MOPME005.
[8] C. Ozkan Loch et al., "System Integration of SwissFEL Beam Loss Monitors", these proceedings, IBIC'15, Melbourne, Australia (2015).
[9] L. Fröhlich et al., "Instrumentation for Machine Protection at FERMI@ELETTRA, Proc. DIPAC'11, Hamburg, Germany (2011), 286, TUOA04.
[10] H. Ego et al., "Transverse C-band Deflecting Structure for Longitudinal Phase Space Diagnostics in the XFEL/SPRING-8 SACLA", Proc. IPAC'11, San Sebastian, Spain (2011), 1221, TUPC092.
[11] P. Craievich et al., "Transverse Deflecting Structures for Bunch Length and Slice Emittance Measurements on SwissFEL, Proc. FEL'13, New York, USA (2013), 236, TUPSO14.
[12] W. Koprek et al., "Overview of Applications and Synergies of a Generic FPGA-based Beam Diagnostics Electronics Platform at SwissFEL", these proceedings, IBIC'15, Melbourne, Australia (2015).
[13] B. Keil et al., "Status of the SwissFEL BPM System", these proceedings, IBIC'15, Melbourne, Australia (2015).
[14] R. Ischebeck et al., "Transverse Profile Monitors for SwissFEL", Proc. IBIC'14, Monterey, USA (2014), 259, TUCYB3.
[15] M. K. Bock, "Measuring the Electron Bunch Timing with fs Resolution at FLASH", DESY-THESIS-2013-008, (2013).
[16] V. Arsov et al., "Commissioning and Results from the Bunch Arrival Time Monitor Downstream the Bunch Compressor at the SwissFEL Injector Test Facility", Proc. FEL'14, Basel, Switzerland (2014), 933, THP085.
[17] P. Juranic et. al., "A scheme for a shot-to-shot, femtosecond-resolved pulse length and arrival time measurement of free electron laser x-ray pulses that overcomes the time jitter problem between the FEL and the laser," JINST, vol. 9, p. P03006, 2014.
[18] M. Dehler et al., "Design Concept for a THz Driven Streak Camera with Ultra-High Resolution", these proceedings, IBIC'15, Melbourne, Australia (2015).
[19] R. Tarkeshian et al., "Plasma Monitor for Ultra-Short SwissFEL Electron Bunch Peak Current Measurement", these proceedings, IBIC'15, Melbourne, Australia (2015).

ISBN 978-3-95450-176-2

MICROBUNCHING INSTABILITY IN RELATIVISTIC ELECTRON BUNCHES: DIRECT OBSERVATIONS OF THE MICROSTRUCTURES USING ULTRAFAST YBCO DETECTORS

E. Roussel, C. Evain, C. Szwaj, S. Bielawski, PhLAM/CERLA, Villeneuve d'Ascq, France
J. Raasch, P. Thoma, A. Scheuring, M. Hofherr, K. Ilin, S. Wünsch, M. Siegel
KIT, Karlsruhe, Germany
M. Hosaka, N. Yamamoto, and Y. Takashima, Nagoya University, Nagoya, Japan
H. Zen, Kyoto University, Kyoto, Japan
T. Konomi, M. Adachi, S. Kimura, M. Katoh, UVSOR, Okazaki, Japan

Abstract

Relativistic electron bunches circulating in accelerators are subjected to a dynamical instability leading to microstructures at millimeter to centimeter scale. Although this is a well-known fact, direct experimental observations of the structures, or the field that they emit, remained up to now an open problem. Here, we report the direct, shot-by-shot, time-resolved recording of the shapes (including envelope and carrier) of the pulses of coherent synchrotron radiation that are emitted, and that are a "signature" of the electron bunch microstructure. The experiments are performed on the UVSOR-III storage ring, using electrical field sensitive $YBa_2Cu_3O_{7-x}$ thin-film ultrafast detectors. The observed patterns are subjected to permanent drifts, that can be explained from a reasoning in phase space, using macroparticle simulations.

INTRODUCTION

Recent coherent synchrotron radiation (CSR) studies in storage rings have heightened the need for understanding the dynamics of electron bunches during the microbunching instability which is a source of intense emission of THz CSR pulses. This instability is known to lead to the formation of structures at millimeter scale in the longitudinal direction of the electron bunch [1]. However, direct observations of the dynamics of these microstructures were an open challenge up to now. Indeed, this requires to detect CSR pulses of hundreds or tens picoseconds length with internal structures at one to tens of picoseconds. Moreover, high-acquisition rate, typically of the order of tens of megahertz, would be required. Thus far, only indirect measurements were achieved by recording the spontaneously emitted coherent signal with slow detectors (at best with microsecond response time) [2–9] or by perturbating the electron bunch with an external laser [10, 11].

In this paper, we report on the first real time recordings of the pulse shape (envelope and carrier) associated with the CSR emitted during the microbunching instability when the electron bunch exceeds several tens of picoseconds [12]. The measurements have been obtained on the UVSOR-III storage ring [13] and have been possible through a new type of detector based on thin-film YBCO superconductor [14–16]. This detector has been developed at the Karlsruhe Institute of Technology (KIT) in Germany. We performed two types of experiments: the first one aims at studying the spontaneous emission of CSR during the microbunching instability; the second one aims at looking at the response of the electron bunch to a localized laser perturbation [2]. We describe the dynamics of CSR pulses from longitudinal phase-space motion.

EXPERIMENTAL SETUP

UVSOR-III Storage Ring

For the study of the spontaneous CSR emission, the UVSOR-III storage ring is operating in single bunch mode and the injected beam current is initially set above the instability threshold (here, around 53 mA). Under these conditions, the electron bunch emits CSR in the sub-terahertz frequency range which is a feature of the presence of longitudinal microstructures in the electron bunch at the millimeter scale. The CSR electric field (envelope and carrier) is detected through a new type of THz detector (YBCO, see next section for details) connected to an ultra-fast oscilloscope (63 GHz bandwidth, Agilent DSOX96204Q) at the BL6B infrared beamline [17](Fig. 1(a)).

A laser-electrons interaction in condition of slicing with picoseconds laser pulses is also possible and is achieved in the undulators U1 [18] (Fig. 1(b)). The beam current is just set below the instability threshold. The laser pulse is generated by an amplified Ti:Sa laser (Mira oscillator and Legend amplifier from Coherent) coupled with a cryogenic Ti:Sa amplifier (Legend Elite Cryo) which delivers a 800 nm, 10 mJ uncompressed laser pulses with a 300 ps duration at 1 kHz repetition rate. The pulses are compressed in the picoseconds range using an adjustable compressor with gratings [19]. Finally, the laser pulse is focused in the undulators U1 where it interacts with the electron bunch. The emitted coherent terahertz radiation is recorded at the BL6B infrared beamline using the YBCO detector and the same 63 GHz bandwidth oscilloscope.

YBCO Detector

The high-temperature superconductor $YBa_2Cu_3O_{7-x}$ (YBCO) is a new technology developed for the detection of radiation in the terahertz frequency range. The detector is composed of a YBCO superconducting thin-film detector

ISBN 978-3-95450-176-2

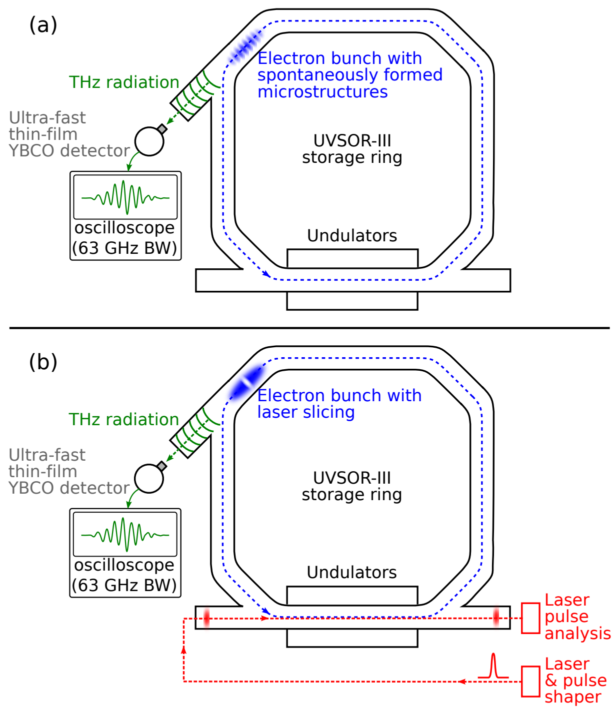

Figure 1: Experimental setups on the UVSOR-III storage ring. (a) Above a threshold beam current, an electron bunch undergoes an instability which leads to spontaneous formation of microstructures at the millimeter scale in the longitudinal direction. (b) Slicing experiment. A short laser pulse interacts with the electron bunch in the undulators U1. In both cases, the emission of coherent synchrotron radiation in the terahertz frequency range is recorded with the YBCO detector on the BL6B infrared beamline.

embedded in a broad-band THz antenna and cooled at liquid Nitrogen temperature and is designed for the analysis of CSR pulses [20].

The YBCO films are fabricated using the pulsed-laser deposition technique. A sapphire layer is used as substrate for the YBCO thin films because of its low dielectric losses which are essential for the back illumination of the YBCO detectors. The YBCO film is embedded between two buffer layers of PBCO ($PrBa_2Cu_3O_{7-x}$) to improve crystalline matching with the YBCO film. For YBCO film thickness above 30 nm, the critical temperature T_c is almost constant and well above the liquid nitrogen temperature of 77 K. To couple a broadband THz frequency range, a planar log-spiral antenna is implemented and embedded into a coplanar readout line. The coupling efficiency of the antenna in the 0.1 to 2 THz frequency range is higher than 90%. The sapphire substrates with antenna-coupled microbridges are glued to the rear, flat side of an elliptical silicon lens and mounted in a shielded holder to reduce interference with the electromagnetic fields at the beamlines.

Measurements at the MLS and ANKA storage rings revealed that the YBCO superconductor is a very sensitive and ultra-fast detector for radiation in the terahertz frequency range. Up to now, measurements achieved with the YBCO have highlighted a temporal resolution of 15 ps FWHM limited by the readout bandwidth (particularly by the 62.8 GHz bandwidth oscilloscope) [14]. They have also shown that the response of the YBCO detector used in zero-bias conditions is sensitive to the electric field of the radiation [14]. The photoresponse of YBCO films to picosecond CSR pulses is explained by direct interaction of vortices with the high-frequency electric field [15].

EXPERIMENTAL RESULTS

Spontaneous CSR Emission

Long-time series recorded at high resolution allow us to study the dynamics of the microbunching instability at different time scales as illustrated in Fig. 2. Therefore, the fast temporal resolution of the YBCO detector unveils the internal structures of the CSR pulse at tens of picosecond time scale. As can be seen in Fig. 2(c), the YBCO detector allows us to monitor the CSR electric field pulse, including the envelope and the optical carrier at ≈ 30 GHz. The CSR pulses have a duration of around 300 ps which is the same order of magnitude as the longitudinal electron bunch length. These CSR pulses are emitted periodically (Fig. 2(b)) with a repetition rate of 5.6 MHz (i.e. a period of 177 ns) which corresponds to the revolution frequency of a single bunch in the storage ring. At the millisecond time scale, slow dynamics of the coherent synchrotron radiation reveals that the emission occurs in a bursting manner far above the instability threshold (Fig. 2(a)). This dynamics is similar to what would be captured by a standard bolometer.

We summarized the dynamics of the CSR pulses as a color map versus a "fast time" (i.e., resolving the pulse shape), and a "slow time" (associated to the number of round-trips). The color map (Fig. 3) displays two features in the dynamics of the CSR pulses. The first one is the presence of structures at the head of the bunch(in the lower part of Fig. 3) which are drifting toward the tail of the electron bunch. The second one is the presence of an other structure which behaves erratically and drifts in both directions (localized around 200 ps in Fig. 3).

Laser-Slicing

The phase space dynamics can also be studied below the microbunching instability threshold, by examining the response to a perturbation to a short laser pulse that create a hole in the longitudinal electron bunch profile. Because the spontaneous microstructures are known to appear at the millimeter scale in the longitudinal direction of the electron bunch, the pulse duration of the perturbating laser is chosen in the tens to single picosecond range.

The experimental response presented in Fig. 4 is obtained using a 15 ps FWHM laser pulse.The perturbation is applied at time t = 0. An immediate response is visible just after the perturbation and a series of delayed response appears periodically with a period approximately equal to a half synchrotron period (at ≈ 25 µs, ≈ 50 µs). The data recorded by

ISBN 978-3-95450-176-2

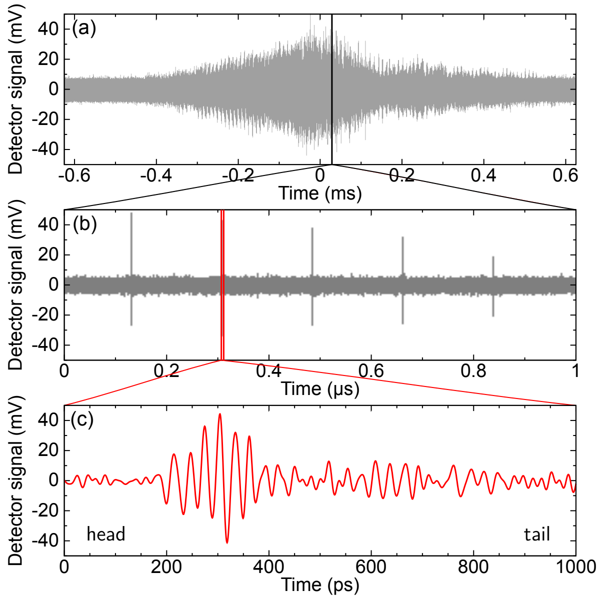

Figure 2: Terahertz CSR burst detected with the YBCO detector for a beam current I = 62 mA. (a) Slow variation of an entire CSR burst. The shape is similar to the traditional recordings with a bolometer or a Schottky diode except the alternating of positive and negative signal due to the sensitivity of the YBCO to electric field. (b) Zoom of (a) showing the CSR pulses emitted at each turn in the storage ring. (c) Zoom at one pulse in (b). The envelope and the carrier of the pulse are visible. The voltage of the detector signal is directly proportional to the incoming CSR electric field.

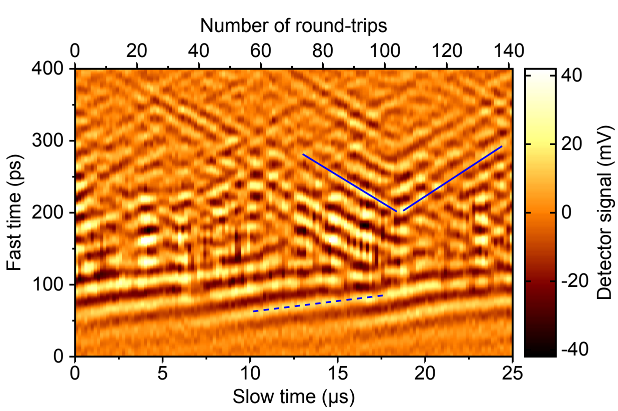

Figure 3: Color map representing the temporal evolution of the CSR electric field over many successive turns in the storage ring.

the YBCO detector display different characteristic features, as the arc shape at half synchrotron period (around ≈ 25 µs), and the cusp (or "Y shape) at the right of the color map.

NUMERICAL SIMULATIONS

The dynamics of the patterns observed in the CSR pulses can be interpreted from a reasoning in the longitudinal phase-

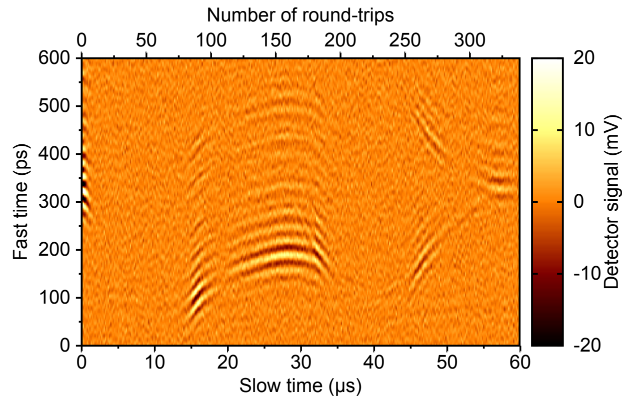

Figure 4: Dynamics following a localized laser perturbation (slicing) at $t = 0$, when the system is below the instability threshold. Note that no CSR emission is detected before $t < 0$.

space (longitudinal position z, energy E) of the electrons, assuming that the relevant motion occurs mainly in the longitudinal direction [21, 22]. For an accurate modeling of the dynamics, one needs to take into account collective effects inside the electron bunch, like, e.g. the shielded CSR impedance as well as the resistive and inductive impedances (see [23, 24] for a detailed description of the used model).

Spontaneous CSR Emission

The link between the electron phase-space distribution and the THz radiation recorded by the YBCO detector is illustrated in Fig. 5. Spontaneous formation of microstructures occurs in the electron bunch distribution $f(z, E, t)$ (Fig. 5(a)). However, only the projection on the z axis is observable, and corresponds to the longitudinal bunch profile $\rho(z, t) = \int_{-\infty}^{+\infty} f(z, E, t) dE$ (Fig. 5(b)). Even though the microstructures-induced modulations are extremely weak compared to the "global" shape of the electron bunch, they lead to a strong emission of CSR (Fig. 5(c)). We notice that the "spiral-shape" that wraps the whole bunch distribution is at the origin of the structures at the borders of the CSR pulse whereas the thin microstructures are responsible for the fast oscillations at the center. Because the electron bunch distribution rotates in phase-space, the structures in the CSR electric field drift along the longitudinal position, i.e. along the fast time axis (Fig. 5(d)). Thus, the structures drifting toward the tail (in the bottom part of Figs. 3 and 5(d)) are associated to the spiral while the structures moving in both directions are associated to the thin microstructures in the central part of the phase-sapce.

Laser-Slicing

A typical numerical simulation of the electron bunch response to a short laser perturbation is presented in Fig. 6. The laser perturbation is applied at time $t = 0$ µs. As in the experimental data (Fig. 4), we find a series of delayed response equally spaced, every half synchrotron period. The characteristic shapes of these responses can be understood

ISBN 978-3-95450-176-2

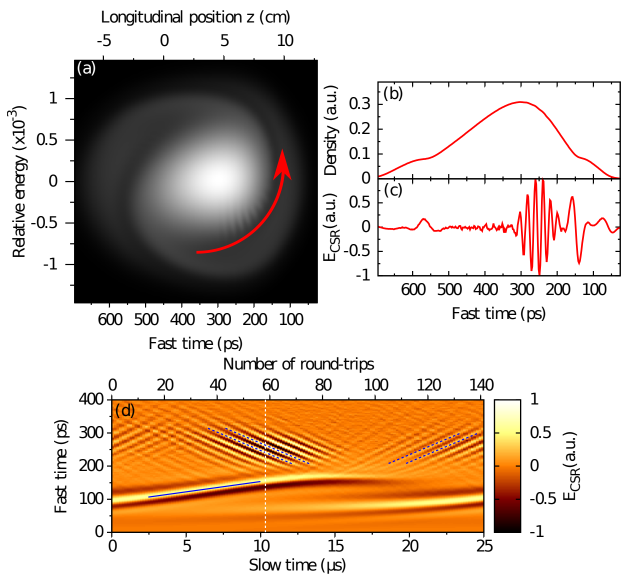

Figure 5: Interpretation of the drifting structures observed in Fig. 3, from numerical simulations. (a) Distribution of the electrons in longitudinal phase space (position z, energy E) at a given time. The CSR instability leads to a microstructure in this phase-space. (b) Longitudinal electron density distribution, i.e., obtained by the vertical projection of the distribution (a). (c) CSR electric field deduced from (b). Note that the structure is more visible in (c) than in (b), because the global shape of the electron bunch is cut off in the CSR process. The temporal evolution of the electric field (d) reveals that the structures are permanently drifting, as in the experiment. This is explained by the rotation of the electron distribution (a). (a,b,c) are taken at time $t = 10.4\,\mu s$ (white dashed line in (d)).

from the study of the phase-space versus time (Figs. 6(b-g)). Following the evolution of the slice, we can see that the Y-shape in Figs. 4 and 6(a) appears as a signature of the transformation of the initially straight slice (Fig. 6(c)) into an "S-shape" slice. The merging of the two branches of the cusp occurs when the inflexion point of the S-shape is almost vertical.

CONCLUSION

We have shown the first direct, real-time monitoring of the CSR pulses turn-by-turn. These experimental observations were possible using the detector based on ultra-fast thin-film YBCO superconductor which is sensitive to the electric field of the detected radiation. Thus, it is now possible to follow in detail the erratic behavior of CSR pulses, including envelope and carrier, in the millimeter wavelength range emitted during the microbunching instability. The detection method can also be extended to the detection of the envelope of pulses where the carrier cannot be resolved, by biasing the detector [16]. We also believe that the YBCO detector is a promising technology which will make it possible to test the validity of the existing or future models.

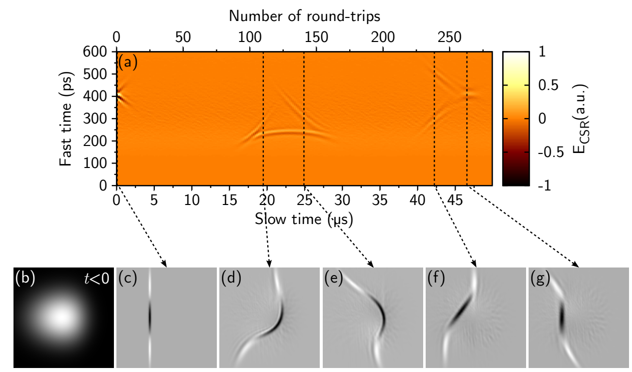

Figure 6: Numerical simulation of the electron bunch response to laser-slicing, and interpretation in phase space. (a) Color map of the temporal evolution of the CSR pulses. (b) Longitudinal electron bunch phase-space before laser-electrons interaction, (c,d,e,f,g) electron bunch distributions at different times after the laser perturbation. For clarity, the initial unperturbed electron distribution (a) has been subtracted.

ACKNOWLEDGMENT

The work was supported by the Joint Studies Program of the Institute for Molecular Science, the JSPS fellowship program for research in Japan (S-09171), the Projet International de Coopération Scientifique PICS project from CNRS, the Grant-in-aid for scientific researches (B20360041) of JSPS, the ANR (Blanc 2010-042301), and used HPC resources from GENCI TGCC/IDRIS (2013- x2013057057, 2014x2014057057). It has also been supported by Ministry of Higher Education and Research, Nord-Pas de Calais Regional Council and European Regional Development Fund (ERDF) through the Contrat de Projets État-Région (CPER) 20072013, and the LABEX CEMPI project (ANR-11-LABX-0007). The CERLA is supported by the French Ministère chargé de la Recherche, the Région Nord-Pas de Calais and the FEDER. The KIT is supported in part by the German Federal Ministry of Education and Research under Grant No. 05K2010.

REFERENCES

[1] M. Venturini *et al.*, Phys. Rev. ST Accel. Beams **8**, 014202 (2005)

[2] J. Byrd *et al.*, Phys. Rev. Lett. **89**, 224801(2002)

[3] V. Judin *et al.*, IPAC 2012, New Orleans, June 2012, TUPPP010 (2012)

[4] M. Abo-Bakr *et al.*, Phys. Rev. Lett. **88**, 254801 (2002)

[5] W. Shields *et al.*, Journal of Physics: Conference Series **357**, 012037 (2012)

[6] E. Karantzoulis *et al.*, Infrared Physics and Technology **53**, 300 (2010)

[7] G. Wüstefeld *et al.*, IPAC 2010, Kyoto, June 2010, WE-PEA015 (2010)

[8] C. Evain *et al.*, Europhys. Lett. **98**, 40006 (2012)

ISBN 978-3-95450-176-2

[9] A. Mochihashi *et al.*, EPAC06, Edinburgh, THPLS041 (2006)

[10] J. Byrd *et al.*, Phys. Rev. Lett. **97**, 074802 (2006)

[11] E. Roussel *et al.*, New Journal of Physics **16**, 063027 (2014)

[12] E. Roussel *et al.*, Phys. Rev. Lett. **113**, 094801 (2014)

[13] M. Adachi *et al.*, Journal of Physics: Conference Series **425**, 042013 (2013)

[14] P. Thoma *et al.*, Appl. Phys. Lett. **101**, 142601 (2012)

[15] P. Probst *et al.*, Phys. Rev. B **85**, 174511 (2012)

[16] P. Thoma *et al.*, IEEE Trans. Terahertz Sci. Technol. 3, 81 (2013)

[17] S. Kimura *et al.*, Infrared Physics and Technology **49**, 147-151 (2006)

[18] M. Adachi *et al.*, IPAC 2010, Kyoto, June 2010, WEPEA038 (2010)

[19] M. Hosaka *et al.*, Phys. Rev. ST Accel. Beams **16**, 020701 (2013)

[20] P. Thoma, Ph.D. thesis, Fakultät für Elektrotechnik und Informationstechnik, Karlsruher Institut für Technologie (KIT) (2013)

[21] M. Venturini and R. Warnock, Phys. Rev. Lett. **89**, 224802 (2002)

[22] G. Stupakov and S. Heifets, Phys. Rev. ST Accel. Beams **5**, 054402 (2002)

[23] E. Roussel *et al.*, IPAC 2014, Dresden, June 2014, TUPRI042 (2014)

[24] E. Roussel, Ph.D. thesis, Université Lille 1, Sciences et Technologie (2014)

ISBN 978-3-95450-176-2

DESIGN OF A COMPACT L-BAND TRANSVERSE DEFLECTING CAVITY WITH ARBITRARY POLARIZATIONS FOR THE SACLA INJECTOR

H. Maesaka, T. Asaka, T. Ohshima, H. Tanaka, Y. Otake, RIKEN SPring-8 Center, Kouto, Sayo, Hyogo, 679-5148, Japan
S. Matsubara, Japan Synchrotron Radiation Research Institute, Kouto, Sayo, Hyogo, 679-5198, Japan

Abstract

For the X-ray free electron laser, SACLA, fine-tuning of the injector part of a drive linac is quite important. Since one of the most effective ways for this tuning is to monitor the temporal structure of an electron beam, we designed a compact L-band (1428 MHz) TM110-mode transverse deflecting cavity (TCAV). The TCAV will be installed at the end of the velocity bunching section, where a bunch length ranges from 10 ps to 1 ns, the kinetic energy of the beam is approximately 1 MeV. In order to measure a short bunch as long as 10 ps, the TCAV system was designed to have less than 3 ps time resolution. The TCAV has 2 input ports intersecting at a right angle in order to excite either of linear and circular polarizations, depending on the measurement condition. The linear polarization is suitable for a short bunch measurement with high temporal resolution and the circular one is useful to measure a long bunch comparable to the rf period (700 ps). Thus, the TCAV system has sufficient temporal resolution and wide measurement range required at the SACLA injector and this system is expected to be beneficial for fine-tuning of the injector.

INTRODUCTION

The X-ray free electron laser (XFEL) facility, SACLA [1], has been stably operated for experimental users for more than 3 years. However, we have encountered some problems that we could not always reproduce the best XFEL performance soon after a long shutdown period. One of the reasons for this problem could be that the temporal profile of an electron beam at the injector part of SACLA was slightly changed at each time. Since a thermionic electron gun and a velocity bunching process are used at the injector, the rf phase and amplitude of a buncher cavity should be accurately adjusted to reproduce the appropriate temporal structure. Therefore, a temporal profile measurement system is demanded at the SACLA injector for fine-tuning of the velocity bunching part.

In order to clarify the necessity of the temporal structure measurement, we introduce the bunching scheme of SACLA. Figure 1 shows a schematic layout of the SACLA accelerator. An electron beam is generated by a 500 kV thermionic electron gun and chopped into a 1 ns-long bunch by a high-voltage pulse chopper. A 238 MHz buncher cavity applies a velocity modulation to the beam, which is afterward accelerated by a 476 MHz cavity. An L-band (1428 MHz) correction cavity (L-COR) operated at a deceleration phase linearizes nonlinear energy modulation on the beam generated by the rf curvature of the acceleration field in the 476 MHz cavity. The kinetic energy after the L-COR is approximately 1 MeV. The beam is accelerated by an L-band alternating periodic structure (L-APS) at an off-crest phase in order to give an energy chirp along the beam bunch for bunch compression. A C-band correction cavity again linearizes the rf curvature given by the L-APS, and the first bunch compressor (BC1) compresses the bunch length from approximately 30 ps to 3 ps. Then, S-band (2856 MHz) accelerator units accelerate the beam at an off-crest phase so as to compress the bunch length at the BC2. The same bunch compression mechanism is utilized to the first 12 units of the C-band (5712 MHz) accelerators and the BC3. After the BC3, a C-band transverse deflecting structure (C-TDS) [2] is installed for temporal bunch structure measurement. The beam is finally accelerated to 8 GeV by remained C-band accelerators.

As mentioned above, there are 5 cavities in the injector part before the BC1. Therefore, we have to adjust all the rf phases and amplitudes of these cavities. These parameters are, at first, set to those from a simulation result or those of the previous operation condition. Then, they are fine-tuned so as to maximize the XFEL power. This tuning process is quite time-consuming. Once the injector is tuned to an appropriate condition, since a temporal beam profile after the BC2 or BC3 can be measured by the C-TDS, we can tune the S-band and C-band accelerators by using the temporal profile information. However, we cannot tune the injector part only by using the C-TDS. In the injector components, the velocity bunching instruments are quite important, because they determine the initial condition of the electron beam. Thus, we designed a transverse deflecting cavity (TCAV) for the temporal bunch structure measurement in the velocity bunching section.

Since the bunch length in the velocity bunching section is variable from 10 ps to 1 ns, the TCAV system is required to have wide measurement range. For a short bunch measurement around 10 ps, this system should have a high temporal resolution of a few ps. For the design of the TCAV system, these requirements should be taken into account.

In this article, we describe the conceptual design of a transverse deflector system according to requirements for the temporal profile measurement. The design of the TCAV is then detailed. Some basics of a transverse deflector system is briefly described in the appendix.

maesaka@spring8.or.jp

ISBN 978-3-95450-176-2

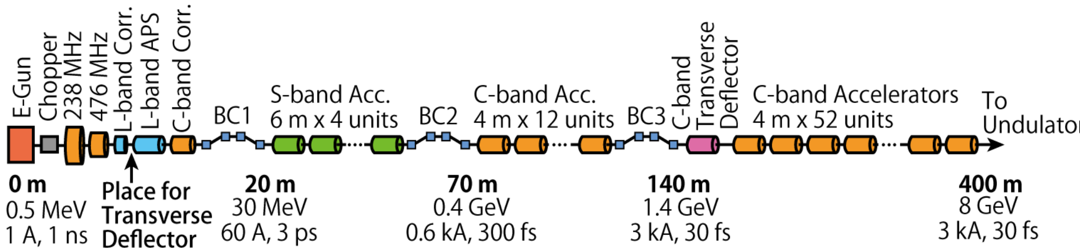

Figure 1: Schematic layout of the SACLA accelerator.

CONCEPTUAL DESIGN OF TRANSVERSE DEFLECTOR SYSTEM

Place for TCAV

In order to measure velocity bunching characteristics, the place for the TCAV should be the end of the velocity bunching section. Therefore, we decided to install the TCAV just before the L-APS, as shown in Fig. 1. In this case, the TCAV can observe the effect from each of 3 cavities, 238 MHz, 476 MHz and L-COR. At this installation point, the beam energy is around 1 MeV, which means that a kick voltage of several 10 kV is enough (several 10 mrad-kick). This kick voltage seems to be generated by a single-cell cavity, which makes the system compact. If we put the TCAV after the L-APS, the kick voltage should be 30 times larger because the beam energy is approximately 30 MeV. To obtain a large kick voltage, we need a large TCAV and a high-power rf source. Thus, the upstream of the L-APS is better for the place of the TCAV, considering the space and cost of the TCAV system. Beam parameters and requirements for this TCAV are listed in Table 1.

Since the space in the injector is limited, we have to use a screen monitor downstream of the L-APS. In addition, the energy of an electron beam is too low to pass through the L-APS without acceleration. Furthermore, there are solenoid lenses and quadrupole magnets after the TCAV. Therefore, the beam dynamics of the L-APS and other focusing devices should also be taken into account for the system design.

Measurement Range and RF Frequency

A bunch length at the entrance of the L-APS can be changed from 10 ps to 1 ns, depending on the rf phase and amplitude of each cavity of the injector. The bunch length is typically 30 ps for XFEL operation. The TCAV should cover this wide measurement range and have sufficient temporal resolution.

In order to meet the measurement range requirement, we considered using both linear and circular polarization rf fields of a TCAV, as described in the appendix. The linear polarization is effective in a short bunch measurement with high resolution by increasing a kick angle. However, it is difficult to measure an electron bunch longer than the linear part of the sinusoidal wave. Especially for a bunch length longer than the half rf period, a part of the deflected image is overlapped due to the folding back of the sinusoidal wave. On the other hand, the circular polarization is suitable for a long bunch

Table 1: Beam parameters and requirements for the TCAV.

Beam energy	~ 1 MeV
Bunch length	10 ps – 1 ns (typically 30 ps)
Normalized emittance	1 mm mrad
Time resolution	< 5 ps for a 10 ps bunch
RF Field polarization	Linear and Circular (Selectable)
Beam size	0.5 mm rms at the screen
Kick angle	> 60 mrad
Screen size	10 mm diameter

measurement because the bunch length comparable to the full rf period of the TCAV can be observed, as mentioned in the appendix. Another reason for using a circular polarization is the existence of a longitudinal magnetic field in a solenoid lens. Although a linearly stretched beam can be distorted by the longitudinal magnetic field, the image of a circularly stretched beam is not distorted but just rotated by the longitudinal magnetic field.

The resonant frequency of the TCAV should be as high as possible for high-resolution measurement, although the frequency should be sufficiently low for a long bunch measurement. Since the longest bunch length is 1 ns, the resonant frequency should be around 1 GHz. We use L-band frequency (1428 MHz) for the TCAV, because there are L-band accelerators in the injector and we can utilize the same apparatus as the L-band accelerator for the TCAV, such as a 2.5 kW solid-state amplifier. In this case, a bunch length measurement range is 700 ps at a maximum. Although this is somewhat smaller than 1 ns, most of the bunch length in the injector can be measured.

Time Resolution and Required Kick Angle

Since the minimum bunch length is 10 ps, a time resolution is required to be less than 3 ps. The time resolution can be calculated from Eq. 13 in the appendix. The beam size at the screen monitor downstream of the TCAV is 0.5 mm rms and the (1,2) element of the beam transfer matrix, m_{12}, from the TCAV to the screen is approximately -0.3 m. Therefore, the required kick angle for 3 ps resolution is estimated to be

$$y'_{\mathrm{max}} = \frac{\sigma_y}{|m_{12}|\sigma_t\omega} \simeq 60\ [\mathrm{mrad}]. \quad (1)$$

ISBN 978-3-95450-176-2

For the circular polarization measurement, the kick angle is limited by a screen monitor size. Since the screen size of SACLA is 10 mm in diameter, the radius of the deflected beam image should be 3 mm at most, for a reliable measurement. In this case, a time resolution is estimated to be 19 ps, which is sufficient for more than a 100 ps bunch length.

Phase Acceptance of L-APS

Since there is the L-APS between the TCAV and the screen monitor, the phase acceptance of the L-APS should be considered especially for a long bunch measurement. The longitudinal phase space orbit of the L-APS can be expressed as [3]

$$\cos\theta - \cos\theta_\infty = \frac{kc}{eE_0}\left[\sqrt{p^2 + (mc)^2} - p\right], \tag{2}$$

where θ is the rf phase with respect to a zero-crossing phase, as shown in Fig. 2, θ_∞ is the constant determined by an initial condition, p is the electron momentum, k is the wave number of the acceleration rf field, E_0 is the average acceleration electric field, c is the speed of light, e is the elementary charge and m is the electron rest mass. The longitudinal phase space trajectory of the L-APS is shown in Fig. 2 [3]. The minimum phase to capture electrons can be calculated from Eq. 2 with $\cos\theta_\infty = -1$. If we set the L-APS acceleration gradient to the typical value, 13.9 MV/m, and the initial kinetic energy to 1 MeV, the minimum phase, $\theta_{\min}$, is calculated to be

$$\cos\theta_{\min} = \frac{kc}{eE_0}\left[\sqrt{p^2 + (mc)^2} - p\right] - 1 \simeq -0.911, \quad \therefore \quad \theta_{\min} \simeq -156\ [\text{deg.}]. \tag{3}$$

To calculate the maximum phase, we firstly evaluate $\cos\theta_\infty$ from the initial condition, $p = \theta = 0$,

$$\cos\theta_\infty = 1 - \frac{kmc^2}{eE_0} \simeq -0.100, \tag{4}$$

Thus, the maximum phase, $\theta_{\max}$, for a 1 MeV electron is estimated to be

$$\cos\theta_{\max} = \frac{kc}{eE_0}\left[\sqrt{p^2 + (mc)^2} - p\right] + \cos\theta_\infty \simeq 0.092, \tag{5}$$

$$\therefore \quad \theta_{\max} \simeq 85\ [\text{deg.}].$$

Thus, the phase interval to capture electrons by the L-APS is approximately 240 degrees, corresponding to 470 ps. This means that we can measure a 470 ps-long temporal structure at once. Nevertheless, we can measure a longer bunch than this value by scanning the L-APS phase.

DESIGN OF L-BAND TRANSVERSE DEFLECTING CAVITY

According to the conceptual design of the transverse deflector system, we designed an L-band TCAV, as shown in Fig. 3. Design values of the TCAV are summarized in Table 2. The TCAV has 2 input rf couplers intersecting at a right angle in order to choose the polarization freely. The cavity diameter is determined to be 256 mm so that the TM110 mode is excited at the resonant frequency of 1428 MHz. The cavity length is 60 mm, corresponding to a quarter wavelength of the rf. The TCAV has 3 tuners: two of them adjust resonant frequencies for the port 1 and 2 and the other is for the orthogonality between the 2 ports.

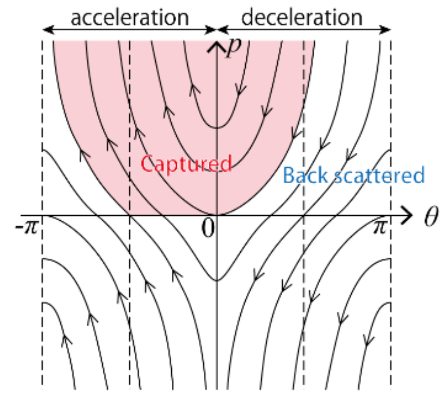

Figure 2: Longitudinal phase space trajectory of an electron beam in the L-APS. The hatched area shows electron-captured region by the L-APS.

By using a 3-dimensional rf simulation code, HFSS [4], the excited field was analyzed and the TM110 mode was confirmed to be properly excited, as plotted in Fig. 4. The unloaded Q factor was calculated to be 2.3 x 10^4. The external Q factor for each port was adjusted to 1.6 x 10^4 and the load Q factor was determined to be 9.5 x 10^3. The coupling factor, $\beta = Q_0/Q_{\text{ext}}$, is 1.44 (strong coupling), which slightly reduces the filling time. The transverse shunt impedance was evaluated to be 2.1 MΩ.When 2.5 kW solid-state amplifiers drive the TCAV, the maximum kick angle for a 1 MeV electron beam is approximately 63 mrad. As calculated in Eq. 1, this angle is sufficient for the requirement of a temporal resolution of 3 ps, which is applicable to a 10 ps long bunch.

Table 2: Design values of the L-band TCAV.

Resonant Frequency	1428 MHz
Resonant Mode	TM110 (linear and circular)
Shunt Impedance	2.1 MΩ
Input Power	2.5 kW max. for each port
Maximum Kick Angle	60 mrad for 1 MeV electrons
Cavity Inner Radius	256 mm
Cavity Inner length	60 mm
Unloaded Q (Q_0)	2.3 x 10^4
Loaded Q (Q_L)	9.5 x 10^3
External Q (Q_{ext})	1.6 x 10^4
Filling Time	6.6 μs

ISBN 978-3-95450-176-2

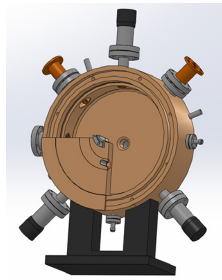

Figure 3: Schematic drawing of the L-band TCAV.

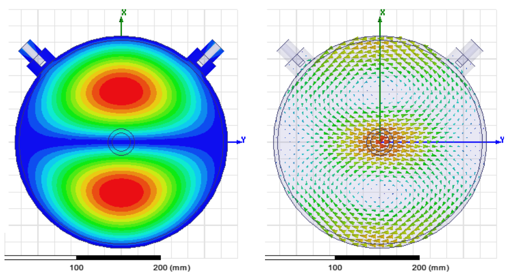

Figure 4: Electric field contour plot (left) and magnetic field vector plot (right) of the TM110-mode in the TCAV.

SUMMARY

In order to measure the temporal structure of an electron beam after the velocity bunching section of SACLA, we designed an L-band TCAV system. Since the bunch length range in the injector is so wide, 10 ps – 1 ns, we considered using both linear and circular polarizations for this system. The temporal structure is linearly stretched by the linear polarization and the time resolution can be enhanced by increasing the deflecting force. Therefore, the linear polarization is suitable for a short bunch measurement. On the other hand, the circular polarization converts the temporal structure to a circular image and enables us to use the full rf period (700 ps). Consequently, the circular polarization is useful to measure a longer bunch. We estimated the performance of the TCAV and the expected time resolution was obtained to be 3 ps for a 1 MeV electron beam. Thus, the designed TCAV system has sufficient performance for the temporal structure measurement at the SACLA injector and meets to the fine-tuning of the injector part.

APPENDIX

Basics of Transverse Deflector System

A schematic setup of a transverse deflector system is illustrated in Fig. 5. A transverse rf field in a TCAV gives a transverse kick to an electron beam. If the rf phase of the cavity is set to zero-crossing, the temporal structure of the beam is converted to a transverse profile. The temporal structure is taken by a transverse image on a screen monitor.

Here, the beam direction is supposed to be z-axis and the beam is to be kicked to y direction. The kick force, F_y, is evaluated from the Lorentz force,

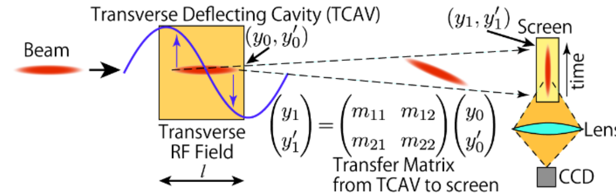

Figure 5: Schematic setup of a transverse deflector system.

$$F_y = -e(E_0 + \beta c B_0)\sin(\omega t + \phi_0), \tag{6}$$

where E_0 and B_0 are the y component of the peak electric field and the x component of the peak magnetic field, respectively, e is the elementary charge, c is the speed of light, β is the beam velocity normalized by c, ω is the resonant angular frequency of the TCAV, and ϕ_0 is the rf phase when an electron is at the cavity center. For simplicity, we assume the TM110 mode of a pillbox cavity from now, because this mode is one of the simplest transverse rf modes. In this case, E_0 can be ignored and B_0 becomes constant, since this mode only generates a magnetic field along the cavity axis and its field strength is independent of the longitudinal position.

The transverse momentum of the electron given by the TCAV is calculated to be

$$\begin{aligned} p_y &= \int_{-\frac{l}{2\beta c}}^{\frac{l}{2\beta c}} F_y dt = -e\beta c B_0 \int_{-\frac{l}{2\beta c}}^{\frac{l}{2\beta c}} \sin(\omega t + \phi_0)\, dt \\ &= -\frac{\sin\frac{\omega l}{2\beta c}}{\frac{\omega l}{2\beta c}} e B_0 l \sin\phi_0 = -e B_0 l\, T \sin\phi_0 , \end{aligned} \tag{7}$$

where l is the cavity length and T is the transit time factor defined to be

$$T \equiv \frac{\sin\frac{\omega l}{2\beta c}}{\frac{\omega l}{2\beta c}}. \tag{8}$$

The kick angle, y_0', can be written as

$$y_0' = \frac{p_y}{p_0} = -\frac{e B_0 l\, T \sin\phi_0}{p_0} \simeq -\frac{e B_0 l\, T \phi_0}{p_0}, \tag{9}$$

where p_0 is the initial beam momentum and ϕ_0 is sufficiently small. We define the maximum kick angle, y'_{max}, as

$$y'_{\mathrm{max}} \equiv \frac{e B_0 l\, T}{p_0}. \tag{10}$$

The transverse position of the electron, y_1, is calculated by using the (1,2) element of a beam transfer matrix in Fig. 5, m_{12},

$$y_1 = m_{12} y_0' = -m_{12} y'_{\mathrm{max}} \phi_0 = -\frac{m_{12} e B_0 l\, T \phi_0}{p_0}. \tag{11}$$

The position-to-time conversion factor, C, on the screen is

ISBN 978-3-95450-176-2

$$C = \frac{\phi_0}{y_1\omega} = -\frac{1}{m_{12}y'_{\max}\omega} = -\frac{p_0}{m_{12}eB_0 l T\omega}. \quad (12)$$

The finite beam size at the screen without deflection, σ_y, limits the time resolution of the transverse deflector system. Therefore, the time resolution, σ_t, is evaluated to be

$$\sigma_t = |C\sigma_y| = \frac{\sigma_y}{|m_{12}|y'_{\max}\omega} = \frac{p_0\sigma_y}{|m_{12}|eB_0 l T\omega}. \quad (13)$$

Thus, in order to obtain a better time resolution, the initial momentum and the beam size at the screen should be small, and the integration of the rf field ($B_0 l T$), the resonant frequency and the (1,2) element of the transfer matrix (m_{12}) should be large.

A screen size or an rf period limits the measurement range. In the case of the limited screen size, the measurement range, $\Delta t_{\max}$, is calculated to be

$$\Delta t_{\max} = |Cy_{\mathrm{scr}}| = \frac{p_0 y_{\mathrm{scr}}}{eB_0 l T\omega m_{12}}, \quad (14)$$

where y_{scr} is the half size of the screen. For the rf period limitation case, we suppose that the approximately linear part of the rf sinusoidal wave is a quarter of the rf period. The measurement range is estimated to be

$$\Delta t_{\max} \simeq \frac{\pi}{2\omega}. \quad (15)$$

Thus, the rf frequency should be sufficiently small for a long bunch-length measurement range. The limitation from the screen size can be relaxed by reducing the rf power instead of decreasing the temporal resolution.

Polarization Control of Transverse RF Field

The polarization of a transverse rf resonant mode, such as TM110 mode in a pillbox cavity, can be freely chosen, if the cavity has 2 input ports intersecting at a right angle, as shown in Fig. 6. The input rf signals at the port 1 and port 2 are defined to be $A_1\cos(\omega t + \phi_1)$ and $A_2\cos(\omega t + \phi_2)$, respectively.

When the rf phase difference between the 2 ports is 0 or π, a linearly polarized rf field is excited. The polarization direction is determined by the arctangent of the amplitude ratio between the 2 ports. The amplitude of the rf field in the cavity is proportional to $\sqrt{A_1^2 + A_2^2}$.

When the rf phase difference between the 2 ports is $\pm\pi/2$ and the amplitudes of the 2 ports are the same, a circularly polarized rf field is excited. The rotation direction depends on the sign of the phase difference. The amplitude of the rf field in the cavity is proportional to A_1 $(= A_2)$.

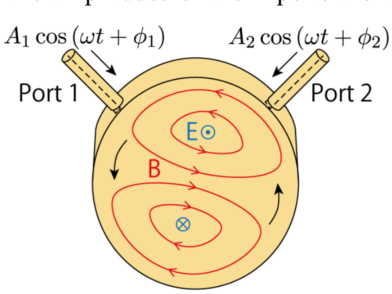

Figure 6: Schematic view of a 2-port pillbox cavity with a circularly polarized TM110 mode.

Characteristics of Circular Polarization Deflector System

If a circularly polarized rf field is excited in a TCAV, the temporal structure of an electron beam is circularly stretched, as shown in Fig. 7. In this case, the full rf period of the TCAV can be used for a temporal profile measurement. Therefore, this mode is suitable for long bunch measurement.

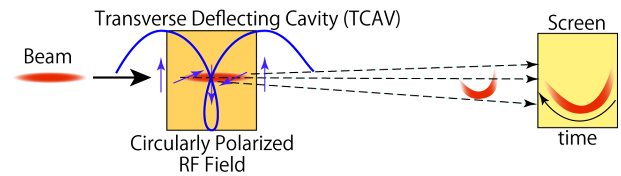

Figure 7: Schematic setup of a transverse deflector system with a circular polarization.

The radial force to an electron in the cavity, F_r can be written as

$$F_r = \beta c e B_0 \cos\omega t. \quad (16)$$

We can get the radial momentum from the kick force, p_y, as follows:

$$p_r = \int_{-\frac{l}{2\beta c}}^{\frac{l}{2\beta c}} F_r dt = eB_0 l T. \quad (17)$$

The kick angle, r'_0, and the radius of an image circle, r_1, are calculated to be

$$r'_0 = \frac{p_r}{p_0} = \frac{eB_0 l T}{p_0}, \quad (18)$$

$$r_1 = |m_{12}|r'_0 = \frac{|m_{12}|eB_0 l T}{p_0}. \quad (19)$$

The time scale of the image is apparently obtained from the azimuthal angle on the screen. For the time resolution, the expression is the same as the rightmost formula of Eq.13. Since the image circle must be within the screen size, the kick strength is limited by this condition. Thus, although the measurement range of the circular polarization case is longer than the linear polarization, the time resolution is not better than the linear polarization case.

REFERENCES

[1] T. Ishikawa, et al., Nature Photonics **6**, 540 (2012).
[2] H. ego, et al., Nucl. Instrum. Methods in Phys. Res., Sect. A **795**, 381 (2015).
[3] R. Helm, R. Miller, Particle Dynamics, in: P. M. Lapostolle, A. L. Steptier (Eds.), Linear Accelerators, North-Holland Publ. Co., Amsterdam (1970).
[4] http://www.ansys.com

ISBN 978-3-95450-176-2

DEVELOPMENT OF A BEAM PULSE MONITOR FOR THE HEAVY ION ACCELERATOR FACILITY

D. Tsifakis#, N.R. Lobanov, P. Linardakis, ANU, Canberra, Australia

Abstract

The Australian National University (ANU) Heavy Ion Accelerator Facility (HIAF) comprises of a 15 million volt electrostatic accelerator (NEC 14UD) followed by a superconducting LINAC booster. The pulsing system consists of a low energy, single gap, gridded buncher and two high energy choppers. The buncher and choppers need to be set in phase and amplitude for maximum efficiency. The LINAC encompasses twelve, lead tin-plated Split Loop Resonators (SLR). Each SLR, as well as the superbuncher and time energy lens, needs to be individually tuned in phase and amplitude for correct operation. The HIAF pulsing system is based on a few techniques. The first one utilises a U-bend at the end of the LINAC. One special wide Beam Profile Monitor (BPM) is installed after the 90 degrees magnet. The technique allows to set up correct phase by observing the displacement of beam profile versus phase shift of the last phase locked resonator. The determination of beam pulse characteristics are based on γ-ray detection produced by beam striking a tantalum target. In this paper, the HIAF set up for pulsed beam diagnostics with sub nanosecond time resolution is described. The system has demonstrated simplicity of operation and high reliability.

INTRODUCTION

The ANU Heavy Ion Accelerator Facility consists of a National Electrostatics Corporation 14UD electrostatic tandem accelerator and a superconducting LINAC booster accelerator. The LINAC comprises of four cryostats, each consisting of three, split-ring resonators, operating at a frequency of approximately 150 MHz. When the beam needs to be accelerated in the LINAC or when the beam is required by the accelerator users to be bunched, the facility's buncher systems are utilised. The first buncher is installed at the low energy section of the 14UD accelerator. It is a gridded, room temperature, buncher using one or three frequencies to produce the field required for bunching. The resulting bunch has a typical width of 1.5 ns FWHM and the bunching efficiency is approximately 0.25.

A second buncher, Super Buncher (SB), is installed at the LINAC entrance. SB is a superconducting, quarter-wave resonator with β=0.1, developed at the ANU and can further compress the beam to bunches with, typically, 100 ps FWHM.

All bunchers as well as the LINAC, are synchronised to the facility's master 150 MHz clock. The low energy buncher operates on the sub-harmonic frequency of approximately 9.375 MHz (1/16 of the master clock) and the two high energy choppers on 37.5 MHz and 4.6875 MHz (1/4 and 1/32 of the master clock).

When the buncher systems are in use, it is important to have a monitoring system which allows the accelerator operator to measure the characteristics of the bunch in the time domain, to assist with the tuning. This paper describes the system used by the facility to produce a time profile of the pulsed beam. This technique of measuring the longitudinal profile is used by other facilities such as [1]. The output of the pulse monitor is used together with other measurement and tuning techniques [2, 3] to optimise the LINAC beam.

The development of this system has happened through the years and with the scientific contribution of the researchers of the Department of Nuclear Physics.

METHOD DESCRIPTION

The beam pulse monitoring system, shown in Fig. 1 is based on the time difference between prompt γ-rays produced by the beam striking a tantalum target and the reference RF used to synchronise the rest of the accelerator.

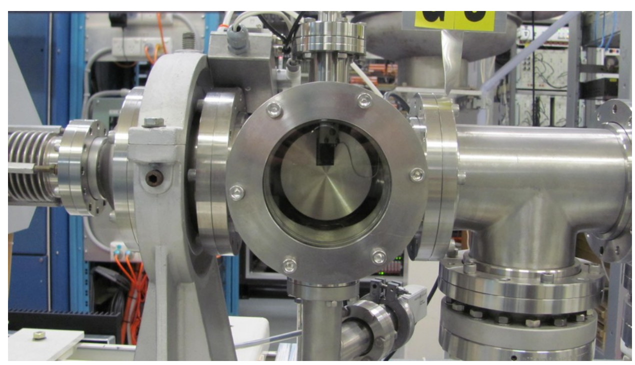

Figure 1: The target station of the beam pulse profile monitor. The target, as seen through the viewing port, can be moved in/out and is rotated by 45 degrees with respect to the beam.

The target is mounted at a 45 degree angle to the beam and it is placed in the path of the beam. This results in prompt γ-rays being produced, which are detected by a barium fluoride (BaF2) scintillation detector. The detector used at the ANU is made by Scionix Holland BV and is model number 38/25B30/2M BaFX2Neg. The BaF_2 detector signal provides the start signal to a time-to-analog converter (TAC) made by Ortec, model 567. The TAC is set to a maximum range of 100 ns. The amplitude signal from the detector is variable as the energy

#Dimitrios.Tsifakis@anu.edu.au

ISBN 978-3-95450-176-2

deposited by the detected γ-ray is not always the same, so in order to produce an accurate timing signal that is not depended on the amplitude of the detector pulse, an Ortec 584 constant fraction discriminator (CFD) is placed between the detector and the TAC. The fast logic signal from the CFD is then fed to the TAC's start signal input. The stop signal comes from the reference RF, which at that point is 9.375 MHz. Figure 2 shows the electronic modules comprising the monitor system. This configuration results in an event rate of the order of 5000/s for a typical beam of 50 nA, which implies that substantially less than one γ-ray per beam pulse is produced. The output of the TAC is connected to a multi-channel analyser (MCA) which produces a histogram representing the time profile of the beam. Since a single beam pulse results in less than one gamma ray detected, over time, the profile of the beam pulse produced in the histogram is considered to be a faithful representation of the profile of the pulse.

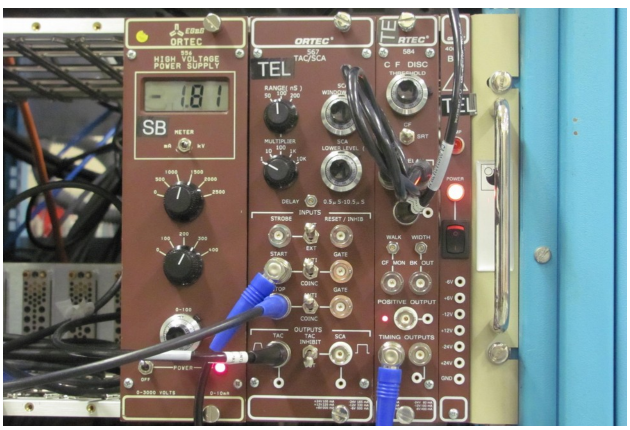

Figure 2: The electronic modules used by the beam pulse monitor system. From left to right: high voltage supply for the BaF2 detector (Ortec 556), time-to-analog converter (Ortec 567) and constant fraction discriminator (Ortec 584). The Single Channel Analyser in the TAC module is not used. The modules are installed in an Ortec 4001C NIM bin.

The MCA used to produce the histogram is a FAST ComTek MCA-3FADC, used on a laptop with a PCMCIA to PCI bridge. This MCA has a maximum conversion range of 8192 channels, which is adequate for this task. The software used to collect the data is written by the manufacturer and the data is stored in ASCII files which can be read and processed by other applications. The histograms presented in this paper were collected at a conversion range of 1024, a range that is adequate for measurements of the beam before the superbuncher.

Calibration of the system is essential in order to produce an absolute measurement of the pulse's FWHM. An Ortec 462 TAC calibrator has been used for this purpose. This TAC calibrator has good long-term stability and absolute accuracy, the latter being ±10 ps for a 10 ns period according to the manufacturer. For the measurements presented in this paper, the calibration factor was found to be approximately 8.47 channels per nanosecond. There are two beam pulse monitor systems, one before the superbuncher and one after the time-energy lens. Their locations are shown in Fig. 3.

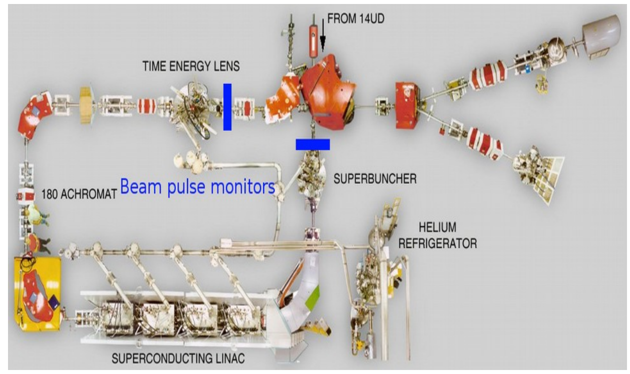

Figure 3: Composite photo of the ANU LINAC facility; the locations of the beam pulse monitor systems are marked in blue colour.

RESULTS

The plots depicted in Fig. 4 are typical plots obtained by the beam pulse monitoring system. The data in this figure are collected by the MCA connected to the first monitoring station, located before the superbuncher. The beam is 72 MeV $^{16}O^{+6}$, produced by the 14UD accelerator with single electron stripper at the terminal.

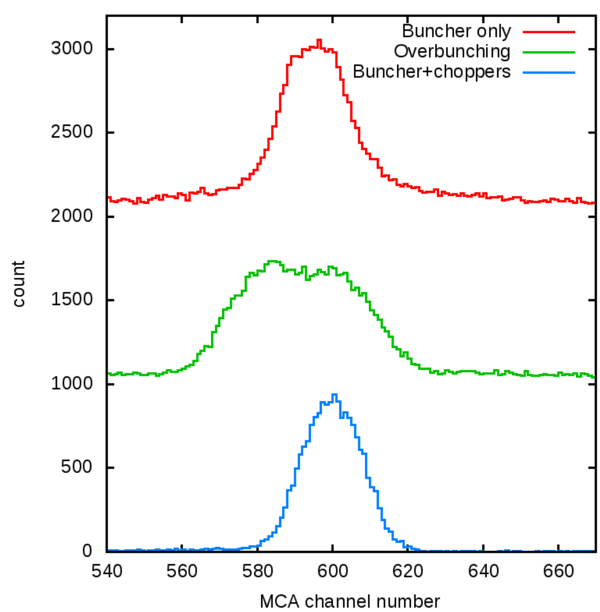

Figure 4: The top histogram (shifted up by 2000 counts) shows the beam pulse with only the low energy buncher enabled. The middle histogram (shifted up by 1000 counts) has a double peak which is typical of overbunching. The bottom histogram is produced with both the low energy buncher and high energy choppers enabled. The collection time for all histograms was 60 seconds.

ISBN 978-3-95450-176-2

DISCUSSION

On the top trace in Fig. 4, only the low energy buncher is in operation. The middle plot shows the characteristic pattern of double peaking which occurs when overbunching. The bottom plot is obtained after the buncher settings are optimised and the high energy choppers are turned on. The reduced background between beam pulses is an effect of the choppers operation.

The process of pulse optimisation consists of adjustment of amplitude and phase of the bunchers and choppers with feedback provided by the beam pulse monitor.

In the latest of a series of LINAC tests, the beam pulse monitor system was found to be affected by mains power noise. The noise is picked up by the lengthy, approximately 100 m, coaxial cable connecting the monitor station to the control room where the MCA is located. This noise results in an artificial widening of the recorded pulses and is currently the subject of an investigation. The noise was found to be about 40 mV peak to peak which, for the selected range conversion of 1024, translates to 3.4 channels or 0.4 nanoseconds. This error is too large for measuring accurately the pulses after the superbuncher. A solution to this problem is the relocation of the MCA computer from the control room to the LINAC hall, combined with remote access to the computer.

ACKNOWLEDGEMENTS

This work has been supported by Australian Federal Government Superscience/EIF funding, under the NCRIS mechanism.

The design of the beam pulse monitor has been made with the contributions of the academic staff of the Department of Nuclear Physics, including Emeritus Professor G. D. Dracoulis and Professor A. E. Stuchbery.

REFERENCES

[1] J. L. Vignet, R. Revenko, “A Bunch Extension Monitor for the SPIRAL2 LINAC”, Proceedings of IBIC2014, Monterey, CA, USA, MOPD26, http://www.jacow.org/

[2] N. R. Lobanov, P. Linardakis and D. Tsifakis, “Tuning the superconducting linac at low beam intensities”, to be published in the proceedings of SRF2015, Whistler BC, Canada.

[3] N. R. Lobanov, P. Linardakis and D. Tsifakis, “Tuning the linac with superconducting resonator used as a phase detector”, to be published in the proceedings of SRF2015, Whistler BC, Canada.

ISBN 978-3-95450-176-2

A COMPACT WEATHER STATION FOR MONITORING ENVIRONMENTAL EFFECTS ON BEAM PROPERTIES AND EQUIPMENT

S. Cunningham#, R. Clarken, A.C. Starritt, Australian Synchrotron, Melbourne, Australia

Abstract

A compact and mobile weather station has been designed and integrated with EPICS (Experimental Physics an Industrial Control System) to assist with environmental monitoring at the Australian Synchrotron. This proved invaluable in correlating the dependence of the Storage Ring RF phase with humidity.

The device is based on Arduino technology and consists entirely of substitutable parts allowing for easy repair and maintenance by people with any degree of technical skill. The project aim is to deploy several of these devices throughout the facility to enhance the understanding of environmental effects on beam properties and equipment.

INTRODUCTION

When considering how to design the weather station, it was essential to try and make it as simple and functional as possible while being low-cost. For this reason the Arduino open-source electronics [1] platform was chosen for the plug and play hardware, simple programming software and pre-existing code available online. The initial prototype utilised an Arduino Uno with an Arduino Ethernet Shield along with a DHT22 temperature-humidity sensor and a digital BMP085, barometric pressure sensor. When choosing these sensors, it was important to take into consideration the operational specifications which are outlined in Table 1 and Table 2 below.

Table 1: BMP085 Technical Data [2]

Variable	Range	Accuracy
Pressure	300-1100 hPa	±2.5 hPa
Temperature	-40°C - +85°C	±2°C

Table 2: DHT22 Technical Data [3]

Variable	Range	Accuracy
Humidity	0 – 100%RH	±5%RH
Temperature	-40°C - +125°C	±0.2°C

Deployment

One practical concern when designing the final weather station device was the capability to isolate and therefore minimise radiation damage. To this end the sensors are housed in their own case separated by a cable from the Arduino and its housing unit. This allows the sensors to be placed near and/or within the plane of radiation of the beam inside the tunnels while potentially minimising the damage to the Arduino itself. Any faulty sensors will therefore be easily replaceable, restoring functionality to the whole module with minimal effort due to the plug and play nature of the device. Figure 1 demonstrates the simplicity of this setup.

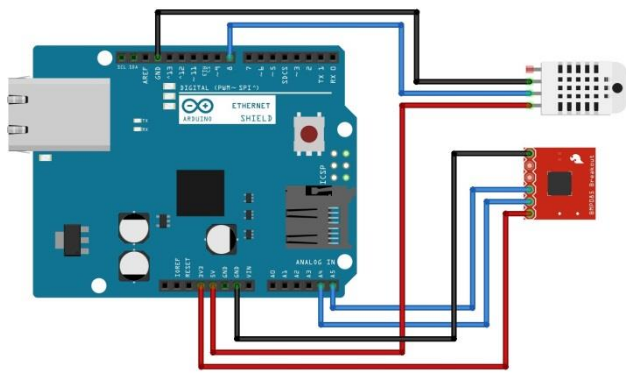

Figure 1: Weather station setup.

To assist with data storage and retrieval, the whole device was hosted on an Input-Output Controller (IOC) to allow integration with EPICS. This removed the need for a real time clock from the device as all data is now saved with a time stamp, as well as enhancing diagnostic capabilities as demonstrated by the correlations in this presentation.

CORRELATIONS DISCOVERED

One of the first correlations discovered was the relationship between beam phase and humidity in the technical hall. It can be clearly seen in Fig. 2 that there is a direct relationship with the humidity leading the phase of the beam.

Another correlation investigated was between the humidity and the vacuum in the linear accelerator (LINAC). Although this has been a known issue for some time, until the development and deployment of the weather station module there has been no way to determine the extent to which this correlation occurs see (Fig. 3).

#Simon.Cunningham@synchrotron.org.au

ISBN 978-3-95450-176-2

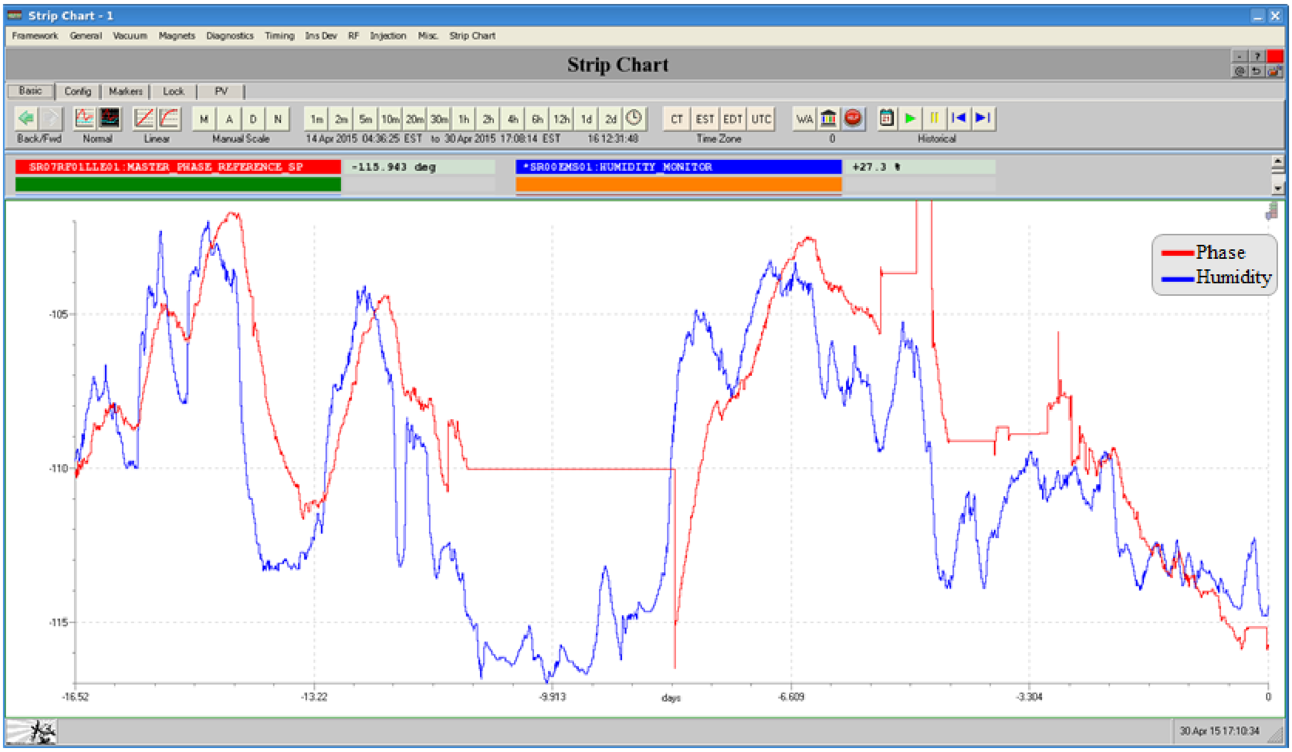

Figure 2: Humidity and phase vs. time.

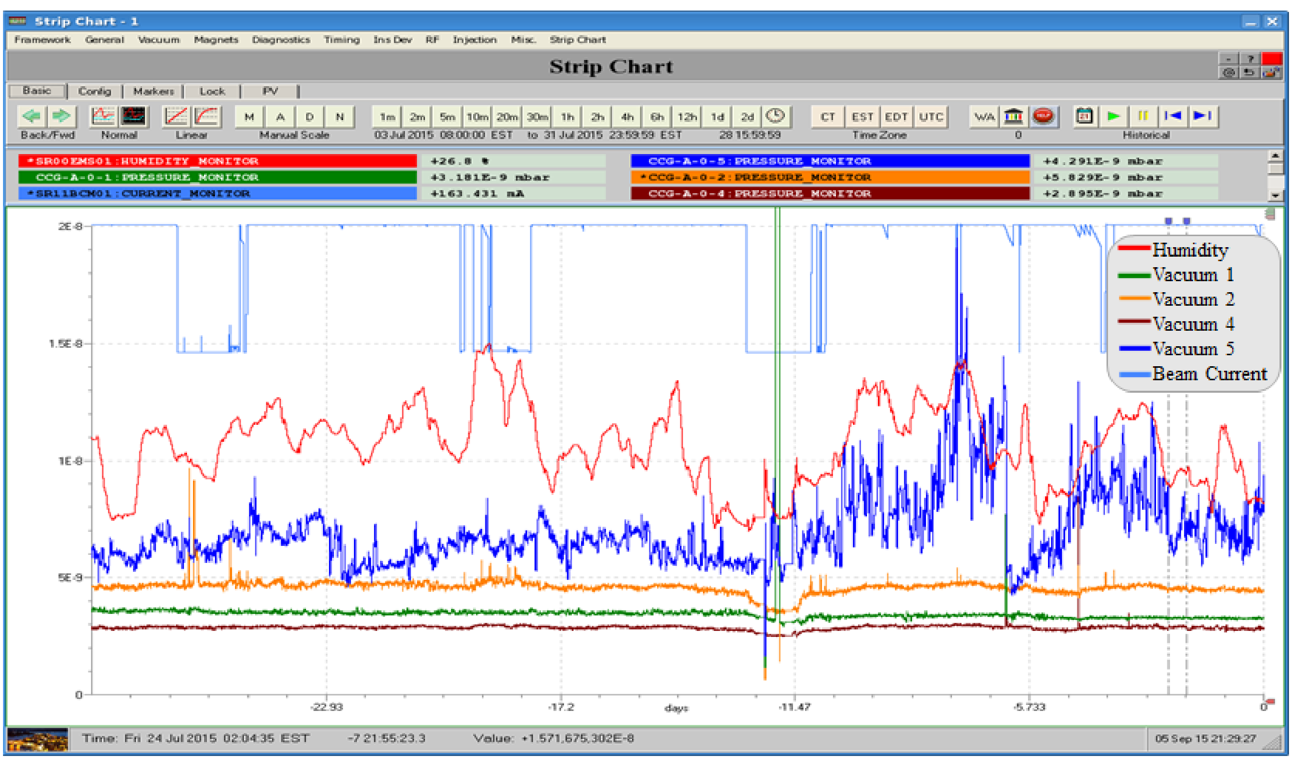

Figure 3: Humidity and LINAC vacuum vs. time.

SECOND GENERATION

The second generation of this device is currently being built with a Freetronics EtherTen module [4] which has power over Ethernet capabilities, eliminating the need for plug packs and proximity to power outlets once deployed. There is also development underway on some in-house support software. The software being developed will allow for future devices to be distributed and integrated into EPICS with ease, in line with the plug and play intent of the overall project. This has the benefit of enabling personnel with any technical skill or knowledge level to maintain and distribute future devices.

ISBN 978-3-95450-176-2

CONCLUSION

A first generation compact weather station has been built and used to discover atmospheric effects between the technical hall and the machine components. A second generation model is currently being developed with the capacity for power over Ethernet, allowing for greater mobility.

Work is also underway on developing code to allow existing and future models to be easily integrated into EPICS.

The correlations presented here show a need for further investigation into the links between atmospheric effects and beam characteristics.

REFERENCES

[1] Arduino website: https://www.arduino.cc/
[2] Bosch, BMP085 Digital pressure sensor data sheet, 15 October 2009
[3] Aosong Electronics Co. Ltd, DHT22 Datasheet
[4] Freetronics website: http://www.freetronics.com.au/

ISBN 978-3-95450-176-2

ELECTRO-OPTICAL MEASUREMENTS OF THE LONGITUDINAL BUNCH PROFILE IN THE NEAR-FIELD ON A TURN-BY-TURN BASIS AT THE ANKA STORAGE RING*

E. Roussel, C. Evain, S. Szwaj, S. Bielawski (PhLAM/CERLA, Villeneuve d'Ascq, France),
A. Borysenko, N. Hiller, A.-S. Müller, P. Schönfeldt, J.L. Steinmann (KIT, Karlsruhe, Germany)

Abstract

ANKA is the first storage ring worldwide with a near-field single-shot electro-optical bunch profile monitor. Previously, the method of electro-optical spectral decoding (EOSD) was employed to record single-shot longitudinal bunch profiles. The readout rate of the required spectrometer detector system limited the acquisition rate to a few Hz and thus did not allow us to study the evolution of the longitudinal bunch shape on a turn-by-turn basis. The setup at ANKA was combined with the novel method of photonic time-stretch [1] for which the modulated laser pulse is not detected in the spectral domain, but stretched to a few nanoseconds by a long fiber and, subsequently, detected in the time domain. This method allows the sampling of the longitudinal bunch profile on a turn-by-turn basis for several milliseconds, uninterrupted. Here, we present first results obtained with the photonic time-stretch method in the near-field at the ANKA storage ring.

INTRODUCTION

During the low-α_c-operation of the ANKA storage ring at the Karlsruhe Institute of Technology, the momentum compaction factor α_c is reduced to compress the bunches longitudinally and thus generate coherent synchrotron radiation (CSR) in the THz range [2]. Previous streak camera measurements have shown a beam current dependent bunch lengthening and deformation effect at ANKA in this special operation mode [3, 4]. In addition, the emitted CSR exhibits a bursting behavior [5–7], which we believe to be caused by dynamic changes of the longitudinal bunch shape (e. g., microbunching). Our near-field EO setup offers the possibility to obtain direct, single-shot measurements of the electric-field of the bypassing electron bunches which is directly linked to the longitudinal bunch profile. For this, the electric field of the electron bunch is modulated on a long, chirped laser pulse which is then analysed subsequently (Fig. 1). The laser pulses are synchronised to the electron bunch revolutions (f_{rev} = 2.7 MHz at ANKA) and with a fast enough detector, the bunch profile could be measured for every turn. Previously, the laser was detected in the spectral domain with a grating spectrometer housing a commercial line array that allowed for single-shot acquisitions, but only at a rather low readout rate of a few Hz (Fig. 1(a)). These measurements have revealed dynamic substructures on the electron bunches on a sub-ps time scale [8–10], but the dynamic evolution of the longitudinal bunch profile could not be studied on a turn-by-turn basis.

* This work is funded by the BMBF contract numbers: 05K10VKC, 05K13VKA.

The novel method of photonic time-strech, based on Dispersive Fourier transform (DFT), also known as real-time Fourier transformation [11], is a powerful method that overcomes the speed of classical cameras and enables real-time measurements of fast non-repetitive events using fast detectors. This technique has already been used in optics, photonics, telecommunications and spectroscopy, etc [11–13]. The principle of time-stretch is simple and consists in imprinting the signal containing the information on laser pulses and then stretch these pulses so that the signal is slowed-down enough and can be acquired with classical oscilloscopes (Fig. 1(b)). The combination of the time-stretch with the electro-optic detection has enabled to reach acquisition rate in the tens of megahertz and thus, revealed the evolution of the microbunching instability on a turn-by-turn basis [1].

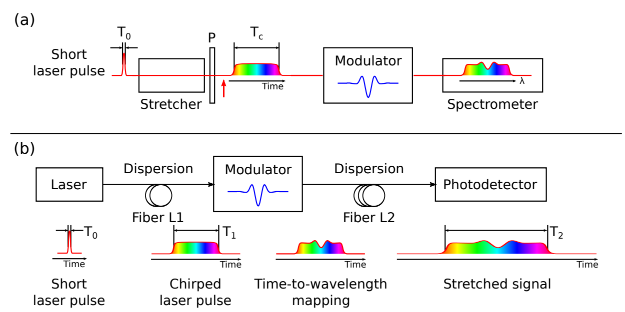

Figure 1: Principle of the detection. The information under inverstigation, here longitudinal bunch profile, is first encoded into a chirped laser pulse, using an electro-optic crystal ("Modulator"). Then the information encoded in the laser pulse is either detected in the spectral domain with a spectrometer (a), or futher stretched by propagation in a long fiber and detected in the time domain with a photodetector (b).

METHODS

Electro-optical bunch length measurement techniques rely on the field-induced Pockels effect to modulate the longitudinal electron bunch profile onto a laser pulse passing through an EO crystal (further reference e. g., [16]).

For the near-field measurements at ANKA, the EO crystal is brought close to the electron beam, so the direct Coulomb field of the bunch induces a time dependent birefringence in the EO crystal and this anisotropy modulates the polarization state of the linearly polarized probe laser pulse. This modu-

ISBN 978-3-95450-176-2

lation can be turned into an intensity modulation with the depicted optical components (quarter- and half-wave plates in combination with a crossed polarizer). Practically, the electric field of the bunch acts as a field-dependent phase retarder for the electric field of the laser pulse with the phase retardation being directly proportional to the field strength. For this to hold true, the crystal axis orientation, the direction of polarization of the Coulomb field and the laser need to be aligned in a specific way. Furthermore, the angles of the wave-plates need to be set in a way that the quarter-wave plate compensates the intrinsic birefringence of the crystal and the half-wave plate regulates the transmission through the crossed polarizer (see e.g. [17] for a detailed description).

The laser system needs to be in sync with the bunch repetition rate and its delay with respect to the electron bunch passing by needs to be adjustable to ensure temporal overlap between the laser pulse and the modulating electric field.

In order to demodulate the desired signal from the laser pulse, it can either be analyzed in a single-shot spectrometer - electro-optical spectral decoding (EOSD) - or the laser pulses are stretched in a long fiber to a few nanoseconds and can then be detected in the time-domain with a fast photodiode in combination with a fast oscilloscope with a bandwidth in the tens of gigahertz - time-stretch method (TS) (Fig. 1). Each method requires some means of absolute calibration of the time for which we delay the laser pulse in well known steps - in our case electronically, with a programmable vector modulator - and measure the shift of the EO signal within our acquisition window.

TIME-STRETCH UPGRADE OF EO SETUP AT ANKA

The EOSD setup at ANKA consists of a laser system (EO-Laser), several single-mode and polarization maintaining fibers, the fiber-coupled EO-Monitor through which the laser beam is coupled into the UHV system of the storage ring, a set of detectors used to measure the modulated laser pulse, a beam position monitor (BPM) which we use as absolute timing reference, and a loss rate counter to ensure that the crystal is far enough from the electron beam to not cause any significant beam losses. We use an Yb-doped fiber laser system (RF synchronized oscillator, pulse picker and amplifier) developed at PSI [18] specifically for electro-optical bunch length measurements for SwissFEL and the European X-FEL. The laser oscillator is tuned to 62.5 MHz (23rd harmonic of f_{rev}) and the amplified laser pulses used for the experiment have a wavelength of around 1050 nm (60-80 nm FWHM) and a repetition rate tuned to 2.7 MHz (f_{rev}). The laser was operated in a bursting regime with one burst every storage ring revolution period. The burst contains 2 or 3 laser pulses (one pulse every 16 ns) in order to get one pulse modulated by the electron bunch through the EO crystal and an other one has a reference background signal (Fig. 2). The reference signal is then subtracted from the modulated signal in the post data analysis.

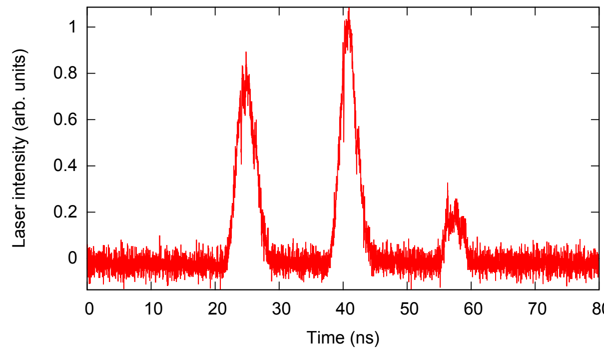

Figure 2: One burst of three laser pulses. The first pulse interacts with the electron beam in the EO crystal while the second one is used as a reference signal. Note that these stretched pulses are recorded using the fast photodetector after propagation in the photonic time-stretch setup.

The laser system is placed outside the radiation protection wall of the storage ring, the amplified laser pulses are then sent via a 35 m long polarization maintaining fiber to the EO-Monitor. The fiber-coupled EO-Monitor transports the laser beam into the UHV of the storage ring and back out to the laser hutch for analysis. It is based on a design from PSI [19,20] which has been extended by a grating compressor to control the laser pulse length right before the pulses are sent to the EO crystal. After the laser enters the UHV through a viewport, it is reflected by a silver coated prism used as a mirror and sent towards the 5 mm thick GaP crystal. The laser light enters the crystal through the front surface and is then reflected by its high-reflex coated back surface (see [10] for a detailed description).

The modulation of the laser pulse by the electric field of the bypassing electron bunch happens when both the electron bunch and the laser pulse co-propagate in the crystal. The distance of the EO-crystal to the electron beam can be adjusted precisely via a linear motion feedthrough that moves not only the crystal, but also the whole EO-Monitor, this ensures that the optical delay remains unchanged when moving the crystal in. For operation at a storage ring, the EO-Monitor has been extended with a movable metallic shutter (impedance protection) that can fully cover the hole inside the UHV vacuum chamber to minimize impedance effects during normal user operation when the crystal is fully retracted from the beam pipe. With the current design, measurements are only possible during single- or dual-bunch operation because of thermal power generated by wake-fields (see [14]). Typical distances of the EO crystal from the electron beam are in the order of 5-6 mm (center of beam pipe to bottom tip of crystal) for which we detect no significant increase in the local beam loss rate with a very sensitive loss detector (lead glass scintillator coupled with a photomultiplier tube) that is placed in a dispersive section a few meters downstream of the EO-Monitor.

For the actual measurement, temporal overlap between the laser pulse and the electron bunch needs to be achieved

ISBN 978-3-95450-176-2

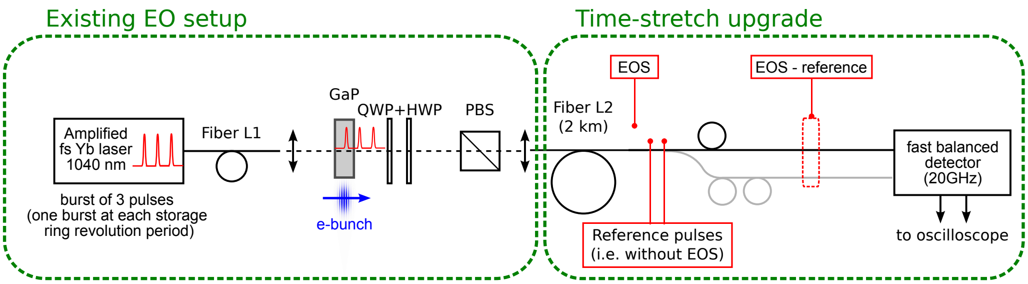

Figure 3: Upgrade of the electro-optical spectral decoding setup with the photonic time-stretch method. The modulated pulses are no more detected in the spectral domain but are stretched in a 2-km-long fiber (L2) and detected in the time domain with a fast photodetector ("Time-stretch upgrade"). With this new strategy, two detection schemes are possible: two laser pulses are detected one a single detector with one pulse that contains the information and an other one as a reference signal; or the signal is split and one part is delayed by one laser period (i.e. 16 ns) and analogically subtracted from the other part in a balanced detector in order to remove the laser envelope background.

inside the EO-crystal. To adjust the temporal overlap with an accuracy in the order of 1 ns, we use the direct signal of one of the four buttons of a nearby button BPM and compare its arrival time in relation to the signal of the laser pulses (measured with a fast photodiode) with an oscilloscope. The fine adjustment of the time delay (sub-ps accuracy) is then done with a step wise scan of the vector modulator that lets us delay the laser pulse very precisely while monitoring the amplitude of the modulated laser signal.

The detection of the modulated laser pulses in the laser hutch was upgraded using the time-stretch strategy (Fig. 3). Instead of detecting the laser pulses with a grating spectrometer, they are stretched in a 2-km-long fiber[1] before detection, in order to get a final pulse duration of around 4 ns and are then detected using a balanced photodetector[2] with a 20 GHz bandwidth and 2800 V/W gain (specified at 1500 nm). The two differential outputs of the detector are sent on a Lecroy LabMaster 10i oscilloscope with 36 GHz bandwidth, 80 GS/s sample rate on each channel, and a memory of 256 Mega samples. This setup permits two different detection schemes. The first one consists in recording the laser pulses on one single detector and to subtract the reference signal containing the envelope of the unmodulated laser pulse in the post-process analysis. The second configuration used a balanced detection strategy. In that case, the signal is split and one part is optically delayed using a fiber longer by one laser period (i.e. 16 ns) (gray path in Fig. 3). The unmodulated laser envelope is then subtracted analogically from the other part in a balanced detector.

The readout of the previous setup using a commercial line array inside the spectrometer has a limited acquisition rate of about 7 fps (193 fps is the limit of the hardware). The time-stretch recording system is able to acquire 62.5×10^6 bunch profiles per second. This allows us to record the longitudinal bunch profiles at each turn in the storage ring, i.e. every 368 ns.

[1] HI1060 from Corning
[2] DSC-R412 InGaAs amplified balanced photodetector (photoreceiver) from Discovery Semiconductors

MEASUREMENT RESULTS

The ANKA storage ring was operated in low-α_c configuration with a beam energy of 1.3 GeV, in single-bunch mode. The current per bunch was around 3 mA.

In order to convert the stretched time of the recorded signal at the input of the oscilloscope, which is in the nanosecond range, we calibrate the time-stretch setup by delaying the probe laser pulse in well-know step over few picoseconds and measure the shift of the EO signal in the stretched laser pulses. Figure 4 shows the calibration curve. The slope gives the conversion factor from the stretched time in ns to the real time of the phenomenon in ps. Here, 1 ns corresponds to a real time of 12.8 ps, which corresponds to a stretch factor of 78.

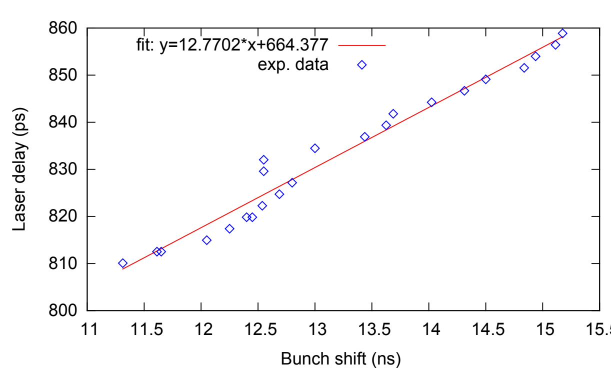

Figure 4: Calibration of the stretch factor. The curve represents the delay in picosecond of the probe laser pulse versus the shift of the bunch profile in the EO signal in nanosecond.

The upgrade of the existing EOSD setup at ANKA with the time-stretch setup allowed us to record longitudinal bunch profile for each revolution turn in the ring. Figure 5 shows 10 successive single-shot longitudinal profiles. In practice, the acquisition is done using one single detector with two laser pulses, one containing the EO signal and an other one used as a reference signal to subtract the laser envelope.

ISBN 978-3-95450-176-2

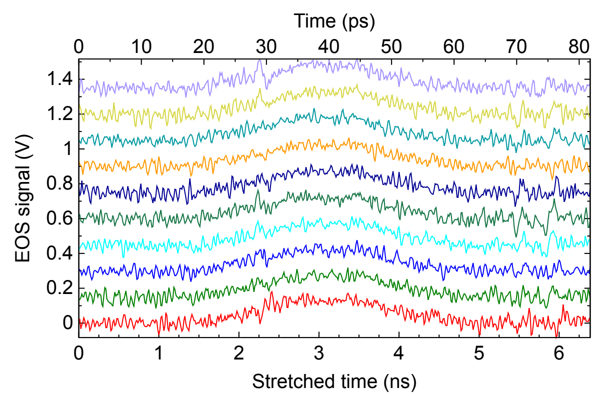

Figure 5: Single-shot recordings of longitudinal bunch profiles using the time-stretch strategy. The curves are shifted vertically for better clarity. The lower scale corresponds to the time at the oscilloscope input (i.e., after the photonic time stretch by a factor 78). The time between pulses is of 368 ns, i.e. equal to electron bunch revolution period.

The EO signal has been compared to the longitudinal bunch profile recorded with the streak camera. The rms bunch length measured with the streak camera was equal to 8 ps. Figure 6 shows a single-shot EO acquisition of a bunch profile (blue dots) and its gaussian fit (red line). The measured bunch length with the EO setup is 8.4 ps, which is in good agreement with the streak camera measurements.

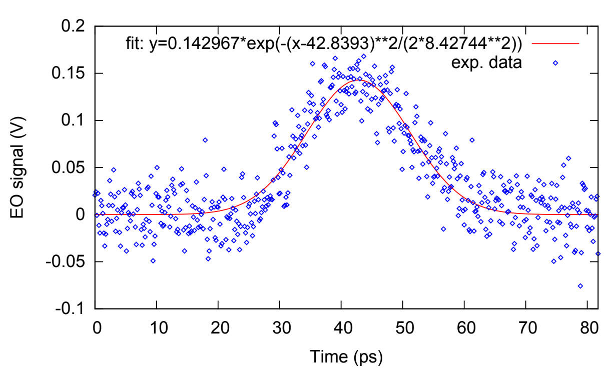

Figure 6: Single-shot longitudinal bunch profile recorded with the time-stretch strategy.

CONCLUSION

We have successfully upgraded the existing near-field EOSD measurements of the ANKA storage with the photonic time-strech. The time-stretch permits single-shot, high-acquisition rate detection of ps shapes. We applied the time-stretch EOSD setup to the direct real-time monitoring of the near-field longitudinal bunch profile turn-by-turn over several milliseconds. These measurements open new perspectives for a detailed comparison between the evolution of the longitudinal bunch shape and the bursting behavior of the CSR emission. In parallel, there is a joint collaboration ongoing for the development of an ultra-fast linear detector array that will allow a continuous data readout at up to 5 Mfps [22].

ACKNOWLEDGMENTS

Many thanks to the colleagues who operated ANKA during our measurement shifts and made our measurements possible.

REFERENCES

[1] E. Roussel *et al.*, "Observing microscopic structures of a relativistic object using a time-stretch strategy", Scientific Reports 5, 10330 (2015).

[2] A.-S. Müller *et al.*, “Far Infrared Coherent Synchrotron Edge Radiation at ANKA”, RPAE038, Proc. PAC’05, Knoxville, TN, USA (2005).

[3] N. Hiller *et al.*, “Observation of Bunch Deformation at the ANKA Storage Ring”, WEPEA020, Proc. IPAC’10, Kyoto, Japan (2010).

[4] N. Hiller *et al.*, “Status of Bunch Deformation and Lengthening Studies at the ANKA Storage Ring”, THPC021, Proc. IPAC’11, San Sebastian, Spain (2011).

[5] V. Judin *et al.*, “Observation of Bursting Behavior Using Multiturn Measurements at ANKA”, WEPEA021, Proc. IPAC10, Kyoto, Japan (2010).

[6] M. Klein *et al.*, “Simulations of the Microbunching Instability at ANKA using a Vlasov-Fokker-Planck Solver”, WEPC095, Proc. IPAC’11, San Sebastian, Spain (2011).

[7] V. Judin *et al.*, “Spectral and Temporal Observations of CSR at ANKA”, TUPPP010, Proc. IPAC’12, New Orleans, LA, USA (2012).

[8] N. Hiller *et al.*, “Electro-Optical Bunch Length measurements at the ANKA Storage Ring”, MOPME014, Proc. IPAC’13, Shanghai, China (2013).

[9] N. Hiller *et al.*, “Status of Single-Shot EOSD Measurements at ANKA”, MOPD17, Proc. IPAC’14, Dresden, Germany (2014).

[10] N. Hiller *et al.*, “Single-Shot Electro-Optical Diagnostics at the ANKA Storage Ring”, MOPD17, Proc. IBIC’14, Monterey, CA, USA (2014).

[11] K. Goda and B. Jalali, "Dispersive fourier transformation for fast continuous single-shot measurements", Nat Photon 7(2), 102-112 (2013).

[12] J. H. Wong *et al.*, "Photonic time-stretched analog-to-digital converter amenable to continuous- time operation based on polarization modulation with balanced detection scheme", Lightwave Technology, Journal of 29(20), 3099-3106 (2011).

[13] Y. Han and B. Jalali, "Photonic time-stretched analog-to-digital converter: fundamental concepts and practical considerations", Lightwave Technology, Journal of 21(12), 3085-3103 (2003).

[14] B. Kehrer *et al.*, “Numerical Wakefield Calculations for Electro-Optical Measurements”, MOPME015, Proc. IPAC’13, Shanghai, China (2013).

[15] A.-S. Müller *et al.*, "Experimental Aspects of CSR in the ANKA Storage Ring", ICFA, Beam Dynamics Newsletter 57, p. 154-165 (2012).

[16] I. Wilke *et al.*, "Single-Shot Electron-Beam Bunch Length Measurements", Phys. Rev. Lett. Vol. 88, No. 12 (2002).

[17] B. Steffen, "Electro-Optic Methods for Longitudinal Bunch Diagnostics at FLASH", PhD thesis, University of Hamburg, Hamburg, Germany (2007).

[18] F. Müller *et al.*, "Ytterbium Fiber Laser for Electro-Optical Pulse Length Measurements at the SwissFEL", TUPD31, Proc. DIPAC'09, Basel, Switzerland (2009).

[19] B. Steffen *et al.*, "A Compact Single Shot Electro-Optical Bunch Length Monitor for the SwissFEL" TUPB42, Proc. DIPAC'09, Basel, Switzerland (2009).

[20] F. Müller *et al.*, "A Compact Electro Optical Bunch Length Monitoring System - First Results at PSI", WEPA09, Proc. FEL'10, Malmö, Sweden (2010).

[21] N. Hiller, "Electro-Optical Bunch Length Measurements at the ANKA Storage Ring", PhD thesis, Karlsruhe Institute of Technology (KIT), Karlsruhe, Germany (2013).

[22] L. Rota *et al.*, "An Ultrafast Linear Array Detector for Single-Shot Electro-Optical Bunch Profile Measurements', TUPD10, Proc. IBIC'14, Monterey, CA, USA (2014).

ISBN 978-3-95450-176-2

SRF GUN CHARACTERIZATION - PHASE SPACE AND DARK CURRENT MEASUREMENTS AT ELBE*

E. Panofski#, A. Jankowiak, T. Kamps, Helmholtz-Zentrum Berlin, Berlin, Germany
P.N. Lu, J. Teichert, Helmholtz-Zentrum Dresden-Rossendorf, Dresden, Germany

Abstract

RF photoelectron sources with superconducting cavities provide the potential to generate high quality, high brightness electron beams for future accelerator applications. At Helmholtz-Zentrum Dresden-Rossendorf, such an electron source was operated for many years. The commissioning of an improved SRF Gun with a new high-performance gun cavity with low field emission and a superconducting solenoid inside the gun cryomodule (SRF Gun II) has started in June 2014. First low current measurements as well as studies of unwanted beam transport using SRF Gun II with a Cu photocathode and an acceleration gradient up to 7 MV/m will be presented. First longitudinal beam characterization of the SRF Gun in combination with ELBE, a two-stage superconducting linear accelerator will be discussed.

INTRODUCTION

Helmholtz-Zentrum Dresden-Rossendorf has provided a test stand for SRF gun technology since 2007. Furthermore, this SRF gun can also be used as an electron source for the two-stage superconducting linear accelerator ELBE. In order to reach a higher acceleration field in the cavity and therefore peak electron energy, a new high-performance gun cavity attended by a superconducting solenoid was assembled in the gun cryomodule in May 2014 [1]. For successful application of the new injector commissioning and full beam characterization of SRF Gun II is required. The presented low current measurements focus on longitudinal phase space characterization and first studies about unwanted beam transport.

For future applications, such as driving X-Ray FEL facilities, the longitudinal phase space distribution plays a critical role. Therefore, good understanding of the longitudinal phase space of the photoelectron source is required. The new high-performance gun cavity design of the photoinjector offers low field emission which will be investigated by measuring dark current from SRF Gun II. Unwanted beam transport to the ELBE beamline is determined by the energy acceptance of the dogleg.

This paper starts with a short overview about the design parameters of the SRF gun as well as the relevant operation parameters of the photoinjector in combination with the linear accelerator ELBE. A review of the experimental technique measuring the longitudinal phase space, followed by a description of the data analysis method is given. All experimental results for the longitudinal phase space are presented. The final section of this paper will summarize first studies of the energy acceptance of the dogleg and therefore the transport of dark current, generated by the SRF gun, into the ELBE beamline.

* Work supported by BMBF & Land Berlin
# eva.panofski@helmholtz-berlin.de

COMMISSIONING OF THE SRF GUN

All beam characterization measurements are done with the SRF Gun II in combination with two-stage linear accelerator ELBE. Figure 1 represents the schematic setup.

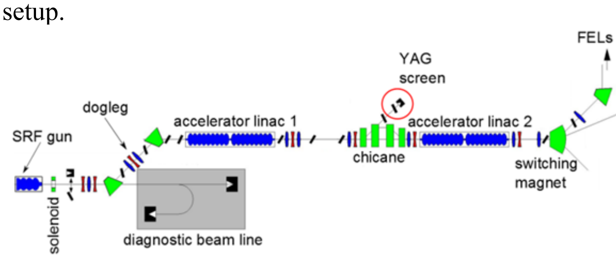

Figure 1: SRF Gun and ELBE beamline at HZDR Dresden [2].

Setup and Operation Parameters

The 1.3 GHz Nb gun cavity consist of 3.5 TESLA cells with a normal conducting Cu photocathode installed in the backplane of the half cell. In order to supress multipacting a DC bias voltage is applied on the photocathode. The cathode is illuminated by 266 nm UV laser light. The drive laser provides 6 ps (rms) long laser pulses with a repetition rate of 100 kHz and an approximately uniform, 2mm transverse profile [1]. Due to the low quantum efficiency of the copper cathode ($\sim 10^{-5}$) only low bunch charges typically smaller than 5 pC are achieved. Therefore, space charge effects can be neglected for all measurements presented in this paper. The generated electron beam is accelerated with maximum gradient (peak field) of 18 MV/m corresponding to a kinetic energy of 3.5 MeV at the gun exit.

Afterwards, the electron beam is guided through the achromatic dogleg to ELBE beamline. The dogleg consists of two bend magnets attended by three quadrupoles which control the horizontal dispersion. The final acceleration up to 19 MeV takes place in the two superconducting cavity modules (C1, C2) of ELBE Linac 1. For all longitudinal phase space measurements presented in this paper the first dipole of the chicane is used to deflect the electron beam with a bend angle of 45° to the YAG screen in the diagnostic beamline.

All relevant measurement conditions and machine settings are summarized in Table 1.

ISBN 978-3-95450-176-2

Table 1: Parameters of SRF Gun II and ELBE

SRF Gun		
Laser wavelength	λ	266 nm
Laser rep. rate	f_{Laser}	100 kHz
Laser pulse length	σ_{Laser}	6 ps
DC bias cathode	V_{bias}	-5 kV
Field (peak)	E_{acc}	7 MV/m (18 MV/m)
ELBE		
Gradient C1	$E_{acc}(C1)$	9.7 MV/m
Gradient C2	$E_{acc}(C2)$	5.3 MV/m

Commissioning of SRF Gun II

The longitudinal phase space of the SRF Gun II can be evaluated at the diagnostic beamline of the photoinjector [3]. Using the 180° dipole together with a YAG screen the energy as well as the energy spread at the gun exit can be determined as function of laser phase. This measurement was done for two different laser phases, 49.4° and 56.6°. The kinetic energy for both phases is 3.59 MeV. After calibrating the screen, an energy spread of $23.04 \pm 0.96\,keV$ is found for 49.4° laser phase while 56.6° corresponds to an energy spread of $13.44 \pm 0.96\,keV$.

The emission length can be estimated by measuring the beam current with a Faraday Cup while varying the laser phase. This so called Schottky Scan for a maximum laser intensity (fully open aperture) and two different DC bias voltages 0 kV and -5 kV is shown in Fig. 2. The beam current measurement without DC bias was done in order to establish the relative phasing between gun and laser. A small current of approximately 20 nA at negative decelerating laser phases provides a measure for dark current. The beam current rises linearly up to 10° laser phase then the whole electron bunch is accelerated in the gun cavity. Due to Schottky effect, the electron beam current is further increased. Finally, the gun cavity design (3.5 cells) limits the plateau length.

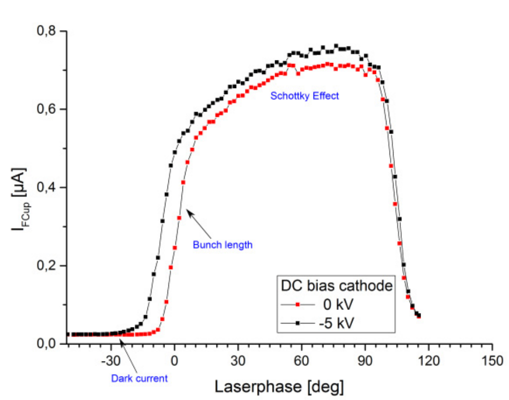

Figure 2: Schottky Scan.

The emission time can be extracted from the slope of the graph. Assuming a Gaussian longitudinal bunch distribution the slope of the beam current can be fitted with a Gauss error function (Eqn. 1) as shown in Fig. 3.

$$F(x) = \frac{1}{2}\left(1 + erf\left(\frac{x-\mu}{\sqrt{2\sigma^2}}\right)\right) \qquad (1)$$

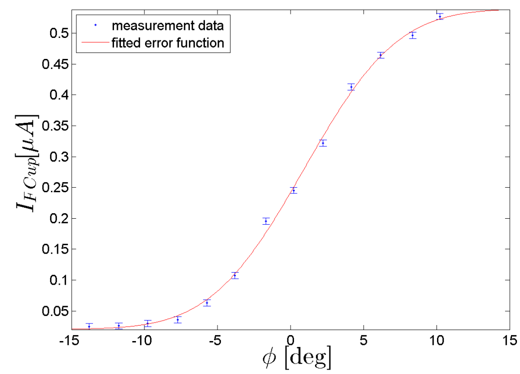

Figure 3: Bunch length estimation from error function fit.

An emission length σ_t of 10.7±2.6 ps is calculated from the fit parameter. Compared to the 6 ps laser pulse the evaluated bunch length is overestimated by at least 4 ps due to the fit quality as well as the accuracy of the displayed laser phase (±0.5°). Furthermore, the rising Schottky effect as well as beam dynamics will influence the measurement values at the end of the slope. Nevertheless, the Schottky scan can be used to estimate the bunch emission length and provides an important control tool in the commissioning procedure.

LONGITUDINAL PHASE SPACE

Phase Scan Technique

The beam characterization of the longitudinal phase space is performed using the phase scan technique illustrated in Fig. 4. Accelerated in a RF cavity module each bunch of finite length receives an energy chirp in longitudinal direction. After passing a dispersive beampath element e.g. a dipole, the energy spectrum is projected in the transverse plane. In the phase scan technique the longitudinal phase space distribution is measured for different RF phases of the linac cavity. Analysis provides the longitudinal parameters at the cavity entrance.

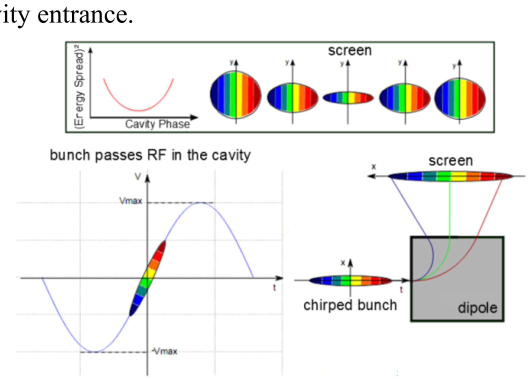

Figure 4: Illustration of phase scan technique [4].

ISBN 978-3-95450-176-2

The assumed longitudinal beam ellipse can be defined by

$$\tau = \begin{pmatrix} \tau_{11} & \tau_{12} \\ \tau_{12} & \tau_{22} \end{pmatrix} = \begin{pmatrix} \sigma_z^2 & \tau_{12} \\ \tau_{12} & \sigma_E^2 \end{pmatrix} \tag{2}$$

In this matrix the element τ_{11} describes the rms bunch length squared σ_z^2 and the element τ_{22} is the rms energy spread squared σ_E^2 [5]. During the phase space measurement the RF phase of the second cavity module in Linac 1 is varied. The first dipole of the chicane acts as a spectrometer. The transverse distribution behind the dipole and therefore the energy spread can be resolved on a YAG screen. The distribution is recorded using a CCD camera.

The transformation matrix of the longitudinal beam ellipse is determined by the linac cavity as well as the drift space up to the imaging point of the dipole onto the screen. Since the electron beam reaches relativistic velocity behind the linac module the drift space transfer matrix in the longitudinal phase space can be written as a unit matrix. Therefore, only the transformation of the beam matrix through the linac (Eqn. (3)) must be considered assuming a simple energy boost from the linac:

$$R_{Linac} = \begin{pmatrix} 1 & 0 \\ -2\pi\lambda_{HF}\dfrac{\Delta E}{E_0}sin\phi_0 & 1 \end{pmatrix} \tag{3}$$

ϕ_0 describes the RF phase of the reference electron. λ_{HF} is the RF wavelength while $\Delta E/E_0$ specifies the relative energy gain in linac C2. The longitudinal beam ellipse $\tau(1)$ at exit of cavity C2 is given by

$$\tau(1) = R_{Linac} \cdot \tau(0) \cdot R_{Linac}^T \tag{4}$$

Multiplying the matrices of Eqn. (4) matrix element $\tau_{22}(1)$ gives energy spread squared behind the linac, respectively on the YAG screen:

$$\delta_1^2 = \frac{4\pi^2\sigma_z^2}{\lambda_{HF}^2}\left(\frac{\Delta E}{E_0}\right)^2(sin\phi_0)^2 - 2\frac{2\pi\,\tau_{12}}{\lambda_{HF}}\frac{\Delta E}{E_0}sin\phi_0 + \delta_0^2 \tag{5}$$

The measured rms energy spread on the YAG screen for several linac phases ϕ_0 are fit with this parabola function in order to obtain the three matrix elements for the longitudinal phase space in front of linac module C2.

The rms bunch length determines the parabola width, while the correlated energy spread is obtained at ϕ_0=0. An offset in the vertex occurs due to the uncorrelated energy spread. The parabola vertex shift from ϕ_0=0 indicates correlation with the laser phase in the SRF gun.

Besides the rms bunch length and rms energy spread the longitudinal emittance can be calculated from the fit parameters (Eqn. (6)). The normalized longitudinal emittance is defined as

$$\varepsilon_{long,n} = \beta\gamma\sqrt{\delta_0^2\sigma_z^2 - \tau_{12}^2} \tag{6}$$

Experimental Results and Discussion

The energy spread for a range of linac phases ϕ_0 was observed for four different gun laser phases. Besides a small laser phase of 10.1° three measurements around the gun minimum energy spread at approximately 57° were performed. Figure 5 presents all experimental results together with their fits.

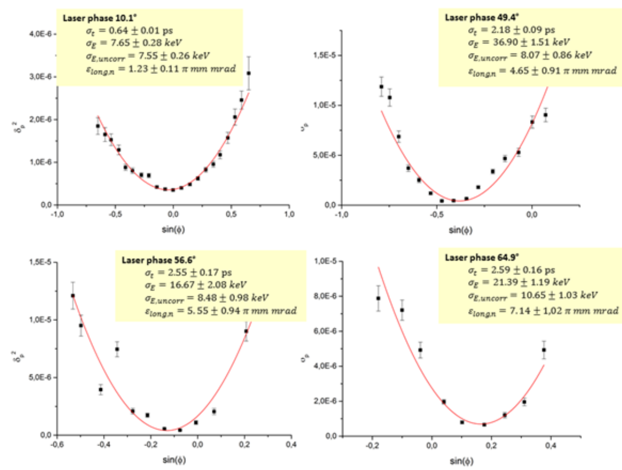

Figure 5: Energy spread measurement for four different laser phases with 19 MeV electron beam.

The measured correlated energy spreads represent the two energy spread minima from the SRF gun at low laser phase as well as at approximately 57°. The vertex shift at both minima is zero. Since there is no significant space charge effect due to the low bunch charge, thermal and RF contributions dominate the uncorrelated energy spread which is nearly constant at 8 keV. Our measurement results confirm the vertex shift correlation with the gun laser phase.

The bunch length is shorter than the rms laser pulse length of 6 ps, slightly reduced by RF bunch compression due to the energy chirp imparted to the beam in the RF field of the gun. Furthermore, bunch lengths seem to grow linearly with laser phase and therefore with bunch charge as evaluated in the Schottky scan in the range [10°, 90°]. The longitudinal emittance shows this linear dependence, as well [see Fig. 6][6].

All error bars shown in Fig. 5 take into account the 12 bit read out resolution of the CCD camera. The deviation of each illuminated pixel is estimated to one bin. Simulations confirm that the pixel resolution can be neglected than more than eleven pixels in diameter are illuminated. The parabola fits in the energy spread distribution measurements are weighted to the error bars. All specified errors for the calculated parameters of the longitudinal phase space refer to the standard deviation of the fit parameters weighted by the resolution of the CCD camera.

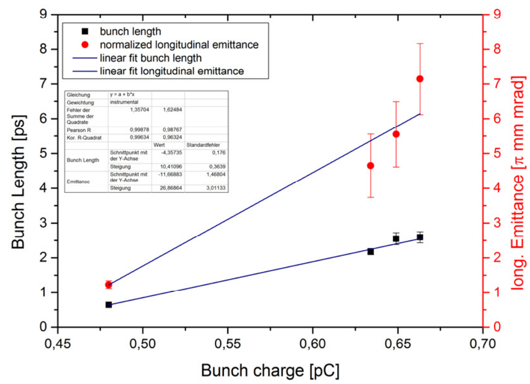

Figure 6: Linear dependence of bunch length and normalized long. emittance vs. bunch charge.

SRF GUN DARK CURRENT AND ENERGY ACCEPTANCE OF THE DOGLEG

In SRF photoinjectors sources of unwanted beam are dark current due to field emission and ghost pulses as well as beam halo due to scattered laser light and non-linear space charge forces. First studies evaluate the dark current at the gun exit. Furthermore, the transport of dark current through the dogleg into the ELBE accelerator which affects user operation and beam loss is investigated.

The current of unwanted beam can be determined using the Faraday Cup while the drive laser of the gun is switched off. A dark current of 18±2 nA is measured. This value is confirmed by the observed offset at negative laser phases in the Schottky scan.

The energy distribution of the dark current can be scanned using the first dipole in the dogleg. Imaged on a YAG screen, one significant dark current peak occurs with an energy of 2.3 MeV [see Fig. 7]. Since this energy is obviously lower than the gun exit energy of the electron beam at 3.5 MeV this low energy peak cannot arise from field emission or light scattering at the photocathode. Contributions from field emission at the cavity walls are assumed to dominate this dark current maximum.

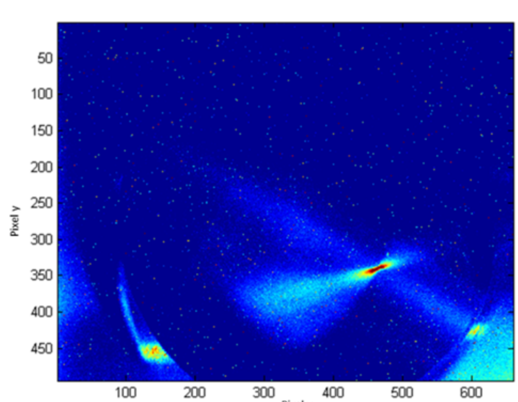

Figure 7: Dark current peak at 2.3 MeV on a YAG screen in the dogleg.

Dark current from the SRF gun can also affects beam operation in the main linear accelerator beamline. Unwanted beam transport to ELBE and therefore any impact of the gun generated dark current onto our beam dynamic measurements is determined by the energy acceptance of the dogleg. Changing the SRF gun gradient around 7 MV/m while all dogleg settings are kept constant the energy boundaries can be found where the electron beam is no longer transported through the dogleg [see Fig. 8]. The displayed beam intensity is assumed to be a convolution of different transmissions though the dogleg which is affected by fluctuations.

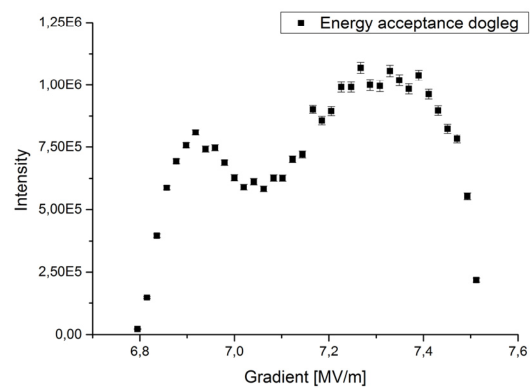

Figure 8: Energy acceptance of the dogleg.

The gradient can be varied between 6.8 MV/m and 7.5 MV/m which corresponds to a kinetic gun exit energy from 3.2 MeV to 3.6 MeV. Therefore, the detected dark current peak at 2.3 MeV does not match the energy acceptance of the dogleg during our beam dynamic measurements at a gun gradient of 7 MV/m.

Contrary to this dark current peak, low intensity unwanted beam can be transported to the linac section. Nevertheless, using a screen behind the dogleg but in front of module linac 1 no dark current contribution from SRF gun can be observed with an energy scan with the second dipole of the dogleg.

Further investigations of the dark current especially at higher gun gradients should be performed. New diagnostics for dark current and beam halo measurements, i.e. a wire scanner, will be installed in the near future.

SUMMARY AND OUTLOOK

The new SRF Gun II in combination with the ELBE accelerator provides promising results. Good characterization of the longitudinal phase space including first estimation of the emission length in the gun as well as measurements of correlated and uncorrelated energy spread, bunch length, longitudinal emittance and correlation to the gun laser phase are obtained in experiments performed with the SRF gun and ELBE accelerator. Dark current studies indicate the energy acceptance of the dogleg as a critical factor for unwanted beam transport to ELBE.

ISBN 978-3-95450-176-2

In order to investigate space charge effects further beam dynamic measurements are planned. The copper cathode will be replaced by Mg and Cs_2Te photocathodes which provide higher quantum efficiencies in order to obtain higher bunch charges. Further dark current and beam halo measurements will be attempted using the proposed wire scanner.

REFERENCES

[1] J. Teichert et al., "Commissioning of an Improved Superconducting RF Photoinjector at ELBE", THP061, Proceedings of FEL'14, Basel, Switzerland (2014).
[2] J. Teichert et al., "Evaluation of Critical R&D Issues of SRF Guns", EuCARD SRF Review 2011.
[3] T. Kamps et al., Rev. Sci. Instrum., 79 (2008) p. 093301.
[4] J. Rudolph, "Bunch Length Measurements and Status of the Slice Diagnostics System for ELBE/SCRF Gun", EuCARD SRF Review 2010.
[5] D.H.. Dowell et al., Nucl. Instr. and Meth. A 507 (2003) 331.
[6] S. Kashiwagi et al., "Photo-electron beam longitudinal phase space tomography studies at the ATF", Proceedings of LINAC'00, Monterey, California (2000).

ISBN 978-3-95450-176-2

BUNCH COMPRESSION DEPENDENT JITTER ANALYSIS WITH LARGE SPECTRAL RANGE

M. Kuntzsch[#], U. Lehnert, R. Schurig, J. Teichert, M. Gensch, P. Michel,
Helmholtz-Zentrum Dresden-Rossendorf, Dresden, Germany

Abstract

At the superconducting continuous wave (CW) accelerator ELBE electron bunch diagnostics have been installed, enabling the investigation of bunch arrival-time jitter for varying bunch compression states [1]. Using these diagnostic systems a comprehensive investigation has been performed that reveals the influence of the bunch compression to spectral noise components up to a frequency of 100 kHz. The contribution describes the measurement results taken for both electron injectors (DC-Gun, SRF-Gun) at the ELBE facility and will give an interpretation of different noise components. Arrival time jitter of the electron bunches is directly transferred into jitter of the secondary radiation generated by the ELBE beam.

INTRODUCTION

Pulse Compression Scheme

The ELBE Accelerator uses two magnetic chicanes to compress the picosecond bunches to the 100 fs regime. The correlated energy spread after the first accelerating module leads in combination with the first chicane to a temporal stretch of the electron bunches. The cavities installed in the second module are operated far off-crest to introduce a large chirp, i.e. a linear correlation between particle energy and longitudinal coordinate. Together with the transport matrix element R56 an energy dependent path deviation in the chicane leads to a longitudinal bunch compression. Figure 1 shows the ELBE accelerators' layout with the two electron injectors and two accelerating modules and illustrates the bunch compression scheme.

Bunch Arrival Time Monitor (BAM)

The bunch arrival time monitor takes advantage of an optical synchronization system that has been installed at ELBE [2]. The stabilized laser pulses provided by that system are used as a timing reference in the BAM. A probe of the electron's electric field passing by is extracted using a broadband electric pickup [3]. The signals are combined in an electro-optic modulator (EOM) which leads to an intensity modulation of single laser pulses according to the phase relation between the reference and pickup signal. Using this technique timing variations are mapped into amplitude modulations of the laser pulses.

The BAM-System installed at ELBE is capable to operate at MHz repetition rates in CW operation and enables arrival time measurements for individual electron bunches with a high resolution [3].

Bunch Compression Monitor (BCM)

The bunch compression monitor uses coherent diffraction radiation or coherent transition radiation generated by the electron pulses passing a boundary of a silicon screen. The intensity of the emitted coherent radiation pulse is dependent on the electron bunch duration [4] and can be used as a qualitative measure for the bunch compression state at the screen position. The shorter the electron bunches the higher the intensity of the coherent radiation pulse. At ELBE the BCMs are used to optimize the compression state of the electron bunches while tuning up the machine. Their application for an active beam-based feedback in order to stabilize the bunch compression state on the target position is currently being evaluated.

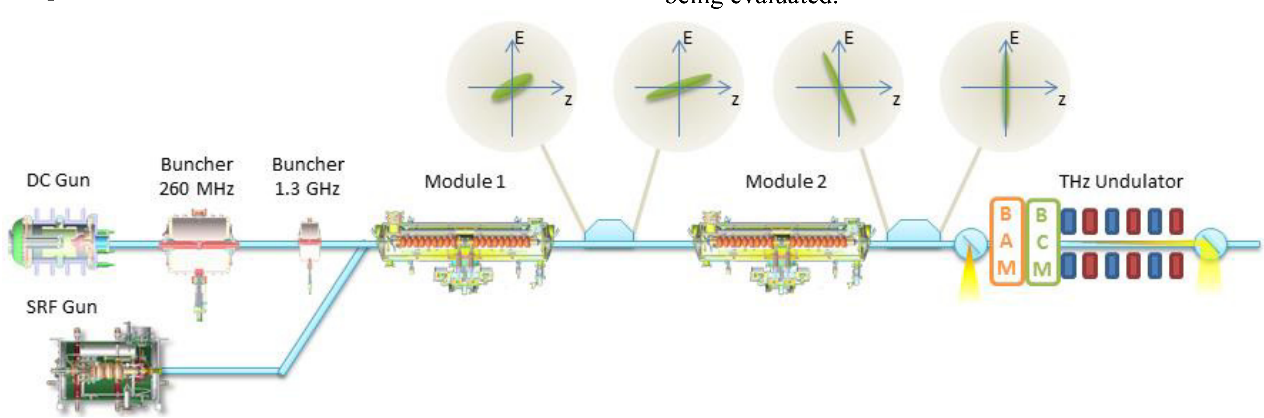

Figure 1: ELBE layout and bunch compression scheme for short pulse operation.

[#]m.kuntzsch@hzdr.de

ISBN 978-3-95450-176-2

MEASUREMENT RESULTS

The diagnostic systems have been used to characterize the behavior of the electron bunches at varying compression states. The investigation was mainly focusing on changes of arrival time of the electron bunches which have direct impact on time resolved experiments with secondary radiation at ELBE.

In order to compress the electron bunches a magnetic chicane after the second accelerating module (LA2) is used. For optimization of the bunch compression process, the R56 of the chicane is kept constant and the phase of LA2 is tuned, while the nominal energy of the electron bunches is maintained by adjusting the accelerating field amplitude. By introducing a very large chirp the over-compression regime is entered where the pulses become longer again.

Thermionic Injector

The user operation at ELBE is mainly served with the thermionic injector. The electrons are accelerated in a DC field up to an energy of 235 keV. The subsequent normal conducting cavities compress the electron bunches from 500 ps RMS to 3 – 5 ps RMS before they enter the superconducting cavities of the main accelerator. The stability of the high voltage supply is a crucial element for the temporal and energy stability of the electron beam entering the main accelerator [5].

Figure 2 shows the normalized output signal of a bunch compression monitor with respect to the phase of LA2. The maximum signal amplitude marks the minimum bunch length. The minimum bunch length can be observed at 156 degree for this specific setting.

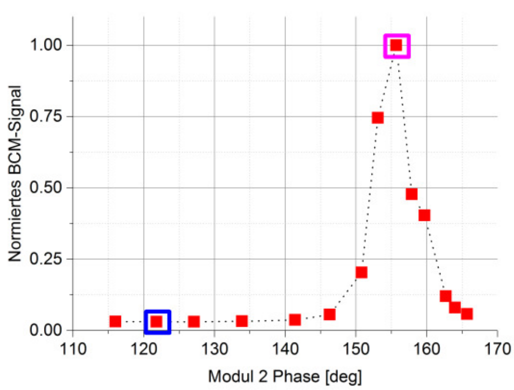

Figure 2: Normalized BCM signal for the thermionic injector changing the bunch compression by adjusting the phase of the 2nd module.

Figure 3 shows the power spectral density of the arrival time measurement and the integrated RMS-jitter for the thermionic injector. For low compression states (blue) the high frequency noise components are more dominant while the low frequency noise components are lower compared to the high compression state (red). The total jitter in the spectral range from 10 Hz to 50 kHz has changed from 750 fs RMS to 1 ps RMS. For all the measurements performed the 50 Hz line frequency and its harmonics are the most dominant noise sources.

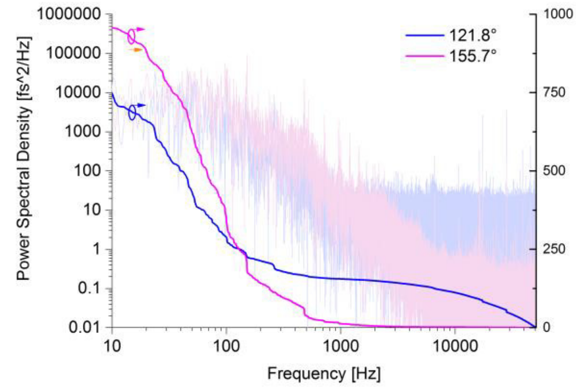

Figure 3: Power Spectral Density of the arrival time measurement and the integrated RMS-jitter at the thermionic injector.

Superconducting RF Injector

A superconducting RF photo injector is currently under development at HZDR [6]. It will provide high average current at low emittance in CW for the ELBE accelerator. For the predecessor of the currently installed cavity the same examination as for the thermionic injector has been performed. That means the chirp and thereby the bunch compression has been varied and the bunch arrival time has been measured.

Figure 4 shows the compression response on the variation of the phase of the second superconducting accelerating module. In this case the maximum compression is achieved at 97 degree phase shift.

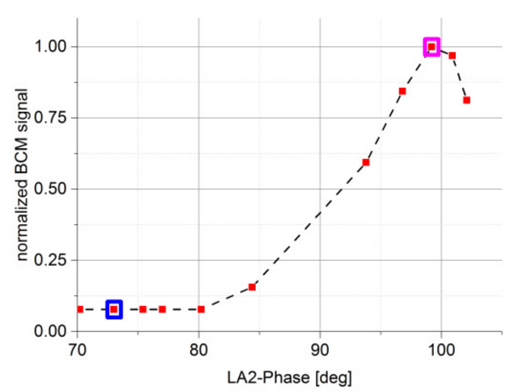

Figure 4: Normalized BCM signal for the SRF injector changing the bunch compression by adjusting the phase of the 2nd module.

In Figure 5 the results of the arrival time measurement are presented. For low compression the arrival time jitter is in the in the order of 100 fs RMS in the displayed spectral range. For high compression, the low frequency

ISBN 978-3-95450-176-2

components become more dominant and lead to a jitter of 220 fs RMS. At the same time the high frequency noise is reduced. The general behavior is very similar to the beam injected by the DC gun but the absolute jitter is by a factor of five lower. The measurement shows that the 50 Hz line frequency is a major jitter contributor.

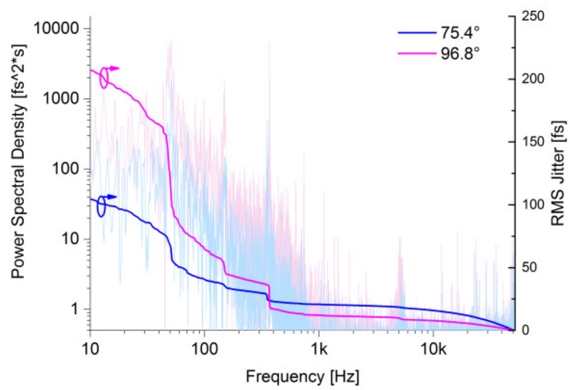

Figure 5: Power Spectral Density of the arrival time measurement and the integrated RMS-jitter at the SRF injector.

CONCLUSION

The measurements performed revealed a strong dependence of the beam arrival time jitter on bunch compression for both injectors used at ELBE. The SRF Gun generates more stable bunches than the thermionic injector. The DC Gun is affected by instabilities from the high voltage and the buncher section [5].

The high frequency noise is believed to be generated by the injectors because it is reduced while increasing the bunch compression. According to [7] the arrival time jitter in front of LA2 is reduced by the bunch compression factor. In addition, the high quality factor of the superconducting cavities suppresses high frequency variations of the RF filed.

The low frequency noise is mainly introduced by the superconducting accelerating modules. The phase and amplitude is varying with the line frequency which is modulated on the electron beam energy. Together with the second chicane these variations appear as arrival time changes.

OUTLOOK

In order to eliminate the jitter components, further accelerator studies have to be performed. The investigation will focus on the high voltage power supply, the pulse generation on the electron gun and on the phase stability of the normal conducting buncher cavities operating at 260 MHz and 1.3 GHz.

In parallel, the RF generation has to be improved to suppress the line frequency noise and a beam based feedback will be installed to eliminate the residual jitter.

REFERENCES

[1] M. Kuntzsch, S. Findeisen, M. Gensch, et al., Electron Bunch Diagnostic at the Upgraded ELBE Accelerator: Status and Challenges, 2nd International Beam Instrumentation Conference (IBIC 2013) Oxford, United Kingdom, 2013.

[2] M. Kuntzsch, A. Buechner, M. Gensch, et al., Status of the Femtosecond Synchronization System at ELBE, Beam Instrumentation Workshop (BIW12), Newport News, USA, 2012.

[3] A. Angelovski, M. Kuntzsch, M. K. Czwalinna, et al., Evaluation of the cone-shaped pickup performance for low charge sub-10~fs arrival-time measurements at free electron laser facilities. In: *Physical Review Special Topics - Accelerators and Beams* 18 (2015), S. 012801.

[4] S. Casalbuoni, B. Schmidt, P. Schmüser, Far-infrared Transition and Diffraction Radiation: Production, diffraction effects and optical propagation. Hamburg, 2005.

[5] M. Kuntzsch, U. Lehnert, R. Schurig, et al., CW Beam Stability Analysis in Time and Frequency Domain, IBIC 2014 - 3rd International Beam Instrumentation Conference, Monterey, USA, 2014.

[6] A. Arnold, M. Freitag, P. Murcek, et al., Commissioning and first RF results of the second 3.5 cell SRF gun for ELBE, 27th Linear Accelerator Conference - LINAC14, Geneva, Switzerland, 2014.

[7] H. Schlarb, Techniques for pump-probe synchronisation of FSEC radiation pulses. In: *2005 IEEE Particle Accelerator Conference (Pac), Vols 1-4* (2005), S. 2541-2545.

ISBN 978-3-95450-176-2

TRIGGER GENERATOR FOR THE SUPERCONDUCTING LINEAR ACCELERATOR ELBE

R. Steinbrück, M. Kuntzsch, M. Justus, Helmholtz-Zentrum Dresden-Rossendorf (HZDR),Dresden
T. Bergmann, Bergmann Messgeräte Entwicklung (BME), Murnau
Alexander Kessler, Helmholtz-Institut Jena (HIJ), Jena

Abstract

The Center for High-Power Radiation Sources ELBE at Helmholtz-Zentrum Dresden-Rossendorf (HZDR) runs a superconducting linear electron accelerator for research applications. A recent machine upgrade enabled new time resolved experiments and made a replacement of the current trigger and clock generation system necessary. The requirements include centralization of trigger generation, improvement of trigger quality, and trigger pattern versatility. To address these needs digital delay generators, developed by Bergmann Messgeräte Entwicklung (BME), have been evaluated. These field programmable gate array (FPGA) based PCI boards have 6 independent trigger channels. Individual PCI modules can be connected by a dedicated trigger bus to extend channel count on demand. The boards are installed in an industrial personal computer (IPC) running Windows 7. Trigger generation runs stand-alone in the FPGA making it independent of operating system timing and ensuring stable phase relation between individual channels. Delay control is possible via C and LabVIEW libraries. A LabVIEW application will offer a graphical user interface (GUI) for local control and an OPC UA interface for control system integration.

INTRODUCTION

The ELBE accelerator is capable of CW operation with a frequency of up to 26 MHz. All timing signals for thermionic injector and superconducting radio-frequency photoinjector (SRF) [1], buncher resonators, macro pulser generator and so on are derived from a 13 MHz master clock oscillator. Currently these signals are generated by independent hardware components. A new structure for the ELBE timing system was proposed that can be seen in Figure 1. This was motivated by:

- a transition to an up to date hardware that is much easier to extend and to maintain,
- an inherent synchronization of all delay channels,
- a precise adjustment of delay channels in reference to each other,
- an increased flexibility of pulse train pattern definition,
- a reduced jitter.

This paper gives an overview of the hard and software structure of the central trigger system currently under development.

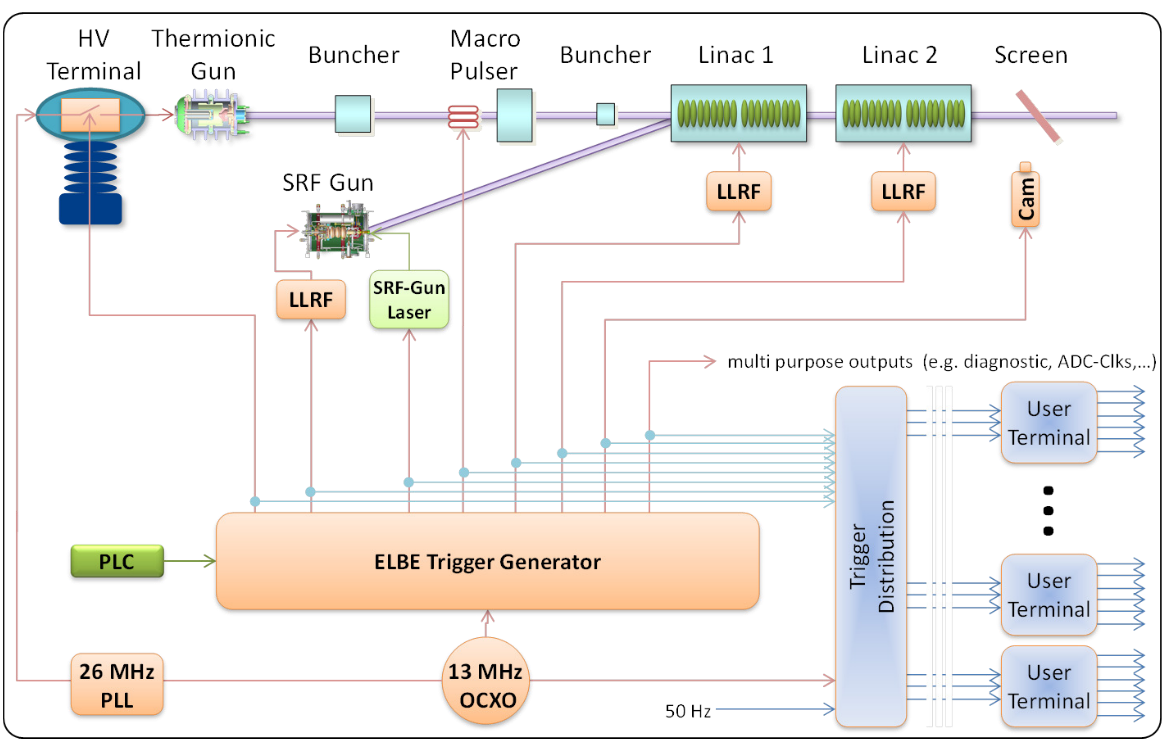

Figure 1: Projected structure of ELBE trigger distribution with central trigger generator. [2]

ISBN 978-3-95450-176-2

DELAY GENERATOR HARDWARE

Delay Generator Modules

BME offers a range of FPGA based digital delay generators. Type BME_SG08p [3] has been selected for the central trigger generator. These PCI modules provide 6 TTL outputs with a delay range from 50 ns to 429 s and a resolution of 25 ps. Trigger repetition rates between 0.002 Hz and 15 MHz are possible. Additionally channels can be pairwise combined by logical OR, XOR or AND operations. This feature is illustrated in Figure 2 where a 26 MHz trigger signal is generated by the disjunction of two 13 MHz signals. In this way it is possible to overcome the 15 MHz repetition limit and to produce the fastest trigger signal needed for the ELBE accelerator.

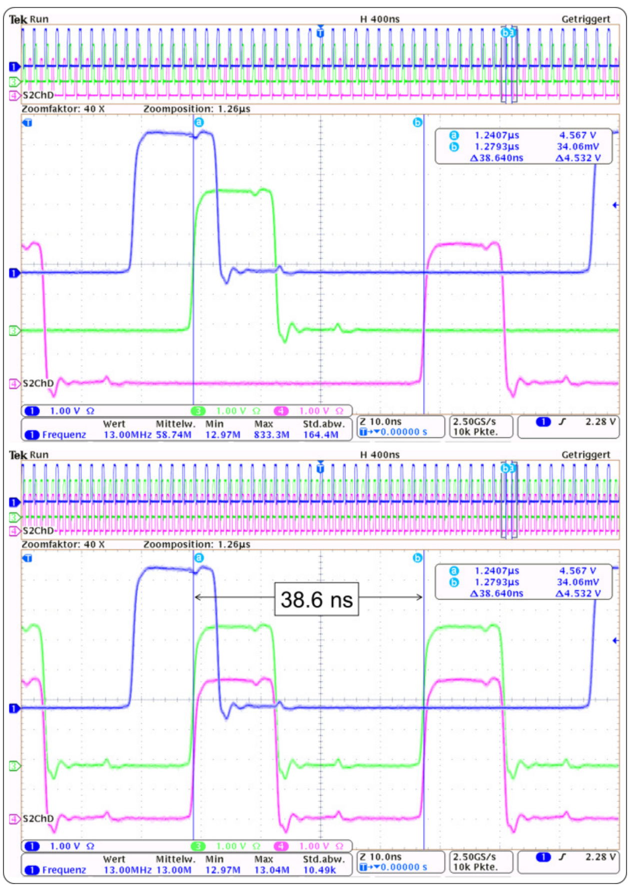

Figure 2: Disjunction of two 13 MHz delay channels (top) to produce a 26 MHz delay signal (bottom).

To increase the number of synchronized delay channels BME_SG08p modules can be connected with a Master/Slave bus cable.

In order to generate asymmetric pulse train patterns it is possible to load delay parameters into FPGA memory tables. These parameters are then cyclically or burst wise transferred into the delay registers after occurrence of selectable trigger events. Any parameter changes are synchronously activated on all delay channels, where any delay channel can be defined as synchronization source, i.e. the trigger for the parameter activation.

Besides standalone control software for Windows operating systems, libraries for C and LabVIEW programming are available.

Hardware Configuration

The PCI delay modules are installed in an IPC with redundant power supplies, high cooling capacity and 20 PCI slots. 18 of these slots are available for delay generators, allowing for up to 108 output channels.

The current system setup comprises five BME_SG08p delay generators. It is used in a laboratory setup (see Figure 3) for further tests and software development.

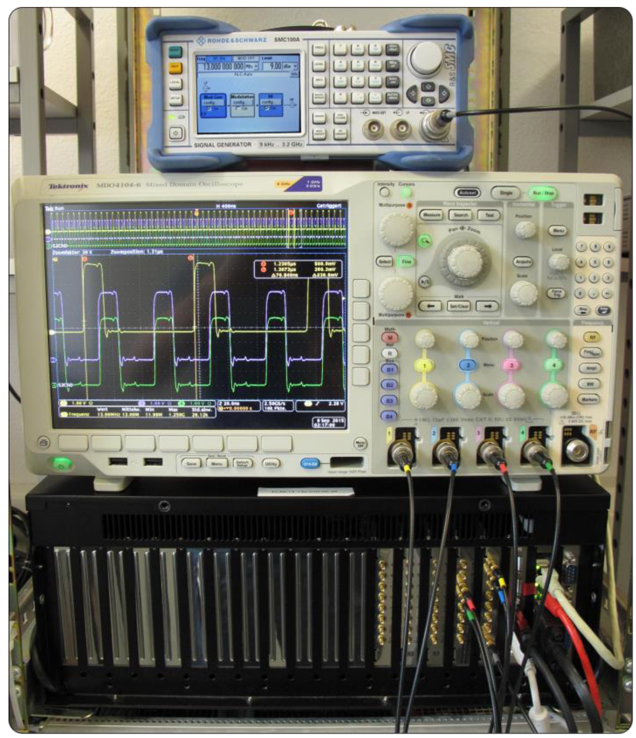

Figure 3: Trigger generator laboratory setup.

DELAY GENERATOR SOFTWARE

Control Application

A control application is under development that will be used to configure the trigger generator according to the ELBE operation requirements. On the one hand this includes configuration of delay generator hardware during setup and system start-up, on the other hand delay channel parameterization for different operating modes. The development environment is NI LabVIEW running on Microsoft Windows 7 64 Bit. Since all time critical operations are executed on the FPGAs of the delay modules, the trigger generation is independent of operating system and software timing issues. The application will run on the IPC and will be available for experts via remote desktop protocol inside the ELBE Ethernet network.

ISBN 978-3-95450-176-2

Only a reduced set of parameters has to be exchanged between the trigger generator and the ELBE control system. The data interface for these parameters is described in the following section.

Control System Integration

The ELBE control system is built with Siemens S7-300 and S7-400 programmable logic controllers (PLCs) [4] and WinCC supervisory control and data acquisition (SCADA). Since the machine interlock system (MIS) is parameterized on PLC level, depending on the machine operation mode, it is desirable to have a direct data connection between the trigger generator and the PLCs.

The LabVIEW Datalogging and Supervisory Control (DSC) Module [5] supports the upcoming OPC UA protocol [6]. Because of its interoperability and platform independence it has been chosen as a candidate for implementing the control system interface of the trigger system.

Although S7 PLCs do not directly support OPC UA, there are ready to use products closing this gap. The OPC UA gateway IBH Link UA [7] from IBH softec has been evaluated. This gateway is acting as OPC UA server, publishing data from Simatic S7 PLCs. At the same time it is an OPC UA client allowing to connect PLCs and external OPC UA servers. The OPC UA address space for PLC data can easily be set up and maintained based on the symbolic data from the according S7 PLC project. With the help of the IBH link UA it was possible to exchange control data between a S7 PLC and a LabVIEW application running on the trigger generator IPC.

Figure 4 gives an overview of the software and communication scheme.

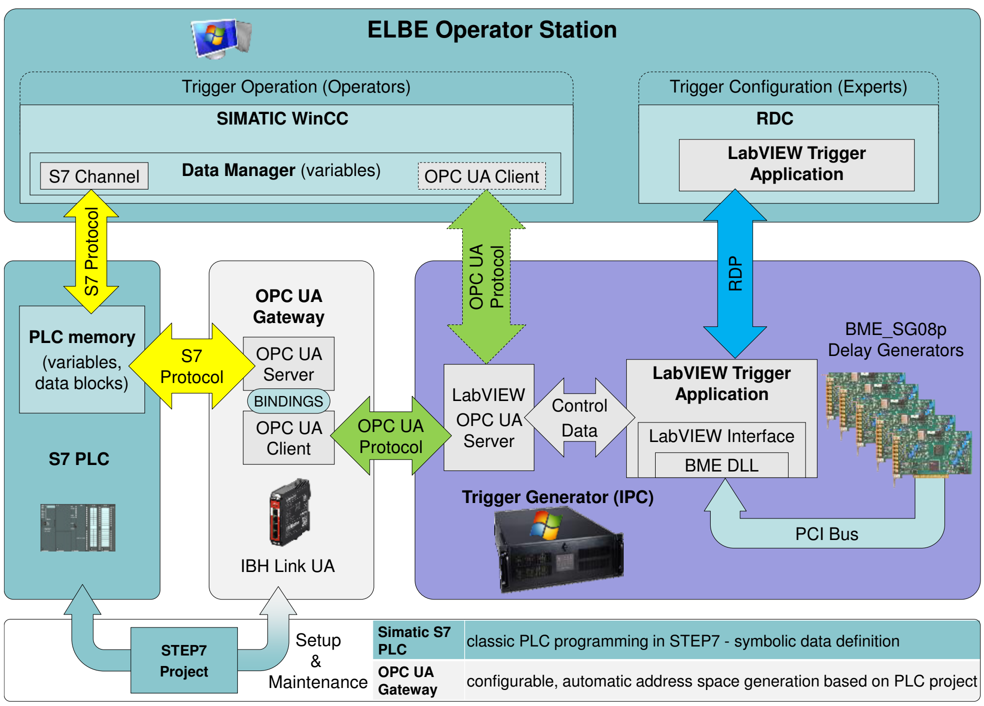

Figure 4:software structure and control system integration.

CONCLUSION AND OUTLOOK

All hardware components for the upgraded trigger system have been selected and evaluated. The trigger generator hardware is ready to use in a laboratory setup. A LabVIEW application to configure and control the trigger generators is under development. OPC UA technology has been successfully tested as an interface to the ELBE control system.

It is planned to finalize development of the trigger control application by end of this year. The trigger generator will then be installed in parallel to the current system to validate operation with the accelerator. After that the final step will be to establish the control system connection and make the trigger generator available for standard machine operation.

REFERENCES

[1] J. Teichert, et al., Free-electron laser operation with a superconducting radio-frequency photoinjector at ELBE, Nuclear Instruments and Methods in Physics Research A 743 (2014) 114.

[2] M. Kuntzsch, A. Büchner, T. Kirschke, U. Lehnert, F. Roeser, Future Timing and Synchronization Scheme at ELBE, Proceeding DIPAC 2011, May 16 – 18, 2011, Hamburg, Germany

[3] http://www.bme-bergmann.de/delay-pci8.htm

[4] http://w3.siemens.com/mcms/programmable-logic-controller/en/advanced-controller/Pages/default.aspx

[5] http://www.ni.com/labview/labviewdsc/d/

[6] https://opcfoundation.org/about/opc-technologies/opc-ua/

[7] http://www.ibhsoftec.com/IBH-Link-UA

ISBN 978-3-95450-176-2

VECTOR POLARIMETER FOR PHOTONS IN keV-MeV ENERGY RANGE

V. Gharibyan*, K. Floettmann, G. Kube, K. Wittenburg, DESY, Hamburg, Germany

Abstract

Light's linear and circular polarizations are analyzed simultaneously by vector polarimeters mainly in astrophysics. At higher energies Compton scattering or absorption is applied for linear or circular polarization measurements in satellites and accelerators. Here we propose a Compton scattering only vector polarimeter for monitoring photon beams in a non-invasive way. The setup is adjustable to match the initial photons' energy and can be used for diagnosing electrons' passage through undulators. In perspective the proposed device could also be explored to measure topological charge of the novel vortex photon beams.

INTRODUCTION AND OVERVIEW

As a consequence of the photon spin a beam of photons could possess an average spin which is often described in classical terms as an elliptical polarization [1]. That is a mixture of linear and circular polarizations - similar to transverse and longitudinal polarizations for a massive spinning particle.

Polarization is an important tool for generating and manipulating light in modern lasers as well as in a fast growing field of X-ray or gamma FEL(Free Electron Laser) research and applications. Recently FELs with tunable [2] or fast switching [3] polarizations have been developed for research in biology, chemistry, physics and material sciences.

For controlling the average spin one needs fast and precise measurement of light beam polarization which is increasingly difficult for high energy photon beams. That is why, the polarimeters, at high energies, are specialized for measuring either the linear or the circular polarization of the beam. In a keV-MeV energy range circular Compton polarimeters are designed [4] or used [5] for FEL radiation diagnostic while examples of linear Compton scattering polarimeters are found, apart from the accelerators, in astronomy (see Ref. [6] and references therein).

Advances in the above mentioned elliptical polarization generating FEL undulator devices require vector polarimeters to measure the linear and circular polarizations simultaneously. Such polarimeters are readily available for low frequency or energy photons within visible or near UV or IR parts of the electromagnetic spectrum (a recent example in astrophysics is described in Ref. [7]; for an undulator radiation see Ref. [8]).

Here we propose a high energy vector polarimeter based on Compton scattering.

* vahagn.gharibyan@desy.de

COMPTON KINEMATICS, CROSS SECTION AND SPIN ASYMMETRY

We review briefly some of the basic features of the Compton scattering process.

Definitions:

ω_0 and ω are the initial and final photon energies;
$E_0 = mc^2$ and E are the initial and final energies of the recoil electron;
θ and θ_e are the scattering angles of the photon and the electron.

The energies are related through energy conservation

$$\omega_0 + mc^2 = \omega + E \tag{1}$$

Furthermore, from momentum conservation follows

$$\omega = \frac{\omega_0}{1 + (\omega_0/mc^2)\,(1 - \cos\theta)} \tag{2}$$

The scattered photon and the scattered electron angles relative to the photon beam direction are

$$\cos\theta = 1 - \frac{mc^2}{\omega_0}\left(\frac{\omega_0}{\omega} - 1\right) \tag{3}$$

$$tg(\theta_e) = \frac{ctg(\theta/2)}{1 + \omega/mc^2} \tag{4}$$

The spin-dependent differential Compton cross section is

$$\frac{d\sigma}{d\Omega} = \frac{d\sigma_0}{d\Omega}\,(1 + P_\gamma^L A_L + P_\gamma^C P_e A_C) \tag{5}$$

with the unpolarized part

$$\frac{d\sigma_0}{d\Omega} = \frac{{r_0}^2}{2}\left(\frac{\omega}{\omega_0}\right)^2\left(\frac{\omega_0}{\omega} + \frac{\omega}{\omega_0} - \sin^2\theta\right) \tag{6}$$

where r_0 is the classical electron radius and

$$\frac{r_0^2}{2} = 39.71\,mb \tag{7}$$

and P_γ^L, P_γ^C and P_e are the linear, circular and longitudinal polarizations of the initial beam photon and the target electron respectively.

ISBN 978-3-95450-176-2

The spin asymmetries are given by

$$A_L = \frac{d\sigma_{L\perp} - d\sigma_{L\parallel}}{d\sigma_{L\perp} + d\sigma_{L\parallel}} = \frac{sin\ \theta^2}{\omega_0/\omega + \omega/\omega_0 - sin^2\ \theta}, \tag{8}$$

for the linear and

$$A_C = \frac{d\sigma_{1/2} - d\sigma_{3/2}}{d\sigma_{1/2} + d\sigma_{3/2}} = \frac{(\omega_0/\omega - \omega/\omega_0)\ cos\ \theta}{\omega_0/\omega + \omega/\omega_0 - sin^2\ \theta}, \tag{9}$$

for the circular photons. The cross-section indices in Eq.(8) stand for photon linear polarization perpendicular($\perp$) or parallel($\parallel$) to a fixed direction (along the axis x) and in Eq.(8) The indices in Eq.(9) correspond to parallel (3/2, along the axis z) and anti-parallel (1/2) spin orientation of the initial photon and electron.

The energy spectra of the scattered photon and electron are mirror images of each other because of equation (1). The spectra are continuous and extend from a minimum photon energy ω_{min} for backward scattering ($\theta = 180^o$)

$$\omega_{min} = \frac{mc^2}{2 + mc^2/\omega_0} \tag{10}$$

all the way up to the beam energy ω_0 for forward scattering ($\theta = 0$).

In Fig.1 we give the unpolarized differential cross section $d\sigma/d\Omega$ as a function of the photon scattering angle θ for monochromatic beam energies of 50, 400 keV and 1 MeV;

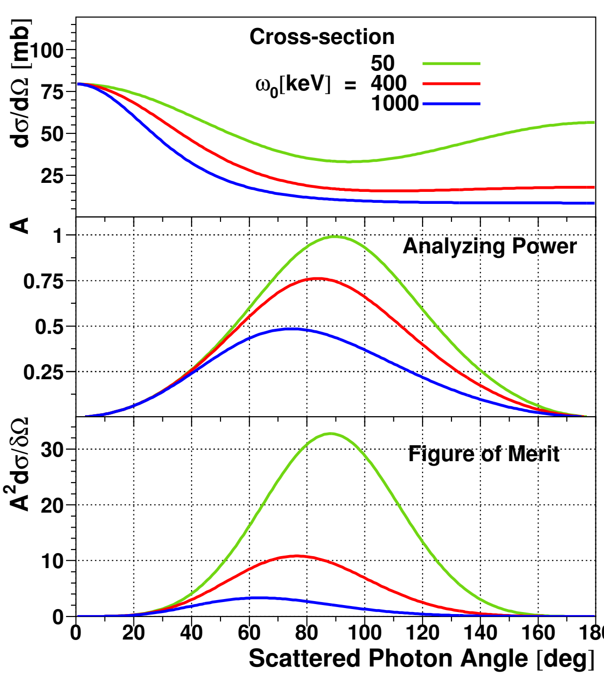

Figure 1: Linearly polarized photons Compton scattering cross-section, analyzing power and figure of merit for polarimetry. Dependence on photon's scattering angle are displayed for 50 keV, 400 keV and 1 MeV initial photon energies.

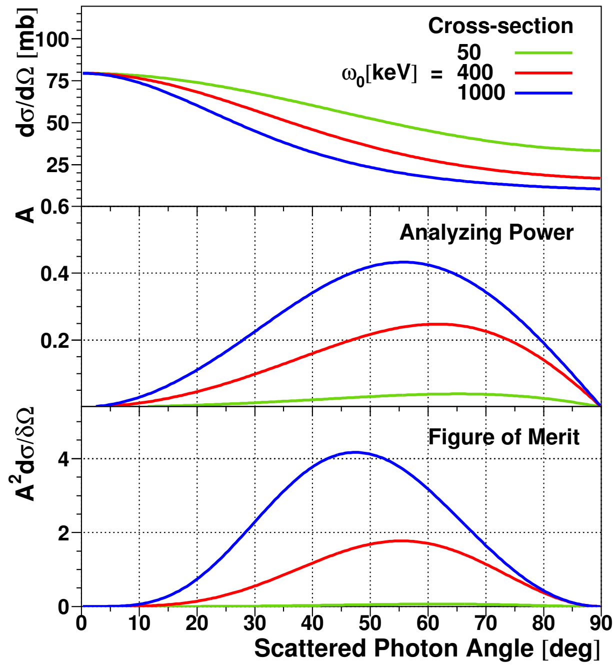

Figure 2: Circularly polarized photons Compton scattering cross-section, analyzing power and figure of merit for polarimetry. Dependence on photon's scattering angle are displayed for 50 keV, 400 keV and 1 MeV initial photon energies.

furthermore the spin asymmetry A and the figure of merit $A^2 d\sigma/d\Omega$ are plotted for the linearly polarized initial photon.

The same quantities are shown in Fig.2 for the circularly polarized initial photon. As it follows from Eq.(8) and Eq.(9) the asymmetries are relative differences of the cross-sections at $P_\gamma^L = \pm 1$ and $P_\gamma^C = \pm 1$ (with P_e=1) for the linear and circular photon polarizations correspondingly. Hence, the calculated asymmetries are Compton process analyzing powers for measuring the photon polarizations.

Within the keV-MeV energy range the formulas and plots indicate a high sensitivity of the Compton scattering to the photons' linear polarization at the lower, keV, energies which is degrading toward the higher, MeV, energies. For the circular photons, contrary to the linear case, the polarized Compton process sensitivity is low at keV energies growing higher at MeV scale.

EXPERIMENTAL CONFIGURATION

In order to obtain the photon beam polarization vector P_γ one needs to measure linear and circular spin asymmetries A_{lin}, A_{circ} as it defined by cross-section indices in Eq.(8) and Eq.(9) and normalize that to corresponding analyzing powers. Then, using Eqs.(8),(9) together with Eq.(5) one obtains polarization degrees:

$$P_\gamma^L = \frac{A_{lin}}{A_L}, \tag{11}$$

for the linear, and

$$P_\gamma^C = \frac{A_{circ}}{A_C P_e}, \tag{12}$$

for the circular case to derive the polarization vector magnitude

$$P_\gamma = \sqrt{(P_\gamma^L)^2 + (P_\gamma^C)^2}. \tag{13}$$

An experimental setup to measure the spin asymmetries A_{lin} and A_{circ} is displayed in Fig. 3 where a Compton target is placed in a reversible magnetic field of a solenoid and the scattered photons are registered by azimuthally displaced detectors.

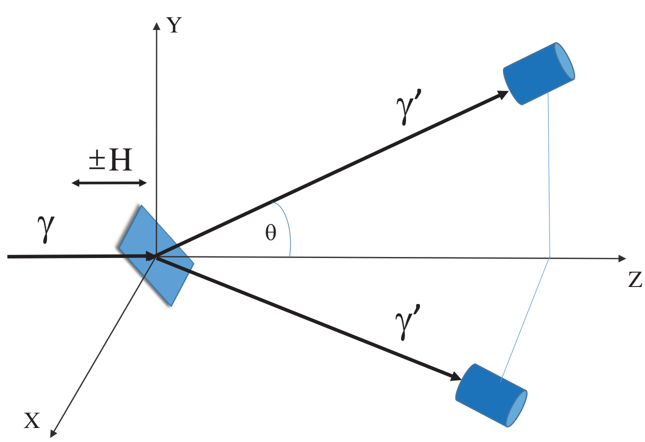

Figure 3: Experimental configuration for measuring photon beam linear and circular polarization.

In the Fig. 3 the photon beam enters from the left and strikes the polarized electron target (at z=0) which consists of a thin ferromagnetic foil tilted by a shallow angle against the beam direction. The foil is magnetized in the z direction by a modest external field $\vec{H}$ to polarize the target electrons to an average degree of $P_e = 8\%$ [9].

Scattered photons are then detected by calorimeters which measure the integrated energy deposition. The scattering angle and the covered solid angle are fixed by the position and aperture of the detector.

In such configuration an asymmetry between horizontal and vertical detector signals $A_{lin} = (S_H - S_V)/(S_H + S_V)$ will be proportional to linear polarization according to Eq.(11). Direction of the linear polarization could be measured either by 45^o rotation of the detectors or by adding a third detector between the two and forming additional asymmetry relations.

The circular polarization will be extracted using Eq.(12), from a measured asymmetry $A_{circ} = (S_+ - S_-)/(S_+ + S_-)$ of the detector signals induced by the solenoid's magnetic field flips.

DETECTORS OPTIMAL POSITIONS FOR VECTOR POLARIMETRY

The figure of merit in the Fig.1 or Fig.2 is changing versus scattered photon (detector) angle. Hence, for maximizing the figure of merit (combination of the signal amplitude and the analyzing power) the detectors should be installed at certain positions to view the target at an optimal polar angle. The optimal angle depends on the initial photon energy and type of measured polarization - linear or circular.

In order to find the optimal detection angle for a given energy of analyzable photon, a maximum of the figure of merit is calculated analytically by zeroing a differential of that expression and solving for θ - the polar angle.

This procedure is done separately for the linear and circular photons with results presented on Fig. 4.

In a vector polarimeter, however, the detector position should be optimized for analyzing both polarizations simultaneously. For that a sum of the linear and circular figure of merits is maximized to achieve the optimal performance. Analytic derivation of the optimal angle for the vector polarimetry is done similar to the linear or circular polarimeters and is plotted on the Fig. 4 versus primary photon energy.

The curves in Fig. 4 show ranges where optimal angles for the vector polarimetry are merging with the linear (below about 100 keV) and the circular (above about 10 MeV) polarimetry angles. These are the energy regions where the Compton scattering is sensitive only to the photons linear (low energy) or the circular (high energy) polarizations. Therefore, at the mentioned energies other photon induced processes should be explored for polarimetry: polarized photoeffect for the circular (<100 keV) and pair creation for the linear photons (>5 MeV) [10].

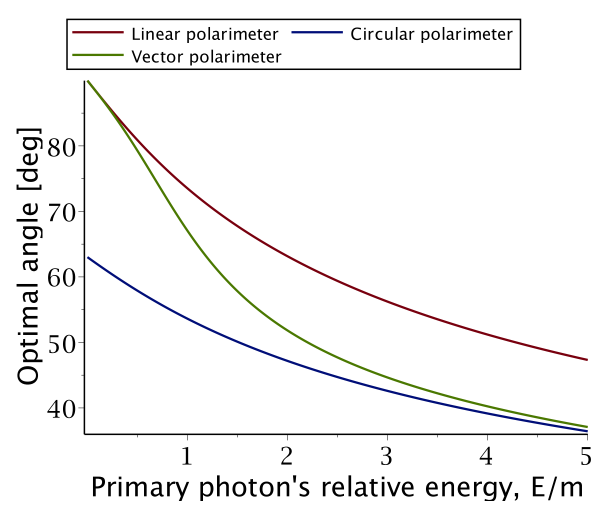

Figure 4: Compton scattered photons optimal detection angle dependence on the energy of the initial photon. Lines at top and bottom correspond to linearly and circularly polarized photons respectively while the middle line shows the maximized figure of merit for the mixed case.

ISBN 978-3-95450-176-2

VORTEX TOPOMETRY

Photons with a phase singularity $e^{im\phi}$ possess an orbital angular momentum and are called vortex or twisted photons [11]; here the ϕ is the azimuthal angle and the integer scale factor m is the topological charge. Vortex optical beams are extensively explored in recent decade or so in photonics and astronomy [12]. There are also prospects to obtain higher energy vortex photons using laser Compton scattering [13] though verifying photons' vortex nature by measuring the topological charge remains a theoretical and experimental challenge. A major gap in knowledge is a missing quantitative description of high energy twisted photons quantum interactions.

Since the orbital angular momentum is described by similar formalism as the light circular polarization, the vector Compton polarimeter described here could be explored to interact with possible beams of high energy twisted photons. As an initial approximation could serve the doubly polarized term in the Compton scattering cross-section proportional to $P_\gamma^C P_e$. Then, a spatial spin-orbital interaction of a vortex photon could possibly be regarded as a correction. Measured asymmetries induced by flips of the topological charge or the electron spin direction at different scattering angles will provide an experimental input for a complete twisted photon quantum theory.

SUMMARY AND CONCLUSION

We applied polarized Compton scattering formulas to derive and demonstrate feasibility of a vector Compton polarimeter. The device can simultaneously measure linear and circular polarizations of a photon beam in a tens of keV to few MeV energy range. Calculations show that outside of this range, at higher(lower) energies, the polarimeter is sensitive to circular(linear) polarization only. Maximizing a convolution of analyzing power and scattered beam intensity, the optimal detection angles are derived for the linear, circular and vector Compton polarimetry. The proposed device could be used at accelerators for undulator radiation polarimetry as well as in X-ray or gamma astronomy. It could also serve in a research and development of the novel high energy vortex photon beams.

REFERENCES

[1] Jackson, J. D., *Classical Electrodynamics (3rd ed.)*, ISBN 978-0-471-30932-1,(1998) [1962].

[2] C. Spezzani, E. Allaria et al. Phys. Rev. Lett. **107** (2011), 084801

[3] H. Deng *et al.*, Phys. Rev. ST Accel. Beams **17** (2014) 2, 020704 [arXiv:1311.3797 [physics.acc-ph]].

[4] V. Gharibyan and K. P. Schuler, LC-DET-2002-011.

[5] G. Alexander *et al.*, Phys. Rev. Lett. **100** (2008) 210801.

[6] S. Antier, O. Limousin and P. Ferrando, Nucl. Instrum. Meth. A **787** (2015) 297 [arXiv:1505.01002 [astro-ph.IM]].

[7] C. Beck, arXiv:1308.4954 [astro-ph.IM].

[8] F. Lie *et al.*, Chin. Phys. C **39** (2015) 028101.

[9] L.V. de Bever, J. Jourdan, M. Loppacher, S. Robinson, I. Sick, J. Zhao, *A target for precise Møller polarimetry*, Nucl. Instr. Meth. A400 (1997) 379.

[10] L. C. Maximon and H. Olsen, Phys. Rev. **126** (1962) 310.

[11] L. Allen, M. W. Beijersbergen, R. J. C. Spreeuw and J. P. Woerdman, Phys. Rev. A **45** (1992) 8185.

[12] Mawet D. *et al.*, J. 2013, The Messenger, 152, 8

[13] U. D. Jentschura and V. G. Serbo, Phys. Rev. Lett. **103** (2011) 013001 [arXiv:1008.4788 [physics.acc-ph]].

ISBN 978-3-95450-176-2

CRYOGENIC CURRENT COMPARATOR FOR STORAGE RINGS AND ACCELERATORS

R. Geithner#, Friedrich-Schiller-Universität Jena, Germany & Helmholtz-Institut Jena, Germany
T. Stöhlker, Helmholtz-Institut Jena, Germany & Friedrich-Schiller-Universität Jena, Germany & Helmholtzzentrum für Schwerionenforschung, Darmstadt, Germany
R. Neubert, P. Seidel, Friedrich-Schiller-Universität Jena, Germany
F. Kurian, GSI Helmholtzzentrum für Schwerionenforschung, Darmstadt, Germany & Helmholtz-Institut Jena, Germany
H. Reeg, T. Sieber, M. Schwickert, GSI Helmholtzzentrum für Schwerionenforschung, Darmstadt, Germany
M. Fernandes, The University of Liverpool, U.K. & CERN, Geneva, Switzerland

Abstract

A Cryogenic Current Comparator (CCC) was developed for a non-destructive, highly sensitive monitoring of nA beams at the planned FAIR accelerator facility at GSI. The sensor part of the CCC was optimized for lowest possible noise-limited current resolution in combination with a high system bandwidth of about 200 kHz. It is foreseen to install the CCC inside the CRYRING, which will act as a well-suited test bench for further optimization of the CCC performance and the cryostat. In the meantime - until the completion of CRYRING - a CCC has been installed and will be tested in the antiproton storage ring (Antiproton Decelerator AD) at CERN. The pulse shape in the AD requires dedicated optimization of the sensor time response. The beam current will increase rapidly during injection from 0 to 12 µA. Since the slew rate of the overall system is limited by the CCC pickup coil, the input signal has to be low-pass filtered to not exceed the slew rate of the CCC system and to ensure a stable operation. For this purpose different low-pass configurations had been tested. In this contribution we present results of the CCC sensor for AD, CRYRING and FAIR, respectively.

INTRODUCTION

The Cryogenic Current Comparator is a well-established device in metrology for current and resistance ratio measurements [1].

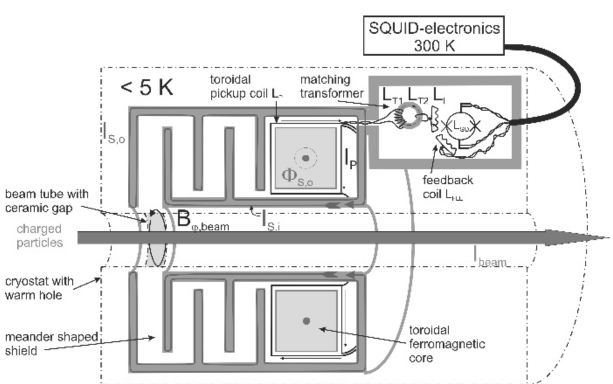

Figure 1: Schematic of the CCC.

Adapting this principle to beam diagnostics it provides a non-intercepting, absolute and precise detection of beam currents in the nA range for continuous as well as bunched beams [2].

The coupling circuit of CCC consists of a superconducting toroidal pick-up coil, a superconducting matching transformer, and a Superconducting QUantum Interference Device (SQUID) and is embedded into a meander-shaped superconducting shielding structure (see Fig. 1). The parts of the coupling circuit are connected by niobium wires and form superconducting closed loops. Due to flux conservation in such superconducting closed loops, it is possible to detect the magnetic field of constant beam currents without modulation techniques like used for DC Current Transformers (DCCT). Using state-of-the-art SQUID systems enables the detection of lowest currents in principle from DC to several MHz, but the overall bandwidth of the CCC is limited by the frequency response characteristic of the coupling circuit, which is specified by the core material embedded in the pick-up coil [3]. All these properties qualify the CCC as a suitable beam charge monitor for storage rings and accelerators.

LEAD-SHIELDED CCC AT GSI

In collaboration between GSI and University of Jena a first version of a CCC working as a beam current monitor was developed in the early 1990's [4]. In this system, the meander-shaped shield was made out of lead, whereas the coupling circuit was made out of niobium. The CCC shows very good results with a current resolution in the nA-range, but the bandwidth was limited by the SQUID-system. Also maintenance issues, like manually refilling of liquid helium prevent the usage as a standard diagnose tool. Therefore for the application in FAIR, a CCC should be developed with lower noise, higher bandwidth having cryostat with automated refilling system. As the existing CCC system at GSI provide a convenient test bench for this development, it has been re-commissioned as a prototype to test new sensor components. The SQUID and the FLL electronics were replaced by state-of-the-art devices. The re-commissioned CCC was then installed in

ISBN 978-3-95450-176-2

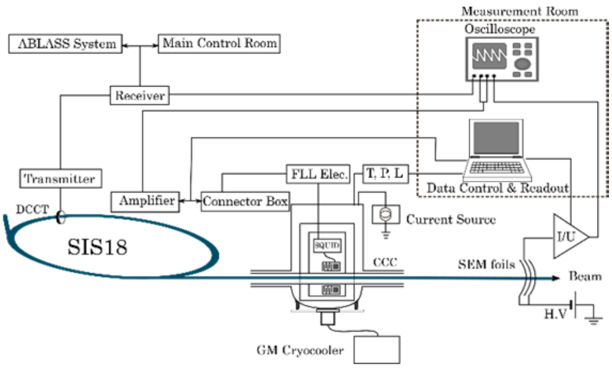

Figure 2: Schematic of measurement setup at GSI.

the extraction line of the GSI synchrotron SIS18 to monitor the extracted beam current (see Fig. 2).

In parallel to CCC measurements, a secondary electron monitor (SEM), which was installed downstream in the beam line, was used to compare the current measurements. With the help of an additional coil wound around the pickup unit, the CCC system is calibrated to a precise known current.

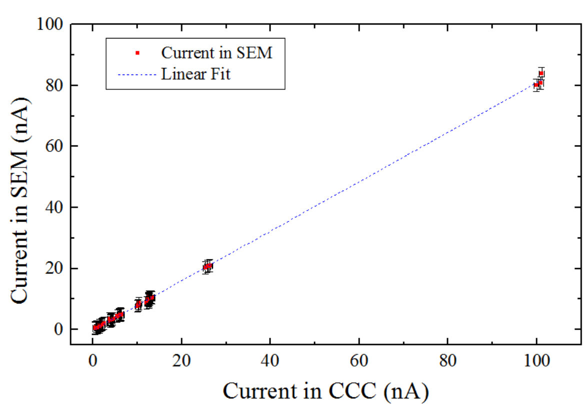

Figure 3: Comparison of beam intensity measured by SEM and CCC.

From a number of slowly extracted beam signals, the intensity measured both CCC and SEM are compared. The comparison of both signals shows a very linear relation (see Fig. 3). However, the slope is not equal to one (~ 0.8). This deviation possibly results from miscalibration of the SEM because the converting factor of the voltage output of the SEM to an equivalent beam current or a particle number strongly depends on the energy of the particles as well as the type of the element and may change with time. In turn, the CCC could also be used to calibrate the SEM.

With a current resolution of 2.3 nA (rms) corresponding to a signal-to-noise ratio of 2 at a bandwidth of 10 kHz, a number of slowly extracted beam signals were measured by CCC. A typical spill structure of a coasting beam measured by CCC and SEM are shown in Figure 4. In the figure, the spill structure is produced by 1.6×10^9 particles of Ni^{26+} extracted over 64 ms giving rise to an average current of 105.5 nA.

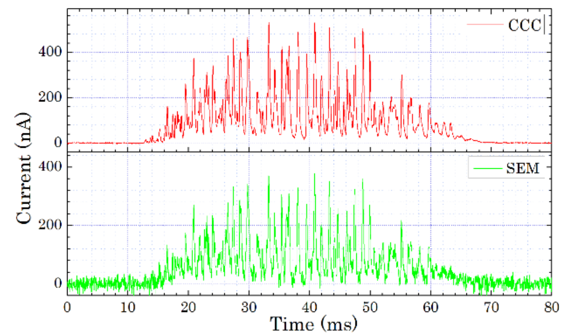

Figure 4: Comparison between SEM and CCC measurement of a 600 MeV/u beam of slowly extracted Ni^{26+} ions.

Both signals show very good temporal agreement. The measured amplitudes differ only by the factor 0.8 (see Fig. 3).

Although ideally one would expect a quasi-dc like spill structure, the beam spill structure typically contains spikes, amplitude of which exceeding several times to the average beam current. These spikes originate from the ripples associated with the power converters of magnets used for slow extraction [5]. These ripples cause over-modulations in the spill structure, i.e., the instantaneous intensity goes down to zero to very high amplitudes. For fixed target experiments (for example, hadron therapy [6]) these fluctuations are not desirable. It was shown that by bunching the beam using rf cavities in the synchrotron SIS18, these over modulation can be reduced [7].

Figure 5 shows the comparison of spill structures of a coasting beam (un-bunched beam) and a bunched beam

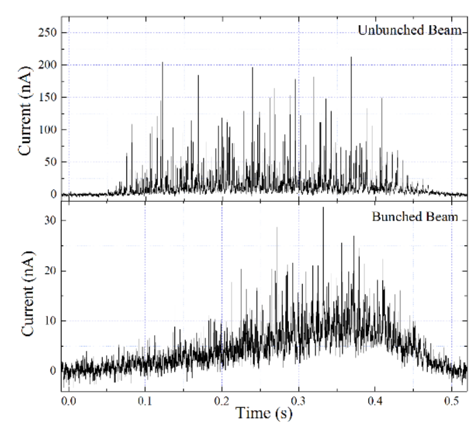

Figure 5: Comparison between the CCC measurements of a 600 MeV/u beam of slowly extracted Ni^{26+} in the unbunched case (top) and with bunching in the SIS18, before the slow unbunched resonant extraction (bottom).

The coasting beam is produced by 1.3×10^9 particles and the bunched beam is produced by 9.7×10^8 particles, both extracted over 500 ms. In the case shown, the particles are bunched with an rf voltage 1/7th of what used for acceleration. As shown in the figure, the bunching removes over modulation and supresses the peak amplitudes to a large extend.

IMPROVED CCC

An improved CCC was developed for the upcoming FAIR-project. A current resolution in the nA-range and a bandwidth of up to 200 kHz were achieved [3]. The CCC should be installed at CRYRING, working as a kind of test bench for FAIR but also as an experimental tool for atomic physics. At the same time, CERN's Beam Instrumentation group also had plans to install a CCC in the Antiproton Decelerator (AD), due to its unique characteristics allowing measurement of low-intensity coasting beams. A collaboration between GSI, Helmholtz Institute Jena and CERN was then put in place, where the CCC developed for FAIR-project would be first be installed in the AD until the completion of CRYRING, after the required modifications in order to adapt it to the AD beam parameters.. The main purpose of this machine is to capture the antiprotons produced by colliding a proton beam against a fixed target, decelerate them (when beam is bunched) to reduce their energy and cool down (by both stochastic and electron cooling when the beam is coasting), to create antiproton bunches suitable to be captured by low-energy anti-matter the experiments. The proposed extra low energy anti-proton facility at CERN (ELENA) will be a new ring installed downstream of the AD, with the purpose of further decelerating and cooling this antiproton beam. The most important figure of merit of these de-accelerators is the number of antiproton delivered to the experiments. Hence, a non-perturbing and absolute measurement of the beam intensity is essential to monitor any efficiency losses during the deceleration and cooling phases. At the same time there is the requirement for having a stable, automated and high-availability system which can work with almost no intervention from an expert operator. Also, the cooling of the different superconducting components should be provided by a stand-alone system, such as a cryo-cooler which should enable a closed cycle cryogenic operation, without the need for manually periodic refills of liquid helium. A special cryostat with an automated helium re-condensation unit was developed. The CCC should meet the following performance specifications: a current resolution smaller than 10 nA, a dynamic range covering currents between 100 nA and 12 µA, and a bandwidth from DC to ~1 kHz [8]. In previous measurements in laboratory environment the resolution and the dynamic range (for slow beams) was demonstrated but instabilities appear when the slew rate of the beam signal exceeds the maximum slew rate of the CCC-system. This means that for signals with higher slew rates, unwanted flux jumps occur and the SQUID electronics in the FLL-mode adjusts to different working point. If this occurs at a single point the absolute measurement offset is lost, and if this occurs continuously the complete measurement is meaningless.

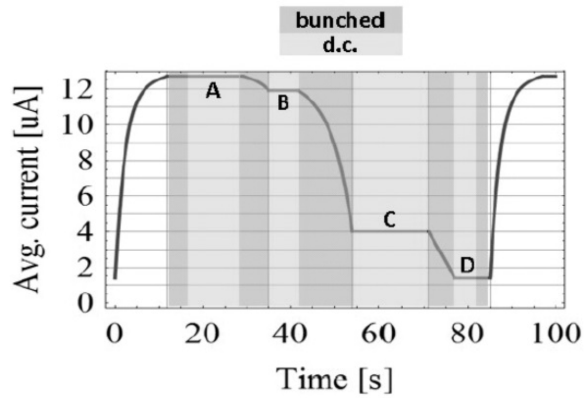

Figure 6: Expected average beam current in AD during injection and deceleration of antiprotons.

Figure 6 shows the high dynamic range of the expected beam current signal, particularly during injection where the current suddenly jumps from 0 to ~12 µA. Using the designed CCC for FAIR without any modification would impose a flux slew-rate on the SQUID of 400 MΦ_0/s, while modern SQUID/FLL systems can handle at most 1 MΦ_0/s to 5 MΦ_0/s.

This difference of two orders of magnitude can be reduced by decreasing the magnetic flux coupling into the SQUID, or by low-pass filtering the magnetic flux signal before it reaches the SQUID input. The latter solution is possible to be implemented due to the low bandwidth specification for the monitor and it is also preferable since it does not entail a loss of current sensitivity. In the AD and ELENA CCC plus cryostat systems, the signal slew-rate will be reduced by a combination of filtering in the CCC coupling circuit, and in the structure of the cryostat developed at CERN.

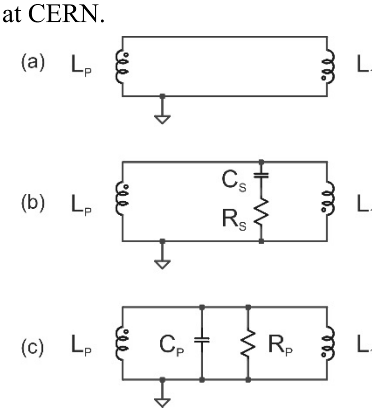

Figure 7: Connection scheme of the tested filter setup ((b) serial connection of R_S and C_S, (c) parallel connection of R_P and C_P) in the coupling circuit between the pick-up coil L_P and the primary coil L_1 of the matching transformer while (a) is the original configuration.

A low pass filter was inserted between the pick-up coil and the primary coil of the matching transformer in consequence of these requirements. Figure 7 shows the different tested setups. The first setup was a serial

ISBN 978-3-95450-176-2

connection of a 1 Ω resistor R_S and a 10 µF capacitance C_S. The bandwidth was reduced to 7 kHz with an additional noise contribution around the resonant peak (see Fig. 8 (b)). That's why a parallel connection of a 0.225 Ω resistor R_P and a 10 µF capacitance C_P was tested. Here, the bandwidth was reduced to 1 kHz with the additional noise contribution evenly distributed from DC to the 1 kHz cut-off frequency (see Fig.8 (c)).

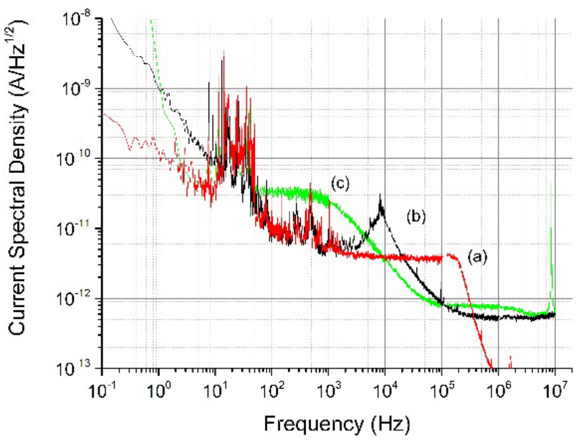

Figure 8: Current noise of the CCC in the original configuration without filtering in the coupling circuit (a), with serial connection of R_S and C_S (b), and with parallel connection of R_P and C_P.

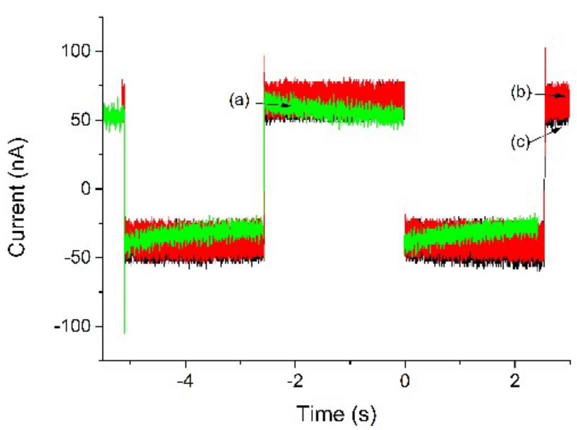

Figure 9: Step function response to a test current of 90 nA with the original configuration without filtering (a) as well as with filtering in parallel connection, applying the test current to beam simulating wire (b) or to the calibration coil (c).

This could also be seen in the step function response in Fig. 9. The test current suddenly increases by 90 nA. Two different methods were used to apply a test current. The test current can be applied by a beam simulating wire along the beam axis or by an additional wire wound around the pick-up coil. In the original configuration without filtering (see Fig 9 (a)), overshooting and a slide creeping occurs. With filtering in the parallel configuration (see Fig. 9 (b) and (c)) some overshooting is visible, too, but the signal is much more stable. In these measurements the SQUID system bandwidth of 12.6 MHz is much higher than the required 1 kHz of the complete detector. This means that the increased noise of the CCC-system could be decreased by filtering the output signal again. Another important feature, regarding measurement accuracy and calibration is also shown in Fig. 9. There is no difference to see if the beam simulation signal is applied to the beam simulating wire (b) or to the calibration coil (c). The comparison between current sensitivity of the CCC depending on whether the test signal is applied to beam simulating wire or to calibration coil is shown in Fig. 10. Both methods show a very linear behaviour in the tested dynamic range from 20 nA to 10 µA. The current sensitivity of the coupling circuit of 96 nA/Φ_0 does not differ in the limits of measurement. That means, that there is an ideal coupling of the beam's azimuthal magnetic field to the pick-up coil without any losses, giving the opportunity of an absolute, linear calibration.

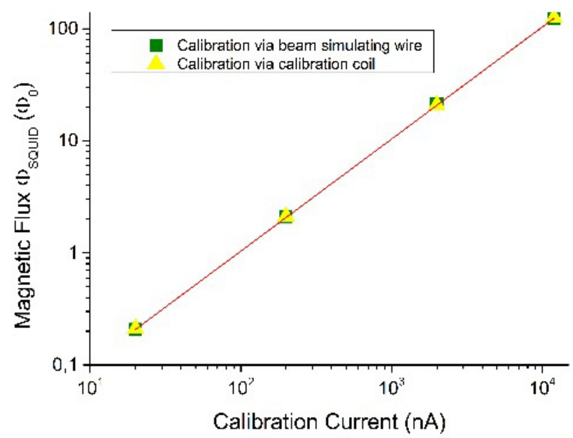

Figure 10: Comparison between current sensitivity of the CCC with test signal applied to beam simulating wire or to calibration coil.

CONCLUSION AND OUTLOOK

The CCC has demonstrated its outstanding performance in the beam line at GSI. Spill structures of extracted beams could be measured with very high temporal (0.1 ms) and current resolution (2.3 nA (rms)). The CCC could also be used for calibration of different devices like SEM, due to its own linear working function which is independent of particle energies. Using improved core materials the current noise could be reduced while the bandwidth of the overall system could be increased. If the bandwidth is not crucial, the detector could be applied to the demands of the signal. For AD the slew rate of the signal (400 MΦ_0/s) would exceed the slew rate of the CCC (< 5 MΦ_0/s). Using low pass filters in the coupling circuit could solve these problems. The CCC is delivered to CERN and installed in AD is a cryostat designed and

ISBN 978-3-95450-176-2

fabricated by CERN with a stand-alone helium re-liquefier system and connected to the control system. Details of the AD installation and first results of beam measurements were presented by in these proceedings [9]. In the meantime the installation of the CCC at CRYRING will be prepared using the results from AD installation.

REFERENCES

[1] W. Vodel et al., *Applied Superconductivity, Handbook on Devices and Applications, Volume 2,* Wiley-VCH, Weinheim, p. 1096 (2015).
[2] R. Geithner, et al., ”A non-destructive Beam Monitoring System based on an LTS-SQUID “ IEEE Trans. Appl. Supercond. 21 3, pp. 444-447 (2011).
[3] R. Geithner et al., “A SQUID-based Beam Current Monitor for FAIR / CRYRING“, WECZB1, In Proceedings of IBIC2014, Monterey, USA (2014).
[4] A. Peters et al., “A Cryogenic Current Comparator for the Absolute Measurement of nA Beams“, AIP Conf. Proc. 451 pp. 163-180 (1998).
[5] D. Ondreka et al., “SIS-18 rf knock-out optimisation studies”. In Conference Proceedings, IPAC13, Shanghai, (2013).
[6] L. Badano, et. al., “Synchrotrons for hadron therapy: Part I”. Nuclear Instruments and Methods in Physics Research Section A: Accelerators, Spectrometers, Detectors and Associated Equipment, 430 pp. 512 – 522 (1999).
[7] A. Peters, et al., “Measurements and improvements of the time structure of a slowly extracted beam from a synchrotron”. In Proceedings of EPAC, Vienna, Austria, pages 2237-2239, 2000.
[8] M. Fernandes et al., “Cryogenic Current Comparator for the Low Energy Antiproton Facilities at CERN“, WEPF04, In Proceedings of IBIC2014, Monterey, USA (2014).
[9] M. Fernandes et al., “A Cryogenic Current Comparator for the Low Energy Antiproton Facilities at CERN“, MOPB043, In these Proceedings of IBIC2015, Melbourne, Australia (2015).

ISBN 978-3-95450-176-2

BEAM DIAGNOSTICS FOR THE HIGH ENERGY STORAGE RING AT FAIR

C. Böhme, A. Halama, V. Kamerdzhiev, F. Klehr, D. Prasuhn, K. Reimers, S. Srinivasan, D. Temme, R. Tölle, Forschungszentrum Jülich, Germany

Abstract

Numerous beam diagnostics systems, with the BPM system considered the most important one, are envisaged for the High Energy Storage Ring (HESR) within the FAIR Project. The BPM design, the corresponding test bench, HESR BLM studies at COSY, status of the ionization profile monitor and other subsystems are presented.

INTRODUCTION

The HESR, part of the FAIR project in Darmstadt, Germany, is dedicated to the field of antiproton and heavy ion physics. The envisaged momentum range is 1.5 GeV/c to 15 GeV/c. The ring will be 575 m long in a racetrack shape. The planned beam instrumentation within the modularized start version is:

76	Shoebox-style BPMs
118	Beam Loss Monitors
2	Beam Current Transformers
1	Ionization Beam Profile Monitor
1	Wall Current Monitor
1	Schottky Pick-up
1	Dynamical Tune-meter
1	Transverse Feedback System
1	Scraper

BPM SYSTEM

The BPM system is foreseen to measure the beam position throughout the ring. 22 BPMs are located in each arc of the ring and will be co-located to each sextupole magnet. An illustration of the elements between two dipoles in the arc sections is given in Figure 1.

The BPM units consist of two shoebox-style pick-ups rotated by 90° around the beam axis in respect to each other. The setup is shown in Figure 3. The inner diameter of the pick-ups is 89 mm and the length 77 mm with a gap of 3 mm between the electrodes using an angle of 55.5°. The expected signal levels are depending on the ion charge, the amount of ions, and the bunch length and can be calculated using

$$U_{img}(t) = \frac{1}{\beta c C_{el}} \frac{A}{2\pi\alpha} I_{beam}(t) \quad (1)$$

$$= \frac{1}{\beta c C_{el}} \frac{L_{BPM}}{2} I_{beam}(t) \quad (2)$$

The capacitance was calculated using a COMSOL Multiphysics 5.0 simulation. For the lowest case, the first injection of antiprotons with 10^7 particles in the ring, the signal level was calculated to 57 μV. For the highest intensity case, with 10^{11} antiprotons stored, the signal level is 390 mV.

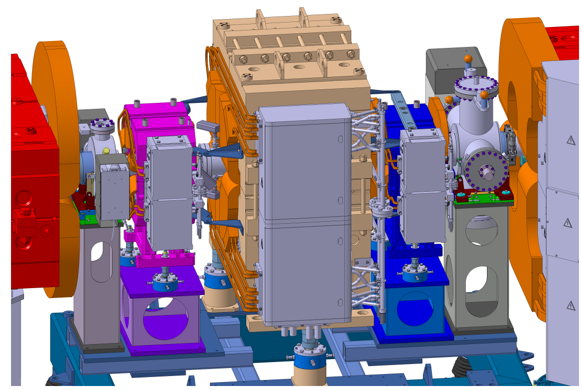

Figure 1: Illustration of the elements between two dipole magnets in the arc. From left to right: Dipole magnet (red), pumping vessel, sextupole magnet (purple), BPM, quadrupole magnet (ocher), steerer (blue), pumping vessel, dipole (red). Magnet coils are in orange.

The achievable resolution ϵ is dependent on the capacity between the pick-ups:

$$\epsilon = \frac{1}{b} = \frac{\alpha}{r_{BPM}} \quad (3)$$

$$\alpha = \frac{1 - \frac{CD}{C_{ges}+CD}}{1 + \frac{CD}{C_{ges}+CD}} \quad (4)$$

with CD the capacity between the pick-ups and C_{ges} the capacitance to ground. The capacity between the pick-ups was determined to 7.8 pF. With this value $\epsilon = 0.0146 mm^{-1}$.

The pick-up design is based upon the COSY BPMs [1]. The length and diameter is shrunk by a common factor in order to keep the length to diameter ratio. As can be seen in Figure 3 the pick-ups themselves are mounted onto a carrier tube which is then mounted within the beam pipe. In order to enhance the signal level, efforts were taken to increase the distance between the electrodes and the grounded carrier tube without changing the inner diameter of the BPM nor the outer diameter of the beam pipe as shown in Figure 2. In detail:

- Increasing the gap between carrier tube and electrodes.
- Shorten all screws to the minimum length.
- Increasing the diameter of holes in the carrier tube for the signal connections.
- Introducing bevels on the small edges of the pick-up cylinder.

ISBN 978-3-95450-176-2

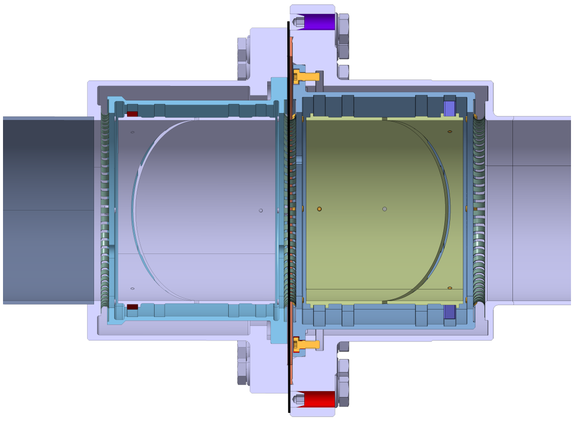

Figure 2: Comparison between the design of the COSY BPM (left) and the HESR design (right). Pictures have been scaled to fit the inner diameter of both BPMs. The gaps between the pick-up electrodes and the grounded carrier tube have been widened in order to reduce the capacitance and so increase the signal level.

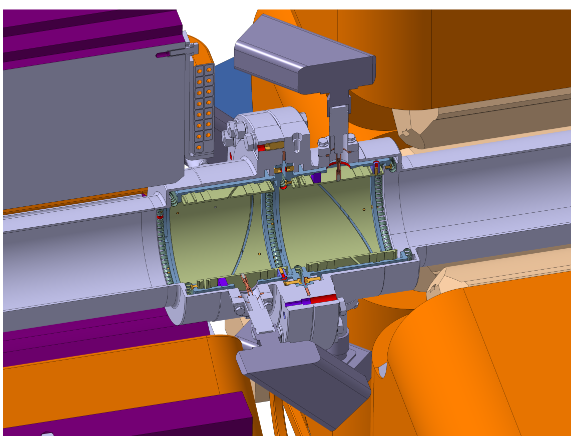

Figure 3: Illustration of the BPM between a sextupole magnet (left) and a quadrupole magnet (right).

- Removing all unnecessary holders of the carrier tube, left from production.
- Increasing the gap between the electrodes to 3 mm.

These efforts lead to an increase of about 50 % in signal level showed in simulation.

Furthermore, the XY coupling in the pick-ups was examined. The coupling reduces the position sensitivity of one plain if the beam moves in the other plain. Also the electrical center is shifted in one plain by introducing a beam offset in another plain. Simulations showed, that by moving the beam 1 mm in e.g. Y direction, the position reading in X direction changes by 2.6 μm.

A prototype of the HESR BPM is currently being manufactured. The test bench measurements are expected to start by the end of 2015.

Ion Clearing

In the antiproton mode of operation of the HESR clearing of residual gas ions trapped in the beam is seen as crucial [2]. Therefore a constant voltage should be applied on at least one pair of each BPM's electrodes. The required field strength on the location of the beam has been calculated to be higher than 2500 V/m. Simulations showed that a voltage of ± 100 V will be sufficient to fulfill this requirement. However it was also shown, that due to the pick-up geometry, the effective length of the field above 2500 V/M at ±100 V amounts to a small fraction of the pick-up length only. Therefor higher voltages might have to be applied in order to effectively clear the ions out of the antiproton beam.

BPM Prototype Wire Test Bench at COSY

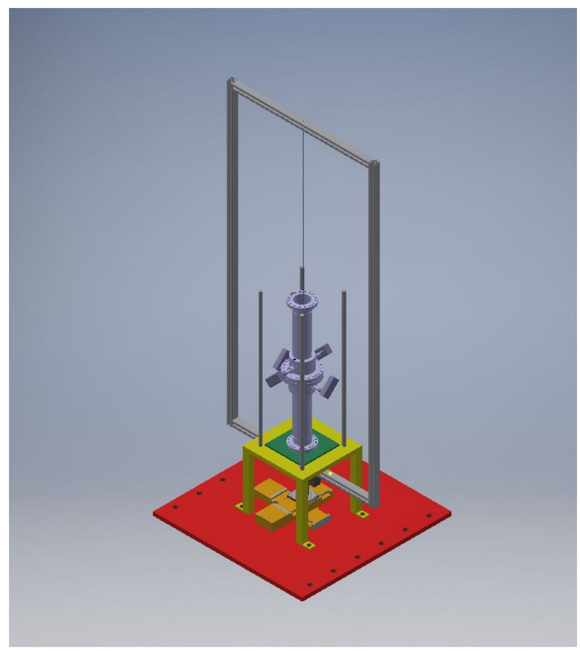

Figure 4: Isometric View of Wire type Test Bench.

Figure 4 (isometric) represents a 3D design view of the test bench with its main elements and the BPM under test. A centered axial line is also depicted to represent the wire that longitudinally passes through the BPM. The fundamental design concept is the upright mounting of the BPM. A movable aluminum frame is used to support a wire, stretched through the BPM. Such an approach allows avoiding any wire sagging due to gravity. With the BPM fixed on the base bench, the aluminum frame carrying the wire is moved by linear stages. Their position readout yields the wire-BPM relative displacement. Moving the wire instead of the BPM will be preferred due to a significant weight of the BPM. The stretched wire will have SMA connectors attached to both ends.

Two linear stages [3] will be orthogonally mounted providing the wire-BPM relative displacement in (x, y) direction. On top, a Y-shaped solid frame made of cast steel will be mounted that holds the aluminum frame. The M-ILS100HA

ISBN 978-3-95450-176-2

will be chosen for each translation stage, being a high performance precision micro-mover driven by DC motors from Newport. The maximum linear travel range is 100 mm with an on-axis accuracy of 3 μm and the smallest incremental linear motion of 0.3 μm. The maximum normal load capacity is 250N (25.5 Kg) which is enough to withstand a weight of approximately 15 Kg by the stage beneath.

The steel base platform serves as the base on which the whole setup will be mounted as shown in Figure 4. The BPM base bench will be made of cast steel and the reference plane will be made of aluminum. Both the base bench and the reference plane have a concentric hollow center for the wire-BPM relative displacement. Finally, two contact brushes will provide electrical contact between the beam pipe and the movable frame (not shown in figure). This is done to avoid the ground current loop that would otherwise form between the wire and the aluminum frame.

BEAM LOSS MONITOR

For machine commissioning, routine operation and further beam optimization detailed beam loss data is very valuable. Unlike other accelerators, the HESR BLM data will not be used for an automated machine protection, as the stored total beam energy will not be high enough to damage the machine. Along the ring 118 BLMs are planned to be used. Although detailed beam loss simulations are yet to be carried out, testing of different detector technologies has already begun.

- LHC-type ionization chamber from CERN [4]
- SNS-type ionization chamber from ORNL [5]
- Liquid scintillator
- Sait-Gobain scintillator crystal 2M2/2 [6]
- PIN-Diode BLMs from Bergoz
- Heliax cable

For the preliminary testing of the ionization chambers a commercially available current amplifier was used. This readout allowed to observe a slowly extracted beam in the extraction beam line of COSY using the LHC ionization chamber. The first test of the SNS type chamber was not successful due to noise dominated signals associated with the test setup. Next series of tests will be carried out using the current measurement module designed and built by iThemba LABS. It is an 8 channel version of a current measurement electronics used to readout harps in the beamlines at iThemba LABS and at COSY [7]. The specifications of both devices are very similar, both measure in the most sensitive range pA by integrating the current, up to 200 ms. Although the integration is done independently for every channel a multiplexer is used to read out the current integrators sequentially. The difference, besides the amount of channels is, that the version with 48 channels can only use the same integration time, and in consequence the same measurement range, for all channels, while the 8-channel one can use individual integration times for every channel. The 8-channel device as well as the newer versions of the 48-channel version have a built-in EPICS server for read-out and controls. In addition further tests using the ionization chambers read out by the CERN electronics to detect beam losses at COSY are planned.

Another test series was carried out using scintillation detectors and PIN-diodes to monitor the beam losses in the COSY tunnel during the JEDI beam time. Standard COSY BLM utilizing a liquid scintillator, a crystal scintillator purchased from Saint-Gobain and a Bergoz BLM based on Hamamatsu PIN-diodes were used. Both scintillation detectors have a PMT and a pre-amplifier built in.

Shown in Figure 5 are results of a comparative test of the PIN diodes and the two scintillation based detectors. These first tests were done using a digital oscilloscope. During this test the beam was slowly steered towards a target on top of the vacuum chamber. Therefor the beam intensity, represented by the BCT signal slowly decreases. As shown, the PIN diode BLM delivers the lowest count rate. This is likely due to a much smaller detector size compared to the scintillator based models. In comparison of the two scintillation based detectors the crystal one has the tendency to saturate slower, which makes this type preferable over the liquid scintillator one.

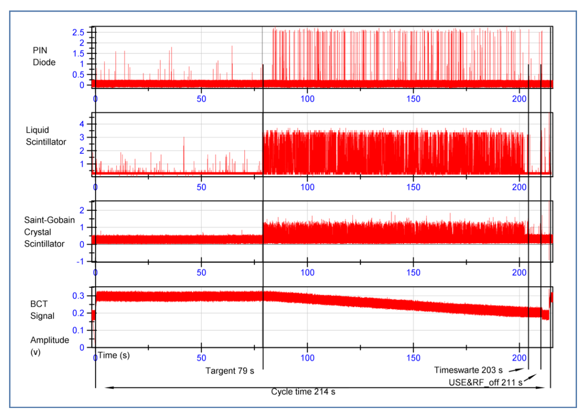

Figure 5: Test of three different Beam Loss Monitor devices. Two scintillator and one PIN diode based (upper trace) during the slow steering of the beam towards a target.

Further evaluations of detectors are planned. Tests of the coaxial cable method [8] are planed using the slowly extracted beam in the extraction beamline. In addition experiments with optical fibers [9] will be performed.

IONIZATION BEAM PROFILE MONITOR

An Ionization Beam Profile Monitor (IPM) shown in Figure 6 was built and tested together with the GSI in 2007. Since then it became a very valuable instrument in beam diagnostics at COSY and GSI [11]. The COSY experience shows, that besides the data acquisition a lot of work goes into reliable automated setting of the voltages needed to

ISBN 978-3-95450-176-2

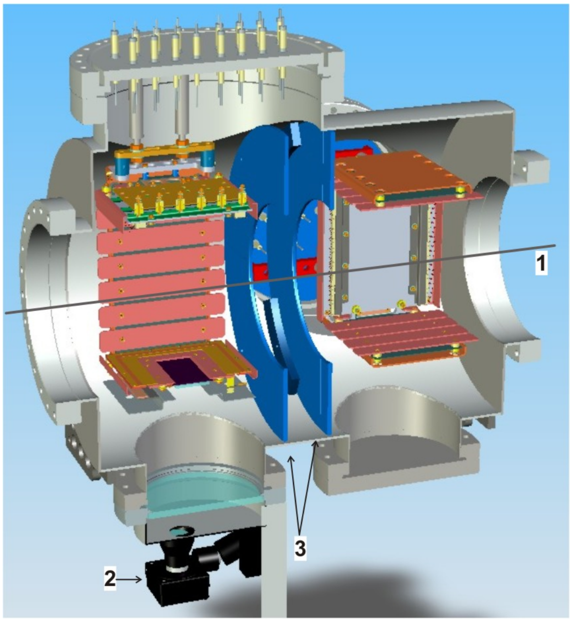

Figure 6: Drawing of the IPM prototype built together with the GSI [10]. The ion beam (1) ionizes residual gas which is accelerated towards a detector and read out by a standard GiGE camera (2). To minimize the effect of the electrical fields towards each other, shielding plates have been inserted between both devices.

operate the instrument at a level where the profiles can be detected, while making sure the built-in micro-channel plates are not damaged. This is due to a wide range of beam densities routinely present in the COSY ring, in particular when beam cooling is applied. The development of automation and interlocks is an ongoing effort to achieve an unattended operation of the IPM. Based on COSY experience a similar device will be developed for the HESR.

CONCLUSIONS

Using anti-protons with a longitudinal stacking injection within the HESR of the FAIR project the beam instrumentation has to be able to measure the beam position with as low as 10^7 particles stored after the first injection. Therefore results from simulations have been used to optimize the design of the shoebox BPM. The manufacturing of the BPM prototype is in progress. The design of the BPM test bench is being finalized. The BPM readout electronics will be provided by Instrumentation Technologies as an in-kind contribution to FAIR. This electronics will also be used for tune measurements and orbit feedback.The first test of BLMs was performed, in order to find a system that best fits HESR needs. Further BLM technologies need to be tested. For dc and bunched beam current measurements commercially available systems will be used. The GSI/COSY IPM utilizing collection of ions will be adopted for HESR.

REFERENCES

[1] R. Maier et. al., “Non-Beam Disturbing Diagnostics at COSY-Jülich,” EPAC’90, Nice, France, June 1990, p. 800.

[2] F. Hinterberger, “Ion Trapping in the High-Energy Storage Ring HESR,” Berichte des Forschungszentrums Jülich 4343, ISSN 0944-2952, October 2011.

[3] Manual of ILS Series, “High-Performance Mid-Range Travel Linear Stages,” MILS100CCHA, Newport Corporation, Irvine, California, USA.

[4] M. Stockner et. al., “Classification Of The LHC BLM Ionization Chamber,” DIPAC 2007, Venice, Italy, WEPC09.

[5] A. Zhukov et. al., “SNS BLM System Evolution: Detectors, Electronics, and Software,” PAC09, Vancouver, BC, Canada, FR5REP038.

[6] Saint-Gobain Ceramics & Plastics, Inc. “Scintillation Detectors with Integrally Mounted PMT,” 05-14.

[7] iThemba LABS, Annual Report 2008, p. 50.

[8] G. W. Bennett et. al., “The Upgraded Ring Loss Radiation Monitoring System at the AGS,” PAC89, Chicago, USA, p. 1477.

[9] F. Rüdiger et. al., “Beam Loss Position Monitoring with Optical Fibres at DELTA,” EPAC08, Genoa, Italy, TUOCM03.

[10] T. Giacomini, GSI Gesellschaft für Schwerionenforschung mbH, Darmstadt, Germany, private communication.

[11] V. Kamerdzhiev et. al., “Results of Electron Cooling Beam Studies at COSY,” RuPAC-2010, Protvino, Russia, WECHZ04.

ISBN 978-3-95450-176-2

A PATIENT-SPECIFIC QA PROCEDURE FOR MOVING TARGET IRRADIATION IN SCANNED ION THERAPY

Y. Hara#, T. Furukawa, R. Tansho, Y. Saraya, K. Mizushima, N. Saotome, T. Shirai and K. Noda,
National Institute of Radiological Sciences, Chiba, Japan

Abstract

Three-dimensional (3D) pencil-beam scanning technique has been utilized since 2011 in NIRS-HIMAC. Beam delivery system and treatment planning software (TPS) require dosimetric patient-specific QA to check each individual plan. Any change in the scanned beams will result in a significant impact on the irradiation dose. Therefore, patient-specific QA for moving target irradiation requires additional procedure.

In an additional QA for moving target irradiation, we placed 2D ionization chamber on the PMMA plate tilted with respect to the beam axis. The PMMA plate was set on the stage of the moving phantom. The moving phantom was moved according to patient data. We measured the dose distribution for both the static target and the moving target. We compared the results for the moving target with those for the static targets by means of a gamma index analysis.

In the additional patient-specific QA, the gamma analysis between the moving and static targets showed the good agreement. We confirmed that this new technique was a beneficial QA procedure for moving target irradiation.

INTRODUCTION

Heavy-ion beams such as carbon-ion beams have attracted growing interest for cancer treatment due to their high dose localization and high biological effect at the Bragg peak. Since clinical trials using the Heavy-Ion Medical Accelerator in Chiba (HIMAC), operated by the National Institute of Radiological Sciences (NIRS), were started in1994 [1], treatments for more than 7000 patients have been successfully carried out with carbon-ion beams. To make the best use of the characteristics of a carbon-ion beam and provide flexible dose delivery, three-dimensional (3D) pencil-beam scanning is an ideal irradiation technique [2-4]. As part of the efforts to achieve ion-scanning therapy, a new treatment facility equipped with a 3D scanning irradiation system was constructed as an extension to the existing HIMAC. The 3D scanning irradiation system has been utilized for treatment since 2011.

In the scanning irradiation method, since the 3D dose distribution is achieved by superimposing doses of individually weighted pencil beams determined in the treatment planning, any change in the scanned beams will cause a significant impact on the irradiation dose. Therefore, the scanning system and its treatment planning system (TPS) require dosimetric patient-specific QA to check each individual plan and its delivery [5]. This patient-specific QA is usually performed before therapeutic irradiation, as follows. After treatment planning, the dose distribution is measured using ionization chambers set in a water phantom. In this measurement, irradiation is performed in the same manner as in the patient treatment. The measured dose profiles are then compared with the dose distribution obtained by recalculation by the TPS using a homogeneous medium instead of the patient CT data. This method allows the quality of the field to be checked.

One of the aims at the new facility is to realize treatment of a moving target by scanning irradiation. In moving target irradiation with a scanned ion beam, the interplay effect between the target motion and scanned beams is a problem, because this effect cause over or under dosage in the target volume. To overcome this problem, we developed fast scanning irradiation system with gating system for moving target [6]. However, the existing patient-specific QA is performed only in static filed. To ensure the validity of both the delivered dose and the gating system, patient-specific quality assurance (QA) for moving target irradiation requires an additional procedure. In this paper, we describe a new patient-specific QA procedure for moving target irradiation and experience with patient-specific QA.

MATERIALS AND METHODS

Patient-specific QA Procedure

The purpose of the conventional patient-specific QA is to compare the dose distribution calculated by TPS and the measured dose distribution in static field. In the additional QA for moving target irradiation, by comparing static and moving measurements, we confirm that there is no difference between them. Additionally, we check that the gating system and fast scanning system work correctly during irradiation.

Figure 1 shows the schematic workflow of patient-specific QA. In the patient-specific QA in HIMAC, the planned dose distribution is converted to the dose distribution in the water phantom, instead of the patient CT data. After that, we perform the measurement and analysis. In the measurement, a commercial 2D ionization chamber array (Octavius Detector 729 XDR, PTW Freiburg, Germany) is employed. The sensitive volume of each chamber is 5 × 5 × 3 mm, and center to center spacing is 10 mm. In total there are 729 chambers in a matrix of 27 × 27, providing a maximum field size of 27 × 27 cm. This ionization chamber array is used with an accordion-type water phantom, which was developed to

#y-hara@nirs.go.jp

ISBN 978-3-95450-176-2

allow measurement depth to be changed easily [5]. The remote control function of the motor makes it possible to shorten successive measurements for different depths. The measured dose distributions are compared with the planned dose by means of a 3D gamma index analysis [7]. This analysis method simultaneously evaluates the dose difference and the distance to agreement quantitatively. In the analysis, a distance to agreement of 3 mm and a dose difference of 3% are employed as accepted deviations. The criterion of QA is that more than 90% of evaluated points should meet the criterion.

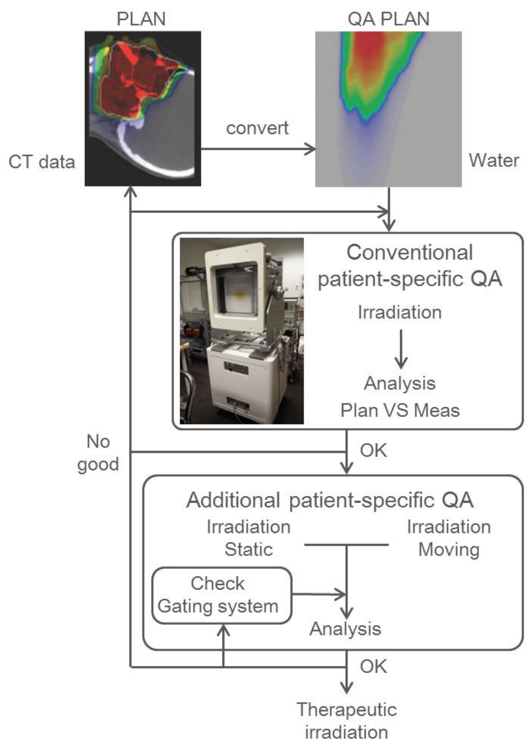

Figure 1: Schematic workflow of patient-specific QA.

In the additional QA for moving target irradiation, we place a 2D ionization chamber on the PMMA plate tilted with respect to the beam axis. Figure 2 shows the additional patient-specific QA measurement setup. The PMMA plate is set on the stage of the moving phantom (Model 008PL, CIRS). The moving phantom can be moved in the transverse direction according to the patient data. We measure the dose distribution for both the static target and the moving target. After the measurement, we derive the displacement that exhibits the smallest dose difference between the measured result for the static target and that for the moving target. The value of half the residual motion is employed as the displacement criterion. Then, considering the displacement, we compare the results for the moving target with those for the static targets by means of a 2D gamma index analysis. We used 3 mm and 3% as the accepted tolerance and the criterion of QA is more than 90% of the passed gamma in the same manner as static QA.

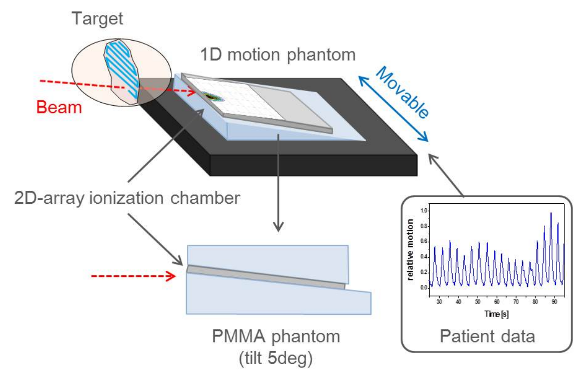

Figure 2: Schematic view of measurement setup for the additional patient-specific QA.

NIRS Scanning Irradiation System for Moving Target

All experiments were performed in the new treatment facility at NIRS-HIMAC, equipped with all the instruments indispensable for 3D scanning irradiation, including a scanning magnet, range shifter, ridge filter and beam monitors. In scanning irradiation, the dose distribution is controlled in the transverse direction by a pair of scanning magnets with beam-scanning velocities of 100 and 50 mm/ms at the isocenter. For depth scanning, the hybrid depth scanning method [8] was employed, in which 11-stepwise energy operation ranging from 140 to 430 MeV/u was used in conjunction with the range shifter. For moving target irradiation, the phase-controlled rescanning (PCR) method is implemented [6]. It can complete the several times rescanning of one slice during a single gated period of the respiration. This scheme is realized by the very fast scanning system and the intensity control system in the beam extraction from synchrotron to provide the optimum beam rate, because the period of the respiration is almost constant but the required dose is different slice by slice.

RESULTS AND DISCCUSION

Patient-specific QA in Static Field

Measurement for conventional patient-specific QA, which we called static QA, was performed after a new treatment plan was approved. The QA measurements of one field typically took 5 min, with three repeated irradiations for three different measurement depths. Figure 3 shows the typical patient-specific QA check sheet. Comparisons of 2D dose distributions, the histogram of dose difference and the histogram of the gamma index for a patient’s plan are shown in the check sheet. The measured dose distributions agreed well with those calculated by the treatment planning system, and the QA criteria were satisfied in all measurements.

ISBN 978-3-95450-176-2

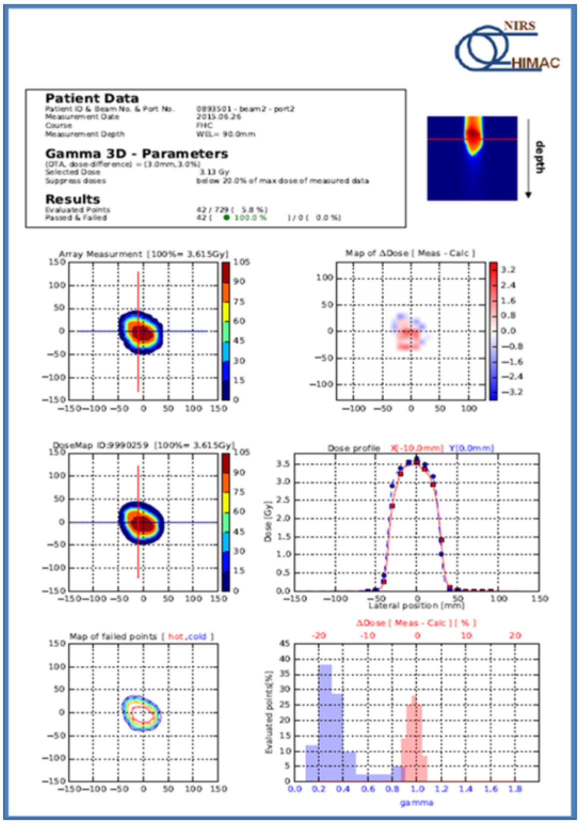

Figure 3: Typical patient-specific QA sheet. Comparison between measured dose and calculated dose by gamma index and dose difference.

Additional Patient-specific QA for Moving Target Irradiation

As a first, we checked the validity of the gating system. Figure 4 shows the time chart of the gated irradiation. The curved line shows the respiratory waveform. The residual motion was 4 mm and the gating duty was the value which was expected.

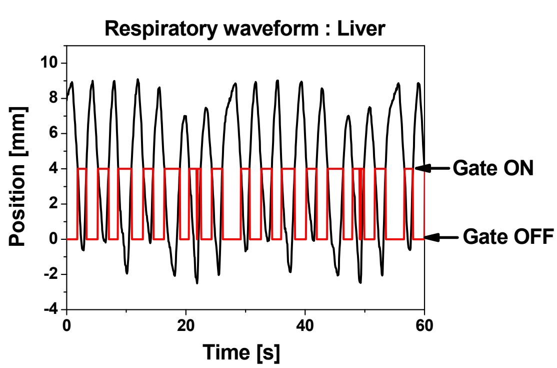

Figure 4: Typical time chart of the gated irradiation.

Figure 5 shows typical results of the additional patient-specific QA. The iso-dose lines of moving target (dashed contour) and static target (solid contour) show the dose difference. The upper and right figures show one-dimensional comparisons. The symbol and solid line show the measured dose distribution in moving field and the measured dose distribution in static field, respectively. The triangle shows the dose difference. The residual motion was 4 mm as shown in Fig. 4 and the displacement between static and moving measurements was 1.5 mm. Therefore, the displacement criterion was satisfied for this QA plan. Additionally, the gamma analysis between the moving and static targets showed good agreement. Figure 6 shows the percentage histogram of dose difference after considering the displacement between static and moving measurement. Dose variation was reasonable. We confirmed that the gating and fast scanning suppressed the interplay effect in the QA measurement.

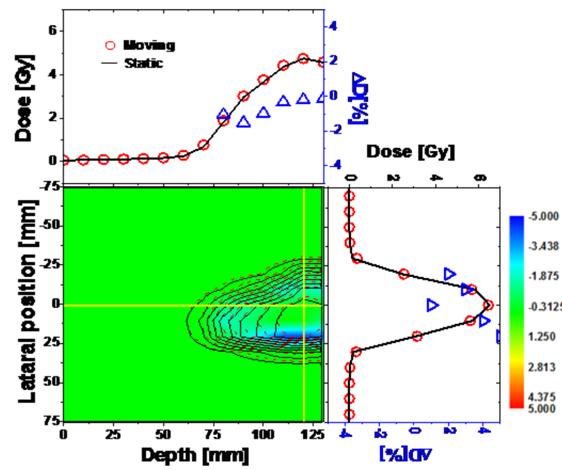

Figure 5: typical result of the additional QA. Comparison between the measured dose distribution in moving field and the measured dose distribution in static field. The upper and right figures show one-dimensional comparisons.

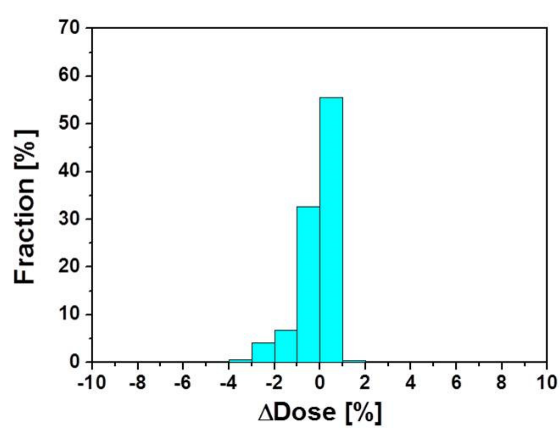

Figure 6: Percentage histogram of dose difference after considering the displacement between static and moving measurement.

ISBN 978-3-95450-176-2

The percentages of passed gamma were compared for fourteen irradiations as shown in Fig. 7 (a). Almost all data reached more than 95% of the passed gamma regardless of the amount of residual motion. However, the passed gamma of the 8th irradiation indicated by arrows in Fig. 7 (a) was less than 95%. In PCR method, it is essential to realize the average displacement during a single gated period of the respiration. As shown in Fig. 7 (b), the probability density functions of the displacement during the gate of the 8th irradiation was not been averaging. This is due to the fact that staying time of target at max displacement was longer. However, the passed gamma was more than 90% of evaluated points and dose difference was within ±2% at almost all evaluated points.

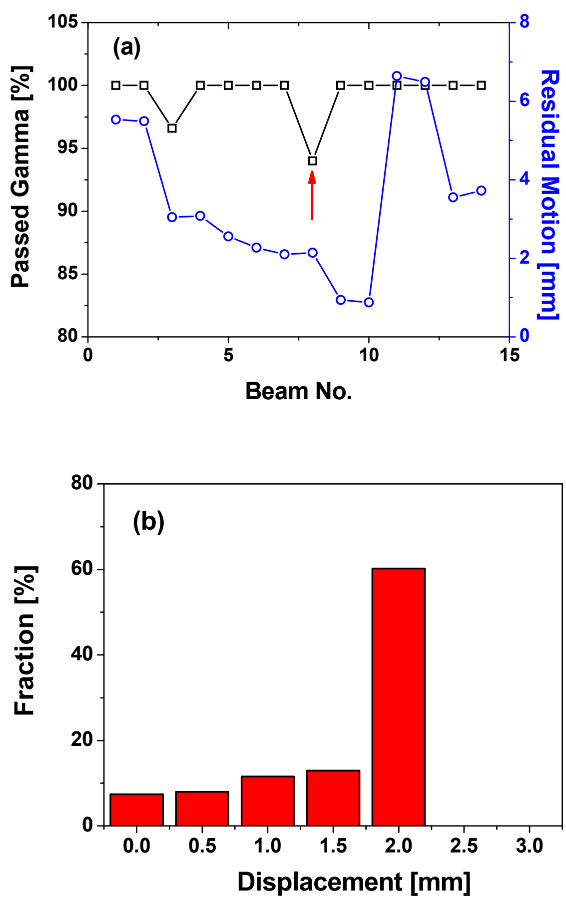

Figure 7: (a) The percentages of passed gamma and residual motion for fourteen irradiations. (b) Probability density functions of the displacement during the gate of the 8th irradiation indicated by arrows in (a).

CONCLUSIONS

We performed the additional patient-specific QA for moving target irradiation with a scanned ion beam. We confirmed that this new technique was a beneficial QA procedure for moving target irradiation. We started the treatment of a moving target by scanning irradiation to the first patient as a clinical study on March 4, 2015.

REFERENCES

[1] Y. Hirao et al., Nucl. Phys. A **538**. 541 (1992).
[2] E. Pedroni et al., Med. Phys. **22**. 37 (1995).
[3] Th. Haberer et al., Nucl. Instrum. Methods Phys. Res. A **330**. 296 (1993).
[4] T. Furukawa et al., Med. Phys. **37**. 5672 (2010).
[5] T. Furukawa et al., Med. Phys. **40**. 121707 (2013).
[6] T. Furukawa et al., Med. Phys. **37**. 4874 (2010).
[7] D. A. Low et al., Med. Phys. **25**. 656 (1998).
[8] T. Inaniwa et al., Med. Phys. **39**. 2820 (2012).

ISBN 978-3-95450-176-2

DEVELOPMENT OF QA SYSTEM FOR THE ROTATING GANTRY FOR CARBON ION THERAPY AT NIRS

N. Saotome#, Y. Hara, K. Mizushima, R. Tansho, Y. Saraya, T. Furukawa, T. Shirai, and K. Noda, National Institute of Radiological Sciences, Chiba, Japan

Abstract

At the National Institute of Radiological Sciences (NIRS), we have been developing the rotating-gantry system for the carbon-ion radiotherapy. This system is equipped with a three-dimensional pencil beam scanning irradiation system. To ensure the treatment quality, calibration of the primary dose monitor, range check, dose rate check, machine safety check, and some mechanical tests should be performed efficiently. For this purpose, we have developed a measurement system dedicated for quality assurance (QA) of this gantry system. The ion beam's dose output are calibrated by measurement using an ionization chamber. A Farmer type ionization chamber is inserted into the center of a water equivalent phantom. The thickness of the phantom could be changed so that employ both calibration of the output at entrance and output checking at center of the irradiation field. The ranges of beams are verified using a scintillator and a CCD camera system. From the taken images, maximum gradient points are determined by some image processing and compared with reference data. In this paper, we describe consideration of the daily QA for the rotating-gantry.

INTRODUCTION

Since carbon ion deposits most of their energy in the last final millimeters of their trajectory, the accuracy of the beam energy/range is required for carbon ion treatment especially for using scanning method. Physical advantages of carbon ion are not only for the beam direction, but also for the lateral direction compare with conventional photon or proton beam. Although QA procedures are necessary for establishing safe and accurate dose delivery of any radiation therapy treatment modality, much high level of QA procedures are required for carbon-ion therapy. There are few guidelines for QA of the particle radiotherapy. The recommendation of the International Commission on Radiation Units and Measurements ICRU [1] that the uncertainties in the delivered dose to patients be limited to within 5% of the prescribed dose is the fundamental principle of the QA guidelines. To ensure the treatment quality, calibration of the primary dose monitor, range check, machine safety check, and some mechanical tests should be performed efficiently. We made the Daily QA list based on the ICRU 78 [2]. Table 1 indicate the list of the daily QA and tolerances. The new treatment room using the rotating-gantry system will be opened at 2016 in addition to existing 4 fixed beam port. Totally 5 of irradiation port have to be check the condition before the treatment within a limited time. For this purpose, we have developed a measurement system dedicated for quality assurance (QA) of this gantry system. The system includes a dose measurement system, a range measurement system, and a slide rail. The system position can be switched for the purpose of the measurement.

#naosao@nirs.go.jp

Table 1: List of Daily QA and Tolerances

Procedures	Tolerances
Calibration of the primary dose monitor	-
output at center of SOBP	2%
Range	0.5mm
Dose rate and monitor ratios for the pencil beam	5%
Performance of the beam-position monitors	Functional
Interlocks	Functional
Isocenter	0.5mm
Gantry angle	0.2 degree

CALIBRATION OF THE PRIMARY DOSE MONITOR

The dose measurement system is used for the calibration of the primary dose monitor. Fig. 1 is the photograph of the dose measurement system. This calibration is performed for the correction of the dose output from the treatment machine. The Farmer type ionization chamber (30013, PTW Freiburg, Germany) was positioned at a depth of 2.0 cm from top of the front surface of a water equivalent phantom. The depth of 2 cm was chosen to ensure that measurements were made in a low dose gradient region of the pristine Bragg Peak curve. The calibration was performed with 10x10 cm2 field size. By comparison of the dose between reference and measured, daily calibration factor is calculated. This measurement is performed at 0 degree of the gantry angle. From the result of the calibration for the existing fixed beam port, our beam control system is very stable. Almost all of the calibration factor from 2011 were within 1 percent. At this moment, only one energy is measured on a daily basis.

ISBN 978-3-95450-176-2

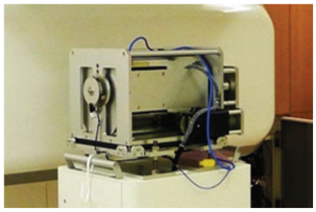

Figure 1: Photograph of the dose measurement system. This is a part of the Daily QA system for the rotating gantry.

OUTPUT MEASUREMENT

After the calibration of the primary dose monitor, to check the combination of the multi devices, the dose output measurements are done at the center of the SOBP width for different carbon beams for the standard 6x6 cm2 field size. The dose measurement system is also used for the output measurement. The Farmer type ionization chamber was positioned at a depth of 10.0 cm from top of the front surface of a water equivalent phantom by inserting the thick phantom. To check the reproducibility of the measurement, we measured 3 times. This measurement was performed at 0 degree of the gantry angle. From the result of the output measurement for the existing fixed beam port, all measurements are within 1 percent.

RANGE VERIFICATION

In the current daily QA at NIRS, Few-points depth dose measurement using ionization chamber is employed for range verification. For the existing fixed beam port, the doses are measured with combination of several range shifter (RSF) plates [3]. It takes about 1 minute for a measurement of one energy beam. Since the gantry beam port is designed for energy scanning method [4], there is not RSF anymore. In order to apply the range check for gantry beam port, independently measureable range verification system is required. For this purpose, we developed the range verification system using a scintillator and a CCD camera (scintillator + CCD system) and to estimate the accuracy of the range verification using the system. The data acquisition of the CCD camera was synchronized with irradiation. We measured pencil-beam having intensities between 8×10^7 and 1.6×10^8 particles per second. Measurement time is 0.1 sec for all energy.

The scintillator + CCD system is shown in Fig. 2. The system is consisted of a scintillator block, CCD camera, and opaque (black) box. Light distribution is detected by CCD camera through a mirror. The optical path length between the scintillator and lens is 400 mm. The system was placed on the treatment couch. The center of the scintillator was placed at isocenter. A EJ-200 plastic scintillator block was selected for pure tranceparent block, similar density with human body, and matching wavelength of maximum emission for CCD camera. The size of cylindrical scintillator block was 200 mm diameter ×20 mm thickness. For shading the light from the treatment room, the scintillator was wrapped by light blocking sheet. The CCD camera (Type BH-61M, 1932x1452 pixels, Bitran Corp., Japan) was installed on the light-shielding house. The spatial-resolution of the system is 0.2 mm/pixels. Measured two-dimensional images were processed by in-house program developed by c++. The workflow of image processing is shown in Fig. 2. After the background correction and median filter, projection on one-dimensional axis is performed. The common reference point of range is distal 80% of the dose distribution. However the system measures the range not with the dose distribution but with the light distribution. From our investigation, DOG method results in smaller discrepancies between the expected and measured ranges for carbon beams compared to the threshold method. DOG method is widely used in edge detection field instead of Laplacian filter [5]. Using DOG method, range position is determined by zero-crossing position in the difference between small-Gaussian smoothed image and large-Gaussian smoothed images. Sigmas for small and large Gaussian are 1 and 1.5 pixels respectively. Only the high-frequency edge position is enhanced when relative small sigma is used. In this work, range-scaling factor is applied. The Range Shifter that gave us the least deviation from the expected relative range for all RSF thickness is then used for all range measurements.

Figure 3 shows the example of depth brightness lines. A total of 124 energy carbon beams that were in the range from 81.7.8 to 326.4 MeV/n were measured sequentially, energy by energy. Relative range differences from the expected range were very small. Root mean square error (RMSE) was less than 0.05 mm for all measurements.

Fig. 4 shows the variation of the measured range for 140, 230, and 290 MeV/n carbon beams over a 6 days. Maximum deviation from mean range is 1.1 mm for 140 MeV/n. From the estimation of the impact of the setup error, beam position or setup error was not negligible, correction of these kind of error have to be considered.

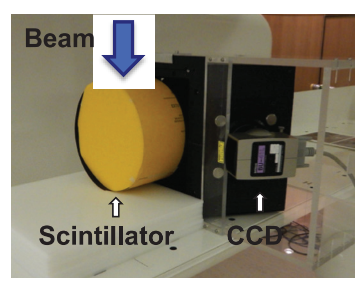

Figure 2: Photograph of the scintillator + CCD system. This is a part of the Daily QA system for the rotating gantry.

ISOCENTER AND GANTRY ANGLE

As a part of the mechanical QA procedures, the accuracy of the isocenter position and gantry angle is tested daily. The beam position is checked the coincidence from the center position of patient positioning system. The gantry angle is checked to ensure

ISBN 978-3-95450-176-2

the accuracy of the digital display and coincidence between mechanical angle and radiation beam angle. Prior technique for isocenter verification in radiation center is to measure the distance between center of the metallic ball and beam center by using screen monitor system. For this technique, preparation of the target and measurement device i.e. screen monitor system are required. We decide to verify the isocenter position and gantry angle using scintillator + CCD system for Daily QA for efficiency. The proposed method extends the basic star shot technique [6]. The star shot test was relatively simple and became quite popular, but it was based on films; therefore, it inherited all film-related problems. The general disadvantages in using films include the cost of films, chemicals and processor maintenance, and occupation of archiving space. we developed the software to analyze the beam angle. we tested for the couch rotation instead of the gantry rotation. Fig. 5 is example of the measured data. Image acquisition was performed sequentially beam by beam.

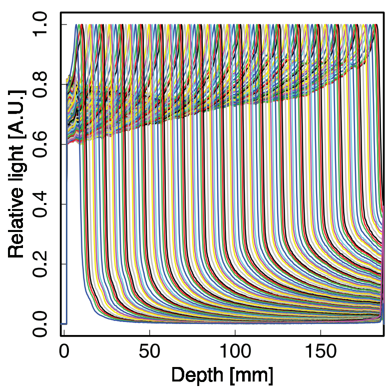

Figure 3: Examples of depth brightness lines. A total of 124 energy carbon beams that were in the range from 81.7.8 to 326.4 MeV/n were measured sequentially, energy by energy.

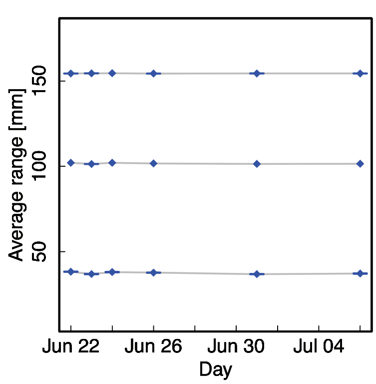

Figure 4: Variation of measured range for 140, 230, and 290 MeV/n carbon beams over a 6-day period.

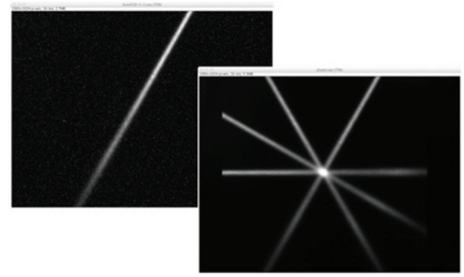

Figure 5: Example of star shot test using scintillator + CCD system. The carbon beam track was measured beam by beam.

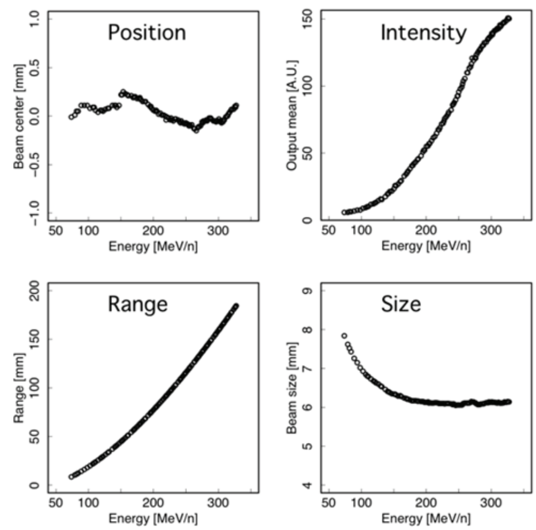

Figure 6: Example of beam position, intensity, range, and size measurement. These data were analyzed using the data for range measurement. A total of 124 energy carbon beams that were in the range from 81.7.8 to 326.4 MeV/n were measured sequentially, energy by energy.

The data acquired by scintillator + CCD system enclose the informative data, such a beam position, intensity, size, and etc. Fig. 6 shows the example of these data. We plan to use utilize these data for analyzing the trend of the machine condition.

CONCLUSION

In this work, Daily QA system for the rotating gantry for the carbon ion therapy with combination of the dose measurement system and range verification system has been developed. We have shown the preliminary result for the range measurement for the gantry beam port. We plan to deliver the carbon ion beam to the gantry beam port in September 2015.

ACKNOWLEDGMENT

The authors would like to express gratitude to Accelerator Engineering Corp. for the skilful operation of the accelerator complex. The authors are grateful to members of the Medical Physics Research Group at NIRS for their warm support and useful discussions.

REFERENCES

[1] ICRU Report 50, Journal of the ICRU, (1993).
[2] ICRU Report 78, Journal of the ICRU, (2007).
[3] T. Furukawa, et al., Med. Phys., 37 (11), 5672-5682 (2010).
[4] Y. Iwata, et al., NIM. A, 624, 33-38 (2010).
[5] D. Mark, et al., Proc. R. Soc. Lond. B, 207, 187-217, (1980).
[6] Gonzalez A, et al., Med Phys. 31, 1489-1493 (2004).

ISBN 978-3-95450-176-2

DEVELOPMENT OF FPGA-BASED TDC WITH WIDE DYNAMIC RANGE FOR MONITORING THE TRIGGER TIMING DISTRIBUTION SYSTEM AT THE KEKB INJECTOR LINAC

Tsuyoshi Suwada*, Kazuro Furukawa, Fusashi Miyahara, KEK, Tsukuba, Japan

Abstract

A new field-programmable gate array (FPGA)-based time-to-digital converter (TDC) with a wide dynamic range greater than 20 ms has been developed to monitor the timing of various pulsed devices in the trigger timing distribution system of the KEKB injector linac. The pulsed devices are driven by feeding regular as well as any irregular (or event-based) timing pulses. For monitoring the timing as precisely as possible, a 16-ch FPGA-based TDC has been developed on a Xilinx Spartan-6 FPGA equipped on VME board with a time resolution of 1 ns. The resolution was achieved by applying a multisampling technique, and the accuracies were 2.6 ns (rms) and less than 1 ns (rms) within the dynamic ranges of 20 ms and 7.5 ms, respectively. The various nonlinear effects were improved by implementing a high-precision external clock with a built-in temperature-compensated crystal oscillator.

INTRODUCTION

Recent advances in FPGA technology have made it possible to apply them to TDCs in which the FPGA is embedded (called FPGA-based TDCs) in high-energy particle and nuclear physics [1] and also in materials science [2]. FPGA-based TDCs are very attractive because of their high performance, high-speed data transfer, and customizability and flexibility in precision timing measurements without any external complex hardware. These excellent features enable high-precision time-duration measurements down to a few picoseconds (see references in [1]). These features also enable the possibility of new applications to precisely monitor various timing pulses with a wide dynamic range in large accelerator complexes, where an accuracy of a few nanoseconds is sufficient.

We have developed a new FPGA-based TDC required for application to the KEKB injector linac. The required specifications of the TDCs are a wide dynamic range greater than 20 ms and an accuracy of 1 nanosecond level, where low-cost fabrication should be also required. The basic design, development, and experimental results of the new FPGA-based TDC for applications to large accelerator complexes are reported in detail.

FPGA-BASED TDC

Required Specifications

All downstream storage rings of the KEKB injector linac [3] will be filled in top-up injections based on a pulse-by-pulse modulation scheme at 50 Hz, which allows the injector linac to perform virtually simultaneous injections [4]. For the virtually simultaneous injections, a new trigger timing distribution system is under development on the basis of the event-based timing and control system [5]. A new additional system is also under development for monitoring all timing pulses generated in the trigger timing distribution system as precisely as possible [6]. The purpose of the introduction of a timing monitoring system is to increase the reliability of the event-based timing and control system. Because the injection beam charges need to be increased to be four to five times greater than those of the previous KEKB, such a timing monitoring system may serve not only the stable operation and complex simultaneous injection but also reliable radiation safety and machine protection of the injector linac.

The fiducial repetition frequency of the injector linac is based on 50 Hz. All pulsed devices are driven by the trigger timing pulses appropriately delayed from the fiducial timing. These trigger timing pulses are fundamentally generated with a frequency of 50 Hz at maximum by obeying the beam injection timing sequences programmed in the control system. However, in a strict sense, the fiducial time duration does not need to be determined exactly to be 20 ms owing to the synchronization condition of the linac and ring RF frequencies on the injection bucket position in the ring.

The allowable width of the fiducial time duration is restricted to the trigger timing condition for the modulators of the high-power klystrons in the injector linac because the modulators should be driven within 20 ± 1 ms to stabilize the applied voltage and to sufficiently allow for stable charging. This specification means that the allowable time duration of the fiducial timing should be monitored to maintain them within 20 ± 1 ms.

The trigger timing for most of other pulsed devices is less than 1 ms delayed from the fiducial timing, and more especially, the trigger timing for the beam-position monitors should be maintained at an accuracy of 1-ns level. Therefore, a resolution of 1 ns and a dynamic range greater than 20 ms are required for the time-duration measurements in the TDC along with a higher accuracy.

Basic Design

The present event-based trigger timing distribution system was constructed in a VME-based system, and accordingly, it was necessary to construct new TDCs (6U VME64x module) in the same VME-based system. The basic specifications required for the VME/FPGA-based TDC are listed in Table 1.

* tsuyoshi.suwada@kek.jp

ISBN 978-3-95450-176-2

Table 1: Basic Specifications Designed for the VME/FPGA-based TDC

Basic parameter	Value	Units
Number of common starts	1	
Number of stops	16	
Number of multistops	4	
Number of bits	32	
Dynamic range (max.)	4.3	s
Resolution	1	ns
Clock frequency	250	MHz
Gigabit Ethernet	available	

The TDC has a common start and sixteen stop input channels. The input voltage level is based on a Nuclear Instrumentation Module (NIM) standard with a 50-Ω input impedance. The fiducial pulse is fed into the common start input channel, and the delayed trigger pulses to the pulsed devices are fed into the stop input channels. Each delay time from the fiducial pulse and the time duration between the fiducial pulses are synchronously measured with 32-bit counters with a resolution of 1 ns. A wide dynamic range of 4.3 s can be implemented at maximum on a Xilinx Spartan-6 (XC6SLX75) FPGA [7]. A multistop function in each stop input channel is available by which the delay timings of successive trigger pulses (up to four at maximum) during one fiducial period generated on one trigger line can be synchronously measured. This is an important specification required for two-bunch acceleration in an RF pulse delivered from the A1 electron gun, in which the time duration between two bunches is exactly 96.3 ns [5]. The content of the buffer data in the FPGA can be accessed via an A32/D32 VME64x interface. The developed TDC module is shown in Fig. 1.

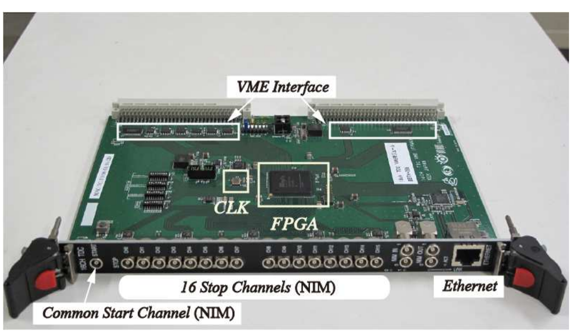

Figure 1: Developed VME/FPGA-based TDC module.

Basic Principle for the Time-duration Measurement

A fundamental principle of the TDC implementation is to count the number of the reference clock pulses generated during the time duration (T) between the leading edges of the start and stop pulses with a coarse counter, as shown in Fig. 2.

In such implementation schemes, the time resolution of the TDC is limited to T_{clk} at maximum, where T_{clk} is the time duration for a period of the reference clock when the

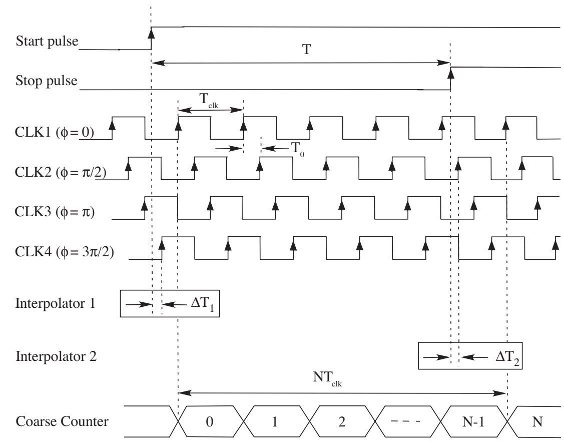

Figure 2: Timing diagram of the fundamental time-duration measurement of the TDC based on the multisampling technique.

start and stop pulses generated in the trigger timing distribution system are not synchronized at all with the reference clock of the TDC. There are several smart methods (sometimes called interpolation methods [8]) to improve the time resolution.

The time duration to be measured may be expressed as

$$T = NT_{clk} + (\Delta T_1 + \Delta T_{\phi 1}) - (\Delta T_2 + \Delta T_{\phi 2}), \quad (1)$$

where ΔT_1 (ΔT_2) is the fractional time duration measured between the leading edge of the start (stop) pulse and that of the next nearest pulse of the valid reference clock (CLK4 (CLK2) in this case), and $\Delta T_{\phi 1}$ ($\Delta T_{\phi 2}$) is the phase delay time of the valid reference clock with respect to the main reference clock (CLK1) ($\Delta T_{\phi 1} = T_{clk}/4$ ($\Delta T_{\phi 2} = 3T_{clk}/4$) in this case), although most of the time duration may be measured as NT_{clk} synchronously with the main reference clock (see Fig. 2). If the fractional time durations can be measured with a higher resolution on the basis of any interpolation method, the time resolution of the TDC may be comprehensively improved.

The multisampling (sometimes called 4×oversampling) technique [1] is one of many smart interpolation methods. In the multisampling technique, four similar reference clocks are generated in the FPGA with a period of T_{clk}, for which each relative phase difference is $\pi/2$, which corresponds to a delay time of $T_{clk}/4$, shown as CLK1–CLK4 (see Fig. 2). The fractional time, ΔT_1 (ΔT_2), for the start (stop) pulse can be measured by detecting the leading edge of the temporally closest reference clock by a first (second) interpolator with a four-times improved resolution of $T_0 = T_{clk}/4$, whereas most of the time duration (NT_{clk}) can be measured with a coarse counter driven by the main reference clock. The total time duration can be simply calculated based on eq. (1) by decoding and adding these results with a resolution of T_0.

Circuit Architecture

Here, the generation of the reference clocks along with their relationships used in the TDC is described in detail. A

ISBN 978-3-95450-176-2

schematic block diagram of the circuit architecture of the TDC along with a block diagram of the phase-locked loop (PLL) are shown in Fig. 3.

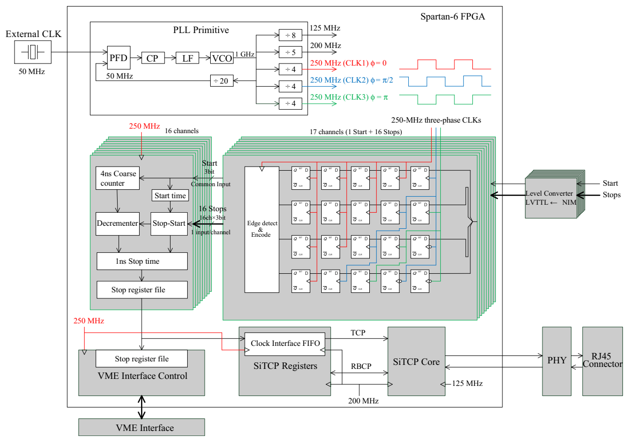

Figure 3: Schematic block diagram of the circuit architecture of the developed TDC. The meanings of the labels are detailed in text.

Three reference clocks, CLK1, CLK2 (delayed by $T_{clk}/4$), and CLK3 (delayed by $T_{clk}/2$), with each clock frequency of 250 MHz ($T_{clk} = 4$ ns) and a phase difference of $\pi/2$ are generated via a voltage-controlled oscillator (VCO) with a frequency of 1 GHz in the PLL primitive, where the frequency of the reference clock is divided by four through a frequency demultiplier. Two other frequencies, 200 MHz and 125 MHz, for the SiTCP and a physical layer transmitter and receiver of Ethernet (PHY) are generated by frequency-demultiplying the VCO frequency by five and eight, respectively. A frequency of 50 MHz is generated by frequency-demultiplying the VCO frequency by twenty, and it is directly phase-locked with the external clock via a standard digital PLL with a bandwidth of 4 MHz, which comprises a phase frequency detector (PFD), a charge pump (CP), and a loop filter (LF). Here, it is important to choose an external clock from a viewpoint of frequency stability because it dominantly influences the characteristics and performance of the TDC in terms of the frequency stability, jitter, skew, and temperature effects. An external 50-MHz temperature compensated crystal oscillator (TCXO, EPSON TG-5501CA [9]) has been selected during TDC development because its frequency stability is guaranteed within ±1 ppm in a temperature (T_e) range of – 40 to 85°C, for which the frequency stability is substantially an order smaller than that of standard crystal oscillators. The basic specifications of the external clock are listed in Table 2.

Table 2: Specifications of the External Clock

Parameter	Value	T_e Range
Frequency	50 MHz	
Stability	$< \pm 1.0 \times 10^{-6}$	25 ± 2°C
Property	$< \pm 0.28 \times 10^{-6}\ ^{o}C^{-1}$	– 40 to 85°C

The fractional time durations (ΔT_1 and ΔT_2) are measured in the 1-ns interpolator as shown in Fig. 3. In the 1-ns interpolator, the start and stop pulses of the input signal are basically sampled and latched at respective D input via a flip-flop array with the use of both the leading and trailing edges of the two reference clocks with a phase difference of $\pi/2$ (CLK2 and CLK3, called sampling clocks), while another reference clock (CLK1, called system clock) is used as a sampling clock for the 4-ns coarse counter, and however, it works as the system clock in the 1-ns interpolator. In such a sampling scheme, the fractional time durations are determined by data sampled at the first row (4 flip-flops) of the flip-flop array. Thus, this sampling scheme is equivalent to that with the use of four different reference clocks with a phase difference of $\pi/2$ as shown in Fig. 2. It should be noted, however, that the system clock (CLK1) is not used at all for determining the fractional time durations in the 1-ns interpolator, while it is used only for determining the coarse time duration (NT_{clk}). This scheme is of advantage to save clock resources in the FPGA as much as possible and it is also due to increase the stability and reliability of the sampling clocks as much as possible by separating them from the system clock. A subsequent 4×4 flip-flop array is required for the two sampling clocks to be synchronized with the system clock domain and also to avoid any metastable states. Thus, the input signal is sampled five times each clock period in total.

In the decision logic (shown as "Edge detect & Encode"), the timing measurement result is converted to a 2-bit information along with an additional bit, which is used for an acknowledgement of both the valid edge detection and the valid phase with respect to the system clock. Then, a 3-bit and sixteen 3-bit information for the start and sixteen stop pulses, respectively, are sent to another logic where the measurement results are decoded. The fractional time duration measured in the 1-ns interpolator is decoded with its sign in a register (shown as "Stop-Start"). On the other hand, the coarse time duration is decoded in the 4-ns coarse counter. Both the coarse time and fractional time durations are simply calculated in a register (shown as "Decrementer") with taking into account the signs of the fractional time durations based on eq. (1). The final result is stored in a register (shown as "1-ns Stop time"). Finally, the same data are moved to another register (shown as "Stop register file") that can be accessed via a VME interface. It should be mentioned that in this decoding scheme the fiducial duration itself can be easily measured on the basis of the nominal start-stop implementation scheme even without any additional stop pulse, in which the next nearest start pulse is applied to the stop pulse.

EXPERIMENTAL TESTS

Characteristic Nonlinearity Measurements

The characteristic nonlinearity measurements were carried out with a high-precision rubidium time-based delay generator (SRS, Model DG645) for investigating these

ISBN 978-3-95450-176-2

systematic-error factors. Because the timing jitter of this delay generator is 10 ps/s (rms), the measurement errors expected from the delay generator are negligibly small. The start and stop pulses were generated with the delay generator, and they were fed into the TDC in an atmospheric environment. The time duration between the leading edges of the start and stop pulses was measured by changing the delay time to be set, where for simplicity, the asynchronous measurements were performed using the delay generator to drive the TDC. The results are shown in Fig. 4.

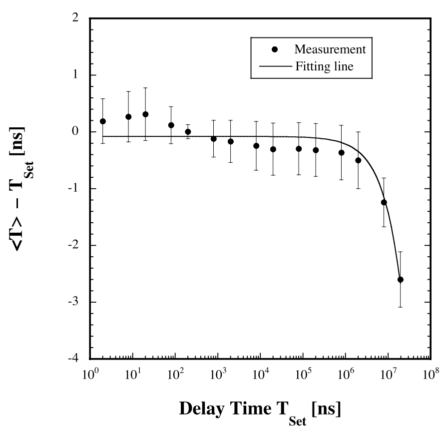

Figure 4: Variations in the time difference between the measured and set delay time with a dynamic range of 20 ms. Each solid point represents the average value over 5000 measurements and only the statistical error bars are plotted. The solid lines show a guide for the eyes only in a straight-line fitting.

Figure 4 shows the variations in the time difference between the measured and set delay time with a dynamic range of 20 ms, which is the required dynamic range. The nonlinear point of the time difference curve is expected to be ~3 ms as shown in Fig. 4, and the absolute time difference at 20 ms is 2.6 ns. An 1-ns accuracy is attainable within the region less than 7.5 ms, and the quantization errors are dominant in this region.

The accuracy is generally given by the absolute time difference divided by the set delay time. The results are shown in Fig. 5 and show that the accuracy reaches a saturation point at which the set delay time is T_{set} ~3 ms, where the attained accuracy is 0.13 ppm, which may originate from the frequency stability of the external clock.

Precision and Integral Nonlinearity

The precision of the TDC is generally defined by a standard deviation of repetitive measurements of the time duration in which the quantization errors are dominant [10] if the systematic nonlinearity is sufficiently smaller within a given dynamic range; that is, the measurement errors are dominated by statistical errors. If in such measurement conditions the decimal part (c) of the ratio (T/T_0) is given by

$$c = \mathrm{Frc}[T/T_0], \tag{2}$$

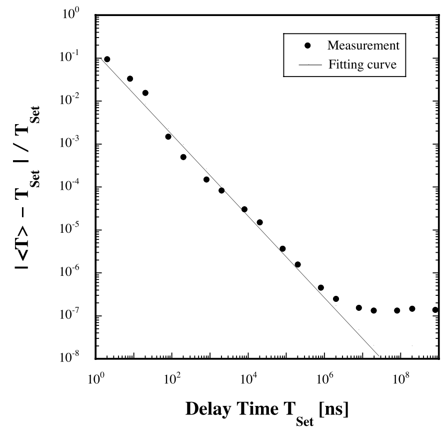

Figure 5: Variations in the accuracy as a function of the set delay time. The solid line is an exponential function fitted to the data.

the measurement precision (σ_T) is expressed by the following equation [8]:

$$\sigma_T = T_0\sqrt{c(1-c)}. \tag{3}$$

The obtained precisions depending on the set delay time are shown in Fig. 6(a).

Here, the solid line shows calculations based on eq. (3), where the average values are applied to the parameter (T). The variations in the precision measurement are in good agreement with calculations. The obtained result means that the precision is mainly caused by the quantization errors within a dynamic range of 20 ms. The maximum (minimum) differential is 0.52 (0.13) ns. This result means that the least significant bit (LSB) due to quantization errors corresponds to 0.52 bits at maximum. The variations in the differential time difference between the measured and set delay time with a straight-line fitting within the same dynamic range are shown in Fig. 6(b).

The integral nonlinearity is defined by the maximum difference within a given dynamic range. The maximum integral nonlinearity is 0.39 ns at the set delay time of 20 ns. This result means LSB = 0.39 bits. Thus, the precision in the time-duration measurement may be expected to be less than 1 ns in total within a dynamic range of 20 ms. The obtained result is sufficiently acceptable for the trigger timing distribution system.

Temperature Stability

The temperature stability of the TDC was measured within a temperature region of 5–35°C by changing the environmental temperature, where the TDC along with a VME crate without any CPUs were placed in a thermoregulated bath while the delay generator was outside. The results are shown in Fig. 7.

Figure 7(a) shows the variations in the difference ($\Delta\langle T\rangle$) between the measured time duration and the set delay time as a function of temperature, and Fig. 7(b) shows the differential coefficient with temperature as a function of the set delay

ISBN 978-3-95450-176-2

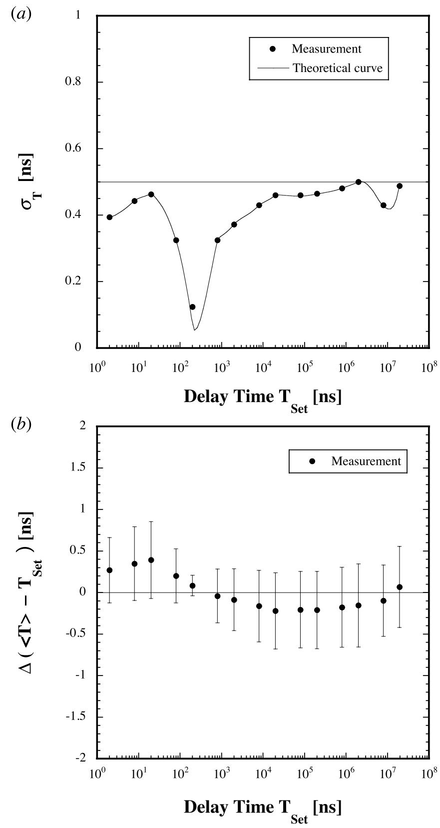

Figure 6: Variations (a) in the precision measurement depending on the set delay time within a dynamic range of 20 ms and (b) in the differential time difference between the measured and set delay time from a straight-line fitting within the same dynamic range.

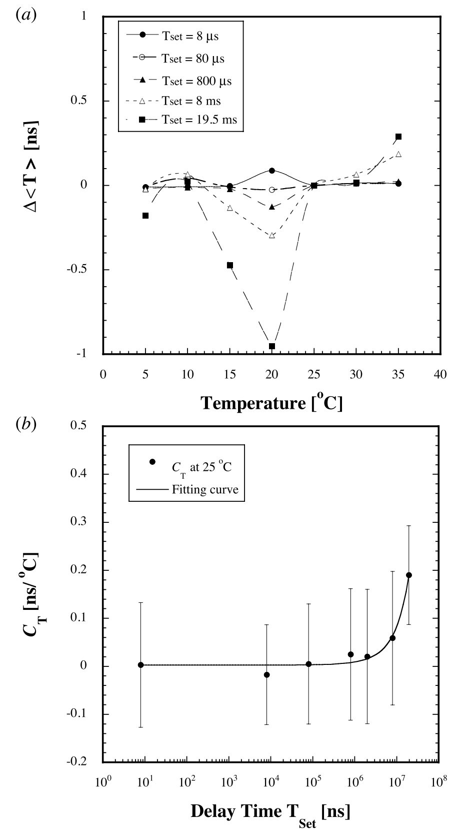

Figure 7: Variations (a) in the difference between the measured time duration and the set delay as a function of temperature, and (b) in the differential coefficient with temperature as a function of the set delay time. The lines indicate a guide for the eyes only in (a) and a second-order polynomial fit to the experimental data in (b).

time. In Fig. 7(a), it should be mentioned that the data points are shown as the differentials from the reference data measured at 25^{o}C (room temperature).

The variations in the temperature stability cannot be expressed by any simple monotonic functions because the temperature effect is automatically compensated by feedback controls embedded in the external clock, and their characteristic feedback patterns may originate from its intrinsic temperature compensation scheme. The maximum measured time duration is $|\Delta\langle T\rangle| \sim 1$ ns at 20^{o}C and a set delay time of 19.5 ms. The variations in the differential coefficient (C_T [ns/^{o}C]) with temperature at 25^{o}C are shown in Fig. 7(b). The magnitude of the coefficient starts to slightly increase at a set delay time greater than 2 ms. The obtained result is sufficiently acceptable for the trigger timing distribution system.

CONCLUSIONS

We have successfully fabricated and tested a new VME/FPGA-based TDC with a wide dynamic range greater than 20 ms and a resolution of 1 ns. The required specifications of the TDC were realized on the basis of the suitable design with a high-precision temperature-compensated external clock with an accuracy of 0.13 ppm. The results are fully sufficient for monitoring the trigger timing distribution system of the injector linac. The developed TDC could be applied to further complex timing systems in large accelerator complexes.

REFERENCES

[1] A. Balla *et al.*, Nucl. Instr. and Meth. A 739 (2014) 75.

[2] S. Kishimoto *et al.*, Nucl. Instr. and Meth. A731 (2013) 53.

[3] M. Akemoto *et al.*, Prog. Theor. Exp. Phys. (2013) 03A002.

[4] K. Furukawa *et al.*, ICALEPCS'13, San Francisco, CA, USA, 2013, pp. 1497 – 1500.

[5] K. Furukawa *et al.*, PAC'09, Vancouver, British Columbia, Canada, 2009, pp. 4797 – 4799.

[6] T. Suwada *et al.*, Nucl. Instr. and Meth. A786 (2014) 83.

[7] Xilinx Inc., http://www.xilinx.com/.

[8] J. Kalisz, Metrologia 41 (2014) 17.

[9] SEIKO EPSON Corp., http://www.epson.com/.

[10] L. Zaworski *et al.*, Metrol. Meas. XIX (2012) 115.

ISBN 978-3-95450-176-2

DATA ACQUISITION SYSTEM FOR SUPERKEKB BEAM LOSS MONITORS

Makoto Tobiyama#, Hitomi Ikeda and John W. Flanagan,
KEK Accelerator Laboratory, 1-1 Oho, Tsukuba 305-0801, Japan.
Graduate University for Advanced Studies (SOKENDAI), 1-1, Oho, Tsukuba 305-0801, Japan.

Abstract

The monitoring of the beam loss distribution along the accelerator is important to prevent damage do delicate detectors around the collision point and to vacuum components such as collimators, and also to suppress the unnecessary irradiation of the accelerator elements. As it is not convenient to construct the readout system synchronized to fast timing such as beam injection, a new 64-ch ADC system which samples the output of the loss monitor signal integrator at a fairly fast rate and automatically keep the peak, mean, and minimum data has been developed. The performance of the ADC system is shown. The control system configuration which reads and resets the hardware interlock signal from the loss monitor integrator for the machine protection system (MPS) is also shown.

INTRODUCTION

The KEKB collider is now being upgraded to the SuperKEKB collider to obtain 40 times higher luminosity than that of KEKB. To realize such high luminosity, the beam energy is re-optimized to 7 GeV for KEKB-HER (HER, electron) and to 4 GeV for KEKB-LER (LER, positron). The maximum beam currents will be roughly doubled to 2.6A for HER, and to 3.6A for LER with much reduced beam emittances and x-y couplings. The beam size at the collision point will be further squeezed with a larger crossing angle. The first commissioning of the HER and the LER without BelleII detector installed (Phase-I operation) is planned to start early 2016. The main beam parameters of the SuperKEKB rings are shown in Table 1.

With the increase of the beam currents and reduction of the beam sizes, the stable beam loss rate along the rings is anticipated to increase greatly. The simulated beam loss rates with designed luminosity are 10 mA/s and 7.2 mA/s for LER and HER, respectively [1]. Those rates are 50 times higher than that of KEKB. In addition, the much smaller vertical beam size could easily cause disastrous damage to the vacuum components due to higher charge density. It is important to monitor the beam loss and to take necessary actions, such as stopping injection or requesting a beam abort before causing disastrous accidents.

For the main rings (HER and LER), we will use a similar configuration for the beam loss monitor system to that used at the KEKB accelerator [2, 3]. It consists of air ion chambers (ICs) and PIN photo-diodes (PINs) [4]. The lengths of the ICs are 5 m and they are distributed roughly every 30 m around the ring, typically near the focusing sextupole magnets (SFs). They are fixed on the cable rack near the outer wall of the accelerator tunnel where the direct distance from the nearest ring is about 2 m, and about 1 m above the medium plane of the rings. For the new positron damping ring (DR) [5] which will start beam commissioning around late FY2016, we plan to install ICs with lengths of 9 m around the ring.

Table1: Main Parameters of SuperKEKB Rings

	HER/LER	DR
Energy (GeV)	7/4	1.1
Circumference(m)	3016	135.5
Max. Beam current (A)	2.6/3.6	0.07
Number of bunches	2500	4
Single bunch current (mA)	1.04/1.44	18
Bunch separation (ns)	4	>98
Bunch length (mm)	5/6	6
RF frequency (MHz)	508.887	
Harmonic number (h)	5120	230
T. rad. damping time (ms)	58/43	11
L. rad. damping time (ms)	29/22	5.4
x-y coupling (%)	0.27/0.28	5
Natural emittance (nm)	3.2/4.6	42.5
Crossing Angle (mrad)	83	
Horiz. beam size at IP(μm)	10.2/7.75	
Vert. beam size at IP(nm)	59/59	
Beam-Beam Parameter	0.90/0.875	
Peak Luminosity ($cm^{-2}s^{-1}$)	8×10^{35}	
Max. injection rate (Hz)	50/50	50
Number of ICs	105	40
Number of PINs	101	optional

The PIN photo-diodes (PINs) are mainly placed near special vacuum components, such as beam collimators, to directly detect large and fast beam loss. Though the number of ICs is almost the same as that of KEKB, we

#makoto.toibyama@kek.jp

ISBN 978-3-95450-176-2

will reinforce the PINs to observe fine, fast beam loss distributions.

Signals from the ICs and PINs are brought to five local control rooms around the rings. The outputs of the ICs are integrated and amplified using NIM 2W-size integrators which handle 8-channels of IC signals. The gain and the integration time constant can be selected from 1X, 10X or 100X, and 0.1 s, 0.3 s and 1 s, respectively. If a loss level exceeds a common pre-defined threshold, it initiates a beam abort request signal which is connected to the machine protection system (MPS).

The outputs from PINs are first integrated with a short time constant of 1 μs, then amplified with the selected gain (1X, 10X, 100X). One output of the amplifier is held with a peak hold circuit with the fixed time constant of 1 s. Other output is directly compared with the pre-defined threshold to initiate beam abort. The size of the module is NIM-2W, and it handles 8 channels of PIN signals. Typical beam abort levels at KEKB were 10 mA/ms and 10 mA/μs for ICs and PINs, respectively [4].

We have developed a 64-ch ADC system which samples the output of the loss monitor signal integrator modules at a fairly fast rate and automatically holds the peak, mean, minimum data. The details and the performance of the system are shown. The control system which reads and resets the hardware interlock signal from loss monitor integrators for the MPS are also shown.

READOUT SYSTEM

Original ADC used at KEKB.

In the original KEKB MR loss monitor systems, we used 16 bit, differential-input, 32-channel scanning VME ADC boards (Internix PVME-332) to read the individual output of the integrators. The original plan was to trigger the ADC synchronized to the injection timing with a reduced integration time constant of the integrator during beam injection, and then to trigger it at 1 Hz with a much longer integration time constant during storage. We prepared an external injection trigger module which mixed the injection timing of both LER and HER, and the control hardware and software to change the integration time constant automatically. Unfortunately, the system did not work so effectively due mainly to insufficient network resources (10Mbps) and a slow user interface due to computing power constraints at the time. Note that it is still not practical to directly handle the data at a high repetition rate such as 50 Hz because no one can utilize the data within 20 ms. We therefore gave up on changing the mode between injection and storage, and fixed the integration time constant to 1 s for the ICs.

New ADC Boards 18K14

There are several unsolved difficulties with the multi-board operation of the PVME-332s. Moreover, the boards have been discontinued and the company that fabricated the board have given up any kinds of support. We therefore have decided to develop a new VME-based ADC board which fulfils following specifications:

- 64-channel single-ended inputs compatible with PVME-332 (bipolar input, with the input range of ±10 V, and the signal input connectors).
- More than 14-bit resolution ADC with simultaneous sampling for all 64 channels.
- On board mathematic function which calculates the peak, the minimum and the mean of the data at a higher sampling frequency, such as 1 kSPS.
- Board to board synchronization function to synchronize the peak, minimum and mean calculation period.

Figure 1 shows the block diagram of the developed ADC board (Digitex 18K14A). It consists of 8, 16-bit, simultaneous sampling, analog-to-digital data acquisition systems (Analog Devices, AD7606) [6] with eight single-ended input channels. The maximum throughput rate of the AD7606 is 200 kSPS. It also includes oversampling function from 1 (no oversampling) to 64 times the timing clock with built-in antialiasing filter (a second-order Butterworth with -3dB frequency of 23 kHz when used with the input range of ±10 V). The SNR and THD is typically 95.5dB and -107dB, respectively. The DC accuracy is ±8 LSB, typically.

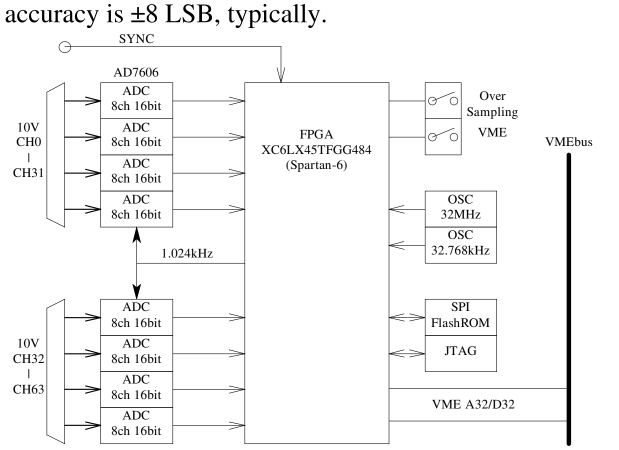

Figure 1: Block diagram of 16bit 64-ch., high-sampling rate ADC (Digitex 18k14A).

The board contains an FPGA (Spartan6 XC6SLX45) to read the AD7606s and to communicate with the VMEbus. It boots up from a SPI flash ROM during initialization of the VMEbus. The boot-up time is very short, typically less than 1 second, much shorter than the boot up time of VxWorks on the VMEbus controller. A J-TAG connector on the board is prepared to update the SPI flash ROM if needed. Timing clock for AD7606 is designed to be 1.024 kHz which is supplied from the FPGA (32.768 kHz / 32) to all AD7606s.

Data from AD7606s are captured and processed by the FPGA using a high speed serial interface. The average (simple average), peak-hold and minimum-hold function is done within the defined time period (1 s: 1024 samples, 0.5 s: 512 samples, 0.25 s: 256 samples). For monitor use, it also can report the raw AD data at the VME access

ISBN 978-3-95450-176-2

which updates once per 1024 samples. The oversampling function of the AD7606s is also usable by setting a DIP switch on the board. We have no plan to use the oversampling function in normal operation, though.

The board supports A32 D32 supervisor (AM=0x0D) and non-supervisor (AM=0x09) access, and occupies 1024 bytes of memory space per board. The interrupter function after finishing mathematical calculations is also supported by the setting of the DIP switch on the board. As simple scan should be enough for most cases, we will not use the interrupter function, however. Figure 2 shows a photo of the 18K14A board installed in the VME64x bus at a test stand. On the front panel, it has two D-sub 37 connectors for analog input, one QLA input for synchronization between boards, three LEDs to show the FPGA status (program done or not), VME access and A/D status (busy, calculation done or standby). On the board ADC chips (AD7606s) are electrically shielded to suppress the noise around the VME. The lengths of the shielded signal cables from the loss monitor integrator to the ADC depends on the configuration of the system rack, typically around 5 m. We have developed EPICS [7] (R314.12.3) device support for VxWorks 6.8.3 on MVME5500 CPU.

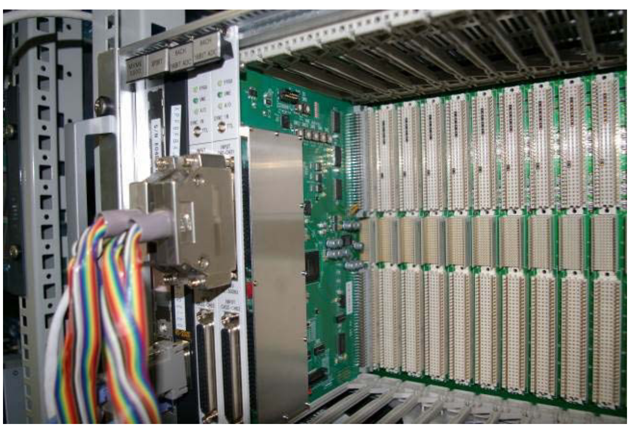

Figure 2: Picture of 18K14A 64-ch 16-bit VME ADC on the test stand.

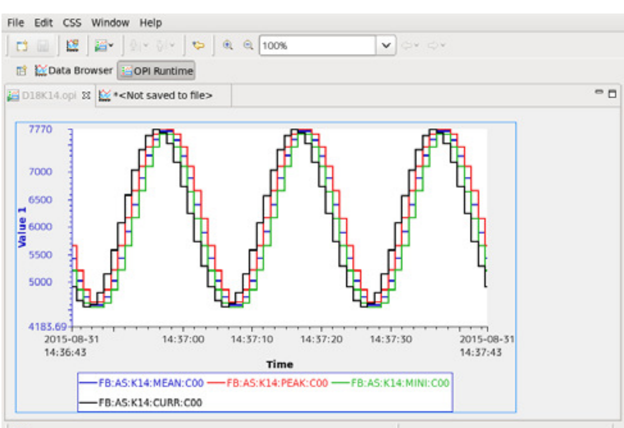

Figure 3: Digitized sinusoidal signal of 0.05 Hz. Mean (blue), Peak (red), Minimum (green) with monitor (black) shows expected behaviours.

The mathematical functions on the FPGA have been evaluated by injecting the known fast signals to 18K14A and checking the ADC outputs (peak, mean, minimum). Figure 3 shows an example of ADC outputs with 0.05Hz sinusoidal input. The scanning of the ADC output is 1 Hz and the calculation period is 1 s (1024 samples). The peak always stays on top and the minimum always stays on the bottom, while the mean stays between the peak and minimum. Note the monitor output shows a different phase from the calculated ones, because it bypasses the mathematical functions, roughly 1 second earlier than those signals.

By injecting a much higher frequency than 1 Hz, for example, a 991 Hz sinusoidal signal, the output shows completely different curves as shown in Fig. 4. All the curves (Peak, Mean and Minimum) show constant lines. The monitor curve shows the aliased remainder from 991 Hz of the function generator to 1 Hz of the 18K14A ADC clock. They also show good frequency response up to 1 kHz.

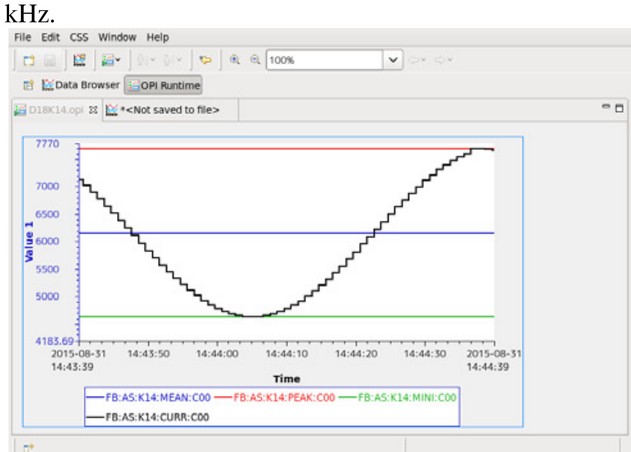

Figure 4: Digitized sinusoidal signal of 991 Hz. The monitor output (black) shows aliased curve to 1 Hz ADC clock.

Synchronization Between the ADC Boards

The ADC boards will be installed in the local control rooms around the rings. They boot up completely independently and process the data following their own system clock. Therefore, the beam loss data obtained with the EPICS scanning period of 1 Hz might be placed into earlier or later scanned data slots depending on the calculation period of the ADC boards. As the precise behaviour of a beam loss which triggers a beam abort is recorded directly using a multi-channel data logger with other useful information such as beam current, RF phase, RF voltage, a one second difference with the slow beam loss data is not a big problem. Nevertheless, the inconsistency might introduce unnecessary confusion during beam tuning especially during the injection tuning with a slow injection rate such as less than 1 Hz. We have implemented two synchronization mechanism among the distributed installed boards to reset the calculation period.

The first method is to inject a hardware synchronization signal to the board to reset the calculation period. On the front panel, we have prepared a timing

ISBN 978-3-95450-176-2

injection port (TTL, rising edge). As in most local control rooms around the ring it is provided an event receiver which could transfer event timing with the timing accuracy of less than one revolution of the ring, 10 μs [8]. Unfortunately it has only four ports on the event receiver and most of the ports are already occupied with other needs.

Another method is to reset the calculation period with a software based signal. On the VME register, we have prepared reset command input which initiates the calculation timing to reset. This could be caused by the EPICS channel access command or by the EPICS sequencer initiated by the interrupt caused by the event system. Though the event system induced software timing might have been expected to have similar timing accuracy among the local control rooms, the arrival time of the EPICS channel access command should have much worse timing jitter.

Nevertheless we will at first evaluate the software timing synchronization scheme based on the EPICS channel access during the phase I operation of SuperKEKB. By observing the calculation time by the flashing timing of LED of 18K14As installed in one VME crate, the phase of the calculation period spread around 45 degree at peak to peak difference per day after the synchronization. It might be needed to re-synchronize the timing twice or more times per day. One such chance might be the period after beam abort—we anticipate having more than one beam abort per day even with normal, stable beam operation.

INTERLOCK MONITOR AND RESET SYSTEM

If the beam loss exceeds a pre-defined threshold, the integrator unit triggers the hardware beam abort request signal to the MPS [9]. The interlock status is latched on the integrator module until receiving signal reset (TTL, falling edge). When the beam abort due to loss monitor has happened, the operator will need to check the place where the loss exceed the threshold as soon as possible, then try to reset all the interlock status to restart beam operation soon. If recovery has been made without difficulty, the detailed beam and beam loss behaviour around the beam abort timing might be investigated during the injection time using data from fast loss logger, RF system data logger and oscilloscopes, and the Bunch Oscillation Recorder (BOR) [10].

During KEKB operation, we used an 80-bit VME-based general purpose I/O (Internix PVME-501) with open collector type 40-inputs/40-outputs daughter card. As in the case of original ADC boards, the board is also discontinued and no support is available now.

To replace and expand the I/O system for the loss monitor, we have selected Yokogawa FA-M3 systems [11] which contain two 32-bit TTL input units (F3XD32-5F) and one 32-bit TTL output unit (F3YD32-1T) with F3PU20-0S power unit on a 5-slot base unit (F3BU05-0D). Those TTL input and output modules are optically isolated. On the Linux-base CPU module (e-RT3), built-in EPICS system is working which enable us fairly easy access to the I/O modules by only defining the EPICS database parameter [12]. Figure 5 shows the installed FA-M3 system at KEKB-D7 local control room. As the signal connectors of those modules are not compatible with existing modules, and as the TTL output unit F3YD32-1T needs external +5V power to be injected to the collector of the photo-couplers, we have prepared a connector box of NIM-2W size. It translates the Dsub-25 connectors from interlock status output of loss monitor modules to Yokogawa A1451JD connectors for F3XD32-5Fs, an A1451JD connector from F3YD32-1T to 8-channels of QLA connectors to reset the interlock status. Driving power for the photo-coupler of the TTL output module is also supplied by the module.

Figure 5: Yokogawa FA-M3 system to read interlock status and to reset the latched interlock. From left, power supply unit, CPU unit, two 32-bit TLL input unit and 32-bit TTL output unit.

Installation of the new ADCs and FA-M3 I/O control system is now in progress. Operation testing of the system has been done at KEKB-D7 local control room and no difficulties have been found, as shown in Fig. 6.

Figure 6: Loss monitor station at KEKB-D7 under installation work.

ISBN 978-3-95450-176-2

The graphical user interface (GUI) must be rewritten almost from scratch due to the addition of many new data (Peak, Mean, Minimum) and the addition of the new monitors. It will be prepared by the end of this year. The complete system test will be done by the end of this year, before the start of the Phase I operation of the SuperKEKB rings.

SUMMARY

We have designed and tested a new 64-ch VME ADC with intrinsic peak, minimum and mean calculation functions for SuperKEKB beam loss monitor systems. Data obtained in the test stand shows excellent performance as expected. The I/O control system to read and reset the interlock status of the loss monitors are also designed and tested and confirmed to be working as expected.

Though the current analog amplifier and integrator unit has long integration or peak-holding functions, the high speed sampling of the developed ADC board might not be so significant. Nevertheless, it might be possible to omit the analog integration circuit which will be installed in the future.

The authors would like to thank our colleague of SuperKEKB beam instrumentation group for numerous supports on the development and construction.

REFERENCE

[1] Y. Funakoshi, talk given at the KEKB review committee (2013).
[2] M. Arinaga et.al., Nucl. Instrum. Meth. Phys. Res. A499 (2003) 100-137.
[3] M. Arinaga et. al., Prog. Theor. Exp. Phys. (2013) 03A007.
[4] H. Ikeda et.al., in proceedings of IBIC2014, Monterey, CA, USA., TUPD22 (2014).
[5] N. Iida et al., in proceedings of IPAC11, San Sebastian, Spain, THYA01 (2011).
[6] Analog Devices website: http://www.analog.com/
[7] EPICS website: http://www.aps.anl.gov/epics/
[8] N. Akasaka et. al., Nucl. Instrum. Meth. Phys. Res. A499 (2003) 138-166.
[9] N. Iida et. al., in proceedings of EPAC2000, Vienna, Austria (2000).
[10] M. Tobiyama, in proceedings of IBIC2014, Monterey, CA, USA (WEPD05).
[11] Yokogawa website: http://www.yokogawa.com/
[12] J. Odagiri et. al., in proceedings of ICALEPCS2013, San Francisco, CA. USA. (2013) MOCBAB02.

ISBN 978-3-95450-176-2

SIGNAL RESPONSE OF THE BEAM LOSS MONITOR AS A FUNCTION OF THE LOST BEAM ENERGY

K. Yamamoto, J-PARC Center, Tokaimura, Japan

Abstract

The 3 GeV rapid cycling synchrotron of the Japan proton accelerator research complex accelerates a proton beam up to 3 GeV and delivers it to the main ring and the material and life science facility. The injection energy of the synchrotron was 181 MeV since 2013, and it was upgraded to 400 MeV in 2014. The main magnets (dipole and quadrupole magnets) of the synchrotron have large aperture, and thickness of yoke is larger than 200 mm. Considering the stopping power of a proton, a shielding effect of the magnets for beam loss monitor strongly depends on the lost beam energy. When the beam loss occurs during injection, the lost proton cannot penetrate the magnet yoke. But when the beam loss occurs after acceleration, lost beam easily pass the magnet. Therefore the signal response of the beam loss monitor is changed even if the number of lost particles is same. To evaluate the beam loss monitor response by the lost beam, we estimated the signal dependence on the lost energy by the simulation.

INTRODUCYTION

The 3 GeV Rapid Cycling Synchrotron (RCS) of the Japan Proton Accelerator Research Complex (J-PARC) provides more than 500 kW beam to the material and life science facility and the main ring[1]. In such high intensity hadron accelerator, the lost protons that are a fraction of the beam less than 0.1 % cause many problems. Those particles bring about serious radio-activation and malfunction of the accelerator components. Therefore, the beam loss monitor (BLM) is one of the most important equipment to observe the state of the beam during operation, and to keep steady operation. Moreover, if we set operation parameters of BLM adequately, it can detect the beam loss that is 10^{-6} fraction of the beam. Thus it enables fine-tuning of the accelerator.

In order to increase the beam power of the RCS, the injection energy of the RCS was upgraded from 181 MeV to 400 MeV in 2014[2]. The main magnets (dipole and quadrupole magnets) of the RCS have large aperture, and thickness of yoke is larger than 200 mm. Therefore it works as a shielding to the BLM from the secondary radiation by the beam loss, and its shielding effect strongly depends on the lost beam energy. When the beam loss occurs during injection, the lost proton cannot penetrate the magnet yoke. But when the beam loss occurs after acceleration, lost beam easily pass the magnet. Therefore the signal response of the BLM is changed even if the number of lost particles is same. To evaluate the BLM response by the lost beam, we estimated the signal dependence on the lost energy by the simulation.

BEAM LOSS MONITOR IN RCS

In J-PARC RCS, We use two kind of BLM. One is a plastic scintillator connected on a photo multiplier tube and the other is a proportional counter.

The plastic scintillation counter has good time resolution (FWHM is less than 100ns) and its wave form data is used for a comparison between the experiment and simulation.

The proportional counter is mainly used to the interlock system for machine protection. The filling gas of the proportional counter is Ar-Co2 mixture, and it was purchased from Toshiba Electron Tube Co., Ltd [3]. A total of 90 proportional counters are set up all over the accelerator beam line. These proportional counters are connected with the machine protection interlock system and it is always checking that the integration of the proportional counter signal is not over a preset value. Integration values are also archived at all times and we can check it when some interlock alerted. The typical location of the PBLM is shown in Fig. 1. In this paper, we evaluate the response of the proportional counter.

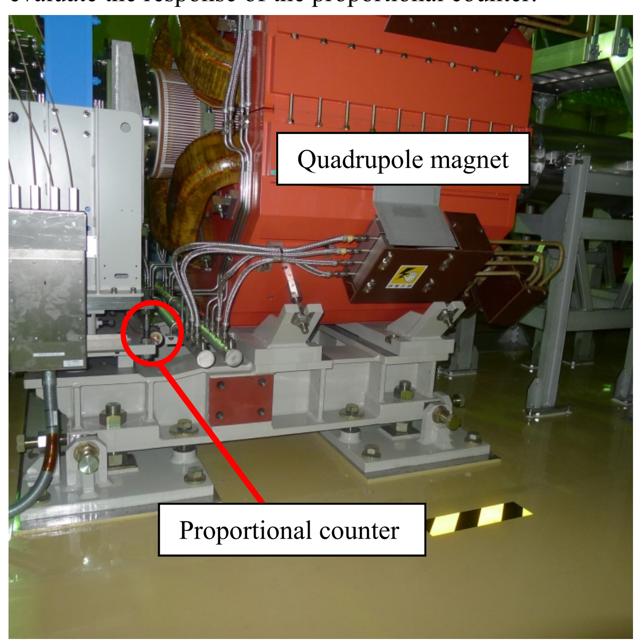

Figure 1: Typical location of the proportional counter.

CALCULATION

The response of BLM would be proportional to the energy deposition by the radiation. Thus we investigated the energy deposition at the monitor as a function of lost beam energy by using the MARS code[4]. The calculation model is shown in Fig. 2. Here, the only quadrupole magnets, proportional counters and vacuum chambers are

ISBN 978-3-95450-176-2

considered. The shape of the quadrupole magnet is regarded as a combination of a cylinder and squares. The cross sections of the actual quadrupole magnet and the model are shown in Fig. 3.

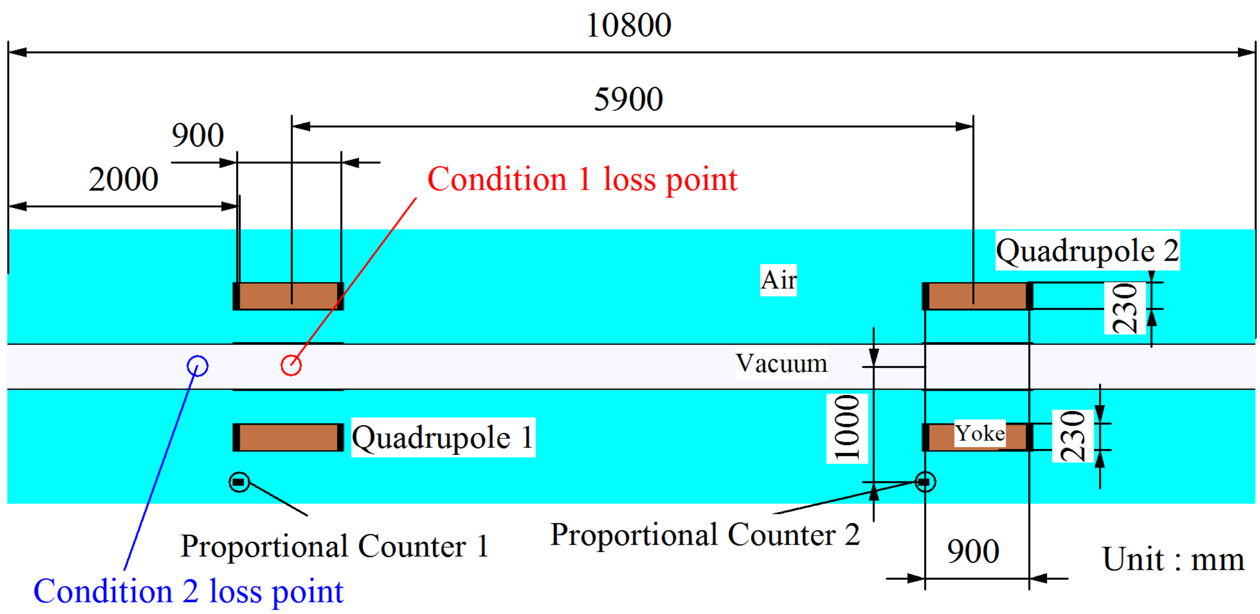

Figure 2: Geometry of the calculation model in MARS code.

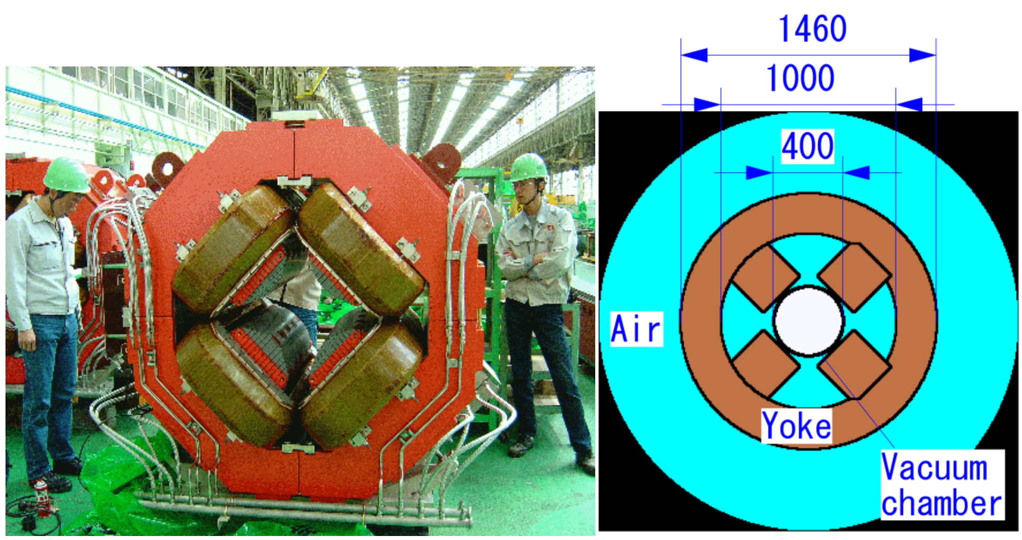

Figure 3: Cross sections of the quadrupole magnet.

The material of the magnets is iron. The vacuum chambers inside of the magnet are ceramic, and the other vacuum chambers are titanium. There is no magnetic field in this calculation. The proportional counters are the iron cylinders in which argon gas is filled. The outer diameter of the proportional counter is 25 mm and thickness of the cylinder is 1.5 mm. Two quadrupole magnets are located in an interval of 5.9m. Each proportional counter is put at the upstream of the magnet's feet.

In this calculation, the beam loss is assumed to be the side of the vacuum chamber. The lost beam shape is a pencil beam with the incident angle of 10 mrad (it has no distribution in the phase space). The number of the test particles is 10^7 in the calculation, and it is considered that those particles corresponded to $2*10^9$ particles per second (corresponded to 1 W loss at 3 GeV energy). In order to evaluate the shielding effect of the quadrupole magnet, we assume two initial conditions. In the first condition, the beam loss occurs in the center of the quadrupole magnet. On the other hand, the beam loss occurs in the 0.3 m upper reaches of the magnet entrance in the second condition (see Fig. 2). The lost beam energy is changed from 181 MeV to 400 MeV, 600 MeV, 800 MeV, 1 GeV, 1.5 GeV, 2 GeV and 3 GeV. We calculated the energy depositions at the argon gases in the proportional counters.

ISBN 978-3-95450-176-2

RESULTS AND DISCUSSION

Result of Condition 1

The energy deposition in the condition 1 as a function of the lost beam energy is shown in Fig. 4, and the trajectories of the protons and secondary particles are shown in Fig. 5.

In this condition, since the beam loss occurred in the middle of the quadrupole magnet, the counter 1 was shielded by that quadrupole magnet. Therefore the energy deposition of the counter 1 was smaller than that of the counter 2 though the distance from the loss point was shorter than the counter 2. When the lost energy was smaller than 1 GeV, the secondary radiation which reaches the counter 1 was so few that the event was too rare (see upper pictures in Fig. 5), and the error bar was very large. The output signals had a tendency to increase in both proportional counters when the lost beam energy became larger due to more production rate of the secondary radiation.

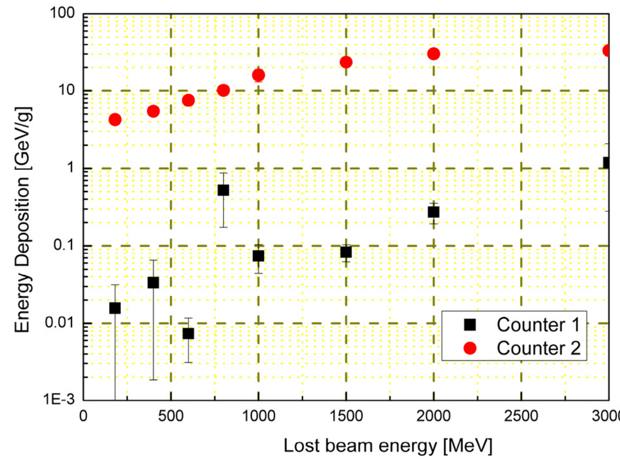

Figure 4: Energy deposition in the condition 1.

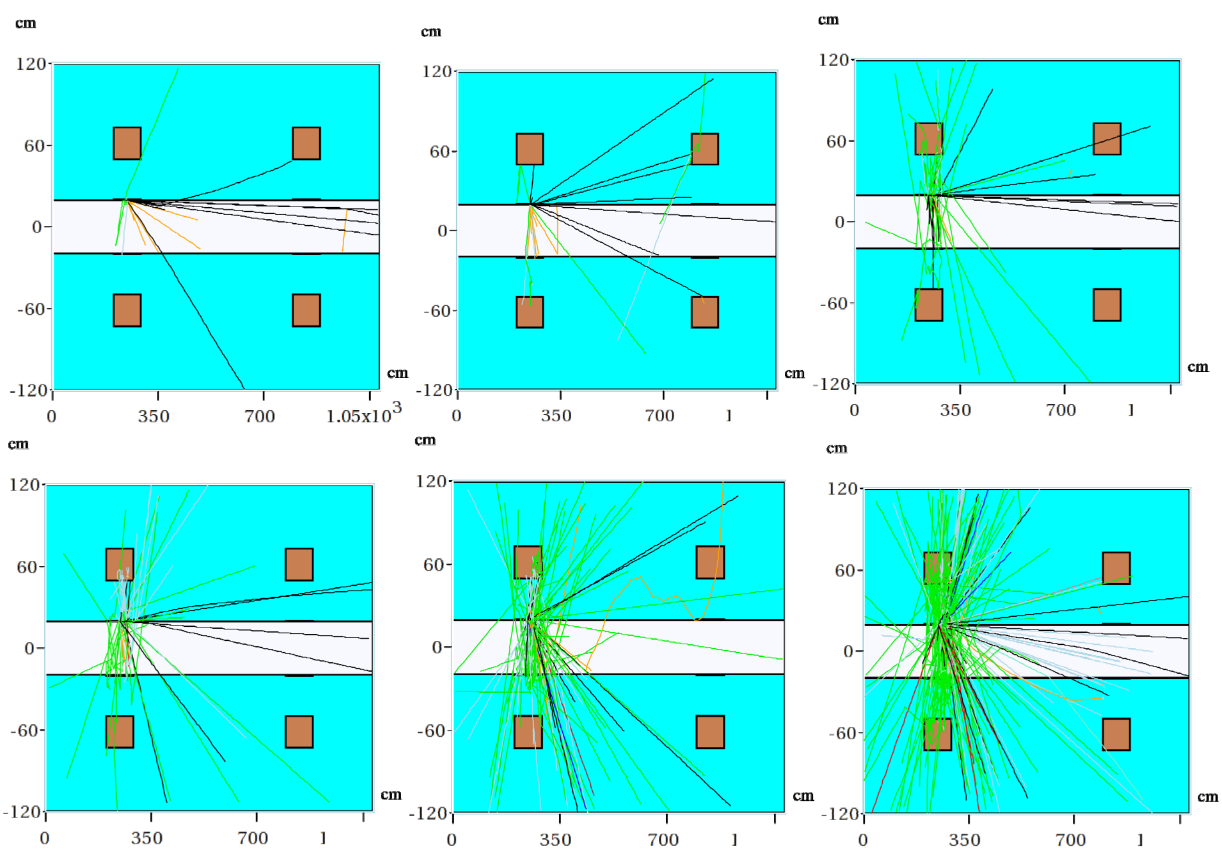

Figure 5: Trajectories of the lost protons and secondary particles in the condition 1.

10 test protons are hit on the vacuum target with the incident angle of 10 mrad at condition 1 lost point. The results are lost proton energy of 181 MeV (upper left), 400 MeV (Upper middle), 600 MeV (Upper right), 1 GeV (Lower left), 2 GeV (Lower middle) and 3 GeV (Lower right). Black lines are protons, green lines are neutrons, light grey lines are gamma-rays, orange lines are electrons, blue lines are pi- and red lines are pi+. Only few deuteron, tritium, alfa-ray, positron and muon from pion are also produced.

ISBN 978-3-95450-176-2

Result of Condition 2

Fig. 6 and 7 show the energy deposition and the trajectories of test particles in the condition 2. Calculation results indicated that the energy deposition of the counter 2 had a minimum at the lost energy of 600 MeV. On the other hand, though the counter 1 was not shielded by the magnet and closer to the loss point, the energy deposition of the counter 1 at 181 MeV was lower than that of the counter2.

The particle trajectories in Fig. 7 revealed this reason. Since the major interaction of 181 MeV proton is the coulomb multiple scattering, the secondary particles were not so generated at the loss point and the counter 1 was not able to receive the energy deposition from those secondary particles. This effect led the larger energy deposition of the counter 2. When the lost beam energy rose to above 400 MeV, the production rate of the secondary radiation at the loss point was also increased. Then more energy was spent in the loss point than the vicinity of the counter 2, and the energy deposition of the counter 1 became larger than that of the counter 2.

Even if the same number of protons were lost, the energy deposition at the lost energy of 3 GeV is nearly 100 times larger than that of 181 MeV.

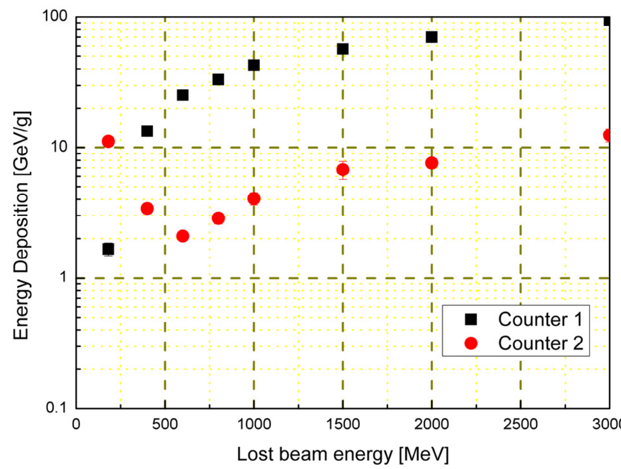

Figure 6: Energy deposition in the condition 2.

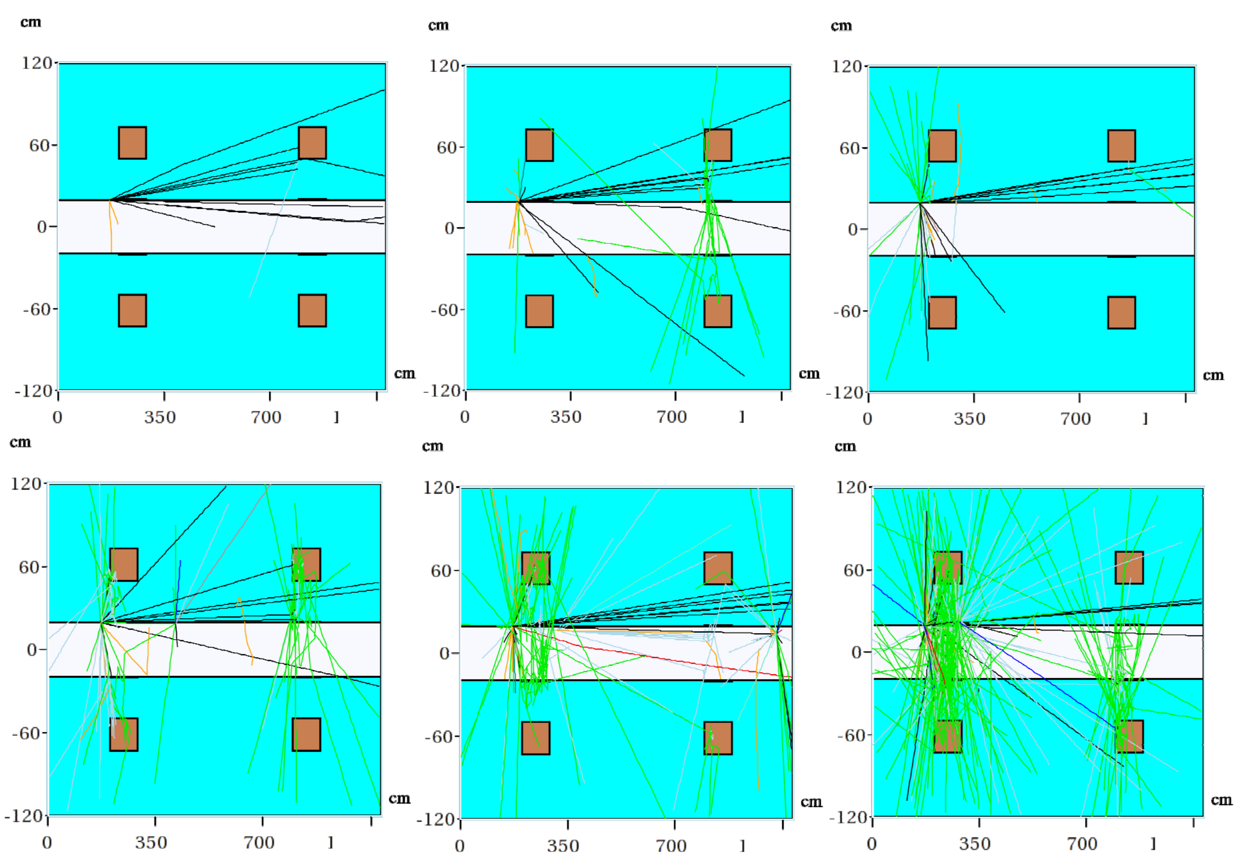

Figure 7: Trajectories of the lost protons and secondary particles in the condition 2.

10 test protons are hit on the vacuum target with the incident angle of 10 mrad at condition 1 lost point. The results are lost proton energy of 181 MeV (upper left), 400 MeV (Upper middle), 600 MeV (Upper right), 1 GeV (Lower left), 2 GeV (Lower middle) and 3 GeV (Lower right). Black lines are protons, green lines are neutrons, light grey lines are gamma-rays, orange lines are electrons, blue lines are pi- and red lines are pi+. Only few deuteron, tritium, alfa-ray, positron and muon from pion are also produced.

ISBN 978-3-95450-176-2

Comparison Between the Condition 1 and 2

From the comparison between the results of the condition 1 and 2, the energy deposition of the counter 1 was different by a factor of one hundred. The difference of the energy deposition of the counter 2 was several times. The large difference of the counter 1 was not only due to the shielding effect of the magnet but also due to the lower density of the hadron cascade at backward direction.

Normalization by the Lost Power

Figure 8 shows the energy depositions normalized by the lost beam power. Except the results of low energy loss and the counter 1 in the condition 1, the energy depositions were almost constant. This indicates that the energy deposition is proportional to the lost power in the energy range of more than 600 MeV.

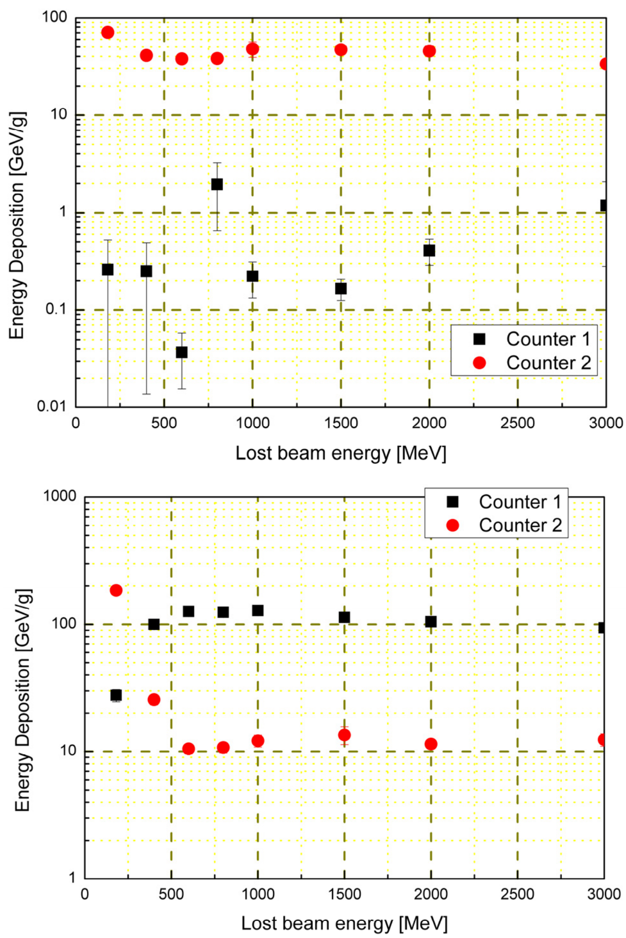

Figure 8: Energy deposition normalized by the lost power.

Results of the condition 1 (upper) and the condition 2 (lower)

CONCLUSION

The J-PARC RCS aims to deliver 1 MW high power proton beam to the downstream facilities. To achieve fine tuning of the accelerator for such high power beam operation, we investigated the response of the BLM with some conditions.

The results of calculation indicated that the response of the beam loss monitor strongly depends on the location of the lost point and lost energy. It is proportional to the lost power except the condition that the magnets become the radiation shielding.

Due to the sensitivity of the monitor response, we have not only to observe the beam loss monitor signals but also to investigate the residual dose distribution. Comparing the monitor signals and residual dose values, we can obtain more precise information of the beam loss.

REFERENCES

[1] M. Kinsho, "STATUS OF THE J-PARC 3 GeV RCS", Proc. IPAC2015, THPF044, (2015).

[2] K. Yamamoto, "J-PARC: The path to 1 MW at J-PARC, including 400 MeV linac improvement, RCS improvements and front-end upgrades", Proc. of ICANS XXI, ABT-01, in printing.

[3] Toshiba Electron Tube Co., Ltd. http://www.toshiba-tetd.co.jp/eng/index.htm

[4] N. V. Mokhov and C. C. James, "The MARS Code System User's Guide Version 15(2014)," http://www-ap.fnal.gov/MARS

ISBN 978-3-95450-176-2

DIAGNOSTICS DURING SESAME BOOSTER COMMISSIONING

H. Al-Mohammad, K. Manukyan, SESAME, Allan, Jordan

Abstract

SESAME* is a 2.5 GeV synchrotron radiation facility under construction at Allan (Jordan), consisting of a 20 MeV Microtron as pre-injector and an 800 MeV Booster Synchrotron. The pre-injector and booster are originally BESSY-I machine with some major changes within power supplies and diagnostics tools. The diagnostic tools are: Fluorescent Screens, BPMs, DCCT, FCT and Synchrotron Radiation Monitor. The Booster had been commissioned in 2014. The installed tools allowed to determine current, orbit, tune, chromaticity and emittance. Set up of the diagnostics and results are presented in this paper.

INTRODUCTION

The SESAME Microtron (MM22) generates an electron beam suitable for injection through Transfer line 1(TL1) into the Booster Synchrotron. The timing system is based on the event generator and receiver system from Micro Research Finland [1], with 1 Hz repetition frequency. The SESAME Booster has a FODO lattice with 38.4 m circumference the main parameters are listed in table 1.

Table 1: Booster Main Parameter

Circumference (m)	38.4
RF frequency (MHz)	499.654
Revolution freq. (MHz)	7.807
Repetition freq.(Hz)	1
Ramping time (ms)	630
Injection/Extraction Energy (MeV)	20/800
Beam Current (mA)	7
H/V Tunes υ_x/υ_y	2.21/1.45
H/V Emittances* ε_x (nm.rad)	180/300
Straight sections β-func.(H/V) (m)	5.2/2.9

*Different optics program give different values (Beta 300 nm, Elegant 180 nm).

In order to properly check the Booster synchrotron performance, the set of diagnostics equipment described in Fig. 1 is installed in the machine. Next, we present the diagnostics elements installed in the Booster and our experience during the commissioning.

* Synchrotron Light for Experimental Science and Applications in the Middle East

FLUORESCENT SCREENS

Fluorescent Screens (FS) are installed in Booster ring which have Aluminium Oxide screens and analog cameras connected to a signal switcher which allows monitoring one camera on the TV monitor in control room. This setup includes manually controlled focus and zoom lenses originally from BESSY-I. All FS are activated pneumatically.

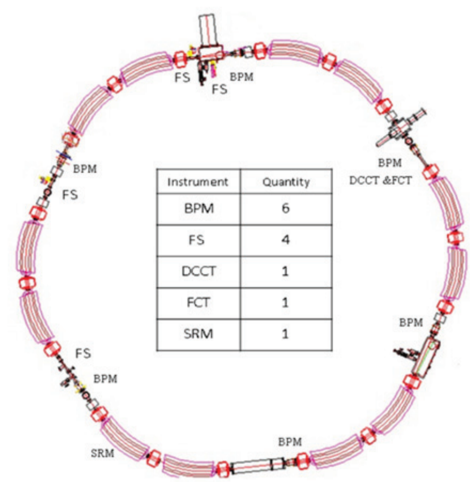

Figure 1: Booster Diagnostics Components.

We placed one FS to monitor the beam path along the Transfer line 1 from the Microtron to Booster (TL1), while 4 more are installed in the Booster to ease the first commissioning goals (injection, first cell, full turn).

Measurements of Microtron emittance were done by Quadruple scan method [2] Fig. 2 shows the results for vertical plane.

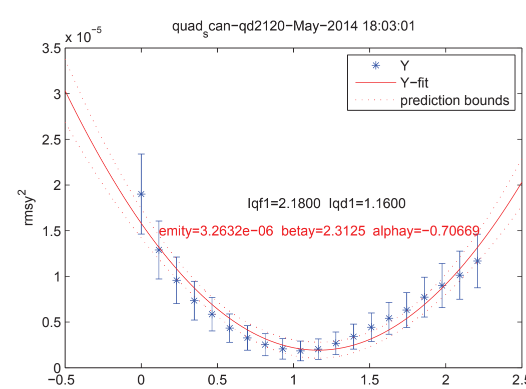

Figure 2: Emittance Measurement of the Microtron in TL1, $\varepsilon_{x/y}$ = 2.6 / 5.2 nmrad.

ISBN 978-3-95450-176-2

BPM SYSTEM

There are 6 beam position monitor (BPM) in Booster ring, 4 of them are strip line and the others are button type. One BPM block can also be used as a shaker (beam exciter) for tune measurement purpose. The length of the stripes is 15 cm designed for 500 MHz and its odd harmonics. The Booster BPM block diameter is relatively large (150 mm) compared to the beam displacement, and the electrode locations in horizontal and vertical planes are symmetric at 45° with a calibration factor K_x, K_y 28.82 and 28.94 respectively, the calculation is done by Matlab code based on analytical calculations from ALBA [3].

All BPMs are connected to Libera Electron [4] to analyse and calculate the position and detailed machine study. Calibrated and phase matched coaxial cable LMR 198 with variety of length (16 m-35 m) are used depending on the location. All Libera's are controlled via wired LAN and receive a trigger and machine clock from Libera clock splitter which is connected and synchronized to the timing system.

EPICS driver is used for Libera Electron; through it all of Libera modes can be used. Basic modes, which are: first turn, demand mode (Turn by Turn) with AGC and DSC off, zero attenuation and fixed switching mode (3), by using this mode we can measure the betatron tune during ramping.

FCT AND DCCT

In Transfer line 1 (TL1) a fast current transformer (FCT) is installed which is a commercial one (Bergoz [5]) which has a sensitivity of 1.25 V/A, The FCT is installed after the FS, it has a ceramic break with a bypass shield, the FCT is directly connected to an oscilloscope (Agilent X2014A) by coaxial cable (LMR200). Figure 3 shows the output pulse of the Microtron via FCT.

The same type of current transformer is used in the Booster (Bergoz) but with different sensitivity 2.5 V/A, furthermore a DCCT with its electronics from the same

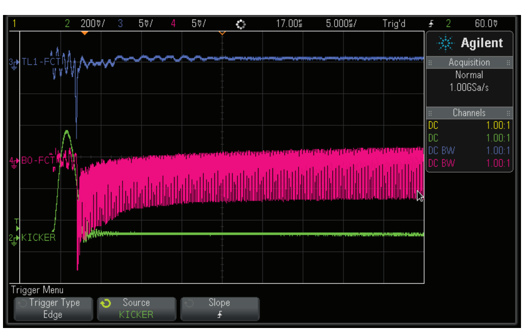

Figure 3: TL1 FCT output (blue), Booster FCT (multi-turn) output (pink) and Kicker Pulse (green).

manufacturer (Bergoz). The vacuum chamber is interrupted by a thin isolation gasket and both FCT and DCCT are located beside each other in the same cell and share the bypass shield. The shield was designed in-house; it consist of two cylindrical half's of low carbon steel. Figure 4 shows the design of the shield and the already installed DCCT in the Booster.

The most precise Booster current measure is done with the DCCT which has 5 uA/sqrt(Hz) resolution in the 20mA range and temperature drift 5 µA/K typically. Both FCT and DCCT are connected to an oscilloscope via coaxial cables and monitored in the control room Fig.5.

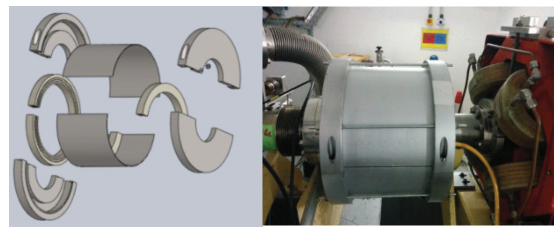

Figure 4: DCCT Shield.

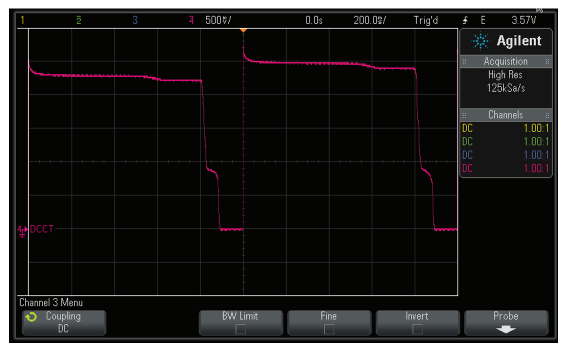

Figure 5: DCCT Reading.

SRM

The Synchrotron Radiation Monitor is taking the light coming from a bending magnet to obtain a transverse image of the electron beam. This image is then analysed to determine the horizontal and vertical beam size. The beam transverse sizes depend on the lattice parameters and the emittance [6]. Figure 6 shows the photon fluxes produced when an electron beam passes a bending dipole in the Booster at full energy.

Completely new vacuum chambers for the dipole had been fabricated for the Booster ring that gave the possibility to fabricate one of the chambers with a glass window for SRM diagnostics. The SRM is located in cell 3 the distance from the glass window to the centre of the magnet is 80cm. Figure 7 shows the visible light that comes from the SRM 300ms after the injection.

To have more and precise measurements and compare it with what we have installed currently, a new optical system is designed with same setup, the optical gages and mirrors are from ThorLabs [7], tubes and gages are SM2 (2") system with 2 ME2-G01 mirrors.

ISBN 978-3-95450-176-2

Figure 8 shows the measured beam sizes during ramping; the trigger for the camera (Basler acA1300-gm [8]) was varied from the beginning to the end of the ramp. For each step 10 shots from the camera were taken fitted to Gaussian distribution and averaged [9].

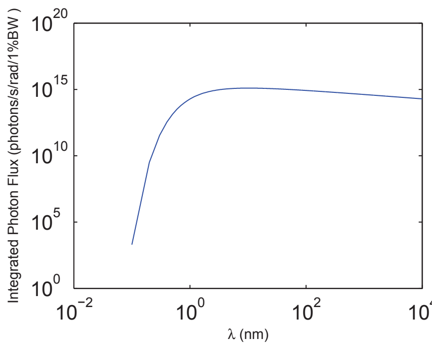

Figure 6: Photon flux from the dipole in the Booster for a beam current 7 mA at full energy.

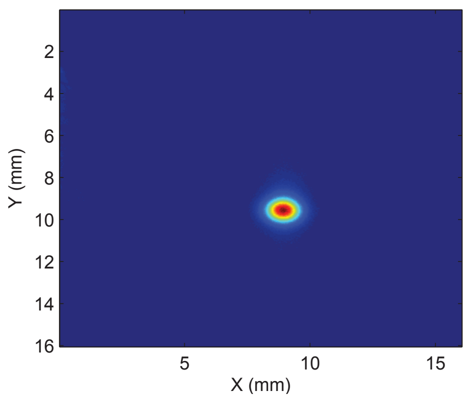

Figure 7: Visible Beam Image After 300 ms of the Injection.

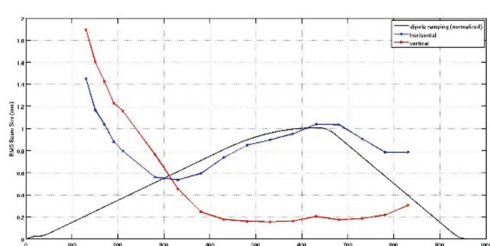

Figure 8: Measured horizontal (blue) and vertical beam size (red) during the ramp, dipole ramping curve (black).

TUNE MEASURMENT

The Booster tune monitor is a diagnostic used to measure the vertical and horizontal oscillation-frequencies (or betatron tunes) of the beam accelerated in the Booster. The beam is accelerated from 20 MeV to 800 MeV in 630 ms. During this ramping cycle, the tunes are not perfectly constant and it is nescessary to precisely measure them along the cycle.To measure the tune the beam is excited using a shaker, the beam position oscillation are recorded using beam position monitors (BPM) by Libera and perform a frequency analysis of these signals in Matlab.

The layout of tune excitation is shown in Fig. 9. The shaker located in cell 1 which also works as beam position monior by RF coaxial switch (TELEDYNE CCS-32). Each stripline will have 2 switches one in the upper stream (Libera and 50 Ω dummy load) and the other in down stream (Amlifier and 50 Ω termination) the switching will be controlled by PLC.

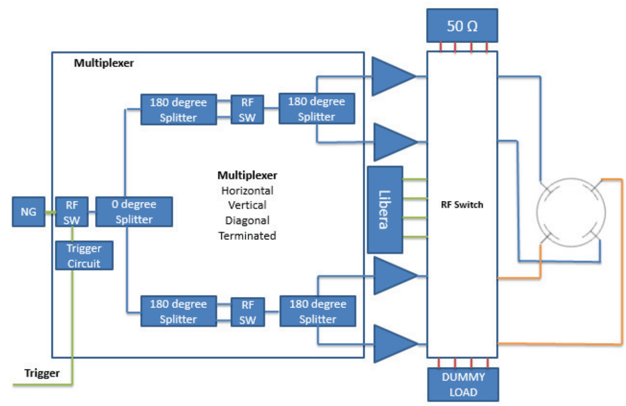

Figure 9: Tune Excitation layout and Switching Between Libera and the Amplifiers.

The source of the excitation is an arbitrary function generator Tek. AFG 3022C, it can give a central frequency and controlled width of white noise on each side.

The amplifer system box consist of amplifers module Modular RF (KMA1040) 50W with frecuency range 200 kHz- 50 MHz 48 dB gain, Mean Well SP-500 power supply and in house designed controller board. The whole system are assembled in 3U rack mounted chassis in the lab.

The tunes can be tracked dynamically during the ramping process across all the turns till 630 ms (full energy of the Booster). To enhance the tune signal after injection a programed code in Matlab started to increase the level of white noise signal as the beam energy increases and synchronize the timing between the Libera and the shaker trigger and shift the time to fit the whole period since Libera electron can take up to 16ms. Figures 10 and 11 show the horizantal and vertical tune the injection and during ramping respectivly.

ISBN 978-3-95450-176-2

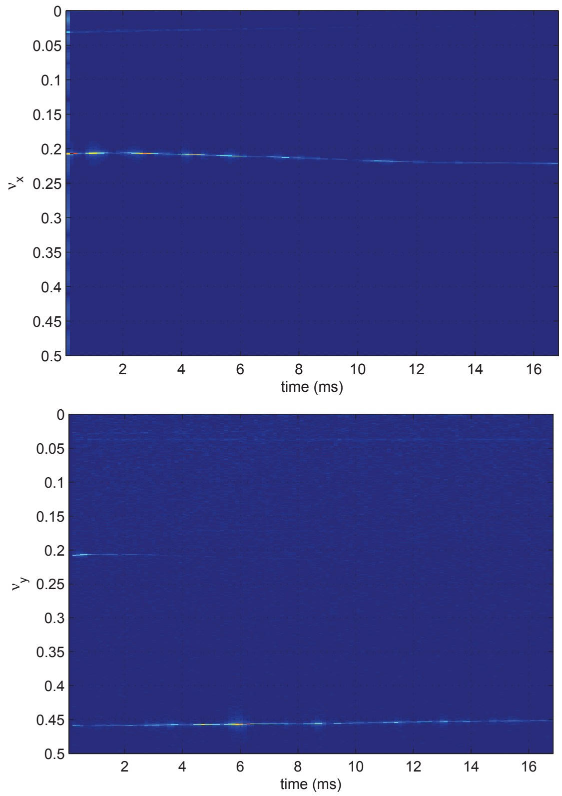

Figure 10: Horizontal (up) and vertical (down) tune at the injection for 16 ms.

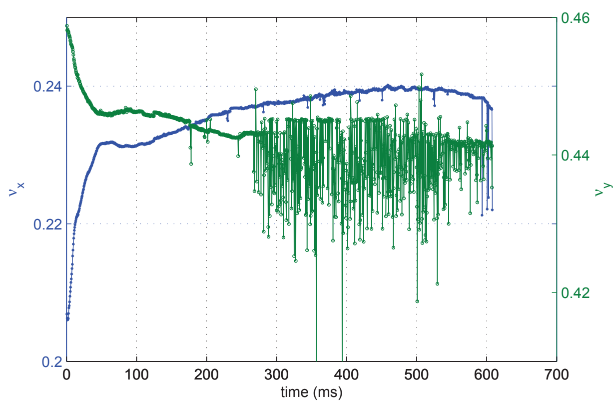

Figure 11: Horizontal and vertical tune during the ramping.

CONCLUSION

The set of diagnostics mentioned in this paper performed satisfactorily and allowed a successful Booster commissioning. Our task now is mainly to perform and upgrade old instruments and make fine adjustments to increase their performance and prepare the new instruments for SR.

ACKNOWLEDGMENT

The authors would like to thank everyone who contributed to this achievement through discussions and suggestions. We are grateful for the support from the entire groups specially control group and special thanks to D. Foudeh (Head of RF&DI Group) for his support and experience to complete this achievement.

REFERENCES

[1] Micro Research Finland, http://www.mrf.fi.
[2] US-Paricle-Accelerator-school-2008, http://uspas.fnal.gov/materials/08UMD/Emittance measurement - Quadrupole Scan.pdf
[3] A. Olmos, F. Pérez, “MATLAB CODE FOR BPM BUTTON GEOMETRY COMPUTATION” Proc. of DIPAC’07, Venice, Italy.
[4] Instrumentation-Technologies, http://www.i-tech.si
[5] Bergoz Instrumentation, http://www.bergoz.com
[6] U. Iriso and F. P´erez, “SYNCHROTRON RADIATION MONITORS AT ALBA” Proc. of EPAC’06, Edinburgh, Scotland.
[7] Thorlabs, http://www.thorlabs.de
[8] Basler, http://www.baslerweb.com/de
[9] K. Manukyan “MEASUREMENTS IN TL1 AND BOOSTER” SESAME internal report SES-TE-AP-TN-0010 Rev 0.2.

ISBN 978-3-95450-176-2

A COMPARATIVE STUDY BETWEEN SIMULATED AND MEASURED BEAM'S QUALITY OF 30 MeV CYCLOTRON AT KFSHRC

F. Alrumayan[1], A.Alghaith[1], A. Hendy[1] and M. Dehnel[2]
[1]King Faisal Specialist Hospital and Research Centre, Riyadh 11211, SA
[2] D-Pace, Inc., Nelson BC, Canada

Abstract

At King Faisal Specialist Hospital and Research Centre (KFSHRC), the C-30 Cyclotron (manufactured by IBA) is used to produce radioisotopes for medical purposes. Working with very expensive machine dedicated for patients needs full attention and understanding of how beam can be controlled safely inside beam transport system. Moreover, knowledge of influence of magnetic lenses on charged particles is desired. Therefore, using off-line source such as PC-based beam simulator allows an operator to immediately see the effect of various magnetic lenses attached to the beam line. Initially, the magnetic field of quadruples and steering magnet was recorded using Hall probe Teslameter. The magnetic field values then uploaded into the Beam simulator in which beam quality was recorded and analysed.

INTRODUCTION

Experience gained since the commissioning of the IBA [3] C-30 Cyclotron at the King Faisal Specialist Hospital and Research Centre (KFSHRC) in 2010, has shown this facility to be viable entity. In addition to the C-30 Cyclotron, the facility includes two other Cyclotrons namely; the RDS-111 and the CS30 Cyclotrons. The latter has dual responsibilities; while is kept as a backup for the other Cyclotrons for radioisotopes production, it's used for proton therapy researches and Bragg Peak measurements at that particular energy [1].

Beam transport system is of high importance to carry particles to their final destination, in case of medical Cyclotrons, are isotopes targets. The amount of current that carried out in beamlines could reach up to 250 uA [2]. Hence, working with very expensive machine dedicated for patients needs full attention and understanding of how beam can be controlled safely inside beamlines. Knowledge of influence of magnetic lenses on charged particles is desired.

Therefore, using off -line source such as PC-based beam simulator allows an operator to immediately see the effect of various magnetic lenses attached to the beam line. This
would eliminate strike of beam on the internal wall of beamline.

In this paper, a comparison study is conducted between real beam shape and position with simulated beam. During experiment the beam was completely stopped using destructive beam viewer supplied on the line.

DESIGN PARAMETER

Optical Elements

Figure 1 shows the layout of beamline 2.1 which attached to the C-30 Cyclotron. The main elements of beamline 2.1 are explained as follows. Steering magnets: The thickness between coil and support is made with two "Nomex" layers of 0.12 mm thickness. Each coil is assembled with conductor made by enamelled round copper wire of 1.4 mm diameter. Each coil has 962 turns per coil. Quadrupole Magnets: On the beam line, there two Quadrupoles installed; one inside the Cyclotron vault and the other on the PET target vault. They are made by Scanditronix Magnet. Each of which contains 4 layers of 25 turns and 1 cooling plate.

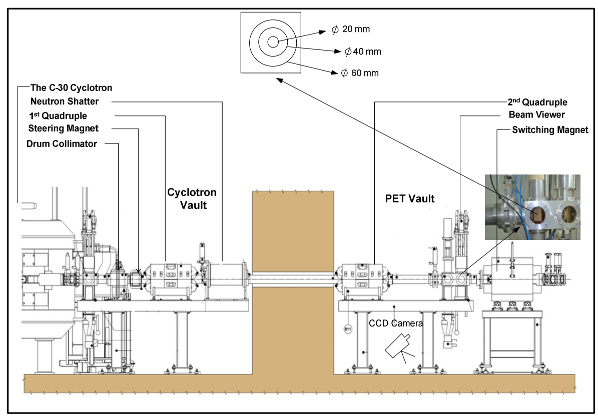

Figure 1: Layout of beamline.

Other Non-magnet elements are installed on the beamline and listed on the figure but outside the scope of simulation of this study.

BEAM MEASUREMENT

On Line Measurement

Real time measurement of beam current was monitored using beam viewer supplied with the C-30 Cyclotron. The Viewer is made of Alumina attached into square piece of copper (the thickness is between 0.2 and 0.3 mm). Within the phosphors screen (figure 1), three indication circles are marked. The diameter of these circles is 20, 40 and 60 mm. A CCD Camera, made by Panasonic, was placed outside the median plane of the Cyclotron. Using very small beam current for short period guarantees the survival of the camera.

Moreover, the beam shape was studied at different beam intensities as shown in Figure 2. The values of the

ISBN 978-3-95450-176-2

magnetic lenses of beamlines were kept unchanged. In some cases and as suggested by figures, changing beam intensity may lead to change the beam distribution horizontally and vertically. This requires varying the values of magnetic lenses, attached to the beam lines, until optimization has been achieved.

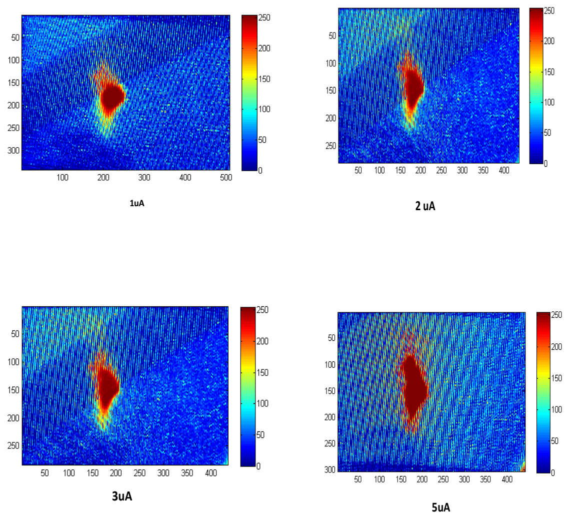

Figure 2: Beam shape at different beam intensities.

Figure 3 shows a beam spot seen on the viewer and its Gaussian shape. This image was used for the comparison study against the simulated beam. The FWHM have been evaluated from the reconstructed images, after normalization, and are plotted with respect to beam width. For image calibration the visible marks seen on the viewer are used.

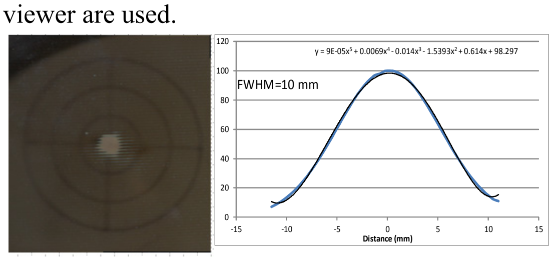

Figure 3: Beam spot on the viewer and its Gaussian shape. The curve describes a polynomial function fit to the experimental data.

SIMULATION ANALYSIS

A beam simulator, ver. 1.4, was used to simulate beamline and its magnetic lenses [4]. Figure 4 shows a snap shot for the developed simulated beam line. The components are explained as follow. Beam Source: It allows for choosing the ion type, its energy and number of particles, as well as ions phase space. Using beam simulator, 10^4 particles were placed in a phase space (X, X', Y, Y'). Drift length it considered as is the region in a beamline where there is no magnetic element. In our design we have three drift lines; one right after the port exit of the cyclotron (0.5 m), second is representing the wall thickness (3 m) and third is just before beam viewer (0.5 m). Steering magnet: is represented by two dipoles. Two quadrupoles.

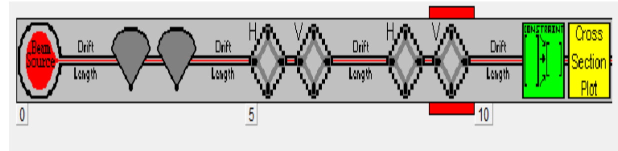

Figure 4: Snap shot of sequential beam icon.

The magnetic field of optical lenses was measured using a Teslameter, Model 3MH5, made by SENIS. The transverse Hall probe can read up to 20 T with a resolution of 100 ppm Fs. Before using the probe, it was calibrated against zero offset using Zero Gauss chamber.

Using the hall probe, linearity curve of quadrupole was measured and plotted as shown in Figure 5. The behaviour of magnetic field as function of power supply current is approximately linear. Temperature of the probe was 22°C.

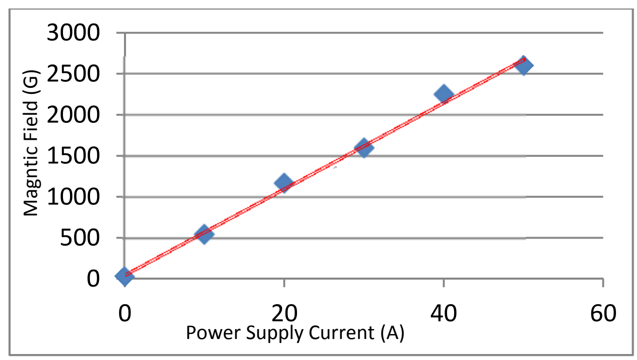

Figure 5: Relation between power supply current and generated field. The curve describes a linear function fit to the experimental data.

The Maximum Beam Half Size (X, X',Y,Y') values for the beam source are, respectively, 1 mm, 0.2mrad, 1mm and 0.2 mrad.The magnetic field values were measured (Table 1) and then uploaded into the Beam Simulator software in which beam shape and position were recorded.

Table 1: Beam Simulator Uploaded Data

Parameter	$I_{supplied}$ (A)	$B_{measure}$ (kG)	L_{effe} (mm)
VQ1	41.9	2.1	0.3
VQ2	45.3	2.3	2.3
HQ1	48.1	2.7	2.7
HQ2	33.7	1.5	1.5
S1*	0.4	0.2	0.2
S2**	41.9	0.3	2.1

*, ** Steering magnets component

ISBN 978-3-95450-176-2

Figure 6 illustrates the horizontal (X) and vertical (Y) envelope along the beamline. The divergence of simulated beam was about 2.9 mrad in the horizontal plane and of 1.3 mrad in the vertical plane.

The preliminary comparison shows a larger beam size from the real beam. It has to be brought in mind that the vacuum level inside the beamline was $5e10^{-6}$ mbar. Such condition and the assumption of the beam phase space at the exit of the beam port could explain the difference between measure and simulated value.

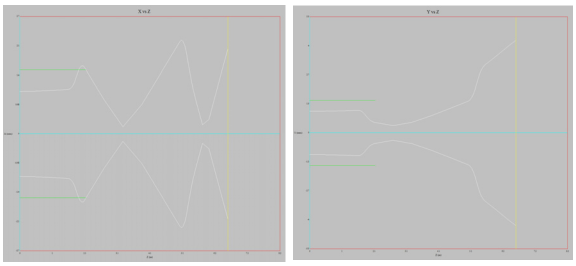

a) X vs Z b) Y vs Z

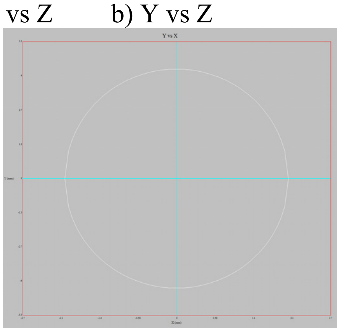

c) X vs Y

Figure 6: Calculated beam envelops, A) the vertical Y component of the beam, B) Shows the horizontal X component and C) shows the overall beam spot.

CONCLUSION

We successfully designed and simulated a beam transport system for C-30 Cyclotron based on empirical values obtained from the magnetic lenses attached to the Beamline. The difference in beam profile between measured beams and simulated one was 15%. Considering the fact that ambient temperature will play role in changing slightly the field. Moreover, vacuum inside the beamline can slightly disperse the beam as it continues traveling along the beamline.

All results were obtained under the assumption that the ion beam has the Gaussian distribution, and the beam moves with no placement from the axis of the beam line.

ACKNOWLEDGEMENT.

This project was supported by NSTIP strategic technologies program in the Kingdome-Award No (14-MAT1233-20).

REFERENCES

[1] F. Alrumayan et. al.," Status Report of the Cyclotrons C-30, CS-30 and RDS-111 at KFSHRC, Saudi Arabia" Proceedings of the 20th International Conference on Cyclotrons and their Applications, Vancouver, Sep 16-20, 2013.

[2] M. Dehnel et. al.," The design and Operation of Industrial Beam Transport System for 15-30 MeVProtons" IEEE Transaction on Industry applications, VOL 28, No. 6, November/December 1992.

[3] www.IBA.com

[4] Beam Simulator, http://www.ghga.com/accelsoft

ISBN 978-3-95450-176-2

HEATING ANALYSIS AND THE SOLUTIONS OF DCCT SYSTEM FOR BEPCII

Y. Zhao, J.S.Cao,J.He,Y.F.Sui,L.Wang

Division for Accelerators, Institute of High Energy Physics, Beijing 100049, China

Abstract

The BEPCII e+ DCCT is damaged due to a high temperature heating. After 8 years operating, it is not working properly in 2014. As the BEPCII is trying to reach high luminosity, the CT will be a defective component with the high beam current, therefore a spare one has replaced it. In order to determine the heating source, some experiments and simulations have been done. A new vacuum chamber structure has been designed to solve the problem. The analysis and result can be also applied to CT designs in the future.

INTRODUCTION

There are two bergoz[1]in air DC current transformers fixed on BEPCII rings on both sides of the interact point(IP). One for positron and another for electron when the machine runs collider mode, both two DCCT can measure the electron current when the machine runs at synchrotron mode. Figure 1 shows the sensor's location. The two DCCT sensors have same parameter and identical mechanical design.

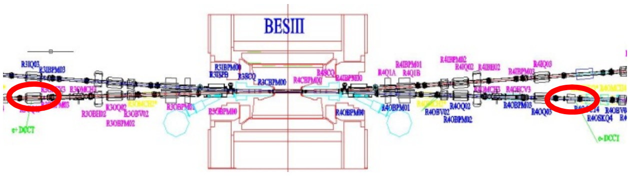

Figure1: Layout of BEPCII DCCT sensor.

Each DCCT has 2 sensors to pick up the temperature. One (e-/e+ T-SU1) is stuck on the DCCT sensor, another (e-/e+ T-SU2) is used to monitor the pipe's temperature. A problem has appeared in e+'s DCCT after once high current operation in 2012: In collider mode ,The e+ DCCT 's temperature is much higher than e- DCCT when the e+,e- beam current is the same. In synchrotron mode, the e+ DCCT's temperature is also slightly higher than e-'s. For the first e+ DCCT sensor was damaged by heating, a spared one with a identical new vacuum chamber made in 2010 has replaced it, but the temperature problem still exist.

The Fig. 2 shows the current and temperature curves when the machine runs at collider mode this year, the peak beam current is 720mA, bunch number is 92, bunch current is 7.9mA for both e+ and e- rings. The e+ T-SU1 is 33°C, 8°C higher than e-'s, the e+ T-SU2 is 50 °C, 10°Chigher than e-'s. The 2 DCCT vacuum chambers have the same water cooling system, they all work normal. The nearby BPMs show the beam position in X,Y direction, no . As the BEPCII will run over 910 mA for collision, and the high temperature will affect the magnetic characters of the DCCT cores [2], the e+ problem should be settled.

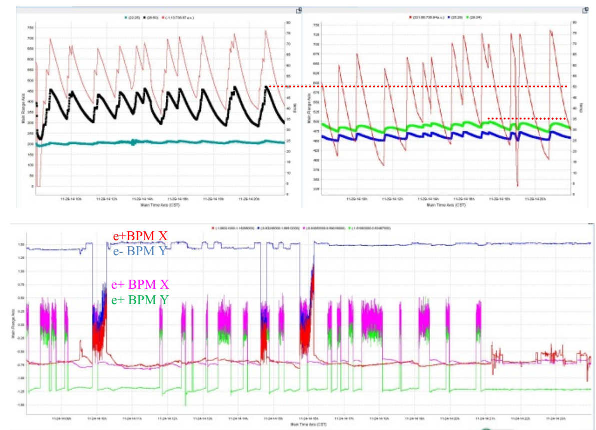

Figure 2: Current and temperature curve for e+ (up left) and e-(up right) DCCT, BPM nearby X,Y position(down).

ANALYSIS AND SIMULATION

For the measurement principle of current transformer, a break is needed in the vacuum chamber to cut off the mirror current. Figure 3 is the structure of DCCT with toroid, bakelite rack and metal shield. The vacuum chamber has a interlayer water cooling. The gap is 2 mm sealed with ceramic ring, kovar alloy is used to weld the ceramic ring to the Steel-316L vacuum pipe. This structure bring a micro vacuum part as a resonate cavity.

BEPCII Bunch length is about 15mm, it means the spectrum of bunch will cover the high frequency part of impedance, which will lead to an enormous heat deposition by the HOM. The HOM power will deposit at places where the wakefield trapped by small discontinuities of the beam duct, such as the ceramic gap. So when charged particles pass through the gap, it loses energy which would transfer into heat power[3].

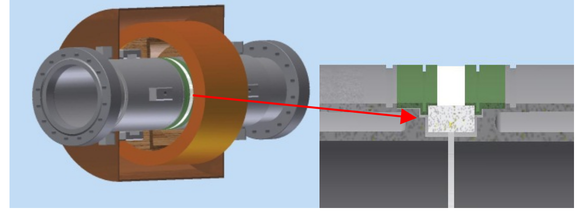

Figure 3: Structure of vacuum chamber.

ISBN 978-3-95450-176-2

The temperature curve also indicates the relevance between heat and bunch current. When the bunch current is above 7mA, the temperature is sharp rising. A large bunch over 10mA is injected into the synchrotron ring for experiment, it means the e+ and e- share the same beam current, the e+ T-SU2 is 69 °C, e- T-SU2 is 37°C, shows in Fig. 4.

Figure 4: Temperature and current curve with bunch current over 10mA.

In order to get the thermal power, a solid model of only vacuum part is built for wakefield simulation. Table 1 shows the BEPCII storage ring main parameters.

Table 1: BEPCII Parameters

Parameter(e+/e-)	BEPCII
Beam current (mA)	910
Bunch current(mA)	9.8
Beam energy (GeV)	1.89
Circumference (m)	237.5

In this case, the loss factor $K_{loss}$is 11.2V/nC when the gap is 2mm, bunch length is 15mm.

$$P_{loss}=I^2\ t\ K_{loss}/N[4]$$

I is the beam current 730mA,t is the revolution time 800ns, N is bunch number 92, so the P_{loss} is about 49.5W.

Eigenmode simulation is used to get the field distribution, the highest field amplitude near the gap is 2.48e+8V/m at 4.4GHz. Figure 5 shows the field distribution.

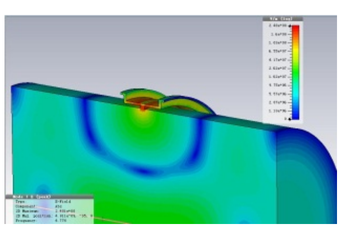

Figure 5: Field distribution of simulation.

A complete model of DCCT toroid, shield, rack and vacuum chamber with flange is established for temperature simulation. The loss power is all used for heat, the mode field distribution is imported to thermal losses [4] and no extra cooling, only the air flow is set on the surface. The temperature is from 20 to 83.8 Celsius degree as shown in Fig. 6.

Then the interlayer water cooling is add to the model by set the heat transfer coefficient in experience. The temperature is between 20 to 44°C, consistent with the e-'s situation. The e+ chamber most likely has other external heat source. As there are no other temperature sensors right now, it's difficult to confirm. We are plan to add a temperature sensor on the asylphon bellowsis connect to the chamber.

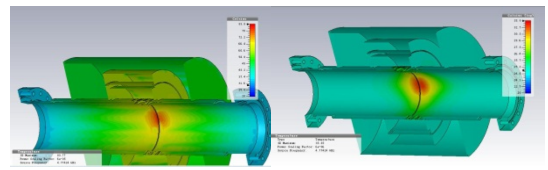

Figure 6: Thermal analysis without and with cooling.

SOLUTION

For not disturbing the machine's operation, a simple way that adding a fan to e+'s chamber for auxiliary cooling is used during last running period. It could lower the temperature for 2, 3°C. F

Examine and avoid the external heat power source is the next step to settle this problem. Meanwhile, for the 910mA or even higher running mode, the heat power will be higher, a new vacuum chamber is designed for spare.

The primary DCCT vacuum chamber has two section which separated by the gap. Both sections have interlayer water cooling. The water route is simple with several blocks to guide the flow, the water may not cover the whole inner surface, and will cause less effect of cooling.

The new vacuum chamber's micro structure will be shielded by improve the welding method, the loss factor may reduce to 6.5V/nC according to the simulation result, so the power will be down to 20W at the same condition above.

A new spiral water route will replace the old one, and the interlayer will increase from 2mm to 4mm as show in Fig. 7. As the water inlet's and outlet's diameter are 10mm, the distance between threads would not be too short or will slow down the water flow.

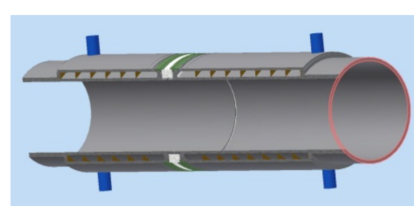

Figure 7: The interlayer of water cooling.

SUMMARY

Reduce the heat source and strengthen the external cooling are the main method to solve the heat problem. Through the simulation and experiment result, we can confirm that the primary mechanical structure and cooling system for DCCT is functional normal, and the analysis procedure could help to optimize the mechanical design for future current transformer. For e+'s special situation, more experiments should to be done for settling it.

ISBN 978-3-95450-176-2

ACKNOWLEDGMENT

The authors would like to thank to all members of the BI group in IHEP for their collaboration. The authors also would like to express their thanks to the colleague in IMPCAS for the assistance.

REFERENCES

[1] www.bergoz.com
[2] Tohru Honda, Yoichiro Hori and MikitoTadano , Suppression Of Bunched Beam Induced HeatingAtthe DCCT Toroid,1526-1528 epac98.
[3] L.Ma, J.Q.Wang, et al, BEPCII operation report (2009).
[4] D. Lipka, Heating of a DCCT and a FCT due to wakelosses in PETRAIII (2013).
[5] CST manual

ISBN 978-3-95450-176-2

PHASE AND ENERGY MEASUREMENT SYSTEM FOR C-ADS INJECTOR I

J.H. Yue, J. Hu, Q.Y. Deng, S.J.Wei, Q.Ye, IHEP, CAS, Institute of High Energy Physics, Chinese Academy of Sciences, Beijing, China

Abstract

For proton linac, phase and energy measurement is very important. Beam phase always can be measured by quadrature sampling [1][2], energy can be calculated by the method of time of flight (TOF), in this way we need to know the beam phase of two points whose distance is given. C-ADS injector I is a 10MeV proton linac with 10mA continuous current. It consists of an ECR (Electron Cyclotron Resonance) ion source, a LEBT (Low Energy Beam Transport), a 3MeV RFQ (Radio-frequency Quadruple) and a superconductivity linac accelerator with 3~10MeV. In the initial phase, the beam energy is about 3MeV. In this paper, phase and beam energy system of C-ADS Injector I have been introduced and some preliminary results have been shown.

INTRODUCTION

The ADS accelerator in China is a Continuous-Wave (CW) proton linac with 1.5 GeV beam energy, 10 mA beam current, and 15 MW beam power [3]. Its main task is to cope with nuclear waste material and produce clean nuclear power. It have two injectors, C-ADS injector I is a 10MeV proton linac with 10mA continuous current made by IHEP. It consists of an ECR (Electron Cyclotron Resonance) ion source, a LEBT (Low Energy Beam Transport), a 3MeV RFQ (Radio-frequency Quadruple) with 325MHz frequency and a superconductivity linac accelerator with 3~10MeV. In the initial phase, the beam energy is about 3MeV. The schematic diagram of C-ADS injector I is shown in Fig.1.

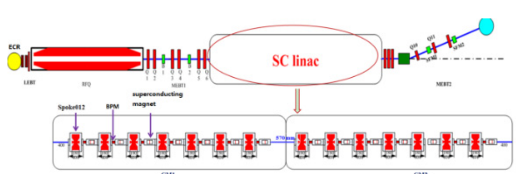

Figure 1: The Schematic diagram of C-ADS injector I.

In order to measure the beam phase and energy, we design the frontend electronics and fast data acquisition system shown in Fig.2. We take the FCT (Fast Current Former) monitors as the pickup, take the quadrature sampling to measure the phase of the FCT1and FCT2 and phase difference between FCTs. We use the method of TOF to get the beam energy.

The phase of sinusoidal signal is can be got by its in-phase and quadrature-phase (I&Q) components. The arctangent of the ratio of I and Q gives the angle of the signal relative to the phase of the sampling clock used to define I and Q.

To get the I and Q components, a signal is sampled at four times its frequency, that means once every 90 degrees. I, Q, -I, and –Q data sequences can be got. I subtract –I produce 2I, Q subtracts –Q makes 2Q, all common-mode errors are consequentially eliminated and low frequency noise is attenuated.

FRONTEND ELECTRONICS

As shown in Fig.2, the pulsed signal from FCT is broadband which comprise 325MHz sine wave. We use a high pass filter and low pass filter to make a narrowband filter. This narrowband signal be sent to DBM (double balanced mixer) to transfer signal to 16.25MHz and to filter again, so here we can get a 16.25MHz sine wave, this signal be input to a 14 bit ADC, the sample frequency is 65MHz, is quadruple of 16.25MHz. 65MHz sample frequency can promise to get a value every 90 degree, so we can get an orthogonal sequence data, the arctangent value of them is phase of the beam. The ADC can receive 325MHz reference signal, then output the 308.75MHz (19/20 of 325MHz) signal as the local signal of DBM.

FPGA CARD AND DAQ

ADC card named 100MAD_DA is selected to sample the waveforms, cope with the data and produce the timing signal. This card has two input tunnels, one is for FCT signal and the other is for reference signal. The analog signals digitize by the ADC, then sent to FPGA, in which we get I/Q data sequence and beam phase, then data are sent to computer by PCI express bus. It also produces the timing signal. The 325MHz reference signal are input to ADC, then 308.75MHz signal are output to send to DBM to down-convert the signal.

PRELIMINARY MEASURE RESULTS

As shown in Fig.3, beam phase of FCT1 and FCT2 have been got. You will find the effective data is not continuous because of two reasons, one is our beam is pulsed mode, not CW mode, the other reason is self-trigger mode. We got the beam phase is -86.98 and 57.66, so the beam phase difference is 144.64 degree. So the time of flight t is (144.64/360)*3.07778ns, equal to 1.237ns, the total flight time is 38.17ns which is 12 high frequency periods plus 1.237ns.

In order to calculate the beam energy, Eq 1, 2, and 3 are needed.

$$V=L/t \tag{1}$$

ISBN 978-3-95450-176-2

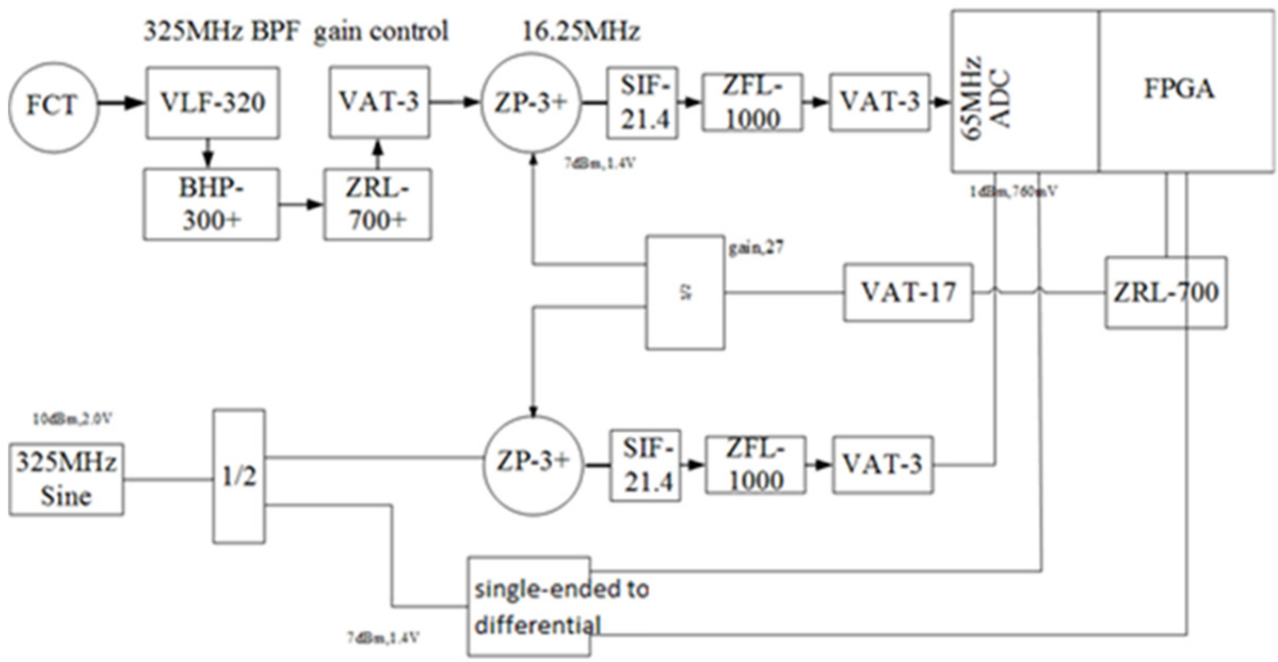

Figure 2: Phase measurement system of C-ADS injector I.

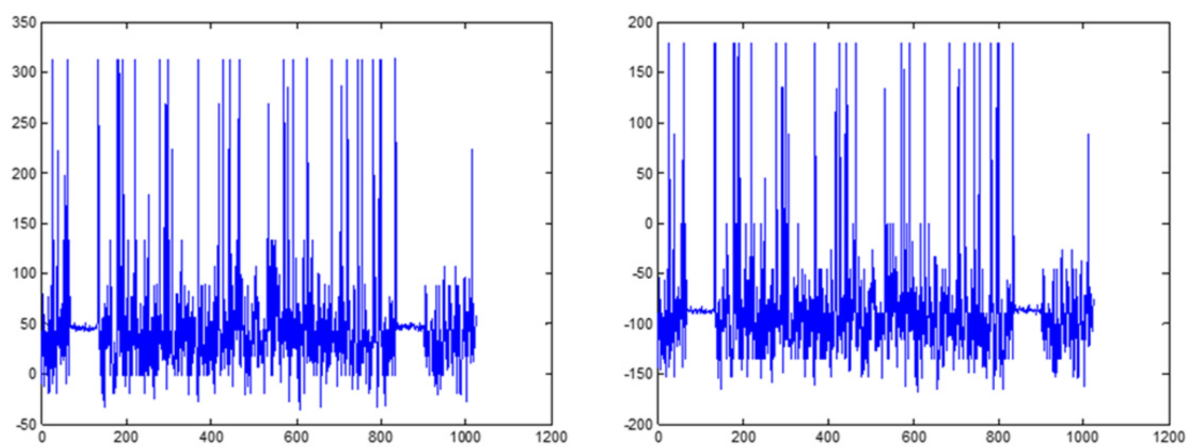

Figure 3: The phase value of different FCTs.

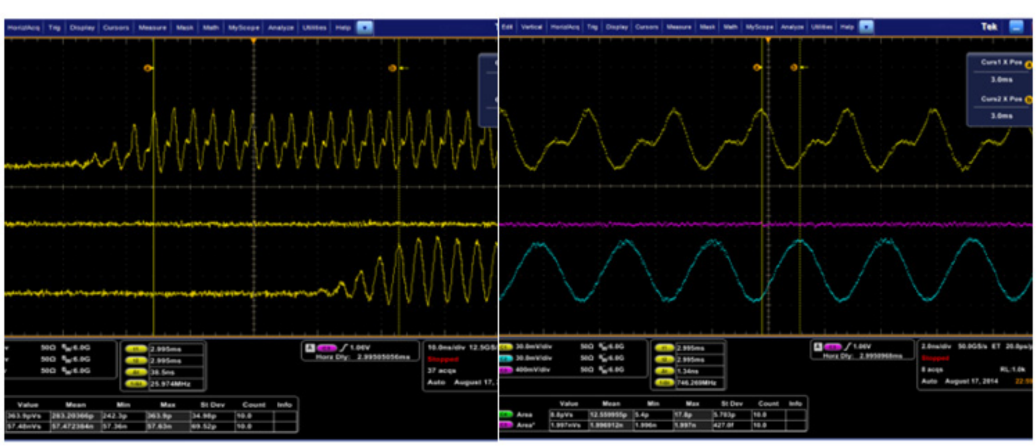

Figure 4: Rough and fine phase difference between FCTs.

$$\gamma = \frac{1}{\sqrt{1-(v/c)^2}} \qquad (2)$$

$$\gamma = \frac{E_k+E_0}{E_0} \quad (E_0 = 938MeV) \qquad (3)$$

Here L is distance of FCT1and FCT2, its value is 0.943m, and E_0 is static energy of proton, we put L, t and E_0 into the above equation, we can get the beam energy is 3.196820MeV.

We also can use the oscilloscope to check the measure results. Fig.4 shows the waveforms of FCT1 and FCT2 on the screen. In Fig.4, we can see the time of signal of FCT1 is in advance of FCT2 12 high frequency periods. That means 36.92ns. In Fig.4, fine time difference between the FCT1 and FCT2 is 1.34ns in one high frequency period, so the total flight time is 38.26ns which is coincide with 38.17ns measured by beam phase measurement system.

CONCLUSION

In this paper, the beam energy system and some preliminary results have been shown. In-phase and quadrature-phase (I&Q) method were taken to get the beam phase, and TOF method were taken to get the beam energy, the measure results is both coincide with design value and the measure results from the oscilloscope, so this method is reasonable, but some further study is need to do like as the resolution of this system.

REFERENCES

[1] J.Power et.al. “Design of a VXI Module for Beam phase and energy measurement for LEDA”, PAC, 1997, Vol.2, 2041-2043.

[2] J.Power, M.stettler, “The Design and initial testing of a beam phase and energy measurement system for LEDA”, AIP Conf. Pro., December 10, 1998, Vol.451, pp459-466.

[3] Z.H. Li. P. Cheng, H. P. Gen, et al. Phys. Rev. ST Accel. Beams, 2013, 16: 080101.

ISBN 978-3-95450-176-2

TIME MEASUREMENT METHOD BASED ON CPLD FOR BEAM LOSS POSITION MONITOR*

Yong Yang, Yongbin Leng#, Yingbing Yan
Shanghai Institute of Applied Physics (SINAP), CAS, Shanghai 201204, P. R. China

Abstract

Beam loss position is of great concern at SSRF. Time measurement is one of the key technologies for beam loss position monitor. This paper introduces a time measurement method based on Complex Programmable Logic Device (CPLD). Simulation has been done to verify the performance of this method.

INTRODUCTION

SSRF is the 3.5GeV electron storage ring facility operated at the Pudong New District of Shanghai. During accelerator operation ionising radiation is detected outside the vacuum chamber, mainly caused by electromagnetic cascades, generated by beam loss electrons hitting the chamber. The total dose is predominantly located at only a few positions of the storage ring, especially at the position of transverse feedback system [1-3]. Optical fiber radiation dosimetry from Cherenkov principle offers the possibility to measure the position of beam loss.

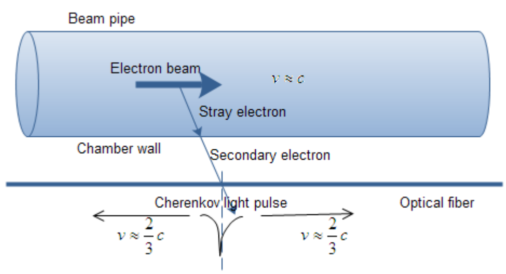

Figure 1: Beam loss position measuring principle.

Figure 1 shows the measuring principle. If some stray electron impact at the vacuum chamber, secondary electron will be excite. The movement of those secondary electron in the optical fiber will bring Cherenkov light pulse. The refractive index of optical fiber (quartz) is 1.5. So the speed of the light pulse in the optical fiber is 0.6666c, where c is the speed of light in vacuum. The Cherenkov light pulse will transmit along the fiber to the both ends [4,5]. The position of the original light pulse can be calculated from the time difference of the light pulse reaching between both ends.

Figure 2 shows an available measurement scheme. The PMT transforms the light pulse to electrical signal, high speed data acquisition card obtains the waveform, and then IOC calculates the time difference by complicated time orientation algorithm from PMT waveform. To measure time accurately, the data acquisition card must be high speed and has enough effective number bits [6,7].

This paper introduces a direct time measurement method to replace the high performance data acquisition card and IOC calculator algorithm.

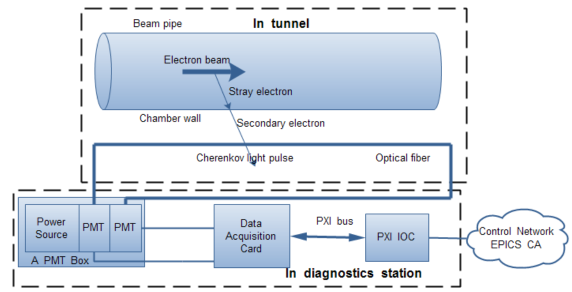

Figure 2: An available measurement scheme for beam loss position.

ARCHITECTURE

In the general purpose CPLD from Altera, there are many dedicated carry lines, which connect adjacent basic logic elements. These dedicated carry lines are normally used to form dedicated carry chains to implement arithmetic functions such as fast adders, counters, and comparators. The delay of each carry line is short and can be considered fixed for a particular physical technology, rail voltage, and temperature range. Using these carry lines as delay cells, a high-resolution time measurement equipment can be implemented in an CPLD [8].

To verify our idea of time interpolation within one clock period using dedicated carry lines, a time measurement equipment based on counter and time interpolation methods was implemented in an CPLD. The block diagram of the time measurement equipment is shown in Figure 3.

Fine Time Measurement

One of the simplest forms used to combine the dedicated carry lines into a carry chain is a multibit adder [9]. The Boolean equations of each adder cell are:

$$Sum = A \oplus B \oplus Ci$$

$$Co = AB + (A + B)Ci$$

where A and B are inputs for the adder, Ci is a carry-in bit, Co is a carry-out bit, and Sum is a sum bit.

*Work supported by National Nature Science Foundation of China (11375255)
#lengyongbin@sinap.ac.cn

ISBN 978-3-95450-176-2

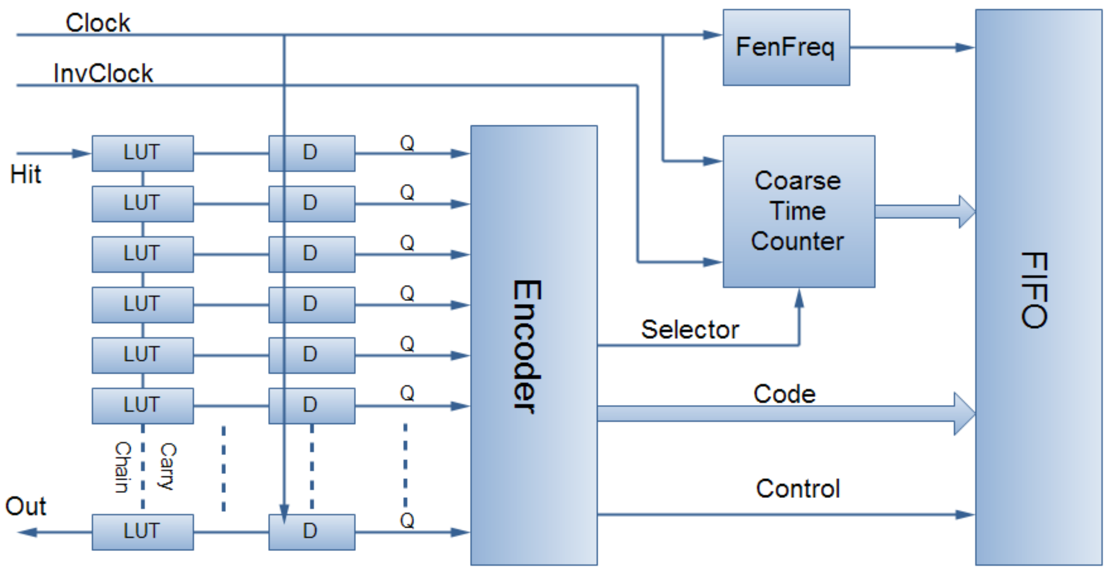

Figure 3: Block diagram of the time measurement equipment.

The delay time of the whole chain must be longer than one period of the system clock. We set all A to logic one and all B except the least significant bit (LSB) to logic zero. The LSB of B is the hit signal. If there is no hit signal, all Sum would be logic one. When there is a hit signal, each bit of the sum, from the LSB to the most significant bit (MSB), will change to logic zero step by step. The changed bits indicate the elapsed time of the hit signal passing along the carry chain. At the next rising edge of the system clock the sum bits will be latched. This is the fine time measurement in a thermometer code.

While trying to latch the adder's output bits at the rising edge of the system clock, we use dual synchronizers to reduce the probability of metastability. There are many kinds of conversion schemes to convert a thermometer code to a natural binary code for the fine time measurement. The binary-search encoder is chosen for its simplicity and easy implementation.

In the fine time measurement, it is very important to keep a uniform delay between the bits of the sum to the input of their corresponding register. A basic logic element that contains a look-up table (LUT) and a programmable register is used to form the 1-bit adder which generates the sum bit and the register for latching the sum bit. In addition, constraints must be set in the design tool and sometimes logic cells must be placed manually.

Coarse Time Counter

A synchronous counter is designed to realize the coarse time measurement. The counter may change its state while the hit arrives. To avoid ambiguous states, two Gray-code counters running at the system clock rate (one in phase and another out of phase) are used. Depending on the phase of the system clock at the arrival moment of the hit signal, one of the two counter's outputs is selected and encoded with a binary code as the coarse time measurement code. If the hit arrives in the first half (0~π) of the system clock period, the output of the 'in phase' counter is selected. Otherwise the output of the 'out of phase' counter is selected. The result of the fine time measurement reflects the phase of the system clock. Using the result of the fine time measurement, a stable coarse time count value is always obtained.

Read-Out Buffer

The result of the complete time measurement (the fine time and the coarse time measurement) is written into a first-in first-out (FIFO) buffer along with a channel identifier. The total time measurement can be expressed as follows:

$$T_{out} = T_{coarse} + T_{fine} = T_{sys} * N_c + T_{bin} * N_e$$

Where T_{out} is the result of the complete time measurement, T_{coarse} is the result of the coarse time measurement, T_{fine} is the result of the fine time measurement, T_{sys} is the period of the system clock, N_c is the coarse time measurement code, T_{bin} is the bin size (the LSB value) of the fine time measurement, and N_e is the fine time measurement code.

SIMULATION RESULT

The delay time of a dedicated carry line is different in CPLD's from different series, capacity and speed-grade. An EPM1270T144C5N MAX II CPLD device from Altera was selected to implement this time measurement equipment design.

Figure 4 shows the simulation result. The horizontal ordinate is the input relative delay time and the vertical ordinate is the code from the read-out buffer in CPLD. The slope of the fit curve is 8.8403. And so the resolution of this time measurement equipment design is 113.1ps.

ISBN 978-3-95450-176-2

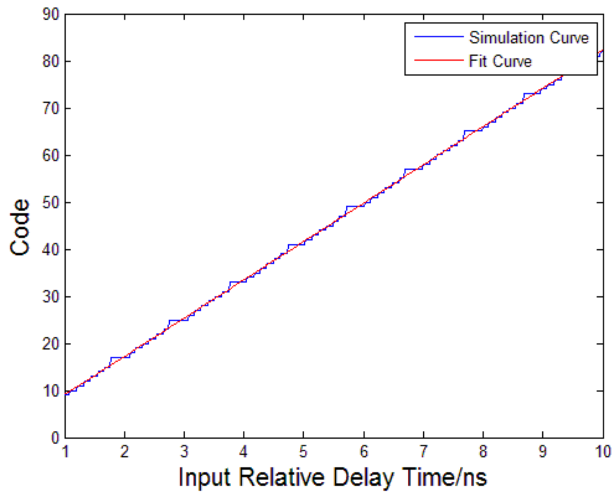

Figure 4: Simulation result and the resolution of this time measurement equipment design is 113.1ps.

CONCLUSION

To monitor the beam loss position in SSRF, a high-resolution time measurement equipment implemented in a general purpose Complex Programmable Logic Device (CPLD) is presented. Dedicated carry lines of an CPLD are used as delay cells to perform time interpolation within the system clock period and to realize the fine time measurement. Two Gray-code counters, working on in-phase and out-of-phase system clocks respectively, are designed to get the stable value of the coarse time measurement. The fine time code and the coarse time counter value are then written into a first-in first-out (FIFO) buffer. Simulation has been done to verify the performance of the equipment design. The resolution is better than 120ps.

REFERENCES

[1] B.Joly, "Beam Loss Monitors at the ESRF", Proceedings DIPAC, Chester, UK, 1999.

[2] Kay Wittenburg, "Beam Loss Montoring and Control", Proceedings of EPAC 2002, Paris, France.

[3] Frank Rudiger, "Beam Loss Montoring and Control", Proceedings of EPAC 2002, Paris, France.

[4] Kay Wittenburg, "Beam Loss Position Monitoring with Optical Fibers at DELTA", DESY, June 2008.

[5] F.Wulf and M.Korfer, "Beam Loss Montoring and Control", Proceedings of DIPAC09, Basel, Switzerland, 2009.

[6] T.Obina, "Optical-fiber Beam Loss Monitor for the KEK Photon Factory", Proceedings of IBIC12, Tsukuba, Japan, 2012.

[7] D.Di Giovenale, "On-line Beam Loss Position Monitors for SPARC", Proceedings of FEL2009, Liverpool, UK, 2009.

[8] P.Carbone et al., *Design, Modeling and Testing of Data Converters*, Signals and Communication Technology, Springer-Verlag Berlin Heidelberg 2014.

[9] Ying Li and Xinglin Che, "Time Interval Measurement for Resonator Fiber Optic Gyroscope based on Slow Light Technolog", Microwave Opt Technol Lett, vol. 50, pp. 3220-2008.

ISBN 978-3-95450-176-2

ELECTRON BEAM UNIFORMITY DETECTION DEVICE FOR IRRADIATION ACCELERATOR*

LG Zhang#, Jiang Huang, Kaifeng Liu, Jun Yang, Chen Zuo
Huazhong University of Sicence and Technology, Wuhan, Hubei, China

Abstract

High-voltage electron accelerator is widely used in irradiation processing industry. Beam uniformity of the accelerator has very important impact on the quality of irradiated products. Accurate measurement of beam uniformity helps to improve product quality and production efficiency. In this paper, the electron beam uniformity detection device is designed based on Faraday cup array followed by the signal shaping circuit and the digital signal processing system. Finally, the computer offers friendly interface to help users understand the operating state of the accelerator and the electron beam uniformity information. This device uses DSP technology to process the signal and optical fibre to communicate, which greatly improves noise immunity capability of the system. Through such a high precision, easy to use detection device, user can get the accelerator beam irradiation uniformity information which is very useful to direct the industry radiation process.

INTRODUCTION

Irradiation accelerator is widely used in many areas, such as irradiation processing industry [1], waste gas treatment [1], food preservation [2], and so on. To ensure the quality consistency of the products, beam uniformity of the accelerator is very important. Accurate measurement of beam uniformity helps to improve product quality and production efficiency. The measurement results can also direct the design of the irradiation accelerator.

To measure the beam uniformity is to measure the beam intensity in the scan area of the irradiation accelerator. Faraday cup is a simple and effective device to measure the beam intensity [3]. It converts the beam intensity to a current signal by collecting the charged particles of the beam. In our design, a Faraday cup array is used to measure the distribution of the electron of the beam, which reflects the beam uniformity.

A high-voltage irradiation accelerator is built in Huazhong University of Science and Technology for biological science and materials science. The structure of the accelerator is shown in Fig. 1. The scan coverage of the beam is 1 *m*. The electron beam uniformity detection device is designed to measure the beam uniformity of this accelerator. As for other irradiation accelerators, the structure of the device is similar, the only differences are the parameters of the components in the measurement circuit and the number of the Faraday cup in the Faraday cup array.

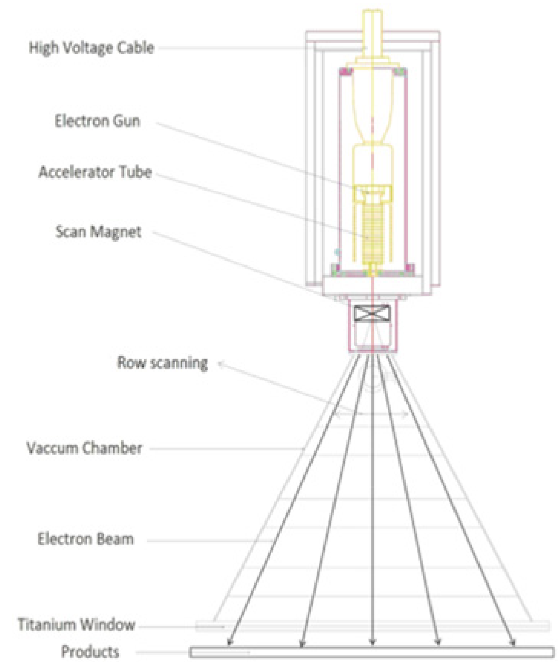

Figure 1: Structure of the high-voltage irradiation accelerator.

SYSTEM DESIGN

The structure of the system is shown in Fig. 2. It consists of four parts: Faraday cup array; measurement circuit; digital processor for optical fibre communication and digital signal processing; and the human-computer interaction interface. Firstly, the Faraday cup array collect the electrons of the beam in the scanning area. The electron current flows from the Faraday cup to the ground, which can reflect the beam density. Then the measurement circuit processes the current signal to reduce the noise and amplify the signal. In order to achieve the remote detection, while reducing EMI noise, a digital processor is used which converts a current signal into a digital signal. Digital filtering method is also used to process signals. In our design the digital filter realised using verilog HDL on the FPGA is a low pass filter. Finally, the beam signal was packaged into data frames and sent to the remote computer, and the graphical interface on a computer written by labVIEW shows the uniformity of the beam, so we can easily achieve the real-time detection of the beam uniformity.

*Work supported by the 2011 Project-Hubei Collaboration Innovation Centre of Non-power Nuclear Technology
#zhanglige @hust.edu.cn

ISBN 978-3-95450-176-2

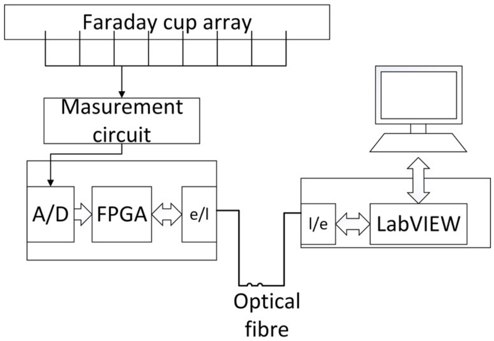

Figure 2: Structure of the system.

Faraday Cup

The Faraday cup structure is shown in Fig. 3. It consists of an inner cup for the collection of electrons and a repeller for biasing the ejected secondary electrons back into the inner cup. Since the high-energy electrons collide with the metal surface of the Faraday cup, the secondary electrons ejected from the surface. In order to reduce measurement error, repeller is used to deflect the ejected electrons. In our design, a electric repeller is used to deflect the secondary electrons. The electric fled between the repller and the inner cup make the secondary electrons reverse accelerated and collected by the inner cup again.

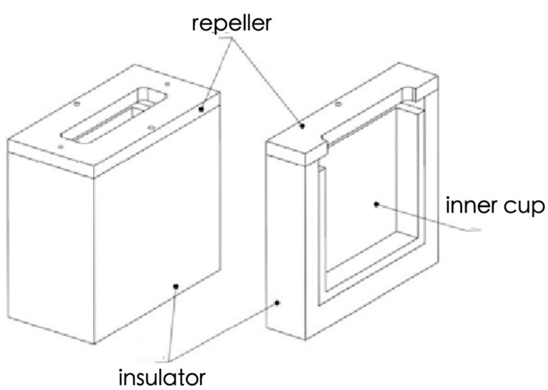

Figure 3: Structure of the Faraday cup.

Measurement Circuit

Electrons flowing from the Faraday cup to the ground will induce a current signal which can be detected. The signal measurement circuit converts the current signal into a voltage signal and amplifies the scope of the signal to the voltage stage of the A/D conversion chip. To ensure the driving capability of the signal, it's required to reduce the output impedance of the conditioning circuit. As used here, two operational amplifiers are used to complete the I/V conversion and the signal amplification. Signal measurement circuit is designed as follows. Preamp circuit converts the current signal into a voltage signal and amplifies the primary voltage. After that, a second-order Butterworth low-pass filter processes the primary amplified voltage signal. Finally, through a forward amplifying circuit, signal voltage is amplified to the dynamic range of the A/D sampling port.

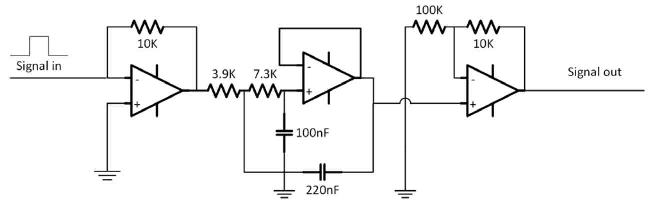

Figure 4: Measurement circuit.

Digital Filtering Algorithm

The digital filter function is implemented as a direct from II transposed structure as shown in Fig. 5. In the algorithm *n-1* is the filter order, which handles both FIR and IIR filters [4].

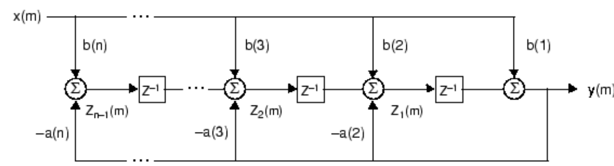

Figure 5: Block diagram of the digital filter.

The input-output description of the filtering operation in the z-transform design is a rational transfer function,

$$Y(z)=\frac{b(1)+b(2)z^{-1}+...+b(nb+1)z^{-nb}}{a(1)+a(2)z^{-1}+...+a(na+1)z^{-na}}X(z) \quad (1)$$

where *na* is the feedback filter order, and *nb* is the feedforward filter order. Due to normalization, assume a(1)=1.

The operation of the digital filter at m-th sample is given by the time domain equation which can be derived by forward difference method.

FIELD AND PARTICLE MOTION SIMULATION IN THE FARADAY CUP

To simplify the evaluation of the electric field in the Faraday cup, we establish a 2D model of the Faraday cup. According to Maxwell's equation, the electron field in the 2D model satisfies,

$$\begin{cases}\nabla\times\boldsymbol{E}=0\\ \nabla\cdot\boldsymbol{E}=0\end{cases} \quad (2)$$

The electric field E can be written as the gradient of the scalar potential φ,

$$\boldsymbol{E}=-\nabla\varphi \quad (3)$$

According to Equ.2 φ satisfies the Laplace equation

$$\nabla^2\varphi=0 \quad (4)$$

Eq. 4 can be easily solved by using FEA method. Figure 6 shows the results of the electric field.

ISBN 978-3-95450-176-2

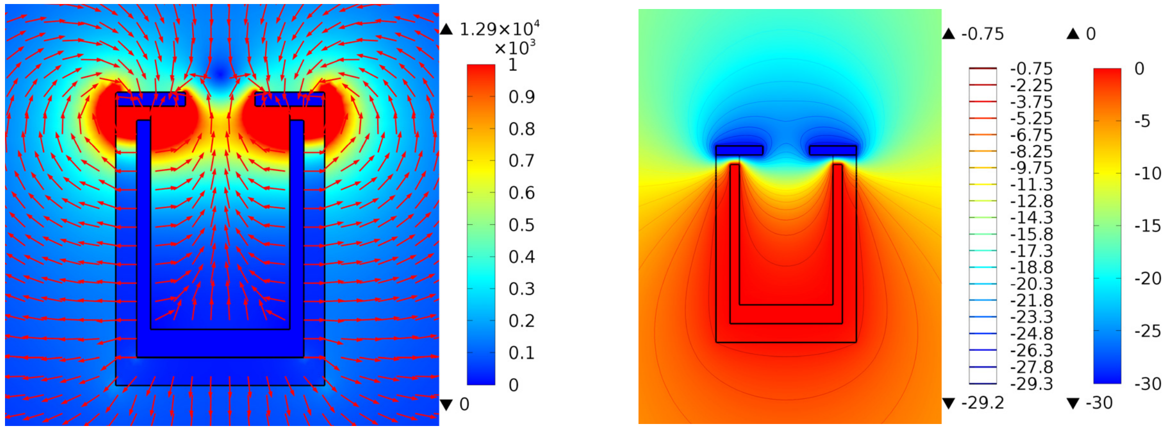

(a) (b)

Figure 6: Electric field in the Faraday cup 2D model. (a) Pseudo-colour image and field lines of $\boldsymbol{E}$. (a) Pseudo-colour image and equipotential line of φ.

The trajectories of secondary electrons at the worst point are investigated. The maximum energy of the ejected secondary electrons satisfies,

$$E_{\max} = A\cos^2\theta \quad (5)$$

Where A is the parameter related to the particle. The energy is high when the angle between the ejected electron and the normal direction of the surface is small. A random simulation of the secondary electrons is conducted as shown in Fig. 7. It shows that the ejected electrons can be captured by the inner cup.

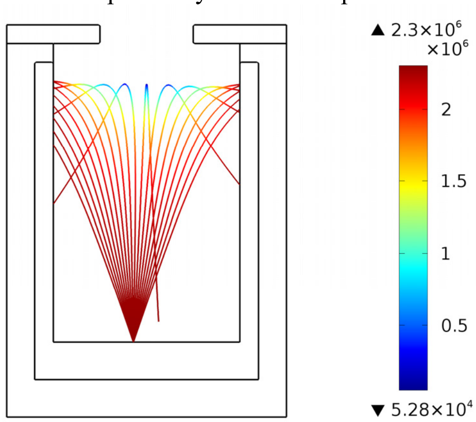

Figure 7: Simulation of the ejected electron' trajectories

RESULTS AND DISCUSSION

The non-uniformity is given as:

$$\rho 1 = \frac{N_{max} - N_{min}}{N_{max} + N_{min}} \quad (6)$$

N_{min} is the minimum dose value, N_{max} is the maximum dose value, $N_{av} = \frac{\sum_0^n N}{n}$, the scanning length is 100cm, and the beam length is 80cm. The non-uniformity is calculated as 7.8% which is better than 10% of the GB/T25306-2010 [5].

CONCLUSION

The proposed beam uniformity detection device demonstrated an efficient, flexible and precise way to measure the uniformity of the beam uniformity, which has very important impact on the quality of irradiated products. The designed Faraday cup array can reduce the error caused by the secondary electrons when collecting the beam electrons. The mixed analog and digital circuit greatly improves noise immunity capability of the system. The graphical interface on a computer written by labVIEW offers friendly interface to help users understand the operating state of the accelerator and the electron beam uniformity information.

ACKNOWLEDGMENT

The authors would like to acknowledge the guidance of Prof. Fan Mingwu. This work, supported by the 2011 Project-Hubei Collaboration Innovation Centre of Non-power Nuclear Technology, was carried out within the help of Hubei Technology College and Wuxi EL PONT Radiation Technology CO. Ltd.

REFERENCES

[1] "Emerging Applications of Radiation Processing", IAEA-TECDOC-1386, April, 2003.
[2] A. G Chmielewski, M Haji-Saeid, "Radiation technologies: past, present and future". Radiation Physics and Chemistry, Volume 71, Issues 1–2, September–October 2004, Pages 17–21.
[3] F.E. Black et al., *This is a Very Interesting Book*, (New York: Knopf, 2007), 52.
[4] P Limão Vieira, Lobo R F M. Low energy electron beam for time-of-flight ionization measurements [J]. Vacuum, 1999, 52:19–22.
[5] GB/T25306-2010, Chinese national general standard for radiation electron accelerator [S].

ISBN 978-3-95450-176-2

DESIGN AND ANALYSIS OF A BEAM UNIFORMITY DETECTOR BASED ON FARADAY CUP ARRAY*

C. Zuo†, J. Huang, J. Yang, L G. Zhang
Huazhong University of Science and Technology, Wuhan, Hubei, China

Abstract

Beam uniformity of electron irradiation accelerator has a great impact results for industrial radiation process. In this paper, a beam uniformity detector, based on Faraday cup array, has been designed for a 400KV electron irradiation accelerator in Huazhong University of Science and Technology. Suitable structure has been calculated for the secondary electrons emission. Cooling system is necessary for the detector in the condition of high-intensity ion beams, and it has been designed by thermo-structural analysis. This detector now has been used for experiments successfully.

INTRODUCTION

Electron irradiation accelerator has been widely used in medicine, food, environmental protection and other industrial fields [1]. Uniformity of electron beam has a great influence on the results in the material and life subjects. Measurement of uniformity can provide accurate parameters for experiments, and important evidence for improving the performance of the accelerator.

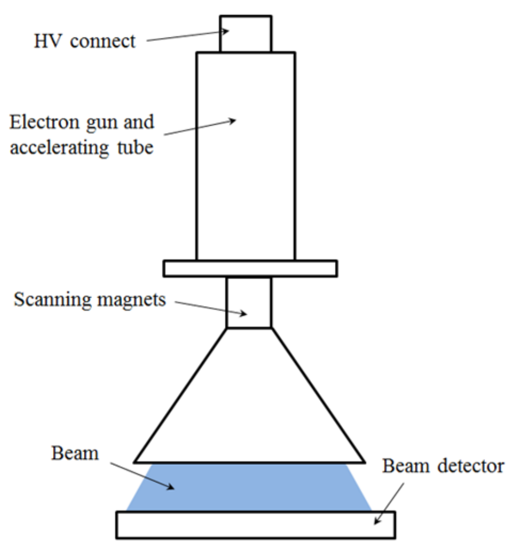

Figure 1: Sketch of a 400kV electron accelerator in HUST.

Faraday cup is a detector designed to measure the intensity of the beam. It is a conductive metal cup hit by a beam of ions or electrons. The metal can then gain a small net charge while the ions are neutralized. By measuring the electrical current in the metal, the number of charges being carried by the ions can be determined. The emission of secondary electrons should been considered, otherwise the result would be less than the actual value. Usually a washer-type metallic electron-suppressor lid, the repeller, is biased at a given voltage to catch the secondary electrons escaped from the metal surface. Faraday cup array is composed of multiple independent Faraday cups arranged in a one (or two) dimension area uniformly. Beam intensity distribution in the area can be obtained by fitting the signals of every Faraday cup. Huazhong University of Science and Technology, HUST, has a 400kV electron irradiation accelerator, as shown in Fig. 1. The length of the beam is about 1000mm. In order to detect the accelerator beam uniformity in the longitudinal direction, a detector based on Faraday cup array has been designed in this paper.

DESIGN DESCRIPTION

Structure

The common structure of Faraday cup is illustrated by Fig. 2 (a). It is composed of a copper cup which collects the electrons and a repeller. The two parts are mounted in an insulated cylinder and they insulate against each other. The metal cup can effectively collect electrons, but the secondary electrons need to be caught again while escaping from the metal surface. For reducing the measurement error, a bias lid mounted on the cup is wildly used. The electric field applied directly on the repeller will reverse and accelerate secondary electrons into the metal cup [2].

As the size of the electron irradiation accelerator's titanium window is 1000mm×100mm, Faraday cup is specially designed to be square, in order to collect more electrons in the beam's longitudinal direction. The inner of the square cup, made up of copper, is 110mm long, 45mm wide and 93mm deep, the surrounding wall is 5mm thick, bottom 7mm thick. The metal square cup is placed into an epoxy square cup with the size of 150mm×75mm× 130mm.The repeller (10mm thick) is mounted on the epoxy cup, so that the distance between bias plate and metal cup is up to 10mm. A square hole (100mm×25mm) is machined in the centre of the lid in order to make the beam enter the Faraday cup directly. A 100V negative bias voltage is given on the electrode.

This beam uniformity detector is composed of a linear array of 10 Faraday cups, as shown in Fig. 2 (b). The distance between each two adjacent is 25mm. Every

*Work supported by the 2011 Project-Hubei Collaboration Innovation Centre of Non-power Nuclear Technology
† cheneyz@hust.edu.cn

ISBN 978-3-95450-176-2

Faraday cup is mounted on a 975mm long grounded copper bar with a 10kΩ resistor.

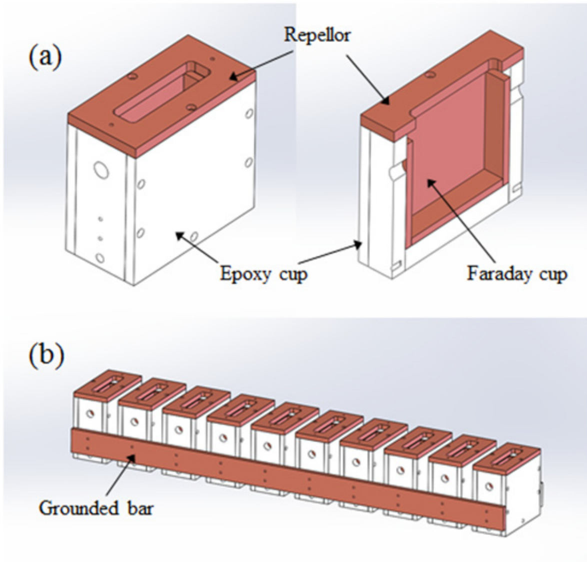

Figure 2: (a)Structure of single Faraday cup (b) Faraday cup array.

Stopping Power in the Bottom

In order to stop the charged particles in the metal, the thickness of Faraday cup's bottom need to be more than the range of particles in copper. The range of electrons for a given material can be approximated by the following expression:

$$R = \int_0^E \left(\frac{dE}{dx}\right)^{-1} dE \tag{1}$$

where R is the range of electrons, E is the initial kinetic energy of the particle.

The ranges of electrons with different energy in different elements is showed in the Atomic Data [3]. As the accelerator beam energy is 400keV, we can found out that the range of electron beam is about 0.8mm, much less than the thickness of the Faraday cup's bottom.

Secondary Electrons Emission

Secondary electrons will be generated by the high power beam hitting the bottom of Faraday cup, it will result in a loss of detection value (see Fig. 3). These electrons escaped from the bottom satisfy the distribution of cos^2h, where h is the angle between reflection line and the bottom surface. If the length of Faraday cup was high enough compared to the inner diameter, the escaped electrons would occur in a lower proportion in all electrons and have little effect on detection value [4].

To simplify we suppose that the beam is just hitting the centre of the bottom, the number of the electrons emitting from the centre is n, and n in the direction along h is in proportion to cos^2h. We can get Equation 2.

$$\theta = \frac{\pi}{2} - h \tag{2}$$

where θ is the angle between secondary electrons emission line and the axis of Faraday cup, so n also satisfy the distribution of $sin^2\theta$. For the angle element $d\theta$,

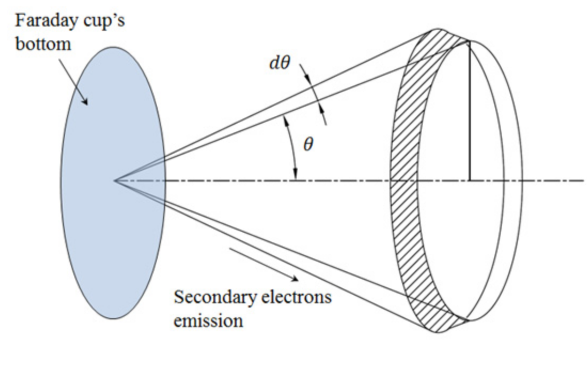

Figure 3: Sketch of secondary electrons emission.

we can get the solid angle dK in the circle face with the radius r.

$$dK = \frac{2\pi r sin\theta \cdot r d\theta}{r^2} = 2\pi sin\theta d\theta \tag{3}$$

$$sin^2\theta dK = sin^2\theta sin\theta d\theta = sin^3\theta d\theta \tag{4}$$

So the number of electrons emitting from dK is in proportion to $sin\theta^3 d\theta$. The rate of the emission electrons can be calculated by the Equation 5.

$$P = \int_0^{\frac{\pi}{2}arctan\frac{b}{a}} 2\pi sin^3\theta d\theta / \int_0^{\frac{\pi}{2}} 2\pi sin^3\theta d\theta$$

$$= \frac{3}{2}\int_0^{\frac{\pi}{2}arctan\frac{b}{a}} sin^3\theta d\theta \tag{5}$$

where a is the length of Faraday cup, and b is the radius of the bottom. When a=12.5mm, b=103mm, the rate is about 0.5%, and the influence can be ignored.

THERMO-STRUCTURAL ANALYSIS

Faraday Cup without Cooling Channels

The Faraday cup should be considered the thermal deformation, as the heat power of the beam will increase the temperature.

The current of the 400kV electron accelerator is up to 3A, the total power is about 1200kW without regard to the secondary electrons emission, a uniform heat power density was applied on the surface of the repeller and the Faraday cup's bottom: the power on the repeller is about 60W, and 30W on the bottom. It is shown in Fig. 4.

A finite element model was developed for the Faraday cup with surface elements to calculate the thermal radiation to the air at 20 °C. The initial temperature of all Faraday cup is set to 20 °C. The properties of copper have been used for all the analyses.

In Fig. 5 the temperature distribution and the thermal deformation in the copper are shown. Obviously, the deformation is too high for normal operation and the high

ISBN 978-3-95450-176-2

temperature would influence the cooper electrical conductivity. Water-cooling channels are necessary for both the repeller and the bottom.

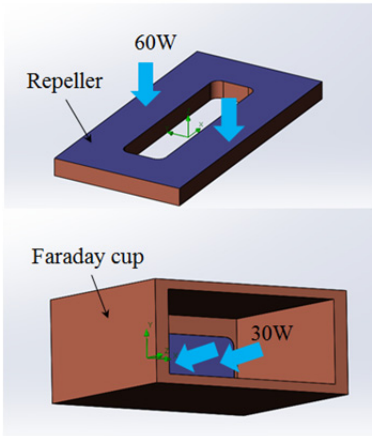

Figure 4: Heat power on the repeller and the bottom.

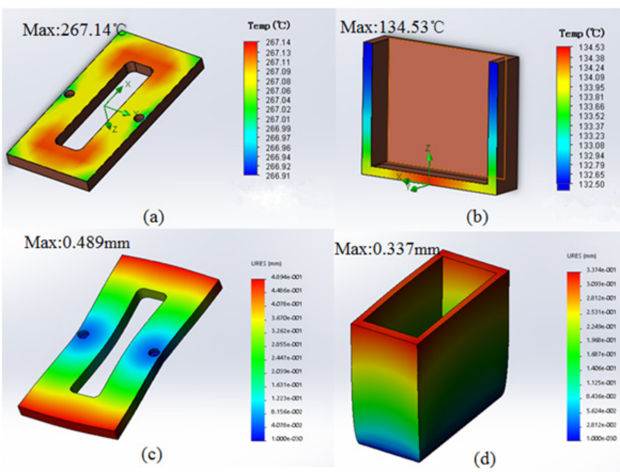

Figure 5: (a)&(b)Temperature (°C) distribution ,(c)&(d) Thermal deformation(mm) in the repeller and the Faraday cup without cooling channels.

Faraday Cup with Cooling Channels

Water-cooling circuits with $\phi 3$ mm inner diameter are processed separately in the repeller and the bottom. Coolant inlet temperature was always set to 20°C. Water velocity was set to 3m/s, water maximum temperature within values that do not influence electrical conductivity (<60-70 ℃), while stress distribution should be preliminarily kept under 107MPa.

The heat transfer process inside the cooling channels in ruled by forced convection in single-phase flow. Fluid-thermal and thermo-structural analyses were carried out to investigate the effect of various parameters (heat flux, water flow, model geometry), in term of temperature of the water and of the cooling channels walls, temperature and stresses in the copper.

In Fig. 6 the max temperature of the repeller and the Faraday cup with water-cooling channels inside is about 22 °C, as the influence on the thermal deformation could became negligible.

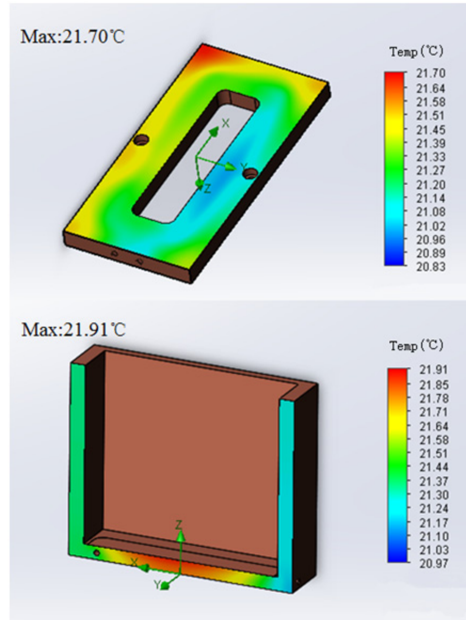

Figure 6: Temperature (°C) distribution in the repeller and the Faraday cup with water-cooling.

CONCLUSION

The beam uniformity detector based on Faraday cup array for electron irradiation accelerator has been designed and used successfully. Compared with other detector, Faraday cup array is simply processed and installed, the matched electric circuit and data processing are both uncomplicated.

The secondary electrons emission is the key of the design. The size of the Faraday cup has been confirmed, by means of numerical calculations: the range of high energy electrons in the copper bottom and the rate of the emitting secondary electrons' number, that was found to be the most critical component.

The water-cooling channels in the repeller and the bottom were found necessary to limit the temperature and thermal deformation in the Faraday cup.

The next step in this work would be to design another detector based on a movable Faraday cup in one or two dimensions. It will help detect the beam uniformity continuously.

ACKNOWLEDGMENT

This work, supported by the 2011 Project-Hubei Collaboration Innovation Centre of Non-power Nuclear Technology, was carried out within the help of Hubei Technology College and Wuxi EL PONT Radiation Technology CO. Ltd.

The authors would like to acknowledge the guidance of Prof. Fan Mingwu.

ISBN 978-3-95450-176-2

REFERENCES

[1] Zhai X L.(1987).Status and applications of foreign accelerators for radiation processing. Nuclear Techniques, 11: 1-5.

[2] Brown K L, Tautfest G W.(1987).Faraday-Cup Monitors for High-Energy Electron Beams. Review of Scientific Instruments, 27(9): 696-702.

[3] Pages, L., Bertel, E., Joffre, H., & Sklavenitis, L. (1972). Energy loss, range, and bremsstrahlung yield for 10-keV to 100-MeV electrons in various elements and chemical compounds. Atomic Data and Nuclear Data Tables, 4, 1-27.

[4] Xu Z G, Wang J C, et al. (2005). Application of Faraday cup array detector in measurement of electron-beam distribution homogeneity. Nuclear Electronics & Detection Technology,25(4): 439-441.

ISBN 978-3-95450-176-2

CW LASER BASED PHASE REFERENCE DISTRIBUTION FOR PARTICLE ACCELERATORS

S. Jablonski *, H. Schlarb, C. Sydlo, DESY, Hamburg, Germany

Abstract

We present a cost-effective solution for the synchronization of RF signal sources separated by tens of kilometers with the femtosecond accuracy. For the synchronization a phase reference distribution system (PRDS) is developed, which is comprised of a CW optical transmitter connected via single mode fiber-optic links to remote receivers. This technique enables to use only one transmitter for multiple receivers and removes the necessity of active stabilization units (e.g. piezo-driven fiber stretchers or laser wavelength tuning), which reduces considerably the system cost.

The concept of the new RF reference distribution, parameters of crucial components, phase drift detection and correction techniques are introduced, which lead to low noise and long-term stable PRDS operation. Detrimental effects of various linear and nonlinear fiber impairments are discussed. One of the most important elements is the phase detector, which is based on a direct RF-sampling ADC and it features a femtosecond measurement precision over 2π phase change. Finally, the long-term performance of the designed PRDS is shown, which was evaluated with a 500-m single-mode fiber and an RF signal of 1.3 GHz.

INTRODUCTION

Modern RF linear accelerators to fulfill high requirements in terms of energy gain per meter must be made much more effective. The accelerator performance is considerably affected by the phase reference distribution system (PRDS), which synchronizes various remote subsystems with femtosecond precision.

In this paper, a prototype of a PRDS is presented, which provides the timebase for the spatially distributed devices with the sub-100 fs pk-pk precision at the distance of a few km over several hours. The designed optical distribution makes use of standard components developed for the telecommunication industry and applies a distribution method that avoids complexity or expensive elements, which cause it attractive for a variety of applications.

Optionally, this PRDS can be also used for the transmission of low jitter RF signals to distant locations with the residual phase jitter lower than 10 fs rms. The transmitted RF signals can substitute local high performance RF sources, which leads to the considerable cost reduction.

The PRDS can be implemented in facilities using different reference signal frequencies ranging from about 100 MHz to up to several GHz, and the distance between the synchronized remote devices can reach dozens of km.

* szymon.jablonski@desy.de

NEW CW OPTICAL DISTRIBUTION CONCEPT

The simplified block diagram of the designed PRDS is shown in Fig. 1. The system is comprised of a CW optical transmitter connected via single mode fiber-optic links to multiple receivers (one is shown in the picture). The optical transmitter is a single-mode laser intensity modulated with an RF reference signal using a Mach-Zehnder modulator (MZM). Optical signal linewidth is broadened by applying a phase modulator to mitigate Rayleigh and Brillouin scattering detrimental effects in optical fibers, which is discussed further in the text below. The modulated laser signal is amplified by a high power erbium doped fiber amplifier (EDFA), and then split to dozens of optical fiber links utilizing a multichannel optical splitter. In a receiver a fraction of the modulated light is coupled out to a photodetector "3" and converted into an RF signal, which is further used for the synchronization of a local RF source to the reference oscillator.

Environmental conditions like temperature, humidity, vibrations or air pressure have the considerable influence on the stability of the distribution system. The major phase drift sources are the optical fibers connecting the transmitter with the remote receivers, which experience mechanical tensions and refractive index changes due to environmental variations [1]. The temperature and humidity sensitivity of a standard SMF28e amounts to 40 fs/K/m and 2.5 fs/%RH/m [2], respectively. Hence, time delay variations in a few kilometer optical fiber can equal even a couple of hundreds ps. However, these variations can be measured using the feedback signal reflected by a mirror located at the end-station. Optical signals propagating forward and backward the SMF experience the same conditions and the delay variations are almost symmetrical in both directions.

To measure time delay fluctuations of the optical fiber, a small fraction of the optical beam is reflected back to the transmitter applying e.g. a Faraday rotator mirror (FRM). In the transmitter, the reflected light is separated from the forward propagating light using e.g. a circulator, then converted into an RF signal by a photodector "2". One channel of the optical splitter is directly connected to the photodetector "1" to measure phase drifts of the components in the transmitter, which are not temperature and humidity stabilized, e.g. Mach-Zehnder modulator or EDFA (see Fig. 1).

Phase drifts between the reference oscillator and a remote RF source are determined using three phase detectors denoted as PD1, PD2 and PD3, which measure the relative phase drifts ϕ_1, ϕ_2 and ϕ_3, respectively. The phase of a remote RF source should be shifted by ϕ_{drift} given by

$$\phi_{drift} = \phi_1/2 + \phi_2/2 + \phi_3 \quad (1)$$

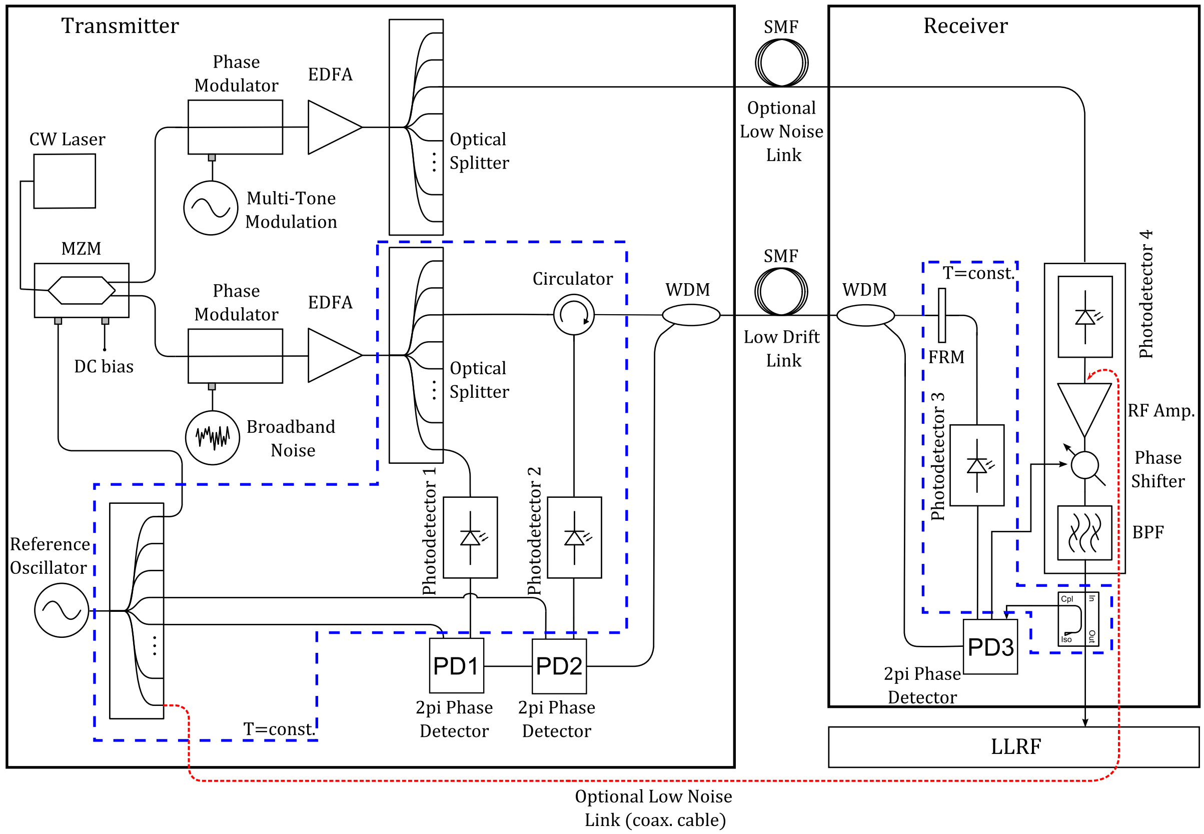

Figure 1: Simplified block diagram of the designed CW optical distribution system.

to be in the synchronization state with the reference oscillator. The drift values are sent digitally from the transmitter to each receiver over the SMF involving the WDM technique.

Phase drifts of a few components, located in blue, dashed frames in Fig. 1, can not be measured and calibrated. Any asymmetric timing variations between output signals of the electrical and optical power splitters lead directly to the synchronization inaccuracies. Phase drifts in the circulators, FRMs and photodetectors result in the PRDS performance degradation as well. Therefore, these components are located in a sealed housing that is actively temperature controlled using a Peltier thermoelectric module and passively humidity stabilized using silica gel beads.

PHASE DETECTOR

The phase detector, discussed in detail in [3] and shown schematically in Fig. 2, is based on a direct RF-sampling dual-channel analog-to-digital converter (ADC) and it features a femtosecond measurement precision over 2π RF signal phase change. Hence, the propagation time can be determined with high precision at all times and sent to a remote receiver where the phase of e.g. a remote RF source can be corrected. Phase correction of the remote RF source can be implemented electronically e.g. by tunning the oscillator frequency or by shifting phase involving a phase shifter or a vector modulator. Alternatively, if no direct phase correction is required, e.g. in digital RF control systems of particle accelerators, the correction can be applied digitally. This advantageously gets rid of the need of cost intensive active link techniques compensating the fiber drift, e.g. piezo-driven fiber stretchers.

A non-I/Q algorithm is used to calculate phase from the RF signal samples. The I/Q demodulation consists of three main steps: down-mixing, low-pass filtering and decimation. The real-valued RF signal is multiplied ("mixed") with two sinusoid signals with 90° phase difference. After down-mixing the signal is low-pass filtered using a FIR filter. The filter bandwidth limits the phase correction bandwidth, which is usually set to be below 10 kHz due to slow phase variations caused by environmental changes.

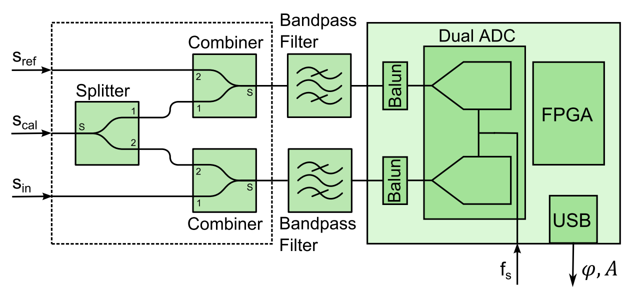

Figure 2: Simplified scheme of the 2π phase drift detector with a two-tone calibration circuit.

ISBN 978-3-95450-176-2

Phase detectors are used to measure relative phase drift between the measured signal s_{in} and the reference signal s_{ref}. Since the relative phase drift is measured, the absolute stability of each detector channel is not critical. The developed phase detector uses a dual channel ADC having both analog-to-digital converters implemented on the same semiconductor substrate. Inside of a single chip temperature variations and ADC input clock changes are common for both channels, which allows for ultra-stable phase difference measurements.

Temperature and humidity drifts of the ADC front-ends comprising attenuators, band-pass filters, RF transformers and microstrip lines (or RF wires) are not perfectly correlated and they decrease long-term measurement stability. To eliminate these potential drifts a two-tone calibration method described in [4] was implemented. For drift calibration a special circuit (a head) with a power splitter and two combiners is applied, which is located in a temperature and humidity stabilized housing. Second RF signal (second tone) s_{cal}, which is synchronized with the signals s_{in} and s_{ref} is fed to the calibration circuit. The combiners are used for combining the measured signal s_{in} and the reference signal s_{ref} with an RF calibration signal s_{cal}. Since the calibration unit can be built drift free, errors in the analog front-ends can be detected through the second tone and digitally corrected.

DISTRIBUTION OF LOW PHASE NOISE RF SIGNALS

RF signals at the remote locations do not have to be generated locally, which is not cost-effective due to the considerable cost of a high performance RF source, but they can be generated once in the transmitter and sent to the distant devices applying coaxial cables or optical-fiber links. The simplest way for the RF signal transmission is the connection of the reference oscillator with the remote electronics via a long coaxial cable that is shown in Fig. 1 (red, short-dashed line). However, coaxial cables have a few disadvantages in comparison to optical fibers like high insertion loss (increasing fast with the frequency), high-cost and the connection of distant devices can cause large ground loops. Therefore, the coaxial cables are usually used to transmit low-noise RF signals up to several hundred meters with the maximum frequency of a few GHz.

The second method for transmitting a low-jitter RF signal is the fiber-optic link. Due to the low loss of SMFs, the relatively high bandwidth of optical components and immunity to electrical interference, RF signals with frequencies up to dozens of GHz can be sent for distances of tens of km applying the RF-over-fiber technique that is shown in Fig. 1. The intensity-modulated light is coupled from the dual output MZM to the multi-tone phase modulation unit for the reduction of Rayleigh and Brillouin scattering. Next, the light is amplified in the EDFA and split to multiple fiber-optic links transmitting optical signals to remote receivers. After direct demodulation in the photodetector "4", the electrical signal is amplified and further its phase is corrected to be constant in relation to the reference oscillator. Next, the RF signal is bandpass filtered using an ultra-narrowband filter to remove harmonics/intermodulation products and to decrease the noise floor. Residual timing jitter of the transmitted RF signals depends on the fiber length and the signal frequency. It was measured that the residual timing jitter is lower than 10 fs rms (integrated from 10 Hz to 1 MHz) for the distances up to 10 km and for the RF signal frequency of 1.3 GHz, which is shown in Fig. 3.

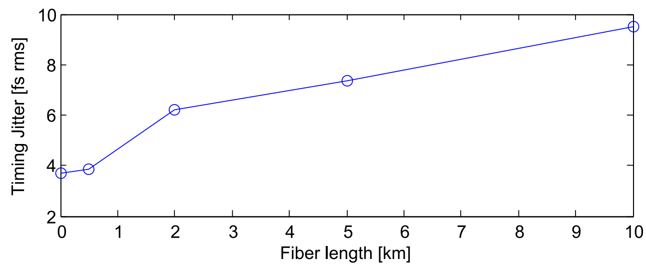

Figure 3: Residual timing jitter integrated from 10 Hz to 1 MHz versus optical fiber length measured with an RF signal of 1.3 GHz.

DESIGN ISSUES FOR ACHIEVING HIGH PRDS PERFORMANCE

In the text above, the new concept of the distribution system for synchronizing remote devices is described. However, to fulfill stringent long-term and short-term stability requirements several engineering and scientific issues had to be considered. Some of them are shortly introduced in this section, but the detailed description is going to be publish elsewhere.

Signal-to-noise ratio (SNR) of the RF signal at the output of the fiber-optic link is decreased by several noise sources like thermal noise of resistive components, shot-noise of photodiodes, relative intensity noise (RIN) of active optical devices (laser source, EDFA). The trade-offs had to be found between the noise reduction and the cost-intensity (or the complexity). The model of the RF-over-fiber link was developed to optimize the performance of the transmitted microwave signals.

Another noise source is the optical fiber, which is susceptible to various linear and nonlinear impairments. The most important linear impairments are chromatic dispersion, polarization mode dispersion (PMD), polarization dependent loss (PDL) and Rayleigh scattering. The nonlinear effects depend on the light intensity and they lead to the generation of new optical frequencies. The potential nonlinear timing error sources in the designed PRDS are stimulated Brillouin scattering (SBS) and self-phase modulation (SPM).

Rayleigh scattering is the scattering of light from non-propagating density fluctuations (molecular vibrations of material), which cause slight modulation of the refractive index [5]. Double backscattered light, called double Rayleigh backscattering (DRB), interferes with the forward propa-

ISBN 978-3-95450-176-2

gating light and due to optical signal phase noise is interferometrically converted to intensity noise, which is called interferometric phase-to-intensity noise conversion. This noise is effectively reduced by wideband and multi-tone modulation of an optical carrier, which lead to the redistribution of noise energy from baseband to higher frequencies [6]. At high frequency, noise is removed by filtering.

Electromagnetic field applied to a fiber generate acoustic waves (through electrostriction), which in turn cause a periodic modulation of the refractive index. The resulting refractive index grating scatters light through Bragg diffraction [7], which is called the stimulated Brillouin scattering. The SBS is completely removed applying the same methods that are used for the reduction of Rayleigh scattering.

SMF fibers feature various deformations and experience external mechanical stress such as bends or twists. This causes birefringence - a slight difference in the propagation constants of both polarization modes, which propagate at different speeds according to a slow and fast axis. These polarization effects degrade the light transmission primarily due to two polarization phenomena as polarization mode dispersion (PMD) and polarization dependent loss (PDL) [8]. PDL causes light intensity fluctuations, which are diminished by a PID control loop involving a variable optical attenuator (VOA). Such a feedback loop is placed in front of each photodiode to reduce the AM/PM conversion (discussed below) and to get the stable amplitude RF signal at the output of the photodiode. PMD causes that light velocity is different for different states of polarization (SOP), which change randomly in time. Currently, the PMD is one of the most important factors limiting the long-term PRDS stability. For long fibers, longer than the correlation length of the birefringence, the PMD value is porportional to $D_p\sqrt{L}$, where L is the fiber length and D_p the coefficient depending on the fiber type. D_p of the best SMFs is of the order of $40\,\mathrm{fs}/\sqrt{\mathrm{km}}$ [9].

Due to the chromatic dispersion, propagation velocities of the optical signal carrier and the modulation sidebands are different, which results both in a SNR penalty [10] and the conversion of laser phase noise to intensity noise (PM-AM conversion). It was calculated that as far as the transmission distance is up to 15 km and the RF modulation frequency is below 10 GHz the SNR penalty due to chromatic dispersion is negligibly small. The discussion about the PM-AM conversion exceeds the scope of this paper - interested readers may found more information in the reference [11].

One of the challenges in the generation of low-noise and low-drift microwave signals is the conversion of optical power fluctuations into phase fluctuations of an electrical microwave signal by a photodiode [12]. However, it mainly concerns the systems in which short optical pulses are detected - a photodiode exhibits highly nonlinear operation under the illumination by high peak-power optical pulses. In the PRDS, the phase-stable conversion is possible by selecting a low AM-PM photodiode and additionally by stabilizing the optical power utilizing the feedback loop, which was already mentioned above.

For achieving the femtosecond synchronization accuracy several other issues must be considered, e.g. frequency stability of the reference oscillator, the directivity of the circulator, the reflections from various optical and electrical components, power supply noise, mechanical vibrations, etc.

EXPERIMENTAL RESULTS OF THE LONG-TERM STABILITY MEASUREMENT

The long-term stability of the PRDS prototype was evaluated using a 500-m length, 3-mm jacketed SMF spool. The transmitter and the receiver were located in a climatized laboratory, in which temperature was stabilized with an accuracy of ±0.1 °C. The sensitive components inside the blue, dashed frames in Fig. 1, discussed earlier in this paper, were additionally temperature and humidity stabilized with the accuracy of about $T = \pm 5\,\mathrm{m}^\circ\mathrm{C}$ and $RH = \pm 0.1\,\%$. The fiber spool was kept outside the climatized laboratory and its temperature fluctuated by about 1.2 °C. Phase drift of the RF signal at the output of the fiber link in relation to the reference oscillator equals about 24.6 ps over 50 h, which is presented in Fig. 4 a. The PRDS precision with the 500-m fiber-optic link is measured to be about 35 fs pk-pk (moving average over 1 hour) that is shown in Fig. 4 b. The phase drift reduction factor equals 703.

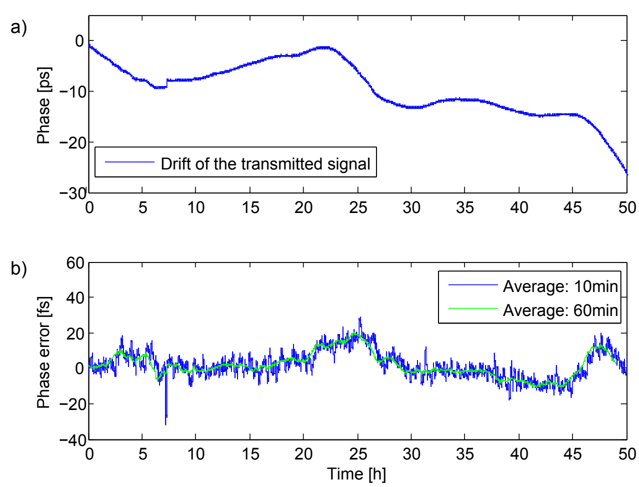

Figure 4: a) Phase drift of the 1.3 GHz signal at the output of the fiber link in relation to the reference oscillator and b) the PRDS accuracy measured with the 500-m SMF.

SUMMARY

The paper presents the cost-effective solution both for the synchronization of distant devices that can be separated by tens of kilometers and for the distribution of low-noise RF signals ranging from about 100 MHz up to several GHz. In the new concept, the intensity modulated light is split to

ISBN 978-3-95450-176-2

many remote receivers. Since the relatively expensive components in the transmitter are used only once for multiple fiber-optic links, this solution is cost-effective and attractive for a variety of applications. Moreover, the calibrated drift-free direct RF-sampling phase detectors feature a femtosecond phase measurement precision over 2π RF phase change. Therefore, the fiber link round-trip propagation time can be determined with femtosecond precision at all times without the need of cost-intensive active link stabilization techniques.

In the paper, the new concept of the CW laser based distribution was presented. Various technical and physical issues influencing the PRDS performance were shortly introduced. The short-term and long-term stability of the built prototype was evaluated. The system can distribute microwave signals at the distance up to 10 km with the residual timing jitter below 10 fs rms. The long-term synchronization precision equals 35 fs pk-pk measured with a 500-m standard SMF.

ACKNOWLEDGEMENTS

This work was supported by the Accelerator Research and Development Grant (ARD-ST3).

REFERENCES

[1] M. Bousonville and J. Rausch. Valocity of signal delay changes in fibre optic cables. In *Proc. of DIPAC09*, pages 248–250, Basel, Switzerland, May 2009.

[2] C. Sydlo et al. Femtosecond timing distribution for the European XFEL. In *Proc. of FEL2014*, pages 1–5, Basel, Switzerland, August 2014.

[3] S. Jablonski, K. Czuba, F. Ludwig, and H. Schlarb. 2π low drift phase detector for high-precision measurements. *IEEE Trans. Nucl. Sci.*, 62(3):1142–1148, June 2015.

[4] G. Huang, L. R. Doolittle, J. W. Staples, R. Wilcox, and J. M. Byrd. Signal processing for high precision phase measurements. In *Proc. of BIW10*, pages 375–378, Santa Fe, USA, May 2010.

[5] R. W. Boyd. *Nonlinear Optics*. Elsevier, 3 edition, 2008.

[6] P. K. Pepeljugoski and K. Y. Lau. Interferometric noise reduction in fiber-optic links by superposition of high frequency modulation. *J. Lightwave Technol.*, 10:957–963, July 1992.

[7] A. Yeniay, J. M. Delavaux, and J. Toulouse. Spontaneous and stimulated brillouin scattering gain spectra in optical fibers. *J. Lightwave Technol.*, 20(8):1425–1432, Aug 2002.

[8] E. Collet. *Polarized Light in Fiber Optics*. Polawave Group, New Jersey, 2003.

[9] Corning. Corning leaf optical fiber. `http://www.corning.com/WorkArea/showcontent.aspx?id=63927`, 2014.

[10] U. Gliese, S. Norskov, and T. N. Nielsen. Chromatic dispersion in fiber-optic microwave and millimeter-wave links. *IEEE Trans. Microw. Theory Techn.*, 44(10):1716–1724, Oct 1996.

[11] S. Yamamoto et al. Analysis of laser phase noise to intensity noise conversion by chromatic dispersion in intensity modulation and direct detection optical fiber transmission. *J. Lightwave Technol.*, 8:1716–1722, Nov 1990.

[12] J. A. Taylor et al. Characterization of power-to-phase conversion in high-speed p-i-n photodiodes. *IEEE Photon. J.*, 3(1):140–151, Feb 2011.

ISBN 978-3-95450-176-2

BEAM PROFILE MEASUREMENTS WITH A SLIT-FARADAY CUP AND A WIRE SCANNER FOR A NEWLY DEVELOPED 18 GHZ SUPERCONDUCTING ECR ION SOURCE AND ITS LEBT*

H. J. You#, S. O. Jang, and W. I. Choo, NFRI, Gunsan, Korea

Abstract

In this presentation we show results of beam profile measurements by a slit-Faraday cup and a wire scanner. Argon 8+ beams were generated in a new liquid helium-free superconducting electron cyclotron resonance ion source (ECRIS). The ECRIS, named SMASHI, was successfully developed at the National Fusion Research Institute in 2014, and in the future it will be dedicated for highly charged ions matter interaction research facility (HIMIRF). Before designing HIMIRF terminals after low energy beam transport (LEBT), it is necessary to characterize the beam properties of the source and its LEBT line. The beam profile measurements have been done after an analyzing dipole magnet (DM). The slit-Faraday cup and the wire scanner were installed at 25 cm and 120 cm from the exit flange of the DM, respectively. Between the two diagnostics an Einzel lens was positioned to control the focusing of diverged beams. Here, with the measurements we checked the present beam alignments in the LEBT, and studied the dependence of beam profile variation on the operations of beam optics such as steering magnets and Einzel lens.

INTRODUCTION

A new superconducting 18 GHz electron cyclotron resonance ion source and its low energy beam transport were developed at the National Fusion Research Institute in South Korea [1]. The source, named SMASHI (Superconducting Multi-Application Source of Highly-charged Ions), will be dedicated for future application of highly charged ions in the area of matter interaction, diagnostic imaging, and probing. In this proceeding, we briefly describe SMASHI and its LEBT. Then, we show preliminary results of beam charge spectra of ^{4}He, ^{16}O, ^{40}Ar, ^{132}Xe ion beams. In order to characterize the beam properties in the LEBT, we also measured beam profiles by a slit-FC system and a wire scanner, by which the beam alignments of the source and the LEBT are checked. Variations of beam profiles are studied with respect to different settings of ion optics in the LEBT.

SOURCE DESCRIPTION

Figure 1 shows the overall section view of SMASHI. As an ECRIS for generating multiply/highly-charged ions, SMASHI has following main features: two-frequency heating(18, 18+Δ GHz), high power-capable plasma chamber, remotely-positional variable gap extraction system, capability to generate a wide range of ion elements from gas to metal, and two diagnostic ports for the extraction region. All these features are highly oriented to the generation of diverse highly charged ions (HCI). Most of all, due to the helium-free SC magnet, SMASHI can be more economically operated with low power consumption, which therefore enabling the full system of ECRIS operated on a high-voltage platform.

Microwave Injection

In Fig. 1, the microwave injection side can be viewed. Normally, the injection electrode is located at the maximum position of the axial magnetic field, and depending on the source condition it can be moved to other optimum positions by adjusting the bellows. In the injection electrode two WR62 waveguide ports, an on-axis sputtering hole, a centered-perforated biased disk, two diagnostic/oven holes, and one gas hole were arranged [1]. The WR62 ports, placed well out of the plasma pattern, are separated by 120◦ from each other. The biased disk is shaped as a triangle with a thru-hole in its center, into which the on-axis sputtering target is inserted. The sputtering target system is remotely positional and designed to easily exchange different materials.

Extraction System

The extraction system, shown in Fig. 1, is a puller-Einzel lens system consisting of 3 electrodes. Each electrode is supported and guided by 4 rods fixed to the extraction chamber. The distance between electrodes can be adjusted when necessary. The whole extraction system is remotely positional by a motor-driven-control, where the gap between the plasma electrode and the puller electrode is adjustable by 20–50 mm. Table 1 summarizes the extraction conditions and beam characteristics. The resulted rms emittance for Ar^{8+} was calculated by using IGUN with the inclusion of the magnetic field and charge state distribution (CSD). The resulting beam radius and the momentum of Ar^{8+} beam are 33 mm and 41 mrad, respectively.

Table 1: Extraction Conditions and Beam Characteristics

Extraction voltage	30 (10-30) kV
Gap distance	33 (20-50) mm
Einzel lens (negative)	30 (10-30) kV
Rms emittance for Ar^{8+} at 500 mm from plasma electrode	48 mm mrad (R_{max}=33 mm, A_{max}=41 mrad)

*This work was supported by R&D Program of 'Plasma Convergence & Fundamental Research' through the National Fusion Research Institute of Korea (NFRI) funded by the Government funds
#hjyou@nfri.re.kr

ISBN 978-3-95450-176-2

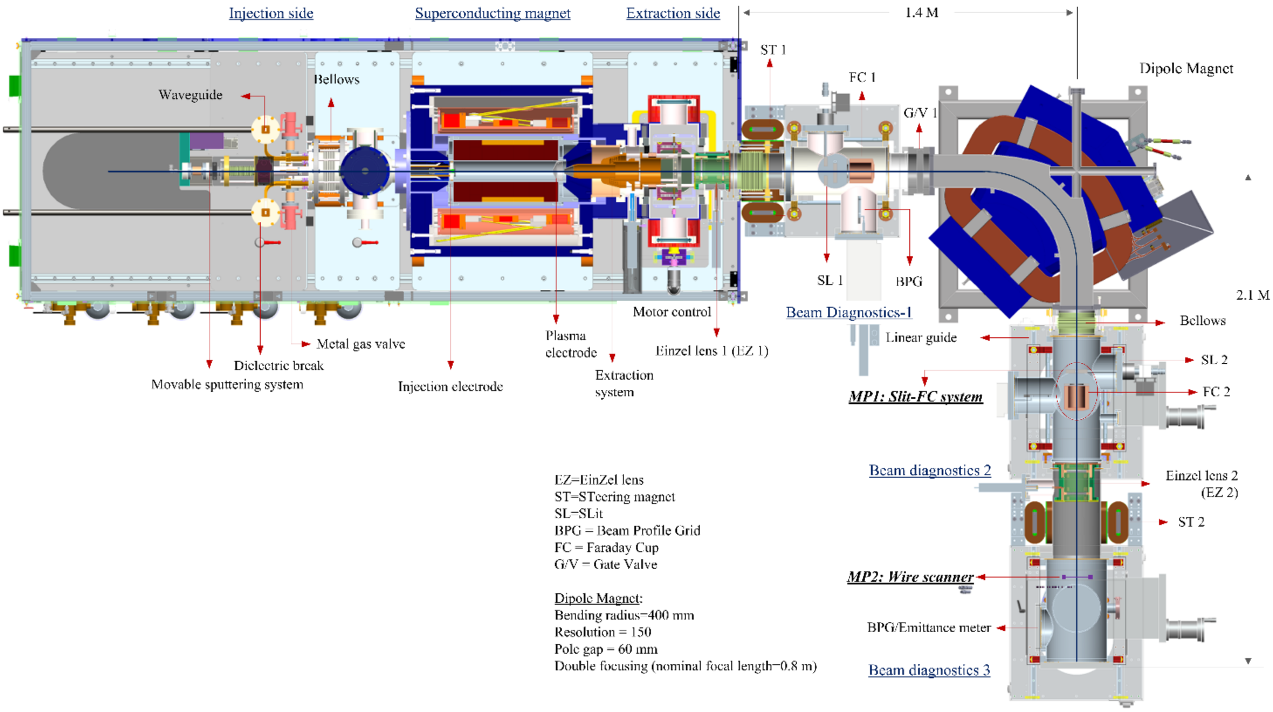

Figure 1: A sectional layout of the NFRI 18 GHz superconducting ECR ion source (SMASHI) & its LEBT.

Magnetic Structure

The magnet system of SMASHI consists of four superconducting(SC) coils sets and a permanent hexapole. The SC coils is designed to be cooled by a single cryocooler (1.5W at 4.2 K) and give axial mirror fields of B_{inj} = 2.0 T and B_{ext} = 1.4 T, where B_{inj} and B_{ext} are the peak fields in the microwave injection region and the beam extraction region, respectively. The hexapole is created by 36 pieces of permanent magnets and gives a radial mirror field of B_{rad} = 1.3 T. Figure 2 shows the magnet design, and Table 2 summarize the main parameters of the magnet. The more detailed design, cooling, and excitation results are found in references [2, 3]

Table 2: Main Parameters Of The Magnet System

B_{inj}	1.7-2.0 T
B_{ext}	1.3-1.4 T
B_{ecr}	0.65 T
B_{rad}	1.3 T
B_{min}	0.4-0.5 T
Superconducting wire	NbTi(Cu) 1.25×0.8 mm for coil 1-3, Ø 0.5 mm for coil 4
Cryocooler	Single GM cryocooler (1.5 W @ 4.2 K/45 W @ 60 K)
Permanent hexapole	36 pieces of NdFeB magnets

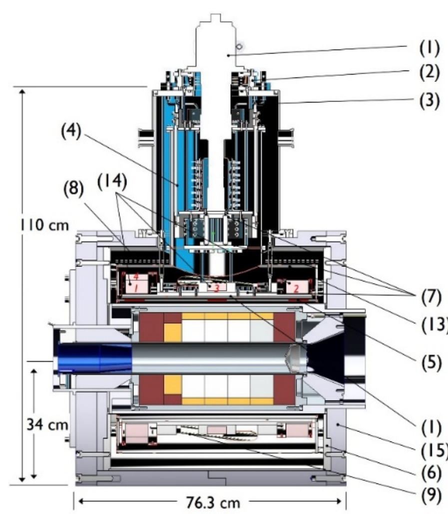

Figure 2: Magnet structure of SMASHI: (1) OFHC bobbin, (2) Superconducting coils, (3) two-step thermal links, (4) HTS lead, (5) copper thermal shield, (6) multilayer superinsulation sheets, (7) thermal insulating supports, (8) vacuum casing, (9) iron yoke, (10) current leads, (11) α-gel anti-vibration, (12) cryocooler, and (13) quench detection loop.

LEBT

Low energy beam transport (LEBT) is designed for the resent 18 GHz superconducting ECR ion source. A sectional layout of the LEBT is shown in the right side of Fig. 1. The LEBT is composed of 5 sections: Einzel lens, beam diagnostics 1(BD-1), double focusing dipole magnet (DM), beam diagnostics 2, and 3 (BD-2, -3). In

ISBN 978-3-95450-176-2

the beam line of the LEBT, extracted ion beams are diagnosed by a Faraday cup (FC) and/or beam profile grid, then specific mass and charge state of beam is selected by the DM. After the DM, the species analysed beam can be profile-monitored by a slit-FC system and a wire scanner in BD-2 and BD-3, respectively. The Einzel lens 1, located just after the extraction system, helps to focus the diverged beam, so that it could go parallel to the DM and be focused at slit 2(SL2). In BD-1, a high power FC are installed for measuring the total ion beam current from the source. The DM is a 90◦ analysing magnet (double focusing) of which bending radius, pole gap, magnetic rigidity, and mass resolution of the DM are 400 mm, 60 mm, 0.36 Tm, and 150, respectively. The inlet and the outlet dimensions of the DM vacuum chamber are both 135 wide and 52 mm high. Bellows inserted before and after the DM are installed to provide good connectivity and beam matching. BD-2 just after the DM also consists of a beam slits (horizontal and vertical) and a FC. A horizontal(x) and a vertical(y) slit can operate to limit the beam divergence and envelope, and they also play a role of analyzing slits in the slit-FC system for beam profile measurement. Thereafter, Einzel lens 2 is installed between BD-2 and BD-3 to re-focus the beam. Steering magnets (ST 1 and ST 2) can be used before and after the DM in case beam paths need to be adjusted.

In Fig. 3 an example of beam envelope calculations is shown. The calculations are done by Trace 3-D Module with electrostatic palette in PBO Lab 3.2.5. The input parameters for Trace 3-D was based on a measured beam current and beam charge spectra. The input emittance value is get from IGUN calculation.

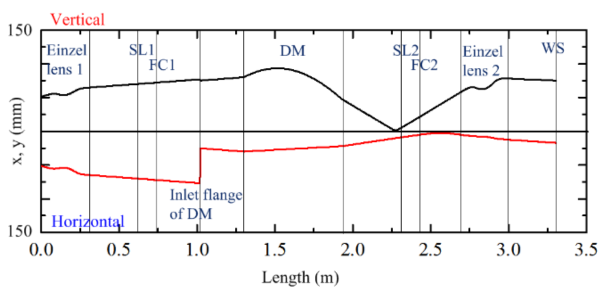

Figure 3: Horizontal and vertical envelopes of Ar^{8+} ion beam in the LEBT.

PRELIMINARY RESULTS OF SMASHI

As the first commissioning results of SMASHI, beam charge spectra of ^{4}He, ^{16}O, ^{40}Ar, and ^{132}Xe ion beams and their intensities are measured. The results are drawn in Fig. 4. So far, the source were operated under the following conditions: Maximum TWT power was limited to 600 W (+300 W). Injection B-field was fixed to 1.7 T (80 % of full intensity). The aperture of plasma electrode and the extraction voltage are Ø8 mm and Max. 20 kV, respectively. The position of the biased disk are optimally adjusted between 10 to 40 mm from the end of the injection electrode, and its biased voltage was -200 to-600 V. Note that, during the operation conditions, we intentionally reduce the microwave power and/or magnetic field level so that the x-ray emission from the source do not exceed the safe dose level of 0.5 µSv/h (at operator position). Until the end of this year, the source shielding will be more strengthened. Though all available operating knobs could not be fully used due to the safety issue from X-ray emission, the performances of SMASHI are promising and will be dramatically enhanced by applying higher microwave power(>1000 W/liter), higher magnetic field (>2 T), extraction potential up to 30 kV, and optimum position of plasma electrode, and improved LEBT transmission.

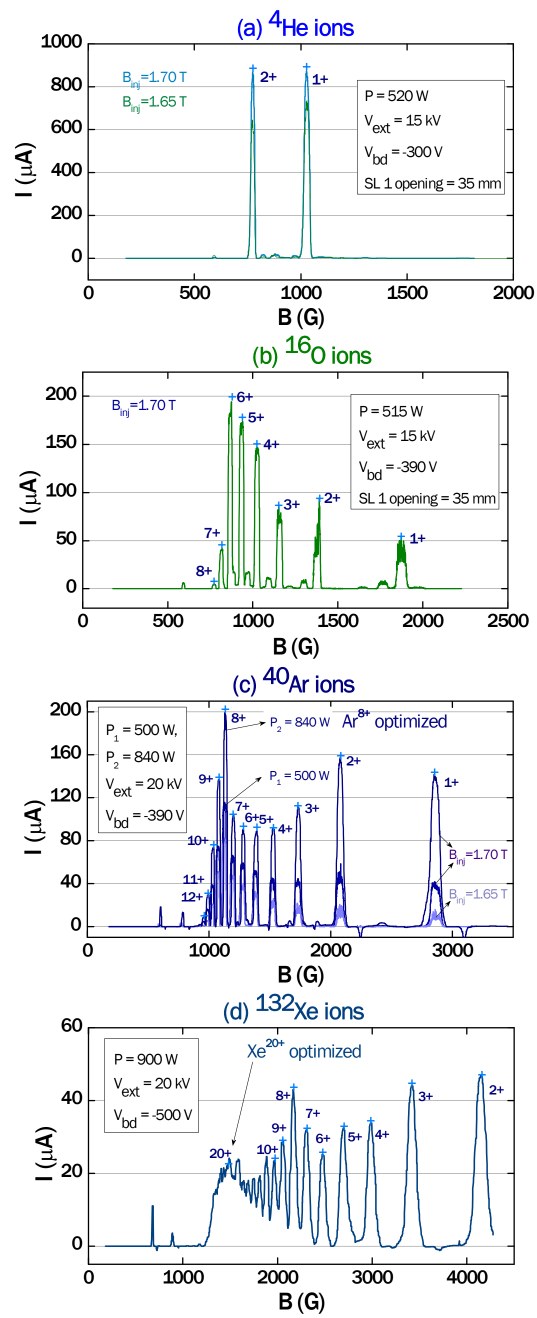

Figure 4: Beam charge spectra of ^{4}He, ^{16}O, ^{40}Ar, ^{132}Xe ion beams from SMASHI.

BEAM PROFILE MEASUREMENT

For BPM, as shown in Fig. 5(a), the x and y slit in the slit-FC system are designed to be independently movable from -25 to 25 mm. Also the gap widths(d's) of the slits are remotely controllable from 0 to 50 mm. When the slit-FC system works for BPM, the gap width of a moving slit is normally set to 2.5 mm, and the other one is set to 50 mm. In other words, when horizontal(x) beam profile is measured, x slit of d=2.5 mm is moved from x=-25 to 25 mm while y slit is fixed at y=0 with its gap width set to 50 mm. The FC is comprise of an isolated metal cup and a high voltage suppression ring close to the entrance of the cup. The cup is ∅50 mm in diameter and 80 mm in length, and the suppression ring can be biased up to -1 kV.

The wire scanner (WS), shown Fig. 5(b), is a fork type scanner. The WS is inserted into the beamline by an angle of 45 degree. The WS is composed of three wires mounted in horizontal(x), vertical(y), and diagonal(s) directions, so that three directions of profiles can be simultaneously measured by one passage. The scanning length of the WS was designed to be 165 mm; The measurement ranges of x, y, and s direction become 50(-25 to 25 mm), 50(-25 to 25 mm), 95 mm(-42.5 to 42.5 mm), respectively.

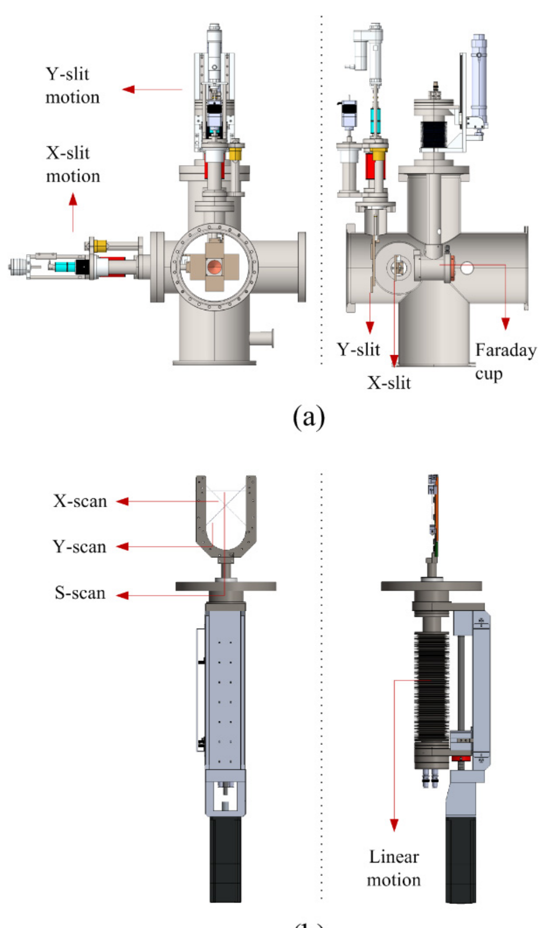

Figure 5: The slit-FC system and the wire scanner in the LEBT.

Beam profile measurements have been done at the positions MP 1 and MP2 (see Fig. 1), which are respectively 25 and 116 cm away from the exit flange of DM. Here target ion beam was selected to Ar^{8+}. TWT microwave power was set to 300 W. The Ar^{8+} beam was

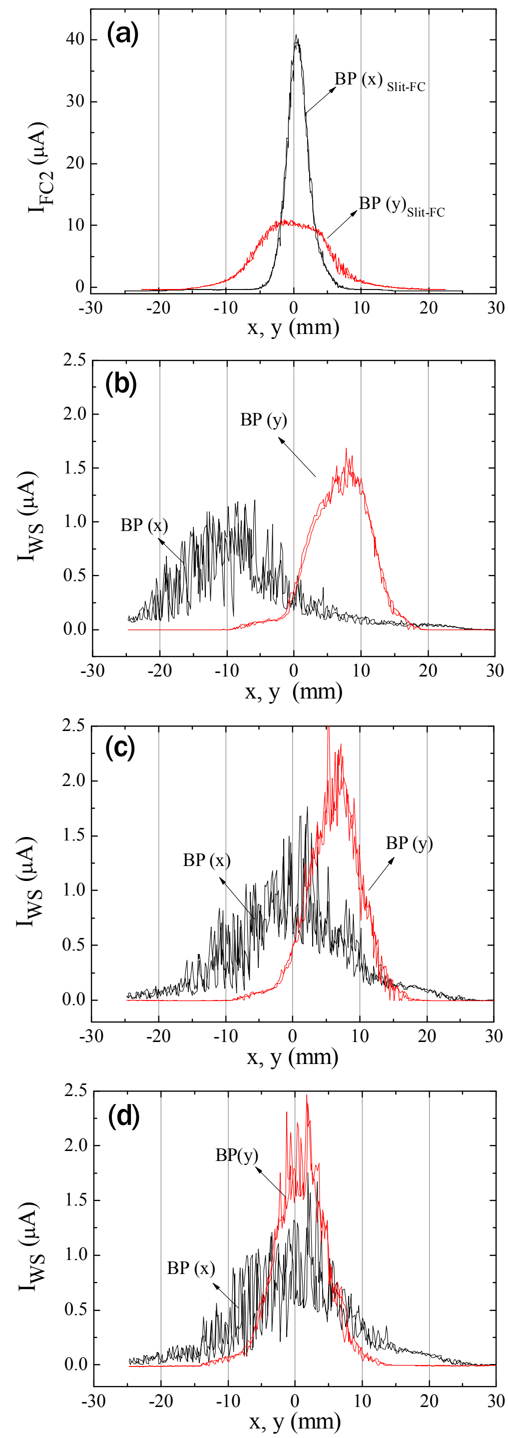

Figure 6: Horizontal (x) and vertical (y) beam profiles measured by (a) the Slit-FC system at MP1 and (b)-(d) the wire scanner at MP2: (b) not steered, (c) x-steered by ST1 (0.24 A), (d) y-steered by ST2 (1.2 A).

ISBN 978-3-95450-176-2

extracted with a source potential of 15 kV. The potential of Einzel lens 1 was tuned to -12 kV, so that the beam was well-focused at MP2 (SL 2 position). The steering magnet, ST1 is also finely tuned for the beam to be directed to the center region of the SL 2. Figure 6(a) shows the beam profiles at MP 1 measured by the slit-FC system. It is shown that x and y profiles are both well positioned at central region. Figure 6 (b)-(d) show the measured beam profiles by the wire scanner. The beam profiles (b), (c), and (d) were taken from three different steering conditions; Figure 6(b) is a beam profile that any further beam steering was not applied at all, Figure 6(c) is a beam profile that x- steering was applied by ST1, and Figure 6(d) is that for y-steering was done by ST2; In Fig. 6(c) and (d), the central positions of the beam were moved by 10 mm in x-direction, and by 6 mm in y-direction, meaning that beam steerings has to be done to locate the beam to center region (x, y=0 at the position of MP 2). Dependence of beam profile on the Einzel lens 2 is shown in Fig. 7, where beam profiles were measured with different center electrode potentials (V_{einzel}=-5, -15, and -25 kV). As expected, it is observed that the higher potential(V_{einzel}) gives the better focusing effect resulting smaller beam width.

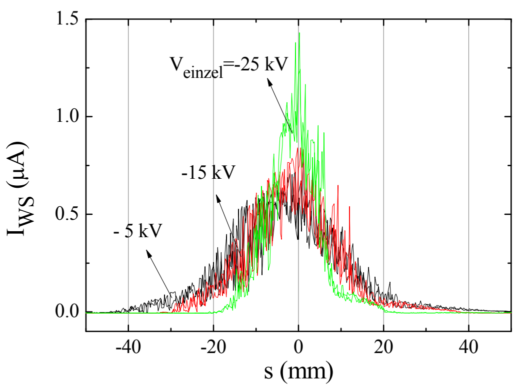

Figure 7: Measured beam profiles dependent on Einzel lens potential (V_{einzel}). The measurements are done at MP2 in diagonal(s) direction with the wire scanner.

First, in Fig. 6(a) showing the result of the slit-FC system, we can find that at MP1 horizontal(x) beam intensity is 4 times higher than vertical(y) beam intensity. It is thought that the smaller vertical(y) beam intensity comes from the unequal x and y dimension (132x52 mm) of the DM vacuum chamber. As shown by the envelop calculations in Fig. 3, the directed beam could be cut by the smaller height of the DM vacuum chamber. Secondly, from the comparison of the results from the slit-FC system and the WS, we see that at MP1 horizontal(x) beam profile is bigger and sharper than vertical(y) beam profile while at MP2 horizontal(x) beam profile becomes smaller and broader than y profile (compare Fig. 6(a) and (d)). This would mean that extracted beam could be rotated, which is possibly caused by the magnetic field gradient in extraction region (the axial magnetic field drops from 1.3 T to 0 T within the extraction system); the decreasing field can give a beam rotation in azimuthal direction [4]. Thirdly, we found that beam steerings are required in both side of the dipole magnet (before and after the DM); as compared the profiles from Fig. 6(a) to (d), aligning the beam at MP1 does not guarantee aligning the beam at MP2. In order to move the beams of MP1 and MP2 to each central region, one needs independent steering magnet such as ST1 and ST 2. Otherwise, the beamlines before and after the DM has to be carefully aligned. Lastly, the full widths at half maximum (FWHM) of Ar^{8+} were estimated that Δx=3.5 and Δy=12 mm at MP1, and Δx=16 mm (Δy=9 mm) at MP2, respectively.

CONCLUSION

As the first commissioning of SMASHI (the ECR ion source in NRFI), preliminary results of the beam charge spectra of ^{4}He, ^{16}O, ^{40}Ar, ^{132}Xe ion beams are obtained. So far, the maximum beam intensities of He^{2+}, O^{6+}, Ar^{8+}, and Xe^{20+} are recorded to be 1000, 200, 200, and 25 μA, respectively. Though all available operating knobs could not be used due to insufficient shielding of X-ray emissions, the present results show that SMASHI is a very promising source and its performance will be dramatically enhanced by applying higher microwave power(>1000 W/liter), higher magnetic field (>2 T), and higher extraction potential(>30 kV), etc. Then, with the beam profile measurements, we found that the LEBT transmission needs to be improved; in the present LEBT setup 1) very high beam losses are expected in front of the dipole magnet due to its small height of the inlet. Better matching of the ion beam to the dipole magnet is needed; 2) Beam steerings are required in both side of the dipole magnet (before and after the dipole magnet). We also found in the beam profile measurements that the extracted beams could be experiencing a rotation. Lastly, measured full widths of half maximum of Ar^{8+} beam are estimated to Δx=16 mm Δy=9 mm at 116 cm from the exit flange of the dipole magnet.

ACKNOWLEDGMENT

The authors would like to gratefully acknowledge Dr. K. Y. Lee for his careful English proofreading and helpful comments.

REFERENCES

[1] H. J. You, S. O. Jang, and W. I. Choo, Rev. Sci. Instrum. 85, 02A916 (2014).

[2] H. J. You, S. O. Jang, Y.-H. Jung, T.-H. Lho, and S. J. Lee, Rev. Sci. Instrum. 83, 02A326 (2012)

[3] H. J. You and K. M. Park, J. Supercond. Nov. Mag. 28, 651 (2015).

[4] M. A. Leitner, D. C. Wutte, and C. M. Lyneis, Proc. 2001 Particle Accelerator Conference, 2001, Chicago, USA.

ISBN 978-3-95450-176-2

PAL-XFEL'S TURBO-ICT FOR BEAM CHARGE MONITORING*

H. Choi†, J.H. Hong, J.H. Han, B.R. Park, S.H. Kim, S.J. Park, H.S. Kang
Department of Accelerator, PAL-XFEL, Pohang, Korea

Abstract

The construction of the PAL-XFEL building, which is a fourth-generation synchrotron radiation-light source, was completed in February 2015. Accelerating devices (Cavities, Klystrons, Modulators) and undulators will be installed by December 2015. The installation of the remaining devices will be completed by the start of 2016. A Beamline user service will be started from the middle of 2016 [1]. The installation of PAL-ITF (Injector Test Facility) was completed at the end of 2012 for the production of high-quality electron bunches. Efforts were made to improve the performance of pre-injector system and diagnostic equipments. In this study, details of the performance improvements of PAL-ITF measurements using a Bergoz Turbo-ICT, which is able to measure the amount of bunch charge from 0.1 to 200pC, and the operating plan of Turbo-ICT which will be installed and operated in PAL-XFEL are introduced.

COMPOSITION OF PAL-ITF

PAL-ITF was constructed to produce the same amount of charge in the range of 0.1~200pC as PAL-XFEL and to test the laser cathode RF gun generating the electronic beams (jitter and drift are less 0.5% of set charge) and the pre-injector accelerating the beam preserving shape, emittance length and energy spread. Figure 1 shows the composition diagram of PAL-ITF [2].

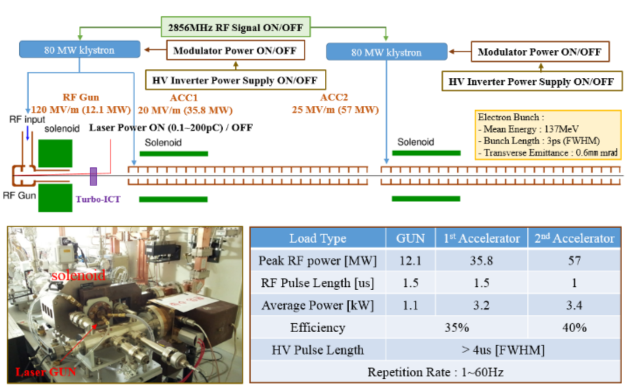

Load Type	GUN	1st Accelerator	2nd Accelerator
Peak RF power [MW]	12.1	35.8	57
RF Pulse Length [us]	1.5	1.5	1
Average Power [kW]	1.1	3.2	3.4
Efficiency	35%		40%
HV Pulse Length	> 4us [FWHM]		
Repetition Rate : 1~60Hz			

Figure 1: PAL-ITF composition diagram.

After completing construction of PAL-ITF at the end of 2012, beam charge was first measured using ICT and faraday cup to monitor beam charge. There were various difficulties measuring the exact charge of 0.1~200pC due to the noise of the pulse power klystron modulator. Turbo-ICT was built in 2013 to accurately measure the charge of beams [3]. A charge of 1pC or more could be measured accurately as shown in Figure 2, after measuring the generated charge of the laser gun while changing the half-wave plate angle inside the laser system. However, it was impossible to measure a charge of 1pC or less due to the noise from the pulse power klystron modulator as shown in Figure 3 [4]. The problem of noise from the pulse power klystron modulator is serious enough to create negative effects on not only the measurement of Turbo-ICT charge but also affects the electronic circuits of all diagnostic units and control devices. Measures had to be prepared to prevent the noise from affecting the exact measurement and operation of electronic devices.

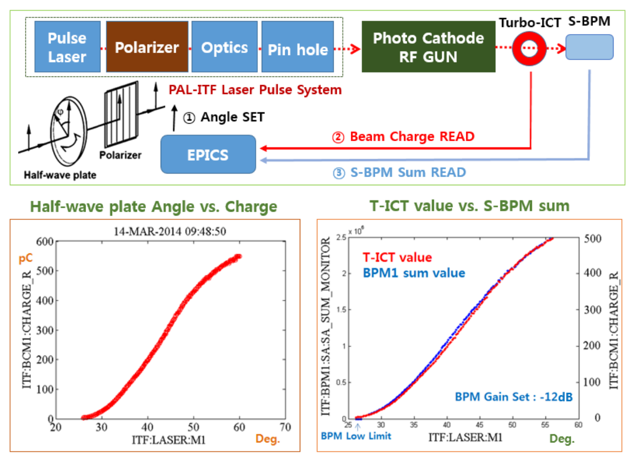

Figure 2: Generation of charge of the laser gun and results of measurement of charge.

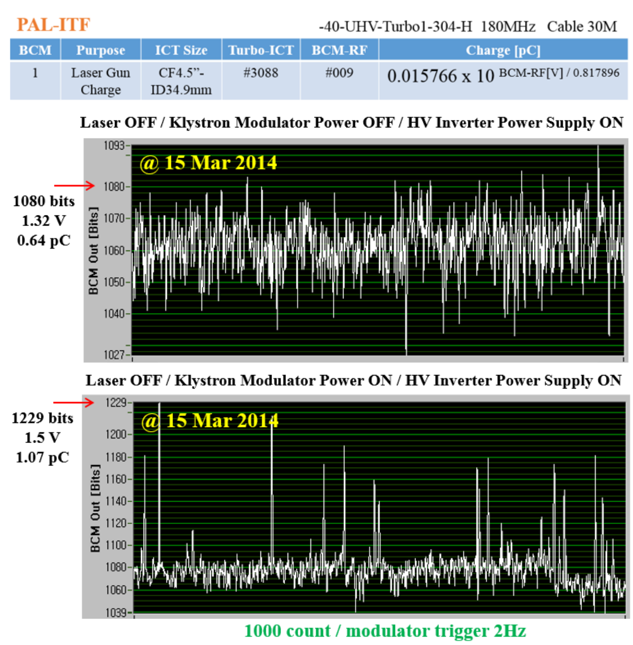

BCM	Purpose	ICT Size	Turbo-ICT	BCM-RF	Charge [pC]
1	Laser Gun Charge	CF4.5"-ID34.9mm	#3088	#009	0.015766 x 10 BCM-RF[V] / 0.817896

Figure 3: Effects of the klystron modulator noise observed from Turbo-ICT.

*Work supported by Ministry of the Science, ICT and Future Planning
†choihyo@postech.ac.kr

ISBN 978-3-95450-176-2

IMPROVEMENT OF PAL-ITF

Existing components of the pulse-forming network (PFN) of the modulator and HV inverter power supply were improved in order to reduce noise from the klystron modulator. The modulator cabinet (panel) shielding was strengthened to prevent noise from inside of the modulator from being discharged to outside as much as possible [5]. As shown in Figure 4, the noise was reduced after improving the klystron modulator. In addition, it was possible to measure 0.1pC as shown in Figure 5.

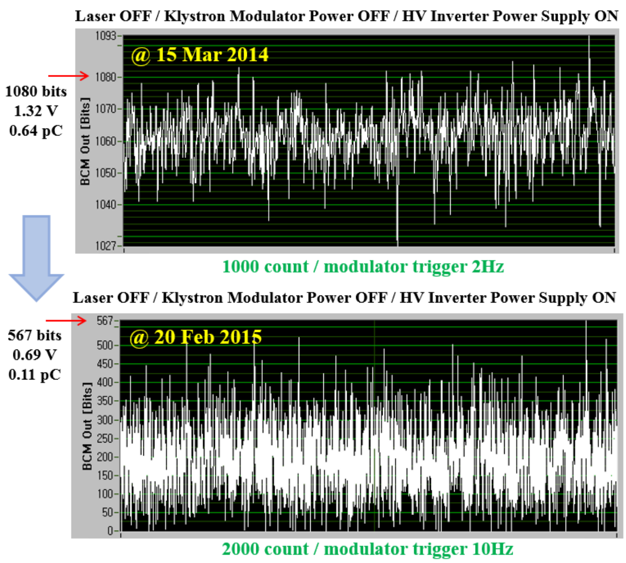

Figure 4: Data of Turbo-ICT measurement after improving the modulator.

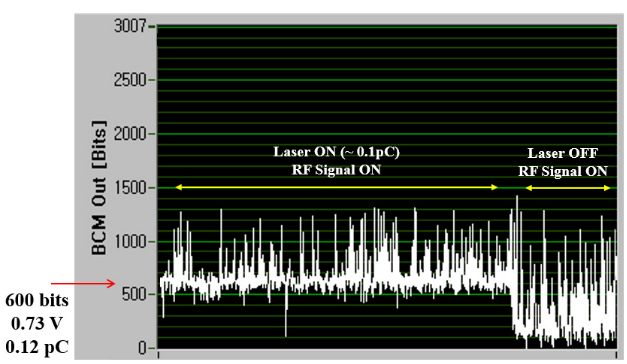

Figure 5: Measurement of 0.1pC of Turbo-ICT.

DARK CURRENT MONITOR

As shown in Figure 6, the noise signal greatly increases if RF power fed into the gun when the laser power is off. Presumably, it is not the noise generated from the modulator but dark currents generated from the laser cathode RF gun. As shown in Figure 8, a plan was prepared to install six 2856MHz Cavity-formed dark current monitors in PAL-XFEL in order to measure dark currents creation from accelerating tubes [6].

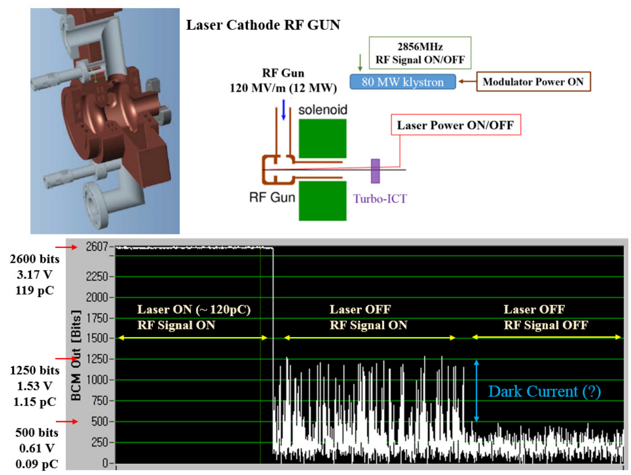

Figure 6: Presumably dark currents.

EMI/EMC

Klystron modulators, power supplies, motor actuator and vacuum pumps handling high voltage and high power are devices producing noise, but some products are designed and operated in violation of regulations regarding EMI (Electro-magnetic Interference) and EMC (Electro-magnetic Compatibility). In consequence, people taking charge of electronic devices related to low voltage should concern themselves with problem of noise. To reduce the effects of noise from the klystron modulator, grounding work of PAL-XFEL was conducted as shown in Figure 7, after dividing the ground into various types, including klystron modulator ground, mesh (220V) ground and data (signal) ground, in the stages of building, designing and ground work.

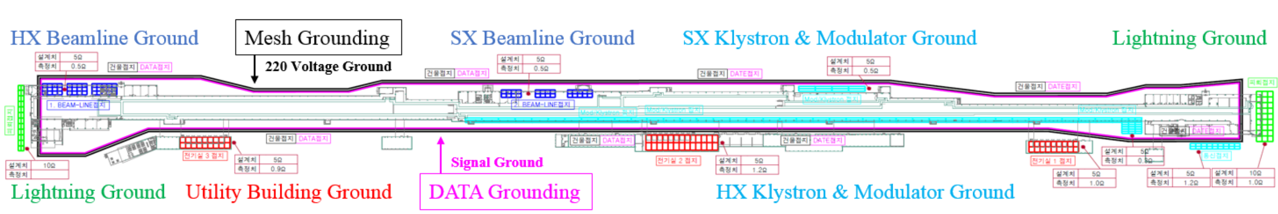

Figure 7: Drawing of locations where the grounding equipments of building grounds are laid and grounding resistance is performed.

Wiring of electric wires was done after installing cable trenches. Cable trenches were divided into those for high voltage, low voltage (220V) and signalling. There also were efforts to reduce EMI while designing the modulator system [7]. Regarding coaxial cables of Turbo-ICT, double-shielded GX03272-D06 cables (BCM-DSC) were chosen to reduce the effects of noise from the outside. Several ferrite cores were attached to both ends of Turbo-ICT cables to filter the noise. To solve the noise problem scientifically, there is a plan to continuously measure the

ISBN 978-3-95450-176-2

strength, cycle and wave form of noise using a spectrum analyzer and FFT and record the results.

PLAN TO OPERATE TURBO-ICT OF PAL-XFEL

Figure 8 shows the installation location of Turbo-ICT of PAL-XFEL. After manufacturing Turbo-ICT, BCM-RF and signal cables a calibration is performed by Bergoz Instrumentation so that the absolute charge of Turbo-ICT can be measured [8]. Figure 9 shows the transfer functions determined by Bergoz Instrumentation after conducting calibration on Turbo-ICT and BCM-RF. Losses of electronic beam charge can be detected using the beam charge monitor (BCM) that can measure absolute charge and can be utilized for machine protection interlock (MPI) systems and personal safety interlock (PSI) systems using BCM measurements [3].

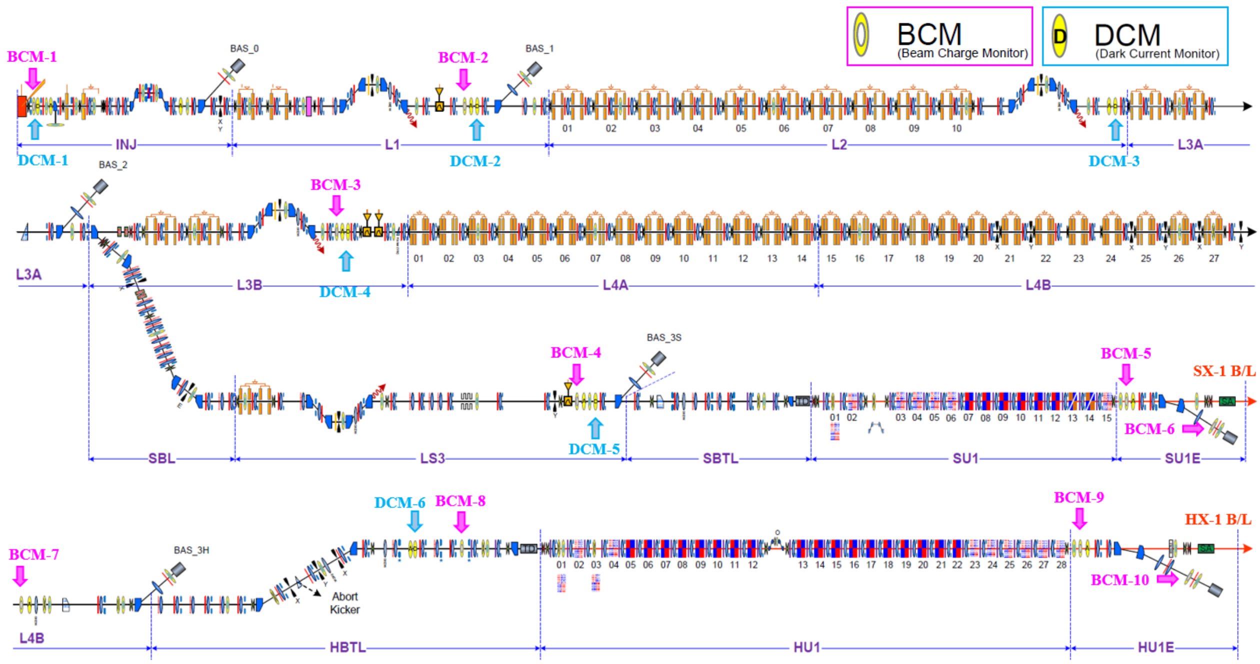

Figure 8: Installation position of Turbo-ICT & DCM.

PAL-XFEL -40-UHV-Turbo1-316LN-H 180MHz / Cable 30M

BCM	Purpose	ICT Size	Turbo-ICT	BCM-RF	Charge [pC]
1	Laser Gun	CF4.5”-ID38.0mm	#3256	#024	$0.01209 \times 10^{\mathrm{BCM\text{-}RF[V]} / 0.85666}$
2	Pre-Injector	CF3”3/8-ID22.2mm	#3188	#014	$0.01970 \times 10^{\mathrm{BCM\text{-}RF[V]} / 0.85405}$
3	L4 Input	CF3”3/8-ID22.2mm	#3189	#015	$0.01997 \times 10^{\mathrm{BCM\text{-}RF[V]} / 0.85946}$
4	SX Input	CF3”3/8-ID22.2mm	#3190	#016	$0.01930 \times 10^{\mathrm{BCM\text{-}RF[V]} / 0.85041}$
5	SX-1 Output	CF4.5”-ID34.9mm	#3257	#025	$0.01413 \times 10^{\mathrm{BCM\text{-}RF[V]} / 0.86111}$
6	SX-1 Dump	CF8”-ID96.0mm	#3193	#019	$0.01786 \times 10^{\mathrm{BCM\text{-}RF[V]} / 0.83559}$
7	L4 Output	CF3”3/8-ID22.2mm	#3191	#017	$0.02129 \times 10^{\mathrm{BCM\text{-}RF[V]} / 0.83897}$
8	HX-1 Input	CF3”3/8-ID22.2mm	#3192	#018	$0.02115 \times 10^{\mathrm{BCM\text{-}RF[V]} / 0.84280}$
9	HX-1 Output	CF4.5”-ID34.9mm	#3258	#026	$0.01871 \times 10^{\mathrm{BCM\text{-}RF[V]} / 0.86590}$
10	HX-1 Dump	CF8”-ID96.0mm	#3194	#020	$0.01855 \times 10^{\mathrm{BCM\text{-}RF[V]} / 0.85722}$

Figure 9: Transfer function of Turbo-ICT.

ACKNOWLEDGMENT

Thanks to Mr. Julien Bergoz, Mr. Hervé Bayle, Mr. Sébastien Artinian, Dr. Frank Stulle and all the colleagues of the Bergoz Instrumentation. They are support many things for implementation Turbo-ICT on PAL-ITF and PAL-XFEL.

REFERENCES

[1] H.S. Kang, et al., “Status of the PAL-XFEL Construction”, Proc. of IPAC2015, WEYC2 (2015).

[2] J.H. Han, et al., “Beam Operation of the PAL-XFEL Injector Test Facility”, Proc. of FEL 2014, WEB02 (2014).

[3] H. Choi, et al., “Presentation about Results Produced after Measuring PAL-ITF Beam Diagnostic Instruments”, Proc. of IPAC 2014, THPRO021 (2014).

[4] H. Choi, et al., “Introduction to the Test Result of Turbo-ICT in PAL-ITF”, Proc. of IBIC 2014, WEPF09 (2014).

[5] S.S. Park, et al., “XFEL Pulse Modulator Test using High Precision High Voltage CCPS”, Proc. of Annual Summer Conference of KIPE, July 2015 pp. 89-90.

[6] D. Lipka, et al., “Dark Current Monitors for the European XFEL”, DIPAC2011, WEOC03 (2008).

[7] C. Kondo, et al., “EMI Noise Suppression in the Klystron Pulse Power Supply for XFEL/SPring-8”, Proc. of IPAC2010, WEPD059 (2010).

[8] F. Stulle, et al., “Turbo-ICT Pico-Coulomb Calibration to Percent-Level Accuracy”, Proc. of FEL 2015, MOP041 (2015).

ISBN 978-3-95450-176-2

DEVELOPMENT OF HIGH PRECISION CAPACITIVE BEAM PHASE PROBE FOR KHIMA PROJECT

Ji-Gwang Hwang*, Tae-Keun Yang, SeonYeong Noh
Korea Institute of Radiological and Medical Sciences(KIRAMS), Seoul, South Korea
Peter Forck
GSI, Darmstadt, Germany

Abstract

In the medium energy beam transport (MEBT) line of KHIMA project, a high precision beam phase probe monitor is required for a precise tuning of RF phase and amplitude of RFQ and IH-DTL. It is also used for measuring a kinetic energy of ion beam by time-of-flight (TOF) method using two phase probes. In this paper, we show the electromagnetic design of the high precision phase probe to satisfy the phase resolution of 1 ° (@ 200 MHz), the test result with a wire test bench to estimate a signal strength and phase accuracy, the design of the 0.2 2.0 GHz broad-band electronics for amplifying the signal strength, and the results of beam energy and RF frequency measurement using a proton beam from the cyclotron in KIRAMS.

INTRODUCTION

The Korea Heavy Ion Medical Accelerator (KHIMA) project is launched to construct a heavy-ion therapy machine using carbon and proton beams. It will provide a carbon beam up to 430 MeV/u and proton beam up to 230 MeV which correspond to a water equilibrium range of 3.0 to 27.0 g/cm^2 [1]. The machine consists of an injector included an electron cyclotron resonance ion source (ECR-IS), low energy beam transport(LEBT) line, RFQ and IH-DTL linacs, and medium beam transport (MEBT) line, synchrotron, and high energy beam transport (LEBT) line. The carbon and H_3^+ beam produced by the ECR-IS with the energy of 8 keV/u and the $^{12}C^{4+}$ and H_3^+ beams were separated from the unnecessary beams by using an analyzing dipole magnet and it is transported through the low energy beam transport (LEBT) line. The low energy beam, 8 keV/u, is accelerated up to 7 MeV/u by the RFQ and IH-DTL [2].

By a carbon foil with a thickness of 100 μg/cm^2 in the MEBT line, the $^{12}C^{4+}$ beam is fully stripped and H_3^+ beam is changed to proton beam and injected to the synchrotron. The $^{12}C^{6+}$ and proton beams is accelerated up to 430 MeV/u and 230 MeV, respectively. A high precision beam phase probe monitor is required in the MEBT line of the KHIMA project for a precise tuning of RF phase and amplitude of the RFQ and IH-DTL to achieve the designed performance and high injection efficiency by adjusting longitudinal beam parameters such as a beam energy and bunch length at the exit of the IH-DTL, and to monitor the status of the carbon foil by measuring the variation of the kinetic energy of ion beam by time-of-flight (TOF) method using two phase probes.

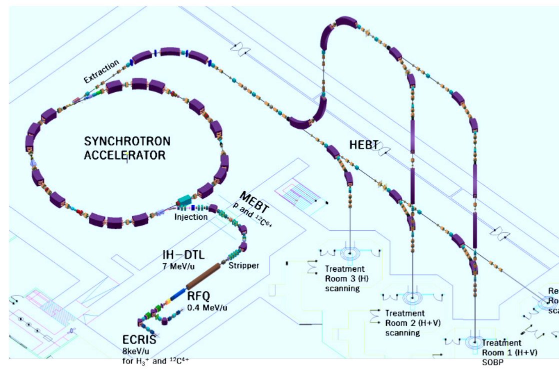

Figure 1: Layout of KHIMA accelerator.

CAPACITIVE PHASE PROBE DESIGN

In the MEBT line, two phase probes are installed to measure the kinetic energy of the ion beams from IH-DTL and to adjust the RF phase and amplitude of IH-DTL by measuring the length of micro-pulses. Since the stripping foil is installed between two phase probes, the status of the stripping foil can be confirmed by the beam energy measurement because the energy loss due to the straggling effects, ~ 16 keV/u, is vanished when the foil is broken. In order to achieve the energy resolution of 10 keV/u, the phase resolution of the phase probe monitor should to be 1° at 200 MHz. Since the beam current is low, ~ 0.1 mA for carbon beam, the capacitive type phase probe monitor is chosen to get the longitudinal distribution without the signal distortion and to get the relatively strong signal. The capacitive pick-up is a stripline bent around the beam pipe axis and then the impedance matching is significant to reduce the ringing effect due to the reflection by the impedance mis-matching. The impedance of the stripline is given by [3]

$$Z_0(l) = \frac{87}{\sqrt{\epsilon_r + 1.4}} \ln\left(\frac{5.98h}{0.8l + d}\right), \qquad (1)$$

where ϵ_r is the relative permittivity, h is the distance between the pick-up ring and surroundings, and d and l are the thickness and length of the pick-up ring. In order to determine the length of the pick-up ring, the impedance as a function of the length when the distance between the inner and outer conductor(h) and the thickness (d) are 14 mm and 3 mm, respectively, that is shown in Fig. 2.

* hwang@kirams.re.kr

ISBN 978-3-95450-176-2

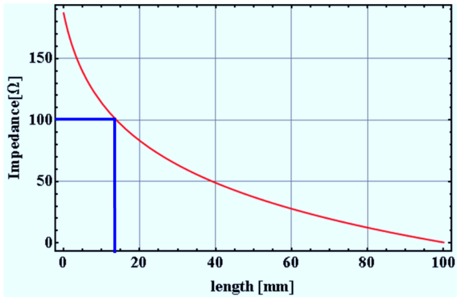

Figure 2: Impedance as a function of length of pick-up ring.

Based on the impedance calculation, the length of the pick-up ring is 14 mm because the impedance of the pick-up ring with surroundings should be matched to be 100 Ω due to the two pathes of the signal. The pick-up ring with the inner diameter of 40 mm and thickness of 3 mm is installed at the center of the double sided CF flange and 1.5 mm thick metal plates are provided on each side to protect the effect by hitting the beam on the pick-up ring. The PEEK (Polyether ether ketone) is used as the insulator material between the pick-up ring and metal plates. The inner diameter of the pick-up ring is determined to be a factor of 2 larger than the full beam size at the installation position to ensure stable operation. The designed capacitive phase probe is shown in Fig. 3.

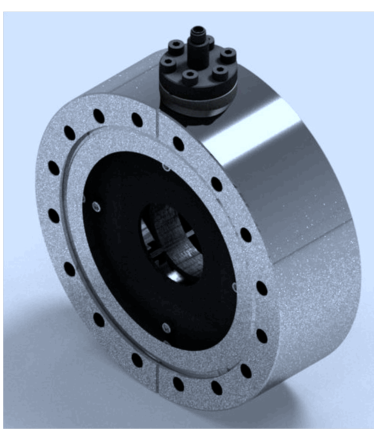

Figure 3: Capacitive phase probe.

Since the distance between the pick-up ring and feed-through, which is required to pick the induced signal at the pick-up ring, is long, about 40 mm, the outer conductor is applied to reduce the signal decay during the signal propagation along the long connector and to prevent the noise signal from surroundings [4]. The inner radius of the outer conductor is determined to match the impedance of 50 Ω based on impedance formula for the coaxial transmission line, $Z = 377\Omega/2\pi \ln\left(r_o/r_i\right)$, where r_o is the inner radius of outer conductor and r_i is the outer radius of the inner conductor. The detail structure for the coaxial transmission line is shown in Fig. 4.

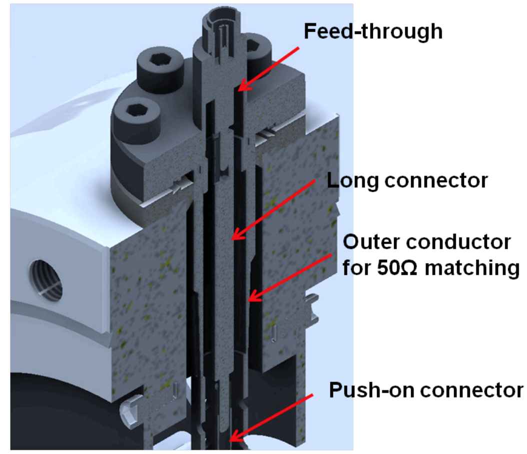

Figure 4: Structure of coaxial transmission line.

In order to determine the proper gain of the pre-amplifier, which is installed near the detector for amplifying the signal, the induced voltage signal from the capacitive phase probe is calculated. The induced voltage signal across the resistor, R, is given by [4]

$$U(t) = R\frac{A}{\beta c 2\pi a}\frac{dI_{beam}}{dt}10^{g/20}, \tag{2}$$

where R is the resistor, A is the area of the pick-up, $\beta = v/c$, a is the radius of pick-up, and g is the gain of an amplifier. Based on the beam parameters, the expected voltage signal with the 60 dB gain pre-amplifier is calculated that is shown in Fig. 5.

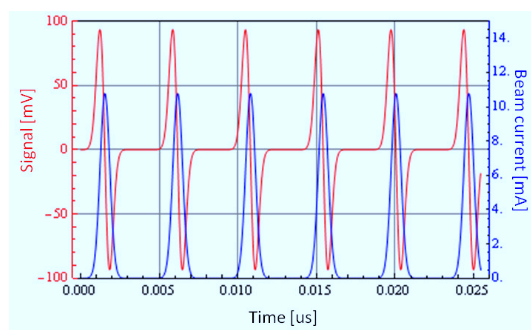

Figure 5: Expected beam current and resulting voltage signal with 60 dB gain pre-amplifier.

From the calculation result as shown in Fig. 5, the maximum gain of the pre-amplifier is determined to 60 dB with 20 dB gain step, minimum gain of 0 dB, and the input power of -50 to 0 dBm. In order to measure the longitudinal distribution of the ion beam by using the phase probe, the time response of the phase probe is significant because the capacitive phase probe has the cutoff frequency due to the structural capacitance and resistance [5]. The half value of time difference between the peak to peak voltage of the induced signal($\Delta t_{P2P}/2$) as a function of the bunch length for a Gaussian distribution is calculated by using CST-PS [6].

ISBN 978-3-95450-176-2

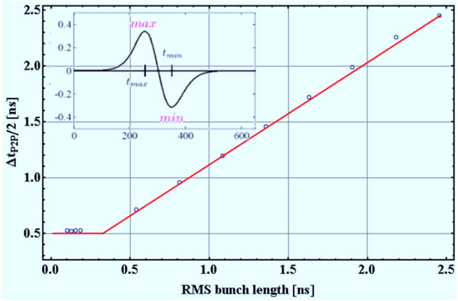

Figure 6: Half value of time difference between peak to peak voltage of induced signal($\Delta t_{P2P}/2$) as a function of rms bunch length for a 7 MeV/u beam.

As shown in Fig. 6, the designed capacitive phase probe has the linear response on a time domain down to RMS bunch length of 0.33 ns, which corresponds to the phase spread of 24° at 200 MHz.

MEASUREMENTS ON WIRE TEST BENCH

The test of the phase probe is performed for measuring the phase resolution of the capacitive phase probe and confirming and the effectiveness of the outer conductor, which is installed to increase the pick-up signal by reducing the propagation loss, using the wire test bench which consists of the linear motor stage and well aligned and stretched wire with two feed-through on the each side. The wire test bench is frequently used to confirm the frequency response and linearity of the pick-up devices from the external signal source. The picture of the test set-up is shown in Fig. 7.

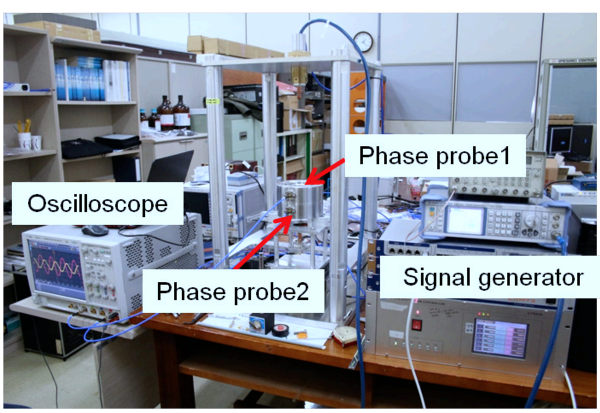

Figure 7: Picture of measurement by using wire test bench.

A 1GHz signal from an RF signal generator is excited on the wire and the induced signal at the phase probe is measured with and without the outer conductor and compared to confirm the effectiveness of the outer conductor. The results are shown in Fig. 8.

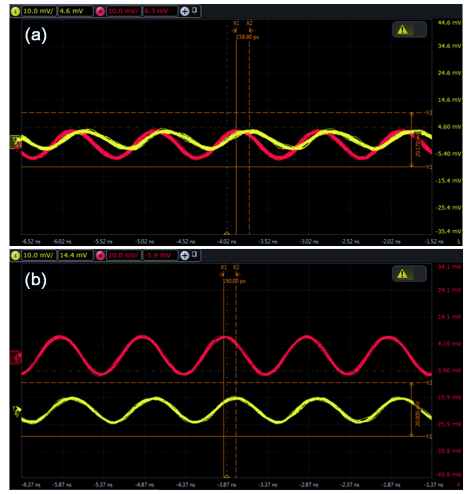

Figure 8: Measured 1GHz signal from two phase probes (a) without outer conductor, (b) with outer conductor.

As shown in Fig. 8, the strength of the pick-up signal is increased about 20 % when the outer conductor is installed.

In order to confirm the phase resolution of the phase probe, two phase probes were mounted on the wire bench with the distance of 50 mm and the signal from the pick-up is measured by using a high sampling speed oscilloscope when the external signal with the frequency of 2 GHz and current of 0.138 mA is excited on the wire. The expected time difference between two phase probes is 167 ps due to the distance of 50 mm. The measured signal and the time difference between two phase probes are shown in Fig. 9.

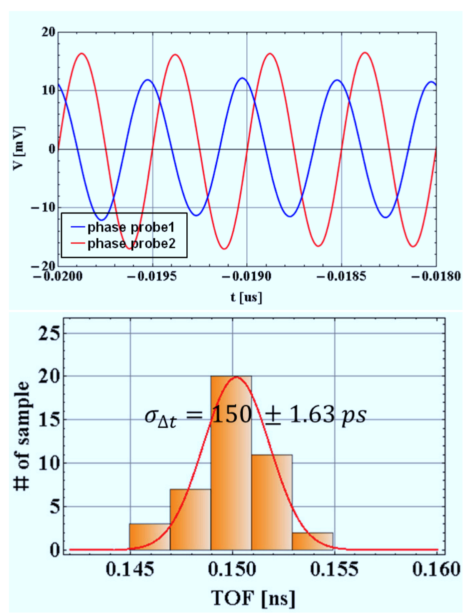

Figure 9: Measured signal (top) and time difference between two phase probes (bottom).

As shown in Fig. 9, the signal from the first phase probe (phase probe1), which is closed to the signal source, is fasten than the signal from the second phase probe(phase probe2). Based on the calculation of the zero-crossing point

ISBN 978-3-95450-176-2

of the each signal, the measured time difference between two phase probes is calculated that is to be 150 $\pm$ 1.63 ps. The difference between the expected and the measured value is 17 ps. It corresponds to the phase of 1.2 ° at 200 MHz.

PRE-AMPLIFIER DESIGN

Based on the calculation and measurement result on wire test bench, the pre-amplifier for amplifying the signal strength from the capacitive beam phase probe is designed. The pre-amplifier for the phase probe is required to have more than three input ports, which is used to the signal from the phase probe, calibration signal, and termination to prevent the damage due to the high power from IH-DTL, respectively, and it has two output port for providing the phase signal to de-buncher in the MEBT line. It was fabricated by EMWISE in Korea [7].

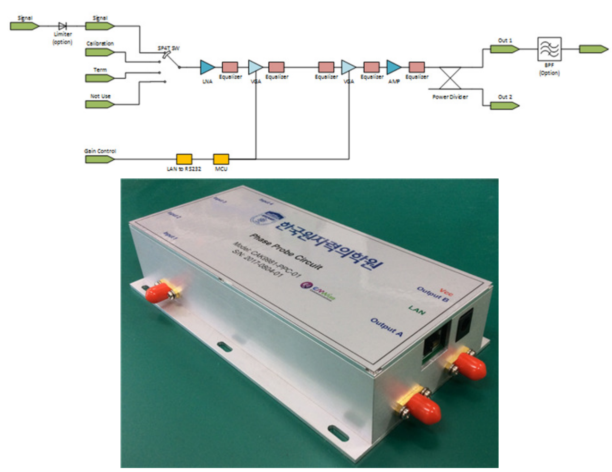

Figure 10: Schematic drawing and picture of pre-amplifier.

As shown in Fig. 10, the amplifier has 4-port RF relay switch, low-noise amplifier (LNA), two variable gain amplifier (VGA), and power divider. The total gain is to be 60 dB with 20 dB step. The gain level and the switch for the selection of input port was controlled via the Ethernet connection. The noise figure of the circuit is 3.69 dB for 500 MHz and 3.93 for 1 GHz. In order to measure the longitudinal distribution of the beam, the wide-bandwidth, 0.2 ~ 2.0 GHz, is required. Then the gain curve as a function of the frequency with 0, 20, 40 , and 60 dB gain is measured. As shown in Fig. 11, the gain flatness in the range of 0.2 GHz to 1.6 GHz is $\pm$ 2 dB.

MEASUREMENTS WITH PROTON BEAM

The time-of-flight(TOF) experiment with the proton beam from the MC-50 cyclotron in KIRAMS is performed to confirm the performance of the phase probe. The extraction energy, average beam current, and RF frequency of MC-50 cyclotron are 30 MeV, 1 uA, and 20.28 MHz, respectively. Then the relative velocity of the beam, $\beta = v/c$, is 0.247. Two phase probes are installed at the extraction

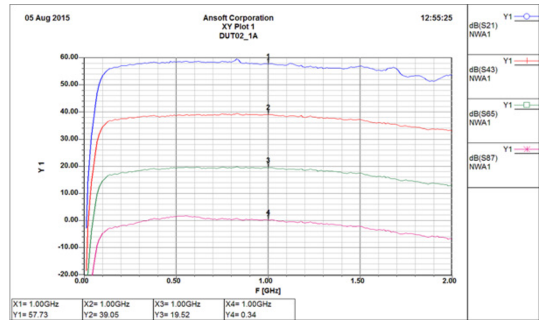

Figure 11: Gain curve as a function of frequency with 0, 20, 40, and 60 dB gain.

line without vacuum condition and the distance between two phase probes is 452 mm. The experimental set-up is shown in Fig. 12.

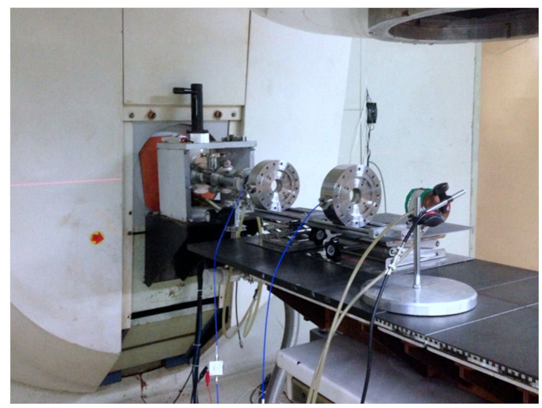

Figure 12: Experimental set-up for TOF measurement with proton beam at KIRAMS.

The signal is amplified by the pre-amplifier with 16.8 dB gain and the bandwidth of 0.1 ~ 1000 MHz and the data acquisition is done by the 2.5GS/s sampling speed digital oscilloscope, DPO4054B. The measurement result is shown in Fig. 13.

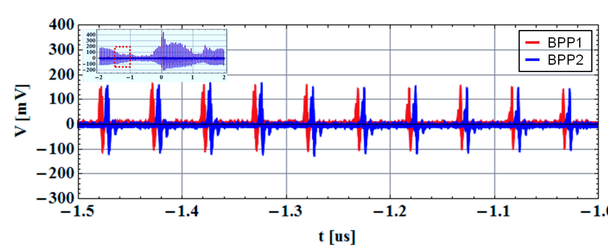

Figure 13: Measured signals from two phase probes.

From the measurement result, the repetition rate of the each signal, T_0, is calculated to confirm the RF frequency,f_{RF}, of the cyclotron because the repetition rate of the beam is well matched to the RF frequency, $f_{RF} = 1/T_0$. The measurement result of the repetition rate of the pulse is shown in Fig. 14.

ISBN 978-3-95450-176-2

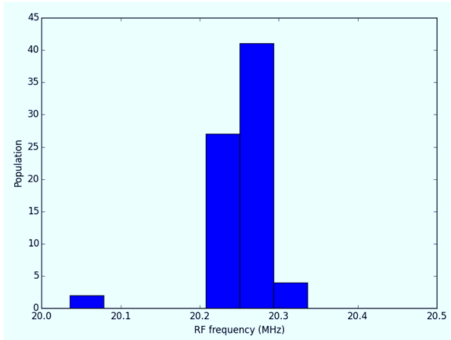

Figure 14: Histogram of the repetition rate of the pulse from the phase probe.

As shown in Fig. 14, the reciprocal of the repetition rate of the pulse, $1/T_0$, is well correspond to the RF frequency, f_{RF}, of the cavity in the cyclotron. The kinetic energy of the beam is defined by measuring the time difference between the zero-crossing points of the signal from each phase probe. The result is shown in Fig. 15.

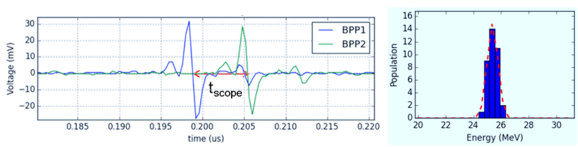

Figure 15: Result of kinetic energy measurement by TOF experiement.

The measured energy is 25.38 ± 0.39 MeV. It is smaller than the extraction energy due to the energy loss in the aluminum window and air.

CONCLUSION

The electromagnetic and mechanical design of the capacitive beam phase probe is performed to achieve the high phase precision, 1° at 200 MHz for identifying the status of the stripping foil and measuring the kinetic energy and the longitudinal distribution of the beam from the IH-DTL in KHIMA project. The time response and expected signal strength of the phase probe is also estimate to determine the proper gain and bandwidth of the pre-amplifier. The pre-amplifier was fabricated and the noise figure, gain flatness, and gain step is measured. The performance of the phase probe is confirmed by measuring the signal response on the wire test bench and TOF experiment with the proton beam.

ACKNOWLEDGEMENT

This work was supported by the National Research Foundation of Korea(NRF) grant funded by the Korea government(MSIP) (no. NRF-2014M2C3A1029534). And this experiment was conducted at the MC50 cyclotron facility operated by KIRAMS supported by the National R&D Program through the Korea Institute of Radiological and Medical Sciences funded by the Ministry of Science, ICT & Future Planning. (No.1711021909).

REFERENCES

[1] http://www.kirams.re.kr/eng/khima.

[2] "KHIMA Handbook of Beam Optics for Accelerator System", private communication.

[3] P. Strehl, *Beam Instrumentation and Diagnostics*, XVII, ISBN 978-3-540-26404-0, Springer, Berlin Heidelberg, Germany (2006)

[4] Peter Forck, *Lecture Notes on Joint University Accelerator School*, Geneva, Switzerland (2011).

[5] Peter Forck, *Lecture Notes on CERN Accelerator School*, Chios, Greece (2011).

[6] CST-MWS and PS website : http://www.cst.com/.

[7] EMWISE website : http://www.em-wise.com/.

ISBN 978-3-95450-176-2

STATUS OF BEAM DIAGNOSTICS AT KHIMA FACILITY

Tae-Keun Yang*, Dong Hyun An, Ga Ram Hahn, Heejoong Yim, Ji-Gwang Hwang, Chang Hyeuk Kim, Seon Yeong Noh, and Chawon Park
Korea Institute of Radiological and Medical Sciences (KIRAMS), Seoul, South Korea

Abstract

The Korea Heavy Ion Medical Accelerator (KHIMA) is the cancer therapy facility based on a synchrotron which can accelerate up to 430 MeV/u for carbon beam and up to 230 MeV/u for proton beam. The facility has 4 sectors Low Energy Beam Transport (LEBT) line from ECR-IS to radio-frequency quadrupole (RFQ) and interdigital H-mode drift-tube-linac (IH-DTL), Medium Energy Beam Transport (MEBT) line from IH-DTL to synchrotron, synchrotron ring, High Energy Beam Transport (HEBT) line from the ring to irradiation rooms, 3 treatment rooms and 1 research room. For the beam diagnostics at the KHIMA, 17 type monitors with total number of 88 are considered and planned including the related instruments such as slit, stopper, stripper and etc. This proceeding introduces specifications of each diagnostic devices and shows test results of several devices.

INTRODUCTION

The Korea Heavy Ion Medical Accelerator (KHIMA) is a project to develop a heavy-ion therapy machine based on a synchrotron. The conceptual design report for each part of the facility has been completed and fabrication of some equipments has been started. The facility can be divided as 4 sectors according to the transferred beam energy; Low Energy Beam Transport (LEBT), Medium Energy Beam Transport (MEBT), synchrotron ring, and High Energy Beam Transport (HEBT) line [1]. A detail information for an ion beam at each sectors are important to transfer well and confirm a beam to a patient with high intensity by minimizing a beam loss. The various monitors are required to measure beam specification such as the beam current, spatial distribution, spill structure, and energy. The beam diagnostic devices can be classified as a destructive or a non-destructive device. The Faraday-cup(FC) is the most famous destructive device and the current transformer(CT) is the most famous non-destructive one to measure the beam current. The DC FCs are installed at the LEBT and AC FCs are the LEBT and MEBT line. The AC current transformers(AC CTs) are installed at the LEBT and MEBT and the DC current transformer (DCCT) is installed at the syncrotron ring. The combination of slit and wire scanner in LEBT line or wire grid monitor in MEBT line, and the pepper-pot device in LEBT line are considered for measuring the beam emittance, which is a significant beam parameter in the accelerator. The transverse beam profile is also measured by the scintillation screen in the synchrotron and HEBT line. Two capacitive pick-up devices are installed in the MEBT line to measure the beam energy by the time-of-flight (TOF) method. Linear-cut beam position monitor, which has the wide linear region, and stripline kicker are adopted to measure the beam position and to use as a RF exciter for tune measurement and RF-KO, respectively. For the interlock, the beam stopper, collimator, and slit is also installed at the each section. In this paper, the beam diagnostics contained at each sectors of the KHIMA facility is introduced.

LOW ENERGY BEAM TRANSFER LINE

The LEBT line is the region of ECR-IS to an entrance of radio-frequency quadrupole (RFQ), see Fig. 1. It has two ECR-IS for producing $^{12}C^{4+}$ and H_3^+ beams. The extraction voltage of the ECR-IS is 24 kV and the required maximum current are 285 euA for $^{12}C^{4+}$ and 765euA H_3^+, respectively. The extracted ion beam is bent by 90° analyzing magnet for ion selection and then the selected beam is transferred into RFQ to accelerate the beam up to 7 MeV/u through the optical components, like solenoid, steering magnet, quadrupole magnet, and electrostatic chopper.

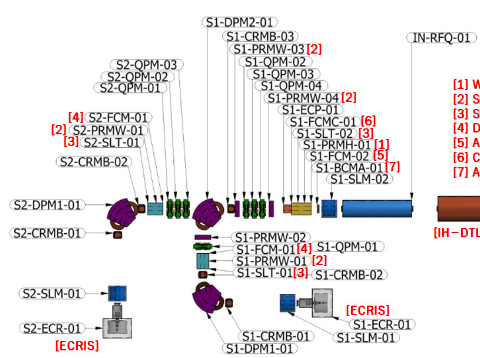

Figure 1: Layout and position of beam diagnostics in LEBT line.

The LEBT line of KIHMA has two emittance measurement systems, which consists of 4 slits with 2 slits at each x- and y-axis, wire scanner with two perpendicular wires, and DC Faraday cup in a vacuum chamber, for measuring the beam emittance after the beam selection by the analyzing magnet and to control the beam optics by measuring the profiles before and after triplet magnets, and an ACCT for measuring beam current after a chopper system. Especially, the Faraday-cup and slit, which is installed in LEBT line, has the cooling channel with the cooling capacitance of 100 W because the beam power of 30 W is fully deposited on

* ytk@kirams.re.kr

ISBN 978-3-95450-176-2

the Faraday-cup. The electric potential with the suppression voltage of -1 kV is calculated and the maximum value of the potential barrier is to be 250 V. It is shown in Fig. 2.

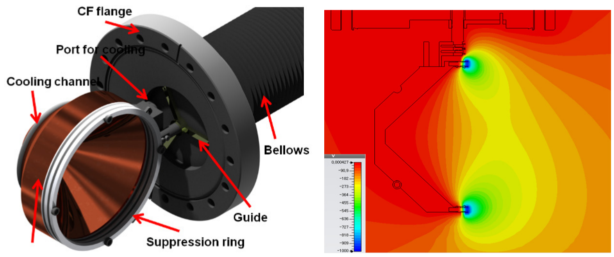

Figure 2: DC Faraday-cup and electric potential map of suppression ring in LEBT line.

Three wire scanners are located near the triplets in the LEBT line for monitoring the beam profile and emittance. For the wire scanner, the device with two wires, which are perpendicular and insulated to each other, is chosen. The actuator is based on a brushless motor to reduce the noise signal from the brush of the motor. Based on the calculation of the heat deposit on the wire, it has moving speed of 100 mm/s and moving range of $\pm$ 200 mm. The diameter of the wire is 0.1mm and the material is tungsten. The emittance measurement is performed by reading current on the wires at each changed positions of slits and wires.

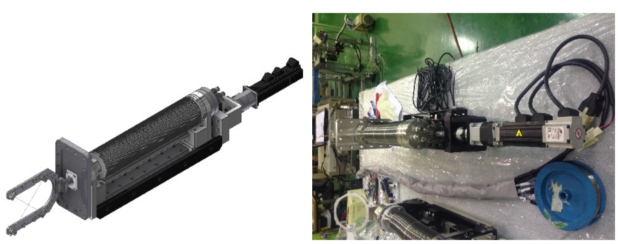

Figure 3: Wire-scanner in LEBT line.

The DC beam from the ECR-IS is changed to be pulsed by an electrostatic chopper. In general, the cylindrical wall typed Faraday-cup was used to collect the beam deflected by the chopper in CNAO and MedAustron [2, 3]. But we choose the DC Faraday-cup on the side of a vacuum pipe to simplify the construction and to lessen the length of the chopper system. The chopper electrodes were designed to be asymmetric so that the deflected beam was well focused at the Faraday cup that is shown in Fig. 4.

After the electrostatic chopper, the emittance of the pulsed beam is measured using x-y slits and wire grid monitor before the RFQ. The wire grid monitor can measure the transverse profile and the central position of a beam. The wire grid monitor consists of horizontal and vertical wire array, 64×64 wires. The active area of it is 105×105 mm^2. The material of wire is tungsten-rhenium alloy and its diameter is 0.1mm. The wire frame is mounted on a pneumatic actuator with 150mm travel range. The pepper-pot device, which consists of mask with the square array

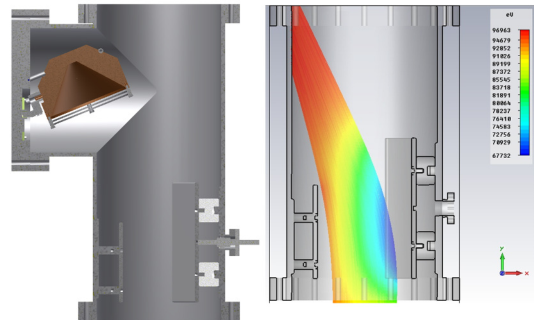

Figure 4: Electrostatic chopper in LEBT line.

holes, microchannel plate (MCP), mirror, and CCD camera, is also considered as a candidate of the emittance measurement equipment. The measurement speed of the device is faster than the combination of the slit and wire-scanner. The design of the pepper-pot device is shown in Fig. 5.

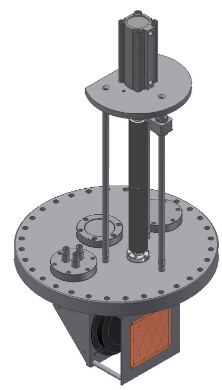

Figure 5: Pepper-pot device in LEBT line.

The pepper-pot mask is made of phosphor bronze and the hole size is measured to be 89.9 ± 1.29 μm by using the scanning electron microscope.

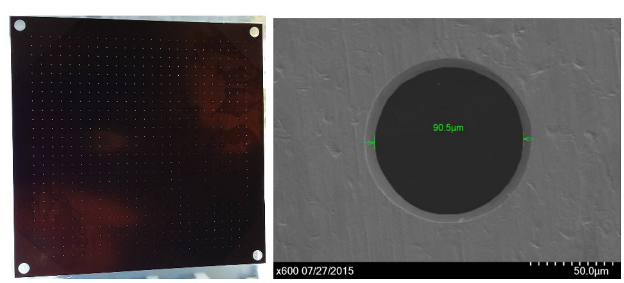

Figure 6: Phosphor bronze pepper-pot mask in Pepper-pot device.

After this wire grid monitor, there are two devices to measure beam current. One is an AC Faraday cup and another is ACCT. The AC Faraday cup has a role of a stopper. Its specification is the same to the DC Faraday-cup except for higher sampling time, $\leq$10 MS/s. The ACCT is non-destructive unlike a Faraday-cup so that it can work as a

ISBN 978-3-95450-176-2

real time monitor during the treatment as well as commissioning.

MEDIUM ENERGY TRANSFER LINE

The pulsed ion beam injected into RFQ is accelerated up to 7 MeV/u by the linac which consists of RFQ and interdigital H-mode drift-tube-linac (IH-DTL). The frequency, repetition rate and duty cycle of the linac are 200 MHz, 4∼5 Hz, and 200 μs, respectively. The accelerated beam is transported to synchrotron through the MEBT line. The layout of the MEBT line is shown in Fig. 7.

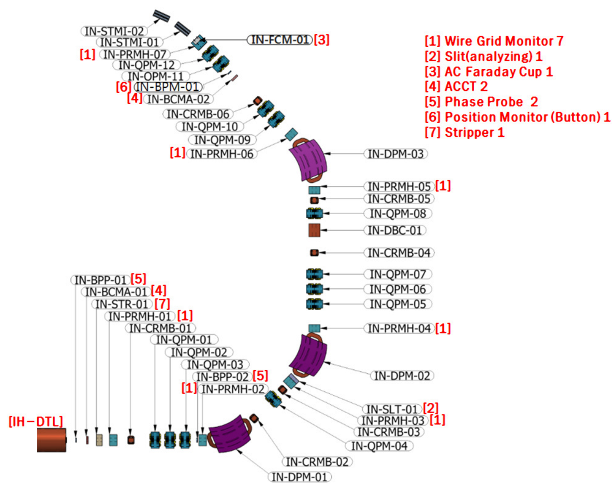

Figure 7: Layout and position of beam diagnostics in MEBT line.

The ACCT and wire grid monitor are located at the exit of IH-DTL to measure beam intensity and to measure the transverse profile of a beam, respectively. The accelerated carbon beam is fully stripped and the H_3^+ beam is changed to proton beam by a thin carbon foil. The equilibrium thickness of the carbon foil for the 7 MeV/u carbon beam is calculated to be 87.8 μg/cm^2 by using code LISE^{++} [4, 5]. The equilibrium thickness means the thickness which does not more change the charge state ratio of transmitted ions. The thickness of carbon foil is chosen to be 100 μg/cm^2. The population of $^{12}C^{6+}$ beam is about 98 % in the case of 100 μg/cm^2 carbon foil. The energy loss and rms angular straggling for the 100 μg/cm^2 carbon foil are 16.1 keV/u and 0.314 mrad, respectively. The five stripper foils are mounted on one ladder and two ladders with step motor are installed in the beam line that is shown in Fig. 8.

The phase probe monitor in a straight section after IH-DTL is used to estimate the spatial beam structure of the accelerated beam by measuring induced current on its electrode as a function of time. The energy of the beam is also determined by applying time-of-flight (TOF) method with output signals from two phase probes. The distance between two probes is about 3 m. The designed phase probe is shown in Fig. 9.

The impedance of the pick-up probe is matched to 100 ohm due to the two passage of the signal. The outer con-

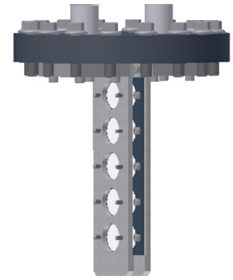

Figure 8: Carbon charge stripper foil mounted on ladder.

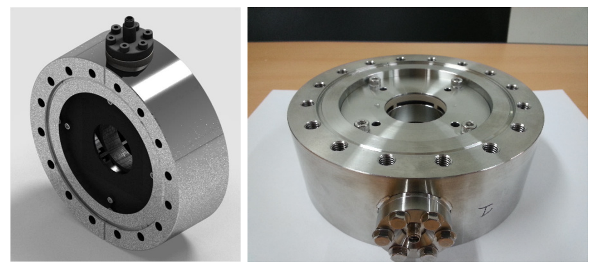

Figure 9: Capacitive beam phase probe in MEBT line.

ductor is applied to reduce the signal decay during the signal propagation along the long connector and to prevent the noise signal from surroundings [6]. The performance of the phase probe is confirmed by measuring the signal response on the wire test bench and TOF experiment with the proton beam in the KIRAMS. The result is shown in Fig. 10.

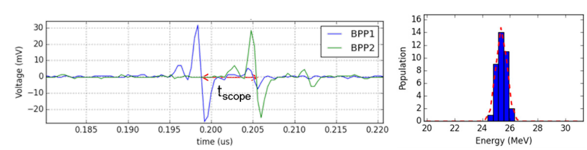

Figure 10: Energy measurement by TOF experiment.

The measured energy is 25.38 $\pm$ 0.39 MeV. It is smaller than the extraction energy due to the energy loss in the aluminum window and air. After first bending magnet in the MEBT line, a horizontal slit is installed to select only a targeted ion with proper charge state, $^{12}C^{6+}$ or H^+, among various ion beams and charge states produced by the stripper. Seven wire grid monitors will be installed to measure the transverse profile of a beam in MEBT. Its specification is similar to one in LEBT with the active area of 70$\times$70 mm^2. Before the injection point, the ACCT and button type beam position monitor are installed to verify the beam current variation and orbit jitter before the injection on the synchrotron, respectively.

SYNCHROTRON RING

The injected beam with the energy of 7 MeV/u is accelerated up to 430 MeV/u for carbon beam and 230 MeV for proton beam in the synchrotron. In order to accelerate beam without the significant beam loss, the monitoring of

ISBN 978-3-95450-176-2

the central orbit, betatron tune, phase stability and synchronization of frequency ramping of the low level RF system for magnetic alloy cavity are important. The layout and position of the beam diagnostics in the synchrotron is shown in Fig. 11.

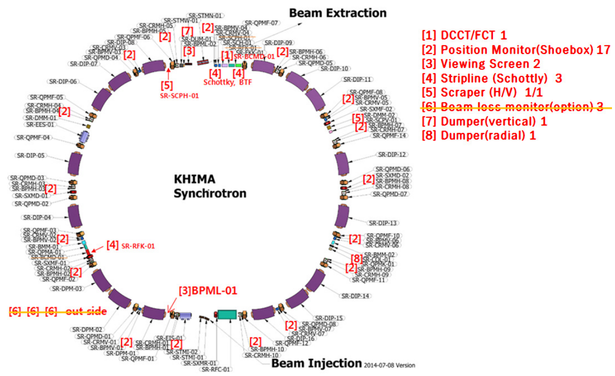

Figure 11: Layout and position of beam diagnostics in synchrotron.

The viewing screen, which is coated P43 scintillation material on Al substrate, is installed at the injection and extraction position to identify the injection beam orbit and profile during first turn in the ring. It is adopted as the beam profile monitor in the HEBT line. The spatial structure of macro-pulse and the beam orbit of the ion beam is monitored by using linear-cut beam position monitor, see Fig. 12. The number of beam position monitor is 10 for horizontal direction and 7 for vertical direction. The position of the position monitor is determined based on the amplitude of the betatron oscillation.

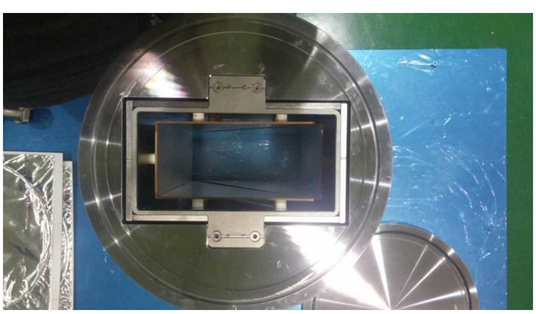

Figure 12: Linear-cut beam position monitor in synchrotron.

It was fabricated based on the design values and the laboratory tests, such as the vacuum leakage test by He leak detector, the measurement of the cross-talk by the Vector Network Analyzer and linearity measurement by the wire test bench, were performed to confirm the performance. The measured cross-talk is less than -40 dB in the operation frequency from 0.48 MHz to 3 MHz, see Fig. 13. The calibration coefficients is measured and it agrees well with the designed parameter calculated by using code CST-MWS [7].

Two stripline kickers are installed to excite the beam

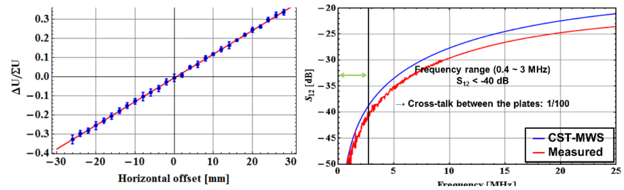

Figure 13: Measurement result of linearity and S-parameter of Linear-cut BPM.

for measuring the betatron tune and to manipulate the spill structure of the extracted beam, respectively. It is also used to measure the beam position and energy spread for the coasting beam. The concave shaped plates are oriented horizontally and vertically to form the capacitors in respective planes. Figure 14 shows the mechanical structure and the field profile of stripline kicker and Schottky pick-up.

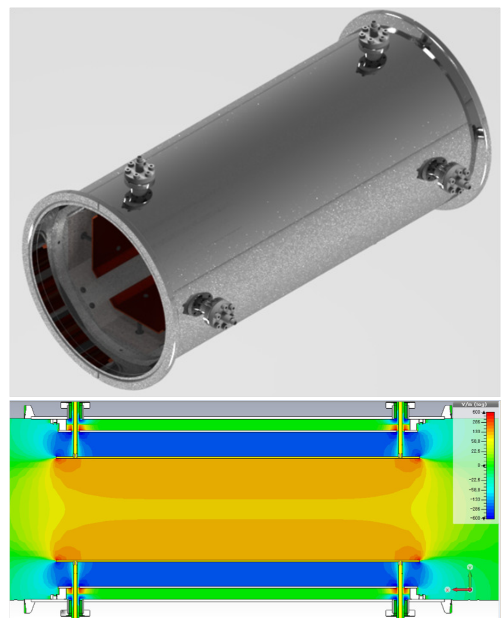

Figure 14: Stripline kicker in synchrotron.

The DCCT and FCT are installed to measure the beam current variation during the injection and extraction cycle. The scraper is also used to control the beam emittance in the ring by removing the halo particles.

HIGH ENERGY TRANSFER LINE

The extracted beam is delivered to the treatment room or research beam line. One horizontal and two vertical treatment room and one horizontal research beam line is planned in the KHIMA facility. The quality of beam extracted from the synchrotron is monitored by the qualification monitor, which is installed between the chopper magnet, to obtain the safety for the therapy. The qualification monitor observes the beam spill structure and profile before the treatment room to confirm the dose on patient. When the stability of the beam intensity and profile is confirmed,

ISBN 978-3-95450-176-2

the beam is delivered to the treatment room or research beam line. The layout and position of the beam diagnostics in the HEBT line is shown in Fig. 15.

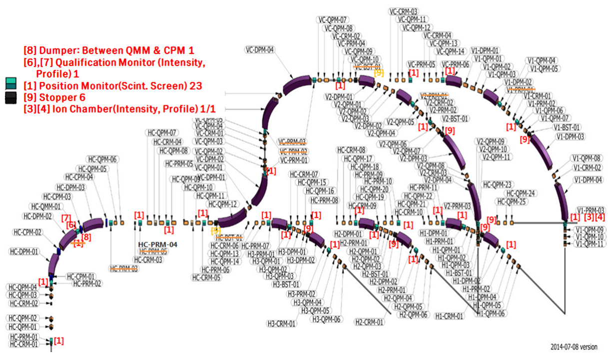

Figure 15: Layout and position of beam diagnostics in HEBT line.

For the optics tuning, the beam profile at the HEBT line is monitored by using the scintillation screen monitor. Since the beam intensity is low, $\sim 5 \times 10^8$ particles/spill, in the HEBT line, the P43 material, which has high light yield, is determined as the scintillation material to obtain the high light output. The thickness of the coating is chosen to be 50 μm with the grain size of 10 μm.

Figure 16: Scintillation screen monitor in synchrotron and HEBT line.

The screen monitor is fabricated and the calibration for the correction of the optics distortion is performed based on the linear mapping. The control and data acquisition system based on the compact single board is under developing. The profile reconstruction and analysis included the suppression of effects of noise and death pixel and the background noise subtraction is done. The beam test with proton beam were performed to confirm the performance that is shown in Fig. 17.

CONCLUSION

The conceptual design of KHIMA facility is completed and we have a plan to construct the 88 beam diagnostics until end of 2017. The beam diagnostic devices such as wire-scanner, Faraday-cup, pepper-pot device, electrostatic chopper, capacitive phase probe, linear-cut BPM, stripline kicker, and scintillation screen monitor, is under developing by collaborating with PAL, GSI, RCNP and KEK.

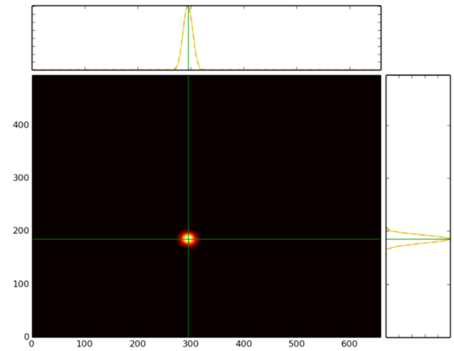

Figure 17: Beam test result with proton beam.

ACKNOWLEDGEMENT

This work was supported by the National Research Foundation of Korea(NRF) grant funded by the Korea government(MSIP) (no. NRF-2014M2C3A1029534)

REFERENCES

[1] KHIMA Handbook of Beam Optics for Accelerator System, private communication.

[2] G. Balbinot et al., "A NOT-INTERCEPTIVE FARADAY CUP IN THE CNAO LOW ENERGY INJECTION LINES", DIPAC09, Basel, Switzerland (2009), TUPD21.

[3] F. Osmic et al., "OVERVIEW OF THE BEAM DIAGNOSTICS IN THE MEDAUSTRON ACCELERATOR: DESIGN CHOICES AND TEST BEAM COMMISSIONING", IPAC2012, New Orleans, USA (2012), MOPPR002.

[4] O. Tarasov, D. Bazin, Nucl. Instr. Meth. B **266** (2008) 4657.

[5] D. Bazin et al., Nucl. Instr. Meth. A **482** (2002) 307.

[6] Peter Forck, *Lecture Notes on Beam Instrumentation and Diagnostics*, Joint University Accelerator School (JUAS), Geneva, Switzerland (2011).

[7] CST-MWS and PS website : https://www.cst.com/.

ISBN 978-3-95450-176-2

INSTRUMENTATION IN DESIREE

A. Källberg, G. Eklund, S. Silverstein, A. Simonsson, M. Björkhage, M. Blom, H. Cederqvist, L. Liljeby, P. Löfgren, A. Paál, P. Reinhed, S. Rosén, H. T. Schmidt, R. D. Thomas, Stockholm University, Department of Physics, SE-106 91 Stockholm, Sweden,
H. Danared, European Spallation Source, Box 176, SE-221 00 Lund, Sweden

Abstract

The instrumentation in the double electrostatic storage rings DESIREE is discussed, In particular, we describe the measurements of the stored beam currents, using a fast kick-out of the beam or Schottky signals. For the Schottky signals, the use of the double-peak structure of the signal is described. Also the preparations to implement stochastic cooling in DESIREE are included in this paper.

INTRODUCTION TO DESIREE

DESIREE is a double electrostatic storage ring at the Department of Physics at Stockholm University. The two rings have similar circumferences, 8.7 m, and a common straight section along which stored ions can interact. The ion optics is housed in one single, double walled cryostat and is cooled to around 13 K by four cryocoolers. Two injectors are able to supply both positive and negative ions to both rings.

The optics of DESIREE is shown in Fig. 1 and a picture of the elements mounted on the 20 mm thick aluminium baseplate of the inner box in the cryostat is shown in Fig. 2. Each ring consists of two 160° bends (CD) and four 10° bends (DE) to complete one turn. Two of the 10° bends are common for both rings. For focussing there are four quadrupole doublets (QD) in each ring and there are also several transverse steerers (CC, CV) in each ring. All elements in DESIREE are electrostatic.

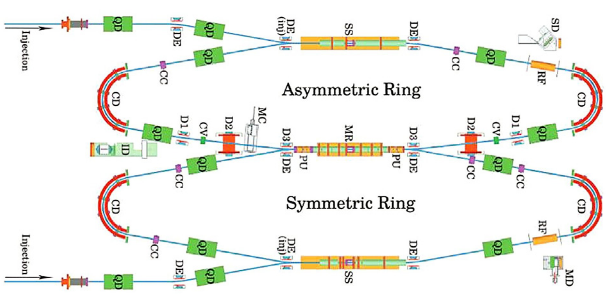

Figure 1: Drawing of the DESIREE optics.

The lattices are similar to the one in ELISA [1]. The main difference is that the injection kicker switches from +10° to -10° instead of from 10° to 0°. This difference was made to minimize the amount of infrared radiation reaching the cold interior in the cryostat from the warm surroundings. It also enables the current measurement described later in this paper.

Ring S, the symmetric ring, has a two-fold mirror symmetry while in ring A, the asymmetric ring, two quadrupole doublets are displaced to permit the installation of two extra bends (D1, D2) on each side of the common section. These are necessary to simultaneously store ions with different energies. Two bends (D3) are common for both rings, they bend 10° in ring S and 0.5°-10° in ring A, depending on the ion mass and energy in ring A.

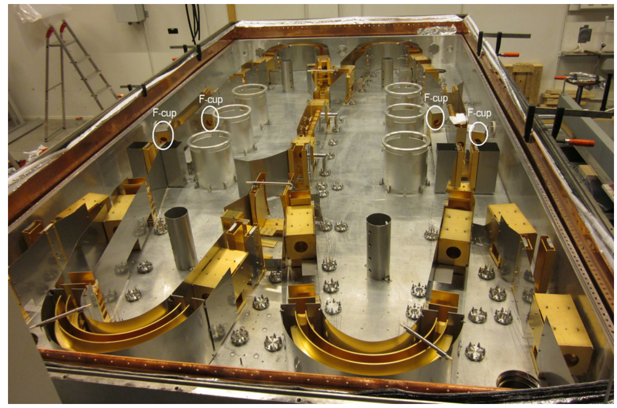

Figure 2: DESIREE inside the cryostat.

Ions can be stored in ring S with lifetimes of several minutes. The lifetimes in ring A are shorter, only in the order of several seconds. This can be expected, since the dynamic aperture in ring A is much smaller than in ring S. For more details about DESIREE see [2] and [3]

MEASUREMENTS OF STORED ION CURRENTS

The most straightforward way to measure the stored ion current would be to use a DC current transformer (DCCT). However, there is no DCCT installed in DESIREE and the stored currents are often weak, often only a few nA or less, so a DCCT would be too noisy to measure such currents. Possibly a squid-based DCCT could be used, but no such device has been incorporated. Instead we are using two other methods.

The Kick-Out Method

Two Faraday cups are available outside and inside of the injection in each ring. These are marked in Fig. 2. The cups on the inside of the rings are used to measure the injected beam when 0 V is applied to the kicker plates (DE (inj)). The outside cups are intended to be used for measurements of the beam after one completed turn. For this measurement the kicker plates are kept at a constant voltage and after having completed one turn, the beam is

ISBN 978-3-95450-176-2

bent 10° outward into the Faraday cup outside the ring, instead of the normal injection procedure of switching the plates to the opposite polarity and thus closing the ring before the injected beam has reached the plates after one turn.

However, the outside cups can also be used to measure a stored beam. If the polarity of the injection kicker is reversed, the stored beam gets kicked 20° out from the closed orbit into the outside cup, which, due to space limitations, is placed 18° outside the closed orbit instead of 20°, but the aperture of the cup is large enough to accept all of the beam kicked out in this way. A benefit of using this method is that the signal from the Faraday cup is always available in the standard ring cycle, since at the end of the ring cycle the polarity of the injection kicker anyway has to be reversed to prepare the ring for a new injection, so the stored ions are always kicked into the outside cup. A 20 MS/ch/s Agilent ADC and a LabVIEW program, which makes features like averaging, background subtraction etc. available, handle this measurement. Figure 3 shows the measurement of the stored current in ring S using this program.

Further developments of this system include the design of an optimized amplifier for the pulsed current and efforts to reduce the noise in the measurements.

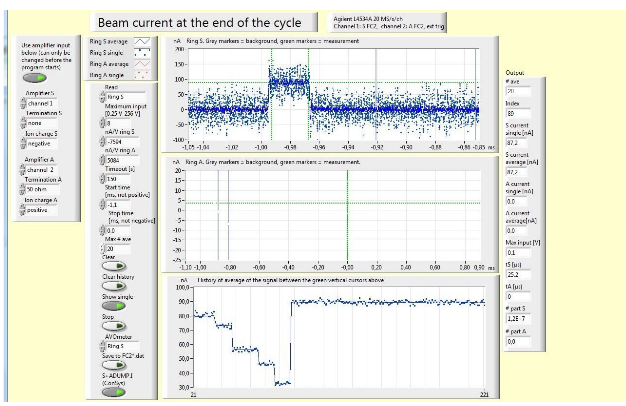

Figure 3: Measuring the stored ion current by kicking the beam into a Faraday cup

The Double-Peak Method

If the beam is cold enough, the individual Schottky peaks can split into a double-peak structure. The double peaks are due to a collective motion in the form of two density waves propagating along the beam direction and opposite to it, in turn a result of the beam interacting with the surrounding beam pipe. The splitting between the peaks is proportional to the square root of the circulating beam current as described in [4], and can thus be used for current measurements.

Figure 4 shows a fit to the expression in [4] of a measured Schottky spectrum of a C_2^- beam at 10 keV total energy, taken at the 23rd harmonic of the revolution frequency. The vertical green lines show the double-peak split which gives the current and momentum spread. However, the expression for the beam current contains the

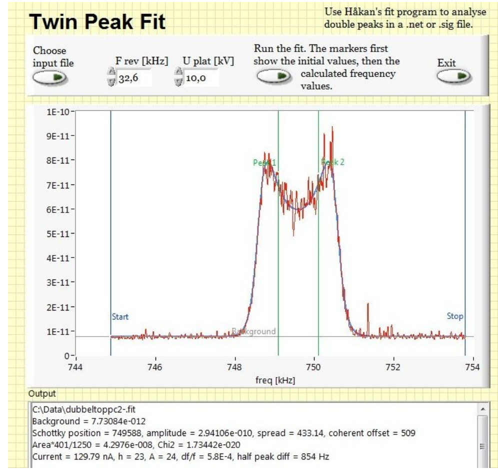

Figure 4: The fit of a double Schottky peak yielding the stored ion current and the frequency spread of the beam.

ratio between the radii of the beam pipe and the beam, a value which is not well defined in DESIREE, since there is actually no beam pipe. Thus the current obtained from the fit has been calibrated with the help of the current in the cup using the kick-out method described in the previous section. The resulting beam current for the spectrum of Fig. 4 was 130 nA.

PREPARATIONS FOR STOCHASTIC COOLING IN DESIREE

Calculations of stochastic cooling in DESIREE have shown that it should be possible to achieve cooling times around 100 s [5, 6]. Since the lifetimes of the beams in the S-ring mostly are much longer than this, a project to implement stochastic cooling has been initiated.

Installing new equipment in DESIREE requires a major effort, since it includes completely dismounting the cryostat. Only minor changes can be made by just opening the cryostat from the top, something which has been done annually. For the initial tests, there is thus no possibility to install dedicated pickups and kickers. Instead the existing RF drift tube has been used as longitudinal pickup and two pairs of transverse steerer plates connected in parallel as a longitudinal kicker. Measurements of the Beam Transfer Function, BTF, between these elements, such as the one shown in Fig. 5, indicate that the available instrumentation should be

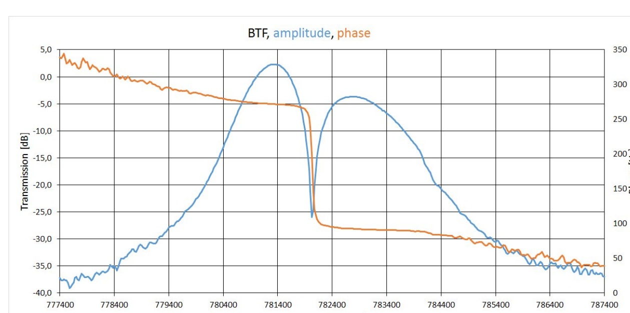

Figure 5: BTF measurement of a 10 keV C_2^- beam.

ISBN 978-3-95450-176-2

appropriate to achieve cooling.

The instrumentation used for the initial tests is shown in Fig 6. The digital notch filter and the delay are implemented in FPGA [7]. The notch filter is designed to suppress the beam orbit frequency and higher harmonics by at least 60 dB. The analog input stage to the notch filter uses an active high-pass active filter to remove low-frequency components of the beam pickup signal below 10 kHz. The following amplifier stage amplifies the high-pass output amplitude to fit the ± 1V range of the notch

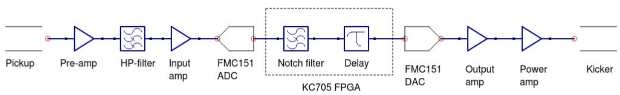

Figure 6: Instrumentation used for the initial cooling tests.

filter's A/D input. A measurement of the transmission of the notch filter is shown in Fig. 7.

The digital notch filter itself comprises a commercial 14-bit A/D and 16-bit D/A conversion daughter card (4DSP FMC151) [8], mounted on a Xilinx KC705 FPGA development board (Xilinx KC705) [9]. The default A/D conversion rate is approximately 124 MHz, allowing the beam orbit period to be set by increments of ~8 ns. An external inhibit signal can be used to disable the output during beam injection and for a period after. The notch filter is remotely controlled via an Ethernet connection from a Windows PC, allowing settings such as the filter frequency and output polarity to be adjusted on the fly.

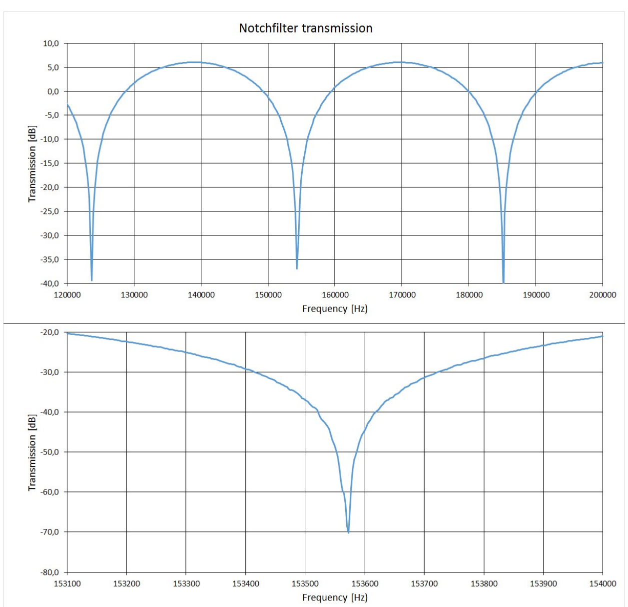

Figure 7: Measured transmission of the digital notch filter.

REFERENCES

[1] ELISA - An Electrostatic Storage Ring for Atomic Physics, S. P. Møller, PAC 1997.

[2] The Double ElectroStatic Ion Ring Experiment: A Unique Cryogenic Electrostatic Storage Ring for Merged Ion-beams Studies, R. D. Thomas et al, Rev. Sci. Inst. 82, 2011.

[3] First Storage of Ion beams in the Double Electrostatic Ion-Ring Experiment: DESIREE, H. T. Schmidt et al, Rev Sci Inst, 2013.

[4] Ordered Ion Beams in CRYRING, H. Danared et al., COOL2001.

[5] Applicability of Stochastic Cooling to Small Electrostatic Rings, H. Danared, EPAC 2008, Genoa, Italy.

[6] Stochastic Cooling at Very Low Energies, Gustav Eklund, Master Thesis, Stockholm University, Dept. of Physics, unpublished.

[7] Momentum stochastic cooling with digital notches, M. Chanel et al., EPAC 1990, Nice, France.

[8] http://www.4dsp.com/FMC151.php

[9] www.xilinx.com

ISBN 978-3-95450-176-2

STUDY OF THE TRANSVERSE BEAM EMITTANCE OF THE BERN MEDICAL CYCLOTRON

K. P. Nesteruk[a,*], M. Auger[a], S. Braccini[a], T. S. Carzaniga[a], A. Ereditato[a], P. Scampoli[a,b]
[a]Albert Einstein Center for Fundamental Physics, Laboratory for High Energy Physics, University of Bern, Switzerland
[b]Department of Physics, University of Napoli Federico II, Naples, Italy

Abstract

The cyclotron laboratory for radioisotope production and multi-disciplinary research at the Bern University Hospital (Inselspital) features an IBA Cyclone 18 MeV proton cyclotron equipped with a Beam Transport Line (BTL), ending in a separate bunker. The horizontal and vertical transverse beam emittances were measured for the first time for this kind of accelerator. Two different techniques were used. A measurement based on quadrupole strength variation and beam width assessment after the last focusing section on the BTL was first performed. A second technique was developed employing 4 beam profilers located at successive positions around a beam waist. These novel beam profile detectors were developed by our group and are based on doped silica and optical fibers. For the data analysis, a statistical approach allowing for estimation of the RMS transverse emittance of a beam with an arbitrary density profile was applied. The results obtained with both methods were found to be in good agreement.

INTRODUCTION

A cyclotron laboratory for radioisotope production and multi-disciplinary research is in operation at the Bern University Hospital (Inselspital) [1]. The facility is equipped with an IBA Cyclone 18 MeV proton cyclotron shown in Fig. 1. The cyclotron is supplied with two H^- ion sources, a redundancy aimed at maximizing the efficiency for daily medical radioisotope production. It provides high beam currents up to 150 µA in single or dual beam mode. Extraction is realized by stripping H^- ions in a 5 µm thick pyrolytic carbon foil.

The Bern cyclotron laboratory is equipped with a Beam Transport Line (BTL), which is a unique feature for a hospital based facility. It allows to carry out multi-disciplinary research in parallel with daily radioisotope production. A schematic view of the BTL is presented in Fig. 2. Alternate beam focusing and defocusing is realized by two horizontal-vertical (H-V) quadrupole doublets, the former located in the cyclotron bunker and the latter in that of the BTL. A movable cylindrical neutron shutter is located at the entrance of the BTL bunker to minimize the penetration of neutrons during routine radioisotope production. For scientific activities, experimental equipment such as particle detectors or specific target stations are installed at the end of the 6.5 m long BTL.

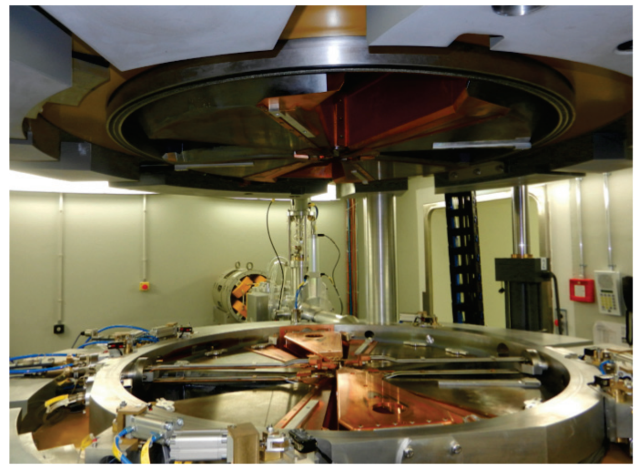

Figure 1: The Bern cyclotron opened during commissioning.

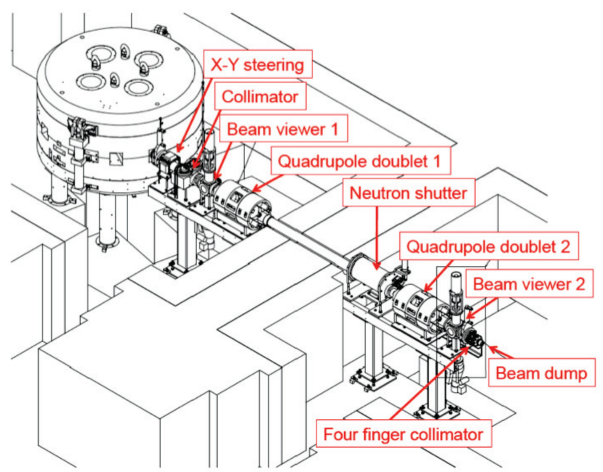

Figure 2: Schematic view of the Bern cyclotron facility, where all the main elements of the BTL are highlighted.

In this paper, we report on the first measurements of the transverse beam emittance of an IBA 18 MeV cyclotron. The measurements were conducted by means of beam profilers developed by our group and named UniBEaM. This detector is a compact device based on doped silica and optical fibers which allows for fully automatized measurements of transverse beam profiles. The first prototype of UniBEaM is described in [2]. For the measurements reported in this paper, a beam current of about 250 nA was used, which is unusual for medical cyclotrons. Such low currents are obtained with the methods described in [3]. This intensity range allows operating the UniBEaM detector in a linear

* Corresponding author: konrad.nesteruk@lhep.unibe.ch

ISBN 978-3-95450-176-2

regime thus avoiding distortions in the beam profiles. The transverse beam emittance was evaluated by applying two different methods, in which the beam profilers were installed along the BTL. Preliminary results are presented in the next sections.

THE TRANSVERSE RMS BEAM EMITTANCE OF AN ARBITRARY DENSITY PROFILE

The beam emittance is the main physical quantity used to characterize an accelerated particle beam. It gives an area in the phase space of the particles. There are two phase space variables for each spatial direction - momentum and position, and the beam emittance describes the correlation between them. The transverse beam emittance can be determined for two planes - horizontal and vertical. The phase space is described by position x and angle x', and position y and angle y' for the former and the latter plane, respectively. In further considerations, only the horizontal plane is discussed being the vertical plane completely analogous.

Realistic beams are usually far from being Gaussian and an appropriate statistical approach is required for a reliable estimation of the transverse beam emittance. In case of an arbitrary density distribution $\rho(x, x')$, the following moments can be defined:

$$\langle x^2 \rangle = \frac{\iint (x-\mu)^2 \rho(x,x') dx' dx}{\iint \rho(x,x') dx' dx} \tag{1}$$

$$\langle x'^2 \rangle = \frac{\iint (x'-\mu')^2 \rho(x,x') dx' dx}{\iint \rho(x,x') dx' dx}, \tag{2}$$

and the covariance:

$$\langle xx' \rangle = \frac{\iint (x-\mu)(x'-\mu') \rho(x,x') dx' dx}{\iint \rho(x,x') dx' dx}, \tag{3}$$

where μ and μ' are the expectation values for x and x', respectively. The beam matrix $\sigma(s)$ at the location s along the beamline is therefore expressed in the following way:

$$\sigma(s) = \begin{pmatrix} \sigma_{11} & \sigma_{12} \\ \sigma_{21} & \sigma_{22} \end{pmatrix} = \begin{pmatrix} \langle x^2 \rangle & \langle xx' \rangle \\ \langle xx' \rangle & \langle x'^2 \rangle \end{pmatrix}. \tag{4}$$

The RMS beam emittance ε_{rms} is then given by the determinant of the σ_s matrix:

$$\varepsilon_{rms} = \sqrt{\det(\sigma(s))}, \tag{5}$$

and is independent of the location s according to Liouville's theorem.

QUADRUPOLE VARIATION METHOD

The quadrupole variation method was first used to measure the transverse beam emittance in both horizontal and vertical planes. The method is depicted in Fig. 3. The last quadrupole magnet of the BTL, located at $s_0 = 0$, is defocusing in the horizontal plane and focusing in the vertical. Its strength was varied and the corresponding beam profiles at the location $s_1 = 694$ mm were measured with the UniBEaM detector for each magnet setting. The measurements were performed for a beam current of 250 nA, which was monitored throughout the experiment by means of a Faraday cup. The profiler and Faraday cup installed on the BTL are shown in Fig. 4. The UniBEaM monitor was rotated by 90° for the corresponding measurements in the vertical plane.

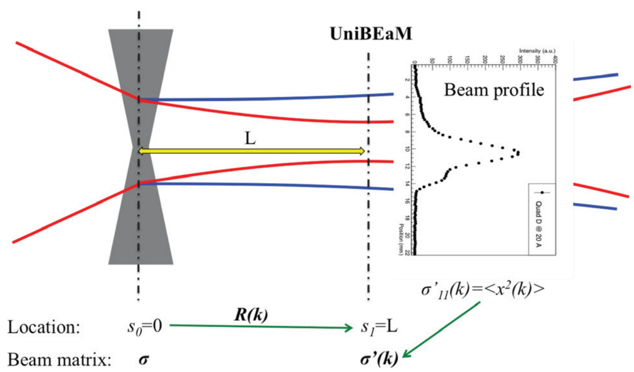

Figure 3: Variation of quadrupole strength for the measurement of the transverse beam emittance.

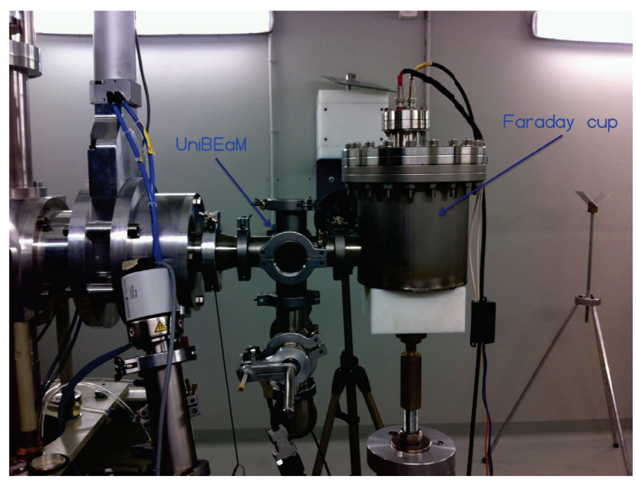

Figure 4: The UniBEaM detector and a Faraday cup installed on the BTL for the quad variation measurement of the transverse beam emittance in the horizontal plane.

Since each profile gives the marginal density distribution, the calculated variance (RMS squared) is an estimate of the $\sigma'_{11}(k)$ component of the beam matrix $\sigma'(k)$ at the location s_1 for a given quadrupole strength k. A defocusing quadrupole magnet of an effective length d set at the strength k can be represented by the following matrix:

$$R_{DQ} = \begin{pmatrix} \cosh\sqrt{k}d & \frac{1}{\sqrt{k}}\sinh\sqrt{k}d \\ \sqrt{k}\sinh\sqrt{k}d & \cosh\sqrt{k}d \end{pmatrix}. \tag{6}$$

A drift of length L follows and leads to the matrix:

$$R_{DR} = \begin{pmatrix} 1 & L \\ 0 & 1 \end{pmatrix}. \tag{7}$$

ISBN 978-3-95450-176-2

Eventually, the beam transfer matrix $R(k)$ is given by the matrix product:

$$R(k) = R_{DR}R_{DQ}, \tag{8}$$

which provides a linear transformation between the beam matrix σ at the entrance to the quadrupole and the beam matrix $\sigma'(k)$ at the location of the UniBEaM detector. The matrix $\sigma'(k)$ is obtained by the following algebraic operation:

$$\sigma'(k) = R(k)\sigma R(k)^T, \tag{9}$$

which gives the $\sigma'_{11}(k)$ component as a function of k, containing three unknown parameters σ_{11}, σ_{22}, and $\sigma_{12} = \sigma_{21}$. It holds:

$$\sigma'_{11}(k) = f(k; \sigma_{11}, \sigma_{12}, \sigma_{22}). \tag{10}$$

The strength k is directly related to the quadrupole current I. During the measurements, the magnet current was varied in the range 17-36 A and 25-63 A for the horizontal and vertical plane, respectively. The factor k was found on the basis of the quadrupole characteristics studies performed by the manufacturer. The components of the beam matrix σ at the entrance to the quadrupole and the corresponding transverse beam emittance value were obtained by performing a fit of the function $f(I; \sigma_{11}, \sigma_{12}, \sigma_{22})$ to the data points. The estimated variance values $\langle x^2 \rangle$ and $\langle y^2 \rangle$ as a function of the quadrupole current together with the fitted curves are reported in Figs. 5 and 6 for the horizontal and vertical plane, respectively. The fit results for both planes and the corresponding emittance values are reported in Table 1. The transverse RMS emittance in the horizontal plane is 3.6 times bigger than the one in the vertical plane. This can be explained by the fact that particles are accelerated in the horizontal plane and therefore the position spread is significantly larger than in the vertical plane.

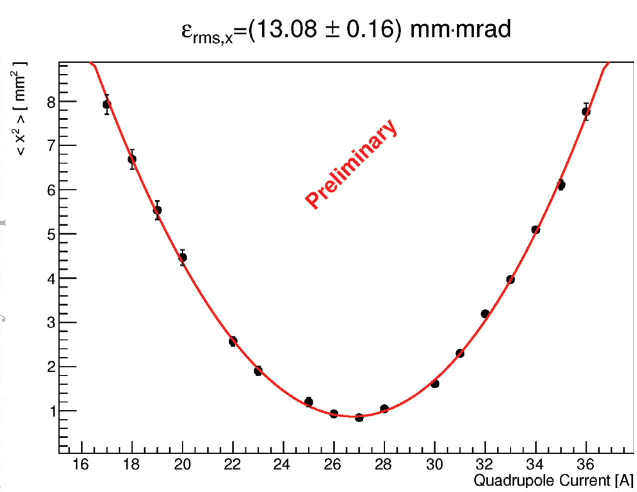

Figure 5: Variance as a function of the quadrupole current obtained in the horizontal plane. The red line corresponds to the best fit.

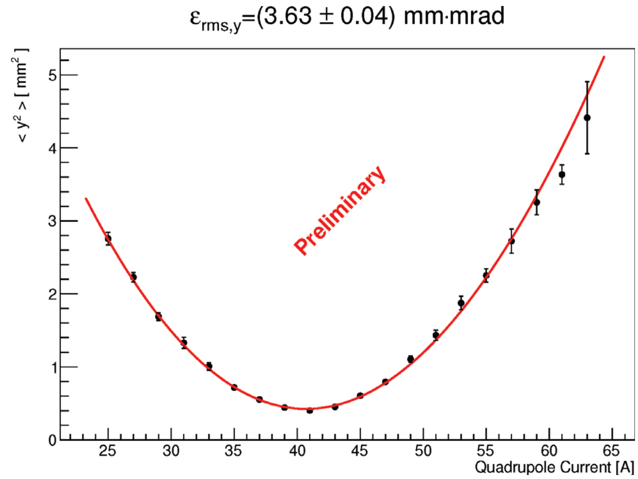

Figure 6: Variance as a function of the quadrupole current obtained in the vertical plane. The red line corresponds to the best fit.

Table 1: Fit Parameters and the RMS Emittance Values Obtained by Quadrupole Variation for Both Horizontal and Vertical Planes

Fit parameter	Horizontal plane	Vertical plane
σ_{11} [mm^2]	200.23 ± 0.08	21.59 ± 0.36
σ_{12} [mm·mrad]	-322.66 ± 0.08	-2.98 ± 0.07
σ_{22} [mrad^2]	520.80 ± 0.22	1.02 ± 0.02
$\tilde{\chi}^2$	0.98	1.04
ε_{rms} [mm·mrad]	13.08 ± 0.16	3.63 ± 0.04

MULTIPLE BEAM PROFILER METHOD

In this method, four UniBEaM detectors were installed on the BTL, as shown in Fig. 7. With respect to quad variation, this method does not require any prior knowledge of the optical elements of the beam line. For a fixed setting of the quadrupole magnets and with a beam current of 250 nA, beam profiles were measured at four succesive locations around a beam waist separated by a drift length $L = 135$ mm, as depicted in Fig. 8. The UniBEaM monitors were rotated by 90° for the corresponding measurements in the vertical plane.

The beam profiles were analyzed in the same way, as in the case of the quadrupole variation method. The variance was calculated for each profile histogram giving an estimate of $\sigma_{11}(s)$ component of the beam matrix $\sigma(s)$ at the location s. The beam transfer matrix $R(s)$ involves now only a drift:

$$R(s) = \begin{pmatrix} 1 & s \\ 0 & 1 \end{pmatrix}. \tag{11}$$

The beam matrix at any location s with respect to the location of the first profiler ($s_0 = 0$) is therefore given by the formula:

$$\sigma(s) = R(s)\sigma(0)R(s)^T. \tag{12}$$

ISBN 978-3-95450-176-2

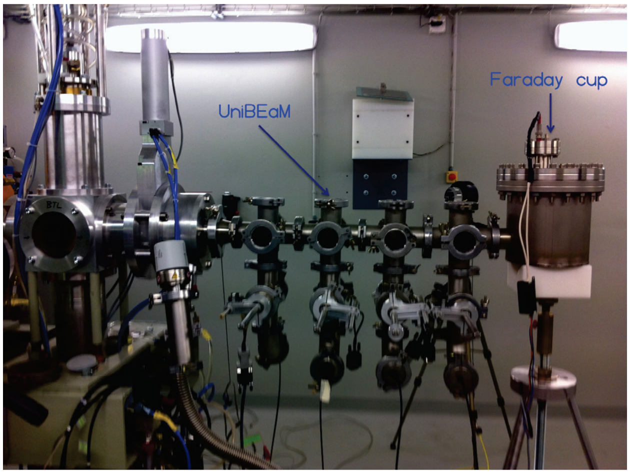

Figure 7: Four UniBEaM detectors and a Faraday cup installed on the BTL for the measurement of the transverse beam emittance in the horizontal plane.

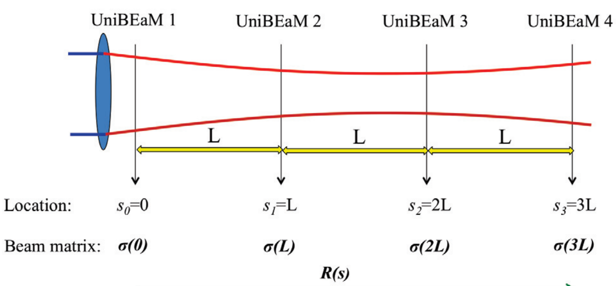

Figure 8: Multiple profilers for the measurement of the transverse beam emittance.

From equation (12) it can be derived that $\sigma_{11}(s)$ is a quadratic function of s:

$$\sigma_{11}(s) = \sigma_{22}s^2 + 2s\sigma_{12} + \sigma_{11} = f(s;\sigma_{11},\sigma_{12},\sigma_{22}), \quad (13)$$

where σ_{11}, σ_{12}, and σ_{22} are the components of the $\sigma(0)$ matrix. These components and consequently the transverse emittance were evaluated by fitting the $f(s;\sigma_{11},\sigma_{12},\sigma_{22})$ function to the four data points representing the estimated variance values as a function of the location s, as reported in Figs. 9 and 10 for the horizontal and vertical plane, respectively. The fit results for both planes and the corresponding emittance values are reported in Table 2.

CONCLUSIONS

The transverse beam emittance of the Bern medical cyclotron has been measured for the first time with the use of a novel beam monitor detector developed by our group. The emittance was evaluated with the two different techniques: quadrupole variation and multiple profilers installed along the beamline. The results were found to be in agreement within 1.65σ and 0.71σ for the horizontal and vertical plane, respectively. The transverse RMS beam emittance in the horizontal plane is almost 4 times bigger than the one in the vertical plane. This is due to acceleration in the horizontal plane, which causes an increase of the particle position spread along the x-direction. The measured emittance values will be implemented in the simulation of the BTL to provide beams of different shapes and sizes for multi-disciplinary research activities.

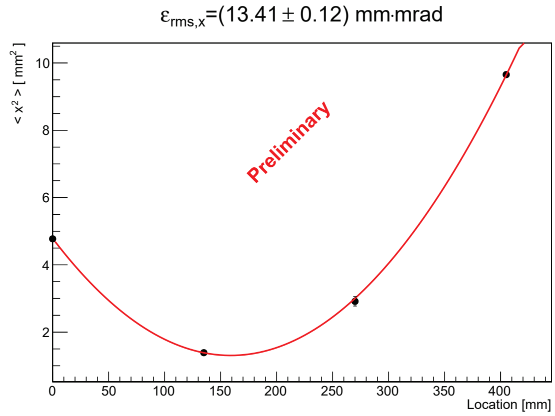

Figure 9: Variance as a function of the location obtained in the horizontal plane. The red line corresponds to the best fit.

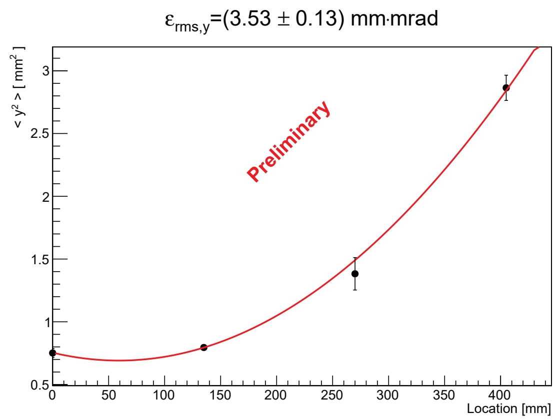

Figure 10: Variance as a function of the location obtained in the vertical plane. The red line corresponds to the best fit.

Table 2: Fit Parameters and the RMS Emittance Values Obtained by Using Multiple Profilers for Both Horizontal and Vertical Planes

Fit parameter	Horizontal plane	Vertical plane
σ_{11} [mm^2]	4.79 ± 0.09	0.75 ± 0.04
σ_{12} [mm·mrad]	−21.90 ± 0.48	−1.06 ± 0.19
σ_{22} [mrad^2]	137.72 ± 2.06	17.99 ± 1.15
$\tilde{\chi}^2$	0.47	0.76
ε_{rms} [mm·mrad]	13.41 ± 0.12	3.53 ± 0.13

ISBN 978-3-95450-176-2

REFERENCES

[1] S. Braccini, *The New Bern PET Cyclotron, its Research Beam Line, and the Development of an Innovative Beam Monitor Detector*, American Institute of Physics (AIP) Conf. Proc. 1525 (2013).

[2] S. Braccini et al., *A beam monitor detector based on doped silica and optical fibres*, 2012 JINST 7 T02001.

[3] M. Auger et al., *Low current performance of the Bern medical cyclotron down to the pA range*, Meas. Sci. Technol. 26 (2015) 094006 (6pp).

ISBN 978-3-95450-176-2

BEAM LOSS MONITORS FOR THE CRYOGENIC LHC MAGNETS*

M. R. Bartosik†, B. Dehning, M. Sapinski, A. Alexopoulos, CERN, Geneva, Switzerland
V. Eremin, E. Verbitskaya, IOFFE, St. Petersburg, Russian Federation
E. Griesmayer, CIVIDEC, Vienna, Austria

Abstract

The Beam Loss Monitoring system of the Large Hadron Collider close to the interaction points contains mostly gas ionization chambers working at room temperature, located far from the superconducting coils of the magnets. The system records particles lost from circulating proton beams, but is also sensitive to particles coming from the experimental collisions, which do not contribute significantly to the heat deposition in the superconducting coils. In the future, with beams of higher brightness resulting in higher luminosity, distinguishing between these interaction products and dangerous quench-provoking beam losses from the circulating beams will be difficult. It is proposed to optimise by locating beam loss monitors inside the cold mass of the magnets, housing the superconducting coils, in a superfluid helium environment, at 1.9 K. The dose then measured by such cryogenic beam loss monitors would more precisely correspond to the real dose deposited in the coil. This contribution will present results of radiation hardness test of $p^+\_n-n^+$ silicon detectors which, together with single crystal Chemical Vapour Deposition diamond, are the main candidates for these future cryogenic beam loss monitors.

INTRODUCTION

Motivation

It has been shown with particle shower simulations [1] that with the present configuration of Beam Loss Monitors (BLMs) close to the LHC interaction points (IPs), the ability to measure the energy deposition in the coil is limited because of collision debris masking the real beam loss signal (see Fig. 1).

In the current BLM system layout the particle showers from beam loss are partly shielded by the cryostat and the iron yoke of the magnets. The system can be optimised by locating beam loss monitors as close as possible to the sensitive superconductive coils. For the high luminosity LHC upgrade (HL-LHC) BLMs are therefore foreseen to be located near the superconducting coils inside the cold mass of the magnets in the superfluid helium at a temperature of 1.9 K [2] (see Fig. 2, courtesy of P. Ferracin).

The advantage of this new location is that the dose measured by the Cryogenic BLM will correspond much better to the dose deposited in the superconducting coil [6].

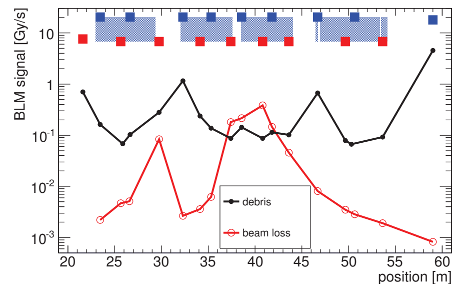

Figure 1: Signal in the coil and in the existing BLMs; Black trace: BLM signal from collision debris (one marker at each BLM location); Red trace: BLM signal from a quench-provoking loss inside the central superconducting quadrupole magnet of the focusing triplet (Q2B).

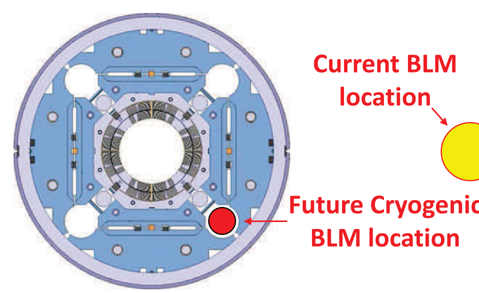

Figure 2: Cross section of a large aperture superconducting insertion magnet (MQXF) foreseen for HL-LHC with the current BLM and the future Cryogenic BLM locations shown.

Cryogenic BLM Requirements

From the electronic point of view the main requirements of the detector are a linear signal relationship with the received dose in the range between 0.1 and 10 mGy/s and a response time faster than 1 ms. The main mechanical challenge of a Cryogenic BLM system is to provide 20 years of maintenance free operation at temperature of 1.9 K [6]. Furthermore the Cryogenic BLM needs to work in a magnetic field of 2 T and be capable of withstanding a fast pressure rise up to 20 bar in case of a magnet quench. The selected detector technologies are based on semiconductor radiation detectors and current readout. The candidates under investigation are single crystal Chemical Vapour Deposition (scCVD) diamond [3] and p^+-n-n^+ silicon [4] detectors.

* This research project has been supported by a Marie Curie Early Initial Training Network Fellowship of the European Communitys Seventh Framework Programme under contract number (PITN-GA-2011-289485-OPAC).
† marcin.bartosik@cern.ch

ISBN 978-3-95450-176-2

CRYOGENIC RADIATION TEST

The specifications for cryogenic BLMs represents a completely new and demanding set of criteria that have never been investigated together before. The main unknown is the combination of the superfluid helium environment with a total ionizing radiation dose of 2 MGy. This motivated the first radiation-hardness tests of the diamond and the silicon detectors in a liquid helium environment, performed at CERN in December 2012 [5]. Degradation curves of scCVD were compared with silicon detectors in forward and reverse mode for a total integrated fluence of 1.22×10^{16} protons/cm^2 (corresponding to an integrated dose of about 3.26 MGy for the silicon and 3.42 MGy for the diamond detectors). Measurements at low doses were, however, missing due to the alignment procedure at the beginning of the irradiation test [6]. In November 2014 a complementary set of cryogenic irradiation measurements were therefore performed.

Setup

The main aim of the cryogenic irradiation test in November 2014 was to investigate the radiation hardness of the new 100 μm thick Si detectors in a liquid helium environment at 4.2 K and evaluate their advantages compared with more common 300 μm thick diodes.

The irradiation experiment was performed in the IRRAD facility in the East Experimental Area at CERN. This irradiation facility is frequently used for sample irradiation and detector performance tests [7].

The IRRAD beam line provides protons with a particle momentum of 24 GeV/c. The beam intensity is 5×10^{11}protons/cm^2 per spill with an rms beam size at the sample location of about 0.25 cm^2. The spill duration is between 400 - 450 ms.

For the final implementation in the LHC, direct current (DC) measurements are required. It was therefore decided to characterise the radiation hardness of the detectors by DC measurements. These measurements were performed using a stand-alone acquisition system developed for the LHC injectors [8] for which data acquisition client and data analysis software has been developed in the Python programming language [9].

The detectors under investigation were $p^+ - n - n^+$ silicon wafers with a thickness of 300 μm and 100 μm, 10 kΩcm resistivity, an active area of 36 mm^2 and aluminium as the metallisation material.

Results

At the end of the irradiation a total integrated fluence of 2.8×10^{15} protons/cm^2 was reached, corresponding to an integrated dose of about 0.75 MGy for the 300 μm Si.

The dependence of the collected charge on voltage (voltage scans) for the 100 μm Si and 300 μm Si detectors at different fluences are depicted in figures 3 and 4 respectively. A positive voltage corresponds to the forward bias operation mode.

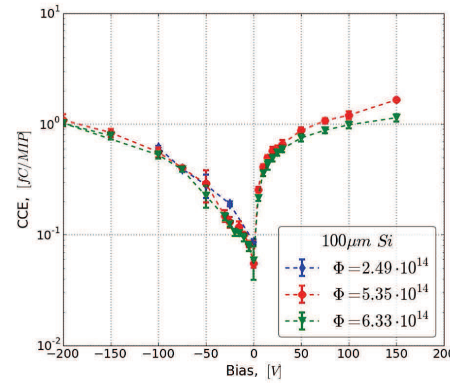

Figure 3: Voltage scan of a 100 μm Si detector for different integrated proton fluences.

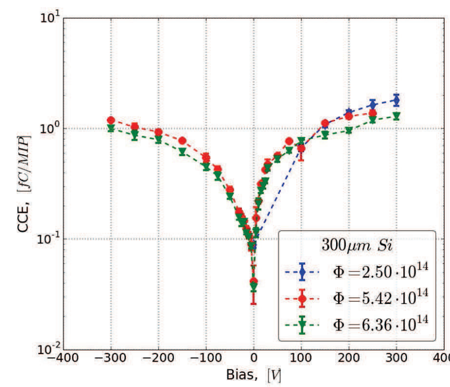

Figure 4: Voltage scan of a 300 μm Si detector for different integrated proton fluences.

The shape of the voltage scans were similar to those observed during the first cryogenic irradiation. The collected charge increases with increasing voltage and shows a slight tendency to saturate. In detectors operated as Current Injection Detector (CID), i.e. at forward bias, the increase was more apparent and the collected charge was larger than that at reverse bias.

This is caused by the reduction of the effective trap concentration due to filling via carrier injection. This implies an effective operation at low voltages which is the main advantage of a CID.

INSTALLATION OF CRYOGENIC BLMS ON THE OUTSIDE OF THE COLD MASS OF THE LHC MAGNETS

As a safety critical system, the long term reliability of the BLM detectors is very important. It was therefore decided

ISBN 978-3-95450-176-2

to install several Cryogenic BLMs on the outside of the cold mass of existing LHC magnets (see Fig. 5).

During the LHC Long Shut-down 1 (LS1) two 500 μm scCVD diamond detectors two 100 μm Si detectors and four 300 μm Si detectors were therefore mounted on the outside of the cold mass containing the superconducting coils in the cryostat of two LHC dipole magnets. Two types of detector holders were used, an Al_2O_3 based ceramic holder for one of the scCVD diamond detectors and seven FR-4 glass-reinforced epoxy laminate based holders for the other locations (see Fig. 6). Taking into consideration that the final Cryogenic BLMs have to be reliable and operate for 20 years radiation hard connectors, feedthroughs and semi-rigid coaxial cables were also installed. A multistep testing procedure with the use of light and ionizing radiation was performed to create signals on all detectors before and after installation [10].

These first cryogenic BLMs installed in operational, superconducting magnets will not only allow the behaviour of the detectors to be tested in realistic conditions, but also determine the validity of the integration in a setup at 1.9 K and in a high magnetic field.

First results of observing LHC beam losses with these detectors are expected in September 2015.

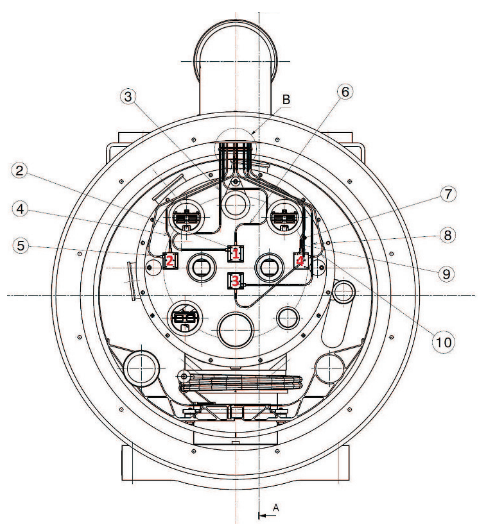

Figure 5: Cross section of an LHC dipole magnet showing the outer cryostat, the inner cold mass housing the superconducting coils and the position of cryogenic beam loss detectors on the end of the cold mass.

CONCLUSIONS

The main results are that the tested Si detectors survive under irradiation to 2.8 × 10^{15} protons/cm^2 in liquid helium environment, and charge carrier transport properties are strongly influenced by the electric field in irradiated detectors.

In order to minimize trapping, current injection into the detector sensitive region CID was tested. It has been shown that current injection developed as a tool for increasing the tolerance of silicon detectors to irradiation at moderate cooling, is still effective in liquid helium environment.

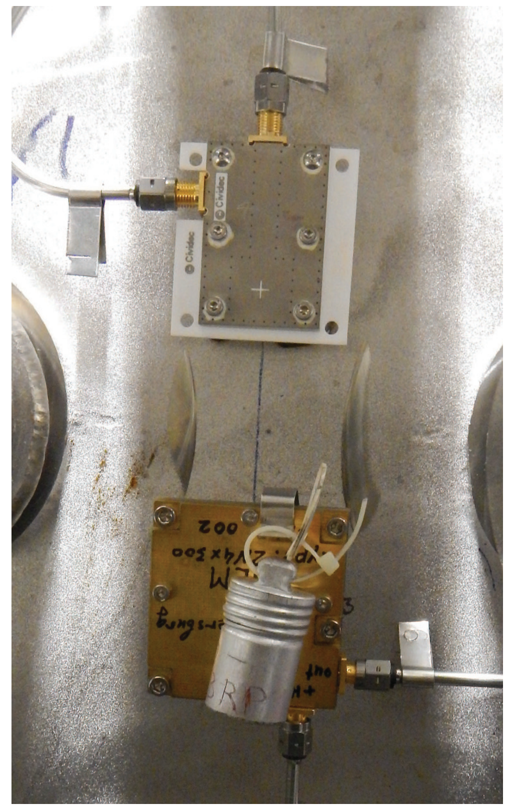

Figure 6: Top: scCVD diamond detector mounted using a ceramic based holder. Bottom: $p^+{-}n{-}n^+$ silicon detector mounted using an FR-4 glass-reinforced epoxy laminate based holder during testing with a gamma-radiation source (capsule).

ACKNOWLEDGMENTS

The project has been supported by: C. Kurfuerst, T. Koettig, J. Bremer, T. Eisel, C. Arregui Rementeria, L. Dufay-Chanat, A. Mereghetti, E. Griesmayer (CIVIDEC Instrumentation GmbH), C. Weiss, L. Gatignon, M. Glaser, F. Ravotti, J. Haerkoenen, E. Verbitskaya and P. Luukka, E. Guillermain, H. Pernegger, H. Jansen, V. Parma, T. Renaglia and a number of other CERN Beam Instrumentation and CERN Cryogenic Laboratory members.

REFERENCES

[1] A. Mereghetti, M. Sapinski et al: Estimation of thresholds for the signals of the BLMs around the LHC final focusing triplet magnets, Proceedings of IPAC 2012, New Orleans, USA.

[2] C. Kurfuerst et al.: Investigation of the use of Silicon, Diamond and liquid Helium detectors for Beam Loss Measurements at 2K, Proceedings of IPAC 2012, New Orleans, USA.

[3] C. Kurfuerst, et al., Radiation tolerance of cryogenic beam loss monitor detectors, proc. of IPAC 2013, Shanghai, China.

ISBN 978-3-95450-176-2

[4] M. R. Bartosik, et al.: Characterisation of SI detectors for the use at 2 K, proc. of IPAC 2013, Shanghai, China.

[5] C. Kurfuerst, et al., In situ radiation test of silicon and diamond detectors operating in superfluid helium and developed for beam loss monitoring, Nuclear Instruments and Methods in Physics Research A 782 (2015) 149158.

[6] C. Kurfuerst, Cryogenic Beam Loss Monitoring for the LHC, PhD thesis.

[7] F. Ravotti, et al., Upgrade scenarios for irradiation lines: Deliverable Report, Advanced European Infrastructures for Detectors at Accelerators AIDA-D8.4.

[8] C. Zamantzas et al., System Architecture for measuring and monitoring Beam Losses in the Injector Complex at CERN, Proceeding of IBIC 12, Tsukuba, Japan.

[9] A. Alexopoulos, Cryogenic Semiconductor Detectors: Simulation of Signal Formation & Irradiation Beam Test, MSc thesis.

[10] M. Bartoisk, et al., Cryogenic beam loss monitoring for the superconducting magnets of the LHC, Proceedings of IBIC2014, Monterey, CA, USA.

ISBN 978-3-95450-176-2

A CRYOGENIC CURRENT COMPARATOR FOR THE LOW-ENERGY ANTIPROTON FACILITIES AT CERN

M. Fernandes*, The University of Liverpool, U.K. & CERN, Geneva, Switzerland
J. Tan, CERN, Geneva, Switzerland
C. Welsch, Cockcroft Institute & The University of Liverpool, U.K
R. Geithner, R. Neubert, T. Stöhlker, Friedrich-Schiller-Universität & Helmholtz Institute Jena, Jena, Germany
M. Schwickert, GSI, Darmstadt, Germany

Abstract

Several laboratories have shown the potential of Cryogenic Current Comparators (CCC) for an absolute measurement of beam intensity down to the nA level. This type of current monitor relies on the use of Superconducting QUantum Interference Device (SQUID) magnetometers and superconductor magnetic shields. CERN, in collaboration with GSI Helmholtz Centre for Heavy Ion Research, Jena University, and the Helmholtz Institute Jena are currently developing an improved version of such a current monitor for the Antiproton Decelerator (AD) and Extra Low ENergy Antiproton (ELENA) rings. The primary goals are a better current measurement accuracy and overall enhanced system availability. This contribution presents the design of the CCC, an estimation of its resolution, dynamic limitations of the SQUID, as well as a description of the modifications to the coupling circuit and cryostat that were required to optimize the monitor for the anticipated beam parameters. First results from beam measurements are also presented. To our knowledge these are the first CCC beam current measurements performed in a synchrotron and the first to be performed with both coasting and bunched beams.

LOW-INTENSITY BEAMS CURRENT MEASUREMENT

Low-intensity charged particle beams present a considerable challenge for existing beam current diagnostics [1]. This is particularly significant for coasting beams with average currents below 1 μA which is the minimum resolution of standard DC Current Transformers. Other monitors, such as AC Current Transformers or Schottky monitors (currently in use in AD) are able to measure low-intensity beam currents, but neither can simultaneously provide an absolute measurement, with a high current and time resolution, which is at the same time independent of the beam profile, trajectory and energy.

At CERN's low-energy antiproton decelerators, the AD and the ELENA (currently under construction) rings, circulate both bunched and coasting beams of antiprotons with average currents ranging from 300 nA to 12 μA. Having a current measurement with the above mentioned characteristics would benefit the machine operation and optimization.

To meet these requirements, a low-temperature SQUID-based Cryogenic Current Comparator (CCC) is currently under development [2,3]. Similar devices have already been developed for electrical metrology [4,5], and have already been used for beam current measurements in particle accelerator [6,7]. The current project, is a collaboration between CERN, GSI, Jena University and Helmholtz Institute Jena to develop this technique further.

The main design specifications for the monitor are: beam current resolution < 10 nA; and measurement bandwidth of 1 kHz.

Overview of the Functioning Principle of the CCC

The CCC (see schematic in Fig. 1) works by measuring the magnetic field induced by the particle beam current. This field is concentrated in a high-permeability ferromagnetic pickup core, from which it is coupled into the SQUID sensor. These are highly sensitive magnetic flux sensors that permit sensing the weak fields created by the beam. A superconducting magnetic shield structure around the pickup-core, as described in [7,8], renders the coupled magnetic field nearly independent of the beam position and makes the system practically immune to external magnetic field perturbations. The unique advantages of the CCC monitor

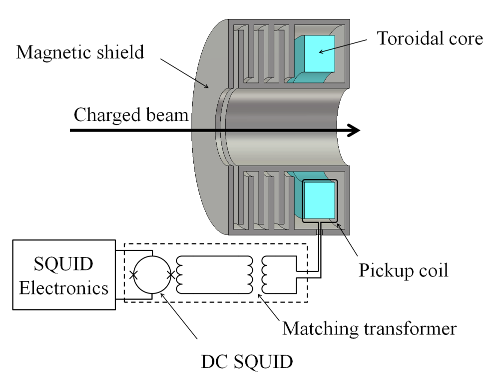

Figure 1: Schematic of the CCC.

are its ability to measure the average current of both coasting and bunched beams with nA resolution, as has been demonstrated by other laboratories. Previous installations of the CCC for beam current measurements were, however, usually

* Funded by the European Union's Seventh Framework Programme for research, technological development and demonstration under grant agreement no 289485.

ISBN 978-3-95450-176-2

restricted to slowly extracted beams in transfer lines. When used for the high-resolution measurement of bunched beams on a circular machine, the stability limitation of SQUIDs, when using a Flux-Locked Loop (FLL) read-out scheme [9], and the immunity to mechanical and electromagnetic (EM) perturbations soon become limiting factors.

CCC CHARACTERISTICS

The superconducting shield and pickup core of the AD CCC were developed by GSI, Jena University and Helmholtz Institute Jena. This core has a single turn inductance $L_P = 104\,\mu$H, while the SQUID device has an input coil self-inductance $L_i = 1\,\mu$H and a mutual inductance $M_i = 3.3\,\phi_0/\mu$A [1].

Coupling Circuit and Resolution

The circuit shown in Fig. 2 couples the beam current signal into the SQUID. An appropriate choice of the pickup core and matching transformer are important to optimize the strength of the coupled signal, and thus improve the Signal to Noise Ratio (SNR). The theoretical dc-gain of this circuit (flux coupled to the SQUID per unit of beam current) is $S_{I_B} = \Phi_S(t)/I_B(t) = 10.5\,\phi_0/\mu$A [3] (in SQUID systems literature it is more commonly quoted the inverse quantity $95.2\,$nA$/\phi_0$). The measured gain of the coupling circuit,

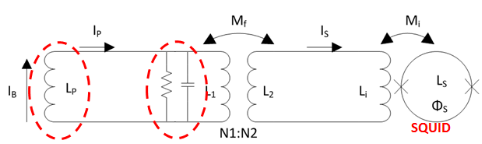

Figure 2: Coupling circuit that converts the beam current into a magnetic flux to be measured by the SQUID.

obtained after factoring the gain of SQUID/FLL electronics, was:

- Calibration winding: $S_{I_B} = 10.46\,\phi_0/\mu$A,
- Beam current wire: $S_{I_B} = 10.44\,\phi_0/\mu$A.

Which are both very close to the computed theoretical value.

Low-pass Filtering in the Coupling Circuit

Flux-Locked Loop (FLL) SQUID systems impose a maximum limit on the slew-rate of the signal to be measured [10]. In order for the SQUID to keep a constant working point an equilibrium between FLL bandwidth, system noise and maximum slew-rate needs to be observed [3]. In modern SQUID/FLL systems, such as the one used in the current AD CCC, the maximum slew-rate of the magnetic flux coupled to the SQUID needs to be $< 5\,$Mϕ_0/s

The nominal beam injected in the AD has the following parameters: $f_{\mathrm{rev}} = 1.59\,$MHz, $h = 6$ with 4 buckets filled, $4\sigma_t^{\mathrm{bunch}} = 30\,$ns and $Q^{\mathrm{bunch}} = 1.25 \times 10^7$e. When such a beam is injected the average current jumps from 0 to 12 µA, and the slew-rate of the flux coupled to the SQUID reaches 400 Mϕ_0/s (assuming a constant gain of the coupling circuit). To reduce the magnetic flux slew-rate, without decreasing the low-frequency coupling strength, a low-pass filtering has been implemented. In order to filter the input signal

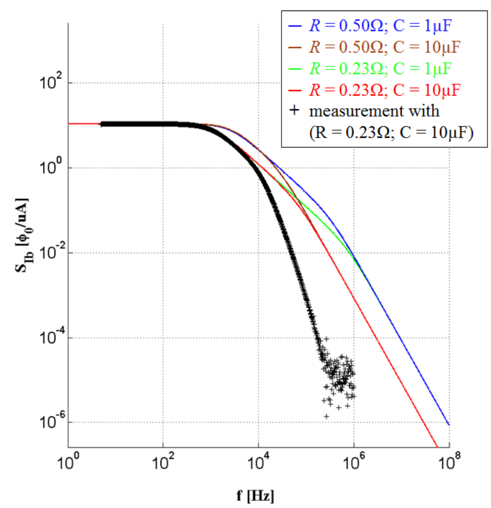

Figure 3: Theoretical frequency response of the coupling circuit alone, for various values of R and C. And laboratory measurement of the frequency response of the complete system (coupling circuit plus cryostat) using a beam simulating wire passing through the cryostat beam pipe (in black).

an RC-parallel filter was added to the primary side of the coupling circuit of the CCC. The theoretical frequency response for different values of the RC values are shown in Fig. 3. The measured transfer function closely follows the theoretical curve until one decade after the cut-off frequency. For higher frequencies a stronger attenuation is observed due to the fact that this measurement takes into account the complete system, coupling circuit plus cryostat (described in next section). Laboratory measurements of different configurations for the coupling circuit filter were also presented by R. Geithner during IBIC'15 conference.

This filter, however, only reduces the maximum slew-rate of the signal coupled to the SQUID, during AD antiproton beam injection to 37 Mϕ_0/s. This is still one order of magnitude above the stability limit of the SQUID/FLL system.

Low-pass Filtering in the Cryostat

In order to further reduce the slew-rate of the signal coupled to the SQUID it was decided to add an RF-bypass to the ceramic gap in the beam pipe. This capacitance in parallel with the high-resistance metallisation on the surface of the ceramic forces the high frequency components of the beam induced mirror current to flow through the beam pipe instead of the outer shell of the cryostat. Thus removing the high-frequency components of the magnetic field reaching the CCC toroid and in so-doing providing the desired low-pass filtering effect. In order to dimension the RF-bypass

[1] $\phi_0 = 2.0678 \times 10^{-15}$ Wb is the magnetic flux quantum which is the unit commonly used for magnetic flux when dealing with SQUID systems.

ISBN 978-3-95450-176-2

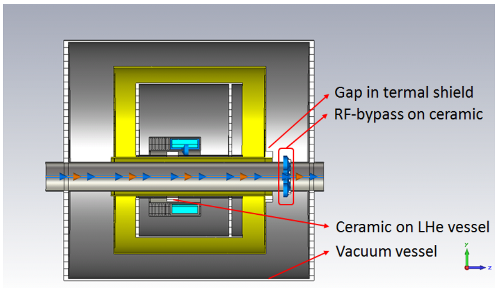

Figure 4: Simplified model of the real cryostat used in time-domain simulation of a single bunch. The CCC shield is shown, but was not considered for the simulation.

the following procedure was followed. First a simulation for a single AD bunch at injection was performed using the Wakefield Solver of the CST Studio Suite. In this simulation a simplified model of the fabricated cryostat was used (see Fig. 4). Since this was a relatively low frequency problem, the RF-bypass impedance was modelled by lumped elements. The signal coupled to the pickup was obtained via a magnetic field probe. By scanning several values of the total capacitance across the ceramic gap, the bunch responses in Fig. 5 were obtained.

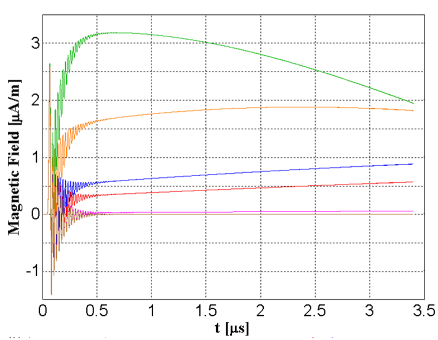

Figure 5: Time domain simulation of the magnetic field coupled to pickup core, induced by the passage of a single bunch of the AD injection beam.

Each iteration of this simulation took a considerable amount of time, so it was not possible to run it for a period of time long enough for the magnetic field signal to decay to zero. Hence the remaining part of signal had to be extrapolated, and this was done using a polynomial function. Despite its limitations in estimating the signal evolution, this analysis should, in principle, always result in an overestimation of the magnetic flux slew-rate of the bunch train, which is the quantity we want to limit.

Having an estimation of the magnetic signal induced by the passage of a single bunch, the signal induced by the passage of the bunch train was synthetised assuming linearity of the system.

In order to use this signal as an input to the transfer function of the coupling circuit in Fig. 2, and estimate the combined filtering effects, the magnetic signal of the bunch train

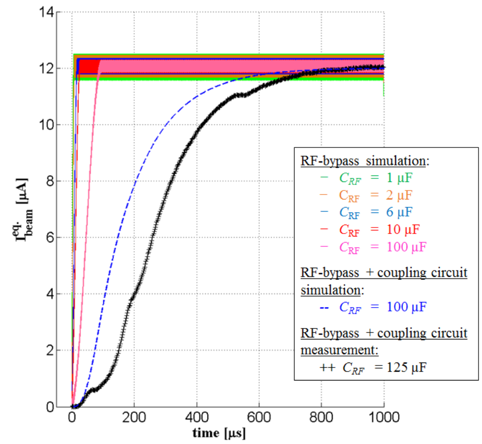

Figure 6: Simulation of the signal (referred to equivalent beam current) coupled to the SQUID at AD beam injection, considering the RF-bypass alone and also the combined effect with the coupling circuit filter. And laboratory measurement using a signal generator passing a similar current signal through a beam simulating wire.

was normalized to an equivalent beam current. For this, the steady-state beam average current $I^{avg.}_{beam} = 12\,\mu A$ was used as a normalization factor. The equivalent beam current signals for the different values of capacitance in the RF-bypass are shown in Fig. 6.

Simulating the passage of these equivalent current signals through the low-pass filtered coupling circuit, one obtains the values in Table 1 for the maximum slew-rate that the SQUID will be subjected to during AD beam injection:

Table 1: Maximum Estimated SQUID Flux Slew-rate for Diffent RF-bypass Capacitance Values

RF-bypass C [µF]	1	2	6	10	100
Max. slew-rate [Mϕ_0/s]	6.06	6.01	5.84	5.63	2.83

For $C \geq 100\,\mu F$ the maximum slew-rate falls below the stability limit of $5\,M\phi_0/s$. The value used in the RF-bypass capacitance in the AD implementation of the monitor is therefore $C = 125\,\mu F$. In Fig. 6 is shown the measured response of the complete system to a current identical to AD injection passing trough a beam simulating wire.

AD BEAM MEASUREMENTS

The newly fabricated cryostat and CCC were installed in the AD-ring before AD operation started in 2015, and beam measurements have been taken on various occasions. Since the CCC measures primarily the beam current, while the most relevant figure of merit of the AD ring operation is the "intensity" or number of accumulated particles, the current

ISBN 978-3-95450-176-2

measurement needs to be normalized against the particles velocity.

Current Measurement

During commissioning and before the first beams were injected two issues were identified that have an impact on the performance of the current measurement. Excessive perturbations were observed at frequencies that are odd multiples of 50 Hz and pulsing the bunch rotation cavities (occurring once per cycle, around 50 µs after injection) was seen to cause a significant flux jump in the SQUID/FLL working point. Both these limitations can be seen in the middle plot

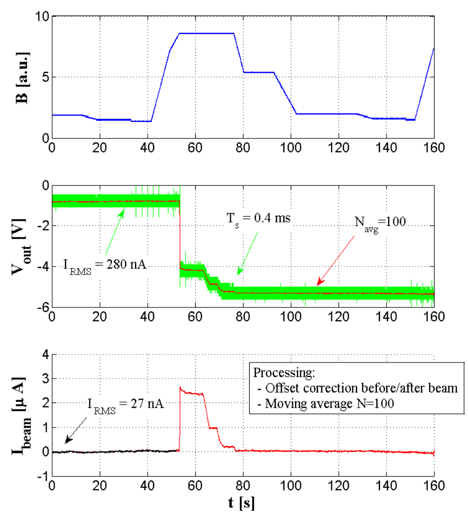

Figure 7: Top Plot: Magnetic Cycle of AD Dipoles in arbitrary Units. Middle plot: SQUID/FLL raw signal of beam current (in green), and same signal filtered with a moving average (in red). Bottom plot: calibrated beam current measurement after filtering and baseline recovery (before beam injection and after beam extraction).

of Fig. 7, with the green trace showing the raw SQUID/FLL voltage signal. The RMS noise (caused essentially by the 50 Hz harmonics) amounts to 275 nA of beam current, while the flux jump is also quite clear as the measured current decreases when it should increase on beam injection.

Both these limitations can be mitigated by post-processing the acquired raw signal. As a first approach the excessive perturbation was filtered out using a time-domain moving average low-pass filter. The flux jump at injection can be corrected by adjusting the offset of the signal before and after injection, knowing that before injection and after extraction the beam current has to be zero.

In Fig. 7 is shown a beam commissioning cycle where the beam was entirely lost during the first cooling plateau. The instant where beam is lost are clearly visible, this represents a clear improvement over the Schottky measurement used to date. This demonstrated that the CCC can be an invaluable tool both for reducing the time needed to setup the beam and for increasing machine efficiency.

Intensity Measurement

The number of circulating antiprotons can be obtained by normalizing the current measurement with the particle velocity (in the AD, $\beta_{\text{inj.}} = 0.97$ and $\beta_{\text{ej.}} = 0.11$). The velocity profile was calculated from the magnetic cycle of the dipole magnets.

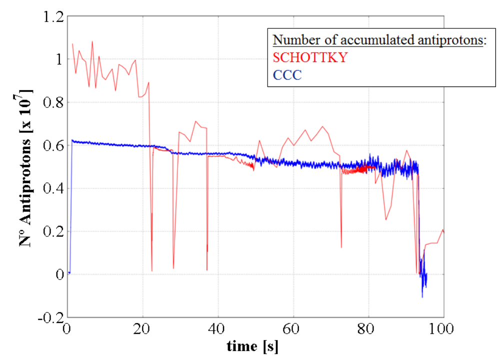

Figure 8: Comparison of the “intensity” (number of antiprotons) measurement between the longitudinal-Schottky and the CCC monitors, during one AD cycle (with 10% of nominal intensity).

From Fig. 8 it is possible to observe that the CCC measurement is much more precise during the coasting beam phases than the Schottky one. One limitation, inherent to the normalization method, is that for small β the errors in the current measurement due to the 50 Hz harmonics are greatly amplified.

CONCLUSION

The different aspects of a CCC current monitor adapted to the measurement of the low-intensity antiproton beams in AD have been presented. A monitor based on this design has been installed, and first beam measurements have been reported. To our knowledge these are the first CCC beam current measurements performed in a synchrotron, on both coasting and bunched beams.

The two major challenges in the adaptation of this type of monitor to the dynamic range and bunched beam of the AD were to guarantee the SQUID/FLL stability when faced with a large input slew-rate at injection, and to avoid the excess noise contamination which may limit the superior current resolution that CCC monitors have shown in other laboratories.

While the first has been successfully addressed the second is still under investigation. It is suspected that this noise may be due to currents flowing in the beam pipe that are then picked up by the monitor. The RF-bypass (needed in order to reduce the beam signal slew-rate) installed in the ceramic gap may therefore be responsible for these two limitations. One solution could be to move this to the gap in the thermal shield. Such optimization is still underway in order to deliver the CCC as a fully operational beam current measurement device for the AD.

ISBN 978-3-95450-176-2

ACKNOWLEDGMENT

The authors would like to acknowledge the work and support of Andrew Lees, Torsten Koettig and Conor Sheehan from CERN's TE-CRG group, who are providing the cryogenic system design, including the cryostat mechanical design, Jean-Pierre Brachet and Didier Lombard from CERN's EN-MME group, and respective teams responsible for the cryostat fabrication, and Ewa Oponowicz and Michael Ludwig from CERN's BE-BI group, who developed the acquisition software. I also thank Patrick Odier, Jeroen Bellemann from CERN, Febin Kurian, Marcus Schwickert and Thomas Sieber from GSI, René Geithner from Helmholtz Institute Jena and Ralf Neubert from Jena University for the many fruitful discussions. Finally I acknowledge the oPAC network support which has made this work possible.

REFERENCES

[1] D. Belohrad, "Beam Charge Measurements," WEOC01, DIPAC2011 proceedings.

[2] M. Fernandes et al.,"Cryogenic Current Comparator for Low Intensity Beam Current Measurement", MOPF25, IBIC'13 Proceedings, Oxford, U.K. (2013)

[3] M. Fernandes et al.,"A Cryogenic Current Comparator for the Low Energy Antiprton Facitilities at CERN", WEPF04, IBIC'14 Proceedings, Monterey, U.S.A (2014)

[4] I.K. Harvey, Rev. Sci. Instrum. 43 (1972) 1626.

[5] W. Vodel et al., "Chapter 9.6: SQUID-Based Cryogenic Current Comparators", In: P. Siedel, Applied Superconductivity Handbook on Devices and Applications, Volume2, (Weinheim: Wiley-VCH, 2015).

[6] R. Geithner et al.,"A SQUID-based Beam Current Monitor for FAIR/CRYRING", WECZB1, IBIC'14 Proceedings, Monterey, U.S.A. (2014)

[7] A. Peters et al., "A cryogenic current comparator for the absolute measurement of nA beams," BIW98, Standford, May 1998, (p. 163), AIP conference proceedings.

[8] K. Grohmann et al., Cryogenics 16(10) (1976) 601.

[9] D. Drung and M. Muck, "Chapeter 4: SQUID Electronics", In: J. Clarke and A. Braginski, The SQUID Handbook. Vol. I: Fundamentals and Technology of SQUIDS and SQUID Systems. Materials and Manufacturing Processes, (Weinheim: Wiley-VCH, 2005).

[10] R. H. Koch, "Maximum theoretical bandwidth and slewrate of a dc SQUID feedback system," IEEE Transactions on Applied Superconductivity 7(2), p. 3259 (1997).

ISBN 978-3-95450-176-2

BLM CROSSTALK STUDIES ON THE CLIC TWO-BEAM MODULE

M. Kastriotou, E. Nebot del Busto, CERN, Geneva, Switzerland; University of Liverpool, UK; Cockroft Institute, Warrington, UK
W. Farabolini, CERN, Geneva, Switzerland; CEA/DSM/IRFU, Saclay, France
S. Doebert, E. Effinger, E.B. Holzer, F.S. Domingues Sousa, W. Viganò, CERN, Geneva, Switzerland
C.P. Welsch, University of Liverpool, UK; Cockroft Institute, Warrington, UK

Abstract

The Compact Linear Collider (CLIC) is a proposal for a future linear e^+-e^- collider that can reach 3 TeV center of mass energy. It is based on a two-beam acceleration scheme, with two accelerators operating in parallel. One of the main elements of CLIC is a 2 m long two-beam module where power from a high intensity, low energy drive beam is extracted through Power Extraction and Transfer Structures (PETS) and transferred as RF power for the acceleration of the low intensity, high energy main beam. One of the potential limitations for a Beam Loss Monitoring (BLM) system in a two-beam accelerator is so-called "crosstalk", i.e signals generated by losses in one beam, but detected by a monitor protecting the other beam. This contribution presents results from comprehensive studies into crosstalk that have been performed on a two-beam module in the CLIC Test Facility (CTF3) at CERN.

INTRODUCTION

The CLIC [1] is a proposal for an electron/positron collider where particles will be boosted to energies up to 1.5 TeV. The required accelerating gradient (100 MV/m) can be achieved via a novel two beam acceleration scheme. RF power from a high intensity (~100 A), low energy (2.37 GeV) Drive Beam (DB) is extracted via Power Extraction and Transfer Structures (PETS), and transferred through a waveguide system to supply the high gradient RF cavities of the high energy, low current (~1 A) Main Beam (MB). The principal constituent of the CLIC linacs is a 2 m long module (the Two Beam Module, TBM), which is a combination of accelerating structures, quadrupoles and PETS. Five different types of TBMs are sufficient for the manufacture of the main CLIC accelerating complex. The simultaneous operation of two parallel accelerators can be challenging for the design of a Beam Loss Monitoring (BLM) system. Losses from one beam line can be detected by the BLMs protecting the other one, reducing the capability of estimating the origin of the losses. This phenomenon is known as crosstalk. In the CLIC Conceptual Design Report the proposed beam loss monitoring system for machine protection is based on ionisation chambers, since they satisfy the requirements in terms of sensitivity and dynamic range. Distributed detectors, such as optical fibres, are also under investigation for their ability to cover the full beam line, preventing potentially dangerous beam losses from going undetected. The present work summarises BLM crosstalk measurements for two different detectors, Little Ionisation Chambers (LICs) and optical fibre BLMs (OBLMs), performed at the prototype TBM hosted at CTF3.

TWO BEAM MODULE LAYOUT AT CTF3

The CTF3 complex at CERN was constructed with the aim of studying the feasibility of the CLIC two-beam technology. CALIFES (Concept d'Accélérateur Linéaire pour Faisceau d'Electron Sonde) is a 26 m electron linac with a Cs_2Te photoinjector pulsed by a UV laser. It provides a flexible electron beam with a bunch charge in the range of 0.05 - 0.6 nC and energy up to 200 MeV with a 1.5 GHz bunching frequency. CALIFES aims to mimic the CLIC main beam [2]. To examine the feasibility of the high current beam production and transport, a scaled version of the CLIC Drive Beam providing an electron beam of up to 28 A with a maximum energy of 120 MeV has been built [3].

The first CLIC Two Beam Module prototype was installed in CTF3 in May 2015. It comprises two PETS and two quadrupoles on the Drive Beam side, four accelerating structures (ACS) on the Main Beam, and instrumentation including one Beam Position Monitor (BPM) for each beam and two wakefield monitors on the main beam.

To study the crosstalk of the BLMs at the CTF3 TBM, four LICs and two optical fibres were installed on both sides of the TBM.

THE BLM EXPERIMENTAL SETUP

The LICs installed at the TBM are cylindrical ionisation chambers, with a diameter of 9 cm and a length of 18 cm. They consist of three circular, parallel plate, Al electrodes separated by 0.5 cm and are filled with N_2 at a pressure of 0.4 bar. Four detectors were used to cover the module. Two of them where installed on the main beam, approximately 5 cm downstream of the TBM accelerating structures, and two on the drive beam, around 10 cm downstream of the quadrupoles.

The OBLM systems consist of an optical fibre coupled to a photosensor. High energy particles generated by beam losses produce Cherenkov light in the optical fibre. These photons propagate in the fibre and are detected by the photosensor, giving information on the intensity of the loss and, if the timing is taken into consideration, also its original location [4]. Two high-OH, pure silica optical fibres from Thorlabs [5] were installed, approximately 15 cm above each beam line. On the Main Beam side, the fibre covers both the TBM and a 4 m upstream segment, while on the Drive Beam side the optical fibre extends over the TBM but only

ISBN 978-3-95450-176-2

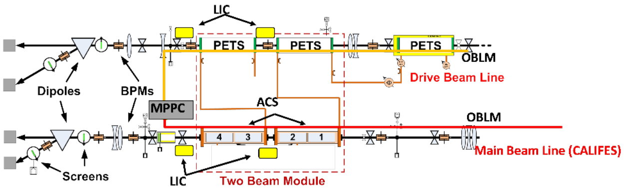

Figure 1: Layout of the BLM installation on the TBM in CTF3 (modified from [2]).

1.5 m upstream. The fibres are located towards the upstream of the TBM to include important elements of the two beam lines (a PETS at the drive beam and an optical transition radiation screen at the main beam). The characteristics of the two optical fibres are summarised in Table 1. In order to achieve higher sensitivity at the low current CALIFES beam line, a fibre of larger diameter (365 nm) than the one of the drive beam was selected. The optical readout consists of a Hamamatsu 14400-pixel Multi-Pixel Photon Counter (MPPC) S12572-25C [6], connected to an AC coupled circuit based on a 50 Ohm resistor and a 100 nF capacitor. In Fig. 1 the schematic layout of the TBM and the BLMs installed is illustrated. Fig. 2 shows the installation of the fibres and the LICs on the main beam. To shield the electronics from RF noise, custom made modules that contain the MPPC readout and a low-pass filter for high frequency noise filtering at the high voltage input have been designed. The modules are mounted in an RF shielded crate with a dedicated back plane for the voltage and ground distribution. The crate is located downstream of the TBM on the main beam side, and only the downstream signal of the optical fibers was acquired. The data acquisition of all BLMs is performed via a 12-bit 100 MS/s SIS-330x ADC card controlled via a VME crate. The schematic layout of the OBLM acquisition electronics is presented in Fig. 3.

Table 1: Optical Fibre BLM

	Main Beam	Drive Beam
Length (m)	7	5
core diameter (μm)	365	200
clad diameter (μm)	400	240
NA(numerical aperture)	0.22	0.22

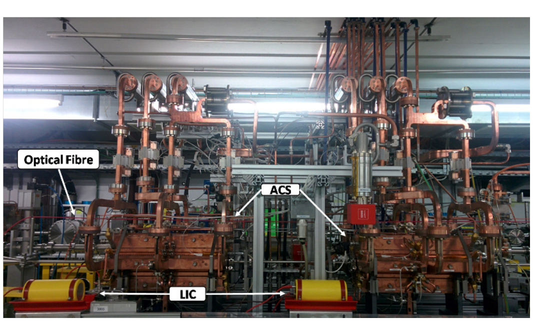

Figure 2: Installation of BLMs at the TBM Main Beam.

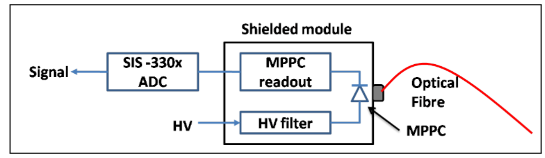

Figure 3: Schematic layout of the OBLM acquisition electronics.

CROSSTALK MEASUREMENTS WITH CALIFES

Beam loss measurements were performed while increasing the beam charge at CALIFES from 0.7 nC (10 bunches) to 11.4 nC (200 bunches), as measured by the beam charge monitor after the electron gun. A set of 100 shots were acquired for each setting. The sum signal from the BPM positioned just upstream of the TBM was used for measuring the relative beam charge on a shot to shot basis.

Califes Normal Operation

For the beam charges observed during this experiment the ionisation chambers did not monitor any losses. The sensitivity limitation is a consequence of the 12-bit resolution of the ADC cards, since these chambers have demonstrated charge measurements down to a few pA. Both drive beam and main beam optical fibre BLMs were sensitive to the losses from the CALIFES beam. The mean signal of the Main Beam optical fibre BLM in the case of a 160 bunch train is presented in Figure 4. The first, low peak can be explained as the contribution of the dark current from the CALIFES electron gun whereas the large peak is induced from beam losses. The detected charge Q was calculated via

$$Q = \frac{1}{R_L} \int_{t_0}^{t_1} V(t)dt \tag{1}$$

where $R_L = 50\,\Omega$ is the measuring load, V(t) the BLM signal and $(t_0, t_1) = (1588.5, 1718.8)$ the integration limits that include only the beam loss signal. Fig. 5 summarizes the BLM detected charge versus CALIFES beam charge, for the two fibres over the TBM. In Fig. 6 the crosstalk of main to

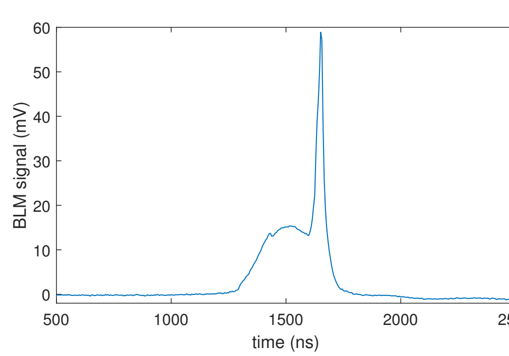

Figure 4: Signal of CALIFES beam losses from the Main Beam optical fire BLM.

ISBN 978-3-95450-176-2

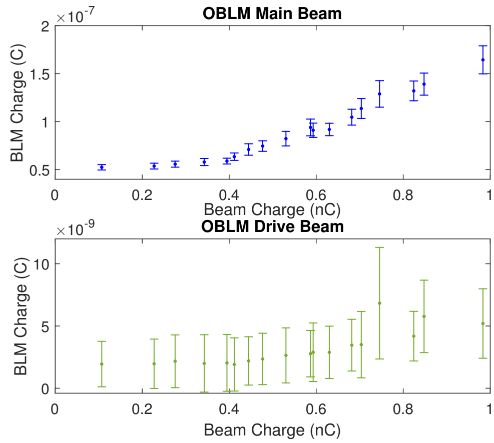

Figure 5: Charge generated in the Main (top) and Drive (bottom) Beam BLMs during CALIFES operation.

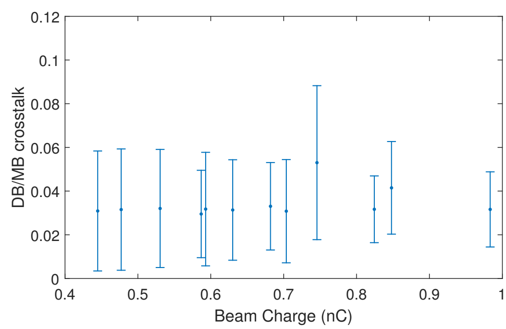

Figure 6: Crosstalk of Main to Drive Beam as measured by the oBLM system.

drive beam has been defined as

$$c_{MB} = \frac{Q_{DB}}{Q_{MB}} \tag{2}$$

where Q_{DB} and Q_{MB} are the total charges detected by the drive and the main beam optical fibres respectively. For the given beam and optics settings, the crosstalk signal on the drive beam OBLM was found to be independent of the beam current and ranges from 3 % to 5.5 % of the main beam OBLM signal, with a mean value of 3.4 %.

Loss scenario with Califes

The measurements were repeated for the case in which an optical transition radiation (OTR) screen [7], located approximately 3 m upstream the TBM, was intercepting the beam. In this case losses were detected by all BLMs. The signals of the main beam optical fibre BLM indicate saturation of the photodetector. As a result, in this case the crosstalk was only computed using the LIC detectors. The calculation was performed via Eq. 3 where Q_{DB} and Q_{MB} were the charges collected from the detectors with the largest signal on the drive and main beam respectively, namely the upstream LICs. Fig. 7 shows the signals of the two fibres and the two upstream LICs for several beam intensities. The signals of the upstream main beam ionisation chamber,

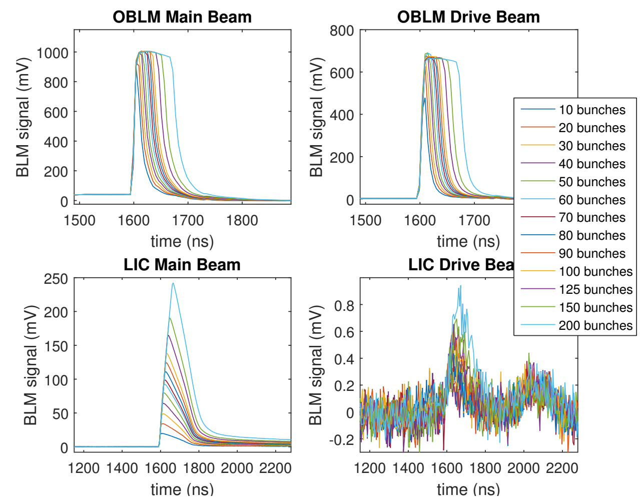

Figure 7: BLM signal after OTR screen insertion to CALIFES.

presented on the right side of Fig. 7, show a very large peak exceeding 200 mV for high beam current (200 bunches). This indicates the generation of significant losses. On the drive beam side, the peak LIC signals are lower than 1 mV and barely exceed the noise level. For the estimation of the

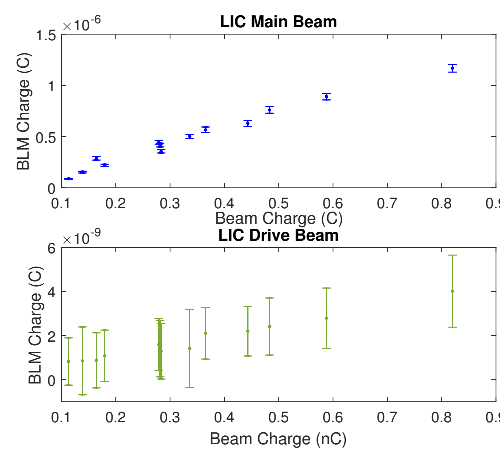

Figure 8: Signal of Main Beam and Drive Beam LIC after OTR screen insertion to CALIFES.

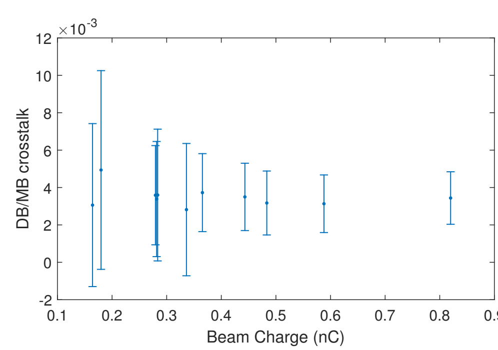

Figure 9: Crosstalk of the Main Beam to Drive Beam LIC after OTR screen insertion into the CALIFES.

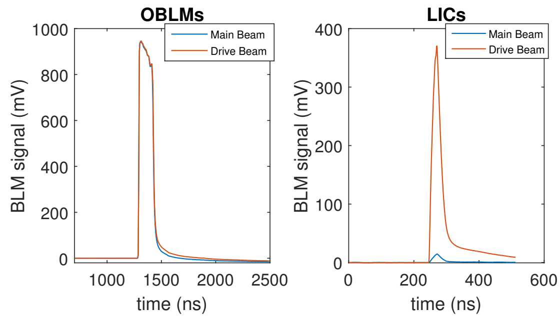

Figure 10: BLM signal induced by drive beam.

charge collected in the LIC, Eq. 1 was used with integration limits $(t_0, t_1) = (1588.5, 1822.9)$ for both detectors.

The BLM signals for losses induced with different beam intensities are summarised in Fig. 8, increasing as expected with higher beam charge. The main beam crosstalk to the drive beam, calculated from Equation 3, is presented in Fig. 9 and is in all cases lower than 0.6 %.

CROSSTALK MEASUREMENTS WITH THE DRIVE BEAM

For the study of the drive beam crosstalk signal to the main beam BLMs a set of 100 shots was acquired with the drive beam on and CALIFES off. The mean beam current, as measured using the BPM located before the TBM, was 1.12 A. During the data-taking, the beam transmission was not ideal and the losses measured by the BLMs were significant. Fig. 10 shows the mean BLM signals for the examined detectors. In both OBLMs the photosensors are clearly saturated, hence no conclusion on the crosstalk for OBLMs can be drawn. The upstream LICs showed the highest signals and were used for the crosstalk estimation. The charge collected by the detector was estimated via Eq. 1, using integration limits that contain only the main peak, in particular $(t_0, t_1) = (1276, 1568)$ for the drive and $(t_0, t_1) = (1276, 1536)$ for the main beam.The crosstalk of the drive beam to main beam ionisation chambers can be calculated from

$$c_{DB} = \frac{Q_{MB}}{Q_{DB}} \qquad (3)$$

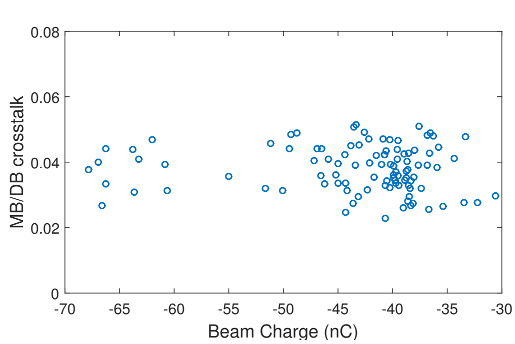

Figure 11: Crosstalk of the Drive Beam to Main Beam.

and the results are illustrated in Fig 11. For the given drive beam settings the crosstalk to the main beam detectors ranges from 2 to 5 % with a mean value of 3.68 %.

CONCLUSIONS

The observations of crosstalk in the CTF3 TBM may be one of the main limitations of a future CLIC BLM system. In this contribution we have presented the first set of measurements performed at the first prototype TBM. The main beam to drive beam crosstalk and vice-versa have been studied independently and estimated at 1 - 5 %. Previous simulations presented at the CLIC Conceptual Design Report have shown that a destructive loss (1 % of the beam) at the beginning of the drive beam (i.e. at 2.4 GeV) would generate a signal similar to those produced by a destructive loss (0.01 %) at the end of the main beam (1.5 TeV). However, note that the measurements presented here correspond to significantly different beam conditions in terms of energy and current with respect to the nominal CLIC values. Hence dedicated simulation would need to be performed to draw conclusions. The final crosstalk achieved in a future CLIC will be a combination of loss location, geometry and bunch structure. Nevertheless it is not expected to be significantly lower than the 1 % level.

ACKNOWLEDGEMENTS

The authors would like to thank the CTF3 collaboration and the CTF3 operators for their invaluable help in providing the beam for these measurements.

REFERENCES

[1] "A Multi-TeV Linear Collider Based on CLIC Technology: CLIC Conceptual Design Report", edited by M. Aicheler, P. Burrows, M. Draper, T. Garvey, P. Lebrun, K. Peach, N. Phinney, H. Schmickler, D. Schulte and N. Toge, CERN-2012-007 (2012).

[2] J. L. Navarro Quirante et al., "CALIFES: A Multi-Purpose Electron Beam for Accelerator Technology Tests", MOPP030, *Proc.* LINAC2014, Geneva, Switzerland (2014).

[3] D. Gamba and F. Tecker,"Emittance Optimisation in the Drive Beam Recombination Complex at CTF3," TUPRI080, *Proc.* IPAC'14, Dresden, Germany (2014).

[4] E. Nebot et al., "Position Resolution of Optical Fibre-Based Beam Loss Monitors Using Long Electron Pulses", MOPB047, *These Proceedings*, IBIC'15, Melbourne, Australia (2015).

[5] Thorlabs, Inc., `http://www.thorlabs.com/`

[6] Hamamatsu Photonics K.K., `http://www.hamamatsu.com/`

[7] M. Bergamaschi et al., "Experimental Study of Optical Transition Radiation Interference", *Proc.*, RREPS-15, St. Petersburg, Russia (2015).

ISBN 978-3-95450-176-2

FIRST K-MODULATION MEASUREMENTS IN THE LHC DURING RUN 2

M. Kuhn[1,2], V. Kain[1], A. Langner[1,2], R. Tomas[1]
[1]CERN, Geneva, Switzerland, [2]University of Hamburg, Hamburg, Germany

Abstract

Several measurement techniques for optics functions have been developed for the LHC. This paper discusses the first results with a new k-modulation measurement tool. A fully automatic and online measurement system has been developed for the LHC. It takes constraints of various systems such as tune measurement precision and powering limits of the LHC superconducting circuits into account. K-modulation with sinusoidal excitation will also be possible. This paper presents the first k-modulation and β^* measurement results in the LHC in 2015. In addition, the measured beta functions will be compared to results from the turn-by-turn phase advance method.

INTRODUCTION

K-modulation is a method for measuring beta functions at locations of individually powered quadrupoles. This method is model independent and often an alternative for locations with a non-optimum phase advance between Beam Position Monitors (BPMs) for the turn-by-turn phase advance measurement [1]. A typical application is the measurement of β^* at the interaction point of a collider or the offset determination of BPMs [2]. Next to β^* measurements, it is also used in the LHC to obtain the beta functions at the transverse profile monitors close to the individually powered quadrupoles in LHC point 4.

K-MODULATION

Changing the strength of a quadruple results in a tune change. The tune change is proportional to the change of strength and the beta function at the location of the quadrupole. If the tune change can be measured accurately, the beta function can be calculated from the change in quadrupole strength following the well-known formula

$$\beta = \frac{2}{l\Delta k}\left[\cot(2\pi Q) - \frac{\cos(2\pi(Q+\Delta Q))}{\sin(2\pi Q)}\right] \qquad (1)$$

where l is the length of the quadrupole, Δk the quadrupole strength change in $[m^{-2}]$, ΔQ the tune change and Q the nominal tune. Changing the strength of the quadrupole changes the tune and the beta function itself. For typical tune changes in the range of 10^{-2}, corresponding to a strength change of several 10^{-4} in the LHC, the resulting beta beat at the quadrupole location amounts to 10^{-3} - 10^{-2}. The expected maximum induced beta beat with k-modulation is in the order of 1 %.

This paper will introduce a new custom-made LHC k-modulation application that offers automated measurements and takes care of the particularities of the LHC individually powered quadrupole circuits. In addition, the first k-modulation and β^* measurement results in the LHC in 2015 will be presented. Furthermore the measured beta functions will be compared to results from the turn-by-turn phase advance method.

K-MODULATION IN THE LHC

The LHC is a superconducting hadron collider with an injection energy of 450 GeV and a design collision energy of 7 TeV per charge. The 27 km ring is designed with eight long straight sections. The matching section cells around them contain individually powered superconducting quadrupoles.

No negative voltage can be applied at the unipolar power converters of the individually powered quadrupoles. Thus a decrease in quadrupole current has to follow the slow natural current decay. The upper power converter limits of the modulation amplitude ΔI and frequency f are given by

$$\Delta I = \frac{\Delta U}{Z} = \frac{IR}{2\pi f L} \qquad (2)$$

with voltage ΔU, impedance Z, resistance R and inductance L. For example quadrupole MQY.5R4.B1 can be modulated with a maximum amplitude ΔI of 26 A at nominal current and 3 A at injection current at a modulation frequency of 0.1 Hz. This is well sufficient for k-modulation in the LHC. The characteristics are different for all circuits. The new k-modulation application takes care of applying appropriate parameters.

Automatic K-Modulation for LHC Run 2

For k-modulation measurements at the LHC in the past, the tune signal and the quadrupole current measurement have been combined offline. The new k-modulation tool offers simultaneous tune and quadrupole current/strength acquisition and display. It executes k-modulation in two modes: step function, where the current is trimmed to different plateaus and tune data is accumulated, and sinusoidal current modulation. Both modulation methods have been tested and the first results are presented in this paper.

The application is fully integrated into the LHC control system [3] where the circuit characteristics of the quadrupoles chosen by the user are available. The modulation frequencies, amplitudes and time over which current changes are applied are pre-calculated by the application according to the power converter limitations.

LIMITATIONS

The precision of the beta function measurement with k-modulation in the LHC is limited by tune noise. The LHC tune noise level is about 10^{-3}. According to the 2012 experience, with k-modulation in current steps, the typical measurement error on the beta function is about 10 %, mainly due

ISBN 978-3-95450-176-2

to tune noise with multiples of 50 Hz lines in the spectrum. However, after extensive progress on the LHC tune acquisition and filtering tool, this uncertainty could be greatly reduced during Run 2. 50 Hz lines in the tune spectrum are very close to the actual tune and sometimes mistaken for the tune peak by the peak find algorithm, see Fig. 1.

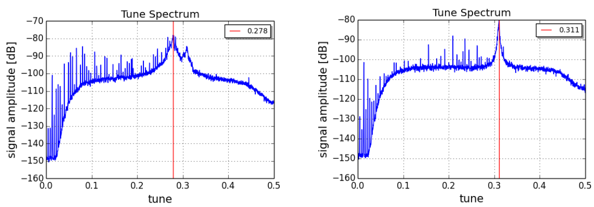

Figure 1: Tune spectrum with dominant 50 Hz lines (left) at injection tunes of nominal 0.28, and with clearer tune peak (right) at collision tunes of nominal 0.31.

The required k-modulation steps have to be significantly larger than the tune noise. Yet the maximum possible tune change is limited by the third order tune resonance in the LHC ($\Delta Q \leq \pm 0.015$ at nominal injection tunes of $Q_x = 64.28$ and $Q_y = 59.31$). Injection tunes are preferred as opposed to collision tunes when the tune separation is larger. Also the transverse damper has to be switched off during k-modulation.

Another limitation of k-modulation is that it cannot be used to obtain measured beta values during the energy ramp or the β^* squeeze. While the power converters are executing functions, they do not allow current modulation on top.

Also, k-modulation can only be carried out with low intensity beams due to tune measurement quality issues with high intensity in the machine and machine protection reasons. Parasitic measurements with physics beams are excluded. As the LHC has been found very reproducible, low intensity test fills during the start-up are, however, representative.

Effects of Hysteresis for Sinusoidal Excitation

The knowledge of the quadrupole strength change is crucial for k-modulation. The quadrupole transfer function links the quadrupole field to the current. The relative error on the measured transfer function is about 0.1 % [4]. The transfer function error on the nominal value due to hysteresis effects is about 0.2 % or smaller, corresponding to the maximum opening of the hysteresis curve [5].

Hysteresis alone would result in an error on the beta function in the order of 10^{-4}. Hence, the hysteresis effects are much smaller than the typical k-modulation measurement precision, which is in the order of 10^{-2}. For the LHC triplet magnets there is no problem of hysteresis as they are at top field during β^* measurements.

Effects of Tune Decay at 450 GeV

At the 450 GeV LHC injection plateau the superconducting magnets are at constant current which leads to a drift of the magnetic field multipoles. This changes the tune and the chromaticity. The tune decay with time is best described by a double exponential function with a fast time constant in the order of 1000 s. The tune decay component is implemented in the LHC control system as a feed forward correction to keep the tune at the reference value. [4] Still, tune decay can be observed on a small time scale, especially for measurements at the beginning of the injection plateau. For k-modulation at 450 GeV it is therefore important to correct the tune and the chromaticity after each measurement. The typical k-modulation measurement length ranges from 60 to 300 s. Thus a linear fit is used to remove the effects of tune decay.

MEASUREMENT RESOLUTION

K-modulation measurements at 450 GeV in LHC point 4 were carried out during the LHC commissioning phase in 2015. Step and sine modulations were performed on the same quadrupoles (MQM.7R4.B1 and MQM.7R4.B2) with identical amplitudes and periods to compare the measurement resolution. An example step modulation is shown in Fig. 2. The same quadrupole with sinusoidal modulation is shown in Fig. 3. In general, the measurement uncertainty is very small. The measurement error for k-modulation in steps ranges from 2.2 to 2.8 %. The measurement error for sinusoidal modulation is smaller, in the range of 0.6 to 1.8 %.

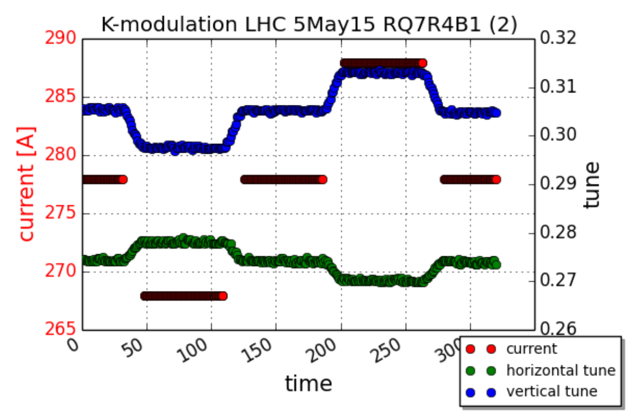

Figure 2: K-modulation in steps at quadrupole MQM.7R4.B1 at 450 GeV injection optics. The current (red) and horizontal (green) and vertical (blue) tune are displayed.

The measurement resolution also depends on the modulation amplitude, frequency and number of periods. If the tune signal is noisy a longer modulation improves the measurement uncertainty. As the frequency is limited by the given amplitude, the measurement error cannot be reduced by modulating faster. The tune acquisition frequency (1 Hz) has to be higher than the chosen modulation frequency to obtain a reasonable fit. When doubling the amplitude the measurement resolution typically improves by 1 %. The same is true for noisy tune signal and doubling the number of periods. The typical k-modulation measurement error is 1 - 3 % depending on the quadrupole. Hence, using the

ISBN 978-3-95450-176-2

optimum modulation parameters can greatly reduce the measurement uncertainty.

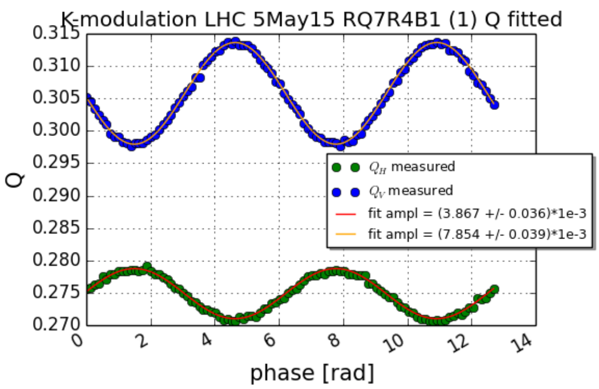

Figure 3: Sinusoidal k-modulation at quadrupole MQM.7R4.B1 at 450 GeV injection optics. The horizontal (green) and vertical (blue) tune are displayed with fits.

β^* MEASUREMENTS

For the 80 cm β^* optics the beta functions at the interaction points (IPs) 1 and 5 were measured in 2015. The quadrupoles closest to the IPs, left and right, were modulated with a sine function. One pilot bunch per beam with an intensity of about 9×10^{-9} protons was used for the modulation. The measurements were carried out after the β^* squeeze with LHC injection tunes and modulation parameters of 10 A and 0.01 Hz. No tune chirp was needed. The measured β was transported to the interaction point. An example measurement can be seen in Fig. 4. The results are listed in Table 1. The measurement uncertainty on β^* as well as the beta beat are smaller than 1 %. This remarkable high precision can be attributed to the good tune signal in the LHC. Each measurement was repeated at least once and it was found that the results are reproducible.

Table 1: Measured β^* Values in IP1/5.

	IP1	**IP5**
β_{1H} **[m]**	0.81 ± 0.01	0.80 ± 0.001
β_{1V} **[m]**	0.81 ± 0.01	0.79 ± 0.01
β_{2H} **[m]**	0.79 ± 0.004	0.80 ± 0.01
β_{2V} **[m]**	0.79 ± 0.01	0.79 ± 0.002

COMPARISON WITH TURN BY TURN PHASE ADVANCE METHOD

Beta function measurement results from k-modulation and the conventional method to measure beta functions in the LHC, the turn-by-turn phase advance method, have been compared. An example analysis of the measured beta beat of quadrupoles in LHC point 4 for each method can be found in Fig. 5. The results are consistent but k-modulation has significantly smaller measurement errors.

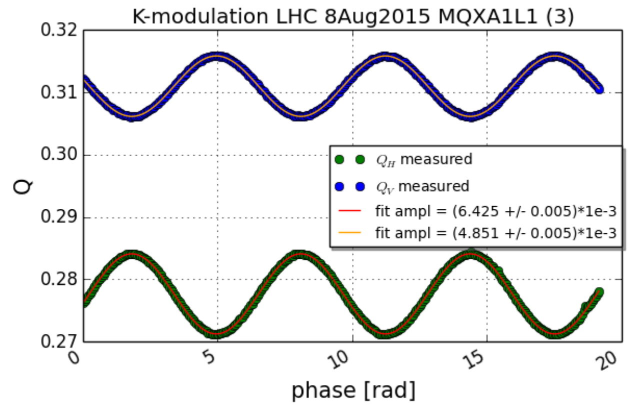

Figure 4: Beta function measurement in LHC IP1 with k-modulation. Quadrupole MQXA1L1 was modulated with a sine function with amplitude 10 A and frequency 0.01 Hz. The horizontal (green) and vertical (blue) tune are displayed with fits.

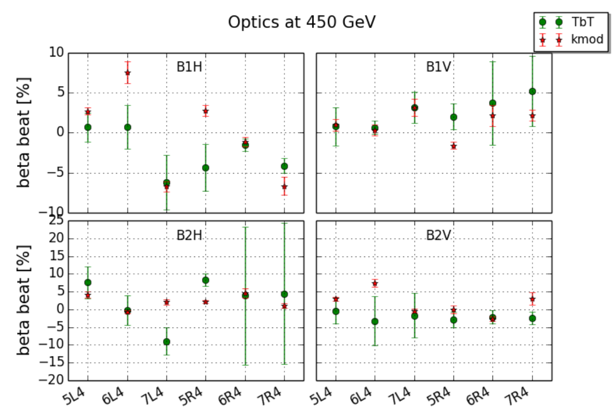

Figure 5: Beta beat for beta function measurements in LHC point 4 with the turn-by-turn phase advance method (green) and k-modulation (red) after the optics measurement correction campaign in April 2015.

CONCLUSION

K-modulation is an alternative method for measuring the beta functions at locations of individually powered quadrupoles. The method was used in 2015 to measure beta functions in LHC point 4 and in the interaction regions. A dedicated online tools is operational since the start of LHC Run 2 which simplified and sped up the measurements. The beta function measurement accuracy via k-modulation in the LHC is mainly limited by tune noise. Nevertheless, measurement errors smaller than 1 % could be achieved with sinusoidal excitation of quadrupoles. These are very promising results and pave the way for high precision beta

ISBN 978-3-95450-176-2

function measurements at the interaction points and beam profile monitors to further decrease the emittance measurement uncertainty.

REFERENCES

[1] A. Langner and R. Tomas, "Optics Measurement Algorithms and Error Analysis for the Proton Energy Frontier," Phys. Rev. ST Accel. Beams 18, 2015.

[2] F. Tecker, "Methods of Improving the Orbit Determination and Stability at LEP," Ph.D. Thesis, RWTH Aachen, 1998.

[3] D. Jacque et al, "LSA - the High Level Application Software of the LHC - and Its Performance During the First Three Years of Operation," ICALEPCS2013, San Francisco, 2013.

[4] E. Todesco et al., "Tune Variations in the Large Hadron Collider, " Nuclear Instruments and Methods in Physics Research Section A: Accelerators, Spectrometers, Detectors and Associated Equipment, Volume 778, pp 6–13, April 2015.

[5] M. Kuhn, "New Tools for K-Modulation in the LHC," IPAC14, Dresden, Germany, June 2014.

ISBN 978-3-95450-176-2

DESIGN CONCEPT FOR A THz DRIVEN STREAK CAMERA WITH ULTRA HIGH RESOLUTION

M. Dehler, V. Schlott, F. Frei, R. Ischebeck, PSI, Villigen PSI, Switzerland
T. Feurer, J. Fabianska, M. Hayati, University of Bern, Berne, Switzerland

Abstract

The resolution of streak camera systems strongly depends on the slew rate of the deflecting element, being proportional to the amplitude and the frequency of the deflector. An attractive approach to reach femto and even sub-femto second resolution are THz driven electron streak cameras, which have been only recently proposed. Here, the ultra fast streaking field is generated by exciting a suitable resonant THz antenna, e.g. a split ring resonator with an intense THz pulse [1]. With today's THz sources streak field amplitudes in excess of 1 GV/m are within reach. Here, we present the concept for a proof of principle system. The THz pulse will be generated by rectifying the pulse from an existing 800 nm laser system in a suitable crystal as LiNbO3 [2]. For the source of the electron beam to be streaked, we plan to use an RF photo gun yielding a relativistic 6.5 MeV beam. We describe the setup of the system and present simulations of the beam dynamics.

INTRODUCTION

Pulsed electron sources are capable of emitting electron bunches with durations in the few hundred femto second regime and, using bunch compressor chicanes, these can be further shortened reaching the few femto second regime. Full temporal characterization of such electron bunches is a prerequisite for their use, for example in seeding of X-ray Free Electron Lasers. This issue is complicated by the non negligible pulse-to-pulse fluctuations of such machines requiring single-shot characterization techniques.

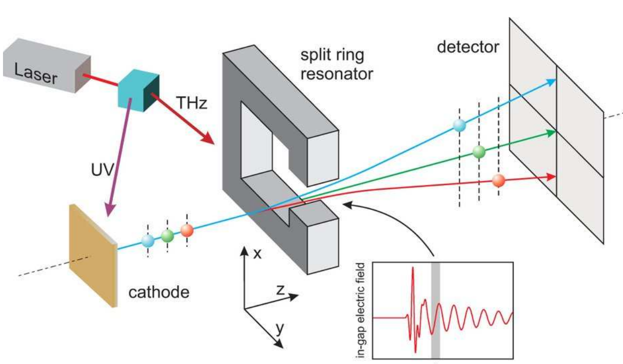

Figure 1: Measurement principle.

In the field of ultra fast electron diffraction, streak cameras have been shown to allow for sub-picosecond bunch duration measurements. Even streak cameras based on deflection mode RF cavities have been demonstrated to operate with sub-100 fs resolution for keV to MeV electron energies [3], yet the issue of phase jitter in RF cavities is a challenge. While obtaining temporal resolutions in the 10-100 fs regime is conceivable with current technologies, few-femtosecond or even sub-femtosecond resolutions seem out of reach. Here, we propose an approach with the potential to achieve a resolution around a femtosecond for electron bunches in the 10 kV to MV energy range [4]. The methodology relies on a resonant THz sub-wavelength structures irradiated with an intense single-cycle THz pulse. The design is reminiscent of a classic streak camera. The deflecting electrodes and the RF streaking field of a standard streak camera are replaced by a split-ring resonator (SRR) and the electric near-field in its gap, respectively. The SRR's resonance frequency can be varied between 100 GHz and several THz simply by changing its geometry, allowing for THz streak field rise times between hundreds of femtoseconds to several picoseconds. The electron bunch passing through the SRR's gap experiences a transverse momentum transfer which sign and magnitude depend on the longitudinal bunch position. Thus, the longitudinal bunch density is mapped onto the transverse axis and can be easily measured with a spatially resolved electron detector. THz-driven streaking should be well adapted to measure ultra short electron bunches, even on a single-shot basis. Ideally, the electron bunches and the THz pulses are generated with the same laser system, that is to say, synchronization between the two is inherently guaranteed.

The planned research builds on the extensive recent work in the field of laser-driven particle acceleration (see e.g. [5]). Particle beams have been accelerated from rest using infrared fields of lasers [6,7]. Due to the small wavelength and corresponding structure size, only low-charge beams could be generated. An acceleration by a field of a few terahertz is described in [8], showing an energy gain of about 7 keV [9]. In the present case, the effective accelerating field is transverse to the direction of motion of the particles, such that particle bunches are streaked rather than accelerated. While the final goal is different, the methods are similar, and we expect to build on the rapid progress made in the field of laser acceleration.

In the following, we describe the principle behind the measurement system, present simulation results for the deflector as well the required electron source and give a first layout of deflector and diagnostics station.

PRINCIPLE

The principle used in the measurement is shown in Figure 1. The photon beam to be measured modulates a photo cathodes and creates an electron beam, which is accelerated

ISBN 978-3-95450-176-2

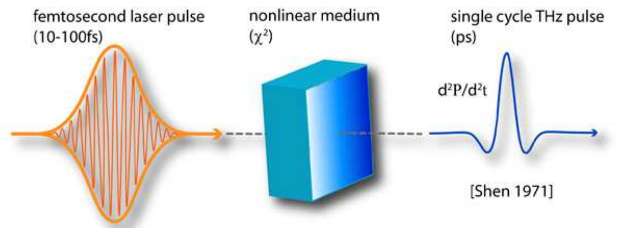

Figure 2: THz generation through optical rectification of laser pulses.

either in a DC or an RF gun. Using optical rectification a plane wave pulse is excited from a second laser pulse, which excites the fundamental mode in a split ring resonator and generates a deflecting field. By letting the electron bunch pass through the zero crossing of the deflecting mode, we obtain a correlation between longitudinal current density and the vertical beam offset. The read out is done via a following transverse electron beam profile monitor.

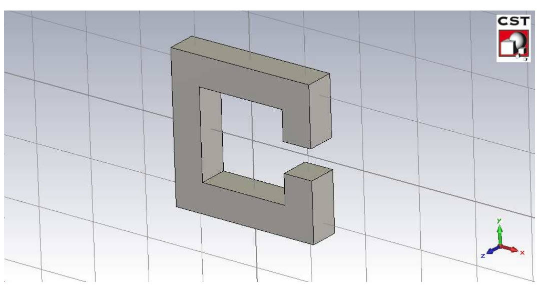

Figure 3: Ring resonator for 1000 GHz resonance frequency.

A first, initial experiment is planned, which will give a proof of principle and will generate both the measurement beam and the THz pulse from the same laser source. By observing the vertical blow up of the beam due to the streaking, laser pulse lengths in the order of a picosecond are sufficient, avoiding major synchronization problems.

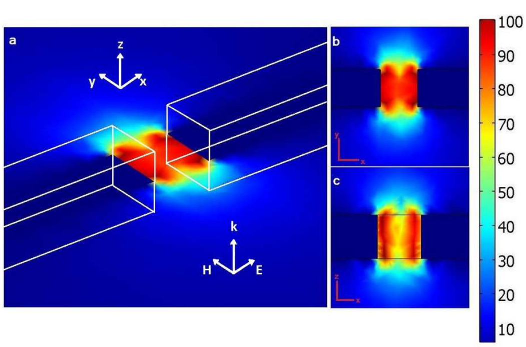

Figure 4: Transverse electric field distribution in the gap.

THz Generation

Currently, high-field single-cycle THz pulses are mostly generated by optical rectification of approximately 100 fs laser pulses in inorganic crystals, such as ZnTe or $LiNbO_3$,

Table 1: Mechanical and Electrical Parameters of the Split Ring Resonators

f (THz)	0.1	0.3	1
width (µm)	370	130	50
deflector gap (µm)	10	10	10
kick (eV/c), 1 MV/m in gap	43.0	27.7	26.5
Q factor	10.8	10.3	11.8

or in organic crystals, such as DAST or OH1 (Fig. 2). Optical rectification is a second order nonlinear frequency mixing process and as such the THz generation efficiency is dominated primarily by three factors, the pump laser intensity, the nonlinear material coefficient, and phase matching. The highest fields to date have been obtained from $LiNbO_3$, DAST and OH1 with electric field strengths in excess of MV/cm.

Split Ring Resonator

For different resolutions and ranges, we are planning to work with three different resonator types, having resonance frequencies of each 100, 300 and 1000 GHz. They have a quadratic shape using a rectangular metallic conductor of 10 µm thickness. As an example, Figure 3 shows the geometry of the 1000 GHz type. The width of the gap, where the beam is passing was chosen at 10 µ for all frequencies.

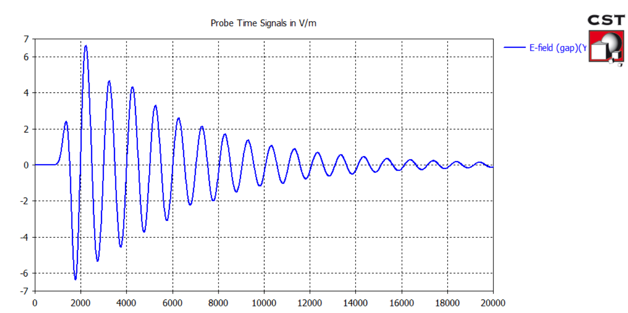

Figure 5: Electric field inside gap of 1000 GHz resonator excited with plane wave pulse of 400 fs FWHM.

The wide band THz pulse can feed only energy into the resonator within its bandwidth. Nonetheless the geometric field enhancement due to the resonator shape gives enhancement factors between 6 and 20 for the deflecting field inside the gap. Figure 5 shows the response of the 1 THz type.

Table 1 gives an overview of the various resonators. The effective kick seen by a relativistic beam passing the gap is given by the electric and magnetic field taken into account the transit time factor. These were calculated for a reference gap gradient of 1 MV/m with CST Particle Studio and are also given in this table. The maximum field inside the resonator is limited by thermal effects due to conductive losses and field emission effects – we assume to be able to reach 500 MV/m peak, which would give us, depending on the frequency, deflections between 13 and 21 keV/c, which are sufficient to work even with low relativistic beams. For

ISBN 978-3-95450-176-2

highly relativistic beams as e.g. a spent FEL beam at several GeV, a phased array of SRRs would be required.

In the simulations, we also looked at secondary effects in the resonators. Even with this high frequencies, conduction effects were not yet visible. Also the variation of the kick over the gap aperture is below 10%.

Generating the Electron Beam

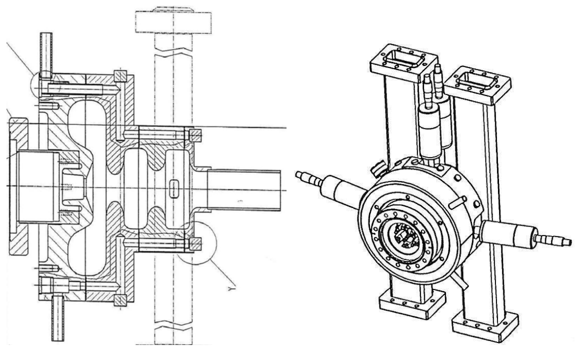

Figure 6: Geometry of the RF gun.

The electron beam generated on the photo cathode should be a faithful replica of the photon signal, this property should be conserved during acceleration and transport through the deflector. Furthermore there is an inherent conflict in choosing the value of the beam current between getting a good detection signal and avoiding space charge effects while focusing the beam through the 10 µm deflector gap.

For a non accelerator, lab based applications, using a compact DC based gun would be preferable. The lower beam energy, 30-100 keV, would be deflected stronger giving a higher resolution. But space charge forces are more visible, making the beam optics even at the design current of 10 mA in such a device quite challenging. A design based on that approach is in development, but not shown here.

The alternative used here is an RF gun. The emitted electrons get rapidly accelerated at gradients up to 100 MV/m, reducing strongly space charge effects. Longitudinal information in the intra bunch density are much better conserved and the dramatically improved transverse emittance allows an efficients focusing of the beam into the 10 µm deflector gap.

The split ring resonator experiment (SRR) was originally planned to be performed using existing equipment at PSI as the RF gun and the solenoid from the SwissFEL Injector Test Facility SITF [10]. But resent discussion with the THz group at KIT centered on doing the setup inside the FLUTE test stand [11], which uses a similar setup. The RF gun is also a 2 1/2 cell gun [12] and solenoid has the same dimensions, so we should expect quite similar behavior concerning the beam dynamics. So the results should apply to both cases.

We modeled the beam dynamics using the geometry of the 2 1/2 cell RF gun, which we had in use in the SwissFEL test injector facility SITF [10]. The gun was originally developed for high current operation in the CLIC test facility CTF-2 [13]. The general geometry is shown in Fig. 6. A specialty

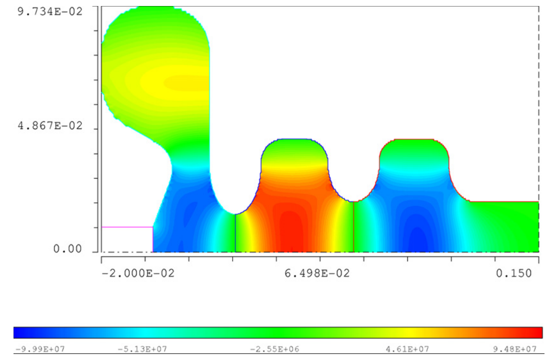

Figure 7: Accelerating mode - contour plot of longitudinal electric field.

compared to other design is the large diameter first half cell, where the TM_{02}resonance is used for the main accelerating mode (Fig. 7). The original reason for this choice is, that this resonance is particularly well suited to generate a bunch train with extremely high beam charges and currents. For the operation at the extremely low currents required this feature has no influence. A second feature, more useful, is the use of large irises between cells minimizing the non-linearity of the RF fields.

The gun is followed by a solenoid focusing the beam into the aperture of the split ring resonator. The operating parameters gun and solenoid are listed in Table 2.

Table 2: Operating Parameters of Gun and Solenoid

RF Gun	
Gradient (MV/m)	100
Emission phase (deg.)	39
laser spot dia. (µm)	50
Beam energy (MeV)	6.5
Solenoid	
Length (mm)	260
Inner diameter (mm)	80
Outer diameter (mm)	385
Peak magnetic field (mT)	290
Beam parameters in focus	
r_{rms} (µm)	0.97
ϵ_n (nm rad)	1.05

Both gun and solenoid are rotationally symmetric, so the beam dynamics could be simulated using the 2 1/2D particle in cell code MAFIA TS2 [14]. To capture space charge forces accurately, grid resolutions down to 5 µm were used. To have reasonable computation times, the solenoid was set to a relatively high field to obtain beam focus already shortly after the solenoid at 520 mm instead having to track the particles in the drift between solenoid and deflector to the design location at 1700 mm.

Figure 8 shows the evolution of the rms beam radius from emission to the focal point for 10 and 20 mA current. The transverse beam parameters in the focal point are also listed in Table 2. As also the transverse phase space plot in Figure 9

ISBN 978-3-95450-176-2

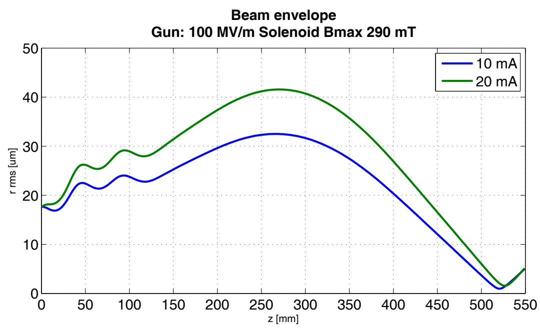

Figure 8: Beam envelope for 10 and 20 mA peak current for an artificially shortened focus position of 520 mm (Design: 1700mm).

shows, we should be able to propagate the beam though the 10 µm sized aperture of the split ring resonator.

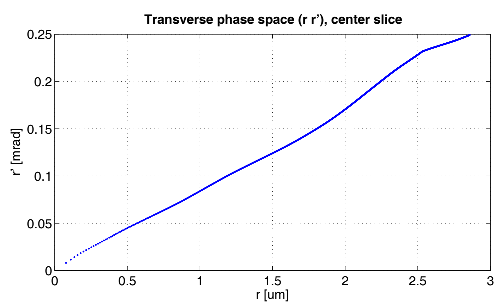

Figure 9: Transverse phase of the center slice of 10 mA beam near the beam focus.

EXPERIMENTAL SETUP

The split ring resonator (SRR) experiment will be performed in the FLUTE test beam line at Karlsruhe Institute of Technology (KIT). A layout of this beam line, indicating the location of the interaction chamber, is shown in Figure 10. The interaction chamber occupies the location of the future bunching cavity.

We only want to have a proof of the principle, showing a transverse blow up as a function due to the streaking action of the SRR. That allows us to avoid synchronization problems between measurement beam and the THz pulse, something, which need to be addressed in a later phase. Also, both the THz pulse and the electron beam can be generated from the same laser pulse with a rather standard optical delay stage to synchronize both.

Terahertz radiation enters the interaction chamber using a crystalline z-cut quartz window from the side. It will be focused onto the SRR with a remotely adjustable paraboloid mirror. A camera will be positioned at the opposite side, allowing for alignment and beam profile measurements.

The effect of the terahertz field on the beam will be measured with a transverse electron beam profile monitor, located 1.2 m behind the interaction zone. Beam profile measurements of 30 fC beams have been performed with such a monitor [15], and an optical resolution of 8 µm according to ISO 12233 has been determined [16].

Experimental Chamber

The split ring resonator will be installed on a hexapod in the experimental chamber. The hexapod allows for a full control of the position and orientation of the resonator, and will be used to align it to the electron beam. It is equipped with six piezo-electric motors, allowing for a nominal accuracy of better than 1 µm. The interaction will take place at the center of the chamber. A CAD model of this chamber is shown in Figure 11. The position and the transverse size of the electron beam will be determined on a scintillating crystal, which can be positioned at the same location as the split ring structure. A microscope lens with a long working distance will be installed to image the scintillator, through the center hole of the mirror, and to alternatively verify the location of the SRR. We aim for a projected pixel size of 650 nm. The resolution of the imaging setup, including vacuum window and mirror, will be determined experimentally.

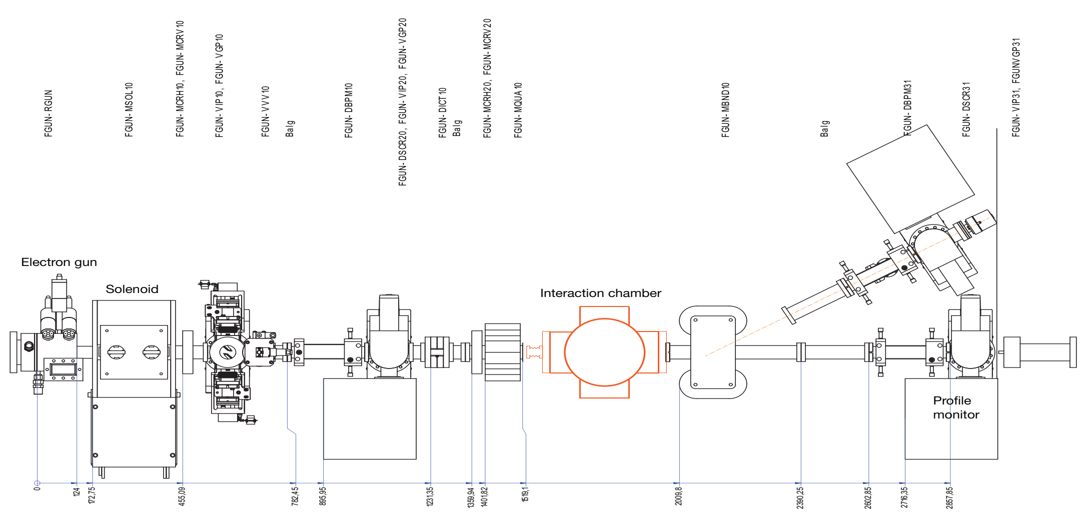

Figure 10: Planned installation in the FLUTE beam line.

ISBN 978-3-95450-176-2

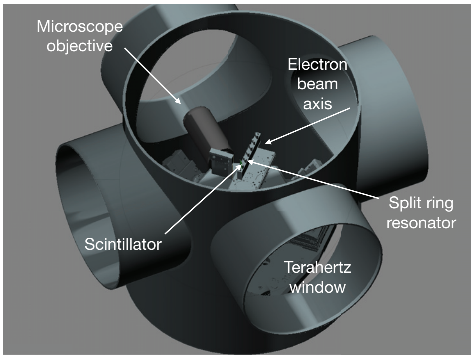

Figure 11: The planned experimental chamber, with the interaction zone for the split ring resonator.

The six-dimensional alignment structure will be equipped with an additional translation stage, mounted diagonally on top of the hexapod. This stage will allow to replace the structure quickly, and to test a series of structures without having to break the vacuum.

SUMMARY AND OUTLOOK

We propose a new concept for a femto to sub femto resolution streak camera. It is based on using micro structure type split ring resonator (SRR), which are fed by a single cycle THz pulse generated by optical rectification of a laser pulse. In order to vary range and resolution of the device, we are working with different designs in the range of 100-1000 GHz. Simulations show, that we can expect up to 20 keV/c maximum transverse kick from a single resonator. To generate the measurement beam, we plan to use a 2 1/2 cell RF gun, which offers the high beam quality to focus the electrons through the micron sized gap of the SRR while preserving the time domain resolution.

We are currently in the design phase for an initial experiment to be conducted at the FLUTE THz beam line at KIT using only the first stage containing the RF gun and the solenoid. Both the photo emission of the measurement beam as well as the THz pulse will be generated by the same laser pulse, that way avoiding synchronization problems. The goal is to prove the principle, by looking at the vertical beam blow up due to the streaking action of the SRR deflector.

REFERENCES

[1] S. Bagiante et al., “Giant Electric Field Enhancement in Split Ring Resonators Featuring Nanometer-Sized Gaps”, Scientific Reports 5, 10.1038/srep08051 (2015)

[2] János Hebling et al., “Generation of high-power Terahertz pulses by tilted-pulse-front excitation and their application possibilities”, J. Opt. Soc. Am. B 25, B6 (2008)

[3] C. Behrens et al., “Few-femtosecond time-resolved measurements of X-ray free-electron lasers”, Nature Communications 5:3762 (2014)

[4] J. Fabianska et al, “Split ring resonator based THz-driven electron streak camera featuring femtosecond resolution”, Scientific Reports 4, Article number: 5645 (2014) doi:10.1038/srep05645

[5] R.J. England et al., “Dielectric laser accelerators”, Rev. Mod. Phys. 86, 1337

[6] J. Breuer and P. Hommelhoff, “Laser-Based Acceleration of Nonrelativistic Electrons at a Dielectric Structure”, Phys. Rev. Lett. 111, 134803 (2013).

[7] E. A. Peralta et al., “Demonstration of electron acceleration in a laser-driven dielectric microstructure”, Nature 503, 91–94 (2013).

[8] W.R. Huang et al., “Toward a terahertz-driven electron gun”, arXiv:1409.8668v2 [physics.optics] (2014).

[9] E.A. Nanni et al. “Linear Electron Acceleration in THz Waveguides”, proc. of IPAC2014, Dresden, Germany (2014).

[10] M. Pedrozzi (ed.), “250 MeV Injector Conceptual Design Report”, PSI Report 10-05 (2010)

[11] S. Naknaimueang et al., “FLUTE, a LINAC based THz Source”, proc. of the IPAC 2011, San Sebastian, Spain, pp. 1458-1460.

[12] R. Bossart et al., “A 3 GHz Photoelectron Gun for High Beam Intensity”, proc. of the 17th International Free Electron Laser Conference, Aug. 21-25 1995, New York, USA, in Nucl. Instrum. Methods A375 (1996) ABS7-ABS8.

[13] R. Bossart, M. Dehler, “Design of a RF Gun for Heavy Beam Loading”, proc. of the EPAC96, June 10-14 1996, Barcelona, Spain, pp. 1544-1546.

[14] http://www.cst.de/

[15] R. Ischebeck et al., “Transverse profile imager for ultrabright electron beams”, Phys. Rev. ST Accel. Beams 18, 082802.

[16] R. Ischebeck et al., “Transverse profile monitors FOR SwissFEL”, proc. of IBIC2014, Monterey CA, USA, pp.259-262.

ISBN 978-3-95450-176-2

AN OPTICAL INTRA-BUNCH INSTABILITY MONITOR FOR SHORT ELECTRON BUNCHES

Thomas G. Lucas, Paul J. Giansiracusa
David J. Peake, Roger P. Rassool, University of Melbourne, Melbourne, Australia
Mark J. Boland, Australian Synchrotron, Clayton, Australia
Ralph J. Steinhagen, GSI, Darmstadt, Germany

Abstract

An improved understanding of intra-bunch instabilities in synchrotron light source electron bunches is crucial to overcoming the imposed limitations of the achievable intensity. A Multiband Instability Monitor, designed specifically for the short bunches of a synchrotron light source, has been developed to perform measurements of intra-bunch dynamics. The MIM performs real-time measurements at a diagnostic beamline using optical synchrotron radiation incident on a high speed photodetector. Three frequency bands up to 12 GHz were used to identify characteristic frequency signatures of intra-bunch instabilities. Mixed to baseband using RF detectors, these high frequency measurements can be performed without the need for similarly high frequency digitisers. This paper reports on the performance of the system at the Australian Synchrotron.

INTRODUCTION

Individual bunch currents are limited by intensity dependent instabilities. Typical Synchrotron light sources operate with bunch length in the tens of picosecond regime, making direct digitisation costly and limited in resolution due to thermal noise and clock jitter. The Multiband Instability Monitor (MIM) Principle, first demonstrated on the Super-Proton-Synchrotron (SPS), avoids the limitations of digitisation using a unique frequency domain approach to measure fast beam dynamics [1]. Incoming signals are split into multiple frequency bands which are downmixed and analysed simultaneously. Allowing the measurement of high frequency dynamics, such as the head-tail instability, without the need for a digitiser of equivalent bandwidth.

TRADITIONAL MEASUREMENTS

Head-tail instabilities were first measured by Sacherer on the Proton Synchrotron at CERN. Bunch structures were easily resolvable in the 200 ns bunches given the digitisers available at the time, allowing bunch profiles of the first 3 head-tail instability modes to be measured [2]. Bunch lengths have reduced dramatically in modern synchrotron light sources such that readily available digitisers do not have the necessary bandwidth. Electron bunch wave-forms for the Australian Synchrotron's 23 ps bunches are shown in Figure 1. The four lowest head-tail instability modes are shown, $m = 0$ corresponding to a rigid bunch instability while $m = 1$ to $m = 3$ are the first three modes of the head-tail instability. Referring to frequency domain plot,

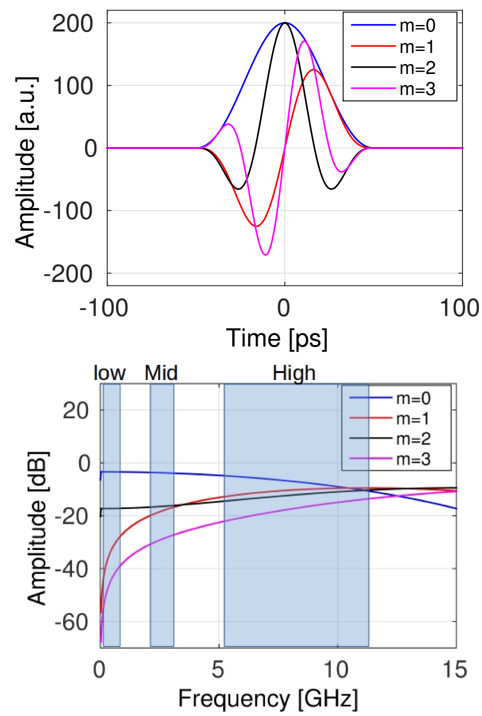

Figure 1: Simulations of the differential BPM signal's waveforms during the lowest four head-tail instabilities modes given the 23 ps bunch lengths seen at the Australian Synchrotron. Displayed in the time and frequency domain, the $m = 0$ represents the shape of the BPM summation signal as well as the differential during rigid bunch motion ($m = 0$). In the frequency domain, a shift in the peak frequency can be seen for the non-zero head-tail instability modes $m = 1$ to $m = 3$. Shading on the frequency plot represents the MIM's frequency bands.

the third mode demonstrates that to measurements would require bandwidths of at least 40 GHz. Such measurements would be limited by the thermal noise, reducing the effective number of bits (ENOB). To resolve the bunch shape bandwidths of hundreds of gigahertz are required, well beyond the capability of digitisers [3]. Thus another technique must be employed to search for these instabilities.

Currently streak cameras are most commonly used to measure intra-bunch dynamics in the picosecond regime. With bandwidths of up to 1 THz these imaging systems are easily capable of resolving intra-bunch structure. Unfortunately

ISBN 978-3-95450-176-2

streak cameras are unable to be implemented as an instability diagnostic tool due to two main limitations:

1. Sampling rates are limited to only a few Hertz
2. Post processing is required so real-time measurements aren't a possibility

These limit streak cameras as diagnostic tools for instability diagnostics as instability rise-times are on the order of microseconds [4].

MIM PRINCIPLE

The MIM principle, first implemented on the SPS and LHC's proton beams uses a unique frequency domain approach to measure intra-bunch motion. By comparing the signals from the Beam Position Monitors (BPM) in different frequency bands, one can determine the presence of a head-tail instability [1]. This is done by measuring the summation (Σ) and the differential signal (Δ) between two opposing BPMs. The Δ signal will contain positional information and therefore be dependent on the bunch profile. Resulting is a shifting peak frequency for different instability modes, as was demonstrated in Figure 1. During a stable bunch, the BPM's Σ frequency spectrum differs from the Δ of the zeroth mode by a multiplication factor. Therefore presence of a non-zero mode head-tail instability can be defined through the ratio of the Σ to Δ signals with respect to frequency. Nominal bunch lengths at the Australian Synchrotron are 23 ps meaning the bandwidths of these frequency bands need to be in the tens of gigahertz regime. High frequency signals from the bands can be processed, in parallel, through RF detectors which downmix the signals to baseband and can be digitised simultaneously.

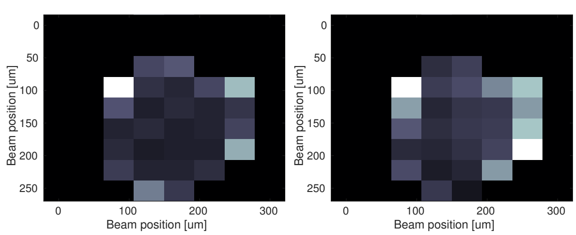

Figure 2: The Q/f_{rev} ratio for the vertical (left) and horizontal (right) tunes. For signals where the total intensity was less than 500 mV, the signal was set to zero as the modulating tune signals became indistinguishable from the noise floor. Transverse fluctuations are seen to be most sensitive on the edge of the active region of the photodetector.

EXPERIMENTAL SETUP

Given the frequency at which the measurements needed to be performed a few novel techniques were implemented. A system was developed to performed the intra-bunch measurements, outlined in Figure 3. Electrostatic BPMs at the Australian Synchrotron are limited to 500 MHz to reduce thermal noise making them unsuitable for the high frequency measurements. Instead a new optical BPM was implemented on the optical diagnostic beamline of the Australian Synchrotron measuring the bunch motion up to 12 GHz. The signals from this BPM were then filtered into multiple frequency bands by the new MIM system and digitised simultaneously.

Optical BPM

Implementing the MIM principle required the determination of the equivalent sum and differential signals from the optical BPM consisting of a single photodetector. Assuming a single bunch is injected in the storage ring, the intensity of the optical synchrotron radiation at the revolution frequency, 1.388 MHz, will represent the sum signal. Transverse oscillations in the focal point result from the betatron motion in the beam and modulate the revolution intensity at 300 kHz and 400 kHz for the vertical and horizontal tunes respectively. This modulation by the tunes will represent the differential signal given it contains positional information. A low noise photodetector was measures the bunch dynamics up to 12 GHz. A 10 V bias on the photodetector improves its sensitivity to small fluctuations. The properties of this photodetector were discussed at a previous proceedings [5].

Vital to the function of the BPM is the location of the synchrotron radiation's focal point. Figure 2 demonstrates the optical BPM's sensitivity to the modulation by the betatron tunes with respect to the focal point location normalised to the beam intensity. Focusing the synchrotron radiation close to the edge of the active region of the photodetector maximises the modulation level making it the optimal position for the MIM system.

Multiband Instability Monitor

Output from the optical BBQ is the bunch motion up to 12 GHz. To prepare the signals for filtering section a 24 dB wideband amplification is applied. Conventional filtering techniques, such as stripline coupling and passive components, could not be used for these high frequency signals. In order to create high frequency band pass filters, and not lose signal through splitting, two diplexers were connected in series. This, along with the analog bandwidth of the subsequent amplifiers, created three frequency bands: 200 – 700 MHz (low), 2.4 – 2.8 GHz (mid) and 5.5 – 12 GHz (high). Transmission plots for each of the bands are demonstrated in Figure 4. Following the filtering, simultaneous downmixing of the three bands is performed with zero-bias RF detectors, bringing the high frequency signals down to baseband frequencies. Removal of higher order f_{rev} signals is performed by band-pass filtering from 200 kHz to 2 MHz after downmixing, consequentially also removing unwanted noise from the system.

EXPERIMENTAL RESULTS

Preliminary measurements from the MIM system were performed during machine studies at the Australian Synchrotron using a single bunch injected into the storage ring.

ISBN 978-3-95450-176-2

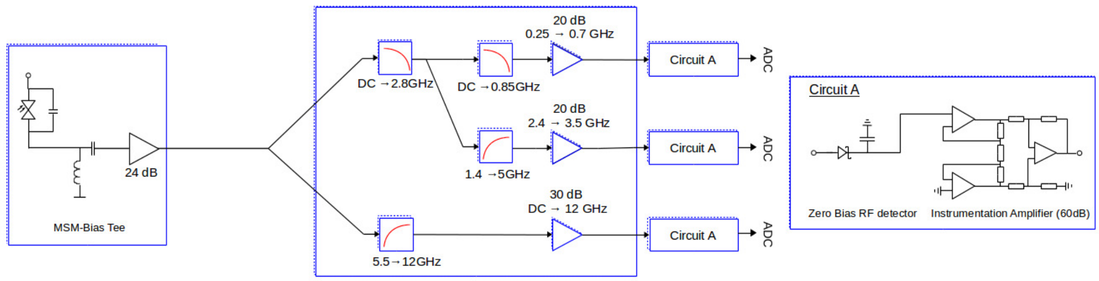

Figure 3: Multiband Instability Monitor at the Australian Synchrotron with a MSM photodetector pickup. The circuit can be separated into three sections: Pickup, Filtering and Downmixing.

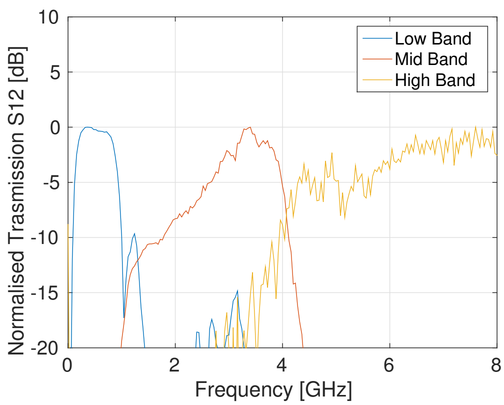

Figure 4: Transmission for the three MIM bands with respect to frequency. It can be seen that there is at least a 10 dB drop between frequency bands.

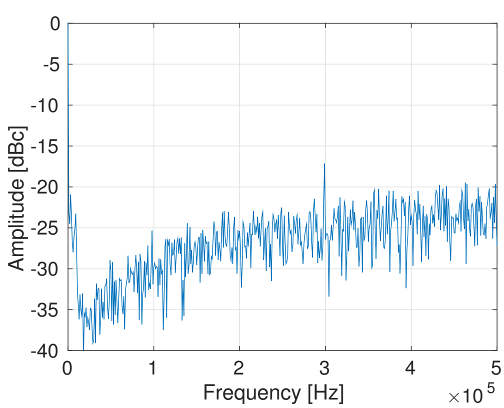

Figure 5: Tune measurement performed on a single bunch injected into the storage ring set to the nominal 0.66 mA. Optimised for the vertical tune the baseband signal can be seen at 300 kHz.

Tune Measurements

Tune measurements using the MSM photodetector have been performed previously and can be found here [6]. The signal-to-noise ratio was found to be similar for the buttons and the photodetector though, with only 500 MHz of analog bandwidth, the button BPMs at the Australian Synchrotron aren't fast enough to measure intra-bunch dynamics.

Measuring single bunches in a bunch train requires a low minimum on the dynamic range. Injecting the nominal user beam bunch current of 0.66 mA into a single bunch in the storage ring, the tunes were measured using a excitation from an injection kicker. Optimised for vertical oscillations, the vertical tune is visible at the nominal 300 kHz, 6 dB above the noise floor (Fig. 5). Given this single bunches could be measured in a bunch train with appropriate gating.

Intra-bunch Instability Measurements

Taking the signal from the optical BPM, the signal was passed through the MIM system. Testing of the system was performed on a 10 mA single bunch injected into the storage ring. Initial testing required the establishment of the noise floor.

Signals from the 3 MIM bands are displayed in the top row of Figure 6 for a stable bunch at nominal chromaticity $(Q'_x, Q'_y) = (3.5, 13)$. Normalising the signals to the carrier, it can be seen there is less than 2 dB variation between the three bands during a stable beam. Reducing the chromaticity incrementally to $(Q'_x, Q'_y) = (-0.8, 0)$, an intra-bunch instability was induced in the bunch. The lower row of plots demonstrates the MIM band signals during this instability. Given the normalised f_{rev}, it can be seen there is a 7 dB decrease in the Q/f_{rev} between the lower band and upper band.

Given the width of the bands for the current prototype, a quantitative analysis of the instability mode is not possible though a qualitative determination on the presence of an intra-bunch instability can be made.

FUTURE WORK

Future work on the system will look at measuring bunches without a catastrophically unstable beam and checking the dynamic range of the system with respect to instability strength. Such measurements will be performed using a statistical analysis on the MIM signals for the stable and unstable beam. To integrate the MIM system into the diagnostics system, it will be important to consider the display of the MIM data. Using a set of bar graph, the MIM data is displayed for a stable and unstable beam in Figure 7. The stability of the bunch can be determined from the gradient between the three bands.

ISBN 978-3-95450-176-2

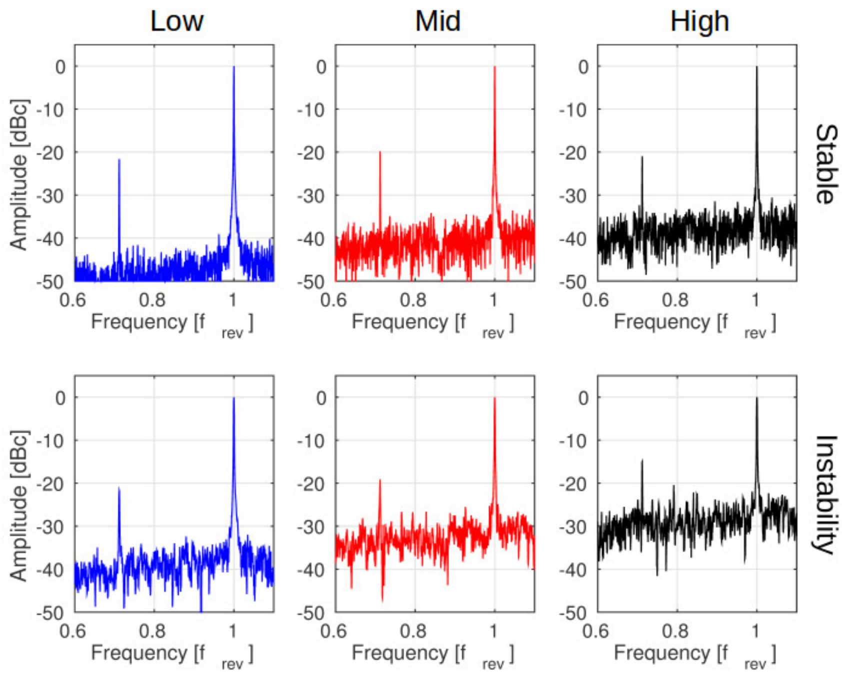

Figure 6: MIM's three frequency band for a stable (top) and unstable (bottom) single bunch. Normalising the signals to the f_{rev} carrier, it can be seen that the stable beam's tune signals are similar amplitudes. In comparison a decrease in the Q/f_{rev} ratio is seen with an increase in frequency during the induced intra-bunch instability.

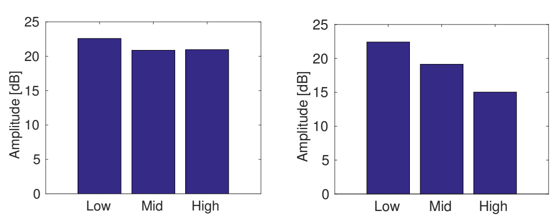

Figure 7: Q/f_{rev} signals for the stable (left) and unstable (right) beam plotted for the three MIM bands. A constant Q/f_{rev} across the bands is indicative of a stable beam whereas a decrease in the Q/f_{rev} ratio is indicative of an intra-bunch instability.

CONCLUSIONS

Initial measurements from the MIM system have displayed the ability to measure intra-bunch instabilities at GHz frequencies. Currently the system is only offers qualitative diagnostics of intra-bunch instabilities but future systems will be designed to offer insight into the instability mode number.

ACKNOWLEDGEMENTS

The authors are grateful to acknowledge the technical expertise of the accelerator and operations group at the Australian Synchrotron.

REFERENCES

[1] R. J. Steinhagen, M. J. Boland, and T. G. Lucas. A Multiband-Instability-Monitor for High-Frequency Intra-bunch Beam Diagnostics. In *Proceedings of the International Beams Instrumentation Conference*, 2013.

[2] F. J. Sacherer. Transverse Bunched-Beam Instabilities. Technical report, European Organisation for Nuclear Research, 1976.

[3] C. E. Shannon. Communication in the Presence of Noise (Reprint). *Proceedings- Institute of Electrical and Electronic Engineers*, 1998.

[4] Ng. *Physics of Intensity Dependent Beam Instabilities*. World Scientific Publishing, 2006.

[5] R. J. Steinhagen, T. Mitsuhashi, M. J. Boland, T. G. Lucas, and R. P. Rassool. Application of Metal-Semiconductor-Metal (MSM) Photodetectors for Transverse and Longitudinal Intra-bunch Beam Diagnostics. In *Proceedings of the International Beams Instrumentation Conference*, page MOPC20, Oxford, United Kingdom, September 2013.

[6] S. Dawson, D.J. Peake, R.P Rassool, R. J. Steinhagen, and M. J. Boland. Storage Ring Tune Measurements Using High Speed Metal-Semiconductor-Metal Photodetector. In *Proceedings of the International Beams Instrumentation Conference*, 2012.

ISBN 978-3-95450-176-2

OVERVIEW OF APPLICATIONS AND SYNERGIES OF A GENERIC FPGA-BASED BEAM DIAGNOSTICS ELECTRONICS PLATFORM AT SwissFEL

W. Koprek, B. Keil, G. Marinkovic, PSI, Villigen, Switzerland

Abstract

For SwissFEL electron beam diagnostics we combine application-specific detectors and front-end electronics with a common solution for digitization, interfacing and FPGA-based digital signal processing. Many key components and standards we use were initially developed by PSI for the European XFEL BPM system, but are equally suited for a broad range of SwissFEL diagnostics systems with little or no modifications. Examples are the FPGA signal processing hardware and firmware/software, ADC and DAC boards, interface boards or peak detection front-end electronics. By following a modular generic hardware and firmware/software design approach, we can cover a larger number of different monitor types with moderate development effort. Applications of our generic platform include BPMs, bunch length monitors, beam arrival time monitors, beam loss monitors. This paper gives an overview of the design, present and future applications of our generic platform, discussing the synergies and differences of the required hardware, firmware and embedded software solutions.

OVERVIEW

In the typical diagnostic system the sensor signals are connected to front-end electronic cards which do analogue signal processing and conditioning. The analogue signals are digitized by analogue to digital converters (ADC) cards and then processed digitally in Field-programmable Gate Array (FPGA) firmware and embedded Central Processing Units (CPU). The processed data is read by control systems over communication interfaces.

Most of the diagnostic systems have this structure therefore one can distinguish in this scheme common and dedicated components. The components may be either hardware modules like an ADC card, can be a firmware component implemented in Very high speed integrated circuit Description Language (VHDL), or software running in embedded processors. The common components - the light grey boxes in Fig. 1 – are present in most applications. The dark grey boxes are specific firmware/software components and are usually different for every application. Having in mind the similarity of various applications we focused on development of common components which can be used by the application developers.

The SwissFEL is a double bunch machine with 28 ns bunch space and 100 Hz repetition rate [1]. In this mode of operation some functions are time critical and have to be implemented in VHDL, but most of the functions can be processed by embedded CPUs between two machine pulses within 10 ms.

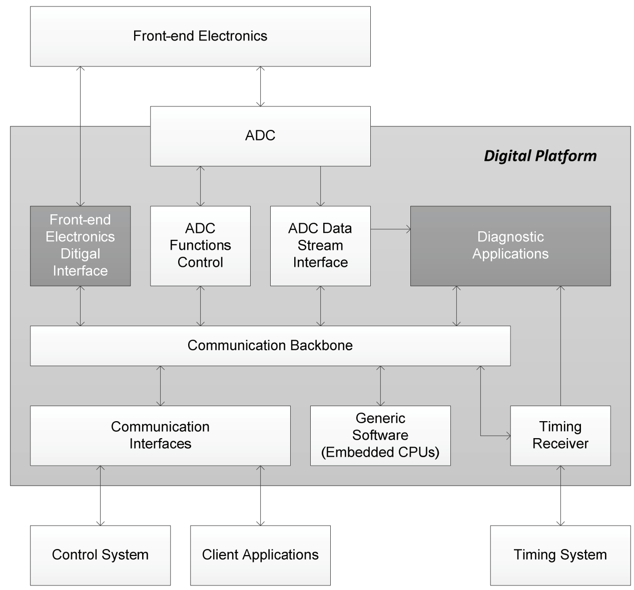

Figure 1: Block diagram of the electronics platform.

The communication backbone is built up of several bus instances and bridges between them and provides access to all components in the system which have bus interface. Communication interfaces block is a set of bridges from communication backbone to other protocols which allow access by control system or various client applications.

Synchronization of the diagnostic systems with the machine is achieved by an embedded timing receiver. This component decodes serial data stream distributed by the timing system over fibre optic links and generates synchronously local triggers and clocks.

HARDWARE PLATFORM

In order to build various systems with common components the system must be modular. Therefore our typical system consists of several hardware cards of various types like carriers, mezzanines or rear transition modules. The hardware platform is based on VERSA Module Eurocard bus (VMEbus) and has been already presented in other publications [2] and the following list gives only brief description:

- General Purpose Analog Carrier (GPAC) is a digital VME card which contains three Virtex-5 FPGA chips, three Spartan3 FPGA chips, and two 500 pin connectors for mezzanine cards. This board is used in every application for digital signal processing - see top left picture in Fig. 2.

ISBN 978-3-95450-176-2

- ADC12FL, ADC16HL – these are two mezzanine cards, one with eight 12-bit ADCs and 500 MSPS sampling rate, and the second with six 16-bit ADCs and 160 MSPS sampling rate. These two ADC cards cover all diagnostic applications - see the top right picture in Fig. 2.
- Radio Frequency Front-end Electronics (RFFE) is a set of various VME size cards where the sensor cables are connected. The cards output processed analogue signals which are connected to ADCs. Each RFFE has digital interfaces which are used to control RFFE functions from GPAC board. The specific RFFE boards are described in diagnostic applications section.
- Rear transition modules (RTM) are boards which are plugged on the rear side of the crate and have two functions. One is to provide digital interfaces between GPAC and RFFEs. The second is to extend functionality of the front board e.g. the COM RTM contains additional interfaces for GPAC.
- Modular BPM Unit (MBU) is a crate initially designed for BPM systems but it can be used as well for other diagnostic systems. This crate has no VMEbus and is meant for modular stand-alone systems - see the bottom picture in Fig. 2.

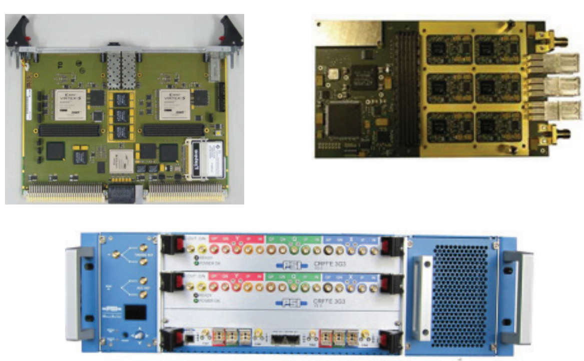

Figure 2: Hardware components.

Configuration Options

Based on the above described hardware components one can build a diagnostic system in two major configurations. One configuration is built with a VME crate and the other with an MBU.

VME Based Configuration The VME crate is able to host several digital cards with VMEbus interface and allows building complete system including the control system as presented in Fig. 3. In the VME crate one can install front-end electronics communicating with GPAC over special transition cards (GPAC/RFFE RTM) deploying user pins from the VME P2 connector. In the same crate the CPU with control software and timing module is installed. The CPU communicates with GPAC over VMEbus. Depending on number of available slots in the VME crate it is possible to have several GPAC boards with corresponding RFFE cards in the same crate.

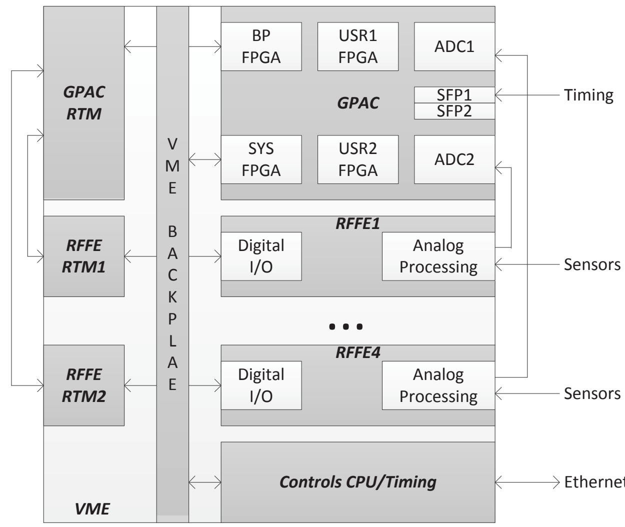

Figure 3: VME based hardware configuration.

MBU Based Configuration In this configuration the control system is not included. The MBU contains only a single GPAC and up to four RFFEs as illustrated in Fig. 4. The MBU contains customized backplane without VME bus since there is only one card with VMEbus interface. The rear transition modules from the VME configuration are replaced by direct connections in the MBU backplane. A dedicated communication RTM board (COM RTM) extends the GPAC interfaces implemented in the VME connectors. The SFPs of GPAC and COM RTM provide physical interfaces for communication protocols between MBU and control systems placed somewhere else in the machine. This solution is preferred for small systems physically distributed along the machine such as BPMs. Many MBUs can be connected to a single Controls CPU by means of Ethernet or fibre optic links. The number of MBUs connected to a single CPU depends on its computation power and it can be easily balanced among many CPUs by reconnecting the MBU.

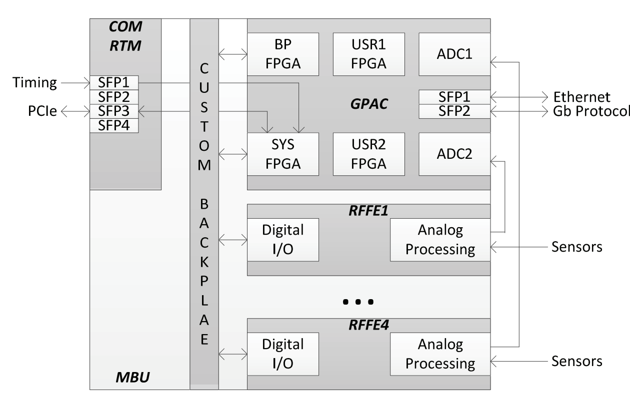

Figure 4: Hardware installation in an MBU.

ISBN 978-3-95450-176-2

GENERIC FIRMWARE AND SOFTWARE

Besides the common hardware components there is also a firmware and software platform which is common for many diagnostics applications and can be used as a base in the diagnostic projects. The following sections describe common firmware and software solutions which are used in various diagnostic applications.

Communication Backbone and Interfaces

The GPAC board has Xilinx Virtex-5 and Spartan3 FPGA chips. Virtex-5 has built-in CPU PowerPC 440, and Spartan3 has synthesized CPU called uBlaze. Both processor types use Processor Local Bus (PLB) for communication. The base firmware configuration of GPAC has three Virtex-5 chips with PowerPC, and two Spartan3 with uBlaze, and the user applications are distributed over those FPGA chips and CPUs. Therefore it was necessary to build a kind of infrastructure which allows communication between all CPU subsystems and the control system. Fig. 5 presents the block diagram of the communication infrastructure.

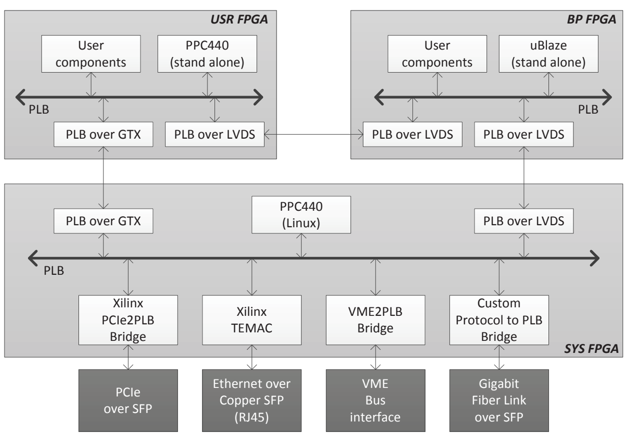

Figure 5: Communication components.

The PLBs are connected to each other by PLB to PLB bridges. The PLB bridge maps part of the PLB address space in remote FPGA to address space of the local PLB based system. The bridge is transparent which means that the PLB Master reads an address on local PLB and the bridge forwards the read transaction to remote PLB, the remote PLB master executes the transaction and sends back the data and the local PLB slave completes the transaction. From PLB Master point of view the difference between local and remote transactions is only in latency. The PLB bridge is implemented in two versions: PLB over GTX and PLB over LVDS. They differ in physical layer. Two Virtex-5 chips are connected by RocketIO (a gigabit serial link called GTX in Virtex-5) and can run with baud rate up to 5 Gbps. Spartan3 has no RocketIO, therefore the link is built on LVDS lines and is scalable depending on the number of available LVDS lines between two FPGA chips.

The communication with external systems is determined by available communication interfaces and protocols in those systems. There are four interfaces currently implemented in GPAC: VME slave, PCIe end-point, 1Gb Ethernet, and PLB over GTX bridge to another system with PLB. The VME, PCIe, and PLB over GTX have PLB master functionality which means that the external system can directly access memory locations in GPAC. The Ethernet interface is used to communicate from client applications by means of TCP/IP protocols with applications running on Linux system in GPAC.

Timing Receiver for SwissFEL

The timing system for SwissFEL consists of a single event generator (EVG) and several event receivers (EVR) connected by fibre optic links [3]. The timing system distributes several events, event clock, and machine status information such as beam on/off, pulse number, charge, etc. The hardware of the timing system is based on the VME standard. The EVR is usually installed in the VME crate next to the controls CPU. But in case of hardware configuration with MBU there is no place for EVR card. Therefore the GPAC board contains a kind of embedded event receiver implemented in FPGA. The block diagram of the receiver is presented in Fig. 6.

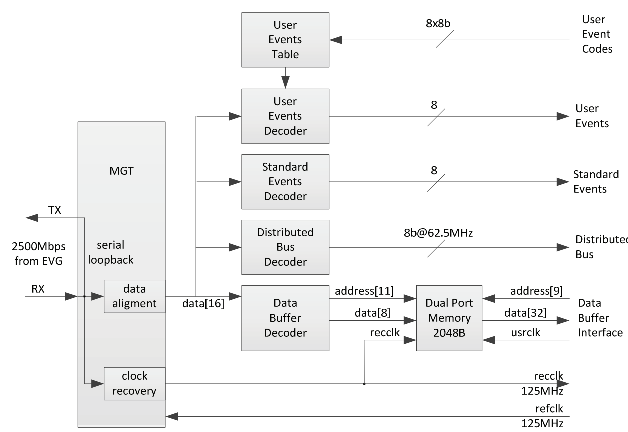

Figure 6: SwissFEL embedded timing receiver.

The fibre link from the timing system network is connected to one of the SFPs on the COM RTM and the data stream is decoded in the FPGA. The firmware allows generation of up to eight triggers from user defined events and it contains a data buffer where the machine status data is received and kept for user applications. The standard events decoder and distributed bus decoder are also implemented according to the specification of the timing system and can be used by the diagnostic applications.

Generic Software

The generic software is implemented in PowerPC in SYS FPGA. The PowerPC is running PetaLinux – this is a Xilinx version of Linux for embedded systems – which was adapted for the GPAC hardware. The Linux system is an open platform for any kind of generic software as well as for user extensions. In PetaLinux environment one can write a new program, cross-compile, and upload it to

ISBN 978-3-95450-176-2

GPAC and run it without disturbing the running system. Among various kind of generic software installed on Linux these are the two most important ones for the application developers: firmware maintenance software and web server.

Firmware Maintenance Software The maintenance software gives possibility to run on Linux several programs to test the system status, read and write any address in the system, and perform remote update of the firmware. The secure copy protocol (SCP) server running on GPAC gives access to file system on a compact flash (CF) card with file system mounted to Linux where configuration files are stored. It is possible to update remotely configuration of all FPGA chips on the GPAC board as well as the Linux image. The firmware update strategy was implemented to keep the system always running and available remotely. It is possible to have several configuration versions and the boot firmware checks if the recently uploaded firmware works and makes the GPAC accessible from outside. If not, the booting firmware loads so-called golden image which works always and gives possibility to upload another, working version of the user firmware.

Web Server The quick way of getting access to the common firmware running on GPAC can be achieved by a web browser. A web server was implemented on the GPAC board. It starts automatically and it has a set of web pages which allows operation of the ADC scope application. The web server is based on open source GoAhead web server. The web server attaches to every requested web page a special library written in JavaScript called WebMAP. This library is responsible for continuous communication of the webpage on the client side with the web server. This library continuously retrieves data from the web server and updates the local web page. An example of such web page is presented in Fig. 7. The screenshot presents a set of control fields with timing and triggers parameters as well as waveforms from four ADC channels.

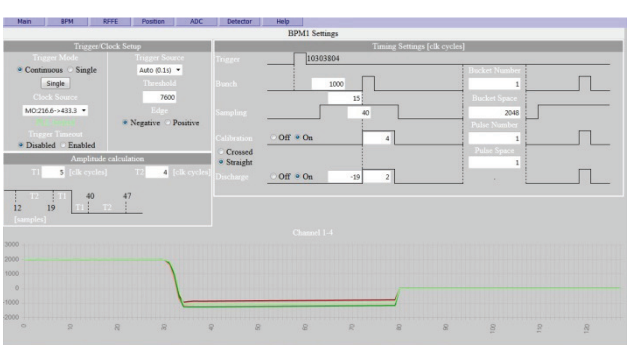

Figure 7: Web page for ADC scope.

The WebMAP library allows building new webpages for user applications by creating new Hyper Text Markup Language (HTML) files without changing the web server. Data embedding in the HTML is done by special use of HTML tags property *title*. This property contains hardware address, data type, and other parameters used by the WebMAP library to access and format displayed data from GPAC. After the web page is loaded by the web browser, the WebMAP library automatically finds tags with defined *title* properties, parses the *title* strings, and performs periodic data update of their content. The new or modified HTML files only have to be uploaded to GPAC CF card by file transfer protocol and can be applied without disturbing the running system.

ADC Based Oscilloscope

Each of the diagnostic applications has analogue signals connected to one of the two types of ADC mezzanine cards. The ADC data stream can be processed directly by VHDL firmware or can be stored in local memory and used for post processing either in embedded CPU or in control system. The ADC based oscilloscope records ADC data and provides interfaces to user applications as presented in Fig. 8.

The parallel data lines coming from ADC have to be aligned in the FPGA to a single clock in order to process them synchronously. Then the data is buffered in FIFOs which keep past samples in order to see what happened before trigger conditions occur. Then the buffered samples are gated by the trigger control component. The trigger can work in auto mode, single mode, or with external trigger. The memory can store up to 4 k samples per channel. This is dual port memory which allows separation of the ADC clock domain from the local clock.

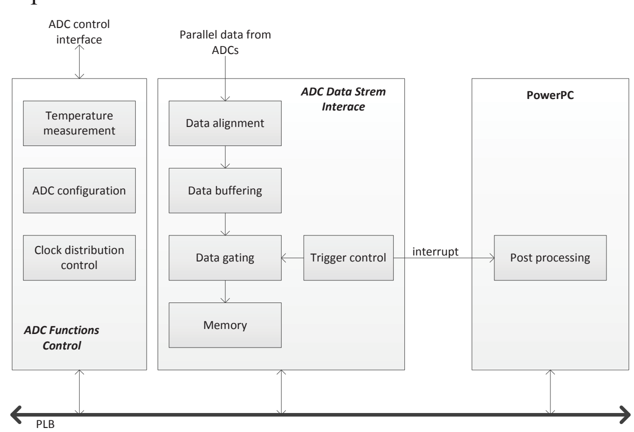

Figure 8: ADC Scope firmware block diagram.

The ADC Functions Control component is used to interface various components on the ADC mezzanines. The ADC cards have configurable clock distribution circuit where one can select local or external clock, set individual clock delays and division factors. The ADC12FL card can also synthesize in phased-lock loop (PLL) different sampling frequencies. The component also provides configuration of the ADC settings. The post processing in PowerPC is a piece of software which calculates basic parameters of the recorded wave forms such as minimum, maximum, mean value, standard deviation, etc.

ISBN 978-3-95450-176-2

DIGITAL PLATFORM APPLICATIONS

The above described digital platform is a base for application specific extensions. If the diagnostic application deploys specific front-end electronics, the developer has to prepare in firmware RFFE specific control components. The firmware library of the digital platform already provides basic VHDL components for typically implemented interfaces such as I^2C, UART, SPI, and 1-Wire. In next step the developer implements application specific ADC data processing. Depending on the latency requirements this can be done either in VHDL or in software in PowerPC. The following applications are based on the GPAC digital platform.

Beam Position Monitors The BPMs for SwissFEL have dedicated RFFEs for two types of cavity pickups for linac and undulators [5]. The data is sampled with 16-bit ADCs. The ADC data is processed directly in FPGA and is supported by pulse to pulse feedbacks implemented in PowerPC [6]. The digital platform was also successfully used for implementation of BPM systems for European XFEL and FLASH accelerator at DESY. The Cavity BPM systems have been running in FLASH since one year [7] and the first Button BPM systems were tested at FLASH and now they are running in XFEL [8].

Beam Loss Monitors The BLMs use a kind of generic RFFE called PAC. The PAC has several connectors for mezzanine cards with analogue circuits for signal conditioning. The BLMs use 12-bit ADCs and the data processing is also done in VHDL and is supported by PowerPC software [9].

Bunch Compression Monitors The BCMs are used in bunch compressors to measure the quality of bunch compression [10]. It deploys specific RFFE for peak detection. The data is sampled by 12-bit ADCs. Due to relaxed condition for latency, the whole processing will be implemented in software in PowerPC. In this case the system will use the external PLB over GTX bridge to communicate with BPM systems in order to normalize the compression measurement.

Bunch Arrival Monitors The bunch arrival monitors have dedicated front-end electronics [11]. Currently it only uses the GPAC platform for sampling signals with 12-bit ADC and the post processing will be implemented in future.

CONCLUSION

The FPGA based digital platform besides common hardware has common firmware and software platform for all diagnostics applications. Deploying of the common firmware/software as a base for specific diagnostics applications reduces significantly the development effort. All the elements have been already tested in some applications. Nevertheless there are still computation resources available for further extensions if necessary.

The next version of GPAC board based on seven series of Xilinx FPGA chips is under development. The new GPAC board will be backward compatible with other hardware components. It will increase the life time and maintainability of existing and future applications by another 15 year.

REFERENCES

[1] Home page of SwissFEL project: http://www.psi.ch/swissfel/
[2] B. Keil et al., "A Generic BPM Electronics Platform for European XFEL, SwissFEL and SLS", IBIC'12, Tsukuba, Japan (2012).
[3] B. Kalantari, "SwissFEL Timing System", presentation given at MRF Workshop: http://www.mrf.fi/index.php/timing-workshop Prague (2014).
[4] Embedded Web Server GoAhead: https://embedthis.com/goahead/
[5] M. Stadler et al., "Development of the SwissFEL Undulator BPM System", IBIC'14, Monterey, USA (2014).
[6] B. Keil et al., "Design of the SwissFEL BPM System", IBIC'13, Oxford, UK (2013).
[7] M. Stadler et al., "Beam Test Results of Undulator Cavity BPM Elecdtronics for the European XFEL", IBIC'12, Tsukuba, Japan (2012).
[8] D.M. Treyer et al., "Design and Beam Test Results of Button BPMs for the European XFEL", IBIC'13, Oxford, UK (2013).
[9] C. Ozkan Loch et. al. "System Integration of SwissFEL Beam Loss Monitors", MOPB051, these proceedings, IBIC'15, Melbourne, Australia (2015).
[10] F. Frei et al., "Development of Electron Bunch Compression Monitors for SwissFEL", IBIC'13, Oxford, UK (2013).
[11] V. Arsov et al., "First Results from the Bunch Arrival-Time Monitor at the SwissFEL Test Injector", IBIC'13, Oxford, UK (2013).

ISBN 978-3-95450-176-2

SYSTEM INTEGRATION OF SwissFEL BEAM LOSS MONITORS

C. Ozkan Loch, D. Llorente Sancho, P. Pollet, G. Marinkovic, R. Ischebeck, V. Schlott,
Paul Scherrer Institut, PSI, Switzerland

Abstract

Scintillator-based Beam Loss Monitors will be used at SwissFEL for monitoring the losses, for optimizing beam conditioning, beam measurements with the wire-scanner and Undulator protection. The optical signals from the scintillators will be detected by PMTs which are located outside the accelerator tunnel. The PMT control and signal conditioning is done via a front-end based on the PSI Analogue Carrier board (PAC). The PAC board allows for amplification/attenuation, offsetting and single-ended to differential conversion of the analog signal, while the Generic PSI Carrier (GPAC) board provides digitization and FPGA-based post-processing, along with bridging the communication to EPICs controls. A fast algorithm was developed to process the signals and trigger the machine protection system (MPS) at 100Hz. The system integration of the BLMs will be discussed in this paper.

INTRODUCTION

In SwissFEL, scintillator screens and wire scanners will be used to monitor the electron beam in the charge range 10 - 200 pC and in the energy range 0.007 - 5.8 GeV. In particular, wire-scanner will be used to resolve the 28 ns time structure of a 100 Hz, two-bunches train [1, 2]. Losses caused during beam conditioning and wire-scanner insertions can travel for tens of meters in the machine. Loss monitors have been designed to track these losses for emittance measurements and to prevent radiation-induced demagnetization of the Undulators.

The beam loss monitor systems have been developed based on the following system requirements to detect losses before an appreciable loss level is reached.

Table 1: Beam Loss Monitor Specifications

Parameters	Specifications	Purpose
Charge range	10 - 200 pC	Full beam loss
Minimum detection	0.1 pC	Wire-scanner measurements
Repetition rate	100 Hz	2-bunch resolving capability, shot-to-shot
Machine protection system	Yes	Beam synchro-nous DAQ

There are a total of 48 BLMs, which will be located at fixed distances with respect to the wire-scanner for slice emittance measurements, and between Undulator segments to monitor the losses reaching at these locations. The BLMs will be interfaced to the machine protection system (MPS), leading to either a beam suppression in the machine or to immediately act on the laser shutter.

#cigdem.ozkan@psi.ch

DETECTORS

The BLMs consist of organic scintillator fibers (BCF12, Saint Gobain), which are then connected to clear duplex plastic optical fibers (POF, Avago Tech) that propagate the scintillator's output light from the accelerator into the technical gallery where the light detectors are located. One of the POFs is optically mated to a PMT (Hamamatsu H10720) [3] and the other to a pulsed light emitting diode (Avago Technologies HFBR-1505AZ/2505AZ) [4]. The LED provides a system-live check and observation of light transmission through the connected fibers for radiation damage, during or outside of beam operation.

DAQ SYSTEM OVERVIEW

The PMTs and preamplifiers, which convert the PMT charge pulse into a time-shaped voltage signal, are mounted on the signal conditioning board called the PSI Analog Carrier (PAC) board. All controls of the PMT, preamplifier and LED voltages, and output signal conditioning is done by the PAC. The output signals are digitized and processed with the Generic PSI Carrier (GPAC) board, which was developed at PSI for application in multiple accelerators (European XFEL, SwissFEL and SLS) [5].

PAC Board

Up to four mezzanine-boards, 2 channels per board may be plugged to the PAC carrier board. Each mezzanine board supports one PMT signal conditioning electronic. This means that a single PAC board can house and control 4 BLMs. All mezzanine boards connectors provides low noise standard linear supply voltages (±12 VDC / ±5 VDC and +3.3 VDC), eight remotely controlled DC voltage supplies, eight general purpose digital controls/status signals and four differential digital I/O signals covering a large spectrum of requests. To avoid digital noise production on sensitive signals, the digital control (Oscillators, FPGA) can be set to standby mode when not in use.

The PAC board communicates with remote systems controls over a serial connection, either through specific user I/O on the VME-P2 connector or over a standard RJ45 network connector located on the front panel for

ISBN 978-3-95450-176-2

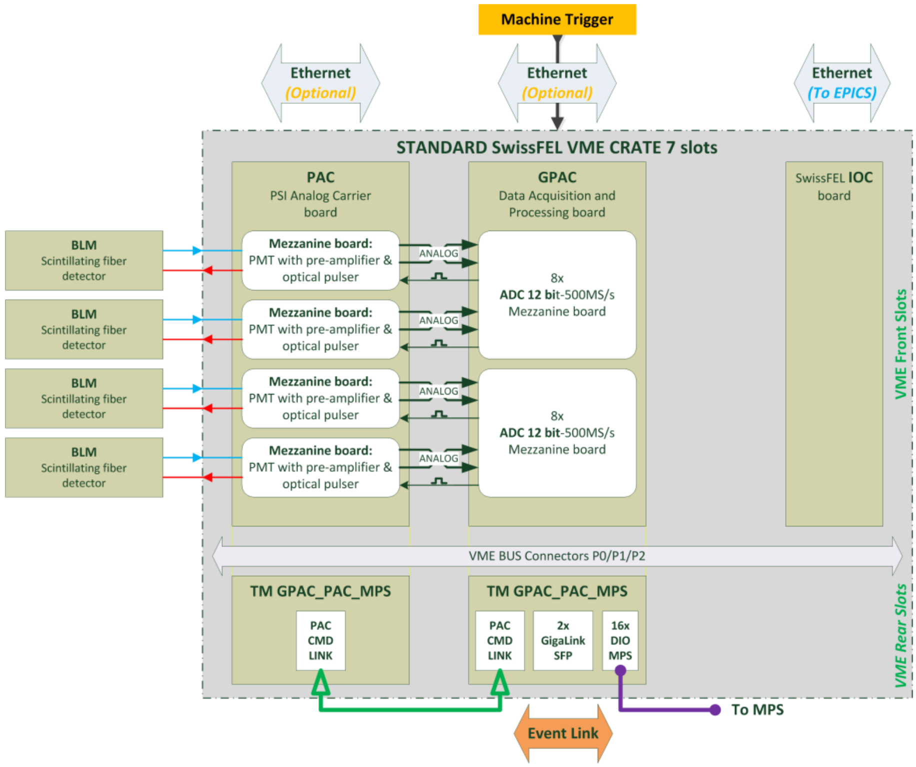

Figure 1: Sketch of the Beam Loss Monitor (BLM) electronic crate overview.

standalone applications. The PAC board supports live insertion.

Analog-to-Digital Conversion

The SwissFEL BLMs use an ADC board originally developed for the European XFEL button BPM system [5]. The ADC board, implemented as mezzanine module for the GPAC, has eight 12-bit 500 MSa/s ADCs (Intersil KAD5512P-50). We plan to interleave up to two/four of such channels for increased resolution, with a 180°/90° degree delay. This delay on the raw signal is introduced digitally with the LMK01020 [6] clock distribution chip on the ADC mezzanine.

The ADC sampling clock is provided externally by the reference distribution system. Differential signalling and coaxial cables are used for the connections to and from the PAC.

Digital Backend

The digital backend consist of one GPAC board and two ADC mezzanine cards as a generic digital platform, as described in [5, 7].

The System (SYS) FPGA handles communication of the GPAC with the machine control system and timing system, via VME bus or SFP fibre optic link. Over VME, the GPAC communicates to the IOC board, responsible for EPICs record processing, as well as linking with the machine network. The digital processing of the ADC signals is done in the two FPGAs (a.k.a. BPM FPGA, Xilinx Virtex-5 [8]), where the signal processing of the mezzanine ADC signals is done in firmware/software (see “Firmware” section). The FPGA provides interfacing via backplane transition modules to the PAC board, over a differential protocol (“FastLink”) running at a clock frequency of 12.5 MHz.

In addition, the GPAC has a so-called backplane (BP) FPGA for controlling slower IOs of front-end electronics via user defined IOs, as well as two FPGAs (CONFIG and SEU) for board and power management. Thanks to the generic firmware/software framework, only part of the BPM and BP FPGA firmware on the GPAC is application-dependent, thus reducing the development effort for new applications and monitors.

Transition Modules

The GPAC will connect to the SwissFEL BLM-Electronics, SwissFEL Machine Protection System (MPS) and SwissFEL event recording system via a transition board mounted on the rear side of a SwissFEL standard VME crate. Communication to the event generating system is achieved by GBit/s optical links connected to the GPAC-VME J0/P0 connector via SFP-modules, while MPS and BLM electronics use the user defined pins of the GPAC-J2/P2 for controls [9].

Triggering

The embedded event receiver consists of a generic IP core capable of decoding the SwissFEL event distribution system [7]. This core is located on the GPAC and connected to the main event generator via optical fiber, using a front-end SFP+ connector on the GPAC. This event is routed to the BPM FPGA, where the appropriate samples from the ADCs are captured and processed.

ISBN 978-3-95450-176-2

This solution has been preferred over the VME-EVR-230 card from Micro Research [10]. Even though it has a jitter of 5ps which is adequate for the needs of the BLM, an integrated event decoder has been preferred for cost-saving reasons.

I/O Controller

Data and statistics obtained at 100 Hz are transmitted through EPICS to the IOC, based on an IFC1210 board from IOxOS [11]. There raw digitized signals and processed results are transmitted to the archiver for both short and long term storage. Control consoles access these records over EPICS, although at a much lower refreshing rate (~5Hz).

SIGNAL PROCESSING

Firmware

The BLM-specific part of the firmware was implemented on the BPM (Virtex-5 FX70T) and BP (Spartan3A) FPGA. Another FPGA (Spartan3A) is located on the PAC board, with a serial protocol to the BP FPGA on GPAC for control of PAC board settings like gain, offset, etc.

The data processing on the BPM FPGA consists of data reception, triggering, buffering and relevant parameter extraction (discussed in the next sections). This is done in real time for every SwissFEL bunch, been able to process a full vector of 4k samples at 100Hz. Raw data is not discarded, it is transferred to the IOC for archiving and for off-line analysis.

On the PAC, a System-on-Chip (SoC) design based on a Microblaze processor has been implemented on its Spartan 3 FPGA. The PAC may receive commands from the GPAC over the FastLink connector or work autonomously, accessed over a XT-Nano-XXL chip [12]. This flexible communication component converts TCP/IP packets to a Serial RS232 format, which is then connected to the PLB bus using an UART core as bridge. Another IP Core interfaces with the 8 DAC available on the PAC via an SPI Bus. Voltage values and operating ranges can be set from EPICS or over the XT-Nano interface.

The PAC board has four slots for extension for detector-specific mezzanine cards. Each mezzanine interface includes eight analogue outputs from two DAC devices, generic lines for SPI/I^{2}C communication and power. This configuration allows for expansion and modularity, highly desirable features in projects of such complexity as the Beam Loss Monitors. By means of an I^{2}C access, an identifier can be read for identifying which mezzanine board has been mounted on the PAC.

Firmware/Software Implementation

The digitized waveforms are processed to determine the pulse integral (see Fig. 2). First a number of samples are picked just before the pulse signals and averaged to give the "baseline" value. Baseline is calculated anew for each bunch.

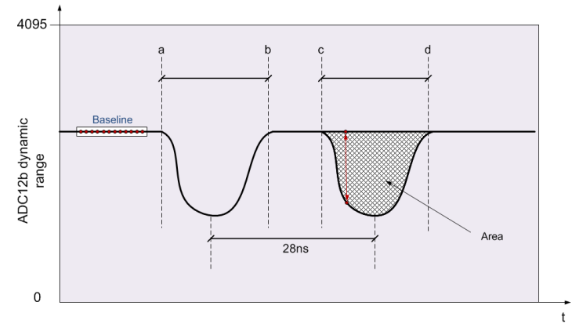

Figure 2: Schematic of the pulse integration.

Then, the regions of interest – sample numbers for the beginning and end of a pulse - are determined by the operator of these monitors. The reason behind this approach is to decouple the two pulses from each other for various locations of the BLMs in the machine, as some variations are to be expected. Region-Of-Interest (ROIs) can be configured over EPICS for double-bunch distinction. The samples in the ROI are summed and the baseline is subtracted. The behaviour of the integral area (shown in Fig. 2) of each pulse is tracked for loss measurements. The value obtained is compared to three thresholds. Two correspond with the MPS alarm levels and a third for device saturation. All three are calculated in <1ms on a per-bunch basis.

Once raw data has been processed, and interrupt to the VME Bust/IOC triggers data fetching from the FIFO on the IP Core to the corresponding waveform record. VME Burst transfers (MBLT, 2eSST) are enabled to support the necessary bandwidth.

MPS Algorithm

The SwissFEL machine protection system (MPS) collects alarms from a variety of monitor systems. Each monitor can generate two types of alarms: level 1 alarm, where no further electron bunches are generated by shifting the radiofrequency (RF) in the gun in order to obtain a timing where no laser is present, and a more severe level 2 alarm, where the RF for the entire machine is turned off.

The calculations are performed at a rate of 100 Hz, independent of the bunch repetition rate of the machine.

1. Determination of monitor reading that enters the calculation (S_0)
2. In case there is no beam measured during the current RF pulse: $S_{calc} = S_0$
3. In case the monitor reading S is saturated: $S_{calc} = S_{sat} .S$
4. Otherwise: $S_{calc} = S$
5. Filtered error signal is calculated
6. Generation of alarms (level 1 or 2) by comparing the filtered signal to the alarm thresholds

Once an alarm is generated, it remains active until its condition is not fulfilled anymore.

For the FPGA implementation, there are four vectors of interest: the integral values extracted from ADC samples

ISBN 978-3-95450-176-2

(S_n), the previously calculated average (avg_n) and the two threshold vectors (one per alarm level).

The proposed formula for alarm level calculation is:

$$\frac{1}{2K}\left(avg_n \cdot (K-1) + S_n\right) \qquad (1)$$

K is a factor for weighted average. A diagram of the algorithm is shown in Fig. 3.

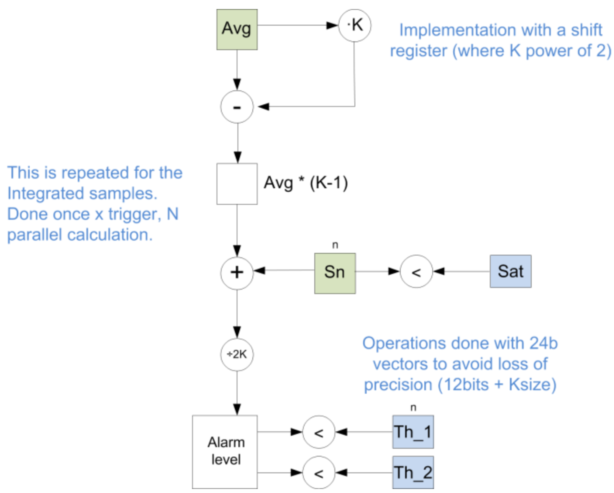

Figure 3: Flow diagram of the MPS algorithm.

This is essentially a low-pass filter which reacts inversely to the number of previous average values calculated (K). This smooths out alarm generation while eliminating spurious alarms (Fig. 4). Divisions and multiplications on the FPGA are implemented with shift registers, which speeds processing while reducing resource use. Hence, K must be a power of two.

Automatic Gain Adjustment

This is where the PMT gain voltage is changed on the PAC board to avoid saturating both the ADC input and the PMT. Each digitized pulse is compared to the saturation threshold. The GPAC issues a command to reduce the PMT control voltage to avoid saturation effect and hence, inaccurate loss measurements. If despite gain reduction the PMTs and/or ADCs are saturated, the machine protection system will trigger Alarm level 2 and prevent beam travelling through the machine.

CONCLUSION

We have presented the DAQ system for the SwissFEL Beam Loss Monitors, which has been designed profiting to a large extent from a generic diagnostics hardware concept. All in all, 48 BLMs will be installed, making it one of the critical instruments for the protections of the accelerator.

Signals obtained from the scintillator fibers are sent to a modular analog front end for signal conditioning before being digitized with 12 bit, 500 MSa/s ADCs. Data is processed in real time on a FPGA, where a specific algorithm compares loss levels to a set threshold and raises the corresponding alarms in case machine protection must be triggered. The DAQ system enables processing at 100 Hz rate and thus, generating an interlock which is fast enough to prevent machine damages.

The firmware for the PAC and GPAC boards have been implemented and tested with realistic input, obtaining satisfactory results. PAC has proven to successfully communicate with the GPAC and the EPICS control system via an IFC1210 IOC.

Further tests of the complete system are ongoing to verify the stable function of the instrument, together with the feasibility of using BLMs as readout for wire-scanner beam profile measurements. This is imperative for accurate emittance measurements. Moreover,

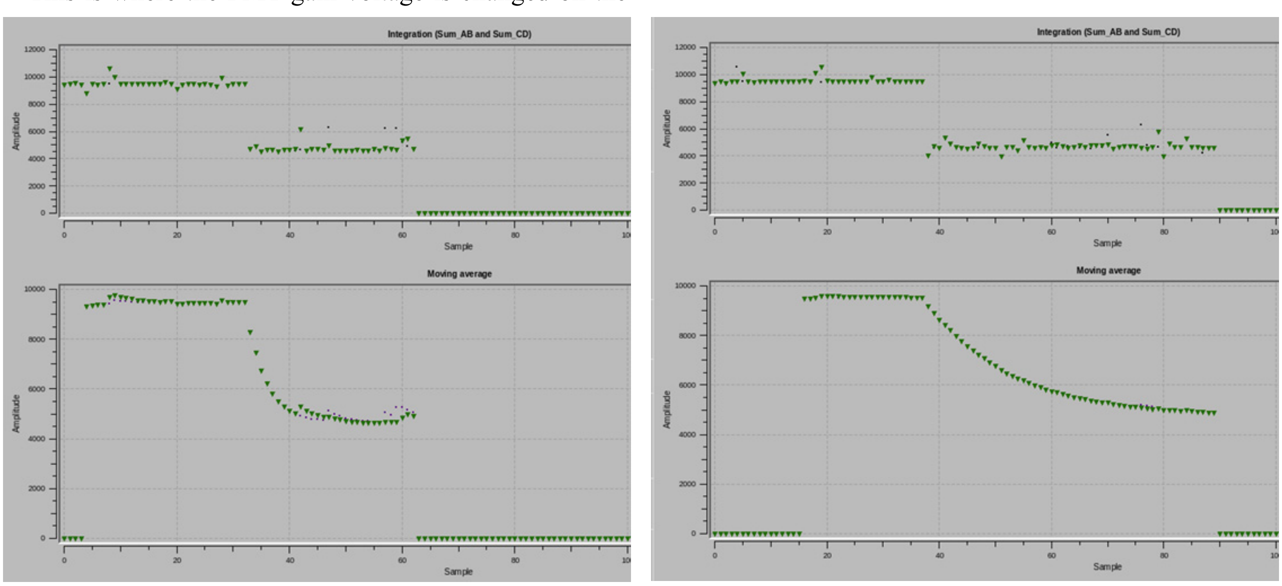

Figure 4: Results of the algorithm implementation shown for two values of K. The algorithm acts as a low pass filter (bottom plot) and removes noise from the shot-to-shot changes of the integrated signals (top plot). The filtered signal is used for triggering the MPS.

ISBN 978-3-95450-176-2

implementation has been successfully completed for the Longitudinal Loss Monitors, where the position of the losses can be determined to within 1 m. Each sample of the digitized output is information relevant for the MPS computation, which means about 2000 computations at 100 Hz.

ACKNOWLEDGMENT

The authors would like to thank W. Koprek for his valuable input in utilizing the GPAC, S. Hunziker for the reference distribution and F. Löhl for the discussions on the algorithm for integrating the loss monitors to the machine protection system.

REFERENCES

[1] R. Ischebeck et. al., "Overview of beam instrumentation activites for SwissFEL", MOPF31, Proceedings of IBIC2014, Monterey, USA (2014)
[2] G.L. Orlandi et. al., "Design and test of wire-scanners for SwissFEL", THP091, Proceedings of FEL2014 Basel, Switzerland (2014).
[3] Hamamatsu photonics, Solothurn, Switzerland.
[4] Acal Bfi, Groebenzell, Germany.
[5] B. Keil et. al. "A generic BPM electronic platform for European XFEL, SwissFEL and SLS", MOCB02, Proceedings of IBIC2012, Tsukuba, Japan (2012)
[6] Texas Instruments: http://www.ti.com/product/lmk01020
[7] W. Koprek et. al. "Overview of Applications and Synergies of a Generic FPGA-Based Beam Diagnostics Electronics Platform at SwissFEL", these proceedings, IBIC 2015, Melbourne, Australia (2015).
[8] Xilinx/Avnet website: http://www.xilinx.com/support/documentation/data_sheets/ds100.pdf
[9] P. Pollet, Transition modules, Private communication
[10] IOXOS website: http://www.ioxos.ch/index.php?option=com_content&view=article&id=136&Itemid=113
[11] Micro Research website: http://www.mrf.fi/index.php/vme-products/76-vme-event-receiver-wo-rf-vme-evr-230
[12] AK-NORD, XT-Nano-XXL website: http://www.ak-nord.de/ak/product_info.php?products_id=33&language=en

ISBN 978-3-95450-176-2

THE BEAM LOSS MONITORING SYSTEM IN TAIWAN PHOTON SOURCE

C. H. Huang, Demi Lee, Jenny Chen, Y. S. Cheng, K. H. Hu, C. Y. Wu, P. C. Chiu, K. T. Hsu
NSRRC, Hsinchu 30076, Taiwan

Abstract

Taiwan Photon Source is a third generation and 3 GeV synchrotron light source during beam commissioning in NSRRC. Several types of beam loss monitors (BLMs) such as PIN diodes, scintillation detectors, Cherenkov BLMs and RadFETs are installed in the storage ring and booster ring to study the beam loss distribution and mechanism. The installation infrastructure, design of reader units and integrated graphic user interface will be described in this report. The preliminary experimental results will also be summarized here.

INTRODUCTION

Taiwan Photon Source (TPS) is a third-generation light source in NSRRC [1]. The circumference of the storage ring is 518.4 m with 24 double-bend achromat cells. There are 6 long-straight sections and 18 standard-straight sections to accommodate insertion devices. In the first initial phase for the beam-line commissioning, seven beam lines with ten inserting devices are installed in the storage ring. At the same time, two superconducting RF (SRF) cavities are also installed during this stage.

To study the beam loss during the SRF and inserting device commissioning, several types of beam loss monitors (BLMs) are setup in the storage ring and booster ring. The PIN diodes can detector the minimum ionizing particles as an electron hits the wall of the vacuum chamber and produce the electromagnetic shower [2]. Cherenkov detector is sensitive to charged particles. The scintillation detector is a kind of secondary emission monitor which combines a scintillating material and photomultiplier tube and can detect both the charged particles and X ray. A radiation-sensing field-effect transistor (RadFET) is a metal-oxide-semiconductor field-effect transistor (MOSFET) with an aluminium gate and a thick layer of silicon dioxide which can be used as a dosimeter [3]. These installed BLMs provide a tool to investigate the beam loss location, beam lifetime, vacuum conditions, beam loss mechanism, specific beam loss, resonance crossing, energy measurement by mean of spin depolarization method, etc. These may be also useful to fine tune the machine during the commissioning, routine operation and beam physics study.

PIN-DIODE BEAM LOSS MONITOR

Bergoz's PIN-diode BLM is made of two diodes mounted face-to-face [4]. For the coincidence readout of the signals of two channels, the dual PIN-diode BLM detects charge particles rather than synchrotron radiation and reduces the dart counts due to the noise. It is widely used in many facilities [5]. There are many kinds of solutions to integrate this BLM. To simplify the wiring, a custom designed version of Bergoz's BLM was adopted in which the original 10 pin connector is replaced by a RJ-45 connector as shown in the BLM photo of Fig. 1. The output of the BLM is coupled by a pulse transformer. Four pairs of twisted cables are used to connect a BLM to the signal translator. This twisted cable provides power to a BLM and sends the coincident pulse back. An 8-channel LVDS to LVTTL translator is used to convert pulses. The pulse complied with LVTTL level is connected to the scaler input.

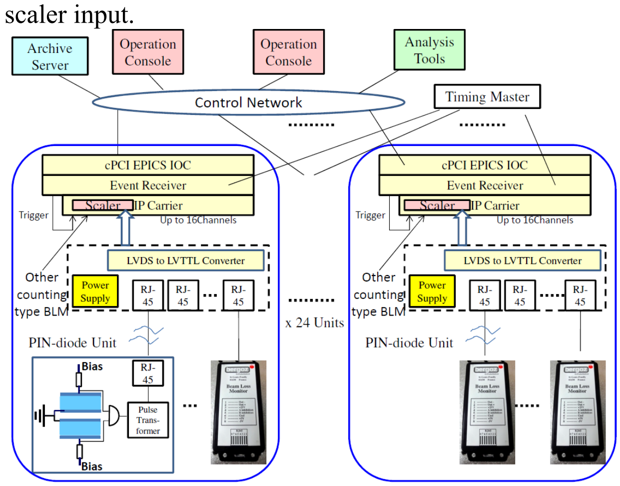

Figure 1: Block diagram of the PIN-diode beam loss monitoring system.

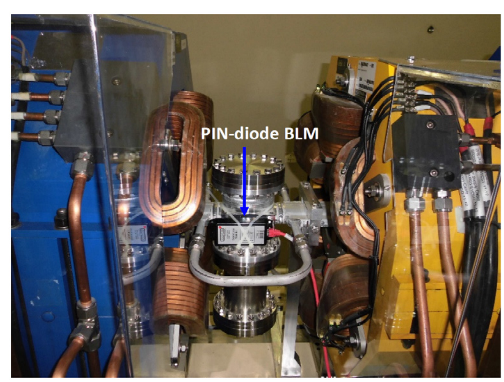

Figure 2: The setup of a PIN-diode BLM.

Data acquisition for BLMs is performed by a 16-channel scaler in an industrial pack (IP) form factor. The IP module is installed on the cPCI carrier board which is located at the cPCI EPICS IOC on the equipment area. All scalers which distributes at 24 IOCs are synchronized by the timing system of the accelerator, shown in Fig. 1. Unused channels of the scalers will be served for another

ISBN 978-3-95450-176-2

kind of counting-type BLMs in the future. Gating period of the scaler is programmable with 1 msec step. The scalar can also operate in the histogram mode with the gate interval in the unit of msec.

Six PIN-diode BLMs in each cell are installed in the inside-wall chamber of the storage ring using cable ties or Kapton tapes as shown in Fig. 2. The setup position of RadFETs for 24 cells is shown Fig. 3. The beam loss distribution in Fig. 4 would be shown with bar chart in the control system.

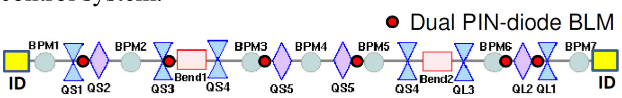

Figure 3: The setup positions of PIN-diode BLMs.

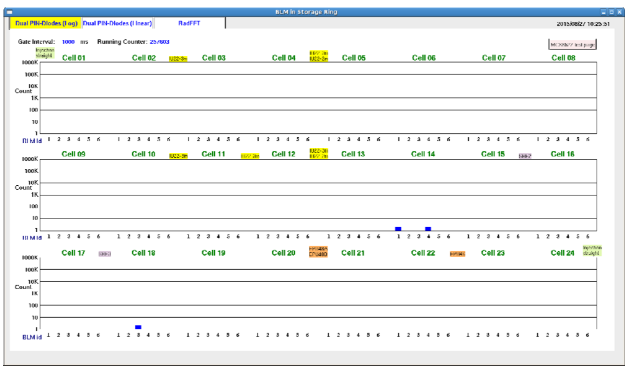

Figure 4: The graphical user interface of PIN-diode BLMs.

RADIATION-SENSING FIELD-EFFECT TRANSISTOR

The RadFET is a discrete p-channel MOSFET optimized for ionizing radiation [6]. The threshold voltage of a RadFET between the gate and source changes due to radiation-induced charges in the oxide layer when applying a constant drain current. The reader of the RadFETs acts as applying constant drain current and reading the threshold periodically. The radiation dose is obtained by a pre-recorded calibration curve between the threshold voltage and radiation dose. The dose rate can be easily obtained by taking time derivative of the recoded dose data.

To obtain high-density installation, the reader is designed up to sixteen channels. A SPI interface is used to read threshold voltage of RadFETs in an ADC. The SPI interface also enables/disables current source in the digital input and output to minimize the interconnecting inside the reader. The process is controlled by the program inside the EPICS IOC, shown in Fig. 5. These sensors can accumulate the radiation dose up to 10K Gray with centigray resolution [7]. Dosage rate is calculated by the EPICS record processing in the EPICS IOC and published into control network.

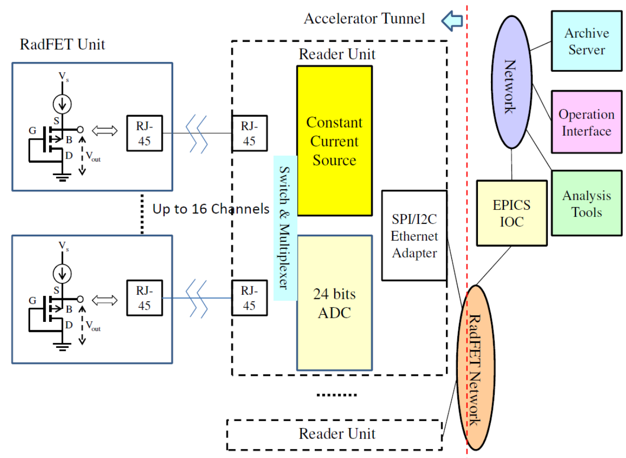

Figure 5: Block diagram of the RadFET setup.

During the Linac and Linac to booster (LTB) commissioning, several RadFETs are installed after the bending magnet, around the dumper and before the stopper. The dose rate updates one minute along accelerator synoptic display, shown in Fig. 6. The threshold voltage of RadFETs are recorded in the archive server, shown in Fig. 7 for further usage. The dose rate or accumulated dose can be processed by a Matlab program from the data in the archive server.

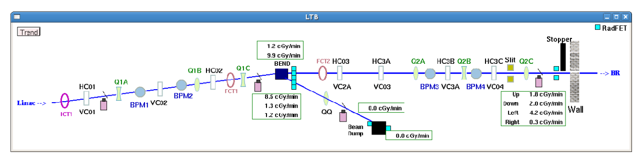

Figure 6: Values along accelerator synoptic display.

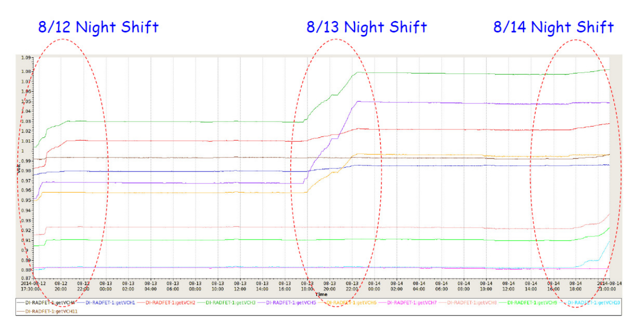

Figure 7: The archived data of the threshold voltages of RadFETs installed in the LTB during the Linac and LTB commissioning form July 12th to 14th, 2014.

RadFETs are also installed before the fifty-four bending magnets of the booster synchrotron in six cells to monitor the beam loss during booster commissioning. Nine RadFETs in each cell are collected by a reader. The threshold voltage, dose, dose rate and beam loss distribution are shown in the control system on line. The beam loss pattern during ramping is shown in Fig. 8.

ISBN 978-3-95450-176-2

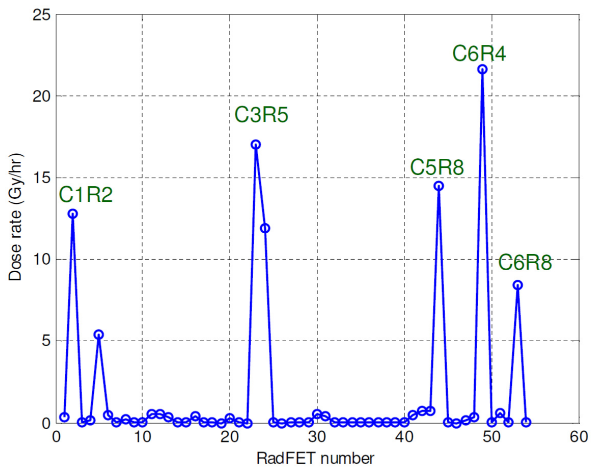

Figure 8: The beam loss pattern as the energy was ramping from 150 MeV to 3 GeV in January 19th, 2015.

In the storage ring, six RadFETs in each cell are installed in the inside wall of the vacuum chamber, shown in Fig. 9(a), in the first stage. These six RadFETs are collected by one reader settled in the cable stray of the tunnel, shown in Fig. 9(b), to minimize the radiation damage and reduce the cable length between the RadFET and reader. Twenty-four readers connect to the EPICS IOC via a private network. The setup position is shown in Fig. 10.

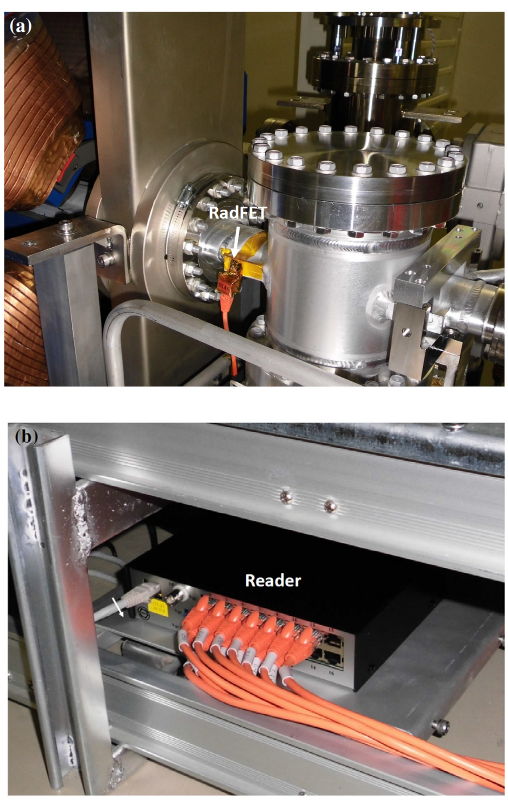

Figure 9: (a) A RadFET and (b) RadFET reader are installed in the inside-wall chamber and cable tray of the storage ring.

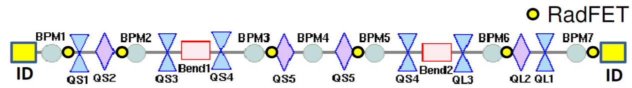

Figure 10: The setup position of RadFETs.

SCINTILLATION-TYPE BEAM LOSS MONITOR

Several high counting rate BLMs are installed in the first cell below the injection straight as shown in Fig. 11. This scintillation detector, in Fig. 12, is consistent of a probe and a photomultiplier tube (PMT) which are connected with a 1m long light pipe [8]. A piece of plastic scintillator which is sensitive to the charge particles is installed in the probe. The diameter of the plastic scintillator is 30 mm and the thickness is 10 mm. The output pulse from the PMT is negative. Another type of signal convert should be designed for the scalar input. In the first stage, the signal is observed by an oscilloscope.

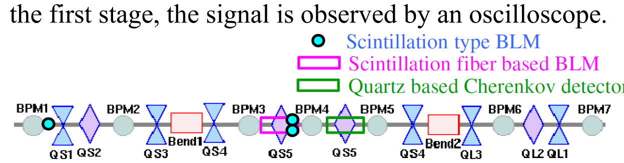

Figure 11: The setup of scintillation and Cherenkov BLMs in the first cell below the injection straight.

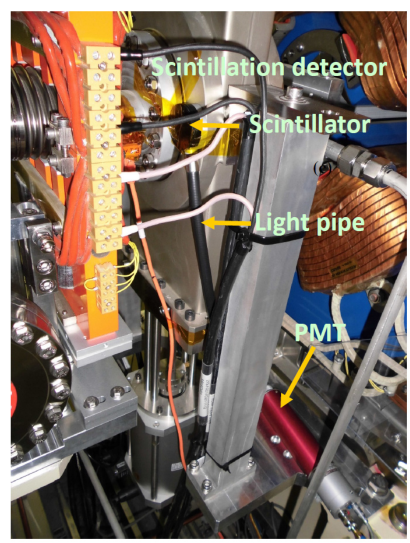

Figure 12: Installation location of a scintillation detector.

MISCELLANEOUS EFFORTS

To equip more beam loss monitors to support various beam loss study, single PIN diode based on solid ionization chamber accompanied with a current to frequency converter is in development. This kind of interface is easy to integrate with the existed scaler. Large volume installation is possible.

Scintillation based BLMs in ESRF type are also considered to be used to support various beam loss study. This detector includes a Zynq based system-on-chip data acquisition unit which supports both the pulse counting

ISBN 978-3-95450-176-2

mode as well as current integration mode. It is above to commercialize soon [9].

A scintillation fiber based BLM which equips with two silicon photomultiplier (SiPM) at both ends is installed in the first cell as shown in Fig. 13. The sensitive volume of the scintillation detector is a plastic scintillating fiber with round cross section of 1 mm diameter. Another quartz rod based Cherenkov-type BLM which equips with two SiPMs at both ends of quartz rode are also installed here to detect the beam loss, shown in Fig. 14. The sensitive volume is a 1.2 cm diameter glass rod with 64 cm sensor length. Signals from both SiPMs can be performed coincident detection to reduce dark counts. These sensors are used to evaluate SiPM type detection at TPS environment. Both kinds of sensors were made by Microsensor S.R.L., Catania, Italy.

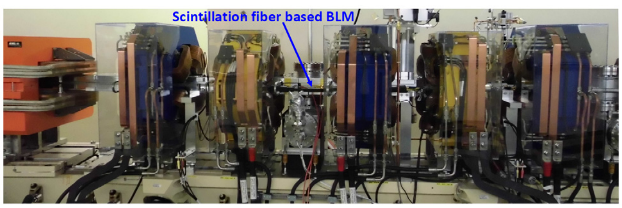

Figure 13: The installation of a scintillation fiber based beam loss monitor.

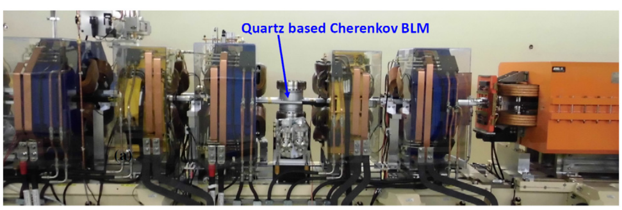

Figure 14: The installation of a quartz based Cherenkov beam loss monitor.

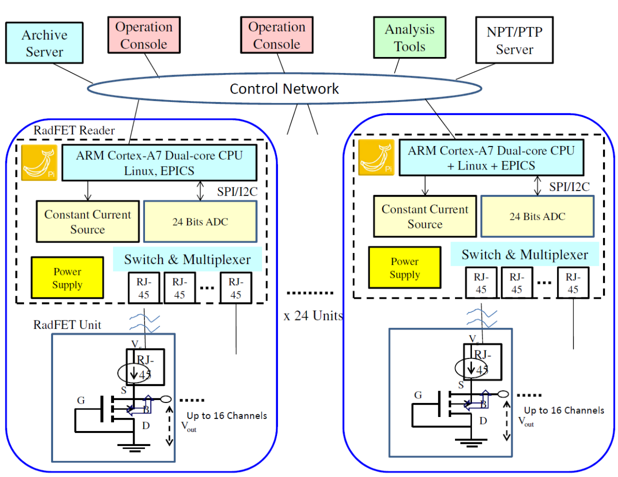

Figure 15: The configuration of the second-generation reader of the RadFET.

Recently, the second-generation reader of the RadFET is in development. The main difference with the first-generation one is that a Banana Pi [10] with ARM Cortex-A7 Dual-core CUP will be embedded inside the reader. Therefore, the Linux, EPICS and controlling program could be installed in the SD card. The configuration is shown in Fig. 15. This reader can also be used stand-alone by recording the data in the SD card as the network is unreachable.

CURRENT STATUS

Phase I commissioning was proceeded with two 5-cell PETRA cavities and without insertion devices from December 2014 to March 2015 [11]. RadFETs are setup in the LTB and booster ring to help beam commissioning. During the long shutdown from April to August, various devices of BLMs are setup in the storage ring. Data acquisition for the counting-type beam loss monitors were setup. The system testing is scheduled in September 2015 which accompanies the phase II commissioning.

ACKNOWLEDGEMENT

Authors thank the brainstorming with Julien Bergoz about how to simplify the cabling of PIN-diode BLMs and conclude a simple twisted-pair solution.

REFERENCE

[1] TPS Design Handbook, version 16, June 2009.
[2] K. Wittenburg, “Beam Loss Monitors”, DESY, Hamburg, Germany.
[3] C. H. Huang et al.,”Beam Loss Study of TLS using RadFETs”, IPAC 2015, Richmond, USA.
[4] Manual of bergoz beam loss monitor, http://www.bergoz.com/
[5] K.T. Hsu et al. “Real-Time Beam Loss Monitoring and its Applications in SRRC”. Particle Accelerator Conference 1997, Vancouver, Canada.
[6] L. Fröhlich, et al., “Online Monitoring of Absorbed Dose in Undulator Magnets with RADFET Dosimeters at FERMI@Elettra”, Nucl. Instr. and Meth. A 703 (2013) 70-79.
[7] Demi Lee et al.,” Online RadFET Reader for Beam Loss Monitoring System”, IPAC 2015, Richmond, USA.
[8] Website of Scionix: http://scionix.nl/.
[9] K. Scheidt and P. Leban, “Prototype Results with a complete Beam Loss Monitor System Optimized for Synchrotron Light Source”, IPAC2015, Richmond, USA.
[10] Website of Banana Pi: http://www.banana-pi.org/ .
[11] C. C. Kuo et al., “Commissioning Results of Taiwan Photon Source”, IPAC 2015, Richmond, USA.

ISBN 978-3-95450-176-2

THE NSRRC PHOTO-INJECTOR DIAGNOSTIC TOOLS FOR INITIAL BEAM TEST

A.P. Lee , M.C. Chou, N. Y. Huang, J. Y. Hwang, W. K. Lau, C.C. Liang, M.T. Tsou,
NSRRC, Hsinchu 30076 Taiwan.
P. Wang, Department of Engineering and System Science,
National Tsing Hua University, Hsinchu 30013 Taiwan

Abstract

The High brightness injector project at NSRRC aims to develop a100 MeV photo-injector system for light source R&D at NSRRC. This photo-injector system equipped with a photocathode rf gun, a solenoid for emittance compensation, an S-band linac as well as various beamdiagnostic tools is designed for operation in two different modes. One is to generate high brightness electron beams for future free electron laser experiments. The other is to produce ultra-short electron bunches by velocity bunching. It also allows us to perform inverse Compton scattering experiment for generation of fs x-ray. In the beginning of this project, the photocathode rf gun was installed in the booster room of TLS at NSRRC. The normalized beam transverse emittance is 5.5 mm-mrad at ~250 pC with Gaussian laser pulse. Recently, a 100 MeV photo-injector system is being installed in the 38 m by 5 m tunnel of the NSRRC linac test laboratory. The rf gun, the 35 MW high power microwave system and a 5.2 m lina has been set up. The UV driver laser system will be set up in the new temperature controlled clean room in the linac test laboratory. For initial beam test, some beam diagnostic tools are considered. They are presented and discussed in this paper.

INTRODUCTION

The development of high brightness beam produced by a photo-injector has been driven mainly by self -amplified spontaneous emission free-electron laser (SASE FEL) applications. The high brightness electron beam is now an important subject of light source research for developing high gain free electron laser. For high gain FEL, the key issue is to produce an ultra-low emittance beam then compress the beam to higher peak current and to accelerate it to the high energy by the main linac system. Since the injector produces the high brightness electron beams that determine the FEL performance, development of injectors show the strong demand in producing high brightness electron beams.

Photo-injectors that deliver low emittance beams at nC bunch charge are commonly used in high gain FELs worldwide. As a result of the continuing developmentfor high brightness electron beam technology, photo-injectors have now become an essential sub system in many x-ray FEL facilities such as LCLS, European FEL, FLASH, Swiss FEL and SPARC etc. A photo-injector system mainly consists of a photocathode rf gun with a emittance compensation solenoid and a traveling wave S-band linac which accelerates the beam up to ~100 MeV. In the rf gun, electrons are emitted from the cathode surface of the cavity by illuminatingan intense UV laser. These electrons are then accelerated to relativistic energy in a few centimeters by the rf field so that the space charge effect degrading the transverse emittance and the beam energy spread is reduced. An emittance compensation solenoid as well as the three-dimensional laser beam shaping is applied for further reduction of space charge emittance growth.

A THz/VUV free electron laser facility isproposed at National Synchrotron Radiation Research Center (NSRRC) in Taiwan [1, 2]. The FEL complex comprises the following parts. A photo-injector is to generate a bright electron beam with energy ~100 MeV, then a 3 m long linac section to modulating theelectron beam with energy chirp. A double dogleg with linearization optics in the middle section of the dog-leg dipole magnets is used as a bunch compressor. Follow the compressor, two 5.2 m linear accelerators in which the beam is time-compressed and accelerated to 325 MeV, then the system to transport the beam to the undulator which is generate the VUV FEL radiation.

PHOTO-INJECTOR SYSTEM

Before constructing the VUV/THz FEL, the high brightness injector project is proposed to develop the photo-injector capable of producing low emittance sub - 100 fs electron beams for the VUV/THz FEL.The 100 MeV high brightness photo-injector of the driver linac system proposed for the VUV FEL facility is under construction in the NSRRC linac test building as shown in Fig. 1. The design of the photo-injector is done by the computer simulation using the particle tracking code, General Particle Tracer (GPT) [3]. A 3.5 MeV low emittance beam with bunch charge of 100 pC is generated from the photocathode rf gun operated at the peak rf accelerating gradient 70 MV/m and optimum laser injection phase23°with respect to rf field. The 5.2 m rf linac with 18 MV/m accelerating gradient is set downstream after the photo-cathode rf gun for boosting beam energy. The optimum location of the linac for getting lowest transverse emittance is according to the Serafini's theory [4]. The linac can be put near the relative local maximum of beam emittance after the solenoid magnet with field strength adjusted correctly for emittance compensation. This optimum location is at 1.35 m from the cathode surface when the solenoid magnet is operated at 1400 Gauss. Beam parameters of the photo-injector in the GTP simulation are summarized in Table 1. Details of hardware components are presented in the following sub sections.

ISBN 978-3-95450-176-2

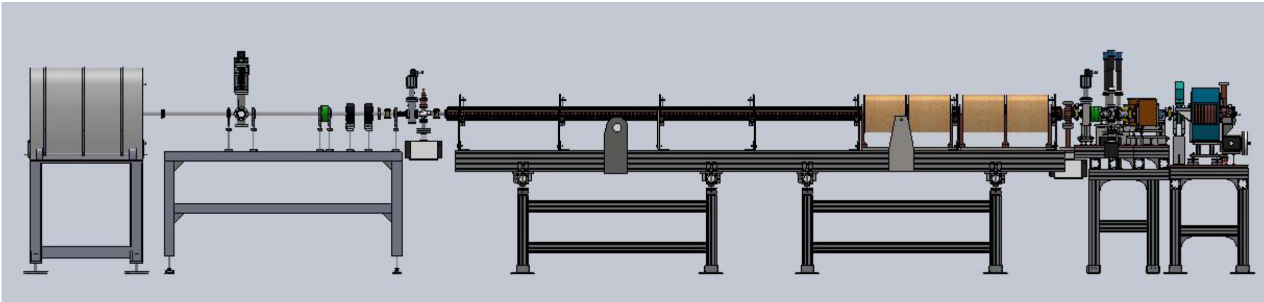

Figure 1: The layout of the photo-injector is being built at NSRRC.

Table 1: Beam parameters at the entrance of the linac.

Initial beam parameters:	
Peak E field in the rf gun	70 MV/m
Laser injection phase	23° (GPT setting)
Initial beam radius	0.6 mm
Initial bunch length	6 ps (FWHM)
Initial beam profile	Uniform cylindrical
Initial beam charge	100 pc
B field of solenoid	1400 Gauss
Beam parameters at the entrance of the rflinac:	
Beam energy	3.54 MeV
Projected energy spread	37 keV
Projected relative energy spread	1.0 %
Sliced energy spread	0.55 keV
Sliced relative spread	0.0016 %
Charge	100 pC
Bunch length	2.25 ps (rms)
Peak current Ip	~ 19 A
Normalized emittance	0.98 mm-mrad
Sliced emittance	0.59 mm-mrad

Photocathode Rf Gun

The photo-cathode rf gun is 1.6-cell BNL GUN-IV type with a polycrystalline copper photocathode except that our operating frequency is set at 2998 MHz. [5]. The dimension of the cavity is scaled to meet the resonant frequency at 2998 MHz. The cathode is illuminated by an 266 nm wavelength UV laser with pulse shaping technique to optimize the final beam quality. Because the measured value of the quantum efficiency of copper at 266 nm is ~10^{-5}, the laser must deliver ~100 μJ on the cathode in order to produce a ~100 pC bunch charge. The gun operates in the fundamental, TM010-π mode of the two-cell cavity. A solenoid magnet is integral to the RF gun operation. The solenoid focuses the beam from the gun exit to the entrance of the linac structure and compensates the emittance growth due to linear space charge.

In the beginning of developing the photo-injector system, a gun test facility (GTF) has been setup in the TLS booster room for testing photo-cathode rf guns. In the spring of 2013, the first operation of the photo-cathode rf gun has been successful accomplished which can be operated at peak field of 58 MV/m. Electron bunches with Gaussian beam shape are characterized with energy of 2.3 MeV, bunch charge of 250 pC and normalized transverse emittance of 5.5 mm-mrad [6]. Since the condition of the rf gun is not optimized, further improvements of the rf gun are in progress. A new photo-cathode rf gun with improved inner wall surface condition will be fabricated for operation at peak field higher than 70 MV/m.

Ultrafast Laser System

The NSRRC ultrafast laser system which was purchased from Coherent Corporation is a Ti:sapphire laser system based on the chirped-pulse amplification technique. This system consists of an oscillator (Mira-900), an amplifier (Legend-F), a third harmonic generator (THG), and a UV stretcher. In 2013 the laser system was successfully used for driving the NSRRC photocathode RF gun [7]. The drive laser system delivers the 3-mJ IR laser pulse with 100-fs pulse duration and the 180-mJ UV laser pulse with 800 fs to 10 ps tunable pulse width at that time. Following the high brightness injector project the whole laser system was moved to the NSRRC linac test laboratory and installed in a temperature-humidity controlled clean room in the beginning of this year.

The laser system will be served as the drive laser for the photocathode RF gun and the seed laser for the VUV FEL. Therefore the laser system will be upgraded by adding a multipass amplifier to increase the laser energy. Figure 1 shows the layout of the upgraded laser system. First, the output energy of the regen is raised from 4.5 mJ to 6 mJ. After that, a beam splitter is inserted in front of the compressor inside the Legend-F. The penetrated stretched 800-nm laser pulse with 80% output energy of the regen amplifier is then compressed to 100 fs and used to generate the UV laser pulse by the THG. The UV laser pulse with 266-nm wavelength, corresponding to photo energy of 4.5 eV, is used to extract photoelectrons from

ISBN 978-3-95450-176-2

the Cu photocathode of the rf gun. The pulse duration of the UV laser can be further stretched from 800 fs to 10 ps by a UV stretcher, which is consisted of four fused silica prisms. Currently, the output energy of the IR laser pulses is 3.8 mJ with energy stability <0.3% RMS. The UV energy is 550 mJ at the exit of the THG and attenuates to 150 mJ with energy stability <1.9% RMS after propagating to the Cu cathode due to energy loss from optical components.

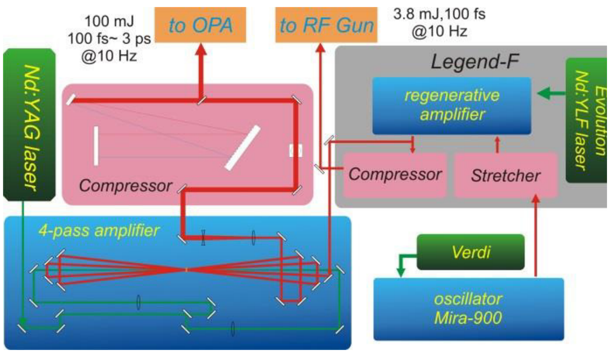

Figure 2: Layout of the upgraded laser system.

The residual laser pulse (20% output energy of the regen amplifier) will be used as the seed pulse for the 4-pass amplifier. The 4-pass amplifier is made of a 10-mm-long, 1.5-cm diameter, 0.25% doping, normal-cut Ti:sapphire crystal and seven folding mirrors in a bow-tie configuration. It will be pumped by a frequency-doubled Q-switched Nd:YAG laser from both ends. With 532-nm pump energy of 600 mJ, the IR laser pulse energy will be expected to amplify to 130 mJ. The amplified laser pulse is further compressed to 100 fs with 100-mJ energy by another grating compressor. Before the compressor the laser beam size will be expanded to 35-mm diameter in clear aperture such that the laser can be propagated in the air after compressed. After that, it can be used to pump the OPA system to generate the UV laser for the FEL seeding. The desired FEL seed laser wavelength is 266 nm, laser pulse energy is 300 mJ, and FWHM pulse width is 1.5 ps, corresponding to the peak power of 200 MW. In addition, in order to match the repetition rate of the RF system, the repetition rate of the upgraded laser system will be tuned from 1 kHz down to 10 Hz by adjusting the pockels' cell timing inside the regen amplifier.

High Power Microwave System

The high power microwave system consists of a 35 MW klystron, a klystron modulator, rf vacuum waveguide system. The high power S-band klystron, Thales model TH2100A,can produce max peak power of 35MW at pulse duration of 4.5 μs. The klystron and focusing magnets has X-ray shields that meet radiation safety requirements. A conventional line-type high voltage modulator consists of 8 sections of pulse forming network which is charged and discharged by a thyratron provide 30kV high voltage to the klystron. A driver amplifier system with the one kilowatt ThalesTH2047 klystron for the high power TH2100A pulsed klystron has been installed. The output microwave is distributed by the vacuum waveguide system, including the hybrid couplers, high power phase shifter and rf windows to the rf gun and the accelerating linac. The amplitude fed to the gun and linac can be adjusted using the high power hybrid. This microwave system is synchronized with the driver laser system, so the phase of microwave fed to gun can be changed by a phase shifter installed after the oscillator and the phase of microwave fed to the linac is controlled using high power phase shifter.

RfLinac

The linac is a 5.2 m, 2998MHz constant gradient traveling-wave structure which is operated at $2\pi/3$-mode. The structure is designed the same as the DESY LINAC-II type and is manufactured by Research Instruments GmbH. It totally has 156 cells with149 normal cells. The power is coupled to the first cell at one arm with the opposite arm shorted and the last 6 cells coated with Kanthal layer for absorbing the power. The shunt impedance, attenuation parameter, and filling time, are 52 M Ω/m, 5dB and 0.69μs, respectively. It can accelerate electron beam to about 97 MeV without beam loading with 35 MW input rf power.

BEAM DIAGNOSTICS

Based on the results of the GPT simulation study, beam diagnostics are designed for characterizing the beam from the rf gun. The instrumentation for the beam diagnostics are set in the gun-to-linac (GTL) drift section as shown in Fig. 4. Two steering magnets allow correcting beam offset and angle. An inductive current transformer is for non-destructive bunch charge measurements. A six-way cross in the beamline allows for on-axis injection of the photocathode drive laser pulse. A rectangular dipole magnet with nominal field 0.05 T is used as the spectrometer bending magnet for energy and energy spread measurements at downstream of the photo-cathode rf gun system. A faraday cup installed after the dipole is used to measure the bunch charge comparing to the ICT.

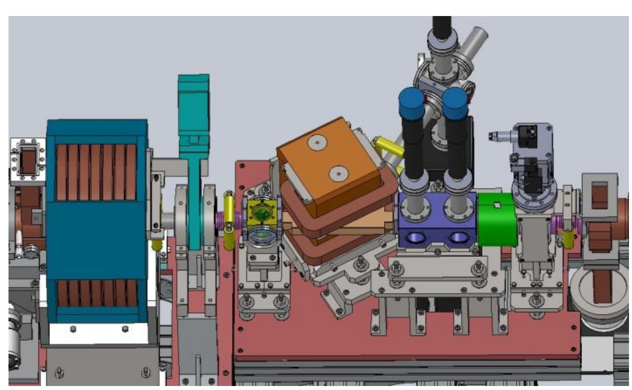

Figure 3: the layout of the beam diagnostic system after the gun.

ISBN 978-3-95450-176-2

Bunch Charge Measurement

Unlike Faraday cup which collects bunch charge by intercepting the electron beam, ICT can be used for non-destructive measurement by passing the beam through the ICT core. The ICT is a transformer which can be used to measure the bunch charge by integrating the beam signal with rise time in the order of picoseconds with no significant loss. To measure the bunch charge with an ICT, a ceramic gap is installed to break the wall current on the vacuum beam pipe and a metallic shield is attached to the vacuum chamber on both sides of the electrical break as wall current bypass as well as rf shield. In our setup, the Bergozin-air type ICT with inner diameter of 82 mm and turn ratio of 5:1 (ICT-082-070-05:1) is chosen to match the dimensions of our beam pipe.

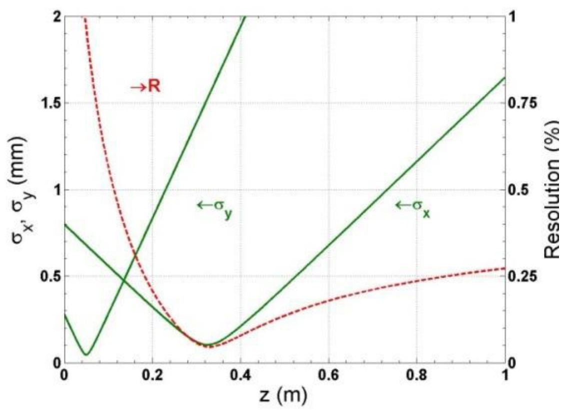

Figure 4: Calculated resolution and beam sizes after a 60° bending magnet. Note that the position at magnet exit is set at z = 0 in these plots.

Energy and Energy Spread Measurement

A 17 cm rectangular dipole magnet with a pole gap of 40 mm will be used as the spectrometer bending magnet for energy and energy spread measurements at downstream of the photo-cathode rf gun system. The physical dimensions of this dipole magnet are shown in Fig. 6. In general, large bending angle and large dispersion are beneficial to improve of beam spectrometer resolution, so we choose 60° as the bending angle. In order to know where to put the screen for best resolution, the analysis of the evolution of beam envelope after the bending magnet without the consideration of momentum spread is necessary. As shown in Fig. 4, the position of optimum resolution is at z ~ 0.33 m which is about the position of minimum horizontal beam size. The estimated resolution is ~ 10 times smaller than the expected beam energy spread of the photo-cathode rf gun. This rectangular dipole magnet with 60° bending angle provides a wider range for putting the screen that allows energy spread measurement at good resolution. A quadrupole pair can be installed before the bending magnet for further improvement of resolution if needed. The position of the screen is located at 33cm away from the exit of the magnet. A 10 x 10 mm screen should be big enough to display the profile of a dispersive beam at this position.

Emittance Measurement by the Multi-slit Method

The design rule of the multi-slit mask is specified by some criteria [8]. The original design of the multi-slit mask that has been used for testing the first prototype photo-cathode rf gun is made of 2 mm thick stainless steel with 50μm slits that are separated at 300μm apart. The slits are cut by electrical discharge machining (EDM) and the edges of the slits are irregular. It is hard to determine the average width of each slit for data analysis. Besides blurred image has been observed on the YAG screen in addition to the image formed by the transmitted beam edge. It is believed that this blurred image is related to the scattering of electrons from the slits. Therefore, an improvement of the multi-slit mask to avoid edge scattering of electrons is considered

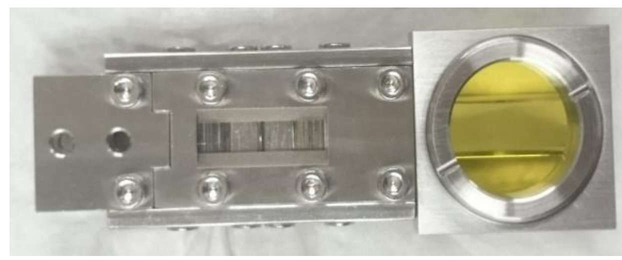

Figure 5: multi-slits stacked in a stainless steel holder.

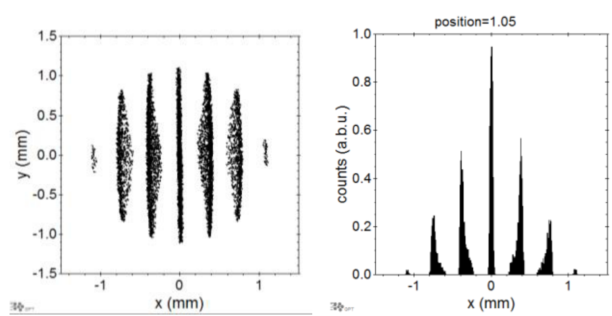

Figure 6: The distribution of the transmitted electron beam at the position of the screen when the multi-slit with the separation of 500 μm. The slit is located at the position 95 cm, and the distance from the slit to the screen is 10 cm.

A new multi-slit mask is fabricated for emittance measurement. The thickness of the stainless steel multi-slit mask should be at least 2.6 mm to stop a 3.5 MeV beam. The mask thickness is set at 5 mm. Slits of 50μm in width and separation of 500μm. Fabrication of C-shaped elements is also possible for slit separation of 300μm.The minimum width and thickness of the slits are limited by the capability of machining methods, so the EDM method is not suitable. The new multi-slit mask is made by stacking C-shaped stainless steels which are machined by precise grinding. A prototype mask has been fabricated in the Mechanical and Systems Research Laboratories of Industrial Technology Research Institute (ITRI) in Taiwan.

ISBN 978-3-95450-176-2

Figure 5 shows multi-slits stacked in a stainless steel holder integrated with a YAG screen. From the GPT simulation while the mask is set at the position 95 cm from the cathode plate, the image of beamlets on the screen will not overlap if the distance from multi-slit to screen is less than 15 cm. Since the edge scattering is not considered in the simulation, the distance is set as 10 cm. The distribution of electron beamlets at the position of the screen is shown in Fig. 6.

SUMMARY

The photo-injector system for the THz/VUV FEL is being builtat NSRRC. The installation has been started in January 2015 and will be finished at the end of 2015. In the first phase, the objective is to generate the ultrashort electron beam via velocity bunching in the 5.2 m linac for THz coherent radiation. Before installing the undulat or, the parameters of beams generated by the photocathode rf gun will be measured. The quadrupole scan is used to measure the transverse emittance and the coherent transition radiation is usedto measure the bunch length after electron beams exit the linac. Then, the RTR experiment will also being carried out [9]. Besides, producing ultrashort x-ray sources through the inverse Compton scattering is to be considered since the 100-MeV electron beam and the 100-mJ laser pulse are ready.

REFERENCE

[1]. N.Y. Huang, et al., “Linac design for the proposed NSRRC THz/VUV FEL facility”, THPRO047, IPAC’14 (2014).

[2]. N.Y. Huang et al., “Study of a THz/VUV free electron laser facility in Taiwan”, THPRO050, IPAC’14 (2014).

[3]. General Particle Tracer, http://www.pulsar.nl/gpt.

[4]. Luca Serafini and James B. Rosenzweig, “Envelope analysis of intense relativistic quasilaminar beams in rf photoinjectors:mA theory of emittance compensation”, Phys. Rev. E 55, 7565 (1997).

[5]. A.P. Lee et al., “Operation of the NSRRC 2998 MHz photocathode rf gun”,WEPWA058, IPAC’13 (2013).

[6]. A.P. Lee et al., “Emittance and bunch length measurement of electron beam from the photocathode gun at NSRRC”, THPRO048, IPAC’14 (2014).

[7]. M.C. Chou et al., “Operation of the drive laser system for the 2998 MHz NSRRC photoinjector”, WEPWA059, IPAC’13 (2013).

[8]. J. Rosenzweig and G. Travish, “Design Consideration for the UCLA PBPL Slit-based Phase Space Measurement”, Lecture Notes (1994).

[9]. P. Wang et al., “Design of a resonant transition radiation source in the soft x-ray range”, TUPJE050, IPAC’15(2015).

ISBN 978-3-95450-176-2

IMPROVEMENT OF TUNE MEASUREMENT SYSTEM AT SIAM PHOTON SOURCE

S. Kongtawong, P. Sudmuang, S. Krainara, P. Klysubun,
Synchrotron Light Research Institute, 111 University Avenue, Muang District
Nakhon Ratchasima, 30000, Thailand

Abstract

A new tune measurement system was recently developed and implemented at Siam Photon Source (SPS) for both the booster synchrotron and the 1.2 GeV electron storage ring. A new electronic module was installed at the SPS booster for collecting the turn-by-turn signal generated when the beam was excited with white noise and fast kicker. The beam excitation was carefully studied in order to determine the optimum beam response. With this system we observed the variation of the tune during energy ramping. The measurement provides information needed to optimize the working tune and to keep it constant. At the SPS storage ring, the excitation signal was changed from swept frequency signal to frequency modulation (FM) signal to reduce the measurement time. Details of the instrumentation setup and its performance will be presented in this report.

INTRODUCTION

The SPS operates a 1.2 GeV electron storage ring to produce synchrotron radiation in a wide energy range, from infrared to hard X-ray. The SPS booster ramps energy of electrons from 40 MeV to 1 GeV in 660 ms before they are transported to the storage ring. The storage ring then further ramps electron energy up from 1 GeV to 1.2 GeV. The maximum stored beam current is 150 mA. This method of electron beam injection previously took ~ 30 minutes. To cut down the number of steps and reduce the injection time, full energy injection system will be set up. The booster will ramp electron energy from 40 MeV to 1.2 GeV before injecting electrons to the storage ring. Therefore, energy ramping in the storage ring will not be required.

To achieve this, a new ramping pattern needs to be applied. Maximum current of the booster dipole magnets will increase from 1300 A to 1700 A and the current pattern of quadrupole magnets will have to change correspondingly. Since all the booster magnets approaches saturation after reaching the energy of 1 GeV, the current patterns of the quadrupole and dipole magnets are not linearly correlated and cannot be obtained from calculation. Therefore, the betatron tune needs to be measured and kept constant during energy ramping [1-3].

The tune measurement system has been set up at the SPS booster to track the tune shift during commissioning of the new pattern. Libera SPARK module was used to collect the turn-by-turn data from button-type Beam Position Monitors (BPM). At the 1.2 GeV electron storage ring, a new tune measurement system was also developed from the old system that used swept frequency signal to excite the beam. The drawback of this excitation signal was the measurement time which was quite long (10-30 seconds per measurement). The excitation was therefore changed to FM signal for faster measurement.

BOOSTER

Layout of the tune measurement system at the SPS booster is illustrated in Fig.1. The system has two subsystems: the excitation system and the signal detection system, which work together synchronously.

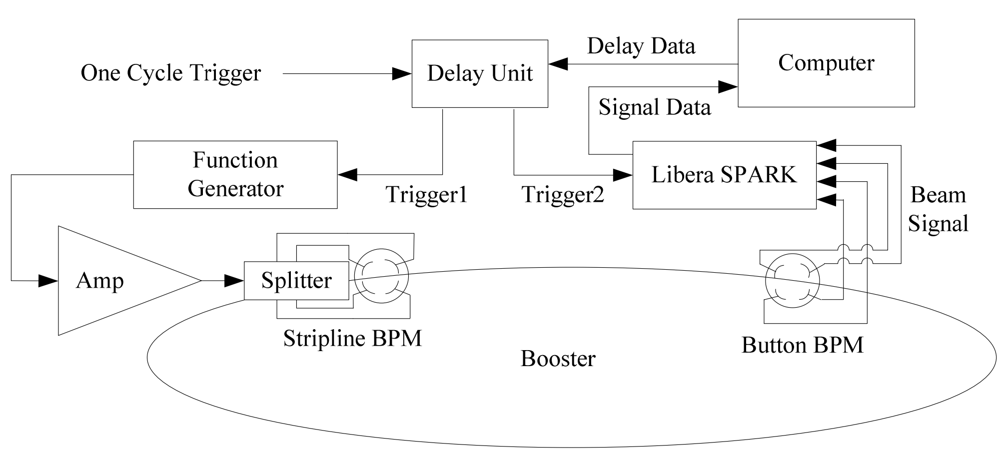

Figure 1: Layout of the tune measurement system at the SPS booster.

ISBN 978-3-95450-176-2

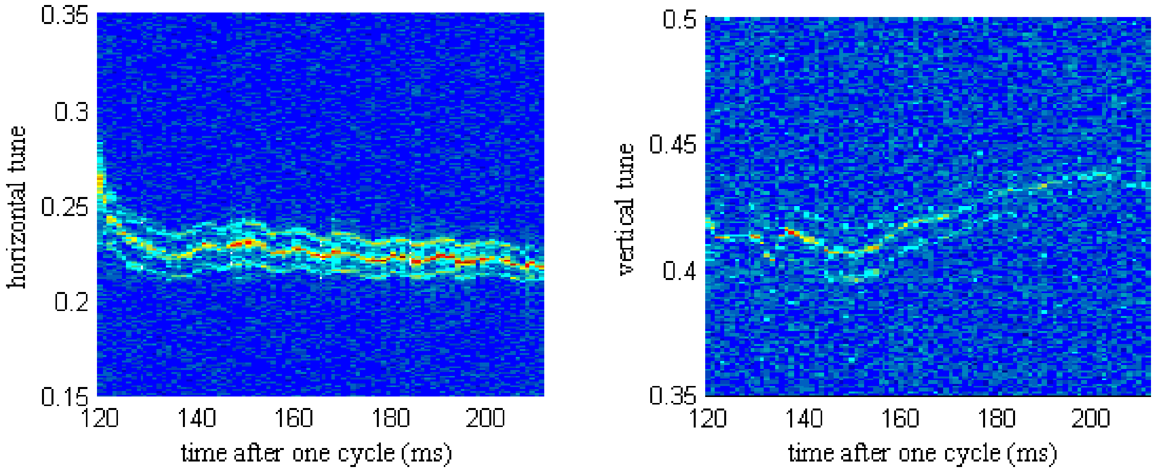

Figure 2: FFT of the signal from BPM showing horizontal tune (left) and vertical tune (right) at the injection point in the booster. Electrons were injected into the booster at 119.5 ms after one cycle trigger.

The tune excitation system consists of a function generator (Agilent 33250A), a 150W rf power amplifier (ENI A150) and a stripline which was used as a kicker. The function generator was used to generate white noise signal with 0 to 3.4 MHz bandwidth. The signal was amplified before being sent to the stripline. In order to excite the whole ramping, the signal amplitude should be increased with the electron energy [1]. However, additional instruments will be required. A workaround for this requirement is to use excitation signal with constant amplitude for one measurement, and excite it before collecting the data. The tune can be measured in approximately 10 ms for one measurement. The next measurements at higher energies are performed with the use of delay unit since it is possible to do only one measurement per one cycle of acceleration. Betatron tune of the whole ramping process is finally constructed from each of these measurements.

The signal detection system consists of a four-button BPM and a Libera SPARK module. The button BPM was used to detect the beam signal and send it to Libera SPARK for data collection. MATLAB routine was used to analyse the data by finding the bunch-by-bunch data and performing Fast Fourier Transform (FFT). Figure 2 shows averaged FFT signal of all bunches when electrons were injected into the booster. The horizontal and vertical tunes can be clearly seen with the resolution of 10^{-3}, which is sufficient for operation. However, the vertical tune cannot be seen after around 500 ms after injection. This is probably because the power of the excitation signal is not high enough, or it may be because the BPM probe was located where the vertical betatron tune is low. Therefore, fast kicker pulse is also used with white noise to measure the tune at higher energy. Using this measurement, the horizontal and vertical tunes can be adjusted to find a new, optimized operating point that provides higher beam current. This was successfully done without any beam loss during energy ramping.

STORAGE RING

The tune measurement system at the SPS storage ring has undergone a minor modification. Layout of the system is illustrated in Fig.3. It should be noted that this system is not a turn-by-turn measurement setup. Real-time spectrum analyser is used to find the tune. The old measurement system used swept frequency signal to excite the stored beam through a stripline. Each measurement took 10-30 seconds, resulted in a long machine study time where the tune measurements are usually involved. FM signal (as shown in Fig. 4) is therefore used instead of the swept frequency signal to improve the measurement speed.

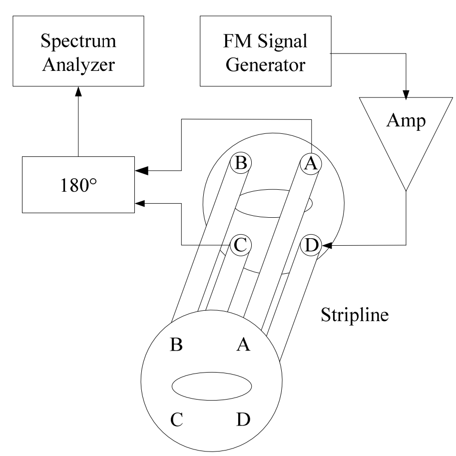

Figure 3: Layout of the tune measurement system at the SPS storage ring.

ISBN 978-3-95450-176-2

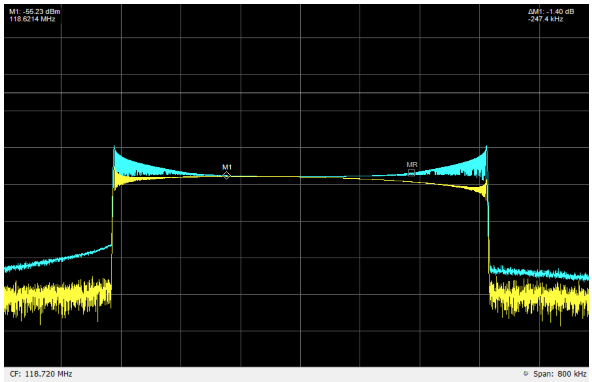

Figure 4: FM signal on spectroscope in real-time mode (yellow) and max hold mode (blue). The center frequency is 118.79 MHz with 500 kHz span.

The FM signal with 118.79 MHz center frequency is created by a signal generator (ROHDE&SCHWARZ SMC100A). The frequency deviation is around 500-800 kHz. The signal is sent to a 300W rf power amplifier (ENI A300) and then to one line (D) of the stripline. Two other lines in diagonal (A and C) were used for data collection of the beam signal. The signal from A and C were combined together with 180° phase difference using a hybrid coupler. The summed signal was then sent to the real-time spectrum analyser (TEKTRONIX RSA5103A). This setup is capable of measuring the betatron tunes with 10^{-3} resolution.

The result of tune measurement using FM signal is presented in Fig. 5. The horizontal and vertical tunes could be measured in real time and the resolution is good enough for operation and machine study.

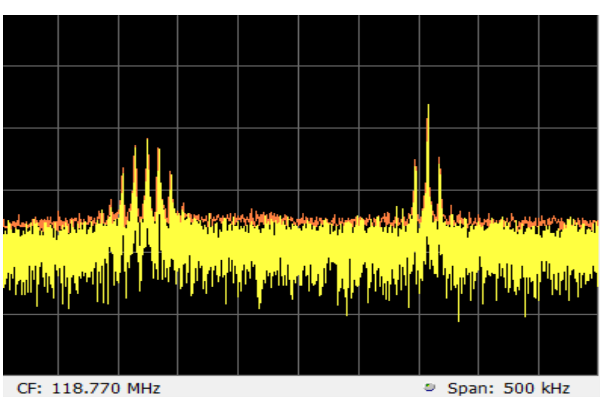

Figure 5: Result of tune measurement using FM signal. Peaks on the left are for vertical tune while peaks on the right are for horizontal tune.

SUMMARY

New system for tune measurement at the booster and storage ring were developed and implemented at Siam Photon Source. The new electronic module installed at the SPS booster will provide betatron tune information during machine commissioning for 1.2 GeV full energy injection. At the SPS storage ring, the use of FM excitation signal can reduce the measurement time from 10-30 seconds per measurement in the old system to real-time in the new system which saves time considerably during machine study.

In the future, some instruments of the system in the booster will be changed or modified to further improve the performance of tune measurement. Some examples are increasing the power of excitation and ramping it with the beam energy, or improving data acquisition system by increasing buffer size of the memory to expand the amount of collected data per one measurement. In the storage ring, the tune can be measured only in machine study time, not when machine is operated for users. This is because the excitation created perturbation to the stored beam. Real-time tune measurement during machine operation is also of interest for future work. However, more work on beam dynamics need to be done in order to reduce the beam distortion induced by the excitation.

ACKNOWLEDGMENT

We would like to thank Dr. Guenther Rehm of Diamond Light Source, UK, who gives us very useful suggestions about electronic module and set up of the system.

REFERENCES

[1] P. C. Chiu et al., “New Booster Tune Measurement System for TLS and TPS Prototype”, MOPF26, Proceedings of IBIC2013, Oxford, UK (2014).

[2] J.M. Koch, J. Meyer, E. Plouviez, “New Tune Measurement System for the ESRF Booster”, POM020, Proceedings of DIPAC 2005, Lyon, France (2005).

[3] U. Iriso, F. Perez, A. Salom, “Tune Measurment System at the ALBA Booster”, BIW10, Santa Fe, New Mexico, USA (2010).

ISBN 978-3-95450-176-2

OBSERVATION OF BEAM LOSS SIGNAL AT THE SPS STORAGE RING

S. Krainara, P. Sudmuang, N. Suradet, S. Teawphet, S. Kongtawong, G. G. Hoyes, and P. Klysubun
Synchrotron Light Research Institute 111 University Avenue, Muang District, Nakhon Ratchasima 30000, Thailand

Abstract

Beam Loss Monitoring (BLM) system is an essential tool for observing beam instabilities and hence for machine protection. At the Siam Photon Source (SPS) storage ring, the BLM system is used to check the beam behavior due to optics perturbation, ion trapping, and vacuum leakage. A network of 50 PIN-diode detectors from Bergoz has been installed around the ring at the positions of high particle density. These positions are at the values of large betatron and dispersion functions in the machine lattice. The operational results of tune scanning verses loss rate in the resonance diagram are described. These results will be useful for improving the beam performance in terms of lifetime and beam stability.

INTRODUCTION

Siam Photon Source (SPS) is a synchrotron light source composed of two 20 MeV linacs, a 1.0 GeV Booster Synchrotron (SYN), and a 1.2 GeV electron storage ring. The SPS storage ring contains four Double Bend Achromat (DBA) super periods with four straight sections. Each symmetric period consists of four focusing quadrupole magnets (QF), three defocusing quadrupole magnets (QD), and two bending magnets (BM). The electron beam is filled twice a day to 150 mA. Three insertion devices; Undulator (U60), Superconducting Wavelength Shifter (SWLS), and Multipole Wiggler (MPW), have been installed and commissioned at three of the straight sections [1]. It was observed that loss rate at the SPS storage ring increased due to the insertion devices operation. A BLM system has been used to investigate the beam loss behavior, which can be a result of optics perturbation, vacuum leakage, and ion trapping. The system can provide information needed to improve the performance of the light source such as beam lifetime and stability. This loss detection system was designed and installed at the SPS storage ring in 2005 [2]. However, the detected signal had a relatively large RF interference. The system was then modified in 2014 in order to better observe the beam fluctuation around the ring.

The BLM detectors are two PIN-diodes from Bergoz. They are sensitive to the minimum ionizing particle (MIP) created when a charged particle hits the vacuum chamber. These detectors generate voltage pulses when active area of the PIN-diodes is struck by the MIPs. BLM signal is counted using the coincidence technique. Figure 1 shows schematic diagram of the BLM system. The real-time loss rate at each position of the detectors is recorded every second by the NI-PXIe system and sent to the control room. The hardware and software improvements of the BLM system are described elsewhere [3].

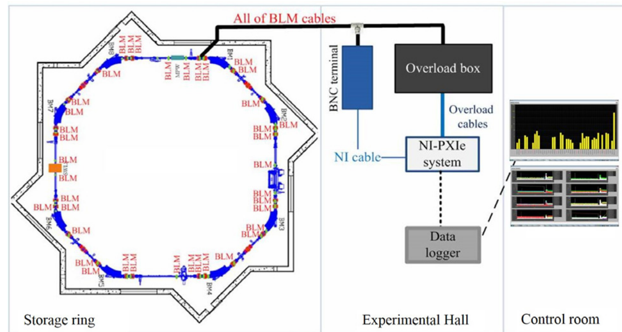

Figure 1: Sketch map of the SPS BLM system.

OPTIMAL BLM LOCATIONS

The loss rate is directly related to the beam lifetime so understanding of all associated mechanisms is necessary for determining appropriate location for BLM installation. In general, the total beam lifetime (τ) is given by three contributions as

$$\frac{1}{\tau} = \frac{1}{\tau_T} + \frac{1}{\tau_q} + \frac{1}{\tau_v} \tag{1}$$

Touschek lifetime (τ_T) originates from the scattering of electrons within the bunch which leads to longitudinal momentum deviation. If the momentum deviation is higher than the RF acceptance, the electron is lost from the system. The best location for BLM installation is thus the section of largest dispersion function.

Quantum lifetime (τ_q) arises from Gaussian energy distribution of the electron particles. It is a result of quantum fluctuations and radiation damping that lead to the loss of energy. The quantum effect may be neglected if the horizontal aperture (determined by RF voltage) is sufficiently large. Therefore, the BLM detector should be installed at the position that exhibits large betatron function where the aperture is small.

Vacuum lifetime (τ_v) originates from the collision of electrons and residual gases. If the energy loss of an electron exceeds a certain amount, it will hit the inward wall of the vacuum chamber. This is likely to happen when electron beam passing through dipole magnets.

ISBN 978-3-95450-176-2

Considering all of these contributions, the BLM detectors should be installed where the betatron and dispersion functions are high. A network of 50 PIN-diode detectors is therefore placed along the SPS storage ring at QF1, QD2, QF3, BM, and insertion devices (IDs) as shown in Fig. 2.

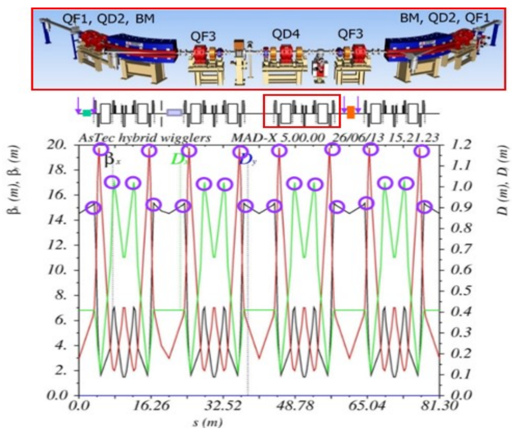

Figure 2: Betatron function and dispersion function along the SPS storage ring. The locations of BLM detectors are presented by purple circles.

OBSERVATION OF BEAM LOSS

Figure 3 shows the count rate from the beam loss monitors during a 24-hour period. The beam loss is large at the injection septum during beam injection. The loss rate goes down immediately after the injection. Moreover, the loss rate is high when the MPW gap is closing and when the SWLS is excited.

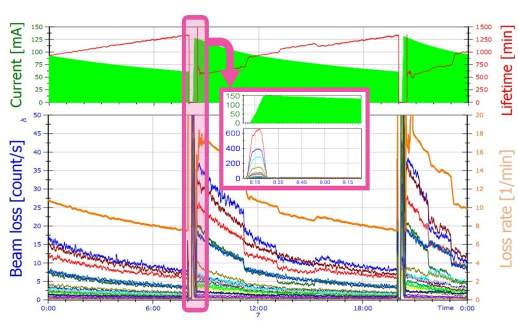

Figure 3: Machine operation status showing the beam current (green), beam lifetime (red), and count rate from beam loss monitors (all others). The beam loss signal during injection process is expanded in the pink box.

It can be seen that the measured beam loss is in agreement with the beam lifetime. The relation between loss rate (α), number of particles (N) and total beam lifetime can be expressed by Eq. 2 where the number of particles exponentially decreases with time [4].

$$\alpha = \frac{1}{\tau} = -\frac{1}{N}\frac{dN}{dt} \qquad (2)$$

Machine operations with IDs

To investigate the effects of ID operation, the beam loss signals of three modes of operation are plotted together in Fig. 4. The three modes are Bare ring (without IDs operation), 2.2 T MPW (operating MPW at 2.2 T), and 4.0 T SWLS + 2.2 T MPW (operating MPW at 2.2 T and SWLS at 4.0 T), respectively. Count rate of the beam loss is generally between 1 to 25 counts/s and jumps up at the IDs due to the beam unstability. The averaged loss rate with IDs operation is also higher than that of the bare ring because of the higher energy loss per turn and mismatched beam.

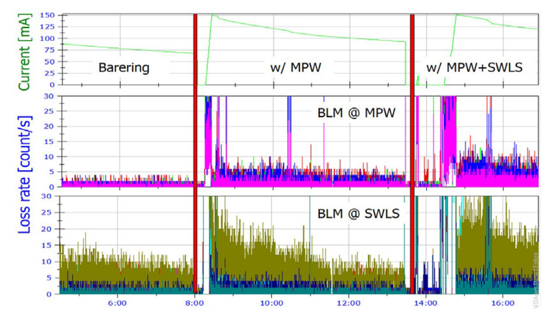

Figure 4: Beam loss for three modes of machine operation (Bare ring w/o IDs, 2.2 T MPW, and 4.0 T SWLS + 2.2 T MPW).

It should be noted that three IDs have been operated since 2013. After machine shutdown in 2015, the beam optics mismatch (betatron and dispersion functions distortion and tune shift) was compensated again using the Linear Optics from Closed Orbits (LOCO) algorithm based on MATLAB [5]. The beam optics parameters are thus nearly the same as the lattice design parameters after the correction. Table 1 lists the parameters of machine operation with IDs. The coupling decreases from 10.21% to 6.78% which results in a smaller vertical beam size and lower beam lifetime. The loss rate is also increased by 40% at the bending magnets.

Table 1: Parameters of machine operation with 4.0 T SWLS, 2.2 T MPW, and U60 before and after LOCO correction

	Lifetime (mA.min)	**Tune (ν_x , ν_y)**	**Coupling (%)**
Before cor.	75,000	4.755, 2.823	10.21
After cor.	74,000	4.766, 2.824	6.78

Vacuum pressure

At the SPS storage ring, a pressure lower than 10^{-10} Torr is desirable. The beam loss measurement will provide more information of pressure distribution because the locations of BLM detectors were carefully chosen, as discussed above. Figure 5 shows the vacuum pressure and loss rate during the beam dump. At BM4 and BM5, the loss rates are higher than that of the others due to high

ISBN 978-3-95450-176-2

pressure at these locations. In addition, it was observed that the loss rate sometimes increases when the front-end is opened for beamline commissioning. This is because the pressure becomes higher than 10^{-9} Torr. BLM system is a useful tool to investigate the vacuum problem and protect the system.

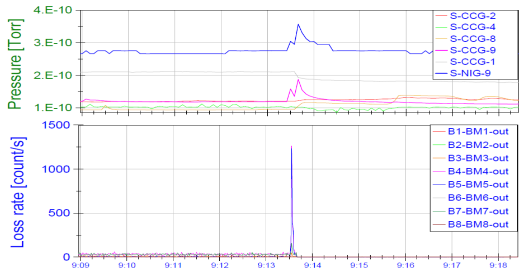

Figure 5: Beam loss and vacuum pressure during the beam dump.

Emittance Issue

In general, low emittance machine is preferable for electron particle accelerators. However, the low emittance results in high density of particles within the bunch which leads to particle loss due to the collision between them (Touschek scattering). Figure 6 shows the loss rate for three different emittances. The loss rate of low-emittance operation is higher than that of the high-emittance operation which is in agreement with the measured beam lifetime.

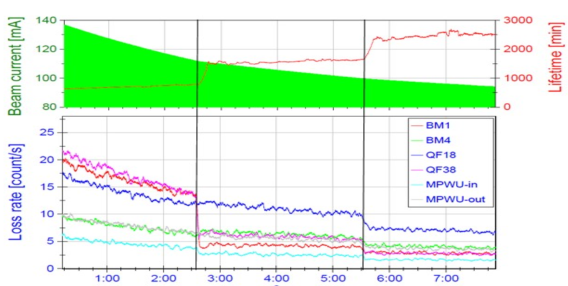

Figure 6: Beam loss for three different emittances without IDs at the beam energy of 1.2 GeV. The working point for each mode remains unchanged at ν_x = 4.768 and ν_y = 2.813 with different emittances.

Tune Scanning Measurement

In addition to beam loss measurement, the betatron tune of the operation was also investigated by changing the quadrupole strengths of QF1 and QD2. The tune scanning was carefully done in steps of 0.05. The working point of the ring without IDs is at the horizontal and vertical tunes of 4.768 and 2.813, respectively. The measured loss rate and tune scanning results are plotted in Fig. 7. In this measurement, the emittance is kept constant at 61 nm-rad. It is clearly shown that the loss rate is high when the horizontal betatron tunes travel across the fourth order resonance lines which cause the unstable beam. On the other hand, the loss rate near the second order resonance is lower because the coupling values are large. Spaces in the resonance diagram with high loss rate should be avoided to prevent beam drop. In adddition, an unstable beam is likely to occur when commissioning the IDs because of the betatron distortion and tune shift. The tune scanning, incorporated with the beam loss measurement, will be useful for optimizing the operation point.

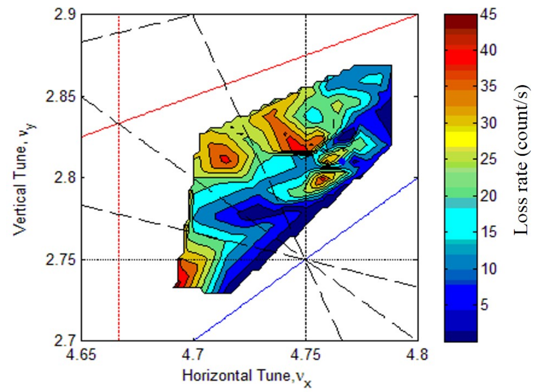

Figure 7: Beam loss rate versus tune scanning for the SPS storage ring with the emittance of 61 nm-rad.

SUMMARY

Beam loss monitor is an important tool to observe the beam instability and understand behaviors of the electron beam. Results of optics perturbation, ion-trapping, and vacuum leakage can be investigated. In addition, the good operation point in the resonance diagram can be chosen when the loss rate is plotted with the tune scanning. These results provide a possibility to improve the beam stability during machine operation of the SPS storage ring.

ACKNOWLEDGEMENT

I would like to thank all members of Accelerator Technology Division for their support.

REFERENCES

[1] P. Sudmuang et al., “Commissioning of the 2.4 T multipole wiggler and 6.5 T superconducting wavelength shifter at Siam Photon Source”, TUPRO068, IPAC’14, Dresden, Germany (2014).
[2] G. G. Hoyes et al., “A Flexible, Low Cost, Beam Loss Monitor Evaluation System”, AIP Conf. Proc., 879, p. 147-150 (2007).
[3] N. Suradet et al., “Improvement of the Siam Photon Source beam loss monitor system”, MOPB058 IBIC’15, Melbourne, Australia (2015).
[4] K. Wile, *The physics of particle accelerators: An introduction*, (New York: Oxford University Press, 2000), 269.
[5] D. Robin et al., “Global beta-beating compensation of the ALS W16 Wiggler”, 6V014, PAC’97, Vancouver, Canada (1997).

ISBN 978-3-95450-176-2

IMPROVEMENT OF THE SIAM PHOTON SOURCE BEAM LOSS MONITOR SYSTEM

N. Suradet, S. Krainara, P. Sudmuang, S. Taewphet, G. G. Hoyes, P. Klysubun
SLRI, 111 University Avenue, Muang District, Nakhon Ratchasima, 30000, Thailand

Abstract

A description of the newly re-built beam loss monitor (BLM) system at the Siam Photon Source (SPS) is presented. The original BLM system was designed and installed in the 1.2 GeV SPS storage ring in 2005. The main problems of this system were poor performance due to RF electromagnetic interference and the use of now obsolete data acquisition electronics. The beam loss detector used is a PIN-diode type from Bergoz. The new BLM system has been implemented using low-noise coaxial cable and an acquisition system based on NI-PXI. The hardware and software modifications incorporated into the new BLM system are presented.

INTRODUCTION

The Siam Photon Source (SPS) is a second generation synchrotron light source operated by Synchrotron Light Research Institute (SLRI) under the Ministry of Science and Technology, and is located in Nakhon Ratchasima, 250 km northeast of Bangkok, Thailand. The accelerator components consist of a 40 MeV linear accelerator, 1.0 GeV booster synchrotron and a 1.2 GeV electron storage ring. The maximum operating beam current is 150 mA in decay mode. The storage ring circumference is 81.3 meters and contains four super-periods of double bend achromat with a total of 8 bending magnets with 3 insertion devices, a permanent magnet undulator, a superconducting magnet wavelength shifter, and a multipole wiggler, providing synchrotron radiation from infrared to hard x-rays to synchrotron light users.

The existing beam loss monitor system (BLM) was designed and installed in the storage ring in mid-2005. The system was intended for measurement and analysis of the closed orbit distortion (COD) with beam loss rate and beam scraping of the vacuum chamber around the storage ring. It used PIN-diode BLMs from Bergoz. The acquisition and control electronics were based on a conventional PCI interface bus using standalone PCs. The major problems of that system were high RF interference in the BLMs and cables and the non-expandable, now obsolete control electronics.

The new system was implemented and subsequently improved in 2014. The major objectives of this improvement are to reduce and protect from RF electromagnetic interference and to better observe the unstable beam around the ring. This paper is organized as follows. Section 2 describes the hardware improvements, while Section 3 presents software improvements. Finally, the measurement results are presented in Section 4.

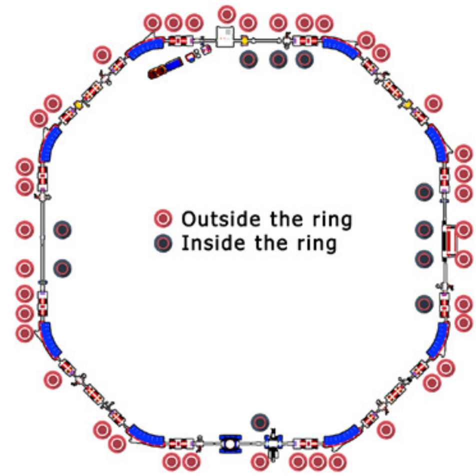

Figure 1: New SPS beam loss monitor positioning layout in storage ring.

HARDWARE IMPROVEMENTS

Sensors and Power Supplies

There are 50 Bergoz's beam loss monitors (Fig. 1), each of which comprises of two pin-photodiodes operating in coincidence mode [1]. The BLMs have been assembled and placed around the vacuum chamber in the storage ring. Regulated low noise power supplies (+5 VDC, -5 VDC, +24 VDC) for up to 10 BLMs is provided from each of 8 transformer units (+12 VDC, -12 VDC, +31.2 VDC) distributed around the ring. The power and signal cables between regulated power supplies and detectors are covered with RF shielding as seen in Figure 2. Also the sources of the RF interference, our bump magnets, were shielded with copper.

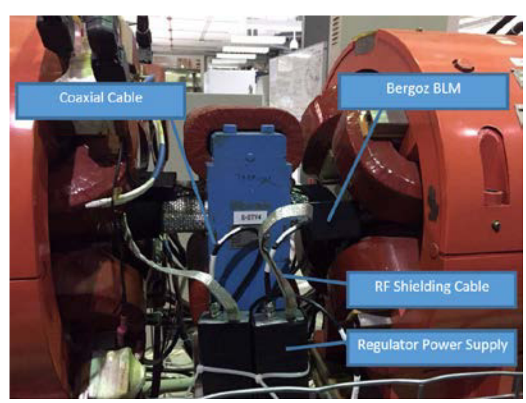

Figure 2: BLMs with RF shielding attached to the vacuum chamber.

ISBN 978-3-95450-176-2

All BLMs have been re-calibrated for background noise count rate with the new cables and acquisition system. Each BLM circuit was re-calibrated to within a spurious count rate of 10 kHz ±800 Hz as per Bergoz's manual [2]. Figure 3 show the comparisons of the count rate in test mode before and after calibration. It shows that the count rate after calibrate is between 10 kHz ± 300 Hz.

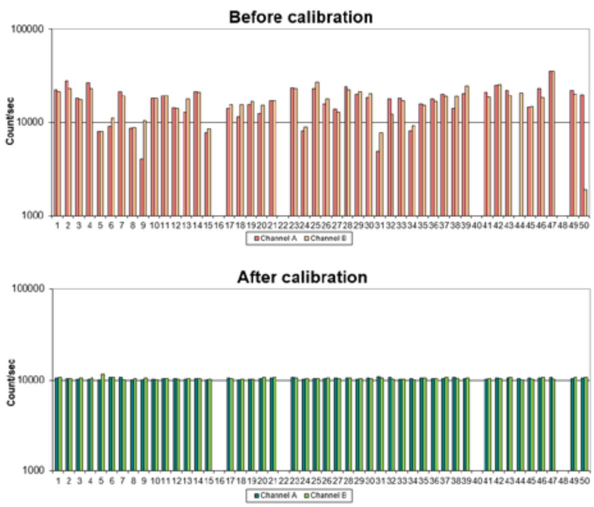

Figure 3: The count rate of BLMs in test mode before and after re-calibration.

Signal Cables

One cause of the RF electromagnetic interference problem is that we previously used low quality signal cables which were susceptible to external interference. Therefore, we replaced the existing cables with HUBER+SUHNER model RG-223/U. This particular cable has double shielding, an impedance of 50 ohms, and operating frequency up to 6 GHz. Both sides of the cable are HUBER + SUHNER BNC 50 ohms. We use 50 ohms terminator to prevent reflection of signals. We also installed all cables in a dedicated mesh-type cable tray, separated from other cables.

Acquisition System

All count signals from the 50 BLMs are collected by NI PXIe-6612 counter modules connecting to BNC terminal boxes as shown in Figure 4. The specifications of these modules are summarized in Table 1. They are based on National Instruments PXI Express platform (NI PXIe) [3] instead of the NI-PCI 6602 counter cards previously used. There are 8 counter modules which are installed in an NI PXIe-1078 PXI Express chassis with a NI PXIe-8820 2.2 GHz Celeron dual-core controller processor and 2 GB, 1333 MHz memory. The PXI is a rugged PC-based platform for measurement and automation systems. It is a high-performance, low-cost deployment platform, and is an especially expandable system for the future.

Table 1: NI PXIe-6612 Counter Module Specifications

Specifications	
Max Source Frequency	80 MHz
Min Input Pulse Width	12.5 ns
Logic Levels	TTL
50 Ohms Terminator	No
Counter Channels	8
Bits	32

Figure 4: BNC terminal boxes installed on rear rack.

SOFTWARE IMPROVEMENTS

In system we use LabVIEW programming platform to collect and analyse input signal from BLM units. The PXIe-6612 counter/timer card from NI is programmed via NI DAQmx software. The block diagram of the program is shown in Figure 5. It first initializes and configures each card for counting up and then starts the counters in the cards. After that it reads data from each input channel at specific intervals, then analyses and displays the count rate.

This program developed in-house can display both real-time and historical data, and has the options to switch between machine layout display, trend chart, and intensity chart. The acquisition system collects the data every 1 second (1 Hz) using controller storage (NI PXIe-8820) and main data logger. This data is broadcasted using NI shared variable protocol via ethernet.

ISBN 978-3-95450-176-2

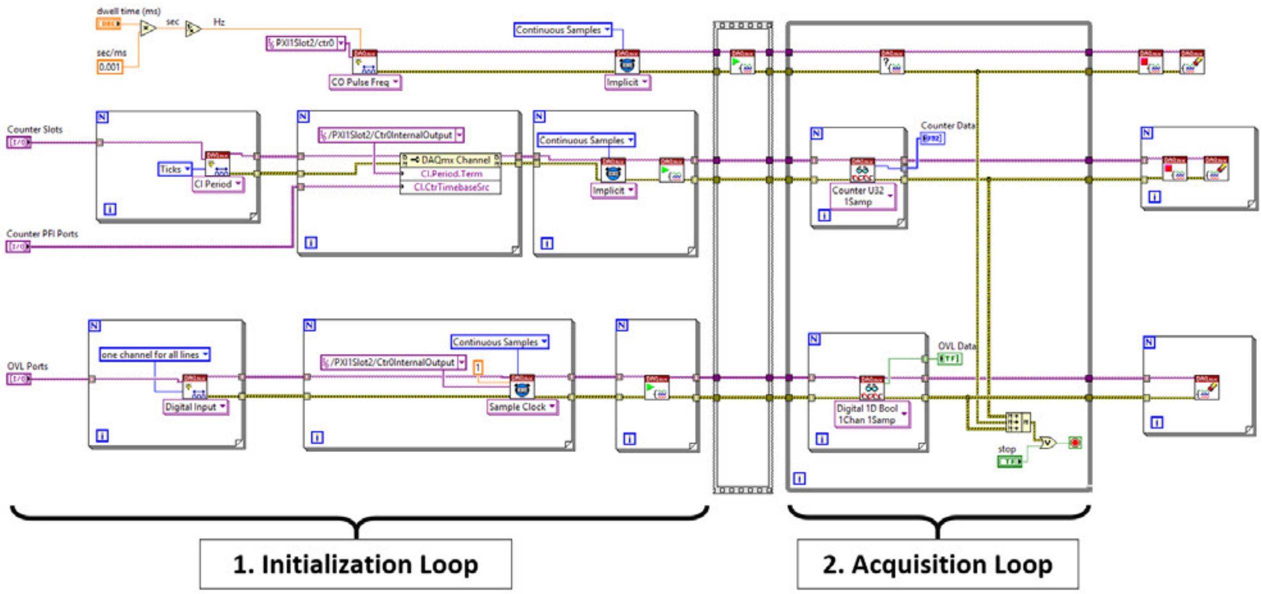

Figure 5: NI LabVIEW DAQmx block diagram.

MEASUREMENT RESULTS

After improving the BLM system, we can clearly detect the variation of beam loss signal during injection, energy ramping, MPW gap change, and excitation of the SWLS. Moreover, we can identify the different loss rates caused by beam instabilities found in the machine during user beam service as shown in Figure 6.

To observe the performance of BLM system, the machine parameters such as working point, beam emittance, machine operation modes were changed to study the effect of loss rate. The details of this study are shown elsewhere [4].

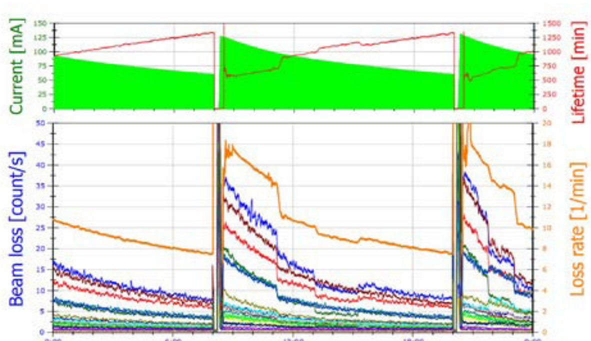

Figure 6: Measured beam loss rate.

CONCLUSION

The improved SPS beam loss monitor system has proved to be extremely useful for machine study and beam loss diagnosis. It is an indispensable tool for our machine physicists for the task to improve the injection efficiency.

ACKNOWLEDGEMENT

We would like to thank all the members of Accelerator Technology Division and the Technical Support team for their assistance, encouragement, and co-operation.

REFERENCES

[1] G. G. Hoyes et al., “A Flexible, Low Cost, Beam Loss Monitor Evaluation System”, AIP Conf. Proc., 879, p. 147-150 (2007).

[2] Bergoz Instrumentation, Beam Loss Monitor User’s Manual: http://www.bergoz.com

[3] PXI Platform National Instruments: http://www.ni.com/pxi

[4] S. Krainara et al., “Observation of Beam Loss Signal at the SPS Storage Ring”, MOPB057, IBIC’2015, Melbourne, Australia (2015).

ISBN 978-3-95450-176-2

FIRST EXPERIMENTAL RESULTS WITH THE CLIC DRIVE BEAM PHASE FEEDFORWARD PROTOTYPE AT THE CLIC TEST FACILITY CTF3*

G.B. Christian, P.N. Burrows, C. Perry, JAI, Oxford University, UK
J. Roberts, CERN, Geneva, Switzerland; JAI, Oxford, UK
A. Andersson, R. Corsini, P.K. Skowroński, CERN, Geneva, Switzerland
A. Ghigo, F. Marcellini, INFN/LNF Frascati, Italy

Abstract

The two-beam acceleration scheme envisaged for CLIC will require a high degree of phase stability between two beams at the drive beam decelerator sections, to allow efficient acceleration of the main beam. There will be up to 48 such decelerator sections for the full 3 TeV design, and each decelerator section will be instrumented with a feed-forward system to correct the drive beam phase to a precision of 0.2 degrees at 12 GHz relative to the main beam, using a kicker system around a four-bend chicane. A prototype system has been developed and tested at the CLIC Test Facility (CTF3) complex, where the beam phase is measured upstream of the combiner ring and corrected with two kickers in a dog-leg chicane just upstream of the CLEX facility, where the resulting phase change is measured. This prototype is designed to demonstrate correction of a portion of the CTF3 bunch train to the level required for CLIC, with a bandwidth of greater than 30 MHz, and within a latency constraint of 380 ns as set by the beam time-of-flight through the combiner ring complex. A description of the hardware will be given and initial results from the first phase of the experiment will be presented.

INTRODUCTION

The RF power used to accelerate the main beam in the proposed linear collider CLIC is extracted from a second 'drive beam'. To ensure the efficiency of this concept a drive beam 'phase feedforward' system is required to achieve a timing stability of 50 fs rms, or equivalently a phase stability (jitter) of 0.2 degrees of 12 GHz (the CLIC drive beam bunch spacing) [1–3]. This system poses a significant hardware challenge in terms of the bandwidth, resolution and latency of the components and therefore a prototype of the system has been designed, installed and commissioned at the CLIC test facility CTF3 at CERN.

A schematic of the CTF3 phase feedforward (PFF) system is shown in Fig. 1. The phase is corrected utilising two kickers placed prior to the first and last dipole in the pre-existing chicane in the TL2 transfer line. By varying the voltage applied to the kickers the beam can be deflected onto longer or shorter paths through the chicane, thus inducing a phase shift. The goal is to demonstrate a 30 MHz bandwidth phase correction with a resolution of 0.2 degrees of 12 GHz. The required hardware consists of three precise phase monitors [4, 5] and two strip line kickers [5] designed and fabricated by INFN/LNF Frascati, and a kicker amplifier and digital processor [6] from the John Adams Institute at Oxford University. More detailed descriptions can be found in [7].

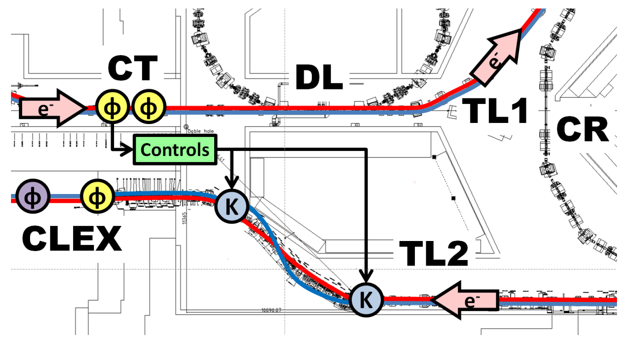

Figure 1: Simplified schematic of the PFF system. Red and blue lines depict orbits for bunches arriving late and early at the first phase monitor, ϕ, respectively. The trajectory through the TL2 chicane is changed using two kickers, K.

The latency of the PFF system, including cable lengths and the latency of each component, is below the 380 ns beam time of flight between the first monitor and the first kicker. This allows the same bunch that was originally measured to be corrected.

COMMISSIONING

The complete PFF system became available in October 2014. Previous results from commissioning of the optics and phase monitors are presented in [8, 9].

The first prototype kicker amplifiers used for the tests presented here provide an output voltage of 340 V. They will be upgraded in stages over the course of 2015, ultimately providing the nominal voltage of 1.2 kV. Constant kick tests demonstrated that applying the maximal 340 V to the PFF kickers resulted in a phase shift of ±3.5°, thus verifying the functionality of the amplifiers, kickers and chicane optics (Fig. 2). The 30 ns rising and falling edges of the response to the kick correspond to 12 MHz amplifier bandwidth when rising from zero to maximum output. This is slew-rate limited and the bandwidth is expected to be 50 MHz for smaller variations.

* Work supported by the European Commission under the FP7 Research Infrastructures project Eu-CARD, grant agreement no. 227579

ISBN 978-3-95450-176-2

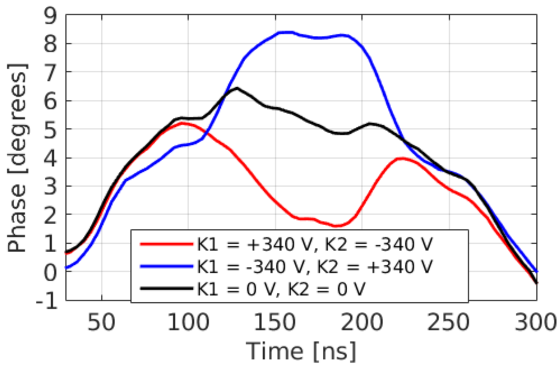

Figure 2: Phase shift resulting from a constant kick applied between 110 ns and 225 ns on the time axis.

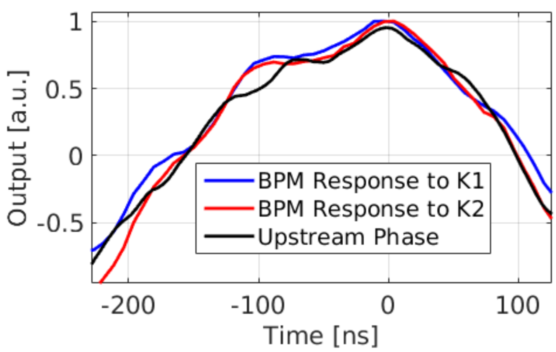

Figure 3: Comparison of the measured downstream position offset and the upstream phase whilst applying the PFF algorithm to one kicker. Note that the phase is normalised to match the sign and amplitude of the position (the actual correction output is the inverse of the input phase).

The PFF algorithm on the digital processor varies the drive signal to the amplifier based on the upstream phase (measured in the CT line, see Fig. 1) in order to correct the downstream phase (after the correction chicane in CLEX) with 30 MHz bandwidth. Its performance was verified by observing the response in a BPM after the correction chicane whilst applying the PFF correction to one kicker at a time. Figure 3 proves that the applied kick has the same shape as the upstream phase.

During the commissioning it was apparent that the upstream phase jitter of up to 1° increased to as much as 4° downstream. The correlation between the upstream and downstream phase was also low, often below 30%. R_{56}, the transfer matrix coefficient relating phase to energy, is a critical parameter for the PFF system and should be exactly zero between the upstream and downstream phase measurements. Any incoming energy jitter will otherwise be converted in to additional downstream phase jitter. This is the dominant source of the low correlation between the upstream and downstream phase at CTF3.

In order to reduce the energy component in the downstream phase, R_{56} for the transfer line TL1 (prior to TL2, see Fig. 1) was therefore tuned to compensate for the non-

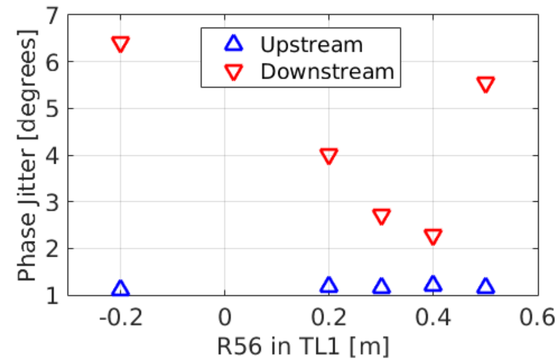

Figure 4: Dependence of phase jitter on R_{56} set in TL1.

zero R_{56} in the TL2 chicane. The downstream phase jitter is reduced to around 2° with an R_{56} of 0.3 m to 0.4 m in TL1 (Fig. 4). Meanwhile, the upstream to downstream phase correlation increased to 40–50%. This improvement in the downstream phase jitter was sufficient to obtain the first PFF results, as shown in the following section. However, further improvements will be needed to reduce the downstream jitter to the CLIC level, as discussed later.

PHASE FEEDFORWARD RESULTS

The drive beam pulses in CLIC are 240 ns long. 100–200 ns pulses (such as shown in Fig. 2) were used to test the functionality of the PFF system at CTF3. As the amplifiers are upgraded during 2015 the increased power will allow tests to be conducted on the full CLIC pulse length.

In the first PFF tests the gain on the digital processor was varied, including both positive (acting to reduce the phase jitter) and negative (acting to increase the phase jitter) values, in order to determine the optimal gain setting and to verify the performance of the correction. Figure 5 shows the relationship between the mean upstream and downstream phase for different gain values, and the upstream-downstream phase correlation is plotted as a function of the gain in Fig. 6. With the PFF system turned off (zero gain) there is 50% correlation between the upstream and downstream phase with a gradient of 1.0. By using a gain of −63 the gradient and correlation are amplified to 1.8 and 63% respectively. Alternatively, with a gain value of +40 the PFF correction acts to remove almost all correlation between the upstream and downstream phase, in fact slightly over-correcting to give a small negative correlation of −0.16.

Figure 7 shows the effect of the PFF correction on the downstream phase jitter. The initial downstream phase jitter of 2° degrees is reduced to 1.4° degrees with a gain of +40, a reduction of 30%. Negative gain values or values above +40 result in the downstream phase being amplified or over-corrected respectively, naturally leading to an increase in jitter.

These results demonstrate a clear improvement in the stability of the mean downstream phase via the PFF correction. However, the goal is to demonstrate not only a correction of

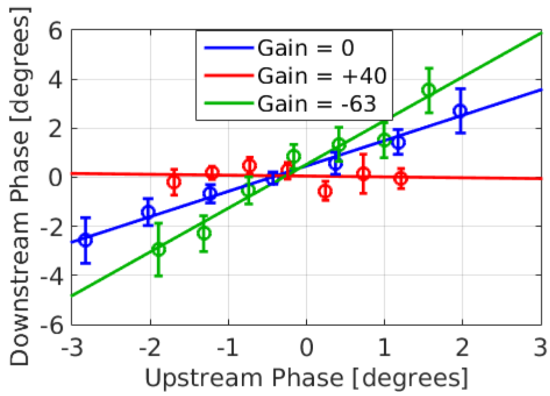

Figure 5: Relationship between the mean upstream and downstream phase for different correction gains.

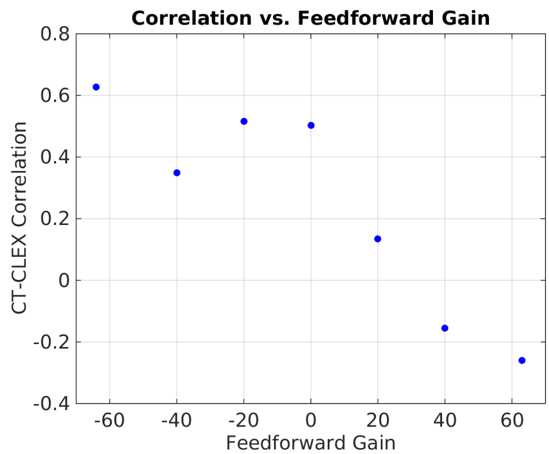

Figure 6: Upstream-to-downstream phase correlation vs feedforward gain.

the mean pulse phase but also flattening of phase variations within the pulse. The effect of the PFF system on the phase within the 200 ns portion of the pulse in which the correction was applied is shown in Fig. 8. With the optimal gain of +40 the phase variation along the pulse is reduced from 7° to 3°. There is a remaining slope in the phase along the pulse as a result of the current limits in correlation and correction range.

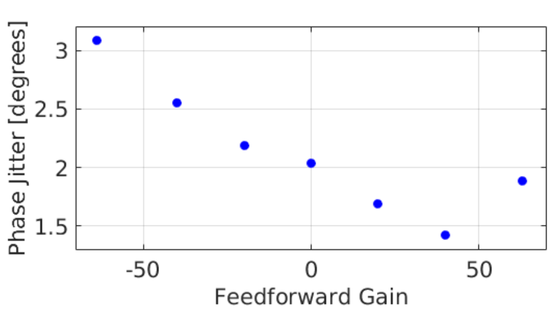

Figure 7: Dependence of the downstream phase jitter on the PFF gain.

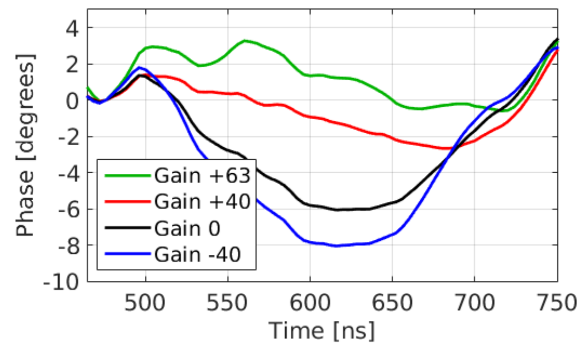

Figure 8: Phase variation along the pulse downstream for different PFF gains. The correction is applied from 510 ns to 710 ns on the time axis.

IMPROVING PERFORMANCE

The theoretical minimum phase jitter achievable using the PFF correction with optimal gain is given by $\sigma_f = \sigma_i\sqrt{1-\rho^2}$, where σ_f is the corrected downstream phase jitter, σ_i is the initial downstream phase jitter and ρ is the correlation between the upstream and downstream phase. A correlation of 97% is therefore required to reduce an initial phase jitter of 0.8° to the CLIC limit of 0.2°. The beam conditions during the first PFF tests were typically 2° phase jitter and 40% correlation, thus important further improvements are needed to achieve this goal.

Despite varying R_{56} in the TL1 line in order to minimise the total residual R_{56} as discussed previously, the adjustments were not precise enough and it was proven that energy was still the dominant source of the low phase correlation. To verify this, the correlation of the upstream and downstream phase with a dispersive BPM (used as an energy measurement) was checked. This is shown in Fig. 9. The high 80% correlation between the downstream phase and the energy compared to the low 2% correlation between the upstream phase and energy confirms that energy jitter is being converted into phase jitter via a residual R_{56} between the upstream and downstream phase monitors.

Simulations have shown that a residual R_{56} of around 0.1 m is enough to recreate the 40% correlation and 2° phase jitter typical of the observed beam conditions. As the R_{56} scan in TL1 shown previously was performed in steps of 0.1 m, it is reasonable to expect that the majority of the remaining energy component in the phase can be removed with finer tuning of R_{56} in TL1. In order to achieve the 97% correlation necessary to correct the downstream phase jitter down to 0.2° the R_{56} must be controlled to within 1 cm.

Additionally, the signal from a dispersive BPM in the same region as the upstream phase monitors can be connected to the PFF processor. The PFF algorithm will then be adjusted to use a combination of the upstream phase and the energy (measured as position jitter in the BPM), thus increasing the correlation of the PFF input with the downstream phase and therefore the capability of the system.

ISBN 978-3-95450-176-2

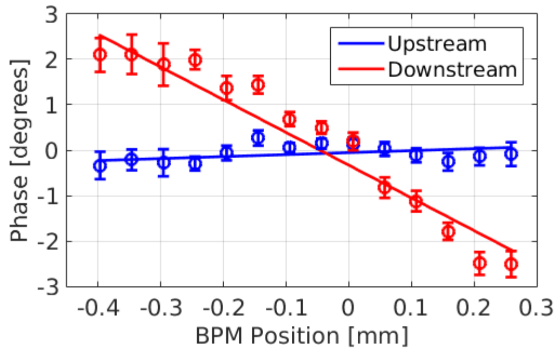

Figure 9: Dependence of the phase on the beam energy (position in a dispersive BPM).

CONCLUSIONS

CLIC requires a drive beam phase stability of 0.2° degrees, which can only be achieved via the use of a high bandwidth PFF correction. Preliminary running of the prototype of this system at the CLIC test facility CTF3 has so far demonstrated a 30% reduction in the drive beam jitter by using kickers to vary the path length through a magnetic chicane. It was identified that in order to reduce the phase stability to the CLIC level at CTF3 energy effects entering the phase via R_{56} must be removed in order to improve the correlation between the upstream and downstream phase from 40% to above 95%. During the 2015 run, finer tuning of R_{56} and including an energy measurement in the PFF algorithm will be tested to achieve this.

REFERENCES

[1] D. Schulte et al. , "Status of the CLIC Phase and Amplitude Stabilisation Concept", MOP024, Proceedings of LINAC10.

[2] CLIC Collaboration, "CLIC Conceptual Design Report", CERN-2012-007.

[3] A. Gerbershagen, "CLIC Drive Beam Phase Stabilisation", PhD Thesis, University of Oxford, 2013.

[4] F. Marcellini et al. , "The CLIC Drive Beam Phase Monitor", WEPEB035, Proceedings of IPAC10.

[5] A. Ghigo et al. , "Kicker and Monitor for CTF3 Phase Feed Forward", TUPC007, Proceedings of IPAC11.

[6] N. Blaskovic et al. , "Development of a Low-Latency, High-Precision, Intra-Train Beam Feedback System Based on Cavity Beam Position Monitors", THOAA02, Proceedings of IPAC2014.

[7] P. Skowronski et al. , "Design of Phase Feedforward System in CTF3 and Performance of Fast Beam Phase Monitors", WEOBB203, Proceedings of IPAC2013.

[8] J. Roberts et al. , "Design, Hardware Tests and First Results From the CLIC Drive Beam Phase Feedforward Prototype at CTF3", MOPP033, Proceedings of LINAC14.

[9] J. Roberts et al. , "First Results from Beam Tests of the CLIC Drive Beam Phase Feedforward Prototype at CTF3", MOPWI001, Proceedings of IPAC15.

ISBN 978-3-95450-176-2

INITIAL WORK ON THE DESIGN OF A LONGITUDINAL BUNCH-BY-BUNCH FEEDBACK KICKER AT DIAMOND

A. F. D. Morgan, G. Rehm
Diamond Light Source, Oxfordshire, UK

Abstract

In 2017 it is planned to install some additional normal conducting cavities into the Diamond storage ring. There is some concern that higher order modes in these devices could cause longitudinal instabilities in the beam. In order to deal with this potential problem we have started work on designing a longitudinal bunch-by-bunch feedback system. This paper will concentrate on the design and simulation of the kicker cavity, which is of the overloaded cavity type.

We chose the overloaded cavity type due to its lack of HOMs, and the wide bandwidth.

INITIAL SYSTEM TESTS

In order to investigate the type of instability we would expect to dominate on the Diamond machine, and to test the capability of our existing sampling electronics, we decided to use the already installed stripline kickers which are used for the transverse feedback system. By operating them in common mode rather than the usual differential mode it is possible to make them act as a weak longitudinal kicker. In order to achieve this, we replaced the existing RF output chain of the transverse multibunch feedback system (TMBF) with the arrangement shown in Fig. 1. Also the striplines were driven in the range 1.5-1.75 GHz rather than the 0-250 MHz they were originally designed for.

For this setup we are only using a mixer as a modulator, thus we are exciting both the upper and lower sidebands. In normal operation, due to our momentum compaction factor (α) of 1.7×10^{-4} and our relativistic gamma factor (γ) of 5870, we are operating above transition ($\eta > 0$) in terms of the Robinson criterion, as shown in Eq. (1).

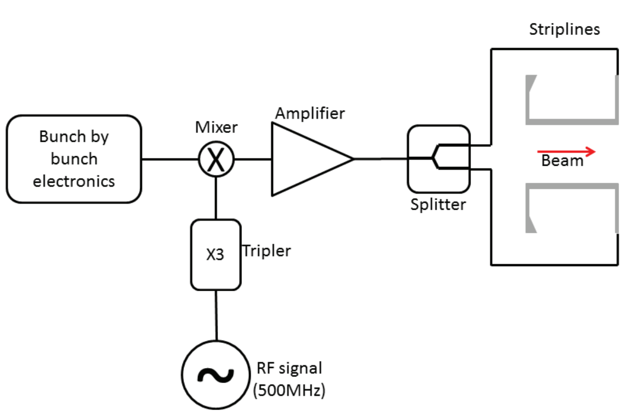

Figure 1: Basic schematic of the modified RF output chain of the TMBF.

$$\eta = \alpha - \frac{1}{\gamma^2} \qquad (1)$$

This means that only the upper sidebands are potentially unstable [1, 2]. Correcting the lower sidebandes is unnecessary, however, for these tests the trade off against simplicity was deemed worth it. In the final system we envisage using IQ mixing to drive single sideband only, which is more efficient and means we are only affecting the modes which the machine is driving towards instability.

For the data capture part of the system, we used our existing frontend and our spare transverse data capture system [3]. The frontend timing was adjusted to sample the zero crossing of the bunch signal in order to maximise the phase sensitivity (and thus the longitudinal position) for each bunch.

With this modified setup we proceeded to run grow/damp studies similar to ones we have done previously for transverse measurements [4], where we excited each mode of oscillation of the bunch train individually, turned off the excitation and recorded the decay. By fitting this to an exponential decay we were able to obtain damping rates on a mode by mode basis.

Our results (Figs. 2 and 3) showed that, unsurprisingly, we are currently comfortably far from a longitudinal instability threshold for normal operating conditions. The most unstable mode would require a beam current of ~ 550 mA to move into an unstable regime. There is a large increase in the noise around mode zero. this is due to the fact that our striplines become particularly weak at those frequencies

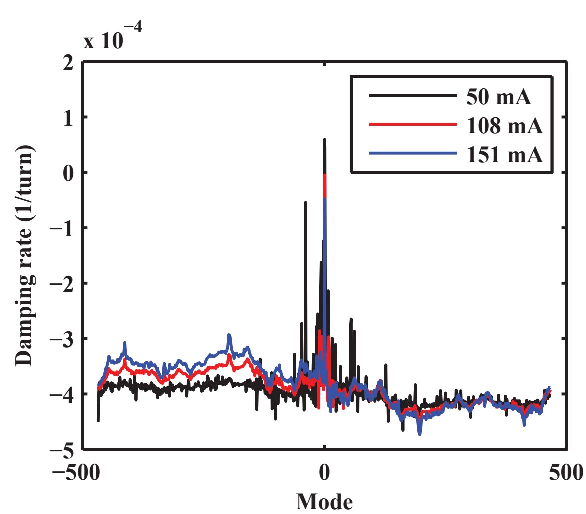

Figure 2: Damping rates for all modes at a range of stored beam currents.

ISBN 978-3-95450-176-2

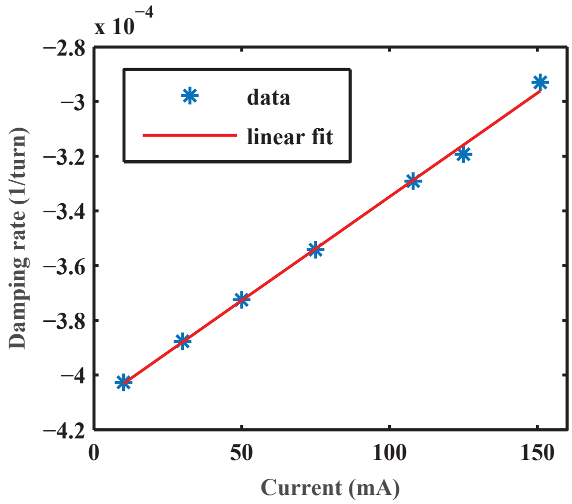

Figure 3: Damping rate against stored beam current for the least damped mode.

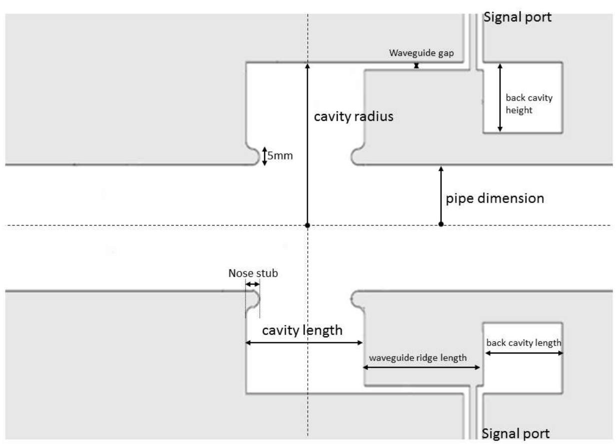

Figure 4: Longitudinal cut of the cavity geometry.

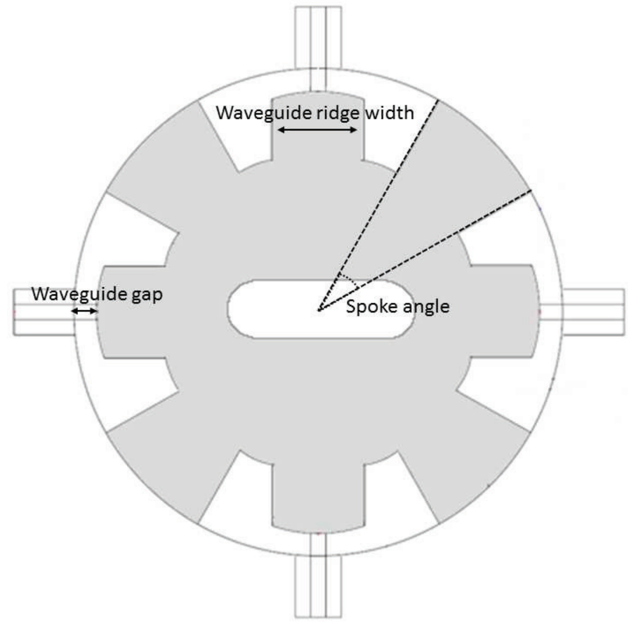

Figure 5: Transverse cut of the cavity geometry.

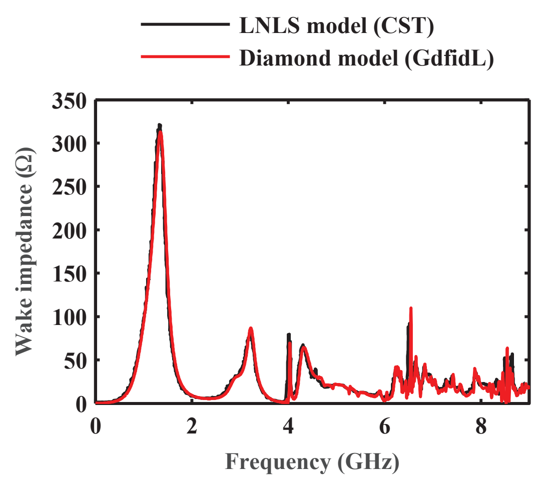

Figure 6: Comparison with the LNLS data.

More studies are planned to investigate the instability thresholds under different operating conditions.

In this benign environment, the stripline kickers would suffice as we are only measuring and need just a small perturbation to the beam. However, this small kick would be insufficient to provide any significant damping of instabilities.

Thus, having tested the basic system, we need to design a longitudinal kicker which is better suited to the expected requirements.

SIMULATION OF THE KICKER

The base design was an overloaded cavity, as used in DAΦNE [5], LNLS [6] and many others [7–9]. An example of which is shown in Figs. 4 and 5.

In order to determine the most suitable parameters, several criteria have to be considered. Firstly, the resonance frequency needs to be correct, in our case the upper sideband of the third RF harmonic is our target, giving a centre frequency of 1.64 GHz. Additionally, the power loss into the structure has to be as low as possible. Sharp resonances in the wake impedance want to be minimised otherwise large variations in heating for different operating conditions may be seen. There also have to be no hot spots, and, to reduce the requirements on the drive amplifiers, the shunt impedance needs to be a high as possible.

We based our initial design on the LNLS version of the cavity [6]. Initially we replicated the design, which gave a useful check as well as an interesting comparison of the CST code used by LNLS, and the GdfidL code used by us. Figure 6 shows the comparison of the wake impedance.

Once we had a suitable initial model, we had to consider how this structure would work installed in the Diamond ring. Being as our pipe dimensions are not the same as the initial model we have to either add tapers to match the

ISBN 978-3-95450-176-2

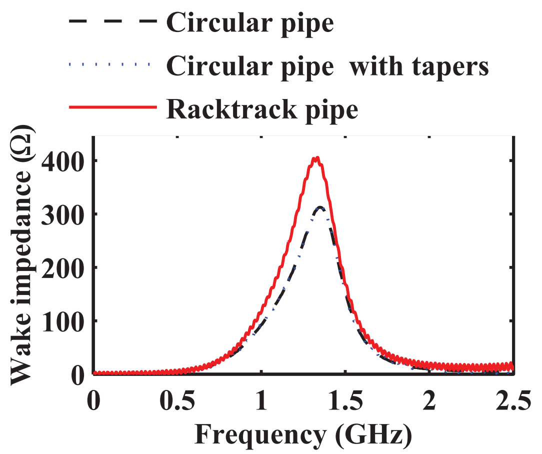

Figure 7: Change in the wake impedance due to pipe cross section changes.

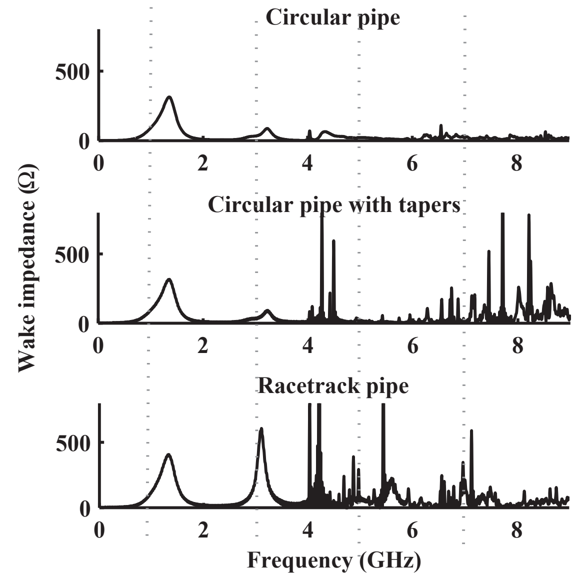

Figure 8: Real part of the wake impedances for different pipe shapes.

external beam pipe shape, or use the racetrack beam pipe cross section throughout the structure. The first case has the advantage of maintaining the rotational symmetry of the cavity, but at the cost that it introduces an additional shallow cavity which would negatively impact the wake loss factor. Conversely, maintaining the racetrack cross section throughout the structure would probably have a reduced wake loss factor but may introduce unwanted features in the wake impedance.

Changing the pipe to a racetrack has only small effects below 2 GHz which can be compensated for with other adjustments to cavity geometry (Fig. 7).

When we look at the wake impedance data we need to consider a much broader frequency range, as the beam can excite up to frequencies of around 20 GHz.

As Fig. 8 shows, although the main operating band below 2 GHz is largely unaffected by the changes in pipe cross section. Both the addition of the taper or the change to a racetrack pipe add new unwanted resonances. The resonances in the taper model are broadly what would be expected from a simple pipe tapering down, as illustrated in Fig. 9, thus the details of the cavity are not dominant.

However, in the racetrack pipe model all the resonance are due to the cavity itself. The new resonances appear as the new beam pipe is smaller and so resonating modes which were well coupled to the larger circular pipe, with its lower cutoff frequency, are unable to couple out of the structure with the smaller pipe in place. This also explains why the resonances stop just above 7 GHz. This is the cutoff frequency of the racetrack pipe for the modes present in the structure.

Using the wake loss factor as a metric, the taper causes a rise from 520 mV/pC from the initial model, to 806 mV/pC. The racetrack model by comparison causes a rise to 1250 mV/pC. Thus in this form, the taper solution would be preferable. However some effort was spent identifying and understanding the structural causes of the racetrack model

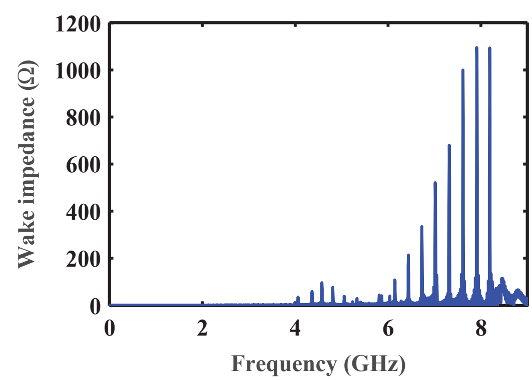

Figure 9: Real part of the wake impedance for the shallow cavity made by the tapers.

resonances, as these may be able to be reduced or eliminated with small design changes to the cavity.

In order to understand the behaviour of the main cavity a model containing just the pipe and cavity was constructed. The results are shown in Fig. 10.

The line of the third harmonic of the cavity is one of the largest of the newly introduced resonances. In order to deal with this the waveguide structure needed to couple out lower frequencies. Ideally we want to couple out all frequencies above the bandwidth around the fundamental cavity resonance. As this coupling structure from the cavity to the signal port is fundamentally a ridged waveguide, one would expect that the ridge height would have the most impact on the cutoff frequency. A simulation was run where the ridge height was increased such that the gap between the ridge and cavity wall was reduced from 5 mm to 1 mm.

ISBN 978-3-95450-176-2

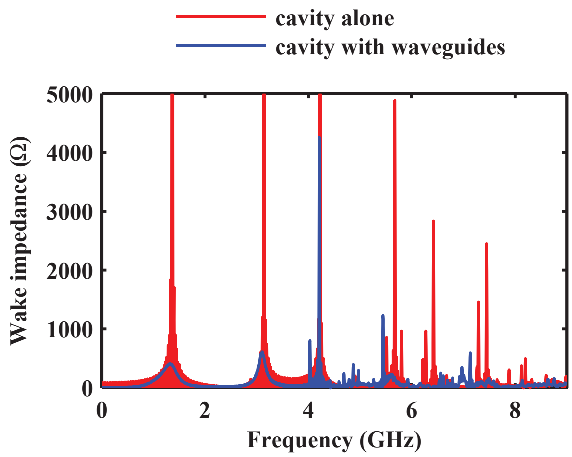

Figure 10: Comparison with and without waveguides.

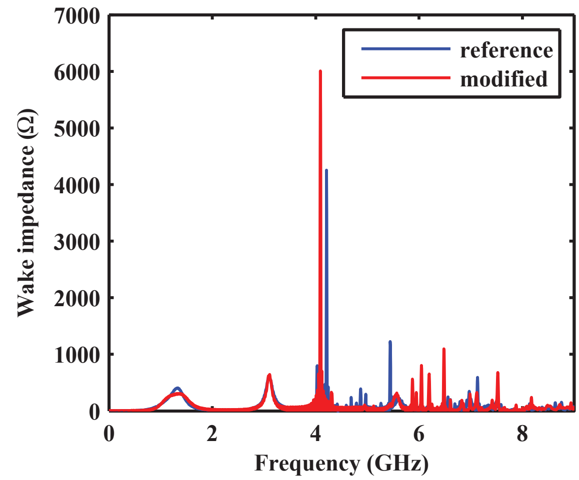

Figure 12: Comparison of the original racetrack model, and new design.

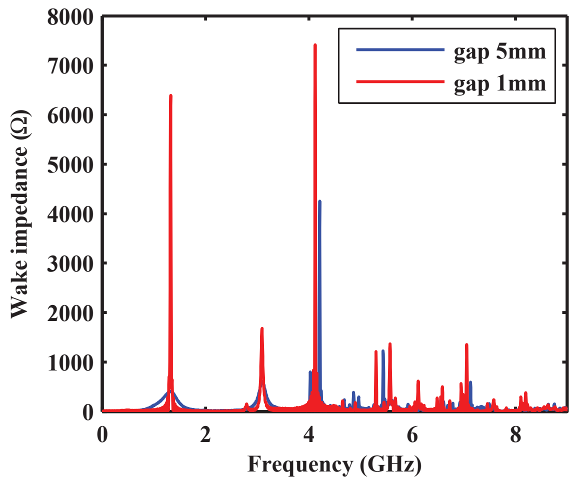

Figure 11: Comparison of the original racetrack model, and one with a reduced gap.

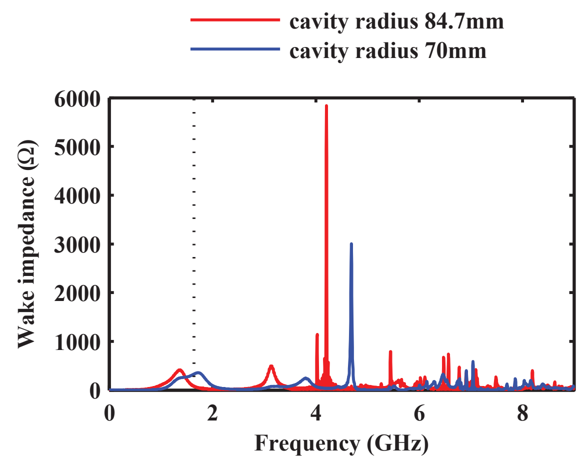

Figure 13: Comparison of the original racetrack model, with a smaller cavity design.

The wake impedance of that simulation is shown in Fig. 11. The resonance at 4.2 GHz is still strongly present which indicates that the cutoff was not lowered enough. It also has the unwanted effect of reducing the bandwidth of the cavity. A more thorough investigation was required.

To that end, a series of simulations was run sweeping various dimensions of the waveguide structure (Figs. 4 and 5). Initially we just looked at how the main design resonance reacted to these changes. For most parameters the design frequency was largely insensitive to changes, with 5 mm changes leading to a few GHz frequency shift. The exceptions were the length of the nose stub, and the waveguide ridge width and height.

Looking more broadly at the higher frequency resonances, the dimensions of the back cavity has quite some impact in the range 4 GHz to 5.8 GHz, as does the nose stub length. A new model with a longer nose stub and a smaller back cavity was tried in an effort to reduce the amplitude of the resonances generally and so bring down the overall wake loss factor.

As Fig. 12 shows, the family of resonances around 5 GHz have been moved to be around 6 GHz. Unfortunately there is also an increase in the amplitude of the third harmonic cavity resonance at 4.2 GHz, which means that the wake loss factor is largely unchanged.

The next step was to modify the cavity radius in order to move the main resonance frequency from 1.35 GHz to 1.64 GHz. By moving the fundamental to a higher frequency we aimed to move the 3rd harmonic above the cutoff for the extraction waveguides.

As Fig. 13 shows, modifying the cavity radius alone is not sufficient. There is a shift of the main peak to 1.64 GHz (as shown by the dotted vertical line) however the bandwidth needs to be optimised. The strong third harmonic line has shifted to higher frequency. Unfortunately it is still below the cutoff of the ridged waveguide structures. Clearly further

ISBN 978-3-95450-176-2

work is needed to optimise the design. One option is to change the resonant frequency to work around a higher RF harmonic.

CONCLUSION

We have demonstrated a longitudinal analysis system using our existing installed striplines. The development of a longitudinal kicker to enable the operation of a multibunch feedback system is progressing. Initial studies have shown that the modifications required from the circular symmetric model to enable installation of such a cavity into the Diamond ring all introduce unwanted sharp resonance lines. Although small modifications to the existing design can impact the behaviour above 4.5 GHz, the third harmonic line of the cavity is trapped in the structure. Further work is needed to improve the coupling out of this cavity harmonic.

REFERENCES

[1] S. Y. Zhang, W. T. Weng, *A new formulation of longitudinal coherent instabilites*, PAC 1993.

[2] A. W. Chao, *Physics of collective beam instabilties in high energy accelerators*, Wiley interscience publication 1993, ISBN 0-471-55184-8

[3] A. F. D. Morgan, G. Rehm, *Performance and features of the Diamond TMBF system*, EPAC 2008.

[4] G. Rehm, M. G. Abbot, A. F. D. Morgan, *New features and measurements using the upgraded transverse multibunch feedback at Diamond*, IBIC2014.

[5] R. Boni et al., *A waveguide overloaded cavity as a longitudinal kicker for the DAΦNE bunch by bunch feedback system*, Particle Accelerators 1996 Vol.52 pp 95-113.

[6] L. Sanfelici et al., *Design and impedance optimisation of the LNLS-UVX longitudinal kicker cavity*, IBIC 2013.

[7] P. McIntosh et al., *An over-damped cavity longitudinal kicker for the PEP-II LER*, PAC 2003.

[8] W. K. Lau et al., *New kicker for the TLS longitudinal feedback system*, PAC 2005.

[9] Y. Lau et al., *Design of longitudinal feedback system kicker for the PLS storage ring*, PAC 1999.

ISBN 978-3-95450-176-2

CONSIDERATIONS AND IMPROVED WORKFLOW FOR SIMULATION OF DISSIPATED POWER FROM WAKE LOSSES

A. F. D. Morgan, G. Rehm
Diamond Light Source, Oxfordshire, UK

Abstract

At Diamond quite some effort has gone into simulating and understanding the dissipation of energy into structures induced by wake losses. Due to changes in the core simulation code we use, it is now possible to extract the dissipated energy information directly from the simulation rather than inferring it from other parts of the simulation output which was, by necessity, our previous method. Various modelled geometries will be used to illustrate the improved approach. Also we will discuss the considerations needed when constructing the model geometries in order to get the most representative results from the simulation.

BASIC WORKFLOW

One of the core principles of our approach is that there should be one core geometry file for each geometry. This can mean some added complexity in the file, but it ensures all the simulations are using the same geometry, and also allows entire simulation sets to be re run for validation. The outline of the approach is shown in Fig. 1

As we are now able to obtain material losses directly from the simulation, only one simulation is required, rather than the N+1 simulations for N materials required by our previous method [1,2]. This gives a large saving in both time and complexity. More importantly it also allows us to remove the assumption that material changes have only a small perturbative effect on the fields in the structure, something we know to be untrue for many of the structures we have studied. Another benefit is that we can now directly compare the total energy lost from the beam to the total energy accounted for from port emission and material heating, giving us an additional valuable check on the self consistency of the simulation.

In order to enable this approach we use a software framework around the core modelling software. The framework (implemented in MatLab [3]) takes the core geometry description and adds any simulation specific information, before running the simulation (CST PS in the past [4], now GdfidL [5]), gathering the results and generating an initial report. As part of the geometry file is programmatically generated it is possible to sweep model parameters (providing the parameters have been set up in the original geometry file). Usually the sweeps involve geometry parameters, however, we have also found it useful to sweep meshing parameters to validate that the model is represented in enough detail to capture all of the resonances and fine structure.

In order to compare the different simulation types, and also to evaluate the effects of geometric changes, we have written high level analysis software in MatLab. This extracts

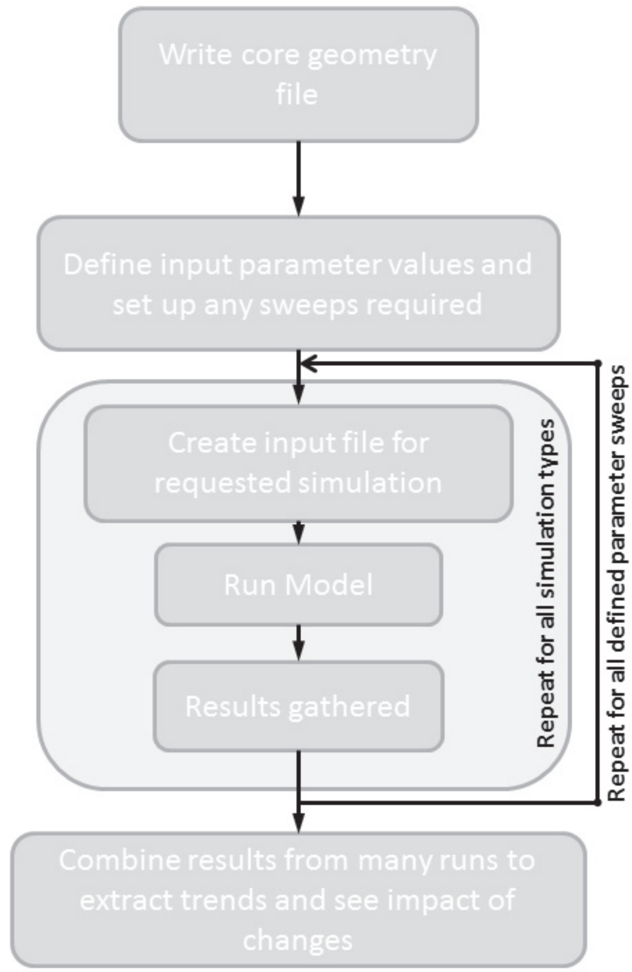

Figure 1: Basic workflow of the simulation process.

information from the output data of the simulations, and combines results in order to help us extract trends and to pull out the more important information for further study. This work is ongoing as we are often finding new ways to combine and look at the data in order to investigate a new aspect of the structures' behaviour.

Currently, this high level analysis is mainly used to track changes in behaviour in S-parameters or energy losses during design studies. In the latter stages of such studies we can perform sensitivity analysis, in order to help define mechanical tolerancing for manufacture. As well as design work, this sort of analysis can be used to improve our understanding of existing devices. It is also useful to validate that

ISBN 978-3-95450-176-2

new versions of the simulation code behave in the expected fashion.

MORE DETAILS OF A SINGLE RUN

In order to get an as complete picture as possible, we use three different simulation modes.

A wake simulation is used to assess wake potentials and wake impedances, as well as energy loss into the structure, and potential disturbances upstream and downstream caused by energy re emission. As described in previous publications this simulation type can be used as a basis to investigate sensitivity to changes in beam and machine conditions [1]. For our purposes, a wake model comprises of a structure with a line charge passing through it representing the beam. There are ports at the beam entry and beam exit, as well as any pick ups (e.g. coaxial outputs from striplines or beam position monitors).

From this simulation we capture energy loss into materials, signals emitted from the ports, and a map of energy deposited into the structure, which helps identify hot spots. Because of the long range nature of the wake potential, we have a correspondingly high resolution wake impedance which gives a clearer picture of structural resonances. When combined with the loss map and the eigenmode results it has the potential to let us identify which mode is causing which effect, and if it is a problem for operation.

An S-parameter simulation excites a single port with a broadband signal. By monitoring the output of the ports, and by repeating the excitation for each port a full S-parameter matrix can be built up. This type of model is useful to assess signal coupling and changes of output due to geometry changes. However its main benefit is to predict signals which can later be measured on the physical device. This being the case, in the simulation we only excite signal ports.

A lossy eigenmode simulation enables us to visualise the modes in the structure, and, depending on the structure being investigated, find the shunt impedance and the Q factors for the modes present in the model. For cavity type structures the shunt impedance helps specify the size of the drive amplifiers required to drive it.

CONSIDERATIONS ABOUT MODEL CONSTRUCTION

Wake Simulation

On top of the usual considerations of using a suitably fine mesh in order to faithfully reproduce the desired geometry, with a suitable time step to describe the input beam, and whether symmetry planes can be used. Additional considerations need to be taken into account. We require a long wake simulation as we require to account for all the energy injected into the simulation by the beam. This implies that we need to wait for the energy in the structure to either couple out of the ports or be absorbed by the materials of the structure.

One of the checks we perform is measuring what fraction of energy lost from the beam is accounted for at the end of the simulation. If it is less than all then we will need to run the simulation for longer. If the accounting returns more than that lost from the beam then there must be an unphysical process in the simulation. A major consideration arises from the behaviour of the ports. Currently the ports cannot distinguish signals arising from a transmitting mode and that from an evanescent mode. Accounting for the former is correct as power is leaving the structure, however, the fields associated with the evanescent modes do not leave the structure. If these evanescent signals touch the port boundary it adds to the account of power leaving the structure which leads to false accounting of the port contribution.

By adding extensions to all ports this reduces the contribution of the evanescent modes to the port signals. Initially we added lossless pipes, but found that with lossy pipes the same effect could be had for a smaller model. Steel was chosen as it is the material used for our vacuum pipes and thus was representative of the installed environment of the machine.

One does not want to capture the output signal due to the original beam signal. Ideally each port can have a capture delay set so that signals are only analysed after the input line charge has fully passed through the port.

Eigenmode Simulation

Currently, the eigenmode simulations return many longitudinal modes which can not exist in the real structure, (ideally it should be possible to match up the resonances between eigenmode and wake solvers). This is due to the need for all pipes and ports to be closed for this type of simulation. A capability to have ports in an eigenmode simulation would mean that the reported modes should be just ones which are present in the physical device and will be a focus for further development.

CHECKING RESULTS FOR SELF CONSISTENCY

In order to build confidence that what is returned by the simulation is a good representation of the real behaviour, we apply many checks to the data to make sure that the results are self consistent and do not violate any physical laws, conservation of energy for example.

The initial check is, whether all the energy has been accounted for. If not, generally the simulation has not run long enough. The aim is to get as close as possible to 100% within a reasonable simulation time. If more than 100% of the input energy is accounted for, this indicates that there is unphysical behaviour in the simulation. Figure 2 shows the energy accounting for a set of button pickups. Most of the energy is accounted for, and in this case the vast majority of the energy is coupled out of the structure through the ports.

In order to determine if the simulation has stabilised we look at several results, as illustrated in Fig. 3. The top graph shows the cumulative sum of the energy out of all

ISBN 978-3-95450-176-2

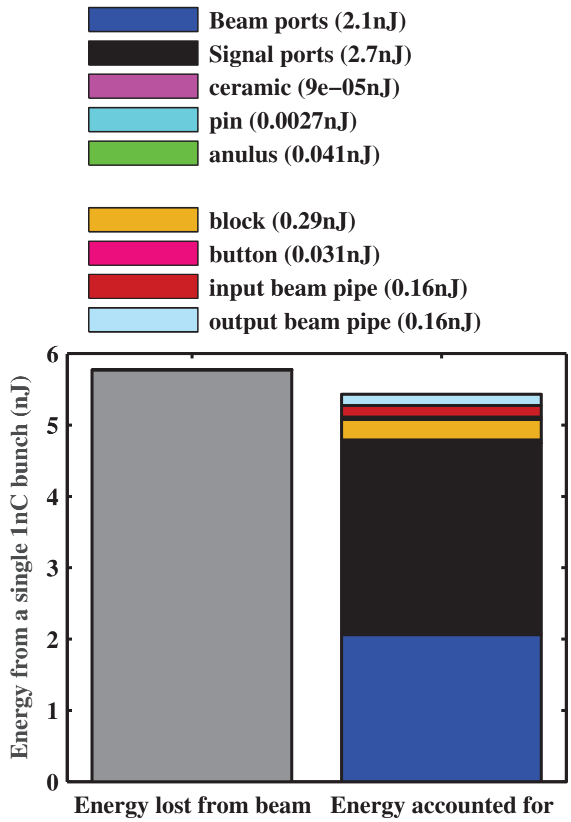

Figure 2: Energy accounting for a beam position monitor button.

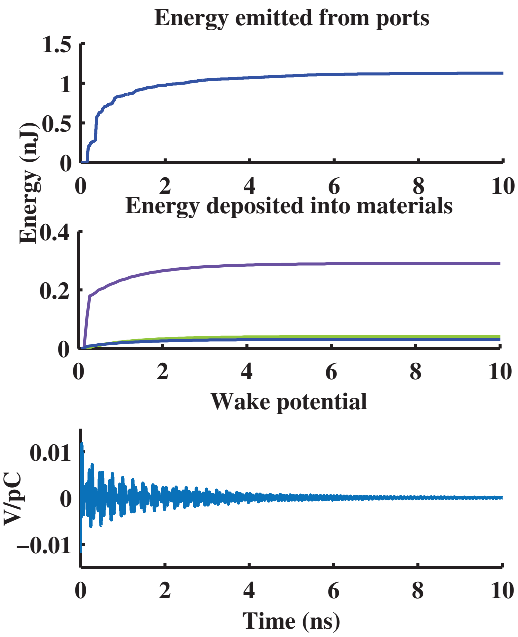

Figure 3: Typical results for a stable model.

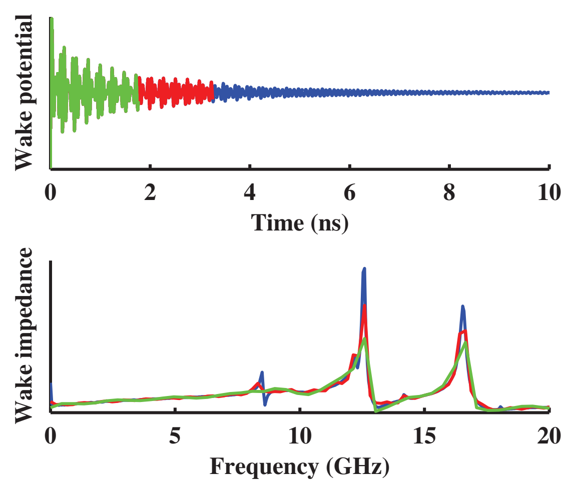

Figure 4: The effects of truncating the wake potential.

ports, so a horizontal line means that the signals out of the ports have decays away, and no further energy will be emitted. The middle graph shows the cumulative sum of all the energy deposited in the different materials in the structure. The lower graph shows the ring down of the wake potential. Often the wake potential will not ring down fully within the simulation time due to high Q resonators in the structure. This introduces errors into any frequency domain analysis such as calculating the wake impedance. How much of a problem this is will depend on the details of the model under scrutiny. Figure 4 illustrates the effects of truncating the time domain wake potential for a button block.

One type of simulation artifact is a resonator which does not decay, and so would ring on for ever. In this case, the simulation will never fully stabilise and the energy from the ports will eventually exceed the total energy put into the structure by the beam.

Once we are satisfied that we have a simulation which has a long enough wake and stabilises well, we move on to more detailed checks.

So far all the checking has been done the the time domain. This next set moves into the frequency domain. As the stimulations are all based on linear equations, then there can be no energy transfer between frequencies. Thus if any frequency has more energy coming out of the ports than was put into the structure, it indicates there is a problem which needs further investigation.

If the discrepancy occurs at a waveguide cutoff of a port, it usually indicates that the simulation is struggling to correctly represent the signal so close to the threshold. In terms of the energy accounting it often has negligible impact due to the sharpness of the resonance. More generally it usually means that either, the port is seeing the fields from evanescent modes, which do not leave the structure or too short a wake has been used causing the time signal to be truncated. Figure 5 shows an example of this. Around 9.6 GHz, the energy from the ports exceeds that deposited by the bunch.

ISBN 978-3-95450-176-2

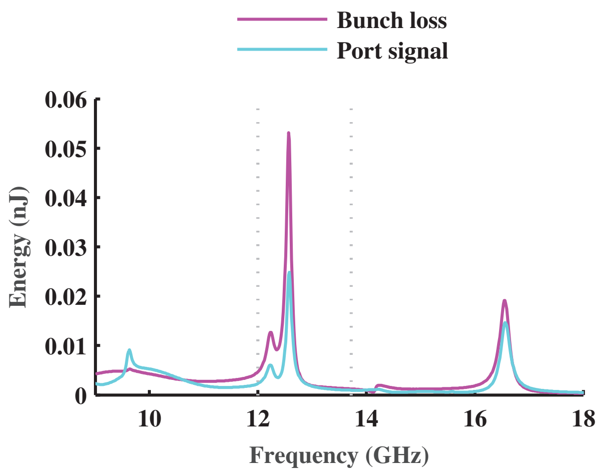

Figure 5: Frequency domain signals emitted from ports and deposited by beam.

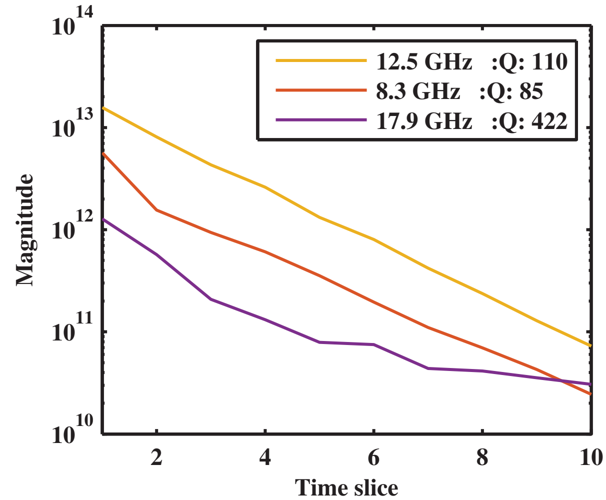

Figure 7: The decay of resonance peaks in a button structure.

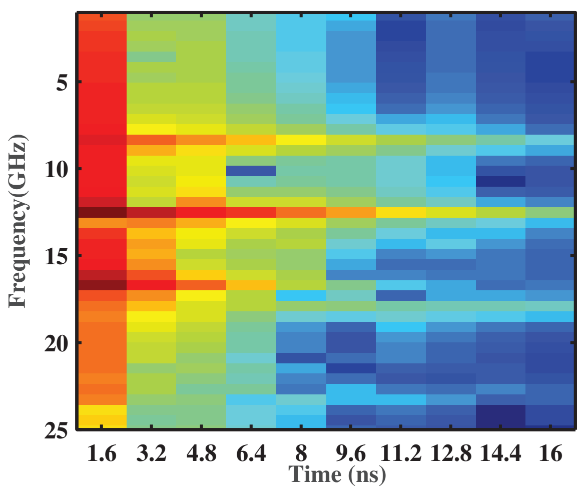

Figure 6: Spectrogram of the wake potential.

Although we have run the simulation long enough for it to stabilise in the time domain, there is still the question of how accurately the resonances in the structure are represented. In order to check this we run the frequency domain processing on a series of increasingly truncated wake potentials. If the Q values obtained for the resonances do not change if additional wake length is added then they are properly represented.

A related check is to separate the wake potential data into chunks of time, and then fourier transform each chunk. This gives a time evolution of the spectrum, and from this one can calculate the decay rate and thus the Q of the resonances. Resonances with extremely high Qs are most likely artifacts but certainly bear further investigation as they could be trapped modes in the structure.

Figures 6 and 7 show a typical result from a button pickup. Figure 6 show the spectrogram of the wake potential. Each collum is the spectrum of 1.6ns of time. three high Q resonances can be seen at 8.3 GHz, 12.5 GHz and 17.9 GHz. An initially strong but fast decaying resonance can to seen at approximately 16 GHz.

Figure 7 shows the trend of the three highest Q resonances in the simulation. The 8.3 GHz and 12.5 GHz lines show the expected exponential decay. However the 17.9 GHz line levels off. This probably indicates the numerical noise floor of the simulation, but a longer simulation could be run in order to see if the other lines also level off when they reach that magnitude.

CONCLUSION

We have described the workflow used in order to investigate many long wake behaviours of the various structures for the Diamond accelerator.

We have also shown how developments in the core simulation code are allowing us to develop new more robust ways of investigation energy losses.

Further work on integrating the output of the wake and eigenmode solvers is expected to improve our understanding of which field patterns contribute to undesired outcomes. Allowing for more targeted solutions.

REFERENCES

[1] A. F. D. Morgan G. Rehm, *Quantifying dissipated power from wake field losses in diagnostic structures*, IBIC 2013.

[2] A. F. D. Morgan G. Rehm, *Finding the distribution of wake field induced losses in diagnostics structures for realistic machine conditions*, ICFA mini-workshop on Electromagnetic wake fileds and imedances in particle accelerators 2014.

[3] Mathworks, www.mathworks.com

[4] Computer simulation technology, www.cst.com

[5] GdfidL, www.gdfidl.de

ISBN 978-3-95450-176-2

STREAK CAMERA PSF OPTIMISATION AND DUAL SWEEP CALIBRATION FOR SUB-ps BUNCH LENGTH MEASUREMENT

L.M. Bobb, A.F.D. Morgan, G. Rehm, Diamond Light Source, Oxfordshire, U.K.

Abstract

Streak cameras are commonly used for bunch length measurement. In normal beam modes, bunch lengths are on the order of 10 ps. For the study of coherent synchrotron radiation, a low alpha single bunch beam mode is implemented with bunch lengths as small as 1 ps and beam current in the tens of μA. In order to reliably measure such a short bunch at low beam currents, the input optics for the streak camera must be optimised for sufficient incident light intensity and high resolution in both sweep directions. This is achieved through the use of reflective input optics in which a pinhole is imaged to provide a small circular PSF. Furthermore, to precisely measure the bunch length the calibration of the dual sweep must be known. Here we describe a calibration method using electrical delays to incorporate calibration information within streak camera images.

INTRODUCTION

Diamond Light Source (DLS) is a third generation synchrotron light source providing high brilliance x-ray beams for user experiments. Nominally a 3 GeV, 300 mA, 900-bunch electron beam is circulated in the storage ring with a revolution period of 1.8 μs. In this normal beam mode the momentum compaction factor α is 1.7×10^{-4} which, given the synchrotron frequency f_s = 2.5 kHz and relative energy spread $\sigma_\epsilon = 10^{-3}$ with Eq. 1, has zero current bunch length $\sigma_{bunch} \approx 10$ ps [1].

$$\sigma_{bunch} = \frac{\alpha}{2\pi f_s}\sigma_\epsilon \qquad (1)$$

In the low alpha beam mode the electron bunch length is reduced to a few picoseconds. Due to the corresponding reduction in x-ray pulse duration, the temporal resolution used for pump-probe or time-of-flight experiments is improved. Furthermore the reduction in bunch length extends the wavelength range in which the electron bunch emits coherently towards the THz/far infrared region of the electromagnetic spectrum [2].

For the low alpha beam mode where $\alpha = 10^{-5}$, f_s = 0.6 kHz and $\sigma_\epsilon = 10^{-3}$ and using Eq. 1, the bunch length $\sigma_{bunch} \approx 2.6$ ps [1, 2].

To measure the longitudinal bunch profile and length, images of the synchrotron radiation (SR) pulses are acquired using a dual sweep streak camera (SC) from Optronis GmbH [3]. The fast deflection unit employs a synchroscan frequency of 250 MHz. This signal is provided to the SC by dividing the 500 MHz master oscillator frequency.

In order for the SC to measure these picosecond bunch lengths at bunch currents of tens of μA, the input optics for the SC must be optimised and the dual sweep calibration must be accurately measured. This report describes the implementation of reflective input optics including a pinhole to ensure maximum light intensity and smallest Point Spread Function (PSF) spot size for high resolution measurements, and presents a method for the dual sweep calibration of the SC using electrical delays.

EXPERIMENTAL SETUP AND ANALYSIS PROCEDURE

The Visible Light Extraction (VLE) system brings visible SR from a bending magnet in the storage to the diagnostics beamline where the SC is located via a series of folding and focussing mirrors. The total path length of the VLE is $\approx$ 25 m, the reader should refer to [4] for further details.

In the diagnostics beamline the visible SR propagates through the input optics and is focussed onto the SC. Inside the SC, visible SR photons are converted to electrons by the photocathode. Electrons are deflected in two directions (horiz. (x) and vert. (y)) within the streak tube. At the end of the streak tube electrons are converted to photons via a phosphor screen. The photons undergo another conversion to electrons as they pass through the intensifier. At the end of the intensifier a second phosphor screen converts the electrons to photons. The readout unit consists of a series of lenses to image the phosphor screen onto the cooled CCD camera for readout. In Figure 1 a schematic overview of the system is illustrated.

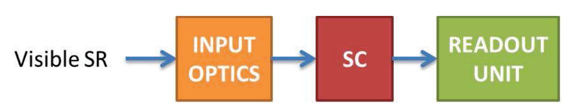

Figure 1: Schematic overview of the streak camera system.

A typical streak camera image with both deflections enabled is shown in Figure 2. The fast 250 MHz sweep and slow sweep run along the horizontal and vertical axes respectively as shown.

To obtain an accurate bunch length measurement the streak image is deconvolved with the PSF (see Figure 3) using the Richardson-Lucy algorithm [5]. The PSF is the measured spot size of the incident light on the SC with both deflections disabled. Next, each row of the deconvolved streak image is fitted with a Gaussian to obtain the r.m.s. bunch length in units of pixels. The bunch length is then converted from units of pixels to picoseconds using the calibration measurement in ps/pixel.

The reader should note that to a first approximation, and assuming the PSF width and bunch profile are Gaussian, the contribution of the PSF width to the bunch length measurement is added in quadrature. The contribution of the PSF to

ISBN 978-3-95450-176-2

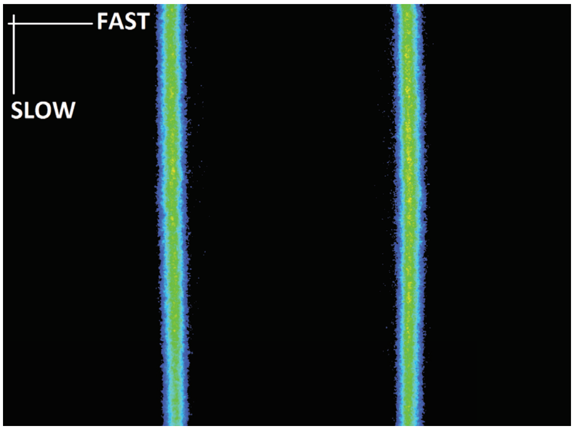

Figure 2: Typical streak camera image in low alpha.

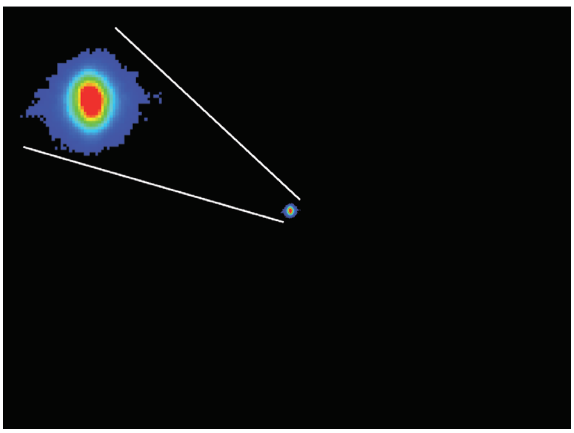

Figure 3: Typical PSF image with zoomed in ROI shown in top left.

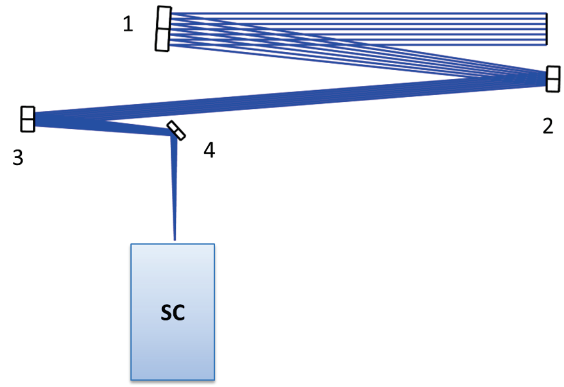

Figure 4: Original reflective input optics where (1) is concave parabolic mirror, (2) is a convex spherical mirror, (3) is a concave spherical mirror and (4) is a flat folding mirror.

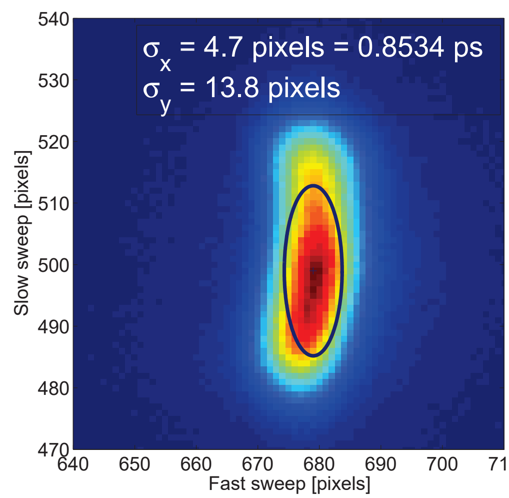

Figure 5: PSF acquired using the previously implemented reflective input optics.

the measured bunch length is shown in Eq. 2 where σ_{bunch} is the real r.m.s. bunch length, σ_{meas} is the measured bunch length and σ_{PSF} is the PSF width.

$$\sigma_{bunch} = \sqrt{\sigma_{meas}^2 - \sigma_{PSF}^2} \tag{2}$$

INPUT OPTICS UPGRADE

For SR studies using the single bunch low alpha beam mode, the input optics for the SC must be optimised to:

1. Propagate the maximum available light intensity to the SC.
2. Focus the incident SR beam to obtain a minimum PSF spot size at the SC.

In Figures 4 and 5 the layout of the previously implemented reflective input optics [6] and corresponding 2D-Gaussian fitted PSF image are shown respectively. The visible SR beam delivered from the VLE is somewhat astigmatic. It was also observed that after propagating through the previously implemented input optics more astigmatism was introduced. In Figure 5 the SC was longitudinally positioned in the horizontal focal plane to ensure the smallest PSF width along the fast sweep axis. With these input optics and astigmatism, the PSF could only be focussed in one direction. Therefore although the PSF contribution would be small for the bunch length measurements along the fast axis, blurring due to overlap along the slow axis reduced the ability to study dynamics along the slow (typically μs to ms scale) axis.

To obtain a small circular PSF a pinhole was inserted into the input optical system. The previously implemented reflective input optics shown in Figure 4 were relocated further upstream relative to the SC and were used to focus the almost-collimated SR beam onto the pinhole aperture for maximal light intensity.

The pinhole was imaged to the SC using two 90° off-axis parabolic (OAP) mirrors as shown in Figure 6. With a totally reflective optical system the maximum available light intensity could be propagated to the SC and the inclusion of a pinhole aperture provided the minimum ($\sigma_x \approx 0.7$ ps) circular PSF spot size as shown in Figure 7.

Due to the beam astigmatism, the PSF width along the fast axis could be favoured by adjusting the longitudinal position

ISBN 978-3-95450-176-2

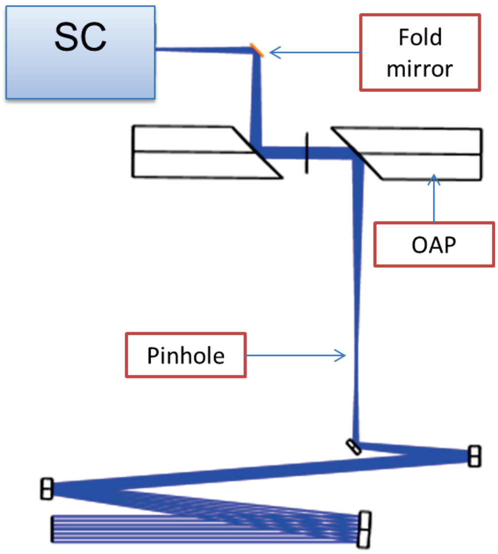

Figure 6: Layout of the upgraded reflective input optics.

of the streak camera. This explains the fit results shown in Figure 7 where the PSF width σ_x along the fast axis is slightly smaller than that along the slow axis σ_y.

The previously implemented reflective optics were left unchanged such that a roll-back could be done easily if required. However, due to the astigmatism introduced it may be preferable to replace this section of the input optics with a simpler single 90° OAP mirror.

The last element of the input optics is a folding mirror mounted on a gimbal holder to allow final alignment adjustments of the incident beam on the SC. The photocathode of the SC has a 2 mm × 2 mm central sweet spot within which the PSF should be located [3].

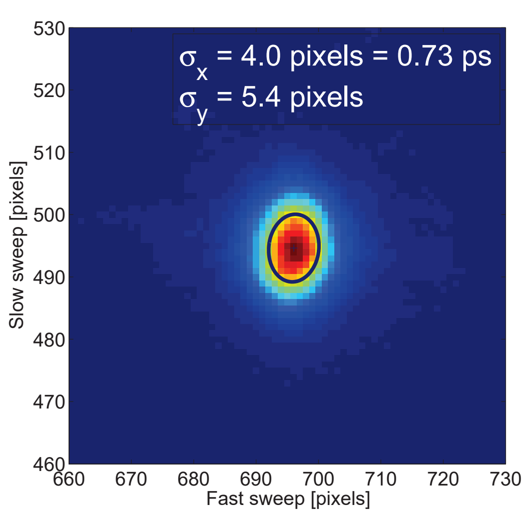

Figure 7: PSF acquired using the upgraded reflective input optics.

CALIBRATION

For bunch length measurements the dual sweep calibration of the SC must be known to a high degree of accuracy. Optical delay lines are most commonly used for SC timebase calibration. One such method is to split a single laser pulse into a train of identical pulses each taking a slightly longer path length and thus having different optical delays. The optical delays introduced are known and can therefore be compared to those measured within the streak image thus providing timebase calibration [7].

Including an optical delay line for the SR beam or for a separate laser source is often time-consuming due to the numerous degrees of freedom and accuracy required. Rather than delaying the arrival time of the incident pulse relative to the fast sweep deflection by a known amount, the same result can be achieved by delaying the fast sweep deflection relative to the arrival time of the incident pulse. For SR, the arrival time of the incident pulse is fixed by the parameters of the storage ring (i.e. the master oscillator frequency) and path length changes due to thermal drifts of the VLE and input optics happen on much longer timescales so can be considered negligible on the order of milliseconds.

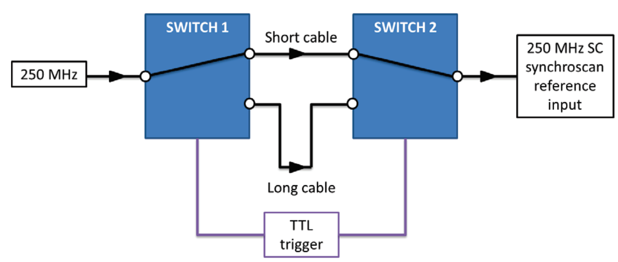

Figure 8: Illustration of the electrical delay introduced using PIN diode switches and cables of different lengths for the fast deflection signal.

In Figure 8 the principle of using the electrical delay difference between two cables of different lengths is illustrated. The 250 MHz signal is the input for the fast deflection unit of the SC. A waveform generator provides a square wave with a specified frequency which triggers the Mini-Circuits PIN diode switches such that the 250 MHz signal travels either via the short or the long cable. This is observed as a characteristic zigzag within the SC image as shown in Figure 9 where the electrical delay is $<$ 20 ps. It should be noted that the calibration can be disabled by simply disabling the output on the waveform generator.

The left and right streaks of the acquired images are analysed separately. Each row of the streak is Gaussian-fitted and the centroid positions are recorded in units of pixels. By taking the mean time shift between the two extreme centroid positions of the zigzag pattern, as denoted by the arrow between the red dashed lines in Figure 9, the electrical delay measured by the SC is obtained in units of pixels.

To obtain calibration values in units of ps/pixel for the left and right streaks the electrical delay must be quantified independently. The electrical delay due to the difference

ISBN 978-3-95450-176-2

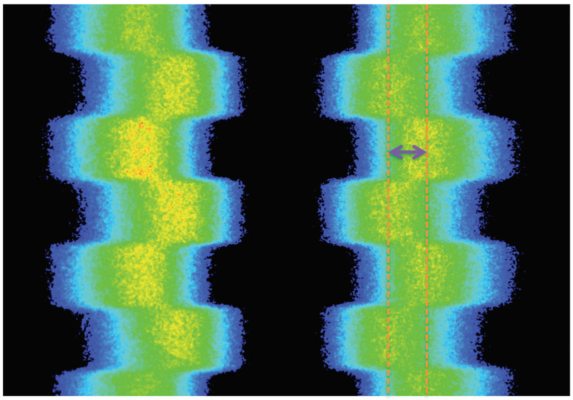

Figure 9: Streak camera calibration image taken in normal user beam where the separation between the dashed red lines is the measured delay used for calibration of the fast timebase. The slow timebase may be calibrated using the period of the square wave.

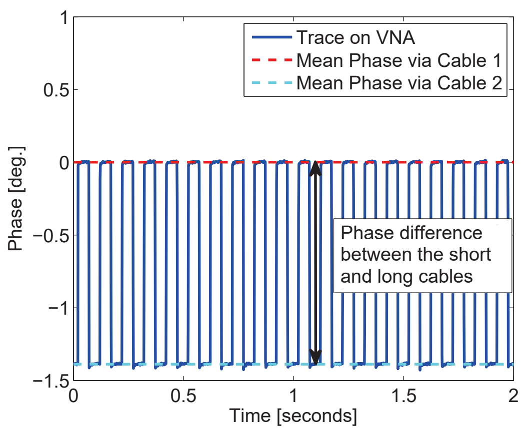

Figure 10: A plot of the 250 MHz VNA trace (blue line) with 10 Hz switching frequency between the short and long cables where the mean phase delays for each cable are shown by the dashed lines.

between the two cable lengths was measured using a Vector Network Analyser (VNA) as shown in Figure 10.

The electrical delay was obtained using the reported phase delay difference between the two cables. Given the phase delay θ in units of degrees, the electrical delay δ_{real} in picoseconds may be calculated using Eq. 3 where $T = 4000$ ps in our case for the 250 MHz deflection signal. Using this system the mean electrical delay was (15.4320 ± 0.0023) ps.

$$\delta_{real} = \frac{T}{360^\circ} \cdot \theta \tag{3}$$

For maximum precision of the phase measurements the VNA was set up with a bandwidth (BW) of 1 kHz for the intermediate frequency (IF) while measuring at a fixed frequency of 250 MHz. Statistics are gathered from 1600 data points of a 2 seconds long trace. However, the narrow IF bandwidth required a low switching rate of 10 Hz.

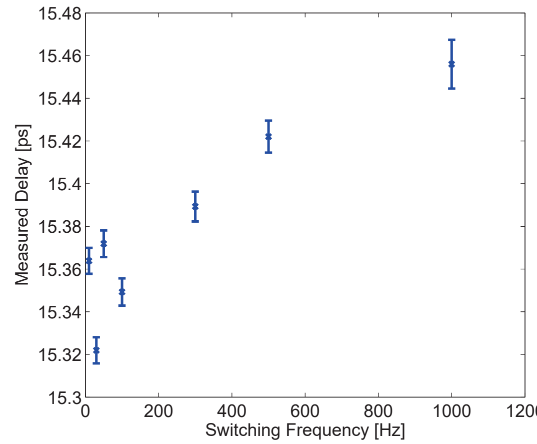

Figure 11: A plot of the measured electrical delay using the VNA for different trigger frequencies provided by the waveform generator. Data points with corresponding standard errors are denoted by crosses and errorbars.

It should be noted that in order to calibrate the timebases of the SC, a trigger frequency on the order of kHz is required. To this end, the VNA was set to a higher IF BW of 10 kHz. The electrical delay was measured for different frequencies as shown in Figure 11. The variation of the electrical delay with switching frequency over a range of 10 Hz - 1 kHz is $< 1\%$.

Given the known electrical delay and the measured time shift from the SC image δ_{SC} in pixels, the fast timebase calibration k_{fast} in units of ps/pixel may be calculated using Eq.4. For the SC at DLS, the fast deflection calibration is regularly measured to four decimal places and varies within the range of 0.17 - 0.20 ps/pixel.

The slow timebase calibration k_{slow} may be obtained by comparing the measured period of the square wave in the SC image (along the slow axis) with the expected period set by the waveform generator (see Figure 9).

$$k_{fast} = \frac{\delta_{real}}{\delta_{SC}} \tag{4}$$

CONCLUSION

For sub-ps bunch length measurements the optimisation of the input optics and calibration of the timebases of the streak camera must be performed.

At DLS, the input optics to the SC have been upgraded to work with white beam and to ensure a high resolution in both the fast and slow sweep directions through the reduction of the PSF spot size using a pinhole aperture. Operation in the low-alpha single-bunch beam mode for SR studies requires all elements in the input optical system to be reflective (vs refractive) to ensure maximum light intensity at the SC and to avoid pulse lengthening due to chromatic dispersion. With these upgraded input optics an r.m.s PSF spot size $\sigma_{PSF} \approx$ 0.7 ps could be achieved.

ISBN 978-3-95450-176-2

An example of the performance of the upgraded SC system is shown in Figure 12. Here the SC bunch length measurements (blue) are plotted against bunch current. The theoretical zero current bunch length is also shown (red). The SC data is in good agreement with the theory and bunch lengths < 2 ps have been measured.

In this report, a simpler method of timebase calibration of the SC using an electrical delay setup is presented. With this method calibration information is contained within the SC images. Calibration measurements can be performed simultaneously with data acquisition to ensure the calibration values are valid for the time at which the data was acquired.

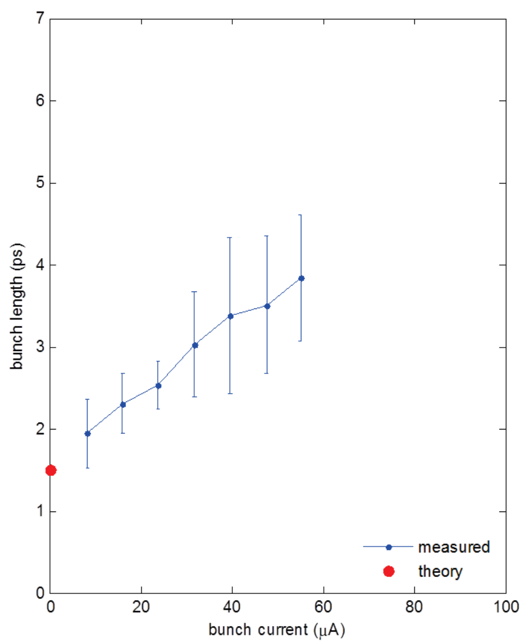

Figure 12: A plot of bunch length at various bunch currents in single bunch low alpha mode at 3.4 MV, $\alpha = -4.6 \times 10^{-6}$ and $f_s = 460$ Hz [8]. The error bars indicate the standard deviation over the ≈ 800 individual profiles analysed in each streak image.

REFERENCES

[1] C.A. Thomas et al., "Investigation of Extremely Short Beam Longitudinal Measurement with a Streak Camera", TUPB41, *Proceedings of DIPAC09*, Basel, Switzerland (2009).

[2] I.P.S. Martin et al., Phys. Rev. ST Accel. Beams 14, 040705 (2011).

[3] Optronis GmbH website: `http://www.optronis.com/en/products/streak-cameras.html`

[4] C.A. Thomas et al., "Diagnostics Beamline Optimisation and Image Processing for Sub-ps Streak Camera Bunch Length Measurement", TUPA42, *Proceedings of IBIC2012*, Tsukuba, Japan (2012).

[5] D.S.C. Biggs et al., Applied Optics 36, 8 (1997).

[6] C.A. Thomas et al., "Performance of a Streak Camera Using Reflective Input Optics", MOPE081, *Proceedings of IBIC2010*, Kyoto, Japan (2012).

[7] S.L. Shapiro, *Ultrashort Light Pulses: Picosecond Techniques and Applications*, (Springer Science & Business Media, 2013), p29.

[8] I.P.S. Martin et al., "Reconstruction of Electron Bunch Motion During CSR Bursts using Synchronised Diagnostics", MOPMA003, *Proceedings of IPAC2015*, Richmond, VA, USA (2015).

ISBN 978-3-95450-176-2

OPTICAL DIAGNOSTICS WITHIN LA3NET*

C.P. Welsch#, Cockcroft Institute and The University of Liverpool, UK

Abstract

The Laser Applications at Accelerators network (LA³NET) is a pan-European project that has received 4.6 M€ of funding from the European Union's 7th Framework Programme. It closely links research into lasers and accelerators to develop advanced particle sources, new accelerating schemes, and in particular beyond state-of-the-art beam diagnostics. This contribution summarizes the research achievements in optical beam diagnostics of this 4 year research and training initiative. It presents the achievable resolution of a laser-based velocimeter to measure the velocity of neutral particle beams, results from the measurement of bunch shape using electro-optical crystals with tens of fs resolution, experimental data using a laser wire scanner, and discusses the resolution limits in energy measurements using Compton backscattering at a synchrotron light source. Finally, it also provides a summary of events that have been organized by the LA³NET consortium.

INTRODUCTION

The LA³NET beneficiary partners have recruited 19 Fellows that are hosted by 11 partner institutions all over Europe. Their individual research projects are often carried out within the frame of PhD studies and distributed over the project's different scientific work packages. The largest of these work packages focuses on R&D into advanced beam diagnostics techniques. Furthermore, the consortium organizes a number of international Schools and Topical Workshops, as well as an international conference and numerous outreach events for the wider laser and accelerator communities, as well as the general public.

RESEARCH

Beam diagnostics is one out of the five scientific work packages within the LA³NET project [1]. It is of central importance as the instrumentation developed by the Fellow is crucial in interconnecting research carried out in the other areas of beam generation, acceleration, detectors and power supplies development. The DITANET project [2] pioneered a new approach to researcher training in beam diagnostics and the concepts developed by this consortium have formed the basis also for LA³NET. The following subsection present research results in this work package from individual LA³NET Fellows.

* This project has received funding from the European Union's Seventh Framework Programme for research, technological development and demonstration under grant agreement no 289191.

carsten.welsch@cockcroft.ac.uk

Electron Bunch Shape Measurements using Electro-Optical Spectral Decoding (EOSD)

FLUTE (Ferninfrarot Linac-Und Test-Experiment – far infrared linac and test experiment) a linac-based light source currently under construction at Karlsruhe Institute of Technology (KIT) is a dedicated accelerator R&D facility. The main R&D goals of FLUTE are to perform systematic bunch compression studies over a wide charge (1 pC - 3 nC) and bunch length (1 fs - 1 ps) range, and to generate THz radiation with high peak fields [3]. The wide range of bunch charges and lengths at a comparatively low energy of 42 MeV requires sophisticated single-shot online-diagnostics. Electro-optical (EO) techniques have proven to be a reliable tool for bunch length measurements at linacs [4, 5]. LA³NET Fellow A. Borysenko had shown previously [6] for a low energy electron beam that longitudinal bunch profile measurements using EO techniques lead to an overestimation of the actual bunch length. This is caused by the electron energy-dependent opening angle of the bunch's Coulomb field that passes the EO crystal during the experiment. The opening angle of the electric field of the bunch is dependent on the electron energy as 1/g due to Lorentz transformation that leads to a longitudinal contraction of the field. Recently, he carried out studies into electro-optical bunch length measurements at beam energies of 40 and 200 MeV at the SwissFEL Injector Test Facility [7], PSI, Switzerland in preparation of measurements at FLUTE.

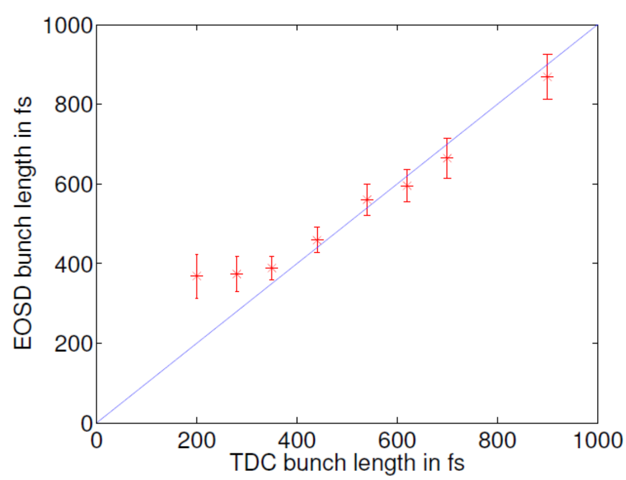

Figure 1: Measurement of bunch profiles using EOSD and a TDC for various electron bunch compressions at a beam energy 200 MeV.

The EO crystal is mounted on a movable arm in a way that the distance to the electron beam can be adjusted during the experiment. The back surface of the crystal has a high reflective coating that reflects the laser pulse. Then it is coupled back into a fibre and transported to the

ISBN 978-3-95450-176-2

experimental station outside of the tunnel for spectral analysis. To record the spectral information of the laser pulse a 512x1-InGaAs photodiode array detector (iDus, Andor) was used that is capable of recording the spectrum of just a single laser pulse. The delay between laser pulse and electron bunch can be adjusted in order to achieve the temporal overlap inside the EO crystal in steps of 188 fs (electronically with a vector modulator) to achieve full temporal overlap inside the EO crystal. Data was compared against measurements using a transverse deflecting cavity (TDC).

The average EOSD bunch profile is depicted together with a single shot EOSD profile in the above Fig. 1. For specified settings of the bunch compressor, each point represents the rms electron bunch length reconstructed from EO measurements and is shown together with the rms bunch length measured with the TDC structure. Each EOSD bunch length is taken as a result of a Gaussian fit for the averaged bunch profile over 300 single shot profiles. The bunch charge was 100 pC. The electron beam energy was set to 40 MeV. The distance between EO crystal and electron beam was set to 1 mm. The EOSD measurement shows good correspondence to the TDC measurement for an electron bunch length longer than 370 fs rms. Moving to a shorter bunch length, the TDC structure is still capable of measuring the bunch length whilst the EOSD system does not measure any shorter than 360-370 fs.

Coulomb Field Strength Measurement by Electro-optic Spectral Decoding

A similar approach has been taken by R. Pan, based at STFC, and co-workers from CERN and the University of Dundee. An EOSD based bunch profile monitor at CTF3 of CERN has been developed and demonstrated [8, 9]. This monitor has a resolution of 1 ps and is suitable for characterizing bunches longer than 3.5 ps with an effective window of 16 ps. The system has a demonstrated single shot signal to noise ratio of 28:1 for a bunch with 0.17 nC charge, 6 ps duration and at a 2 mm offset. Recently, this technique was applied at the CALIFES beam line at CERN's CTF3 facility.

In the measurement the background signal is eliminated by rotation of a λ/2 wave plate. This allows the absolute value of the Coulomb field to be determined and also for the polarity of the field to be observed. All measurements were taken at 0.3 nC bunch charge, 200 MeV beam energy and observed at 2 mm away from the bunches. A laser pulse centred at 780 nm, with 130 fs FWHM initial duration chirped to 13.8 ps FWHM was used. The nonlinear crystal is 4 mm thickness ZnTe.

As can be seen from Fig. 2 there is a small bump following the main peak between 20-30 ps. This bump can be easily mistaken as a bunch structure in the tail within one electron bunch for the crossed polarization detection.

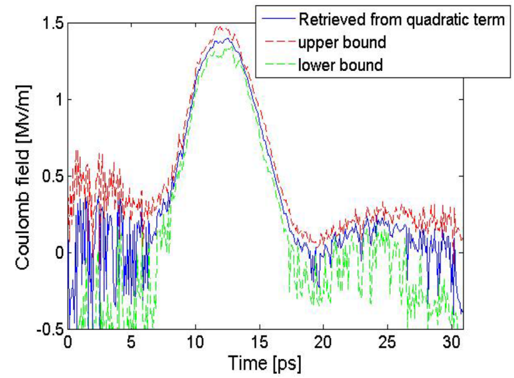

Figure 2: Retrieved Coulomb field from the quadratic term, the 95% confidence intervals determined bounds are shown in red (upper) and green (lower).

However, this bump comes from the negative part of the retrieved Coulomb field, since the cross polarization detection measures the Coulomb field square and represents a measurement of the wakefield of the bunch. The developed analysis techniques and the measured signal-noise characteristics are expected to be of use in the evaluation of the full potential for EO-based beam profile monitors [10].

Beam Characterization using Laser Self-Mixing

The increasing importance of supersonic gas jets for applications at accelerators [11, 12] means that their detailed characterization becomes very important. A sensor that can provide information about the jet's velocity, density and temperature in a least-destructive way would thus be an ideal tool to have. Laser self-mixing (SM) has been investigated as a simple to integrate, compact and cheap device for such purposes by Fellow A. Alexandrova, based at the Cockcroft Institute/University of Liverpool [13].

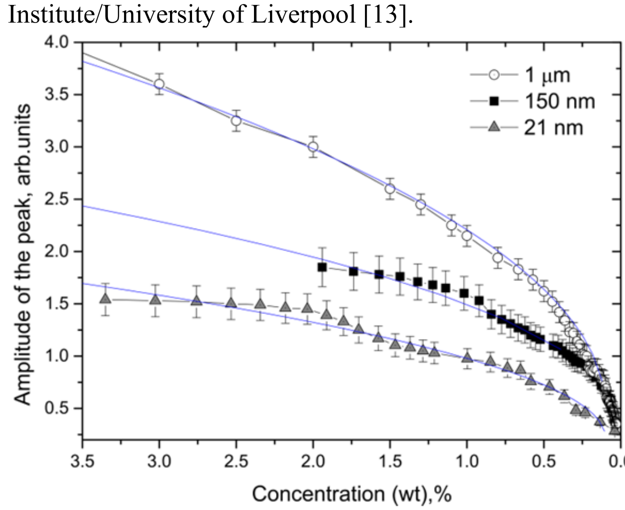

Figure 3: Measured influence of the concentration of TiO_2 seeders in water on the spectrum of the SM signal. Seeder diameter is indicated by different markers.

Laser self-mixing is based on the coupling of laser light reflected or scattered off a moving target back into the cavity. The backscattered light will have experienced a wavelength shift as a result of the Doppler effect. Its

ISBN 978-3-95450-176-2

intensity depends on the detailed characteristics of the target, including velocity, density, optical properties, etc. The interaction between emitted and incoming signal will create a signal determined by a number of important target properties that can be directly derived. Direct measurements on a gas jet traveling at velocities of up to 2,000 m/s, however, are very demanding and hence investigations were started using liquids in combination with different seeder particles [14].

The concentration of the seeders is responsible for the amount of light being backscattered into the cavity. Varying concentrations of different seeder sizes have been studied to understand the influence on both the amplitude of the spectrum peak and its bandwidth. Figure 3 shows the measured amplitude of the peak signal as a function of seeder concentration and for different seeder sizes. The amplitude was averaged over 100 measurements. It can be seen that the overall trend of all plots is identical, irrespective of particle size, but that the amplitude can be changed using different seeders. Future studies will focus on the efficient seeding of gases and extension of the method to even higher velocities.

A Laserwire Emittance Scanner for LINAC4

Photo-detachment of electrons in an H^- ion beam provides an interesting way of non-invasive, reliable and maintenance-free diagnostics [15, 16]. Since the reduction of accelerator downtime is a major target for any accelerator and in particular for high current accelerators this technique can help to maximize machine efficiency. T. Hofmann who is based at CERN has successfully applied this technique at the new LINAC4 facility [17, 18]. He used a 1080 nm laser with 154 µJ pulse energy, 80 ns pulse length (FWHM), 60 kHz repetition frequency and an M^2 of 1.8. Due to its comparatively low pulse energy, the laser can be efficiently delivered to the accelerator by means of a long optical fiber. The laser is focused into the vacuum vessel with a final diameter of approximately 150 µm. Due to the quasi-monomode beam quality the laser diameter remains almost constant when colliding with the millimeter-size particle beam. Vertical scanning of the laser is performed by a remote controlled stage. A CCD camera and a fast photodiode are used to continuously monitor the laser beam quality. To detect the neutralized H^0 atoms a 20 mm x 20 mm polycrystalline diamond detector with 5 strip channels was used.

Figure 4 shows the resulting emittance values, measured with both a laser-diamond detector system, as well as with a 'classic' slit/grid reference system as a function of the applied threshold.

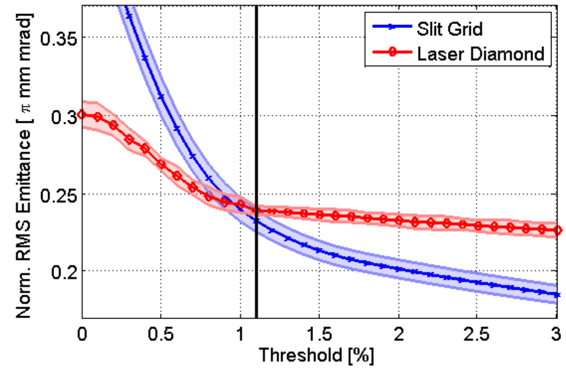

Figure 4: Normalized emittance value resulting from both instruments as a function of threshold used for noise suppression.

The characteristic kink in this curve marks the spot where the noise is largely suppressed and the sampled signal starts to originate from impinging particles. It can be seen that for the laserwire system this point is quite well-defined at 1.1%. The equivalent position for the slit/grid is not so clearly defined but can be marked down in the same region. Assuming the same threshold of 1.1% for both systems the resulting emittance values are 0.232 π mm·mrad for the slit/grid system and 0.239 π mm·mrad for the laserwire. SD represents the uncertainty of the emittance measurements at intervals along the LINAC4 pulse.

It is planned to use a modified version of the instrument during LINAC4 commissioning at 50 MeV and 100 MeV with the aim to measure the detached electrons and reconstruct the beam profile in a non-invasive manner [19]. In preparation for permanent operation the electrode design of the diamond detector and its data acquisition readout chain are in the process of being re-designed to provide even higher angular resolution and faster emittance measurements. Furthermore, it is foreseen to modify the system such that scans in horizontal and vertical planes will be possible.

Energy Measurement using Compton Backscattering at ANKA

Compton Back-Scattering (CBS) has some significant advantages for non-invasive beam energy measurements as compared to other techniques such as spin depolarization, reduced measurement times and that a polarized beam is not required. Several facilities have reported energy measurements based on CBS using a head-on collision geometry with relative accuracies reaching 10^{-4} to a few 10^{-5} [20, 21]. LA³NET Fellow C. Chang who is based at KIT and his co-workers have developed a CBS geometry that applies a transverse configuration ($\varphi=\pi/2$). This setup has several advantages: It is very compact and can therefore be used at rings with restricted space. Furthermore, the transverse setup reduces the energy of Compton edge photons by a factor of two which either makes measurements and detector calibration easier or enlarges the measurable range of a

ISBN 978-3-95450-176-2

specific setup. They have used a High Purity Germanium (HPGe) spectrometer to determine the energy of the emitted photons [22]. Fig. 5 shows a typical spectrum that was acquired from a 1.3 GeV electron beam over 120 seconds. The mechanical centers of two quadrupoles were used as the reference line and the laser direction measured relative to this line with a laser tracker and a camera.

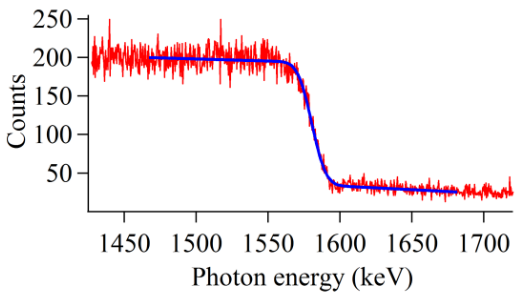

Figure 5: Measured CBS spectrum at 1.3 GeV with fit to determine the Compton edge energy.

The collision angle φ was determined from this measurement and yielded an average value of the beam energy of 1287.0 MeV ± 0.2 MeV. As compared to conventional CBS methods for energy measurement, a compact setup based on a transverse scheme has been successfully tested at ANKA. These measurements have been extended to beam energies of 0.5 GeV, 1.6 GeV and 2.5 GeV and gave promising initial results. It was shown that longer acquisition times can help further reduce statistical uncertainties in the Compton edge and hence beam energy. This might give access to measurements uncertainties to below a few 10^{-5} in the future.

TRAINING EVENTS

The primary training that all Fellows receive is training through their individual research projects. This is complemented by local courses and lecture series that are provided by their host institute or partner university. In addition, a series of network-wide training events has been organized by the consortium. These have brought all Fellows together on a regular basis training them in aspects that significantly stretch beyond their core research projects, thus maximizing their skills and increasing employability.

International Schools

A first international school on laser applications was held at GANIL, France in 2012 [23]. 80 participants from within and outside the LA³NET Consortium were introduced to the state of the art in this dynamic research area. The five day event followed the successful format pioneered earlier in the DITANET project. Renowned lecturers covered topics such as introduction to lasers and accelerators, beam shaping, laser ion sources, laser acceleration, laser based beam diagnostics and industrial applications. In addition to the lectures there were study groups, poster sessions and two evening seminars on major international initiatives in the laser and light sources field. All newly recruited LA³NET fellows joined this school and benefited not only from the excellent lectures, but also from discussions with participants from the wider community.

Between 29 September and 3 October 2014 the consortium held an Advanced School on Laser Applications at Accelerators. This event was hosted by the Spanish Pulsed Lasers Centre (CLPU) in Salamanca, Spain and attracted over 70 participants from all over the world [24]. It started with lectures about an introduction to lasers, the history of accelerator development in Europe, accelerator applications, as well as beam generation, acceleration and diagnostics. Day two included lectures on laser ion sources, photo injectors and Free Electron Lasers (FELs), in addition to a two-hour study session giving delegates a chance for a hands-on look at some of the topics covered. The following days covered more advanced topics in ion and electron acceleration, commonly used simulation codes for accelerator design and optimization, as well as industry applications of accelerators and lasers. Both Schools stimulated many fruitful discussions. In addition, the network has organized two researcher skills schools for all Fellows, covering wider skills, such as presentation, scientific writing, project management and CV writing in the first and final year of the project. The training scheme that was developed for the network's Fellows was specifically praised by a number of bodies, including the REA, HEA and UKRO and has since been implemented for many additional student cohorts at partner universities.

Topical Workshops

In order to stimulate knowledge exchange and help the Fellows in building up an international contact network LA³NET has organized a number of targeted scientific workshops at venues across Europe. These lasted 2-3 days and focused on expert topics within the network's scientific work packages. Fellows were given the opportunity to give talks about their individual projects and invited research leaders complemented the program of each event.

The first Topical Workshop covered laser based particle sources and was held at CERN in February 2013 [25]. It covered photocathodes for the production of high brightness electron beams, RF and DC photo injectors, hot cavity and gas cell ion sources for radioactive ion beam facilities, laser systems for efficient resonance ionization, as well as in-source spectroscopy of rare nuclides. A second workshop on laser technology and applications was hosted by the ILT in Aachen in 2013 [26] and included session on optics and laser design. The third workshop focused on novel acceleration techniques and was held in Dresden in 2014 [27]. It covered laser and particle beam plasma wakefield acceleration, as well as dielectric laser acceleration. A "Scientists Go Industry" workshop hosted by the Helmholtz Association in Berlin provided the Fellows and external delegates with an insight into the full range of job opportunities available for them outside of academia [28]. Finally, a Workshop

ISBN 978-3-95450-176-2

on Beam Diagnostics was held in 2015 on Mallorca and included presentations about the state of the art in optical diagnostics, beam profile and emittance measurements and the use of optical techniques for ultra-short bunch diagnostics. On the second day longitudinal measurements of ultra-short Bunches, novel sensors and technologies and advanced diagnostics technologies were covered [29].

Conference on Laser Applications and Outreach Symposium

In March 2015 the network held a Conference on Laser Applications at Accelerators on Mallorca, Spain [30]. Following an introductory overview, methods for particle beam generation including laser ion sources and photoinjectors were presented. In the afternoon laser-based ion acceleration and dielectric laser acceleration were the focus as two examples of novel acceleration techniques with demonstrated performance gains. The conference also included sessions on electron acceleration and industrial applications including a seminar about the new Extreme Light Infrastructure (ELI). Finally, beam diagnostics methods were covered, linking to the efforts in the other work packages and indicating how existing and future facilities can be further optimized.

As the final project event an international Symposium on Lasers and Accelerators for Science & Society took place on the 26th of June in the Liverpool Arena Convention Centre. The event was a sell out with delegates comprising 100 researchers from across Europe and 150 local A-level students and teachers. The aim was to inspire youngsters about science and the application of lasers and accelerators in particular. All presentations are now available as an online resource, including videos of the talks that were given [31]. The Symposium also showcased the LA³NET projects through an interactive poster session with Q&A, giving young people the opportunity to see how scientists just a few years older than themselves are pushing back the boundaries of knowledge.

CONCLUSION AND OUTLOOK

Over the past four years, the LA³NET consortium has successfully trained 19 researchers and organized a large number of scientific events for the laser and accelerator communities. The network has established new training schemes that promote international collaboration. This paper described the progress made in the beam diagnostics work package and the results obtained by the project's Fellows.

In its last meeting the LA³NET Steering Committee decided to continue promoting the activities of the network's Fellows beyond the original project duration via various communication channels and to also continue organizing events for the wider research community. Details will be announced via the network's social media channels, website and quarterly newsletter.

REFERENCES

[1] http://www.la3net.eu
[2] http://www.liv.ac.uk/ditanet
[3] M. Nasse et al., Rev. Sci. Instrum. 84, 022705, (2013)
[4] B. Steffen et al., FEL 2005, THPP039.
[5] G. Berdenet al., Phys. Rev. Lett. 93, 114802, (2004).
[6] A. Borysenko et al., IPAC 2014, THPME123.
[7] A. Borysenko, et al., Phys. Proc. (2015), *submitted*.
[8] R. Pan, et al., "Synchronization scheme of a bunch profile monitor based on electro-optic spectral decoding", Proc. BIW, Newport News, USA (2012).
[9] R. Pan, et al., "Electro-optical bunch profile measurement at CTF3", Proc. IPAC, Shanghai, China (2013).
[10] E. Pan, et al., "Coulomb field strength measurement by electro-optic spectral decoding system at CALIFES beam line", Phys. Proc. (2015), *submitted*.
[11] V. Tzoganis et al., "A non-invasive beam profile monitor for charged particle beams." Applied Physics Letters, 104-20, p 204104 (2014).
[12] Yu. Kudryavtsev et al., "The in-gas-jet laser ion source: Resonance ionization spectroscopy of radioactive atoms in supersonic gas jets." Nucl. Instrum. Meth. B 297, p 7-22 (2013).
[13] A. S. Alexandrova et al., "Laser diode self-mixing interferometry for velocity measurements." Optical Engineering, 54.3, p 034104 (2015).
[14] A. S. Alexandrova et al., "Beam Characterisation using laser self-mixing", Proc. IBIC, Melbourne, Australia (2015).
[15] W. B. Cottingame et al. "Non-interceptive techniques for the measurement of longitudinal parameters for intense H-beams." IEEE NS-32, 1985.
[16] Y. Liu et al, "Laser wire beam profile monitor in the spallation neutron source (SNS) superconducting linac", Nucl. Instr. and Meth. A 612, 241, (2010).
[17] T. Hofmann et al, "Laser based stripping system for measurements of the transverse emittance of H− beam at the CERN LINAC4" MOPME075, Proceedings of IPAC2013, Shanghai, China
[18] T. Hofmann, et al., "Experimental results of the laserwire emittance scanner for LINAC4 at CERN", Phys. Proc. (2015), submitted.
[19] T. HOfmann, et al., "Design of a Laser Based Profile-Meter for LINAC4 Commissioning at 50 Mev", Proc. IBIC, Melbourne, Australia (2015).
[20] R. Klein et al., Nucl. Instrum. Methods Phys. Res., Sect. A 384, 293 (1997).
[21] C. Sun et al., Phys. Rev. ST Accel. Beams 12, 062801 (2009).
[22] C. Chang, et al., "First results of energy measurements with a compact Compton backscattering setup at ANKA", Proc. IPAC, Richmond, USA (2015).
[23] indico.cern.ch/conferenceDisplay.py?confId=177701
[24] indico.cern.ch/conferenceDisplay.py?confId=285698
[25] indico.cern.ch/conferenceDisplay.py?confId=212365
[26] indico.cern.ch/conferenceDisplay.py?confId=266133
[27] indico.cern.ch/conferenceDisplay.py?confId=285723
[28] indico.cern.ch/conferenceDisplay.py?confId=318719
[29] indico.cern.ch/conferenceDisplay.py?confId=340153
[30] indico.cern.ch/conferenceDisplay.py?confId=340153
[31] indico.cern.ch/conferenceDisplay.py?confId=368273

ISBN 978-3-95450-176-2

ADVANCED BEAM DIAGNOSTICS R&D WITHIN oPAC

C.P. Welsch#
Cockcroft Institute and the University of Liverpool, UK

Abstract

oPAC 'Optimization of Particle Accelerators' is a European research and training network that has received funding within the EU's 7th Framework Program. With a total budget of 6 M€ and 23 Fellows that are employed within the project, it is the largest Marie Curie network that was ever funded by the European Union. oPAC was started in 2011 and would usually come to an end at the end of 2015.

The network currently joins more than 30 partner institutions from all around the world, including research centers, universities and the private sector. One of the project's largest work packages addresses advanced R&D in beam diagnostics. This includes studies into advanced instrumentation for synchrotron light sources and medical accelerators, enhanced beam loss monitoring technologies, ultra-low emittance beam size diagnostics, beam diagnostics for high intensity beams, as well as the development of compact electronics for beam position monitors.

This paper presents the research outcomes of the diagnostics work package and discusses the demonstrated performance of each monitor. A summary of the various events the network has organized for the accelerator community is also given together with an outlook on future opportunities.

INTRODUCTION

An efficient optimization of particle accelerators and light sources requires close collaboration between beam dynamics experts, instrumentation specialists, along with powerful accelerator and electromagnetic field simulations tools. The oPAC network covers all these aspects in its different scientific work packages [1]. The project's Fellows carry out a broad yet closely interconnected R&D program in all these areas. The consortium consists of partners from industry, universities, as well as national and international research centers, such as ALBA, GSI and CERN. Selected associated and adjunct partners contribute to the research activities and complement the network's training program. The primary goals of oPAC are to provide the best possible training to its Fellows thus maximizing their career opportunities, as well as advancing knowledge through a cutting edge research program.

*This project has received funding from the European Union's Seventh Framework Programme for research, technological development and demonstration under grant agreement no 289485.

#c.p.welsch@liverpool.ac.uk

BEAM DIAGNOSTICS R&D

A versatile beam diagnostics system is crucial for the successful operation and optimization of any particle accelerator or light source. Between 2011-2015 the DITANET consortium [2] set out to define improved training standards in this research area and the development of advanced beam diagnostics is also a key aspect in the oPAC project. Here, a summary of results from Fellows in beam diagnostics R&D is given.

Cavity BPM Electronics

In the last few years the number of projects and applications requiring sub-micrometer resolution for their beam position monitoring systems has increased dramatically. This trend is mainly driven by an increasing number of Free Electron Laser (FEL) projects and by specific applications such as inverse Compton scattering where the high resolution is required in the beam-laser interaction region. Depending on the characteristics of the beam, different cavities and resonant frequencies are used, ranging from single-bunch applications in high-Q cavities to low-Q for long bunch train cavities.

Because of the increased demand in these systems, the requirements for the readout electronics have been collected and extensive simulations run for different scenarios by oPAC Fellow Manuel Cargnelutti, based at Instrumentation Technologies. The idea is to develop a system flexible enough to deliver excellent performance over a broad range of cavities. The compact hard-/software platform on which this instrument will be developed is already in use for other applications [3,4], but several changes will now be introduced in the RF front-end: (1) Down-conversion: A PLL locked to an external reference is used to down-convert the cavity input signal from the cavity resonant frequency to a given intermediate value. (2) Variable attenuators: These are used to adjust the cavity input signal level to the ADC full-scale to maximize the signal-to-noise ratio. (3) ADC: The sampling rate is increased to 500 MS/s. This enables bunch-by-bunch position measurements for low-Q cavities, as well as bunch-train applications. The data acquired is processed by an FPGA of the Xilinx ZYNQ 7045 system-on-chip. Here, a special deconvolution filter and a parametrized time-domain processing of the input signal pulses enable to deliver the beam position for every electron bunch and with sub-micrometer resolution. Fig. 1 presents the simulation of the system position resolution where the internal attenuators setting is parametrized. The cavity used as reference for these simulations is the model BPM16 from the SwissFEL project [5].

ISBN 978-3-95450-176-2

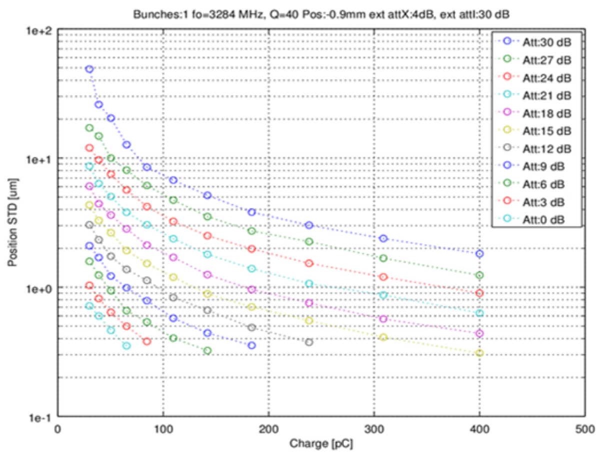

Figure 1: Position resolution for a single-bunch e⁻ beam.

The project is currently in the high-level design phase. During this phase, a complete set of requirements is being collected to ensure that as many as possible use-cases are covered. Based on feedback from users the design will then be finalized and the implementation phase started.

Position Detection for Ultra-Low Intensity Heavy-Ion Beams

The Collector Ring (CR) at the Facility for Antiproton and Ion Research (FAIR) will mainly be used for collecting and pre-cooling high-intensity radioactive ion beams and antiprotons. It can also be used for isochronous mass spectrometry for neutron-rich or neutron-deficient exotic nuclei when it is tuned to a special ion-optical setting. The ultra-low intensity of these beams then imposes stringent sensitivity requirement on beam detection techniques. An RF cavity as a Schottky noise detector has proven to be an extremely sensitive beam diagnostic device with its ability to detect even single ions [6]. As an upgrade of the existing Schottky resonator installed in the Experimental Storage Ring (ESR) a position-resolving cavity has been proposed for the CR. This cavity, together with the intensity-sensitive one, will be able to distinguish the revolution orbits of stored ions for nuclear mass measurements. The measured positions will be used as a key input for subsequent analyses to correct for the anisochronism effect in the measurement and help improve the accuracy and precision of the evaluated atomic masses [7]. In contrast to a conventional cavity-based BPM the present design offsets the beam pipe to a side of the cavity and utilizes the resonant monopole mode [8]. Consequently, the shunt impedance, which is a measure of the coupling strength between the cavity and the beam exhibits an inclined trend over the aperture around a fairly high mean value. Having normalized the signal to a reference from the intensity cavity the position can be deduced by means of magnitude discrimination. In order to enhance the intensity sensitivity and position resolution of the cavity much effort has been devoted to the optimization of the cavity geometry so as to attain adequate mean value and slope of the shunt impedance. oPAC Fellow Xiangcheng Chen, based at GSI, carried out analytic and numerical studies into the design. First, the electric field inside the cavity was solved for a rectangular box and elliptic cylinder. The optimum dimensions were then selected in accordance with the experimental requirements. Second, an electromagnetic field solver was used to investigate changes in resonant frequency and shunt impedance taking into account realistic values for beam pipe and plunger. In order to verify the design two scaled prototypes have been manufactured and tested by Chen on a purpose-built benchtop. The electric fields inside the prototypes were measured by perturbation with a ceramic bead. The latter was held by a cotton thread while the cavity was moved by a motorized displacement unit. The resonant frequency was obtained from transmission measurements using a vector network analyzer. A dedicated Java application coordinates the movement-measurement cycle. In order to account for any temperature drift a reference measurement was taken before each perturbation measurement. The entire profiling process takes 5 hours and is fully automated. As an example the measured shunt impedance of the rectangular prototype is shown in Fig. 2. It is in very good agreement with the associated simulation studies.

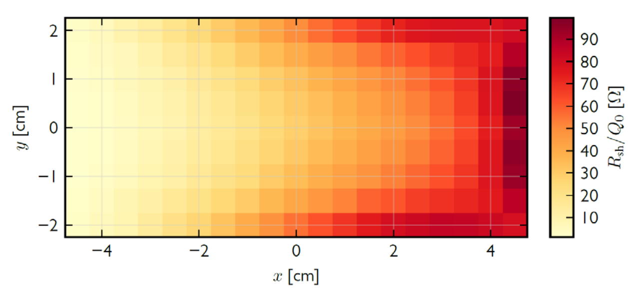

Figure 2: Measured shunt impedance of the rectangular Schottky monitor prototype.

Beam Profile Monitors for High Intensity Beams

The European Spallation Source (ESS) [9], currently under construction, consists of a partly superconducting linac which will deliver a 2 GeV, 5 MW proton beam to a rotating tungsten target. Two different types of devices are currently been designed for the ESS linac to monitor the beam profile, an invasive and a non-invasive one, which will both be located in the same module. The invasive device will be a wire scanner and will be used during the commissioning at low beam current and short pulse. Because this invasive system would get damaged by the beam under nominal conditions the development of an additional non-invasive device became necessary.

The Non-invasive Profile Monitor (NPM) chosen for ESS are based on the interaction of the beam with the residual gas. Two different devices are being developed by Charlotte Roose and colleagues to meet the ESS

ISBN 978-3-95450-176-2

constraints: a Beam Induced Fluorescence monitor (BIF) [10] and an Ionization Profile Monitor (IPM) [11]. The BIF monitor is based on the fluorescence emission of the excited residual gas. In the warm linac, the main constraint is the 10 cm available space for the NPM. This compact monitor is a good answer to that issue as both horizontal and vertical profile measurements can be performed at the same place. Furthermore, its design is rather simple and can be easily changed since all the device components, except for the beam pipe viewport, are outside the beam pipe.

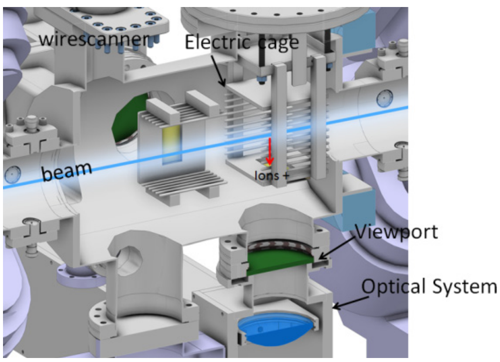

Figure 3: ESS IPM - current model.

The IPM uses charged particles produced during the interaction of the beam with the residual gas to obtain the profile. Fig. 3 shows the current model of the ESS IPM. The electric field created by the IPM cage has two purposes: First, it guides secondary ions to a screen. Second, it decreases the space charge effect [12] of the beam which would otherwise disturb the ion trajectories and hence distort the profile. Due to the anticipated high dose rate in the cold linac a scintillator screen is used to collect the secondary ions. This is then imaged by a conventional camera system placed outside the vacuum.

Cryogenic Beam Loss Monitors

Beam Loss Monitors (BLMs) close to the interaction points of the Large Hadron Collider (LHC) are currently located outside the cryostat, far from the superconducting (SC) coils of the magnets. In addition to their sensitivity to lost beam particles they also detect particles coming from the experimental collisions which do not contribute significantly to the heat deposition in the SC coils. In the future, with beams of higher energy and brightness resulting in higher luminosity, distinguishing between these interaction products and dangerous quench-provoking beam losses from the primary proton beams will be challenging. The system can be optimized by locating BLMs as close as possible to the SC coils, inside the cold mass in a superfluid helium environment at 1.9 K. The dose then measured by cryogenic BLMs would more precisely correspond to the real dose deposited in the coil. The candidates under investigation for such detectors are based on p+-n-n+ silicon and single crystal Chemical Vapour Deposition (scCVD) diamond, of which several have now been mounted on the outside of the cold mass of the SC coil in the cryostat of the LHC magnets. The cryogenic BLM specifications represent a completely new and demanding set of criteria that have never been investigated in such a form before. A certain knowledge about radiation hardness of particle detectors is available for the temperature of outer space (2.7 K), i.e. from the requirements of space-based experiments, but little is known for detectors below this temperature. The main unknown was the combination of the cold environment with a total ionizing radiation dose of 2 MGy. This is why the first radiation-hardness test of the diamond and the silicon detectors in liquid helium environment were recently performed at CERN.

The main aim of the cryogenic irradiation test was to investigate the radiation hardness of ionizing radiation detectors in liquid helium at 1.9 K. After careful preparations, the irradiation experiment was performed in the IRRAD facility at CERN. At the end of the cryogenic irradiation a total integrated fluence of $1.22 \cdot 10^{16}$ protons/cm^2 was reached, corresponding to an integrated dose of about 3.26 MGy for the silicon and 3.42 MGy for the diamond detectors.

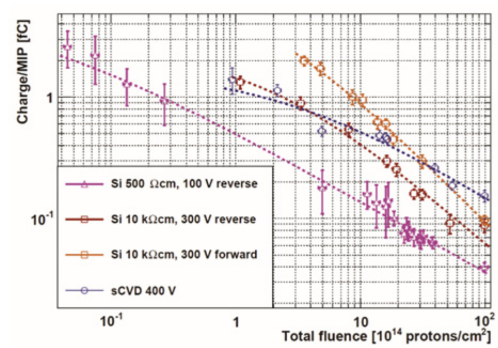

Figure 4: Degradation curves of scCVD diamond detector at 400 V compared with a 10 kΩcm silicon detector at 300 V and 500 Ωcm silicon at 100 V reverse as reference curve (courtesy of C. Kurfuerst).

It can be seen that the silicon has a larger signal than the diamond at the beginning of irradiation, but the situation changes rapidly, see Fig. 4. The reduction in signal corresponding to 20 years of LHC operation (2 MGy) is of a factor of 52 ± 11 for the silicon device at 300 V and of a factor of 14 ± 3 for the diamond detector at 400 V. As a safety critical system, the long term stability of the BLM is a high priority criterion. During Long Shut-down 1 of the LHC four cryogenic radiation detectors were mounted on the outside of the cold mass containing the SC coils in the cryostat of two LHC dipole magnets. These four detectors consisted of one 500 µm scCVD diamond detector, one 100 µm silicon detector and two 300 µm silicon detectors. Once the interconnection between the two magnets where the detectors were located was closed and the cryostat was under vacuum a Current-Voltage (IV) curve measurement of the detectors was performed [13]. The results show that the leakage current is at a reasonably low level which should allow

ISBN 978-3-95450-176-2

the measurement of beam losses with a high signal to noise ratio. These first cryogenic radiation detectors installed in operational SC magnets will not only allow the behavior of the detectors to be tested under realistic conditions, but also determine the validity of the integration in a setup at 1.9 K, in a magnetic field and under vacuum. First results with beam are expected in September 2015.

Beam Size Measurements at ALBA using Interferometry

Synchrotron radiation interferometry is now a reliable method to measure the horizontal and vertical beam size at the ALBA storage ring in Barcelona, Spain. The technique, developed by T. Mitsuhashi, allows determining the beam size by measuring the visibility of the interferogram, obtained by making the visible part of the synchrotron radiation interfere using a double slit interferometer. Due to the layout of the ALBA diagnostic beam line Xanadu interferometry measurements were not completely straight forward. Fellow Laura Torino introduced several enhancements to the existing set-up to overcome existing limitations, in particular: The light selected by a photon shutter cuts the light horizontally whilst the first extraction mirror selects only the upper lobe of the produced radiation. This generates a final footprint that is dominated by Fraunhofer diffraction. The use of a double slit system allows the selection of several different fringes of the footprint. Fringes generated by Fraunhofer diffraction don't have necessarily the same phase. This might provoke a loss of contrast affecting the visibility measurements. To reduce this effect the slits were substituted by pinholes to select a more compact region of the footprint and consequently, a reduced number of fringes. Furthermore, the 7 mirrors guiding the light up to the Xanadu optical table are "in-air". The air turbulence in the tunnel or in the beam line can provoke vibrations of the optical elements that are converted in a rigid displacement of the centroid of the interferogram image on the CCD sensor.

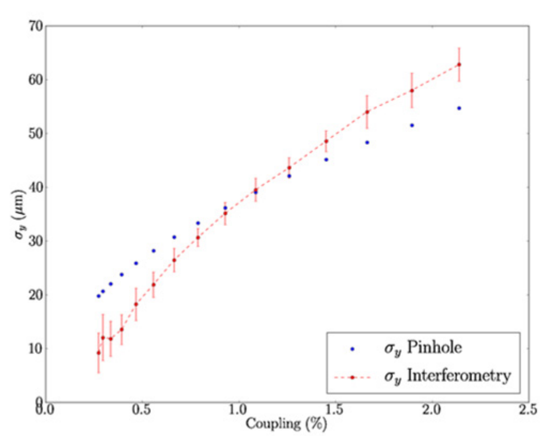

Figure 5: Vertical beam size measurements σ_y from the pinhole (blue) and the interferometer (red).

The incoherent sum of artificially displaced images also produces a loss of contrast in the visibility measurements. Reducing the CCD exposure time is an intuitive and efficient way to solve this problem, but also causes a reduction in intensity of the image which leads to an impossibility in the visibility measure, due to the reduced dynamic range of the CCD camera. To overcome this problem a matching algorithm was developed to superimpose low exposure time images (0.1 ms) and improve the contrast and the dynamic range of the interferogram. The reliability of these measurements, both for horizontal and vertical beam size, was verified in several ways. It was possible to study depth of field effects on the horizontal beam size by performing measurements for different distances between the pinholes. In addition, the effectiveness of vertical beam size measurements was verified by performing so-called coupling scans: By changing the emittance coupling using skew magnets the vertical beam size also varies. The results obtained with the interferometer follows the ones obtained with the x-ray pinhole. The x-rays used for pinhole measurements, and the visible light for the interferometry come from two consecutive bending magnets at slightly different locations. For this reason the measurements do not exactly coincide, but the trend is nicely confirmed, as shown in Fig. 5. Further details are given in [14].

TRAINING EVENTS

Training within oPAC is provided locally by the host institute, primarily through cutting edge research, specialized lectures and seminars, as well as network-wide training offered by the whole consortium. In addition, oPAC has organized a series of Topical Workshops and Schools for its Fellows which were also open to the wider accelerator community.

International Schools

At the start of their training all oPAC Fellows participated in either the established CERN Accelerator School or the Joint Universities Accelerator School. This provided them a sound training basis as they took on their projects within the Network. Both Schools included lectures and tutorials covering accelerator physics, relativity and electro-magnetism, particle optics, longitudinal and transverse beam dynamics, synchrotron radiation, linear accelerators, cyclotrons and general accelerator design. An oPAC School on Accelerator Optimization was then organized by the consortium between 7th-11th July 2014 at Royal Holloway University of London, UK. It covered advanced techniques for the optimization of particle accelerator performance - in particular the combination of different fundamental techniques to push the limits of accelerators ever further.

All Fellows initially met for a dedicated researcher skills School in Liverpool, UK in June 2013. During the week-long School they were provided with subject-specific training in addition to generic topics, including

ISBN 978-3-95450-176-2

project management, scientific writing, problem solving techniques and building bridges between academia and industry. The Fellows were asked to present a short summary of their projects as part of presentation skills training and also to develop a detailed project plan of their oPAC projects. Towards the end of their projects all Fellows followed a 4-day advanced researcher skills workshop which brought them again to Liverpool. The transition to permanent employment from postgraduate research is a challenging prospect in an ever more competitive job market. The workshop provided dedicated and practical support to help the Fellows in their future careers. External and internal trainers provided an extremely broad training throughout the week. This included support in career planning by providing practical and specific advice on CV writing and interview skills, writing competitive grant applications and science communication and networking. The university's business gateway team and Dr. Marco Palumbo, IPS Fellow in the physics department, contributed dedicated sessions on intellectual property rights, commercialization and entrepreneurship that were very positively received by the course participants.

Topical Workshops

oPAC also organized a whole series of Topical Workshops. This included expert training days on 'Simulation Tools' (CST, Germany) and 'Beam Diagnostics' (Bergoz, France), a 2-day Topical Workshop on the Grand Challenges in Accelerator Optimization at CERN, Switzerland on June $27^{th}/28^{th}$ 2013 [15], a workshop on Beam Diagnostics hosted by CIVIDEC [16] and one on Libera Technology at Instrumentation Technologies. Most recently, a workshop on Computer-Aided Optimization of Accelerators (CAoPAC) was held at the GSI Centre for Heavy Ion Research in Darmstadt, Germany from 10 – 13 March 2015 [17]. This was a special event for the network as it was organized by the Fellows of the network, providing them with the opportunity to take charge of a whole event from scratch, with a limited time-frame, limited resources, and the challenge of offering an interesting event to attract a good number of participants.

Accelerator Symposium and Conference on Accelerator Optimization

An international Symposium on Lasers and Accelerators for Science & Society took place on the 26th of June in the Liverpool Arena Convention Centre. The event was a sell out with delegates comprising 100 researchers from across Europe and 150 local A-level students and teachers. The aim was to inspire youngsters about science and the application of lasers and accelerators in particular. It is now possible to share the enthusiasm of the accelerator experts through online presentations [18]. Finally, the network will organize a 3-day international conference on accelerator optimization which will be hosted by CNA in Seville, Spain.

SUMMARY

An overview of the beam diagnostics R&D results within the oPAC project was given in this paper. The network has successfully trained 23 early stage researchers and achieved all of its scientific deliverables. The project's Steering Committee has recently decided that the network will continue to organize events for the accelerator community and disseminate research results from its Fellows. Despite the enormous success and impact that oPAC has had, there remains a considerable shortage of skilled accelerator experts to meet the demand of the most advanced accelerator-based research facilities. The consortium plans to propose additional training initiatives in the future to help overcome this problem.

REFERENCES

[1] http://www.opac-project.eu
[2] http://www.liv.ac.uk/ditanet
[3] G. Jug, M. Cargnelutti, B. K. Scheidt, "Development of Compact Electronics Dedicated to Beam Position Monitors in Injectors and Boosters", Proc. IBIC, Oxford, UK (2013).
[4] M. Znidarcic, E. Janezic, M. Cargnelutti, "Compact Single Pass BPM", Proc. IPAC, Richmond, USA (2015).
[5] B. Keil, "Cavity BPM Pickups for SwissFEL", DEELS Workshop 2014.
[6] F. Nolden, et al., "A fast and sensitive resonant Schottky pick-up for heavy ion storage rings". Nucl. Instrum. Meth. A 659 (2011) 69.
[7] X. Chen, et al., "Accuracy Improvement in the Isochronous Mass Measurement Using a Cavity Doublet." Hyperfine Interact., (in press, 2015).
[8] M.S. Sanjari, et al., "Conceptual Design of Elliptical Cavities for Intensity and Position Sensitive Beam Measurements in Storage Rings." Phys. Scr., (in press, 2015).
[9] S. Peggs et al., "ESS Technical Design Report", Lund, Sweden (2013).
[10] F. Becker, "Non-destructive Profile Measurement of Intensive Heavy Ion Beams", PhD Diss., Darmstadt, Germany (2010).
[11] T. Giacomini et al., "IPM@GSI", Proc. DIPAC2011, Hamburg, Germany (2011).
[12] C. Roose et al., "Methods for Measuring the Transverse Beam Profile in the ESS High Intensity Beam", Proc. IBIC, Monterey, USA (2014).
[13] M.R. Bartosik, et al., 'Cryogenic Beam Loss Monitors for the Superconducting Magnets of the LHC', Proc. IBIC, Melbourne, Australia (2015).
[14] L. Torino et al. "Limitations and Solutions of Beam Size Measurements via Interferometry at ALBA", Proc. IBIC, Melbourne, Australia (2015).
[15] indico.cern.ch/conferenceDisplay.py?confId=243336
[16] indico.cern.ch/conferenceDisplay.py?confId=293158
[17] indico.cern.ch/conferenceDisplay.py?confId=333414
[18] indico.cern.ch/conferenceDisplay.py?confId=368273
[19] indico.cern.ch/conferenceDisplay.py?confId=380975

ISBN 978-3-95450-176-2

FRIB MACHINE PROTECTION SYSTEM DESIGN AND VALIDATION STUDIES*

S.M. Lidia#, M. Ikegami, Z. Li, Z. Liu, T. Russo, R. Webber, Y. Zhang, Q. Zhao, Facility for Rare Isotope Beams, East Lansing, Michigan, USA 48824

Abstract

The FRIB heavy ion superconducting linac will become the highest peak power heavy ion beam facility, with beams carrying up to 400 kW power with kinetic energy ≥ 200 MeV/u. Fast protection systems are required to detect and remove beam within 35 μs. Detection of beam losses in the low energy linac segment is confounded by two effects: small fluxes of secondary radiation from beam impacts, and large fluxes due to cross-talk from neighboring, higher energy linac sections. We describe a machine protection scheme based on multiple families of diagnostics and diagnostic networks. On-going fault mode studies are utilized to assess risk and to assist in the definition of specific detection networks for high reliability and responsivity.

INTRODUCTION

The Facility for Rare Isotope Beams (FRIB) is a high-power, high-brightness, heavy ion facility under construction at Michigan State University under cooperative agreement with the US DOE [1]. The linac will accelerate ions to energies above 200 MeV/u, with up to 400 kW of beam power on target. The linac facility, shown in Fig. 1, consists of a Front End, three Linac Segments (LSs) connected by two Folding Segments (FSs), and a Beam Delivery System (BDS) leading to the production target. Ion sources are located on the ground level and beam from one of two ion sources is delivered to the linac tunnel through a vertical beam drop. An electrostatic chopper upstream of the vertical beam drop is the primary control of the time structure and duty cycle of the ion beam.

The FRIB linac is designed to support multiple operating modes with varying time structure and peak intensity of the ion beams. These modes can be grouped into four general categories:

- Short pulse (<5 – 50 μs), low duty cycle (< ~1 Hz), varying intensity (50 to 650 μA)
- Moderate pulse length (~0.01 s to s), low duty cycle (< ~1 Hz to 5% duty factor), nominal intensity (3 – 10 pμA)
- Approximately CW (50 μs gap @ 100 Hz), low to nominal intensity (<10 to 400 kW)
- Dynamic ramp to high power (variable intensity, pulse duration, and repetition rate) to slowly increase the target temperature (~10 minutes)

*This material is based upon work supported by the U.S. Department of Energy Office of Science under Cooperative Agreement DE-SC0000661, the State of Michigan and Michigan State University.
#lidia@frib.msu.edu

Several additional modes are used for commissioning the front end and fragment separator. These modes exhibit a wide range in intensity: 2–650 eμA for Front End commissioning, and 0.0001–30 pnA for fragment separator commissioning and secondary beam development.

MACHINE PROTECTION SYSTEM

Machine protection systems (MPS) exist to avoid prompt and long-term damage to the accelerator and experimental instrumentation, are required to minimize the number of false trips that limit production, and provide evidence of failures or fault events when interlock systems stop beam operation.

Machine failures can derive from several sources. Hardware failures can include power supply trips, magnet or cavity quench, RF trips and loss of low-level control, loss of vacuum, etc. Control system failures may include incorrect calibrations, improper updates of settings, timing distribution errors or mistimed triggers, and feedback malfunctions. Operator actions may introduce tuning and steering errors that generate errant beams.. Beam instabilities at high current or high brightness might develop quickly and damage components.

The time response for MPS interdiction ranges over many orders of magnitude. Fast protection systems (FPS) serve to protect against prompt damage from beam impacts. Typical FPS response times can vary from several to some hundreds of microseconds, and reflect thermodynamic changes of accelerator materials caused by errant beams. Run permit systems (RPS) operate on a slower time scale, from milliseconds to many seconds, and are used to verify machine state and identify conditions that may lead to unintended damage or long term irradiation effects that limit personnel access. As the FRIB accelerator facility may function in many different operating modes with varying thresholds for beam induced damage, the complete machine protection system must be flexible and configurable.

FRIB Challenges

The challenges for the FRIB MPS derive from multiple sources, including physics of the interaction of heavy ions with the vacuum chamber components and the proximity of high energy to low energy linacs The high power and brightness, and short (< mm) Bragg range of the FRIB heavy ion beam places critical importance on the fast protection system to detect and limit prompt beam losses [2]. The performance and lifetime of sensitive superconducting cavity surfaces can be affected by small losses (< 1 W/m) occurring over long durations.

ISBN 978-3-95450-176-2

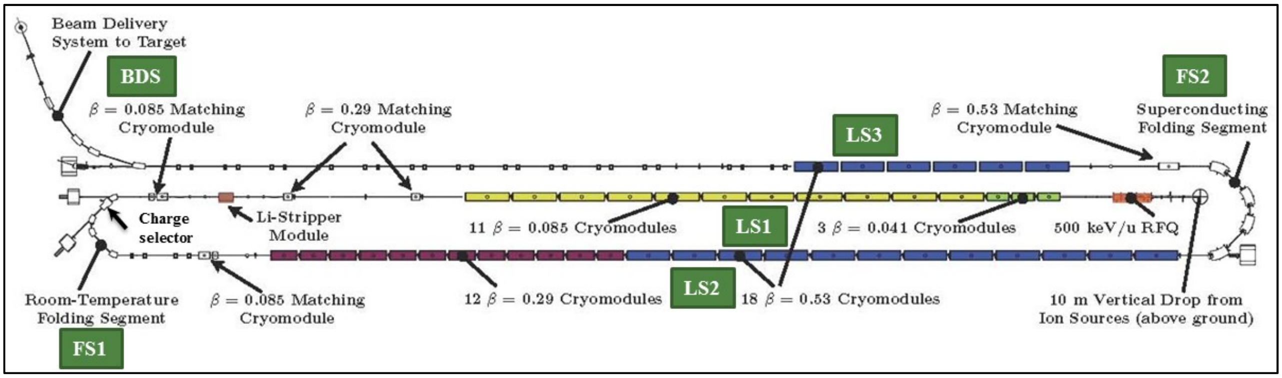

Figure 1: FRIB accelerator layout.

The twice-folded geometry of the FRIB linac places the high energy linac segment in close proximity to the low energy linac segment. Traditional loss monitors, eg. ionization chambers and scintillation-based neutron detectors, will be unable to differentiate the low-amplitude loss signals arising in LS1 from the high-amplitude signals generated in LS3 due to radiation cross-talk [3]. Additionally, x-ray background sources originating from field emission in the RF cavities might also overwhelm the relatively low-amplitude beam-generated signals in the low energy linac modules.

MPS Controls and Mitigation

The MPS network for detection and mitigation employs an optical fiber network to establish communication between an FPS Master and multiple Slave nodes, and the beam inhibit devices. The FPS Master queries and receives input from 7 chains of FPS Slave nodes every 8 µs. Each chain is composed of 8 Slave nodes. The input to each Slave node is a single RS-422 bit, which originates from beam or component monitoring systems.

The FPS Master activates the MPS interlock whenever the status bit changes from OK to NOK, as reported by the FPS Slave nodes or the RPS monitoring system. The time budget for activating the beam mitigation system is 10 µs from the first instance of a NOK signal from any Slave node. The primary beam inhibit is to initiate a fast (< 1 µs) HV switch to de-energize the electrostatic dipoles in the Low Energy Beam Transport section (see Fig. 2). Defense-in-depth requires a reach-back to the ion source HV platforms which terminate beam production. A secondary reach-back to the electrostatic chopper power supply can be used to direct beam to a local beam dump in the vacuum chamber.

BEAM LOSS DETECTION METHODS

Multiple overlapping and redundant systems will continuously monitor the state of individual beamline components and power supplies, control feedback, and beam sensing diagnostics.

The RPS (100 ms scale) continuously queries the machine state and controls permission to operate with beam.Fast loss detection methods are integrated with the FPS to terminate the beam within 35 µs. These schemes limit damage from acute beam loss by quickly activating the beam inhibit device. They require sensitivity for fast detection of large losses (~10% - 100%). Additionally, slow losses are detected and measured with high sensitivity over longer time scales (sec to hours) to prevent slow degradation of SRF system under small beam loss. FPS mitigation is activated once a loss threshold is exceeded.

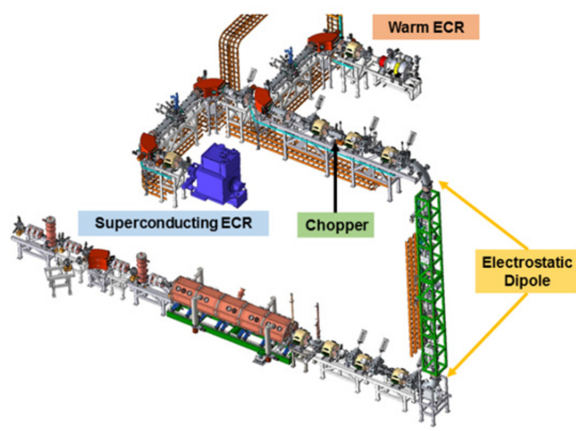

Figure 2: Front End beamline schematic.

Layering Strategy for Beam Loss Monitors

Beam diagnostics systems supplying inputs to the Machine Protection System offer a range of sensitivities and time responses to beam losses incurred along an accelerator chain. To mitigate risk and increase the probability of a robust detection scheme, a network of sensors is established. Redundant loss monitor systems for both fast and slow losses will be implemented. In many cases, the signals from the same physical monitor will be analyzed over multiple time scales with varying sensitivity.

The loss monitoring scheme for FRIB is shown in Table 1. Fast and slow loss detection methods are shown for each segment of the accelerator, and primary as well

ISBN 978-3-95450-176-2

as backup detection schemes are indicated. At low energy, the primary fast detection schemes are based on direct beam monitoring. Secondary radiation monitoring methods only come into play as the primary beam energy increases to a suitable production threshold. The slow loss schemes are based on time-averaging of signals as well as thermal monitoring in cryomodules.

Table 1: Beam Loss Monitor Network (DBCM – Differential Beam Current Monitor; HMR – Halo Monitor Ring; BLM – beam loss monitor; FTS – Fast Thermometry Sensor; Cryo – Cryogenic System Monitors)

		LS1	FS1	LS2 Low Energy	LS2 High Energy	FS2	LS3	BDS
Fast Loss	Primary	DBCM	DBCM	DBCM	DBCM	DBCM	DBCM	DBCM
< 35 µs	Secondary	HMR	HMR	HMR	BLM	BLM	BLM	BLM
	Tertiary				HMR	HMR	HMR	
Slow loss	Primary	HMR	HMR	HMR	BLM	BLM	BLM	BLM
> 100 ms	Secondary	FTS		FTS	HMR	HMR	HMR	
	Tertiary	Cryo		Cryo	Cryo		Cryo	

A multi-time scale signal processing scheme for the Halo Monitor Rings is shown in Fig. 3.

In Vacuum Monitors

The direct measurement of beam properties, on a suitably fast basis, can directly inform the machine protection system to cease beam production and to dump stored beam. Robust monitoring of beam current at the 1-10% level of the normal current on a fast time scale (several µs) is required to detect changes in the beam intensity that may require MPS interdiction. Beam position monitors, capacitive pickups, and current sensing interceptive devices near the limiting beam aperture can also provide reliable detection sensitivity. Modern FPGA electronics systems are gaining wide acceptance for fast and flexible beam loss detection and interface to MPS decision and control systems.

Differential Beam Current Monitoring

Differential beam current monitoring (DBCM) for MPS has been demonstrated at SNS using AC-coupled current transformers (ACCTs) [4]. ACCTs generally have higher frequency response than DC-coupled current transformers and so can better detect relatively fast changes in beam current (<10 µs). However, lacking DC response, an ACCT signal must be periodically re-baselined to define the 'no current' condition and additional signal conditioning is necessary to compensate for signal 'droop'. [5].

A network of 12 ACCTs will be deployed at FRIB to provide fast detection of beam losses throughout the linac segments and transport arcs. The individual ACCT beam current monitor (BCM) signals will be acquired, conditioned, digitized, and analysed with Struck 8300-L2 digital cards and Struck 8900 MTCA.4 RTM boards [6]. A single pair of boards will receive 4 BCM signals. A single MTCA.4 chassis will house the 3 pairs of boards, and provide a fast digital link to daisy chain the FPS status to the FPS slave node.

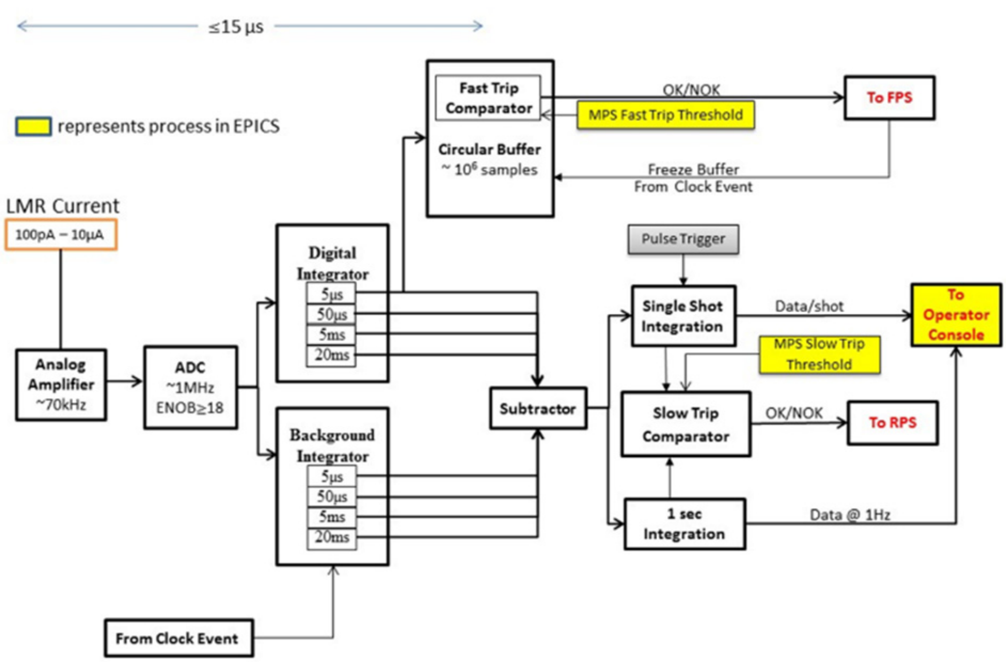

Figure 3: Halo ring signal processing scheme.

ISBN 978-3-95450-176-2

The halo monitor ring (HMR) was designed as a minimally interceptive device [3], with high sensitivity (~0.1 nA) to small losses and fast response (<10 µs) to large losses. The HMR is designed to be mounted within a diagnostic box between two cryomodules, with inner aperture that approximately matches the limiting beam aperture in the cryomodule. Tests of the loss ring sensitivity were performed at the National Superconducting Cyclotron Laboratory. The FRIB HMR design is shown in Fig. 4.

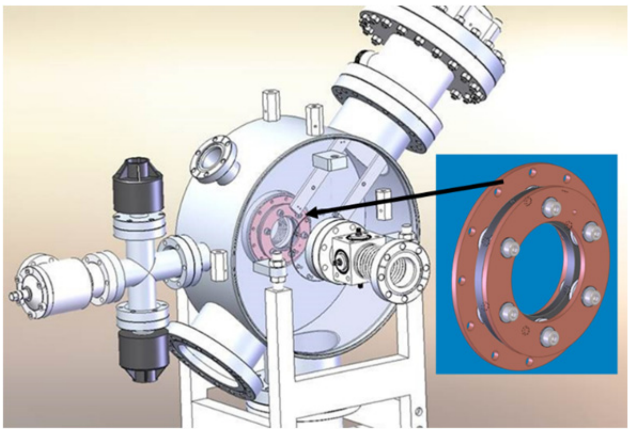

Figure 4: FRIB halo monitor ring implementation.

Secondary Radiation Monitoring

Beam loss monitors (BLMs) based on detection of radiation from primary beam losses will be used extensively. Sensitive, pressurized gas ionization chambers will be used in the warm transport areas and along LS3 for fast and slow monitoring. Scintillator based neutron monitoring will be used along LS2 and LS3 for overall background radiation monitoring. During commissioning, they will be deployed along LS1 for fast and slow loss monitoring.

Cryomodule-Based Monitors

Low intensity, chronic beam losses are a prime factor in the degradation of superconducting RF cavity performance. Losses of primary beam interact thermodynamically with the cryomodule system. Systems employing fast thermometry or calorimetry have been developed to monitor the temperature of cryogenic components and beamlines [7][8]. Resistance temperature detectors (eg. Cernox RTDs) are employed to monitor the surface temperature of components.

Fast thermometry techniques are currently being explored to detect low level, slow beam losses at limiting apertures in cryomodules [9]. ANSYS models can predict the magnitude and rate of change in component temperature under thermal loading conditions due to beam loss [10] (Table 2).

Table 2: Cryogenic Beam Loading Response

Rising time for 0.1K temperature difference from beam loss		
Beam loss in cryomodule	0.1 W/m	1 W/m
0.1K rising time	1 min	7 sec
Maximum temperature rising	1.83 K	8.9 K
Total rising time	30 min	20 min

Measurements of thermal loading and RTD pickups were conducted at FRIB [9]. Initial sensor response is encouraging for detection of several mK temperature rise with a time response of 10's seconds. Improvements to the sensitivity and time response are expected with higher sampling and averaging rates (1-10kHz).

A fast thermometry system (FTS) [7] will be installed in the cryomodules in LS1 (Fig. 5) and the low energy portion of LS2 to provide enhanced beam loss detection. Pairs of resistance temperature detectors (RTDs) will be installed at the entrance and exit of each cryogenic solenoid in these cryomodules to detect changes in local temperature from beam interception. Fast (~10 kHz) signal conditioning and digitizing modules provide sensitivity to 0.1 K temperature changes on a seconds-order time scale.

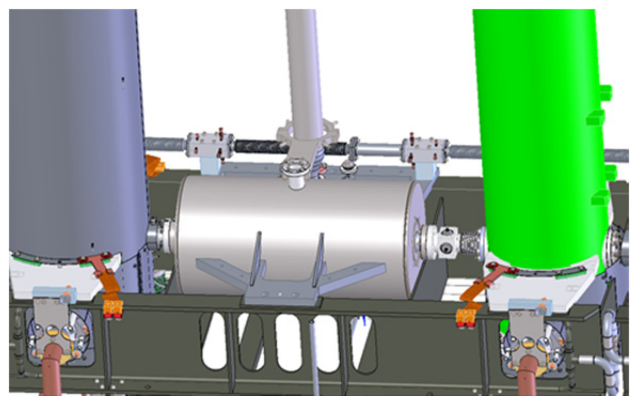

Figure 5: FRIB β=0.085 cryomodule segment.

Additional methods are under consideration to monitor the heat load in the 2K (cavity) and 4.5K (solenoid) cryogenic circuits due to beam loss. Such signals include the cavity/solenoid vessel temperature sensors (CERNOX 1010), vessel heater supplies, and the 2K/4/.5K bath pressure. These can provide temperature sensitivity to 0.1K but may require long time averaging (1000s seconds).

Fault Mode Studies to Improve Network Response

Fault mode and errant beam studies are being conducted to assess the risk of large beam energy density deposition from component failure or operator error. A beam and accelerator model is used to generate distributions of beam power and energy density deposition along the beamline due to discrete fault conditions [11]. Particular cases under study are single cavity and solenoid magnet failures from quench and

ISBN 978-3-95450-176-2

room temperature magnet mis-powering and steering errors.

Fault mode and errant beam loss patterns are used to identify high risk loss events and then analyse the responses of BLM sensors (using secondary radiation) as well as BCM, BPM, and HMR fast responses. This data can then be used to optimize the network density of FPS-serving sensors and improve the robustness of beam loss decision making algorithms [12][13].

COMMISSIONING AND VALIDATION SCHEME

During the initial FRIB commissioning phases, the peak and average beam intensity will be limited. Increasing the average beam power to the design value will require validation of machine and personnel protection mechanisms. It is currently envisioned to progressively validate and commission the FPS systems in three stages.

The first stage has sufficiently low peak and average beam power that safe operation requires no fast MPS response. MPS will only be needed to inhibit the next pulse in case of a fault situation. In this stage, the DBCM, HMR, and BLM diagnostic systems will be established to terminate the beam within 50 ms.

In the second stage, MPS is required to terminate the beam within 50 ms. The diagnostic systems have been established and demonstrated in the previous stage. In this second stage, fast DBCM, HMR, and BLM systems will be verified to terminate beam within 500 μs. The increased sensitivity provided by slow HMR and BLM monitoring systems and by cryomodule temperature monitoring will be initially demonstrated.

The third stage requires fast MPS systems, starting with 500 μs response times. Further demonstration and verification of beam termination within 35 μs will be performed before full power beam production is allowed.

REFERENCES

[1] J. Wei, "The very high intensity future," Proceedings of IPAC2014, MOYBA01; http://www.JACoW.org

[2] S. Lidia, "Diagnostics for high power accelerator machine protection systems", Proceedings of IBIC 2014, Monterey, CA; http://www.JACoW.org

[3] Z. Liu, *et al.*, "A new beam loss monitor for low-energy protons and heavy-ion accelerators," Nucl. Instrum. Methods Phys. **A**, *in press* (2014).

[4] W. Blokland, C. Peters, "A new differential and errant beam current monitor for the SNS accelerator," Proceedings of IBIC13, THAL2; http://www.JACoW.org

[5] R.C. Webber, "Charged particle beam current monitoring tutorial," AIP Conf. Proc. 333 (1995), p. 3-23.

[6] www.struck.de

[7] D. Orris, *et al.*, "Fast thermometry for superconducting rf cavity testing," Proceedings of PAC07, WEPMN105; http://www.JACoW.org

[8] J. Knobloch, *et al.*, Rev. Sci. Instrum. **65**, 3521 (1994).

[9] Z. Zheng, et al., "Cryogenic thermometers as slow beam loss detectors for FRIB", these proceedings, IBIC 2015, Melbourne, Australia (2015), MOPB073; http://www.JACoW.org.

[10] Y. Zhang, et al., "Analysis of beam damage to FRIB driver linac," Proceedings of SRF2011, MOPO058; http://www.JACoW.org

[11] Q. Zhao, et al., "FRIB accelerator beam dynamics design and challenges," Proceedings of HB2012, WEO3B01 (2012).

[12] Z. Liu, et al., "Optimization of beam loss monitor network for fault modes", Proceedings of IPAC 2015, TUAC3; http://www.JACoW.org.

[13] Z. Liu, et al., "Optimization of beam loss monitor locations using data mining techniques", these proceedings, IBIC 2015, Melbourne, Australia (2015) MOPB072; http://www.JACoW.org.

ISBN 978-3-95450-176-2

OVERVIEW OF BEAM DIAGNOSTIC SYSTEMS FOR FRIB*

S.M. Lidia#, S. Cogan, D. Constan-Wahl, J. Crisp, M. Ikegami, Z. Liu, F. Marti, I. Nesterenko, E. Pozdeyev, T. Russo, R. Shane, R.C. Webber, Y. Zhang, Q. Zhao, Facility for Rare Isotope Beams East Lansing, Michigan, USA

Abstract

The Facility for Rare Isotope Beams will extend the intensity frontier of heavy ion linac facilities, with continuous beam power up to 400 kW and beam energy ≧200 MeV/u. Strict demands are placed on the beam diagnostics in the front end, linac, and beam delivery systems to ensure delivery of high quality beams to the target with minimal losses. We describe the design of diagnostic systems in each accelerator sector for commissioning and operations.

INTRODUCTION

Facility for Rare Isotope Beams (FRIB) is a high-power, high-brightness, heavy ion facility under construction at Michigan State University under cooperative agreement with the US DOE [1]. The linac will accelerate ions to energies above 200 MeV/u, with up to 400 kW of beam power on target. The linac facility, shown in Fig. 1, consists of a Front End, three Linac Segments (LSs) connected by two Folding Segments (FSs), and a Beam Delivery System (BDS) leading to the production target [2].

CHALLLENGES FOR BEAM INSTRUMENTATION

FRIB employs a superconducting linac to accelerate the high power, high brightness hadron beam. As such, it shares operational issues with other facilities (SNS, ESS, RHIC, LHC, JPARC, etc.) with regards to power handling, cleanliness of components, restricted access to the beam line, prohibitions against actuated diagnostics near cryomodules, etc. Additional challenges for beam instrumentation presented by FRIB include the low energy of the heavy ion beams, the folded linac geometry, and the plan to transport and accelerate multiple charge states simultaneously.

Low-beta Beam Position Monitoring

The relatively low velocity of the ion beams in the driver linac has implications for accurate beam position monitoring. With low β, the electric field lines spread out resulting in longer, slower image current, and reduced high frequency content. The significance of this effect depends on the proximity to the button and it results in frequency response dependent on position and velocity [3][4][5].

*This material is based upon work supported by the U.S. Department of Energy Office of Science under Cooperative Agreement DE-SC0000661, the State of Michigan and Michigan State University.
#lidia@frib.msu.edu

Multiple Charge State Beams

The acceleration, transport and delivery of a multiple charge state composite beam presents particular complications to the beam instrumentation design and functionality necessary to establish the machine tune. Representative ion species for FRIB are listed in Table 1, where Q1 is the beam charge state in the Front End and LS1, and Q2 is the beam charge state following the stripper and charge selector in FS1. In the case of Uranium, two charge states are transmitted to the stripper, with five states selected for additional acceleration and target delivery.

Table 1: Representative Ion Species in FRIB

Ion Species	A	Emax (MeV/u)	Q1	Q2-center	Q2-spread
U	238	200	33, 34	78	76-80
Xe	136	221	18	49	48-50
Kr	86	257	14	35	35
Ca	48	264	11	20	20
Ar	36	320	8	18	18
O	16	320	6	8	8

In LS1, orbit oscillations in both longitudinal and transverse phase space arise due to charge state dispersion (ΔQ/Q) in neighboring rf buckets. A challenge to beam instrumentation is to spatially resolve the phase dispersion of the charge states so that the oscillation can be monitored, and growth in both longitudinal and transverse emittance be minimized. This may be accomplished by utilizing the network of linac BPMs and incorporating digital sampling techniques to determine the oscillation phase.

Large Dynamic Range of Beam Intensity

The FRIB linac is designed to support multiple operating modes with varying time structure and peak intensity of the ion beams. These modes can be grouped into four general categories:

- Short pulse (<5 – 50 µs), low duty cycle (< ~1 Hz), varying intensity (50 to 650 µA)
- Moderate pulse length (~0.01 s to s), low duty cycle (< ~1 Hz), nominal intensity (~650 µA)
- Approximately CW (50 µs gap @ 100 Hz), low to nominal intensity (<10 to 650 µA)

ISBN 978-3-95450-176-2

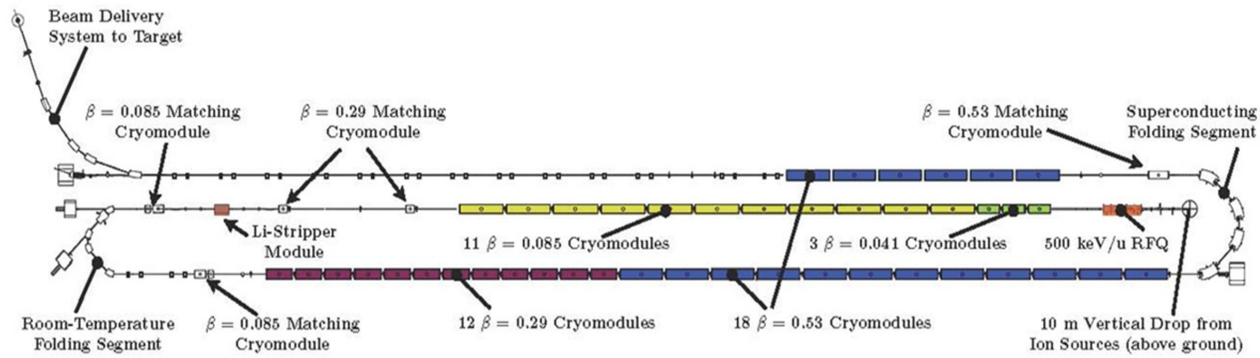

Figure 1: Schematic layout of FRIB drive accelerator facility.

- Dynamic ramp to high power (variable intensity, pulse duration, and repetition rate) to slowly increase the target temperature (~30 s for warm re-start to 10 minutes for cold start).

Several modes used for commissioning the front end and fragment separator lack quantitative definition, but may be mapped to one of the other categories. These modes exhibit a wide range in intensity (2 – 650 eμA for Front End commissioning, and 0.0001–30 pnA for fragment separator commissioning and secondary beam development).

The previously discussed beam modes define the range of conditions that the beam instrumentation must serve. Beam instrumentation is required to detect beam currents ranging from ~1 mA to ~1 μA, with bandwidths sufficient to provide sensitivity over many orders of magnitude in duty cycle or pulse duration (CW to 50 μs pulse duration at 1 Hz). Additional operating modes, albeit a small fraction of the operating schedule, require lower peak intensities and average beam power. The baseline resolution requirements for the diagnostic systems assume CW operation with 100 μA beam current. Operationally, for reduced average beam currents, longer integration or averaging times may be used to restore resolution. In the extreme case of ion beam fluxes ~100 pfA, intercepting diagnostics may be utilized with long integration times to acquire flux density information on the transported beams.

Machine Protection System

The high power and brightness, and short (< mm) Bragg range of the FRIB heavy ion beam places critical importance on the fast protection system to detect and protect against prompt beam losses [6]. The performance and lifetime of sensitive superconducting cavity surfaces can be affected by small losses (< 1 W/m) occurring over long durations.

The twice-folded geometry of the FRIB linac places the high energy linac segment in close proximity to the low energy linac segment. Traditional loss monitors, eg. ionization chambers and scintillation-based neutron detectors, will be unable to differentiate the relatively low-amplitude loss signals arising in LS1 from the high-amplitude signals generated in LS3 due to radiation cross-talk [7]. Additionally, x-ray background sources originating from the RF cavities themselves can also potentially overwhelm the beam-generated signals in the low energy linac modules.

OVERVIEW OF BEAM DIAGNOSTIC INSTRUMENTATION

The suite of beam instrumentation systems is designed to facilitate initial commissioning and tuning activities preceding user operations, and to monitor beam transport and acceleration function and provide sensors for machine protection during operations. Diagnostic systems will be provided to continuously measure beam position and orbit deviations, beam current and transmission at several points, and beam loss induced radiation fields. On-demand diagnostics will produce measurements of beam phase space densities, bunch duration, 1-D beam profiles and 2-D transverse (x-y) or hybrid (x-z) distributions. Time of flight measurements using a dense network of beam position monitors will enable phase and amplitude tuning for all RF cavities in the linac sections [8].

Overall Requirements and Sensitivities

To meet the demands of the FRIB experimental systems, stringent requirements on the linac driver and beam delivery system are imposed. These are summarized in Table 2.

Table 2: Required Beam Parameters at Target for Five-Charge-State Uranium

Parameter	Value	Required (% beam)
Beam spot size	1 mm	≥ 90%
Angular spread	±5 mr	≥ 90%
Bunch duration	3 ns	≥ 95%
Energy spread	±0.5%	≥ 95%

FRONT END

The instrumentation package in the Front End section will enable selection and tuning of two charge states to be simultaneously accelerated and transported to the first linac segment, while maintaining beam quality. The two

ISBN 978-3-95450-176-2

ion source lines in the FRIB front-end (Fig. 2) will each include a diagnostic station, capable of intercepting up to 300 W of continuous beam power, comprising (i) horizontal and vertical charge-selecting slits; (ii) a Faraday cup; (iii) view screen and optics; and (iv) horizontal and vertical Allison scanners [9].

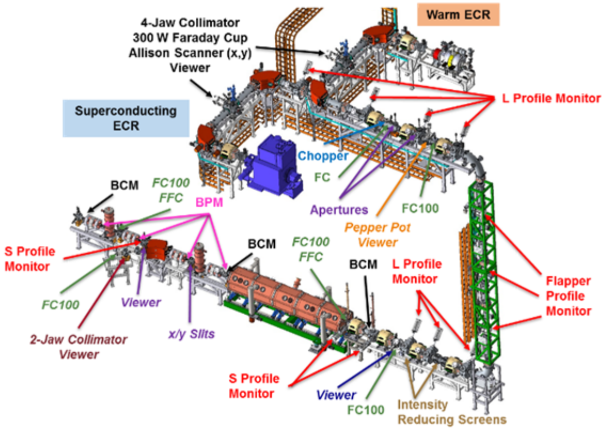

Figure 2: Schematic of diagnostic systems in the FRIB Front End.

The Low Energy Beam Transport (LEBT) beamline transports and manipulates the beam between the ion source and charge selector, and the RF quadrupole accelerator (RFQ). The initial stage of the LEBT uses an electrostatic, deflecting chopper to limit the beam pulse duration and to impress an ~100 Hz intensity modulation on the otherwise CW beam. Following the chopper are collimating apertures to remove off-angle beam tails and limit the beam emittance along the modulated pulse. A sequence of 1-D profile monitors (Fig. 3) and pepperpot emittance monitor support analysis of the beam quality and assurance that the transport lattice and beam distribution are well matched. Following the multi-harmonic buncher and velocity equalizer [8], a pair of fast Faraday cups (BW 5-10 GHz) will be utilized to monitor the longitudinal distribution prior to injection to the RFQ, and to the downstream linac section..

AC-coupled beam current transformers (ACCTs) [10] continuously monitor the beam transmission through the RFQ and at the exit of the MEBT. A 50 µs, 100 Hz current notch or beam gap is imposed by the chopper so that the current baseline can be periodically recovered with the ACCTs. Beam position monitors (BPMs), tuned to a harmonic of the 80.5 MHz cavity frequency, are introduced following the RFQ. Nearly all BPMs in the FRIB lattice use 20-mm diameter buttons to sense the beam [3].

LINAC SEGMENTS

The first linac segment (LS1) accelerates the two-charge-state ion beam from 500 keV/u to 16 MeV/u. Beam position monitors are located both within the cryomodule assemblies, between superconducting solenoids and RF cavities (Fig. 4), and in the warm sections between cryomodules (Fig. 5). In the two higher energy linac segments (LS2 and LS3), BPMs are located only in the warm sections between cryomodules.

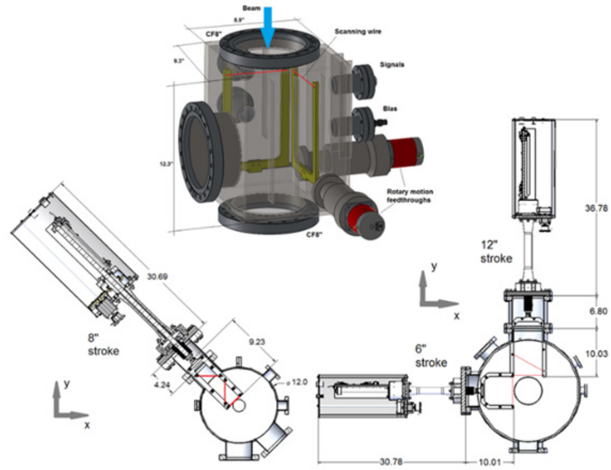

Figure 3: FRIB wire profile monitors. Flapper (top), Small (left), Large (right).

There are a total of 39 cold BPMs integrated with the LS1 cryomass assemblies. Steel jacketed, ceramic dielectric (SiO_2), 50 Ohm cables are used within the cryomodule insulating vacuum to carry the BPM signals from the ~4 K beam line to a 300 K feedthrough. The small cable diameter (0.090 inch) limits the static heat load presented to the cryogenic system. This system has been installed on the prototype FRIB 0.085 cryomodule cold mass, and verified with a network analyser at ambient and cryogenic temperatures [11].

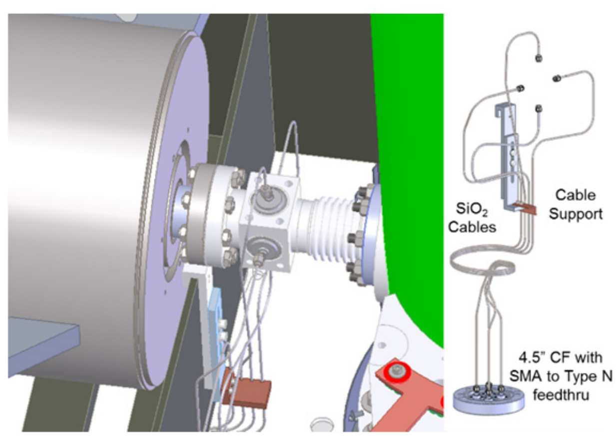

Figure 4: Cryogenic BPM installed between solenoid and cavity in LS1 (left), and cryogenic cable assembly (right).

All FRIB BPMs will be mapped with a purpose-built stretched wire, RF-driven test stand. Polynomial correction removes geometric nonlinearities from the difference-over-sum algorithm, providing position error <100 µm over ~2/3 of the BPM aperture.

RF phase referencing for each BPM will be accomplished with a dedicated tap from the local (10.625

ISBN 978-3-95450-176-2

MHz) RF reference line. Each BPM reference is transmitted along with the individual BPM button signals in a bundle of 5 phase matched cables to a common digitizer board. A custom analog board (based on the FRIB LLRF board) will be used to condition and digitize the input signals, which will then be passed to the FRIB General Purpose Digital Board (FGPDB) for signal processing and reporting. This system will be incorporated within a MTCA.4 standard chassis.

Beam current monitors are installed along each straight section in the folded linac. These are Bergoz AC current transformers (ACCTs) with ~300 kHz high frequency cutoff. An integral Hereward feedback circuit extends the low frequency response to ~3 Hz yielding a 100 ms *L/R* time constant. The positions of the current monitors have been optimized to reduce residual DC magnetic fields from nearby, large bore magnets. Additional magnetic shielding is added to further reduce the effects of stray flux that limit the low frequency response.

Halo Monitor Rings [7] with apertures closely matching the physical apertures of the cryomodules are installed in the warm sections between cryomodules (Fig. 5). They are capacitively-coupled to the electrical ground of the diagnostic box and provide a measurement of intercepted current (down to ~10 nA) whether from halo scraping or transverse excursions of the beam core. Current work is examining the optimum ring aperture as a compromise between detection sensitivity, tuning flexibility, and ring lifetime.

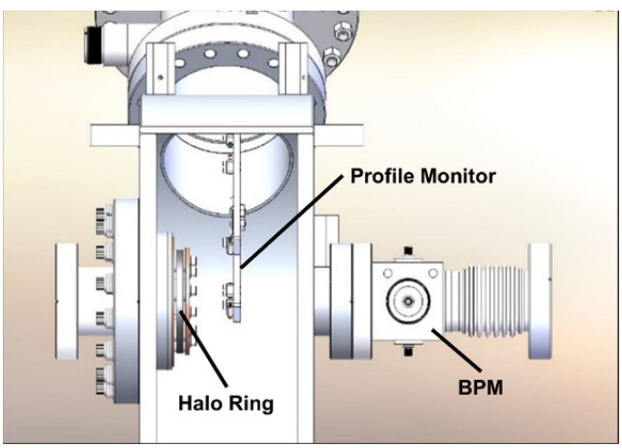

Figure 5: Warm section diagnostic box, with wire profile monitor, BPM, and halo monitor ring. The profile monitor (shown) is absent in stations between cryomodules.

External beam loss monitors (ionization chambers and scintillator-PMT-based, moderated neutron detectors) will be placed along LS3 and the high energy end of LS2 for prompt detection of x-rays and gammas, and for more sensitive detection of neutron fluxes.

A fast thermometry system [12] will be installed within the cryomodules in LS1 and the low energy portion of LS2 to provide enhanced beam loss detection. Pairs of resistance temperature detectors (RTDs) will be installed at the entrance and exit of each cryogenic solenoid in these cryomodules to detect changes in local temperature from deposited beam power. Fast (~10 kHz) signal conditioning and digitizing modules provide sensitivity to 0.1 K temperature changes on a seconds-order time scale.

FOLDING SEGMENTS AND BEAM DELIVERY SYSTEM

The low energy (~16 to 20 MeV/u) Folding Segment 1 (FS1, see Fig. 6) serves several purposes: (i) to provide a warm magnet transport lattice to connect LS1 to LS2; (ii) to strip the ions in the beam to a higher charge state; (iii) to select up to five charge states for transport and injection in LS2; and (iv) to provide a straight-ahead beam dump line for commissioning and tuning LS1. A second beam dump in FS1 facilitates tuning the charge state selector and beam optics. The high energy (≥150 MeV/u) Folding Segment 2 (Fig. 7) provides a transport lattice with four superconducting dipole magnets to connect LS2 to LS3, as well as a straight ahead beam dump for LS2 commissioning and tuning.

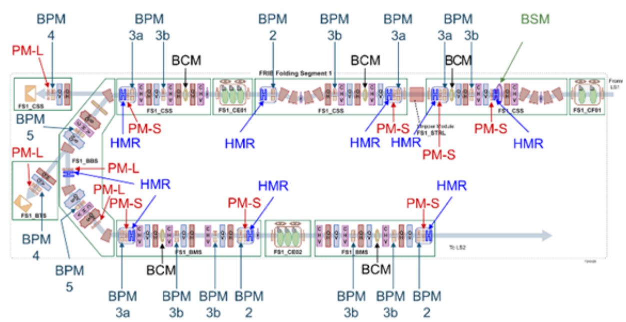

Figure 6: Ideogram of Folding Segment 1.

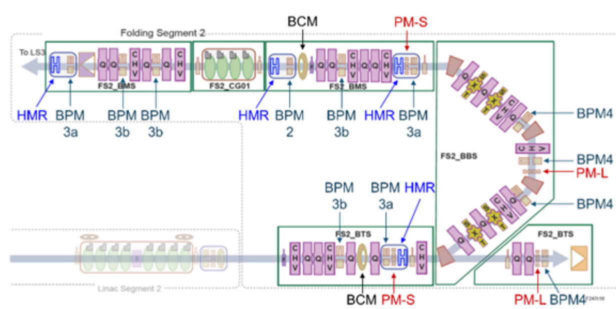

Figure 7: Ideogram of Folding Segment 2.

A separate issue with multi-charge state beams arises in the Folding Segments due to dispersion. In FS1, the beam distribution at the BPM following the charge selector is dispersed horizontally by up to ~80 mm. A large (150 mm) aperture, elliptical, split plate BPM design (Fig. 8) provides a larger linear response aperture [13].

ISBN 978-3-95450-176-2

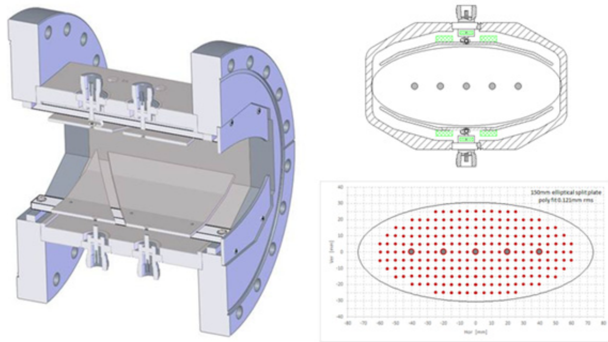

Figure 8: 150 mm, large aspect ratio BPM in dispersive section of FS1 (left). (Right) BPM cross-section and linearized response map with multi-charge-state beam component positions indicated.

Additional BPM instrumentation is required to provide beam tuning capability in the Folding Segments. Custom vacuum chambers within specific quadrupole magnets will incorporate BPMs (Fig. 9).

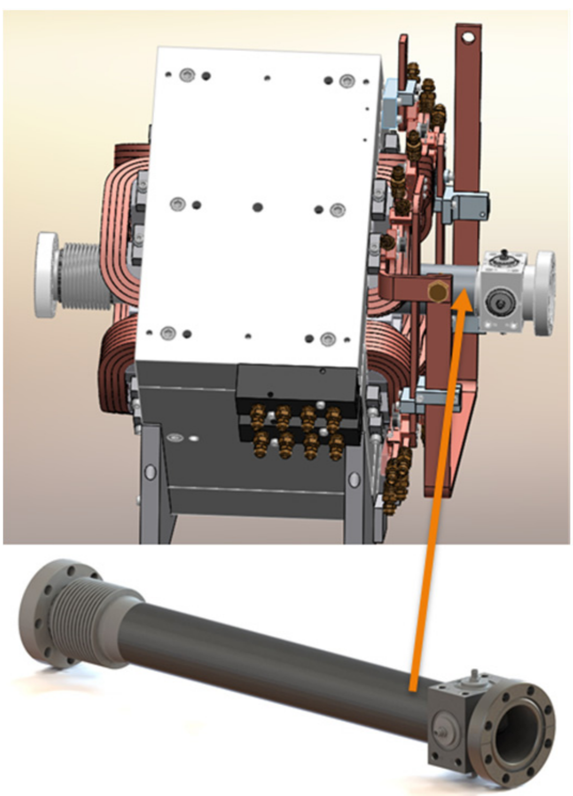

Figure 9: (Top) Vacuum chamber with integrated BPM in quadrupole magnet (FS1, FS2). (Bottom) Type 3b BPM assembly.

The basic instrumentation suite includes beam position monitors, transverse profile monitors, and beam current monitors. The charge stripper imposes requirements on the incoming beam distribution to minimize the resulting energy spread and beam emittance growth. A Feschenko-type bunch shape monitor [14] will be used to monitor the transverse and longitudinal bunch profile and to enable upstream tuning to match the beam on to the stripper foil or curtain.

The final transport lattice, the Beam Delivery System (BDS), delivers the multi-charge-state beam to the target with parameters as given in Table 1. The BDS beam instrumentation design includes beam position, transverse profile, and beam current monitoring. A full energy, ≥200 MeV/u, straight ahead beam dump is used for commissioning and tuning of LS3 and the linac-to-BDS transport line. This dump however is not rated for full beam power.

REFERENCES

[1] J. Wei, et al., “FRIB accelerator status and challenges”, LINAC’12, Tel Aviv, August 2012, p. 417; http://www.JACoW.org
[2] F. Pellemoine, et al., “Development of a production target for FRIB: therm-mechanical studies”, J. Radioanal Nucl Chem, DOI 10.1007/s10967-013-2623-7.
[3] O. Yair, et al., “FRIB beam position monitor pick-up design”, Proceedings of IBIC2014, Monterey, USA, TUPF16; http://www.JACoW.org
[4] A. Lunin, et al., “Development of a low-beta button BPM for the PXIE project’, Proceedings of IBIC2013, Oxford, UK, TUPC14; http://www.JACoW.org
[5] R.E. Shafer, “Beam position monitor sensitivity for low-β beams”, AIP Conf. Proc. 319 (1994).
[6] S. Lidia, “Diagnostics for high power accelerator machine protection systems”, Proceedings of IBIC 2014, Monterey, CA; http://www.JACoW.org
[7] Z. Liu, et al., “A new beam loss detector for low-energy proton and heavy-ion accelerators”, Nucl. Instrum. Methods Physics Res. A767 (2014), 262.
[8] Q. Zhao, et al., “FRIB accelerator beam dynamics design and challenges”, Proceedings of HB2012, Beijing, China, WEO3B01; http://www.JACoW.org
[9] P.W. Allison, et al., IEEE Trans. Nucl. Sci. NS-30, (1983), 2204.
[10] http://bergoz.com/
[11] S. Miller, et al., “Construction and Performance of FRIB Quarter Wave Prototype Cryomodule”, SRF’15, Whistler, Canada (2015).
[12] D. Orris, *et al.*, “Fast thermometry for superconducting rf cavity testing,” Proceedings of PAC07, WEPMN105; http://www.JACoW.org
[13] E. Schulte, in *Beam Instrumentation*, J. Bosser (ed.), CERN-PE-ED 001-92.
[14] Feschenko A.V., Ostroumov P.N. “Bunch Shape Measuring Technique and Its Application For an Ion Linac Tuning”, *Proc. of the 1986 Linear Accelerator Conference*, Stanford, 2-6 June, 1986, pp. 323-327.

ISBN 978-3-95450-176-2

CRYOGENIC THERMOMETERS AS SLOW BEAM LOSS DETECTORS*

Z. Zheng#, Z. He, S. Lidia, Z. Liu, R. Shane, Y. Zhang, Facility for Rare Isotope Beams, East Lansing, Michigan, USA 48824

Abstract

Due to the folded geometry of the linac, beam loss monitoring at the Facility for Rare Isotope Beams (FRIB) [1], especially for small losses, is extremely challenging in the low energy section of the linac. Fast detection is not required for slow/small beam losses, and we therefore propose thermometers installed in the cryomodules at potential hot spots, such as the locations upstream of solenoids. Cryogenic thermometry tests were implemented in the ReA6 cryomodule with heaters and RTD thermometers. The preliminary study shows that the 10 mK signal resolution of thermometers corresponds to ~5 mW heat power in 100 seconds, or ~1 W heat power in 10 seconds, which is sufficient to satisfy the requirement for small beam loss at FRIB.

INTRODUCTION

The unique paper-clip geometry of the FRIB linac leads to radiation cross-talk between the low-energy segment and the adjacent high-energy segment. This creates a background which can obscure beam losses, especially small losses in the low-energy segment. Ion chambers, proposed for beam-loss detection in the high-energy sections, are not suitable for the low-energy sections due to this radiation cross-talk and also the x-ray background from field emission in the RF cavities. Neutron detection in these areas is similarly affected.

In this paper, we investigate the suitability of cryogenic thermometers as a tool to measure small beam losses in which prompt detection is not critical (also referred to as "slow" losses). The first section analyzes potential beam-loss hot spots in the FRIB cryomodules. The next section describes the simulation of thermal sensitivity and response time at possible thermometer locations. The final section presents the results of cryogenic thermometry tests implemented in the ReA6 cryomodule.

LOSS HOT SPOTS IN CRYOMODULES

Beam Loss Simulation

The most probable cause of beam loss at FRIB is the failure of solenoids or cavities. Three classes of beam loss were simulated using the code IMPACT [2]:

- 1 of 69 solenoids is tripped (including 69 cases);
- 1 of 332 cavities tripped (including 332 cases);
- 2 of 332 cavities tripped randomly (including 170 cases).

A summary of the beam-loss simulation results is shown in Fig. 1. The largest peaks in power loss occur at positions 284 m and 446 m, corresponding to the second and third Folding Segments of the FRIB linac. The large beam loss in these locations is due to cavity failure. To protect the cryomodules from damage, however, we are more interested in detecting small losses which may occur over a long period time. These occur mainly in the lower-energy Linac Segments 1 and 2, as shown in Fig. 2.

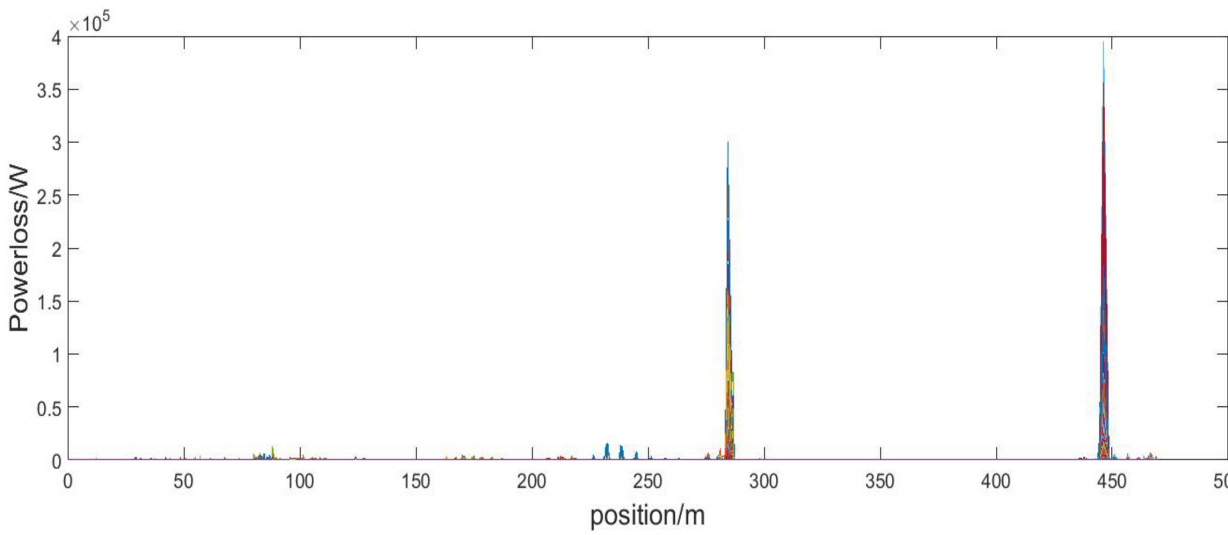

Figure 1: Summary of beam-loss results from IMPACT simulations. The corresponding FRIB linac segments are: Segment 1 = 0 - 126.5, Segment 2 = 136.5 m - 283.3 m, Segment 3 = 301.5 m - 443.7 m.

*Work supported by the U.S. Department of Energy Office of Science under Cooperative Agreement DE-SC0000661

ISBN 978-3-95450-176-2

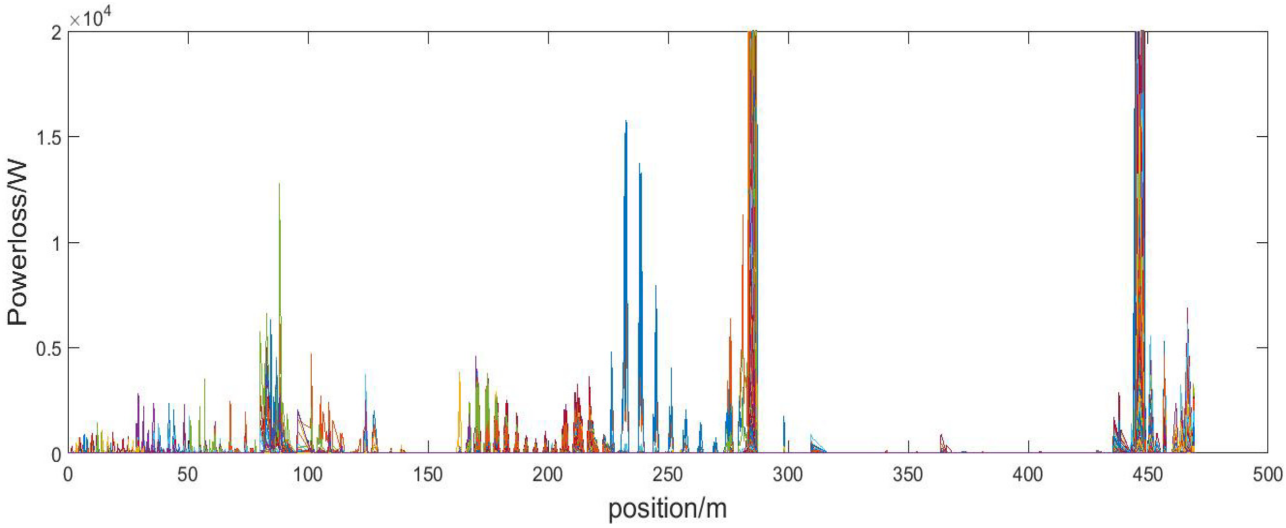

Figure 2: Close-up of small losses occurring in Segments 1 and 2 of the FRIB linac.

Slow-Loss Hot Spots

Since the cryogenic thermometers will be used to detect slow/small beam losses, they will be distributed mainly in Linac Segments 1 and 2, and possibly in a few of the potential beam loss positions in segment 3.

Almost 90% of the beam loss occurs in either the cavities (70.24% of total beam loss inside cryomodule), the drift spaces before solenoid (12.36%), or the solenoids (6.84%). Beam loss inside a cavity or solenoid cannot be measured directly by temperature sensors because they are inside helium jackets. Therefore, we plan to install thermometers close to the solenoids in the drift space before and after.

SIMULATION OF THERMAL SENSITIVITY AND RESPONSE TIME

A cavity and a solenoid are connected by a flexible coupling (bellows), providing a short section of drift space between them. To decide the attachment point for the thermometers, a simulation of sensitivity and response time was performed. For the simulation, sensors were placed on both bellows flanges and the bellows wall, as shown in Fig. 3.

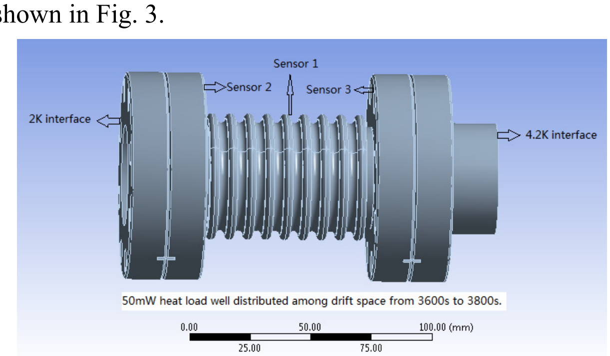

Figure 3: Thermal simulation for the drift space between cavity and solenoid. Left bellows flange is connected to the cavity flange (2K interface), right one is connected to the solenoid flange (4.2K interface). There is 50 mW heat load well-distributed among the drift space from 3600s to 3800s during the simulation.

Since it is difficult to attach a thermometer to the ridged surface of the bellows wall, we examined the response time at the bellows flanges. The simulation shows that the temperature rises faster for the solenoid-side flange (Fig. 4) than the cavity-side flange (Fig. 5). A 10 mK rise in temperature takes about 30 seconds at the solenoid-side flange, while it takes about 50 seconds at the cavity-side flange. Also, the temperature of the solenoid-side flange has a much higher saturation temperature than cavity-side flange. Thus, we see higher thermal sensitivity on the solenoid side.

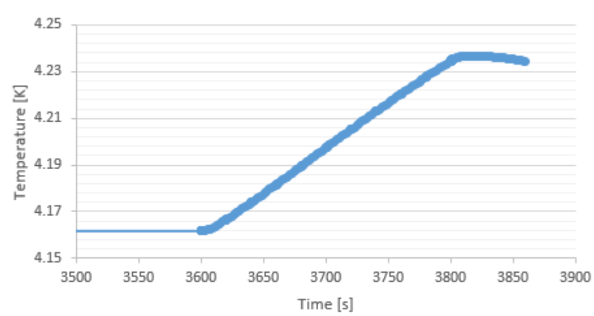

Figure 4: Solenoid-side bellows flange, Temperature vs. Time.

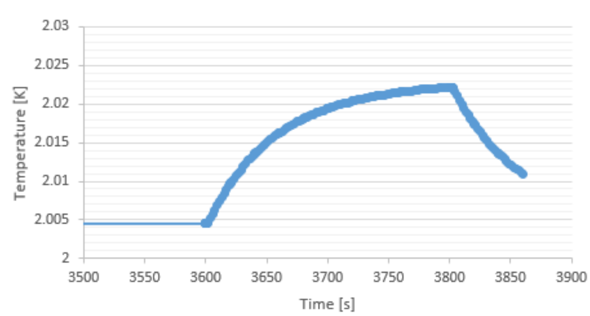

Figure 5: Cavity-side bellows flange, Temperature vs. Time.

ISBN 978-3-95450-176-2

The simulation result is consistent over a range of heat loads from 5mW to 100mW. Based on these results, the thermometer should be attached on the bellows flange nearest the solenoid.

CRYOGENIC THERMOMETRY TESTS

A proof-of-concept test for the cryogenic thermometry was performed in the ReA6 cryomodule [3]. A 5Ω heater was used to mimic small beam loss. Three Cernox RTD sensors (TI79, TI81 and TI82) were attached near solenoid helium jacket and one (TI1) on the jacket itself (see Fig. 6). All measured signals were processed by a digital low-pass filter to reduce the white noise.

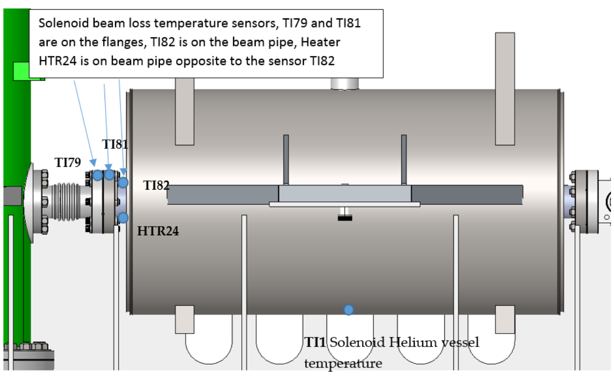

Figure 6: Schematic of thermometry test in ReA6 cryomodule. TI79, TI81, TI82 and TI1 are thermometers. HTR24 is 5 Ω heater.

The background temperature was measured by sensor TI1 in order to characterize the noise. Temperature fluctuations were about ±5 mK, and the average temperature drifted no more than a few mK over the course of the 1.5-hour test (see Fig. 7). This simple noise measurement indicates that a ΔT of 10 mK is certainly distinguishable by the Cernox sensors without "heroic" signal conditioning.

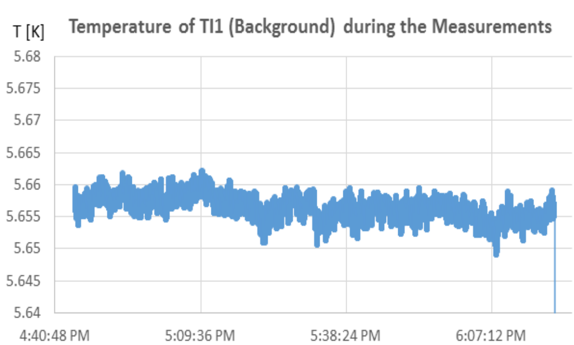

Figure 7: Background temperature fluctuation during the test, spanning about 1.5 hours. Temperature background fluctuations are about ±5 mK.

The step response of each sensor was recorded for heat loads from 2 mW up to 1 W. Fig. 8 shows the 4.5 mW heat load case for TI82. Sensors at the other two locations (TI81 and TI79) have similar results. The stated sensitivity of the sensor is 2 mW according to the technical specifications. However, a more reasonable lower bound for this measurement appears to be 5 mW.

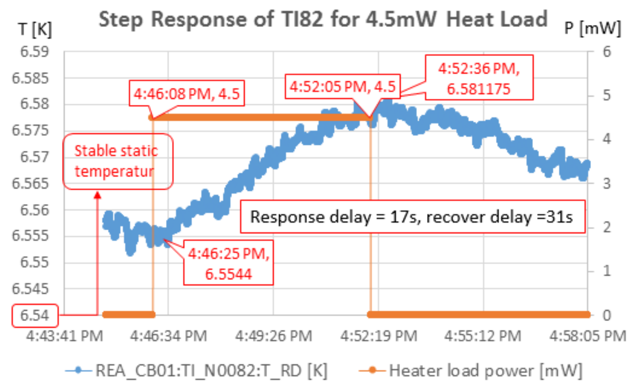

Figure 8: 4.5-mW-heat-load step response for TI82. Response delay is the time until the temperature begins to rise after heater turned on. Recover delay is the time until the temperature begins to drop after the heater is turned off.

Table 1 summarizes the measurement data for TI82 with heat loads from 2 mW to 1 W. The response time is less than 20s when heat load is > 5 mW. Since it has been indicated that the Cernox sensor can distinguish a ΔT of 10mK, we define beam loss (BL) detection time as the time for the temperature to rise 10mK after the heater is turned on. For example, if FRIB's local slow/small beam loss is 50 mW, the thermometer should detect it within 21 seconds.

Table 1: Summary of TI82 Measurement Data

Heat Load	Response Time	BL detection time
2 mW	83 s	303 s
4.5 mW	17 s	107 s
12.5 mW	14 s	50 s
32 mW	11 s	29 s
50 mW	10 s	21 s
98 mW	11 s	17 s
1013 mW	10 s	11 s

The location of the thermometers will affect the results, and this was also considered in the test. The effect is apparent in Fig. 9, which shows the results for a 50 mW heat load. The beam-loss detection time increased when the distance from thermometer to heater increased. Using the average beam-loss detection time (about 30 s), we get good agreement between our measurements and the thermal simulation for the 50 mW heat load case, which also took about 30s to rise 10 mK (Fig. 4). In summary, the thermometry measurement technique showed a 5mW lower bound for beam loss and it will detect beam loss at expected power levels (< 100mW) in the time scale of a minute.

ISBN 978-3-95450-176-2

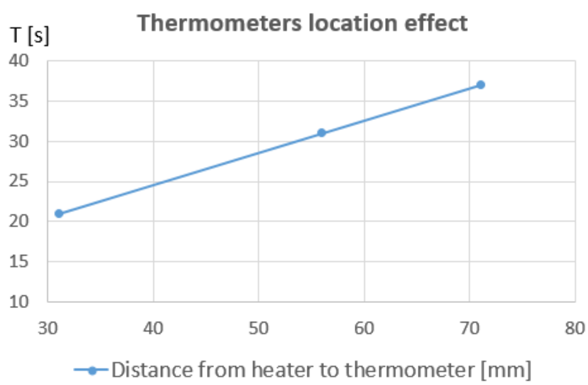

Figure 9: Beam loss detectable time vs. Distance from heater thermometer.

CONCLUSION

Slow/small beam-loss monitoring is extremely challenging in the low-energy segment of FRIB, but critical in order to protect cryomodule from degradation due to radiation damage. Thermometry has been proposed as a method for detecting these small losses without interference from radiation cross-talk. Beam-loss simulations determined that the slow-loss hot spots in the cryomodules are within the cavities and solenoids, and in the drift space before a solenoid. Thermal-sensitivity and response-time simulations were performed in order to determine the suitability of several sensor locations. A proof-of-concept test was implemented in the ReA6 cryomodule, showing a reasonable loss detection limit of 5 mW. At the power levels specified for slow losses at FRIB (< 100mW) the sensor response is less than a minute, as required for FRIB slow beam loss monitors.

ACKNOWLEDGMENT

The authors would like to thank Dan Stout, Joseph Ozelis and Genfa Wu for generously providing information. The authors also would like to thank Ting Xu and Yoshishige Yamazaki for their support.

REFERENCES

[1] FRIB website: http://www.frib.msu.edu/
[2] IMPACT website: http://amac.lbl.gov/~jiqiang/IMPACT/index.html
[3] ReA6 website: https://people.nscl.msu.edu/~iwasaki/rea6.html

ISBN 978-3-95450-176-2

REFERENCE SIGNAL DISTRIBUTION FOR BEAM POSITION AND PHASE MONITORS AT LANSCE*

R. C. McCrady, H. A. Watkins, Los Alamos National Laboratory, Los Alamos, NM 87545 U.S.A.

Abstract

The new beam position and phase monitors at LANSCE measure the phase of the beam relative to a reference signal from the master reference oscillator. The distribution of the reference signal along the 800m-long linac is subject to thermal effects, and phase drifts of the reference signal are observed to be greater than 15 degrees. We are investigating stabilization schemes, one of which involves distributing two RF signals of different frequencies. By observing the phase difference between the two signals, the phase drift of the reference signal can be deduced. Initial tests indicate that the reference can be stabilized to within 0.5 degrees using this scheme. In this paper we will present the principles of operation of this stabilization scheme and results from tests of the system.

INTRODUCTION

Deployment of instrumentation for beam position and phase monitors (BPPMs) is imminent at LANSCE, and a 201.25 MHz reference signal is necessary at each of the instrumentation chassis for the phase measurement. Measurement of the beam phase provides time-of-flight information for the tune-up process, as well as diagnostic data for troubleshooting accelerator systems.

The short-term stability requirements for the reference are stringent in order to enable the tune-up process, but long-term stability requirements are fairly relaxed, at about ±1°.

The instrumentation systems are distributed throughout the ~1 km-long klystron gallery, so thermal effects on the reference distribution medium are significant; variations of almost 20° have been observed in tests over the course of a few days, mostly following the diurnal temperature cycles. While this magnitude of variation is not a show-stopper for the system, greater stability would facilitate the use of the phase measurements for long-term monitoring and for troubleshooting.

The original plan for the system had the reference signal tapped off of a thermally-stabilized transmission line that serves as the distribution medium for the accelerator klystrons; this is illustrated in Figure 1. The signal would then have been routed along the same path as the signals from the BPPM electrodes to the instrumentation chassis. This would compensate for thermal effects, as the beam signals and the reference would be subjected to the same environment. This part of the project has been delayed indefinitely, so we are seeking an economical alternative solution.

In an effort to leverage existing infrastructure, we have been exploring the possibility of distributing the reference signal on spare fibres in some recently-installed fibre-optic bundles. In addition to being an economical solution, our experience with analog fibre-optic links gave us confidence that the reference signal could be distributed over long distances with low attenuation, and we were hopeful that we could implement a stabilization scheme. One such scheme is presented in the following sections.

*Work supported by the United States Department of Energy under contract DE-AC52-06NA2596.

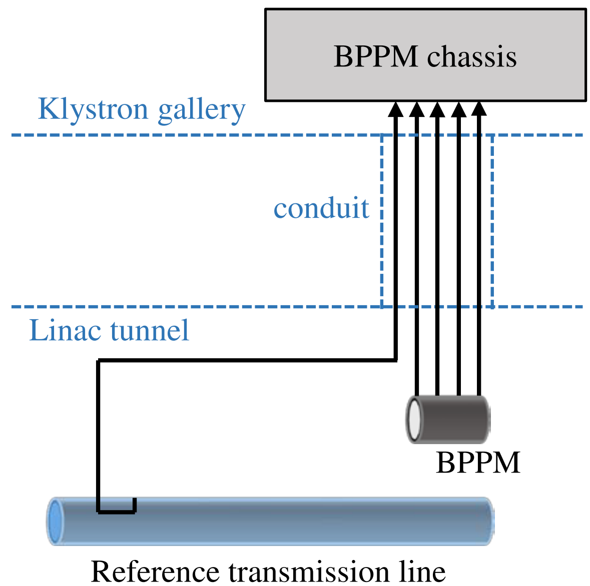

Figure 1: The original plan for distribution of the 201.25MHz reference signal.

THE BPPM SYSTEM

The transducers for the BPPMs are four-electrode, shorted-striplines about 4.8 cm long. These aren't ideally tuned for the 201.25 MHz beam-bunch frequency, as they were designed to replace existing phase-only, single-electrode transducers without modification of the beam pipes.

Coaxial cables transmit the beam-induced signals from the beam tunnel to the instrumentation chassis in the klystron gallery.

The instrumentation has 5 inputs ports, one for each electrode and another for the 201.25 MHz reference signal that serves as a fiducial for the beam phase measurement. Because the input hardware is an off-the-shelf, general-purpose card, additional input ports are available. The significance of this is discussed below.

DISTRIBUTION ON OPTICAL FIBRE

To test the idea of distributing the 201.25 MHz reference signal on optical fibre, we identified a pair of spare fibres in an existing fibre bundle to use in a loop-back

ISBN 978-3-95450-176-2

measurement, as illustrated in Figure 2. The total signal path length for the test was about 2 km. The network analyser used to generate the test signal and to measure the phase of the return signal was stabilized with a GPS-derived 10 MHz reference.

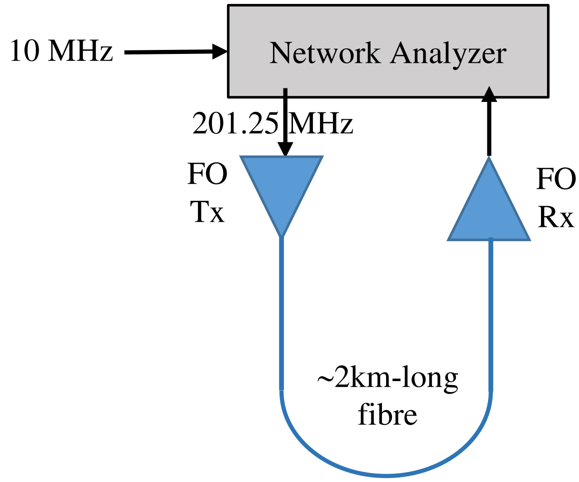

Figure 2: Schematic diagram of the loopback setup for testing the phase stability of the reference signal distributed on a fibre-optic link.

The 201.25MHz RF signal generated by the network analyser was fed into a Miteq LBL-10M3G analog fibre-optic link (FOL) transmitter, which sent the signal on the ~2km fibre path, and the FOL receiver fed the RF signal on coaxial cable back into the network analyser for the phase measurement.

The phase of the received signal relative to the transmitted signal is shown in Figure 3. A variation of >15° was seen over the course of the test period of a few days.

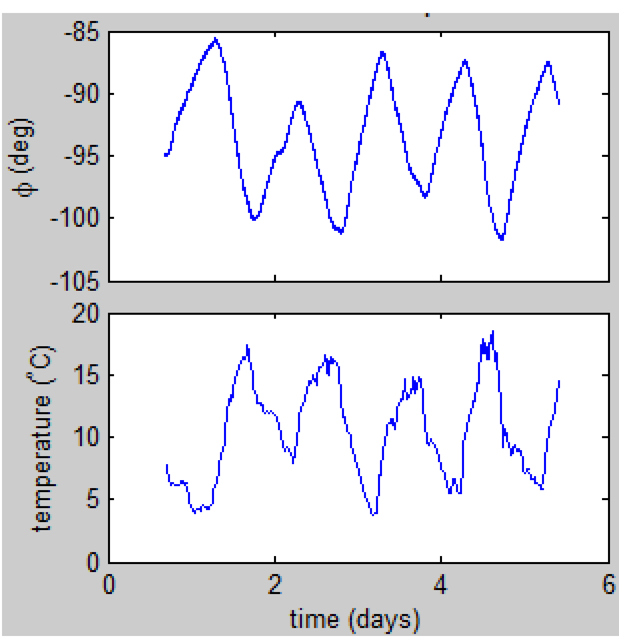

Figure 3: Results of the loopback test.

The shorter (several minute) stability of the signal phase would enable the Δt linac tune-up process, but we were motivated to find a way to stabilize the phase to enable greater use of the phase measurements.

Because the reference distribution was not part of the original scope of the BPPM project, an economical solution is highly desired.

STABILIZATION SCHEME

The stabilization scheme described here works as follows: Both 201.25MHz and 805MHz reference signals are transmitted to a BPPM chassis. Assuming the changes in group delay are the same for the two signals, the changes in phase of the 805MHz will be four times those of the 201.25MHz signal. By monitoring both signals at the BPPM chassis, the change in phase of the 201.25MHz signal can be deduced and corrected.

The individual changes to the phases of the 201.25MHz and 805MHz can't be measured, but the phase of one relative to the other can. The phase of the 805MHz signal will change four times as much as the 201.25MHz:

$$\Delta\phi_{805} = 4 \times \Delta\phi_{201}$$

$$\theta \equiv \Delta\phi_{805} - \Delta\phi_{201} = 3 \times \Delta\phi_{201}$$

The change in the relative phase between the two signals is 3 times the change in phase of the 201.25MHz signal. This is illustrated in Figure 4.

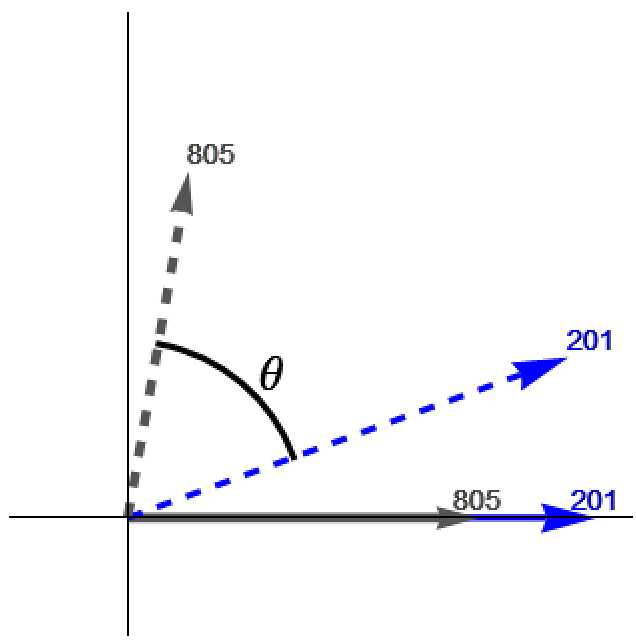

Figure 4: Phasor diagram illustrating the stabilization scheme. The original phasors are shown as solid arrows, and the phase-shifted phasors, at some hypothetical later time, are shown as dashed arrows. The quantity that can be measured is the relative phase of the two signals, θ. In this example, the 201.25MHz signal has shifted by 20° and the 805MHz has shifted by 4 times that amount, 80°. The phase between them is 60°, which is 3 times the shift of the 201.25MHz signal.

ISBN 978-3-95450-176-2

This stabilization scheme relies on identical group delays for the two signals. On coaxial cable this would probably not be the case, however on the fibre-optic link the signals are transmitted as light of a single wavelength; the group velocity doesn't depend on the signal frequency.

To test the feasibility of this correction scheme we set up a single 4-port network analyser to transmit and receive both 201.25MHz and 805MHz signals on two FOLs, with all the fibres within a single bundle to ensure that they were subjected to nearly identical environments. (See Figure 5.)

The result of this test is shown in Figure 6. The corrected 201.25MHz reference signal varies by about 1° over the few-day test.

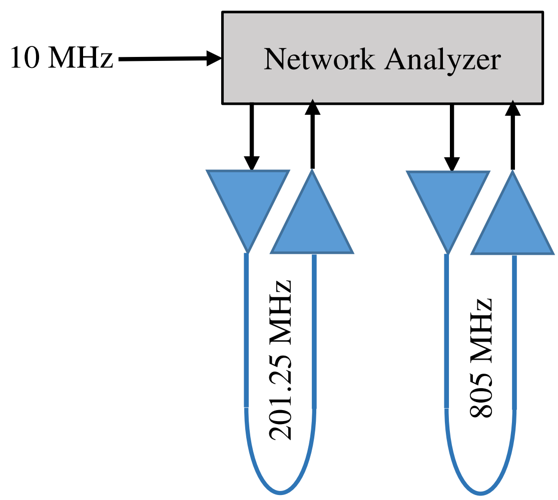

Figure 5: The loopback test setup for the dual frequency test.

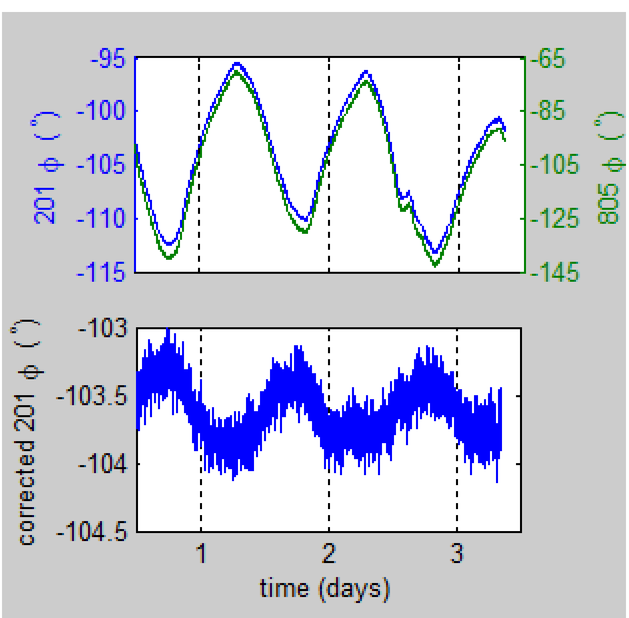

Figure 6: Results of the dual-frequency loopback test. The top plot shows the phases of the two signals, and the bottom plot shows the 201.25MHz phase corrected as described in the text.

PHASE MEASUREMENT

We are considering a couple of techniques for measuring the relative phase of the two signals. The challenge lies in the fact that they are of two different frequencies. One possibility is to use a diode-based frequency multiplier to convert the 201.25MHz signal to 805MHz. This requires several external analog components including the multiplier, filter, and a splitter (because the 201.25MHz signal must be sampled also.)

Another possibility is to sample both signals; the extra ADC input ports on the BPPM processor mentioned above could accommodate the additional signal. A copy of the 201.25MHz signal can then be digitally converted to 805MHz as shown in the following equations:

$$\cos(4wi) = 8\cos^4(wi) - 8\cos^2(wi) + 1$$

Where w is the phase advance per sample interval and i is the sample index number. By defining $\cos(wi)$ to be the 201.25MHz reference samples, it can be up-converted to 805MHz to allow a phase measurement.

The RF signals into the BPPM system are sampled at 240Msamples/sec; this is below the Nyquist frequency for both reference signals. Numerical simulations of the process indicate that the technique works well even with such under-sampling.

This digital up-conversion and the subsequent phase measurement require several arithmetic blocks in the FPGA-based signal processing unit, and few FPGA resources are available beyond those required for the BPPM functionality; we are evaluating whether this can be accommodated.

SUMMARY

We've described a scheme for stabilizing a reference signal for a beam phase measurement that involves distributing a harmonic of the reference signal and observing the change in phase between the reference and its harmonic. A correction for the reference can be deduced from this relative phase measurement. We are currently evaluating how to implement this correction scheme.

ACKNOWLEDGEMENT

We thank Dan Young for help with the fibre-optic infrastructure at LANSCE, and Phil Torrez, Lawrence Castellano, and Mark Prokop for providing access to the signals from the master reference oscillator.

ISBN 978-3-95450-176-2

DIAGNOSTICS CHALLENGES FOR FACET-II*

C. Clarke†, S.Z. Green, C. Hast, M.J. Hogan, N. Lipkowitz, G. White, V. Yakimenko, G. Yocky, SLAC National Accelerator Laboratory, CA 94025, USA

Abstract

FACET-II is a prospective user facility at SLAC National Accelerator Laboratory. The facility will focus on high energy, high brightness beams and their interaction with plasma and lasers. The accelerator is designed for high energy density electron beams with peak currents of approximately 50 kA (potentially 100 kA) that are focused down to below 10x10 micron transverse spot size at an energy of 10 GeV. Subsequent phases of the facility will provide positron beams above 10 kA peak current to the experiment station. Experiments will require well characterised beams however the high peak current of the electron beam can lead to material failure in wirescanners, optical transition radiation screens and other instruments critical for measurement or delivery. The radiation environment and space constraints also put additional pressure on diagnostic design.

INTRODUCTION

FACET (Facility for Advanced Accelerator Experimental Tests), a User Facility that delivers uniquely high powered multi-GeV electron and positron beams to its experimental program, completes its operations in 2016. FACET-II is a proposed upgrade to FACET currently at the conceptual design stage (Fig. 1). Its primary purpose is to support the development of advanced high-gradient techniques for acceleration (e.g. plasma wakefield acceleration [1,2] (PWFA) and dielectric wakefield acceleration [3] (DWA)). The high power beams, particularly in combination with the facility's multi-terawatt laser system [4], are also in demand by groups developing diagnostics in extreme regimes and studying materials, for example by using terahertz (THz) radiation in THz pump-laser probe experiments.

FACET-II will deliver improved electron beam quality due to advances in technology predominantly the radio frequency (RF) photocathode gun and injection system. It is expected that there will be a factor five longitudinal peak current improvement over FACET and a factor three improvement in transverse area. Though beam energy is 10 GeV (half that of FACET), the tighter bunches will produce much higher peak currents and associated electromagnetic fields (Table 1).

Note that the beam parameters are not independent and configurations are developed for experiments with an understanding for what parameters are most critical and what can be compromised on. Delivering both electrons and positrons adds additional constraint as the two systems are tied together in a shared linac and changing parameters of one may affect the other. Anticipated starting beam parameters are given in Table 2 and are a more relaxed set of beam parameters that can satisfy the requirements for early experiments.

Table 1: Ranges for FACET-II Beam Parameters Considering Design Limits for Electrons and Positrons Delivered to the Experimental Area. Note that the Start-up Beam Configuration will be Relaxed Parameters Shown in Table 2.

Parameter	Electrons	Positrons
Energy [GeV]	4.0-13.7	4.0-13.7
RMS Energy Spread [%]	0.4-1.8	0.5-1.5
Charge per pulse [nC]	0.7-5.0	0.6-2
Bunch Length σ_z	1-20	7-11
Beam size transverse σ_x [μm]	6-20	10-25
Beam size vertical σ_y [μm]	6-10	7-10
Peak Current [kA]	10-100	12-15
Repetition Rate [Hz]	1-30	1-5
Average beam power [kW]	0.1-4.2	0.005-0.14

FACET-II Challenges

The FACET-II injector, linac, chicane and final focus performance has been studied through the 6D particle tracking codes *Impact-T* [5] and *Lucretia* [6] which includes longitudinal and transverse wakefields, coherent synchrotron radiation (CSR), incoherent synchrotron radiation (ISR) and third order optics (e.g. chromatic effects). Dynamic errors from sources of jitter were studied (the dominant sources are phase jitter in the first stage of the linac, timing jitter on the laser used for the injector and position jitter of the laser).

At FACET-II, we expect many of the first experiments to be studies of PWFA with the requirement on the beam parameters that peak current for both the electron bunch and the positron bunch is greater than 10 kA. For this beam configuration, the tracking studies with errors from jitter sources showed that some shots may have a peak current of 80 kA though the average is 30 kA. It cannot be prevented that we achieve sporadic shots of high peak current which can damage intercepting material in a single shot.

The configuration for PWFA does not lead to the highest peak current FACET-II can deliver. Figure 2 shows the variation of peak current and bunch length with electron bunch charge which is controlled through collimation of high and low energy parts of the beam in the bunch compressor chicanes. When the configuration is optimised for high peak currents, peak currents in excess of 100 kA can be achieved.

These extreme beams present challenges for diagnostics just as they create opportunities for experiments.

* This work performed under DOE Contract DE-AC02-76SF00515.
† cclarke@slac.stanford.edu

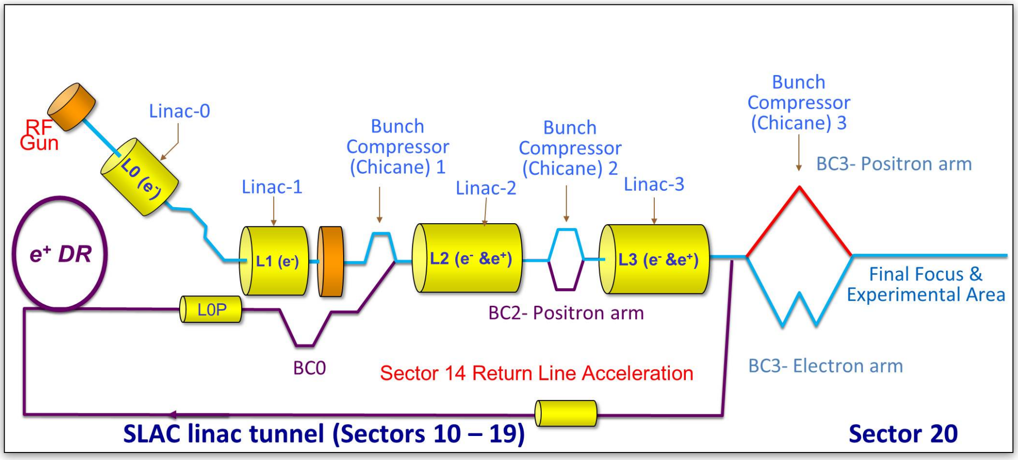

Figure 1: Overview of FACET-II. Electron and positron beams are delivered to the experimental area after multiple compression stages resulting in high peak current beams at the point of delivery.

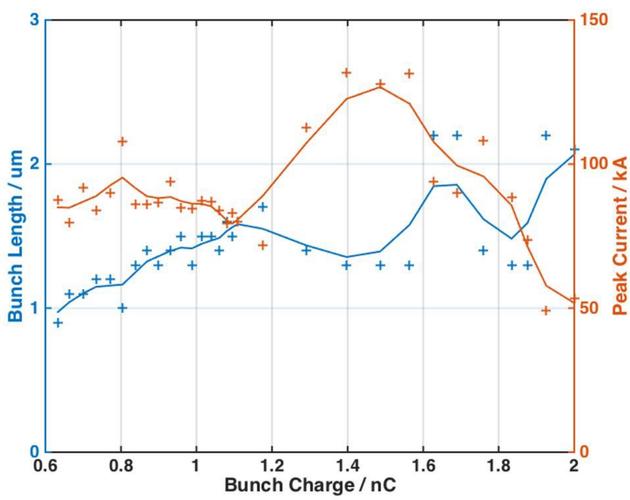

Figure 2: Charge is controlled with collimators in the bunch compressors (magnetic chicanes) that selectively collimate high and low energy offset tails of the beam from an initial charge of 2 nC from the RF photocathode gun. This affects the bunch length as shown. Maximum peak current occurs around 1.5 nC for electrons.

EXPERIENCE FROM FACET

FACET's experimental area is situated after three bunch compression stages and a final focus resulting in beams 20 μm r.m.s both transversely and longitudinally. Peak current is typically above 10 kA. Diagnostics in the experimental area change regularly depending on the experiments installed and many are built or otherwise provided by the experiment teams.

Optical Transition Radiation Profile Screens

Profile monitors based on optical transition radiation (OTR) were installed in the experimental area. Thin (1 μm) titanium foils were used to minimise emittance growth such that the profile screens upstream of experiments could be inserted during data-taking, giving shot-by-shot measurements of the transverse beam size entering the experiment.

During beam operation, these titanium foils broke. A single shot, when the beam was high enough density, was sufficient to make the entire screen unusable as the thin screen tore from a single hole.

This led to a redesign of the foil holder to allow several screens to be installed at once and driven in with a stepper motor vacuum feed-through. This allows the operator to move on to a fresh screen once one is damaged.

For screens installed at or close to the beam waist, thicker targets (500 μm) were installed which would not tear after a single spot of damage. If the thicker targets accrued a damage-spot, the target could be moved a few hundred microns to a fresh area. Figure 3 shows a 500 μm thick titanium disk that has been damaged in several places by the electron beam at FACET. Figure 4 shows a magnified image of one of the holes formed by multiple beam shots. When the beam is high enough density to cause damage, it can cause damage in a single shot.

FACET experience has shown limited success in using OTR screens for beam size tuning at the beam waist. However, they been used very effectively away from the beam waist. Screens are placed upstream and downstream of the beam focus to image transverse tails that appear at different phases. At these locations, the beam size is larger and the screens are not damaged.

Wirescanners

Beam size tuning at FACET most commonly relies upon wirescanners. The FACET optics can be set to move the waist of the beam to various locations in the experimenter area. Beam tuning usually occurs with the beam waist set to a wirescanner location. After beam tuning, the waist is shifted to the experiment "interaction point" (IP).

The wire scanners installed at FACET use 60 μm thick tungsten wires with gold coating to enable them to be sol-

ISBN 978-3-95450-176-2

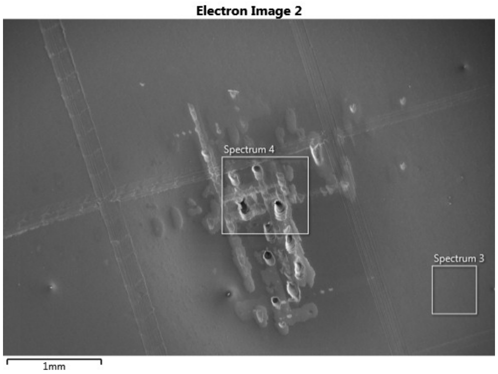

Figure 3: Titanium target with multiple regions of damage caused by multiple shots of the FACET electron beam.

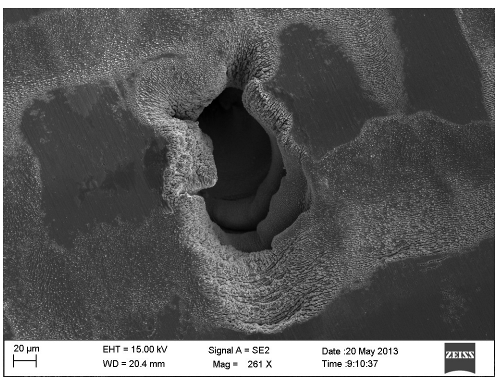

Figure 4: Magnification of a hole caused by the FACET electron beam. Material is 500 μm titanium.

dered. A particular wirescanner was installed close to the PWFA IP. After three months of beam operations, the wires were inspected. The gold had melted but the tungsten showed no signs of damage (Fig. 5). At FACET's beam parameters, wirescanners with tungsten wires were usually a reliable diagnostic for beam size but did break due to the beam on a couple of occasions.

Figure 5: Gold coating melted off wires used at IP for 20 by 20 beams.

Development by Experiment Teams

Other beam diagnostics have been implemented or developed by user groups to complement the basic tools for operators to deliver. Many diagnostics when developed by one team are subsequently used by other teams or the accelerator operators to deliver beam parameters that match specific needs for an experiment.

These additional diagnostics include electro-optic sampling for measuring the timing between laser and electron beam developed by the E-210 Trojan Horse experiment [7] team. Their experiment requires a laser pulse 250 fs in advance of the electron beam and their developed diagnostic allows them to adjust the timing of the laser appropriately and record the delay on a shot by shot basis.

Diagnostics to understand the beam-plasma interaction for PWFA experiments included a Cherenkov light-based profile monitor [8] and a KODAK LANEX (efficient rare-earth phosphor) screen to use in combination with a magnetic spectrometer to measure the energies of the "spent" wakefield-driving bunch and the plasma-wakefield-accelerated trailing bunch. LANEX screens were also used to image the x-rays which inform on the beam dynamics within the plasma. Thin metal sheets of various materials were used to convert the x-rays and provide information on the x-ray energy. An x-ray spectrometer consisting of bricks of alumina and x-ray sensitive diodes was tested in FACET but the backgrounds were high and the data hard to interpret leading to the preference to use screens.

Bunch profile diagnostic development based on reconstructing the profile from the Smith Purcell radiation [9] has also taken place as has measuring the properties of coherent transition radiation [10] and extrapolating electron bunch properties.

Any system that introduces materials to the beam path suffers some degree of beam damage and needs to be extracted from the beam path when not critical and needs a regular replacement schedule. In particular, this includes the LANEX screen which needed replacement after a few days of use.

Mechanisms for Material Failure

The damage to the foils and wires in FACET is primarily due to heating of the material from Ohmic losses. Contributions from electromagnetic showers are small in comparison and the average beam power is low due to the low repetition rate (1-10 Hz).

The impinging beam has strong electromagnetic fields that induce currents in the material. Calculations [11] solving for the induced currents indicated that with the optimally tuned FACET beam (20 μm for σ_x, σ_y and σ_z with 3.2 nC bunch charge), we were close to the critical conditions for failure of tungsten wires and titanium screens due to melting. This matches our operational experience. Usually once beam conditions were already sufficient for experiment delivery, they were not tuned further.

Failure of material will certainly occur if the material temperature rises above the melting point of the material. Typically, flaws in the material mean that failure occurs earlier. FACET experience saw this in particular for the 1 μm foils which were deposited thin films and not rolled material. Also, initially ductile materials could become brittle and eventually fracture due to repeated and excessive temperature increases below the melting point. This meant

ISBN 978-3-95450-176-2

that material failure occasionally happened without the beam density being unusually high.

FACET-II EXPECTATIONS

FACET-II diagnostics at the point of delivery will initially be based on FACET diagnostics. Initial beam parameters are not expected to be pushing to the highest peak currents but instead will be ~10 kA, similar to FACET (Table 2). Experiments that require consistently higher beam currents will be scheduled for later in the operation when experience and development of new diagnostics is more mature.

Table 2: Objective performance for FACET-II upon first operation.

Parameter	Electrons	Positrons
Energy [GeV]	10	10
Charge per pulse Q [nC]	2	1
Bunch Length σ_z	20	20
Normalised emittance [μm]	10	20

Estimates for Damage

The temperature increase from Ohmic losses go as $(\frac{Q}{\sigma_z})^2$ [12]. FACET-II is capable of both higher charge and shorter bunch lengths than FACET (the two parameters are coupled as shown in Fig. 2) and therefore material damage through heating by image currents is a high concern.

Through analytical calculation of induced image charges, the temperature increase due to Ohmic losses can be estimated. Assuming the optimal design parameters for the electron beam for the expected linac and compressor set up to deliver >10 kA electron and positron beams to the experimental area simultaneously, the temperature increase when the beam impinges upon tungsten wires is estimated by Equation 24 in analysis by Lin and Whittum [12]. This assumes round Gaussian bunches for simplicity and leads to the approximate result that the temperature rise in the wire is above 2 million degrees Celsius.

It is clear from both analytic calculation and FACET operational experience that the materials are already being used at their limits. Any increase in peak current for FACET-II is at the expense of using diagnostics at the beam waist. Intercepting materials should be positioned in locations where the beam size is over 200μm to avoid Ohmic heating about the melting point of tungsten.

Wirescanners at FACET-II

Following from the OTR strategy of installing many targets at once, our planned wire scanner design for FACET-II includes many wires. A prototype card was wired and is shown in Fig. 6. Although this would not permit measurement of the high peak current beams at the waist, this will mitigate against the case were the beam configuration has nominally more relaxed parameters with dynamic errors producing errant high peak charge shots. Software will be used

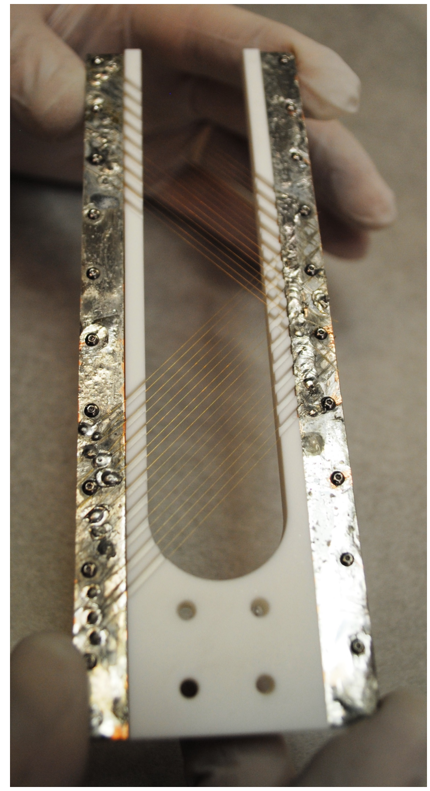

Figure 6: New wire card with multiple wires.

to "park" the beam as the card is being moved to go from wire-to-wire (as opposed to during wirescan measurements) to prevent all the wires from being broken if beam density is high enough. This is the initial plan for resuming beam operations with nominal delivered beam parameters close to FACET, sufficient for a great deal of the early experiments planned.

Multiple wirescanners can be used to interpolate the minimum beam size. A constraint on this is the limited beam line space available to be shared between delivery diagnostics and experimental apparatus. Compact wire scanners with integrated bellows that only need 4 inches of beam line have been designed for this area.

OTRs at FACET-II

The ladder design of multiple targets will continue to be used. Tungsten targets can be used and have already been effective for OTR in FACET. Normally, the screens are not used at the beam waist and will continue to be installed upstream and downstream of experiments.

Measuring Shorter Bunch Lengths

FACET uses a transverse deflecting cavity (TCAV) as its primary diagnostic for setting up the linac bunch compression correctly and adjusting collimators to deliver two bunches with parameters suitable for the wakefield experiments.

The TCAV has seen great success at FACET due to its operational simplicity. The existing X-band TCAV is in the

ISBN 978-3-95450-176-2

electron arm of the final bunch compression chicane (BC3 in Fig. 1). FACET-II plans to install a second TCAV in the positron arm of BC3 (the positron arm does not currently exist and will be installed for FACET-II) for setting up the bunch compression for positron delivery.

The resolution of an X-band TCAV is predicted to be 7 μm [13]. LCLS have measured bunch lengths as small as 1.5 μm with an S-band TCAV [14]. We expect to study the technology choice for FACET-II and the theoretical resolution limits further.

Measuring Two Beams

FACET-II will deliver two bunches to the experiments. Uniquely in the world, there will be a two bunch delivery configuration that will be one electron bunch and one positron bunch. In this configuration, positrons will be accelerated in the same linac as the electrons and compressed in reversely polarised chicanes (Fig. 1). Peak to peak separation for electron and positron bunches for PWFA are of the order 200 μm. FACET-II's design includes adjustment of the bunch separation.

Techniques for resolving the two bunches and measuring their separation were evaluated [13]. Two techniques were implemented for FACET (where the two bunches are created by collimation of a portion of a stretched electron bunch): the X-band TCAV and electro-optic sampling (EOS).

EOS was an effort by the E-210 Trojan Horse experiment team, an example of the close relationship between facility and user development of diagnostics. This single-shot, non-invasive diagnostic is still being developed and is planned to continue through FACET-II.

No concerns have been identified yet with operating EOS in FACET-II. Higher electric fields will permit the electro-optic crystal to be placed further from the beam. Experience at FACET shows that the electro-optic crystal surface can be damaged by a single direct hit from the electron beam but is still functional.

The TCAV could also be used to measure bunch to bunch separation. However, to streak both beams simultaneously to tune on the bunch separation would require a TCAV downstream of the separate electron and positron chicanes. Magnet density is high in this region as it is the final focus but finding a location in the shared beamline will be investigated. Downstream of the experimental area, apertures need to be large as there are many particles deflected due to the beam-plasma interaction that could damage a structure.

CONCLUSION

FACET-II will be a facility that will deliver high-density beams of electrons and positrons, ideal for creating exotic states of matter and researching advanced accelerator technologies such as PWFA and DWA. However, to take advantage of the capability of >100 kA peak current beams, diagnostics need to be designed for this regime. Typical operations are expected to start with peak currents close to those of FACET (10-20 kA) where we have operational experience and overcome concerns by building in redundancy.

ACKNOWLEDGMENT

We would like to thank Dieter Walz and Doug McCormick for diagnostic development at FACET and also the many experimenter groups that contributed to shared diagnostics for the FACET User Facility (E-200, E-201, E-206, E-210 and E-224).

REFERENCES

[1] M. Litos et al., "High-Efficiency Acceleration of an Electron Beam in a Plasma Wakefield Accelerator", Nature, vol.515 7525 (2014).

[2] S. Corde et al., "Multi-gigaelectronvolt acceleration of positrons in a self-loaded plasma wakefield", Nature, vol.524 7566 (2015).

[3] B. O'Shea et al, "Demonstration of Gigavolt-per-meter Accelerating Gradients using Cylindrical Dielectric-lined Waveguides", Proc. of IPAC, Dresden, Germany, TUOBB02 (2014).

[4] S.Z. Green et al., "Laser ionized preformed plasma at FACET", Plasma Physics and Controlled Fusion, vol.56 084011 (2014).

[5] J. Quiang, S. Lidia, R. D. Ryne and C. Limborg-Deprey, "Three-dimensional quasistatic model for high brightness beam dynamics simulation" Phys. Rev. ST Accel. Beams 9, 044204 (2006).

[6] `http://www.slac.stanford.edu/accel/ilc/codes/Lucretia/`

[7] B. Hidding et al, "Ultracold Electron Bunch Generation via Plasma Photocathode Emission and Acceleration in a Beam-Driven Plasma Blowout" Phys. Rev. Lett. 108, 3, 035001 (2012).

[8] E. Adli et al, "Cherenkov light-based beam profiling for ultrarelativistic electron beams" Nucl. Instrum. Methods Phys. Res., Sect. A, 783, 35-42 (2015).

[9] H. Andrews et al, "Reconstruction of the time profile of 20.35 GeV, subpicosecond long electron bunches by means of Coherent Smith-Purcell radiation" Phys. Rev. ST Accel. Beams 17, 5, 052802 (2014).

[10] Z. Wu et al, "Intense terahertz pulses from SLAC electron beams using coherent transition radiation" Rev. Sci. Instrum. 84, 022701 (2013).

[11] G. Stupakov, "Melting thin foils by incident relativistic electron bunch," SLAC-PUB-15729 (2013).

[12] X. E. Lin and D. H. Whittum, "Image Current Heating on a Metal Surface" Phys. Rev. ST Accel. Beams 3, 101001 (2000).

[13] M. D. Litos et al, "Evaluation of Temporal Diagnostic Techniques for Two-Bunch FACET Beam," Conf. Proc. C 110328, 568 (2011).

[14] H. Loos, "LCLS accelerator operation and measurement of electron beam parameters relevant for the x-ray beam," SLAC-PUB-15422 (2013).

ISBN 978-3-95450-176-2

SUB-PICOSECOND SHOT-TO-SHOT ELECTRON BEAM AND LASER TIMING USING A PHOTOCONDUCTIVE THz ANTENNA

E. Curry, P. Musumeci, UCLA, Los Angeles, CA 90095, USA
B. T. Jacobson, A. Murokh, RadiaBeam Technologies, Santa Monica, CA 90404, USA

Abstract

Temporal synchronization systems, which measure electron beam time of arrival with respect to a laser pulse, are critical for operation of advanced laser-driven accelerators and light sources. State-of-the-art synchronization tools, relying on electronic e-beam response and photodetector laser response are limited to few GHz bandwidths in most practical configurations. This paper presents a temporal diagnostic instrumentation based upon a photoconductive THz antenna, which could offer an inexpensive and user friendly method to provide shot-to-shot relative time of arrival information with sub-picosecond accuracy. We describe the overall instrument design and proof-of-concept prototype results at the UCLA PEGASUS facility.

INTRODUCTION AND MOTIVATION

Many experiments today involve the careful coordination and synchronization between pulsed laser beams and accelerated charged particle beams. Examples include inverse Compton light generation, laser driven plasma wakefield acceleration, and plasma photocathode injectors. The two most widely used diagnostic systems for measuring synchronization which are capable of providing sub-ps or better timing resolution are BPM pick-ups [1] and fast photodiodes equipped with very high bandwidth oscilloscopes and electro-optical based encoding techniques [2]. The first method requires careful cable trimming and very expensive oscilloscopes. Electro-optic sampling (EOS) methods require careful optical alignment of birefringent crystals and many optical components and relatively high fields to induce non-linear processes.

THz photoconductive antenna (PCA) devices can both detect and produce single-cycle THz fields when used in conjunction with a pulsed laser system (typically < 100 fs pulse widths) [3]. The devices are comprised of a substrate wafer of photoconductive material, such as low-temperature GaAs, which is grown to have modified properties to enhance the carrier mobility in order to respond at ps and sub- ps timescales. Conductive metal is patterned onto the photoconductive substrate in the form of a resonant antenna (dipole, log-spiral, or other geometries) with a small gap left in the antenna structure. When the LT-GaAs in the antenna gap is illuminated with laser radiation with a photon energy above the photoconductive threshold, any incident THz fields will drive current on the antenna which can be measured with a transimpedance amplifier. The device will in this way be “gated” by the laser pulse, the width of which sets a lower limit on the temporal resolution of THz field amplitude detection.

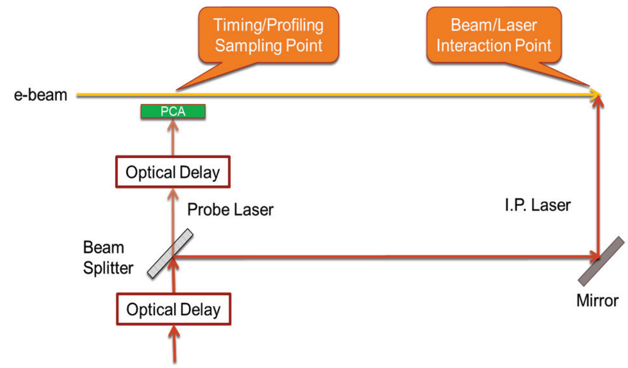

Figure 1: Schematic overview of a THz photoconductive antenna used as a timing synchronization instrument for short pulsed beams. The system could be used for longitudinal profile measurements for beams of longer bunch lengths

BENCH-TOP TESTS

For our proof of concept measurements, we have used the Menlo Systems Tera8-1 photoconductive antenna. The THz pulse used to test the detection capabilities of the PCA was produced through pulse-front-tilted optical rectification [4][5] of a 45 fs Ti:sapphire laser pulse centered at 800 nm with a 30 nm bandwidth. A beam splitter removed a fraction of the initial IR to act as the gating pulse for the PCA. Pulse-front tilting of the remaining IR was accomplished with a grating and then imaged onto stoichiometric lithium niobate to produce a picosecond-scale single-cycle THz pulse. The peak field of the THz pulse was set by the incident IR power and ranged from 300 kV/ m to 4.6 MV/ m. The THz pulse was collimated and then refocused down to a 2 mm spot size at the PCA using a pair of off-axis parabolic mirrors.

Initial measurements with the PCA varied greatly depending on the spot size of the IR pulse that illuminated the antenna. A 50 μm diameter pinhole was placed in front of the PCA to ensure a reproducible IR spot size and limit the IR illumination to the region of the antenna gap. Proper alignment of the pinhole with the antenna gap introduced a substantial challenge to the THz detection set-up, but resulted in significant improvement to the detection sensitivity and timing resolution. The pinhole was incorporated into the antenna mount design and alignment was optimized using the bench-top THz source. With the pinhole locked in place, the antenna mount could then be illuminated with a large (several mm) IR spot size, eliminating the challenge of precise optical alignment.

ISBN 978-3-95450-176-2

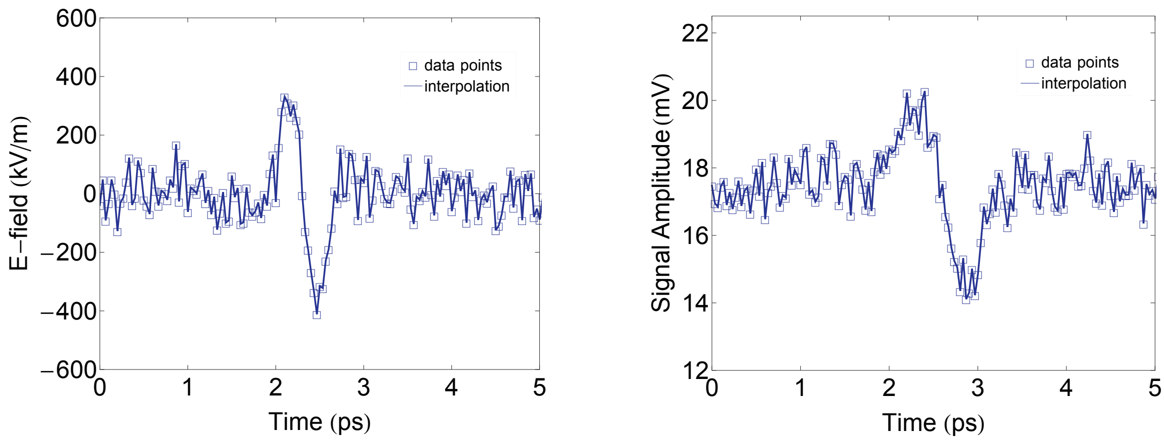

(a) (b)

Figure 2: (a) EOS measurement and (b) PCA measurement of the single-cycle THz pulse generated through optical rectification on the bench-top set-up. The temporal profiles obtained by the two methods show comparable sensitivity to low THz power.

The temporal field profile measured by the PCA was compared to an EOS measurement taken with zinc telluride at the focus of the THz pulse. The IR pulse that provided the gating for the PCA was used as the probe pulse for EOS. Within ZnTe, a THz field results in a rotation of the slow and fast axis of the crystal. When the THz pulse and linearly polarized probe pulse were coincident on the ZnTe, the polarization of the probe pulse was rotated. In the "balanced detection" configuration, after a quarter waveplate and Wollaston prism, a pair of photodiodes measured the orthogonal polarization components of the probe pulse to detect the rotation. The change in relative intensity was used to calculate the THz field.

Using the EOS diagnostic, we were able to determine the THz field seen by the PCA. At 350 kV / m the PCA sensitivity was comparable to that of the EOS measurement, as shown in Fig. 2. The temporal profile and timing resolution of the two methods were also in good agreement.

INSTALLATION AND BEAM TEST AT PEGASUS

The PCA has been mounted on the beamline at the UCLA PEGASUS laboratory [6] [7]. A schematic of the facility is shown in Fig. 3. The antenna is situated perpendicular to the beamline with the polarization of the dipole oriented vertically in order to pick up the radially-polarized single-peaked THz pulse that is produced by the electron bunch passing above the detector. A manually operated actuator controls the proximity of the PCA mount to the beam axis, as seen in Fig. 4. The time of arrival of the IR gating pulse for the PCA has been measured and adjusted to match the expected arrival of the electrons. Fine tuning of the IR pulse delay will be made using a remotely operated translation stage. Measurements of the electron bunch charge produced at PEGASUS for this test by a downstream Faraday cup give

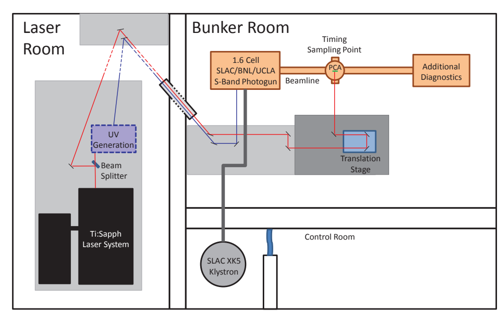

Figure 3: Simplified schematic of installation on the PEGASUS beamline.

an estimated charge of 50 pC. The electron beam can be steered and focused using the steering magnets and solenoid mounted on the beamline. The position of the electron beam relative to the PCA mount can be monitored using a YAG screen and CCD camera.

The operation of the klystron results in significant distortion of the PCA signal. While the photocurrent established by the IR pulse is distinguishable from background, indicating that we should be able to see the time-dependent THz signal, we are making additional modifications to the signal amplification equipment in order to filter the noise associated with the klystron. Once we have optimized the signal to noise ratio of the photocurrent, we will begin measurements of the PCA signal for varying IR pulse delay to detect the time-dependent THz signal.

CONCLUSION

Bench-top results using commercially available THz photoconductive antenna chips are promising, indicating temporal resolution on the order of several 100 fs and sub-ps synchronization. At the time of this publication, installation

ISBN 978-3-95450-176-2

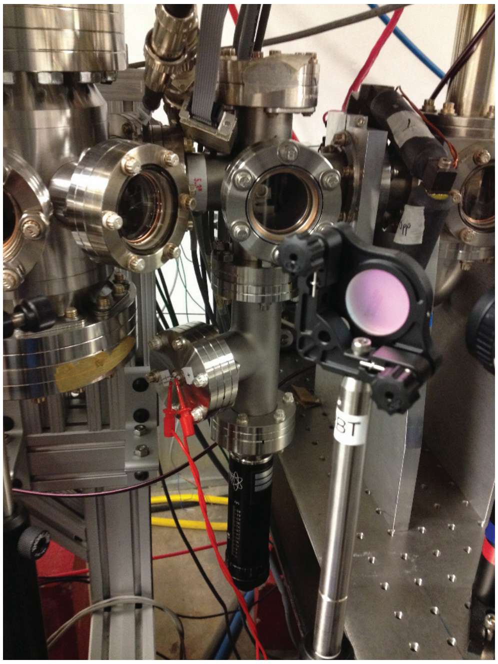

Figure 4: PCA mount with actuator installed in cross on PEGASUS beamline.

is complete and beam based measurements are underway. The first experimental runs have demonstrated THz and laser correlated signal, however noise from the accelerator system may be large enough to hinder acquisition of delay scans. In order to enhance sensitivity for optimal use in accelerator diagnostics in noisy environments, a collaboration with chip-level device manufactures producing customized photoconductive THz detectors is expected to yield up to 30 times sensitivity gain. Next generation detectors are expected in late October for testing. The results from these upcoming experiments at PEGASUS will serve to evaluate the use of photoconductive antennas for synchronization of GHz repetition rate accelerator diagnostic systems and for plasma photocathode injection requiring sub-picosecond time of arrival precision.

REFERENCES

[1] Aleksandar Angelovski et al. In: *Physical Review Special Topics-Accelerators and Beams* 18.1 (2015), p. 012801.

[2] M. Brunken et al. DESY, 2003.

[3] Daryoosh Saeedkia. In: *Proceedings of the 5th European Conference on Antennas and Propagation (EUCAP)*. 2011.

[4] A.G. Stepanov, J. Hebling, and J. Kuhl. In: *Applied physics letters* 83.15 (2003), pp. 3000–3002.

[5] J Hebling et al. In: *Applied Physics B* 78.5 (2004), pp. 593–599.

[6] P Musumeci et al. In: *Physical review letters* 100.24 (2008), p. 244801.

[7] J. T. Moody et al. In: *Physical Review Special Topics-Accelerators and Beams* 12 (7 2009), p. 070704.

ISBN 978-3-95450-176-2

NSLS2 FILL PATTERN MONITOR AND CONTROL*

Weixing Cheng#, Bel Bacha, Yong Hu, Guimei Wang, Om Singh
NSLS-II, Brookhaven National Laboratory, Upton, NY 11973

Abstract

NSLS2 storage ring has harmonic number of 1320. Possible fill patterns include multi bunch train(s) followed by ion cleaning gap(s), hybrid fill with single bunch in the ion gap. Storage ring filling pattern can be measured using button BPM sum signal together with high speed digitizer or oscilloscope. Button BPM sum signal typically has dynamic range of 10^-2 to 10^-3. Nonlinearity of BPM sum signal dependence on beam position has been characterized. In preparation for high dynamic single bunch current measurement, a filling pattern monitor system using synchrotron radiation is under development. Besides, the storage ring filling pattern can be controlled using the bunch cleaning function integrated in the bunch-by-bunch feedback system. Results of these two filling pattern monitors and bunch cleaning will be presented.

INTRODUCTION

NSLS2 storage ring has been commissioned recently and it's open for user operation. The ring is using super conducting 500MHz single cell cavity. There are maximum of 1320 bunches that can be filled in the ring. There is one cavity available with RF voltage at 1.78MV. 300mA total beam current were able to be stored with this cavity. Once the second super-conducting cavity is available in the coming months, high storage current can be achieved. NSLS2 storage ring was designed to have weak dipoles and damping wigglers (DW) to further decrease the horizontal emittance to sub-nm level. Depending on RF gap voltage, number of DWs used and bunch lengthening due to broadband impedance, typical bunch lengths at NSLS2 storage ring are between 15-40ps.

Arbitrary fill pattern can be generated in the NSLS2 storage ring. Typical fill pattern includes a long bunch train of about 1000 bunches (80% fill) followed by an ion-clearing gap. Bunches are separated by 2ns in the bunch train. Camshaft single bunch can be added in the ion gap for future time correlated experiments. At the current user operation, a single bunch is filled with similar bunch current to the main train bunches. The single bunch is used to monitoring betatron tune continuously. Even with the ion gap, fast ion instabilities have been observed [1,2] along the long bunch train. With bunch by bunch feedback, ion instabilities can be suppressed well up to 300mA, bare lattice at nominal chromaticity of +2/+2. As the total beam current increasing and machine emittance (especially vertical plane) decreasing like coupling correction, fast-ion effect will be more severe. There is possibility to fill the ring with 4 (or 6) bunch trains. Each train will have ~250 bunch filled followed by a short ion gap of 80 buckets. Camshaft single bunches can be populated in the ion gaps as well.

During top-off operation at 500mA, beam lifetime is expected to be around 3 hours. To keep the total beam current variation within 1% and top off injection period > 1 minute, 7nC charge per shot are required to be delivered to the storage ring. Relative bunch to bunch current variation is specified to be within 20%. It's desired to measure the bunch to bunch current with better than 1% resolution. Fill pattern monitor and control is also important to various machine studies.

Button BPM SUM signal is not only determined by the bunch current, it may depend on the button size and BPM chamber geometry, cable attenuation, electronics attenuations, beam position and bunch lengths. For the fill pattern monitor BPM SUM signal, button geometry, cable and electronics attenuations are fixed once the system is installed. SUM signal nonlinearity dependence on the beam position has been analyzed in [3]. Figure 1 plots the two diagonal buttons SUM signal nonlinearity of the FPM BPM pickup. As can be seen, if the beam orbit is controlled within +/-6mm horizontally and +/- 3mm vertically, BPM SUM signal dependency on beam position is within 1%. With stored beam and orbit corrected, beam position at the FPM pickup is well within 1mm from the BPM geometric center, typically the SUM signal dependency on beam position can be neglected.

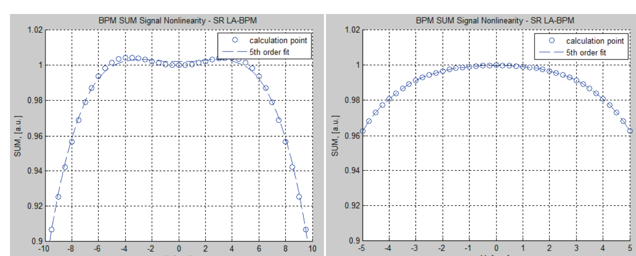

Figure 1: BPM SUM signal nonlinearity of two diagonal buttons. Two diagonal buttons SUM signal is used to measure the NSLS2 storage ring fill pattern.

Reflection of the button signal could lead to inaccurate measurement of the fill pattern, especially when there are high current bunches filled in the ring. As the capactive button is not 50 Ohm matched to the detection electronics, reflection signal is unvoidable. 3 dB attenuators have been added right after the button feedthrough which helped to supress the reflection signal but not able to eliminate it. Reflection signal can come from the HOM of the vacuum chamber structure where BPM pickup is mounted on. Figure 2 shows an example of 0.2mA single bunch filled in the ring, the signal peak amplitude was about 800mV (out of scale), there were

*Work supported by DOE contract No: DE-AC02-98CH10886
chengwx@bnl.gov

ISBN 978-3-95450-176-2

reflection peaks observed at ~40ns and 200ns away from the main peak. The reflection peaks had amplitude about 5mV, which is ~ 0.6% of the main peak signal.

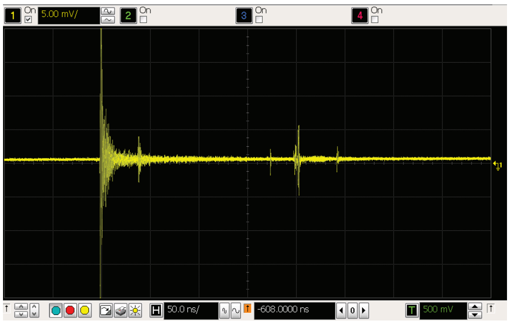

Figure 2: Reflection signals observed when a high current signal bunch was filled.

A time correlated single photon counting system (TCSPC) has been tested using visible light in the SLM diagnostic beamline. The setup is similar to other 3rd generation light sources [4,5], it has large dynamics range to measure the single bunch purity. The system can be used to measure the bunch to bunch fill pattern with better dynamics range and reasonable measurement time. As synchrotron light is used, TCSPC system has no position dependency or reflection issue.

FPM FROM BPM SUM SIGNAL

Storage ring filling pattern was measured from a dedicated BPM. Broadband hybrid SUM signal from diagonal buttons was send to high speed digitizer or 20GHz oscilloscope. Bunch filling pattern was calculated from pulse area or peak amplitude. Meanwhile bunch centroid can be used to measure beam synchronous phase, if the digitizer jitter is small. This could be a useful tool to detect the transient beam loading effect with long bunch train and ion gap fill. Shown in Fig. 3 is a typical bunch pulse observed on storage ring filling pattern monitor, using 20GHz oscilloscope. Red diamonds are the raw sampled data with 50ps separation.

To retrieve the peak amplitude and location with better resolution, 10 times interpolation was applied to the raw data. Interpolated data points are plotted as blue circles. Searched peak of interpolated point gives the green square in the figure, its amplitude was considered to be proportional to bunch current and its position as measured bunch arrival time (synchronous phase). Interpolated points have 5ps separation, the measured synchronous phase shall have accuracy better than 5ps, not including the trigger jitter. Storage ring revolution fiducial clock 378kHz was used for the 20GHz scope trigger, the fiducial signal from event timing system has jitter typically around 17ps relative to the beam signal. A lower jitter fiducial clock divided from the RF reference signal has been tested with jitter less than 3ps.

Synchronous Phase Measurement

To validate the synchronous phase measurement method, preliminary study was done by varying RF cavity voltage and recording the synchronous phase. From the synchronous phase vs. cavity voltage curve, energy loss per turn can be estimated. Assume bunch synchronous phase:

$$\phi_s = \phi_m + \phi_0 \tag{1}$$

Where ϕ_m is the measured synchronous phase and ϕ_0 is the constant due to delays.

At low bunch current, parasitic energy loss due to wakefield can be neglected, bunch synchronous phase and energy loss per turn due to synchrotron radiation has the relation:

$$eV_{rf} \sin\phi_s = U_{sr} \tag{2}$$

Where V_{rf} is RF gap voltage; U_{sr} is energy loss due to synchrotron radiations. Substitute Eq. 1 in to Eq. 2, we get:

$$eV_{rf} \sin\phi_m \cos\phi_0 + eV_{rf} \cos\phi_m \sin\phi_0 = U_{sr} \tag{3}$$

Let's define:

$$\begin{aligned} x &= eV_{rf} \cos\phi_m \\ y &= eV_{rf} \sin\phi_m \end{aligned} \tag{4}$$

Eq. 3 can be written as:

$$y\cos\phi_0 + x\sin\phi_0 = U_{sr} \tag{5}$$

From Eq. 4 and Eq. 5, one can see that by measuring the synchronous phase ϕ_m at different V_{rf} and fitting the *x, y* variables, energy loss per turn can be calculated from the fitting slope.

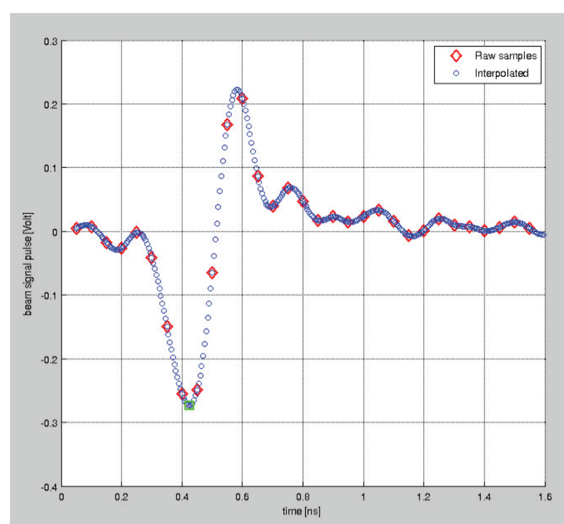

Figure 3: Storage ring filling pattern monitor signal from 20GHz real time sampling scope. Red diamonds were raw sample data points while blue circles were interpolated points by a factor of 10. Green Square is the searched peak of interpolated point, its amplitude was considered to be bunch current and its position was measured synchronous phase.

ISBN 978-3-95450-176-2

Figure 4 is the FPM measured synchronous phase at different RF gap voltage, with bare lattice (no DWs). 20 bunches were filled to 0.7mA, averaged synchronous phase from these 20 bunches was considered as measured results. Fitting the *x, y* values as defined in Eq. 4 yields the energy loss per turn for bare lattice to be 286.6 keV, this agrees well with the theoretical value of 287 keV. Three DWs in C08, C18 and C28 can be open/close at different gaps. Figure 4 (c) gives the measured energy loss per turn results with DW28 at different gaps.

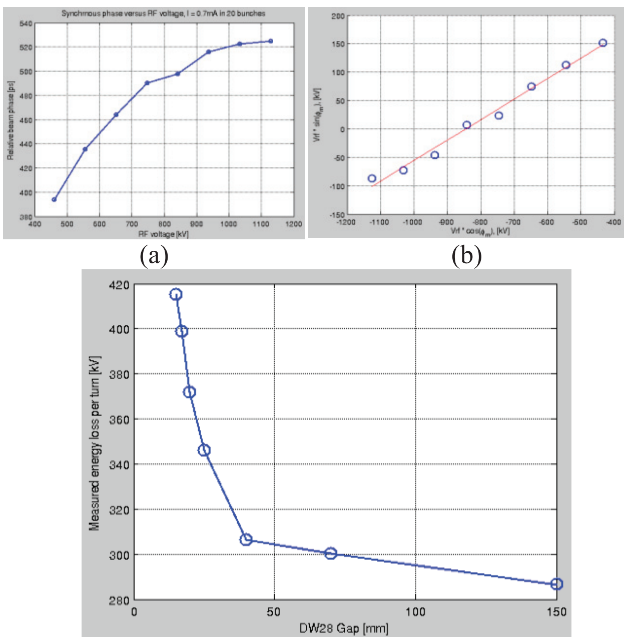

(a) (b) (c)

Figure 4: (a) measured synchronous phase at different Vrf; (b) Fitting the *x, y* values as defined in Eq. 4, blue points are the measured points, red line is the linear fit. Energy loss per turn is measured from the fitted line; (c) Measured energy loss per turn with DW28 closed at different gaps. The other two DWs were fully open.

FPM Calibration

As the bunch to bunch current varies a lot, it's important to check linearity of measured bunch peak voltage with different stored bunch current. With single bunch filled in the ring at 0.1mA to 0.6mA with 0.1mA steps, Fig. 5 plots the interpolated peak voltage at different single bunch current. FPM scope had fixed vertical scale of 500mV per division.

With bare lattice and Vrf = 1.78MV, measured bunch length changed from 15 ps to 22 ps with bunch current varied from 0.1mA to 0.6mA [6]. Peak voltage vs. bunch current had good linearity with this bunch lengthening effect.

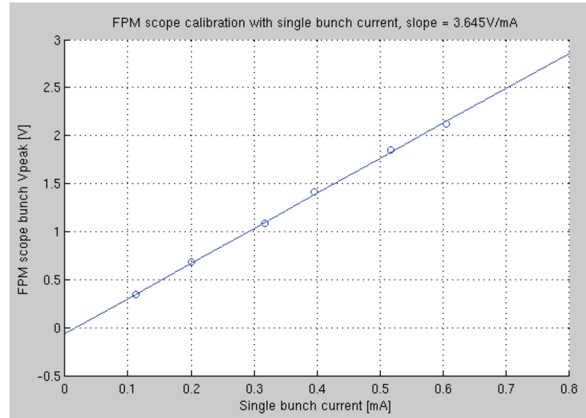

Figure 5: FPM scope measured peak voltage at different single bunch current. Scope vertical scale was fixed at 500mV per division.

Uniform Fill Pattern

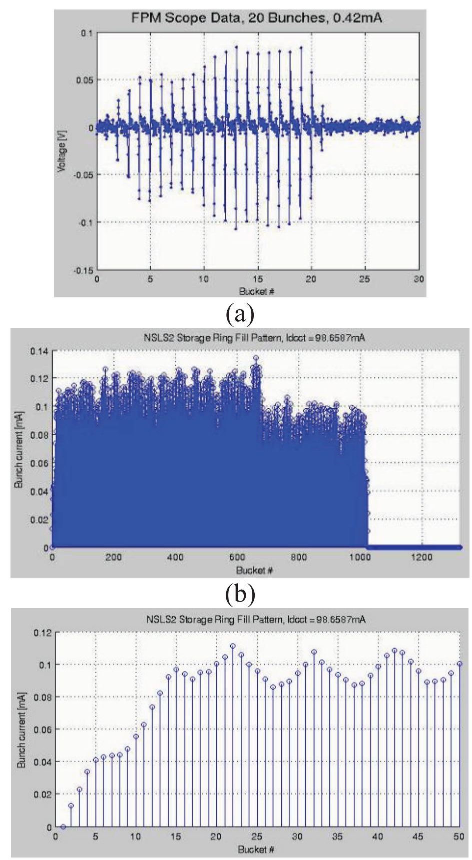

(a) (b) (c)

Figure 6: NSLS2 storage ring rill patterns. (a) Single shot injecting of 20 bunches stored in the ring, bunch to bunch current variation is mainly coming from the electron gun. (b) Typical fill pattern with 50% overlap fill, 20 bunches train was injected in the ring with target bucket increased by 10 between different shots of injections. Machine was filled to 99mA with 1000 bunches. (c) Zoom in the head bunches of the 1000-bunch train.

ISBN 978-3-95450-176-2

As discussed earlier, top-off injection requires ~7nC delivered to the storage ring per shot. Electron gun and injector are typically operated in multi-bunch mode to generate high charges. Gun pulse width can be adjusted to generate a pulse train of different bunches. At present 150mA user operation, typical bunch train from the injector includes 20 bunches with 2ns bunch to bunch separation. Bunch to bunch current variation is pretty big, as can be seen in Fig. 6 top plot. To have a more uniform fill pattern, overlap filling is typically used in between different injection pulses. With 20 bunches injection and 50% overlap fill, fill pattern at 100mA is typically like in Fig. 6 (b, c). RMS bunch to bunch current variation was able to be controlled within 10%, not including bunches in rise/falling edges.

As can been seen from Fig. 6 (c), even with the overlap fill, head/tail bunches in the long bunch train still have large bunch to bunch current variations, which is inherited from the un-even fill pattern of the injector. These head/tail bunches can be trimmed away using the bunch cleaning functions integrated in the bunch by bunch feedback system. After knock out the rise/falling edge bunches, rectangular shape bunch train can be generated. The best achieved fill pattern had 0.8% RMS bunch to bunch current variation, with 100mA stored in 1000 bunches.

FPM FROM TCSPC

Button BPM SUM signal may suffer from the position dependency nonlinearity, reflections and bunch length dependency etc. To avoid these issues, synchrotron radiation detection with a photon diode looks to be a good solution. For the isolated single bunch in the ion gap, it is important that there are no (very little) diffused electrons in the nearby buckets so that experiments will see a clean isolated x-ray pulse. Due to dark current from the gun and scattering, there will always be electrons escape from the main single bunch and captured in the nearby buckets. Single bunch purity is defined as ratio of electrons in nearby bunches to the main bunch. It's of great interest to measure the single bunch purity for the potential time resolved users. NSLS2 bunch by bunch feedback system has the integrated function to knock out unwanted bunches, similar to trim the head/tail bunches in the long bunch train. This method is very helpful to create a 'pure' single bunch so that there will be no polluted electrons nearby. While cleaning the bunches, there is little disturbance to the main bunch.

Using the visible light in SLM hutch, a time correlated single photon counting (TCSPC) system has been tested. Visible light was guided on to a test branch where a fast photo diode will generate a pulse whenever single photon was detected. The pulse was then amplified with an integrated broadband amplifier. PicoHarp300 [7] system was used to measure the photon arrival time relative to the ring revolution clock, which is 378kHz for NSLS2 storage ring. To avoid pile up, a pinhole and optical density filters are added before the photo diode to detect less than one photon per turn. Figure 7 shows the preliminary single bunch purity measurement results. A single bunch was filled in the ring with current ~0.2mA, TCSPC system was counting photons for 2 minutes. Before bunch cleaning, one can see there are unwanted photons coming 2ns, 4ns and 6ns later from the main single bunch. After cleaning these buckets were not seeing photons within the measurement duration. The single bunch purity was better than 1e-5. It's worth to note that with higher current in the single bunch, scattered electrons from the main bunch can be re-captured in the following buckets, depends on the bunch in-purity growth rate, periodical bunch cleaning may be necessary to guarantee a high purity single bunch.

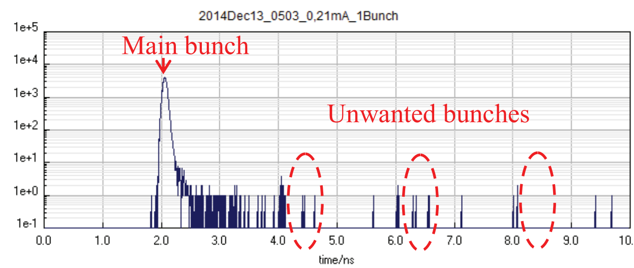

(a) Before bunch cleaning

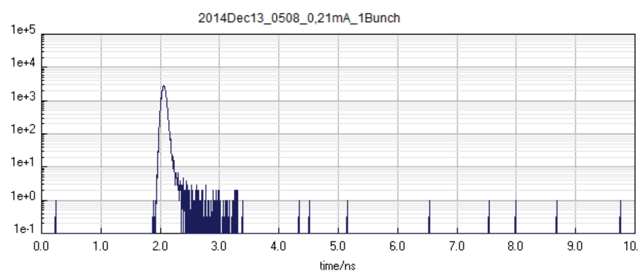

(b) After bunch cleaning

Figure 7: Single bunch purity measurement using timing correlated single photon counting (TCSPC) system. It counted photons for about 2 minutes with 0.2mA single bunch stored in the ring. Vertical scale is number of photons detected with the photo diode. (a) Before bunch cleaning, the single bunch purity was measured to be ~3e-4. (b) After bunch cleaning, single bunch purity is better than 1e-5.

If there are more than one bunches filled in the ring, photon counting system can count the photons from different bunches and determine which bunch is the photon coming from, this can actually be used to precisely measure the electron bunch fill patterns. Usually for fill pattern measurement, it can count with shorter time to have loose dynamics range.

Figure 8 plots are the fill pattern measured with 20 bunches stored in the ring, machine was delivering beam to beamline commissioning with low average current of 0.33mA. Upper plot shows the raw photon counting data generated from these 20 bunches. Processed fill pattern is in the lower plot. Both plots have linear vertical scale. Compared to the fill pattern measured from BPM SUM signal, photon counting system has better dynamics range, for example, bunch # 24 in Fig. 8 had ~ 0.7uA which is not easy to detect with button signal.

ISBN 978-3-95450-176-2

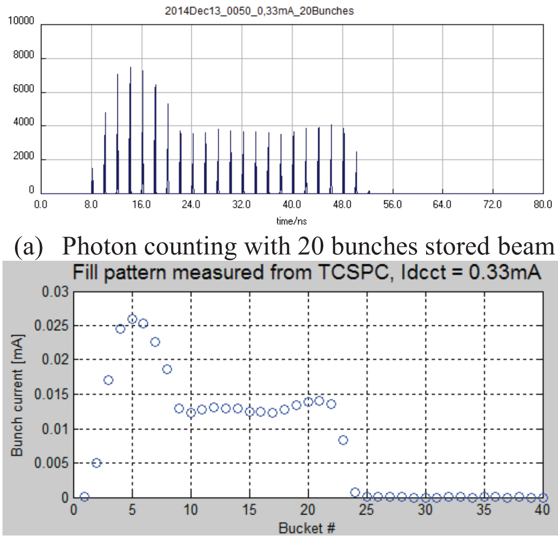

(a) Photon counting with 20 bunches stored beam

(b) Measured fill pattern

Figure 8: Fill pattern monitor from TCSPC system. 20 bunches were fill in the ring with average beam current of 0.33mA.

SUMMARY AND DISCUSSION

Two types of fill pattern monitors at NSLS2 storage ring have been used. Button BPM SUM signal digitized with high sampling rate scope (or digitizer) is the currently operational system. The system has dynamics range ~1% which is sufficient to measure the bunch to bunch current variation of 20%. Button SUM signal dependency on beam position has been calculated to be small. For the future camshaft fill pattern for time resolved experiments, when a high current single bunch filled together with a long bunch train with low bunch current, reflection signal from the high current bunch may overlap with the low current bunch signal, which might cause inaccurate fill pattern measurement.

Bunch synchronous phase can be measured by interpolating the 20GHz sampled data. With low jitter revolution fiducial as trigger, bunch phase can be measured with resolution of 5ps. This method has been used to measure the energy loss per turn with bare lattice and different DW gaps. The measured energy loss per turn agrees well with the theoretical calculation. When the beam had longitudinal instability during several studies, scope measured synchronous phase saw ~50 ps bunch to bunch motion. This had been cross checked on streak camera.

To generate a uniform fill pattern, overlap fill is implemented during the storage ring initial fill and top off. After trimming the rise/falling edges, typical bunch to bunch variation is within 10%.

A TCSPC system has been tested using visible light in the SLM diagnostic beamline. The photon counting system can measure the single bunch purity of the camshaft bunch. After bunch cleaning, single bunch purity was measured to be better than 1e-5. The system can be used to precisely measure the storage ring fill pattern. Compared to the button BPM based fill pattern system, photon counting fill pattern monitor will have better dynamics range with reasonable measurement time (~ 1 min). However, TCSPC is not able to measure the bunch synchronous phase and other transient effect like bunch current at injection.

The author thanks Dr. Takashi Obina from KEK, Dr. Guenther Rehm from Diamond Light Source and Dr. Jeff Corbett from SLAC on various information of photon counting measurement.

REFERENCES

[1] W. Cheng, et. al., "Commissioning of Bunch-by-bunch Feedback System for NSLS2 Storage Ring", IBIC'2014
[2] W. Cheng, et. al., "Observation of Ion-induced Instabilities at NSLS2 Storage Ring", this proceeding.
[3] W. Cheng, et. al., "Performance of NSLS2 Button BPMs", IBIC'2013
[4] C.A. Thomas, et. al., "Bunch purity measurement for Diamond", Nucl. Instr. Meth. A 566 (2), 762 (2006)
[5] J. Corbett et. al., "Bunch Pattern Measurement via Single Photon Counting at SPEAR3", IBIC'2014
[6] W. Cheng, et. al., "Longitudinal Bunch Profile Measurement at NSLS2 Storage Ring", this proceeding.
[7] https://www.picoquant.com/

ISBN 978-3-95450-176-2

LONGITUDINAL BUNCH PROFILE MEASUREMENT AT NSLS2 STORAGE RING*

Weixing Cheng#, Bel Bacha, Alexei Blednykh, Yongjun Li, Om Singh
NSLS-II, Brookhaven National Laboratory, Upton, NY 11973

Abstract

Longitudinal bunch profile has been measured at NSLS2 storage ring using streak camera. From the measured profile, bunch lengthening and synchronous phase information can be derived to study the single bunch collective effect. Single bunch lengthening effect has been measured for bare lattice and for other lattices with different insertion devices. The streak camera can also be setup for other beam physics studies, for example to measure the injection beam dynamics and fast ion effects. Y-z imaging was measured using cylindrical lenses. Single bunch y-z profile was measured at threshold current.

INTRODUCTION

Visible synchrotron light monitor (SLM) diagnostic beamline has been constructed and commissioned at NSLS2 storage ring. The diagnostic beamline utilizes the radiation from Cell 30 bending magnet B (BM-B), which is the second dipole magnet after injection straight section. The nominal source point is ~2.75mrad into the dipole. The beamline has acceptance of +/-1.5mrad horizontal and +/-3.5mrad vertical. Visible light from the dipole synchrotron radiation is reflected by in-vacuum mirror through a vacuum window. The visible light is guided into SLM hutch located on the C30 experimental floor. There are various optics setups on the 4'x10' optical table, currently there are four setups: 1) CCD camera for continuous beam profile monitoring, spatial resolution of the CCD camera was analyzed to be around 60 μm, which makes the direct imaging method possible to measure horizontal beam sizes (~100 μm). Vertical beam size at SLM source point is ~10 μm which is not possible to measure with direct x-y imaging. There are methods that can be tested using the CCD camera, such as double slit interferometer and π-mode beam size measurement. Preliminary test of double slit interferometer has been carried out during user operations. 2) Fast gated camera for transient x-y profile measurements. The camera has minimum gate width of 3ns which makes it suitable to measure turn to turn profile of individual bunches. 3) Test branch which is used for Time Correlated Single Photon Counting (TCSPC) system to measure the single bunch purity and fill pattern. 4) Streak camera for various longitudinal beam dynamics studies. Visible light can be directed to different cameras/detectors through beam splitter and flip mirrors. More information on the diagnostic beamline design and the commissioning results can be found at [1, 2].

Streak camera has been used for longitudinal bunch profile measurements. The camera is Hamamatsu C5680 with 2ps resolution and it includes synchroscan module M5675, slow sweep module M5677 and dual sweep module M5679. Synchroscan frequency was chose to be 125MHz, which is 1/4 of the NSLS2 storage ring RF frequency. The sweeping clock signal is getting from master oscillator through long Heliax cables. Phase jitter of the clock signal was measured to be less than 1ps. Small jitter is important for precise bunch length measurements. The long Heliax cable runs inside the NSLS2 buildings where the temperature is well regulated. Phase drift of the streak camera 125MHz synchroscan signal should be small, this is helpful to measure the relative synchronous phase from streak camera profiles.

Depends on the applications, optics setup for streak camera measurement can be different. There is different optical density (OD) filters (OD = 0.5, 1, 2, 3, 4) mounted on a rotation wheel so that different filters can be easily selected according to the beam current. A band-pass filter with center wavelength of 500nm and bandwidth of 10nm is typically used to limit the chromatic aberrations. For a typical bunch length measurement setup, 20x objective lens mounted on a 6-dimesional stage (x/y/z/x'/y'/z') right in front of the streak camera slit. The lens forms a very tight image on the camera slit which is then relayed to photocathode through streak camera input optics.

There are cases to observe the vertical and longitudinal (y-z) profile to understand the single bunch and coupled bunch instabilities. Dove prism was used to rotate the image by 90 deg and cylindrical lenses are used to image on the streak camera slit. Vertical lens has focal distance of 500mm and horizontal lens has focal distance of 50mm to make the beam image tight in horizontal plane and with reasonable magnification vertically. This setup is suitable to detecting the head-tail coupling motions. Fast ion has been observed as the most dominant instability since beginning of NSLS2 commissioning. Using the slow sweep module and y-z imaging setups, streak camera can monitor the bunch motions in vertical plane along the bunch train.

In the following sections, measurement results with different optics setups and streak camera modules will be presented, starts with single bunch profile measurement at different bunch current and RF voltage. Injecting beam longitudinal dynamics has been checked to optimize the phase and energy mis-match of injecting beam. Y-z imaging to study the head-tail coupling due to chromaticity and Transverse Mode Coupling Instability (TMCI) will be followed. Direct observation of fast-ion motions along the bunch train using slow sweep module will be discussed as well.

*Work supported by DOE contract No: DE-AC02-98CH10886
#chengwx@bnl.gov

ISBN 978-3-95450-176-2

SINGLE BUNCH PROFILE

Single bunch profile has been typically measured in synchroscan mode. Beam was stored in the ring with different single bunch current and RF voltage. Proper OD filters are used to minimize the space charge effect of cathode generated electron pulse. Measurement resolution can be checked with streak camera operatesd in focus mode, where smallest focused image gave ~ 6 pixels FWHM. This is corresponding to measurement resolution of 1.74ps RMS in the most used synchronscan range. Adding 1ps jitter of 125MHz signal, total measurement resolution should be around 2ps RMS. A typical measured longitudinal profile is shown in Fig. 1. Single bunch with current of 0.11mA was stored in the ring with three damping wigglers (DWs) gap closed to 15mm. As the single bunch current increase, bunch lengthen is expected to increase due to imagninary broadband impedances, in the meantime, real part impedance will cause synchrnous phase move towards the bunch head.

As detailed in Ref [1], longitudinal bunch profile was fitted to a skewed Gaussian function. Figure 1 lower plot shows the raw profile data and its fitting results. Bunch lengthes and centroids are available from the fitting. This sets of profile were measured with three DWs closed at different single bunch current up to 3.5mA. RF voltage was fixed at 1.78MV. Blue dots are the raw data from the streak camera image, red lines are fitted curves. When

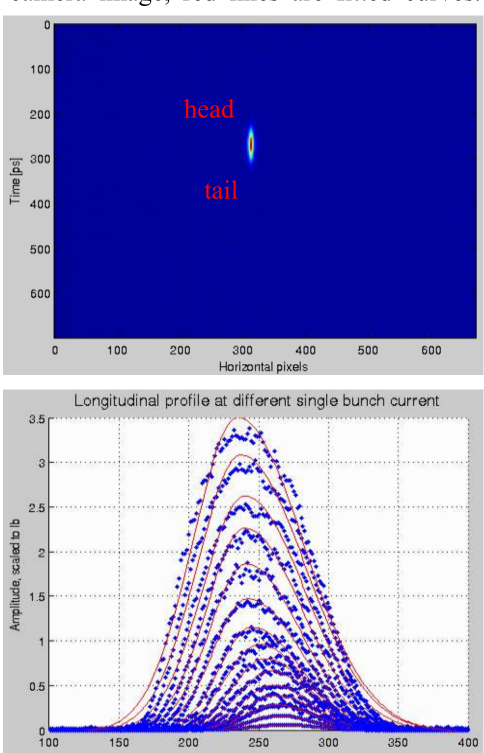

Figure 1: (Upper) Streak camera measured longitudinal profile in synchroscan mode, single bunch was stored in the ring at 0.11mA with all three DWs gap closed to 15mm. (Lower) Measured profile at different single bunch current (blue dots) and its fitting results (red line), vertical peak amplitude scaled to the bunch current.

bunch current was below 2mA, fitted curve is quite close to the raw data. When bunch current is above 2mA, fitting is not that well, probably due to more complicated longitudinal distributions.

NSLS2 has three DWs to further decrease the horizontal emittance below 1nm.rad. With bare lattice (dipole radiation only, no DWs), horizontal emittance is about 2nm.rad, energy spread is ~0.05%. Energy spread will be increased when DWs are closed hence 0-current bunch lengthes will be longer. Bunch lengthes have been measured during early commissioning stage with bare lattice and lower RF voltage. Recent developments at NSLS2 include commissioning of DWs and In-Vacuum Undulators (IVUs), RF voltage was increased to 1.78MV for normal operation, we measured bunches with different configuration of insertion devices and RF voltages. Results of recent measurements are summrized in Fig. 2. All data were collected at 1.78MV RF voltage. Single bunch instability appears at around 0.7mA [3] with nominal chromaticity +2/+2, bunch by bunch transverse feedback was switched ON to accumulate single bunch with higher current. Single bunch lengthening effect was measured twice in April and August, 2015. Those data are plotted with blue circles and red stars in Fig. 2. The results agree well. With one DW gap closed to 15mm, bunch length at different single bunch current results are shown as green diamonds. Magenta triangles are results with all three DWs gap closed. Lattice was well characterized and corrected to the model before collecting the bunch length data. As more DWs close, bunch length at 0-current increases, bunch lengthening effect is not as strong as bare lattice. Bunch length was measured with all commissioned insertion devices (three DWs, two EPUs and four IVUs) gap closed, the results are shown as cyan triangles (feedback OFF) or cyan diamonds (feedback ON). IVUs gap close doesn’t change bunch lengthening much.

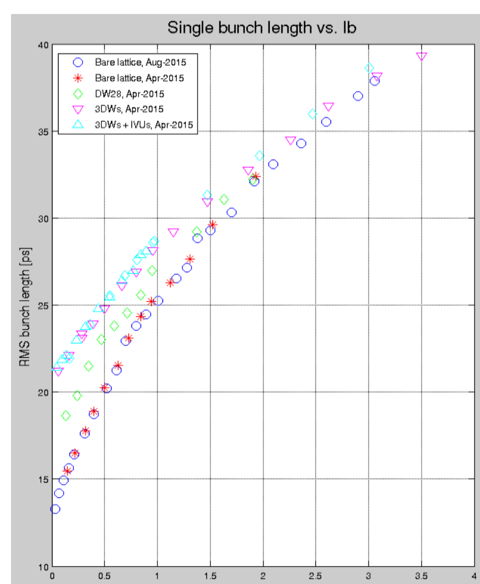

Figure 2: Single bunch lengthening effect with different insertion devices configurations.

ISBN 978-3-95450-176-2

As can been seen from the bunch lengthening curves, bare lattice, one DW and three DWs curves merged at higher bunch currents, which indicate microwave instability happens. Preliminary horizontal beam sizes measurement at different single bunch current shows energy spread increase from pretty low current. Further measurements and analysis will help us to understand the issue.

Assume 125MHz synchro scan signal has no drift during the streak camera measurement, bunch centroid (synchrotron phase) can be measured from the profile. There is concern that this assumption may not be true even though the long Heliax cable is housed in temperature regulated environment. Precise bunch synchronous phase can be measured with reference bunch(s) filled with low charge, as described in [4]. To have balanced image intensity of main bunch and reference bunch(s), multi buckets can be filled with very low bunch current. Precise bunch to bunch current measurement will be important to determine the main bunch currents. In the future, we plan to use the photon counting system to measure the bunch current with high dynamic range and precision [5], accurate synchrotron phase drift can be measured at different single bunch current. Combined the bunch lengthening and synchrotron phase information, real and imaginary longitudinal impedance of NSLS2 storage ring can be understood better.

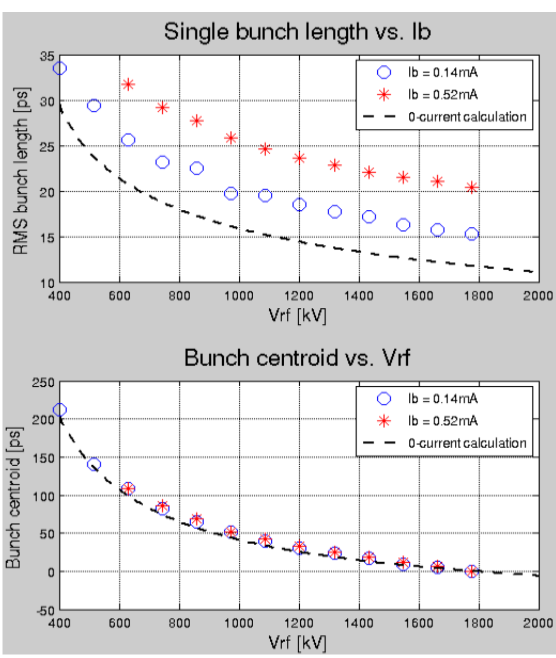

Figure 3: Measured bunch length and bunch centroid drift while scanning the RF voltage. (Upper) Single bunch length at different RF voltage, measured at single bunch current of 0.14mA and 0.52mA with bare lattice. Black dash line is the calculated bunch length. (Lower) Relative synchronous phase measured plot together with calculation result, while RF voltage varied.

Bunch profile while scanning the RF voltage has been measured as well. Figure 3 gives an example of such measurement for the bare lattice, RF voltage was varied from 1.78MV down to 400kV, at single bunch current of 0.14mA and 0.52mA. Calculated 0-current bunch length and synchronous phase drift are plotted as well. While scanning the RF voltage, measured synchronous phase drift agree well with the calculation. Other measurements using fill pattern monitor has shown synchrotron frequency drift at different RF voltage agrees with theoretical calculation. Based on this, it's fair to say that synchro-scan signal used for streak camera had no large phase drift during the period of data recording (~30 minutes).

INJECTION BEAM DYNAMICS

Streak camera dual sweep measurement is a powerful tool to observe the injection beam phase/energy mismatch. Two dual sweep images with 20 deg RF phase difference are presented in Fig. 4. Injection beam was captured and kept in the ring for 100ms before it was kicked out, this way there is no stored beam in the ring and only fresh injecting beam dynamics can be studies. 20-bunch trains were injected during the shift, that's the reason there are two strips on the image.

Left image shows injecting beam came in with phase mis-match, beam was doing synchrotron oscillation (fs ~2.5kHz, oscillating period ~ 0.4ms) start at 90 deg phase. After adjusting the storage ring RF phase by 20 deg, we achieved minimum synchrotron oscillation as shown in the right image. Injecting beam was still doing a smaller amplitude synchrotron oscillation start with 0 phase, which means there was slightly energy mis-match. This energy mis-match induced oscillation can be corrected by adjusting the Booster extraction energy or tune the storage ring RF frequency slightly.

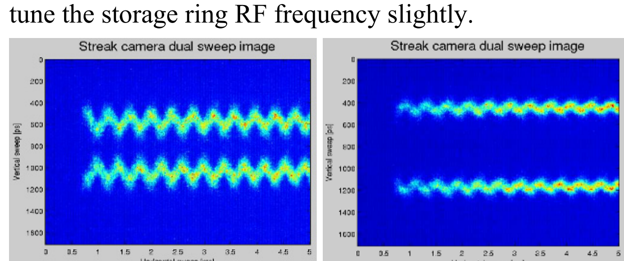

Figure 4: Injection beam phase and energy mis-match observation on the streak camera. (Left) Storage ring RF phase was 20 deg above the matched value. (Right) Storage ring RF phase best matched to the injector.

Synchrotron oscillation will be eventually damped down due to synchrotron radiation. Energy or phase mis-match will couple to horizontal motion due to dispersion. Turn by turn data from dispersive BPMs can be used to optimize the injection beam as well. Due to large horizontal betatron motion added on top of the synchrotron motion and filament in phase space, limited number of turns data is available and typically one needs to filter out the high frequency betatron motions to observe the clean synchrotron oscillations.

ISBN 978-3-95450-176-2

Y-Z IMAGING

It has been observed since early stage of NSLS2 storage ring commissioning, single bunch was getting unstable vertically at 0.7mA. This rather low single bunch threshold current has been studies carefully and it was determined due to TMCI when mode 0 and mode -1 of vertical tune sidebands collide [3,6]. CCD camera measured x-y profile saw blowup in vertical plane. To understand the bunch motions at single bunch threshold current, optics of the streak camera has been modified to monitor y-z profiles, dove prism and cylindrical lenses were added for the streak camera branch. Typical synchroscan and dual sweep images are shown in Fig. 5. Stable single bunch was stored in the ring while taking the images. In dual sweep, horizontal sweep time was set to 10 μs to see four consecutive turns image.

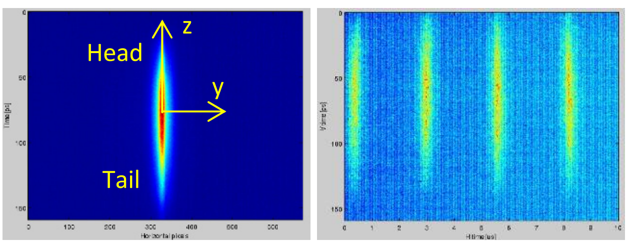

Figure 5: y-z image on the streak camera with stable single bunch stored in the ring. Left image is a synchroscan image while right side shows a dual sweep image with horizontal sweep time of 10 μs.

At nominal chromaticity of +2/+2, single bunch instability threshold was around 0.76mA. Figure 6 shows the x-y (measured with SLM CCD camera) and y-z profiles captured at the threshold current, horizontal sweep time was at 2μs to see one turn profile. Without bunch by bunch feedback, single bunch vertical beam

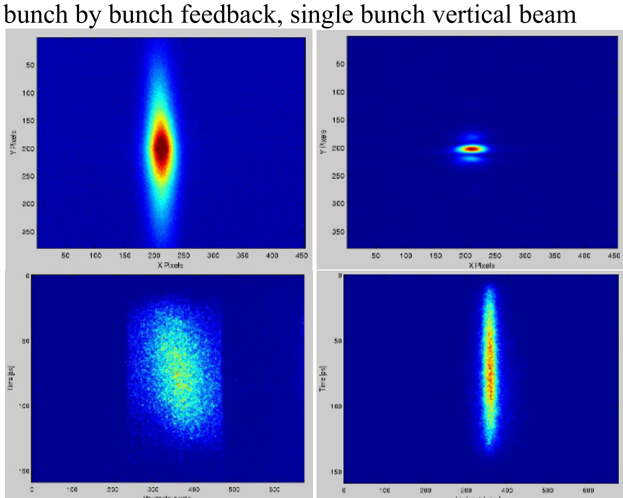

Figure 6: x-y CCD image and y-z streak camera image at single bunch current of 0.76mA. Without BxB feedback, beam was blow up vertically as shown in two left images. Longitudinal and vertical coupling motion was observed. With BxB feedback turned ON, single bunch was kept stable up to 6mA. Right side images show the stable beam profiles.

sizes were blown up. Longitudinal and vertical coupling motion was observed, y-z image was tilted. With BxB feedback turns ON, single bunch was kept stable up to 6mA single bunch current. Right side images show the stable beam profiles. Similar observations were noticed at different chromaticity (0, +1, +5), although threshold current was increased at higher chromaticity.

Using the same streak camera setup, chromatic head-tail motion (synchro-betatron coupling) has been observed as well, as shown in Fig. 7. Several single bunches separate by 8ns (4 RF buckets) were filled to get a better streak camera image, beam was kicked using vertical pinger at turn #0, streak camera trigger was adjusted to see the images at different turns after the kick. Single bunch current was measured to be ~0.28mA per bunch and chromaticity was measured at +2.18/+1.94. Vertical pinger was set to 0.15kV kicker, from BPM turn by turn data, bunch centroid oscillation amplitude at SLM source point was measured to be around 0.8mm peak-to-peak, right after the pulse kick.

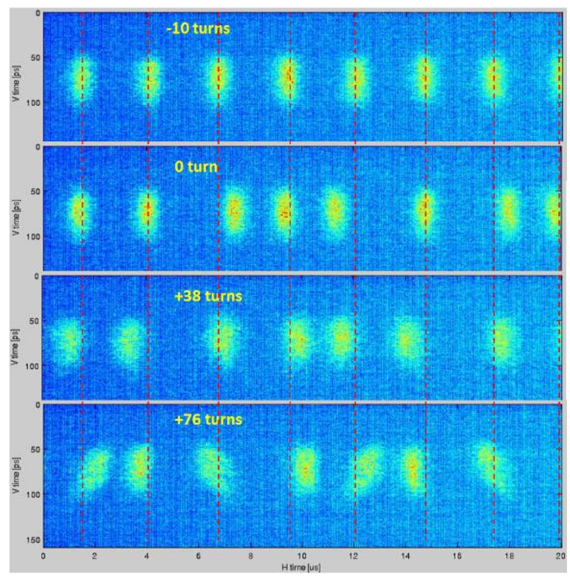

Figure 7: y-z profile at different turns after pulse kick of 0.15kV, oscillation amplitude was measured to be 0.8mm peak-to-peak from BPM TbT data.

Beam was kicked vertically at turn #0 and started betatron oscillation. Red dash lines are added in the figure to mark when the nominal vertical beam position should be when there is no pulse kick. Due to chromaticity, head and tail bunches will have slightly different betatron frequency, head and tail bunch betatron oscillation phase difference will be maximum at half synchrotron period T_s. Synchrotron oscillation frequency was ~2.5kHz with RF voltage of, which is ~150 turns. As can been seen, tilted bunch profile was observed at $T_s/4$ and more apparent at $T_s/2$. Passing the tilted bunch through a slit at primary image plane, several pico-second short pulses can be generated. High repetition rate of short x-ray pulses generation of this method may have attractive application as it will have little impact on general high flux user. Short x-rays pulses had been demonstrated at APS [7],

ISBN 978-3-95450-176-2

NSLS2 is developing a plan for high repetition rate (~ kHz) excitation using transverse feedback stripline kicker.

FAST ION DIRECT OBSERVATION

Fast ion instabilities have been observed when there was 25mA multi bunches stored in the ring in May 2014. Ion instability has been improved as the vacuum condition is getting better. At present average vacuum pressure of 3e-9 Torr, fast ion is still observed as the major coupled bunch instability during 150mA user operation. At shorter bunch train and higher bunch current fill, fast ion instability is getting stronger.

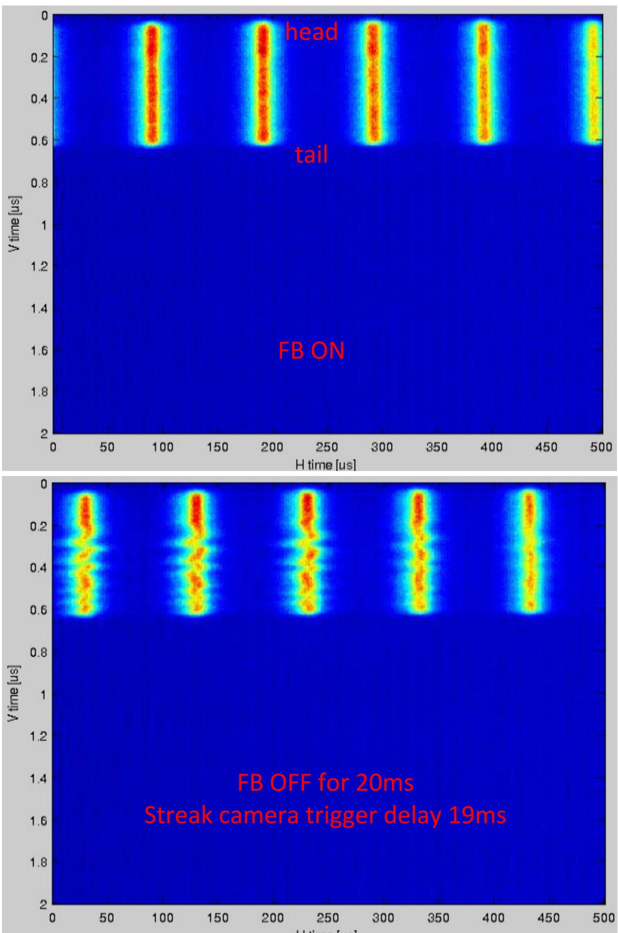

Figure 8: Dual sweep streak camera image using slow sweep module. (Upper) with bunch by bunch feedback ON, there was no instability observed on the streak camera y-z image. (Lower) with feedback turned OFF for 20ms, and streak camera trigger delay adjusted to see 19ms after the feedback OFF, bunches after #100 saw vertical motions on the streak camera image.

Use the same y-z imaging optics and streak camera slow sweep module, vertical motions along the bunch train can be directly observed. Fig. 8 gives the streak camera image taken with 300 bunches fill to total beam current of 63mA (~0.2mA per bunch). Vertical sweep was set to 2µs to see one turn profile of stored multi bunches, sweeping clock was adjusted to 10kHz period. Horizontal sweep was at 500µs to see five turns of profile with 100µs separation. Each vertical strip in the figure is one turn image, head bunches are at the top. With bunch by bunch feedback system, there was no instabilities observed hence head and tail bunches had no vertical motion. To see the fast ion instability build up, feedback was gated OFF for 20ms and streak camera horizontal trigger delay was adjusted to see the turn to turn profiles at 19ms after feedback OFF. As shown in the botton image, head bunches were still stable while tail bunches (> bunch #100) were doing vertial motions. Further information of fast ion instability observations can be found at [8].

SUMMARY AND DISCUSSION

Various measurements using streak camera have been carried at SLM diagnostic beamline, to characterize the single bunch and multi-bunch longitudinal motions.

Significant single bunch lengthening was observed at bare lattice and different insertion devices. Single bunch threshold current was noticed to be ~0.7mA which is lower than expected. Y-Z imaging of single bunch profile at threshold current reveals how the longitudinal and vertical motions were coupled. Further analysis of measured longitudinal profile will help to understand the storage ring longitudinal impedances.

Streak camera has also been used to optimize injection beam energy/phase mis-matches. It is also a powerful tool for direct observation of synchro-betatron coupling and fast ion instabilities along the bunch train.

We thank NSLS2 operation group's help during machine studies. Continuous support from NSLS2 management is essential to make these measurements possible.

REFERENCES

[1] W. Cheng, et al., "NSLS2 Visible Synchrotron Light Monitor Diagnostic Beamline Commissioning", IBIC'2014

[2] W. Cheng, "Synchrotron Light Monitor System for NSLS-II", BIW'2010

[3] W. Cheng, et al., "Commissioning of Bunch-by-bunch Feedback System for NSLS2 Storage Ring", IBIC'2014

[4] Weixing Cheng, Alan Fisher, Jeff Corbett, "Streak-Camera Measurements at High Currents in PEP-II and Variable Optics in SPEAR3", BIW'2008

[5] W. Cheng, et al., "NSLS2 Fill Pattern Monitor and Control", this proceeding

[6] A. Blednykh, et al., "First Collective Effects Measurements in NSLS2 with IDs", IPAC'2015

[7] B. Yang et al., "Streak Camera Studies of Vertical SynchroBetatron-Coupled Beam Motion in the APS Storage Ring", PAC'2005

[8] W. Cheng, et al., "Observation of Ion-induced Instabilities at NSLS2 Storage Ring", TUPB086 these proceedings.

ISBN 978-3-95450-176-2

BEAM ARRIVAL TIME MONITORS

J. Frisch SLAC National Accelerator Laboratory, Stanford CA 94305, USA

Abstract

We provide an overview of beam arrival time measurement techniques for FELs and other accelerators requiring femtosecond timing. This paper will discuss the trade-offs between the various techniques used at different facilities.

ARIVAL TIME MONITORS

Beam timing is only meaningful relative to some reference, and in general what matters is the relative timing of two different systems. Pump / Probe experiments in FELs, UEDs etc. generally have the most critical requirements: down to a few femtoseconds. Proton HEP experiments can require few-picosecond coincidence detection, but bunch lengths are typically long, so precision arrival times are not required.

It should be noted that the thermal expansion of conventional materials, cables, optical fibers etc. is typically on the order of 10^{-5}/°C, corresponding to 30fs/°C. Because of this, most arrival monitors are coupled to some form of stabilized timing transmission system, and the design of that system will influence the monitor technology choice.

As the arrival monitors are typically not the "weak link" in a timing system [1], trade-offs between cost and efficiency should be considered.

Timing System Architecture

A typical timing system includes the beam arrival monitor, a timing distribution system, and an experimental laser system as shown in figure 1:

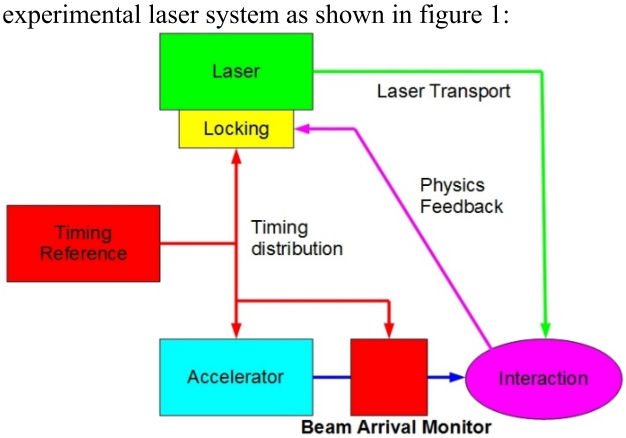

Figure 1: Typical timing system

The information from the beam arrival monitor may be used in a variety of ways:

- Provide feedback to the accelerator timing to reduce timing jitter [2]
- Correct the timing drift in the reference signal from the accelerator to the experiments [1]
- Provide offline correction of experiment data for shot to shot timing jitter [1]

DETECTING BEAM FIELDS

Frequencies

The electric fields from relativistic bunces diverge at an angle of 1/γ so that the fields at the beam pipe radius can contain high frequency components, in most cases above the maximum frequency (~50GHz) of conventional electronics. For high energy machines (γ>~300) the fields at the beam pipe will have frequency components higher than the response time of electro-optical system (~100fs).

Signal Levels

The field probes for arrival time monitors can be described as having a geometric impedance, for accelerator structures this is denoted by "R/Q", and for a cavity is typically 100Ω. The single pulse energy deposition is given by [3]

$$E = q^2\left(\frac{\omega_0}{2}\right)\left(\frac{R}{Q}\right)$$

A 100pC bunch in a 3GHz cavity with 100Ω R/Q will deposit 10nJ. When this is compared to thermal noise of $2\text{x}10^{-21}$J it corresponds to a timing resolution of 20 attoseconds. Other effects will limit the monitor resolution well before this level, and in most cases thermal noise is not the primary limitation in arrival time monitors.

Other types of beam pickoffs, including "buttons" may have much lower coupling and signal levels can be a performance limit.

Broadband vs. Narrowband Detection

Conventional electronics typically has ~1ps timing resolution for single shot measurements [4]. However if the beam electrical impulse is converted to a narrow band repetitive signal this allows multiple measurements to be averaged on a single pulse. Beamline cavities can perform this narrow-banding for low frequency systems.

Electro-optical systems can have very high bandwidths (100 fs response time) and provide few-femtosecond single shot resolution. These can be used without ringing filters.

Sources of Beam Fields – Working Above Cutoff

Electron beams will emit electromagnetic radiation whenever they encounter a change in beam pipe impedance. Components of this radiation above beam-pipe cutoff of 1.8412C/(2πR). (9GHz for a 1cm radius pipe) will propagate.

ISBN 978-3-95450-176-2

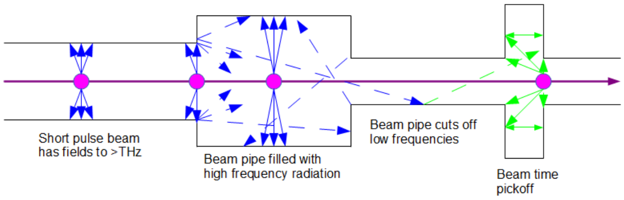

Figure 2: Fields above cutoff propagate from upstream.

The fields from upstream will have a position dependence that may interfere with the measurement of timing at the arrival time monitor. Note that most arrival time monitors have a measurement resolution that is much smaller than the operating frequency so even a small interfering signal can produce a significant timing distortion. (A 3GHz system has a time constant of ~50ps, so a -60dB interfering signal can result in 50fs errors).

Signals above cutoff will propagate with a group velocity less than C:

$$V_g = c\sqrt{\left(1-\left(\frac{f_c}{f}\right)^2\right)}$$

allowing them to be separated temporally. However, as the difference in velocities is small, using timing prevents the use of narrow band systems. The reduction in performance from using broadband detection makes operation slightly above cutoff an unattractive option in most cases.

At frequencies far above cutoff, propagation is essentially free space at the speed of light. This provides a very small delay – 150 fs for a 1cm radius beam pipe, at a distance of 1M.

Above cutoff operation has been used successfully at DESY / FLASH and other labs, [5] so provide few-femtosecond timing measurements. However, great care is needed in these systems to ensure that signals propagating from upstream do not result in position dependent time measurements.

Frequency / Bandwidth Choice

In general arrival time monitors fall into two types: Low frequency (<10GHz) cavity systems with low bandwidth that operate below cutoff, or high frequency (>10GHz – THz) systems with high bandwidth that operate above cutoff.

Dark Current, Tails and Halo

Most accelerators produce some unwanted beam charge in incorrect buckets from the gun or structure field emission. Defocused halo or tails may arrive at a different time from the main beam.

Beam pickups will see this dark current and it can interfere with the timing measurement. For example 10^{-3} charge out of time in a 3GHz arrival time monitor can produce a 50 femtosecond error.

Narrowband and low frequency systems are more susceptible to dark current / halo issues.

BEAM PICKUP TYPES

Cavities

For operation below cutoff cavities provide a narrow band high-Q beam pickup with good beam coupling. They are mechanically robust and the readout electronics use conventional RF techniques.

The largest disadvantage of cavities is their very high temperature sensitivity which needs to be corrected – described in a later section.

RF cavity based arrival time monitors have been used with few-femtosecond resolution at SLAC / LCLS. [1]

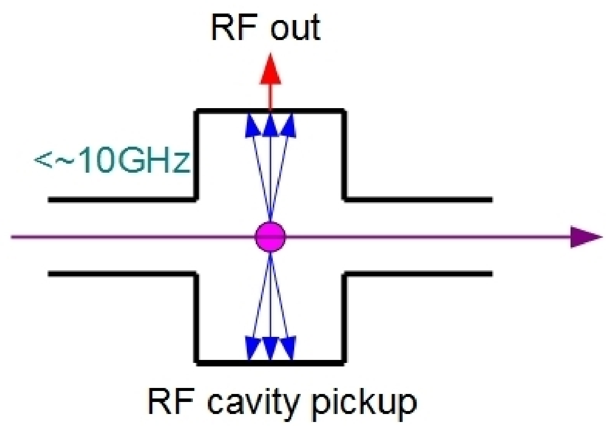

Figure 3: Cavity pickup.

Waveguide Pickup

Commercial RF waveguide components including mixers are available at frequencies up to several hundred GHz. [6] this allows high bandwidth systems to be built without optical components. However note that dispersion in the waveguide to the mm-wave mixer can prevent temporal separation of fields generated from upstream and propagating down the beam pipe.

Tests at SLAC / LCLS have shown >300GHz response from waveguide coupled systems of this type. However these have been used for bunch length, not bunch timing measurements.

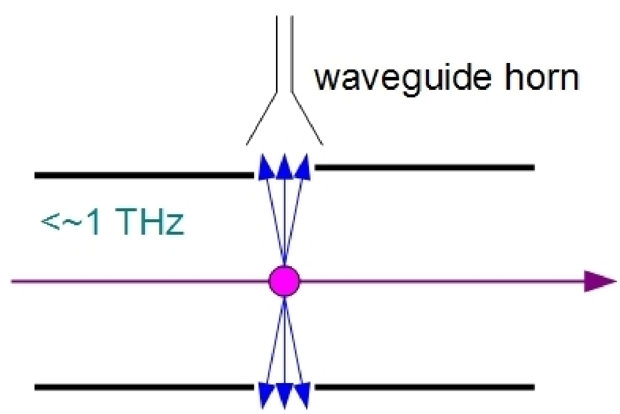

Figure 4: Waveguide based pickoff.

ISBN 978-3-95450-176-2

Direct Electro-Optical Pickup

A fiber coupled electro-optical element placed near the beam will be directly exposed to the high bandwidth beam fields. If the electro-optical crystal is used to modulate a femtosecond optical pulse, extremely high bandwidth is available – generally limited by the phase matching requirements in the EO crystal to approximately 200fs. [7]

Direct EO systems have demonstrated few-femtosecond resolution [5], however care must be taken to avoid damage to the EO crystal from ionizing radiation or high electric fields due to its proximity to the electron beam.

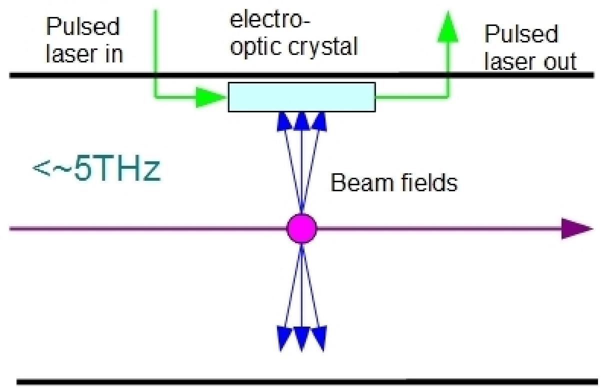

Figure 5: Direct EO sampling.

Indirect EO Sampling

The practical issues with direct EO sampling can be improved at the expense of bandwidth by using a fast electrical beam pickoff coupled to a commercial high bandwidth EO modulator. The bandwidth of such systems is typically limited to < 50GHz. A system of this type is planned for the European XFEL [8].

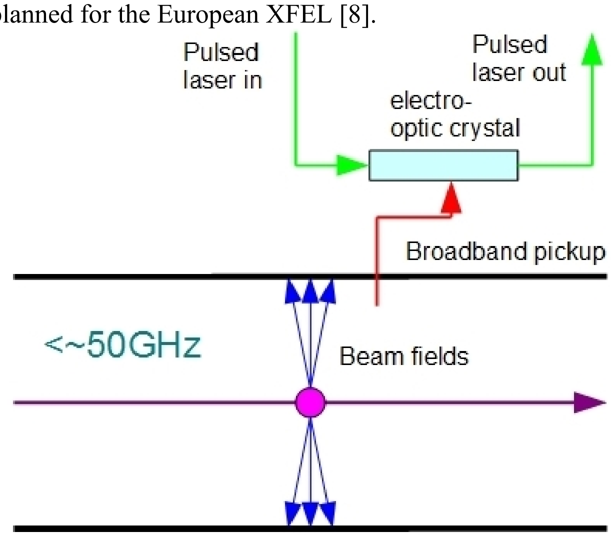

Figure 6: Indirect EO sampling.

OTHER SCHEMES

The majority of arrival time monitors rely on coupling out the beam fields, however a number of other schemes have been considered and many tested.

Transverse Deflection Cavities

Transverse deflection cavities are most commonly used to measure beam longitudinal profiles, however they can be used to measure beam arrival times. The transverse deflection of a beam in a TCAV is proportional to the relative arrival time of the beam to the cavity fields. [9]

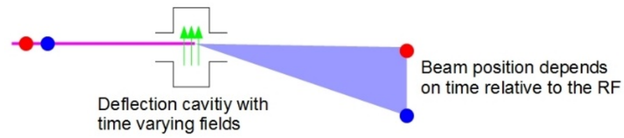

Figure 7: Transverse deflection cavity.

The fields in the TCAV are generally controlled through a feedback system based on a structure field probe. This system is very similar to a conventional cavity based arrival time monitor, so in most cases there is no performance improvement. However for very low charge beams where there is insufficient signal to noise for conventional arrival time monitors, a TCAV can provide improved resolution.

Free Space Radiation

An electron beam can radiate into free space through interaction with a foil (OTR) or undulator. Since the radiation source is well defined, spatial filtering can be used to reduce the effects of emission from upstream. The bandwidth is limited by the bunch length and can be very high. Mixing in nonlinear crystals can be used to interact the signal with a femtosecond laser to provide timing information.

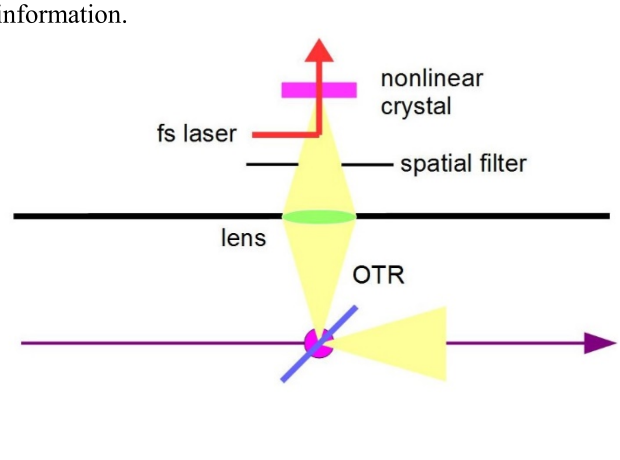

Figure 8: OTR signal generation.

Note that for an undulator it may be impractical to have a large enough K and wiggler wavelength for use with high energy electron beams.

Relative to direct EO modulation the OTR / Undulator technique has the following advantages

ISBN 978-3-95450-176-2

- Higher signal intensity which allows the use of thinner nonlinear crystals and higher bandwidths
- Spatial and Spectral filtering can reduce interference from upstream signals
- External attenuation can provide large dynamic range.

The disadvantage is the substantially greater cost and complexity relative to conventional EO techniques. The authors are not aware of OTR being used as part of an experiment timing system.

X-ray Timing

Since the goal of X-ray FEL timing systems is to provide timing to experiments, schemes that directly measure the X-ray vs. laser timing are attractive. This type of system can provide the primary timing to experiments. Note that usually a conventional arrival time monitor is needed to keep the X-ray system within its dynamic range and for beam conditions where the X-ray system is unable to function. When available, X-ray / laser timing systems will generally provide the higher performance than other options.

In the system used at SLAC / LCLS the experiment laser is directed into an optical continuum generator and the resulting white light is temporally chirped. That chirped pulse then intersects the X-rays in a thin foil. The attenuation and index of refraction of the foil changes when it is hit by X-rays and this modified the spectrum of the transmitted light. [10]. Note that other schemes involving a special cross-correlation in an non-co-linear geometry have also been used at SLAC.

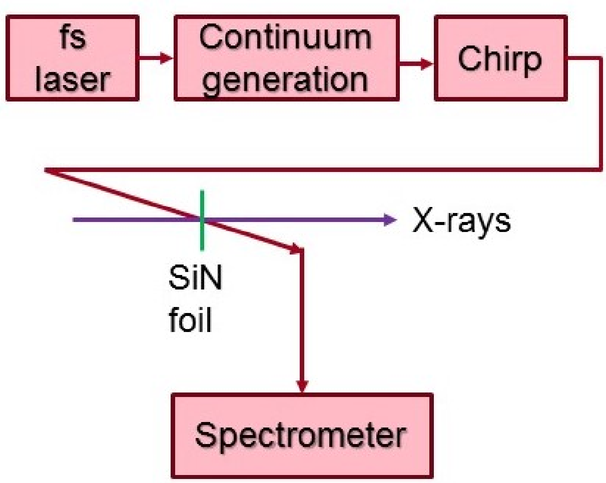

Figure 9: X-ray/optical cross correlator at SLAC/LCLS.

The improvement in timing resolution from using the X-ray / Optical arrival time monitor can be seen in figure 10 where a timing scan of the non-thermal melting of Bi is displayed. This experiment also demonstrated <15fs drift over 5 hours of operation.

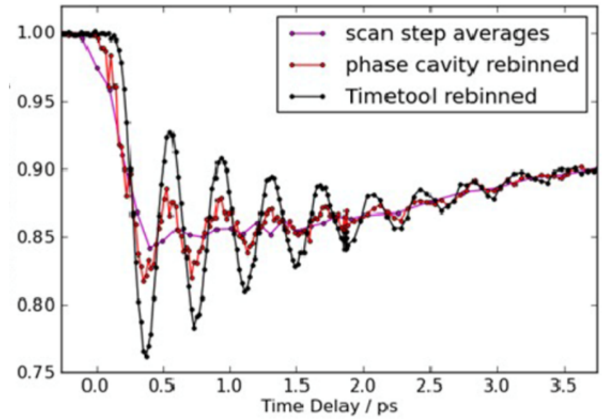

Figure 10: X-ray / Optical correlator (Time tool) improves resolution for non-thermal melting of Bi.[11]

RF CAVITY ARRIAL TIME MONITOR: SLAC / LCLS

The timing system for the LCLS is an all-RF based system. We present it as an example of the sorts of engineering to be considered in the design of a beam arrival monitor. The LCLS operates at 3-15 GeV, at 120Hz, with bunch charges from 20-250pC, and few kA peak currents.

Timing System Architecture

The LCLS timing system uses a reference signal from the accelerator transmitted through a ~1.5 km un-stabilized cable. The arrival time monitor measures the beam time in the undulator hall and corrects for the drift of the long cable. The resulting stabilized signal is then transmitted to the experiment stations using a bidirectional RF link. All long distance transmission uses 476MHz, 1/6 of the 2856 main accelerator frequency.

The bidirectional link operates as phase locked loop: The loop feedback fixes the time at the arrival time monitor. If the cable length changes (due to temperature), the change in the transmitted and reflected phases are equal and opposite, so an average of those phases is first order corrected for temperature.

Precision timing is provided by the X-ray / optical cross correlator "time tool".

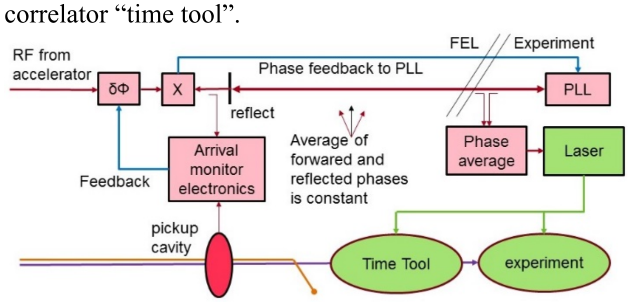

Figure 11: LCLS timing system overview.

Arrival Time Monitor Cavities

The LCLS uses beam pickup cavities at S-band, 2805MHz, different from the GUN and Accelerator RF of

ISBN 978-3-95450-176-2

2856MHz in order to avoid measuring dark current The cavities are high Q (~7000) copper. Two cavities are used, each has a heater for calibration.

Note that he couplers are NOT designed to reject dipole modes and no measurement of position sensitivity has been performed. (This is expected to be fairly small, and cavities are located after the undulator where the orbit is very stable).

Arrival Time Monitor Electronics

The electronics mixes the 2805MHz from the cavity with 2856MHz (6X the 476MHz reference). The resulting 51MHz IF is digitized at 119MHz (locked to the reference). High linearity electronics used throughout to reduce amplitude -> phase conversion. The electronics is 8 years old, and could be improved, but it is not the performance limiting part of the timing system. Also note that the specific frequency choices were driven by the available hardware and are not optimal.

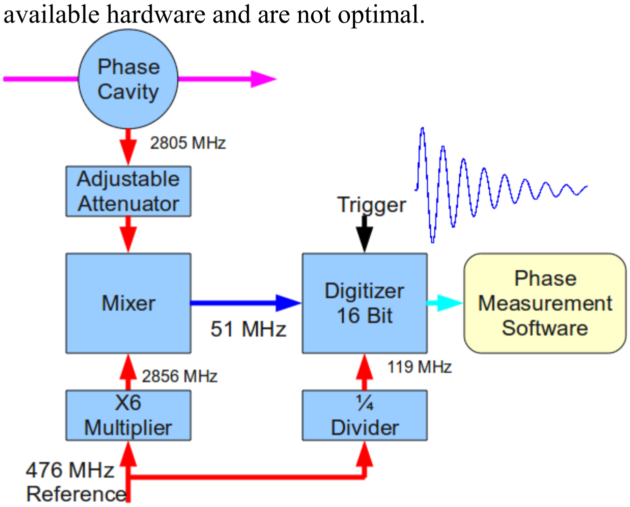

Figure 12: Arrival time processing electronics.

Temperature Coefficient Correction

The high Q cavities ring at ~3GHz for ~10^4 radians and the thermal expansion of Copper is ~2×10^{-5}/°C From this we expect 10ps/°C temperature sensitivity.

The ringing frequency is directly proportional to temperature, in fact it is the change in frequency that is causing the problem in the first place. This allows us to measure the changing resonant frequency and use it to correct the timing

We calibrate by heating first one cavity, then the other, and fitting the change in delay times relative to measured cavity frequencies. For details see [12]

Note that the LCLS undulator hall where the arrival time monitor is located has a very stable temperature ~0.1 C.

Arrival Time Monitor Performance

The arrival time monitor has been in operation for approximately 8 years. After a recent upgrade to the processing algorithm the following performance was observed:

- RMS difference between measured timings for two cavities: 13fs RMS for a 1 minute measurement.
- Drift difference between timings for two cavities: 340fs pk-pk for 2 week measurement.

Note in figure 13 that the drift is not diurnal. The cause of this drift is not understood, there are a number of possible candidates:

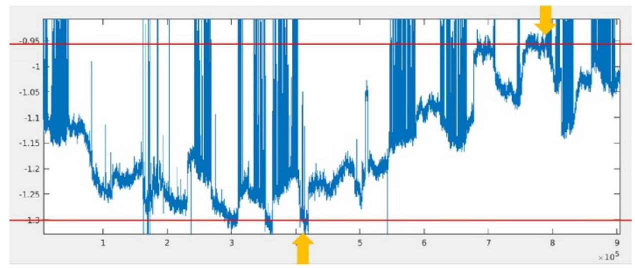

Figure 13: Drift over 2 week measurement ~340fs pk-pk.

The source of the residual drift is not understood. There are a number of possible causes that have not yet been investigated:

- Humidity: Water has a high dielectric constant at RF frequencies. Water absorption in cables can change their phase length
- Physical motion: The 300fs drift corresponds to 100um motion. The cavity mounts could move due to changes in air pressure acting on bellows
- Beam conditions: changing satellite bunches, dark current etc. could cause timing changes.

In practice for LCLS the drift is not a significant problem as other drifts in the timing system are larger, and all are corrected by the Time Tool cross correlator for most experiments.

RF Arrival Time Monitor Reliability

Since its commissioning in 2007 the arrival time monitor has been in nearly continuous operation. It has had a single hardware failure, where automatic fail-over to the redundant system allowed experiments to continue. There have been several software / network issues, primarily related to the communication of the real-time data to the experiment data acquisition system.

PULSED FIBER ARRIVAL TIME MONITOR

Several variants of a common design concept have been used, or are under development for FLASH and the European FEL. Here we show a "generic" version.

The timing system uses a 216MHz, 100fs soliton laser as a master source and the arrival time monitors use high frequency RF pickups which drive commercial electro-optical modulator. The system is designed for 20pC to 1nC charges, with beam burst rates to MHz [13].

Fiber Timing System

The fiber timing system samples the forward and reflected laser pulses in the long haul fibers. The pulse overlap is measured by correlating in a nonlinear crystal –

ISBN 978-3-95450-176-2

providing a measurement at the full bandwidth of the laser. Changes in delay are corrected by adjusting the length of the transmission fiber (fiber stretcher or mechanical delay line). In some variants polarization preserving fiber is used, in others a polarization feedback is used to control polarization.

This stabilized fiber backbone is used to synchronize the arrival time monitor and the experiment laser system.

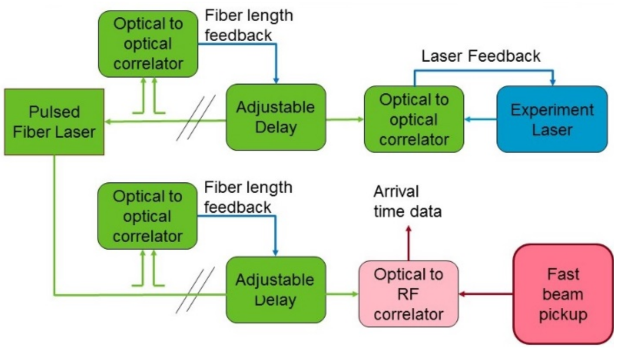

Figure 14: Fiber timing backbone.

EO Arrival Time Monitor

The electro-optical arrival time monitor uses indirect EO sampling with a broadband pickup with 10GHz (coarse) and 40GHz (fine) channels. The beam field's amplitude modulates the pulsed fiber signals whose intensity are then detected by low bandwidth receivers. The large required dynamic range necessitates the use of attenuators and limiters, so care is required to avoid amplitude -> phase conversion.

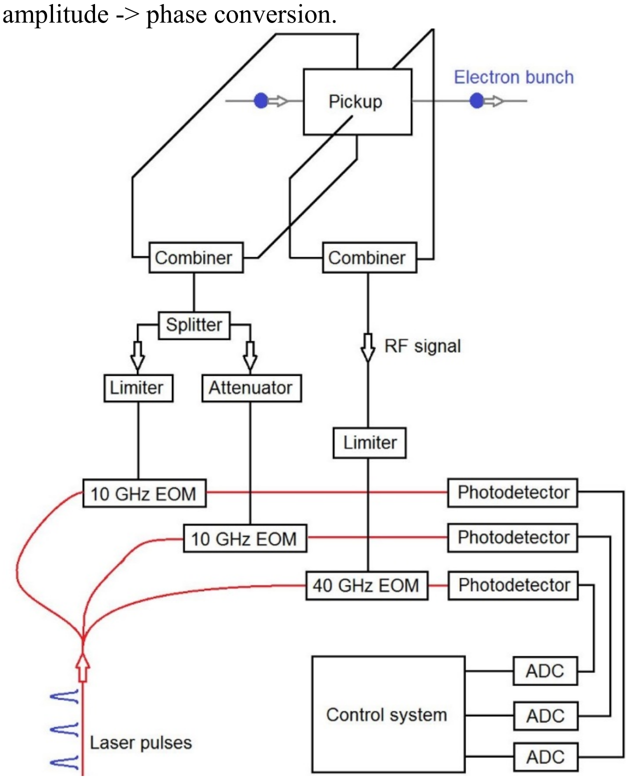

Figure 15: Fiber BAM front end. [14]

EO Arrival Time Monitor Performance

A 5GHz version of the EO system tested in 2008 at DESY FLASH where it demonstrated 9.5fs RMS difference over a 1 minute interval between two arrival monitors [13]. The long term drift was not published but is expected to be low.

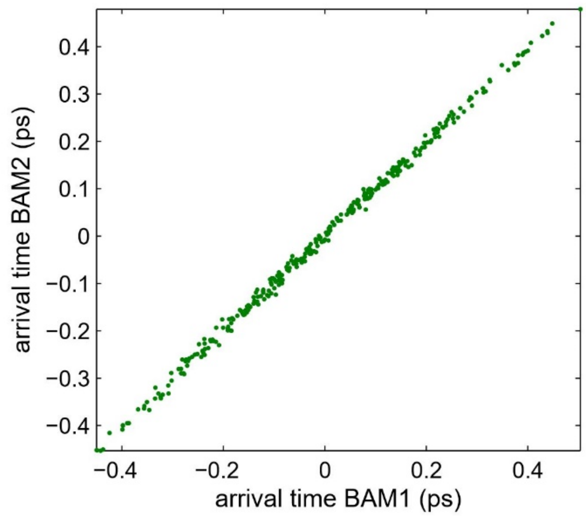

Figure 16: EO Arrival time monitor 9.5fs RMS difference over 1 minute measurement at DESY / FLASH.

DESIGN CHOICES

Fiber vs RF

Both Fiber and RF based arrival time monitors have been used successfully. RF systems generally operate below beam-pipe cutoff and are relatively simple, rugged and inexpensive. Fiber based Electro-optical systems generally operate at as high a frequency as is practical, above the beam-pipe cutoff. They in general provide better performance than RF systems, but are more complex to construct and maintain.

System Overview

The Arrival Time Monitor is just one component of an experiment timing system and many other components may be larger contributors to the overall timing error:

- Are the electrons you are measuring the ones that contribute to the physics?
- Dark current? Tails? Does the entire beam laser in the FEL?
- **Arrival Time Monitor?**
- Timing transport system?
- Laser locker?
- Laser amplifier and compression chain?
- Laser transport to the experiment?

All these sub-systems should be considered when designing a timing system.

ISBN 978-3-95450-176-2

REFERENCES

[1] J. Frisch et al, Status of the LCLS Experiment Timing System, SLAC-PUB-15254, http://slac.stanford.edu/pubs/slacpubs/15250/slac-pub-15254.pdf 2012

[2] C. Behrens "Intra-train Longitudinal Feedback for Beam Stabilization at FLASH", DESY FLASH Seminar, November 11, 2010. http://flash.desy.de/sites2009/site_vuvfel/content/e870/e68614/infoboxContent68969/FlashSeminar_WK.pdf

[3] T. Wangler, "RF Linear Accelerators", Wiley 2008.

[4] Tektronix tech note "Triggering Fundamentals", http://www.tek.com/

[5] F. Lohl et al, "Electron Bunch Timing with Femtosecond Precision in a Superconducting Free-Electron Laser" Phys. Rev. Lett. 104, 144801 – Published 5 April 2010

[6] www.vadiodes.com

[7] B. Steffen et al. "Spectral Decoding Electro-Optic Measurements for Longitudinal Bunch Diagnostics At the DESY VUV-FEL", Proc. 27th International Free Electron Laser Conference.

[8] A. Kuhl et al. "Comparative Analysis of Different Electro-Optical Intensity Modulator Candidates for the new 40GH Bunch Arrival Time Monitor System for Flash and the European XFEL", IBIC 2013.

[9] D. Ratner et al. "Time-resolved imaging of the microbunching instability and energy spread at the Linac Coherent Light Source", Physical Review Special Topics: Accelerators and Beams, 18, 030704 (2015).

[10] D. Zhu et al. "Development and Status of Temporal Diagnostics at LCLS", Photon Diagnostics Workshop, June 2015, Trieste.

[11] H. Lemke, M. Weaver, et al., Proc. SPIE, 87780S (2013)

[12] K. H, Kim et al, "Implementation of Phase Cavity Algorithm for Beam Arrival Time Monitoring System for LCLS", K. H, Kim et al. MOPB076, IBIC2015

[13] F. Loehl et al, "Experimental Determination of the Timing Stability of the Optical Synchronization System at FLASH", EPAC08, Genoa Italy.

[14] A. Kuhl et. al. "Analysis of the Electro-Optical Front End For the New 40GHz Bunch Arrival Time Monitor", IBIC2012, Tsukuba Japan.

ISBN 978-3-95450-176-2

TRANSVERSE PROFILING OF AN INTENSE FEL X-RAY BEAM USING A PROBE ELECTRON BEAM*

P. Krejcik, SLAC National Accelerator Laboratory, Menlo Park, CA 94306, USA

Abstract

Monitoring the pulse by pulse output intensity and profile of an FEL is a critical measurement both for users and for optimizing the accelerator drive beam. The diagnostic challenge is to find a technique that is not susceptible to damage at high output power, is noninvasive and can be performed at high repetition rates. Fluorescent screens are invasive, susceptible to damage and limited in repetition rate by the camera readout. Gas cell monitors are noninvasive but only yield intensity information and suffer from residual ionization at high repetition rates. The technique described here uses the scattering of a beam of low-energy electrons as they are scanned across the photon beam to measure the transverse intensity profile of the photon beam. Two different geometries are compared. One is where a finely focused electron beam is scanned transversely across the photon beam to measure the transverse profile. The second is where the electrons are bent onto the axis of the photon beam and are scattered by the counter propagating beam of photons. Here the electron beam is kept larger in diameter than the photon beam so that the photon pulse intensity can be measured by the scattering.

INTRODUCTION

The pulse by pulse photon energy output of an FEL is a vital parameter for both the experiment users of the photon beam and the operators tuning the electron drive beam to optimize the FEL performance. The energy output varies greatly shot to shot because of the stochastic nature of SASE FELs and experimenters need that information for each shot. The photon output energy depends on many parameters of the electron drive beam such as charge, emittance, bunch length, peak current, energy, energy spread and so on. The pulse energy is therefore the bottom line tuning parameter for optimization of the accelerator. The value is displayed prominently in the LCLS control room on a scrolling display to give an immediate indication of the overall machine performance.

Measurement of the photon beam size is also important in any photon experiment involving focusing of the beam so that knowledge of beam size, beam divergence and the virtual source position can be used to set up the x-ray optics.

The LCLS relies on two main measurement techniques to measure size and intensity. The first is an invasive technique where a fluorescent YAG screen is inserted in the photon beam and the image recorded by a camera[1]. Beam cannot be delivered to user experiments during this measurement process. The size and position of the beam can be measured on the screen with good precision to a few microns. The camera intensity also gives a good measure of the intensity of the x-ray beam at intensities below saturation of the YAG screen.

At high intensities the YAG output saturates, and this is readily observed if the screen is used with small or focused spots. At still higher intensities the YAG screen becomes permanently damaged with reduced light output, and at very high intensities the YAG crystal does not survive a single shot.

Although it can be regarded as a single shot measurement, the repetition rate is limited by the camera read out speed and would not keep up with the high repetition rate of superconducting machines like LCLS-II.

The intensity measurement of the YAG screen needs to be calibrated against an absolute measurement of the x-ray intensity such as with the gas cell monitor.

The gas monitor at LCLS is a low pressure gas cell separated from the photon beam line vacuum by differential pumping. The x-ray photons passing down the axis of the cell ionize the gas and the number of ions is counted by sweeping them to them side with a clearing electrode into a detector [2].

In this way the individual pulse energy of the FEL can be monitored continuously and non-invasively during beam delivery to users, making it a valuable diagnostic tool. No information on beam size or position is available though.

A problem arises when we move to the high repetition rate beams of superconducting machines such as LCLS-II. Ions in the gas monitor move relatively slowly and are not fully cleared by the time the next pulse arrives in a 1 MHz bunch train. There are therefore significant transient effects in the detector response at the beginning of the pulse train compared to later in the train when residual ionization builds up. A diagnostic with a faster response suited to LCLS-II parameters is therefore sought.

ELECTRON PROBE DETECTOR

In its simplest form an electron beam is directed across the beam of x-ray photons so that they scatter off each other, as shown in Figure 1. The interaction can be described by the Compton scattering process, but since the energies considered here are quite low it is in the Thompson elastic scattering regime.

Compton scattering measurements have been routinely performed at high energy accelerators, usually with a laser directed at the high energy electron beam in order to measure the transverse profile of the electron beam. A laser is used when the intensity of the electron beam is so

*This material is based upon work supported by the U.S. Department of Energy, Office of Science under Contract No. DE-AC0276SF00515.
#pkr@slac.stanford.edu

ISBN 978-3-95450-176-2

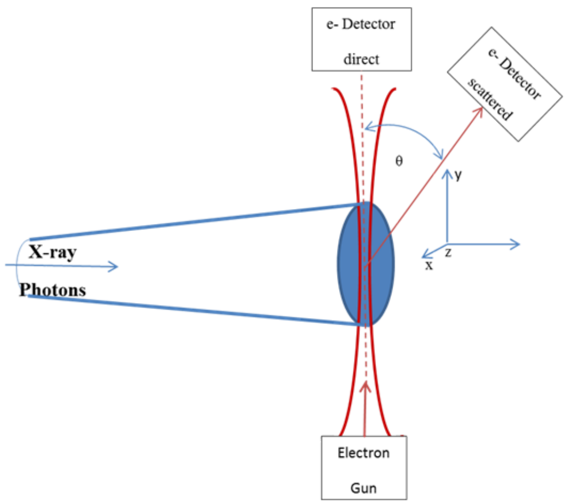

Figure 1: A high intensity x-ray beam from an FEL can be measured with a probe beam of low energy electrons by detecting the scattered electrons.

high that it would destroy a conventional scanning wire used for the beam profiling measurements, or the wire would be too invasive. For this reason such a device is often referred to as a 'laser wire scanner' [3]. In a laser wire scanner the usual procedure is to measure the number of Compton scattered photons. However, in the case of a low energy electron probe beam the electrons impart very little energy to the photons. In this case, detecting the scattered electrons instead becomes a more viable solution.

ELECTRON PHOTON INTERACTION

The Compton scattering process is usually analysed in terms of a photon striking a stationary electron and using conservation of energy and momentum to calculate the energy, as shown in Figure 2.

The incident photon has energy

$$E_0 = h\nu_0$$

and momentum

$$p_0 = \frac{h\nu_0}{c}$$

If the electron is assumed to have zero initial momentum

$$p_{e_0} = 0$$

The scattered electron energy is

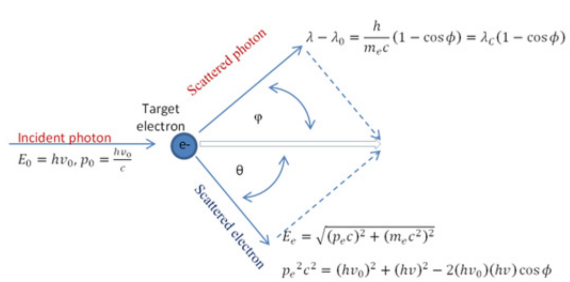

Figure 2: Compton scattering geometry for a photon scattered from a stationary electron.

$$E_e = \sqrt{(p_e c)^2 + (m_e c^2)^2}$$

where the magnitude of the scattered electron momentum is

$$p_e{}^2 c^2 = (h\nu_0)^2 + (h\nu)^2 - 2(h\nu_0)(h\nu)\cos\phi$$

and the change in wavelength of the scattered photon is

$$\lambda - \lambda_0 = \frac{h}{m_e c}(1-\cos\phi) = \lambda_C(1-\cos\phi)$$

with the $\frac{h}{m_e c}$ term is usually referred to as the Compton wavelength, λ_C.

At low energies the cross section is energy independent and is given by the Thompson cross section

$$\sigma_0 = \frac{8\pi}{3}\left(\frac{\alpha\lambda_C}{2\pi}\right)^2 \approx 66.5\,(fm)^2$$

where α is the fine structure constant.

At high energies the cross section is modified according to the Klein-Nishina formula[4]

$$\sigma_C = \sigma_0 \frac{3}{4}\left\{\frac{1+\epsilon}{\epsilon^3}\left[\frac{2\epsilon(1+\epsilon)}{1+2\epsilon} - \ln(1+2\epsilon)\right] + \frac{1}{2\epsilon}\ln(1+2\epsilon) - \frac{1+3\epsilon}{(1+2\epsilon)^2}\right\}$$

where $\epsilon = \gamma\frac{\omega_0}{m_e}$ is the normalized energy of the laser photons in the electron rest frame and γ is the Lorentz factor associated with the incident electron beam energy.

The number of scattering events, N_γ, is

$$N_\gamma = N_b \frac{P_L \sigma_C \lambda}{c^2 h}\frac{1}{\sqrt{2\pi}\sigma_s}$$

where N_b is the number of electrons in the bunch (or overlapping in time with the photon pulse) σ_s is the beam overlap area.

P_L is the FEL laser power output at wavelength λ.

Some typical photon parameters for LCLS are:

P_L = 100 GW

σ_C = 66.5 (fm)^2

λ = 0.1 nm

σ_s = 1 mm

For the electron beam, the number of electrons is related to the velocity, βc, of the electrons (and hence their energy) and to the electron beam current, I. Over an interaction length, L, the number of electrons is

$$N_b = \frac{L}{\beta c}\frac{I}{q_e}$$

As an example, for a 1 keV electron beam there are:

N_γ = 5.14x10^4 scattering events per ampere per meter of interaction length.

For the transverse scattering geometry shown in Figure 1with a photon beam diameter of 1 mm we obtain

N_γ = 5.14x10^2 total scattering events per ampere.

If, after various detector efficiencies are taken into consideration, we find that this number is too low, we can also consider alternative scattering geometries.

BACKSCATTER GEOMETRY

The electron beam in this case is bent onto the axis of the photon beam with a dipole magnet, as shown in Figure 3. The electrons counter propagate against the photon beam over a length, L, before being bent out of the way by a second dipole which directs the electrons towards a detector. The interaction length between the

ISBN 978-3-95450-176-2

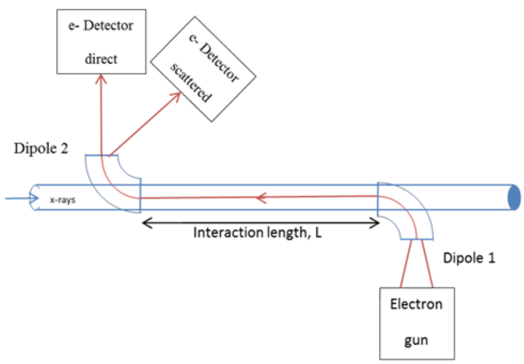

Figure 3: Back scatter geometry where the probe electron beam counter propagates over a length L against the x-ray beam.

dipoles can be chosen to ensure that sufficient scattering events occur to give a reliable signal. One detector measures the straight ahead unscattered component of the electron beam, and a second detector is placed at an angle to intercept lower energy electrons that have been scattered by the x-rays. The normalized scattered intensity can be determined by taking the ratio of these two detectors.

Measurement of the scattered fraction by detection in the energy spectrometer arrangement shown is not the only option. Some electrons are also scattered transversely and can be detected by annular detectors around the photon beam pipe. The x-ray photons are also scattered and although the bulk are forward directed some fraction is also scattered at an angle to the beam pipe and Compton shifted in wavelength.

Another possible geometry is to have the electrons and photons propagate in the same direction over a distance, L, as before. The electrons will gain energy in this geometry and be predominantly scattered in the forward direction.

IONS VERSUS ELECTRONS

It is worth considering whether other particles would have a higher cross section for interaction with the x-rays than the electron beams considered here. The gas monitor used at the LCLS relies on the detection of ions, so why not, for example, use an ion beam to interact with the photons. Since the photons always interact with the electrons, regardless of whether they are bound to an ion or are free electrons, the cross section of the interaction is the same. So the question becomes which technology allows the highest density of electrons to be delivered to the beam. Electron guns are by far the most efficient in this respect. However, ions travel much slower so that for a given energy and current the number of interactions over a length L is higher.

The electron gun design involves several trade-offs. High current operation requires pulsed operation, rather than dc operation, in order to keep the average power low. Although the electron density increases as the electron energy is lowered (increasing the number of scattering events) care must be taken in avoiding space charge effects that would limit the transverse size of the electron beam at very low energies.

Yet another approach would be to use a high brightness RF gun and use pulse compression techniques to achieve high peak electron currents.

SUMMARY

The electron probe technique permits single shot measurement of the x-ray intensity. At favorable electron-photon intensities it is also possible to scan the beam and measure the transverse profile. The technique is non-invasive and can be used while delivering beam to users. Since the electrons are “replenished” on each shot the technique is neither susceptible to damage nor limited in repetition rate. Since the technique is not limited by intensity it is also suitable for focused x-ray beams.

A rich parameter space exists that can be optimized for different measurement configurations. The challenge is to ensure that a sufficient number of scattering events can be recorded for each measurement. In general, the yield of scattered electrons can be increased by:

- Increasing the interaction length
- Lowering the energy of the electrons
- Increasing the peak current of the electrons

REFERENCES

[1] K. Tiedtke et al., "Absolute pulse energy measurements of soft x-rays at the Linac Coherent Light Source," Opt. Express 22, 21214-21226 (2014);

[2] K. Tiedtke et al., "Absolute pulse energy measurements of soft x-rays at the Linac Coherent Light Source," Opt. Express 22, 21214-21226 (2014);

[3] H. Sakai et al., “Measurement of a small vertical emittance with a laser wire beam profile monitor”, PRSTAB, Vol 5, 122801 (2002).

[4] K. Tiedtke et al., "Absolute pulse energy measurements of soft x-rays at the Linac Coherent Light Source," Opt. Express 22, 21214-21226 (2014);

ISBN 978-3-95450-176-2

BEAM BASED CALIBRATION FOR BEAM POSITION MONITORS

M. Tejima, KEK/J-PARC, Tsukuba, Ibaraki, Japan

Abstract

Beam position monitoring is one of the most fundamental diagnostic tools in an accelerator. To get good performance of the BPM system, the beam-based alignment method has been developed and used for more precise BPM alignment and maintaining the performance. The signal from a BPM is transferred by coaxial cable, and processed by signal processing circuit. The beam position is calculated from the relative ratios between the 4 outputs of the BPM head. The circuit gain is calibrated in the beginning on a test bench. But this calibration changes with each passing year. To escape from this problem, a method for calibration of the gain similar to beam-based alignment is a key issue to maintain the good performance of the BPM system. For this propose, a beam-based gain calibration method has been developed and used at KEK. Both beam-based alignment and beam based gain calibration methods are presented using concrete examples.

INTRODUCTION

For high energy accelerators, the measurement of the beam position is one of the basic diagnostics along with the beam intensity and the betatron oscillation frequency. Stability of the closed orbit is very important for stable operations to maintain good performance in an accelerator. Therefore we have prepared a BPM at each quadrupole magnet. For example, there were 186 BPMs in the J-PARC Main Ring. The BPM system requires a high accuracy measurement. In order to satisfy the requirement, we have done careful calibration of the BPM system in three steps before the commissioning. But, in KEKB, we found noticeable errors larger than 0.1 mm in almost all BPM readings.

These errors come from the alignment error of a BPM to its adjacent quadrupole magnet, and the imbalance among 4 output data of the BPM. Beam-based alignment (BBA) is a method for correcting the offset of a BPM head based on beam measurement [1]. The center position of each BPM should be known in terms of offset from the magnetic center of the adjacent quadrupole magnet. The relative gain of the output data may drift due to unpredictable imbalance among output signals from the pickup electrodes, because the output signals must travel through separate paths, such as cables, connectors, attenuators, switches, and then are measured by the signal detectors. For this reason, the gains of every BPM of KEKB have been calibrated by a non-linear least-square method [2]. The same process of gain calibration used in KEKB has been tried with the BPM system in J-PARC Main Ring, however the fitting result gave indefinite solutions.

A new beam-based method to calibrate the gains of BPMs at the J-PARC Main Ring has been developed using the Total Least Square method (TLS) [3].

CALIBRATION DURING INSTALLATION

The output data from a BPM system was usually calibrated in the following three steps on the test bench at KEKB [4].

1. Mapping measurement of BPM system
   The BPM heads were fabricated to within a ± 0.1 mm tolerance. However, variations of frequency response between button electrodes cannot be ignored considering the accuracy requirements. All BPMs were mapped at a test bench with a movable antenna to identify the electrical zero position of each BPM.
2. Alignment of geometrical offset
   Most BPMs (~97%) were aligned in relation to their nearest quadrupole magnet. After installation of BPM heads in the ring, we measured the geometrical offsets of the BPM heads relative to the quadrupole magnet. But the measured offsets were not the offset from the field center of quadrupole magnet.
3. Attenuation ratio of transmission line
   We employed 4 twisted coaxial cables with foamed Polyethylene insulation between BPMs in the tunnel and electronics at a local control room above ground. To measure signal attenuation at the detection frequency, the cables together with the electronics were also calibrated to 50 μm accuracy.

BEAM BASED ALIGNMENT

In order to align a BPM to the field center of a quadrupole magnet, the BPM offset is calibrated by finding the position of the closed orbit at that BPM which is insensitive to a change of the field strength of the adjacent quadrupole magnet. Calibration data are taken for different beam orbits and different field strengths of the quadrupole magnet. The orbit change due to the field gradient change Δk of the quadrupole magnet is proportional to the closed orbit displacement Δx from the magnetic center of the quadrupole magnet. Figure 1 shows an example of BPM offset measurement by BBA in the main ring at J-PARC [5]. A correction coil wound on each pole of a quadrupole magnet was used to change the field strength. The current on the correction coil, I_Q was changed from -4 A to 4 A nominally. To change the

ISBN 978-3-95450-176-2

orbit, a bump orbit Δx was set to three different orbits of -8 mm, 0 mm and 8 mm. When the beam orbit is in the vicinity of the center of the quadrupole magnet, even if the current of the correction coil is changed, the orbit does not change significantly (Fig. 1-(a) ~ (c)). In the measurement, three $\Delta x / \Delta I_Q$ values were obtained for the 3 bump orbits as shown Fig.1-(d). The beam position which gives $\Delta x / \Delta I_Q = 0$ is the offset of the BPM.

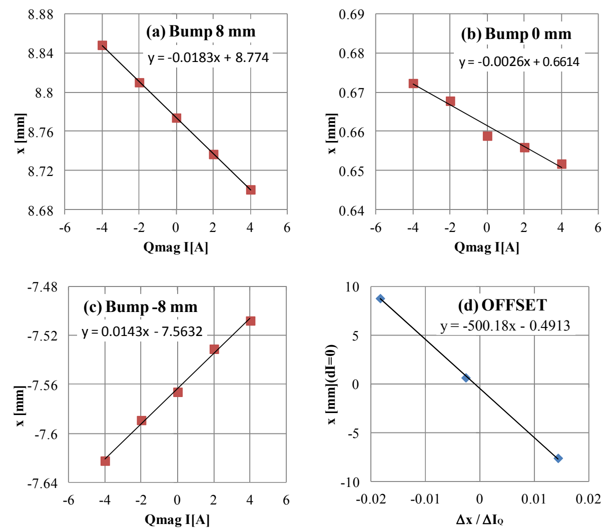

Figure 1: x-COD vs. QM current I_Q. (a) bump ~ -8 mm, (b) bump ~ 0 mm, (c) bump ~ +8 mm.

The orbital change due to ΔI_Q can be monitored not only the BPM but by any other BPMs in the ring. Figure 2 shows the offset positions observed by all BPMs when the field strength of quadrupole magnet is changed.

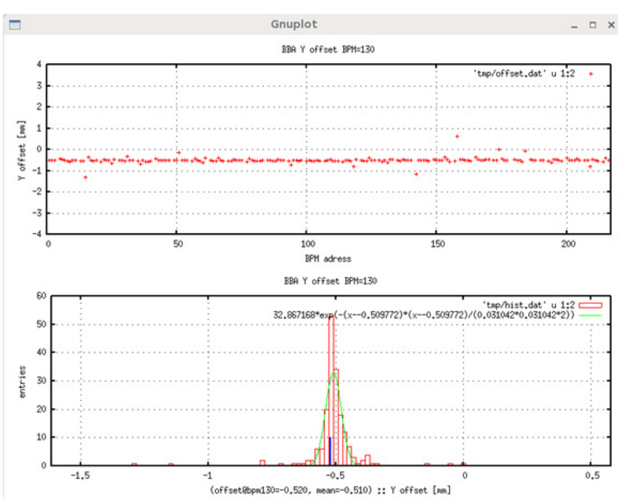

Figure 2: Offset values calculated with the all BPM response. y_0 at BPM#130 at J-PARC.

The vertical and horizontal offsets were obtained for almost all BPMs in the J-PARC MR by this BBA method. Figure 3 shows the offset distributions for MR BPMs. The BPM Offsets measured by this method were installed in the data base.

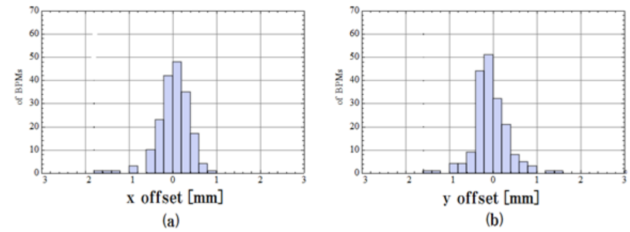

Figure 3: Distribution of BPM offsets obtained with BBA in J-PARC MR. (a) x-plane, (b) y-plane.

The effects of the BPM offset correction can be seen in the beam orbit. Figs. 4(a) and (b) show the closed orbit distortion (COD) with and without the offset correction for the MR. The closed orbit was corrected better than it was without the correction, especially the vertical closed orbit.

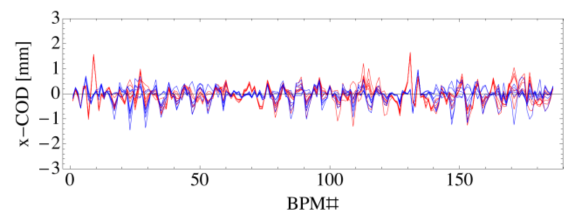

(a)

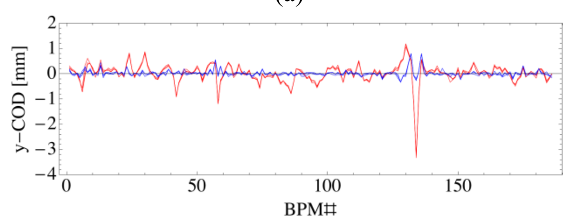

(b)

Figure 4: CODs along the MR, corrected without / with the BBA offset data (red / blue lines, respectively).

(a) x-COD, (b) y-COD.

Figure 5 show the offset distribution obtained by BBA in the LER and the HER at KEKB. We have also set the offset data in the data base of BPM system.

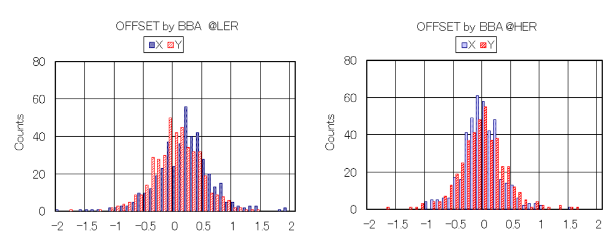

Figure 5: BPM offsets. Blue bars and red bars show horizontal offsets and vertical offsets, respectively.

The effects of the BPM offset correction can be seen in the beam orbit. Figures 6 upper and lower show the COD

ISBN 978-3-95450-176-2

before and after the beam based alignment for the LER. The orbit is smoother, especially in the arc sections, after the offset correction is included.

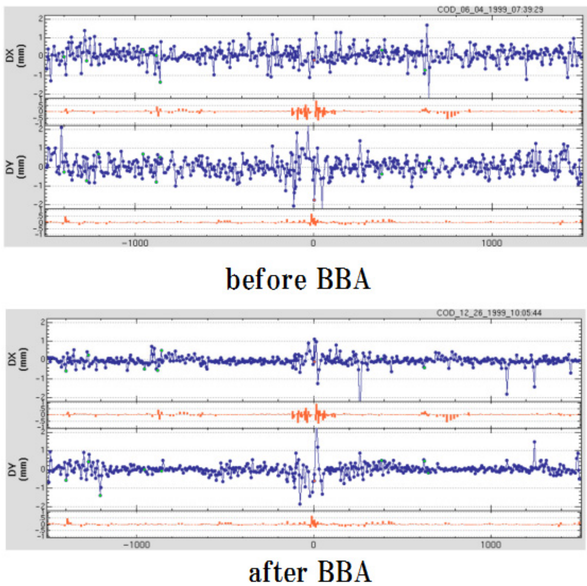

Figure 6: COD change by BBA in the LER at KEKB.

BEAM BASED GAIN CALIBRATION

The beam based gain calibration (BBGC) is a very effective method for achieving BPM accuracy. We introduce the two gain analysis methods that have been developed at KEKB and J-PARC. .

BBGC for BPM with Four Buttons

The BPM model assumes the configuration with four electrodes as illustrated in Fig. 7. The output voltage of the i-th electrode for the beam position (x, y) against the BPM center is expressed as:

$$V_i = q g_i F_i(x,y),$$

where g_i is the relative gain factor, $F_i(x,y)$ is the response function normalized to $F_i(0,0)=1$, and q is the proportional factor to the beam current. The response function depends only on the geometrical structure of the BPM head.

The beam positions are measured m times with a pick-up head, by changing the orbit at the monitor each time, the signal from the i-th electrode at the j-th measurement is given by,

$$V_{i,j} = g_i q_j F_i(x_j, y_j), \quad i = 1,,,4,\ j = 1,,,m$$

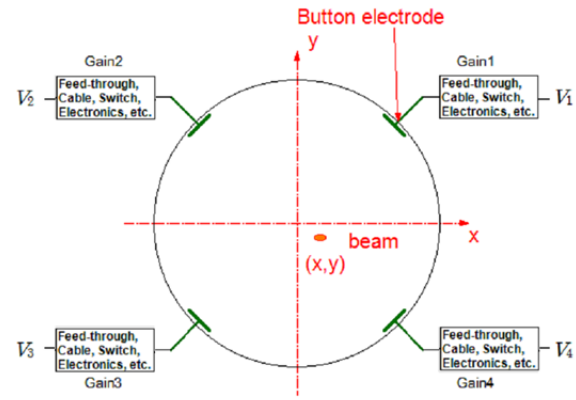

Figure 7: BPM model with 4 electrodes.

Since we can set g_1 to 1 with a proper scaling factor for the beam charge, there exist only 3 unknown gains, g_2, g_3 and g_4. We measure $V_{1,j}$, $V_{2,j}$, $V_{3,j}$ and $V_{4,j}$ at each measurement. Since g_i will not change at each measurement, q_j, x_j and y_j are unknown parameters. After the m-th measurement the number of the unknown parameters is 3+3m. The known parameters are 4m. When m is larger than 4, then 4m exceeds 3+3m, and the unknown parameters, including the gains, can be calibrated using a non-linear least-square method,

$$J(a) = \sum_{i=1}^{4} \sum_{j=1}^{m} \left[V_{i,j} - g_i q_j F_i(x_j, y_j) \right]^2$$

$$a = (g_2, g_3, g_4, q_1, x_1, y_1, \cdots, q_m, x_m, y_m),$$

where a denotes the array of fitting parameters. The fitting analysis has been performed using the Marquardt method [6] which is able to obtain the optimum value with sufficient accuracy. This BPM model has the nice symmetry that all of the response functions can be expressed with only one function,

$$\begin{aligned} F_1(x,y) &= 1 + a_1 x + b_1 y \\ &+ a_2(x^2 - y^2) + b_2(2xy) \\ &+ a_3(x^3 - 3x^2 y) + b_3(3xy^2 - y^3) \\ &+ a_4(x^4 - 6x^2y^2 + y^4) + b_4(x^3 y - xy^3), \end{aligned}$$

$$F_2(x,y) = F_1(-x,y), \quad F_3(x,y) = F_1(-x,-y),$$

$$F_4(x,y) = F_1(x,-y)$$

The expansion coefficients $(a_1,,,a_4)$ and $(b_1,,,b_4)$ are determined by fitting the measured mapping at the calibration stand or the calculated mapping by the finite boundary element method. Figure 8 shows the example of the relative gains of g_2/g_1, g_3/g_1 and g_4/g_1 of all BPM pickups in the ring which were obtained by BBGC at KEKB [6].

ISBN 978-3-95450-176-2

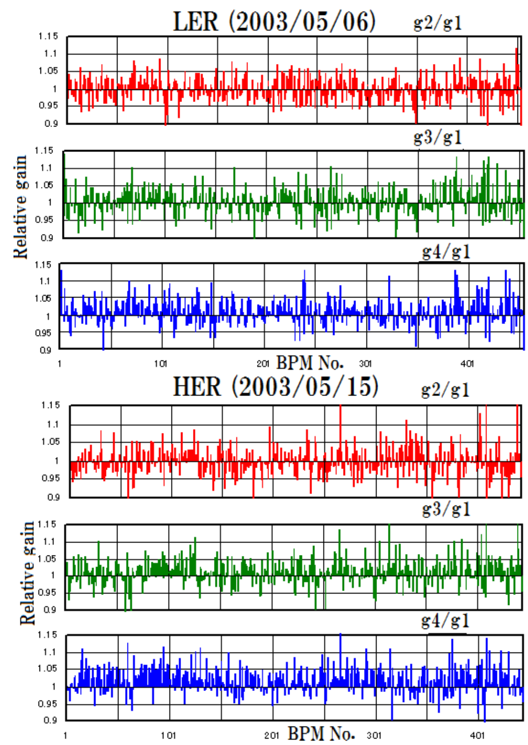

Figure 8: The Relative gains obtained by BBGC in LER (upper) and HER (lower) at KEKB. Here, horizontal scale is BPM No.

The results of the figure are the first measurement for BBGC at KEKB, where the spread of these gains is -8% ~ +8%. The gain data are used into the software to calculate the beam position, to correct the gains of all BPMs.

We converted the measured value of BPM gain into BPM offset value. We tried to compare the offset with the offset from BBA. Figure 9 shows the correlation of both offsets in the LER and the HER at KEKB. From these correlations we believe that BPM gain drift has caused the offset change.

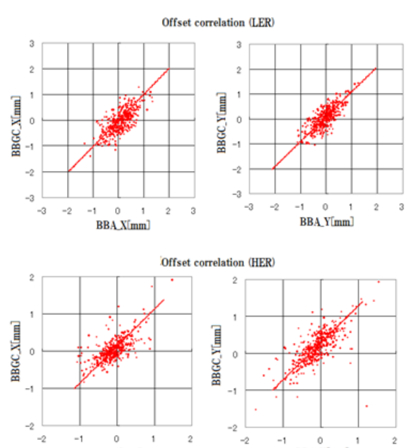

Figure 9: The correlation of both offsets in the LER and the HER at KEKB.

BBGC for BPM with Diagonal Cut

In the J-PARC MR, we adopted an electrostatic pickup with a diagonal-cut cylinder type duct as shown in Fig. 10, where the horizontal and vertical beam positions are independently detected by two pairs of pickup electrodes. The simulation was performed by using the method in the previous section to estimate gains of the MR BPMs. For these linear response pickups, the above-mentioned least squares (LS) method minimizing the sum of the square of the difference between each electrode output and the model response function is not applicable. The simulation showed the result that these gains were changed depending on the given initial values for q_j, x_j and y_j in the fitting process. The non-linear fitting method was not able to be used for the gain analysis of such diagonal cut electrodes.

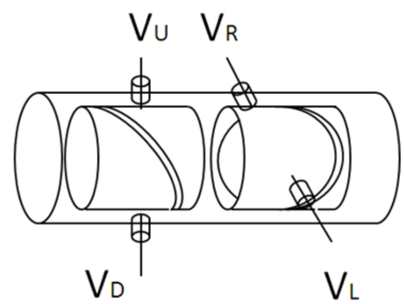

Figure 10: BPM heads with diagonal cut electrodes in J-PARC MR.

The outputs of diagonal cut electrodes for the beam position (x, y) are given by

$$V_L = \lambda\left(1+\frac{x}{a}\right), \quad V_R = g_R\lambda\left(1-\frac{x}{a}\right), \qquad (1)$$

$$V_D = g_D\lambda\left(1-\frac{y}{a}\right), \quad V_U = g_U\lambda\left(1-\frac{y}{a}\right), \qquad (2)$$

where λ is the proper normalization factor proportional to the beam current, g_R , g_U and g_D are the relative gains to the electrode L and g_L is normalized to 1, and a is the radius of the diagonal cut electrode. By eliminating λ, x, y and *a* in the above formula, we obtain the equation

$$V_L = -\frac{V_R}{g_R} + \frac{V_U}{g_D} + \frac{V_D}{g_D}$$

This linear equation express three gains in terms of four outputs. When beam positions are measured m times, the simultaneous linear equations are expressed in a matrix representation of

ISBN 978-3-95450-176-2

$$\boldsymbol{Ax} = \boldsymbol{b}\,,$$

where

$$\boldsymbol{A} = \begin{pmatrix} -V_{R,1} & V_{U,1} & V_{D,1} \\ & \vdots & \\ -V_{R,j} & V_{U,1} & V_{D,j} \\ & \vdots & \\ -V_{R,m} & V_{U,m} & V_{D,m} \end{pmatrix},$$

$$\boldsymbol{x} = \begin{pmatrix} 1/g_R \\ 1/g_U \\ 1/g_D \end{pmatrix}, \quad \boldsymbol{b} = \begin{pmatrix} V_{L,1} \\ \vdots \\ V_{L,j} \\ \vdots \\ V_{L,m} \end{pmatrix},$$

Then $V_{L,j}$, $V_{R,j}$, $V_{U,j}$ and $V_{D,j}$ denotes the measured output at the j-th measurement. The approximate solution by least squares (LS) of the linear system $\boldsymbol{Ax} = \boldsymbol{b}$ is given by

$$\boldsymbol{x}_{LS} = \left(\boldsymbol{A}^T \boldsymbol{A}\right)^{-1} \boldsymbol{A}^T \boldsymbol{b}\,,$$

when the components of matrix $\boldsymbol{A}$ have no errors. On the other hand, when $\boldsymbol{A}$ has errors, the best approximated solution is given by total least squares (TLS) method [7]. The solution of TLS is given by

$$\boldsymbol{x}_{TLS} = \left(\boldsymbol{A}^T \boldsymbol{A} - \sigma_{n+1}^2 I\right)^{-1} \boldsymbol{A}^T \boldsymbol{b}\,,$$

where n is the rank of $\boldsymbol{A}$ and σ_{n+1} is the smallest singular value of the matrix $[\boldsymbol{A}\ \boldsymbol{b}]$.

We compare the TLS method with the LS method by using simulations. In this simulations, the mapping data were generated from model outputs with the defined Eq. (1)-(2), 12500 points at 25 displaced positions with 0.2% Gaussian noise, as shown in Fig. 8. The gains were given reasonable values, set $g_R = 1$, $g_L = 1.01$, $g_U = 1.005$, $g_D = 0.975$.

Table 1: Simulation Result

	g_L	g_U	g_D
LS	1.034	1.015	0.988
Variation	0.024	0.01	0.013
TLS	1.012	1.005	0.977
Variation	0.002	0.0	0.002

The results of values given to relative gains and variation from true gains in both TLS and LS simulations are summarized in Table 1. The TLS gives smaller variations than LS. Corrected positions by obtained gains are shown as black points in Fig. 11.

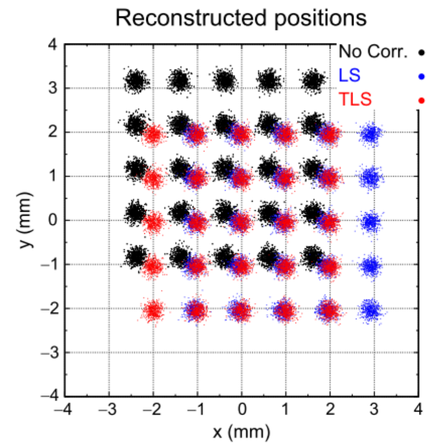

Figure 11: Reconstructed mapping data. Red: (x, y) without correction, Black: (x, y) with TLS.

By using real beam, we tested both the TLS and the LS method for diagonal cut BPMs in the J-PARC MR. The position measurements were done in nine displacements of beam positions at the BPM as shown in Fig.12. The results of gain calibrations are summarized in Table 2. We can see differences in the relative gains depend on the fitting method. The beam positions corrected by the new gain are overlapped on Fig. 14.

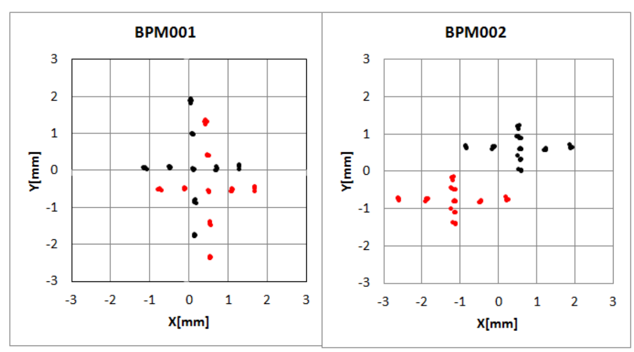

Figure 12: Measured mapping data and corrected mapping data. Red points are the measured positions without gain correction. Black points are the corrected positions with TLS method.

Table 2: Corrected Relative Gains by TLS and LS Methods

BPM001	g_L	g_U	g_D
TLS	1.0062	1.0024	0.9873
LS	1.0103	1.0045	0.9892
BPM002	g_L	g_U	G_D
TLS	0.9568	0.9811	0.9463
LS	0.9617	0.9838	0.9487

ISBN 978-3-95450-176-2

We analyzed the gains using the data obtained with actual beam. In order to obtain the mapping data of beam positions the beam orbit was kicked by a steering magnet.

The gains g_R, g_U and g_D are plotted in Fig. 13(a),(b) and (c), respectively, as functions of the address number along MR. The gains for two cases of beam intensities (low and high) are plotted as blue and red solid circles, respectively. The beam amounts of "Low" and "High" intensities are 10^{13} and 10^{14} -order protons per pulse, respectively. The gains are different by a maximum of 2–3% between the cases of "Low" and "High" intensity. The accompanied error bars are calculated as follows.

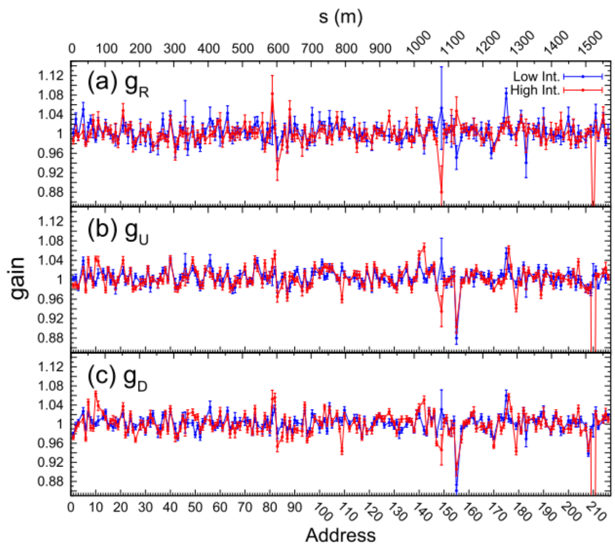

Figure 13: Relative gains calculated by TLS method. g_R, g_U and g_D are plotted. The gains for low intensity (blue line) and high intensity (red line) are plotted Here, horizontal scale is BPM No.

EVALUATION OF GAIN CORRECTION

Examination of Four Button Pickups at KEKB

Usually the beam position is calculated from the output of four electrodes as Fig.1. We obtain the normalization of the signals (X, Y) as

$$X = \frac{V_1 - V_2 - V_3 + V_4}{V_1 + V_2 + V_3 + V_4}, \quad Y = \frac{V_1 + V_2 - V_3 - V_4}{V_1 + V_2 + V_3 + V_4}.$$

Mapping measurement was made at many mesh points in the central area. We fitted third order polynominals (F_x, F_Y) of two variables (X, Y) for these mesh data to describe the relation between (x, y) and (X, Y) for each BPM as follows

$$x = F_X(X,Y),\ y = F_Y(X,Y),$$

where

$$F_X(X,Y) = a_0 + a_1 X + a_2 Y + a_3 X^2 + a_4 XY + a_5 Y^2 \\ + a_6 X^3 + a_7 X^2 Y + a_8 XY^2 + a_9 Y^3,$$

$$F_Y(X,Y) = b_0 + b_1 X + b_2 Y + b_3 X^2 + b_4 XY + b_5 Y^2 \\ + b_6 X^3 + b_7 X^2 Y + b_8 XY^2 + b_9 Y^3,$$

where the coefficients ($a_n, b_n \cdots n = 1,2,,,9$) are obtained by fitting of the mapping data.

The beam position is also obtainable from the output voltage of any three electrodes chosen out of four electrodes. Using the same data, we also obtained the normalizations of two electrodes as

$$\begin{cases} X_1 = (V_1 - V_2)/(V_1 + V_2),\ X_2 = (V_3 - V_4)/(V_3 + V_4) \\ Y_1 = (V_2 - V_3)/(V_2 + V_3),\ Y_2 = (V_1 - V\ )/(V_1 + V_4) \end{cases}$$

Then it gives the four relations between the beam position and the normalization as follows:

$$\begin{cases} (x_1, y_1) = \left(F_X^{ABC}(X_1, Y_1),\ F_Y^{ABC}(X_1, Y_1)\right) \\ (x_2, y_2) = \left(F_X^{BCD}(X_2, Y_1), F_Y^{BCD}(X_2, Y_1)\right) \\ (x_3, y_3) = \left(F_X^{ACD}(X_2, Y_2), F_Y^{ACD}(X_2, Y_2)\right) \\ (x_4, y_4) = \left(F_X^{ABD}(X_1, Y_2), F_Y^{ABD}(X_1, Y_2)\right) \end{cases},$$

where functions (F_X, F_Y) are third order polynominals for three electrodes of BPM.

If the four outputs have ideal correlation, these four beam positions ((x_1, y_1), (x_2, y_2), (x_3, y_3), (x_4, y_4)) should coincide with each other. The software procedure for the BPM system performs calculation of not only beam positions using four electrodes, but also four beam positions using three electrodes to examine consistency among these positions. The deviations among the four beam positions are represented by the standard deviation formula as follows:

$$\begin{cases} \sigma_X = \sqrt{\frac{1}{4}\sum_{i=1}^{4}(X_i - \bar{X})^2} \quad with \quad \bar{X} = \frac{1}{4}\sum_{i-1}^{4}(X_i) \\ \sigma_Y = \sqrt{\frac{1}{4}\sum_{i=1}^{4}(Y_i - \bar{Y})^2} \quad with \quad \bar{Y} = \frac{1}{4}\sum_{i-1}^{4}(Y_i) \end{cases}, \quad (3)$$

where σ_x and σ_y are the standard deviations among four beam positions called the consistency error of beam position measurement.

Figure 14 shows an example of the distributions of the consistency error at KEKB.

As a result of having corrected the output voltage with new gains, the consistency error became very small.

ISBN 978-3-95450-176-2

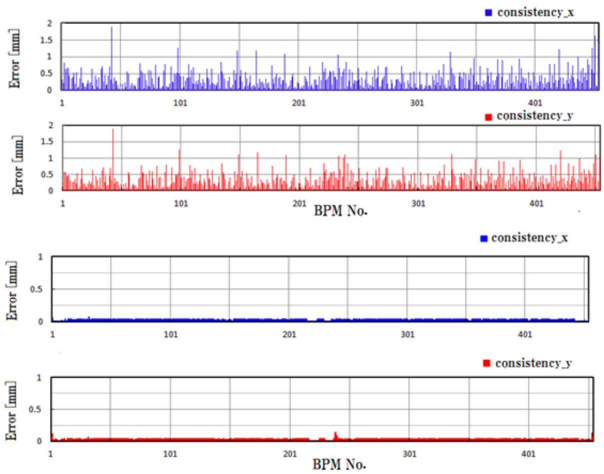

Figure 14: Consistency before (top) and after (bottom) gain calibration in LER at KEKB, horizontal scale is BPM No.

Examination of BPM Gain at J-PARC MR

To evaluate the analyzed gains, we checked the consistencies of four positions calculated from Eqs. (1) and (2) as following,

$$x_1 = \frac{V_L - V_R/g_R}{V_L + V_R/g_R}a, \quad y_1 = \frac{V_U/g_U - V_D/g_D}{V_U/g_U + V_D/g_D}a$$

$$x_2 = \frac{V_L - V_R/g_R}{V_U/g_U + V_D/g_D}a, \quad y_2 = \frac{V_U/g_U - V_D/g_D}{V_L + V_R/g_R}a$$

$$x_3 = \left(\frac{2V_L}{V_U/g_U + V_D/g_D} - 1\right)a, \quad y_3 = \left(\frac{2V_U/g_U}{V_L + V_R/g_R} - 1\right)a$$

$$x_4 = \left(\frac{-2V_R/g_R}{V_U/g_U + V_D/g_D} + 1\right)a, \quad y_4 = \left(\frac{-2V_D/g_D}{V_L + V_R/g_R} + 1\right)a$$

where (x_1, y_1) is the position using two electrodes in the horizontal or vertical direction, (x_2, y_2) is the position using four electrodes, and (x_3, y_3) and (x_4, y_4) are obtained using three electrodes. We also defined the consistency of x and y as σ_x and σ_y in Eq. (3).

Table 3 shows improvement of consistency error by using BBGC.

Table 3: Consistency Before and after Gain Calibration of BPM at J-PARC MR

	Before		After	
	σ_X[mm]	σ_Y[mm]	σ_X[mm]	σ_Y[mm]
BPM001	0.524	0.518	0.018	0.018
BPM002	0.964	0.954	0.025	0.025

CONCLUSION

We should pay some special attention to guarantee precise measurement of beam positions over a long time. The BBA measurement is useful for correction of the BPM offset error. The gain balance among four outputs of a BPM changes gradually over a long period. The imbalance among the gains gives offset errors to beam position. The most probable source of the gain drift is the change in the electrical characteristics of the transmission line of the signal by temperature drift, because we found seasonal variation in the gain drift at KEKB. We have achieved a high-accuracy BPM system by monitoring the consistency error and applying beam-based gain calibration [8].

REFERENCES

[1] M. Masuzawa et al. Proceedings of EPAC 2000, Vienna, Austria, p.1780.
[2] K. SATOH and M. TEJIMA, Proceedings of the 1997 Particle Accelerator Conference, Vancouver, 2087.
[3] M. Tejima et al. Proceedings of DIPAC2011, Humburg, Germany, p. 275.
[4] M. Tejima et al. Proceedings of the 11th Symposium on Accelerator Science and Technology, Spring-8 Ako, Hyogo Japan, from October 21 - 23, 1997.
[5] T. Toyama et al., "Beam-Based alignment of the BPMs at J-PARC MR", Proc. of Particle Accelerator Society Meeting 2014, Aomori, Japan, 739–743, 2014.
[6] D. Marquardt, "An algorithm for least-squares estimation of nonlinear parameters," SIAM J. Appl. Math., 1963, Vol. 11, pp. 431–441.
[7] I. Markovsky and S. V. Huffel, Signal Processing 87 (2007) 2283.
[8] M.Arinaga et al.,"Progress in KEKB beam instrumentation systems", Prog. Theor. Exp. Phys. 2013, 03A007 (31 pages).

ISBN 978-3-95450-176-2

PROGRESS TOWARDS ELECTRON-BEAM FEEDBACK AT THE NANOMETRE LEVEL AT THE ACCELERATOR TEST FACILITY (ATF2) AT KEK

N. Blaskovic Kraljevic, D. R. Bett, T. Bromwich, P. N. Burrows, G. B. Christian, M. R. Davis, C. Perry,
John Adams Institute, Oxford, UK

Abstract

Ultra-low latency beam-based digital feedbacks have been developed by the Feedback On Nanosecond Timescales (FONT) Group and tested at the Accelerator Test Facility (ATF2) at KEK in a programme aimed at beam stabilisation at the nanometre level at the ATF2 final focus. Three prototypes were tested: 1) A feedback system based on high-resolution stripline BPMs was used to stabilise the beam orbit in the beamline region c. 50m upstream of the final focus. 2) Information from this system was used in a feed-forward mode to stabilise the beam locally at the final focus. 3) A final-focus local feedback system utilising cavity BPMs was deployed. In all three cases the degree of beam stabilisation was observed in high-precision cavity BPMs at the ATF2 interaction point. Latest results are reported on stabilising the beam position to approximately 50nm.

INTRODUCTION

A number of fast beam-based feedback systems are required at future single-pass beamlines such as the International Linear Collider (ILC) [1]. For example, at the interaction point (IP) a system operating on nanosecond timescales within each bunch train is required to compensate for residual vibration-induced jitter on the final-focus magnets by steering the electron and positron beams into collision. The deflection of the outgoing beam is measured by a beam position monitor (BPM) and a correcting kick applied to the incoming other beam. In addition, a pulse-to-pulse feedback system is envisaged for optimising the luminosity on timescales corresponding to 5 Hz.

The Feedback on Nanosecond Timescales (FONT) project has developed ILC prototype systems, incorporating digital feedback processors based on Field Programmable Gate Arrays (FPGAs), to provide feedback correction systems for sub-micron-level beam stabilisation at the KEK Accelerator Test Facility (ATF2) [2]. Previous results [3], [4] have demonstrated an upstream closed-loop feedback system that meets the ILC jitter correction and latency requirements. Earlier results demonstrating the propagation of the correction obtained using the upstream stripline BPM feedback system at ATF2 are reported in [5]. The ultimate aim is to attempt vertical beam stabilisation at the nanometre-level at the ATF2 IP [6]. An overview of the extraction and final focus beamlines at the ATF, showing the positions of the FONT5 system components in both the upstream and IP regions, is given in Fig. 1.

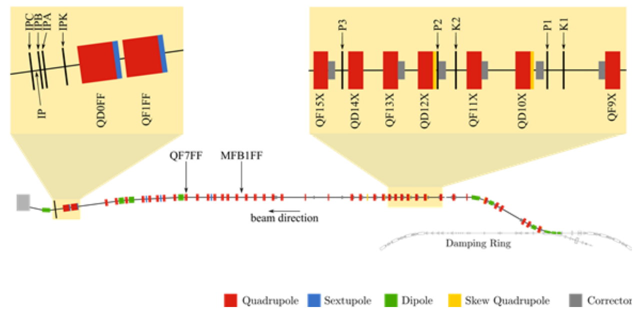

Figure 1: Layout [7] of the ATF extraction and final focus beamline with the FONT regions zoomed in.

We report here the latest developments and beam testing results from the FONT project using both the upstream stripline BPM system as well as near-IP cavity BPMs [8,9] to drive feedbacks for stabilising the beam at the IP.

UPSTREAM FEEDBACK SYSTEM

The upstream feedback system (Fig. 1) comprises 3 stripline BPMs and 2 stripline kickers. The design goal for this system is to stabilize the vertical beam position to the 1 µm level at the entrance to the final-focus system. This requires BPMs capable of resolving bunches separated in time by around 100 ns, and with a position resolution at the submicron level. For tests of the FONT5 system the ATF is operated in a mode whereby a train of two or three bunches is extracted from the damping ring and sent down the ATF2 beam line. The bunch separation is determined by the damping ring fill pattern and typically is chosen to be between 140 ns and either 154 ns (3-bunch mode) or 300 ns (2-bunch mode).

Stripline BPMs (Fig. 2) were used due to their inherently fast, broadband response and capability to resolve bunches with the required time resolution. In the FONT5 system only the vertical plane of the BPMs is routinely instrumented (Fig. 3) with an analogue processor (Fig. 4), which functions [7] so as to deliver the stripline pickoff-pair difference and sum signals in a form that can be easily recorded by the digitizer for calculation of the position-dependent, beam charge-independent ratio of the two. Ten processors were built and are used in beam operations at ATF2. A single BPM processor can be used to process the beam position data in either the horizontal or vertical plane; from here on only the vertical plane is considered.

ISBN 978-3-95450-176-2

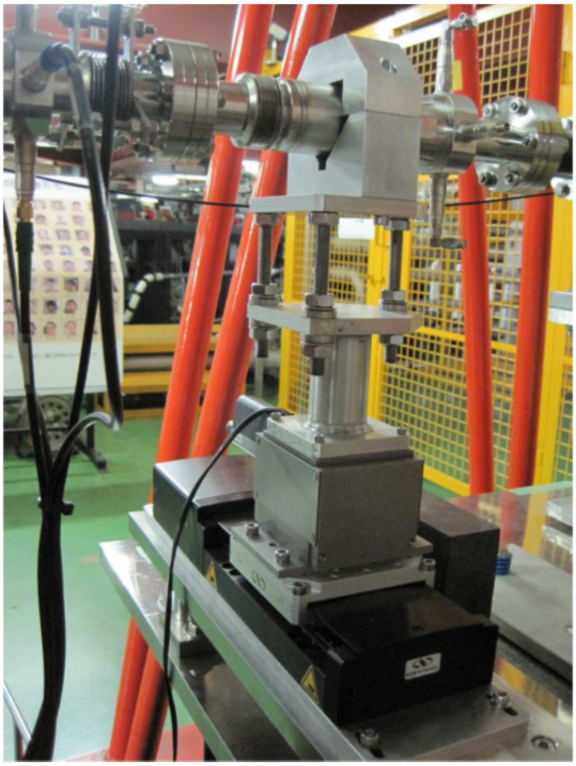

Figure 2: Photograph of FONT5 stripline BPM P3 and its mover in the ATF2 beam line.

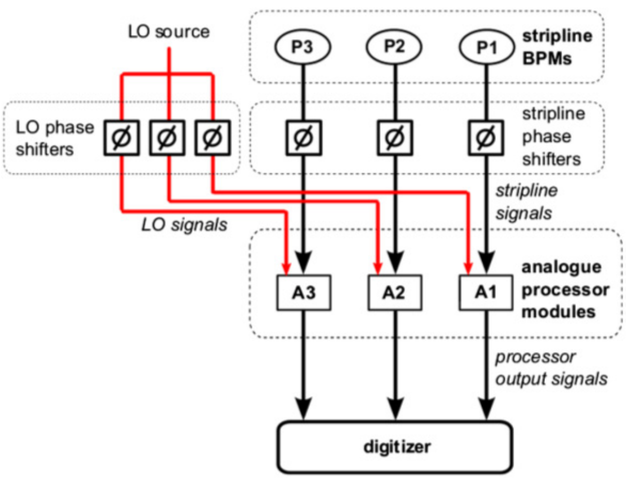

Figure 3: Schematic of the BPM system. For each BPM, a phase shifter is used on one of the stripline signals to adjust the relative path lengths of the two input signals at the BPM processor, and another phase shifter is used to adjust the phase of the LO signal at each processor.

Analogue Processor Latency

The latency of the processor is defined to be the time interval between the arrival of the stripline signals at the inputs and the peak of the signals at the outputs. One of the principal design goals was that the latency should be low, while providing baseband output pulses that are amenable to convenient digitization. The latency was measured by using a test bench to provide realistic beam-proxy input signals and observing on an oscilloscope the arrival time of the processed output signal (Fig. 6). Subtracting from this the time of arrival at the oscilloscope of the input when the processor is bypassed, the processor latency before the amplifier stage was found to be 10.4+-0.1 ns, and 15.6+-0.1 ns including the amplifier stage (Fig. 4).

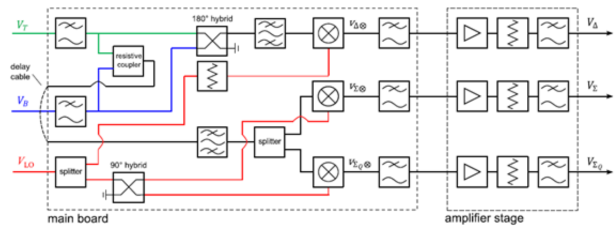

Figure 4: Schematic diagram illustrating the structure of the FONT5 analogue processor.

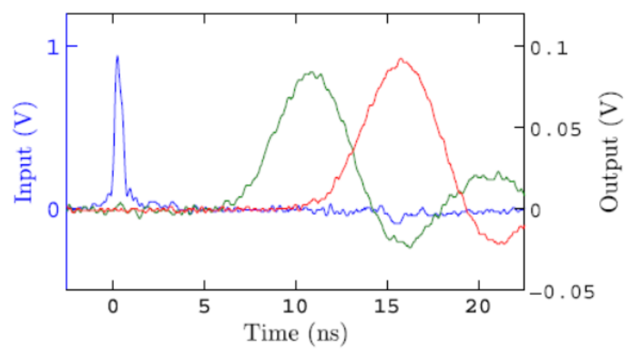

Figure 5: Input beam proxy signal (blue, left-hand scale) and processor output difference signal before the amplifier stage (green, right-hand scale, with factor 5 multiplication), and after the amplifier stage (red, right-hand scale), vs time (ns). The amplifier stage delays the output signal by an additional 5.2 ns.

Digitisation

The BPM processor outputs are digitised by the FONT5 custom digital feedback processor board (Fig. 6). The board has nine analogue signal input channels digitised using ADCs with a maximum conversion rate of 400Ms/s

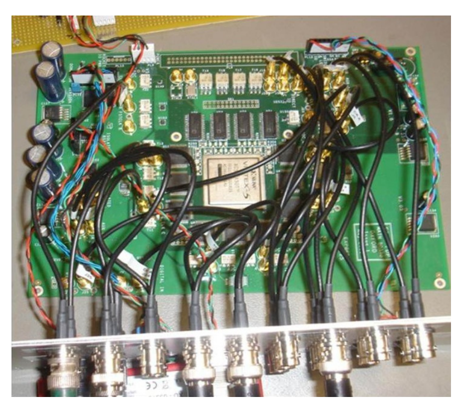

Figure 6: FONT5 digital feedback board.

ISBN 978-3-95450-176-2

and two analogue output channels formed using DACs, which can be clocked at up to 210 MHz. The digital signal processing is based on a Xilinx Virtex5 FPGA. The FPGA is clocked with a 357 MHz source derived from the ATF master oscillator and hence locked to the beam. The ADCs are clocked at 357 MHz.

BPM Performance

The range of linear response is defined to be the range over which the system responds linearly to a change in beam position. A nonlinear response is expected if the input signal to a mixer (Fig. 4) is large enough to cause its output to saturate. Saturation will be avoided if the mixer RF input signal level is small compared with the design LO input signal level, ~7 dBm. For optimum resolution, the stripline BPM signals can be attenuated to ensure that for the nominal beam charge (~1 nC) the sum-channel signal level is comfortably below the mixer saturation point. The processor output is then expected to be linear for $|y| \lesssim 400$ µm, in agreement with corresponding measurements [7].

The resolution of the system is determined by comparing the beam position measured in one BPM with the position predicted at that BPM on the basis of the beam positions measured in the other two BPMs. Assuming that the three BPMs have the same resolution, σ, these residuals yield a resolution estimate, for a centred beam with a bunch charge of approximately 1 nC, of σ = 291+-10 nm [7] which is world leading in terms of the position resolution obtained in stripline BPMs in single-pass beam mode. Such a level of performance is achieved routinely in beam operations. For comparison, a global least-squares fit can be performed to explicitly minimize σ. For the same data set this yields a value for the resolution of 262+-11 nm. As this method removes any correlated components of the BPM position data, and also allows for variation in the individual BPM scale factors, this result represents the minimum possible resolution that could, in principle, be attained, if for example any residual correlated effects were accounted for. In contrast, the value obtained using the beam line model better represents the actual minimum sensitivity attainable in a given position measurement. The value attained with the least-squares fit is consistent with that expected from the measured system noise.

Upstream Feedback System Performance

Fig. 7 shows the vertical position of bunches 1 and 2 recorded in the feedback input BPMs, P2 and P3, as well as in the downstream BPM MFB1FF (see Fig. 1), which acts as an independent witness of the beam correction by the feedback loop. By construction bunch 1 is not corrected, but provides the input position information for the correction of bunch 2. The feedback reduced the vertical beam jitter from an r.m.s. deviation of 1.9um to 0.5um (P2) and from 1.7um to 0.6um (P3), representing a jitter reduction by a factor of slightly more than 3. The jitter at BPM MFB1FF, roughly 30m downstream, was reduced by the same factor, from 26um to c. 8um, thus demonstrating no detectable additional sources of beam jitter between P3 and MFB1FF.

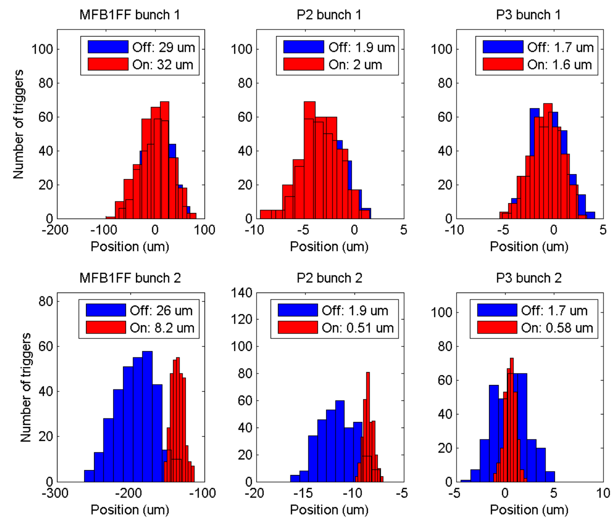

Figure 7: Distribution of vertical beam position measured in BPM (left to right) MFB1FF, P2 and P3 for bunch 1 (top row) and bunch 2 (bottom row) with feedback off (blue) and on (red) respectively.

A detailed simulation of the ATF2 beamline was used [8] to model the tracking of the vertical beam position from the measured inputs at P2 and P3 to the downstream locations of MFB1FF and the IP. The simulation reproduced accurately the measured position distribution at MFB1FF [8]. The implied jitter reduction at the IP was from c. 9.5nm to c. 3.6nm. Hence the upstream stripline-based feedback system is capable of delivering beam stabilisation at the IP at the few nanometre level. Though the beam position near the IP can be monitored using the local cavity BPMs (see Fig. 1), as described in the next section their resolution is not yet sufficient to be able to resolve beam jitter at the nanometre level, so that the predicted degree of beam stabilisation cannot yet be verified.

IP FEEDBACK SYSTEM

The IP feedback system (Fig. 8) comprises a C-band cavity BPM (IPB) [8,9] and a short stripline kicker (IPK). The final focus magnets (QF1FF, QD0FF) can be used to steer the beam by introducing a position offset or to move the x and y beam waists longitudinally along the beamline. The offset of the QF7FF magnet can be used to change the pitch of the beam trajectory through the IP region.

Determining the position of the beam at IPB requires both the dipole mode signal of IPB and the monopole mode signal of a reference cavity (Ref). The cavities were designed such that the y-port frequency of both signals is 6.426 GHz [8]. The signals are down-mixed to baseband using a two-stage down-mixer [10], as follows. The first stage down-mixer (M1) takes the 6.426 GHz reference

ISBN 978-3-95450-176-2

and IPB signals and mixes each with an external, common 5.712 GHz local oscillator (LO) to produce down-mixed signals at 714 MHz. The second stage down-mixer (M2) mixes the IPB 714 MHz signal using the reference 714 MHz as LO, giving two baseband signals: I (IPB and reference mixed in phase) and Q (IPB and reference mixed in quadrature). The I and Q signals are subsequently digitised in the FONT5 digital board and normalised by the beam bunch charge; the charge is deduced from the amplitude of the reference cavity signal. The charge-normalised I and Q signals are calibrated against known beam position offsets (by moving the beam using QD0FF), allowing the IPB vertical beam position to be known in terms of a linear combination of charge-normalised I and Q.

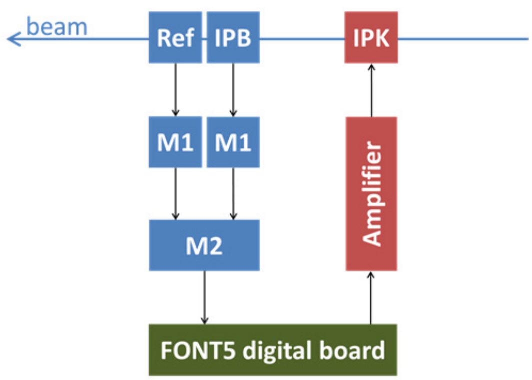

Figure 8: Schematic of IP feedback system showing the cavity BPM (IPB), reference cavity (Ref), first and second down-mixer stages (M1 and M2), FONT5 digital board, amplifier and kicker (IPK).

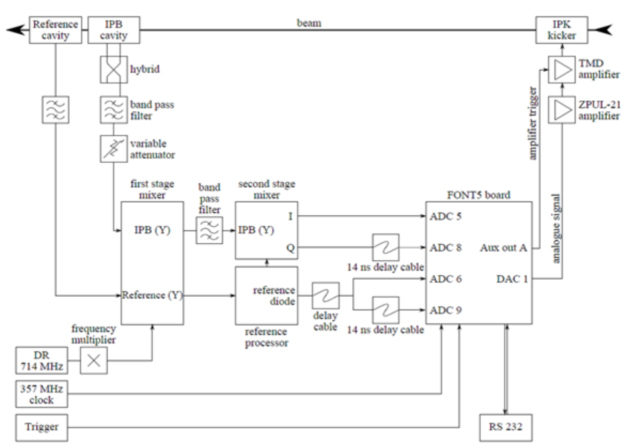

Figure 9: Schematic of operation of IP feedback system.

IP Feedback System Performance

We report the results of beam tests of the FONT5 system in the 2014 running period; earlier tests were reported in [11,12]. A detailed schematic of the hardware configuration is shown in Fig. 9.

The ATF was set up to provide two bunches per pulse of beam extracted from the damping ring, with a bunch separation of 274.4 ns. This separation was found typically to provide a high degree of measured vertical spatial correlation between the two bunches. The feedback tests therefore involve measuring the vertical position of bunch one and correcting the vertical position of bunch two. The system was typically operated in an 'interleaved' mode, whereby the feedback correction was toggled on and off on alternate machine pulses; the feedback 'off' pulses thereby provide a continual 'pedestal' measure of the uncorrected beam position. For the purpose of recording data with BPM IPB the longitudinal location of the beam waist in the IP region was adjusted by varying the strengths of the two final focus magnets QF1FF and QD0FF. For the results reported here the beam waist was typically set near the position of IPB.

The IP feedback system latency was measured and found to be 134 ns; however this could be reduced if, for example, a greater effort was made to optimise cable lengths. The performance of the feedback system was measured using IPB. Figure 10 shows the vertical position of bunch two recorded in IPB. The IP feedback reduced the vertical beam jitter from an r.m.s. deviation of 410 nm to 67 nm. The time-sequence of the data from the same run is shown in Fig. 11.

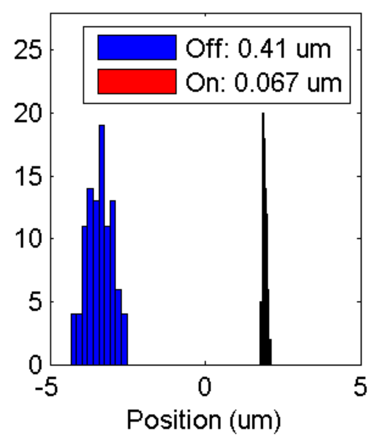

Figure 10: Distribution of the vertical position of bunch two in IPB with (red) and without (blue) application of the IP feedback correction.

In order to study the feedback operation a scan was performed of the beam waist longitudinal position around the nominal centre of IPB by varying the current in the QD0FF magnet (Fig. 1). As the focal point is moved longitudinally away from the centre of IPB, the vertical beam jitter measured in IPB increases (Fig. 12b). Also, due to their slightly different incoming beam trajectories, this scan had the effect of changing the vertical position of bunch 2 w.r.t. bunch 1 (Fig. 12a). Both changes allow a test of the feedback performance. The range of vertical position change of bunch 2 was roughly +-4 um w.r.t. nominal centre, and the incoming beam jitter varied up to about 400 nm. Figure 13b shows that the feedback reduced the incoming beam jitter at all scan points. The expected bunch 2 feedback-on jitter can be computed

ISBN 978-3-95450-176-2

using the feedback-off jitter and bunch 1-2 position correlation measurements; this is shown in Fig. 12b, and agrees remarkably well with the measured bunch 2 jitter.

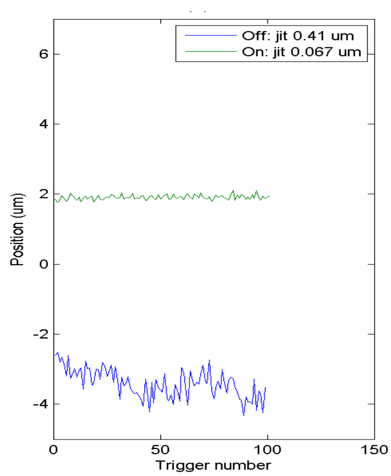

Figure 11: Time-sequence of the vertical position of bunch two in IPB with (green) and without (blue) application of the IP feedback correction.

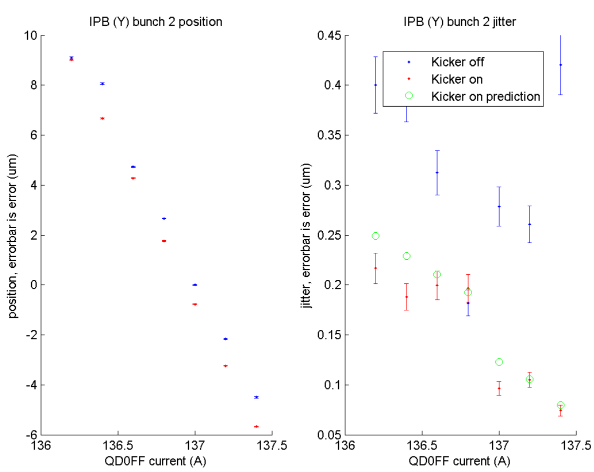

Figure 12: Bunch two mean position (a, left) and position jitter (b, right) with (red) and without (blue) application of the IP feedback correction. The green circles in (b) represent the predicted performance (see text).

Assuming that the FB performance is currently limited by the resolution of the cavity BPMs employed, the best position jitter stabilisation achieved, 67 nm, implies a BPM resolution of around 50 nm. This is consistent with direct estimates of the resolution determined using the system of three C-band BPMs at the ATF2 IP [8]. This is also consistent with fine scans of the longitudinal beam waist position at IPB, which yield a minimum measured beam jitter of around 50 nm (Fig. 13).

CONCLUSIONS

Beam stabilisation at the ATF2 IP using both stripline and cavity BPMs has been demonstrated. Vertical beam position stabilisation was achieved at the level of 0.5um in the upstream system, corresponding to an implied 3nm stabilisation at the IP. Local IP feedback was used to stabilise the beam directly to the level of 67nm. Work is ongoing to improve the resolution of the cavity BPMs near the IP from the currently measured value of c. 50nm in order to obtain improved results.

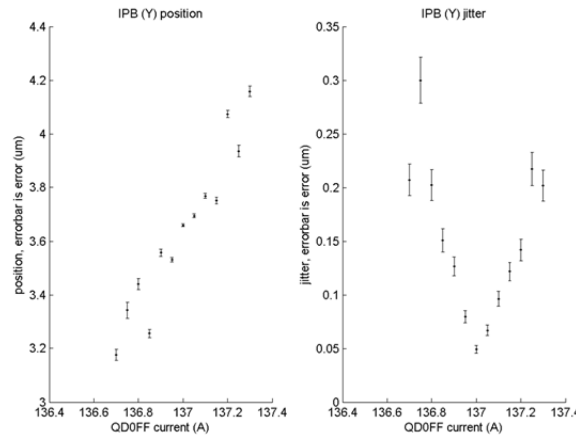

Figure 13: Bunch two mean position (a, left) and position jitter (b, right) vs. QD0FF current.

ACKNOWLEDGMENTS

We thank the KEK ATF staff for their outstanding logistical support and beam time and our ATF2 collaborators, especially from KNU and LAL, for their help and support. Financial support was provided by the UK Science and Technology Facilities Council and CERN contract KE1869/DG/CLIC.

REFERENCES

[1] C. Adolphsen et al., The ILC technical design report, volume 3: Accelerator, JAI-2013-001, 2013.
[2] G. R. White et al., Phys. Rev. Lett., vol. 112, p. 034802 (2014).
[3] R. Apsimon et al., Proceedings IPAC11, MOPO17.
[4] D. R. Bett et al., Proceedings IPAC12, WEPP068.
[5] P. N. Burrows et al., IPAC2014 Proceedings, TUPME009.
[6] B. I. Grishanov et al., ATF2 proposal, vol. 2, KEK Report 2005-9, 2005.
[7] R.J. Apsimon et al., Phys. Rev. ST Accel. Beams, vol. 18, p. 032803 (2015).
[8] N. Blaskovic Kraljevic, DPhil thesis, Oxford University, 2015.
[9] Y. I. Kim, PhD thesis, Kyungpook National University, 2012.
[10] Y. Inoue et al., Phys. Rev. ST Accel. Beams, vol. 11, p. 062801, 2008.
[11] M. R. Davis et al., Proceedings IPAC13, WEPME053.
[12] N. Blaskovic Kraljevic et al, Proceedings IPAC14, THOAA02.

ISBN 978-3-95450-176-2

DIRECT OBSERVATION OF ULTRALOW VERTICAL EMITTANCE USING A VERTICAL UNDULATOR

K. P. Wootton*,†, The University of Melbourne, Parkville, VIC, 3010, Australia

Abstract

In recent work, the first quantitative measurements of electron beam vertical emittance using a vertical undulator were presented, with particular emphasis given to ultralow vertical emittances [K. P. Wootton, et al., Phys. Rev. ST Accel. Beams, 17, 112802 (2014)]. Using this apparatus, a geometric vertical emittance of 0.9 ± 0.3 pm rad has been observed. A critical analysis is given of measurement approaches that were attempted, with particular emphasis on systematic and statistical uncertainties. The method used is explained, compared to other techniques and the applicability of these results to other scenarios discussed.

INTRODUCTION

The low emittance ring community expects direct observation of beam size as demonstration of ultralow vertical emittance in electron storage rings. In particular, the development of low emittance tuning routines at electron storage rings for proposed linear collider damping rings has motivated the measurement of pm rad vertical emittances. A variety of techniques for measuring vertical emittance have been developed, typically utilising imaging, interferometry or projection of the distribution of spontaneous synchrotron radiation produced by the electron beam.

Recent experiments and simulations have demonstrated that undulator radiation from a vertical insertion device is particularly sensitive to pm rad vertical emittance [1]. However the use of a vertical undulator beamline for direct measurement of pm rad vertical emittance in a storage ring presented several challenges. This work is a critique of several experimental approaches to the measurement of vertical emittance using a vertical undulator.

THEORY

The use of a vertical undulator for measurement of vertical emittance in an electron storage ring was first proposed by S. Takano in 1997 [2]. Using simulations, it was demonstrated that a measurement of the on-axis flux from a short vertical insertion device could be used to evaluate the vertical emittance in the SPring-8 storage ring.

The spectral brilliance of a planar undulator yields a distribution with odd harmonics of high intensity, and null even harmonics. The angular distribution of radiation for the first harmonic illustrated in Fig. 1(a) of Ref. [3] could be approximated by a Gaussian distribution. However, using the first harmonic for a vertical emittance monitor with an opening angle of order $\approx 1/\gamma$ limits the minimum electron beam emittance which can be deconvolved from a measured photon distribution to approximately the same order.

This approximation breaks down at high undulator harmonics. High harmonics yield an angular distribution of undulator radiation which can be described as the fine structure of a narrow interference pattern within the usual cone of undulator radiation. This pattern exhibits minima on axis for even harmonics, and maxima on axis for odd harmonics, and enables measurement of emittances smaller than the undulator radiation opening angle. Employing a narrow interference pattern convolved with the electron beam distribution, this technique is similar to several other emittance diagnostics, such as the π-polarisation technique [4], synchrotron radiation interferometer [5], X-ray Fresnel diffraction [6] and the coded aperture X-ray emittance monitor [7].

PREVIOUS MEASUREMENTS OF ULTRALOW VERTICAL EMITTANCE

Vertical emittance measurements in 2008 at the SLS using the π-polarisation technique demonstrated $\varepsilon_y = 3.2 \pm 0.7$ pm rad [4].

Experiments conducted in 2010 using the AS storage ring demonstrated through indirect measurements a vertical emittance of $\varepsilon_y = 1.2^{+0.3}_{-0.2}$ pm rad [8].

In 2012, a new vertical emittance of $\varepsilon_y = 0.9 \pm 0.4$ pm rad was observed using the direct π-polarisation technique at the SLS storage ring [9].

With the goal of optimising the AS storage ring for lower vertical emittance, a beam-based survey of storage ring magnets was undertaken [10], culminating in 2012 in the mechanical alignment of individual sextupole magnets within vertical tolerances of $\Delta y < \pm 25$ µm [11]. Indirect measurements of the bunch volume by the Touschek lifetime demonstrated vertical emittances below 1 pm rad [11].

The goal of the work presented in [3, 12] was direct measurement of picometre electron beam vertical emittance beams at the AS storage ring.

MEASUREMENT APPROACHES

The flux ratio of the 14$^{\text{th}}$ to 15$^{\text{th}}$ harmonics was measured using the approaches of energy scans, time-averaging and electron beam orbit bumps. These harmonics were selected as they were the highest undulator harmonics (greatest sensitivity to vertical emittance) which were still lower in photon energy than the Au absorption edge cutoff of 2150 eV for the beamline, which arises from Au coatings on the beamline mirrors [13].

* k.wootton@student.unimelb.edu.au
† Present address: SLAC National Accelerator Laboratory, Menlo Park, CA, 94025, USA.

ISBN 978-3-95450-176-2

Photon Energy Spectrum

Initial experiments were conducted by scanning the beamline monochromator [1, 14]. The positions of four blades were optimised to minimise the size and vertical position of the on-axis pinhole passing undulator radiation. In those experiments, the size of the pinhole was not measured, hence the emittance could not be directly inferred. Instead, the vertical emittance of the electron beam was set based on model values determined using LOCO [15].

In practice, it was not possible to simultaneously minimise the position and size of the pinhole within the tolerance required to directly measure emittances. The fitted pinhole dimension and position were the principal systematic uncertainty limiting the direct measurement of vertical emittance.

Time Averaging

One way to minimise the statistical uncertainty in a given measurement is to increase the number of acquisitions of that quantity. For a given mean of the sample population μ, the statistical uncertainty $\delta\mu$ for n acquisitions is [16]

$$\delta\mu = \frac{\sigma}{\sqrt{n}}, \tag{1}$$

where σ is the standard deviation of the sample population. This approach was used effectively to minimise the statistical uncertainty in the measurement of vertical emittance [17]. However, the systematic uncertainty arising from the pinhole position remained.

Blade Scans

Instead of optimising for a pinhole dimension, a single blade was scanned vertically through the undulator radiation distribution [18]. The vertical angular distribution of undulator radiation was recovered from by numerically differentiating the transmitted intensity with respect to vertical position. The recovered and simulated vertical distribution of undulator radiation for vertical emittances of 100 pm rad and 1 pm rad are plotted in Fig. 1.

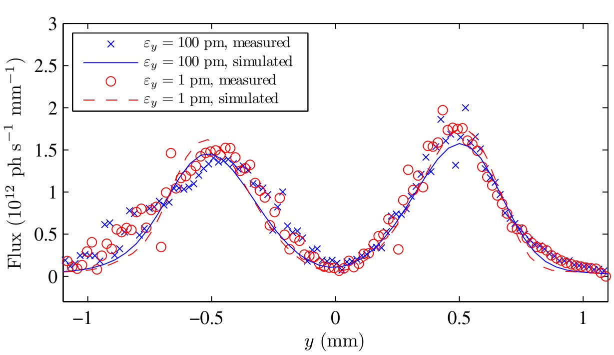

Figure 1: Measured undulator radiation distribution profile recovered from blade scan at the 6th undulator harmonic. With the electron beam set to vertical emittances of 100 pm rad and 1 pm rad, there is not sufficient sensitivity for a direct emittance measurement.

Figure 1 shows that there is a small difference in the measured radiation distributions for significantly different vertical emittances. However, this technique is not sufficiently sensitive to discriminate emittances on the order of pm rad.

Orbit Bumps

Instead of optimising for both the centred position and minimum pinhole size, the decision was made to optimise only the vertical pinhole dimension. The blade positions were optimised with the beamline monochromator aligned to pass a high, odd undulator harmonic (the 15th). With one blade positioned near the centre of the undulator radiation distribution, the second was closed by moving vertically in steps. As illustrated in Fig. 3 of Ref. [3], it was possible to close the two blades to a sensible pinhole height of 5 ± 5 µm. However, this minimised pinhole size was not necessarily correctly positioned to pass the centre of the undulator radiation distribution.

To scan through the centre of the undulator radiation distribution, vertical orbit bumps were made across the two sectors of the AS storage ring adjacent to the insertion device. Figure. 10 of Ref. [3] illustrates the trajectory arising from a four-corrector closed orbit bump which results in a vertical angle kick through the insertion device. The vertical distribution of undulator radiation was measured passing the optimised pinhole by scanning the bump magnitude of the electron beam in the storage ring.

RESULTS

The flux ratio of the 14th to 15th harmonics was measured using the several approaches outlined. The AS storage ring was set using LOCO with lattices of various ultralow vertical emittances below 100 pm rad, and the vertical emittance was measured at these setpoints. Measurements ultralow vertical emittance using orbit bumps were presented in Ref. [3]. Here, measurements using energy scans and time averaging are also compared, and presented in Figs. 2 and 3.

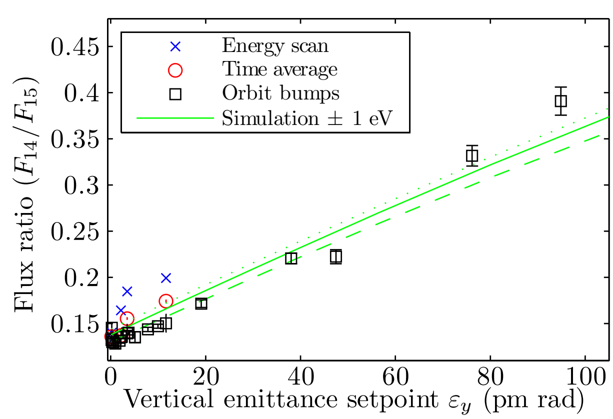

Figure 2: Measured flux ratio F_{14}/F_{15} compared for several measurement approaches. The simulated flux ratio for various vertical emittances is indicated by a line.

ISBN 978-3-95450-176-2

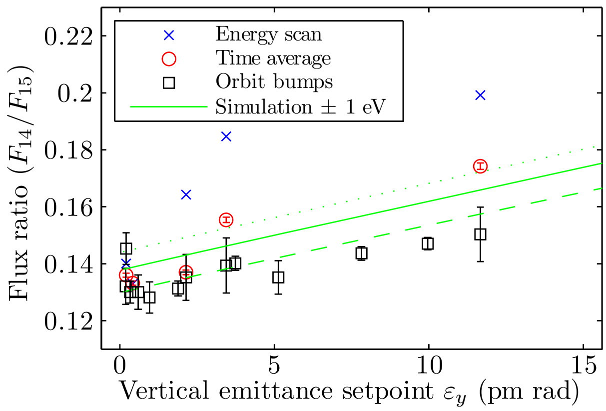

Figure 3: Measured flux ratio F_{14}/F_{15} compared for several measurement approaches, for vertical emittances below 15 pm rad.

The flux ratio for various emittance setpoints was simulated using SPECTRA [19], importing the measured magnetic field map of the insertion device [20].

The most successful measurement technique was orbit bumps through the insertion device. As outlined in Ref. [3], the smallest vertical emittance measured using the vertical undulator technique was $\varepsilon_y = 0.9 \pm 0.4$ pm rad. The vertical emittance measured using LOCO, with the quantum limit of vertical emittance [21] added in quadrature was $\varepsilon_y = 0.4 \pm 0.1$ pm rad. Although these direct and indirect measurements disagree within uncertainty, the vertical emittance measured using the vertical undulator is equal to the world-record low of Ref. [9].

DISCUSSION

Diffraction-Limited Storage Rings

Brilliance-optimised diffraction-limited storage rings are currently under construction or proposal in several countries. A survey of horizontal and vertical emittances of current and proposed electron and positron storage rings is presented in Fig. 4.

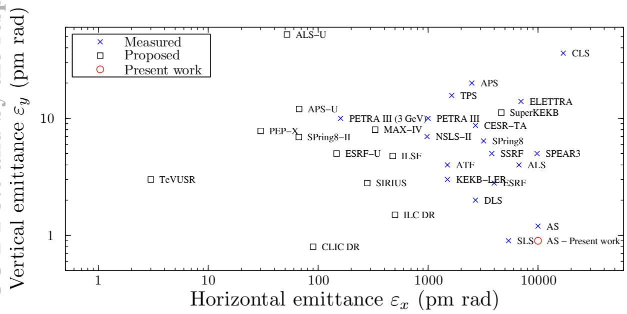

Figure 4: Survey of horizontal and vertical emittances of several current (measured) and proposed electron and positron storage rings. The measurement of Ref. [3] is denoted by ∘.

The designs call for orders of magnitude increase in storage ring brightness compared to existing third-generation storage ring facilities. Principally, this will be achieved with insertion device beamlines in multi-bend achromat storage ring lattices with horizontal emittances below 500 pm rad. This emittance regime has been tested using vertical insertion devices in existing storage rings.

Of particular interest are measurements of the angular distribution of undulator radiation at high undulator harmonics. For ultralow vertical emittances, the angular profile of undulator radiation departs significantly from typical Gaussian distributions, resulting in a narrow diffraction pattern, as highlighted in Fig. 3 of Ref. [18]. Photon beamlines utilising high-undulator harmonics at diffraction-limited storage rings should carefully evaluate this departure from Gaussian-approximated spatial distribution of photon beams at existing storage ring facilities.

Emittance Growth Resulting from Undulator Self-Dispersion

It is well-known that the vertical dispersion of a lattice increases the equilibrium vertical emittance. Vertical emittance optimisation routines seek to minimise coupling and dispersion terms simultaneously. The inclusion of a vertical insertion device in a lattice has the well-known effect of increasing vertical emittance, which lattice designs have exploited with the intent of creating round beams [22]. This suggests that designs for ultralow vertical emittance avoid introducing vertical dispersion.

Vertical emittance growth due to undulator self-dispersion was calculated according to the method of Ref. [22], for the APPLE-II undulator and the normal AS user lattice with 0.1 m distributed horizontal dispersion in the insertion straights. The vertical emittance growth in a ring from self-dispersion in a vertical wiggler is given by [22],

$$\frac{\Delta\varepsilon_y}{\varepsilon_{x0}} = \frac{\dfrac{5\pi}{6}\dfrac{\beta_y(s)}{\langle\mathcal{H}_0\rangle}\dfrac{\rho_0}{R}\left(\dfrac{\rho_0}{\rho_w}\right)^2 N_w\theta_w^3}{1+\dfrac{2}{\pi}\dfrac{\rho_0}{\rho_w}N_w\theta_w}. \tag{2}$$

For a ring, the mean of the curly-$\mathcal{H}$ function can be approximated by [22],

$$\langle\mathcal{H}_0\rangle = \frac{\varepsilon_{x0}\rho_0}{C_a E^2}\frac{\rho_0}{R}\mathcal{J}_x. \tag{3}$$

Using the parameters in Table 1 for this experiment at the AS, the curly-$\mathcal{H}$ function was evaluated as $\langle\mathcal{H}_0\rangle = 0.0027$ m rad.

For the parameters of the storage ring and undulator at the AS given in Table 1, the vertical emittance increase due to self-dispersion of Eq. 2 is presented in Fig. 5 for an increasing number of vertical undulator poles.

The APPLE-II undulator used at the AS has a total of 50 poles, giving a calculated increase in vertical emittance due to self-dispersion of $\Delta\varepsilon_y = 0.012$ pm rad. Increasing the vertical emittance to $\varepsilon_y \approx 1$ pm rad by self-dispersion

ISBN 978-3-95450-176-2

requires approximately 6500 undulator poles, at a total undulator length of 240 m. Hence it can be concluded that the increase in vertical emittance due to self-dispersion is negligibly small for practical devices in present storage ring light sources.

Table 1: Parameters Used in the Calculation of Vertical Undulator Self-Dispersion.

Parameter		Value	Units
Beam			
Energy	E_0	3.0	GeV
Energy spread	σ_E	0.11	%
Horizontal emittance	ε_x	10	nm rad
Undulator			
Period length	λ_u	75	mm
Peak field	B_u	0.55	T
Deflection parameter	K_u	3.8	...
Number of full periods	N_u	25	...
Number of poles	N_w	50	...
Deflection angle	θ_w	6.5×10^{-4}	rad
Bending radius	ρ_w	29.0	m
Storage ring			
Damping decrement	$\mathcal{J}_x$	1.37	...
Bending radius	ρ_0	8.5	m
Ring radius	R	34.4	m
Curly-$\mathcal{H}$ function	$\langle \mathcal{H}_0 \rangle$	2.3×10^{-3}	m rad

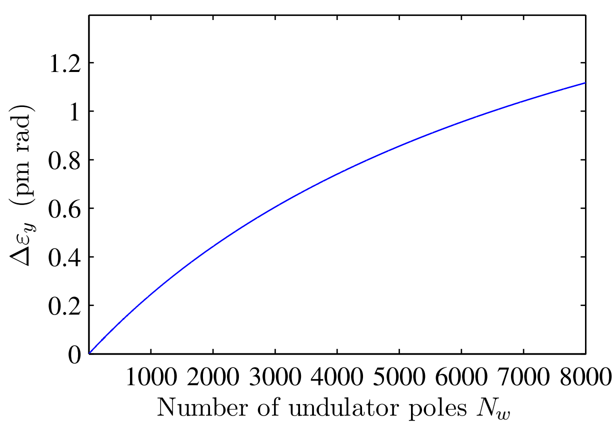

Figure 5: Increase in vertical emittance due to vertical undulator self-dispersion for an undulator of N_w poles. The APPLE-II undulator at the AS has 50 poles.

Emittance Growth Resulting From Orbit Steering

Making use of the electron beam orbit correctors in the storage ring, it was possible to steer the electron beam with vertical angle bumps through the insertion device, which is counter-intuitive for a vertical emittance measurement. A four-corrector vertical angle bump was made across the two sectors of the storage ring adjacent to the APPLE-II insertion device, which steered the electron beam vertically off-axis through lattice quadrupoles and sextupoles. This has the effect of introducing skew betatron coupling and vertical dispersion, which are well-known to contribute significantly to vertical emittance.

The magnitude of local orbit bump required for the orbit bump measurements is of the order < 10 µrad. In Ref. [3], it was demonstrated that for a well-corrected storage ring lattice this would result in a negligible vertical emittance growth of $\varepsilon_y = 0.07 \pm 0.01$ pm rad.

Ideal Vertical Insertion Device

At the time of construction, the APPLE-II insertion device used was shimmed to correct multipole field errors while operating in the horizontal polarisation mode: operation as a usual horizontal undulator [20]. For operation principally as a vertical undulator, it would be beneficial to shim the insertion device for use in the vertical polarisation mode.

Ideal Detector

The principal uncertainty in the vertical undulator technique is the uncertainty in the pinhole vertical dimension and position. For future experiments to measure vertical emittance, there are two complementary directions for an ideal detector – either a single pinhole of fixed dimensions, or a pixel detector for profile measurements of the undulator photon beam. Future experiments to measure vertical emittance should consider using a pinhole of known diameter, as in other work to characterise a tandem APPLE-II undulator [23].

A pixel detector observing the angular distribution of undulator radiation at a fixed photon energy could be used to measure the vertical emittance in much the same way as orbit bumps through the insertion device. A candidate detector particularly appropriate to this photon energy range is the DiagOn device developed at SOLEIL. Recently, direct projections of undulator harmonics have been measured at SOLEIL [24]. Designed as a beam diagnostic for APPLE-II insertion devices operated in the horizontal polarisation orientation, the reported device measures the distribution of horizontally-polarised undulator radiation at a fixed photon energy. As the desired polarisation for vertical emittance measurement using a vertical undulators corresponds to vertical linear polarised radiation, the device would need to be rotated about the beam axis to pass photons of vertical polarisation.

CONCLUSION

Measurement of vertical emittance using a vertical undulator in an electron storage ring has been achieved. This is a direct measurement of emittance, based on the convolution of the angular divergence of the electron beam with the single-electron undulator radiation distribution. The smallest measured vertical emittance at the AS storage ring was $\varepsilon_y = 0.9 \pm 0.3$ pm rad.

These measurements of undulator radiation distributions with ultralow electron beam emittances have highlighted that the angular distribution of undulator radiation departs from usual Gaussian approximations, at high undulator harmonics.

ISBN 978-3-95450-176-2

This is a consideration that photon beamlines at proposed diffraction-limited storage ring light sources should be aware of.

ACKNOWLEDGEMENTS

This research was conducted using the storage ring and soft X-ray beamline at the Australian Synchrotron, Victoria, Australia. The author gratefully acknowledges useful discussions with Roger P. Rassool (The University of Melbourne), Mark J. Boland, Rohan Dowd, Yaw-Ren E. Tan, Greg S. LeBlanc, and Bruce C. C. Cowie (Australian Synchrotron) during these experiments.

REFERENCES

[1] K. P. Wootton, et al., Phys. Rev. Lett. 109, 194801 (2012).

[2] S. Takano, "On Emittance Diagnostics of Electron Beam by Observing Synchrotron Radiation from a Vertical Undulator", Proc. of Workshop on "Precise measurements of electron beam emittances", KEK, Tsukuba, Japan, KEK Proceedings 97-20, p. 18-29, (1998).

[3] K. P. Wootton, et al., Phys. Rev. ST Accel. Beams 17, 112802 (2014).

[4] Å. Andersson, et al., Nucl. Instrum. Methods Phys. Res., Sect. A, 591, 437-446 (2008).

[5] T. Mitsuhashi, "Beam Profile and Size Measurement by SR Interferometers", Beam Measurement: Proceedings of the Joint US–CERN–Japan–Russia School on Particle Accelerators, Montreux and CERN, Switzerland, 11 – 20 May 1998, World Scientific, Singapore (1999).

[6] M. Masaki, et al., Phys. Rev. ST Accel. Beams, 18, 042802 (2015).

[7] J. W. Flanagan, et al., "X-ray Monitor Based on Coded-Aperture Imaging for KEKB Upgrade and ILC Damping Rings" Proc. of EPAC 2008, Genoa, Italy, TUOCM02, (2008). `http://www.JACoW.org`

[8] R. Dowd, et al., Phys. Rev. ST Accel. Beams, 14, 012804 (2011).

[9] M. Aiba, et al., Nucl. Instrum. Methods. Phys. Res., Sect. A, 694, 133-139 (2012).

[10] R. Dowd and Y.-R. E. Tan, "Beam Based Sextupole Alignment Studies for Coupling Control at the ASLS", Proc. of IPAC 2011, San Sebastián, Spain, WEPC001, (2011). `http://www.JACoW.org`

[11] R. Dowd, et al., "Beam Based Magnet Alignment for Emittance Coupling Minimization", Proc. of IPAC 2013, Shanghai, China, TUPWA003, (2013). `http://www.JACoW.org`

[12] K. P. Wootton, PhD thesis, The University of Melbourne, Parkville, VIC, Australia (2014) `http://hdl.handle.net/11343/39616`

[13] B. C. C. Cowie, et al., AIP Conf. Proc. 1234, 307-310 (2010).

[14] K. P. Wootton, et al., "Vertical Emittance Measurements Using a Vertical Undulator", Proc. of IBIC 2012, Tsukuba, Japan, MOCB04, (2012). `http://www.JACoW.org`

[15] J. Safranek, Nucl. Instrum. Methods Phys. Res., Sect. A, 388, 27-36 (1997).

[16] Joint Committee for Guides in Metrology, (unpublished), Bureau International des Poids et Mesures Report No. JCGM 100:2008 (2008).

[17] K. P. Wootton, et al., "Vertical Undulator Emittance Measurement: A Statistical Approach", Proc. of IBIC 2013, Oxford, United Kingdom, TUPF18, (2013). `http://www.JACoW.org`

[18] K. P. Wootton, et al., "APPLE-II Undulator Magnetic Fields Characterised from Undulator Radiation", Proc. of IBIC 2013, Oxford, United Kingdom, TUPF19, (2013). `http://www.JACoW.org`

[19] T. Tanaka and H. Kitamura, J. Synchrotron Radiat., 8, 1221-1228 (2001).

[20] C. Ostenfeld, et al., "APPLE-II and TESLA FEL Undulators at Danfysik A/S", Proc. of PAC 2007, Albuquerque, USA, TUPMN006, (2007). `http://www.JACoW.org`

[21] M. Sands, (unpublished), Stanford Linear Accelerator Center Report No. SLAC-R-121, (1970).

[22] H. Wiedemann, Nucl. Instrum. Methods Phys. Res., Sect. A, 266, 24-31 (1988).

[23] J. Bahrdt, et al., Phys. Rev. Lett. 111, 034801 (2013).

[24] T. Moreno, et al., J. Synchrotron Radiat. 19, 179-184 (2012).

ISBN 978-3-95450-176-2

RECENT PROGRESS IN X-RAY EMITTANCE DIAGNOSTICS AT SPRING-8

S. Takano*, M. Masaki
Japan Synchrotron Radiation Research Institute (JASRI/SPring-8), Hyogo 679-5198, Japan
H. Sumitomo
SPring-8 Service Co. Ltd. (SES), Hyogo 679-5165, Japan

Abstract

At the SPring-8 storage ring, we have recently developed two X-ray instruments for emittance diagnostics. The one for a bending magnet source is the X-ray pinhole camera which directly images the beam profile. A pinhole in the atmosphere is composed of combined narrow X-Y slits made of tungsten. A scintillator crystal is used to convert the X-ray beam image to a visible image. The spatial resolution is about 7 μm. It is operated for continuous emittance diagnostics and coupling correction of user operation of SPring-8. The other for an undulator source is the X-ray Fresnel diffractometry monitor. Monochromatic X-rays are cut out by a single slit, and the vertical beam size is deduced from the depth of the central dip in a double-lobed diffraction pattern. Resolving beam size less than 5 μm is feasible.

INTRODCUTION

Light source rings are competing to achieve lower emittance and emittance coupling ratio for higher brilliance. Serious and elaborate efforts are being paid for upgrade plans of existing synchrotron radiation (SR) rings or new plans of low emittance rings.

X-ray SR is the key diagnostics probe for non-destructive beam emittance [1]. Both direct imaging and interferometric techniques can resolve the micrometer-order transverse beam size. The beam emittance is obtained from the measured beam size with the knowledge of the betatron and dispersion functions and the beam energy spread.

At the SPring-8 storage ring, we have recently developed two X-ray instruments for emittance diagnostics. The one for a bending magnet source is the X-ray pinhole camera which directly images the beam profile. The spatial resolution is about 7 μm. It is operated for continuous emittance diagnostics and coupling correction of user operation of SPring-8. The other for an undulator source is the X-ray Fresnel diffractometry (XFD) monitor [2,3]. Monochromatic X-rays are cut out by a single slit, and the vertical beam size is deduced from the depth of the central dip in a double-lobed diffraction pattern. Resolving beam size less than 5 μm is feasible.

X-RAY PINHOLE CAMERA

The layout of the SPring-8 X-ray pinhole camera is shown in Fig. 1 and the specifications are summarized in Table 1.

The source point is in a dipole magnet (29B2), 1.0 mrad inside from the edge. The magnetic field and the critical photon energy of emitted X-rays is 0.5 T and 21.1 keV, respectively. The X-ray window is located at a distance of 6.2 m from the source point. The window material is aluminium alloy of 3 mm thickness. The window separates the ultra-high vacuum and the atmosphere, and the X-rays emitted in the source dipole magnet go out to the atmosphere.

The pinhole assembly in the atmosphere is located at a distance of 11.4 m from the source. It is composed of

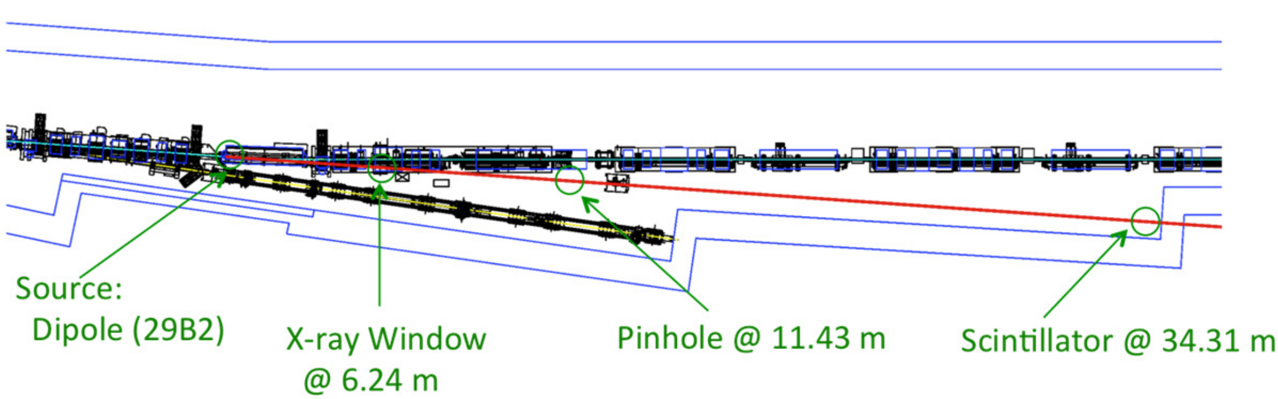

Figure 1: Layout of the X-ray pinhole camera of SPring-8.

*takano@spring8.or.jp

Table 1: Specifications of the SPring-8 X-ray Pinhole Camera

Light Source	Bending Magnent (29B2)	
Pinhole	Distance from Source (m)	11.4
	Aperture Size (µm)	20 x 20
Scintillator	Distance from Source (m)	34.3
	Material	$CdWO_4$
Camera	Number of Pixels	2448 x 2050
	Pixel Size (µm)	3.45 x 3.45
Magnification Factor	x 4 (Pinhole: x 2, Lens: x 2)	
Resolution (rms) (µm)	7.2 (Pinhole: 6.9, Scintillator & Camera: 2.2)	

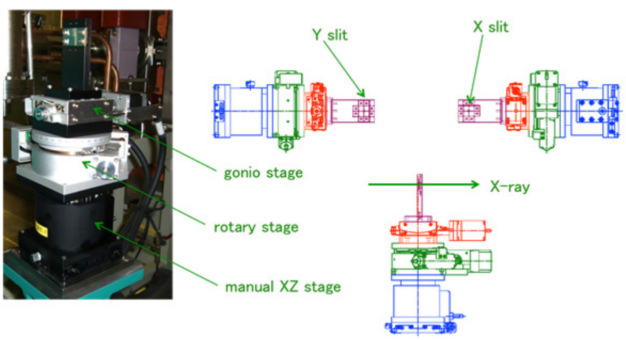

Figure 2: Pinhole assembly.

combined narrow X-Y slits made of tungsten (Fig. 2). The thickness of each slit is 3mm, and the aperture size of the pinhole is 20 µm x 20µm. The pinhole assembly is equipped with remote controllable gonio and rotary stages for adjustments of pitch and yaw of the pinhole. It is mounted on a manual XZ stage for alignment.

The X-ray image of the electron beam formed by the pinhole is converted to a visible image by a scintillator located at a distance 34.3 m from the source. The magnification factor of the pinhole is accordingly two. The visible image is measured by a CCD camera through a lens. The details of the scintillator and camera assembly

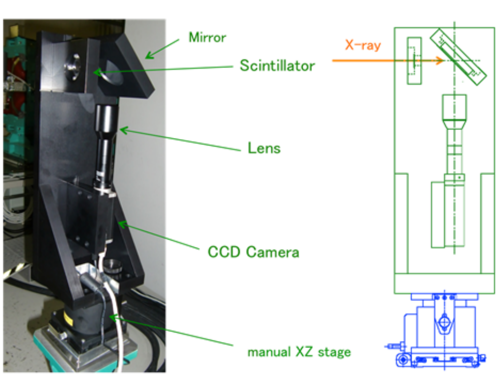

Figure 3: Scintillator and camera assembly

are shown in Fig. 3. The scintillator is made of CdW_4O with a thickness of 0.5mm. The lens is object-space telecentric with a magnification factor of two. The CCD camera (Basler AG, piA2400-17gm) has 2448 x 2050 square pixels of 3.45 µm size. It is connected to a remote computer through the Gig-E (Gigabit Ethernet) interface.

The total spatial resolution of the pinhole camera σ_{XPC} is expressed as,

$$\sigma_{XPC} = \sqrt{\sigma_{diff}^2 + \sigma_{CAM}^2} \qquad (1)$$

where σ_{diff} stands for the contribution of diffraction of pinhole and σ_{CAM} for that of the scintillator and camera assembly.

The pinhole resolution σ_{diff} was evaluated according to numerical calculation of the point-spread function (PSF) based on wave optics by using diffraction formula. Examples of PSFs of the pinhole for monochromatic X-rays, pinhole diffraction patterns for a monochromatic point source, are shown in Figs. 4(a) and (b). The resolution σ_{diff} was defined by width of a Gaussian curve fitted to the PSF. Fig. 5 (a) shows the monochromatic pinhole resolution as a function of the X-ray energy.

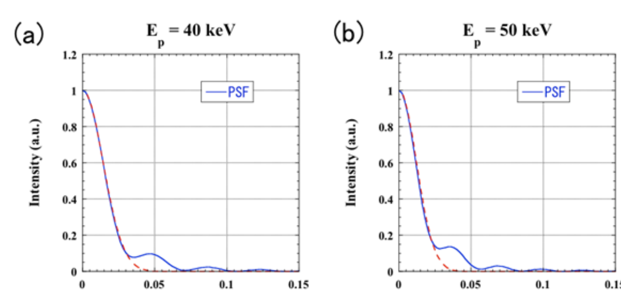

Figure 4: Examples of the point-spread functions (PSFs) of the pinhole for monochromatic X-rays (blue), and fitted Gaussian curves (red).

ISBN 978-3-95450-176-2

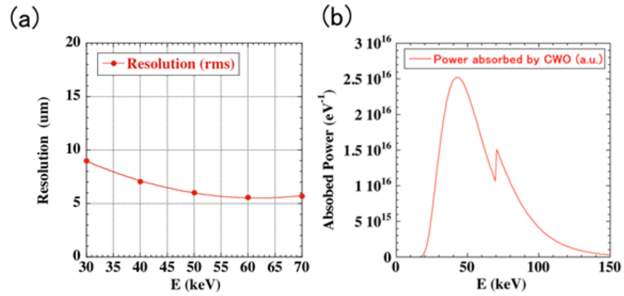

Figure 5: (a) Monochromatic pinhole resolution as a function of the X-ray energy. (b) Spectral power absorbed by the scintillator.

Spectral power absorbed by the scintillator was calculated by the calculation code SPECTRA [4], and found to peak at an X-ray energy of 42 keV as shown in Fig. 5(b). The resolution of the pinhole σ_{diff} was evaluated to be 6.9 µm from the width of the monochromatic PSF at 42 keV.

The resolution of the scintillator and camera assembly σ_{CAM} was calibrated by the sharpness of the observed edge of a tungsten bar placed in front of the scintillator. Fig. 6(a) shows the tungsten bar and 6(b) an observed

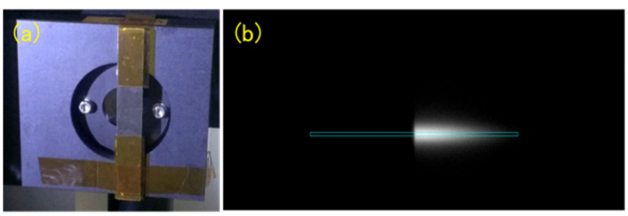

Figure 6: (a) Tungsten bar placed in front of the scintillator for calibration of the resolution of the scintillator and camera assembly. (b) Edge of the bar observed in a beam image.

beam image with an edge cut by the bar. The profile of the observed edge and its derivative are shown in Figs. 7(a) and (b). The resolution σ_{CAM} of the scintillator and

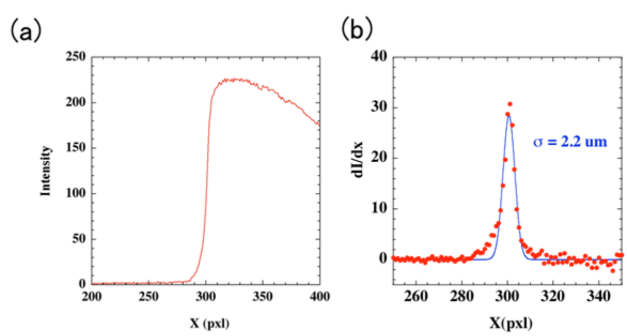

Figure 7: (a) Profile of the observed edge with the bar. (b) The derivative of the edge profile (red) and a fitted Gausiian curve (blue).

camera assembly was evaluated as 2.2 µm on the beam coordinate (4.4 µm on the scintillator) from the width of a Gaussian curve fitted to the derivative in Fig. 7(b). The total spatial resolution of the pinhole camera σ_{XPC} given by Eq. (1) is accordingly 7.2 µm.

The scale of the camera pixel to the beam coordinate was calibrated by introducing vertical bump orbits (Fig. 8). The calibrated scale is 0.848 µm/pixel, which is

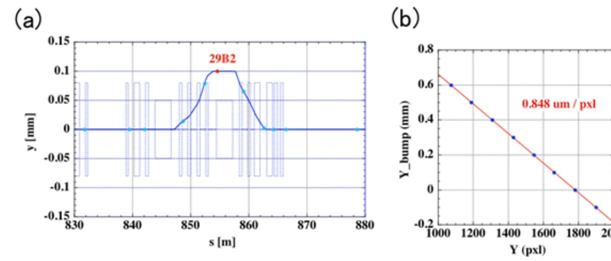

Figure 8: (a) Schematic of the vertical bump orbit. (b) The observed relation between the beam position and the image position on the CCD camera.

consistent with the designed value of 0.863 µm/pixel within the manufacturer's specified accuracy of the lens magnification factor.

The display for the X-ray pinhole camera in the SPring-8 control room is sown in Fig. 9. Live beam image view

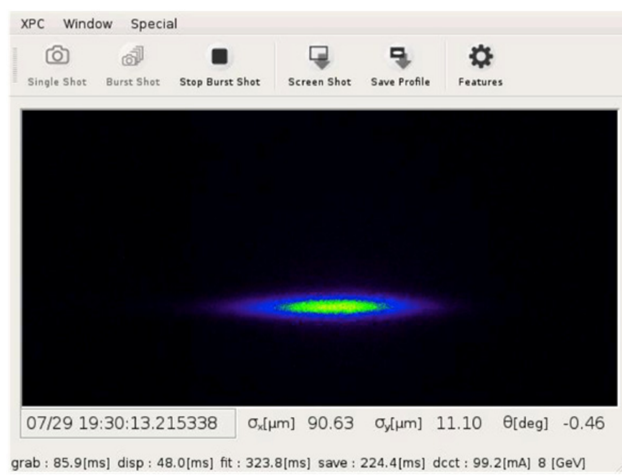

Figure 9: The display for the X-ray pinhole camera in the SPring-8 control room.

is available with the refreshing rate of approximately 15 frames per seconds.

Parameters of the beam profile, including the horizontal and vertical bean sizes σ_x and σ_y and the beam tilt angle θ, are obtained periodically with a cycle time of 1s by fitting a two-dimensional Gaussian profile to the beam image. They are logged to the control system database.

The SPring-8 X-ray pinhole camera was installed in March 2014. After commissioning and calibration, it has been operating as a real time emittance diagnostics since September 2014. It is a indispensable diagnostics tool for both beam tuning and user operation of SPring-8.

ISBN 978-3-95450-176-2

X-RAY FRESNEL DIFFRACTOMETRY MONITOR (XFD)

X-ray Fresnel diffractometry monitor (XFD) is a diagnostic technique for light source rings to measure vertical beam size at ID (undulator) source point [2,3]. Schematics of XFD are illustrated in Fig. 10. It employs a

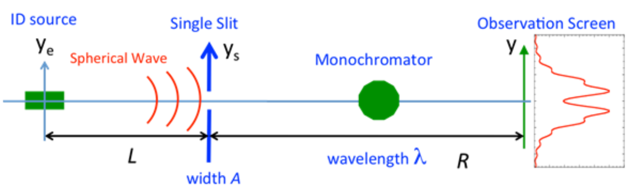

Figure 10: Schematics of X-ray Fresnel diffractometry monitor (XFD).

single slit and a monochrometer and an imaging device (X-ray camera). Diffraction patterns observed on the screen of the imaging device depend on a width A of the slit. By adequitely tuning the slit width, a double-lobed Fresnal diffraction pattern is available. The optimum slit width for the deepest median dip is expressed as,

$$A \approx \sqrt{7\lambda \frac{LR}{L+R}}.$$

The depth of the median dip correlates with the light source size.

The setup for the initial XFD experiment at SPring-8 is shown in Fig. 11 [2,3]. The source is a planar undulator

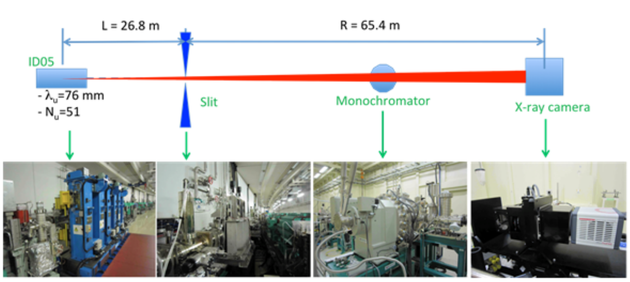

Figure 11: Setup for the initial XFD experiment at SPring-8.

(ID05) with 51 magnetic periods of 76 mm long. The vertical beam size at the source point of ID05 smaller than 10 μm was successfully resolved [2,3].

In order to improve the performance of the XFD, we have recently replaced an X-ray imaging device and increased the observing photon energy. The new setup

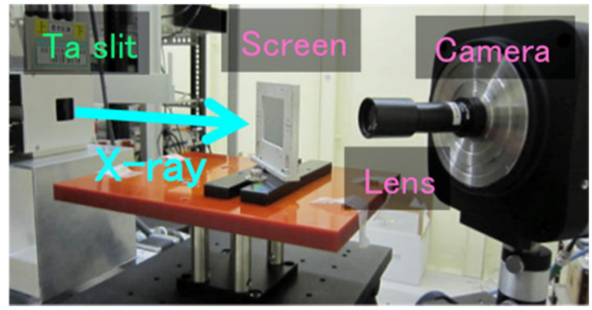

Figure 12: New X-ray imaging setup for XFD experiment at SPring-8.

for X-ray imaging is shown in Fig. 12. The screen material is YAG(Ce) of 50 μm thick. The pixel size of the camera is 16 μm x 16 μm. Minimum available exposure time of the camera is 0.2 ms five times shorter than that of the previous camera of 1ms. The shorter exposure time reduces the influence of the vibration of the cryogenically cooled monochromator crystals. The resolution of the X-ray imaging device was calibrated by the sharpness of the observed edge of a tantalum slit installed in front of the screen. The obtained resolution as converted to the source

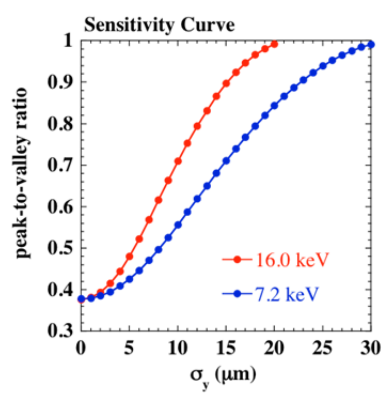

Figure 13: Sensitivity curve of XFD for the increased observing energy 16 keV (red) and for the previous 7.2 keV (blue).

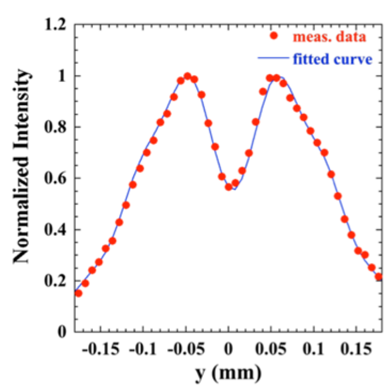

Figure 14: Example of observed diffraction pattern (red) and fitted model function (blue). The deduced source vertical beam size is 6.3 μm (rms).

ISBN 978-3-95450-176-2

point coordinate is 2.2 μm, which is three times better than the previous device. The sensitivity curve, peak-to-valley-ratio of the median dip of the double-lobed diffraction pattern as a function of vertical beam size, is shown in Fig. 13. Improvement of the sensitivity for small beam size below 5 μm is evident for the increased observing energy (16 keV). An example of diffraction pattern observed with the new imaging device at the increased X-ray energy (16keV) is shown in Fig. 14. By fitting the theoretical model function [3] to data, vertical beam size (rms) of 6.3 μm was deduced.

CONCLUSION

The SPring-8 X-ray pinhole camera was installed in March 2014. It images a dipole magnet source with a spatial resolution (rms) of 7.2 μm. It has been operating since September 2014 as a real time emittance diagnostics indispensable for both beam tuning and user operation of SPring-8.

The XFD developed at SPring-8 is a diagnostic technique for light source rings to measure vertical beam size at ID (undulator) source point, feasible to resolve beam size smaller than 5 μm (rms). It requires only slit, monochromator, and imaging device (X-ray camera), and has potential universal availability to ID beamlines of the diffraction limited storage rings (DLSRs).

REFERENCES

[1] S. Takano, “Beam Diagnostics with Synchrotron Radiation in Light Sourecs”, IPAC’10, p2392. (2010).
[2] M. Masaki, Y. Shimosaki, S. Takano, M. Takao, “Novel Emittance Diagnostics for Diffraction Limited Light Sources Based on X-ray Fresnel Diffractometry”, IBIC’14, p274. (2014).
[3] M. Masaki, S. Takano, M. Takao Y. Shimosaki, “X-ray Fresnel diffractometry for ultralow emittance diagnostics of next generation synchrotron light sources.”, Phys. Rev. ST Accel. Beams 18, 042802 (2015).
[4] T. Tanaka and H. Kitamura, “SPECTRA: a Synchrotron Radiation Calculation Code”, J. Synchrotron Radiat. 8, 1221 (2001). http://radiant.harima.riken.go.jp/spectra/index.html

ISBN 978-3-95450-176-2

DESIGN OF CORONAGRAPH FOR THE OBSERVATION OF BEAM HALO AT LHC

T. Mitsuhashi#, KEK, Ibaraki, Japan
E. Bravin, R. Jones, F. Roncarolo, H. Schmickler, G. Trad, CERN, Geneva, Switzerland

Abstract

An observation of the beam halo using the coronagraph is planned in LHC in two phases. In the first phase, a coronagraph is designed using some optical components of the coronagraph constructed in KEK in 2005. The diffraction and Mie-scattering backgrounds from optical components near the coronagraph are analysed. Result of this analysis, we can observe a beam halo with a contrast of 10^{-4} range to the peak intensity of beam core. The coronagraph is under construction and will be finished by the end of 2015.

INTRODUCTION

In the LHC, the beam halo can lead to an important beam loss. Measurement of the beam halo distribution is therefore important for understanding and controlling the beam halo. The coronagraph is a spatial telescope to observe the sun-corona by an artificial eclipse [1]. The concept of this apparatus is to block the glare of central image and to observe a hidden image such as the sun-corona. We applied this concept for the observation of the surrounding structure (halo, tail) of the beam core. For this purpose, a coronagraph was constructed at Photon Factory, KEK in 2005 [2]. The project of using the coronagraph for the observation of beam halo image in the LHC will be performed in two phases. We plan an observation test in the first phase where the coronagraph is designed and constructed by modifying the optical design of the KEK coronagraph. This coronagraph is aiming for a halo observation with 10^3 to 10^4 contrast to the beam core, and will be set in B2 optical monitor line. In the second phase an optimum coronagraph will be designed for the LHC, to reach 10^5 to 10^6 contrast. The optical design and diffraction analysis of the coronagraph for phase 1 is described in this paper. Also Mie-scattering from lens surface or optical component in front of the objective lens is discussed and analysed.

THE CORONAGRAPH

The coronagraph was first developed by Lyot for the observation of sun corona without waiting for an eclipse [1]. The optical layout of the coronagraph is illustrated in Fig. 1. The first lens (objective lens) makes a real image of the object (beam image) onto a blocking disk which makes artificial eclipse. The second lens (field lens), located just after the blocking disk, makes a real image of the objective lens pupil onto a mask (Lyot Stop).

The diffraction fringes are re-diffracted by the field lens aperture and transferred to the diffraction fringes on the focal plane of the field lens. The Lyot's genius idea of the coronagraph is to remove the majority of this diffraction fringes by a mask (Lyot stop), and relay the hidden image by a third lens onto final observation plane. By applying a very well polished lens for the objective, we can observe the hidden image with very high contrast (Sun corona has 10^5 contrast to the photosphere). With this coronagraph, we can observe a hidden image surrounding from the bright image of beam core.

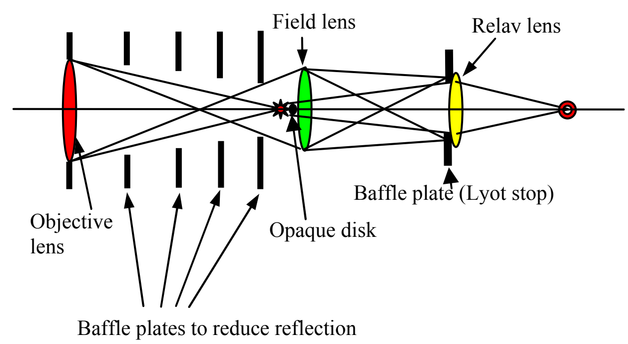

Figure 1: Layout of optical system of the coronagraph.

OPTICAL DESIGN OF CORONAGRAPH FOR PHASE 1

For the first phase, we modified the optical design of coronagraph which was constructed in Photon Factory (PF) in 2005 in KEK [2]. The previous design of the coronagraph is optimized for the conditions at PF as listed in table 1. The same conditions of optical monitor line in B2 of LHC are also listed in table 1.

Table 1: Conditions for Design the Coronagraph at PF and LHC

	PF (BL28)	LHC(B2)
Distance between source point and objective lens	8m	28.5m
Horizontal beam size (1σ of beam core)	263μm	270μm
Vertical beam size (1σ of beam core)	80μm	350μm
Minimum size of opaque disk against beam core	6σ of beam core	5σ of beam core

Modification points of the optical design are 1) the transverse magnification reduction of the objective lens caused by the long distance between the SR source point and the objective lens, 2) Redesigning the re-diffraction system to obtain a larger image of the objective lens for a

toshiyuki.mitsuhashi@kek.jp

ISBN 978-3-95450-176-2

convenient Lyot stop size, 3) Redesigning the relay system to obtain enough transverse magnification of the halo image for a convenience of observation with CCD.
The optical design of previous coronagraph and new one are listed in table 2.

Table 2: The Optical Design of Previous and New Coronagraph

	PF (BL28)	LHC(B2)
Focal length of objective lens	2000mm	2000mm
Objective lens aperture	50 x 50mm	25 x 25 mm
Transverse magnification	0.333	0.0754
Opaque disk size	1mm	0.110mm
Focal length of field lens	500mm	800mm
Movable range of Lyot stop	2 x 2mm to 20 x 20mm	2 x 2mm to 20 x 20mm
Focal length of relay lens	36mm	500mm

DIFFRACTION ANALYSIS

The aperture of the objective lens causes the diffraction fringes surrounding from the central image. The disturbance of the diffraction pattern of the first objective lens aperture is given by the Fraunhofer diffraction of the entrance pupil as follows:

$$F(\xi,\eta)=\frac{1}{i\cdot\lambda\cdot f_{obj}}\int f_{obj}(x,y)\exp\left\{-\frac{i\cdot 2\cdot\pi\cdot(x\cdot\xi+y\cdot\eta)}{\lambda\cdot f_{obj}}\right\}dxdy$$

In here, $f_{obs}(x,y)$ is inout disturbance to entrance pupil and f_{obj} is denotes the distance between the objective lens and its imaging plane. For a rectangular shape aperture, this Fourier transform results a sinc function. The result of calculation for the cross section of diffraction intensity by the objective lens is shown in Fig. 2.

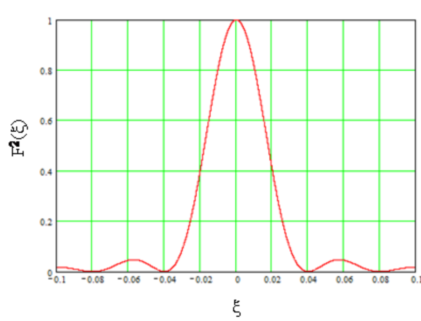

Figure 2: Intensity of diffraction pattern by objective lens pupil.

The diffraction pattern by next field lens on Lyot stop is given by Fourier transform of the disturbance $F(\xi,\eta)$ on the field lens pupil. The field lens pupil is defined by both its outer aperture and the opaque disk. The input disturbance of the light for this pupil is the diffraction fringes without the airy disk in the diffraction pattern of objective lens. This disturbance is diffracted again with re-diffraction system, and resulting diffraction fringes on the imaging plane of the field lens. Using Babinet's principle [3], the disturbance of re-diffracted light $F_{\mathrm{field}}(X)$ on the imaging plane of the field lens is given by,

$$F_{field}(X,Y)=\frac{1}{i\cdot\lambda\cdot f_{field}}\left[\int_0^{\xi 2}F(\xi,\eta)\exp\left\{-\frac{i\cdot 2\cdot\pi\cdot(\xi\cdot X+\eta\cdot Y)}{\lambda\cdot f_{field}}\right\}d\xi d\eta\right.$$
$$\left.-\int_0^{\xi 1}F(\xi,\eta)\exp\left\{-\frac{i\cdot 2\cdot\pi\cdot(\xi\cdot X+\eta\cdot Y)}{\lambda\cdot f_{field}}\right\}d\xi d\eta\right]$$

Where λ denotes wavelength of input light, $\xi 1$ denotes radius of stop, $\xi 2$ denotes the aperture radius at the field lens pupil and f_{field} denotes the distance between the field lens and its imaging plane (location of Lyot stop), respectively. The result of calculation for the cross section of intensity distribution $|F^2(X)|$ using a square-pupil at the objective lens is shown in Fig. 3.

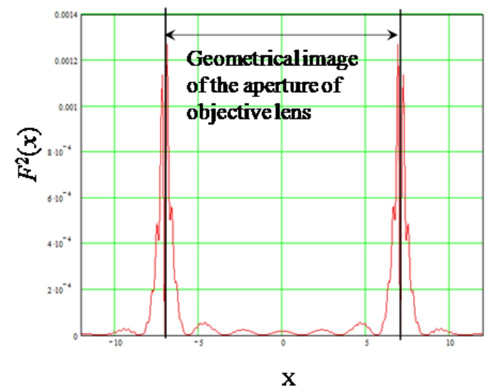

Figure 3: Intensity distribution $|F_{field}{}^2(X)|$ on imaging plane of field lens.

From this figure, we can see the majority of diffraction fringes located in the inside and outside of the geometrical image of the objective lens edge (it is called the Schlieren image of objective lens edge). Blocking this majority of diffraction fringes with a mask (Lyot Stop), prevents most of the diffraction fringes light from reaching later stages of the coronagraph. Since the width of the two diffraction fringes is inverse proportional to the opaque disk diameter, increasing the latter reduces the light leakage from the diffraction fringe inside of Lyot stop.

A diffraction pattern on the imaging plane of the relay lens is produced by the remaining disturbance of light inside of Lyot stop. This diffraction pattern is given by an Fourier transform of the disturbance $F_{field}(\xi,\eta)$ in the field lens pupil (Opening of the Lyot stop),

$$F_i(\xi,\eta)=\frac{1}{i\cdot\lambda\cdot f_{field}}\int F_{field}(x,y)\exp\left\{-\frac{i\cdot 2\cdot\pi\cdot(X\cdot X_i+Y\cdot Y_i)}{\lambda\cdot f_{field}}\right\}dXdY$$

This is the diffraction background in the coronagraph. A result of calculation for the diffraction pattern by relay lens pupil is shown in Fig. 4, where the peak intensity of this diffraction fringe is $3.7\mathrm{x}10^{-4}$. Except of the two central fringes, most of diffraction fringes have intensities ranging from 10^{-5} to 10^{-6} range. In the usual condition of the coronagraph, the opaque disc diameter is in the range

ISBN 978-3-95450-176-2

of few mm [2], resulting a diffraction background of 10^{-6} to 10^{-7} range. In the present case, the diffraction fringes eliminated by Lyot stop is wider corresponding to small opaque disk diameter as shown in Fig. 3, thus the leakage of diffraction fringe light becomes larger.

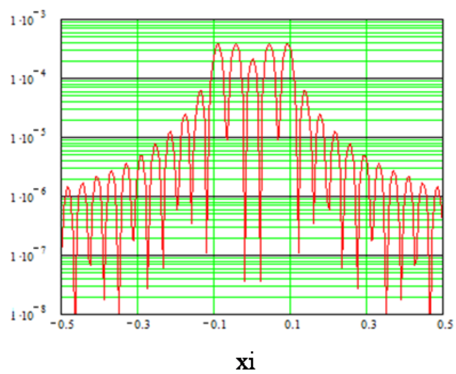

Figure 4: Intensity of diffraction pattern on imaging plane of relay lens.

BACKGROUND NOISE DUE TO MIE-SCATTERING

After blocking the central bright core image and cutting the light from the diffraction fringes, we still have some scattered light noise from the objective lens of the coronagraph. The defects in the objective lens such as scratches and digs on its surface and some defects on the optical components such as mirrors in near front of the objective lens and dust in air will produce the Mie-scattering. The intensity of these Mie-scattered lights possibly reaches the 10^{-3} order. In this chapter, we discuss a diffraction treatment of the Mie-scattering.

Let us approximate the i-th noise source in the pupil as an opaque disk having a diameter of r_0 as shown in Fig. 5.

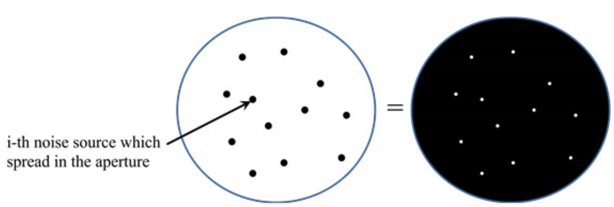

Figure 5: The pupil with Mie scattering sources.

Using the Babinet's principle again [4], the pupil is given by reversing the contrast and its function is expressed by,

$$P_i(r_0, x, y) = -circ(r_0, x_i, y_i)$$
$$P(\bar{r}, x, y) = \sum_i P_i(r_0, x, y) \cdot \exp(-ik(x_i + y_i))$$

When the distance between the opaque disks is assumed to be longer than the transverse coherent length, the pupil function becomes,

$$P(\bar{r}, x, y) = \sum_i P_i(r_0, x, y)$$

Case 1 Mie-scattering Source on the Objective Lens

First we consider the case where the Mie-scattering sources are on the objective lens. A sketch of this case is shown in Fig. 6.

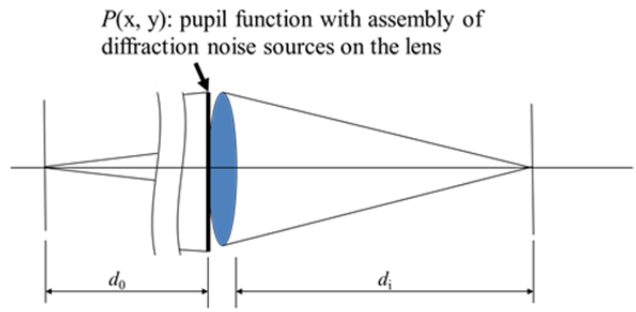

Figure 6: Case 1, Mie-scattering sources on the objective lens.

The impulsive response on the image plane is then given by,

$$h(x_i, y_i; x_0, y_0) = \frac{1}{\lambda d_0 d_i} \iint P(\bar{r}, x, y)$$
$$\exp\left\{-i\frac{2\pi}{\lambda d_i}\left[(x_i + Mx_0)x + (y_i + My_0)y\right]\right\} dxdy$$

where $M = d_i / d_0$ denotes the geometrical magnification. This result means Mie-scattering from small opaque disk on the objective lens is given by the Fraunhofer diffraction of the holes. Since the diffraction intensity is inverse-proportional to the following extinction rate,

Extinction rate = entrance pupil aperture area / total area of noise source

the total intensity of Mi-scattering against diffraction intensity by lens pupil is scaled by this extinction rate.

Case 2 Mie-scattering Sources in Front of Objective Lens

In the following, we consider the pupil which has the Mie-scattering source in front of the objective lens as shown in Fig. 7.

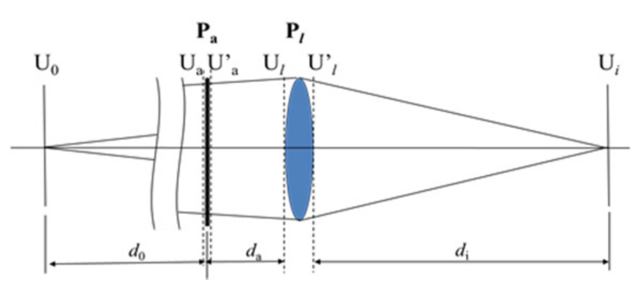

Figure 7: Case 2, Mie-scattering source in front of objective lens.

This is the case of some optical components such as the mirror in front of the objective lens. Since the disturbance of light U_a' after the pupil P_a propagates in free space reaching the front of the objective lens, U_l is given by Fresnel transfer of U_a'. When passing through the lens, the disturbance U'_l is given by the lens transfer of U_l. Finally the disturbance on the imaging plane U_i is given by Fresnel transfer of U'_l. The result of these calculations is given by,

$$U_i(x_i, y_i) = \iint \left[\iint P_a(x_a, y_a) exp\left\{ i\frac{k}{2}\left(\frac{1}{d_0 - d_a} - \frac{1}{d_a}\right)\left(x_a^{\ 2} + y_a^{\ 2}\right) \right\} \right.$$
$$\left. \cdot exp\left\{ -ik\left(\left(\frac{x_0}{d_0 - d_a} + \frac{x_l}{d_a}\right)x_a + \left(\frac{y_0}{d_0 - d_a} + \frac{y_l}{d_a}\right)y_a \right) \right\} dx_a dy_a \right]$$

$$\cdot P_l(x_l, y_l) exp\left\{ i\frac{k}{2}\left(\frac{1}{d_l} + \frac{1}{d_i} - \frac{1}{f}\right)\left(x_l^{\ 2} + y_l^{\ 2}\right) \right\}$$
$$\cdot exp\left\{ -i\frac{k}{d_i}\left(x_i x_l + y_i y_l\right) \right\} dx_l dy_l$$

The first double integral originates from the diffraction of Mie-scattering source while the second double integral results from the diffraction of lens pupil.

Actual Mie Scattering Source on the Surface of Optical Component

A photograph of a surface with the optical polishing quality of scratch & dig 60/40 is shown in Fig. 8 [2]. The optical surface quality 60/40 guarantees no larger scratches than 6µm width, and no larger dig than 400µm. The side of this photograph is 5mm. This photograph is taken with the dark field illumination method. The surface with optical polishing "scratch & dig 60/40" still has many digs (small shiny spots in the photograph).

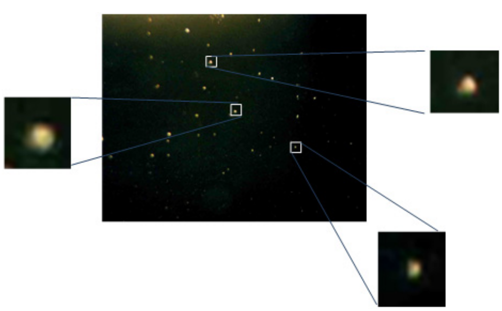

Figure 8: A photograph of surface with the optical polishing quality of scratch & dig 60/40. The side of this picture is 5mm.

Actually, no recognisable scratch can be found on this surface, and the maximum diameter of dig is about 100µm.

Simulation of Mie-scattering Background from Lens Surface

Results of simulation of the Mie-scattering background for dig diameters of 400µm, 200µm, 100µm, 50um on the imaging plane of objective lens are shown with the diffraction of objective lens pupil in Fig. 9. The diffraction patterns are shown for field of ±10mm on the imaging plane of the objective lens. The dig diameter of 400µm corresponds to the maximum possible size in dig 40. In this simulation, an extinction ratio corresponding to number of dig 20digs/5mm^2 was assumed. A zoom-up plot of the diffraction patterns for a significant field is shown in Fig. 10. This field corresponds to 20σ of the beam core size, and a significant beam halo image will be appeared in this field.

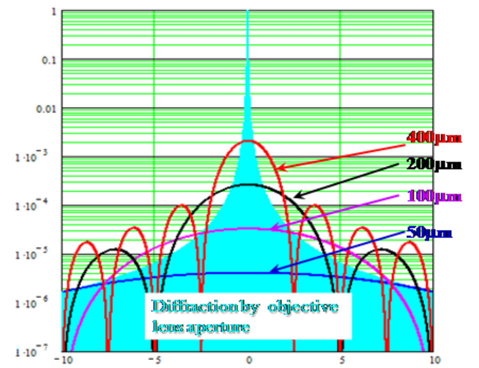

Figure 9: Results of simulation of Mie-scattering background for dig diameter of 400µm, 200µm, 100µm, 50µm on imaging plane of the objective lens with the diffraction of objective lens pupil.

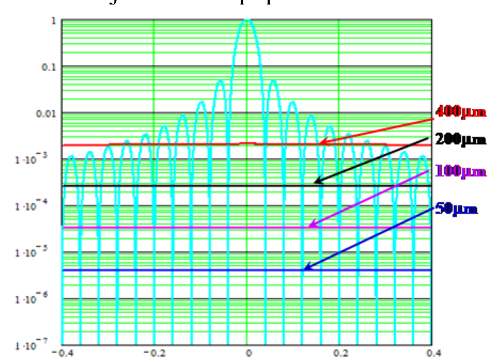

Figure 10: A zoom up plot of diffraction patterns.

According to Fig. 9, the Mie-scattering intensity corresponding to 400mm dig has an intensity of 2 x 10^{-3} of the peak intensity of the objective lens diffraction. Moreover, a 3 x 10^{-4} peak is found for a 200µm dig, 3 x 10^{-5} for 100µm dig and 4 x 10^{-6} for 50µm dig respectively. The Mie-scattering background can be an important contribution to the overall coronagraph background.

Example of Observation of Mie-scattering Noise

An example of Mie-scattering background observation is shown in Fig. 11 [2], where in (a) a result of beam halo observation in PF is found while in (b) same image taken with some intentionally sprayed dust onto a mirror located 1m in front of the objective lens. In this example, the beam halo image is totally hidden by the bright Mie-scattering noise. This case corresponds to the Case 2, and out of focus image of noise source plus its Fresnel like diffraction due to a shorter D_0.

ISBN 978-3-95450-176-2

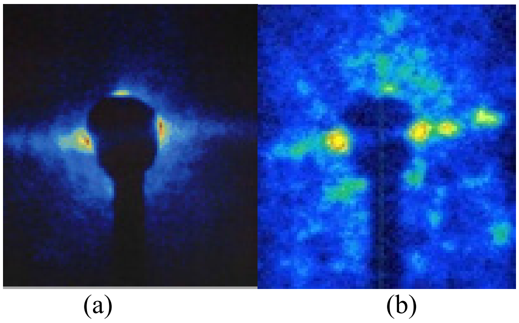

Figure 11: Observation of Mie-scattering noise in beam halo observation at PF. Observed beam halo at PF (a), same image taken with some intentionally sprayed dust onto a mirror located 1m in front of the objective lens (b).

ARRANGEMENT OF CORONAGRAPH SETUP IN B2 OPTICAL HUT

The coronagraph layout is proposed to fit in the SR monitor hut of B2 in the LHC. The objective lens of the coronagraph which is constructed in PF [2] is reused for phase 1 LHC coronagraph. However, the rest of the optical system is redesigned. The optical hut has 4.8mx0.8m optical table housing an imaging line and a calibration. To fit in the coronagraph, the calibration line will be dismounted and the imaging line rearranged. A proposed rearrangement on the optical table is shown in Fig. 12. Due to a limitation of the length of the optical table, and long length of the coronagraph, the coronagraph optical axis is folded two times by 90 deg after the field lens (this tilting in the coronagraph is very common due to their long length). The existing imaging line will be set surrounding the coronagraph.

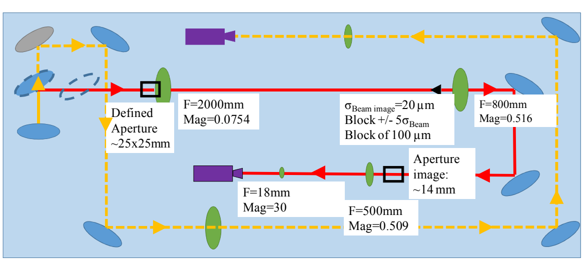

Figure 12: Arrangement of the coronagraph on the optical table at B2.

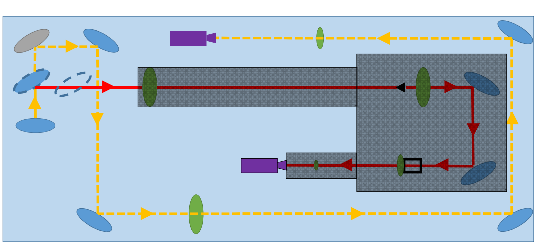

Figure: 13 Surrounding tubes and dark box.

In this arrangement, we have three relay mirrors set in front of the objective lens: the in-vacuum SR extraction mirror followed by an optical widow for separation of the vacuum and two steering mirrors. Surfaces on these optical components can serve as the Mie-scattering noise sources. The optical components of the coronagraph will be covered with surrounding tubes in a dark box to escape from external parasitic light noise and also to reduce the air turbulence of in long optical path. The layout of the coronagraph surrounding structure is shown in Fig. 13.

SUMMARY

Coronagraph optics for phase 1 observation of beam halo is designed for B2 SR monitor beam line at LHC. From diffraction analysis, the background in this coronagraph from leakage of diffraction fringe is estimated to be 3.7×10^{-4}. The diffraction fringes from the relay lens square aperture is mainly localized in the horizontal and vertical medium plane, we possibly can distinguish beam halo image between diffraction fringes by rotating the aperture pupil. Since the existing B2 SR line is not optimised for coronagraph observation, the performance of coronagraph will also be limited by the Mie-scattering noise from existing optical components such as mirrors. On the surface of actual optical components with scratch & dig of 60/40, the 400μm dig is very rare. The digs having a diameter smaller than 100μm are the majority. For this reason, an order of 10^{-4} to 10^{-5} background can be expected for phase 1 using the B2 SR monitor line. The Mie-scattering noise from small digs is almost flat distribution over the significant field as shown in Fig. 10, we have a possibility to subtract this background. We expect to observe the beam halo with a contrast of 10^4 using coronagraph set in B2. Actual arrangement of coronagraph on B2 optical table is also studied. The designed coronagraph is now under construction and should be ready by the end of 2015.

LODESTER FOR PHASE 2 CORONAGRAPH DESIGN

The background is caused by from diffraction fringe leakage in Lyot stop that limits the theoretical contrast in the coronagraph. Since leakage of diffraction fringe is reduced by increasing the opaque disk diameter, we can achieve a better contrast by increasing the beam core image size. Therefore we should design the focal length of the objective lens. Since the chromatic shift on the optical axis is given by the focal length divided by the Abbe number, designing a long focal length implies increasing the chromatic focal shift. Reflector focusing system for the objective should be considered instead of the objective lens system in stage 2. Actually, recent space coronagraph such as LASCO coronagraph [4] applied reflective system for objective system.

REFERENCES

[1] B.F.Lyot Month. Notice Roy. Ast. Soc,p580,**99** (1939).
[2] T. Mitsuhashi, Proc. Of DIPAC 2005, p7 (2005) Lyon.
[3] G.E.Bruecknere, et.al., Solar Physics,**162**,p357 (1995)
[4] M. Born and E. Wolf,"Principal of Optics", p424, 7th ed., Cambridge University Press (1999).

ISBN 978-3-95450-176-2

FAST ORBIT FEEDBACK SYSTEM AT THE AUSTRALIAN SYNCHROTRON

Y.-R. E. Tan, T. D. Cornall, E. J. Vettoor, A. Michalczyk, N. Basten, SLSA, Clayton, Australia
D. J. Peake, The University of Melbourne, Melbourne, Australia

Abstract

Since the end of commissioning of the facility in 2006, implementing top up (completed 2012) and fast orbit feedback have been top priority upgrades to improve the stability of the light source for users. The fast orbit feedback system is currently being implemented and will be commissioned late 2015. The feedback system has a star topology with an FPGA based feedback processor at its core. The system will utilise the existing 98 Libera Electron beam position processors, with Libera Grouping for data aggregation, as the source of position data at 10 kHz. The corrections are calculated in a Xilinx Vertex 6 FPGA and are transmitted to 14 corrector power supplies in the 14 sectors. These power supplies are six-channel bipolar 1 Ampere and have been developed by a local company. The corrector magnets are tertiary coils on the existing sextupole magnets in the storage ring. This report shall present the design, results of Simulink simulations, the current status of implementation and future plans.

INTRODUCTION

The Australian Synchrotron (AS) is a 3rd generation light what was commissioned in 2006 [1]. The storage ring is a 14 fold symmetric Chasmann-Green lattice with leaked dispersion. In each of the 14 sectors there are 7 beam position monitors (BPMs) giving a total of 98 BPMs [2].

As the technology and techniques on the beamlines mature, their sensitivity to source stability has increased. The stability requirement at the AS is to maintain the transverse beam motion to be less than 10% of the beamsize at the source. The tightest constraint on the beam motion is at the insertion device straights where the beamsize is the smallest. With the nominal configuration (optics) the one sigma beamsize is 320 μm horizontally and 16 μm vertically at 1% emittance coupling and 5 μm for the natural coupling of 0.1%. The integrated motion at the insertion device straights is shown in Figure 1 where in the vertical plane the beam motion exceeds 10% of the vertical beamsize of 16 μm at 100 Hz.

The fundamental requirement for the fast orbit feedback (FOFB) system is to reduce the beam motion to less than 10% of the beamsize up to 100 Hz [3]. To achieve this the system was designed to try and meet a closed loop bandwidth of 300 Hz. However as shall be shown this was always going to be challenging. The second design requirement was to, where possible, reuse the existing infrastructure and equipment. The following sections will introduce the design of the system, the results of simulation studies, the different subsystem and the current state of the project.

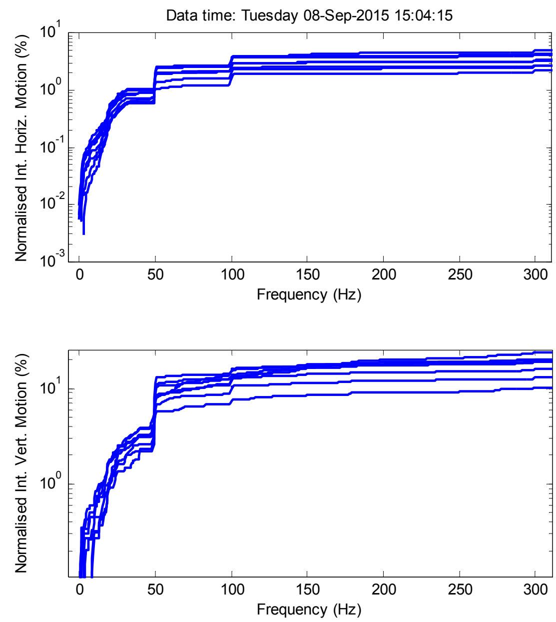

Figure 1: Integrated beam motion at all insertion device straights normalised to the beamsize in percent (320 μm and 16μm). The largest contributor to the perturbation on the beam is the 50 Hz mains frequency. At 100 Hz the integrated beam motion in the vertical plane exceeds 10%.

DESIGN

The design of the system can be broken down into 3 sub-systems as shown in Figure 2: (1) beam position measurement and aggregation, (2) feedback controller and (3) corrector magnets and power supply.

Beam Position Measurement

The beam position in the storage ring is measured using Instrumentation Technologies' Libera Electron beam processor. The processors have a real-time stream of position data at 10 kHz (Fast Acquisition data) and are aggregated across the 98 BPMs by using Libera Grouping [4]. The topology of Libera Grouping implemented here is a single a ring with one level of redundancy. The Libera Electrons transmit 98 horizontal and 98 vertical positions at a rate of 10 kHz via UDP using a GbE link.

Feedback Controller

The feedback controller receives the data, decodes packet information and translates this into corrector current values using an inverted BPM-Corrector response matrix. In the first instance the controller will be a single

ISBN 978-3-95450-176-2

global P controller. The corrector current values are then sent to the magnet power supplies via optical fibres using a serial protocol. The chosen platform for the controller is a Xilinx Vertex 6 FPGA (on a development board).

The choice of an FPGA platform was two-fold, a strategic decision to build expertise within the Australian Synchrotron in developing on such platforms as well as the future potential of such a system to do more intensive computations without significantly compromising on the system performance.

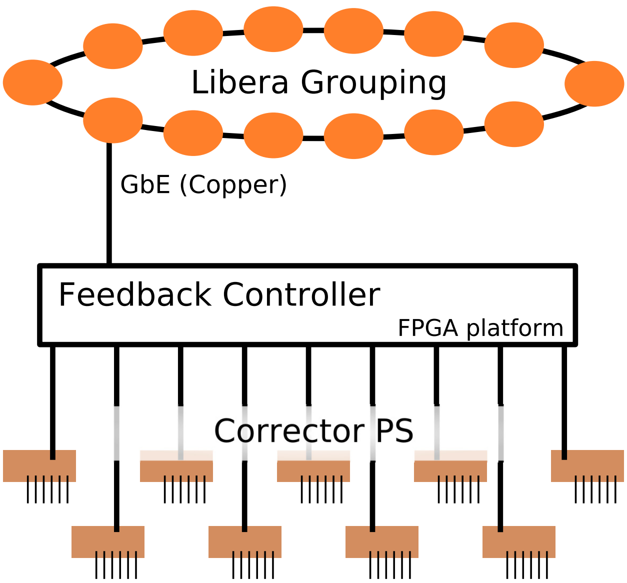

Figure 2: The three sub-systems are: (top) beam position measurement and aggregation, (middle) feedback controller and (bottom) power supplies connected to tertiary coils on the sextupole magnets.

Corrector Magnets and Power Supplies

There are three Horizontal "Fast" Corrector (HFC) and three Vertical "Fast" Corrector (VFC) in each of the 14 sectors giving a total of 84 "Fast" corrector magnets in total. These corrector magnets are tertiary coils installed on the existing sextupole magnets in the storage ring.

In the development of the design for the FOFB system the following were considered:

1. Replacing or modifying existing corrector magnets: this would have been too costly and risky.
2. Trim power supply in series: this was tested however the interaction between the slower and trip power supply introduced instabilities as certain frequencies.
3. Independent freestanding corrector magnets and power supplies: new magnets just around the insertion devices, not insignificant cost of magnets and stands.
4. Independent coils on sextupoles and power supplies: lower cost of magnets and can have correctors in the arcs. Trade off lower bandwidth due to the vacuum chambers.

The decision was made to use the coils on the sextupoles due to the lower cost and distributed nature.

LATENCIES

To estimate the bandwidth of the system it is necessary to quantify the latencies in the system. To measure the latencies of the system a simplified prototype of the feedback controller was developed to decode the position data from the Libera Electron and to output a digital signal which is triggered when the reported position changes. The change in the position is systematically created by a 10 Hz pulse that attenuates one of four input signals to the Libera Electron resulting in step changes to the position at a rate of 10 Hz. By measuring the delay between the onset of the pulse and the digital output from the comparator it is possible to measure the latency of the Libera Electron processor and position aggregation (see Figure 3). After 12000 samples the spread of the latency showed an equal distribution between with a minimum of 86 μs and a maximum of 191 μs. In the following analysis and simulations we have assumed a conservative latency of 200 μs to account for the Libera Electron processing and aggregation. The Libera Grouping's data packet contains data for 98 BPMs with a total of 1610 bytes (including headers). At 1 Gbps the transfer time is 13 μs.

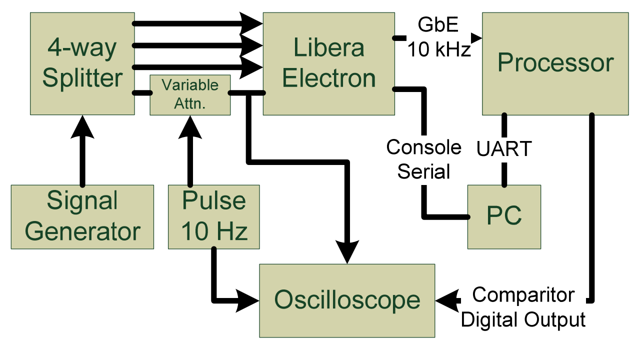

Figure 3: Setup used to measure the latency of the Libera Electron processor and the position aggregation. The pulse attenuates just one of four of the 500 MHz RF signal to the Libera Electron. The result is a step change in the position. By setting the appropriate level the comparator output will indicate when the reported position on the 10 kHz data stream changes.

Another system that can be quantified is the response of the vacuum chamber. Due to the screening effect of the 3 mm thick stainless steel vacuum chamber walls it acts as a low pass filter. The cut-off frequency was measured and shown to be 400 Hz and 1000 Hz in the horizontal and vertical planes respectively (see Figure 4).

Figure 5 shows all the known latencies in the system as well as the screening effect of the vacuum chamber. This is the fundamental limit of the feedback system. At the start, conservative limits were placed on latencies of the systems that we would be implementing (processor and the power supplies).

ISBN 978-3-95450-176-2

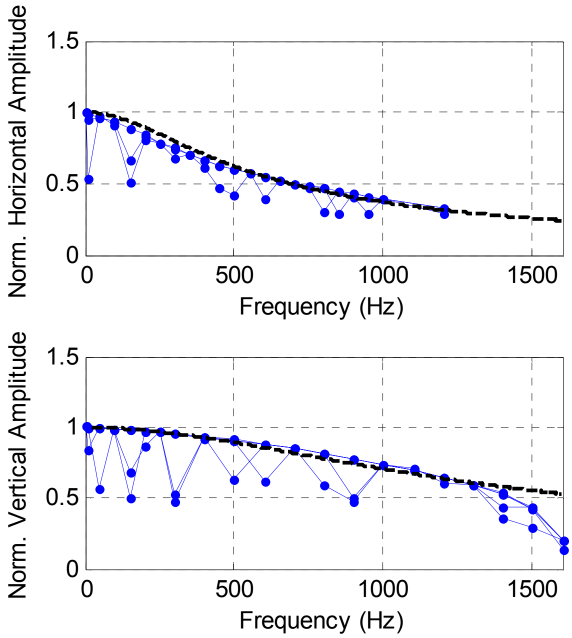

Figure 4: Measured peak amplitude of the closed orbit perturbation as a function of frequency. The corrector magnet was driven with a sinusoidal current at a constant peak amplitude of 230 mA at different frequencies (solid lines). Simulated low pass filter with a cut-off frequency of 400 Hz (H) and 1000 Hz (V) shown as a dashed line.

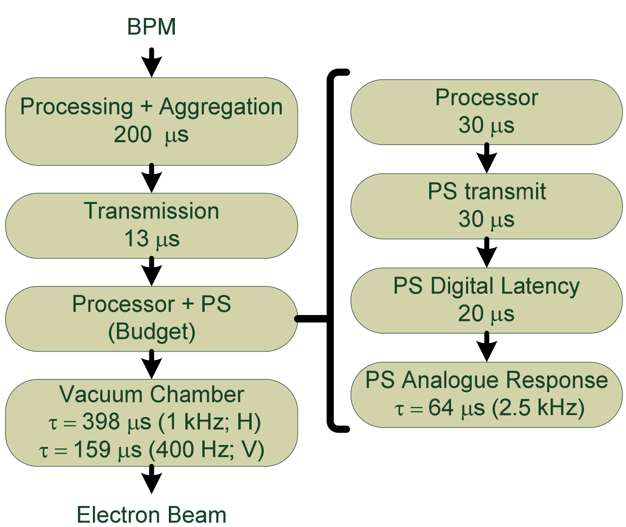

Figure 5: Summary of the estimated latencies in the various sub-systems that are fixed and the budgeted latency for the processor and power supply.

SIMULATIONS

With the above assumptions a Simulink model was created to determine the closed loop bandwidth of the system. To simulate the disturbance, 2 seconds of real position data was collected. The fast acquisition (FA) data (10 kHz) was streamed to a PC running Diamond's Fast Acquisition Archiver [6] to store and later retrieve data. A whole ring response matrix was calculated using a model of the Storage Ring using the Accelerator Toolbox (AT) [7]. The whole ring response places dipole perturbation terms in all the quadrupole and sextupole locations creating a total of 182 parameters. By using the whole ring response, the perturbations, including noise on observed on the storage ring can be modelled by 182 parameters.

The Simulink model shown in Figure 7 takes into account the fixed and budgeted latencies (Figure 5) as well as models the feedback controller and responses of the power supply and the vacuum chamber. The comparison of the closed loop gain in both planes is shown in Figure 6. Using this result the estimated bandwidth of the feedback system is 220 Hz and 310 Hz in the horizontal and vertical planes respectively.

The current design only implements a simple P controller however if the implementation over the coming months go well we will investigate the feasibility of implementing a PI or modal controller [8].

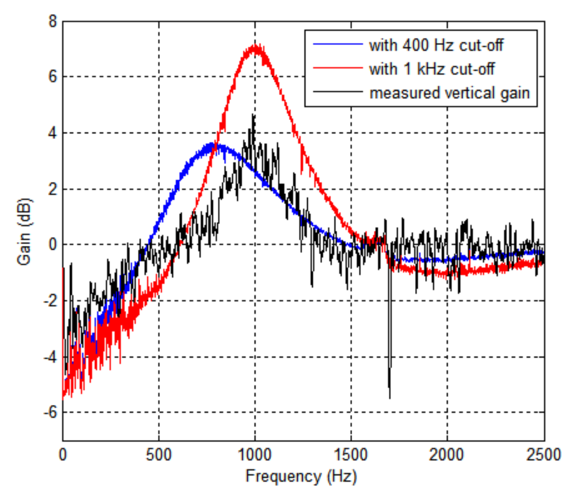

Figure 6 Simulated closed loop gain of the feedback system in both planes with the two differ cut-off frequencies of the vacuum chamber and measured vertical gain with a prototype controller. The closed loop bandwidth is estimated to be 220 Hz (Horizontal; blue) and 310 Hz (Vertical; red). Above 450 Hz (Horizontal) and 610 Hz (Vertical) perturbations are amplified. All of the above use a P coefficient of 0.9.

Prototype Test

Early in the project a prototype of the feedback controller was developed to test various components (ability to decode the Libera data packets, matrix multiplication, P controller and control of the power supplies) and determine if we could do it on an FPGA. In this test only two correctors were used in the feedback loop and results shown in Figure 6 (black) compare reasonably well with the simulations. It so happened that the power supply that we were trialling (ITEST Bilt power module) had a bandwidth ~2.5 kHz, latency of 50 μs, transmission latency of 20 μs.

ISBN 978-3-95450-176-2

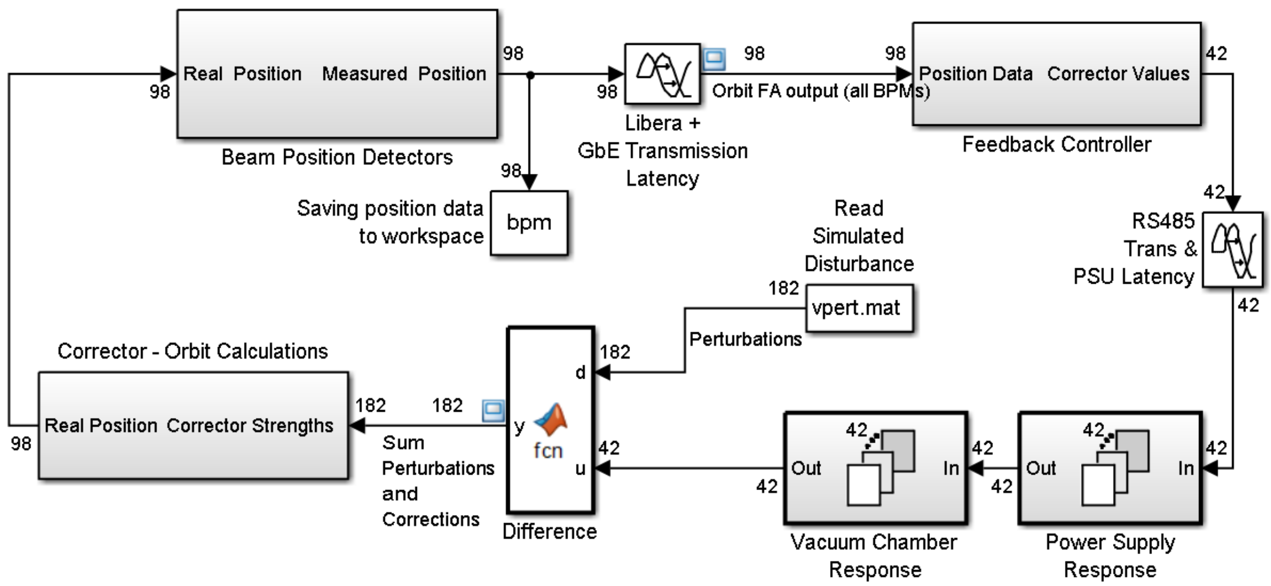

Figure 7: Simulink model of the feedback system. The perturbations are simulated by distributed dipole kicks around the ring (modelled with 182 parameters) which is converted back into position (bottom left). The BPM processors include a 220 µs transport delay (top left). The feedback processor uses an inverted fast corrector-BPM response matrix to calculate the corrections needed with a P controller (top right). The power supply is modelled by a fixed transport delay of 80 µs and a low pass filter of 2.5 kHz. The vacuum chamber is modelled by a low pass filter of 400 Hz and 1000 Hz for the horizontal and vertical planes (bottom right).

FEEDBACK CONTROLLER DESIGN

The feedback controller on a built on a Virtex 6 FPGA will be connected directly to the controls system and to a Libera Electron for the FA data (10 kHz position data). The design philosophy is to modularise the functionality as much as possible to ensure future modifications are simplified. A schematic of the design is shown in Figure 9. The control system's EPICS IOC will communicate with the controller via a GbE connection.

The primary processing chain decodes the data packet from the Libera Electron to extract the transverse position ID and status data. The transverse position is sorted by id number to form a vector to be multiplied by the inverse response matrix and scaled by a proportional factor, P. When all corrector values are updated a signal is given to the UART handler to transmit the data via the digital IO channels on the FMC. A separate daughter board has been developed to transmit the UART data to the power supplies via optical fibre links (see below).

The system operates in three modes: stop/initial, run and diagnostic. The parameters can only be updated when in the stop mode, (no queuing feature has been implemented). The data is processed when in run mode and in diagnostic mode the user can set the input position vector and/or the calculated corrector values. A software trigger then forces the calculation of the corrector values based on the input position values and another software trigger can be set to transmit the corrector values. In all modes it is possible to request a snapshot of the position data and corresponding calculated corrector values.

The modularity will ensure that future algorithms can be easily added to the system and eventually utilise the on-board 1GB DDR RAM to create a circular buffer to store diagnostic data.

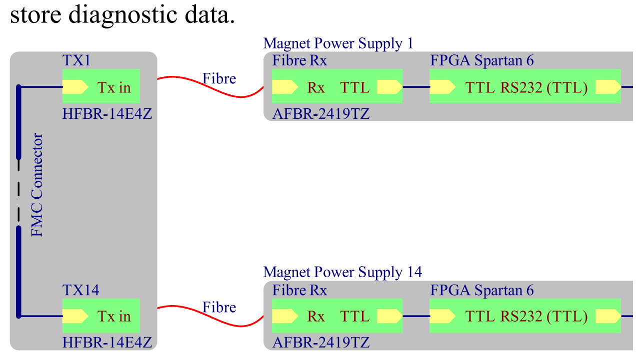

Figure 8: FPGA controller to power supply communications modules using optical fibres. The system has been tested at a baud rate of 10 MBps.

Power Supply Communications

To transmit the corrector values to the 14 power supply units a daughter board was designed to transmit the UART data via optical fibre. The transmitter uses a custom encoding scheme to pass the data to an optical receiver on the power supply at a baud rate of 10 MBps.

ISBN 978-3-95450-176-2

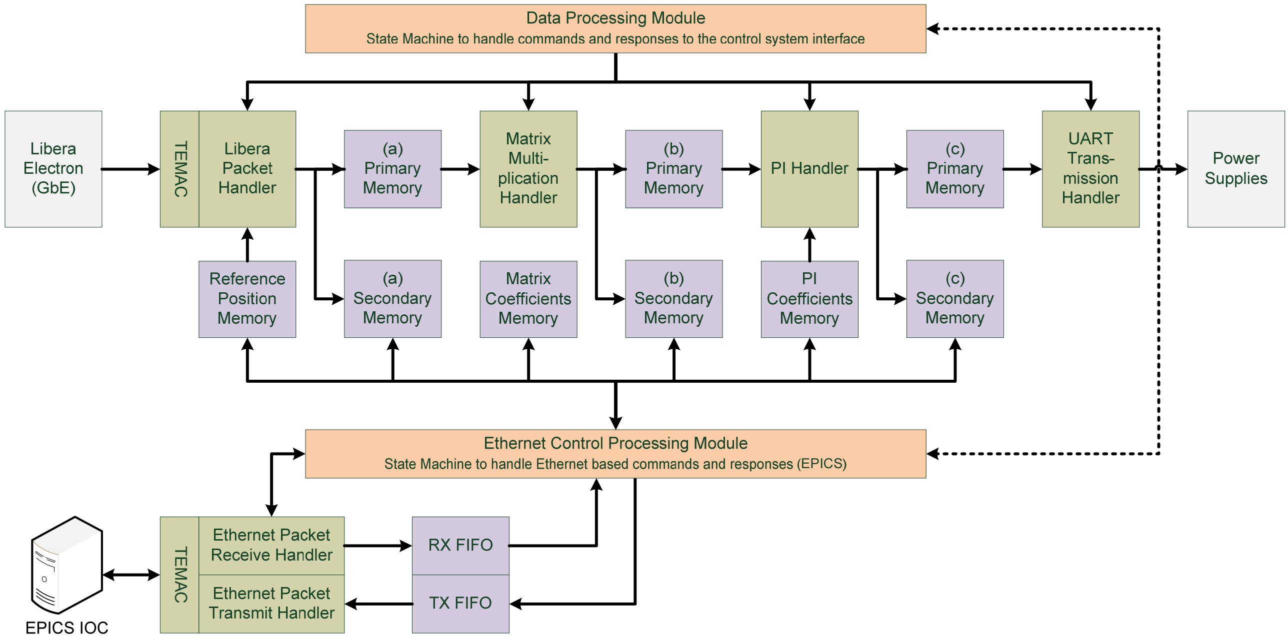

Figure 9: Feedback controller design.

POWER SUPPLY

The power supplies have been developed locally by DETECT and have supplied the AS with 15 units (1 spare) with performances listed in Table 1. These have been delivered and tested at the AS and has been shown to perform well. In some instances the actual performance exceeded the specifications by a large margin. For example the long term stability was measured at 400 mA ±70 uA and the temperature coefficient was < 100 ppm/°C. The system latency was also measured at 31 us and the bandwidth at amplitude of 400 mA was close to 4 kHz.

Table 1: Specifications for the FOFB Power Supplies

Total number of channels	84 (14 units × 6 ch)	
Output Current	± 1.0 A, bipolar	
Load Inductance range (@ 100 Hz)	0.99 mH	2.7 mH
Load Series Resistance*	1.4 Ω	2.4 Ω
Setting and readback current resolution better than	1 mA	
Current accuracy	50 mA	
Current noise, 10 kHz bandwidth	< 0.3 mA (300 ppm)	
Long term stability (8 hr)	± 0.3 mA (300 ppm)	
Temperature coefficient	< 300 ppm/°C	
Setting data rate	10kHz	
Minimum bandwidth with maximum load†	> 2.5 kHz	
Max latency (end data arrival to DAC output)	50 us	

* Including resistance of wire from the power supply rack to the magnet coils. Minimum of 0.6 Ω Maximum of 1.1 Ω.

† AC with peak amplitude of 0.4 mA (peak-peak of 0.8 mA) into an inductive load of 2.7 mH and 2.4 Ω.

ACKNOWLEDGMENT

Sincere thanks to Brian Jensen and Rahul Banerjee in the Electrical and power supply group for work on the power supply.

REFERENCES

[1] G. LeBlanc, “Status of the Australian Synchrotron Project”, APAC’07, Indore, India (2007).
[2] Y.R. E. Tan, et al., “Storage Ring Turn-by-Turn BPMs at the Australian Synchrotron”, PAC’07, Albuquerque, USA (2007).
[3] Y.R. E. Tan, et al., “FPGA Based Fast Orbit Feedback System for the Australian Synchrotron”, IBIC’12, Tsukuba, Japan (2012).
[4] A. Bardorfer, et al., “Libera Grouping: Reducing the data encapsulation overhead”, EPCA’08, Genoa, Italy (2008).
[5] P.C. Chiu, “Conceptual Design and Performance Estimation of the TPS fast orbit feedback system”, EPAC’08, Genoa, Italy (2008).
[6] M.G. Abbott, “A new fast data logger and view at Diamond: the FA archiver”, ICALEPCS’11, Grenoble, France (2011).
[7] A. Terebilo, “Accelerator Modelling with Matlab Accelerator Toolbox”, PAC’01, Chicago, USA (2001).
[8] A. Terebilo, T. Straumann, “Fast Global Orbit Feedback System in SPEAR3”, EPAC’06, Edinburgh, Scotland (2006).

ISBN 978-3-95450-176-2

ADVANCEMENTS IN THE MANAGEMENT MEASUREMENTS & VISUALISATION OF NEC BEAM PROFILE MONITORS

D. Button#, D. Garton, M. Mann, ANSTO, Lucas Heights, Australia
S. Yan, National Instruments, Macquarie Park, Australia

Abstract

In DC ion beam tandem accelerator facilities commonly Helix Rotating wire Beam Profile Monitors/scanners (BPM) are used to monitor the shape and location of the ion beam. These BPMs are used in combination with a BPM Selection station which activates and conditions signals visualisation on an Oscilloscope. At ANSTO we have been developing an alternative system to allow firstly the management and operation of concurrent National Electrostatics Corp (NEC) BPMs, secondly to construct a 2D approximation of the particle beam parameters based on programmable hardware and software, and thirdly to give advanced functionality to control systems. This paper will review the current status of the development, and the potential features which can be gained with this technological approach.

BACKGROUND

Beam Profile Monitors BPMs are an important diagnostic device used during the tuning of electrostatic ion beam accelerator particle beams. These provide effectively real-time information back to the operator to indicate the location of the beam and the X and Y intensity profile of the beam. There are generally two types of these monitors/scanners used in DC electrostatic ion beam facilities, the oscillating Y-Shaped wire scanner manufactured by HVEE, and the helix rotating wire scanner manufactured by NEC (see Fig.1). The NEC rotating helix wire scanner is the subject of this paper and development.

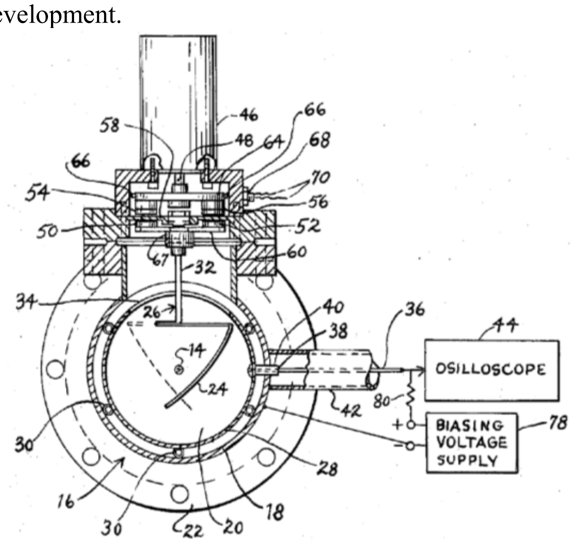

Figure 1: Original general assembly drawing of the NEC BPM taken from the 1971 patent application [1].

dbu@ansto.gov.au

Principle of NEC BPM Operation

The NEC BPM uses a helix shaped wire attached to a rotating disc as shown in Fig. 2, this disc rotates which due to the geometry of the system has a pseudo effect of sweeping the wire through the cross-section of beam firstly in the Y direction, and then the wire sweeps through the X direction, see Fig. 2(a,c). The shaft on the axis of rotation has magnets attached at known positions that a stationary sensor/coil pick-off produces an analogue stream of pulses. These pulses are used to indicate firstly the start of a rotation cycle (Fig. 3(1)), the wire passing the centre of the Y axis (Fig. 3(2)), and the wire passing through the centre of the X axis (Fig. 3(3)), these are referred to as the "Fiducial" markers, see Fig. 3.

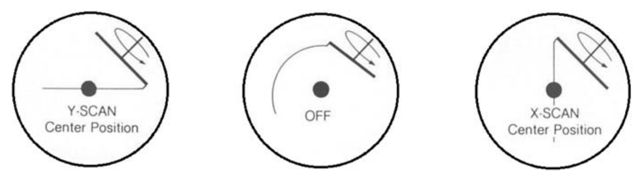

(a) (b) (c)

Figure 2: The rotating axis of the helix wire as indicated in (a-c) is setup at an angle of 45° to the horizontal plane. (a) shows the wire "sweeping" through the pseudo Y plane of the beam as the wire is effectively horizontal through this part of the rotation, (b) the wire is free of intersection/interacting with the beam, (c) the "sweeping" motion through the pseudo X plane of the beam as the wires direction is effectively vertical in this part of the rotation [2].

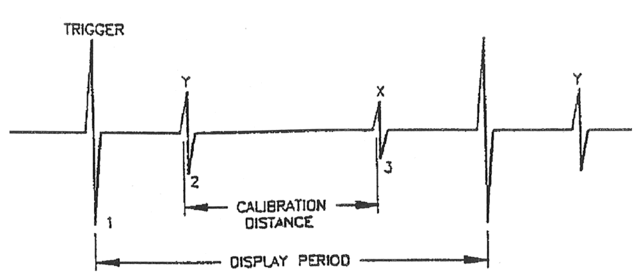

Figure 3: Shows the fiducial markers produced during the rotation of the helix wire shaft (see Fig. 1(26)) [3]. The larger trigger pulse indicates the start of the rotation followed by the Y centre marker, and finally the X centre marker, as the shaft continues to rotate the same pattern continues during operation.

ISBN 978-3-95450-176-2

As the wire passes through the region of beam the impact of the ions on the wire generates secondary electrons which are proportional to the flux of the ions striking the wire at any one time. These electrons are collected by an insulated positively biased shield (see Fig. 1(34)) which feed into a gain amplifier to produce the "Collector" signal. This collector signal gives the profile detail of each plane as it travels through the beam from different directions. When the "Fiducial" and "Collector" signals are combined using a NEC BPM-SS6 Selector Station the unit interoperates and produces more user friendly signals for an oscilloscope which are, a Trigger, Collector signal, and Centre Marker signals (*On CRO's this controlled the beam brightness Z channel)*, see Fig. 4.

The existing BPM-SS6 units are limited to only display and select one BPM at a time and display on one oscilloscope. This is a mode of operation devised primarily from when an oscilloscope was the intended means of visualisation. To operate and display multiple BPMs would require an unreasonable number of oscilloscopes and other components. Thus it can be reasonably concluded that using an oscilloscope and selector station to run multiple BPMs is economically unviable, likewise the only data is visual feedback to the operator and not interactive to provide active engagement with a control system or real parameters. With the availability of modern instrumentation the existing method of visualisation and management is limited and may not be the most economical solution.

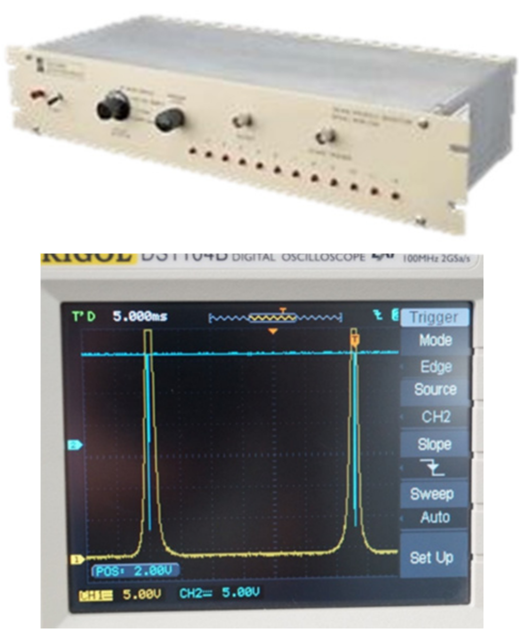

Figure 4: The top photo shows and BPM-SS6 BPM selector station which can receive the Fiducial and Collector signal from up to 12 BPMs. It selects any one of the attached BPMs to operate, and processes the Fiducial and Collector signals into signals to feed into an oscilloscope to display the beam profile and position in the Y (first peak) and X plane (second peak).

DEVELOPMENT OF NEW BPM INTERFACE

Many electrostatic accelerator facilities have seen great advances in throughput and general operational ease as they have progressed from so called "knob based" controls systems to computerised control systems. This has many advantages in reducing cable run requirements which made equipment susceptible to interference, ground loop problems, and by consequence the majority of all chassis and cabinets had to be custom made making it an expensive undertaking [2].

The ANSTO electrostatic tandem accelerator facilities have a combination of partially and fully computerised control systems for the operation of our existing 4 facilities. Even where the BPMs are activated by the computer system there is still the limitation to run and display one BPM at a time with the existing oscilloscope display method employed.

With access to modern programmable instrumentation it has been considered to extract more information to present to the operator from one or more BPMs. Currently the operator has to be familiar with how to interoperate the displayed profile, and even be familiar with qualitative estimates of the preferred tuned paths through the accelerator and beamlines for best performance by prior experience. Likewise the operator has to iterate individually through the BPMs one at a time to evaluate the optics through the system as changes are made. Even when completed tuning, the operator only knows a rough estimate of beam location relative to the axis, and roughly the beam shape via mental evaluation of the oscilloscope display. Likewise it is of note that most oscilloscopes used for this purpose of display have a resolution of 8 bits which can limit sensitivity with low current beams.

Digitizing the BPM

In researching this topic post initial development of the ANSTO digitized interface to the NEC BPM, I should acknowledge the few examples of people producing similar concept developments of digitized helix wire beam scanners/BPMs. For example one of the most similar used a Commodore 64 PC with a basic system demonstrated at TRIUMF [4], and was able to produce a basic 3D plot interpretation of the signals see Fig. 5.

Though inspiration to some aspects of a solution can't be demonstrated as being unique or new, by utilising a National Instruments FPGA platform, and LabVIEW code we plan to achieve a greater expansion of useful parameters of the beam and system control capabilities which our current system is not capable of, these are detailed in Table 1.

ISBN 978-3-95450-176-2

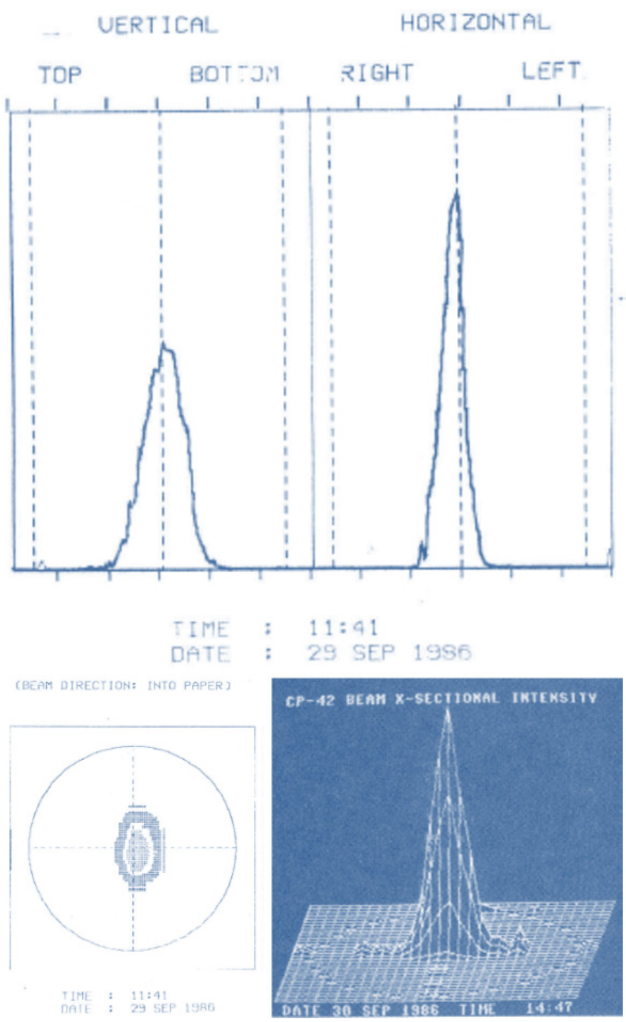

Figure 5: Original figure adapted from TRIUMF paper [4] of figures (4 - 6), demonstrating a 1986 version of a digitized helix wire beam scanner.

Current Development Activities

Firstly in summary the goals which have been achieved and will be detailed below are indicated in blue text in Table 1.

Initial proof of principle of conducted with the aid of a National Instrument development engineer to verify the suitability and capability of both software and hardware which was ultimately selected as the base platform for the BPM development work. Figure 6(a-c) shows the initial proof of principle using the digitized capture of live signals from a BPM to generate firstly the equivalent display as a current system, and secondly the sub-sequential calculated and generated 2D and 3D intensity plots (see Fig. 6).

The acceptance of the proof of principle allowed for the investing in FPGA hardware and PXI chassis to advance the development. This was done as the FPGA platform would deliver a solution which can behave deterministically, have true parallel processing, and be able to perform pre-processing of some data to reduce the process overhead of the associated computer system. Each R series FPGA card used in this development is able to support up to 4 BPM with the native I/O on board, with full functionality of a NEC BPM81 profile monitor. Due to the FPGA data pre-processing ability this make the platform effectively scalable by adding more BPM inputs by adding additional R series FPGA I/O cards.

Engaging with the National Instruments engineer a migration of the PC based code to a FPGA target solution was produced. This application can be screen in Fig. 7. The demonstration was successful in allowing the capture, manipulation, and display of data with no lag detectable to the accelerator operator. Though the demonstration in Fig. 7 is not the final solution, it has demonstrated progress, and that our current development platform has not shown any current limitation for the future refinement of this development.

Table 1: Long Term Goals of BPM Development

Basic • Drop-in replacement for the BPM-SS6 unit. • Capture basic signal information to mimic current oscilloscope display.
Expansion System Operation • Scalable solution, the ability to add more BPMs to a common platform without creating system performance lag. • To allow operation of multiple units concurrently.
Expansion of Information • To convert the two scan peaks into a pseudo 2D and 3D intensity plot of the beam on a Cartesian plane. • To give dimensional measurement of the size position and pseudo shape of the beam. • To allow integration of the beam intensity for calibration studies again a faraday cup for continuous beam monitoring. • To allow dynamic real-time optics diagram to be generated throughout the beam path of flight path cross-section.
Control System Integrations • Controls a reading publish on network for concurrent display and operation. • Targeted and beam quality automated tuning of the ion beam through accelerator beamlines. • Alternative feedback system for Slit based Terminal Potential Stabiliser control and magnet stabilisation based on beam position. • Implantation dosage control. • Auto correction centring beam with grouped steerers.
Note: *Item listed in* ***Blue****, have been demonstrated.*

ISBN 978-3-95450-176-2

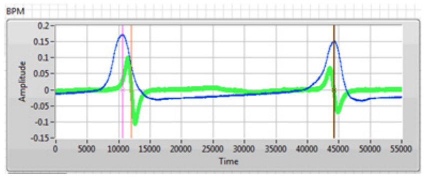

(a)

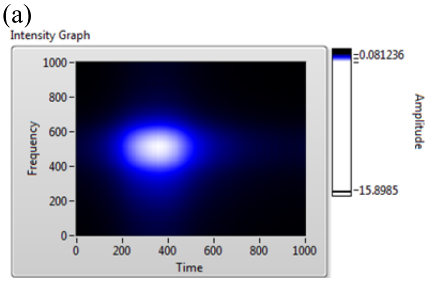

(b)

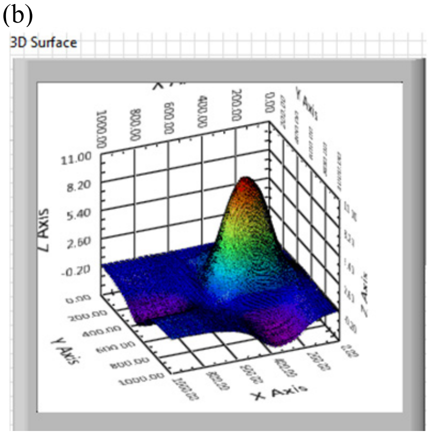

(c)

Figure 6: This shows the initial proof of principle results of digitizing the BPM signal to generate the equivalent oscilloscope display (a), the 2D intensity plot and pseudo beam shape (b), and the 3D intensity plot (c).

REFERENCES

[1] National Electrostatics Corp. Inventors; Raymond G. Herb, 1971 July 29. Beam Scanner. United States patent US 3,789,298.

[2] R. Hellborg (Ed.), Electrostatic Accelerators Fundamentals and Applications, ISBN-10 3-540-23983-9 Springer Berlin Heidelberg New York (2005).

[3] National Electrostatics Corp., Instruction Manual, Beam Profile Monitor Model BPM81.

[4] P. Bloemhard, Z. Gelbart, "High Current Beam Profile Monitor (Wire Scanner)", Proceedings Elevenses International Conference on Cyclotrons and their Applications, Tokyo, Japan (1986).

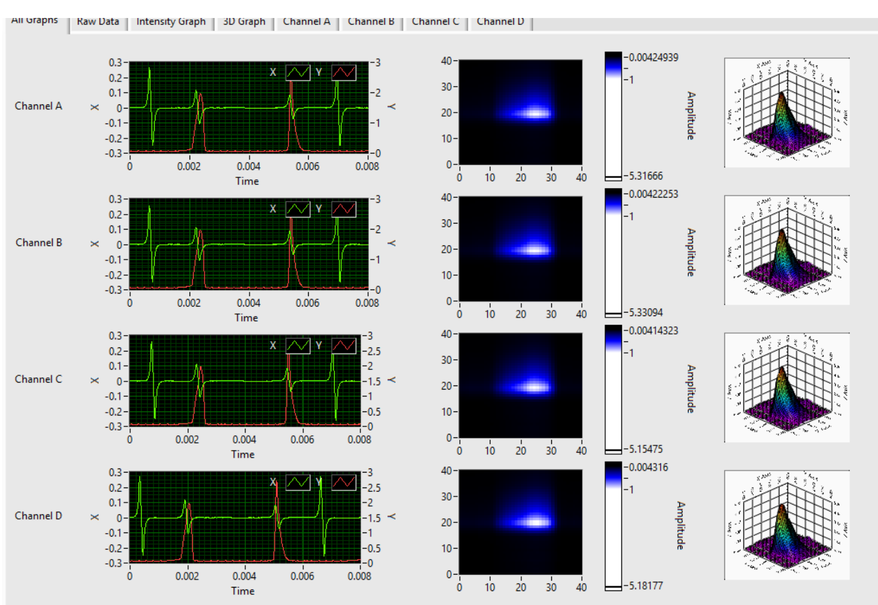

Figure 7: The above screen shot is of the first results of the FPGA based quad BPM monitor. Note, in this test only 1 signal was feed into all 4 BPM inputs, with each input processing individually still. The test demonstrated that the unit was capable of rendering the data in real-time with effectively no delay to the operator.

ISBN 978-3-95450-176-2

IMPEDANCE OPTIMIZATION OF SIRIUS STRIPLINE KICKER

H.O.C. Duarte*, S.R. Marques, LNLS, Campinas, Brazil

Abstract

Two approaches to design a transverse feedback (TFB) stripline kicker are well known in the accelerators community: one with bare strips in a tapered cavity and other whose shrouded strips are ended with parallel-plate capacitive gaps. This work presents a comparison between both models in terms of electromagnetic performance, proposes alternative solutions for increasing the gap capacitance and analyzes the performance of a hybrid stripline kicker design.

INTRODUCTION

Studies of collective beam instabilities for Sirius, the 3 GeV light source under construction in Brazil [1], have shown the need of the transverse bunch-by-bunch (BBB) feedback system in the storage ring since day one [2]. For the longitudinal plane, at least for the initial phases, the use of BBB feedback system is not planned since superconducting RF cavities will be used.

The digital signal processing for the BBB system will be performed by the front/back-end and iGp processor units from Dimtel, Inc. [3] and the actuators will be one $\lambda/2$ stripline kicker for each plane. A $\lambda/4$ stripline tune monitor is also planned.

This contribution describes the evolution of the stripline kicker design for Sirius. At first, several concepts were tested regarding their transverse geometric factor and longitudinal coupling impedance. Then the best suited geometry was optimized following the compromise between the reflection parameter at the input coaxial ports and the geometric loss factor of the structure. Shunt impedance was also evaluated and finally the mechanical project and thermal simulation results are shown.

GEOMETRY ALTERNATIVES

The electromagnetic design evolution for Sirius stripline kicker was carried out by analysing three different concepts to further optimize the longitudinal impedance spectrum and the reflection parameters of the chosen one. GdfidL [4] was used for the electromagnetic simulations.

Transverse 2D Analysis

All presented stripline geometries can be grouped in either of these two transverse profiles: Bare Strip and Shrouded Strip designs, whose dimensions are shown in Fig. 1. While solving the 2D Laplace's equation for an electric boundary condition (BC) characterizes the odd mode, which is the kicker operation mode, the solution for a magnetic BC would give the field distribution for the even mode [5]. Both profiles in Fig. 1 had their geometry parameters set to match a 50 Ω characteristic impedance (i.e., 25 Ω for the full structure containing two electrodes). An impedance mismatching can impact the beam coupling impedance [6] and the port signal reflection.

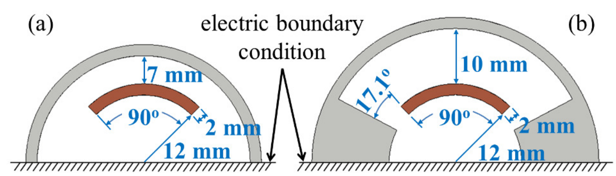

Figure 1: The considered transverse profiles for the vertical striplines: a) Bare Strip and b) Shrouded Strip designs.

From the mentioned 2D electrostatic analysis one can also determine the transverse geometric factor $g_\perp$. For the Bare Strip (Fig. 1a) and Shrouded Strip designs (Fig. 1b), $g_\perp$ is equal to 1.09 and 1.01 respectively. The geometric factor allows determining the transverse beam impedance [5]:

$$Z_\perp(k) = \frac{g_\perp^2 Z_{ch,\perp}}{kr^2}[\sin^2(kL) + j\sin(kL)\cos(kL)] \quad (1)$$

where k is the wave number, $Z_{ch,\perp}$ the full structure characteristic impedance for the odd mode (25 Ω), r the stripline inner radius (12 mm) and L the stripline lenght, which determines the kicker operation bandwidth (BW). Choosing $L = \lambda/2 = 30$ cm provides 250 MHz shunt impedance BW [7], which is enough for correcting Sirius transverse coupled-bunch instabilities (CBMIs) [8] since Sirius RF frequency is ~500 MHz. The shunt impedance can be calculated by [5]

$$R_{sh}^{\perp} = \frac{4 \times \Re e Z_\perp(k)}{k} \quad (2)$$

For a kicker, the shunt impedance is an important parameter since it quantifies its efficiency relating the injected power with the kick energy absorbed by the beam. Given that both transverse profiles in Fig. 1 only differ by the geometric factor, it is straightforward to see in Eq. 1 that a transverse kicker with Bare Strip transverse profile is 16.5% more efficient than one with the Shrouded Strip design type. However, the stripline ends affect other aspects of the kicker and a three-dimensional analysis must be performed for a satisfactory characterization.

Longitudinal 3D Analysis

Figure 2 shows the simplified geometries for the simulation models of three different stripline concepts. The Tapered Cavity Stripline is the design approach considered by NSLS-II [9]. Its adapted model consists of bare strips (see Fig. 1a) placed inside a 1/15 linearly tapered cavity that reaches the 24 mm diameter vacuum chamber profile

* henrique.caiafa@lnls.br

ISBN 978-3-95450-176-2

on both ends. Another design type, the Capacitive Gap, which was inspired by SOLEIL stripline [10], consists of shrouded strips (see Fig. 1b) with 0.5 mm capacitive gaps at both ends and thus following the vacuum chamber profile. Based on these two approaches, a hybrid design was also simulated and considered for comparison. It consists of the Bare Strip transverse profile with the stripline ended by capacive gaps whose capacitance was set to keep the same as of the Capacitive Gap type. The chamber transitions follow the 24 mm diameter round profile in the vertical plane (limited by the 90° stripline aperture angle) but a 1/15 tapered transition, that finally reaches the vacuum chamber profile, is found in the horizontal plane.

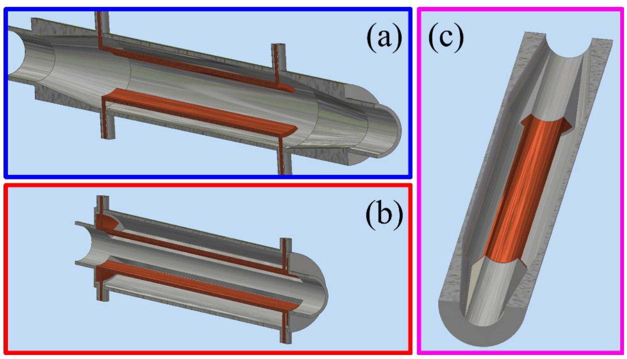

Figure 2: Analysed stripline approaches: a) Left half of the Tapered Cavity type. b) Right half of the Capacitive Gap type. c) Bottom half of the Hybrid type.

Figure 3 compares the real part of longitudinal beam impedance of the three discussed design approaches. The Tapered Cavity design shows higher broadband impedance than the other two geometries. Its lower frequency portion, below 17 GHz, is most impacted by the bare ends of the stripline, because the spectrum of the power sum signal of the feedthrough ports approximately matches the impedance within this frequency range. On the other hand, the energy lost by the beam caused by the tapered cavity shape, flows through the beam ports and impacts the high frequency part of the impedance [9]. One can also notice the gap capacitance effect for both Hybrid and Capacitive Gap geometries, where the feedthrough output signals start to be filtered out right above 500 MHz, although stronger HOMs are generated.

To allow further comparison, the geometric single-bunch (SB) and multi-bunch (MB) loss factors were evaluated for the simulated bunch length σ_s = 2.65 mm and the 3.8 mm length expected for Sirius Phase 1 [11]. Their values are shown in Table 1.

Table 1: Geometric SB and MB Loss Factor Comparison among Tapered Cavity, Capacitive Gap and Hybrid Stripline Types for Two Bunch Length Scenarios

Geometry type	**Geometric κ_{loss}, mV/pC**			
	σ_s = 2.65 mm		**σ_s = 3.8 mm**	
	SB	**MB**	**SB**	**MB**
Tapered Cavity	614.7	559.7	423.9	361.6
Capacitive Gap	74.9	43.2	48.5	21.8
Hybrid	131.2	75.3	84.9	40.6

Both SB and MB loss factors were evaluated from the impedance spectra presented in Fig. 3 through the Eqs. 3 and 4, respectively [12, 13]. For the later, a uniform filling pattern is considered.

$$\begin{aligned}\kappa_{loss}^{SB} &= \frac{\omega_0}{\pi}\sum_{p=1}^{\infty}\Re e Z_{\parallel}(p\omega_0)\mathrm{e}^{-(p\omega_0\sigma_s/c)^2} \\ &\simeq \frac{1}{\pi}\int_0^{\infty}\Re e Z_{\parallel}(\omega)\mathrm{e}^{-(\omega\sigma_s/c)^2}\,\mathrm{d}\omega\end{aligned} \tag{3}$$

$$\kappa_{loss}^{MB} = \frac{M\omega_0}{\pi}\sum_{p=1}^{\infty}\Re e Z_{\parallel}(pM\omega_0)\mathrm{e}^{-(pM\omega_0\sigma_s/c)^2} \tag{4}$$

where c is the speed of light, M = 864 is the harmonic number and ω_0 = 3.634 Mrad/s the revolution frequency of Sirius storage ring.

As can be seen in Table 1, all MB loss factors were smaller than the SB ones, since no strong HOM was sampled in the impedance spectra and local minima at RF frequency multiples (i.e., $pM\omega_0$) are found below 4 GHz. Despite having stronger HOMs and 16.5% lower shunt impedance due to the Shrouded Strip transverse profile, the Capacitive Gap geometry was preferred since its beam load is ~2 and ~15 times weaker than the Hybrid and Tapered Cavity types, respectively.

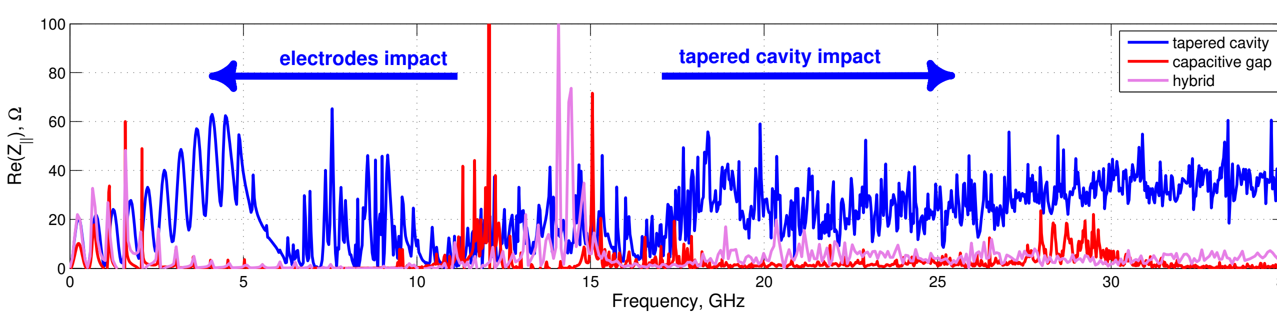

Figure 3: Real part of longitudinal beam impedance of the Tapered Cavity, Capacitive Gap and Hybrid stripline geometries.

ISBN 978-3-95450-176-2

CAPACITIVE GAP ALTERNATIVES

After selecting the Capaticitve Gap geometry type, the idea of studying alternative gap types was welcomed not only for increasing the gap capacitance, but also for allowing alternative mechanical solutions for expected thermal expansions. Therefore, besides the previously analysed Standard Gap type, three gap geometries were proposed: Sliding Gap, Upper Gap and Comb-type Gap, as shown in Fig. 4 below:

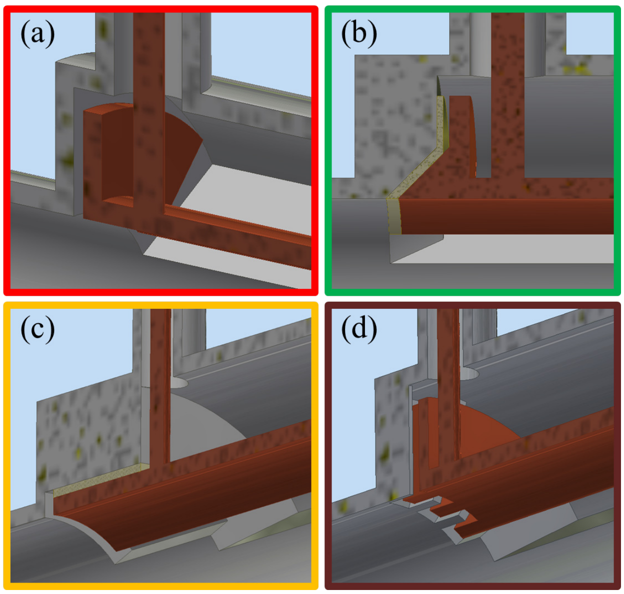

Figure 4: Considered capacitive gap types: a) Standard Gap b) Sliding Gap c) Upper Gap d) Comb-type Gap.

The previously analysed Standard Gap is a 0.5 mm gap transverse to the beam axis. For the Sliding Gap this size is 1 mm, filled by a 0.5 mm thick alumina insulator that lies in the 45° and 5 mm chamfered transverse wall of the cavity. Such slope turns any longitudinal expansion of the stripline into a transverse motion. The Upper Gap type contains a 20 mm length and 1 mm thick ceramic slit that touches the upper face of the stripline end, which has a 2 mm longitudinal clearance. Finally, as shown in Fig. 5, the Comb-type Gap, inspired by the RF shielding for KEK bellows and gate valves [14], consists of 5 mm length (a parameter) nested teeth whose parallel side faces are separated by a 0.5 mm gap b and the front faces by a longitudinal gap c of 2 mm. For Standard and Sliding Gap types as well, the plates, whose 10 mm height also follows d from Fig. 5, stay radially 2 mm away from the cavity wall.

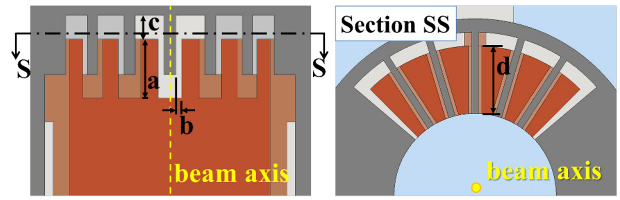

Figure 5: Comb-type Gap geometry parameters. Left: beam/bottom view. Right: Transverse cut (Section SS) view.

Figure 6 shows the real part of the longitudinal impedance of the four capacitive gap striplines and the correspondent SB and MB loss factors are found at Table 2. Due to the highest wake losses, the Upper Gap design was discarded. Among the remaining three, the Standard Gap type was the least desired as a gap size lower than 0.5 mm was not acceptable, considering the risk of short-circuiting the gap by thermal expansions and/or mechanical tolerances. Finally, since the Sliding Gap requires a complex three-dimensional ceramic slit due to the chamfer in the round edge cavity profile, the Comb-type was preferred even though its MB loss factor gets higher than the SB one. This occurs because three HOMs are sampled by RF multiples.

Table 2: Geometric SB and MB Loss Factors of the Standard, Sliding, Upper and Comb-type Gaps for Two Bunch Length Scenarios

Geometry type	Geometric κ_{loss}, mV/pC			
	σ_s = 2.65 mm		σ_s = 3.8 mm	
	SB	MB	SB	MB
Upper	202.0	185.5	94.7	79.5
Standard	74.9	43.2	48.5	21.8
Sliding	45.2	17.4	30.8	8.2
Comb-type	35.5	40.0	24.6	23.7

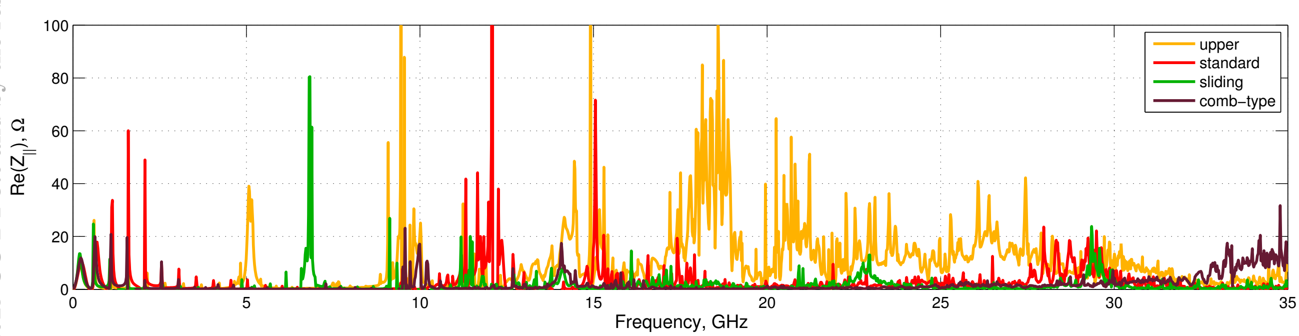

Figure 6: Comparison between the real part of longitudinal beam impedance of the Standard, Sliding, Upper and Comb-type Capacitive Gap striplines.

ISBN 978-3-95450-176-2

S1,1 OPTIMIZATION

For the the initial S-Parameter analysis, a pin holder was included, whose design, shown in Fig. 7, was proposed from the idea of allowing longitudinal offsets between the stripline and the pin through elastic deformation of its 0.3 mm thick slits, without stressing the feedtrough ceramic insulator. Although the holder was included in the simulation models, the feedthrough ceramic insulators were not considered since the use of commercial components is planned.

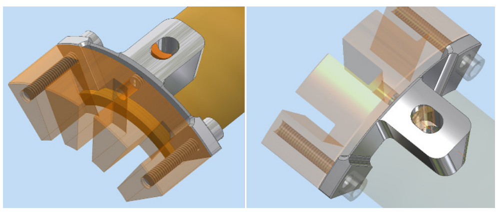

Figure 7: Mechanical design of the pin holder.

The first analysis have shown that the Comb-type gap capacitance was too high for a satisfactory reflection at the input coaxial port (S1,1) within the 250 MHz operation BW, showing a -12 dB (25%) maximum. A -16.5 dB (15%) goal was set to provide a good balance between signal distortion and wake losses, since reducing the mentioned capacitance increases the beam power outgoing the feedthroughs.

The S1,1 optimization shown in Fig. 8 can be separated into two stages. In the first one, a rectangular waveguide (WG), centered with the pin, was inserted between the coaxial line and the gap teeth in order to add an inductive component for compensating the gap capacitance, but was not enough for achieving the desired goal. In the second stage, as depicted by Fig. 9, two alternative geometries for reducing the the gap capacitace have been designed: Geometry 1 has the gap between teeth (*b* from Fig. 5) equal to 0.7 mm and the lateral gaps increased as much as possible; Geometry 2 has 4 teeth instead of 6 and kept the geometry parameters *a*–*d* to their original values. Both geometries have reached -16.4 dB maximum within the 250 MHz BW.

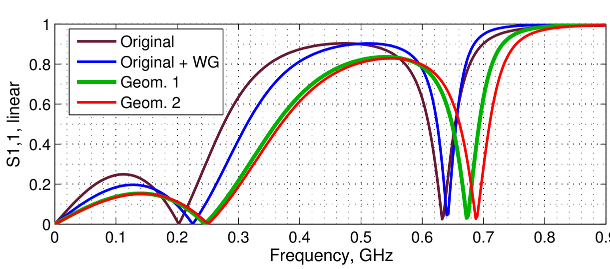

Figure 8: Optimization stages of the S1,1 parameter for the comb-type gap stripline.

Although good equivalence in the S1,1-parameters performance was found for both geometries, Geometry 2 was preferred as it drains lower beam load than Geometry 1. The SB and MB loss factors form the former were 55.15 mV/pC and 42.91 mV/pC, respectively, while the later achieved 29% and 84% higher corresponding values.

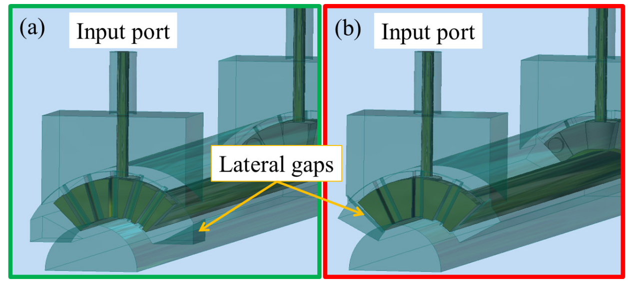

Figure 9: Vacuum profile of the geometry alternatives to reduce the gap capacitante: a) Geometry 1 b) Geometry 2.

TRANSVERSE SHUNT IMPEDANCE

The vertical coupling impedances for Geometry 2 and original Comb-type Gap design were simulated and their shunt impedances obtained by Eq. 2. In Fig. 10, the results are compared with the one calculated from Eqs. 1 and 2 and good agreement was found. The gap capacitance interferes with the shunt impedance frequency response by distorting the symmetry of the vertical impedance's fundamental mode.

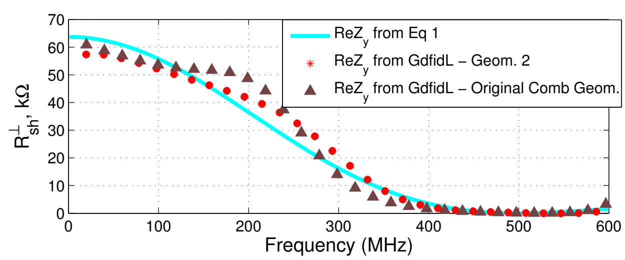

Figure 10: Vertical shunt impedance for Geometry 2 and original design, compared with the one from Eqs. 1 and 2.

THERMO-MECHANICAL ANALYSIS

The power dissipated in the structure by Joule effect can be obtained by two different approaches. The first is taking the difference between the resistive-wall $\kappa^{MB}_{loss,RW}$ and the geometric $\kappa^{MB}_{loss,geom}$ loss factors:

$$P_{loss} = \frac{2\pi}{M\omega_0}(\kappa^{MB}_{loss,RW} - \kappa^{MB}_{loss,geom})I^2_{av} \qquad (5)$$

where I_{av} is the beam average current. The second approach is subtracting the coaxial and beam ports output power from the $\kappa^{MB}_{loss,RW}$ total power loss alone [15]. In the following analysis the first method was employed, but both of them give similar results.

The difference between RW and geometric loss factors is 11.71 mV/pC for Geometry 2, considering 2.65 mm bunch length. Assuming 500 mA average current as a worst case scenario, Eq. 5 provides P_{loss} = 5.86 W. Twice this input power was considered and distributed, according to GdfidL result, among the geometry parts as shown by Table 3 in the thermal simulation model. Electrical conductivities for Copper and Stainless Steel were considered as 5.80×10^7 S/m and 1.43×10^6 S/m respectively.

ISBN 978-3-95450-176-2

Table 3: Power Loss Distribution among the Geometry Parts

Component	Material	Power %	Power, W
Cav. + end pipes	SS	33.17	3.888
Cavity ridges	SS	39.97	4.685
WG + outer coax.	SS	2.91	0.341
Stripline (SL)	Cu	8.57	1.004
SL teeth	Cu	1.48	0.173
Chamber Teeth	SS	10.85	1.271
Feedthrough pins	SS	1.04	0.122
Holder slits	SS	0.53	0.062
Holder–center	SS	1.01	0.118
Holder–sides	SS	0.47	0.055

Figure 11 depicts the mechanical design used in the thermo-mechanical simulation shown in Fig. 12. Two alumina insulators were considered: a tiny saddle-shaped ceramic spacer, to avoid short-circuiting the gap and a 5 mm thick washer in the feedthrough for holding its pin. Thermal analysis have shown the stripline center and the pin holder as the hottest spots, reaching temperatures up to 50°C and a 9°C gradient was found along the pin. Mechanical results provides only 20 μm longitudinal gap contraction and also shows that the holder was not optimized to avoid the pin bending. Even though the consequent von Misses equivalent stress over the ceramics feedthrough is 80 MPa, much below the ceramics breaking point, modifications in the geometry and material of the pin holder will be analysed in order to reduce the stresses at the feedthrough.

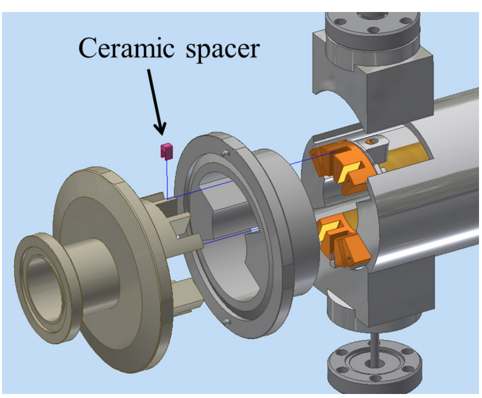

Figure 11: Mechanical design of the stripline kicker.

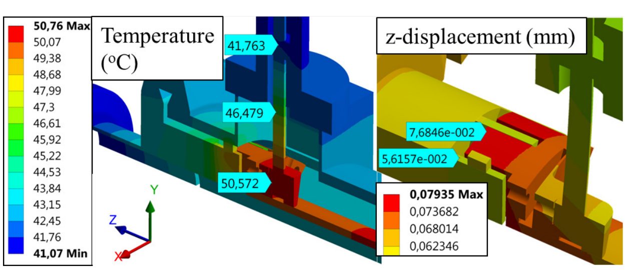

Figure 12: Thermal (left) and mechanical (right) simulation. On the later, 80× distortion magnification is shown.

CONCLUSION

The stripline kicker Comb-type gap stripline choice and its optimized Geometry 2 were shown by this work. The comb-type gap design have helped reducing wake heating in the components and beam load outgoing the feedthroughs. However, a HOM analysis in frequency domain is desirable for improving the accuracy of such wake heating evaluation. The first kicker prototype is scheduled for late this year.

ACKNOWLEDGMENT

The authors would like to thank not only Thiago M. Rocha (from LNLS Vacuum Group) for his tremendous support and execution of the mechanical design and thermal simulations, but also E. Plouviez, G. Rehm, A. Morgan and J.J. Sebek for the fruitful discussions. Last but not least, special thanks must go to SINAPAD [16] colleagues for the clusters infrastructure and their excellent technical support.

REFERENCES

[1] A.R.D. Rodriques et al., "Sirius Accelerators Status Report", TUPWA006, Proc. IPAC2015, May 2015.

[2] F.H. Sá et al., "Study of Collective Beam Instabilities for Sirius", TUPRI041, Proc. IPAC2014, June 2014.

[3] Dimtel, Inc., `http://www.dimtel.com`

[4] W. Bruns, GdfidL, `http://www.gdfidl.de`

[5] D. A. Goldberg and G. R. Lambertson, "Dynamic Devices – A Primer on Pickups and Kickers" LBL-31664, Nov. 1991.

[6] A. Blednykh et al., "Stripline Beam Impedance", WEPBA06, Proc. PAC2013, September 2014.

[7] M. Schedler et al., "A Broadband RF Stripline Kicker for Damping Transversal Multibunch Instabilities", MOPO003, Proc. IPAC2011, September 2011.

[8] M. Lonza, "Digital signal Processing – Multi-bunch feedback systems", CERN Accelerator School, May 2007.

[9] A. Blednykh, "Beam Impedance and Heating for Several Important NSLS-II Components", Mini-Workshop, DIAMOND, January, 2013.

[10] C. Mariette et al., "Excitation Stripline for SOLEIL Fast Transverse Feedback", WEPC16, Proc. DIPAC 2007, May 2007.

[11] L. Liu et al., "Update on Sirius, The New Brazilian Light Source", MOPRO048, Proc. IPAC2014, June 2014.

[12] B.W. Zotter and S.A. Kheifets, *Impedances and Wakes in High-Energy Particle Accelerators*, ISBN: 9810226268, World Scientific, Singapore (1997), pp. 98-99.

[13] M. Furman et al., "Energy Loss of Bunched Beams in SSC RF Cavities", SSC-116, Proc. PAC1987, March 1987.

[14] Y. Suetsugu et al., "Application of Comb-type RF-shield to Bellows Chambers and Gate Valves", RPPE052, Proc. PAC2005, May 2005.

[15] A. Morgan and G. Rehm, "Finding the Thermal Distribution of Wake Losses", Mini-Workshop, DIAMOND, January, 2013.

[16] SINAPAD, `https://www.lncc.br/sinapad/`

ISBN 978-3-95450-176-2

MULTIFUNCTION INSTRUMENT DESIGNS WITH LOW IMPEDANCE STRUCTURES FOR PROFILE, ENERGY, AND EMITTANCE MEASUREMENTS FOR LEReC AT BNL*

T. Miller†, M. Blaskiewicz, A. Fedotov, D. M. Gassner, D. Kayran, J. Kewisch, M. Minty, I. Pinayev, P. Thieberger, J. Tuozzolo, Collider-Accelerator Dept., BNL, Upton, NY, 11973, U.S.A.

Abstract

The low energy RHIC electron cooling (LEReC) upgrade project [1], being installed over the next two years will require a low impedance beam line so that the soft 1.6MeV electron beam will not be perturbed by induced electromagnetic fields, especially in the instrumentation chambers. Novel designs of the Profile Monitors, Emittance Slit Scanners and BPMs are presented along with Particle Studio simulations of the electron beam wake-field induced electric potentials. The design of a new instrument incorporating a button beam position monitor (BPM) and YAG screen profile monitor in the same measuring plane is presented as part of a method of measuring beam energy with an accuracy of 10^{-3}.

INTRODUCTION

In support of the Beam Energy Scan Phase-II physics program, in search of the QCD critical point and verification of several QCD models [2], a bunched beam electron cooler based on a SRF LINAC is being developed with operation planned for 2018-19. Effective cooling of the low energy Au ion beams below 20 GeV can be accomplished by co-propagating low energy electron beams of 1.6 – 5.0 MeV [2]. With the portion of this new electron machine sharing vacuum space with RHIC, an aggressive design and installation schedule has been set forth to allow the installation of the cooling section components, as shown in Fig. 1, during this year's 2015 shutdown. This has accelerated the design and fabrication of specialized beam instrumentation components for measurements such as profile, position, emittance, energy and energy spread. A key critical requirement of these components is that this instrumentation present minimal impedance to the electron beam; thereby minimizing the effects of longitudinal wake fields to preserve the strict requirements on intrabunch longitudinal beam energy spread An impedance budget of 5.0 V/pC has been set for the entire beamline. As a result, all beam line elements will be evaluated for their impact on this budget.

This low impedance requirement has necessitated the specialized design of the vacuum chambers within which YAG crystals are held for profile measurements, emittance slit masks are scanned for slice emittance measurements, and capacitive pick-up electrodes are mounted for position monitoring. These three chamber types, supporting instruments in the cooling section, were designed to minimize the rate of change of the beam transport aperture; thereby minimizing perturbations in the beam's wake field that can set up oscillating electromagnetic fields and in turn impacting the quality of the beam. Modeling in Particle Studio [3] has led to a refining of the chamber design resulting in a balance of lowest possible induced electric potentials within the chamber against a minimum compromise of the beam aperture to support insertion components and viewing ports.

Finally, the optimized profile monitor design was combined with a newly designed BPM chamber to produce a new hybrid device capable of using optical beam measurement techniques to calibrate integrated BPM pick-ups for better than 50µm absolute position accuracy. This high level of absolute accuracy is provided by the use of BPMs upstream and downstream of and in conjunction with the 180° dipole magnet between cooling sections to make absolute beam energy measurements to an accuracy of 10^{-3}.

Beam Parameters

The electron beam has a nested pulse structure, as previously illustrated [1], so that 120 ps bunches at 705MHz are grouped in macro bunches and positioned to overlap with the RHIC ion beam. These macro bunches (and ion bunches) are spaced at 9.1 MHz and grouped into a train of macro bunches. The train length is one turn around RHIC with a gap between consecutive trains that aligns with the RHIC abort gap. Other key parameters of the electron beam are listed in Table 1.

Table 1: Electron Beam Parameters in the Cooling Section

Parameter	Value
Energy	1.6 – 5 MeV
Bunch Charge	100 – 300 pC
Macro bunch Charge (γ_{ion} = 4.1–10.7)	3 – 5.4 nC
Average beam current	30 – 50 mA
Bunch / Macro bunch Rep Rates	704 / 9.1 MHz
Bunch Length	37 mm
Max. Allowable Energy Spread (Δp/p)	5×10^{-4}
Beam trans. size	σ = 3.84 mm

† tmiller@bnl.gov

*Work supported by Brookhaven Science Associates, LLC under Contract No. DE-AC02-98CH10886 with the U.S. DOE

ISBN 978-3-95450-176-2

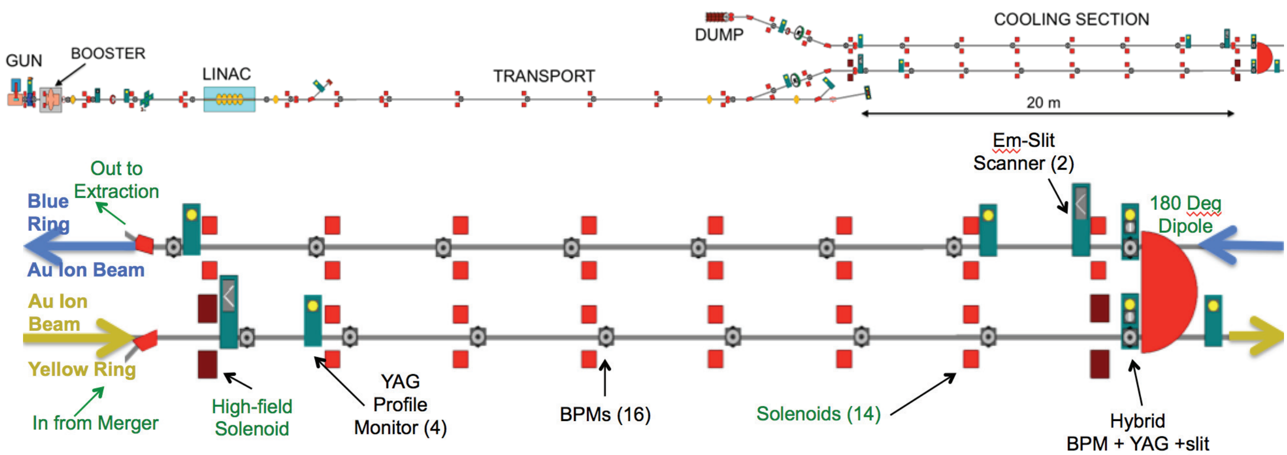

Figure 1: Overall layout of the LEReC machine (top) and the detail of the cooling section (bottom).

The macro bunch charge shown in Table 1 is not a constant. As the ion bunch length reduces when RHIC operation changes from $\gamma = 4.1$ to $\gamma = 10.7$, the number of bunches in the copropagating and overlapping macro bunch will be reduced from 30 to 18. In compensation, the charge per bunch will be increased from 100 pC to 300 pC. Note also that the beam transverse size in the cooling section has a full width of nearly 20 mm.

CHAMBER DEVELOPMENT

To meet the strict demand of low impedance to the electron beam, the typical use of a 6-way cube or cross as a vacuum chamber for instrumentation was abandoned. Starting from a cylindrical design, matching the 4.78" I.D. beam pipe, orthogonal ports were added to accommodate the insertion of detectors as well as viewports for imaging.

Profile Monitor

Requirements for profile measurements in the LEReC cooling section ask for a relaxed resolution of 10% of the beam size (23 mm at 3σ or 99% full width in the cooling section) on a screen measuring 45 mm in diameter in order to make profile measurements at the beginning and end of each of the two cooling sections. The design started with four typical YAG crystal based profile monitors with two-position actuators, placed at each end of each of the two cooling sections as shown in Fig. 1. These units are being designed and built in-house in order to meet an aggressive project schedule and to cope with the demand of presenting low impedance to the electron beam. Both the actuator and optics view ports were kept as small and short as possible to accommodate the YAG-mirror holder assembly and allow imaging & illumination through the optics port.

The YAG-mirror assembly holds a 0.1 × 50 mm YAG crystal with a 100 nm Al-coating and is optimized for an aperture of 45 mm. The YAG crystal is held normal to the beam and therefore is imaged through a polished copper mirror held at 45° just behind the crystal. Fig. 2 shows the assembly model.

The large aperture introduced by the actuator port was shown, by simulation of wake filed induced electric potentials in its vacuum chamber and on the in-vacuum components using Particle Studio code, to have peak values that were higher than desired. Thus, a NiZn ferrite absorbing block, type CMD5005, was selected and designed to have a surface area of 23.42 in^2 and volume of 4.83 in^3 and positioned in the actuator port.

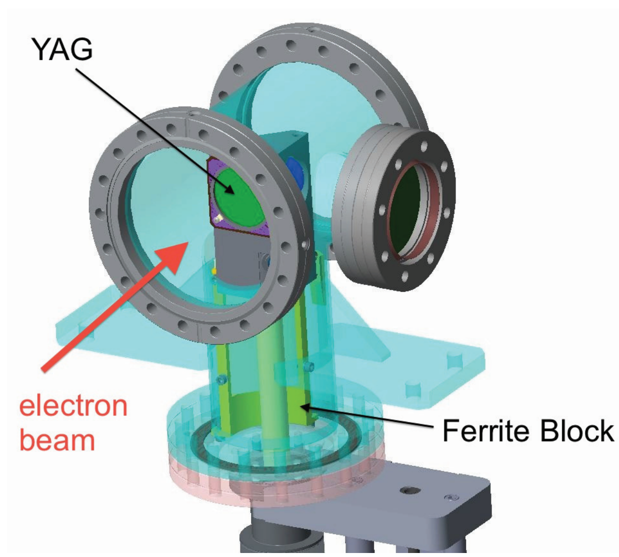

Figure 2: Model of the profile monitor with ferrite absorber, actuator not shown.

Emittance Slit Scanner

Requirements for emittance measurements in the LEReC cooling section demand a measurement with better than 10% error at the beginning of each of the two cooling sections. Although a 2mm thick Tungsten mask was chosen for its low penetration depth of the 1.6 – 5 MeV electrons and mechanical rigidity, the 150 μm wide slits at this plate thickness will cause an aperture reduction of > 23 %/degree of misalignment error. Considering a thinner plate, compensation for the "detour factor," [4] where electrons follow zigzag path through the material (exceeding the penetration depth), would

ISBN 978-3-95450-176-2

suggest a mask thickness of 1.0 mm in order to stop the electrons. However, simulations previously reported [5] made with beams energetic enough to penetrate a pepper pot mask showed negligible blurring of the resultant image because the degraded electrons that pass through the plate are so widely scattered over a large angular range that the background they generate is very small. Therefore, we are considering milling a ~5 mm wide area along the slits down to a thickness of 300 – 500 μm, thereby reducing the aperture reduction factor down to under 6 %/degree. Thus design calls for a 1° alignment error during installation and must be held to within a rotational tolerance of 5 mrad during operation to hold the effective slit width constant.

In order to provide both horizontal and vertical slice emittance measurements at each location, two dual slit stepper-motor-driven mask scanners were designed with similar constraints on their vacuum chambers. Although only an actuator port is necessary from which to insert the large tungsten plate-mask, the length of the plate required to support both horizontal and vertical slits on a single 45° scan axis exceeded the chamber diameter; thereby requiring an opposing port to receive the over-travel of the mask during a scan. Since only the thin mask need be inserted into the beam aperture, the chamber walls remain contiguous with the exception of two opposing narrow slits through which the mask travels. This relieved much of the effect of the aperture otherwise created by the 2.56” I.D. actuator and over-travel ports accommodating the 2” wide orthogonal-slit mask. Figure 3 shows the assembly model. Figure 4 shows the slit mask in four key positions through a scan over the horizontal and vertical slits with an overlay of the beam spot.

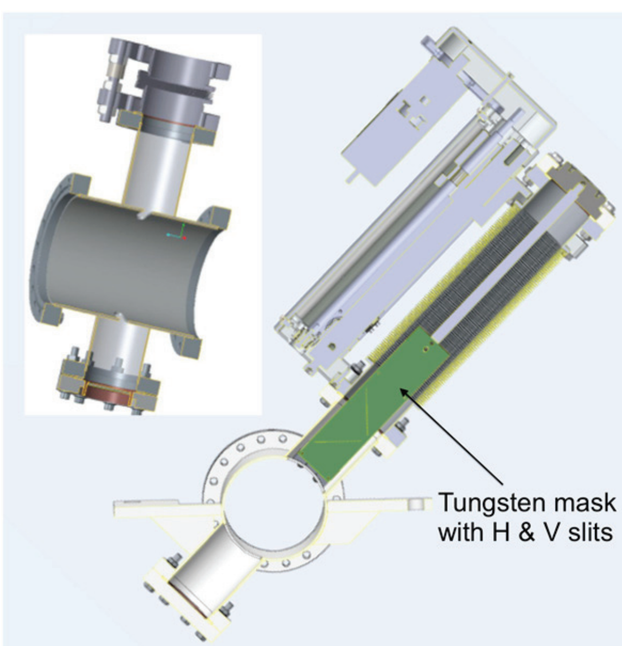

Figure 3: Cut-away model of the emittance slit scanner and cut-away view of the chamber.

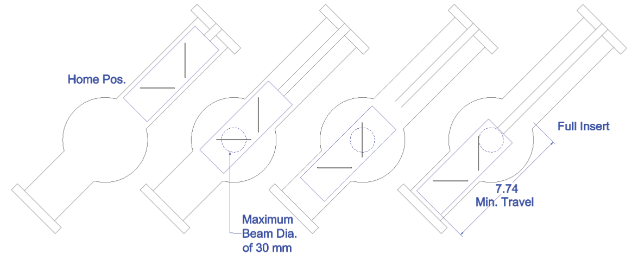

Figure 4: Detail of the emittance slit mask in its key positions along the scan with the beam spot shown.

MODEL SIMULAITON

Although the mechanical models of the profile monitors and emittance slit scanners were made with best efforts to reduce the impact on beam loading, an iterative refining process of numerical simulation of the wake-field induced electric potentials by a short bunched packet of charge followed by adjustments to the mechanical design in an effort to arrive at a final design with as low a wake potential as possible.

To do this, simplified 3-D models of the chambers were made to run in a Particle Studio simulation with a representative electron bunch passing through the chamber. The induced electric potentials were plotted to express the impedance vs. frequency as well as wake potential per beam charge as a function of distance behind the bunch.

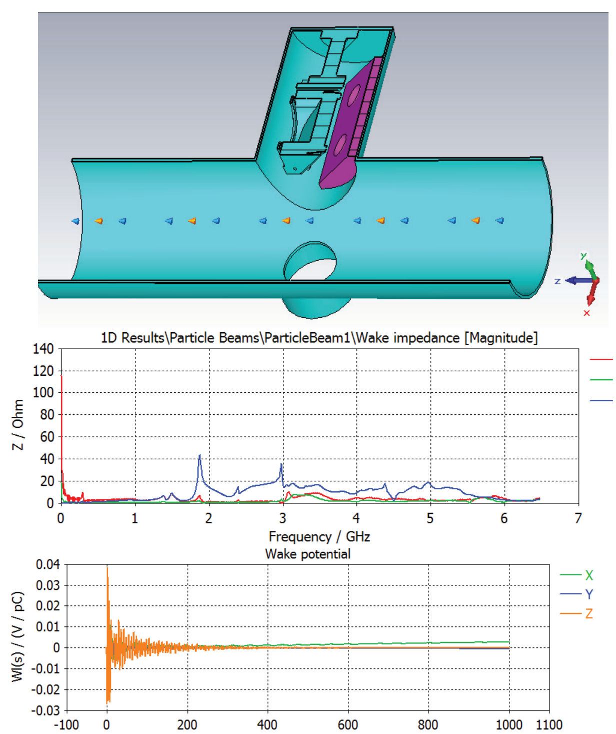

Figure 5: a) Simulation model for profile monitor with b) resulting impedance and c) wake potential plots.

ISBN 978-3-95450-176-2

The latter is used to confirm that the ringing electromagnetic fields in the chamber dampen before the next beam bunch arrives. Figure 5 shows the simplified version of the model used in the simulation for the profile monitor with the beam path indicated, along with the resulting impedance vs. frequency spectrum and the wake potential plot vs. trailing distance. As the preliminary design of the emittance slit scanner chamber contained a minimally intrusive opening for only the mask to protrude, no design modifications resulted from the simulations.

In order to determine how low the wake induced potential must be; all beam line devices are being analyzed and tabulated to ensure that the 5.0 V/pC budget is not compromised. Table 2 summarizes the potentials of various beamline components found from Particle Studio simulation ran with 300 pC bunches, 1.5 cm_{rms} long. Thus far, efforts have been concentrated on devices in the cooling section. Some of the devices remaining to be analyzed include the 180° dipole chamber, various Y-chambers, "Flying Wire" profile monitors, RF cavities, and transport section BPMs. Analysis of the Conflat® flanges where the copper gasket I.D. is larger than the beam pipe I.D. must be analyzed as well since the resulting tiny cavities can also "ring."

Table 2: Device Wake Loss Factor

Device	(V/pC)
Cooling Section Profile Monitor	2.33×10^{-2}
Cooling Section Emittance Slit Scanner	1.68×10^{-2}
Cooling Section BPM	5.30×10^{-3}
Welded Bellows	9.07×10^{-2}
Formed Bellows	3.00×10^{-2}
40cm of 4.78" ID beam pipe	5.70×10^{-4}
Hybrid BPM+Profile Monitor+Slit	6.28×10^{-2}

Grounding

Another effect of wake-field induced potentials by the short bunched electron beam are those induced on the YAG crystal and its holder as well as on the large surface of the tungsten emittance slit mask. These voltages can set up large "ringing" "L-C" oscillations on these elements that can be significant enough to distort the electron beam; thereby corrupting the attempted measurement.

Models of the instruments were made for simulation with their in-vacuum elements in the retracted position to aid in the design of the cavity. Simulations were also made of the instruments with their in-vacuum elements in the inserted position. This provided insight into the magnitude of the induced voltages on the elements that interact directly with the beam. The determination was made that local grounding connections were necessary to shunt the wake-filed current to mitigate these ringing electromagnetic fields.

Parallel design efforts continue for the inclusion of a sliding electrical contact within the actuator port of the vacuum chamber to electrically ground the in-vacuum element, as shown in Fig. 6. Simulations will be run with and without this ground connection to determine its effectiveness.

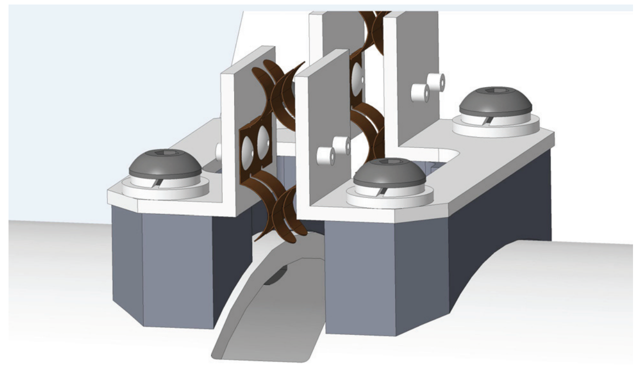

Figure 6: Sliding ground contact in emittance slit scanner mounted over entrant slot (mask removed).

POWER & EXPOSURE CALCULATIONS

Profile Monitor

Tests were made at the electron lens (eLens) test bench at BNL in 2012 [6] with YAG crystals used to image a 5keV, 5 mm (FWHM) Gaussian electron beam. Results showed a linear response of the crystal without saturation under beam pulses up to 40 µs long at up to 500 mA. Although this is under investigation in order to scale the results to fit the LEReC beam parameters, the tests were made with single shots and thus don't contain the steady state temperature effects needed for scaling. The approach will be to determine a maximum local temperature rise at the beam spot on the YAG crystal above which the response of the YAG begins to degrade, resulting in a flattening of the Gaussian profile. This ΔT limit will then be used to find an exposure limit to the LEReC beam at maximum charge and repetition rate. Saturation mechanisms other than those due to heating are being explored. If these other mechanisms can be neglected, then the resulting ΔT limit will then be applied to the profile monitor located in the merger section of the LEReC beam line where the beam size is the smallest with $\sigma = 0.3$ mm. A limit for the cooling section profile monitors, where the beam $\sigma = 3.84$ mm, will scale with σ^2, thus allowing many more macro bunches resulting in a longer exposure time in the cooling section.

With this approach of using the eLens test bench results, estimates will be conservative because the minimum beam spot considered is much smaller than that of the beam on the test bench, thus allowing heat conduction to play a more significant role, where the temperature gradients will be larger. These estimates may be made even more conservative by improving radiative

ISBN 978-3-95450-176-2

cooling of the crystal by applying a thin carbon coating on top of the aluminum coating on the YAG crystals.

Emittance Slit Scanner

The emittance slit mask and support assembly is intended to safely absorb 10 W of average power from the electron beam on the mask with a mask $\Delta T < 200$ °C without the need for water-cooling inside the vacuum chamber, based on a 1 minute exposure to 10 W of average beam power, allowing a 5 minute cool down period between exposures with a maximum of 5 exposures per hour.

The slit is scanned over the entire beam diameter in 0.5 mm steps. The measurement rate is limited by the 1-second image capture rate of the associated Profile Monitor. Thus to scan the largest beam diameter of 30 mm, in 0.5 mm steps, a scan time of 60 seconds is required. As this mask contains two slits for both horizontal and vertical scan data, the mask is planned to endure two consecutive 60-second scans.

Equation 1 gives the exposure time (T) corresponding to the 10 W limit, based on the beam energy and macro bunch charge & frequency

$$\mathrm{T} = \frac{P \cdot t}{V} \cdot \frac{1}{Q_{MB} \cdot f} \quad (1)$$

where P = 10 W average power, V = 5 MeV max. beam energy, t = 1 s repetition rate, Q_{MB} = 5.4 nC max. charge per macro bunch (18 × 300 pC = 5.4 nC [2]) and f = 9.1 MHz macro bunch repetition rate. This results in a total charge of 2000 nC each second, distributed over 370 macro bunches, for an exposure time of 40 µs per pulse train per second; thereby limiting the beam power to under 10 W.

HYBRID DESIGN

Absolute Energy Measurement

In order to support an absolute beam energy measurement with an accuracy of 10^{-3}, two BPMs will be used with the 180° dipole magnet in the cooling section as a spectrometer. The beam entry and exit points in the dipole are separated by 700 mm. Hence, an accuracy of position measurement to better than 700 µm is required from the BPMs to guarantee the 10^{-3} energy measurement accuracy. In order to provide a real time calibration of these two BPMs, a YAG screen profile monitor is inserted into the BPM chamber in the same X-Y plane as the BPM buttons. To accommodate the actuator port for the YAG screen, one plane of buttons was eliminated, leaving only the horizontal sensing plane of the BPM. These BPMs shall only be used for horizontal position measurement in the spectrometer arrangement. Therefore, the optics viewport opposes the actuator, requiring a special design of the YAG and mirror holder, as shown in Fig. 7

A Particle Studio simulation was run on this model and found that a ferrite absorber was needed to reduce the wake-field induced oscillations in the extracted position. Moreover, a grounding contact was added to mitigate large oscillations on the structure from the effects of the 704 MHz and 9 MHz beam structures. A ferrite ring was chosen to fit into the optics port due to limited space in the design.

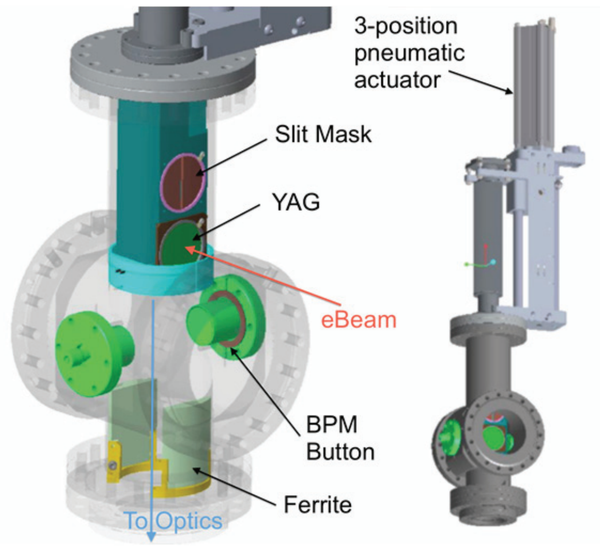

Figure 7: left: Hybrid BPM + Profile Monitor + Slit Mask, shown in the extracted position; right: transparent view of chamber only, full assembly view.

Energy Spread Measurement

An energy-spread measurement is required with a resolution of better than 10% of the maximum Δp/p of $5{\times}10^{-4}$. To perform this measurement in the cooling section, the 180° dipole magnet is used in conjunction with the two new Hybrid monitors to measure the horizontal dispersion due to energy spread. The Hybrid monitors are equipped with a 3-position actuator such that a vertical slit can be inserted at the station upstream of the dipole (#1). There is a standard profile monitor down stream (or behind) the dipole (#2) that will image the beam through the slit with the dipole turned off, giving a measurement of initial condition. With the dipole turned on, the beam will propagate around the dipole bend radius to the downstream Hybrid monitor (#3) where its profile will be imaged by the YAG screen. The path length between monitors #'s 1 – 2 and 1 – 3 are equivalent.

The solenoid just upstream of the dipole is a high field solenoid that will be used to focus the beam to a minimum at the Hybrid monitor (#3). Simulations using Parmela, not accounting for the use of the slit, predicts an increase of the horizontal beam size from 0.71 –1.30 mm (rms). This difference of 590 µm on the 45 mm YAG screen using a 2MP CCD camera will be resolved over 13 pixels, providing a 7.6% resolution measurement. This will require optics with better than 40 µm resolution (limited only by pixel resolution).

ISBN 978-3-95450-176-2

BPM Calibration Procedure

Relying on mechanical survey data of fiducial points on the profile monitor, an accurate absolute position of the YAG crystal can be known. Four optical features on the YAG holder (whose positions are fixed to the survey data) can be imaged along with a beam profile, as shown in the simulated representation in Fig. 8. The center of gravity (CoG) calculation of the beam center is compared in position to the center of the reference circle drawn through the optical features. The two resulting X and Y offset values are then fed into the BPM data processing as offsets from actual center. The expected resolution of the profile monitors at this low energy is 50 – 100 μm. This should be sufficient to support the calibration of the BPM with the required accuracy of 700 μm.

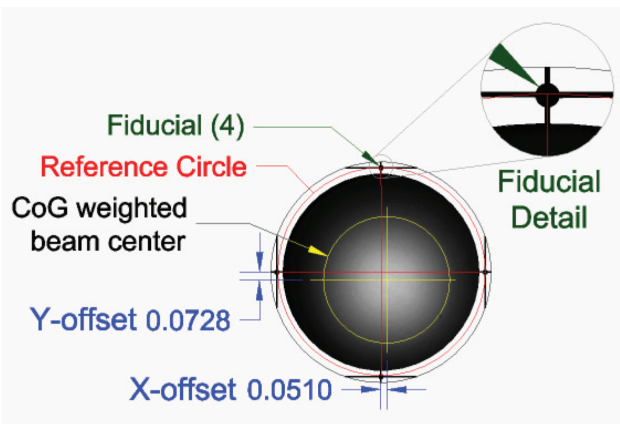

Figure 8: Hybrid BPM + Profile Monitor + Slit Mask simulated calibration procedure (4 fiducials, reference circle, example beam image with center, and X-Y offsets.)

STATUS AND CONCLUSION

The design of the Profile Monitors, Emittance Slit Scanner and Hybrid Unit were tailored to minimize the impedance of these three new instruments for LEReC in order to preserve the quality of its "soft" low energy electron beam. The large beam diameter in the cooling section has necessitated a large aperture YAG crystal and hence required large ports into the chamber, requiring damping with ferrite absorbers.

The tight requirement for absolute position measurement near the 180° dipole magnet for energy measurements has led to a novel hybrid design incorporating a combination of three typical instruments. Although the mechanical design has been relatively straight forward, the challenge to design suitable optics in order to achieve the required optical resolution is a challenge that awaits completion.

The chamber and in-vacuum elements of the profile monitors and emittance slit scanners were designed in-house and are being fabricated on site; while the actuators were outsourced with custom specifications. The design of the hybrid BPM+PM was made in-house and the in-vacuum elements will be fabricated on site; while the fabrication of the vacuum chamber and actuator will be out sourced. The goal is to install the total of eight devices before the RHIC start-up in January 2016.

Ongoing work includes continued beam component modeling to completely account for wake field potential factors throughout the entire beam line and ensure the budget of 5.0 V/pC is not exceeded. Other work includes the design of the profile monitor optics as well as the fabrication, testing and installation of the component vacuum chambers and in-vacuum components by the end of the year.

ACKNOWLEDGEMENTS

The authors would like to acknowledge the contributions of C. Liu, T. Shaftan, D. Weiss, and other members of the Accelerator R&D Division, as well as M. Fedurin and M. Babzien from the BNL Accelerator Test Facility, as well as members of the Accelerator Components & Instrumentation Group, especially A. Curcio, L. DeSanto, and A. Weston, as well as members of the design room, especially V. De Monte, G. Whitbeck and K. Hamdi.

REFERENCES

[1] D. Gassner et al, " Instrumentation for the Proposed Low Energy RHIC Electron Cooling Project ", IBIC2013, Oxford, UK, TUPF24
[2] A. Fedotov et al., "Bunched Beam Electron Cooler for Low-Energy RHIC Operation", PAC2013, TUOAA1, http://jacow.org
[3] Particle Studio Simulation Software https://www.cst.com/products/cstps
[4] T. Tabata, et al. Nuclear Instruments and Methods in Physics Research, Section B, "Beam Interactions with Materials and Atoms"; v. 119(4)
[5] J. G. Power, "Slit Scattering Effects in a Well Aligned Pepper Pot", Proceedings from PAC 2003
[6] X. Gu et al, "The E-Lens Test Bench for RHIC Beam- Beam Compensation", Proceedings of IPAC 2012, New Orleans, LA, USA, WEPPD084

BEAM DIAGNOSTICS OF THE LIPAC INJECTOR WITH A FOCUS ON THE ALGORITHM DEVELOPED FOR EMITTANCE DATA ANALYSIS OF HIGH BACKGROUND INCLUDING SPECIES FRACTION CALCULATION

B. Bolzon#, N. Chauvin, S. Chel, R. Gobin, F. Senée, M. Valette, CEA, Gif-sur-Yvette, France
K. Shinto, JAEA, Rokkasho Fusion Institute, Rokkasho, Japan
J. Knaster, Y. Okumura, IFMIF/EVEDA Project Team, Rokkasho, Japan

Abstract

To prove the technical feasibility of the IFMIF accelerators concept, the EVEDA phase will commission in Japan the LIPAC accelerator, which will deliver a 125 mA/9 MeV CW deuteron beam. LEDA already managed 100 mA in CW at 6.7 MeV in 2000. The different subsystems of LIPAC have been designed and constructed mainly by European labs with the injector developed by CEA-Saclay. This injector must deliver a 140 mA/100 keV CW deuteron beam at 99% D^+ ratio, which is produced by a 2.45 GHz ECR ion source. The low energy beam transport line (LEBT) is based on a dual solenoid focusing system to transport the beam and to match it into the RFQ. The normalized RMS target emittance at the RFQ entrance is targeted to be within 0.25π mm·mrad. This article describes the diagnostics installed in the LEBT to measure beam parameters such as intensity, profile, emittance, species fraction and degree of space charge compensation. The article also focuses on the algorithm developed to analyze emittance data of high background from an Allison scanner. Species fractions (D^+, D_2^+, D_3^+) using mass separation technique were also calculated during the on-going commissioning campaign with the Allison scanner installed between the two solenoids in a first stage.

INTRODUCTION

The IFMIF project (International Fusion Materials Irradiation Facility) will generate a neutron flux of 10^{18} $m^{-2}s^{-1}$ with a broad energy peak at 14 MeV in order to characterize and study candidate materials for future fusion reactors. To reach such a challenging goal, two parallel deuteron accelerators of 5 MW each will deliver a high intensity D^+ beam of 2 x 125 mA CW (Continous Wave) at 40 MeV against a liquid lithium target [1]. In the present final phase before construction, called EVEDA (Engineering Validation and Engineering Design Activities), a 125 mA/9 MeV CW deuteron demonstrator accelerator called LIPAc (Linear IFMIF Prototype Accelerator) is being assembled, commissioned and will be operated in Rokkasho [2, 3]. LIPAc has been designed and constructed mainly in European labs with participation of JAEA in the RFQ couplers. It is composed of a deuton injector delivered by CEA-Saclay [4], a Radio Frequency Quadrupole (RFQ) [5] to be delivered by INFN, eight superconducting half-wave resonators (SRF Linac) designed by CEA-Saclay [6], Medium and High energy beam transfer lines and a beam dump designed by CIEMAT.

The injector is composed of a 2.45 GHz ECR ion source based on the CEA-Saclay SILHI source design [7] and a LEBT line that will transport and match the beam into the RFQ. After acceptance tests performed at CEA-Saclay [8, 9], it has been shipped to Japan in 2013 and is currently under commissioning in Rokkasho [10, 11]. According to requirements, the D^+ beam injected into the RFQ must be 140 mA/100 keV CW with a normalized RMS emittance lower than 0.30π mm·mrad (with a target value of 0.25π mm·mrad). Under these conditions, simulations demonstrated that the deuteron beam can be accelerated to 5 MeV by the RFQ with less than 10% losses in order to reach the specified 125 mA CW. This paper details the different beam diagnostics available in the LEBT, not only during this commissioning phase, but also during operation. A particular focus is made on the validation of the algorithm developed to analyze data of high background from an Allison scanner in order to compute emittance and determine species fraction ratio (D^+, D_2^+, D_3^+) extracted from the ion source.

BEAM DIAGNOSTICS IN THE LEBT

The LEBT consists of an accelerator column (containing the ion source extraction system), two solenoids with integrated H/V steerers, a diagnostic box located between the solenoids and an injection cone located just upstream the RFQ. During the injector commissioning, a specific diagnostic box, equipped with a beam stopper designed to handle a 15 kW beam, is placed after the injection cone. To minimize the emittance growth driven by the high beam space charge, the LEBT length has been minimized to 2.05 m from the plasma electrode to the internal face of the RFQ entrance. In such a short line and due to the radiation environment induced by the D-D fusion reactions from beam losses and deuterium adsorbed in the beam pipe walls, only few diagnostics can be installed: Charge Injection Device (CID) cameras, a deported spectrometer beyond the shielding walls via a radiation hardened optical fiber, an Allison scanner, a Four Grid Analyser, an ACCT and a movable beam stopper have been selected to characterize the beam during commissioning and operation.

A 3D view of the LIPAc injector with its dedicated beam diagnostics is shown on Fig. 1.

#benoit.bolzon@cea.fr

ISBN 978-3-95450-176-2

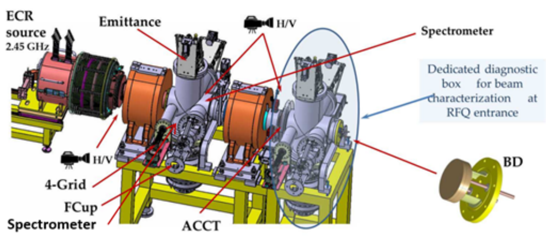

Figure 1: Scheme of the LIPAc injector with its dedicated beam diagnostics.

Beam Current Measurement

The total current extracted from the ECR source (including D^+, D_2^+ and D_3^+ ion species) is provided with an error of a few percent by the output current flow of the main high-voltage power supply. The beam current can also be estimated between the two solenoids thanks to a movable beam stopper which is initially used to protect the valve isolating the LEBT vacuum from the rest of the system (for space optimization reasons, the sector valve is placed between both solenoids). At the end of the LEBT, the beam current can be measured with an ACCT (AC Current Transformer) located at the end of the injection cone and with the beam stopper located inside the diagnostic box. The ACCT, capable of measuring pulsed beams above few microseconds, will allow estimating the current transmission of the RFQ by comparison with another ACCT located at the beginning of the MEBT. A DCCT (DC Current Transformer) would have obviously been preferable for CW operation but space constrains, driven by space charge induced emittance growth, were in place.

Improvement of Beam Stoppers Measurements

In high intensity and low energy beam lines, the interaction of charged particles with a beam stopper (metallic surface) induces the production of secondary electrons (from few tens of eV to 100 eV) and overestimations of the beam current measurements can take place (see Fig. 2). This potential difficulty has been partly solved in LIPAc injector by an auto-polarization of the beam stopper; however, this polarization induces the attraction of electrons which are trapped into the beam (in turn, allowing the space charge compensation) and of secondary electrons emitted by the beam losses hitting the beam pipe. In these cases, the real current is underestimated unavoidably given the subtracting contribution of the electrons in the measurement values.

A study of a dipolar magnetic system is planned to be done in order to remove the contribution of secondary electrons on the current measurements. Two solutions can be considered: 1) a dynamic and adjustable dipole or 2) a static dipole by means of a permanent magnet, which is perceived as simpler and substantially cheaper. In the case of the movable beam stopper, the permanent magnets may slightly deflect the primary beam when the equipment would be pulled out; at the same time, the power supply of a dynamic dipole can be cut off when the beam stopper is pulled out. A static dipole can thus be considered for the beam stopper installed at the end of the LEBT, while a dynamic dipole has to be designed for the movable beam stopper installed between the two solenoids.

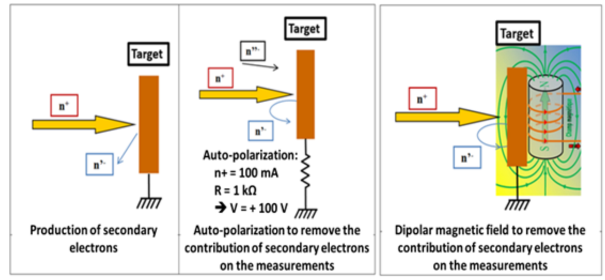

Figure 2: Suppression of the contribution of secondary electrons on current measurements with a beam stopper.

Optical Beam Diagnostics

In the LEBT of LIPAc, optical diagnostics based on the fluorescence of residual gas are used to characterize the high intensity ion beam [12, 13]. These devices are radiation hardened since high neutron and gamma rays flux are emitted when operating the LEBT with deuterons; in that case, even activation of materials will take place [9].

Four CID cameras (radiation hardness up to ~30 kGy), known to be more resistant to radiation than more usual Coupled Charge Device (CCD) cameras, have been installed perpendicularly to the beam direction in the LEBT in order to measure both horizontal and vertical profiles at two different locations. Their resolution and sensitivity to light are low and the beam profile cannot be clearly observed when the beam is lightly focused (see Fig. 3 showing typical pictures of CID cameras beam profiles). CCD cameras will be thus installed close to the emittance meter to provide a clear image of the beam in any experimental condition. They will be used during the commissioning phase with proton operation, whose radiation and induced activation at 100 keV is negligible.

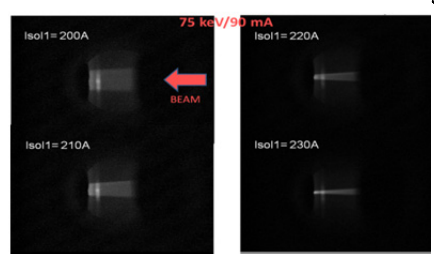

Figure 3: Deuteron beam profiles measured with CID cameras for different coil currents of the 1st solenoid.

The analysis of ion species fraction (such as D^+, D_2^+ and D_3^+) is done by the Doppler Shift technique between the two solenoids of the LEBT, by means of a CDD camera installed with 20° angle to the focal plane of a monochromator. The weak radiation hardness of these devices is overcome with a 20 m long Fujikura radiation hard fiberscope to transport the fluorescence light from the vault to the monochromator located outside the accelerator vault. This last one is set to the wavelength of the D_α Balmer series (± 40 nm) to isolate the fluorescence coming only from the interaction of the beam with the

ISBN 978-3-95450-176-2

residual gas. Species fraction (spectroscopy), species fraction beam profile (imaging) and source impurities can then be analysed. Results of measurements from the commissioning at Rokkasho are reported elsewhere [11, 14].

Measurement of Space Charge Compensation

The high space charge of LIPAc, due to the low energy and high intensity beam, can be partially compensated in the LEBT when the beam interacts with the residual gas of D_2 [15, 16]. A Four Grid Analyser has been installed in the first diagnostic chamber of the LEBT in order to perform measurements of the beam potential well of the compensated beam, and to calculate the degree of space charge compensation. Either secondary electrons or D_2^+ ions can be analysed. The experimental space charge compensation values found using such a device for the 75 keV, 130 mA proton beam of the LEDA injector range from 95% to 99% [17]. It has been theoretically [18] and experimentally [19, 20, 21] observed that the beam emittance can be improved by injecting some heavy gas in the beam line, and that this improvement depends strongly on the gas species. During deuteron operation at Rokkasho, measurements of space charge compensation and of beam emittance have been performed with and without Krypton gas injected inside the LEBT [11].

EMITTANCE DATA ANALYSIS

Emittance Measurement Unit (EMU) that is used for the LIPAC injector is an Allison scanner [22] which can be installed either on the first or second diagnostic box. Its design has been optimized to sustain 15 kW of beam power in CW and for a critical beam diameter of 30 mm. It allows reconstituting the beam projection in the vertical plane of phase space. Emittance measurements are performed during the commissioning between the two solenoids to characterize the beam as close as possible to the source, and after the injection cone to characterize the beam at the entrance of the RFQ. Plans to measure the emittance in a third phase at the exit of the accelerator column are being discussed, but possibly are not needed if thorough understanding is being achieved during the last quarter of 2015.

The ECR source produces not only D^+ but also D_2^+ and D_3^+ molecular ions, with D^+ fraction ratio which should be of at least 80% with a suitable optimization of the source parameters. The extraction system has thus been optimized to extract a total beam current from 150 mA to 175 mA in order to be able to reach the required D^+ current of 140 mA at the energy of 100 keV at the RFQ entrance. A ϕ12 mm cone shaped with an angle equal to the D^+ beam theoretical convergence (half-angle of 8°) is installed just upstream the RFQ injection to stop the undesired particles, mainly D_2^+ and D_3^+.

During the first stage of the commissioning phase, the Allison scanner has been installed between the two solenoids and the three species are thus still significantly present. Figure 4 shows raw data from the Allison scanner for a deuteron beam of 91 mA/100 keV and in CW operation.

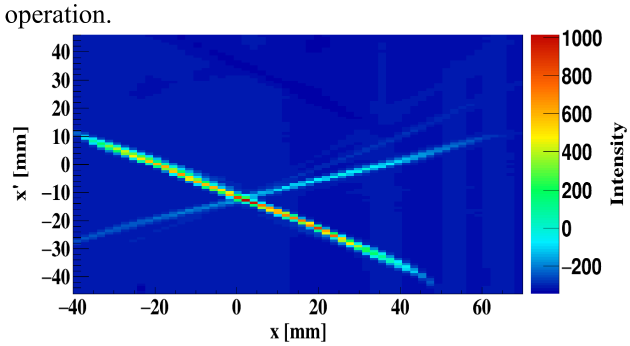

Figure 4: Raw data from the Allison scanner for a deuteron beam of 91 mA/100 keV and CW operation.

The two solenoid coil currents were set to maximize the beam transmission to the RFQ injection cone in order to be in the same condition than for the operation of the whole LIPAc. D^+ ion species are in this case convergent, as it can be observed on Fig. 4. D_2^+ and D_3^+ ion species diverge due to their higher magnetic rigidity and the three species are mixed on the beam axis (X-position = 0 mm). A high and non-homogeneous background is present in the data as described later in the article. In order to calculate the emittance of the desired species (i.e. D^+), D^+ spectrum needs to be isolated and the different steps are described below to perform this task automatically:

- Detection and removal of the background
- Detection and isolation of D^+, D_2^+, D_3^+ spectra
- In the area where the three species are mixed, interpolation of D_2^+ and D_3^+ spectra
- Subtraction of this interpolation to D^+ spectrum

Species fraction ratio can moreover be obtained by calculating the integrated intensity of each isolated species. An algorithm has been developed to perform these different steps automatically. The emittance and the D^+ fraction ratio can thus be obtained on-line for the beam tuning. Results of species fraction ratio measured with the Allison Scanner and the deported spectrometer have been compared [14].

Background Detection

The algorithm is written in Python [23] using ROOT [24] libraries (pyROOT). For background detection, the function member “Background” of the class “TSpectrum” of ROOT is used. It allows separating useless spectrum information (continuous background) from peaks, based on Sensitive Nonlinear Iterative Peak Clipping Algorithm [25, 26]. This function performs one-dimensional background estimation and it is used to detect background for each X-position of the Allison Scanner, i.e. for each abscissa of the emittance histograms. Its input parameters are optimized in order to remove only background and not real signal. Figure 5 shows a typical background detected by “TSpectrum” from the raw data shown on Fig. 4. A negative signal which seems to be homothetic to the beam can be clearly seen, probably due to secondary electrons produced inside the Allison scanner. Neutral particles

ISBN 978-3-95450-176-2

(due to beam neutralisation) can also be observed at the X-position of 20mm.

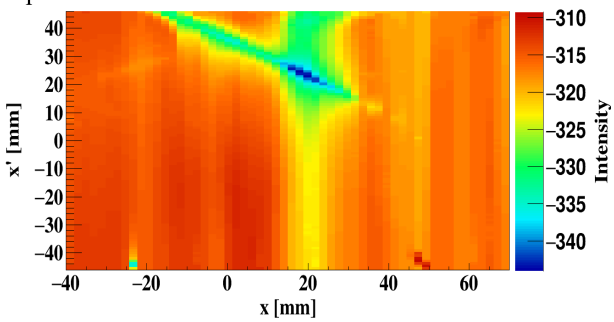

Figure 5: Typical background detected by "TSpectrum" from raw data of the Allison scanner shown on Fig. 4.

Ion Species Detection

Once the background has been detected and subtracted from the raw data, the algorithm can detect the three species. To perform this task, the function member "Search" of the class "TSpectrum" is used. It allows identifying one-dimensional peaks in a spectrum with the presence of continuous background and statistical fluctuations, i.e. noise. The algorithm is based on smoothed second differences that are compared to its standard deviations [25, 26].

Peaks detection of the three ion species are performed in one dimension, using this function at different X-positions where the different ion species are well separated. To make a matching between the peaks and the three ion species, several criteria are used depending on the X-position such as the highest intensity and the distance between peaks. A polynomial fit is then performed for each species using the identified peaks in order to identify the peaks at each X-position. For each species, pixels which do not have a null value around the polynomial fit are kept. A finer criterion using "TSpectrum" is applied to know the boundary between species when they are close to each other. On Fig. 6, peaks detections of the species are shown with their polynomial fits after background subtraction. D^+, D_2^+, D_3^+ and H_2O can be clearly seen.

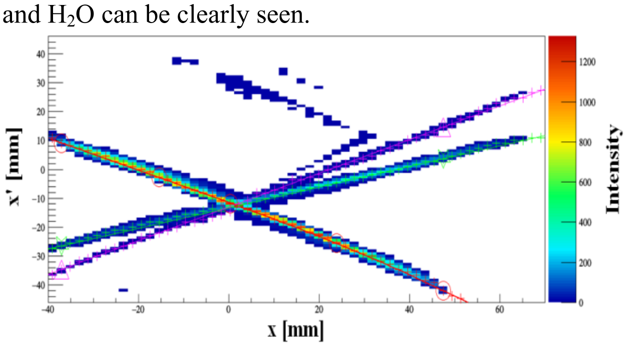

Figure 6: Peaks detections of D^+, D_2^+ and D_3^+ ion species after subtracting the histogram background of Fig. 4.

Interpolation of D_2^+ and D_3^+ Ion Species

From the Scipy library of Python, a smooth bivariate spline approximation function of order 5 is used to perform the interpolation of D_2^+ and D_3^+ species in the area where the three ion species are mixed. The data where D_2^+ and D_3^+ species are mixed are given to the interpolation function in order to perform the interpolation of both species in the same time. In fact, D_2^+ and D_3^+ species are mixed in a large position range and D_2^+ and D_3^+ species cannot be interpolated separately. This interpolation is then subtracted to the D^+ species spectrum and the emittance of D^+ species can be then calculated (see Fig. 7). First emittance results of the injector commissioning at Rokkasho, obtained with our method, are reported in [11].

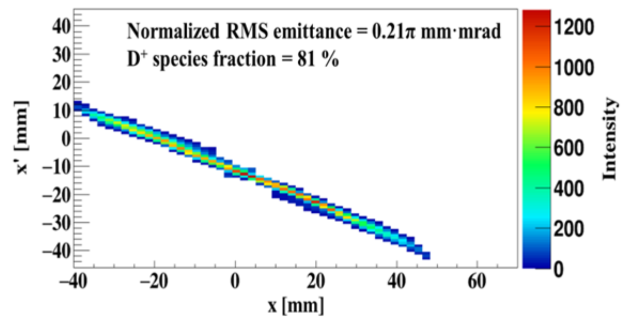

Figure 7: Example of an Histogram of D^+ after interpolation subtraction.

Figure 8 shows the histogram of D_2^+ after interpolation with the area where D_2^+ and D_3^+ are mixed. Figure 9 shows the histogram of D_3^+ where the gap corresponds to the area where D_2^+ and D_3^+ are mixed. The calculation of D^+ species fraction is performed as below:

$$D^+ \text{ species} = \frac{A1}{A1+A2+A3}$$

where A1 corresponds to the area of Fig. 7, A2 to the area of Fig. 8 and A3 to the area of Fig. 9.

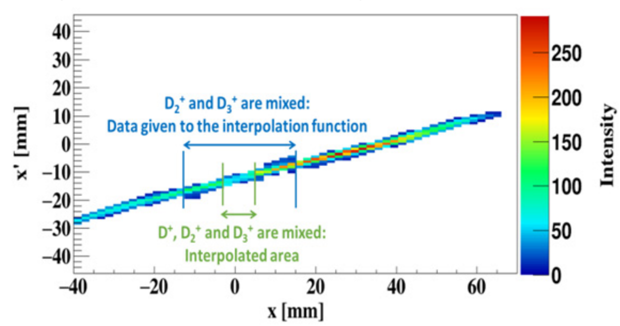

Figure 8: Histogram of D_2^+ after interpolation.

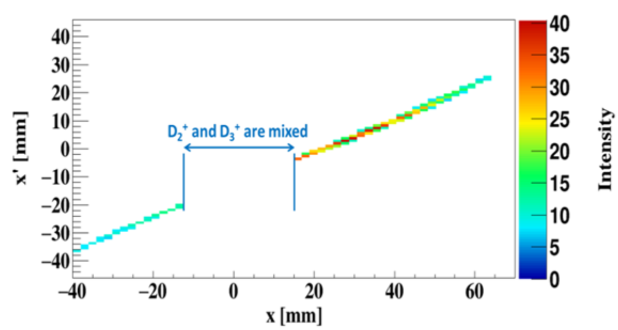

Figure 9: Histogram of D_3^+ without interpolation.

ISBN 978-3-95450-176-2

Separation of the Ion Species Experimentally

The three species have been experimentally separated by setting the solenoids coil currents to a null value and by using instead the magnetic steerer which is integrated to the first solenoid. This experimental set-up can be seen as a kind of Wien filter [27]. Figure 10 shows an example of emittance data obtained between the two solenoids from the Allison scanner with such a set-up. The proton beam current was 90 mA for an energy of 50 keV. No interpolation needs thus to be done to analyse these data.

A second set-up has been performed without using the steerers but with the coil current of the first solenoid set to focus enough strongly H^+ species on the emittance meter to avoid large emittance aberrations coming from non-linear magnetic fields on the edge of the solenoid. Interpolation was thus included in the data analysis.

Emittance measurements have been performed with these two set-ups for different parameters of the injection source, implying a significant variation of the H^+ fraction ratio. The results of H^+ fraction and of emittance obtained with these two set-ups have been compared for each setting of the source parameters and show a difference of less than 1%. This gives a strong confidence on the accuracy of emittance measurements and analysis.

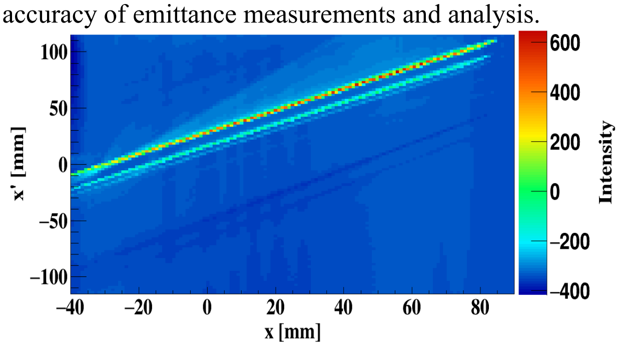

Figure 10: Raw data from the Allison scanner with the solenoids coil currents set to 0 A and with the magnetic steerer integrated to the first solenoid set to 150 A.

Test of the Algorithm Efficiency

Beam dynamics simulations [15, 18] have been performed with a 170 mA/50 keV proton beam. Emittance histograms have been obtained between the two solenoids for a normalized RMS emittance of 0.45π mm·mrad and for two different H^+ fraction ratios, i.e. 55% and 72%. Background detected with “TSpectrum” from arbitrary real measurements have been first multiplied by a fixed factor and then added to the simulated histograms. Figure 11 shows the histogram obtained for the H^+ fraction ratio of 55%.

The algorithm was used to calculate the emittance of the H^+ beam and the H^+ fraction ratio from these noisy simulations. The results were compared with the ones given by the simulations (before adding the background) and differences from less than 1% to a maximum of 4% have been observed. This shows that the background is accurately removed and that the interpolation accuracy is sufficient with this algorithm.

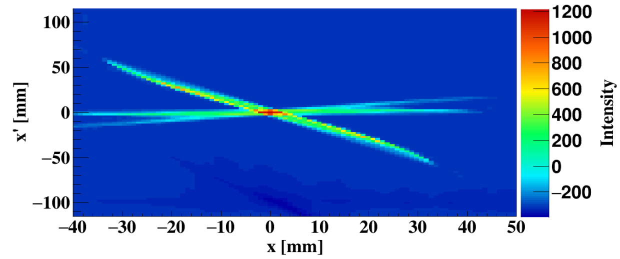

Figure 11: Emittance simulation between the two solenoids for a 170 mA/50 keV proton beam; RMS normalized emittance = 0.45π mm·mrad; H^+ ratio = 55%.

CONCLUSION

Beam diagnostics of the LIPAc injector have been commissioned at Rokkasho and are indispensable tools to achieve the required challenging beam characteristics at the RFQ entrance to allow CW operational mode. Modifications to enhance performance are planned such as the installation of a dipolar magnetic system to get a more accurate measurement of the beam current with the beam stoppers and the installation of CCD cameras during proton beam commissioning.

In order to analyse raw emittance data of high and non-homogenous background from an Allison scanner, an algorithm has been developed that allows both an automatic on-line calculation of the emittance rms values and of the species fraction ratio.

REFERENCES

[1] J. Knaster et al, Nuclear Fusion 55 (2015) 086003.
[2] J. Knaster et al, Proc. IPAC 2013, TUOAB101, Shanghai.
[3] A. Mosnier et al, Proc. IPAC 2012, THPPP075, New Orleans.
[4] R. Gobin et al, Proc. IPAC 2013, THPWO003, Shanghai.
[5] M. Comunian et al, Proc. LINAC 2008, MOP036, Victoria.
[6] H. Dzitko et al, Proc. IPAC 2015, THPF006, Richmond.
[7] R. Gobin et al, Rev. Sci. Instrum., 79 (2008) 02B303.
[8] N. Chauvin et al, Proc. IPAC 2013, THPWO006, Shanghai.
[9] R. Gobin et al, Rev. Sci. Instrum. 85, 02A918 (2014).
[10] R. Gobin et al, Proc. ICIS 2015, C151517-MonPS05, New-York, Rev. Sci. Instrum. (2016).
[11] Y. Okumura et al, Proc. ICIS 2015, WEDM04, New-York, Rev. Sci. Instrum. (2016).
[12] F. Senée et al, Proc. DIPAC 2011, TUPD46, Hamburg.
[13] F. Senée et al, Proc. DIPAC 2009, TUPB14, Basel.
[14] K. Shinto et al, Proc. ICIS 2015, C151669-ThuPS18, New-York, Rev. Sci. Instrum. (2016).
[15] N. Chauvin et al, Proc. HB 2012, THO3A03, Beijing.
[16] N. Chauvin et al, Rev. Sci. Instrum. 83, 02B320 (2012).
[17] R. Ferdinand et al, Proc. PAC 1997, 6W010, Vancouver.
[18] N. Chauvin et al, Proc. LINAC 2008, MOP072, Victoria.
[19] R. Gobin et al, Rev. Sci. Instrum. 70 n° 6, 2652 (1999).
[20] R. Hollinger et al, Proc. Linac 2006, TU3001, Knoxville.
[21] P.-Y. Beauvais et al, Rev. Sci. Instrum. 71 (2000) 1413.
[22] P.W. Allison et al, IEEE Trans. Nucl. Sci. NS-30, 2204-2206 (1983).
[23] https://www.python.org/.
[24] https://root.cern.ch/drupal/.
[25] M. Morháč et al, NIM, A401 (1997) 113-132.
[26] C. G Ryan et al, NIM, B34 (1988), 396-402.
[27] D. Catana et al, Report WP10 IDRANAP 15-01/2001.

ISBN 978-3-95450-176-2

A NEW BEAM ANGLE INTERLOCK AT SOLEIL

N. Hubert#, Y-M. Abiven, L. Cassinari, L. Chapuis, F. Dohou, M. El-Ajjouri, A. Loulergue, L.S. Nadolski, O. Marcouillé, P. Monteiro, D. Pédeau, P. Rommeluere, Synchrotron SOLEIL, Gif-sur-Yvette, France

Abstract

Anatomix and Nanoscopium beamlines are collecting photons generated by two 5.5 mm gap in-vacuum insertion devices installed in a canted straight section. Simultaneous operation of those two beamlines requires particular precautions in terms of alignment of the electron (and photon) beam in the undulators. With the high stored beam current (500 mA), any mis-steering in the upstream undulator could quickly damage the downstream one. Using the classical beam position interlock to guarantee the undulators protection would have constrained too much the operation due to very restrictive position thresholds. Then the machine protection system has been modified to incorporate a new interlock based on the electron beam angle combining two adjacent BPM readings. A description of the system and its performances will be presented.

INTRODUCTION

SOLEIL [1] is the French third generation synchrotron light source located south of Paris. It delivers photon beams to the users since 2008 is shown in Table 1. Today the 2.75 GeV facility has received more than 20,000 users. A total of 27 beamlines (BLs) take beam on a daily basis.

Table 1: Main SOLEIL Storage Ring Parameters

Parameters	Values
Circumference	354 m
Energy	2.75 GeV
Maximum current	500 mA
Revolution period	1.18 µs

Among them two recently constructed long (160 m) beamlines Anatomix and Nanoscopium bring challenges in term of operations. Both BLs use in-vacuum undulators (IVU) as radiation sources that are installed in the same canted straight section. The configuration at SOLEIL is specific since a 12 m long straight section has been transformed and equipped with a strong horizontal chicane for beam separation and a quadrupole triplet for optics adaptation to allow the host of two 5.5 mm minimum gap insertion devices [2]. Their point sources are 6.75 m away (Fig. 1) and make the first undulator a potential hazard for the downstream IVU in term of power deposition. Therefore the radiation angle issued from the upstream insertion has to be precisely and continuously watched for in order to prevent any radiation hitting the NiCu liner sheet of the downstream IVU.

#nicolas.hubert@synchrotron-soleil.fr

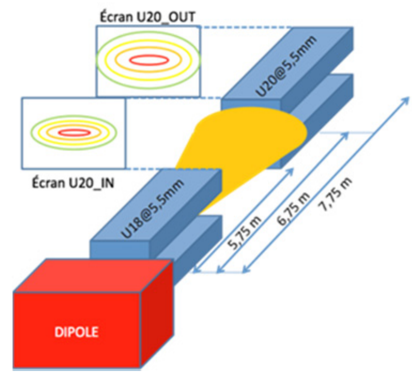

Figure 1: Schematics of the two insertion devices for Anatomix and Nanoscopium beamlines on the same (canted) straight section. In case of mis-steering of the beam in the upstream undulator, radiations may damage the downstream one.

Unfortunately SOLEIL experienced once this issue in 2011: the downstream undulator lower liner sheet was strongly damaged during the first simultaneous gap closing with a 500 mA stored beam leading to the removal of this insertion. Inadvertent mis-steering of the electron beam was aggravated by a wrong vertical offset of the undulator jaws with respect to the beam trajectory. This undulator has then been replaced, and thorough studies were carried out to prevent any such situation to occur again. One of the findings was that the electron beam trajectory in the upstream undulator has to be very carefully aligned and maintained within limits below what was earlier expected so that produced photons pass right into the centre of the downstream one. One of the mandatory steps before allowing again the simultaneous use of the two insertion devices at their minimum gap was an upgrade of the machine protection system (MPS) to protect the device from any accidental beam mis-steering during operation. This will permit simultaneous operation of insertions during the fall of 2015 for an intermediate configuration of the gaps (with gap values respectively 8 and 5.5 mm of the first and second IVUs).

The fastest and easiest way to do that would have been to reduce the vertical position thresholds (currently +/- 300 µm) of the already existing beam position interlock [3] for the two BPMs on each side of the upstream undulator. This would have led to +/-50 µm new threshold values too much constraining for the day-to-day operation (high probability of fake interlocks and strong impact on the beam availability). As a consequence, it has

ISBN 978-3-95450-176-2

been decided to develop an additional and new type of fast interlock based on the beam angle detection.

REQUIREMENTS

The beam angle interlock system must be robust and present a high reliability. It must trigger the MPS in less than 100 ms in order to prevent both heating up of the magnets of the IVU (demagnetization hazard) and damage of its liner sheets. The three conditions to be met simultaneously are:

- Machine stored current > 20 mA
- Both undulator gaps < 25 mm
- Beam vertical angle in upstream undulator > 25 µrad

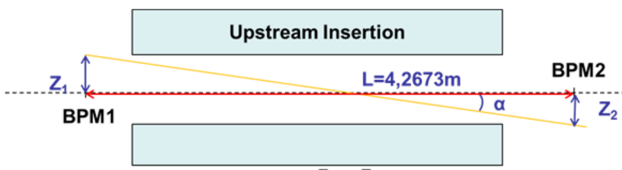

$$\alpha = \frac{Z_2 - Z_1}{L}$$

Figure 2: The new beam angle interlock should detect beam angle default between the two BPMs around the upstream insertion device.

As any interlock system, the beam angle detection should be designed on hardware/firmware based technology. It will be connected to the global machine protection system as a new input [4]. This latter turn off the RF switch of the main storage ring radiofrequency cavities and quadrupoles (redundancy). To ensure one-turn loss of the stored beam in the highly shielded injection section, one of the injection kickers is trigged at the same time since a few years.

IMPLEMENTATION

The beam angle interlock system must collect information from different subsystems, namely:

- Two BPMs for angle calculation,
- DCCT for current threshold detection,
- Undulator gap motion controllers for gap threshold detection.

Then this information has to be treated in order to generate the logical signal that will trigger the machine protection system (Fig. 3).

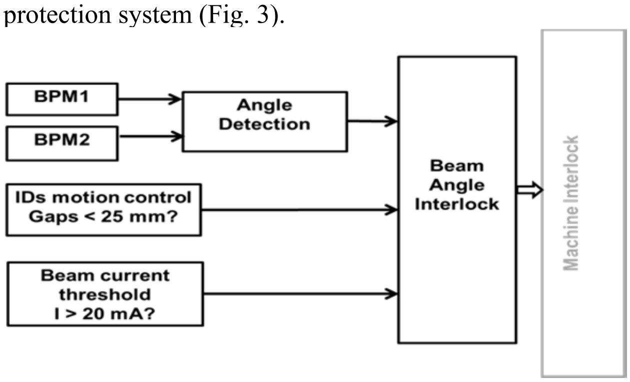

Figure 3: General architecture of the beam angle interlock system.

BPM Electronics

SOLEIL BPM system is based on Libera Electronics [5] that provides, among other data flows, Fast Acquisition (FA) position data sampled at 10 kHz. This data flow is already used for the position interlock system (internally of the Libera) and for the fast orbit feedback correction system.

In order to use the same data flow for the angle interlock, Libera FPGA design has been modified. FA data are distributed in one of the two RS485 frontside ports for serial communication (Fig. 4).

Figure 4: SOLEIL BPM Electronics based on Libera units have been modified to output the 10 kHz sampling position data in one of the RS485 port.

Position data are coded into 16 bits and transported over the RS485 link using an UART protocol adding start/stop and parity bits (Fig. 5). The baud rate on the transmission lane is 1.25 Mbit/s. Data distribution is started automatically as soon as the Libera module is switched ON.

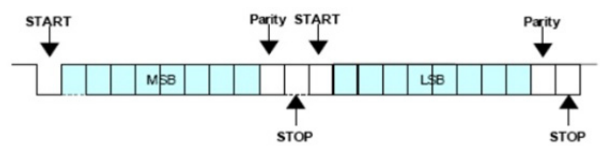

Figure 5: Data protocol over the RS485 transmission line.

Angle Detection

A first electronic board is used to convert the data electrical format from RS485 (differential link) to TTL. Then, the output of this conversion board is connected to a FPGA board (Tews Technologies TCP631) on which the frame decoding is done but also the angle calculation, and the angle fault detection (Fig. 6).

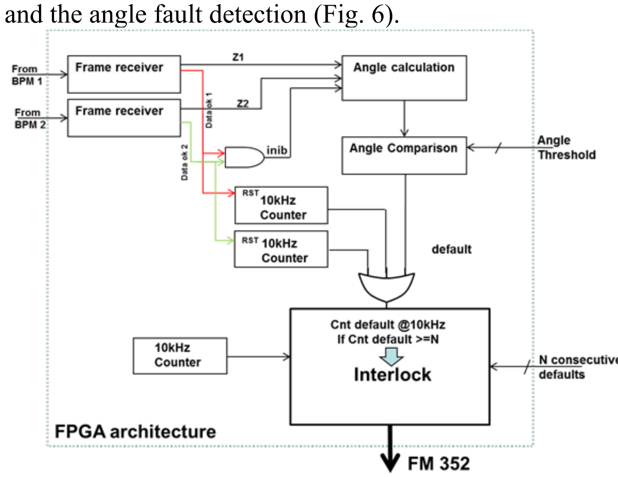

Figure 6: FPGA architecture for the angle detection.

ISBN 978-3-95450-176-2

Calculated angle is compared to user configurable thresholds and the angle interlock signal is emitted if several consecutive angle faults (outside thresholds) are detected. The angle interlock signal is not emitted after a single detected default in order to prevent beam trips due to false errors (BPM spikes for example). This number of consecutive faults needed to emit the interlock is also user configurable.

Moreover, the logic is able to detect a fault in the incoming position data rate (≠10 kHz) or corrupted data. Any communication error is considered as a default.

Insertion Device Motion Control

Information from gap motor encoders is collected by a TLCC that compare the gap position reading value to the gap threshold (25 mm) and generate a fault signal if gaps of the two undulators down crossed threshold.

Beam Current Threshold Detection

Beam current value in the storage ring is measured with a DC current transformer. On top of it, a Programmable Logic Controller (PLC) is already used to generate ON-OFF signal depending on the beam current value to inhibit/uninhibit different systems like top-up injection, beam position interlock, injector...

An additional output of this system has been allocated for the beam angle interlock with a threshold that is presently set to 20 mA (typical maximum low current for commissioning and machine dedicated studies with possible orbit distortion).

Beam Angle Interlock

The logic combining the different faulty signals to generate the interlock signal is implemented in a PLC module (Siemens FM352). Interlock output is trigged when all the three conditions, namely beam angle, gap positions and beam current are met. Any interlock is latched and hold until acknowledgment by the user.

PERFORMANCE

The beam angle interlock system is configured to trigger the machine protection system after ten consecutive faulty conditions (recorded at 10 kHz). As explained earlier this margin is taken in order to improve the robustness of the system against false detections.

With this configuration, the total time needed to trip the beam after a beam angle fault has been measured equal to 1.9 ms. This delay is the sum of ~1.1 ms for beam angle error detection itself (system wait for 10 consecutive faults) and 0.8 ms for the machine protection system. Dedicated measurement has been performed using a fast air coil corrector to steer the beam outside the limits, and measuring the delay between angle default and beam loss on BPM post-mortem data (Fig.7).

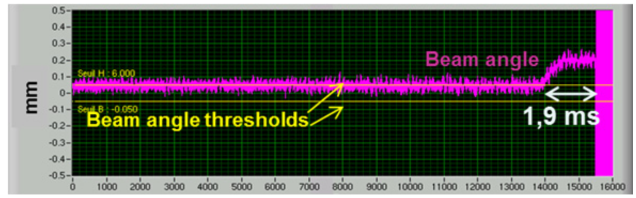

Figure 7: The beam is killed 1.9 ms after the beam angle exceed the threshold.

OPERATION

The beam angle interlock system has been put in operation since May 2015 in order to allow the simultaneous use of the two undulators installed on the same canted straight section. Since then, the system has been fully operational and did not constrain the day-to-day operation. The system has also shown both high reliability and robustness.

CONCLUSION

This new vertical beam angle interlock system has been in operation at SOLEIL since May 2015 to allow the simultaneous operation of two in vacuum insertion devices mounted on the same (canted) straight section for an intermediate configuration of their gaps.

Additional diagnostics like a post-mortem buffer of the beam angle measurements just before the beam loss will be implemented soon.

In order to ensure a safe operation of simultaneously both undulators closed to their minimum gap (5.5 mm), the addition of a dedicated photon absorber is mandatory. This latter is under final design and should be installed in front of the downstream absorber beginning of 2016. This will require an extension of the angle interlock system: it will be duplicated in the horizontal plane to protect the absorber.

It will also be possible in the future to integrate as a new input in the system, the photon BPM reading installed in the frontend of the BLs to provide a redundant signal and additional information about the variation of the pointing angle of the photon beam produced by the upstream undulator.

REFERENCES

[1] A. Nadji et al., SOLEIL Status Report, IPAC2015, Richmond, Virginia, pp. TUPWA012, 1419-1421
[2] A. Loulergue et al., Double Low Beta Straight Section For Dual Canted Undulators at SOLEIL", WEPEA011, IPAC2010, Kyoto, pp. 2496-2499.
[3] J-C. Denard et al., « BPM System Interlock for Machine Protection at SOLEIL », WEPC169, IPAC2011, San Sebastian, pp. 2379-2381.
[4] Y-M. Abiven et al., « Machine Protection and Interlock Systems at Synchrotron SOLEIL », WEP089, ICALEPCS2009, Kobe, pp. 576-578.
[5] Instrumentation Technologies : http://www.i-tech.si/

ISBN 978-3-95450-176-2

DIGITAL PROCESSING OF PICK-UP SIGNALS FOR POSITION AND TUNE DETERMINATION

R. Singh, A. Reiter, P. Forck and P. Kowina, GSI, Darmstadt, Germany

Abstract

With the advent of fast high resolution Analog to Digital Converters (ADCs) and Field Programmable Gate Arrays (FPGAs), "all digital systems" for pick-up data processing to determine position and tune have become commonplace. This contribution compares the frequently used position estimators used in the digital systems in terms of measurement variance, bias and robustness to external interference. An analytical beam model, along with simulated pick-up signal and actual pick-up signal from the SIS-18 synchrotron are used for the comparison. The effect of precise position estimation on the tune spectra is discussed.

INTRODUCTION

High precision position estimation requires the optimization of the beam position measurement system in all the stages of development, which starts from EM simulations to optimize the pick-up design against unwanted resonances, establishing linearity while minimizing the cost of manufacturing [1]. The mechanical construction and installation of pick-ups with respect to the magnetic center of magnets within the specified tolerances is also a challenging task. Finally, the electronics required for acquisition and processing of the pick-up signals demand low noise and high dynamic range as well as periodic and precise calibration. The typical methods for signal processing and calibration are described in [2–4]. In the recent years, the signal processing have completely shifted to digital domain due to availability of fast high resolution ADCs and FPGAs and this contribution will focus on this aspect of position measurement system for circular accelerators.
The concepts of pick-up position sensitivity and offset are presented along with the typical signal spectra for bunched and coasting beams in the next couple of sections. Following that, the frequently used digital position estimation methods are discussed and a new approach to position estimation based on "linear regression model" is introduced. All the presented methods are compared with an analytical beam model, simulated beam data and the pick-up signal from the SIS-18 synchrotron in terms of estimated position bias and variance. The effect of position estimation methods on tune spectra calculated from the turn-by-turn position is discussed.

POSITION SENSITIVITY AND OFFSET

The pick-up position sensitivity and offset estimates are obtained from the EM simulations [5] or on-bench wire based measurements [6, 7]. The uncertainty in the position sensitivity measurement is given by the precision of the measurement equipment used for bench measurements and simulation time/resources which are often < 0.1% of absolute values as shown in [5, 8]. In careful pick-up designs, the pick-up sensitivity is found to be constant within 0.1% of the absolute sensitivity value in the frequency region of interest [5]. Once the pick-up sensitivity and offset are known, the beam center-of-mass can be determined from the difference of the signal induced on opposite pick-up plates. There are two important features of pick-up signal which are relevant for digital position estimation a) Most of the pick-up types are "capacitive" or AC coupled, which leads to rejection of the DC component of the beam signal and b) The signal is sampled with fast ADCs such that many samples are acquired in each time interval for the position measurement. Thus the problem of position estimation is that of an overdetermined system whose low frequency components are significantly suppressed. The lower cut-off is given by the termination impedance of the pick-up [2].

PICK-UP SIGNAL SPECTRUM

The pick-up signal spectrum of a ring accelerator is unique due to the periodic crossing of beam particles through the pick-up. A beam of particles traversing the synchrotron or

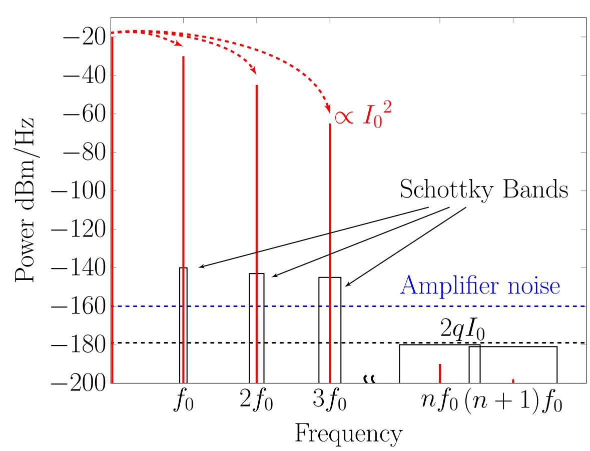

Figure 1: A bunched beam power spectrum of a U^{28+} bunched beam with 10^9 particles at injection energy in SIS-18. $2qI_0$ is the shot noise level while blue dashed line represents the electronics noise. The Schottky bands are shown for reference.

storage ring with a constant energy is referred to as coasting beam. The beam is said to have no coherent longitudinal structure due to absence of any longitudinal focusing. However, due to finite momentum spread, finite number of particles and periodic traversal of particles through the BPM, signals proportional to the square root of number of particles are induced at the revolution frequencies. The power in each revolution band is given by $2qI_0$, where q is the charge

ISBN 978-3-95450-176-2

state and I_0 is the beam current. They are called Schottky signals due to their origin in shot noise [9]. When an external field imposes a longitudinal structure on the beam, power is transferred from the DC component of the beam to higher harmonics at the revolution frequency. Any harmonic with sufficient power in the difference signal spectrum can be used to obtain the position information. This coherent power is proportional to the number of particles and is usually large enough for calculation of bunch-by-bunch beam position measurement. Figure 1 shows the estimated power spectra of a U^{28+} bunched beam with 10^9 particles at injection energy. In comparison, the power in the Schottky bands of the unbunched beam with the same current is also shown. Though the beam position measurement usually implies bunched beam position measurement; with high beam intensities and long measurement times, Schottky signals can be utilized for beam position measurements of a coasting beam. Detailed introduction to pick-up signal spectra can be found in [10].

POSITION ESTIMATORS

Each pick-up electrode signal is either individually sent through an amplifier/attenuator chain or passive "hybrids" are utilized to create sum and difference signals before amplifying the signal. Hybrids are preferred when the pick-up signals are large and require to be attenuated before digitization. The electronics chain is designed to match the pick-up signal to the ADC input range, while the ADCs are selected such that the effective number of bits ENOB is matched to the amplifier noise. The sampling rate is kept as high as possible while satisfying the criterion mentioned above. The ADC selected for SIS-100 has 12 effective number of bits and sampling rate of 250 MSa/s. A calibration scheme is used to periodically correct the amplifier gain and offset drifts as well as the ADC offset drift. This is performed to eliminate the systematic biases in the measurement. The N digitized signal samples from opposite electrodes are denoted by $U_{l,i}$ and $U_{r,i}$, where $i \in \{1, N\}$ denotes the sample index.

There are two classical approaches which are frequently used for calculation of beam position. The first and most frequent approach referred to as integral method resurrects the lost DC or baseline, which is lost due to AC coupling of the pick-up [11]. The baseline of the signal from each capacitive plate is individually determined from the samples in between the bunches (See Fig. 4 and 7) . In frequency domain, it translates to the reconstruction of the DC signal from the higher harmonics (See Fig. 1). If the baseline of each electrode is denoted by B_l and B_r, the beam position of the whole bunch $< x >$ can be calculated from the difference-over-sum ratio:

$$\frac{< x >}{k} = \frac{\sum_{i=1}^{N}(U_{l,i} + B_l) - \sum_{i=1}^{N}(U_{r,i} + B_r)}{\sum_{i=1}^{N}(U_{l,i} + B_l) + \sum_{i=1}^{N}(U_{r,i} + B_r)} \tag{1}$$

Here k is the pick-up sensitivity in mm units. Obviously, this method is very prone to biases resulting from baseline calculation.

The second position estimator is based on the power of individual signals and uses the root-sum-square (RSS):

$$\frac{< x >}{k} = \frac{\sqrt{\sum_{i=1}^{N} U_{l,i}^2} - \sqrt{\sum_{i=1}^{N} U_{r,i}^2}}{\sqrt{\sum_{i=1}^{N} U_{l,i}^2} + \sqrt{\sum_{i=1}^{N} U_{r,i}^2}} \tag{2}$$

This approach is a reasonable substitute to the earlier approach since the baseline restoration is not required. In the frequency domain, this estimator weights each harmonic with its magnitude, and thus the noise characteristics are significantly better than integral method.

The third and the newer approach represents the position estimation problem as the case of simple linear regression and solves it with the ordinary least square (OLS) approach which takes a simple closed form [12]. For the conciseness of the formulation, the electrode signals are represented in difference $U_{d,i} = U_{l,i} - U_{r,i}$ and sum forms $U_{s,i} = U_{l,i} + U_{r,i}$ and the estimator can be given as,

$$\frac{< x >}{k} = \frac{N \cdot \sum_{i=1}^{N}(U_{d,i}U_{s,i}) - (\sum_{i=1}^{N} U_{d,i})(\sum_{i=1}^{N} U_{s,i})}{N \cdot \sum_{i=1}^{N} U_{s,i}^2 - (\sum_{i=1}^{N} U_{s,i})^2} \tag{3}$$

This estimator has two important advantages over the difference-over-sum approach. The first is the minimization of the residuals in the least square sense. The second is immunity to any slow offset errors which might occur due to ADC offsets, external interferences or any amplifier offsets. This is especially advantageous for operating in asynchronous mode or closed orbit mode, when position is calculated from long data sets.

Bias and variance

The bias and variance characteristics for each estimator are evaluated using a simple triangular beam model analytically. The triangular model is chosen for the simplicity in performing the error propagation calculations while capturing many relevant features of a real beam. Figure 2 shows the triangular beam model, where the dashed line with blue dots represents the AC coupled signal from pick-up plates, while the solid line with red dots represent the baseline restored signal. σ_V is the std. deviation of the individual data samples. V_{FS} is the full scale voltage while A is the relative amplitude of the signal with respect to the full scale voltage. N_S is the number of "signal samples" inside the triangular bunch while N_B is the number of "baseline samples" outside the bunch. It should be noted that for a raw signal, the distinction between signal samples and baseline samples is not clear since, baseline samples also carry position information. Since the analytical calculations rely on this distinction, perfect baseline restoration is assumed.

ISBN 978-3-95450-176-2

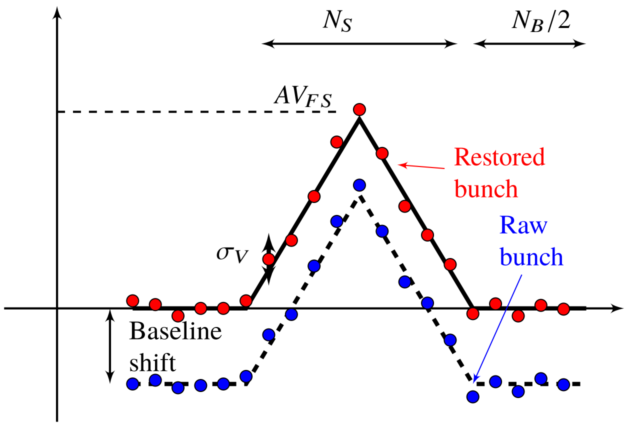

Figure 2: Triangular beam model.

Using error propagation of independent samples, it can be shown that for a perfectly restored baseline, the std. deviation of the position calculated for a centered beam by the estimators in Eq. 1, Eq. 2 and Eq. 3 are given by,

$$\frac{\sigma_{<x>}}{k} = \sqrt{2} \cdot \left(\frac{\sigma_V}{A \cdot V_{FS}}\right) \cdot \frac{\sqrt{N_S + N_B}}{N_S + 2} \qquad (4)$$

$$\frac{\sigma_{<x>}}{k} = \sqrt{3/4} \cdot \sqrt{2} \cdot \left(\frac{\sigma_V}{A \cdot V_{FS}}\right) \cdot \frac{1}{\sqrt{N_S + 3 + 2/N_S}} \qquad (5)$$

$$\frac{\sigma_{<x>}}{k} = \frac{\sqrt{3}}{\sqrt{2}} \cdot \left(\frac{\sigma_V}{A \cdot V_{FS}}\right) \cdot \sqrt{\frac{N_S(N_S + N_B)}{(N_S + 2)(\frac{1}{4}N_S^2 + N_S N_B)}} \qquad (6)$$

The detailed calculations can be found in [13]. Figure 3 shows the std. deviation as a function of ratio of number of baseline samples N_B to the number of signal samples for each method. The number of signal samples within the triangular beam is $N_S = 80$, and the number of baseline samples is varied. It gives an interesting insight on how each estimator treats the baseline samples. The std. deviation of the integral method increases with the addition of baseline samples since the samples do not contain any position information. The std. deviation of RSS method is shown to be independent of inclusion of baseline samples. The OLS method, calculates the slope by fitting the difference signal to the sum signal, and each point improves the estimate, including the baseline samples. This is evident in reduction of the std. deviation as more baseline points are added.

The outcome of the triangular analytical beam model is compared with a beam generated with MADX particle tracking [14] through the SIS-18 lattice. The generated beam traverses the SPICE model of the capacitive pick-up and acquisition electronics. The simulated pick-up data has the same characteristics as the SIS-18 injection pick-up signals. Figure 4 shows the bunches along with the processing windows, in order to select the different number of baseline samples for the position calculation. The positions are calculated

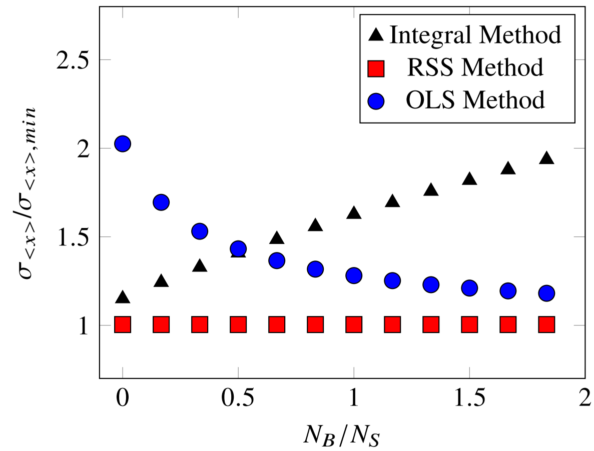

Figure 3: Predictions of the std. deviation of positions calculated for the analytical beam model against the ratio of number of baseline samples to number of signal samples ($N_S = 80$). Each std. deviation value is normalized to the smallest value.

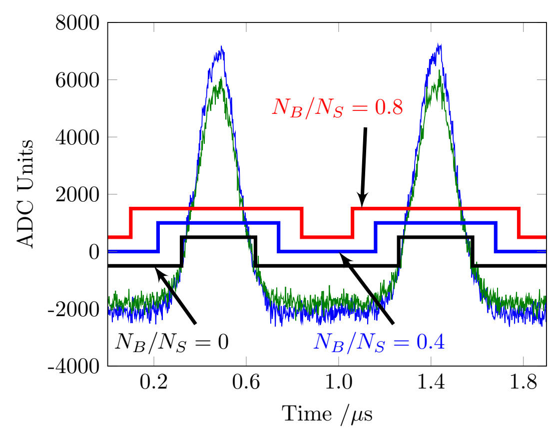

Figure 4: The simulated beam and different processing windows with selected samples for position calculation.

for both restored and non-restored data for 800 consecutive bunches. Figure 5 shows std. deviation of the calculated positions as a function of the baseline samples and signal samples for comparison with Fig. 3. The restored beam case can be directly compared with the analytical model. The negative values of N_B/N_S depict the cutting into the bunches or removing some signal samples. The behavior is similar to the predictions from the analytical model, the OLS estimate improves with inclusion of the baseline samples, while the performance of integral method worsens with inclusion of more samples. The crossing point where OLS produces better results compared to the integral method is at $N_B/N_S = 0$ in comparison to $N_B/N_S = 0.5$ in case of analytical model. The position values obtained from RSS has the smallest std. deviation and is independent of the number of samples included in the calculation. For $N_B/N_S > 0.6$, the OLS closes into RSS performance. Figure 6 shows the mean of the calculated position with restored and non restored beam.

ISBN 978-3-95450-176-2

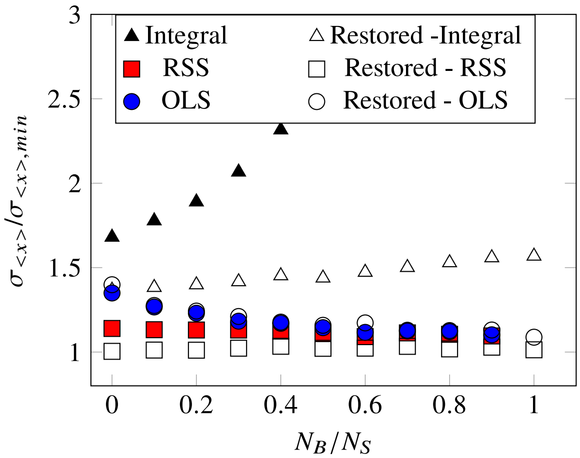

Figure 5: Std. deviation of the position calculated from the simulated pick-up data.

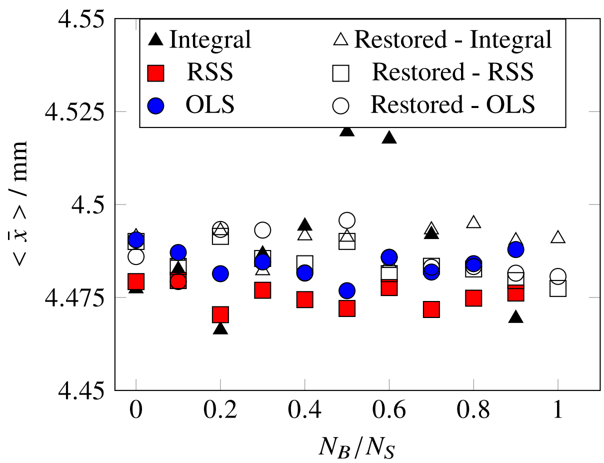

Figure 6: Mean of the position calculated from the simulated pick-up data.

All the algorithms predict the true position value correctly in the scanned range.

Finally, the actual beam data is chosen for comparison with the predictions of the analytical model and results from the simulated beam. The beam data is carefully chosen at the injection plateau of SIS-18 in the vertical plane where no transverse oscillations and beam drifts were visible. This is important to distinguish the variance due to the electronics noise from actual beam oscillations or beam drifts. Figure 7 shows the longitudinal bunch structure along with the processing windows. 1000 consecutive bunches were used to calculate the positions. The std. deviation and mean for the positions calculated by each algorithm are shown in Figures 8 and 9 respectively. The integral algorithm expectantly diverges in the non-restored beam case. Even in the case of baseline restoration, it has the largest std. deviation, and thus offers the least position resolution of all methods. The surprising outcome is that the performance of the OLS method has bettered the RSS method in the whole range of N_B/N_S in contradiction to the simulated beam data. On further in-

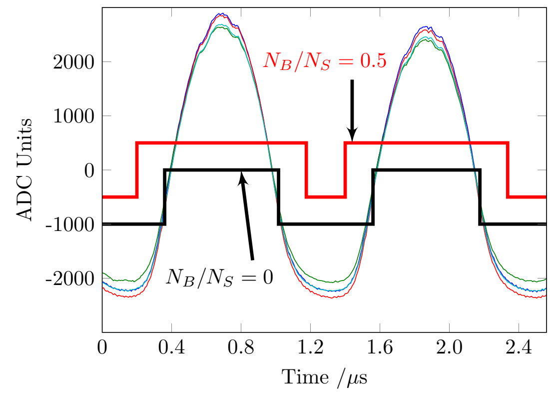

Figure 7: The pick-up data from SIS-18 injection beam along with the processing windows with samples used for position calculation.

vestigation, a slow 5KHz common mode interference (CMI) on the pick-up signal seems to cause the difference. OLS method strongly suppresses any common mode signal while the RSS output is disturbed by external interferences. In the

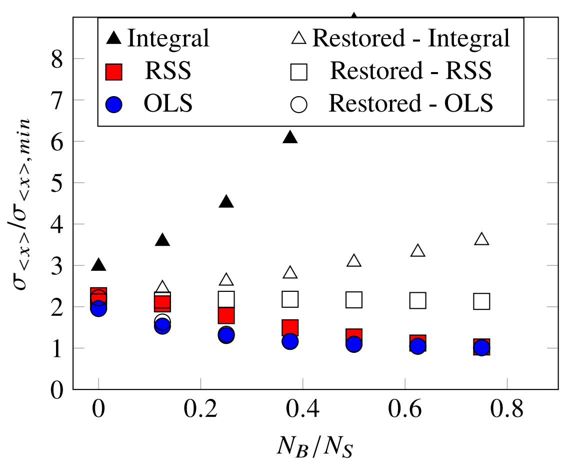

Figure 8: Std. deviation of the position calculated from the SIS-18 injection beam pick-up signal.

mean calculation, the baseline restoration seems to produce a bias in the estimated position for integral and RSS methods, while OLS estimates are independent of the baseline restoration. It is clear from the results in this section that the integral method is not suited for position calculation. In addition, the baseline restoration is a non-linear latent procedure which seem to cause bias under external interferences, and is actually not required by both RSS and OLS procedures. One can thus conclude, that the baseline restoration and the integral method should be avoided for position calculation altogether. Rest of the document will only deliberate on the RSS and OLS methods.

Robustness

The robustness of the position estimators in this context is defined as its ability to cope with electronic baseline drifts e.g. ADC or amplifier offset drifts, external electromagnetic

ISBN 978-3-95450-176-2

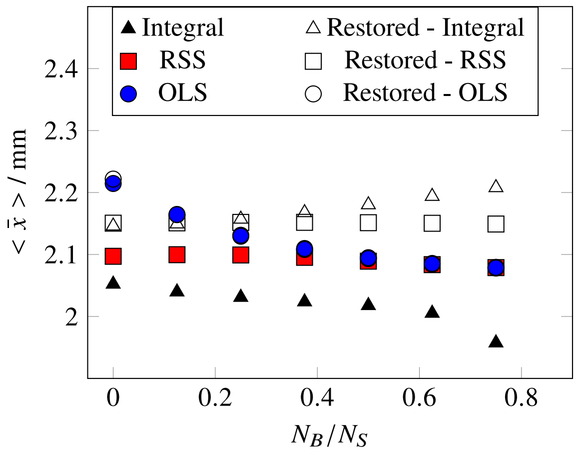

Figure 9: Mean of the position calculated from the SIS-18 injection beam pick-up signal.

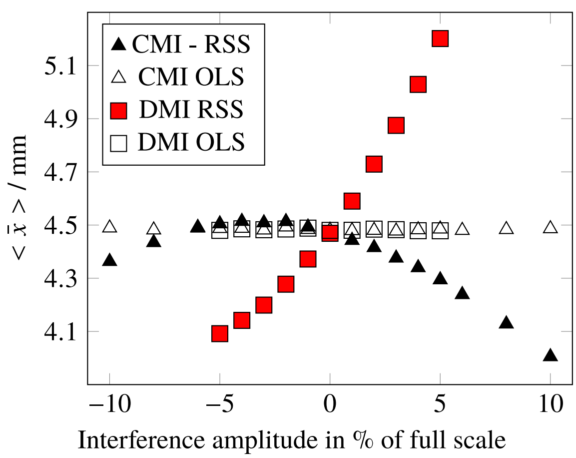

Figure 10: The effect of common mode and differential mode interferences on the position estimate by RSS and OLS fit.

interference, bunch detection errors and dependency on the external signals. The performance of RSS method with the SIS-18 beam data in presence of common mode interference shown to be poor in the last section. Here we illustrate the performance of RSS vs OLS method to common mode interference (CMI) and differential mode interference (DMI). Non-beam related constant offsets are added to the simulated beam signal shown in Fig. 5 in common mode and differential mode. First the common mode signal in the units of % of full scale voltage are added and mean of estimated position is plotted in Fig. 10. The OLS method is immune to the CMI while the RSS has an asymmetric response depending on the the sign of CMI. Similarly, the effect on positions calculated by OLS to DMI is negligible while the gradient for the position calculation error for the RSS method to DMI is large. In real beam scenario, these interferences are unavoidable, and the ability of OLS to suppress them is a big advantage over the RSS method. The next section emphasizes this point further.

TUNE CALCULATION

Tune is the measure of transverse phase advance of the beam after one turn around the synchrotron. The discussions on the robustness of algorithms to non-beam related interferences become extremely important when tune from bunch by bunch position data since any arbitrary external interference can significantly modify the tune spectrum as clearly suggested by Fig 10. Figure 11 shows the tune spectra calculated from the positions calculated by (a) integral method, (b) RSS and (c) OLS on the baseline restored pick-up data of U^{28+} beam which is excited with a wideband noise exciter. The spectra from integral method and power method look similar except for the noise floor, which is higher for integral method. However, the spectra from OLS fit method is strikingly different the other methods, and demonstrates its ability to suppress external disturbances and improve the tune spectrum estimate.

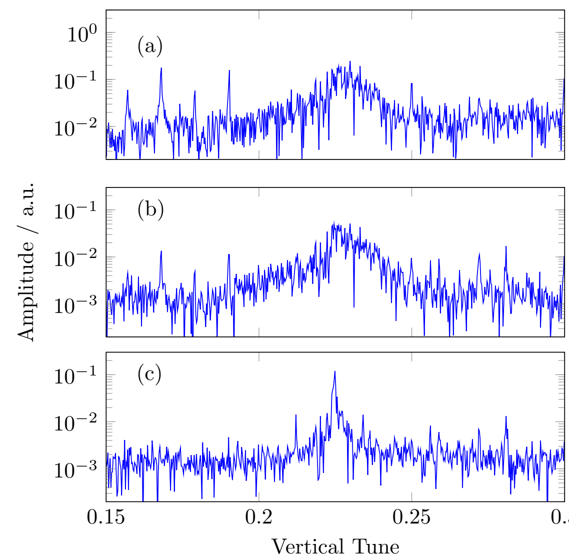

Figure 11: The vertical tune spectrum calculated for an excited beam at SIS-18 injection from the positions calculated from (a) Integral method (b) RSS method (c) OLS method.

SUMMARY

A new regression based approach to position calculation is presented. It is compared with traditionally utilized estimators with the help of triangular beam analytical model, simulated pick-up signals and SIS-18 injection beam pick-up signals. The performance of the new approach is superior to the traditional algorithms. The robustness of the new OLS based position estimator to external interference is of special significance for bunch-by-bunch position calculations and betatron tune measurements.

REFERENCES

[1] P. Kowina et al., FEM simulation- a Powerful Tool for BPM Design, DIPAC 2009.

ISBN 978-3-95450-176-2

[2] P. Forck, P. Kowina, D. Liakin, "Beam Position Monitors", Beam Diagnostics, CAS2009, Darmstadt, 2009.

[3] G. Vismara, "Signal processing for beam position monitors" Proc. Beam Instr. Workshop BIW 2000, Cambridge AIP 546, p. 36, 2000.

[4] D. Liakin et al.,"Advanced digital signal processing for effective beam position monitoring", Proc. of DIPAC 2011, Hamburg, 2011.

[5] P. Kowina et al., "Optimization of Shoe-box type beam position monitors using the finite element methods", DIPAC 2005, Lyon, France.

[6] F. Caspers, "Impedance determination from bench measurements" CERN-PS/2000-004(RF), 2000.

[7] Maurice Cohen-Solal, "Design, test, and calibration of an electrostatic beam position monitor" Phys. Rev. ST Accel. Beams 13, 032801, 2008.

[8] I. Podadera, L. Soeby, "Precision beam position monitor for EUROTEV", Proc. of DIPAC 2007, Venice, Italy.

[9] F. Caspers , "Schottky signals", Beam Diagnostics, CAS2009, Darmstadt, 2009.

[10] J. M. Byrd, "Bunched Beam Signals in the time and frequency domain", in Proceeding of the School on Beam Measurement, Montreux, p. 233 World Scientific Singapore (1999).

[11] A. Galatis et al., "Digital Beam Position Measurement at GSI-SIS and CERN-PS", Proc. of DIPAC 2005, Lyon, France.

[12] R. Singh, "Tune measurements at SIS-18: Methods and applications", PhD Thesis, TU Darmstadt, 2013.

[13] A Reiter, R. Singh, "Statistical treatment of the pick-up signals", GSI Internal note 2015.

[14] Methodical accelerator design tool, http://mad.web.cern.ch/mad/

ISBN 978-3-95450-176-2

MICRON-SCALE VERTICAL BEAM SIZE MEASUREMENTS BASED ON TRANSITION RADIATION IMAGING WITH A SCHWARZSCHILD OBJECTIVE

L.G. Sukhikh*, A.P. Potylitsyn, A.V. Vukolov, Tomsk Polytechnic University, Tomsk, Russia
S. Bajt, G. Kube, DESY, Hamburg, Germany
I.A. Artyukov, P.N. Lebedev Physical Institute, Moscow, Russia
W. Lauth, Institute for Nuclear Physics, Johannes Gutenberg University, Mainz, Germany

Abstract

This report presents preliminary results of a measurement of a micron–scale vertical beam size based on imaging of optical transition radiation in the visible region. The visualization of point spread function dominated beam images was carried out using a Schwarzschild objective that provides high magnification and that is free of some of aberrations. According to the preliminary data treatment, a vertical rms beam size of 1.37 ± 0.07 μm was measured at the 855 MeV beam of the Mainz Microtron MAMI (Germany).

INTRODUCTION

Optical Transition Radiation (OTR) is generated when a charged particle crosses the boundary between two media with different optical properties. It is an important tool for beam diagnostics, mainly for transverse profile beam imaging in modern linear accelerators. OTR in backward direction is generated directly at the screen boundary in an instantaneous process with a linear response and a rather high light output. The radiation is emitted in the direction of the specular reflection in a small lobe with an opening angle which is defined by the beam energy. Unfortunately, the diffraction limit of the optical system imposes a limitation that makes the method ineffective for reliable diagnostics of micron–scale beams in modern accelerators.

The point spread function (PSF) defines the minimum beam size that can be resolved using OTR. The PSF was investigated for the first time by M. Castellano and V.A. Verzilov [1] and later in more details by A.P Potylitsyn [2], D. Xiang and W.-H. Huang [3] and by G. Kube [4]. It was shown that the PSF has a double lobe structure which is defined by the observation wavelength and the acceptance of the optical system. The minimum beam size that can be measured using OTR with a wavelength of 400 nm and a reasonable optical system is about 3 μm.

In principle it is possible to overcome the limitation by decreasing the observation wavelength used for the beam imaging. A proof–of–principle experiment that demonstrated the possibility to image beam profiles using backward transition radiation (BTR) in the Extreme Ultraviolet (EUV) region at $\lambda \simeq 20$ nm was published in [5].

In the case of small beams and OTR in the visible region, it is possible to obtain PSF dominated images that at the first glance could be treated as convolution of the PSF with the beam profile. In this situation, beam size information could be extracted as it was shown in [6–8]. In [6, 7], the authors used a thin lens as the main part of the optical system, and in the experiment described in [8] imaging was performed by a spherical mirror. Such optical schemes resulted in a decrease of the resolution because of aberrations, especially due to spherical and chromatical ones. In the present report we describe an experiment devoted to PSF dominated beam imaging using a Schwarzschild objective that is free of this kind of aberrations [9].

EXPERIMENTAL SETUP

The experiment was carried out at the 855 MeV electron beam of the Mainz Microtron MAMI (Institute of Nuclear Physics, Johannes–Gutenberg–University, Mainz, Germany). The quasi–continuous beam of the racetrack microtron (mean beam current 52 nA) was operated in macro–pulse mode with a pulse duration of 0.8 s in order to allow CCD frame readout in the gaps in between.

Figure 1 shows a scheme of the experimental setup. A set of targets was mounted onto a motorized stage which allowed rotational and linear motion across the beam axis in horizontal and vertical direction. The target set consisted of Mo and Al single layer targets, a Mo/Si multilayer target which was optimized to generate 20 nm wavelengths, two wire–scanners (10 μm thick and 4 μm thick tungsten wires), and a LYSO:Ce scintillator. The electron beam interacted with the target, generating OTR in a wide spectral range, and the beam spot was imaged using this OTR with

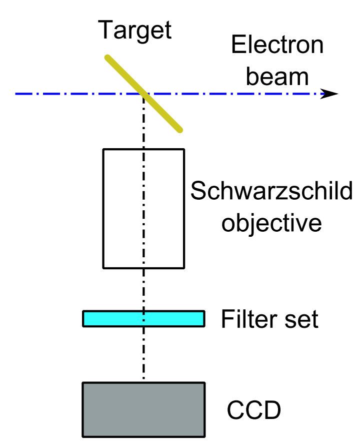

Figure 1: Experimental setup.

* sukhikh@tpu.ru

ISBN 978-3-95450-176-2

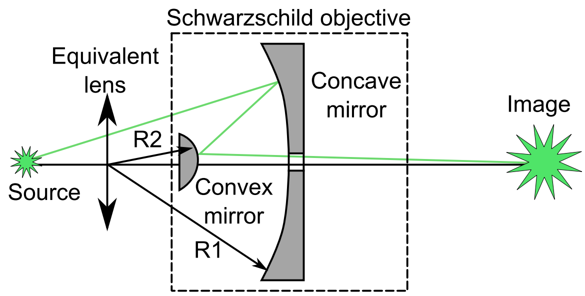

Figure 2: Schwarzschild objective scheme.

the Schwarzschild objective. The resulting beam image was recorded with a CCD detector. A set of filters was mounted in front the CCD camera in order to selectively detect different parts of the spectrum. The present report describes results obtained for the Mo/Si multilayer target and a bandpass filter with central wavelength $\lambda = 400$ nm and full width half maximum equal to 140 nm. Beam size measurements using the LYSO:Ce scintillator are reported in [10].

The working principle of the Schwarzschild objective is illustrated schematically in Fig. 2. It consists of two spherical mirrors, one is concave and the second convex. Both mirrors have the same center of curvature, and the equivalent thin lens is located in this center [9]. A Schwarzschild objective used for our experiment was developed and produced at the Lebedev Physical Institute (Moscow, Russia). It consisted of two mirrors with a multilayer coating which was optimized for wavelengths of about 20 nm, nevertheless it had also a good reflectivity in the visible part of the spectrum. The nominal numerical aperture amounted $NA = 0.19$ and the equivalent lens focal length was equal to 26.9 mm. In the experiment, the distance from the target to the lens amounted 27.54 mm and the distance from the lens to the CCD 1155.46 mm. As result, the magnification was equal to $M = 41.95$. Due to the fact that the secondary mirror of the Schwarzschild objective blocked most of the OTR radiation when the target was tilted at 45 deg, a tilt angle of 49 deg was chosen in order to maximize the radiation intensity.

The beam images were recorded with a scientific grade CCD camera (ANDOR DO434-BN-932) with 1024×1024 pixels and a pixel size of $13 \times 13 \mu m^2$. Special feature of this in–vacuum CCD camera was a rather high sensitivity in the range from 1 eV up to 10 keV due to the back illuminated chip without coating. The CCD was cooled down to −40 °C in order to decrease dark current and CCD noise. Both, background and CCD noise were measured with the beam while the optical path was blocked by a 1 mm thick aluminum plate.

BEAM IMAGING IN THE VISIBLE REGION

Figure 3 shows a beam image accumulated over 10 accelerator shots which was obtained in the visible region using

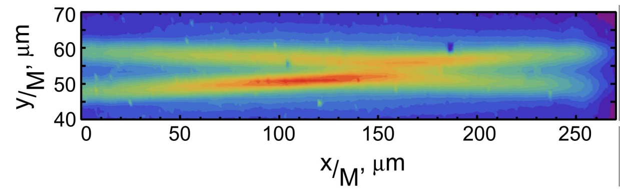

Figure 3: Beam image obtained in the visible region.

the bandpass filter. The radiation intensity is expressed in CCD counts per pixel.

The recorded image shows a pronounced double lobe shape that is a clear signature for a PSF dominated image in the case of a measurement using the vertical OTR polarization component [6,7]. In the measurement Fig. 3 no external polarizer was used, the obtained image is the result of the natural polarization due to the reflection at the target. The banana–like shape is caused by the depth–of–focus effect, the target was tilted and the beam tails are out of focus. For details concerning this topic see also [8, 11]. In the present experiment, no possibility exists to determine the horizontal beam size because the left part of the beam image is out of the view field of the CCD camera. This is the payback for the high magnification of the Schwarzschild objective, but nevertheless it is possible to determine the vertical beam size using the PSF dominated image.

Figure 4 shows the vertical projection with a projection width of 1.5 μm, taken at the horizontal CCD position $x = 160\ \mu$m in Fig. 3. Together, the blue dots and the green triangles in this figure represent the measured vertical projection. In order to estimate the beam size, the following approximation for the central part of the distribution was proposed in [11]:

$$f(y) = q_3 + \frac{q_0\, q_1^2}{q_2\sqrt{2q_1^{-2} + q_2^{-2}}} \frac{2q_2^4 + q_1^2(q_2^2 + y^2)}{(q_1^2 + 2q_2^2)^2} e^{-\frac{y^2}{q_1^2+2q_2^2}}, \quad (1)$$

with y the vertical coordinate and q_0, q_1, q_2, q_3 free fit parameters. Parameter q_1 defines the peak position and q_2 the vertical rms beam size (see [11] for details). Parameters q_0 and q_3 serves for scaling of the distribution amplitude and zero level.

The red solid line in Fig.4 shows a fit to the experimental data according to Eq. (1), and it was carried out only for the points indicated by the green triangles. The reason for this restriction is that the beam size in mainly sensitive on the contrast ration between the maxima and the central dip of the distribution, the distribution tails are far less sensitive on beam size effects. The selected data range allowed to carry out the best fit using Wolfram Mathematica built–in function `NonlinearModelFit`. The fit procedure resulted in the following parameter values: $q_1 = (2.04 \pm 0.04)\ \mu$m, $q_2 = (1.37 \pm 0.07)\ \mu$m.

In the experiment with the LYSO:Ce scintillator carried out at the same time under the same conditions, an rms beam size of $\sigma_y = 1.44\ \mu$m was deduced [10].

ISBN 978-3-95450-176-2

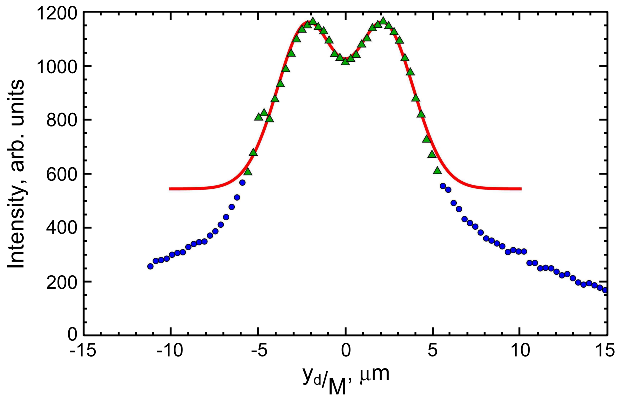

Figure 4: Beam image projection. Green triangles - experimental points used for the approximation, blue dots - experimental points excluded from the approximation, solid line - fit function Eq. (1).

The obtained value for the q_1 fit parameter is very surprising due to the fact that it is equal to $q_1 \simeq 5\lambda$ at $\lambda = 400$ nm. According to the OTR PSF theory, in an ideal optical system the PSF peak position is defined by the numerical aperture and the radiation wavelength [1,4]. In the case of $NA = 0.19$ and $\lambda = 400$ nm, the peak position should be equal to approx. 1 μm. The obtained value of $q_1 = (2.04 \pm 0.04)$ μm is more expected at the $NA \simeq 0.1$ at $\lambda = 400$ nm. In the LYSO:Ce experiment, the numerical aperture value was estimated to be equal to $NA = 0.2$ that is much closer to the manufacturer information [10]. This measured difference is not clear yet and may be caused by the fact that the scintillator light is emitted isotropically while the OTR cone is very narrow. This fact needs additional theoretical investigations.

SUMMARY AND OUTLOOK

This report presents preliminary results of an experiment devoted to the measurement of micron–scale vertical beam size using OTR in the visible range with a Schwarzschild objective based optical scheme. The advantage of the selected Schwarzschild objective was a high magnification and low aberrations that allow a precise measurement of PSF dominated images. Based on the fit proposed in [11] a beam size was deduced that amounted σ_y=(1.37 ± 0.07) μm, showing very good agreement with scintillator measurements performed in the same experiment [10]. Such an agreement for micron–based beam size measurements is very promising and indicates the high potential of the optical scheme used.

Despite the fact that the agreement in the beam size measurement is rather good, the numerical aperture of the Schwarzschild objective deduced from both beam size measurements is different: according to the manufacturer it is $NA = 0.19$, the scintillator measurement best fit results in $NA = 0.2$, and from the OTR measurement it is expected to be $NA \simeq 0.1$. Such a difference is not clear yet and may be caused by the fact that scintillator light is emitted isotropically while OTR obeys a strong directivity with a very narrow emission cone. However, this fact needs additional investigations and will be carried out as one of the next steps.

ACKNOWLEDGMENT

The work was partially supported by the Russian Ministry of Education and Science within the program "Nauka" Grant No. 3.709.2014/K and RFBR grant 14-02-01032.

REFERENCES

[1] M. Castellano and V. A. Verzilov, Phys. Rev. Spec. Top. Accel. Beams 1 (1998) 062801.

[2] A.P. Potylitsyn, in *Advanced Radiation Sources and Applications* ed. by H. Wiedemann (2006) 149.

[3] D. Xiang, W.-H. Huang, Nucl. Instr. Meth. Phys. Res. A 570 (2007) 357.

[4] G. Kube, Imaging with Optical Transition Radiation, Transverse Beam Diagnostics for the XFEL, TESLA-FEL 2008-01 (2008).

[5] L.G. Sukhikh, G. Kube, S. Bajt, W. Lauth, Yu. A. Popov, and A. P. Potylitsyn, Phys. Rev. Spec. Top. Accel. Beams 17 (2014) 112805.

[6] A. Aryshev, N. Terunuma, J. Urakawa, S.T. Boogert, P. Karataev, and D. Howell in *Proceedings of the 2011 International Particle Accelerator Conference, San Sebastian, Spain, 2011*, (JACoW, New York, 2011), p.1965, WEOBB01.

[7] K. Kruchinin, S.T. Boogert, P. Karataev, L. J. Nevay, B. Bolzon, T. Lefevre, S. Mazzoni, A. Aryshev, M. Shevelev, N. Terunuma, and J. Urakawa in *Proceedings of the 2013 International Beam Instrumentation Conference, Oxford, UK, 2013*, (JACoW, New York, 2013), p.615, WEAL2.

[8] G. Kube, S. Bajt, Yu.A. Popov, A.P. Potylitsyn, L.G. Sukhikh, W. Lauth in *Proceedings of the 2014 International Particle Accelerator Conference, Shanghai, China, 2013*, (JACoW, New York, 2013), p.488, MOPME010.

[9] Igor A. Artyukov, Proc. of SPIE 8678 (2012) 86780A.

[10] G. Kube, S. Bajt, A.P. Potylitsyn, L.G. Sukhikh, A.V. Vukolov,I.A. Artyukov, and, W. Lauth, these proceedings, TUPB012, IBIC 2015, Melbourne, Australia (2015).

[11] L.G. Sukhikh, G. Kube, and A. P. Potylitsyn, Transverse Beam Profile Diagnostics based on Optical Transition Radiation De-Focusing Effect, submitted to Phys. Rev. Spec. Top. Accel. Beams.

ISBN 978-3-95450-176-2

TRANSVERSE BEAM PROFILE IMAGING OF FEW-MICROMETER BEAM SIZES BASED ON A SCINTILLATOR SCREEN

G. Kube, S. Bajt, DESY, Hamburg, Germany
A.P. Potylitsyn, L.G. Sukhikh, A.V. Vukolov, Tomsk Polytechnic University, Tomsk, Russia
I.A. Artyukov, P.N. Lebedev Physics Institute, Moscow, Russia
W. Lauth, Institut für Kernphysik, Mainz, Germany

Abstract

Standard beam profile measurements of high–brightness electron beams based on optical transition radiation (OTR) may be hampered by coherence effects induced by the microbunching instability which render a direct beam imaging impossible. As consequence, for modern linac based 4^{th} generation light sources as the European XFEL which is currently under construction in Hamburg, transverse beam profile measurements are based on scintillating screen monitors. However, the resolution of a scintillator based monitor is limited due to intrinsic material properties and the observation geometry. In this report, a beam size measurement in the order of a few micrometer is presented using a LYSO scintillator, and discussed in view of the possible achievable resolution.

INTRODUCTION

Transverse beam profile diagnostics in electron linacs is widely based on optical transition radiation (OTR) as standard technique which is generated when a charged particle beam crosses the boundary between two media with different dielectric properties. Unfortunately, microbunching instabilities in high–brightness electron beams of modern linac–driven free–electron lasers (FELs) can lead to coherence effects in the emission of OTR, thus rendering it impossible to obtain a direct image of the particle beam. The observation of coherent OTR (COTR) has been reported by several facilities (see e.g. Ref. [1]), and in the meantime the effect of the microbunching instability is well understood [2]. In order to allow beam profile measurements in the presence of the instability, transition radiation based imaging in the EUV spectral region was successfully tested [3,4]. An alternative concept is to use scintillation screens because the emission of the scintillation light is a stochastic process from many atoms which is completely insensitive to the longitudinal bunch structure. A comprehensive overview over scintillating screen applications in particle beam diagnostics is given e.g. in Refs. [5, 6].

In a series of test measurements performed in the past few years, the applicability of inorganic scintillators for high resolution electron beam profile measurements was investigated [7, 8]. Most notably, the dependency of the resolution on the scintillator material and on the observation geometry was studied with respect to resolve beam profiles in the order of several tens of micrometers. Based on these measurements, high resolution screen monitor stations were designed for the European XFEL which is currently under construction at DESY in Hamburg (Germany) [9]. Prototype monitors of this type are successfully in operation since about two years at the FLASH2 undulator beamline of the free-electron laser user facility FLASH at DESY [10]. These monitors use a 200 μm thick LYSO screen as scintillator.

The objective of the present study was to investigate the achievable resolution for micrometer beam sizes. For this purpose, scintillator based beam size measurements were performed at the 855 MeV beam of the Mainz Microtron MAMI (University of Mainz, Germany) which are presented in the following. Based on these measurements, the dependency of the beam size sensitivity on different experimental parameters was studied theoretically using a simple model to describe the scintillator influence.

EXPERIMENT AND DATA TAKING

The experiment was performed at the 855 MeV electron beam of MAMI with a beam current of about 250 pA. Fig. 1 shows a sketch of the experimental setup. The surface of

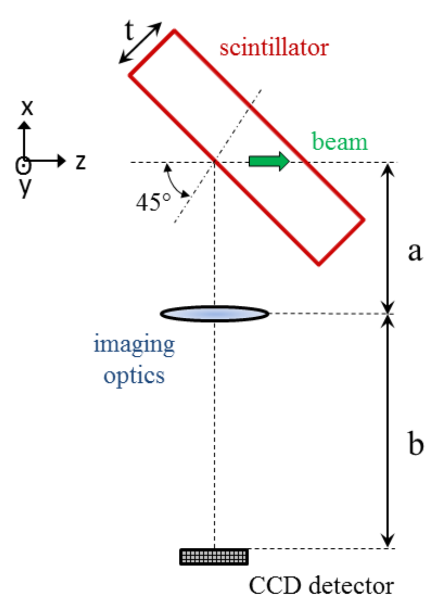

Figure 1: Sketch of the experimental setup (not to scale). The scintillator surface is rotated by 45 deg around the y–axis, observation is performed under 90 deg with respect to the beam axis.

a LYSO ($Lu_{2-x}Y_xSiO_5$:Ce) scintillator with thickness t = 200 μm from the company *OmegaPiezo* [11] was tilted by 45 deg with respect to the beam axis, and observation was performed under 90 deg. The scintillating light generated by the electron beam inside the scintillator was imaged via an imaging optics onto a spatial resolving detector (CCD). As imaging optics, a Schwarzschild objective with nominal numerical aperture NA = 0.19 and focal length f = 26.90 mm was used which is described in detail in Ref. [12]. With an object distance a = 27.54 mm and an image distance b = 1155.46 mm, the overall optical magnification of the system amounted to M = 41.95. The spatial resolving detector was a scientific grade CCD camera (ANDOR DO434 BN) with 1024×1024 pixels and a pixel size of 13×13 μm^2. For the measurements presented in the following, in vertical direction the range of interest was restricted to 275 pixels.

The scintillator measurements were performed in conjunction with an experiment to resolve sub–micron beam sizes based on OTR which required the chosen experimental geometry [4]. However, for resolution studies with a scintillator the 90 deg observation geometry is counteractive in the tilted horizontal ($x-$) plane because of the strong resolution broadening contribution, see Ref. [8]. Therefore, in the following only the vertical ($y-$) plane is considered for the resolution analysis.

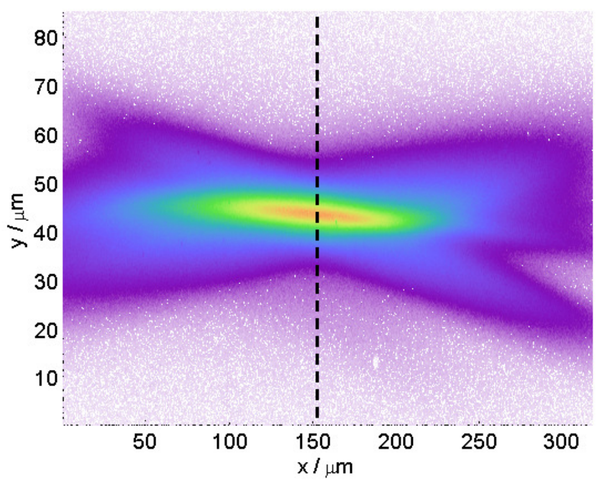

Figure 2: Beam image from LYSO scintillator, recorded with the CCD. The horizontal resp. vertical scales correspond to the object plane. The dashed line indicates the position onto the CCD chip which was used for the vertical profile analysis.

In Fig. 2 a beam spot measurement is shown which is the basis for the subsequent discussion. As can be seen, the beam image has a central core which resembles a Gaussian distribution, but it exhibits additional tails. These tails are caused by the scintillator, but also by the depth–of–focus effect of the optical system because the object plane (scintillator surface) was tilted versus the image plane (CCD chip). The horizontal position along the CCD at which the imaging condition is fulfilled is determined by the waist in the vertical intensity distribution, cf. Fig. 2. This fact could simply be verified in the experiment by moving the Schwarzschild objective slightly along the optical axis, thus observing a horizontal shift of the waist onto the CCD.

ANALYSIS

In order to get rid of the depth–of–focus contribution, the analysis was performed only for that part onto the CCD for which the focusing condition is fulfilled. Therefore, in the following only the cut along the CCD column indicated by the dashed line in Fig. 2 is considered to represent the measured vertical beam distribution.

For the description of the scintillator properties and for the direct comparison with the experiment, the scintillator resolution was simulated using the optical ray–tracing program ZEMAX© [13], applying a simple model which was used earlier to describe the impact of the observation geometry [7, 8]. In this model, the scintillation light emission from a single electron is represented by a line source located inside the LYSO crystal which emits isotropically. The scintillator material properties are described by the wavelength dependent index of refraction, using a Sellmeier representation based on the data in Ref. [14]. The experimental setup in Fig. 1 is used as optical configuration, but for the sake of simplicity the imaging optics is described by a paraxial lens with the same focal length and NA than the Schwarzschild objective. For each configuration under investigation, in total 10^8 rays at a fixed emission wavelength (normally at the LYSO peak emission wavelength of 420 nm) are traced from inside the scintillator to the CCD, applying non–sequential ray–tracing. The resulting 2–dimensional intensity distribution is used as single particle resolution function (SPF), thus characterizing the scintillator influence. Finally, the resulting SPF is convolved with a 2–dim. Gaussian describing the electron beam profile, and the vertical cut through the maximum of this con-

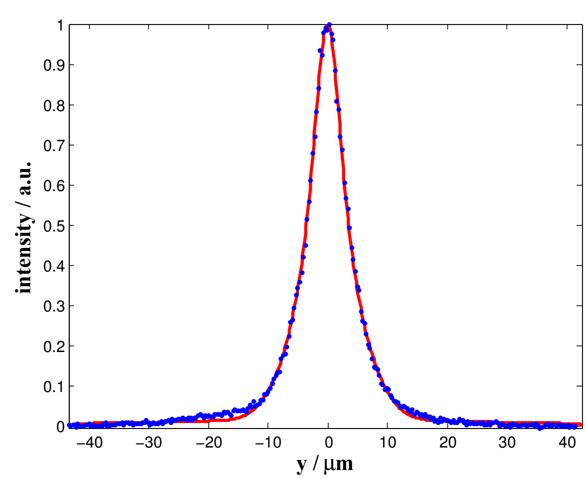

Figure 3: Comparison between measurement (blue dots) and simulation (red line). Both data sets were normalized to their maximum values. The calculation was performed for NA = 0.20 and a beam size of σ_y = 1.44 μm.

ISBN 978-3-95450-176-2

volution is compared with the cut along the experimentally recorded and background corrected CCD data as explained before. The agreement between simulation/convolution and the experimental data is evaluated based on a χ^2 calculation.

The comparison between the vertical beam profile measurement and the simulation shown in Fig. 3 suggests that the observed profile is described in a satisfactory way by means of the scintillator model described before. Moreover, the beam size of $\sigma_y = 1.44\ \mu$m used for the calculation indicates that it is possible to resolve transverse beam sizes down to the few micrometer level, perhaps even in the sub–micrometer range. The numerical aperture of NA = 0.20 for which the best agreement between measurement and simulation was achieved is slightly larger than the expected one of 0.19, which may be caused by the simplified description of the optical system by a paraxial lens. However, in the following the influence of some parameters is investigated and discussed in view of sensitivity for beam size determination.

Beam Size Fig.4 shows a comparison between the measured beam profile and a simulated SPF which was convolved with different Gaussian distributions with beam sizes from 1-2 μm. As can be seen from this comparison, the difference in beam size is clearly visible, and the variation in the beam size affects the profile in the central part of the distribution. From this comparison it can be concluded that the sensitivity of the scintillator based beam size measurement is better than 1 μm.

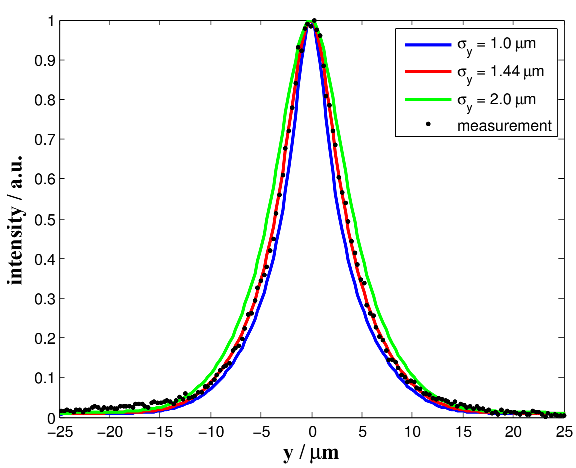

Figure 4: Comparison between measurement (black dots) and simulated SPF with subsequent convolution for three different vertical beam sizes (solid lines). The simulation was performed for NA = 0.20 at the LYSO peak emission wavelength $\lambda = 420$ nm.

Numerical Aperture In the next step, SPFs were simulated for different numerical apertures and then convolved with beam distributions. Based on the χ^2 calculation, for each NA the vertical beam size was determined which resulted in the best agreement with the experimental data. As

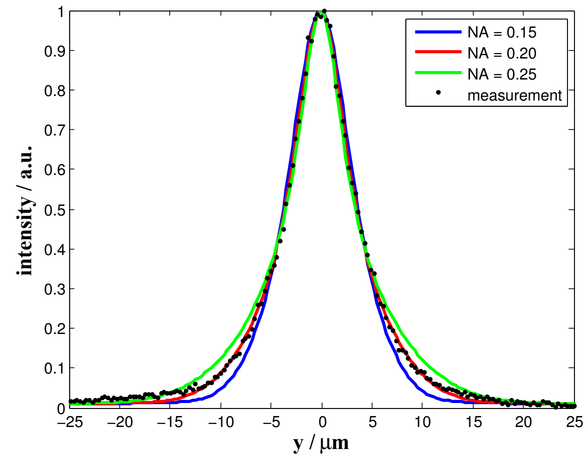

Figure 5: Comparison between measurement (black dots) and simulated SPFs for three different NAs (solid lines) with subsequent convolution. The simulations were performed for $\lambda = 420$ nm.

an example, Fig. 5 shows a comparison for three different NA simulations. As can be seen from this figure, a difference in NA affects the profile in the tails of the distribution. Hence, variations in beam size and NA have different effects on the vertical beam distribution and can therefore be disentangled.

Fig. 6 summarizes the results of this investigation. As can be seen, with increasing NA the beam size decreases. This effect is probably caused by the minimization procedure: with increasing NA there is an increased contribution from the tails of the distribution, cf. Fig. 5, which is compensated by decreasing the beam size. However, as can be seen from the bottom of Fig. 6, there is a well defined parameter set (NA, $\sigma_y)_{opt}$ by which the measured distribution can be

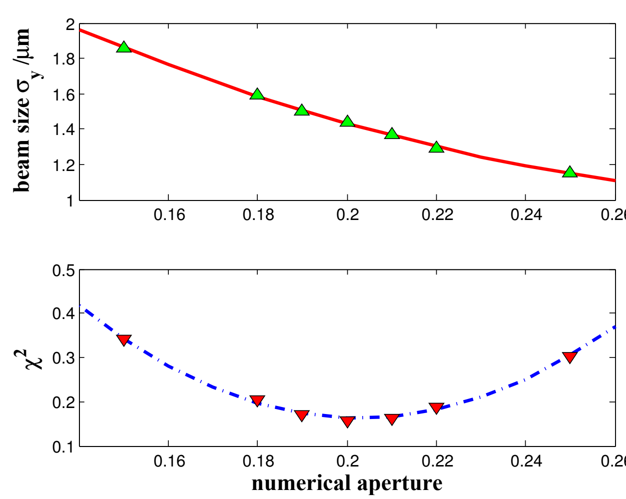

Figure 6: Top: Vertical beam size as function of the numerical aperture. The solid line shows a parabolic fit simply to guide the eyes. Bottom: The calculated χ^2 as function of NA indicates a well defined minimum.

characterized. As a conclusion, if there is an uncertainty in the numerical aperture it will be possible to determine both, beam size and aperture, from the experiment. At the other hand, according to Fig.6 the beam size variation required to compensate the uncertainty in NA is well below 1 μm , i.e. the sensitivity of the scintillator based beam size measurement is still better than 1 μm, even if the NA is not exactly known.

Wavelength As last point the dependency of the vertical beam size determination on the emission wavelength was investigated. LYSO has an emission spectrum from λ = 350 nm up to 620 nm with the peak emission at 420 nm. In the geometric ray–tracing model used to describe the scintillator properties, the wavelength dependency is introduced by the wavelength dependent index of refraction n which influences the refraction at the boundary between scintillator and vacuum. However, in the wavelength region from 360 nm up to 500 nm, where data for n were accessible [14], it decreases only slightly from $n(360nm) = 1.88$ down to $n(500nm) = 1.83$. Different SPFs were simulated for wavelengths between 400 nm and 500 nm, and the vertical beam size was deduced as described before. However, the variation in σ_y between 1.42 μm and 1.46 μm is negligible compared e.g. to the NA influence, therefore the wavelength dependency plays a minor role following the model simulations.

It should be noted that according to the manufacturer the LYSO refractive index at the peak emission wavelength amounts to $n(420nm) = 1.82$ [11] instead of 1.85 according to the Sellmeier parametrization [14]. However, due to the wavelength insensitivity this offset is negligible.

IMPROVEMENTS

Based on the model simulations described before, in this section possible improvements will be discussed which may help to increase the beam size sensitivity of a scintillator based profile measurement. In Fig. 7 the calculated vertical profile is shown for illustration together with the simulated SPF and the vertical electron beam profile. As can be seen from this comparison, the calculated profile is dominated by the SPF contribution. The best way to increase the beam size sensitivity is therefore to minimize this contribution.

A possibility to decrease the SPF contribution in vertical direction is to use a thinner scintillator. Fig. 8 shows simulated SPFs for different scintillator thicknesses and the same parameter set as before. As can be seen, for thinner scintillators the SPF contribution shrinks down and the beam size sensitivity increases. Going to much smaller thicknesses would even further reduce the SPF contribution, however from technical point of view the handling of a 50 μm thick scintillator is already difficult.

It is interesting to note that there is no significant difference between the SPF of a 200 μm and a 500 μm thick scintillator, in Fig. 8 they cannot be distinguished from each other. This observation can be interpreted such that from a

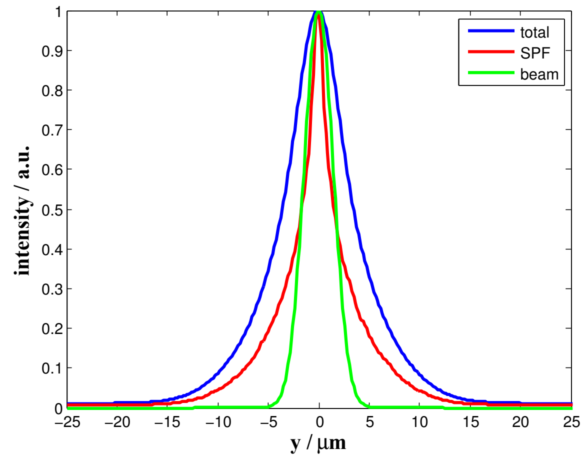

Figure 7: Contribution of the SPF (red curve) for NA = 0.20, λ = 420 nm and the vertical beam profile (green curve) for σ_y = 1.44 μm to the best fit of the observed beam profile (blue curve).

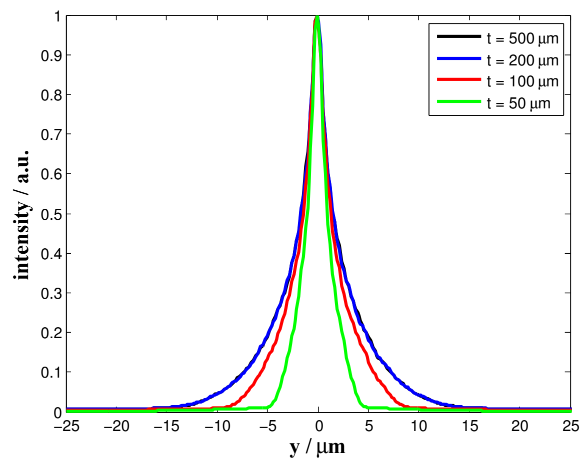

Figure 8: Simulated SPFs for different scintillator thicknesses. The simulations were performed for NA = 0.20 and λ = 420 nm.

certain depth inside the scintillator, the radiation does not contribute significantly to the image formation, a point that has to be investigated more detailed in the future.

A further possibility to reduce the SPF is to change the observation geometry. As already mentioned in the introduction, the horizontal resolution is strongly affected by the observation geometry, and especially the 90 deg geometry used in this experiment is not optimal, see e.g. Refs. [7, 8]. In the vertical plane there exists additionally a dependence which is far less pronounced and which is beyond the scope of this investigation.

An important step towards a reliable high–resolution profile measurement can be achieved if the full 2–dim. information recorded by the CCD will be available for the analysis. In the present experiment the drawback was the depth–of–focus influence which allowed to use only a small region of the CCD. In order to correct perspective distortion

ISBN 978-3-95450-176-2

caused by the observation geometry over the whole CCD chip, the Scheimpflug principle can applied, see e.g. Ref. [15]. This principle which states that a planar object (scintillation screen) not being parallel to the image plane (CCD chip) will be completely in focus if the extended object-, lens- and image planes will intersect in one line, is already successfully applied for the screen monitors at the European XFEL [9]. In this case the SPF would correspond to the classical Point Spread Function (PSF), and the full 2–dim. beam profile could be reconstructed by classical deconvolution algorithms known from image processing, as for example the Lucy–Richardson algorithm [16].

SUMMARY AND DISCUSSION

In this report, a high resolution beam profile measurement based on a scintillating screen monitor is presented. Using a 200 μm thick LYSO:Ce screen it was possible to resolve a vertical beam size of σ_y = 1.44 μm. Based on a simple model to simulate the scintillator properties, the impact of different parameters on the sensitivity for beam size determination was investigated and improvements were pointed out.

However, care has to be taken specifying an absolute value for the beam size, the extracted value of 1.44 μm can be considered only as an upper limit. In this context one has to keep in mind that the resolution of a scintillator based profile measurement depends on the light generation and the light propagation. So far only the latter case was considered, i.e. the resolution contribution when the light produced inside the scintillator crystal has to reach the detector to contribute to the measurement, and for this it has to cross the boundary between scintillator and vacuum. But the light generation mechanism itself is a multi–stage process: according to Ref. [17], the sequence of processes leading to scintillation in a medium consists of 4 phases: (1) energy conversion, i.e. initial energy release with the formation of "hot" electrons and holes, (2) thermalization, i.e. the formation of electron-hole (e-h) pairs with an energy approximately equal to the band gap, (3) energy transfer to the luminescent centers, and (4) radiative relaxation of the excited centers. In Ref. [7] it was assumed that the first stage in this sequence dominates the resolution contribution, and the effect was estimated via the Fermi radius R_M for high–energetic electrons to be negligible. To estimate the contribution of the light generation process, an independent beam profile measurement is required which is not affected by this effect.

Such a measurement is available because the scintillator investigations presented here were performed in conjunction with an experiment to resolve sub–micron beam sizes based on OTR [4], and according to that experiment a beam size of σ_y = 1.37 μm was deduced [18]. Under the assumption that the discrepancy in both beam size measurements is caused by the light generation process inside the scintillator, this contribution can be estimated by subtracting both values quadratically, resulting in σ_{res} = 0.44 μm. This value can be considered to be an estimate for the fundamental resolution limit of a scintillator based profile measurement using a LYSO crystal. If a better resolution is required it will be necessary to find an appropriate scintillator material.

ACKNOWLEDGMENT

This work was partly supported by the by the Russian Ministry of Education and Science within the program "Nauka" Grant No. 3.709.2014/K.

REFERENCES

[1] S. Wesch and B. Schmidt, Proc. DIPAC'11, Hamburg, Germany, May 2011, WEOA01, p.539 (2011).

[2] G. Stupakov, Proc. IPAC'14, Dresden, Germany, June 2014, THYA01, p.2789 (2014).

[3] L.G. Sukhikh, G. Kube, S. Bajt *et al.*, Phys. Rev. ST Accel. Beams **17** (2014) 112805.

[4] L.G. Sukhikh, G. Kube, I.A. Artyukov *et al.*, these proceedings, TUPB011.

[5] B. Walasek–Höhne and G. Kube, Proc. DIPAC'11, Hamburg, Germany, May 2011, WEOB01, p.553 (2011).

[6] B. Walasek–Höhne *et al.*, IEEE Trans. Nucl. Sci. **59** (2012) 2307.

[7] G. Kube, C. Behrens, W. Lauth, Proc. IPAC'10, Kyoto, Japan, May 2010, MOPD088, p.906 (2010).

[8] G. Kube *et al.*, Proc. IPAC'12, New Orleans (Louisiana), USA, May 2012, WEOAA02, p.2119 (2012).

[9] Ch. Wiebers, M. Holz, G. Kube *et al.* Proc. IBIC'13, Oxford, UK, September 2013, WEPF03, p.807 (2013).

[10] N. Baboi and D. Nölle, Proc. IBIC'14, Monterey (CA), USA, September 2014, THIXB1, p.712 (2014).

[11] `http://omegapiezo.com/index.html`

[12] I.A. Artyukov *et al.*, Opt. Commun. **102** (1993) 401.

[13] `http://www.zemax.com`

[14] M. Kronberger, PhD thesis, Technical University of Wien (2008), CERN-THESIS-2008-043.

[15] H.M. Merklinger, *Focusing the View Camera*, Bedford, Nova Scotia: Seaboard Printing Limited (1996). `http://www.trenholm.org/hmmerk/download.html`

[16] L.B. Lucy, Astronomical Journal **79** (1974) 745. W.H. Richardson, J. Opt. Soc. Am. **62** (1972) 55.

[17] P. Lecoq *et al.*, *Inorganic Scintillators for Detector Systems*, (Springer Verlag, Berlin–Heidelberg, 2006).

[18] L.G. Sukhikh, private communication (2015).

DEVELOPMENT STATUS AND PERFORMANCE STUDIES OF THE NEW MICROTCA BASED BUTTON AND STRIP-LINE BPM ELECTRONICS AT FLASH 2

Bastian Lorbeer*, Nicoleta Baboi, Hans-Thomas Duhme, Frank Schmidt-Foehre, Kay Wittenburg
DESY, Hamburg, Germany

Abstract

The FLASH (Free Electron Laser in Hamburg) facility at DESY (Deutsches Elektronen-Synchrotron) in Germany has been extended by the new undulator line FLASH 2 providing twice as many experimental stations for users in the future [1] . After the acceleration of the electron bunch train up to 1.2 GeV in FLASH, a part of the beam can be kicked into FLASH 2, while the other is going to the old undulator line of FLASH 1. The commissioning phase started in early 2014 and continues parasitically during user operation in FLASH 1. One key point during first beam commissioning is the availability of standard diagnostic devices such as Beam Position Monitors (BPMs) [2]. In the last couple of years new electronics for button and strip-line BPMs have been developed, based on the MTCA.4 standard [3–6]. This new Low Charge BPM (LCBPM) system is designed to work with bunch charges as small as 100 pC in contrast to the old systems at FLASH initially designed for bunch charges of 1 nC and higher. This paper summarizes the development status of the new BPM system and discusses the results of resolution studies of the BPM system.

INTRODUCTION

The demand for beam time at the user facility FLASH increased substantially in the past. In order to fulfill this need the facility has been extended by a new undulator beam line for SASE generation called FLASH2. The desired charges for FLASH 1 and FLASH 2 can be adjusted separately from two laser systems. FLASH2 has seen the first beam on 4th March 2014 and was able to provide SASE (Self Amplified Spontaneous Emission) for the first time on 20 August 2014 [7, 8]. This was done simultaneously to SASE delivery in FLASH1. The electron beam delivered to FLASH2 is accelerated together with the beam for FLASH 1 within the same RF (Radio Frequency) pulse to up to 1.2 GeV after approximately 150 m from the gun and is then kicked....Part of the diagnostics in FLASH2 are button and strip-line monitors at 16 locations in the machine utilizing new MTCA.4 electronics designed at DESY [3–6]. Challenges in the development of this system are the single-bunch resolution requirement of 50 µm, operation at charges below 100 pC and a high bunch repetition rate of up to 4.5 MHz. These requirements were chosen to be compatible with the requirements for the European XFEL [9]. The development status and resolution studies of the BPM system are summarized in this paper.

* bastian.lorbeer@desy.de

MACHINE AND SYSTEM OVERVIEW

The new FLASH2 undulator beam line runs in parallel to the old FLASH1 undulator beam line as it can be seen in Figure 1. It is divided into several sections namely EXTRACTION, SEED, SASE, BURN, and DUMP. Button and strip-line monitors are installed in different locations.

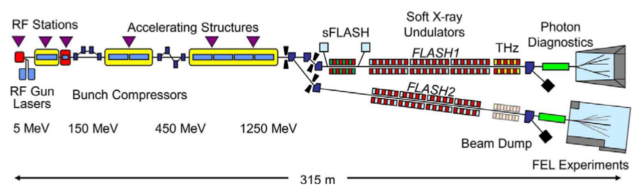

Figure 1: Section overview FLASH.

Most of the LCBPMs are distributed along the EXTRACTION section at the beginning of FLASH2 with nine BPMs. Four BPMs are in the BURN/DUMP section. Due to space limitations in the SASE section three button BPMs have been installed here as well instead of using the more preferable cavity BPMs which offer the required resolution for orbit tuning in the SASE section [10, 11]. A variety of different beam pipe diameters for the button BPMs and a few refurbished strip-line BPMs, with different RF cable lengths ranging from 35 to 58 m, required the development of a very robust but also flexible BPM electronics. Table 1 summarizes all types of BPMs for which the electronics are currently in operation. Electromagnetic field simulations [12] delivered the monitor constants. The button type concept is similar as for the European-XFEL that has been reported in [13], while the strip-line monitors are an old design described in [14].

Table 1: Types of Beam Position Monitors Installed in FLASH2 and Corresponding Monitor Constants

Type	amount	Beam Pipe	Monitor constant
button	2	40 mm	10.6 mm
button	4	34 mm	9.06 mm
button	3	100 mm	23.84 mm
strip-line	4	44 mm	8.678 mm
in-air	1	100 mm	31.25 mm
button	3	10 mm	2.55 mm

An overview of a BPM system can be seen in Figure 2.

The beam excited RF signals in the horizontal and vertical plane respectively are combined after a delay of 100 ns to suppress interference with the next bunch in the train. This so-called Delay Multiplex Single Path Technology (DM-

ISBN 978-3-95450-176-2

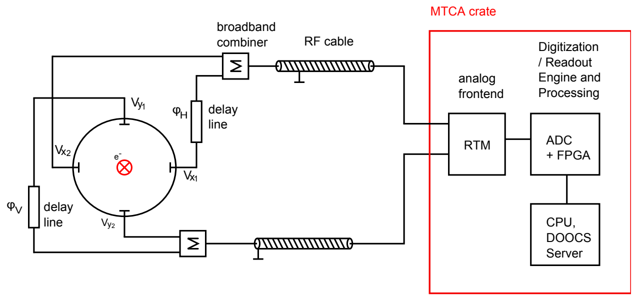

Figure 2: Beam Position Monitor System Overview.

SPT) [15, 16] method has been successfully in operation for many years in HERA[1] at DESY. It successfully proved to suppress the common mode EMI disturbances on the RF cable from the tunnel to the electronic racks. It also halves the number of necessary ADC (Analog Digital Converter) channels for each BPM. The electronics for signal conditioning and processing are separated into an analog RTM (Rear Transition Module) and a digital card. The two cards are housed in a MTCA.4 crate. The position calculation takes place in the Firmware on the digital card and is given by the normalized difference of the signal on opposite electrodes [17]. This position information can then be read from a device server which sends the position information to a so called middle layer server. This collects the data to be displayed in an orbit panel for operation and sends the data to a digital Data Aquisition System (DAQ).

ELECTRONICS

Analog Signal Conditioning

A typical input and output signal for one channel of the radio frequency receiver from a button BPM is shown in Figure 3. The raw data for a single bunch in one plane of the BPM is shown. The data has been taken on a test output port on the analog front-end with a 2 GHz oscilloscope. In order to meet the requirement to measure bunch trains with a repetition rate of up to 4.5 MHz, a delay of 100 ns between opposite electrodes and a peak detector with discharger topology has been chosen. With this method the bunches in the train can be well separated. Moreover the receiver has a large dynamic range to adapt to the specified charge range from 1nC down to 20pC and the measurement at large beam offsets. More details of the analog front-end can be found in [6].

Digital Raw Signal

The position calculation takes place in an FPGA (Field Programmable Gate Array) on a digitizer card. The sample rate of the signal is 125 MHz and the resolution is16 Bits. A typical digitized raw signal for one plane of a single bunch is shown in Figure 4. Due to the additional buffer amplifier and anti aliasing filtering the signal shape looks different from what is measured on the analog test port.

[1] Hadron Elektron Ring Anlage

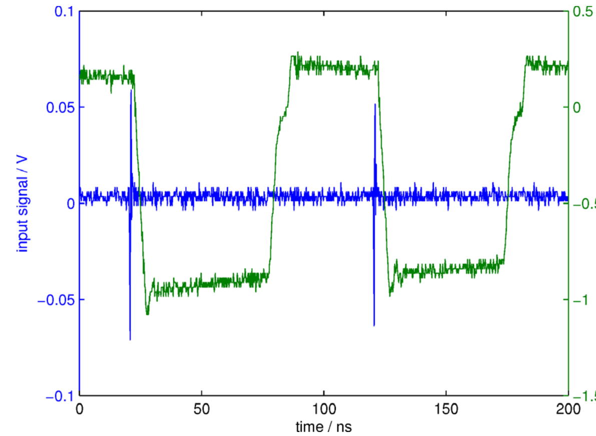

Figure 3: Blue: A typical input signal for the BPM electronics. Green: A typical output signal from the analog front-end before digitization.

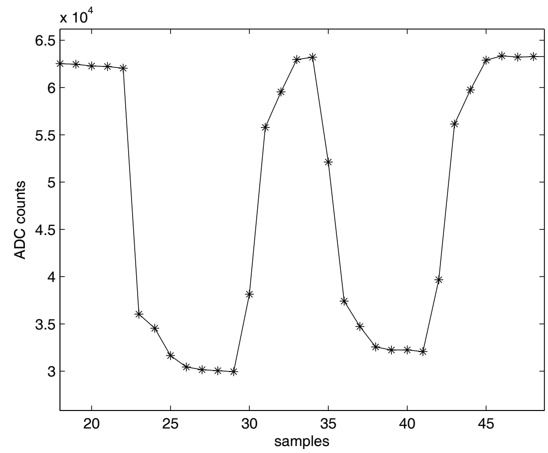

Figure 4: Typical digital raw data.

The custom made firmware (FW) is operating in real time and delivers bunch by bunch information at its output registers. The FW contains registers to adjust the step attenuators on the analog RF front-end. Currently the FW is operating in the so-called quasi-autarchic mode. In this mode the FW receives an external pre-trigger from the accelerator timing system. All other bunch related information is derived from this initial trigger inside the FW. The measured resolution of this mode is discussed in the later section. The best resolution is expected for the fully timing coupled mode in which the sampling points are more stable in the aquired signal.

SYSTEM STATUS

The beam positions calculation has been processed in the FW and are then collected by a device server after the bunch train and are then sent to a BPM middle layer server which displays the beam position for steering purposes to the operator. The middle layer server also provides a time stamp to the event based measurements which is necessary for later data analysis. The insufficient signal strength for three button monitors in the SASE section has been overcome

ISBN 978-3-95450-176-2

by the installation of custom made pre-amplifiers inside the tunnel. The position reading is also possible at these locations now.

RESOLUTION MEASUREMENTS

One key feature in the characterization of the BPM is its electronics resolution. In [6] it has been shown that this BPM system already fulfils the single shot resolution of 50 µm. Nevertheless these measurements were not free of beam jitter . In order to characterize the true electronics resolution the beam based fluctuations and the electronics noise contribution to the position measurement from each BPM have to be sparated . One method to separate the two sources relies on the fact that the transverse beam movement for the single bunch position measured by all BPMs in the machine is a correlated contribution to the measurement while the individual noise of each BPM remains uncorrelated. Under such conditions a prediction method based on linear regression can be applied. One pre condition to identify correlated and uncorrelated contributions to the BPM readings is the synchronous reading of beam positions from all BPMs. The implementation of the middle layer allows this. After taking data of 300 subsequent bunches at a charge of 85 pC and applying the method which has been described in detail in [18] a position prediction vector could be identified.

It is based on all 16 button and strip-line BPM readings in FLASH 2 excluding the BPM under test. An example for one button and one strip-line BPM under test plotted against their prediction vectors are shown in Figures 5 and 6.

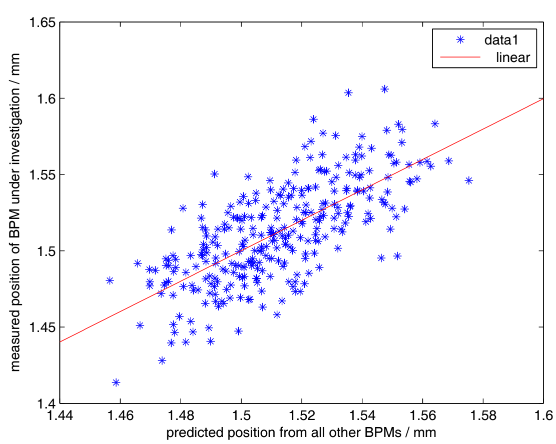

Figure 5: Strip-line monitor correlation plot.

The standard deviation for the strip-line and button monitors are 33 µm and 54 µm respectively. These values include correlated and uncorrelated contributions to the measurement. The residual standard deviation of electronics under test is 23 µm for the strip-line monitor and 32 µm for the button BPM. These values represent the uncorrelated contribution to the measurement and identify the electronics resolution.

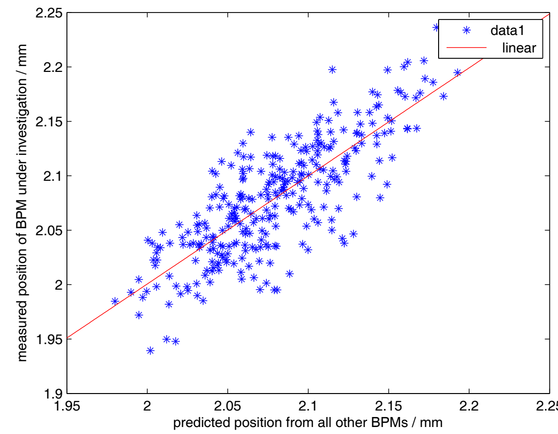

Figure 6: Button monitor Correlation plot

SUMMARY AND OUTLOOK

A new MicroTCA based BPM system has been summarized in this paper. Its performance has been studied using linear regression and it has been found to fulfil the resolution specifications. An improved resolution is expected when a fully timing-coupled FW mode is calculating the BPM position. The development of this mode is under way. In addition a FW upgrade of the Register Interface to a DMA(Direct Memory Access) driver for advanced data throughput is currently investigated.

REFERENCES

[1] `http://flash2.desy.de`

[2] N.Baboi et. al., "Commissioning of the FLASH2 Electron Beam Diagnostics in Respect to its use at the European XFEL", THXB1, IBIC14, Monterey, USA.

[3] PICMG MTCA.4 Revision 1.0, "MicroTCA Enhancements for Rear I/O and Precision Timing", August 22, 2011 `http://www.picmg.com`

[4] B. Lorbeer et al., TUPA19, IBIC2012, Tsukuba, Japan.

[5] F. Schmidt-Föhre et al., THPME117, IPAC2014, Dresden, Germany.

[6] B. Lorbeer et al., TUPF08, IBIC2014, Monterey, USA.

[7] S. Schreiber, B. Faatz, "First Lasing at FLASH2", MOA03, presented at FEL2014, Basel, Switzerland.

[8] K. Honkavaara et al., "FLASH: First Soft X-ray FEL Operating Two Undulator Beamlines Simultaneously", WEB05, FEL2014, Basel, Switzerland.

[9] D. Nölle, "The European XFEL Beam Position Monitor System", Conceptual Design Report, 2010.

[10] M. Stadler et al., "Low-Q Cavity BPM Electronics for E-XFEL, FLASH 2 and SwissFEL", WEPD12, IBIC14, Monterey, US.

[11] D. Lipka et al., "FLASH Undulator BPM Commissioning and Beam Characterization Results", TUPF07, IBIC14, Monterey, US.

[12] D. Lipka private communication.

[13] D. Lipka et. al., "Button BPM Development for the European XFEL", MOPD19, DIPAC2011, Hamburg, Germany.

ISBN 978-3-95450-176-2

[14] D. Nölle, M. Wendt, "TTF2 Beam Monitors for Beam Position, Bunch Charge and Phase Measurements", TUP72, LINAC 2004, Lübeck, Germany.

[15] R. Neumann private communication.

[16] F. Schmidt-Föhre et. al, "BPM system upgrades in the Petra 3 Pre-accelerator chain during the 2008 shutdown", MOPD20, Proceedings of DIPAC09, Basel, Switzerland.

[17] G. Vismara et al., "From Narrow to Wide Band Normalization for Orbit and Trajectory Measurements", BIW98, SLAC, USA.

[18] N. Baboi et. al., "Resolution Studies at Beam Position Monitors at the FLASH Facility at DESY", AIP Conference Proceedings 868, 227 (2006); doi: 10.1063/1.2401409.

ISBN 978-3-95450-176-2

DEVELOPMENT OF NEW BEAM POSITION MONITORS AT COSY

F. Hinder*, F. Trinkel, IKP, Forschungszentrum Jülich, 52425 Jülich, Germany
H.-J. Krause, PGI-8, Forschungszentrum Jülich, 52425 Jülich, Germany
H. Soltner, ZEA-1, Forschungszentrum Jülich, 52425 Jülich, Germany
for the JEDI collaboration†

Abstract

The existence of permanent Electric Dipole Moments (EDMs) of fundamental particles would violate parity and time reversal symmetry. Assuming the CPT-theorem, this leads to CP violation, which is necessary to explain the matter over antimatter dominance in the Universe. Thus, a measurement of a non-zero EDM would be a hint to new physics beyond the Standard Model. The JEDI collaboration (Jülich Electric Dipole moment Investigations) has started investigations towards a direct EDM measurement of protons and deuterons at a storage ring. To measure an EDM signal, systematic effects have to be controlled with high precision. One way of studying systematic effects is the use of new Beam Position Monitors (BPMs) based on a Rogowski coil as a magnetic pick-up. The main advantage of such coil is their high response to an RF signal, i.e. the particle bunch frequency, and their compactness. In a first step the BPMs have been benchmarked in a laboratory test system. In the next step the calibrated BPMs have been installed and tested at the storage ring COSY (Cooler Synchrotron) at Forschungszentrum Jülich. First measurement results are presented.

INTRODUCTION

The JEDI collaboration investigates the feasibility of measuring EDMs of charged particles, namely protons and deuterons, in the magnetic storage ring COSY [1, 2]. The method of choice is the usage of an RF Wien Filter to introduce a build-up of the vertical polarization, which is proportional to the EDM of the particle [3, 4]. A measurement of the orbit is necessary to control systematic effects, which contribute to a polarization build-up which is not related to the EDM [5]. The existing orbit control system, including electrostatic BPMs [6, 7], has to be improved to reduce systematic effects. One step of this improvement is an update of the existing BPM readout electronics [8]. In addition, new BPMs are being developed. These BPMs are magnetostatic pick-ups in a Rogowski coil configuration [9]. In industry the Rogowski coil is a well known device to measure alternating currents (ACs). The primary concept of a torus wound with a wire to measure the current, is modified towards a device which measures the centroid of the current. The spatial sensitivity is reached by winding the torus in parts and measuring the induced voltages in these parts. One advantage of the new device is its thickness of 1 cm compared to the length of the existing BPMs of 13 cm. Due to its small dimension the BPM can be installed at various places in the storage ring.

DESIGN OF ROGOWSKI PICK-UP COILS

The presented concept is based on the idea of determining the position of the beam by measuring the magnetic field induced by the particle flux. The developed Rogowski coil BPM consists of a torus with the following geometric parameters:

- Radius of the torus $R = 40$ mm
- Radius of the tube $a = 5$ mm.

The tube of the torus is wound with one layer of cooper wire with a diameter of 150 μm. The geometric form of the wiring determines the field of application. A full winding is sensitive to the AC beam current going through the torus. Cutting the wiring into two equal halves leads to a measurement of the beam position in one direction of the transversal plane. Dividing the wiring into four segments allows to determine the beam position in both directions of the transversal plane. Figure 1 shows the Rogowski coil in a halved and a quartered configuration. The depicted coordinate system is used in the following mathematical derivation. The two halves of the coil are labeled R and L. The four quarters are labeled R, U, L and D.

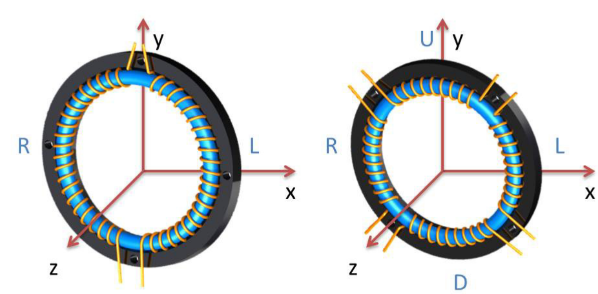

Figure 1: Half and quarter wound Rogowski coils in our coordinate system. The configuration shown on the left hand side permits a position measurement in x-direction. The configuration shown on the right hand side facilitates a measurement of the beam displacement in both directions: x and y.

Magnetic Field of the Particle Beam

The beam current assumed to be a pencil current in z direction perpendicular to the torus. The position with respect

* f.hinder@fz-juelich.de
† http://collaborations.fz-juelich.de/ikp/jedi/index.shtml

ISBN 978-3-95450-176-2

to the center of the torus is given by

$$\vec{r_0} = x_0\vec{e_x} + y_0\vec{e_y} = r_0\cos\varphi_0\vec{e_x} + r_0\sin\varphi_0\vec{e_y}.$$

The magnetic field $\vec{B}$ induced by a particle beam with a current $\vec{I}$ is described by the Biot-Savart law:

$$\vec{B} = \frac{\mu_0}{2\pi}\vec{I}\times\frac{\vec{r'}}{|\vec{r'}|^2} \qquad \text{with} \qquad \vec{r'} = \vec{r} - \vec{r_0},$$

where μ_0 is the vacuum permeability, $\vec{r_0}$ is the beam center and $\vec{r}$ is the position of the point where the magnetic field is measured. The magnetic flux through the Rogowski coil can be calculated by:

$$\Phi = \int_A \vec{B}d\vec{A}, \tag{1}$$

where $\vec{A} = A\vec{e_\varphi}$. For convenience, first the projection of the magnetic field to the $\vec{e_\varphi}$ direction is calculated. The expansion of the projected magnetic field in a Taylor series up to second order for small position deviations from the center of the torus ($r_0/R \ll 1$) leads to:

$$\begin{aligned}\vec{B}\cdot\vec{e_\varphi} = \frac{\mu_0 I}{2\pi}\frac{1}{r}\Bigg[&1 + \cos(\varphi-\varphi_0)\frac{r_0}{r} \\ &+\cos(2\varphi - 2\varphi_0)\left(\frac{r_0}{r}\right)^2 + O\left(\frac{r_0}{r}^3\right)\Bigg].\end{aligned} \tag{2}$$

Induced Voltages

Solving the integral Eq. 1 by using Eq. 2, multiplying the result with the number of windings N and calculating the time derivative lead to the induced voltage in the coil:

$$U_{\text{ind}} = -N\frac{d\Phi}{dt}.$$

For a fully wound coil the induced voltage is:

$$U_{\text{ind},1/1} = \mu_0 N\frac{dI}{dt}\left(R - \sqrt{R^2 - a^2}\right).$$

The result is the same as an analytical solution of Eq. 1 without using a Taylor expansion of the magnetic field [10]. The induced voltage for one half of the coil reads:

$$U_{\text{ind},1/2} = \frac{U_{\text{ind},1/1}}{2}\cdot\left(1 - \frac{2}{\pi\sqrt{R^2-a^2}}x_0\right),$$

if the full coil is cut in the two halves along the y-direction. The induced voltage of a quartered coil features additional terms including $x_0\cdot y_0$, x_0^2 and y_0^2:

$$U_{\text{ind},1/4} = \frac{U_{\text{ind1},1}}{4}\cdot\left(1 - \frac{2\sqrt{2}}{\pi\sqrt{R^2-a^2}}x_0 + O\left(x_0 y_0, x_0^2, y_0^2\right)\right).$$

The position of the particle beam can be computed by calculating the difference and the sum of the voltages of two opposite halves:

$$x_0 = \frac{\pi\sqrt{R^2-a^2}}{2}\frac{\Delta U_{\text{ind},1/2}}{\Sigma U_{\text{ind},1/2}}. \tag{3}$$

For two opposite quarters the corresponding term features non-linear corrections:

$$\frac{\Delta U_{\text{ind},1/4}}{\Sigma U_{\text{ind},1/4}} = \frac{2\sqrt{2}}{\pi\sqrt{R^2-a^2}}x_0 + O\left(x_0\cdot y_0, x_0^2, y_0^2\right).$$

Figure 2 shows the calculation of the difference over sum ratio of two quarters for a beam position in the range of $-35\,\text{mm} < x_0, y_0 < 35\,\text{mm}$.The center of the two quarters are at $x_R = -R$ and $x_L = R$. This configuration leads to a sensitivity to the position x_0 of the particle beam. Using the two other quarters ($y_D = -R$ and $y_U = R$) leads to an equivalent sensitivity for y_0 displacements. The color-coded

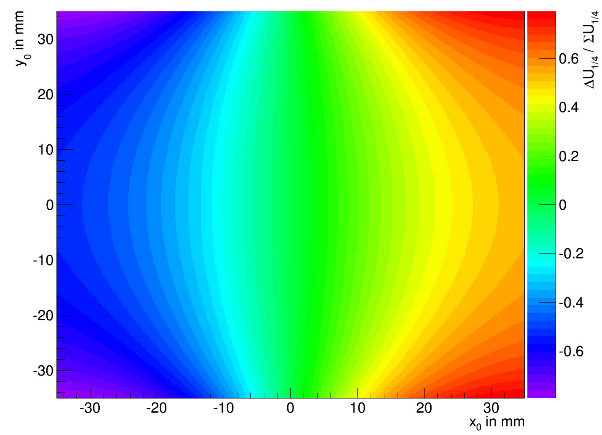

Figure 2: Calculated response signal of a quartered Rogowski coil BPM to the position of an ideal particle beam.

z-axis is the calculated ratio $\frac{\Delta U_{1/4}}{\Sigma U_{1/4}}$,which to first order is proportional to x_0. The influence of the higher-order terms increases with the distance to the torus center.

LABORATORY MEASUREMENTS

A first test of the measurement principle described was carried out in a laboratory setup [11]. With a live wire representing the particle beam. This wire is connected to two $x-y$ micro tables, one at each end. The current parameters are chosen to represent a typical Gaussian bunched particle beam in COSY. The frequency was set to 750 kHz, the intensity corresponds to 10^{10} particles and the width of the longitudinal bunch profile is chosen to be $\frac{\Delta T}{T} = 10\,\%$. The first measurement with this setup was done with a quartered Rogowski coil, aligned as sketched in the right hand side of Fig. 1.

With this installation two measurements were performed. One with the wire centered at $y_0 = 0\,\text{mm}$ and moved along x-direction in the range $x_0 = -30\,\text{mm}$ to 30 mm and the second one under the conditions: $y_0 = 15\,\text{mm}$ and $x_0 = -30\,\text{mm}$ to 30 mm. For both measurements the induced voltages of the two quarters L and R are measured. The calculated ratio $\frac{\Delta U_{LR}}{\Sigma U_{LR}}$ is plotted against the position of the wire in Figs. 3 and 4.

Both measurements show that a position determination using the Rogowski coil BPM is possible. The sensitivity of

ISBN 978-3-95450-176-2

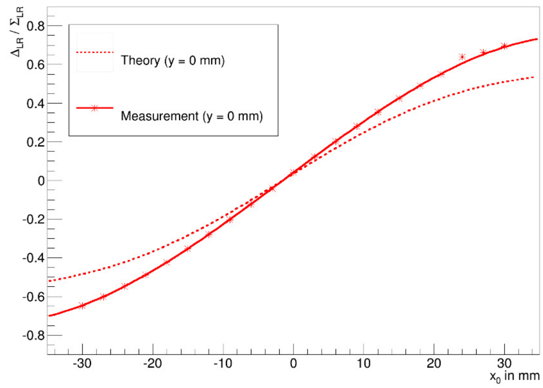

Figure 3: The ratio $\frac{\Delta U_{LR}}{\Sigma U_{LR}}$ for the wire positioned at $y_0 = 0$ mm and $x_0 = -30$ mm to 30 mm. The dotted line represents the theoretical expectation, the solid line is a fit to the data points.

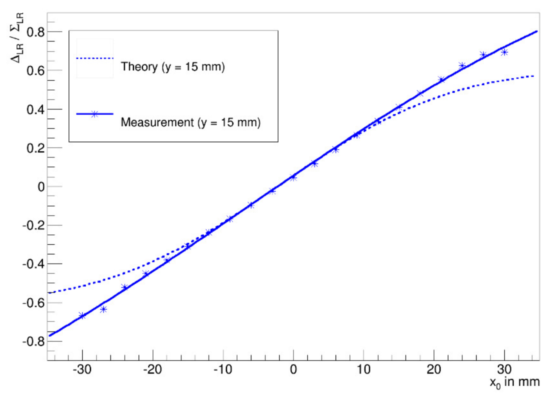

Figure 4: The ratio $\frac{\Delta U_{LR}}{\Sigma U_{LR}}$ for the wire positioned at $y_0 = 15$ mm and $x_0 = -30$ mm to 30 mm. The dotted line represents the theoretical expectation, the solid line is a fit to the data points.

the BPM, the linear term of the measurement, is around 10% higher than the expected value. In addition the non-linear corrections seem to be smaller than those calculated by using the described Taylor expansion. These discrepancies are under investigation and will be analyzed by using a new test bench. This test bench is specially designed to characterize the Rogowski coil BPM for further developments within the EDM experiment of the JEDI collaboration.

MEASUREMENTS AT COSY

Accelerator Setup

To test the measurement principle in a real accelerator environment, a halved Rogowski coil was installed at COSY. The measurements were performed with a bunched deuteron beam with a momentum of 970 MeV/c and a revolution frequency of 750 kHz. One series of measurements was dedicated to the response to a horizontal orbit shift of the beam at the position of the Rogowski coil BPM. This response was induced by applying a local orbit bump. The deflection of the bump was controlled by the change of two corrector magnets. A deuteron beam of about 10^9 particles was injected, accumulated and accelerated to its final momentum. After 33 s the orbit bump with a certain strength was applied. The beam position was measured before and after the orbit bump. The first measurement probed the reference orbit, the second the orbit after the bump. The difference between both measurements is the displacement of the beam, induced by the corrector magnets. Two fills were taken for each bump strength. After these two fills the bump strength was varied and the measurement repeated. Figure 5 illustrates the measurement sequence for two different corrector strengths.

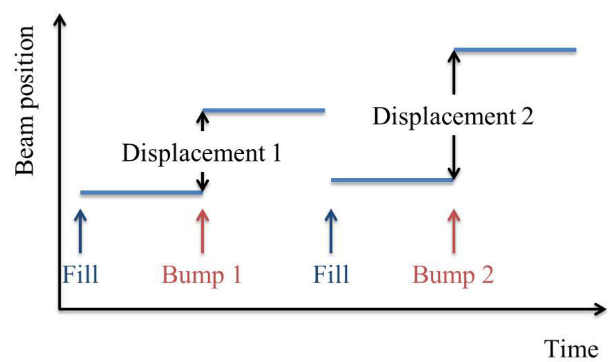

Figure 5: Schematics of the measurement sequence with two different local orbit bumps.

Readout Scheme

Each pick-up coil of the BPM is connected to a pre-amplifier with a high input impedance with an amplification of 13.5 dBm. The pre-amplified signals are fed into a two channel lock-in amplifier[1]. The reference frequency of the lock-in is the beam revolution frequency, defined by the bunching cavity. Figure 6 shows a schematic drawing of the wiring. The chosen 3 dB filter width of the lock-in amplifier was 15.7 Hz. This filter leads to an effective averaging time of 10.2 ms. The sampling rate of the device was set to 225 Sa/s.

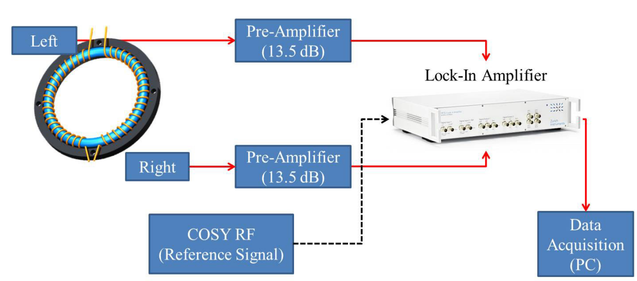

Figure 6: Readout scheme for the signals of the two halves of the Rogowski coil.

[1] HF2LI from Zürich Instruments (`http://www.zhinst.com/`)

ISBN 978-3-95450-176-2

Analysis of the Data

The displacement of the beam induced by the orbit bump is determined by using two measurement intervals. Each interval has a length of 4.45 s. For each data point the beam position is calculated using Eq. 3. The measured beam position $P_{1,2}$ at each interval is calculated by averaging the 1000 data points. The statistical error of the measured beam position is $\sigma_{P_{1,2}} = 3\ \mu$m for each interval. The difference of these two measurements corresponds to the displacement:

$$\Delta P = P_2 - P_1 \pm \sqrt{2} \cdot \sigma_{P_{1,2}}. \tag{4}$$

In addition to the statistical uncertainty a systematic uncertainty is estimated from the variations of the measured displacement ΔP_{fill} from the first fill to the second fill for constant magnet settings. The variations of the change in the displacement is plotted in Fig. 7. The RMS value

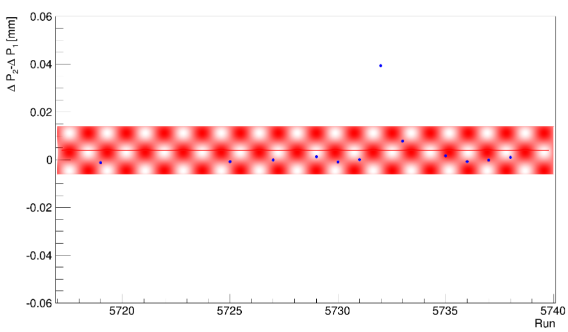

Figure 7: Displacement variations from fill to fill for constant magnet settings. The width of the colored band represents the RMS of the shown variations.

$\sigma_{var} \approx 10\ \mu$m of this variation is considered as an additional source of uncertainty. In summary, the uncertainty is given by:

$$\sigma^2_{\Delta P} = 2 \cdot \sigma^2_{P_{1,2}} + \sigma^2_{var} \approx 10\ \mu\text{m}. \tag{5}$$

Measurement Results

The performance of the Rogowski coil BPM is analyzed by plotting the measured displacements ΔP against the change of the strength of the two corrector magnets. Figure 8 displays the corresponding plot for 13 different settings of the corrector magnets. The data suggest a complete linear dependence on the beam position over a range of about ±8 mm. The linear fit describes the given data points very well, the reduced $\chi^2 = 9/11$ confirms the expected linear behavior. In addition the residua show no significant systematic effect, they are uniformly distributed.

Since the existing BPM system at COSY does not provide a measurement of the beam position at the shown accuracy, a calibration against the existing system isn't done. An absolute calibration will be carried out with the new test system, described before.

In addition to the precisely linear sensitivity of the BPM, the influence by a change of the particle beam perpendicular

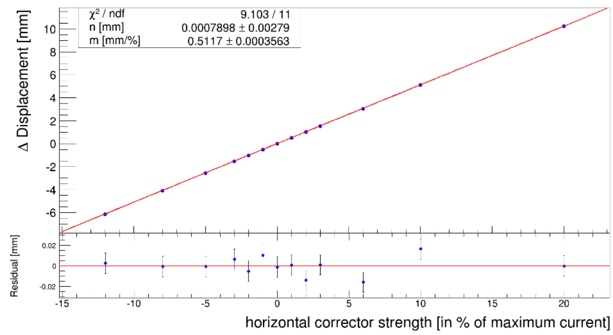

Figure 8: Test of the linearity of the BPM response to the corrector magnet excitation, which is proportional to a horizontal beam displacement at the BPM.

to the measurement direction is studied. The measurement principle is similar to the one used for the horizontal measurement: The beam is moved in y-direction with a vertical orbit bump, induced by two corrector magnets. The strength of the magnets is directly proportional to the vertical beam displacement at the position of the Rogowski coil. With a perfectly aligned BPM and no vertical-horizontal coupling, the measured displacement should be independent of the change of the beam position in y-direction. The corresponding measurement result is shown in fig. 9.

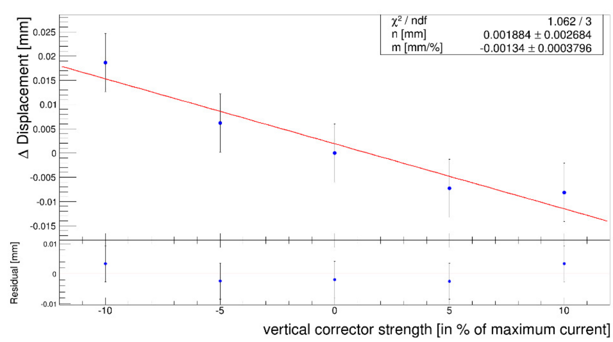

Figure 9: The measured horizontal beam displacement plotted against the corrector strength, which is proportional to the vertical beam movement.

A linear function is fitted to the data points. The slope is $m = (1.3 \pm 0.4)\ \mu$m/%, which is 3σ larger than 0. This small deviation from 0 can be driven from tilts in the magnets or from a tilt of the BPM itself. Both these effects may be distinguishable with an upgraded BPM system. In comparison to the horizontal case, the vertical sensitivity is about 400 times smaller.

SUMMARY

A new concept of a magnetostatic BPM, described by a simple mathematical model, is presented. First measurements in a laboratory demonstrate the applicability of Rogowski coils as BPMs for bunched particle beams.

ISBN 978-3-95450-176-2

For a Rogowski coil BPM wound with two wires, each covering an angle of 180°, the spatial sensitivity of the coil is completely linear. This prediction has been proven by a first operation of the BPM in an accelerator environment. In the measured range of ±8 mm, the sensitivity was found to be completely linear. In addition the measured sensitivity to the perpendicular axis is at least 400 times smaller and can be regarded as negligible within the confidence interval. All in all, the Rogowski coil BPM in the configuration with two opposite windings allows a precise measurement of the beam position in one direction, independent of the beam position in the second, perpendicular direction. In future work, the Rogowski coil BPMs will be analyzed in more detail in a new test bench which is specially designed to calibrate the BPMs. After the calibration, the BPMs will be installed in COSY in the vicinity of a new RF Wien Filter to enable an alignment of the particle beam with respect to the center of the Wien Filter. This configuration allows a study of systematic effects relevant for EDM measurements.

Outlook toward Future Developments

To reduce the noise of the measured voltages and the resulting position uncertainty, the coils can be cooled down. By changing the geometric form of the windings, the pickups may be used for measurements of higher moments of the beam distribution. Further sensitivity improvement can be achieved by fabricating the coils from superconducting wire and couple them to a SQUID magnetometer.

ACKNOWLEDGMENT

The authors acknowledge the COSY operation group and the diagnostics group for their helpful support during the installation of the Rogowski coil in COSY as well as during the measurements.

REFERENCES

[1] R. Maier, "Cooler synchrotron COSY — Performance and perspectives", *Nuclear Instruments and Methods in Physics Research Section A: Accelerators, Spectrometers, Detectors and Associated Equipment 390*, pp. 1–8 (1997) `http://dx.doi.org/10.1016/S0168-9002(97)00324-0`

[2] C. Weidemann, F. Rathmann, H. Stein, et al., "Toward polarized antiprotons: Machine development for spin-filtering experiments", *Physical Review Special Topics - Accelerators and Beams 18*, 020101 (2015) `http://dx.doi.org/10.1103/PhysRevSTAB.18.020101`

[3] F. Rathmann, A. Saleev, N.N. Nikolaev, "The search for electric dipole moments of light ions in storage rings", *Journal of Physics: Conference Series 447*, 012011 (2013) `http://dx.doi.org/10.1088/1742-6596/447/1/012011`

[4] W. M. Morse, Y. F. Orlov, Y. K. Semertzidis, "rf Wien filter in an electric dipole moment storage ring: The "partially frozen spin" effect", *Physical Review Special Topics - Accelerators and Beams 16*, 114001 (2013) `http://dx.doi.org/10.1103/PhysRevSTAB.16.114001`

[5] M. Rosenthal, A. Lehrach, "Spin Tracking Simulations Towards Electric Dipole Moment Measurements at COSY", *in Proceedings 6th International Particle Accelerator Conference*, IPAC'15, Richmond, VA, USA (2015). `http://jacow.org/IPAC2015/papers/thpf032.pdf`

[6] J. Biri, M. Blasovszky, J. Gigler, et al., "Beam position monitor electronics at the cooler synchrotron COSY Jülich", *IEEE Transactions on Nuclear Science 41*, pp. 221–224 (1994) `http://dx.doi.org/10.1109/23.281493`

[7] R. Maier, J. Bojowald, R. Danzglock, et al., "Non-beam disturbing diagnostics at COSY-Jülich", *in 2nd European Particle Accelerator Conference Proceeding*, EPAC 90, Nice, France (1990), pp. 800–802

[8] C. Böhme, M. Bai, F. Hinder, et al., "Studies for a BPM Upgrade at COSY", *these proceedings*, TUPB017, IBIC'15, Melbourne, Australia (2015)

[9] W. Rogowski, W. Steinhaus, "Die Messung der magnetischen Spannung", *Archiv für Elektrotechnik 1*, pp. 141–150 (1912) `http://dx.doi.org/10.1007/BF01656479`

[10] M. Rezaee, H. Heydari, "Mutual inductances comparison in Rogowski coil with circular and rectangular cross-sections and its improvement", *in 2008 3rd IEEE Conference on Industrial Electronics and Applications (ICIEA)*, pp. 1507–1511 `http://dx.doi.org/10.1109/ICIEA.2008.4582770`

[11] S. Kirfel, S. Mikirtytchiants, R. Schleichert, et al., "Construction of a test station for beam current measurement device", *IKP Annual Report from 2013*, pp. K21f (2013) `http://www.fz-juelich.de/ikp/EN/Service/Download/download_node.html`

ISBN 978-3-95450-176-2

UPGRADE OF THE BEAM PROFILE MONITORING SYSTEM IN THE INJECTION BEAM LINE OF COSY

K. Reimers, C. Böhme, R. Gebel, A. Halama, V. Kamerdzhiev,
Forschungszentrum Jülich, Germany
J.L. Conradie, M.A. Crombie, H.W. Mostert, iThemba LABS, South Africa

Abstract

The cyclotron Julic is used as an injector for the COSY synchrotron and storage ring of 183 m circumference. The 93 m long injection beam line (IBL) transports polarized and unpolarized H^-/D^- ions which are injected into the ring via multi-turn stripping injection. 8 profile monitoring stations are installed in the IBL. Each station contains two harps having 39 wires at 1mm spacing. Each harp is read out by a multichannel pico-amperemeter module designed by iThemba LABS, South Africa, delivering profile data to the COSY control system. The technical details of the upgrade and recent beam profile measurements are presented.

INTRODUCTION

The cooler synchrotron COSY shown in Fig. 1 is operated at the Nuclear Physics Institute at the Forschungszentrum Jülich. It delivers high precision beams of protons and deuterons for experiments in the momentum range of 290 to 3850 MeV/c.

Injection and Beam Cycle

A typical COSY machine cycle consists of injection of particles from the cyclotron into the ring, beam acceleration and storage. Injection momentum is 293 MeV/c for H^- and 538 MeV/c for D^- ions. The shortest cycle at COSY is the test cycle with duration of 2 s. This cycle just contains the injection without acceleration. Injection of particles into the COSY ring is gated by the so called macro-pulse of typically 5-20 ms duration. Only during this time interval beam profiles in the IBL are measurable. The macro-pulse signal therefore is used to trigger the beam profile measurement.

IBL Beam Instrumentation

Figure 2 shows the COSY IBL consisting of 4 bent and 4 straight sections with an overall length of 93 m. Phase probes and harps are installed in the IBL for longitudinal and transverse beam diagnostics. This paper deals with transverse beam diagnostics only. The harps allow the detection of beam shape, beam position and intensity.

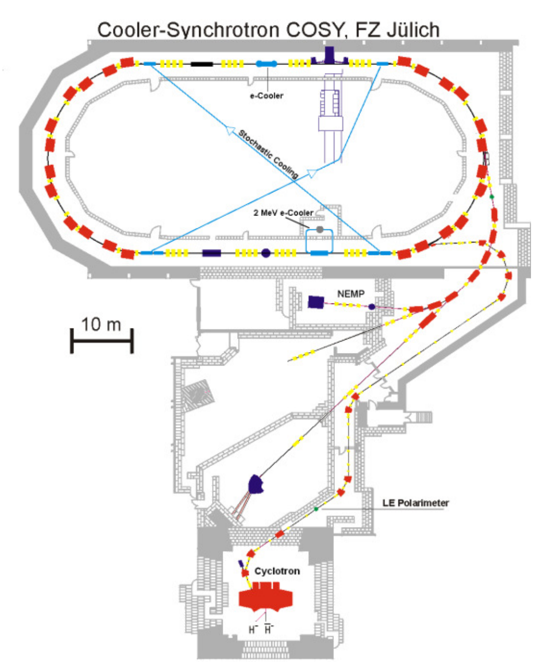

Figure 1: Layout of the COSY accelerator facility. For clarity only a few insertion devices are shown.

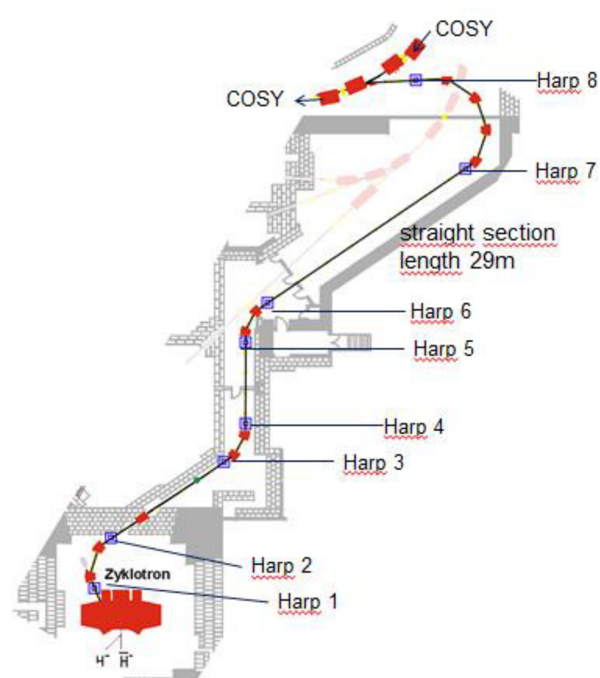

Figure 2: Distribution of harp stations in the IBL.

ISBN 978-3-95450-176-2

Harp Stations

Harps rely on the effect of secondary electron emission. Some particles of ion bunches hit the wires. When fast ions enter a metal surface secondary electrons are emitted [1], which can be detected as electric signal by a sensitive current measurement system [2]. Many wires mounted in parallel allow detecting a transverse charge profile at that position (see Fig. 3).

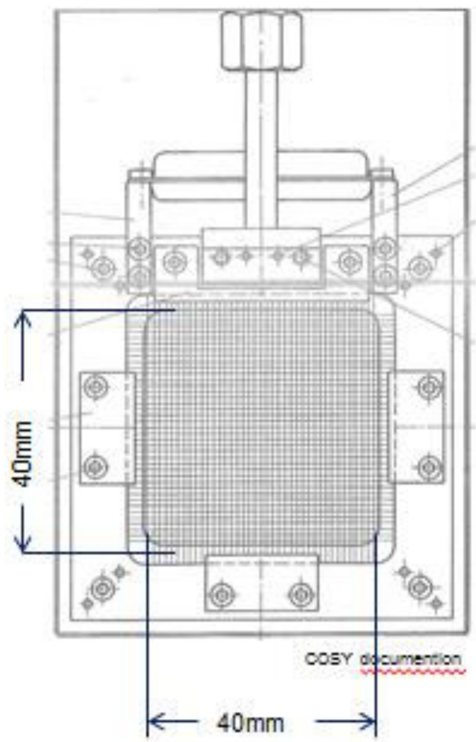

Figure 3: Drawing of a harp installed in the IBL [3].

A harp station is installed at each intersection between straight and bent sections. Each of the 8 profile monitoring stations consists of two harps performing measurement in one transverse plane (see Fig. 4). They have 39 wires with 1mm spacing covering 40mm.

UPGRADE

Motivation

The IBL was commissioned in the early 1990's and has always been in use since then. Originally having been equipped with a harp system as a major means of beam diagnostics the initial readout electronics has reached end of life resulting in time consuming beam setup procedures. The centralized architecture of the readout system allowed only for one profile grid to be used at an instance. The initial harp readout system had an rs232 based communication. There were a multiplexer station for the first group of 4 harp stations and another one for the second group.

Figure 4: Harp station 4 in the IBL contains a vertical and a horizontal harp moved by one pneumatic drive. Two multichannel pico-amperemeters are mounted below the cable tray.

Reliable operation of the beam profile measurement system is crucial for achieving reasonable beam transfer efficiency from the cyclotron to the COSY ring and keeping the IBL setup times short. Furthermore the ability to perform simultaneous profile measurements at all harp stations is regarded as very useful.

Boundary Conditions

Over the years no issues caused by the harp sensors have been reported. The pneumatic drives are considered to be in good working condition. Due to these reasons only the harp read out electronics is replaced. As there were concerns regarding the signal to noise ratio, the read out cables are kept as short as possible, so the read out electronics is placed close to the harps. Radiation effects need to be regarded.

The communication to the controls will be established by use of an EPICS client/server configuration to be integrated into the existing control system.

New Readout Electronics

A multichannel pico-amperemeter current measurement module for harps was designed and manufactured at iThemba LABS. A similar module has already been used for the luminescence profile monitor at COSY [5]. It is based on the charge integrator chip ACF2101 by Burr Brown [6]. The electronics is controlled by a BeagleBone microcontroller board. It controls the integrator chips,

ISBN 978-3-95450-176-2

timing, trigger input and ADC's of the electronics, performs the data acquisition and communicates to the COSY-control system via Ethernet.

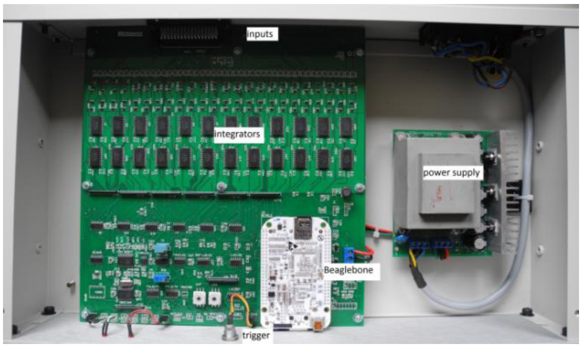

Figure 5: Opened pico-amperemeter current measurement module.

The modules shown in Fig. 5 are capable of measuring currents from 10 pA to 200 µA with 1 pA resolution and use 6 measurement ranges. The module has 48 channels, 39 of them are connected to a harp via a 2 m, 39-wire double shielded coax cable. Free channels are disabled by software. The macro-pulse signal connects to the trigger input by a single coax RG58 cable for synchronization.

Software System

The Experimental Physics and Industrial Control System (EPICS) is an open source architecture hosted by ANL. It has the properties of a client/server and publisher/subscriber systems. It also is capable of real time behavior. EPICS is widely used in the accelerator community. On the BeagleBone microcontroller the EPICS server software runs in an Ubuntu 13 environment. It is distributed on micro-SD cards and can easily be updated.

Control System (GUI)

The existing GUI was adapted to the new protocol. All harps can be read out simultaneously. All beam profiles are shown in one window (see Fig. 6). The profile measurement can be performed in free run mode or in triggered mode, which synchronizes to injection sequence.

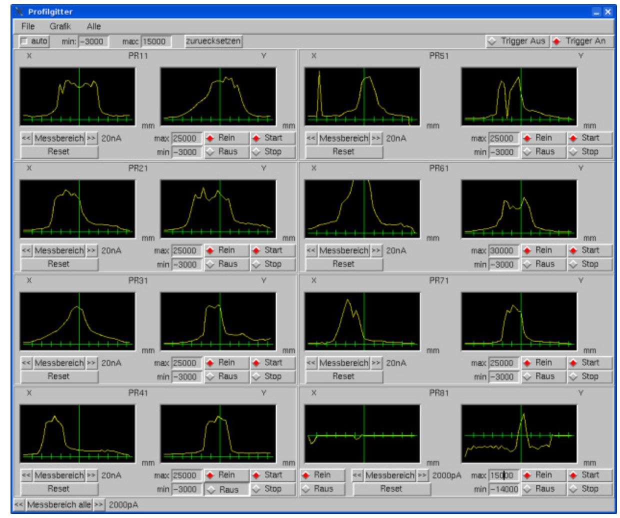

Figure 6: All 16 harps in the beam (H^- at 45MeV) deliver profile data showing a good alignment. At harp station 8 the y-plane covers the x-plane minimising the x-profile.

SUMMARY

The upgrade of the profile monitoring system of the COSY IBL was completed by the beginning of 2015. The system is now in routine operation. The GUI has been modified to work with the new hardware. Occasional hardware resets are required due to radiation and software issues. An upgrade to a better maintained OS-version (Ubuntu 14 LTS) is envisaged.

Outlook

An automatic procedure of determining the beam position, width and intensity based on the harp profile measurements is yet to be implemented. This data will then be used for an automated model-based IBL optimization routine. Long term archiving of the measured data is yet to be implemented as well.

REFERENCES

[1] E.J Sternglass, Theory of secondary electron emission by high speed ions, Physic rev 108,1957.
[2] G.W. Tautfest and H. R. Fechter, A Nonsaturable High Energy Beam Monitor, Rev. Sci. Instr. 26, 229 (1955).
[3] COSY Documentation, drawing CY-PG20, Jülich, 1990.
[4] iThemba Labs, Annual report 2007-2008, 2008.
[5] Böhme, C., Untersuchungen zur Profilmessung von Hadronenstrahlen mittels Restgaslumineszenz und -ionisation, Technical University Dortmund, 2011.
[6] Texas Instruments, Datasheet ACF2101, www.ti.com/products/acf2101.

ISBN 978-3-95450-176-2

STUDIES FOR A BPM UPGRADE AT COSY

C. Böhme, M. Bai, F. Hinder, V. Kamerdzhiev, F.Trinkel
Forschungszentrum Jülich, Germany

Abstract

For the planned Electric Dipole Moment (EDM) precursor experiment at the COoler SYnchrotron (COSY) synchrotron and storage ring an accurate control of the beam orbit is crucial. The required beam position measurement accuracy demands an upgrade of the Beam Position Monitor (BPM) readout electronics. The BPM system currently in operation is described. The required performance and the possible upgrade scenarios are discussed.

INTRODUCTION

The COoler SYnchrotron (COSY) of the Forschungszentrum Jülich is a 184 m long racetrack-shaped synchrotron and storage ring for protons and deuterons from 300 MeV/c (protons) or 300 MeV/c (deuterons) up to 3.65 GeV/c. Built in are devices for stochastic as well as electron cooling. The stored ions can be polarized or unpolarized. Commissioned in 1993, some of the components are not only outdated, but start failing while spare parts for repair are hard to acquire. In addition, for the planned EDM [1] precursor experiment a higher beam position measurement accuracy is needed than can be reached with the used components. Therefore different upgrade scenarios are investigated.

CURRENT STATUS

COSY is equipped with 30 shoebox-style BPMs. During commissioning 27 BPMs of two types were installed, a cylindrical type with 150 mm diameter and a rectangular type 150 mm · 60 mm [2]. The selection was made to fit into the beam pipe, which is round in the straight sections and rectangular in the arcs in order to fit into the dipole magnets. Later on 3 BPMs were added, with special geometries to fit within the beam pipe of a different diameter close to experiments, giving a total number of 30. 2 of them are installed within the recently added 2 MeV electron cooler [3] and use their own electronic for readout, which is different from the others. One of them at the ANKE experiment, which uses a standard readout hardware. All other BPMs are read out by the same type of electronics [4], whose concept is shown in Figure 1. The readout electronic for each BPM, except for the pre-amplifiers, is housed in one VXI crate, consisting of 2 analog modules, 2 digital modules, one CPU, and one timing receiver. The pre-amplifiers are directly connected to the N-type vacuum feedthrough of the pick-ups. This pre-amplifier has a fixed gain of 13.5 dB with an input impedance of 500 $k\Omega$ and a bandwidth of 100 MHz. The gains and offsets of two pre-amplifiers have to be exactly matched for one plane of one BPM in order to avoid incorrect measurements. The preamplified signals are then fed into an analog module, where sum and delta signals are produced

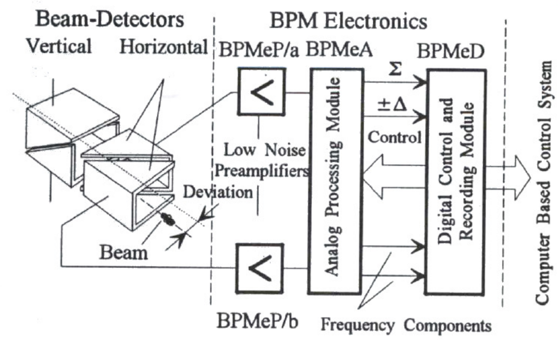

Figure 1: Current Beam Position Monitor electronics assembly [4].

using a hybrid. These signals are then treated separately and can be further amplified in 6 dB steps from 0 dB to 66 dB. Both the sum and the delta branches have two signal paths. A narrowband path features 3 possible filter settings with bandwidths of 10 kHz, 100 kHz, or 300 kHz and an additional amplifier that can be set from 0 dB to 18 dB in 6 dB steps. The broadband path with 10 MHz bandwidth can be used for turn-by-turn measurements while the narrowband signals are used for closed orbit measurements. The analog outputs are unipolar, the sign of the narrowband delta signal is detected separately and the information is transmitted by a separate TTL signal line. After the analog signal processing the signals are digitized in a digital module. This is done using 20 MHz 8 bit ADCs. For the narrowband signal the sampling frequency is lowered to 1 MHz or 100 kHz, depending on the selected analog bandwidth. For the sum signal only 7 of the 8 bits of the ADC are used, the 8th bit is used to indicate the polarity of the delta signal. The digital module generally has the possibility to buffer 4096 data points, while few modules can store up to 32768 data points for turn-by-turn measurements. The CPU of the VXI crate then calculates out of the narrowband signal the beam position using a scaling factor for the specific BPM geometry. It is also possible to transfer the raw data to the control system, display and export it.

LIMITATIONS OF THE CURRENT HARDWARE

First, the position measurement is highly dependent on the pre-amplifiers used for the two pick-up electrodes of one plain having identical characteristics, even better than usual production variations of electronic components. Therefore, at the time of construction, extensive tests have been performed to figure out identical pairs of the produced pre-amplifiers. Recent tests of selected pairs showed that the matching of the pairs is still good, even after years of opera-

ISBN 978-3-95450-176-2

tion. In addition, until now no defects were found for this part, so that there is no pressing need to replace those.

The analog modules have several issues [5]. They are failing at an increased rate, although until now most modules could be repaired. The modules require an extensive calibration procedures performed regularly, otherwise parameter drifts decrease the measurement accuracy . Therefore using an in situ calibration signal seems to be more promising than the calibration procedure by adjusting potentiometers.

The digital modules seem to be most outdated with only 8 bit sampling resolution, from which for the sum signal uses only 7 bits. The modules don't show a high failure rate so that the low resolution and the limited storage for turn-by-turn measurements are basically the main drivers of an upgrade.

As described above, the position calculation is done by the embedded CPUs. If introducing a calibration signal into the signal chain, the calibration data gathered has to be used for calculating the position. Here the hardware limitations, especially the low memory of the CPU modules, come into account, which does not allow the storage of larger lookup tables of correction values.

REQUIREMENTS

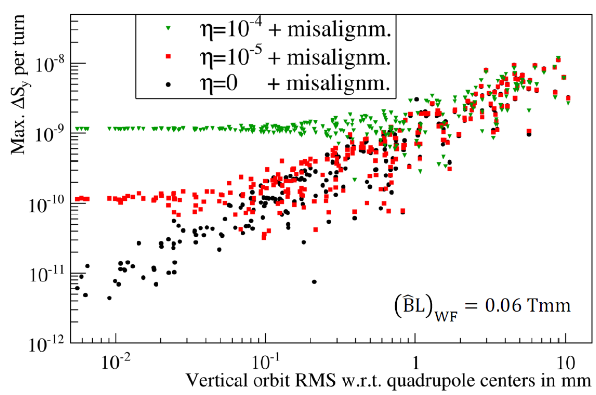

Figure 2: Calculated spin buildup per turn for different presumed EDM values. Depending on the real EDM value the beam has to be aligned in respect to the quadrupole magnets with a certain accuracy. This leads to the accuracy required from the BPMs [6].

Shown in Figure 2 is the required beam positioning accuracy of the EDM experiment for different presumed EDM values [6]. This accuracy reflects the possibility to align the beam in respect to the quadrupole magnets. In order to do this, the BPM accuracy is of cause only one part, other elements of the accelerator like the steering magnets are as well involved. As assumption a closed orbit measurement accuracy of 100 μm is the goal of the upgrade. The mechanical design of the COSY BPM does not support an accurate positioning of the pickups themselves e.g. by use of fiducial marks. A beam based alignment could reduce the BPM positioning uncertainty significantly and has to be considered.

UPGRADE SCENARIOS

Several upgrade scenarios have been discussed. In all scenarios some constraints have to be considered.

- The BPM pick-ups will remain unchanged, although they are not equipped with position markers, so their absolute position is only known within some error margin.
- Up to now no test signal for calibration purposes is used. In every upgrade scenario the introduction of test signals is mandatory.

Calibration Signal

Up to now the BPM system doesn't have a calibration signal path. Independent of the selected upgrade scenario, even if the old electronics will be kept, it appears crucial to inject a calibration signal in front of the pre-amplifier. The design of the calibration signal has to be adapted to the specific solution. While keeping the old analog electronics in place, with the early generation of the sum and delta signal, two test signals with variable amplitudes have to be provided. This is necessary for acquiring the gain and offset data for all possible gain settings in the delta and sum branches. A pure digital solution may only need one test signal that will be switched through the channels, in order to make sure the test signal will be identical for all channels.

To feed the test signal into the signal path, passive couplers or active switches are under consideration. With the advantage of the passive coupler, that it is less likely to fail, and the disadvantage, that during beam operation a calibration will not be possible. These facts have to be considered.

Another design choice under discussion is the central generation of a calibration signal vs. the local one. While a central signal generation can be performed with one high precision instrument, the distribution introduces signal variations from BPM to BPM. A local generation would have to be performed by a cheaper generator, here the later presented Red Pitaya board is under discussion, but will probably have a lower precision. In case of a purely digital solution, where only one signal is needed the local generation might be the better solution. When keeping the analog electronics in place, the two signals fed into it would have to be matched to each other and so a central generation might be the better solution.

Upgrade of the Digital Part Only

From the point of view of improving the performance of the BPM system an upgrade of the digital part seems to be the most urgent one. Furthermore, replacing the digital part only promises significant cost savings, as the amplifiers, both, the pre-amplifiers directly at the pick-ups and the ones in the analog modules, wouldn't have to be replaced, as shown in Figure 3. As candidate for a replacement a Red

ISBN 978-3-95450-176-2

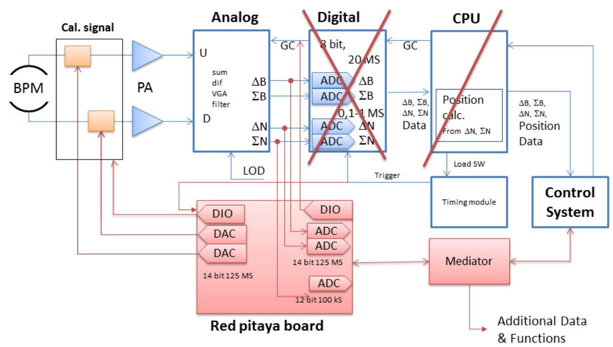

Figure 3: Concept of an upgrade, only replacing the digital part. Existing parts in blue, new parts in red. For the necessary trigger, the old CPU modules would have to be kept, as the timing modules require them during boot. All other functions of the old CPUs would be no longer used.

Pitaya board is under consideration. This board is a compact device featuring:

- 2 · 125 MS/s 14 bit ADCs with 50 MHz analog bandwidth
- 4 · 100 kS/s 12 bit ADCs
- 2 · 125 MS/s 14 bit DACs with 50 MHz analog bandwith
- 4 · 100 kS/s 12 bit DACs
- 16 · digital I/Os
- Xilinx Zynq 7010 SoC FPGA
- GBit Ethernet communication

One could use one fast ADC for capturing of the broadband delta signal of the old analog module and the other one for the narrowband delta signal, but not for speed but for the 14 bit resolution. The sum signals will be captured by two slow ADCs. The two other ADCs will capture the TTL signals indicating the polarity of the delta signals. The 16 digital I/Os are used to set the amplification and filtering mode of the analog module. And finally, the 2 DACs will be used to provide a test signal to be fed into the signal chain in front of the pre-amplifiers in order to calibrate the signal chain.

Another candidate is using fast electronics from the CERN open hardware initiative. The philosophy there is to have carrier boards on which mezzanine cards for different applications can be attached. This way we could use VXI carrier boards to fit into our existing crates. A set of fast ADCs and digital I/Os could replace the old digital modules. There are existing projects with 4 · 130 MHz 16 bit ADCs, which could be used. On the carrier boards the possibility to use FPGAs is foreseen, giving the possibility to do complex calculations of the beam position in short times.

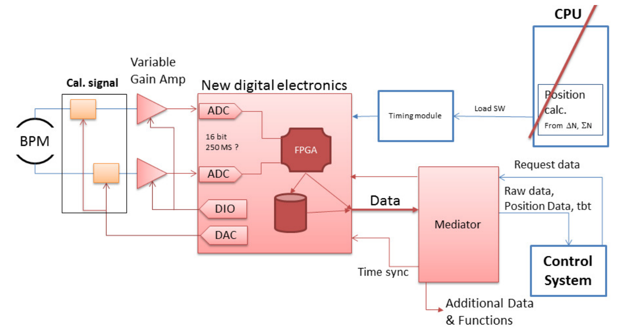

Figure 4: Concept of a complete electronics upgrade. Existing parts in blue, new parts in red.

Upgrade of the Entire System

Like other recently planned BPM systems e.g. [7, 8] the goal is to digitize the signals as early as possible in the signal chain. The downside of this upgrade scenario is that all components, including the pre-amplifiers, have to be replaced. The concept, as shown in Figure 4, is, that instead of the currently used fixed-gain amplifiers, variable gain amplifiers will be used in order to match the signal of the pick-ups to the input range of the ADC. Depending on the amount of stored particles and the beam energy, the induced voltage can range from hundreds of μV to tenths of mV. The input range of ADCs are usually in the range of up to 1 V. In order to use the resolution of the ADCs optimally, the signal should be amplified close to the this signal level.

After digitizing the individual pickup signals, further processing is done digitally. Usually an FPGA is used for real-time bunch detection, filtering and beam position calculation.

Several hardware options are under consideration:

- Instrumentation Technology Libera Hadron
- CERN Open Hardware
- DESY / XFEL / ESS solution based electronics

The Libera hadron platform was chosen for the BPM readout within the FAIR project [9]. Due to the fact that the Research Center Jülich is responsible for the design and construction of the HESR, the same hardware was chosen as a potential candidate for the COSY BPM upgrade as well. This approach insures an efficient use of resources. Unfortunately, while extensive tests with the Libera Hadron A were already performed, this device is no longer produced and is replaced by version B, which differs in design and features. The new Libera B is based on μTCA and is a modular system. Each chassis can host the electronics to read out 4 BPMs. The maximum sampling frequency is 250 MHz with 16 bit resolution. Most of the software provided by the manufacturer was build to FAIR specifications, with some extensions for other use-cases.

For the CERN open hardware the solution would be similar as the one described in the partial upgrade scenario, with

ISBN 978-3-95450-176-2

the difference that the analog amplifiers also would have to be replaced. Also the software component will be more complex, as the old analog electronics already provides a lot of the peak detection and filtering mechanisms.

Although not being identical, latest developments from DESY including XFEL and the ESS could be a prototype for a COSY solution. At least for the ESS case most of the designated hardware is commercially available, using Struck fast digitizer cards.

Control System Adaption

For all upgrade solutions, significant adaptions within the existing control system are necessary. Since the COSY control system is self-developed and outdated, evaluations are made if a modern control framework like Control System Studio (CSS) or FESA could be used as a mediator between the new electronics and the current control system to minimize the effort extending the existing control system. Within the current control system only features already existing for the old hardware would be available, while the full set of features would become available using the new framework. With this approach other accelerator sub-systems undergoing an upgrade in the future could as well use the new framework as mediator, replacing the control system currently in operation completely in a medium to long time frame.

CONCLUSIONS

Although the old electronics is performing within the specifications it was designed for, the much tighter specifications for the EDM precursor experiment require an upgrade of the BPM electronics. By introducing calibration signals, the uncertainties of the existing analog electronics can be minimized. A rather cost effective way would be to just replace the outdated digital part of the existing electronics. Nevertheless, the rate of failures of the analog modules increases. Therefore the need of a complete replacement becomes evident. The electron cooling capabilities of COSY demand for a BPM system capable of dealing with bunch lengths down to 20 ns. Current activities involve identifying a potential manufacturer of variable gain pre-amplifiers. Once the choice is made, test setups for different digital solutions will be performed in order to test their performance. As the time frame is rather short, the system should be ready for installation in late 2016, a solution providing the necessary software components might be preferred over a hardware where FPGA programming has to be done from scratch.

REFERENCES

[1] A. Lehrach on behalf of the JEDI Collaboration, "Beam and Spin Dynamics for Storage Ring Based EDM Search," IPAC2015, Richmond, VA, USA, WEAB2.

[2] R. Maier et. al., "Non-Beam Disturbing Diagnostics at COSY-Jülich," EPAC'90, Nice, France, June 1990, p. 800.

[3] V. B. Reva et. al., "Cosy 2 MeV Cooler: Design, Diagnostic and Commissioning," IPAC2014, Dresden, Germany, MOPRI075.

[4] J. Biri et. al., "Beam Position Monitor Electronics at the Cooler Synchrotron COSY Jülich," Eigth Conference on Real-Time Computer Applications in Nuclear Physics, Vancover, June 1993.

[5] F. Hinder et. al., "Beam Position Monitors @ COSY," JEDI Collaboartion Internal Note, 13/2015, June 16, 2015.

[6] M. Rosenthal et. al., "Spin Tracking Simulations Towards Electric Dipole Moment Measurements at COSY," IPAC2015, Richmond, VA, USA, THPF032.

[7] H. Hassanzadegan et. al., "System Overview and Current Status of the ESS Beam Position Monitors," IPAC2014, Dresden, Germany, THPME166.

[8] K. Lang et. al., "Performance Tests of Digital Signal Processing for GSI Synchrotron BPMs," PCaPAC08, Ljubljana, Slovenia, TUP002.

[9] M. Znidarcic et. al., "Hadron BPM For The FAIR Project," IPAC2015, Richmond, VA, USA, MOPTY040.

ISBN 978-3-95450-176-2

COMPACT AND COMPLETE BEAM DIAGNOSTIC SYSTEM FOR HCI AT IUAC

R.V.Hariwal, [1, 2, #] H.K.Malik, [2] R. Mehta, [1] S.Kedia, [1] and V. Verzilov [3]
[1]Inter-University Accelerator Centre, Aruna Asaf Ali Marg, New Delhi, India
[2]Plasma Waves and Particle Acceleration Lab, Department of Physics, I.I.T Delhi, India
[3]Accelerator Division, TRIUMF, 4004 Wesbrook Mall, Vancouver, B.C., Canada

Abstract

Design efforts result into the fabrication of a compact and complete beam diagnostic system for High Current Injector (HCI) accelerator system [1] at Inter-University Accelerator Centre (IUAC), New Delhi, India. HCI is an upcoming accelerator facility and will be used as an injector to the existing SC-LINAC. It consists of high temperature superconducting Electron Cyclotron Resonance (HTS-ECR) ion source [2], normal temperature Radio Frequency Quadrupole (RFQ), IH-type Drift Tube Linear (DTL) resonators [3] and low beta superconducting quarter wave resonator cavities to accelerate heavy ions having $A/q \leq 6$. The diagnostic system is especially designed and fabricated to get the complete beam information like current, profile, position, transverse and longitudinal emittances, bunch length and energy of incident ion beam at the entrance of DTL resonators. The compactness is preferred to minimize the transverse and longitudinal emittance growth at the entrance of DTL resonators. Various beam parameters of heavy ion beams at different energy have been carried out to validate the design and fabrication of the system. Here, the design, fabrication and various test results are presented.

DIAGNOSTIC SYSTEM FABRICATION

Compact Diagnostic System

A compact diagnostic box in Fig.1 is made of 10 mm thick stainless steel material. As the drift space between two DTL cavities is crucial, to accommodate the diagnostic chamber and quadrupole triplet, we need to minimize the drift. A highly compact diagnostic chamber has been designed and fabricated indigenously at IUAC. The diagnostic chamber is of 70 mm longitudinal length. The radial dimension of the box is approximately 160 mm and the beam aperture is 20 mm. The diagnostic box is circular in shape. There are four ports available in the box. Three will be used for Faraday cup, slit scanner and capacitive pick-up. One is left for pumping purpose. The chamber was leak tested at the leak rate of 1×10^{-11} mbar.l/s. Without any separate pumping station, the vacuum of 1×10^{-7} mbar was achieved, but this can be further improved by adding a separate pumping station.

Faraday Cup

A water cooled Faraday cup (FC) has been fabricated to

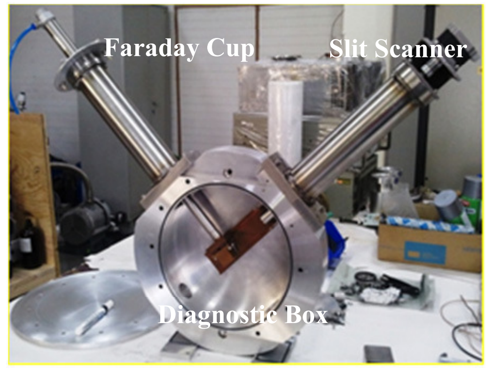

Figure1: Compact diagnostic box.

measure the current. The cup has a beam aperture of 25 mm and its length is 20 mm along the beam direction (Fig. 2). It is made of Oxygen Free High Conductivity (OFHC), copper material. Based on the expected beam power from HCI the FC is designed for few hundred watts of beam power. The suppressor ring, which retains the secondary electrons on the cup, is made of SS 304 material. The FC is completely shielded by the 3 mm thick tantalum sheet. The linear movement of FC is controlled by a pneumatic cylinder, which provides the 60 mm strokes in the diagnostic box.

Figure 2: Faraday cup.

It can be used to measure the current of the order of few nanoamperes to hundreds of microampere current.

Slit Scanner

The slit scanner in Fig. 3 is fabricated indigenously for the measurements of beam positions and beam profiles in HCI beam line. It scans the beam in two transverse directions with the help of two 500 micron slits. The slits are made orthogonal to each other and moves linearly in such a way that they cut the ion beam in x and y directions. The linear motion of the slit scanner is done by a computer controlled stepper motor. The microcontroller programming and data processing have been done with the help of LabVIEW programs. It is possible to see the online beam profiles on the two dimensional graphs of the beam intensity versus the beam positions.

#hariwal@gmail.com

ISBN 978-3-95450-176-2

Figure 3: Slit scanner.

Capacitive Pick-up

The compact diagnostic box will also consist of capacitive pick up for bunch length measurement at the entrance of DTL resonators in Fig. 4. This will be installed opposite to the Faraday cup. Once the Faraday cup will be taken out, the pick up will be moved in along the beam centre. The capacitive pick-up is designed for relative velocity (ß)~0.05 and it is under fabrication process. The time of flight will also be measured between the DTL resonators with the help of capacitive pick-up.

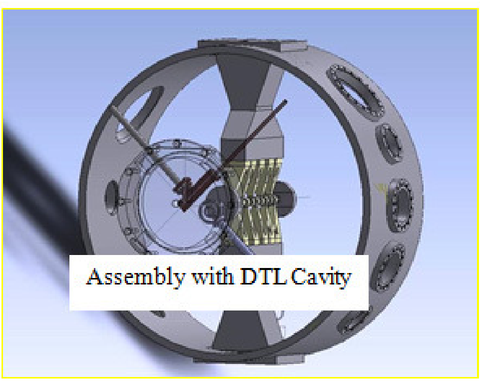

Figure 4: Design assembly of compact diagnostic box with DTL.

ONLINE BEAM TEST SET -UP

Diagnostic Box Installation in LEIBF

The prototype compact diagnostic box, along with the Faraday cup and slit scanner, were installed in the Low Energy Ion Beam Facility (LEIBF) at IUAC in Fig.5 to perform the online ion beam test and validate the various design parameters.

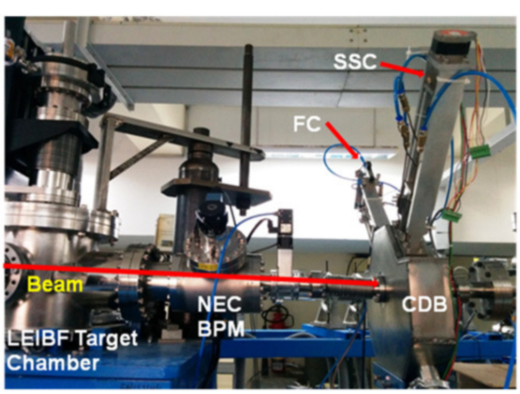

Figure 5: Prototype Diagnostic Box installed at IUAC LEIBF beam line.

The beam profile and current measured by the diagnostic system matched very closely to the one measured by the National Electrostatics Corporation (USA) made FC and BPM devices. The diagnostic system was further verified by the measurements of currents and beam profiles of the various ion beams such as N and O ion beams with different energy and currents. All the results demonstrated good agreement with those measured by standard devices confirming the operational aspect of the system.

Online Beam Test Set-up

A Keithely 6517 B electrometer is used to measure the ion beam current directly from the Faraday Cup. There is GPIB to USB connector, which connects the electrometer to CPU. The stepper motor controller was also connected to CPU by USB connector. The Faraday cup will give the current values and stepper motor provides the position information. The current signal from the Faraday cup can also be displayed on the control panel by using log amplifier. The linear motion of the slit scanner has been controlled by the stepper motor controller unit which is connected to a computer running the LabVIEW program in Fig. 6. When the scanner moves, FC collects the charged particles passed through the slits. It provides current signal and thus measures the ion beam current intensity vs the beam position.

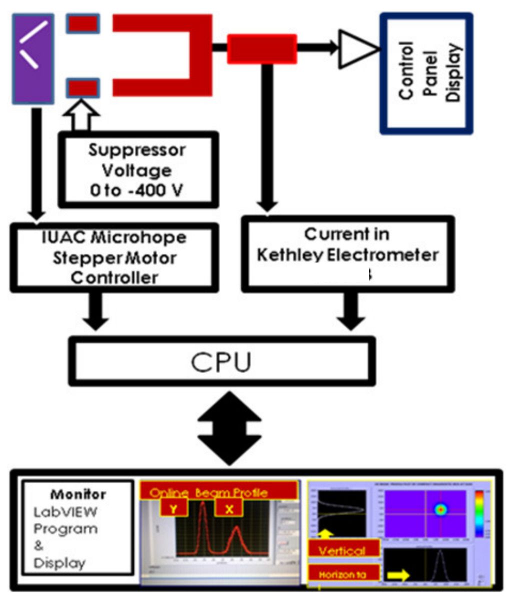

Figure 6: Electronic set up.

RESULTS AND DISCUSSION

The beam current and profile measurements of various heavy ion beams at different energy have been carried out to validate the design and fabrication of the Faraday cup and slit scanner. We have tested the Faraday cup and slit scanner by measuring the current and profiles of various ion beam viz. Nitrogen and Oxygen at different energy and current. The experimental details and its results are given below.

ISBN 978-3-95450-176-2

Beam Parameters Measurements

The Faraday cup and beam profile monitor have been tested and verified with the following ion beams. (Table1).

Table1: Current Measurement by Faraday Cup

Ion Beam	Energy (keV)	Current (FC) (µA)	Current (NEC) (µA)
N^{1+}	250	72.5	74
N^{5+}	1250	1.3	1.3
O^{1+}	250	2.77	2.77
O^{5+}	1250	0.421	0.421

Nitrogen and Oxygen Ion Beam Test

The determinations of beam profiles through the slit scanner have been carried out for N and O ion beam in the material science beam line. The measurements of various types of the beams at various energies and current are really useful for the evaluation of the performance of the various optical devices installed into the beam line [4-8]. The results are shown in the following in Fig. 7.

The lower as well as higher currents were measured by the Faraday cup very accurately from tens of picoamperes to few hundreds of microamperes. Various ion beam profiles, obtained with the LabVIEW program, provide the digital signature of the charged particles distribution, i.e. the current intensity along the ion beam positions.

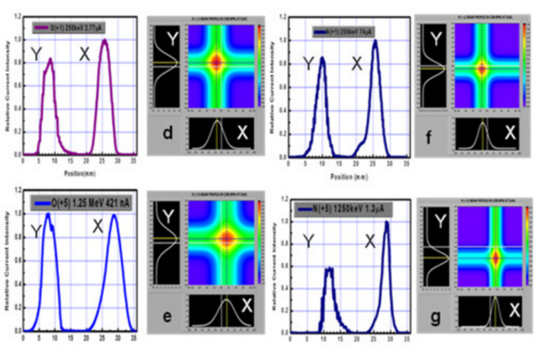

Figure 7: Beam profiles.

The experimental results provide the information not only on the beam current, profile and spot size but the beam positions also. The Oxygen and Nitrogen ion beam profiles along with their positions from the centre point of the beam line are shown above.

CONCLUSIONS

We have developed indigenously a very compact diagnostic system, which can replace any conventional beam diagnostic components in the beam line. The motivation behind the development of such devices came to investigate and avoid the beam losses in the low energy ion beam line section of an accelerating system. The low cost, high accuracy, high reliability and simplicity are the figures of merit of this system. This system plays a significant role in the current measurements and beam tuning to enhance the performance of accelerators by providing the good quality beam, especially at the entrance of each DTL cavities in the HCI accelerator system.

ACKNOWLEDGEMENTS

The author would like to acknowledge the IUAC workshop personnel and Jimson Sakarias to provide the machining and welding facilities during the fabrication of compact diagnostic system. The author is also thankful to the Director, IUAC New Delhi for giving the permission for installation of diagnostic system and online testing with the various ion beams in LEIBF. Lia Merminga, R. Laxdal and Josef Holek from TRIUMF Canada are specially acknowledged for their support and fruitful technical suggestions.

REFERENCES

[1] A. Roy, Curr. Sci.76, 149(1999).
[2] G.Rodrigues, P.S.Lakshmy, Sarvesh Kumar, A.Mandal and D.Kanjilal, Rev. Sci. Instrum. 81, 02B713 (2010).
[3] R. Mehta, J. Sacharias, R.V. Hariwal et .al, Design Validation of IH Type Drift Tube Resonator at IUAC in ADS conference 2011, BARC, Mumbai, India.
[4] Valery Dolgashev et al, Appl. Phy. Lett. 97,171501 (2010).
[5] O.Kamigaito, M.Kase, N.Sakamoto,Y.Miyazawa, Eikezawa et al., Rev. Sci. Instrum.76, 013306 (2005).
[6] R.B. Fair, J. Phys. E: Sci. Instrum. 4, 35 (1971).
[7] Probyn B. A., J. Appl. Phys.D:Appl.Phys. 1, 457-65 (1968).
[8] Jacob L Phil, Mag. 28, 81-85 (1939) [1]Peter Fork, Lecture Notes on Beam instrumentation And Diagnostics, Joint University Accelerator School, 2008.

ISBN 978-3-95450-176-2

DESIGN AND DEVELOPMENT OF CONFIGURABLE BPM READOUT SYSTEM FOR ILSF

M. Shafiee[1,2], J.Rahighi, M.Jafarzadeh, [1]ILSF, Tehran, Iran
A.H.Feghhi, [2]Shahid beheshti University, Tehran, Iran

Abstract

A configurable electronic system has been developed for button BPMs readout in the storage ring of Iranian Light Source Facility (ILSF). This system calculates the beam position through the output voltage of BPMs. Output signals of BPMs pass through a 500 MHz and 50ohm front-end for noise filtering and also gain control purposes. Then the signal is digitized based on under sampling method by a 130MHz ADC for further analysis in FPGA. Safe dynamic range of 0dBm to -90 dBm can be covered by this electronic system with white noise measured to be around -110dBm. Trigger for this electronic is 2-10Hz as Slow data acquisition for Slow orbit feedback system and 4-10 KHz as Fast data acquisition for fast orbit feedback system. This paper describes the design, analysis, and measurements of the developed electronic system.

INTRODUCTION

The Iranian Light Source Facility (ILSF) is a 3 GeV third generation synchrotron light source facility which is in design stage [1]. In diagnostics group, we have designed different instrument and fabricated some prototypes. Since Beam Position Monitors (BPMs) are the most frequently used non-interceptive diagnostic in particle accelerators [2], we have designed and developed BPM and its readout system. To monitor closed orbit, It is needed to employ 160 BPMs around the storage ring of ILSF. Important criteria in the design of BPMs are to have the intrinsic resolution of less than *1um*, to have as highest and as flattest transfer impedance as possible, to have less higher-order mode (HOMs) resonances, and excellent impedance matching which will result in well-separated bunch by bunch signals with high signal-to-noise ratio [3]. Fig. 1 shows BPM design and vacuum chamber schematic at ILSF.

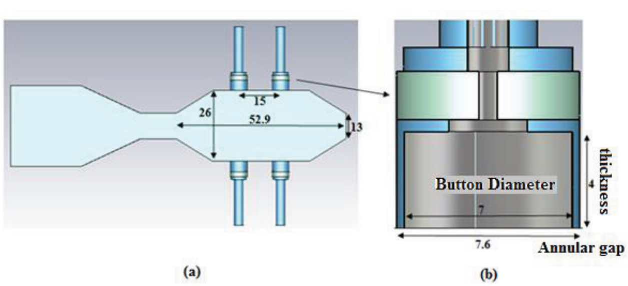

Figure 1: (a) Location of BPMs around vacuum chamber (b) Button BPM structure. All units are in mm.

To simplify BPM parameters calculation, a code was developed in C# [4]. After optimization of BPM design, we have designed and developed a new BPM readout system to improve important parameters of high precision, high speed and high digital processing capability. The developed BPM readout system consists of three parts: the analog front-end, the mixed-signal and the digital circuit. In the analog front-end circuit, each RF input signal is filtered and amplified individually by using two successive accurate IF-band passband filters, and two voltage gain controllers (VGAs) which has been implemented based on combination of attenuators and accurate narrowband amplifiers. Then the four filtered and amplified signals are fed to the mixed-signal section of the circuit to be digitized with high sampling rate and with low noise. Therefore, we used four accurate high speed ADCs and under-sampled the signal using accurate clock signals generated using LVDS clock distributors. Then the digital output and synchronization signals are fed through the FMC connector connected to the main signal processing module (digital circuit). In FPGA (ML605) buffers implemented to transfer raw data to PC by Ethernet for further calculation and analyses in MATLAB [5].

After laboratory tests of this system, final tests were done using the real beam in ALBA. The tests showed precision and resolution of 1 micro meter.

BPM FOR THE ILSF STORAGE RING

As mentioned high sensitivity, high transfer impedance and less parasitic and coupling impedance are the desired features of BPM Design in ILSF. To achieve these features, a code was developed to calculate parameters of BPM such as sensitivity, intrinsic resolution and power dissipation vs bandwidth and current.

It is known that less annular gap causes less parasitic impedance, HOM resonances at higher frequency, and more capacitance. In general more capacitance is equal to less parasitic losses, then increasing it by increasing thickness of button and decreasing annular gap can be helpful. Larger button diameter causes more sensitivity but also increase risk of thermal noise through beam dissipation power on longer button and somehow mechanical deviation at button [6]. Fig. 2,3 shows calculated parameters of designed BPM by using developed code. Fig. 2 shows that BPM sensors supposed to have linear response for almost 10 mm displacement. Fig. 3 also shows induced power on buttons for different

ISBN 978-3-95450-176-2

beam current. In 100mA beam current, induced power is around -22.8 dBm equal to 46 mV Peak-to-peak.

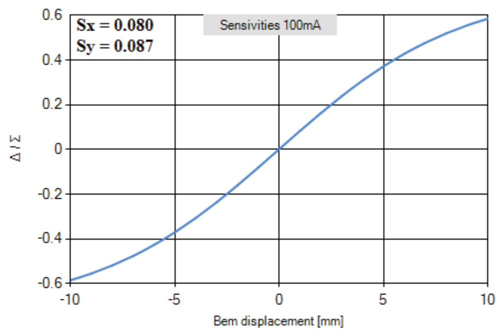

Figure 2: BPM sensitivity vs Beam Displacement.

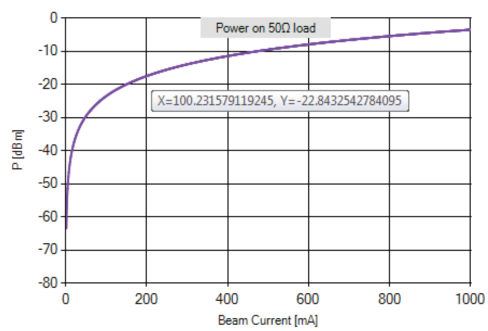

Figure 3: Induced power on buttons vs beam current.

An intensive particle beam moving in a vacuum chamber induces quite strong electromagnetic field named wake field affecting the beam itself. From here the most significant results of collective effects are various instabilities of beam motion, which can lead to beam losses or beam quality deterioration. To calculate Wakefield and induced voltage of BPMs, CST code was used [7]. In this method beam shape was considered Gaussian with standard deviation of 2.9mm. Fig.4 shows calculated induced voltage when beam placed at the centre of vacuum chamber.

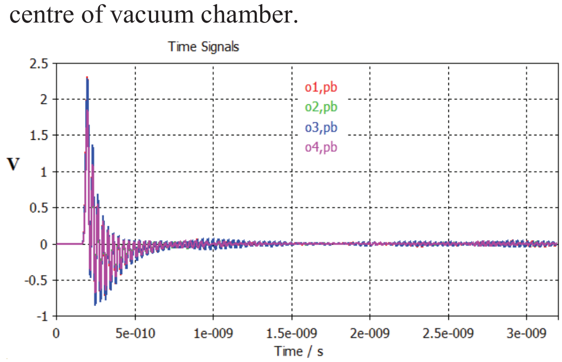

Figure 4: Induced voltage of BPM for single pass beam at centre of vacuum chamber.

Wakefield impedance (coupling impedance) at Fig. 5 shows that resonances are far enough from working frequency range then it confirms assurance of BPM design.

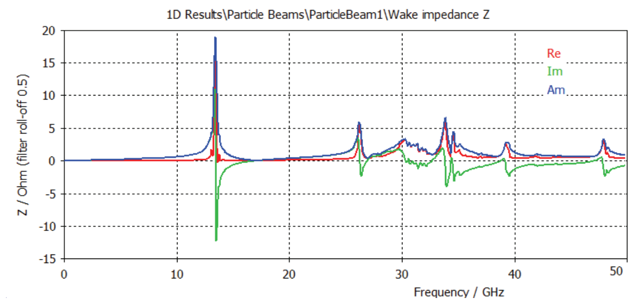

Figure 5: Real and Imaginary parts of longitudinal coupling impedance for a BPM.

Wake potential also calculated by CST as shown at Fig. 6 loss factor for a bunch was also calculated by CST and formula $P_{diss} = \frac{K_l I_{beam}^2}{f_{RF}}$. The power dissipated in the component for a beam is 2.2 Watt which is within the normal value.

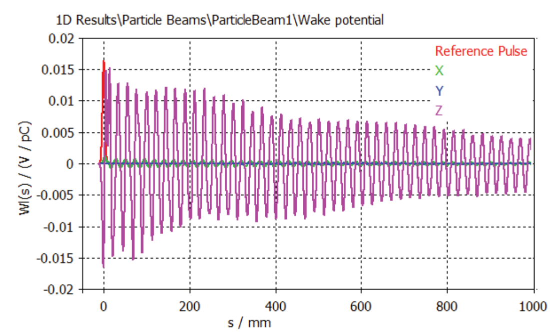

Figure 6: Wake potential as function of distance from bunch for a BPM.

BPM READOUT SYSTEM

After we have done the design of button BPM successfully, we have decided to develop Electronic readout system for beam position monitoring purposes. Based on design, it consists of 3 different parts, the analog front-end, the mixed-signal and the digital circuit (Fig. 7).

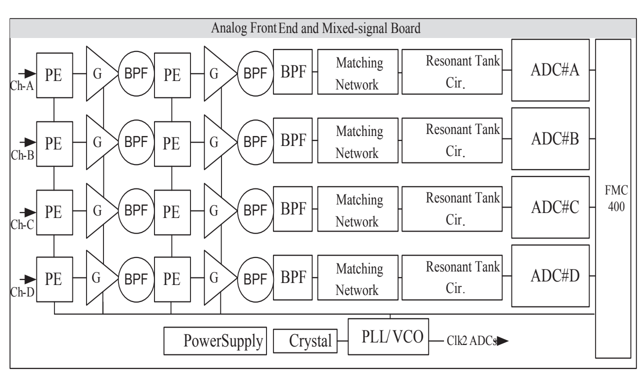

Figure 7: The schematic of electronic components in the board of Analog front end and the mixed signal sampling board.

ISBN 978-3-95450-176-2

The Analog Front-end Circuit

This circuit is composed of VGAs and band-pass filters, which are implemented individually for four IF input channels. In each channel, the VGA module has been designed using two digital controllable attenuators (DAT-31R5-SP+) and two fixed IF low-noise amplifiers (TAMP-72LN+). Each attenuator could be used to attenuate the input signal in the range of 0 to 31.5dB in 0.5dB steps, by setting 6 digital bits in an online or offline way. In the RF front-end, the IF signals are being amplified/attenuated and filtered in the single path configuration, individually. To have a good band-pass filter, we utilized the SAW filters. We used SAW filter, TA0979A, which is a 8th Butterworth band-pass filter with the central frequency of 500MHz and a bandwidth of 6MHz. In addition, it's low insertion loss of 2.5 dB is an advantage for the overall SNR of signals

The Mixed-signal Circuit

This is the most important part of the instrument since there are both analog and digital signals in the circuit. Therefore, we took care of the mixed-signal issues in both circuit and PCB design to minimize the crosstalk, signal and power noise, as well as to increase the SNR and dynamic ranges of the system. To have a better quality of pre-processed IF signals, first we used to parallel a RF-transformer and a Balun transformer to convert the single ended signal to differential signal in order to make the SNR of the signal better by decreasing the EMI noises. Then, the signals have individually have passed the anti-aliasing low pass filter and resonant tank circuit and then have fed to the differential high-precision single-channel ADCs. The ADC of LTC2208 was used which has a trade-off between accuracy and sampling rate. It digitizes the signals to 16-bits digital data with the sampling rate of up-to 130MHz and high-precision SNR of 75dB@100MHz. The output data and synchronized signal of each ADC has been buffered and the voltage is changed to 2.5V to be compatible to digital circuit powers. The input clock of each ADCs has been sourced using a LVDS clock distributor (AD9510). We used a very accurate crystal oscillator to source the LVDS clock distributors. The advantage of AD9510 clock distributor is to flexibly control the clock outputs, currents and clock rate by using SPI interface. In our study, we have set the clock rate to 122MHz. To have a connection between analog and mixed-signal circuits and digital circuit, all the ADC signals, power and ground signals, digital control signals were passed through a FMC-400PIN connector compatible with ML605 FPGA board module.

Digital Circuit

The digital circuit is composed of digital modules in order to implement various tasks including data read-out and storage, voltage gains adjustment, ADC and Clock PLL configuration, digital signal processing and communication with computer through the Ethernet and USB interfaces. By considering the complexity of the required digital circuit, we used an advanced ML605 board which contains digital electronic components including FPGA Virtex-6, Ethernet physical layer and USB controller, DDR3 memory, high speed flash and so forth. We utilized FPGA to program and control all the required sub-modules. All the FPGA VHDL codes have been compiled in the ISE 14.7 development software released by Xilinx Company [8]. Final shape of developed readout system is shown at Fig. 8.

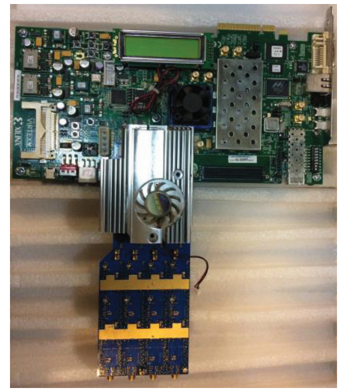

Figure 8: The overall hardware implemented design of BPM system.

Developed GUI Monitor in PC

To monitor beam position and also induced voltage on button BPMs, a code was developed in visual C++ [9] in windows. In this code Mitov GUI [10] has been used to monitor signal push for samples, average of peak-peak voltage and also beam position values. Schematics of this developed GUI are shown at Fig. 9.

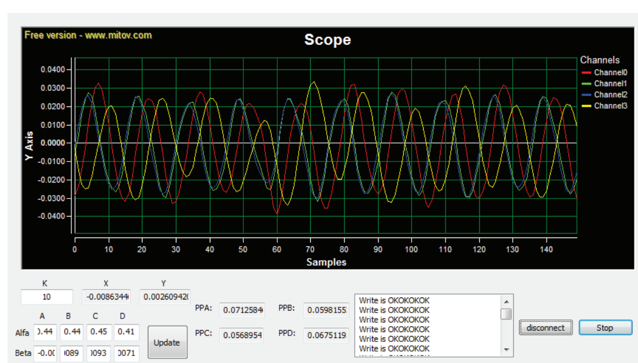

Figure 9: Schematic of developed code for monitoring beam parameters according to the recorded signals from BPM.

Tests in ILSF Lab

In ILSF lab tests were done by signal generator (E8663D Agilent) for 500MHz with different amplitudes as input. Measurements showed that the system works completely linear. Then by calibrating and finding calibration

ISBN 978-3-95450-176-2

coefficients, we could measure the input voltage by the readout voltage.

Tests in ALBA

We had a great chance to test developed readout system in ALBA (Spain) on real beam. To get information about induced signal on buttons, measurement by oscilloscope with 50-ohm termination showed peak to peak voltage around 221mV equal to -9 dBm which is quite in our system's dynamic range. Resolution is around 0.2 um due to wide dynamic range up to -90 dBm and $K(\Delta V)=\Delta x$ formula which K is 10. After calibration of our system by using signal generator for each channel and finding coefficients due to its linear behaviour between BPM output voltage and readout voltage, we started beam position measurements. Beam position calculation was done based on peak-peak voltage measurements and Δ/Σ equation. Fig. 10 shows beam position measurement for an hour in storage ring of ALBA with 3 Hz as system trigger.

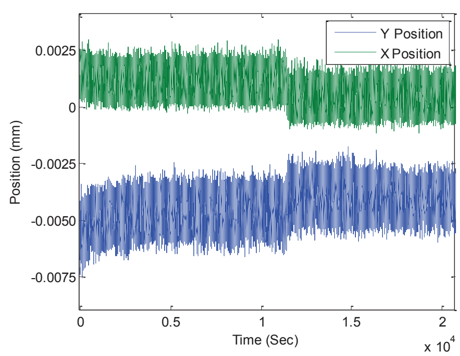

Figure 10: Sample of X-Y position measurement by our designed BPM device.

Results show 0.0016 mm and 0.0015 mm displacement in both horizontal and vertical directions respectively with 0.0014 mm precision (Standard Deviation). The readout system also was tested on ALBA booster. In top-up mode at ALBA accelerator facility, a two-third storage ring filling pattern is used, in which 320 out of 448 buckets of the SR are filled with electrons. For filling these buckets, the LINAC is operated in multi-bunch mode, and it delivers 10 shots with repetition rate of 3Hz including the trains of 32 bunches per shot at each 20 minutes [11]. Fig. 11 shows the measurement of injection pattern by our developed readout system based on the induced voltage on BPMs at ALBA booster.

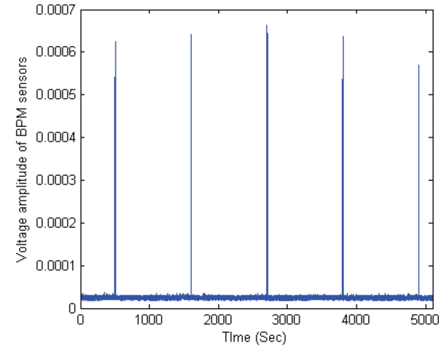

Figure 11: Peak-peak voltage of readout system through measurements at booster.

However the precision of around 1 micro meter for the beam position measurements by this electronic system achieved but higher precision is required. To find out optimized mathematical method to decrease the standard deviation, and consequently increase the precision, we analyzed the recorded raw data offline by different methods. One solution is using PCA (Principal Component Analyses) to reduce the noise through finding the frequency range of max data quantity [12]. By filtering position Data x,y, we got that max data quantity can be found less than 2.9 Hz. Then using PCA technique for these data decreased the precision down to 0.25 micro meters. One of disadvantage of this method is its long processing time, because of that it is applicable for slow rate data acquisition. Fig. 12 shows noise reduction results based on PCA technique in measurement of beam position at ALBA storage ring.

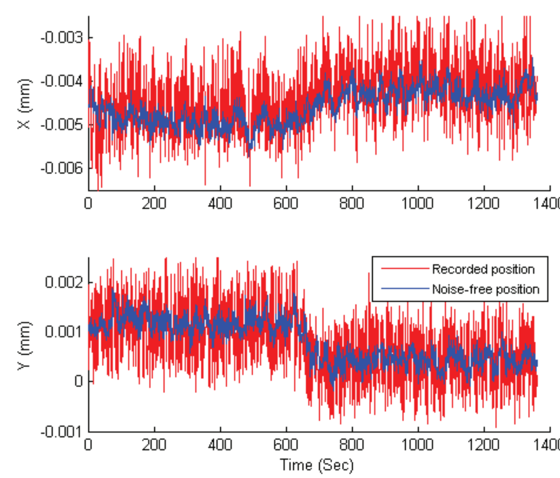

Figure 12: The recorded positions and processed low-noise positions based on PCA.

ACKNOWLEDGMENT

We would like to Thank Dr Francis Perez for his kind suggestion and support to test developed readout system in ALBA. We are also thankful of Dr. Ubaldo Iriso and Angel Olmos for their kind comments and technical supports in ALBA.

ISBN 978-3-95450-176-2

REFERENCES

[1] H. Ghasem, Others, "Beam Dynamics of a new low emittance third generation synchrotron light source facility", Physical review special topics, Accelerators and beams, 18, 030710 (2015).
[2] L.Muguira,Others, "A Configurable electronics ssytem for the ESS-BILBA beam position monitors", Nuclear Instruments and Methods in Physics Research A, 721, (2013) 50-59.
[3] Zhichu Chen, Others, "Beam position monitor design for a third generation light source", Physical review special topics-Accelerator and beams 17,112801 (2014).
[4] A.Molaee, Others. "General Consideration for button BPM", IPAC2014, Dresden, Germany.
[5] www.mathworks.com
[6] S.R.Marques, Others, "Design of Button Beam Position Monitor for the Brazilian Synchrotron Light Source", IPAC2007, USA.
[7] www.cst.com
[8] www.xilinx.com
[9] www.visualstudio.com
[10] www.mitov.com
[11] R.Munoz Horta, Others, "Operation and Improvements of the ALBA LINAC", ACDIV, September 2014.
[12] Svante Wold, Others "Principal Component Analyses", Chemometrics and Intelligent Laboratory Systems, 2, p. 37-52, 1987.

ISBN 978-3-95450-176-2

LONG-TERM STABILITY OF THE BEAM POSITION MONITORS AT SPRING-8

T. Fujita#, H. Dewa, M. Masaki, S. Matsubara, S. Sasaki, S. Takano,
Japan Synchrotron Radiation Research Institute (JASRI/SPring-8), Hyogo, Japan
H. Maesaka, Y. Otake,
RIKEN SPring-8 Center, Hyogo, Japan

Abstract

Stability of the BPM system is critical for synchrotron light source rings to keep the quality of photon beams and to stabilize the photon beam axes. The BPM system of SPring-8 has suffered from fluctuating gain imbalances among 4 electrode channels, which results in variations of offsets for beam position measurement. We recently surveyed the logged data of the BPM and the operating environment, and revealed several features of variations of the offset errors of the BPM. To cure step variations of the offsets, inspections of switch modules of the readout circuit are necessary. For variations correlated with the dew point of the environment, we consider that a possible cause is change of reflection coefficients in the BPM cables damaged by radiation. Further investigations are necessary to find the causes of other variations of the BPM offset errors.

INTRODUCTION

For synchrotron light source rings, accuracy of the BPM system is crucial for the quality of the source electron beam. Elaborate efforts are paid for calibration of BPM offsets including pre-installation bench calibration, survey at installation and beam-based alignment after commencement of operations. Stability of the BPM system is even more important as it is critical to keep the quality of photon beams and to stabilize the photon beam axes as well.

The BPM system of the SPring-8 storage ring has suffered from fluctuating gain imbalances among four 4 electrode channels. A major origin of the imbalances is voltage standing waves in the cables of the BPM caused by reflections at locations with impedance mismatching. While the imbalances are routinely corrected in accordance with a beam-based measurement [1] for several time per year, they fluctuate during the operation periods and result in variations of offsets for beam position measurements. Fluctuating BPM offset errors could degrade stability of the beam orbit and the photon beam axes.

Stability of the BPM system would be affected also by mechanical and electrical stability of the components comprising the BPM system, vacuum chamber and supporting girder of BPM, signal cables and readout electronic circuits. In order to find and cure the causes of variations of offset errors of the SPring-8 BPM system, we recently surveyed extensively the logged data of the BPM and the operating environment, such as the temperature and the dew point (DP).

SPRING-8 BPM SYSTEM

The SPring-8 storage ring consists of 48 cells and six BPMs are regularly placed in each cell. The totals of 288 BPMs are processed at 24 stations of BPM readout circuit. The electrode of the BPM is button-type and four buttons are placed in skew positions. Signal from each button electrode is transferred from the accelerator tunnel to the BPM circuit outside the tunnel through 3 coaxial cables connected; 2.5-m long flexible "a-cable", ~25-m long low loss "b-cable" and 5-m long flexible "c-cable". A block diagram of the BPM circuit is shown in Fig. 1 [2]. The circuit employs multiplexing method. Three BPMs are processed by one common channel comprised of an RF amplifier, a mixer, an IF amplifier and an ADC. A reference signal supplied for the frequency down-converter is delivered from a master oscillator through a phase-stabilized optical fiber cable, which is commonly used for 12 BPMs from two cells.

Beam positions at each BPM are continuously calculated with a repetition of 1 kHz and sent to a ring-buffer on a DSP board. The position data sampled by 1 kHz can be used for analyses of the orbit fluctuations and of error source position at sudden beam loss. Slow position data averaged for 600 ms are sent to a control workstation for routine global orbit correction with 1 Hz repetition [3]. Typical resolution of the averaged position data is 0.1 μm (rms).

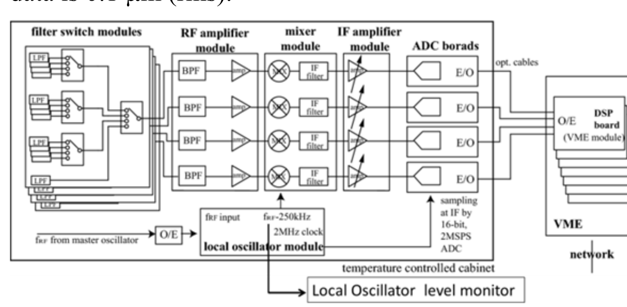

Figure 1: Block diagram of the SPring-8 BPM circuits.

#tfujita@spring8.or.jp

ISBN 978-3-95450-176-2

BALANCE ERROR OF BPM

In order to distinguish instrumental fluctuations of the BPM system from real orbit fluctuations, we introduce an index, "balance error" of BPM.

For a BPM comprising four electrodes at skew positions, beam positions x and y are generally calculated by using four channel voltages, as $x = k_x \Delta_x/\Sigma_x$ and $y = k_y \Delta_y/\Sigma_y$. Beam positions are also available by using three voltages out of the four. There are four combinations to choose the three electrode channels yielding four pairs of x and y positions as,

$$x_1 = F_1(V_2,V_3,V_4), y_1 = G_1(V_2,V_3,V_4), \quad (1)$$
$$x_2 = F_2(V_1,V_3,V_4), y_2 = G_2(V_1,V_3,V_4), \quad (2)$$
$$x_3 = F_3(V_1,V_2,V_4), y_3 = G_3(V_1,V_2,V_4), \quad (3)$$
$$x_4 = F_4(V_1,V_2,V_3), y_4 = G_4(V_1,V_2,V_3), \quad (4)$$

where V_1, V_2, V_3, V_4 are voltages of each channel. The functions F_1, F_2, F_3, F_4, G_1, G_2, G_3, G_4 are the mapping functions of BPM determined by the geometry of the BPM chamber. If the whole BPM system is ideal without any errors, the four position pairs must be identical. The discrepancies reflect relative errors among the four BPM channels. We define an index of "balance error" of BPM as,

$$\Delta_x = \max(x_1,x_2,x_3,x_4) - \min(x_1,x_2,x_3,x_4), \quad (5)$$
$$\Delta_y = \max(y_1,y_2,y_3,y_4) - \min(y_1,y_2,y_3,y_4). \quad (6)$$

The balance error is related to the offset error of the BPM. For the geometry of the BPM chamber of SPring-8, the vertical balance error Δ_y is about 1.5 times larger than horizontal Δ_x. Hereafter, the vertical BPM balance error Δ_y is used as an index to evaluate the stability of BPM.

FEATURES OF BALANCE ERROR OF SPRING-8 BPM

An example of trend of the balance error of the SPring-8 BPM for one operation cycle of SPring-8 (2nd run of 2015FY, May/07-June/06) is shown in Fig. 2. The upper panel shows balance error defined in the previous section with the environment data, the temperature and the DP. The temperature is measured in the accelerator tunnel near the BPM. The DP is calculated from the temperature and humidity measured by the air-conditioning system for the tunnel. The lower panel of Fig. 2 shows voltages for each electrode channel normalized by the mean of the four, subtracted by the initial values in the plot. The BPM shown in Fig. 2 is stable and the balance error is less than 5 µm. Slight fluctuations in each voltage reflect actual orbit fluctuations.

Through the extensive survey of the logged data of the BPM and the operating environment, we have revealed several features of variations of balance error of the BPM. Figure 3 shows an example of BPM with balance error correlated with the DP. Drift of balance error is 48 µm. Voltages of some channels are also correlated with the DP.

Figure 4 shows an example of BPM of which balance error varies like step functions. Some of discontinuous jumps of balance error are identified to occur at occasions after beam abort and changeover of beam filling-pattern. Jump of balance error is 10 µm. Voltages of some channels jumped simultaneously with the balance error. Sources of the jumps could be failed behaviors of RF switches in the BPM circuits which select one of 4 BPM electrodes. Inspections of the switch modules and exchanges of the faulty ones are planned.

Figure 5 shows an example of BPM balance error variating with a period of approximate one day. Voltages of some channels also varied with the same period. Variation of balance error is 25 µm. The period of approximate one day suspected the environment temperature as suspected cause of variations. However, no significant correlation has been found so far. Further investigations are necessary to find the cause.

Figure 6 shows an example of BPM with fast variations of balance error. Voltages of some channels also varied. Variation of balance error is about 7 µm. No significant correlation has been found so far with other parameters. The behavior of variations seems to change at the changeover of beam filling patterns, suggesting that the source of the variations could be the beam, for example higher-order modes of electro-magnetic waves excited in the vacuum chamber.

The features of variations of the balance errors of the SPring-8 BPM are summarized in Fig. 7. The BPMs with variation smaller than 5 µm are counted as stable BPMs. When the balance error of a BPM has both the correlation with the DP and the step behavior, both "DP" and "step" are counted up. The variations correlated with the DP and the step variations are the majority, accounting for 20% and 18%, respectively. For BPMs with step variations, of balance error, inspections of the switch modules of the readout circuit and exchanges of the faulty ones are planned. We will discuss possible causes of variations correlated with the DP in the next section.

DISCUSSION

Among the BPMs showing variations of balance errors correlated with the DP, we have found that the BPMs with cables damaged by radiation have large variations (C05-6, C17-6 and C42-2 in Fig. 7). Figure 8 shows TDR waveforms of the cables of the BPM C05-6. Reflections in portions of the cables irradiated by radiation scattered by a photon absorber is evident (Fig. 9). To investigate the cause of the imbalance variation, we replaced the damaged cables with new ones and covered them with Pb tube with 3 mm thickness for shielding radiation. The cables removed from the BPM C05-6 were installed in the BPM C07-1 which did not show variations correlated with the DP.

ISBN 978-3-95450-176-2

We also removed the cables from the BPM C29-6 which showed variations with the DP. TDR waveform of the cables also indicated unusual reflection similar to that of the BPM C05-6 caused by the radiation from the photon absorber. We measured TDR waveforms of the removed cables in a humidity controlled chamber to investigate the effect of the DP to reflections. Fig. 10 shows TDR waveforms measured by changing humidity at a fixed temperature (28℃). Significant changes of voltage reflection coefficient were revealed near the end of the damaged cables on the button side. A new cable was measured for comparison, which had small reflection coefficient independent of the DP.

We have found that the reflection coefficient of a radiation damaged cable is affected by the DP. Therefore, we consider that a possible cause of the BPM balance error correlated with the DP is the variations of standing waves in the BPM cables damaged by radiation which is dependent on the DP. To confirm this idea, we will carefully observe the imbalance variations for the BPMs C05-6 and C07-1 after the machine operation is restarted in September.

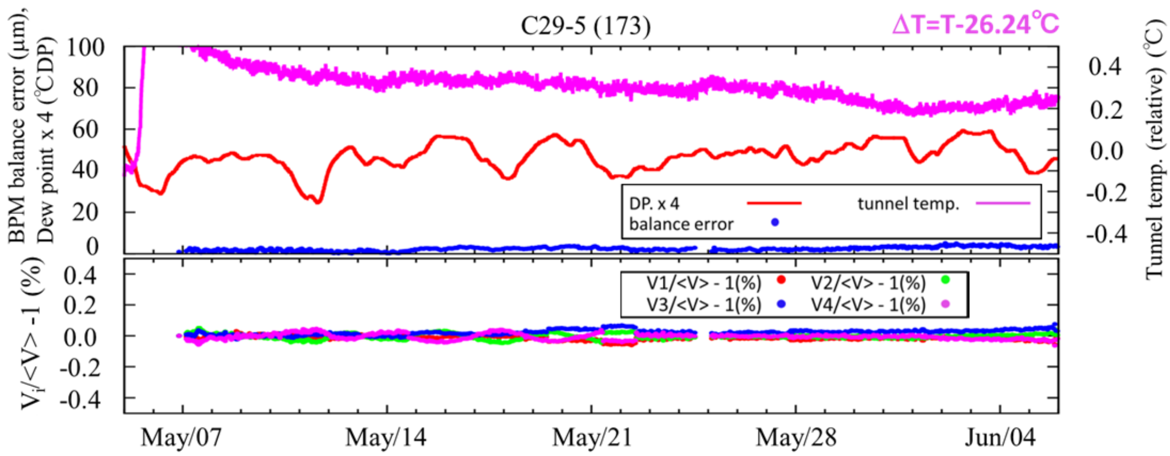

Figure 2: An example of stable BPM. Peak-peak variation of balance error was ~5 μm. Slight variations in voltages are due to beam orbit variation. Legends are common for Figs. 3-6.

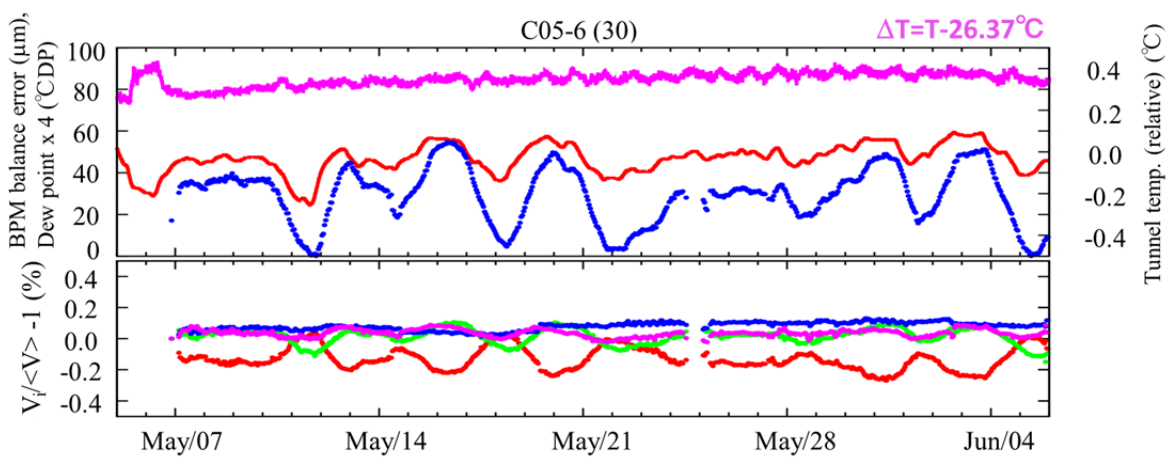

Figure 3: An example of BPM with balance error correlated with the DP. See Fig. 2 for legends.

ISBN 978-3-95450-176-2

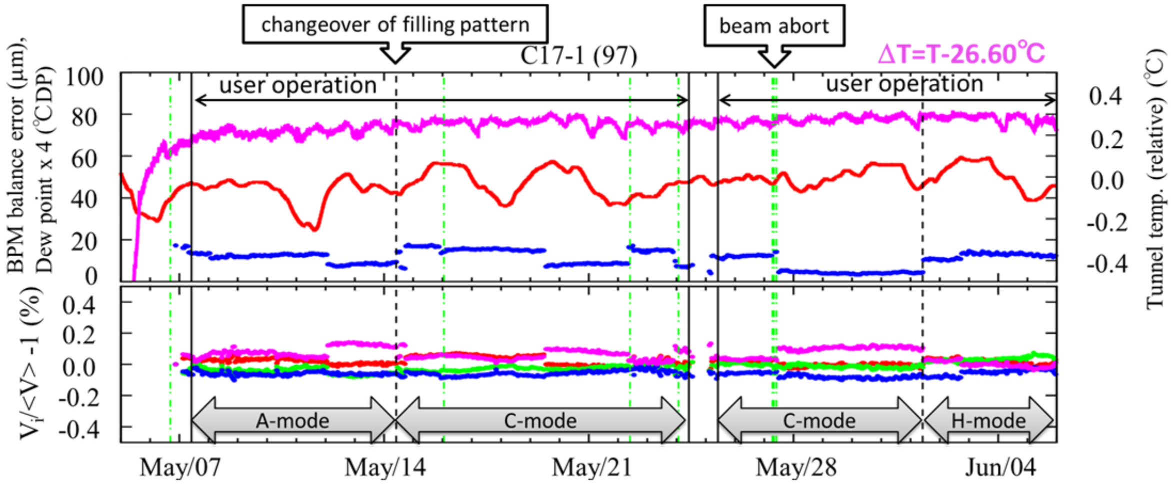

Figure 4: An example of BPM with step function like variations of balance error. See Fig. 2 for legends. In operation modes given in the figure, bunches are stored as follows [4]; A-mode : 203 bunches with each bunch current of 0.5 mA are equally spaced, C-mode : 29 bunch trains are equally spaced. Each train consists of 11 bunches with the bunch current of 0.3 mA, H-mode : one bunch train which consists of 924 bunches with the bunch current of 0.1 mA and one isolated bunch with the bunch current of 5mA. In every operation-modes, the total beam current stored in the ring is 100 mA.

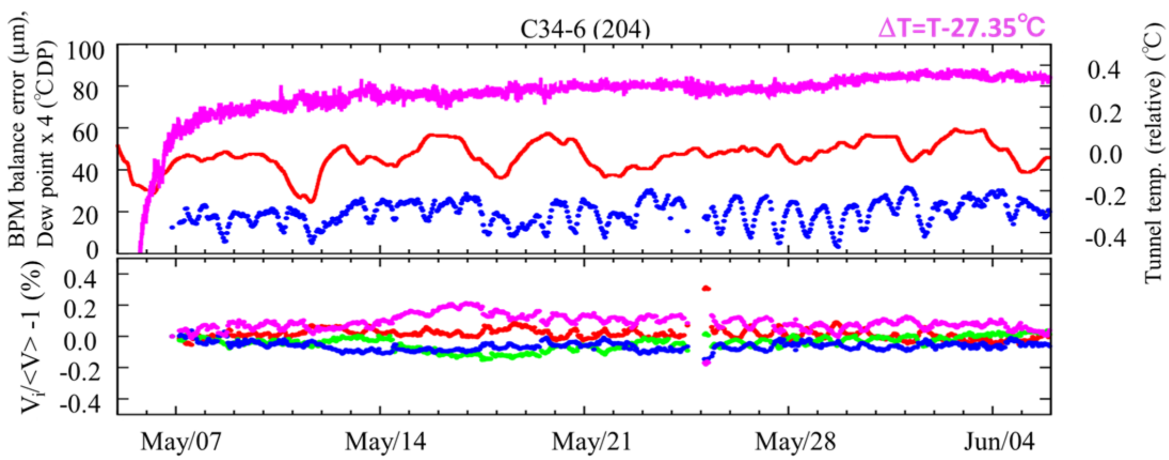

Figure 5: An example of BPM with balance error varying with a period of approximate one day. See Fig. 2 for legends.

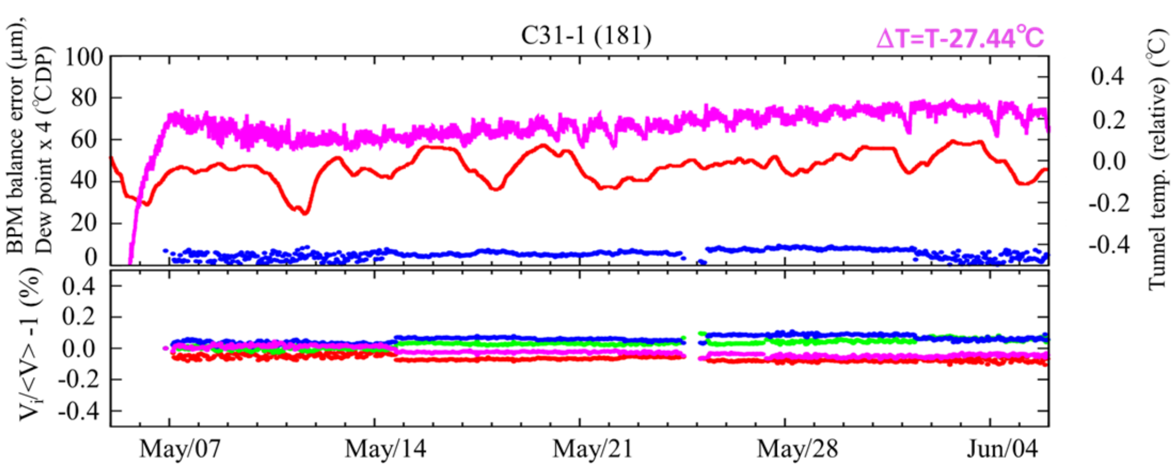

Figure 6: An example of BPM with fast variation of the BPM with balance error. See Fig. 2 for legends.

ISBN 978-3-95450-176-2

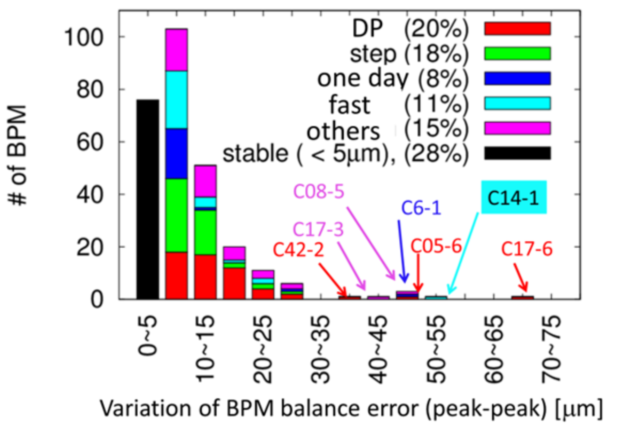

Figure 7: Histogram of the peak-peak variations of the BPM balance error. BPMs with variations smaller than 5 µm are counted as stable.

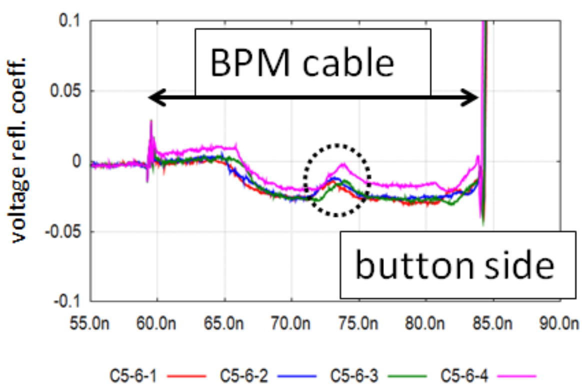

Figure 8: TDR waveforms for the cables of BPM C05-6. Humps around 73 ns correspond to shade of a steering magnet girder placed between the cables and a photon absorber (Fig.9).

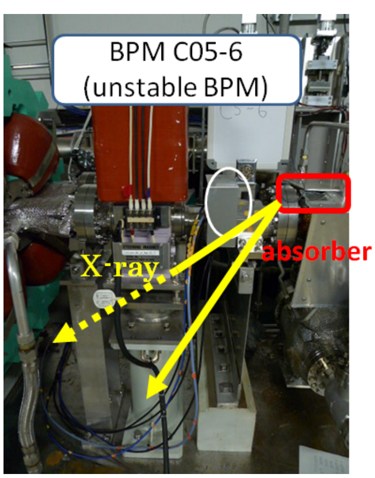

Figure 9: Layout of the BPM C05-6 and the photon absorber

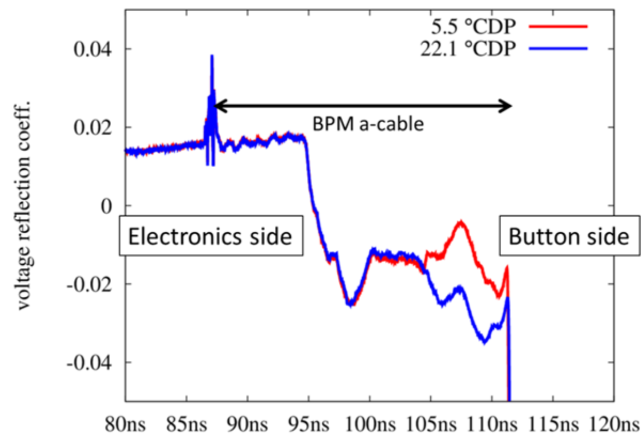

Figure 10: TDR waveforms of the damaged BPM cable (C29-6-2) measured by changing the DP at a fixed temperature (28℃) .

SUMMARY

In order to find and cure the causes of variations of offset errors of the SPring-8 BPM system, we recently surveyed extensively the logged data of the BPM and the operating environment, such as the temperature and the DP. We have revealed several features of variations of the offset errors. To cure the step variations, inspections of the switch modules of the readout circuits and exchanges of the faulty ones are planned. For variations correlated with the DP, we consider that a possible cause is the variations of standing waves in the signal cables damaged by radiation which is dependent on the DP. Further investigations are necessary to find the causes of other variations of BPM offset errors.

REFERENCES

[1] M. Masaki et. al, A Method of Beam-based Calibration for Beam Position Monitor, Proc. of the 11th Symp. on Accel. Sci. and Technol., SPring-8, 1997, p.83.

[2] S. Sasaki, T. Fujita et al., Proc. of the DIPAC 2007, Venice, Italy, (2007) p. 114

[3] T. Fujita, S. Sasaki et.al, Proc. of the IPAC2014, Dresden, Germany, (2014), p. 274

[4]http://www.spring8.or.jp/en/users/operation_status/schedule/bunch_mode

ISBN 978-3-95450-176-2

CHARACTERIZATION OF THE SR VISIBLE BEAM POLARIZATION STATE AT SPEAR3†

Chunlei Li[1], Jeff Corbett[2] and Toshiyuki Mistuhashi[3]
[1]East China University of Science and Technology, Shanghai, China
[2]SLAC National Accelerator Laboratory, Menlo Park, USA
[3]KEK, Tsukuba, Japan

Abstract

Synchrotron radiation has the well-known property of horizontal field polarization in the midplane with increasingly elliptical polarization in the vertical plane. By measuring the beam intensity transmitted through a linear polarizer, it is possible to characterize the beam polarization state, determine the Stokes' parameters and solve for the beam polarization ellipse in the visible portion of the SR spectrum. The results can be compared with Schwinger's equations for synchrotron radiation taking into account the effect of extraction mirrors.

INTRODUCTION

Synchrotron radiation (SR) has both partially-coherent and fully-polarized electromagnetic field properties, each used for a wide range of scientific research. With the advent of high-power, short-pulse free-electron lasers, applications depending on the spatial beam coherence are growing at a rapid rate. Similarly elliptically polarized x-rays have become an increasingly powerful tool to study magnetic dichroism and chirality at both storage rings and FEL facilities [1]. The large vertical opening angle of visible light in the diagnostic beam line at SPEAR3 provides a unique opportunity to study both the transverse spatial coherence [2] and electromagnetic polarization state of the beam [3].

The polarization state in particular can be characterized by measuring beam power transmitted through a polarizer oriented at systematic angles with respect to the x-y beam axis. In this way is it possible to obtain 'slice' measurements of the beam polarization ellipse which can be combined to represent the beam polarization state in terms of the Stokes parameters [3,4].

To cross-check the measurements we compare with Schwinger's equations for the SR field [5]. These 'classical' equations express the horizontal and vertical field intensities $E_x^2(\omega,\psi)$and $E_y^2(\omega,\psi)$ in terms of radiation frequency ω and, conveniently, vertical observation angle ψ. For SR the relative phase difference between E_x and E_y is $\pm\delta=\pi/2$ at all emission angles depending on whether the observer is above (+) or below (-) the midplane, and $E_x \neq E_y$ so the radiation is i general elliptically polarized. Using the SPEAR diagnostic beam line it is possible to measure an calculate the SR polarization state in the visible ligh regime as a function of vertical observation angle.

†Work sponsored by U.S. Department of Energy, Office of Basic Energy Sciences under Contract No. DE-AC02-76SF00515 and the China Scholarship Council.
corbett@slac.stanford.edu

MEASUREMENT SYSTEM

Figure 1 shows a plan view of the SPEAR3 diagnostic beam line. The beam line contains a horizontal 'cold finger' to block the on-axis hard x-ray SR component followed by a rhodium-coated mirror to horizontally reflect visible dipole radiation into the diagnostic laboratory. The cold finger blocks ±0.6 mrad of the beam at the midplane and the surrounding apertures have an acceptance of 3.5 mrad x 6 mrad. A pair of near-incidence Aluminum mirrors is used to reject any stray x-ray Compton scattering and align the SR beam with the optical bench. An image of the 60mm x 100mm unfocused visible SR beam showing the shadow of the cold finger at the measurement station is seen in Fig. 2.

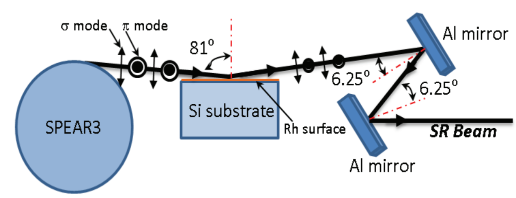

Figure 1: Plan view of the diagnostic beamline.

For the beam polarization measurements, we constructed a remote- controlled scanning system rotatable polarizer, 532nm bandpass filter (BP) and power meter on a continuous-motion vertical stage [6]. An insertable quarter waveplate (QWP) optically matched the bandpass filter is used to determine helicity of the to elliptically polarized light.

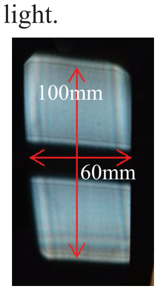

Figure 2: Unfocused visible SR Beam.

As shown in Fig. 3, the polarizer was installed on a computer controlled rotation stage (Newport URS50BPP) to adjust the polarizer axis.

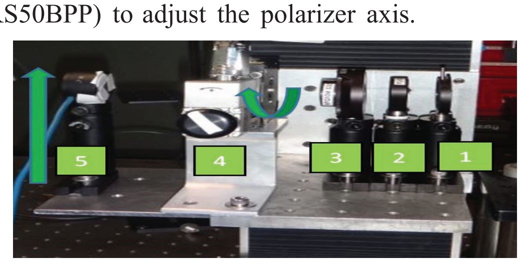

Figure 3: Measurement apparatus: 1-iris, 2-BP filter, 3-quarter wave plate, 4-polarizer, 5- power meter.

ISBN 978-3-95450-176-2

remotely. The complete optical system was installed on a vertically-adjustable stage to measure the beam intensity at different observation angles.

The automated measurement system contains two main parts - one for motor control and the other for data acquisiton. A block diagram of the system is shown in Fig. 4. The motor control system is composed of 3 components: (1) an SSRL in-house motor controller, (2) an in-house motor driver, and (3) Allied Electronics stepper motor M062-LS03E. The data acquistion system also contains 3 parts: (1) Newport 1815-C power meter with 818-UV sensor, (2) Nova R&D Inc., N101 voltage-to-requency converter, and (3) in-house counter/timer electronics.

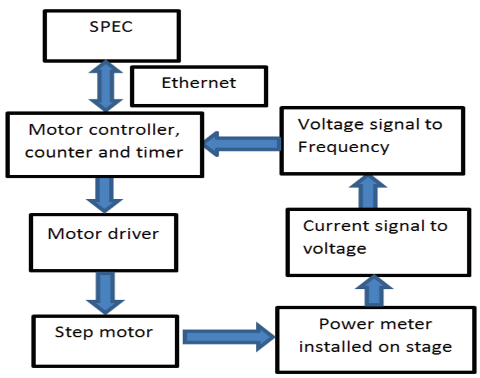

Figure 4: Block diagram for continuous-scan system.

To record beam intensity the Newport 1815-C voltage signal was first converted to a frequency-modulated pulse train through the voltage-to-frequency module. The frequency signal was then detected using the SSRL counter/timer electronics. SPEC software version 6.02.08 (Certified Scientific Software, USA) was used to communicate with both the motor controller and the counter/timer to move the vertical stage at a continious rate while synchronously collecting intensity data [6].

In general five parameters need to be defined for the trajectory of the vertical stage. They are start position (s), end position (f), number of intervals (n), data acquisition time for each interval (t) and the motor acceleration time (t_{acc}). The distance of each interval can be calculated according to Eq. 1a, and the velocity v calculated from Eq. 1b:

$$d = \frac{f-s}{n} \tag{1a}$$

$$v = \frac{d}{t} \tag{1b}$$

In order to make the detector system move at constant velocity during the measurement process, an acceleration segment d_{acc} and deceleration segment d_{dec} were added before the start and after the end positions. The distance of the acceleration and deceleration segments can be calculated from Eq. 2a. The start position s_{start} and end position s_{end} of the acceleration part are calculated from Eqs. 2b-c, and the deceleration part from Eqs. 2d-e.

$$d_{acc} = d_{dec} = 0.5 \times v \times t_{acc} \tag{2a}$$

$$s_{start} = s - 0.5 \times d - d_{acc} \tag{2b}$$

$$s_{end} = s - 0.5 \times d \tag{2c}$$

$$s_{start} = f + 0.5 \times d \tag{2d}$$

$$s_{end} = f + 0.5 \times d + d_{dec} \tag{2e}$$

BEAM LINE MIRROR EFFECTS

The first optical element in the SR beam line is the rhodium-coated pickoff mirror. Due to geometric constraints, the mirror intercepts the SR beam at a steep incidence angle of 81° to the surface normal [7]. The reflected field attenuation and phase shift can be calculated from Fresnel's laws [8]

$$r_s = \frac{R_s}{E_s} = \frac{n_1 \cos\theta_i - n_2 \cos\theta_t}{n_1 \cos\theta_i + n_2 \cos\theta_t} \tag{3a}$$

$$r_p = \frac{R_p}{E_p} = \frac{n_2 \cos\theta_i - n_1 \cos\theta_t}{n_1 \cos\theta_t + n_2 \cos\theta_i} \tag{3b}$$

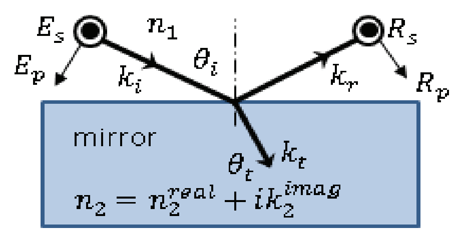

Figure 5: S- and P-wave reflection at a mirror surface.

where as seen in Fig. 5 E_s, E_p and R_s, R_p are the incident and reflected electric field values, respectively, $n_1=1$ is the free-space index of refraction, and n_2 is the complex-valued refraction index for the mirror. θ_i and θ_t (complex) are related by Snell's law:

$$n_1 \sin\theta_i = n_2 \sin\theta_t \tag{3c}$$

Of note horizontally-polarized σ-mode SR radiation corresponds to the P-polarized field component at the horizontally reflecting Rh mirror in the parlance of optics (parallel to the plane of incidence). Similarly, π-mode SR radiation corresponds to the S-polarization component at the mirror. Designations {σ,π}={P,S} will be used in context below for consistency with both nomenclatures.

Table 1 lists the complex refraction index value n_2 and calculated reflectivities r_s and r_p for the Rh mirror at 81° incidence angle at three different wavelengths. Also shown are the ratios for intensity reflectance $I_p/I_s = (r_p/r_s)^2$ and net phase shift $\Delta\phi_{s/p}$ between field components E_s and E_p. According to the calculation, the ratio I_p/I_s is ~0.5 indicating the intensity of the SR σ component should be attenuated twice as much as the π component due to optical activity of the rhodium mirror.

Figure 6 shows a plot of intensity *reflectance* for the S and P polarization components as a function of incidence angle on the Rh surface at λ=532nm [9]. At an incidence angle of 81° the P-polarization reflectance is near the minimum value.

ISBN 978-3-95450-176-2

Table 1: Rh mirror reflection parameters at 81° incidence. $\Delta\emptyset_s$ and $\Delta\emptyset_p$ are phase change of S and P waves at the mirror surface. $\Delta\emptyset_{s/p}$ is the net phase change (see Fig. 7).

Wavelength (nm)		430	532	650
Refractive index		1.64	1.93	2.19
Extinction index		4.37	4.89	5.74
Reflectivity	r_s	0.98	0.98	0.98
	r_p	0.70	0.68	0.68
	I_p/I_s	0.51	0.48	0.48
Reflection phase	$\Delta\emptyset_S$	-176.4°	-176.9°	-177.3°
	$\Delta\emptyset_P$	-70.1°	-77.2°	-87.0°
	$\Delta\emptyset_{S/P}$	-16.3°	-9.7°	-0.3°

In terms of phase, Table 1 indicates at 532nm the S-wave is delayed by -176.9° and the P-wave is delayed by -77.2°. Figure 7 shows how the delays act on the two polarization components. As pictured, the S-wave (π–mode) begins 90° *ahead* of the P-wave prior to reflection. After reflection the S-wave is 10° *behind* the P-wave so that light is more linearly polarized and the helicity reversed. On the opposite side of the midplane the S-wave leads the P-wave by 170° after reflection.

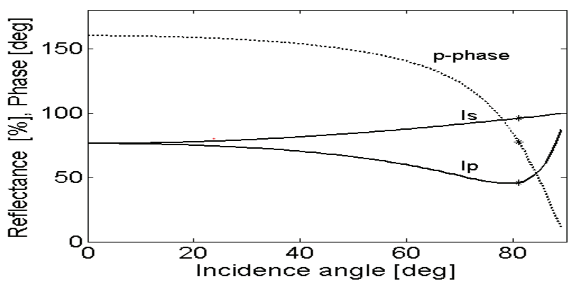

Figure 6: Calculated intensity reflectance for S and P waves at the Rh mirror for λ=532nm. Dashed line is the phase retardation for P-waves.

The net effect of the Al mirrors is to produce a reflectance ratio I_p/I_s near unity and relative phase shift of order 1° for visible light.

STOKES LAW AND THE BEAM POLARIZATION ELLIPSE

At optical and x-ray frequencies oscillations of the electromagnetic field are too fast for direct measurement. Detectors can only record beam intensity $I = EE^*$ and phase information is lost. This problem has confounded scientists for centuries. In a seminal paper published in 1852, G.G. Stokes proposed a theoretical framework to characterize the polarization state of light without direct measurement of the oscillating field [10]. The measurements require use of a single polarizing element in conjunction with a phase retarder (waveplate). For our application, when the SR beam passes through a polarizer oriented at angle θ with respect to the x-axis, the transmitted field is

$$E = E_{x0}\cos\theta + E_{y0}\sin\theta e^{i\delta} \tag{4}$$

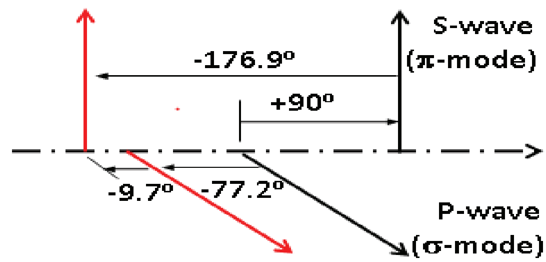

Figure 7: Electric field phase shift at the Rh mirror. S-wave is +90° at incidence and -10° after reflection.

where E_{xo} and E_{yo} are the Cartesian field amplitudes and δ the relative phase difference. Substituting E into $I = EE^*$ yields a simplified version of Stokes' Law for beam intensity as a function of polarizer angle θ in the absence of a phase retarder:

$$I(\theta) = E_{xo}^2 cos^2\theta + E_{yo}^2 sin^2\theta \\ +2E_{xo}E_{yo}\cos\theta\sin\theta\cos\delta \tag{5}$$

Examination of Eq. 5 reveals that three field parameters $\{E_{xo}, E_{yo}, \delta\}$ are sufficient to describe the basic polarization state of the SR beam. Knowledge of these three parameters also provides a graphical representation in terms of the beam polarization ellipse:

$$\frac{E_x^2}{E_{x0}^2} - 2\frac{E_xE_y}{E_{x0}E_{y0}}\cos\delta + \frac{E_y^2}{E_{y0}^2} = sin^2\delta \tag{6}$$

The polarization ellipse is a statistically time-average quantity that is readily derived by eliminating the propagator term $\omega t - kz$ from parametric plane wave expressions for E_x and E_y, namely [4]

$$E_x = E_{x0}e^{-i(\omega t - kz + \delta)} \tag{7a}$$
$$E_y = E_{y0}e^{-i(\omega t - kz)} \quad . \tag{7b}$$

where again δ is the relative phase between E_x and E_y. For SR radiation E_{x0} and E_{y0} obey Schwinger's equations as a function of ω and vertical observation angle ψ. Mathematically the beam polarization ellipse is closely related to the intensity modulation curve in Eq. 5 but provides a more intuitive picture of the field polarization characteristic.

From Stokes Law, the first three Stokes parameters can recovered by recording beam intensity without the QWP in place and the polarizer oriented at angles θ=0°,45°,90° and 135° with respect to the x-axis. By definition of the Stokes parameters and inspection of Eq. 5 we have

$$S_0 = I_{0^o} + I_{90^o} = E_{x0}^2 + E_{y0}^2 \tag{8a}$$
$$S_1 = I_{0^o} - I_{90^o} = E_{x0}^2 - E_{y0}^2 \tag{8b}$$
$$S_2 = I_{45^o} - I_{135^o} = 2E_{x0}E_{y0}\cos\delta \tag{8c}$$

ISBN 978-3-95450-176-2

As demonstrated in [3], measurements of I_{0^o} and I_{90^o} yield E_{xo} and E_{yo} which can be used to calculate the phase parameter δ from Eq. 8c.

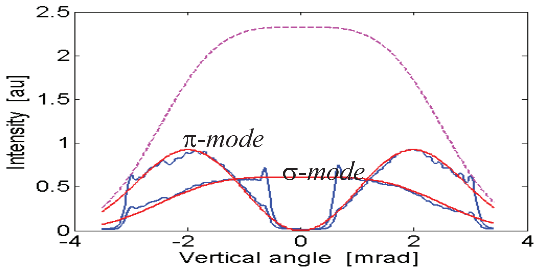

Figure 8: Horizontal (σ-*mode*) and vertical (π-*mode*) polarization intensities vs. vertical observation angle. Blue=measured, red=model, magenta=free space.

Introduction of the quarter waveplate yields the forth Stokes parameter (S_3) associated with right/left 'handedness' of the electromagnetic field polarization:

$$S_3 = I_{45^o}^{QWP} - I_{135^o}^{QWP} = 2E_{x0}E_{y0} sin\, \delta \qquad (8d)$$

where the superscript *QWP* indicates the quarter waveplate has been inserted with fast axis oriented along one of the principle x-y axes.

MEASUREMENTS AT 532nm

Figure 8 shows the measured SR polarization intensities E_{x0}^2 and E_{y0}^2 as a function of vertical elevation angle. Compared with Ref. [3], the data spans a larger vertical observation angle and the storage ring vacuum chamber has been re-aligned to reduce edge diffraction at the limiting apertures. Some diffraction at the top, bottom and cold finger is still apparent.

Calculated beam intensity curves based on Schwinger's equations are superimposed on the data. For the σ-mode calculation, the curve was reduced by a factor of 0.26 relative to the calculated value. Referring to Table 1, the anticipated reduction due to the Rh mirror is only 0.50. The difference may be attributed to electro-chemical coating of the Rh mirror surface after years of SR fluence altering the complex index of refraction. The *un-scaled* theoretical σ-mode curve is shown as a dashed line.

Figure 9 shows the measured beam intensities with the polarizer oriented at 45° and 135°. Substituting the Schwinger model for field values $E_{x0}$and E_{y0} deduced from Fig. 8 into the expression for field projection Eq. 4, the model beam intensities were again calculated for polarizer angles of 45° and 135°. In this case, the relative phase angle δ was set to 10° to account for optical activity at the Rh mirror (see Table 1). The dashed line shows the theoretical result in the absence of the Rh mirror, i.e. no beam attenuation and $\delta = \pi/2$.

Notably for both the top and bottom segments of the SR beam the beam intensity changes dramatically as the polarizer is rotated from 45° to 135°. This is indicative of a near-linear polarization state of the light. The result is consistent with a small phase angle δ between the

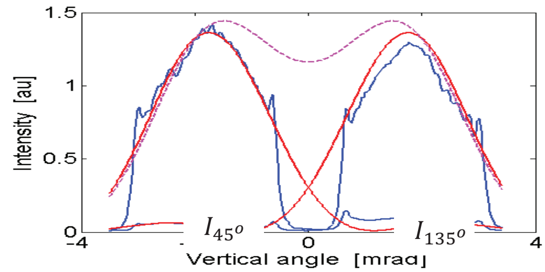

Figure 9: Beam intensity measured with polarizer oriented 45° and 135°. Blue=measured, red=model magenta=free space.

σ and π mode radiation components after reflection.

The beam polarization ellipse at 1mrad vertical observation angle is plotted in Fig. 10 to demonstrate the near-linear polarization state with the major axis of the ellipse much larger than the minor axis. Referring to Fig. 8, at 1mrad the horizontal and vertical fields are approximately equal. The large magenta ellipse plotted in Fig. 10 is the free-space result predicted from Schwinger's equations in front of the mirror.

In this case the horizontal field amplitude is a factor of two more than the vertical field and the ellipse is upright because the free-space SR phase angle δ=90°.

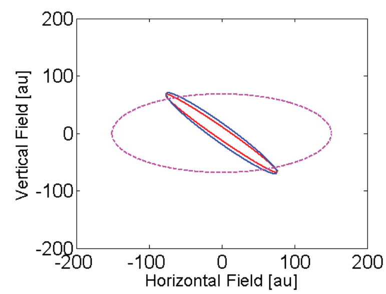

Figure 10: Beam polarization ellipse at ψ=1mrad. Blue=measured, red=model, magenta=free space.

In order to analyse polarization helicity, recall quarter waveplates can convert linearly polarized light into circular polarized light and vice versa. In our case the quarter waveplate was inserted with fast axis aligned vertical so the horizontal σ-mode light was delayed 90°.

Following the prescription for measurement of S3 (Eq. 8d) the polarizer was again oriented at 45° and 135° and vertical scans of beam intensity recorded. Both the raw data and the calculated curves based on Schwinger's model are plotted in Fig. 11, again using the model phase angle of δ=10°. The different between the 45° and 135° data yields polarization helicity.

As expected, the phase retarding effect of the QWP causes the polarization state to change from a near-linear condition (Figs. 9,10) to a more circular state, i.e. the length of major and minor axes of the beam polarization ellipse are now more equal in magnitude and the relative phase between E_x and E_y is closer to 90°. The data again

ISBN 978-3-95450-176-2

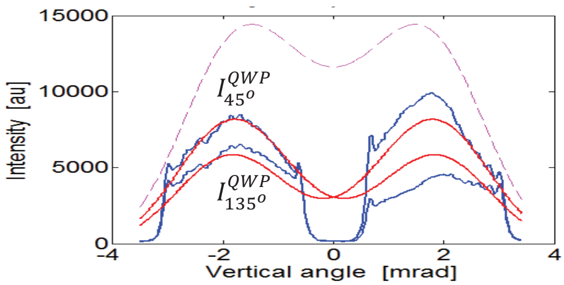

Figure 11: Beam intensity measured with QWP installed and polarizer oriented 45° and 135°. Blue=measured, red=theory, magenta=free-space.

shows an asymmetry between the top and bottom portions of the beam. The cause of the asymmetry is under investigation.

PHASE SHIFT AT THE Rh MIRROR

To further analyse the top/bottom asymmetry we can calculate the relative phase shift δ between the polarization components directly from the measured data. In this case the field amplitudes E_x and E_y are derived from the σ- and π–mode intensity measurements in Fig. 8, this time using the raw data instead of the model. These values are again substituted into the Eq. 8c where measured data is also used for $I_{45^o} - I_{135^o}$ to solve for the phase angle δ. As seen in Fig. 12, this method yields a phase factor $\delta \sim$ -15° in the bottom half of the beam, close to the calculated value of δ=-9.7°. (Without the Rh mirror the phase differential would be δ=+90°.) The resulting 'measured' beam polarization ellipse is superimposed on the calculated ellipse in Fig. 10. The measured ellipse is slightly more 'elliptical' because the phase angle δ is larger.

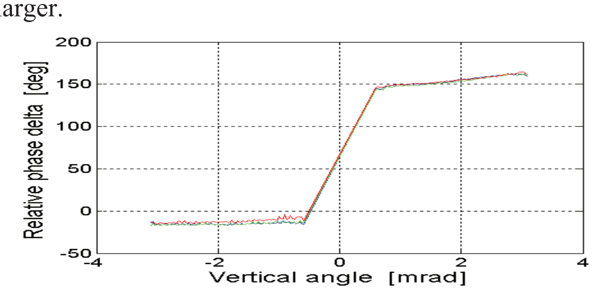

Figure 12: Relative phase angle δ between σ-mode and π-mode polarization components after Rh mirror.
Blue: 430nm, green: 532nm, red: 650nm.

Figure 12 also shows the result of the same calculation process applied to data recorded with 430nm and 650nm bandpass filters. In the lower portion of the beam the measured phase is near the calculated value but does not show the trend toward δ=0° seen in Table 1 at longer wavelengths. Since the phase angle is a sensitive function of incidence angle the measurements are nonetheless considered plausible. In the upper portion of the beam the phase is observed to change with the vertical elevation angle indicating either surface contamination or more likely physical distortion of the mirror surface.

CONCLUSIONS

Beam polarization measurements at the SPEAR3 diagnostic beam line were evaluated taking into account both field attenuation and phase shift of the SR beam at the Rhodium pickoff mirror. The vertical beam polarization profile is found to be in good agreement with Schwinger's theory for highly relativistic synchrotron radiation emission. A factor of 2 anomaly in reflectance is observed leading to a larger than expected reduction in the σ-mode component. Accepting the validity of Schwinger's equations in the visible regime we attribute the difference to as-yet unexplained optical activity at the surface of the pickoff mirror.

The relative phase between E_x and E_y is close to the predicted value after reflection from the Rh mirror leading toward a more linear polarized beam than the free-space SR beam condition before the mirror. Across the bottom surface of the mirror the relative phase is nearly constant as anticipated. The phase shift slews across the top of the mirror indicating a possible physical distortion of the mirror.

ACKNOWLEDGMENTS

The authors would like to thank the China Scholarship Council, A.Knowles, D.Van Campen, M.Polyanskiy, W.J.Zhang, and SPEAR3 staff for support of this work.

REFERENCES

[1] R. Kukreja, et al., *X-rays Expose Transparent Spins*, Physical Review Letters, 24 August 2015.
[2] T.Mitsuhashi, *Measurements using Spatial Coherence of SR*, IPAC15, Richmond, VA (2015).
[3] J.Corbett, C.L.Li, et al., *Characterization of Visible SR at SPEAR3*, IPAC15, Richmond, VA (2015).
[4] E.Collett, *Polarized Light: Fundamentals and Applications*, Marcel Dekker, Inc., NY (1992).
[5] A.Hoffmann, *The Physics of Synchrotron Radiation*, Cambridge University Press (2004)
[6] C.L.Li, A.M.Kiss and W.J.Zhang, *Investigation of Continuous Scan Methods for Rapid Data Acquisition,* IPAC15, Richmond, VA (2015).
[7] C.Limborg, et al., *An Ultraviolet Light Monitor for SPEAR3*, EPAC02, Paris, France (2002).
[8] E.Hecht, *Optics*, 2nd Edition, Addison-Wesley (1987).
[9] A useful calculator for reflectivity at mirror surfaces can be found at http://refractiveindex.info/
[10] G.G. Stokes, *On the Composition and Resolution of Streams of Polarized Light from Different Sources*, Trans. Camb. Phil. Soc., Vol. IX, 399 (1852).

HIGH POSITION RESOLUTION BPM READOUT SYSTEM WITH CALIBRATION PULSE GENERATORS FOR KEK e+/e- LINAC

F. Miyahara#, K. Furukawa, M. Satoh, Y. Seimiya, T. Suwada, KEK, Tsukuba, Ibaraki, Japan
R. Ichimiya, JAEA, Rokkasho, Aomori, Japan
H. Saotome, KIS, Tsuchiura, Ibaraki, Japan

Abstract

The KEK e+/e- injector linac will be operated in multiple modes for the electron beam injection to three independent storage rings, the SuperKEKB HER, Photon Factory (PF) Ring and the PF-AR, and the positron beam injection into the damping ring and the SuperKEKB LER. The beam current ranges between 0.1 and 10 nC/bunch. The beam current depends on the beam mode. The operation modes can be switched every 20 milliseconds. The injector linac is under upgrade for the SuperKEKB, where the required resolution of beam position measurement is less than σ=10 μm. However, the current beam position monitor (BPM) readout system based on oscilloscopes for stripline beam position monitors has the position resolution of 50 μm approximately. Thus, we have developed a new BPM readout board with narrow band pass filter, 16-bit, 250 Msps ADCs and calibration pulse generators. The system is based on VME standard and the beam position is calculated by FPGA on board. The calibration pulse follows every position measurement. The calibration pulse is used for the gain correction and the integrity monitor of the cable connection. We will report details of the system.

INTRODUCTION

In the SuperKEKB, the injector linac is required to inject 5 nC/bunch, 7GeV electron and 4 nC/bunch, 4 GeV positron beams with the emittance less than 20 mm-mrad. The electron beam with emittance of about 10 mm-mrad, is generated by a photocathode RF gun [1]. The initial emittance is low enough for the requirement, but an emittance growth due to the short range transverse wakefield which is caused by misalignment is not negligible. The emittance growth can be suppressed by using the offset injection method [2]. Numerical studies show the emittance at the end of the linac is less than 20 mm-mrad under the condition of alignment error of 0.1 mm [3,4]. To perform the offset injection in the linac, at least resolution of 10 μm is required. However, the resolution of current oscilloscope based BPM readout system [5] is about 50 μm. The beam is also transported to the PF ring. The bunch charge for the PF ring is 0.2 nC/pulse during the top-up operation. By contrast, primary electron beam for positron production will be 10 nC/bunch. Those operation modes are switched every 20 ms. Thus, the wide dynamic range for beam currents is required. The dynamic range can be ensured by setting attenuation of the BPM signal for every beam modes or currents. That means several gain parameter sets and a calibration system to fix those parameters are needed. The calibration system allows the monitoring of a variation of the gain and integrity of the cable connection. The newly developed board was designed to have the high position resolution with dynamic range from 0.1 to 10 nC/bunch and to be equipped calibration pulse generators. A position resolution of σ=3 μm for 0.1 nC/bunch beam was achieved [6]. The board is also designed to have wide dynamic range for the position. The detail of the design is reported in previous studies [6,7]. There are 93 stripline BPMs on the linac, 20 VME crates with 3-8 readout boards are set on klystron gallery. The old system will be replaced with the new one stepwise after this summer. In this paper, we report a whole system of the BPM, calibration scheme and stability of the gain.

#fusashi.miyahara@kek.jp

BPM SYSTEM

The BPM readout system consists of a VME CPU board (MVME5500), a RAS (Reliability, Accessibility, Serviceability) board, an Event Receiver (VME-EVR-230RF) [8] and BPM readout boards. An EPICS IOC [9] runs on the CPU. The RAS board monitor status (such as power, temperature) and control the fan of the VME crate. The event receiver is used for the distinction of the beam mode and the generation of triggers to BPM boards. The readout board has 4 signal input channels for one stripline BPM. The calibration signal is also sent from one of those channels to the corresponding electrode.

BPM Readout Board

The BPM readout board is composed of four RF units which detect the signal from BPM electrodes, 16-bit 250 MSPS ADCs, sub FPGAs for the ADC and a main FPGA. The position and charge of the beam are calculated in the main FPGA. Those results and parameters for the calculation and the operation of the board are recorded in the registers on main FPGA. Figure 1 shows the block diagram of the board and the RF unit. The setting value of the variable attenuator, sum of ATT1A and ATT1B, depends on bunch charge. In particular, the beam is away from BPM center, a nonlinearity of the ADC gain causes a measured position drift. The readout board has a good

ISBN 978-3-95450-176-2

linearity, less than ±5 μm drift in position, for the relative input signal of ±10 dB.

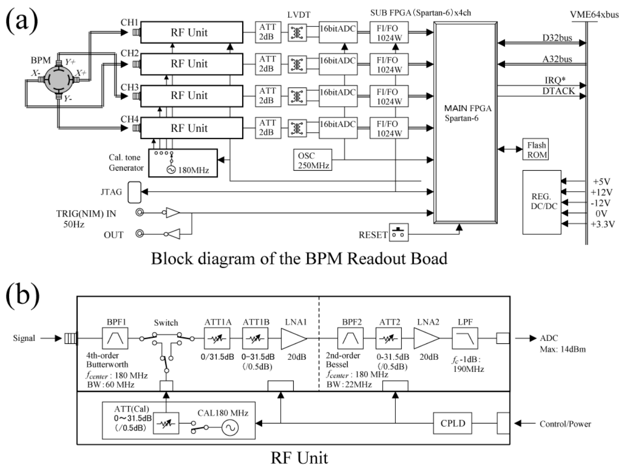

Figure 1: Schematics the BPM readout board (a) and the RF Unit (b).

The signal from the stripline BPM is filtered by 4th-order Butterworth filter which has a bandwidth (BW) of 60 MHz with center frequency (f_{center}) of 180 MHz and the 2nd-order Bessel filter (BW=22 MHz, f_{center}=180 MHz). The double bunch operation with time interval of 96 ns is required in the operations for SuperKEKB. Thus, the Bessel filter is used to convert a bipolar signal to ringing sinusoidal waveform with full-width of ~90 ns. The Butterworth filter is used to compensate rather broad cut-off characteristic of the Bessel filter. The beam position is given by,

$$x = A_0 + \sum_{m=0}^{3}\sum_{n=0}^{3} a_{mn} (\Delta_H / \Sigma_H)^m (\Delta_V / \Sigma_V)^n \tag{1}$$
$$y = B_0 + \sum_{m=0}^{3}\sum_{n=0}^{3} b_{mn} (\Delta_H / \Sigma_H)^m (\Delta_V / \Sigma_V)^n ,$$

where

$$\Delta_H = W_1 - W_2, \Sigma_H = W_1 - W_2 \tag{2}$$
$$\Delta_V = W_3 - W_4, \Sigma_H = W_3 - W_4$$

$$W_i = G_i G'_i \sqrt{\sum_j \left(V_{i,j} - V_{i,ped}\right)^2} \,. \tag{3}$$

The coefficients a_{mn} and b_{mn} were given by fitting the function to the mapping data taken from stretched wire measurement. The variables A_0 and B_0 stand for the offset of electrical center from the quadrupole magnet center and are determined by beam based alignment. An output signal from an electrode is given by root sum square of ADC values within a window which covers the beam/calibration signal and correction factor G and G'. The variable $V_{i,j}$ and $V_{i,ped}$, are ADC value of the i-th electrode (see Fig. 1), where j represents ADC channel, and the pedestal, respectively. The factor G stands for static signal balance between electrodes and depends on signal attenuation in the coaxial cable and a variation of circuit element. The G', dynamic gain factor, represents gain drift which strongly depends on the environmental temperature. Those factors are discussed in the next section.

Calibration Pulse

The calibration pulse is used for a correction of gain balance between electrodes and a monitor of gain drift and cable connection. The signal is shown in Fig. 2. The signal is sent to one of the four electrodes, and then return signals are measured by the readout system. Figure 3 shows ADC signals for the output pulse which was sent from Ch1. Both Ch3 and Ch4 correspond to adjoining electrodes and detect large signal at around 2400 ns. The small signal after the large signal, delayed about 350 ns, represents reflection. The calibration pulse can be set from a short pulse to CW. The pulse width is controlled by the switch after the RF module. Due to response to the CW contains superposition of refection signals; a short pulse is adopted for the calibration. The attenuator after the calibration module, ATT(CAL) in Fig. 1, is used to avoid saturation of the amplifiers and ADC. The power of the RF at the BPF1 input is 36 dBm in ATT(CAL)=0 dB. In case of a largest attenuation setting which corresponds to 10 nC/bunch, we confirmed that signal level enough for the calibration can be obtained.

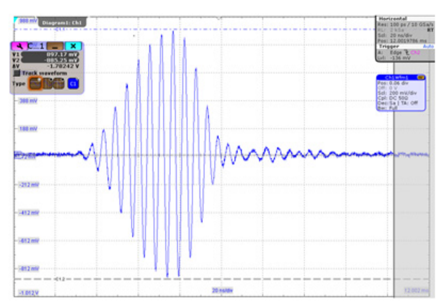

Figure 2: Calibration pulse signal.

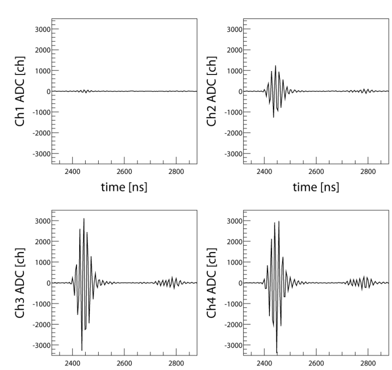

Figure 3: ADC response to the calibration pulse. The pulse was sent to the BPM from Ch1(X+).

ISBN 978-3-95450-176-2

Control and Operation

The readout system is controlled by EPICS framework which was utilized for most devices in the injector linac. The EPICS IOC works on VxWorks 5.5.1. All parameters for the operation and results of a measurement such as position, charge and waveform can be taken from EPICS records. To reduce data acquisition (DAQ) time, the waveform of the signal is not transferred in normal operation. It takes about 3.5 ms to take four waveforms in the board. The waveform is used for setting/confirming the ADC gate. The development of the software is ongoing. The detail of the software will be reported in elsewhere [10].

DAQ scheme is the following:

1. External Trigger
   →Beam Data acquisition
   →Writing parameters for calibration
2. Internal Trigger (6.6 ms after the ext. trigger)
   → Calibration Data acquisition for Horizontal
   →Writing parameters for calibration
3. Internal Trigger (13.2 ms after the ext. trigger)
   → Data acquisition for calibration (vertical)
   →Writing parameters for a next beam.

The external triggers are synchronized the beam timing which is distributed by the EVR. The writing parameter required for each process because parameters such as attenuation setting, gain factor could be changed. The repetition rate of the linac is 50 Hz; three DAQ processes are performed in 20 ms interval. Thus, one DAQ process must be less than 6 ms. Figure 4 shows total elapsed times for one DAQ process in case of maximum load with 8 readout boards. The DAQ time is much faster than required time.

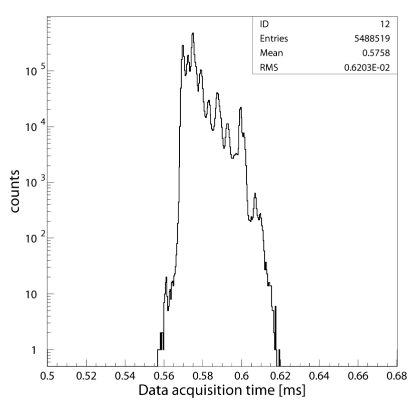

Figure 4: Total elapsed time for one data acquisition process with 8 BPM readout boards.

SIGNAL STABILITY AND GAIN BALANCE

Studies of the gain drift and gain balance between opposite electrodes have been performed by using the calibration pulse. The drift of signal level and gain balance lead to variation of measured charge and position, respectively. The gain balance reflects variation in circuit elements. In particular, the amplifier has a rather large temperature-dependence compared with other elements. Thus, the temperature dependence of the system and the gain drift has been studied. The response to the calibration signals for different environmental temperatures measured by putting a BPM, 30 m coaxial cables and the readout system in a thermostatic chamber. The signal level W_3, W_4 and gain balance W_3/W_4 for the calibration pulse from CH1 are plotted with the temperature in Fig. 5. Where, $G = G'=1$ in Eq. 3. Three sets of the attenuation settings correspond to different bunch charge, 0.5, 1 and 5 nC/bunch. In case of Att(In)=25 dB, in order to keep the signal level to be in good linearity region, the attenuator just after the pulse generator was set to 9 dB. Each data point shown in Fig. 5 is an average of 500 events, and a statistical error is less than 1 ch. The environmental temperature was changed every ~5 hours. The signal and gain balance are very stable and shows quick response and good reproducibility to the temperature, except in the case 9 dB attenuation for the calibration pulse. It appears that the attenuator needs much more time to be an equilibrium state due to high output power of the pulse generator. This variation is less than 1% and the absolute value of the signal does not affect the beam position but the charge. The temperature dependence of the signal level is -1%/°C in the system.

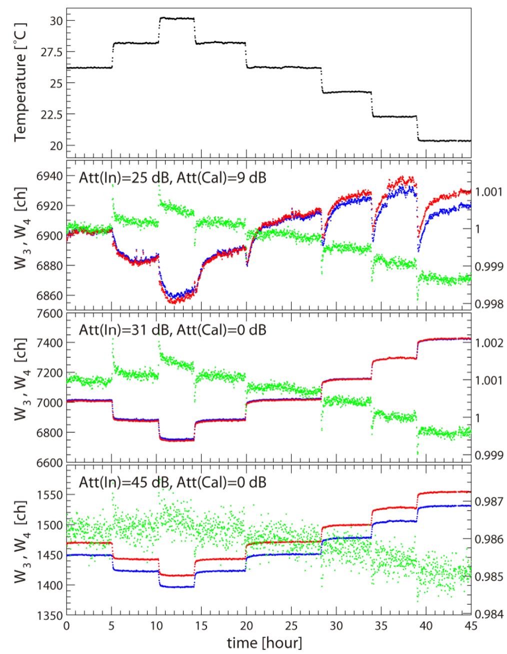

Figure 5: Signal level and gain balance variation. Temperature is shown in the top. Signal levels of CH3(Y+) and CH4(Y-) are plotted by red and blue dots, respectively. The green dots show the ratio of both signals. The Att(In) and Att(Cal) stand for attenuation value for the input (ATT1A+ATT1B) and output of the calibration.

ISBN 978-3-95450-176-2

Figure 6 shows temperature dependence of the gain balance. The data are averages of 10 minutes just before changing the temperature setting. It has been found that the temperature dependence of the gain is very small, less than 0.02%/°C which corresponds to about 1 μm/°C, and shows same gradient for different attenuation settings. In the injector linac, the room temperature is kept in 23 to 26 °C. As a result, the position drift due to a temperature fluctuation is negligible and a correction of the gain drift, *G'*, is not required. By contrast, the value of the gain balance depends on the attenuation value, Att(In), that corresponds the beam charge. The static gain factor *G* will be set so that the signal ratio of opposite electrodes becomes 1 for any attenuation setting. The calibration pulse can be powerful equipment to perform the gain calibration in our linac. More precise gain correction can be performed by using the beam.

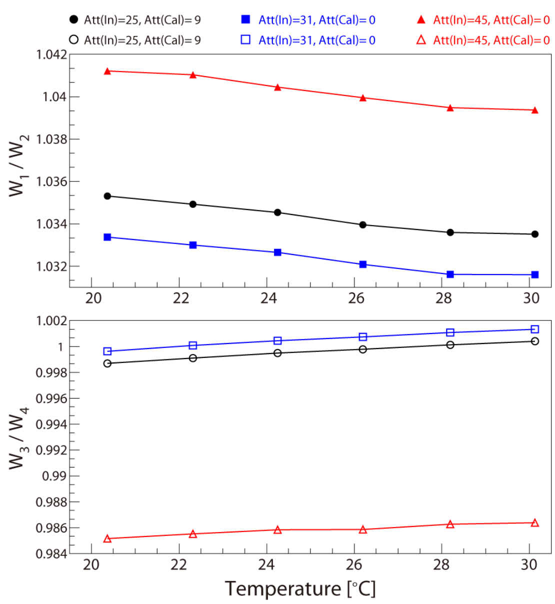

Figure 6: The gain ratio vs. the environmental temperature.

CONCLUSION

In order to suppress the emittance growth in the KEK e+/e- linac, a new BPM system with high position resolution and wide dynamic range in beam charge and position is required. We have developed the new VME-based BPM readout system which consists of CPU board, RAS board, EVR for event timing system and the new readout board with a calibration pulse generator. The system shows negligible gain drift, less than 1 μm, in the environmental temperature of the injector linac. The calibration system gives easy ways to correct the gain balance for any attenuation settings that correspond to beam currents.

ACKNOWLEDGMENT

We greatly thank Dr. Steve Smith (SLAC) and Dr. Andrew Yang (SLAC) for providing us with the important information of the developing of BPM readout system and meaningful suggestions. The authors would like to express thank to Dr. Makoto Tobiyama (KEK) for useful suggestions. We grateful Kyosuke Yamada (DIGITEX LAB. CO.) for his support in the fabrication of the readout board.

REFERENCES

[1] T. Natsui et al., “Quasi-Traveling Wave RF Gun and Beam Commissioning for SuperKEKB”, TUPJE003, IPAC’15, Richmond, Virginia, USA (2015).
[2] A.W. Chao, B. Richter and C.Y. Yao, Nucl. Instrum. Methods 178, 1(1980).
[3] M. Satoh, “Injector commissioning”, The 19th KEKB Accelerator Review Committee, KEK, Tsukuba, Japan (2014); http://www-kekb.kek.jp/MAC/2014.
[4] S. Kazama et al., “Emittance Preservation in SuperKEKB Injector”, MOPWA071, IPAC’15, Richmond, Virginia, USA (2015).
[5] M. Satoh et al., “EPICS IOC of WindowsXP-based Oscilloscope for Fast BPM Data Acquisition System”, WEP086, ICALEPCS2009, Kobe, Japan (2009).
[6] R. Ichimiya et al., “Development of High Precision Beam Position Monitor Readout System with Narrow Bandpass Filters for the KEKB Injector Linac towards the SuperKEKB”, WEPC14, IBIC2013, Oxford, UK (2013).
[7] R. Ichimiya et al., “High Position Resolution and High Dynamic Range Stripline Beam Position Monitor (BPM) Readout System for the KEKB Injector Linac Towards the SuperKEKB”, WEPD04, IBIC2014, Monterey, USA (2014).
[8] Micro-Research Finland Oy website: http://www.mrf.fi
[9] Experimental Physics and Industrial Control System: website: http://www.aps.anl.gov/epics/
[10] M. Satoh et al., “Development of BPM Readout System for SuperKEKB Injector Linac”, MOPGF034, ICALEPCS2015, Melbourne, Australia (2015).

ISBN 978-3-95450-176-2

BEAM HALO MEASUREMENT UTILIZING YAG:CE SCREEN

Takashi Naito #, Toshiyuki Mitsuhashi
KEK, 1-1 Oho, Tsukuba, Ibaraki 305-0801 Japan

Abstract

We are aiming to produce an extremely small beam having a vertical beam size of 37nm at KEK-ATF2. The beam halo surrounding the beam core will make the background for the beam size measurement using a Laser interferometer beam size monitor. An understanding of beam halo distribution is important for the measurement of the beam size at the final focus point of the KEK-ATF2. In order to measure the beam halo distribution, we developed a beam halo monitor based on fluorescence screen. A YAG:Ce screen, which has 1mm slit in the center is set in the beam line. The image on fluorescence screen is observed by imaging lens system and CCD camera. In this configuration, the beam in the core will pass through the slit. The beam in surrounding halo will hit the fluorescence screen, and we can observe the distribution of beam halo. The intensity contrast of beam halo to the beam core is measured by scanning the beam position for the fixed fluorescence screen position. The results of observation of beam halo are presented.

INTRODUCTION

ATF2 is a test beam line for developing the final focus system for the International Linear Collider (ILC). The very low emittance beam is supplied from the damping ring(DR). The energy is 1.3GeV and the design emittances for the horizontal and vertical are 1.3nm and 10pm, respectively. The final focus optics in the ATF2 beam line generates an extremely small beam. The design vertical beam size is 37nm at the virtual focal point [1]. A laser interferometer beam size monitor is used for the beam size measurement [2]. The collision of the electron beam and the fringe of two laser beams makes the Compton scattered photons. The beam size is estimated from the modulation depth of the Compton signal when scaning the fringe position of the laser beams. A Gussian distribution is assumed for the electron beam in this estimation. The beam halo causes the background of the Compton signal and the measurement error. The beam halo distribution is important for the measurement of the beam size.

The beam-gas scattering, beam-gas bremsstrahlung and intra-beam scattering cause the beam halos in the storage ring. The beam halo distribution in the case of the ATF damping ring was estimated in reference [3]. The vertical beam distribution with different vacuum pressure due to the beam-gas scattering is shown in Fig. 1. The calculation shows some deviation at 10^{-3} of the intensity in the case of 10^{-7}Pa of the vacuum level.

We developed a screen monitor utilizing a YAG:Ce screen, which has both high resolution and high sensitivity[4]. This monitor is also used at the KEK LUCX (Laser Undulator Compton X-ray) facility [5]. The beam halo monitor is an application system of the screen monitor, which can visualize the beam halo distribution.

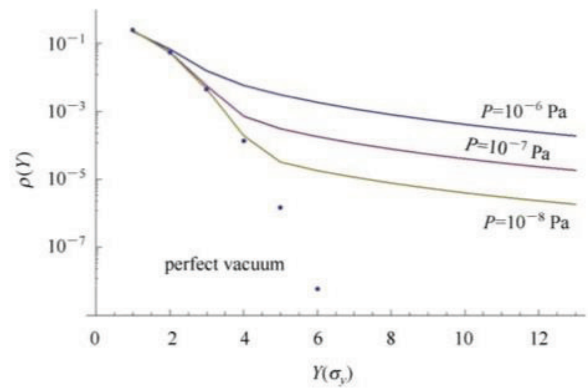

Figure 1: Vertical beam distribution with different vacuum pressure (vertical axis:provability, Horizontal axis : normalized RMS beam size), from Chinese Physics C, Vol. 38, No. 12 (2014) 127003

HARDWARE

The beam halo monitor consists of a YAG:Ce screen held on the air actuator and an imaging system. The YAG:Ce screen has 1mm slit in the center. The size is 10mmϕ and the thickness is 100μm. The picture of the YAG:Ce screen on the actuator holder is shown in Fig. 2.

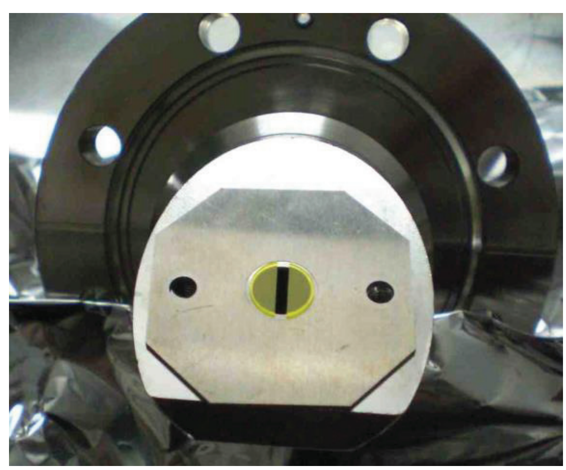

Figure 2: YAG:Ce screen on the actuator holder: The beam core goes through a slit at the center of the screen without any interaction for the scintillator.

In this configuration, the beam in the core passes through the slit and the beam halo hit the screen. The

takashi.naito@kek.jp

ISBN 978-3-95450-176-2

fluorescent light is observed by the imaging lens and the CCD camera. An example of the measured image of the beam halo monitor is shown in Fig. 3. The beam core passes through the right side and the beam image suddenly disappear at the slit location. We can observe only the beam halo. The amount of the beam halo is measured by scanning the beam position.

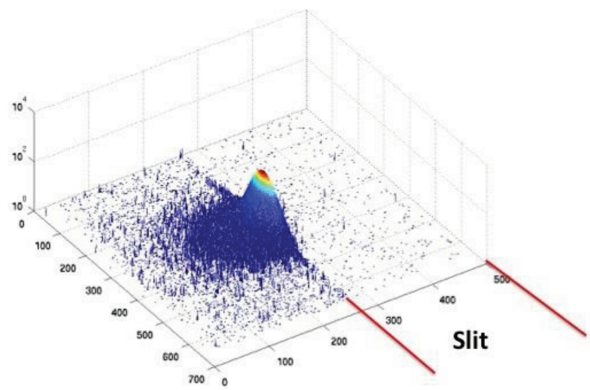

Figure 3: Example of the beam halo image

Figure 4 shows the layout of the YAG:Ce screen and the imaging lens. The screen is inserted into the beam orbit with a 45-degree angle for horizontal direction by the air actuator. The CCD observes the scintillation light of the screen from a perpendicular direction. The optical system can fully focus on the screen when the beam position moved. This layout can be avoided the reflection of the synchrotron radiation (SR) and coherent optical radiation (COTR), which are reflected to a 90-degree angle.

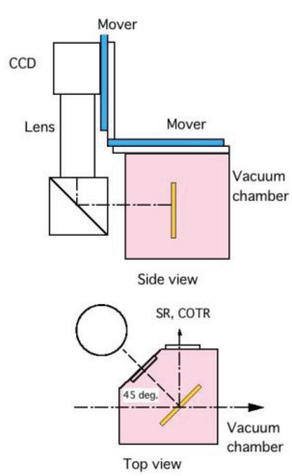

Figure 4: Layout of the YAG:Ce screen and the imaging lens

The scintillation light is delivered onto the CCD using a 90-degree reflective mirror and a zoom lens. The reflective mirror is used for changing the optical axis and avoiding the X-ray on the CCD. A zoom lens (TS-93022: Sugito Co.) is used for the lens. The lens has three times of the magnification ratio, 0.3mm of the focal depth and 4.3μm of the resolution. The point spread function (PSF) is estimated from the Fourier transform of the modulation transfer function of the lens. The PSF is shown in Fig. 5. The resolution is estimated from the Gaussian fitting of the PSF. The lens has enough resolution to measure less than 10μm of the beam image.

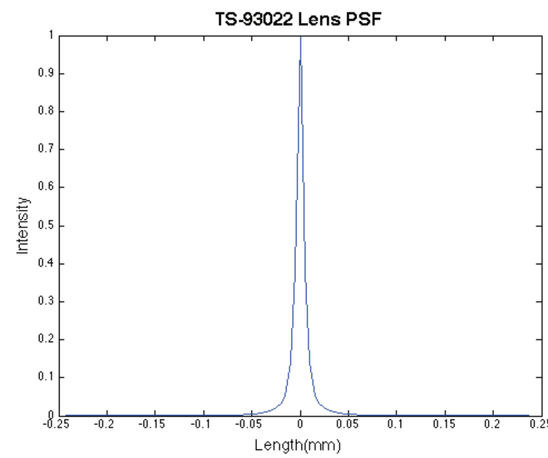

Figure 5: Point spread function (PSF) of the TS-93022 lens

CCD IGV-B0610M (IMPREX Co.) is used for the imaging. The CCD has 648 x 488 resolution with 7.4μm^2 pixel size and the external trigger function with 2μs of minimum exposure time. The scintillation time of the YAG:Ce is 100ns.

BEAM MEASUREMENT

Saturation of the YAG:Ce Screen

The beam halo monitor is located at the diagnostic section of the ATF beam line. The assumed beam sizes for horizontal and vertical are 50μm x 25μm, respectively, at the location. The electron density is very high at the location. YAG:Ce has the saturation of the scintillation light for high beam density. The measured saturation level is 0.25pC/μm^2. [4] It is difficult to measure the peak intensity of the beam image for the saturation in this measurement. We measured the saturation effect as a function of the beam intensity when set the beam center on the screen. The peak intensity is estimated from the liner fitting of the non-saturated area. The measured light intensity of the YAG:Ce as a function of the beam charge is shown in Fig. 6. The saturation starts from less than 0.05x10^9 electrons.

Vacuum Dependence

The beam halo measurement was done with following procedure. 1) The screen is inserted into the beam line. 2) The beam position for the screen slit is scanned using a

ISBN 978-3-95450-176-2

steering magnet located at the upstream. It is better to change the slit position for the beam, however we don't have the mover of the screen. The dispersion effect is negligible when the beam position is changed. 3) The halo image is acquired and the peak intensity of the halo is estimated from the acquired image.

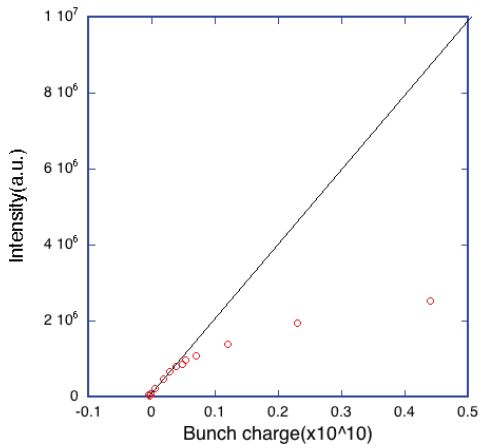

Figure 6: Light intensity of the YAG:Ce as a function of the beam charge

The distribution of the beam halo for the different vacuum condition is plotted in Fig. 7 in the case of the beam intensity 0.23 x 10^{10} electrons. Three different vacuum conditions are plotted, 4.3x 10^{-7}Pa, 7.6 x 10^{-7}Pa and 12.0 x 10^{-7}Pa, respectively. The Ion pumps in the damping ring were turned off to change the vacuum level. The core part of the beam is not plotted for the saturation of the screen. The red line in Fig. 7 shows sigma=25µm of Gaussian distribution. The peak of the Gaussian distribution was estimated from the saturation characteristics in Fig. 6, which is shown as a red cross. There is a clear difference of the beam halo for the different vacuum level. The core part is same for the different vacuum level.

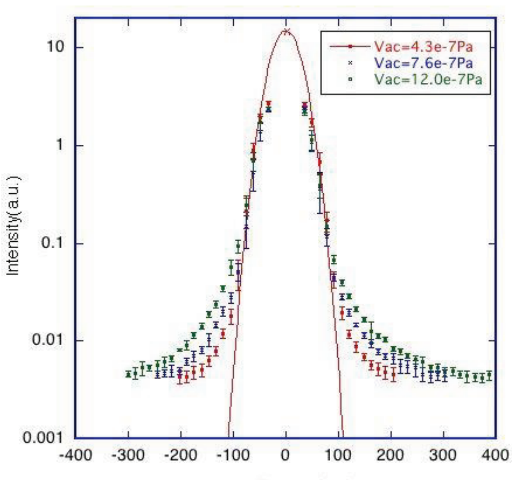

Figure 7: Distribution of the beam halo for the different vacuum condition in the case of the beam intensity 0.23 x 10^{10} electrons

The intensity of the halo for the position is plotted in Fig. 8 in the case of the beam intensity 0.45 x 10^{10} electrons. Three different vacuum conditions are plotted, 4.3x 10^{-7}Pa, 8.7 x 10^{-7}Pa and 13.1 x 10^{-7}Pa, respectively. The red line in the Fig. 8 shows sigma=27µm of Gaussian distribution. The peak of the Gaussian distribution was estimated from the saturation characteristics in Fig. 6, which is shown as a red cross.

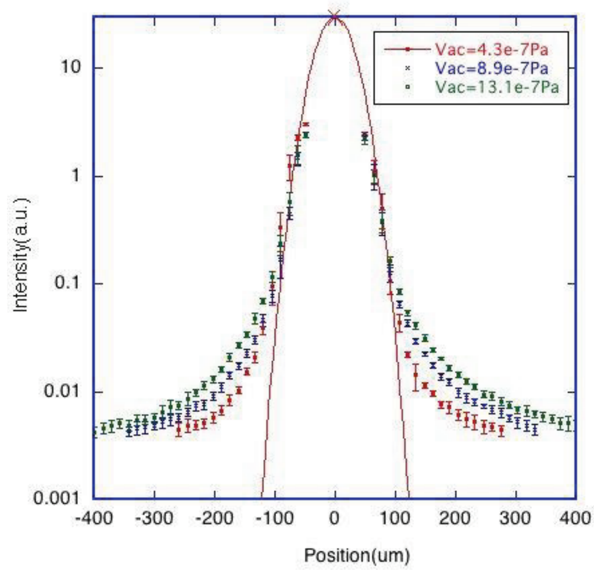

Figure 8: Distribution of the beam halo for the different vacuum condition in the case of the beam intensity 0.45 x 10^{10} electrons

RF Voltage Dependence

The distribution of the beam halo for the different rf voltage of the damping ring is plotted in Fig. 9 in the case of the beam intensity 0.23 x 10^{10} electrons. Two different rf voltages are plotted, Vrf=283kV and Vrf=110kV, respectively. The bunch length of the beam is a function of the rf voltage and the difference is about 10% for the two cases. The bunch length affects the core beam size by the intra-beam scattering. The measurement shows almost same beam halo and a little bit increased the beam core. The red line in the Fig. 9 shows 25µm of Gaussian distribution. The peak of the Gaussian distribution was estimated from the saturation characteristics in Fig. 6, which is shown as a red cross.

ISBN 978-3-95450-176-2

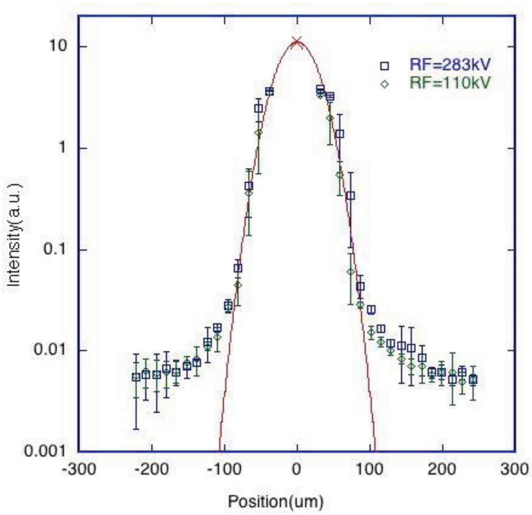

Figure 9: Distribution of the beam halo for the different rf voltage of the damping in the case of the beam intensity 0.23 x 10^{10} electrons

SUMMARY AND FUTURE PLAN

We developed a beam halo monitor to measure the electron beam distribution utilizing a YAG:Ce screen. The beam halo measurement at the KEK-ATF2 beam line showed the clear deviation from the Gaussian distribution. The amount of the deviation was from 10^{-2} to 10^{-3} of the peak intensity, which was a function of the vacuum level of the damping ring. The measurement agrees with the simulation result. The beam halo was no change for the rf voltage of the damping ring. In these measurements, the peak intensity of the beam core was estimated from the saturation characteristics. The beam density of the core was too high for the YAG:Ce screen measurement. We have a plan to install an OTR screen monitor at same location to measure the peak of the beam core. By super impose the data of the OTR screen monitor and the data of the beam halo monitor, we will get the wide range of the beam profile from the peak to the halo.

ACKNOWLEDGMENT

We acknowledge to Professors S. Michizono, A. Yamamoto and S. Yamaguchi for their encouragement. We also thank to the members of the ATF group for giving machine time for testing of the monitor. This work was supported by Photon and Quantum Basic Research Coordinated Development Program from the Ministry of Education, Culture, Sports, Science and Technology, Japan.

REFERENCES

[1] ATF collaboration, "ATF2 Proposal", KEK Repoert 2005-2, August 2005
[2] T. Okugi, et al., "Linear and second order optics corrections for the KEK Accelerator TestFacility final focus beam line" PRST-AB 17, 023501(2014)
[3] WAN Dou, et al., "Analytical estimation of ATF damping ring" Chinese physics C Vol. 38, No.12(2014) 127003
[4] T. Naito, et al., " YAG:Ce Screen Monitor using a gated CCD camera", IBIC14, TUPD08(2014)
[5] A. Arishev, Private communication

ISBN 978-3-95450-176-2

DESIGN OF CODED APERTURE OPTICAL ELEMENTS FOR SUPERKEKB X-RAY BEAM SIZE MONITORS

E. Mulyani, Sokendai, Tsukuba, Ibaraki, Japan
J.W. Flanagan, KEK and Sokendai, Tsukuba, Ibaraki, Japan

Abstract

We describe the design of coded aperture optical elements for the SuperKEKB x-ray beam size monitors. X-ray beam profile monitor are being installed in each ring of SuperKEKB (LER and HER) to provide high resolution bunch-by-bunch, turn-by-turn measurement capability for low emittance tuning, collision tuning and instability measurements[1,2]. We use two types of optical elements, single-slit (pinhole) and multi-slit optical elements (coded apertures, CA). CA imaging offers greater open aperture than a single pinhole, for greater photon throughput and better statistical resolution for single-shot measurements. X-rays produced by a hard-bend magnet pass through a pinhole or CA optical element onto a detector. The resolution is obtained by calculating the differences between the images recorded by the detector for various simulated beam sizes, for a given number of photons. The CA elements that we have designed for use at SuperKEKB are estimated to provide 1.25-2.25 microns resolution for 10-25 microns of vertical beam sizes at 1 mA bunches. We present the design principle and optimizing process used to optimize the resolution at various beam sizes for SuperKEKB.

INTRODUCTION

Precision measurement of vertical bunch size plays an important role in the operation and tuning of electron storage rings [3], including the e^+ e^- collider SuperKEKB[4]. For this machine, luminosity or brightness is directly related with vertical emittance and vertical beam size. To meet bunch-by-bunch beam profile monitoring with high resolution and fast response, we are building an x-ray imaging system based on coded aperture (CA) imaging [5]. The basic concept of CA imaging is shown in Fig. 1. The system consists of a pseudorandom array of pinholes (apertures) that project a mosaic of pinhole images onto a detector. The detector image is then decoded using the known mask pattern to reconstruct the original image. With a single pinhole, the resulting image is relatively easy to understand and analyze, though the usable photon flux is limited.

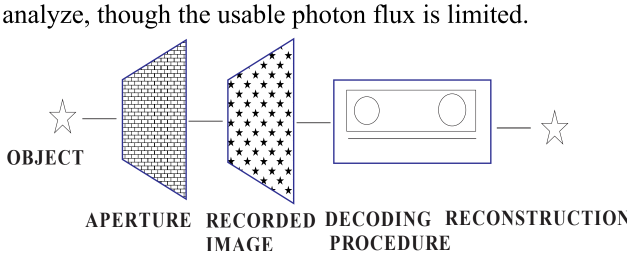

Figure 1: Basic concept of CA imaging [6].

CA imaging offers greater open aperture than a single pinhole, for greater photon throughput and better statistical resolution for single-shot measurements. One traditional example of such a pattern is the Uniformly Redundant Array (URA)[6], which has been tested for beam size measurement at CesrTA[7], Diamond Light Source[8], and the ATF2[9]. Other patterns have also been developed which are optimized for better performance at small beam sizes [10]. At SuperKEKB, x-ray beam monitors will be used primarily for vertical bunch profile measurement, with two types of optical elements, single-slit (pinhole) and multi-slit optical elements (coded apertures, CA). A schematic view of the x-ray beam size monitor line is shown in Fig. 2. Beryllium filters are placed upstream of the optics to reduce heat load, with the whole line being in vacuum up to the 200 μm Be extraction windows at the end. The detector is 128 channels of silicon with 2 mm of sensing depth, and a pixel pitch of 50 μm. SuperKEKB has two rings, the Low Energy Ring (LER) and the High Energy Ring (HER). Parameters for each beam line and the optical elements shown in Table 1.

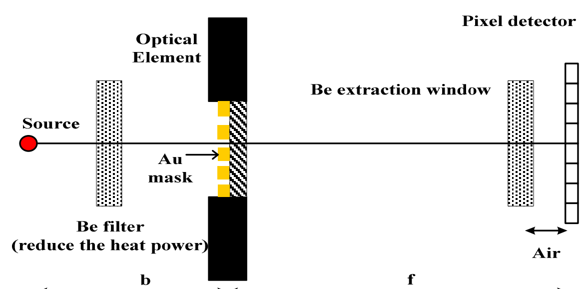

Figure 2: Simplified schematic of x-ray beam size Table monitor (not to scale).

Table 1: Parameter for Beam Lines and Optical Element

Parameter	LER	HER	Unit
Beam energy	4	7	GeV
Source bend radius ρ	31.74	106	m
Distance from source to mask (b)	9.43	10.33	m
Distance from mask to detector (f)	31.38	32.35	m
Au thickness	20	20	μm
Total Be thickness (filter+window)	0.7	16.2	mm
Diamond thickness	600	600	μm
Air gap (window-det.)	10	10	cm

ISBN 978-3-95450-176-2

SIMULATION METHODS

The formalism used to simulate the detected image follows K.J.Kim's formulation [11, 12]

$$\begin{pmatrix} A_\sigma \\ A_\pi \end{pmatrix} = \frac{\sqrt{3}}{2\pi}\gamma\frac{\omega}{\omega_c}\left(1+X^2\right)(-i)\begin{pmatrix} K_{2/3}(\eta) \\ \dfrac{iX}{\sqrt{1+X^2}}K_{1/3}(\eta) \end{pmatrix} \quad (1)$$

where

$$\begin{aligned} \eta &= \frac{1}{2}\frac{\omega}{\omega_c}\left(1+X^2\right)^{3/2} \\ X &= \gamma\psi \\ \omega_c &= 3\gamma^3 c/2\rho \end{aligned} \quad (2)$$

where $A_{\sigma,\pi}$ are the components of the complex wavefront amplitude of the synchrotron radiation (SR) with angular frequency of photon ω, γ is the Lorentz factor for the particle beam, ω_c is the critical frequency, ρ is the radius of instantaneous curvature of the electron trajectory (in practical units $\rho[m] = 3.3E[GeV]/B[T]$), ψ is the observation angle in the vertical plane and K are the modified Bessel functions. The angular density of the spectral flux in frequency band $\Delta\omega/\omega$ is defined as[11]

$$\begin{bmatrix} \dfrac{d^2F_\sigma}{d\theta d\psi} \\ \dfrac{d^2F_\pi}{d\theta d\psi} \end{bmatrix} = \alpha\frac{\Delta\omega}{\omega}\frac{I}{e}\begin{vmatrix} A_\sigma \\ A_\pi \end{vmatrix}^2 \quad (3)$$

where $d\theta$ is the horizontal angel element, α is the fine-structure constant, I is the accelerator beam current and e is the charge of the electron. As has been explained previously[13], for a one dimensional mask, the path integral in the vertical direction from a point in the source distribution to a point on the detector can be written using the Kirchhoff approximation as[14]

$$\begin{aligned} A_{\sigma,\pi}\,(\text{detector}) &= \frac{iA_{\sigma,\pi}\,(\text{source})}{\lambda} \\ &\times \int_{mask}\frac{t(y_m)}{r_1 r_2}e^{i\frac{2\pi}{\lambda}(r_1+r_2)}\left(\frac{\cos\theta_1+\cos\theta_2}{2}\right)dy_m \end{aligned} \quad (4)$$

where λ is the wavelength, y_d and y_m are the vertical coordinates at the detector and mask, r_1 and θ_1 are the distance and angle from the source point to the mask point at y_m, and r_2, θ_2 are the distance and angle from the mask point y_m to the detector point y_d. For each pixel in the detector, the wavefront amplitude from each source point is calculated by equation (4) and converted to detected flux.

The single-shot resolution of the system is limited by the statistical fluctuations in the number of detected photons. To estimate the resolution of the system as a function of beam size, simulated images are calculated for Gaussian beams of various sizes. The simulated detector images for different-sized beams are then compared pair-wise against each other. The differences between two images in signal height for each channel are used to calculate the χ^2 per degree of freedom as[15]

$$\frac{\chi^2}{\nu} = \frac{1}{N-n-1}\sum_{i=1}^{N}\frac{\left[s_i' - s_i\right]}{\sigma_i^2} \quad (5)$$

where N is the number of detector channels (pixels), and n is the number of fit parameters, which is in this case is one. The residual weighting σ_i for channel is taken to be proportional to the square root of the signal height (number of photons) in that channel (s_i). The resolution is then defined as the change in beam size, Δσ, where the χ^2 per degree of freedom is one.

MASK DESIGN

The optical elements for the x-ray beam size monitor consist of 20 µm thick gold masking material on 600 µm thick diamond substrates. The diamond substrate mask is more robust than silicon (due to the better heat conduction of diamond), so it can better tolerate the LER and HER power densities [16]. The design of the pinhole and CA masks proceeded as follows. First, the pinhole size was optimized by simulating detector images for a point source in both rings, with various pinhole (slit) sizes. The minimum widths of the resulting Point Response Functions (PRFs) were found to be the same (within 1 µm) at 33 µm for both the LER and the HER, so this size pinhole was taken as the optimum for both rings. Next, pairs of 33 µm slits were simulated, with varying separations between the pairs.

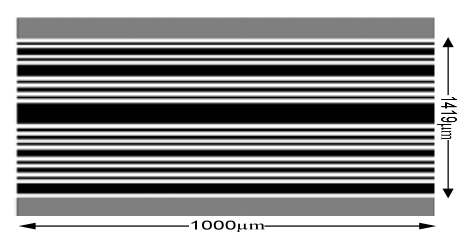

Figure 3: CA1 mask with 17 slits.

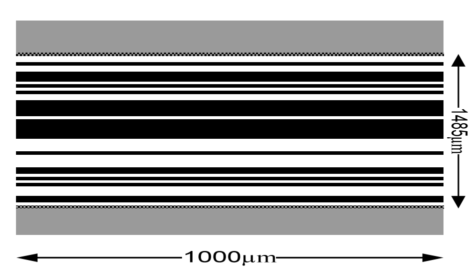

Figure 4: CA2 mask with 12 slits.

ISBN 978-3-95450-176-2

For each separation, the resolution curves for different beam sizes at a standard bunch current of 1 mA were calculated, to determine the range of beam sizes for which each slit separation was optimal. Then a series of multi-slit patterns were devised by hand, incorporating a suitable range of slit separations to cover the dynamic range of interest, with emphasis on covering the smallest beam sizes. The hand-optimized pattern that was chosen based on its resolution curve over a range of beam sizes is denoted CA1, shown in Fig. 3. Finally, a 12-slit URA pattern was constructed using 33 μm as the basic unit size. This pattern, called CA2, is shown in Fig. 4.

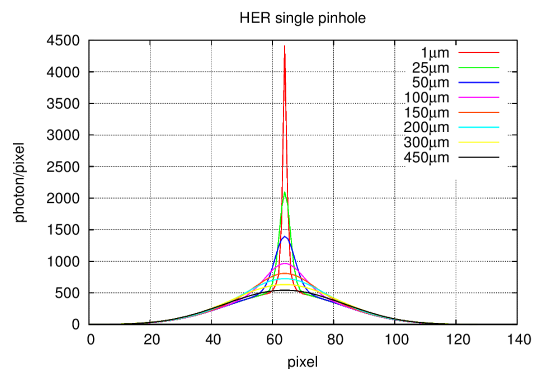

(a)

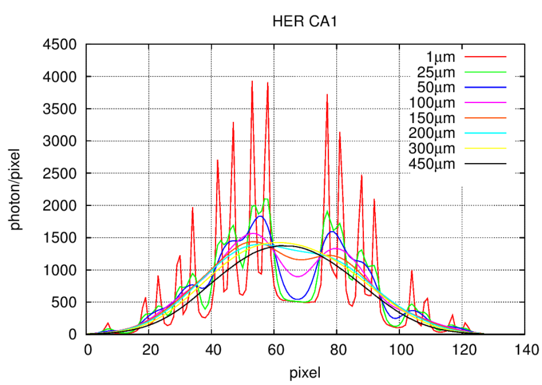

(b)

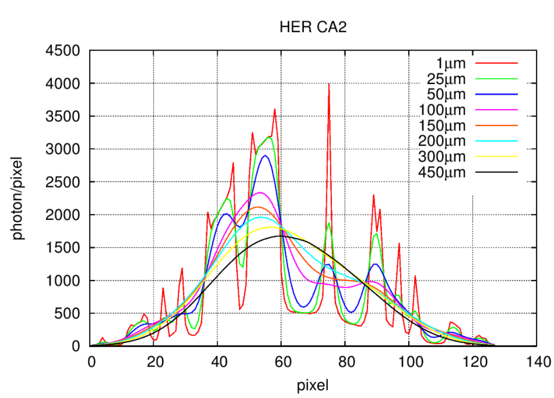

(c)

Figure 5: Simulated detector images showing the number of photons/pixel for 1 mA bunches for different beam sizes at HER: (a) single pinhole; (b) CA1; (c) CA2.

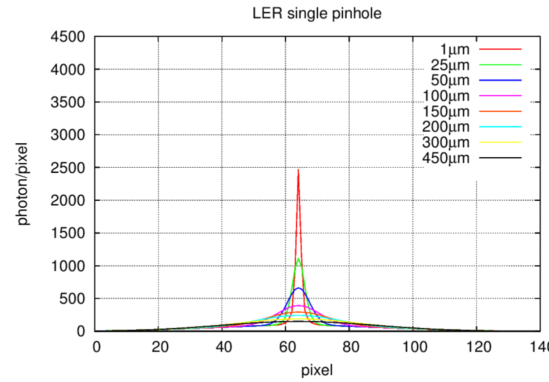

(a)

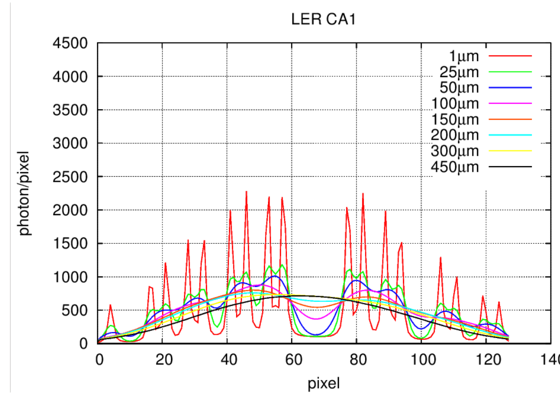

(b)

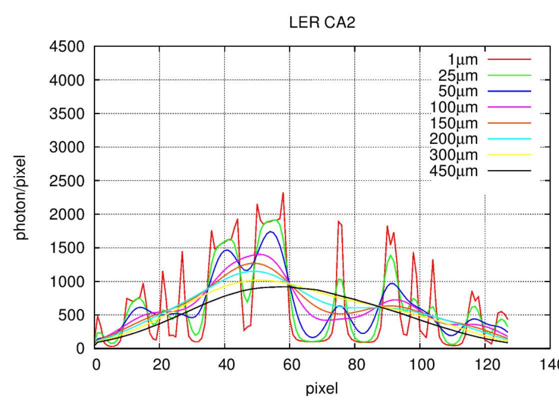

(c)

Figure 6: Simulated detector images showing the number of photons/pixel for 1 mA bunches for different beam sizes at LER: (a) single pinhole; (b) CA1; (c) CA2.

RESULTS

The detector images for all three optical elements at the HER and LER are shown in Figs. 5 and 6, respectively.

We calculated the resolutions for the pinhole and the CA masks for both rings (LER and HER) with the number of photons in the LER being 1942.96 photon/turn/mA/bunch, while at the HER it is 3341.63 photon/turn/mA/bunch, for hole regions. Figs. 7 and 8 show the estimated resolution for the single-slit, CA1 and CA2 for various bunch currents.

ISBN 978-3-95450-176-2

At lower beam sizes (10-25 microns), the CA1 has better single-shot resolution than the single pinhole and CA2. It is estimated to provide 1.25-2.25 microns resolution for 10-25 microns of vertical beam sizes at 1 mA bunches. For smaller currents the resolution of vertical beam sizes changes, e.g at 0.1 mA and 0.01 mA bunches the resolution drops to 4-7.5 microns and >20 microns respectively due to lower photon throughput and statistical resolution. For higher beam sizes (> 30 µm), the CA2 mask performs better than CA1.

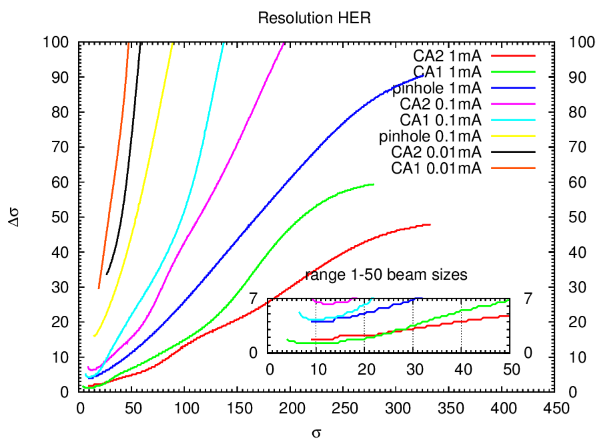

Figure 7: Vertical beam size resolutions at HER for various bunch currents (1 mA, 0.1 mA and 0.01 mA) and optical elements (single pinhole, CA1 and CA2).

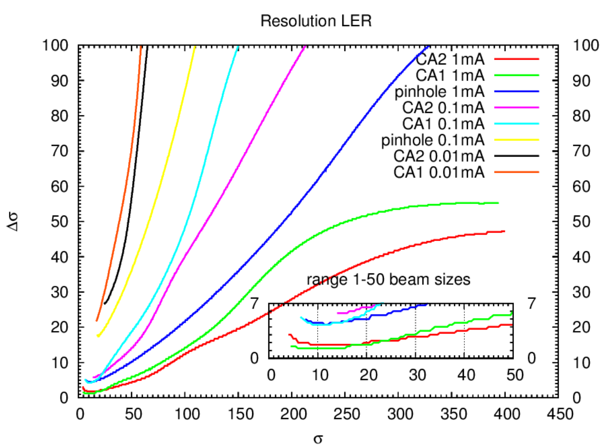

Figure 8: Vertical beam size resolutions at LER for various bunch currents (1 mA, 0.1 mA and 0.01 mA) and optical elements (single pinhole, CA1 and CA2).

SUMMARY

The CA1 elements that we have designed for use at SuperKEKB are estimated to provide 1.25-2.25 microns resolution for 10-25 microns of vertical beam sizes at 1 mA bunches. For larger beam sizes (> 30 µm), CA2 mask is better than CA1.

The pinhole and CA masks are in fabrication for use at SuperKEKB. The study of the resolutions available with these mask patterns will be refined to incorporate noise and low-count (Poisson) statistics, and compared with data taken following beam commissioning in Spring 2016.

REFERENCES

[1] H. Fukuma, et al., Proc. IBIC2013, 6 (2014).
[2] J.W. Flanagan, et al., Proc. PASJ10, Himeji, (2010).
[3] J.W. Flanagan, Proc. IPAC11, 1959 (2011).
[4] Z. Dolezal, for the Belle Collaboration, PoS EPS-HEP2009, p. 143 (2009).
[5] R. H. Dicke, Astrophys. Journ., 153, L101 (1968).
[6] E. E. Fenimore, T. M. Cannon, Appl. Optics, Vol 17, No.3, 337 (1978).
[7] J.P. Alexander et al, Nucl. Instrum. Methods Phys. Res., Sect. A **748**, 96 (2014).
[8] C. Bloomer, et al., Proc. IBIC2014, TUCBZ2 (2014).
[9] J.W. Flanagan, et al., Proc. IBIC2012, 237 (2012).
[10] J.P. Alexander et al, Nucl. Instrum. Methods Phys. Res., Sect. A **767**, 467 (2014).
[11] K. J. Kim, AIP Conf. Proc. **184**, 565 (1989).
[12] A.Thompson et al., X-ray Data Booklet, (Berkeley : Lawrence Berkeley National Laboratory, 2009), 2-1.
[13] J.W. Flanagan et al., Performance of Coded Aperture X-Ray Optics with Low Emittance Beam at CESRTA, Proc. PAC09, Vancouver, BC, Canada, pp. 3561-3563 (2009).
[14] J.D. Jackson., *Classical Electrodynamics*, (Second Edition), John Wiley&Sons, New York (1975).
[15] P.R. Bevington, *Data Reduction and Error Analysis for the Physical Sciences*, McGraw-Hill, New York (1969).
[16] J.W. Flanagan et al., Proc. IBIC2013, 844 (2013).

MACHINE STABILITY ANALYSIS BY PULSE-BASED DATA ARCHIVER OF THE J-PARC RCS

N. Hayashi*, JAEA/J-PARC, Tokai, Ibaraki, Japan

Abstract

The J-PARC RCS runs with a repetition rate of 25 Hz. The beam intensities from current monitor data and beam loss monitors (BLM) data are archived for all pulses and are analyzed to study machine stability. It was found that after replacing ion source, the beam intensity seems to be more stable than before. In addition, beam position monitors (BPM) data are regularly recorded. In this paper we report a few examples of the data recorded by BLM or BPM in the case of magnet power supplies feedback problem or vacuum problem, respectively. In case of the bending magnet problem, not all BLMs show increasing signal, some BLMs' signal were decreasing. In case of the vacuum pump trouble, within a few seconds, the beam losses were quickly increasing. It is described these incidents with various data.

INTRODUCTION

The Japan Proton Accelerator Research Complex (JPARC) has three accelerators and three experimental facilities. The Linac upgrade was upgraded in two stages, namely energy upgrade and intensity upgrade [1]. The energy upgrade from 181 to 400 MeV was performed in the end of 2013 by adding annular-ring coupled structure (ACS) cavities [2]. The intensity upgrade, involving increasing the peak beam current from 30 to 50 mA, was realized by replacing the front-end part of the Linac during the summer shutdown of 2014. The front-end part comprises an RF driven ion source [3] and a 50 mA RFQ [4].

The second accelerator is a Rapid-Cycling Synchrotron (RCS). The RCS injection system, bump magnets power supplies, was also upgraded to adapt the system to higher Linac energy. RF harmonics of the RCS is $h = 2$, and there are two bunches inside the ring. The proton is accelerated up to 3 GeV and is extracted with a 25 Hz repetition rate. The RCS delivers an intensive primary proton beam to the Materials and Life Science Experimental Facility (MLF) and serves as a booster for the Main Ring (MR) proton synchrotron with a period of 2.48 s or 6 s. Four consecutive batches (eight bunches in total) are delivered in every MR cycle. The MR has two beam-extraction modes, fast and slow extraction mode. The first one is for neutrino experiment (NU), and the second one is for hadron experimental facility (HD). By the end of June 2015, nominal beam power of the MR was 330 kW for NU and 33 kW for HD. These are correspond to $4.4\times10^{1}3$ protons per pulse (ppp) and $1.010^{1}3$ ppp for NU and HD, respectively, at the RCS intensity.

The designed output beam power of the RCS is 1 MW, and the corresponding beam intensity is $8.3 \times 10^{1}3$ ppp. Even though it was only pulsed mode, the RCS achieved the design intensity in the beginning of 2015 [5]. It was a successful demonstration, but it revealed several issues pertaining to continuous 1 MW operation. The beam power of the routine user operation has been increased step-by-step. It commenced from 300 kW in fall 2014, increased to 400 kW in March, and reached 500 kW in the spring 2015. Development to achieve 1 MW user operation is underway. In addition, it is required to provide high availability and stable operation. A data-archiving system might be useful for analyzing accelerator stability and investigating the cause of any interruption in accelerator operation. Using these pieces of information, one can improve accelerator stability. In this paper, various examples are presented.

* naoki.hayashi@j-parc.jp

DATA ARCHIVING SYSTEM

The RCS has a threefold symmetric lattice with a circumference of 348 m. The RCS has three straight and three arc sections in the ring. The RCS houses various types of beam instruments [6], and a few important monitor data are continuously recorded and archived. These instruments include 54 beam position monitors (BPM) [7], intensity monitors DCCT and SCT, and beam loss monitors (BLM). The circulating beam current from the raw DCCT data is divided by the revolution frequency to obtain intensity, and the raw BLM signal is integrated in signal processing units. Most of BLMs are proportional chamber type (PBLM), and ninety PBLMs are distributed all over the ring.

The archive system employs reflective memory to read all 25 Hz, 20 ms-long pulses [8]. Although time resolution is limited, these data, BLM and DCCT, are recorded thrice every pulse with a 10 ms interval. BPM data is recorded every 1 ms. Although the system can store all data, 50 consecutive pulses are recorded every minute as archived data.

The Machine Protection System (MPS) is an interlock, triggered by any machine failure or large beam loss detected by BLM. If it is due to a machine failure on the beam, some amount of beam loss is expected. An MPS event triggered by BLM only is an indication of hidden problems.

INTENSITY STABILITY

It is mentioned already that the ion source was replaced in the intensity upgrade stage. The old ion source was of the LaB_6 filament type without cesium. The new one is a cesium feed RF-driven ion source. Figure 1 shows an example of a one-day intensity plot of the new source. The beam destinations were both NU and MLF. Only a few interruptions were observed over the course of a day, and they were caused by MPS. The new ion source seems to be more stable than the old one.

ISBN 978-3-95450-176-2

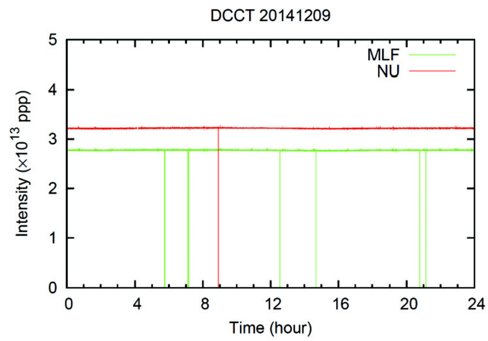

Figure 1: Stable DCCT intensity plot for one day. Data of NU and MLF mode are plotted separately.

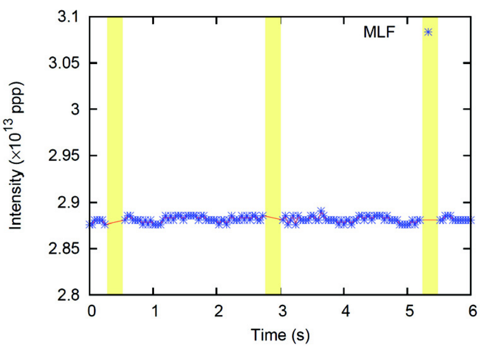

Figure 2: Stable intensity from the Linac to RCS. Only the MLF beam is operated, and the NU beam is not operated. Seven empty pulses are employed at intervals of 2.48 s. There is no fluctuation even just after each interval, which is unlike the case when using the old front-end system. The yellow hatched region represents the time gap for seven pulses.

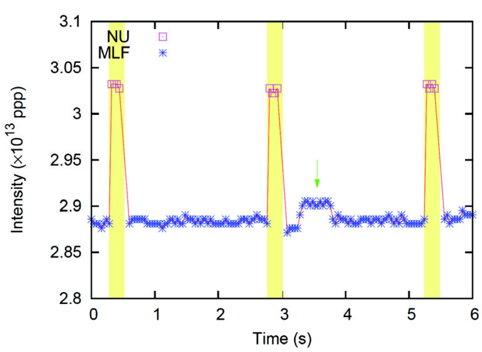

Figure 3: Similar to Fig. 2, but with NU beam under operation. Occasionally small fluctuations are seen after NU pulses (green arrow). The yellow hatched region corresponds to the NU pulses and three empty pulses.

In case of the old source, a few empty or very-lowintensity pulses were present. Moreover, slight variations (~2% higher) were observed right after the pulse gap[1] [9]. Upon replacement with the new ion source, these phenomena seemed to disappear (Fig. 2). Only slight fluctuation is seen as in Fig. 3, in the NU mode.

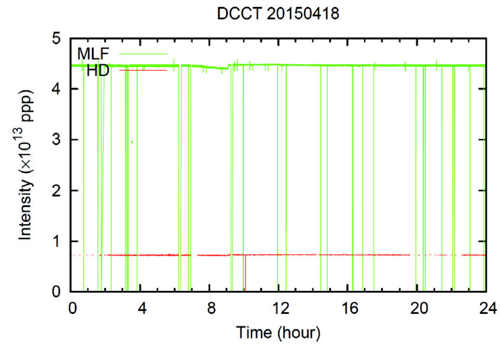

Figure 4: DCCT plot of full day. MLF beam power is 500 kW, and the MR is in the HD mode.

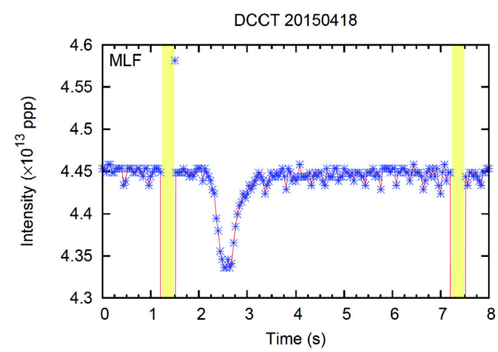

Figure 5: DCCT plot of 8 s duration around 4:09. Two gaps represent time of HD beam, and a small fluctuation was observed (2 % drop). The yellow hatched region corresponds to the HD pulses and three empty pulses.

Figure 4 shows another DCCT plot after the MLF beam power reached 500 kW in the HD mode. Contrary to Fig. 1, on that day, the ion source was unstable. It was found that the ion source plasma disappeared for some seconds and intensity fell immediately without recovery. We had to increase the hydrogen low rate to the ion source to stabilize it. There is no interlock for such event on the accelerator side. However, the neutron target system should stabilize their temperature, and the target system prohibits sudden changes in intensity within a few seconds. Irregular small fluctuations were detected as well, as shown in Fig. 5.

PBLM PATTERN AND TREND

In this section, a few examples of the PBLM pattern and the trends in the PBLM signal are described.

[1] This gap is due to the switching of the beam destination to the MLF and the MR. Four consecutive pulses are delivered to the MR. Because of residual field of pulse bending magnet in the beam transport line, three more empty pulses follow. If the beam for the MR stops for any reason, seven consecutive pulses are empty from the MLF viewpoint. Recently, a compensation scheme of the pulse bending magnet residual field is taken care, three empty pulses will be filled with MLF pulses.

ISBN 978-3-95450-176-2

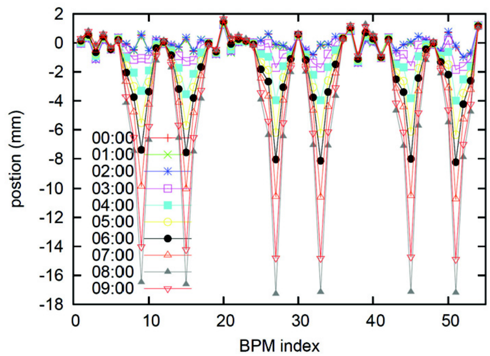

Figure 6: Horizontal COD excursion during BM feedback of. The excursion seems to start around 3:00 and evolves within several hours.

Main Magnet Feedback Error 1: BM

The RCS main bending magnet (BM) and quadrupole magnets (QM) power supplies have a feedback system to stabilize. The system uses recorded waveforms of output current, analyzes them, and provides feedback to the power supplies through a network. In one instance, this feedback loop was cut of owing to network trouble. There was no direct warning, although the power supply was drifted. It was only noticed when a beam orbit excursion occurred as a result.

Given that the RCS has six dispersion peaks in three arc sections, mismatch signature between bending field and particle momentum appears on these peaks. Figure 6 shows horizontal closed-orbit distortion (COD) excursion during the problem. In the beginning, COD was only about 1 ~ 2 mm, but it developed to almost 16 mm at the peak after several hours. Because the dispersion peak is η ~5 m, it corresponds to field mismatch of 3×10^{-3}.

The RCS was operated in NU and the MLF modes. The PBLM patterns of the NU and MLF modes are shown in Fig. 7, and their time evolutions are shown in Fig. 8. The trend in the PBLM signal is shown in Fig. 9. The PBLM19 (C05-01) signal gradually decreased, especially in the case of the NU-beam. In contrast, the PBLM47 (C16-01) signal increased. As stated above, in some BLM cases the loss decreased, whereas in other cases, it increased. However, their absolute signal sizes were different, which was not very apparent. There was no MPS interlock trigger by the BLMs, which is one of the reasons why it took some time to realize the problem.

Main Magnet Feedback Error 2: QM

The same network problem occurred a few days later. One of a quadrupole magnet family power supply (QFL) was affected. At this time, a noticeable number of BLM MPS events were detected. Figures 10 and 11 present the PBLM pattern and the signal trends of PBLM19 and PBLM47, respectively. The trends clearly indicate the increase in beam loss. There are many red-colored interruptions in the trend graph, which means that many MPS events occurred in the NU mode.

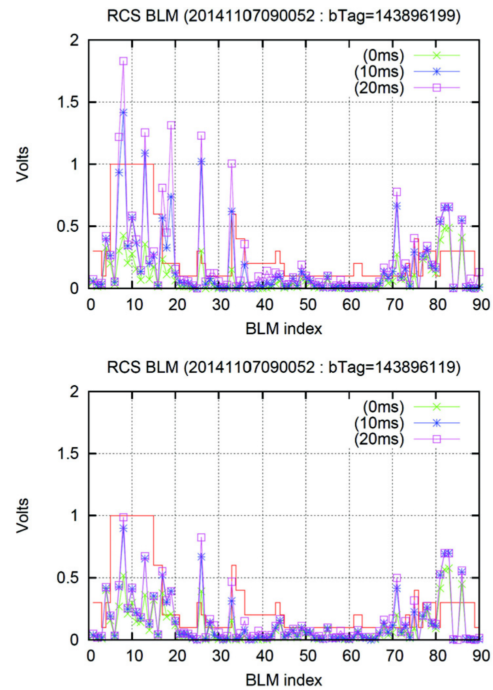

Figure 7: PBLM pattern data of NU (upper) and MLF (lower) modes. The horizontal axis represents the BLM index, and the vertical axis represents the magnitude of the BLM signal.

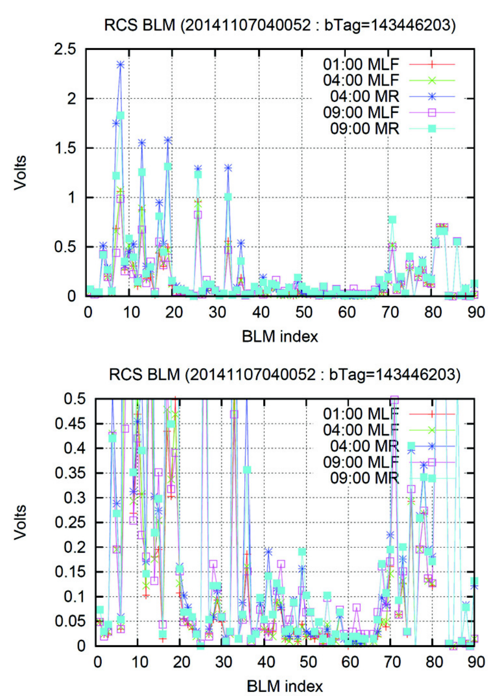

Figure 8: Evolution of PBLM pattern data during BM feedback problem. Vertical scale is zoomed in lower figure.

Vacuum Pump Failure

After the beam power for the MLF was increased from 300 to 400 kW, three turbo molecular pumps (TMP) around the RCS injection area failed within two weeks. The PBLM loss pattern and the short-term PBLM08 (C03-02) trend

ISBN 978-3-95450-176-2

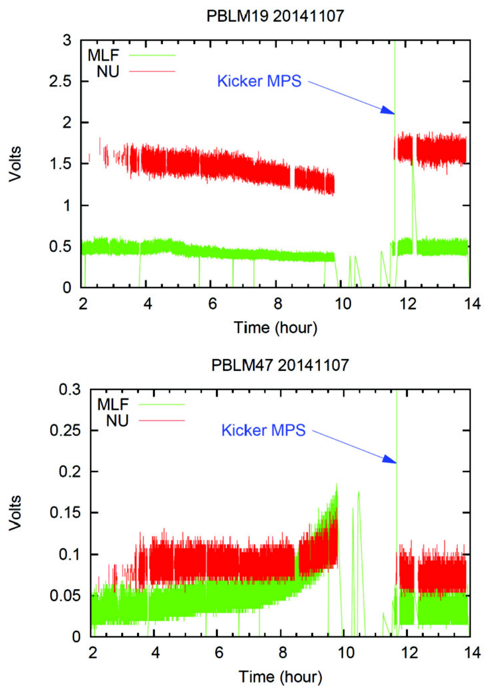

Figure 9: PBLM19 (upper) and PBLM47 (lower) signal trends are shown within 12 hours. The large beam loss at time at 11:40 was ascribed to an external cause, namely an MPS event due to the misfiring of the RCS extraction kicker magnet. The problem was solved at that time, and the loss signal is back to its previous level.

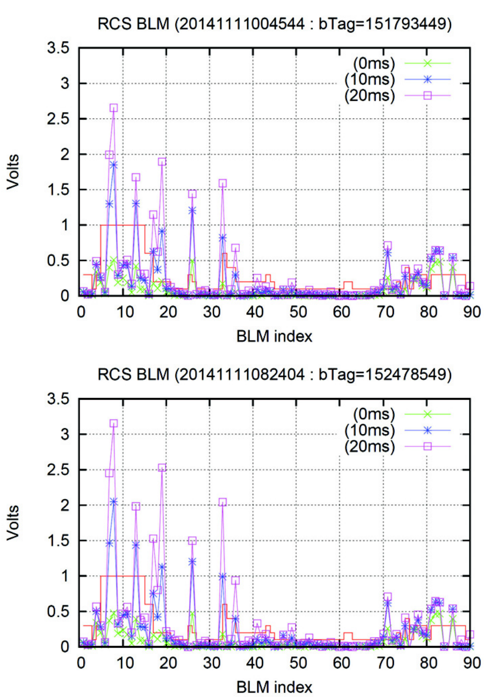

Figure 10: PBLM pattern in the NU mode. Before the trouble (upper) and the last moment of the problem (lower).

of the events are shown in Fig. 12. Vacuum level MPS (exceeding 10^{-3} Pa) stopped the beam. Neither the TMP itself nor PBLM was related to MPS. Certainly, the signal of the NU mode was higher than that of the MLF mode. The PBLM08 signal grew quickly within a few seconds.

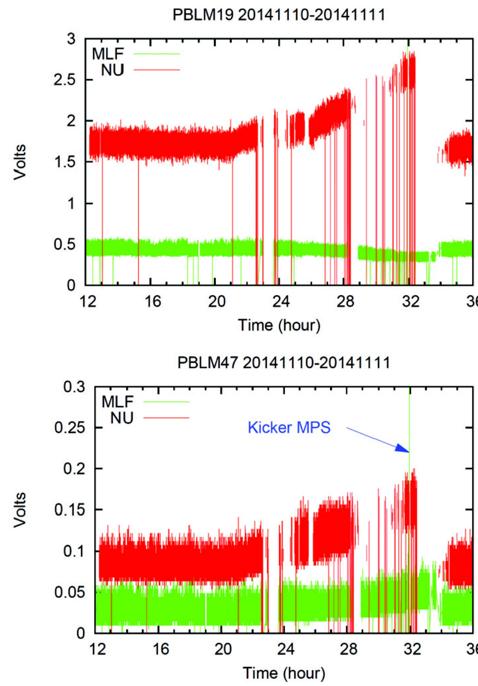

Figure 11: PBLM19 (upper) and PBLM47 (lower) data during QFL trouble. Beam loss started to increase at around 22:00. A large beam loss at time around 32 h ascribed to an external cause, which is the misfiring of the RCS extraction kicker magnet. The problem was fixed after 34 h (second day 10:00).

BLM Trend

Figure 13 shows the DCCT and PBLM19 trend plots of the day on which beam power to the MLF increased from 400 to 500 kW. The BLM19 signal clearly increased. In this period, the MR was operated in the HD mode. Thus, the beam intensity is lower than that in the NU mode and the beam loss is smaller as well.

SUMMARY

In this study, we describe how beam intensity became more stable after the introduction of the new ion source. However, small and random fluctuations were observed occasionally, especially, when the MR was running along with the HD operation. PBLM patterns and PBLM trend data are also displayed for various incidents. In most of cases, the PBLM signal is below the MPS threshold, but it contains some useful information. These evidences are elaborated owing to the data-archiving system, which can distinguish whether each pulse is in the MR or the MLF mode and record all 25 Hz pulses without dead time. The system can be improved and used to establish even more stable accelerator operation in the future. A new scheme to synchronize various events recorded by different instruments or digitizers

ISBN 978-3-95450-176-2

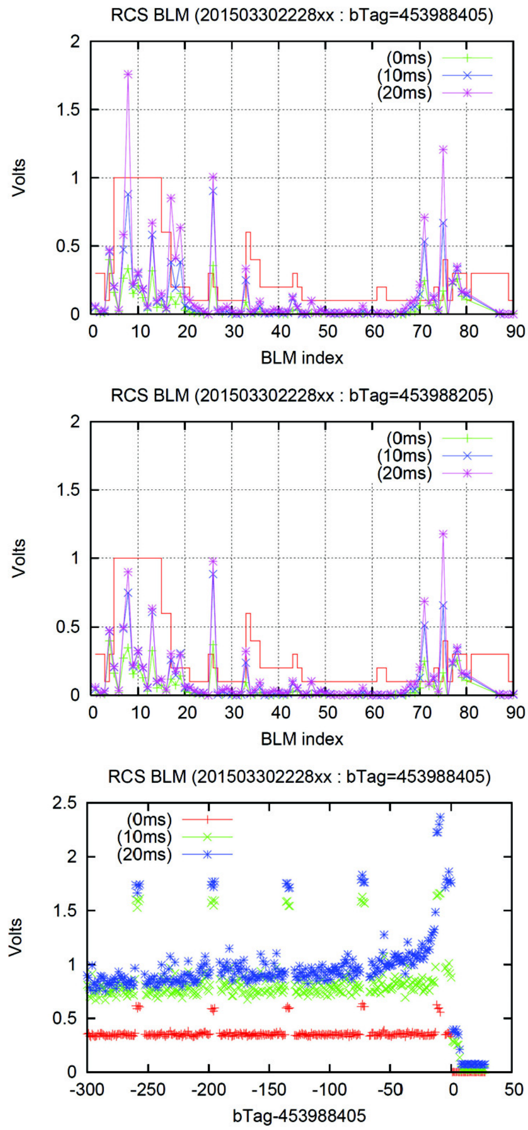

Figure 12: PBLM pattern data in MLF mode and short trend of PBLM08 signal (14 s in full range) in the event of TMP failure.

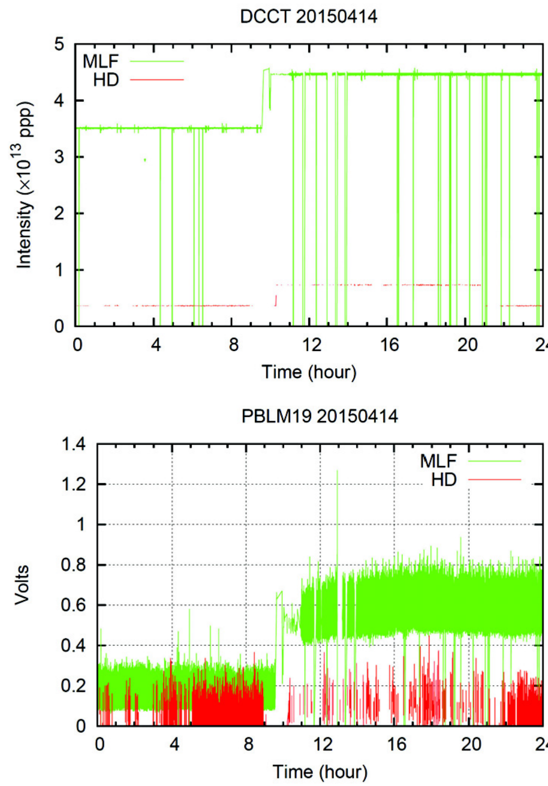

Figure 13: DCCT plot from 400 kW to 500 kW (upper) and PBLM19 trend at the same time scale (lower).

is also planned. The scheme might generate more useful information owing to the better time resolution on offer.

REFERENCES

[1] K. Hasegawa, "Commissioning of Energy Upgraded LINAC of J-PARC", Proceedings of of the 27$^{\text{th}}$ Linear Accelerator Conference, Geneva, Switzerland, August 31 – September 5, 2014, pp. 417–422 (2014). **TUIOB03**

[2] H. Ao et al., "Annular-Ring Coupled Structure Linac for the J-PARC Linac Energy Upgrade", Proceedings of the 4$^{\text{th}}$ International Particle Accelerator Conference, Shanghai, China, May 12–17, 2013. **THPWO036**

[3] A. Ueno et al., "Over 60 mA RF-driven H^- ion source for the J-PARC", NIBS 2012, Jyväskylä, Finland, September 3–7, 2012. AIP Conf. Proc. **1515**, 331 (2013).

[4] Y. Kondo et al., "Beam Test of a New RFQ for the J-PARC LINAC", Proceedings of of the 27$^{\text{th}}$ Linear Accelerator Conference, Geneva, Switzerland, August 31–September 5, 2014, pp. 267–269 (2014). **TUIOB03**

[5] H. Hotchi, "Recent progress of J-PARC RCS beam commissioning — Toward realizing 1-MW Output Beam Power", Proceedings of the 6$^{\text{th}}$ International Particle Accelerator Conference, Richmond, VA, USA, May 3–8, 2015. **TUBB3**

[6] N. Hayashi et al., "Beam Instrumentations for the J-PARC RCS Commissioning", Proceedings of EPAC 2008, pp.1125–1127., Genova, Italy (2008). **TUPC034**

[7] N. Hayashi et al., "Beam position monitor system of J-PARC RCS", Nucl. Instr. Meth. **A677**, pp.94–106. (2012)

[8] H. Takahashi et al., "Synchronized Data Distribution and Acquisition System Using Relective Memory for J-PARC 3GeV RCS", Proceedings of EPAC 2008, pp.1553–1555., Genova, Italy (2008). **TUPP013**

[9] N. Hayashi et al., "Pulse Based Archive System and Analysis for Current and Beam Loss Monitors in the J-PARC RCS", Proceedings of of the 5$^{\text{th}}$ International Particle Accelerator Conference, Dresden, Germany, June 12–17, 2014, pp.3800-3802 (2014). **THPRIO016**

ISBN 978-3-95450-176-2

BUNCH LENGTH ANALYSIS OF NEGATIVE HYDROGEN ION BEAM IN J-PARC LINAC *

A. Miura#, N. Hayashi
J-PARC Center, Japan Atomic Energy Agency, Tokai, Ibaraki, JAPAN
T. Maruta, Y. Liu, T. Miyao,
J-PARC Center, High Energy Accelerator Research Organization, Oho, Tsukuba, JAPAN
S. Fukuoka
Graduate School of Pure and Applied Sciences, University of Tsukuba, Tsukuba, Ibaraki, JAPAN

Abstract

We used bunch shape monitors (BSMs) to measure the longitudinal bunch length of a negative hydrogen ion beam in the J-PARC linac. Because we experienced a vacuum degradation to suspend a beam operation during the BSM operations, BSMs were once dismounted for vacuum conditioning. We installed one BSM again in the beam line with additional vacuum equipment. We stared to measure the 191-MeV beam again to tune the buncher amplitude after checking a functioning BSM by comparing its results with those of a simulation. To evaluate the measurement errors with peak beam current increasing, we observed waveforms with various beam currents. Therefore, the RMS bunch length depends on the peak beam current and the bending at the pulse head grows with the peak beam current. Furthermore, to avoid the thermal stress, we compared the data taken at an off-center beam with the ones taken at an on-center beam, because a target wire will be exposed to a higher peak beam current. In this study, we introduced the peak beam current dependence of the bunch length waveforms, and an effect of on-/off-centering of the wire position. Finally, the new buncher tuning method using one BSM is discussed.

INTRODUCTION

In the 1-MW upgrade project at the J-PARC at the experimental laboratories connected to the downstream of the linac and the rapid cycling synchrotron (RCS), we have two big projects, particularly, the energy upgrade from the 181-MeV linac to the 400-MeV linac and the front-end improvement using a new RF ion source and replacing it with the upgraded radio frequency quadrupole (RFQ) linac cavity. To meet with the 400 MeV of the linac, 21 ACS cavities have been developed and installed in the beam line; we have developed the beam monitors for the ACS cavity tuning. Because the acceleration frequency of ACS cavities is 972 MHz, which is three-fold higher than that of upstream RF cavities, we need to take longitudinal matching at the upstream part of the new ACS beam line.

We started the development of a bunch shape monitor (BSM) for the J-PARC linac. Three years into the project, three BSMs were fabricated. In the summer of 2012, prior to the installation of ACS cavities, we installed all three BSMs at the upstream of the new ACS section to conduct some test measurements using 181-MeV beams [1]. During the BSM measurements, a problem with the degradation in vacuum conditions was found. A major reason for this problem was outgassing from materials when the high voltage and RF power were supplied. To mitigate this problem, BSMs were dismounted from the beam line and the off-line conditioning with outgas analysis was performed. The impacts of the bias voltage to the target wire and static lens and the RF power to the deflector were examined in the vacuum test [2].

The improved arrangement of the vacuum system for installing the BSM was also proposed. We installed a BSM in at the upstream of the ACS again in the summer of 2014 with the additional vacuum arrangement. We started to use the BSM to conduct the buncher amplitude tuning. In the study on space-charge driven transverse–longitudinal coupling resonance, we measured the longitudinal emittance with the BSM. The results are expected to contribute to the design of the beam operational parameters for the energy-upgraded linac. The high-intensity linac design follows the equipartitioning (EP) condition. Fortunately, J-PARC linac could find its EP solution as the baseline design without sacrificing hardware efficiency. It also has the applicability for a wide range of off-EP conditions, offering opportunities not only for investigating the basic beam physics principles but also for further optimizing the machine operation [3].

To evaluate the measurement errors in the high-intensity beam operation, we observed waveforms with various beam currents. We discuss the longitudinal bunch length taken at an off-center position to avoid the thermal stress from the higher peak beam current. Finally, we introduce a proposal for the new buncher tuning method with one BSM.

STRUCTURE OF BSM

A BSM comprises the body, RF deflector, steering magnet, actuator, and electron detector as shown in Fig. 1. An RF deflector and an actuator which holds a target wire are vertically installed against the beam axis on the body. Secondary electrons that pass through the collimators on the RF deflector travel to the pipe connected to the electron detector [4]. Finally, secondary electrons pass

* amiura@post.j-parc.jp

ISBN 978-3-95450-176-2

through some collimators and the bending magnet before reaching the electron multiplier.

During a BSM operation, we set the wire position at the beam center by observing the beam loss signals at the downstream beam loss monitor. The stroke of the wire reaches about 5.0 mm from the duct center (to the right in Fig. 1). It means that the wire is relatively closer to the detector.

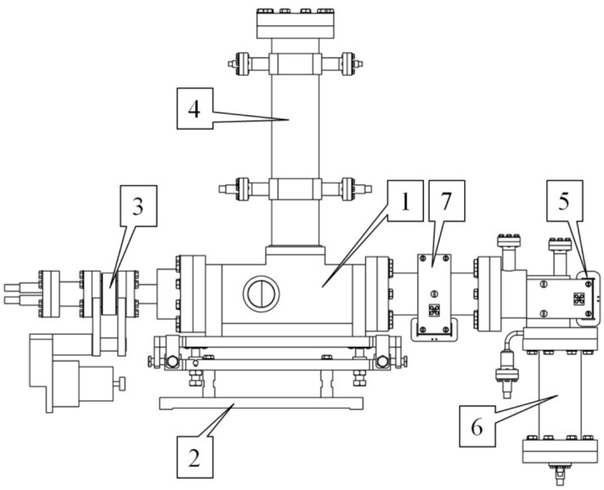

Figure 1: Overview of BSM (1: body, 2: support, 3: target actuator, 4: RF deflector, 5: bending magnet, 6: electron detector, and 7: steering magnet).

Installation layout of the BSM is shown in Fig. 2. The BSM locates at the downstream of SDTL16 and ACS-type bunchers. The specification of the measured beam is 5–30 mA for the peak beam current, 191 MeV for the beam energy, and 100 μs for the longest pulse duration.

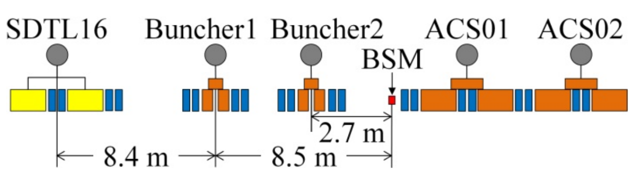

Figure 2: One BSM installation layout after SDTL16 with their distances shown.

EFFECT OF THE RF FEED FORWARD SYSTEM

When the beam operation started, we usually tuned an RF feed forward (FF) system for the compensation of the RF power loss due to the passing of charged particles to the RF cavity. To investigate the behavior of the pulse head, we took waveforms at various peak beam currents. In the 30-mA operation, the peak beam current can be squeezed by the scraper in the upstream of linac to make 5–30 mA with 5-mA intervals.

The electrical field in an RF cavity is caused by the travelling electrical field induced by the charged beam pulse. The strength of the field directory depends on the travelling electrical field, i.e., the peak beam current. The field counteracted the beam pulse, particularly, by slowing down the beam particles.

Figure 3 shows the waveforms affected on the beam pulse. In the figure, pulse heads are on the left and the tails are on the right. The color contour means the intensity of the signal. At 5 mA, phases were not affected by the travelling field and the profiles were almost straight. When the peak beam current increased, pulse heads were effectively bent. This is usually compensated by the RF FF system; if there is no compensation, then it is usually difficult to calculate pulse width accurately. These results suggest the importance of RF FF adjustment to compensate the electrical field for the measurement at the high peak beam current operation.

RMS bunch lengths are calculated using the last half of the measurement results, because the effect of the RF FF system is negligible in the last half. The calculated RMS bunch length grows with beam current. It is considered that the cause of the growth is due to the space-charge effect.

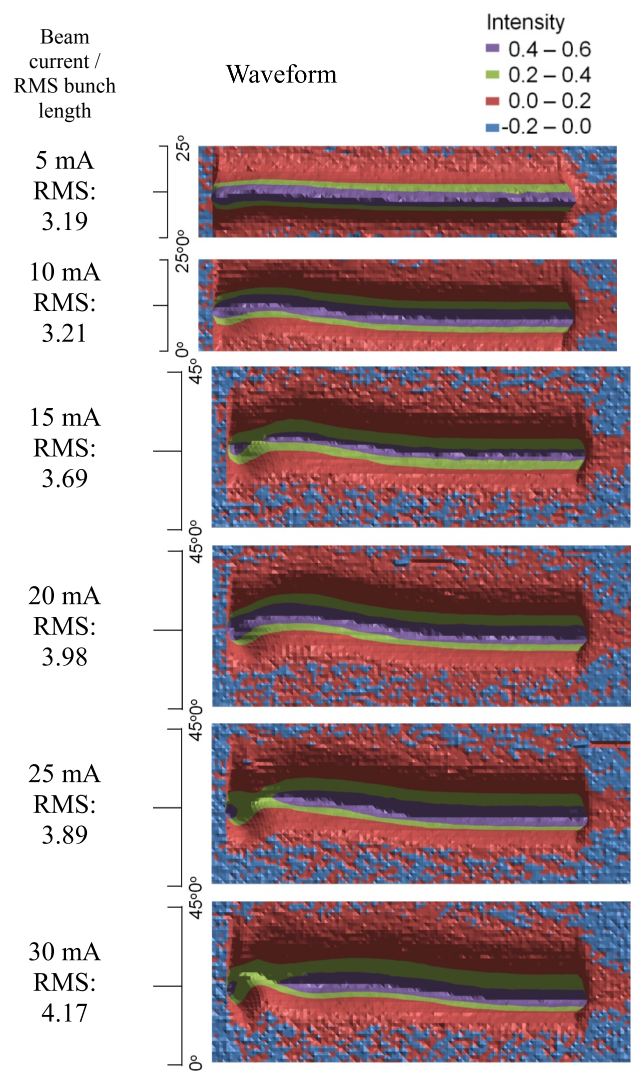

Figure 3: Effect of the FF system on waveform of bunch length.

ISBN 978-3-95450-176-2

EFFECT OF OFF-CENTERING BEAM

When the peak beam current is increasing, a target wire will be exposed to a higher peak beam current and the thermal stress will become serious. The misalignment with the beam axis should be evaluated. Several measurements were conducted for different horizontal wire positions scanning from −2 mm to +2 mm in steps of 0.5 mm as shown in Fig. 4. Here the positive position means the wire is inserted to the right of the detector in Fig. 1. To control the thermal stress, we evaluated the data taken at an off-center beam with those taken at an on-center beam. The minimum phase spread can be seen at −1.0 mm where the maximum signal was detected by the electron multiplier and the Gaussian fitting is shown to underestimate the actual RMS bunch length. This tendency agrees with the frontend bunch length of the 3-MeV beam measured at Linac4 at CERN [5]. The absolute bunch length of the 3-MeV beam is quite larger than that above 191 MeV in J-PARC. The signal level shift with wire position is considered to be caused by the mechanical structure.

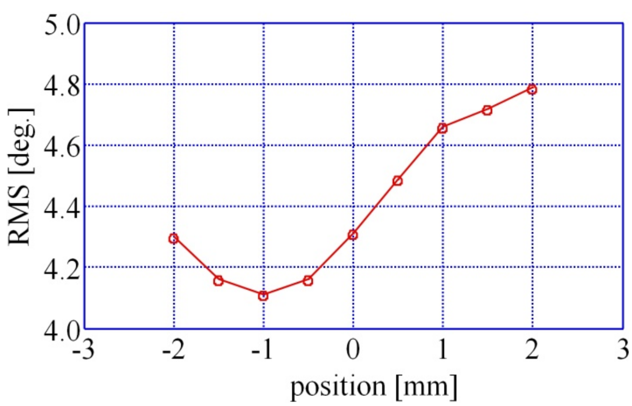

Figure 4: RMS phase spread at different horizontal wire positions.

Because the BSM is a type of wire scanning device, the possibility of using it as a horizontal profile monitor is incidentally discussed [5]. However, the signal level is a function of the wire position; therefore, the measurement results include the functional errors. We usually defined the wire position of the beam center by the beam loss signal taken at the downstream beam loss monitor. When the beam hits the wire, secondary particles are generated and lost to the transport. A part of the lost particles are detected by the beam loss monitors, and the signal levels depend on the beam intensity. We usually obtained the horizontal beam profiles by the beam loss signal with the horizontal wire scan.

LONGITUDINAL TUNING

We propose a new buncher tuning method. Because currently we can use only one BSM, we need to consider the new method to tune the longitudinal bunch length. One BSM was installed in front of ACS01 as shown in Fig. 4. We can measure the longitudinal pulse width using SDTL16, buncher 1, and buncher 2. We can obtain the amplitude scan curve as shown in Fig. 5. From previous discussions of EP tuning [3], the EP condition should be far from the resonance region to avoid transverse–longitudinal emittance exchange. We propose a tuning method using the amplitude scan curve and Twiss parameters obtained by transverse profiles.

We use the following formula [6].

$$\sigma^2_{BSM} = \varepsilon_z[(1+Lk)^2\beta_B - 2L(1+Lk)\alpha_B + L^2\gamma_B], \quad (1)$$

where ε_z is emittance, L is drift length, α_B, β_B, and γ_B are Twiss parameters at the BSM position, and k is longitudinal focusing force. We substituted σ^2_{BSM} and k, which are obtained from Fig. 5. In Fig. 5, blue dots were taken at 30 mA and red ones were at 50 mA. We can obtain the smallest bunch length at 3 MV for the buncher 1 amplitude. This curve means longitudinal focusing and defocusing by the buncher amplitude. The amplitude at the minimum bunch length means the focusing point that is the most important for fitting the simulation results.

We made iterated calculations to obtain a free parameter set of ε_z, α_B, β_B, and γ_B estimated by a 3D-PIC simulation. We adopted the above parameter set for the buncher and quadrupole settings and the total beam loss measurements, and we finally decided the proper settings for the minimum beam loss situation.

We obtained the longitudinal beam parameters as listed in Table 1 at the position of buncher 1. The emittance at the RFQ exit from the RFQ simulation is 134.4 [π deg. keV] and the measured emittances at buncher 1 are 149.9 at 30 mA and 224.0 at 50 mA. Emittances glowed approximately 10% and 60% at 30 mA and 50 mA, respectively.

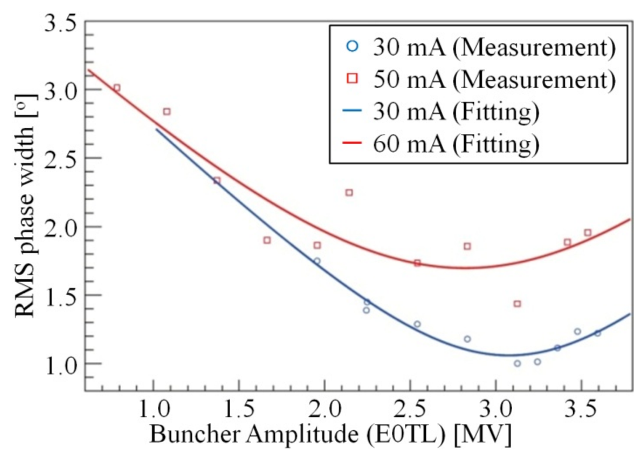

Figure 5: Amplitude scan curve of buncher 1 at 30 (blue) and 50 mA (red). Solid curves are fitted.

Table 1: Measured longitudinal beam parameters at the MEBT2 entrance by buncher 1 amplitude scan [6]

	Measurement	
	30 mA	50 mA
α_x	0.138	−0.622
β_x [deg./keV]	0.0182	0.0183
ε_x [π deg. keV]	149.9	224.0

ISBN 978-3-95450-176-2

CONCLUSION

We successfully developed a BSM for the J-PARC linac and used it for the buncher amplitude tuning. The effect of the electric field generated by the travelling charged particles was observed using various beam currents. Furthermore, we showed the RMS phase spread at different horizontal wire positions. One possible cause is the mechanical structure. However, there still mains an unknown beam dynamics cause. The high-intensity linac design follows the EP condition. We measured the longitudinal emittance with BSMs. The results supported minimum beam loss conditions; however, the emittance growth was recognized at 30 and 50 mA. We proposed a new tuning method using one BSM, which is similar to the Q-scan method. We have a plan to develop the BSM for the frontend; there is not sufficient space to install a number of BSMs. In this case, we will install only one BSM and use this method. This method will play an important role in the frontend tuning.

REFERENCES

[1] A. Miura, et. al., "Bunch Shape Measurement of 181 MeV Beam in J-PARC Linac", JPS Conference Proceedings Vol. 8, to be published in Oct., 2015.

[2] A. Miura, et. al., "Vacuum Improvement of Bunch Shape Monitor for J-PARC Linac", Proc. International Beam Instrumentation Conference (IBIC2014), TUPD09, Monterey, California, USA, 2014.

[3] Y. Liu, et. al., "Stability Studies for J-PARC Linac Upgrade to 50 mA/400 MeV", Proc. Int. Proc. Part. Acc. Conf. (IPAC15), THPF039, Richmond, Virginia, USA, May, 2015.

[4] A. V. Feschenko, "Methods and Instrumentation for Bunch Shape Measurements", Proc. Part. Acc. Conf. PAC 2001, Chicago, p. 517, 2001.

[5] G. Bellodi, et. al., "Longitudinal Beam Profile Measurements in Linac4 Commissioning", Proc. LINAC2014, MOPP025, Geneva, Switzerland, 2014.

[6] T. Maruta, et. al., "Recent Progress of Beam Study in the J-PARC Linac", Proc. Part. Acc. Soc. of Japan, WEP014, Fukui, 2015 (in Japanese).

ISBN 978-3-95450-176-2

STATUS OF BPMS IN THE FIRST STAGE OF COMMISSIONING AT CADS INJECTOR I*

H.Z. Ma#, J.S. Cao, Y.F. Sui, Q. Ye, IHEP, 100049, China
Key Laboratory of Particle Acceleration Physics and Technology,
IHEP, Chinese Academy of Science

Abstract

The paper will introduce the status for BPMs in the first stage of commissioning at CADS (China Accelerator Driven Subcritical System) Injector I. The measurement principles and results of BPM at injector I are presented. The measurement of BPM is rigorous in the first medium energy beam transport line of CADS Injector I. To ensure the safety of test cryomodule, beam orbit should be corrected to the minimized region. The third order fitting way is used to calculate the position of beam for BPM non-linearity. And the average of data in the single pass window should improve the resolution. Then BBA of BPM can help tracking beam position accurately. Finally the interlock circuit of BPM is tested with the beam.

INTRODUCTION

China Accelerator Driven Subcritical system (CADS) is a strategic plan to solve the nuclear waste problem and the resource problem for nuclear power plants in China[1]. CADS has two injector linacs named Injector I and II to ensure its high reliability, which are respectively built by Institute of High Energy of Physics (IHEP) and the Institute of Modern Physics (IMP).

With the energy of about 3.4MeV in the first stage of commissioning, the injector I in IHEP is composed of ECR ion source, Low Energy Beam Transport line (LEBT), Radio Frequency Quadrupole (RFQ), Test Cryomodule (TCM), Medium Energy Beam Transport line (MEBT) and beam dump. The layout of BPMs for the ADS Injector I at the first stage of commissioning is illustrated in Figure. 1.

The injector I linac at the test stage includes total 10 BPM detectors of three types, which are strip line, capacitive and button. Two of BPMs are cryogenic mechanical structure. The rest of them are designed to work in the normal temperature environment. Here are the parameters of BPMs and beam characteristics as Table 1.

Table 1: The Parameters of BPM and Beam Characteristics of 3.4 MeV C-ADS Injector I

Parameter	**Value**
Electrode type	Strip Line /Capacitive/Button
Beam pipe diameter	30/50/35 mm
Beam max displacement (with ref. to beam pipe)	50%
Position accuracy	±100um
Position resolution	30um
Beam energy	3.4MeV
Bunch repetition rate	325MHz
Beam pulse length	30us-CW
Pulse repetition rate	5Hz/10Hz
Peak current	10mA

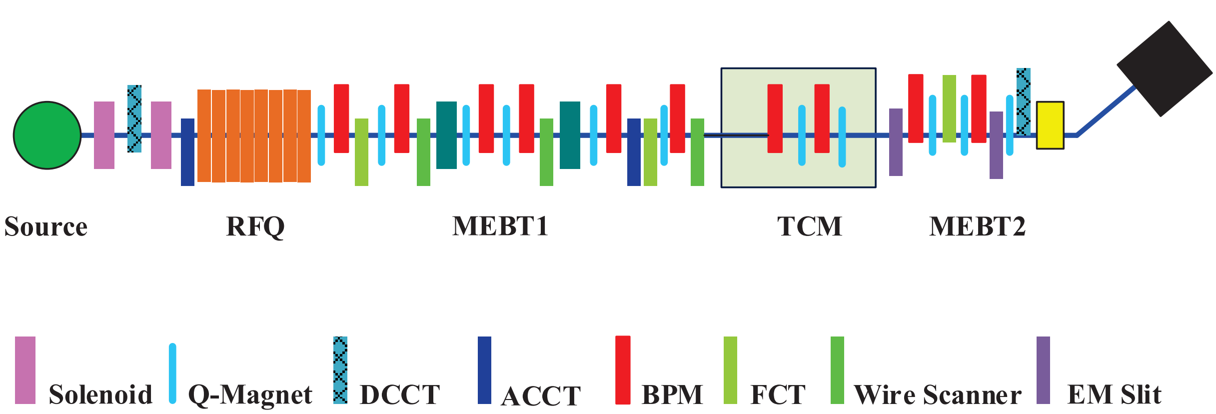

Figure 1:The layout of BPMs of the ADS Injector I.

*Work supported by China ADS Project (XDA03020000)
#mahz@ihep.ac.cn

ISBN 978-3-95450-176-2

BEAM POSITION MONITOR MAPPING

First, the BPM should be calibrated on the test stand before installed on the injector. The standard signal generator is used to do the mapping test. The figure 2 shows the result of mapping for BPM. Then in order to improve the accuracy of BPM, the third fitting way is adopted to decrease measuring error due to the non-linearity effect. The formula 1 for calculating the beam position can be described to be the third order of function. U and V in the formula 1 stand for the normalized data of 4 digitized electrode signal for BPM. The fitting coefficients A and B can be estimated according to the database of mapping. The RMS for fitting error is about 0.2-0.3mm. Finally, the data of measurement for calculating beam position by the formula 1should be more accurate.

$$x = \sum_{i=0}^{3}\sum_{j=0}^{i} A_{i-j,j}U^{i-j}V^{j}$$
$$y = \sum_{i=0}^{3}\sum_{j=0}^{i} B_{i-j,j}U^{i-j}V^{j} \qquad (1)$$

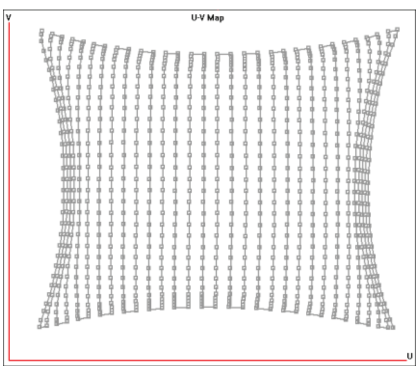

Figure 2: Sensitivity mapping of 4 electrodes for BPM.

THE MEASUREMENT OF BAEM POSITION MONITOR

Signal Processing Electronics

Libera Single Pass H (LSPH) is an instrument intended for position and phase monitoring in hadron and heavy ion linacs [2]. Starting from the four BPM signals, beam position is calculated by delta-over-sum formula. With a stable 325 MHz sine signal using as a reference, the four phases measured by each input are then averaged. Figure 3 shows the status of LSPH equipped with BPM label.

Figure.3 Libera Single Pass H.

DAQ

The data acquisition system of BPM is based on EPICS. The position data obtained by BPM IOC is only linear fitting. Therefore, the new third order fitting way for calculating position. The average of the position and phase data in the single pass window is realized by the soft IOC in the DB level.

Beam Measurement

At the first stage of commissioning for injector I, the Beam Based Alignment (BBA) of BPM on the first MEPT should be carried out. Table 2 gives the deviation of BPM detector from beam centre, which are within 0.5mm.

Table2 : BBA Measurement for BPM on First MEPT

OFFSET	X(mm)	Y(mm)
BPM2	-0.28	0.05
BPM3	0.3	0.08
BPM4	0.055	-0.5

Orbit correction on the first MEPT can be completed according to the BBA test. Stability of the beam orbit should be kept in the range of ± 0.15 mm [3], especially for the safety of spoke cavity in TCM.

INTERLOCK TEST FOR BPM

In the case of injector I, the Interlock of BPM electronics is an optoisolated open collector output [4]. The circuitry outside should be externally connected as shown in Figure 4. Depending on applied 24 V power supply, R should be calculated to not exceed 8 mA over resistor. Finally it is chosen to be 2K ohm.

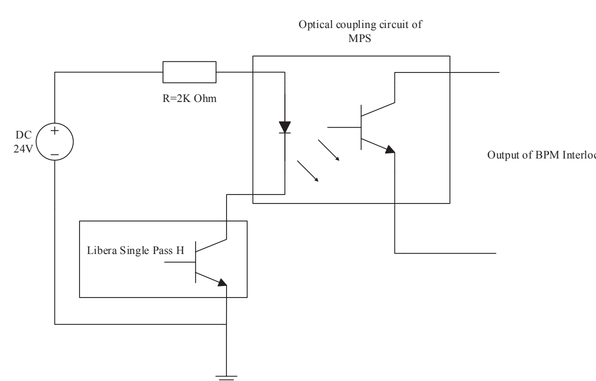

Figure 4: The BPM Interlock Circuit.

The circuitry test with BPM electronics. The output signal is DC high level or negative pulse 5V, which can be checked in Figure 5.

ISBN 978-3-95450-176-2

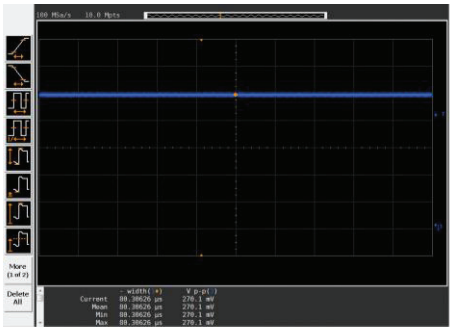

a

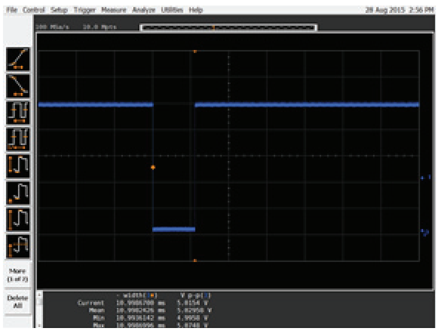

b

Figure 5: Output of BPM Interlock. a) Interlock enabled b) Interlock disabled.

CONCLUSION

All type of BPM detectors are installed on injector I linac for the 3.4MeV beam testing. BPM mapping, position data reconstruction by SOFT IOC and BBA improve the accuracy of beam measurement. Preliminary research of BPM interlock guarantees stable operation of the superconducting cavity in TCM. Although the BPMs work well during the operation of Injector I, there is detailed research to be done to optimize the whole system.

ACKNOWLEDGMENT

We acknowledge Matjaz. Žnidarčič from I-Tech for the help in test of the Libera Single Pass H. The authors are grateful for the help and cooperation from the operators of the test beam line. Thanks are also given to the members of the beam instrumentation group for their useful discussions and suggestion.

REFERENCES

[1] Jingyu Tang and Zhihui Li (ed.), Conceptual physics design of the C-ADS accelerators, IHEP-CADS Report/2012-01E.
[2] Libera SPH page - http://www.i-tech.si/.
[3] Weimin Pan, Internal Report in IHEP.
[4] Libera Single Pass H User Manual 2.80.

ISBN 978-3-95450-176-2

MEASUREMENTS OF BEAM HALO BY WIRE SCANNER MONITOR*

Hongping Jiang#, Key Laboratory of Particle & Radiation Imaging (Tsinghua University), Ministry of Education, Beijing 100084, China
Peng li, Taoguang Xu, Institute of High Energy Physic, Chinese Academy of Sciences, Beijing 100049, China

Abstract

A wire scanner is used in the beam halo experiment at the Institute of High Energy Physics (IHEP) to measure the beam halo for the study of beam halo dynamics. The beam energy in the FODO transport line is 3.5 MeV and the peak current is 24 mA. Firstly we get the emittance value for the vertical and the horizontal plane respectively by measuring the matched beam. Then we measure the beam halo of the mismatched beam.

INTRODUCTION

The beam halo formation is an important characteristic of high intensity beams. Beam halo particles are more easily lost on the walls and increase unwanted radioactivity [1]. The experimental study of beam halo formation is very important and necessary. So we built a 28-quadrupole beam transport line after the IHEP RFQ [2]. We have designed a beam profile and halo measurement system and have installed the system in the transport line [3]. In the experiments we used the measured beam profile data to character the proton beam with quadrupole scans method, firstly [4]. Then we measured the RMS matched beam profiles. We also measured the mismatched beam profiles and beam halos, lastly.

In this paper, we introduce the beam profile and halo measurement system and the beam halo experiments. Then we present the measured RMS matched beam profiles with beam halo and the measured mismatched beam profiles with beam halo.

THE BEAM PROFILE MEASUREMENT SYSTEM

We have designed a wire scanner system to measure the transverse beam profile and the emittance. The schematic view of the wire scanner is shown in Fig. 1. The wire scanner will be mounted at 45 ° to the horizontal plane. The outer assembly that resides outside the vacuum consists of a stepper motor, a linear encoder and an electric control platform. The inner consists of a movable frame that carries a sensing wire. And the 32micron diameter carbon wire is selected for use.

* Work supported by National Natural Science Foundation of China (Major Research Plan Grant No. 91126003)
#Jianghp@ihep.ac.cn

Figure 1: The Schematic view of the wire scanner.

BEAM HALO EXPERIMENT

The 28-quadrupole beam transport line is installed at the end of the IHEP RFQ, which accelerates the proton beam to 3.5MeV and operates at the frequency of 352MHz [2]. The block diagram of this transport lattice is shown in Fig. 2.

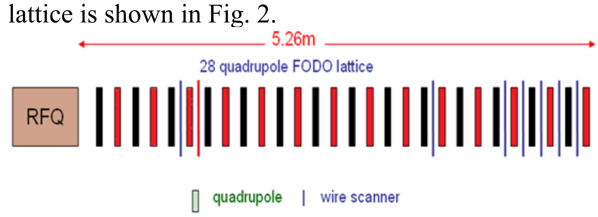

Figure 2: Block diagram of beam halo experiment transport line.

The squares mean quadrupoles, and we change the focusing strength of the FODO channel to obtain the different zero current phase advances. The lines mean wire-scanners. The red line is used to measure the vertical beam profile; the blues are used to measure the horizontal beam profiles at the different locations. Quadrupole scans method is used to charactering the beam, firstly. And the results are presented in Table 1.

Table 1: The Beam rms Parameters

Direction	Alpha	Beta	Emittance (RMS Normalized)
Horizontal (x)	3.287	0.4466 (mm/mrad)	0.29 (mm-mrad)
Vertical (y)	-0.165	0.1005 (mm/mrad)	0.47 (mm-mrad)

ISBN 978-3-95450-176-2

THE MATCHED BEAM PROFILES

Due to the lack of vertical wire scanners at the end of transport line, the beam was matched by adjusting the first four quadrupoles to produce equal rms sizes in horizontal position at the last 6 wire scanners. A least-squares-fitting procedure was used based on measurements of derivatives of rms sizes with respect to matching quadrupole gradients. Under matched conditions, the beam is expected to be transported along a linear transport channel with minimal emittance growth, and no significant change in the equilibrium distribution [5]. The measured results with different location equilibrium horizontal beam profiles were shown in Fig. 3.

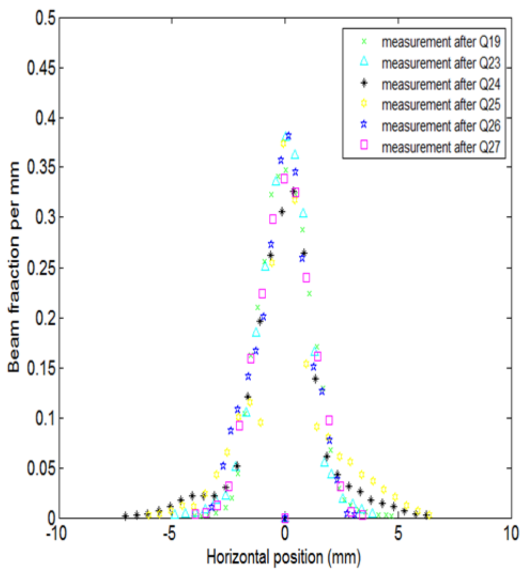

Figure 3: The measured equilibrium horizontal profiles at different locations.

We have used the IMPACT code to simulate the matched beam with the measured initial beam parameters and simulations can reproduce the beam profiles properly [3]. The results for matched beam are shown in the Fig. 4. From the measured results Fig. 4, we can see that the scanner can provide intensity measurements over a dynamic range of about 10^3. And it can cover the scope of 3 RMS radiuses of the beam profiles, it is enough for measure of the beam halo, Shoulders [7].

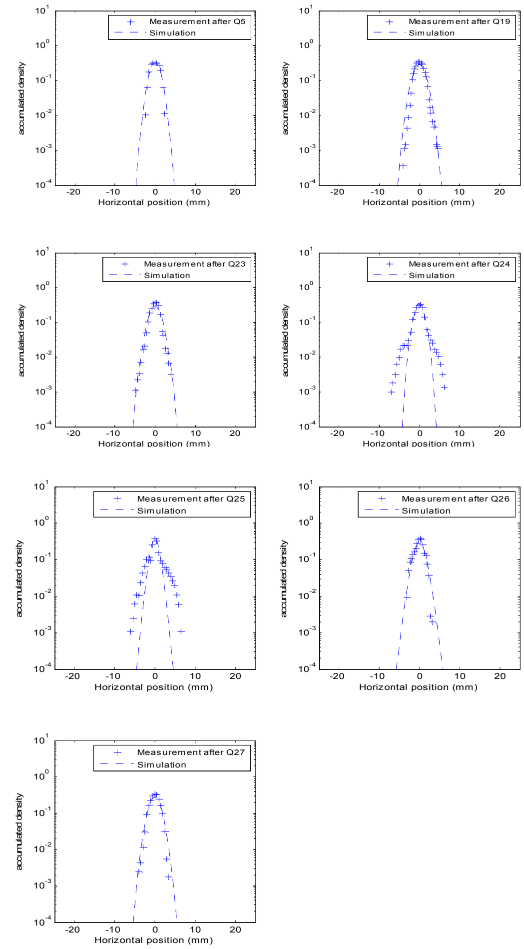

Figure 4: The measured and simulated matched beam profiles.

From the Fig. 4 we also can see in the most locations the simulations can properly reproduce the measured beam profiles without beam halo, but there are a little halo particles in two locations. That means the beam in the phase space is not elliptic symmetry. If we want to know there are beam halo particles or not in beam phase space, we need change the strength of the quadrupole to measure more 1-D beam profiles, the different projections of the 2-D phase space.

We also analyse the matched beam transported in a weaker focusing FODO channel, and the results are shown in Fig. 5.

ISBN 978-3-95450-176-2

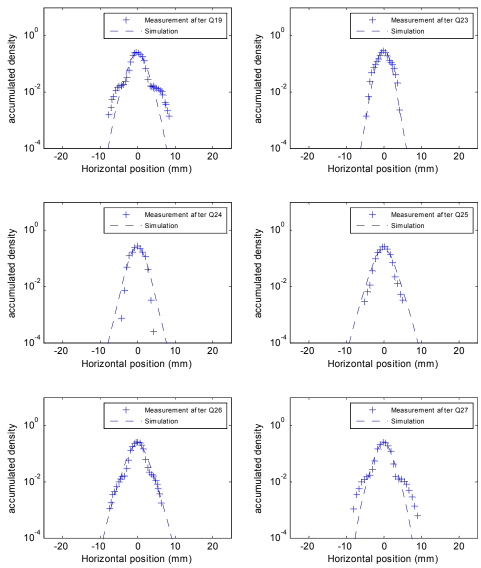

Figure 5: The measured and simulated matched beam profiles.

From Fig. 5 we can see the beam profiles have larger radius and more obvious beam halo 'shoulder' at two locations.

THE MEASURED MISMATCHED BEAM PROFILES

Then we obtain mismatched beam by adjusting the matching quadrupoles and measure the beam profiles. We use the IMPACT to simulate the beam.

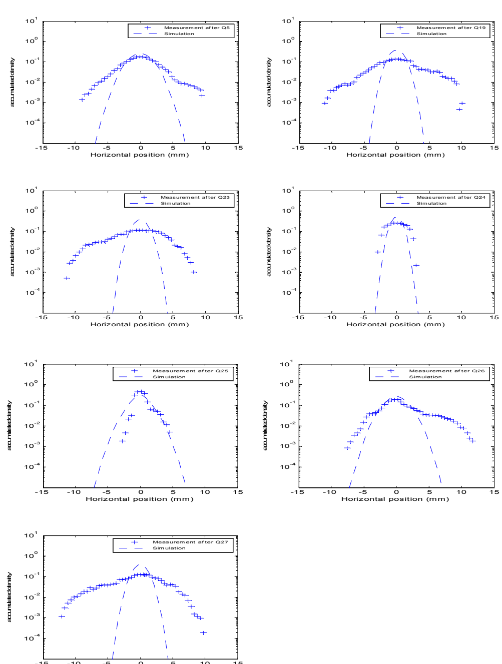

Figure 6: The measured and IMPACT simulated mismatched beam profiles.

From Fig. 6 we find that the beam halos are formed in measured profiles at all locations, and we can see the simulations can't reproduce the measured beam profiles with beam halo.

CONCLUSION

We have built a transport line and designed a wire scanner system to measure the transverse beam profile and the emittance. We find dynamic range of the wire scanner is enough for us to measure the beam halo. And if we want to know there are beam halo particles or not in beam phase space, we need change the strength of the quadrupole to measure more 1-D beam profiles, the different projections of the 2-D phase space, because there are still a little halo particles in two locations for the matched beam profiles.

REFERRENCE

[1] P. L. Colestock, T. Wangler, C. K. Allen, "The Beam Halo Experiment at LEDA". *Proc. of the XX International Linac Conference.* Monterey, California, 2000. 806-808.

[2] P. Jun, H. Tao, L. Hua-Chang, et al. *Beam halo experiment at IHEP [J]*. Chinese Physics C, 2013, 37(3): 037002.

[3] R. Yu-Fang, H. Lu-Xiang, L. Hua-Chang, et al. "Design and simulation of a wire scanner for the CSNS linac [J]". Chinese Physics C, 2010, 34(10): 1655.

[4] J. Hong-Ping, F. Shi-Nian, P. Jun, et al. "Characterizing a proton beam with two different methods in beam halo experiments [J]". Chinese Physics C, 2014, 38(8): 087002.

[5] M. Reiser, "Theory and design of charged particle beams [M]". John Wiley & Sons, 2008

[6] H. Jiang, S. Fu, P. Chen, T. Huang, F. Li, P. Li, B. Sun, "Macroparticle Simulation Studies of a Beam-core Matching Experiment", Shanghai, IPAC 13.

[7] C. K. Allen, K. C. D. Chan, P. L. Colestock, et al. "Beam-halo measurements in high-current proton beams [J]". Physical review letters, 2002, 89(21): 214802

ISBN 978-3-95450-176-2

BUNCH-BY-BUNCH STUDY OF THE TRANSIENT STATE OF INJECTION AT THE SSRF*

Zhichu Chen, Yongbin Leng, SSRF, Shanghai, China

Abstract

High current and stable beams are preferred to a light source, so the suppression of the oscillations due to the frequent injections during top-off operations get the attention at the Shanghai Synchrotron Radiation Facility (SSRF). To evaluate the possibility of further optimizations, a bunch-by-bunch position monitor is used to study the behavior of the injected bunch. The injected part is isolated from the stored one by decomposing the position matrix of all the bunches in the storage ring. Frequency feature, motion lifetime and other characteristic parameters of the injection mode have been compared with those of the stored mode.

INTRODUCTION

The SSRF is a third generation light source aiming to provide stable and brilliant synchrotron radiation. The high brilliance target was achieved by operating under top-off mode. But the frequent injections required by the top-off mode will decrease the stability of the beams. The behavior of the injected bunch has to be studied before finding a solution to minimize the effect of the injection.

BUNCH SEPARATION

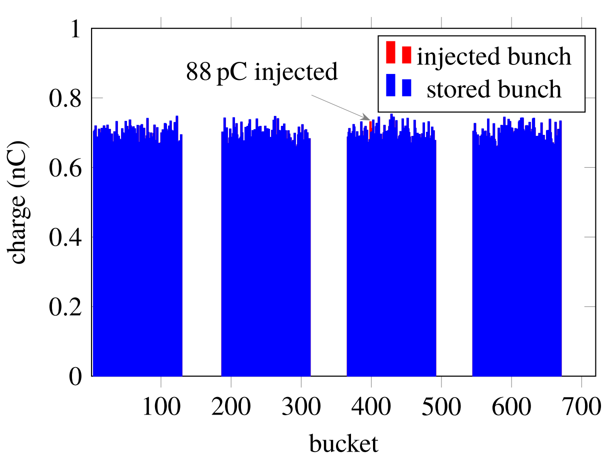

Figure 1: Filling patterns before and after an injection.

The goal of the study is to build an on-line feedback system to stabilize the injected bunch, so it's better to leave the beam undisturbed while getting its information. Signals from the electrodes of the bunch-by-bunch position monitor can easily be used to get the positions as well as the filling pattern of the bunch train. The data succeeded the injection were saved for further study.

* Work supported by National Natural Science Foundation of China (No. 11305253)

The injected bunch can be found by using the filling patterns (as shown in Figure 1). The adjacent bunches are used to interpolate the orbit of the stored bunch and the position of the injected bunch can be obtained by deducting the weighted stored part from the raw position data. The injected bunch can also be separated by decomposing the motion matrix of all bunches by using the singular value decomposition (SVD) [1]. Both methods gave the same—or extremely close—results.

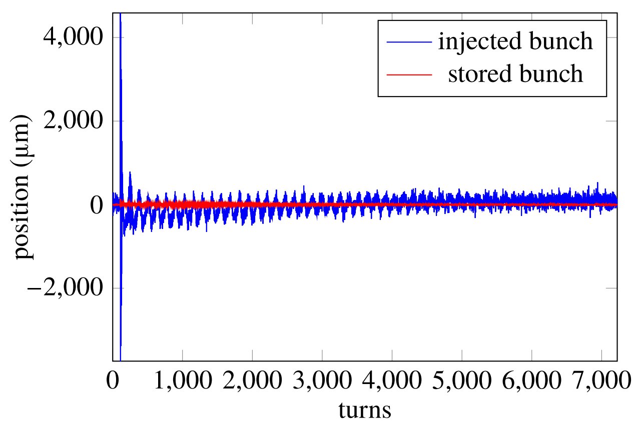

Figure 2: Horizontal positions of the injected bunch separated from the stored one.

The behavior of the stored bunch (red line in Fig. 2) is considered trivial, while the motion of the injected one (blue line in Fig. 2) shows the potential to give more information at the first glance.

A motion matrix was constructed to decompose the source signals. The columns of the matrix are shifted segments of the total waveform, so that the sources (the five major sources are shown in Fig. 3) can be separated after the independent component analysis (ICA) [2, 3]. The waveforms and the spectra (as shown in Fig. 4) of the sources indicates that the motion is dominated by the energy oscillation and its harmonics. The signal source 5 is pure horizontal betatron oscillation, and the rest sources are mixtures of horizontal and vertical betatron oscillations, judged by their characteristic frequencies.

The ICA is a time-consuming and semi-automatic method which requires human interference. Considering the on-line processing requirement in the future, the SVD method would be used and the ICA results would serve as a reference.

The singular values of the aforementioned motion matrix show that only the first ten modes make sense and the rest modes can just be considered as random noise (as shown in Fig. 5). The singular values and the spectra of the left-singular vectors implies that the modes are in pairs and the

ISBN 978-3-95450-176-2

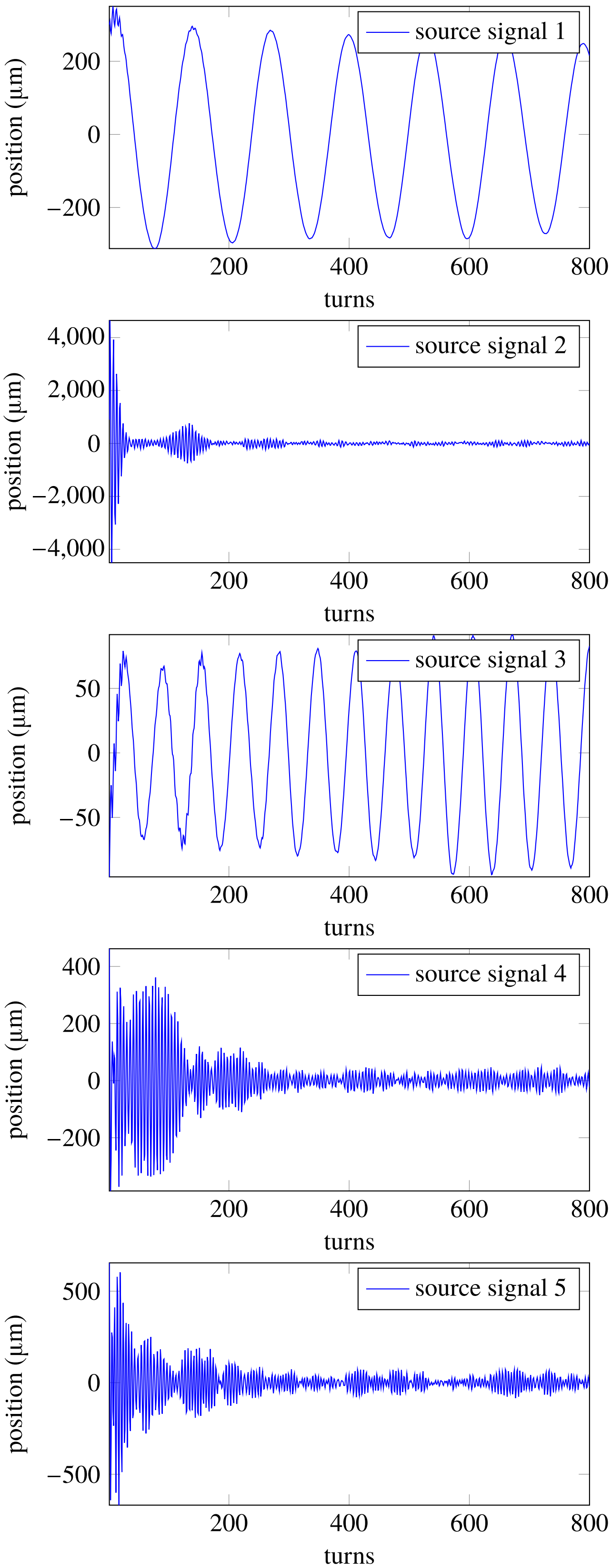

Figure 3: Sources separated from the motion matrix using ICA. The signals 1 and 3 are energy oscillation related and do not decay with time.

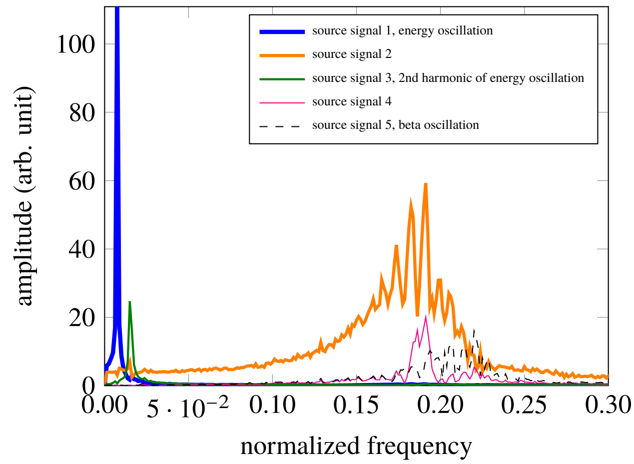

Figure 4: Spectra of the sources in Fig. 3.

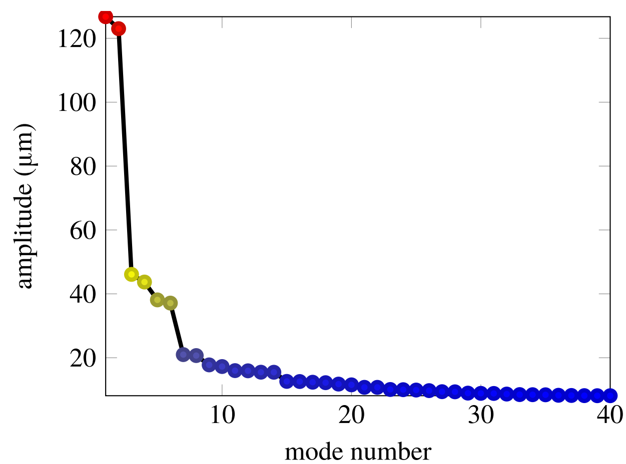

Figure 5: Singular values of different modes.

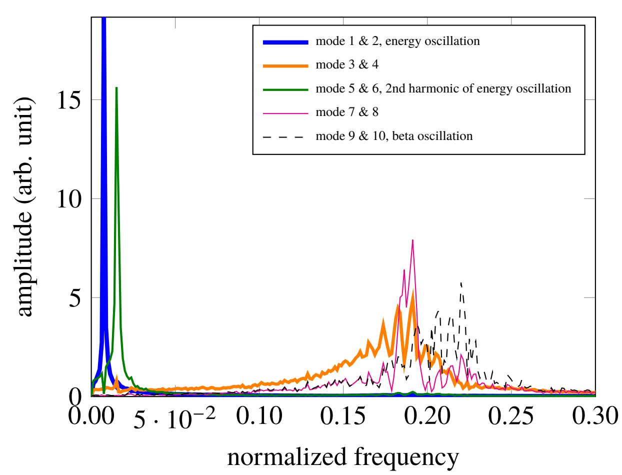

Figure 6: Spectra of the modes separated by SVD.

energy oscillation mode pair is still found to be the dominant modes. Comparing the spectra of both results (as shown in Figs. 4 and 6), the distributions of the components of the separated signals (or the corresponding modes) and their characteristics are roughly the same. It is safe to say that the

ISBN 978-3-95450-176-2

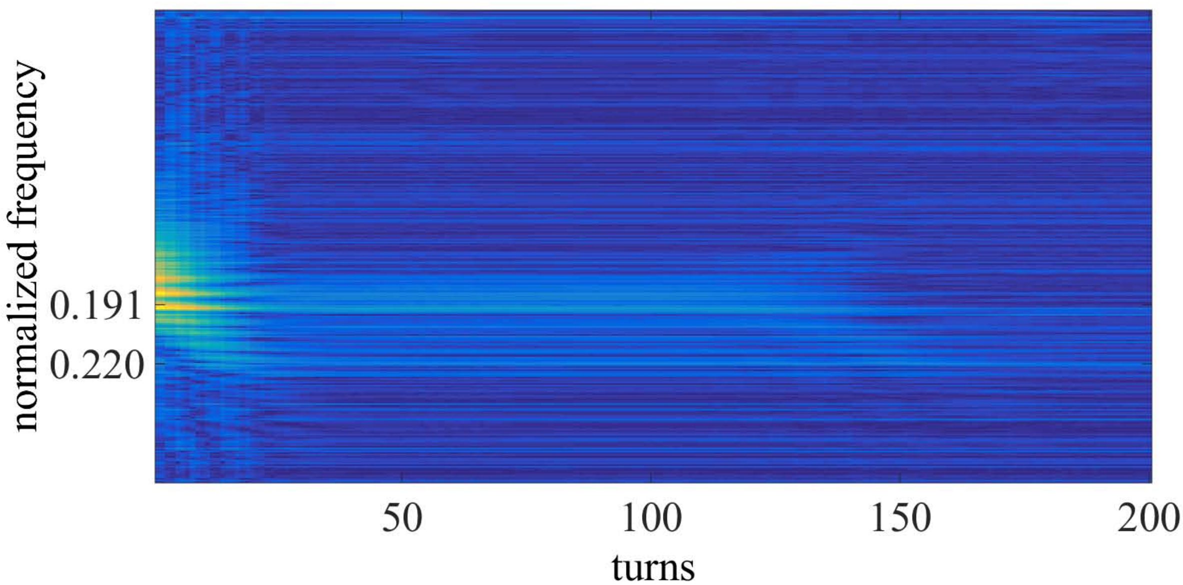

Figure 7: Spectra waterfall of the motion of the injected bunch.

ICA procedure can be replaced by the SVD method in this situation.

The spectrum of the injected bunch (blue line in Fig. 2) is not constant. The waterfall plot of the spectra (as shown in Fig. 7) shows that the distribution of the modes may vary with time. The detailed evolution of the modes can be obtained by using the right-singular vectors of the motion matrix of the injected bunch (as shown in Fig. 8).

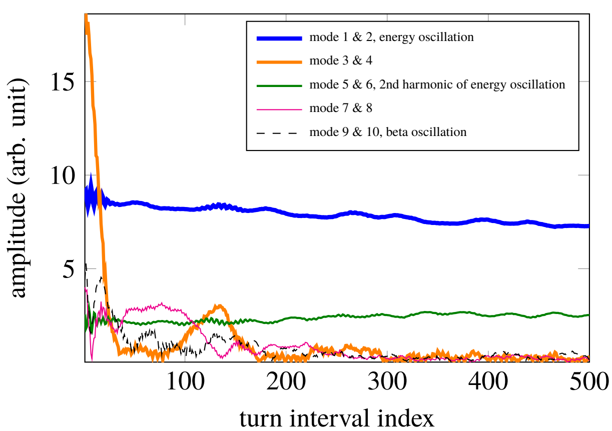

Figure 8: Samples from real measurements and its shifted, scaled reflection signal.

CONCLUSION

The motion of the injected bunch can be extracted from the stored bunch by singular value decomposing. It can be separated into the energy oscillations and the betatron oscillations on-line based on the SVD method. The betatron oscillation due to the mismatch between the transport line and the storage ring decays rapidly within 20 turns.

The second harmonic of the energy oscillation is obvious. The reason might be that the stored bunch and the injected bunch forms a two-body system, so the two parts are interfering with each other.

REFERENCES

[1] Zhichu Chen, Yong Yang, Yongbin Leng and Renxian Yuan, Phys. Rev. ST Accel. Beams **17**, 112803 (2014). `http://link.aps.org/doi/10.1103/PhysRevSTAB.17.112803`

[2] Stone, James V., *Independent component analysis : a tutorial introduction*. Cambridge, Mass. MIT Press (2004). ISBN 0-262-69315-1.

[3] Aapo Hyvarinen, Juha Karhunen and Erkki,Oja, *Independent component analysis* (1st ed.). New York: J. Wiley (2001). ISBN 0-471-22131-7.

ISBN 978-3-95450-176-2

PROGRESS OF CAVITY BEAM POSITION MONITOR AT SXFEL

L.W. Lai , Y.B. Leng, L.Y. Yu, R.X. Yuan, W.M. Zhou, Z.C. Chen, Y.B. Yan
SSRF, SINAP, Shanghai, China

Abstract

Shanghai Soft X-ray FEL Test Facility (SXFEL) has started the infrastructure construction in 2015. All beam diagnostic systems are under processing and measurement, including C-band Low-Q cavity BPMs. This paper presents the progress of the cavity BPM system, including design and the measurements on a lab platform. Measurements shown that the cavity BPM frequency is 4.7GHz ± 8MHz, and the complete test platform verify that the cavity BPM system, which including signal processing electronics can work as expected.

INTRODUCTION

The SXFEL project at the Shanghai Synchrotron Radiation Facility (SSRF) campus serves as a test facility of China's future hard X-ray FEL user facility, while it can be easily upgraded to a FEL user facility at "water-window" spectral region for scientific investigations with high brilliance X-ray pulses of ultra-fast and ultra-high resolution processes in material science and physical biosciences.

The construction of the SXFEL has started since April 2015, and the first X-ray FEL light is planned to be delivered to the beam line in 2017.

The SXFEL consists of following parts:

1. A photo-injector generating a bright electron beam and accelerating it to ~ 130 MeV.
2. The main linear accelerator, where the electron beam is longitudinally compressed and accelerated to ~ 840 MeV.
3. The FEL undulator complex where X-ray radiation is generated.
4. The photon beam transport & diagnostic line.

To achieve the physical design of SXFEL, the diagnostic system need to achieve requirements listed in Table 1, and the dynamic is 0.1nC~0.5nC.

CAVITY BPM SYSTEM

The cavity BPMs have been chosen for the real time measurements of the electron beams positions along the undulator of the SXFEL. The layout is shown in Fig. 1.

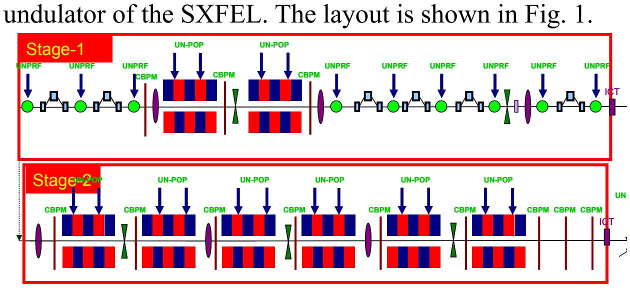

Figure 1: Layout of cavity BPM along undulator.

Table 1: Beam Diagnostics System Specification

Parameter	Main technical specifications
Position	Stripline BPM, Resolution: 10μm@0.5nC
	Cavity BPM, Resolution: 1μm@0.5nC
Size	YAG/OTR, Resolution:30μm@1nC, Repeatablity:50μm
Charge	ICT, Resolution:1%
Length	CSR, Resolution:100fs
Arrive time	Phase cavity, Resolution:200 fs

Cavity BPM Pickups

The cavity BPM system consists of the cavity BPM probes, the RF front-end and data acquisition (DAQ) electronics is shown in Table 2. The working frequency of the position mode and the reference cavity of the CBPM are designed to be 4.7GHz preliminary to avoid the interference of the dark current caused by the frequency multiplication of the RF. The signals will be lead out through the 50Ω load and the system quality factor will be mainly determined by the external quality factor.

Table 2: The Cavity BPM Design Parameter

Parameter	TM110	TM010
Frequency	4.7GHz	4.7GHz
Q	~60	~60
Ports number	4	2
Signal amplitude@50Ω	12mV/μm/nC (peak)	100V/nC (peak)

CBPM responses with a series of simulated electron beams passing the CBPM at different positions have been modeled with MAFIA. The output signal and the corresponding spectrum at the electrode of the CBPM are shown here in Fig. 2.

ISBN 978-3-95450-176-2

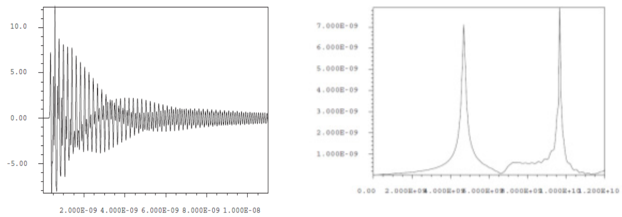

Figure 2: Simulation of output signal and spectrum at the electrode of the CBPM.

The suppression of the fundamental mode in the design of the CBPM is about 106dB and the sensitivity of the electrode at peak voltage is about 12mV/μm/nC. The estimated resolution is about 0.07μm@1nC by comparing the data with those from Spring-8. The radius of the reference cavity is 20.25mm. The inner and the outer radius of the ring structure are 15mm and 20.25mm, respectively. The length of the pipe is 10mm. The working frequency is optimized to be 4.7GHz.

The cavity BPM is shown in Fig. 3.

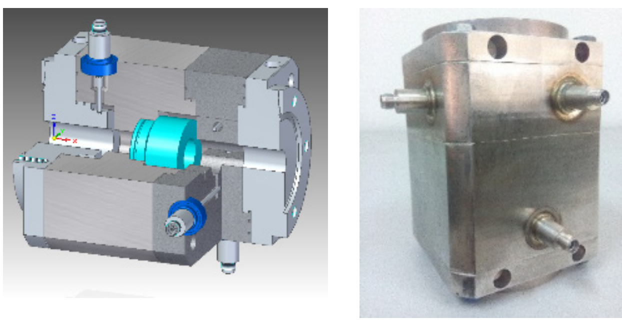

Figure 3: The cavity BPM.

Signal Processing

The cavity BPM signal processing consists of RF front-end electronics and DAQ electronics. The RF front-end converts the RF signals down to IF signals before DAQ. The diagram of RF front-end shows in Fig. 4[1].

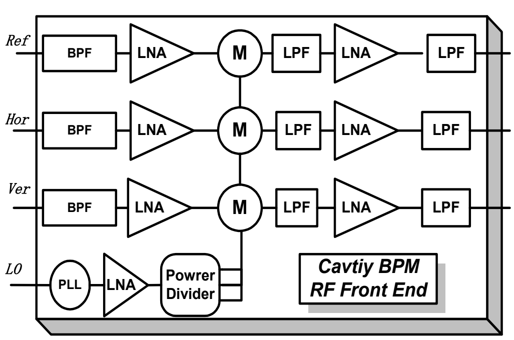

Figure 4: RF front-end diagram.

DAQ electronics will sample signals output from the RF front-end. Then the FPGA on the DAQ electronics will process the sampled digital signal to get position data.

CAVITY BPM TESTS

Network Analyser Measurement

The BPM has been measured with Agilent N5230A PNA-L network analyser. Figure 5 is the screen shot of the analyser measurement, it shows that the pickup central frequency is 4.7GHz±8MHz.

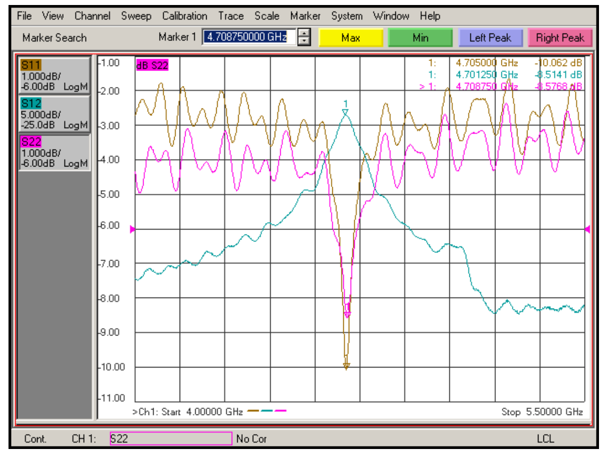

Figure 5: Screen shot of analyser measurement.

Lab Test

A lab test platform has been constructed to simulate beam environment, Fig. 6 is the platform diagram and Fig. 7 is the scene photo.

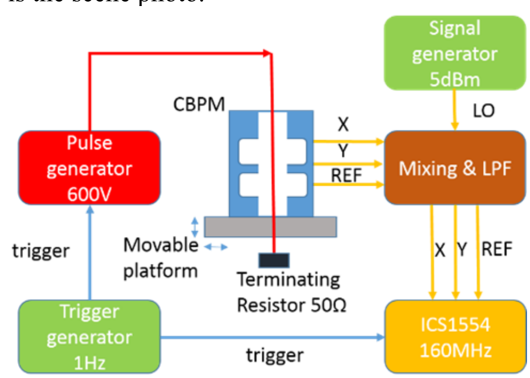

Figure 6: Lab test platform diagram.

Figure 7: Lab test photo.

The BPM was located on a movable platform, and a 600V pulse signal was fed into the cavity through a cable across the BPM to simulate beam passing. A trigger generator drives the pulse generator with 1Hz signal, which signal was also used to trigger DAQ electronics—ICS1554[2]. The reference and position signals were down converted to about 20MHz IF signal with a 4.72GHz local oscillator and RF front-end. The commercial DAQ board ICS1554, which consists of four 16bits 160MHz ADCs and FPGA, was used to sample the IF signal.

The raw RF signal was sampled with a 6GHz oscilloscope at 25G samples/s. Figure 8 and 9 are the sampled RF position signal and reference signal respectively, the signal decay time is about 20ns.

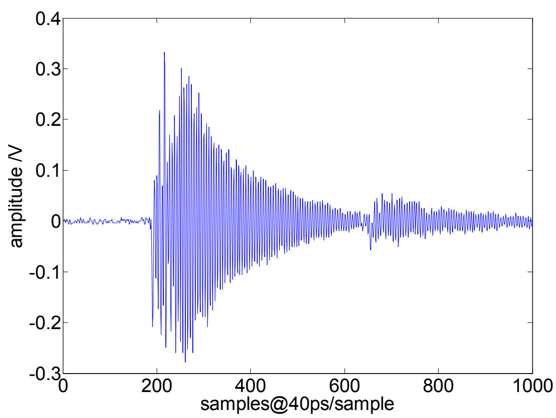

Figure 8: Raw RF position signal.

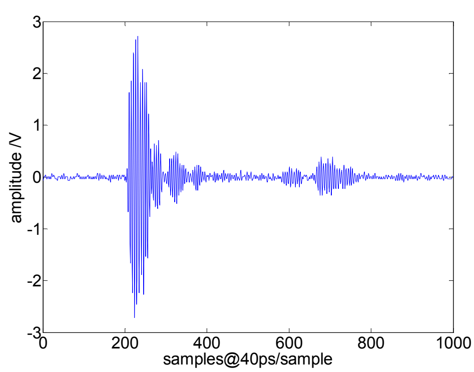

Figure 9: Raw RF reference signal.

The IF signal is sampled with ICS1554 at 160M samples/s. Figure 10 shows sampled ADC data of both position cavity and reference cavity.

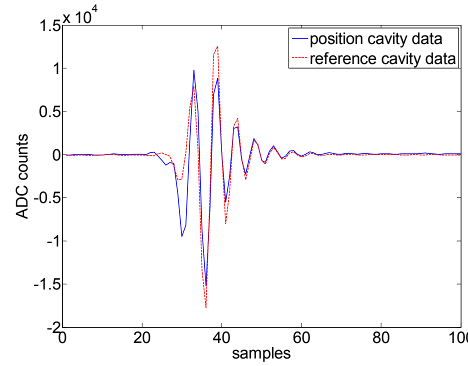

Figure 10: IF data sampled with ICS1554.

To get the amplitude of position cavity and reference cavity from the sampled IF signal, several algorithms have been studied, including square root of the IF signal's absolute integration and curve fitting to the IF signal. The algorithm will be implemented later in FPGA. And beam tests will be carried out later on SDUV FEL.

SUMMARY AND OUTLOOK

The measurement of the SXFEL cavity BPM showed that the frequency deviation value is about 8MHz from the designed 4.7GHz, and deviation within ±5MHz can be achieved with fine-tuning in future volume production. A complete lab test platform used to simulate beam environment has been constructed, which verified that the BPM pickup, the RF front-end electronics and DAQ electronics can work as expected. Recently, beam test will be carry out on SDUV FEL, results will be given in future paper.

REFERENCES

[1] B.P. Wang, Y.B. Leng, et al., "Development of cavity beam position monitor system", IPAC'13, Shanghai, China, 2013.

[2] Hardware Reference Manual: ICS1554 Operating Manual, GE Fanuc Intelligent Platforms Ltd, 2008:3~4(2008); http://defense.ge-ip.com/products/2234.

ISBN 978-3-95450-176-2

INTERFEROMETER DATA ANALYZING USING THE PCA METHOD AT SSRF *

Y.B. Leng#, H. J. Chen, J. Chen, Z. C. Chen, Y.B. Yan, SSRF, SINAP, Shanghai, China.

Abstract

An SR interferometer, which was used to monitor the transverse beam size in the SSRF ring, had been implemented and put into operation since 2009. The direct projection and curve fitting was adopted for raw image data processing. Any CCD alignment error could introduce some beam size measurement error in this case. Using primary component analyzing (PCA) method to process raw image data, the horizontal and vertical distribution information can be decoupled and the misalignment information of CCD can be derived. Beam experiment results will be discussed in this paper.

INTRODUCTION

Shanghai Synchrotron Radiation Facility (SSRF) is the 3.5GeV third generation light source with the emittance of 3.9nm.rad. The typical transverse beam sizes are 53μm in horizontal plane and 22μm in vertical plane with 1% vertical coupling. To monitor such small transverse beam dimension and motion, a set of interferometer was implemented since 2009 [1].

The source point of SRM is inside the second bending magnet of the cell#2. The synchrotron light is extracted by a water-cooled beryllium mirror. Then three mirrors guide the light to the dark room.

Two Harsherian-type reflective SR interferometers are installed to measure the both of vertical and horizontal beam sizes. The double slit is set at 18 meter apart from source point. A focusing mirror, f=2000mm, is used as an objective mirror. A small off axis diagonal mirror is set for the convenience of the observation. A band-pass filter, which has 50nm or 80nm bandwidth at 550nm, is used to limit the wavelength of input light. The σ-polarization of SR is selected by dichroic polarization filter.

The 800Mb/s interface enables full frame rate and even more cameras on the same bus. The IEEE-1394b cable with jack screws allows a more secure connection to the camera. 12-bit A/D converter, Via external trigger, software trigger (on same bus), This equipment has been tested and found to comply with the limits for a Class A digital device, have good linearity It provide reasonable protection against harmful interference when the equipment is operated in experimental environment. After all environments and system calibration, Interferometer is good enough for the measurement of a few μm small beam size. [2]

Figure 1 shows a set of typical interference image data and corresponding data processing method. In order to minimize measurement uncertainty, CCD exposure time was set to a large number (for example 200ms) to get strong visible light signal. Meantime the edge part of raw image with poor SNR was cut and only central part was reserved to get interference flange profile using direct projection method.

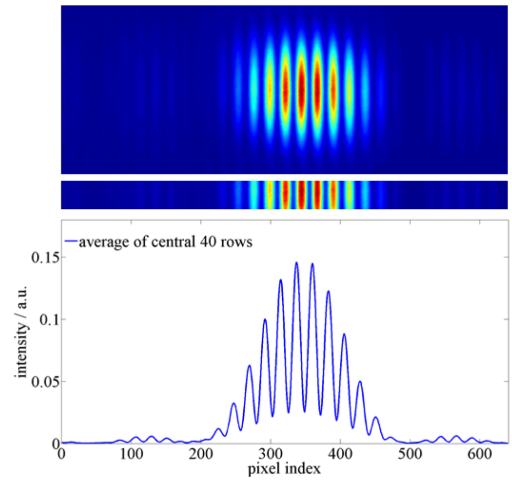

Figure 1: Typical interference image (top), central slice of 40 rows (middle) and projected interference flange (bottom).

The SNR of the final profile can be guaranteed with above CCD configuration and data processing method. But two disadvantages were introduced into the system at the same time. The first, not all information of the raw image was used. The second, any misalignment between the double slit and CCD will contribute measurement error and this contribution is hard to find and fix with direct projection method.

So we propose to use PCA method to process raw image data, reduce random noise, detect misalignment angle and decouple the horizontal and vertical profile.

IMAGE PROCESSING USING PCA

PCA method is originally used in image processing filed to reduce data dimensions and now widely used in accelerator field to do BPM turn-by-turn data analyse. [3]

The interference image matrix can be decomposed into three terms by using SVD:

$$IMG=USV \tag{1}$$

where U and V are unitary square matrices and S is a diagonal matrix. U is the matrix of the eigenvectors of the covariance matrix IMG and each column of U corresponds to the horizontal distribution pattern of a specified mode; V is the matrix of the eigenvectors of the covariance matrix IMG and each column of V corresponds to the vertical distribution of a specified mode; Each element of S is nonnegative and real, and it corresponds to the intensity of a specified mode.

*Work supported by National Nature Science Foundation of China (11375255)
#lengyongbin@sinap.ac.cn

ISBN 978-3-95450-176-2

For 1D interferometer application, the horizontal and vertical distribution is totally independent with ideal configuration. In this case interference image can be fully decoupled using SVD method and interference flange can be retrieved from horizontal matrix U directly. Since the whole IMG matrix was used to do SVD analyse there is no information abandoned and the maxima SNR can be get with this method.

Figure 2 shows a typical SVD result of interference image acquired with almost perfect system configuration. Only the mode #1, which horizontal vector is interference flange, vertical vector is guassian distribution and singular value is much larger than other modes, is true physical mode. The all rest modes stand for random noise which can be removed.

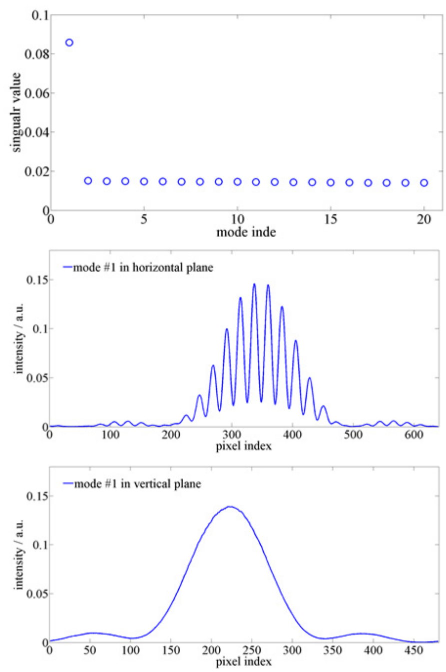

Figure 2: Raw image data processing result using PCA method: singular value (top), horizontal distribution of mode #1 (middle) and vertical distribution of mode #1.

If there is any misalignment between double slit and CCD the independency between horizontal and vertical distribution pattern will be crashed. Then SVD will give us more than one mode and the singular value of mode #2 will be large than noise floor. Let's define a new factor

$$\sigma 12 = S11/S22 \quad (2)$$

as normalized singular value of mode #2. This factor σ_{12} will be very sensitive to misalignment angle and can be used to detect and fix this misalignment.

BEAM EXPEIRMENT

To verify the feasibility of PCA method two set of beam experiments were carried out in the SSRF ring. Low beam current (10mA) experiment was set to investigate random noise reduction effect. High beam current (240 mA) experiment was set to check the feasibility of misalignment angle detection and comprehension.

Random Noise Reduction

Usually we can get high quality data from interferometer during daily operation since visible light signal is strong enough due to high beam current (large than 200 mA), low CCD gain (minimal) and large exposure time (typical 0.2s). But if we want to increase data updating rate or measure beam size with very low beam current we have to decrease exposure time and increase CCD internal gain. In this case the SNR of raw image will be poor and pre-processing will be required.

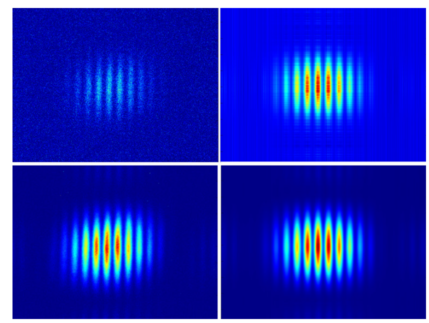

Figure 3: Interference image before and after noise reduction using PCA method: shutter speed 50ms before noise reduction (left-top); 50ms after noise reduction (right-top); 1s before noise reduction (left-bottom); and 1s after noise reduction (right-bottom).

To investigate the feasibility of random noise reduction of PCA method series of image data were taken with different shutter speed configuration under 10mA low beam current condition. Fig 3 shows the image pre-processing result, which indicates that PCA is very effective for poor SNR data (shutter speed 50ms) but not so effective for good SNR data (shutter speed 1s).

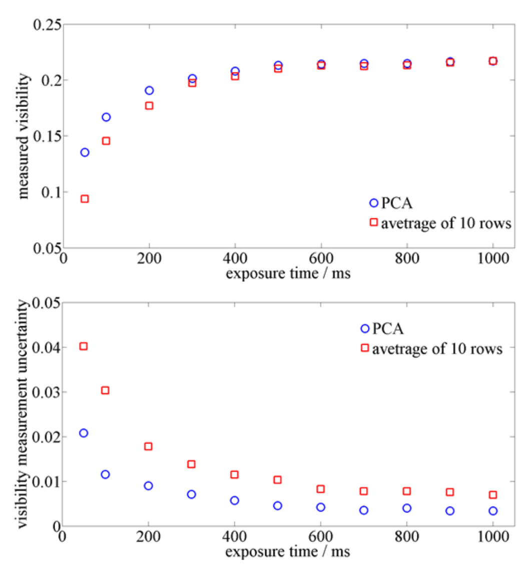

Figure 4: Investigation of shutter speed effect: measurement error (top) and measurement uncertainty (bottom).

ISBN 978-3-95450-176-2

Figure 4 shows the measurement error comparison of PCA method and old projection method. It is obvious that PCA method has better performance.

Misalignment Angle Detection

Another series of beam experiment was carried out to demonstrate the misalignment angle detection using PCA. By rotating CCD angle from 166 degree to 194 degree with step of 2 degree we can simulate misalignment between double slit and CCD from -14 degree to +14 degree.

Figure 5 shows the singular value variation depends on misalignment angle. It is easy to find that more independent modes show up with angle increasing from 0 degree to 14 degree just like expecting.

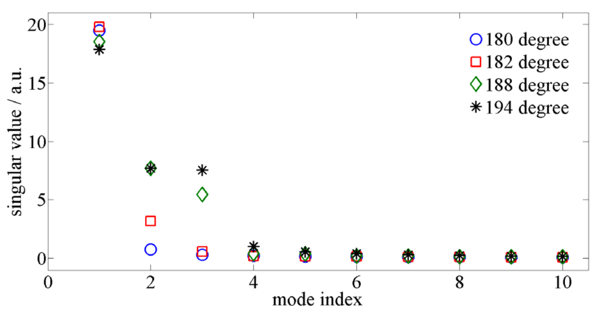

Figure 5: Singular value VS misalignment angle.

Figure 6 shows the dependency between rotation angle and normalized singular value of mode #2. The sharp peak at the zero degree (180 degree) indicates that we do find a very sensitive flag for misalignment angle detection.

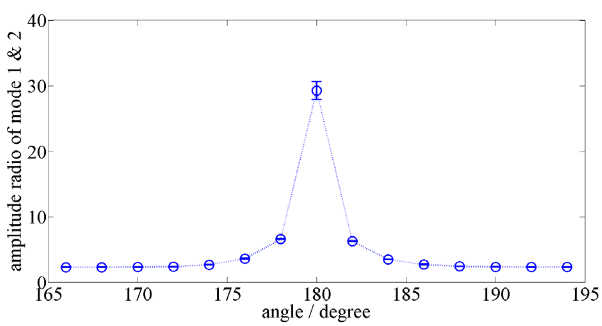

Figure 6: Normalized singular value of mode #2 VS misalignment angle.

For acquired image the following pre-processing can be used to check if there is misalignment angle or not: a) rotate digitized image in two direction (clockwise and anti-clockwise); b) do SVD for every rotated image and get the normalized singular value of mode #2; c) plot the normalized singular value of mode #2 VS rotating angle, the peak index indicates the misalignment angle; d) the corresponding rotated image is corrected data.

Figure 7 shows an example of misalignment angle detection. In this example a small angle of 3.75 degree was detected.

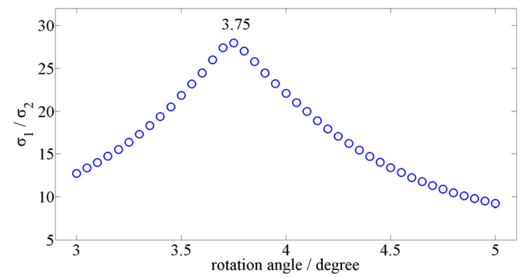

Figure 7: Misalignment angle detection using normalized singular value of mode2 as flag.

In order to find the relationship between mode #1 and mode #2, the horizontal and vertical vector of mode #2 and the differential curve of mode #1 were plotted together in Fig. 8. It is obvious that they match each other very good.

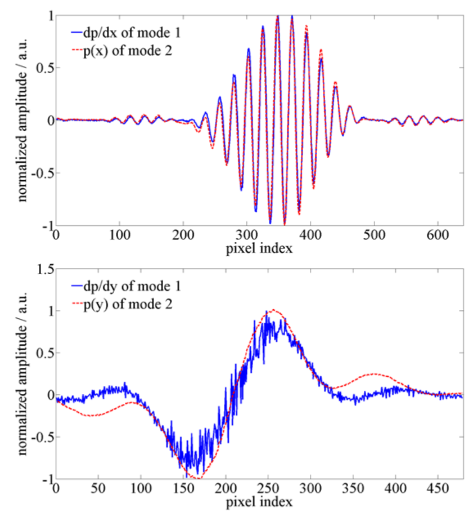

Figure 8: Horizontal vectors (top) and vertical vectors (bottom) using PCA in small misalignment angle case.

CONCLUSION

The PCA was applied in interferometer image data analysing. Compared with direct projection method PCA is better to retrieve more information and improve image data quality especially in poor SNR condition. The PCA has also been proved to be a very sensitive tool to detect the misalignment angle between double slit and CCD.

REFERENCES

[1] Y.B.Leng, K.R.Ye, W.M.Zhou, etc., "SSRF Beam Diagnostics System Commissioning", Proceedings of DIPAC2009, Basel, Switzerland, 2009.

[2] J.Chen, Z.C.Chen, Y.B.Leng, etc., "The Synchrotron Radiation Diagnostics Line at SSRF", Proceedings of IBIC 2012, Tsukuba, Japan, 2012.

[3] Z.C.Chen, Y.B.Leng, Y.B.Yan, etc., "Correlation analysis of Beam Diagnostic Measurements in SSRF", Proceedings of IPAC 2012, New Orleans, USA, 2012.

ISBN 978-3-95450-176-2

DEVELOPMENT OF CAPACITIVE LINEAR-CUT BEAM POSITION MONITOR FOR HEAVY-ION SYNCHROTRON OF KHIMA PROJECT

Ji-Gwang Hwang *, Tae-Keun Yang, Seon Yeong Noh
Korea Institute of Radiological and Medical Sciences, Seoul, Korea
Peter Forck, GSI, Darmstadt, Germany
Changbum Kim, Pohang Accelerator Laboratory, Pohang, Kyungbuk, Korea

Abstract

Since the beam intensity after the injection and capturing process in the KHIMA synchrotron is $\sim 7.4 \times 10^8$ particles for the carbon beams and $\sim 2.07 \times 10^{10}$ for the proton beams, the linear-cut beam position monitor is adopted to satisfy the position resolution of 100 μm and accuracy of 200 μm with the linearity within the wide range. In this paper, we show the electromagnetic design of the electrode and surroundings to satisfy the resolution of 100 μm, the criteria for mechanical aspect to satisfy the position accuracy of 200 μm, the measurement results of position accuracy and calibration by using a wire test-bench, and the beam-test results with long (~ 1.6 μs) electron beam in Pohang accelerator laboratory (PAL).

INTRODUCTION

Main purpose of the Korea Heavy Ion Medical Accelerator(KHIMA) project is to construct a proton and carbon therapy accelerator based on a synchrotron and it is currently under construction in Korea [1]. A low intensity proton and carbon beam with an energy in the range of 110 to 430 MeV/u for a carbon beam and 60 to 230 MeV for a proton, which corresponds to a water equilibrium beam range of 3.0 to 27.0 g/cm^2, is produced by the accelerator for a cancer therapy [2]. The accelerator consists of the low energy beam transport (LEBT) line, radio-frequency quadrupole (RFQ) linear accelerator (linac), interdigital H-mode drift-tube-linac (IH-DTL), medium beam transport (MEBT) line, synchrotron, and high energy beam transport (HEBT) line [3]. In the KHIMA synchrotron, a high precision beam position monitor, which has a position resolution and accuracy of 100 μm and 200 μm, respectively, is required to match and control the beam trajectory for the beam injection and closed orbit [4]. It is also used for measuring Twiss parameters, betatron tunes, and chromaticity in the synchrotron. Since the bunch length in the heavy ion synchrotron is relatively long, a few meters, and the intensity of the beam is low, a box-like device with long plates of typically 20 cm is used to enhance the signal strength and to obtain a precise linear dependence with respect to the beam displacement [5]. The number of the horizontal and vertical beam position monitors in the synchrotron are 10 and 7, respectively. The position of the monitor is determined based on the amplitude of the betatron oscillation. It is shown in Fig. 1.

* hwang@kirams.re.kr

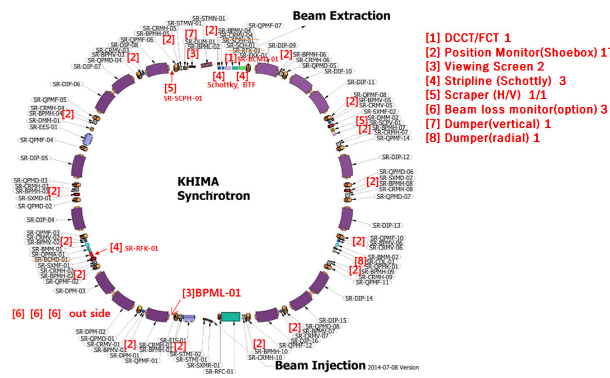

Figure 1: Layout and position of beam diagnostics in KHIMA synchrotron.

LINEAR-CUT BEAM POSITION MONITOR

The linear-cut beam position monitor consists of two electrodes with the width of 136 mm and the thickness of 2 mm, 5 mm thick body, insulator, holder and vacuum chamber. The distance between the body and electrode is maintained to be 8 mm to increase the induced signal by reducing the capacitance. The designed beam position monitor is shown in Fig. 2.

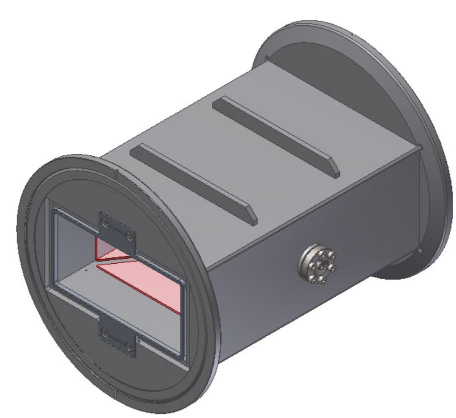

Figure 2: Linear-cut beam position monitor in KHIMA synchrotron.

The transverse and longitudinal dimensions of the beam position monitor is restricted because the beam position monitor would be installed inside the steering magnet yoke. The length of horizontal and vertical monitor are 290 mm and 244 mm, respectively. The transverse dimension of

ISBN 978-3-95450-176-2

the electrode was kept as large as possible within a limited chamber size to increase the signal strength. Since the cross-talk between two electrodes determines mainly the position resolution of the beam position monitor, the cross-talk as function of the distance between two electrodes is investigated to optimize the distance between two electrode. The result is shown in Fig. 3.

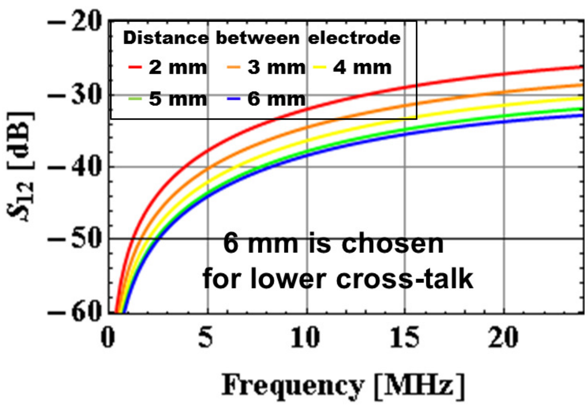

Figure 3: Cross-talk(S_{12}) as a function of the distance between two electrodes.

When the distance between the electrodes is larger than 5 mm, the cross-talk is almost saturated to be -40 dB in the operating frequency range of 0.48 to 3 MHz. The distance between the electrodes is determined to be 6 mm to achieve the cross-talk of less than -40 dB. For the cross-talk of -40 dB, the position reading error due to the cross-talk is about 2 %. The linearity of the beam position monitor is also calculated by using CST-PS that is shown in Fig. 4 [6].

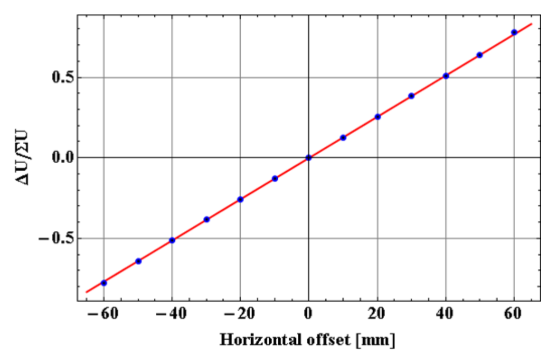

Figure 4: Linearity of the beam position monitor.

The beam position is determined by the ratio of difference and sum of the signals generated by the two electrodes that is given in Eq. 1.

$$x = a_0 \frac{\Delta U}{\Sigma U} + a_1 = a_0 \frac{U_{left} - U_{right}}{U_{left} + U_{right}} + a_1, \qquad (1)$$

where a_0 is coefficient which is proportional to the transverse dimension of the electrode, a_1 is coefficient which is related with the mechanical central position, the U_{left} and U_{right} are voltage output from the left and right electrodes, respectively. The ideal values of a_0 and a_1 for the designed beam position monitor are 72 mm and 0 mm, respectively. Due to the internal structure, such as the insulator and surroundings, the beam position monitor, however, has the a_0 and a_1 coefficients of 78.10 mm and -72.7 μm. It is enough to satisfy the desired position accuracy of 200 μm.

CROSS-TALK MEASUREMENT AND CALIBRATION

The beam position monitor consists of two electrodes, body, insulator, holder, two feed-through and vacuum chamber. The triangular shape electrodes are made by the oxygen free copper (OFC), and the body, holder, and vacuum chamber is made by stainless steel, SUS304. The 99.6 % alumina-ceramic is chosen as the insulator material which is used to attach two electrodes inside the body with well defined distance of 8 mm. The picture of the fabricated horizontal beam position monitor is shown in Fig. 5.

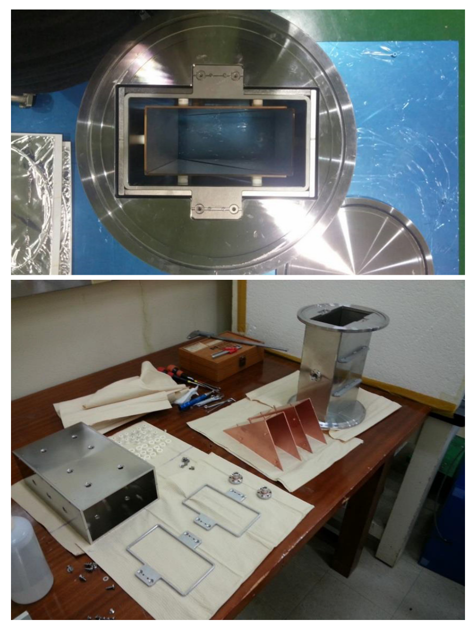

Figure 5: Picture of fabricated beam position monitor.

Based on the results of the electromagnetic and mechanical design, the beam position monitor is fabricated by the Korean company, I.T.S, and the leakage test is performed by using the helium leak detector to check the the defect during the welding process [7]. The requirement of the vacuum pressure for the beam position monitor is 10^{-9} Torr to reduce the beam loss and electron capture in the synchrotron. In order to confirm the performance of the fabricated beam position monitor, the cross-talk between two electrodes is measured by using Vector Network Analyzer. The result is shown in Fig. 6.

The measured cross-talk between two electrodes is lower than the -40 dB in the range of operation frequency, 0.48 $\sim$ 3 MHz, which is required to achieve the desired position resolution. The measurement result agrees well with the calculation result using code CST. By using the wire test

ISBN 978-3-95450-176-2

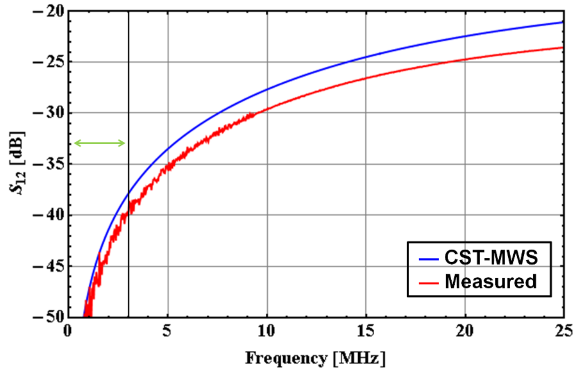

Figure 6: Measurement result of the cross-talk.

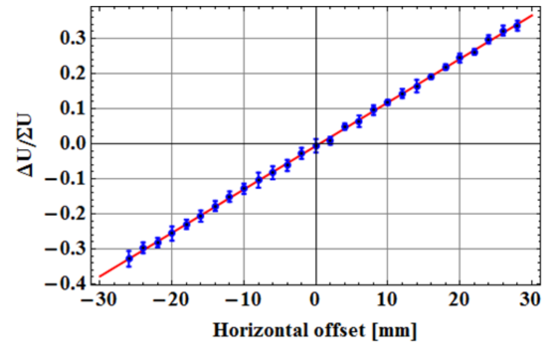

Figure 8: Calibration and linearity measurement of beam position monitor using wire test bench.

bench, which consists of the linear motor stage and well aligned and stretched wire with two feed-through on the each side, the signal response as a function of the offset was measured to confirm the linearity of the beam position monitor. The wire test bench is frequently used to confirm the frequency response and linearity of the pick-up devices from the external source. The test set-up is shown in Fig. 7.

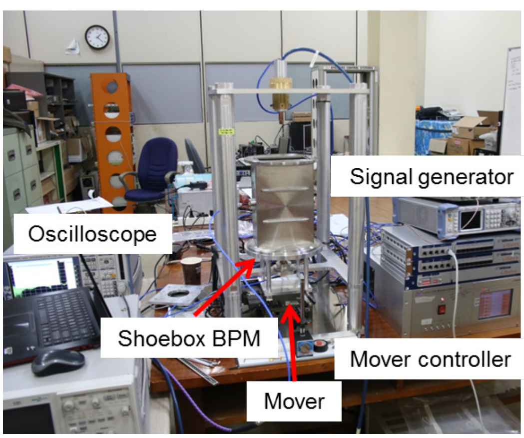

Figure 7: Picture of the test by using wire test bench.

The higher frequency noise signal is filtered by digital low-pass filter during the data processing. It suppresses all frequencies higher than the cut-off frequency and leaves smaller frequencies unchanged. The $\Delta U/\Sigma U$ as a function offset in the range of -28 mm to 28 mm is calculated to obtain the calibration coefficients, a_0 and a_1 that is shown in Fig. 8. The linearity of the beam position monitor in the range of -28 mm to 28 mm was confirmed. The calibration coefficients of a_0 and a_1 are measured to be 80.64 mm and 475 μm, respectively.

PRE-AMPLIFIER DESIGN

The pre-amplifier for amplifying the signal strength from the beam position monitor is designed. It has 1 MΩ input impedance. Two input ports are required for the pre-amplifier of the beam position monitor to calibrate the electronics on the operation. It has two individual channels because the beam position monitor has two signal ports. The bandwidth is determined to be DC ~ 50 MHz to measure the spatial structure of the beam. It was fabricated by EMWISE in Korea [8].

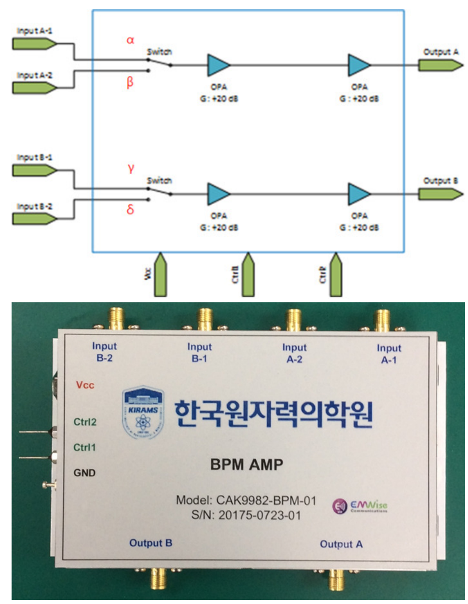

Figure 9: Schematic drawing and picture of pre-amplifier for beam position monitor.

As shown in Fig. 9, the amplifier consists of 2-port RF relay switch and two op-amplifier. The total gain is fixed to be 40 dB. The noise figure of the circuit is 9.9 dB for 10 MHz and 9.8 for 50 MHz. The gain curve as a function of the frequency is measured that is shown in Fig. 10.

MEASUREMENT WITH ELECTRON BEAM

The beam test with the long electron bunch train, ~ 1.6 μs, which corresponds to the frequency of 630 kHz, is performed to confirm the performance of the beam position monitor with pulsed beam at the test linac in the Pohang Accelerator Laboratory (PAL). Since the beam position monitor has large capacitance, ~ 120 pF, and the input impedance of the pre-amplifier is also high, 1 MΩ, the cut-off frequency is low

ISBN 978-3-95450-176-2

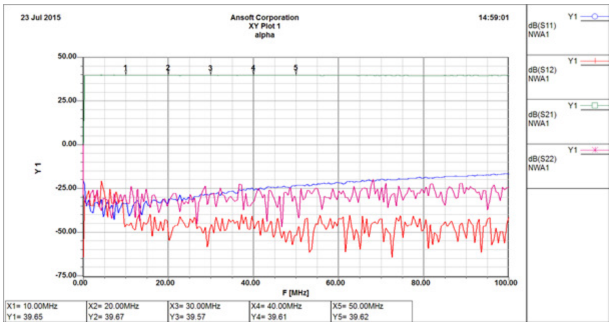

Figure 10: S-parameter of high impedance pre-amplifier for beam position monitor.

enough to collapse the effects of the micro-pulse [9]. The picture of the beam test set-up is shown in Fig. 11.

Figure 11: Picture of beam test set-up with moving stage after beam window of test linac.

The length of the macro-pulse agrees well with the operation frequency although the length of the micro-pulse is very short, less than nano-second, due to the RF frequency of the S-band linac, 2.856 GHz. The energy and current of the electron beam are 60 MeV and less than 1 mA, respectively. The beam position monitor is installed on the moving stage and the high impedance amplifier is installed near the beam position monitor. The gain of the pre-amplifier is set to be 40 dB. The signal as a function of the horizontal offset of the moving stage is measured to calculate the calibration factor and to confirm the linear response of the beam position monitor. The measured signal is shown in Fig. 12

The higher frequency noise signal from the surroundings is observed and it is filtered by digital low-pass filter during the data processing. By using the filtered signal, the $\Delta U/\Sigma U$ as a function offset of the moving stage is calculated to obtain the calibration coefficients, a_0 and a_1 that is shown in Fig. 13.

The non-linear behavior is observed when the offset of the moving stage is large. It may cause due to the large beam size and halo particles at the exit of the beam window because the signal strength is decreased when the electron hit the electrode directly. The calibration coefficients of a_0

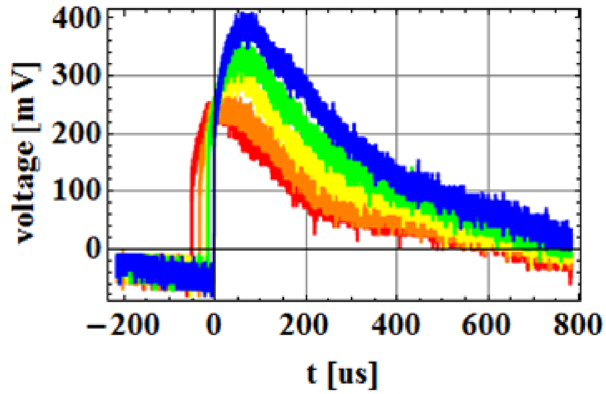

Figure 12: Measured signal as a function of horizontal offset of moving stage.

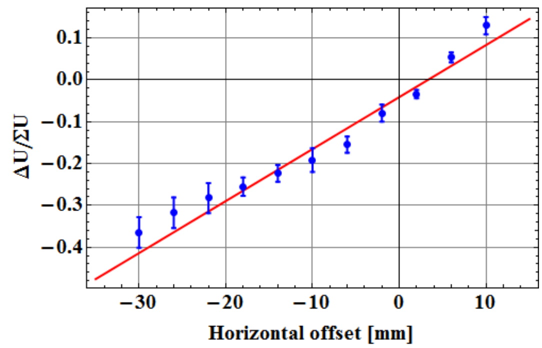

Figure 13: Calibration and linearity measurement of beam position monitor using electron beam.

and a_1 are measured with electron beam to be 80.83 mm and -0.255 mm, respectively.

CONCLUSION

The linear-cut beam position monitor, which will be installed in the synchrotron ring of KHIMA, is under developing. The design study of the beam position monitor to achieve the desired position resolution of 100 μm and the accuracy of 200 μm was performed. And it was fabricated based on the design values and the laboratory tests, such as the vacuum leakage test by helium leak detector, the cross-talk measurement and linearity measurement using the wire test bench, were performed to confirm the performance. The measured cross-talk and calibration coefficient agree well with the designed parameter by the numerical simulation using code CST-MWS and CST-PS. The pre-amplifier with the 1MΩ input impedance is designed and fabricated. The beam test with the long electron bunch train at the test linac in PAL is performed and the measured calibration coefficients is also well agree with the result of wire test bench.

ACKNOWLEDGMENT

This work was supported by the National Research Foundation of Korea(NRF) grant funded by the Korea government(MSIP) (no. NRF-2014M2C3A1029534). And the

ISBN 978-3-95450-176-2

beam test was conducted at the test linac operated by Pohang university of science and technology funded by the Ministry of Science, ICT & Future Planning.

REFERENCES

[1] http://www.kirams.re.kr/eng/khima.

[2] Chawon Park *et al.*, in *The 18th International Conference on Accelerators and Beam Utilization (ICABU2014)* , Daejeon, Korea (2014).

[3] "KHIMA Handbook of Beam Optics for Accelerator System", private communication.

[4] Heejoong Yim, *The 18th International Conference on Accelerators and Beam Utilization (ICABU2014)* , Daejeon, Korea (2014).

[5] Peter Forck, *Lecture Notes on Joint University Accelerator School*, Geneva, Switzerland (2011).

[6] CST-MWS and PS website : http://www.cst.com/.

[7] I.T.S website : http://itsvac.com/.

[8] EMWISE website : http://www.em-wise.com/.

[9] P. Strehl, Beam Instrumentation and Diagnostics, XVII, ISBN 978-3-540-26404-0, Springer, Berlin Heidelberg, Germany (2006).

DEVELOPMENT OF A SCINTILLATION SCREEN MONITOR FOR TRANSVERSE ION BEAM PROFILE MEASURMENT AT THE KHIMA PROJECT*

Seon Yeong Noh#, Se Duk Chang, Tae-Keun Yang Ji-Gwang Hwang, and Ga Ram Hahn
Korea Institute of Radiological and Medical Sciences
75 Nowon-gil, Nowon-gu, Seoul, 01812, Korea

Abstract

The scintillation screen monitor measures transverse profile of ion beam in beam transport line. The Korea Heavy Ion Medical Accelerator Project (KHIMA) has developed a scintillation screen monitor in the high energy beam transport (HEBT) line. The images of each beam pulse were recorded by CCD camera and evaluated the beam properties by the LabVIEW®-based in-house program in real time. We designed a scintillation screen monitor using phosphor screen, P43. In order to investigate the limits of scintillating screen during beam profile monitoring at low intensity, we designed a remote control device of iris for the incoming light adjustment to the CCD camera. In this paper, we present details of the image processing system using the LabVIEW® and the beam profile measurement results from the in-beam test.

INTRODUCTION

In the Korea Heavy Ion Medical Accelerator (KHIMA) project at the Korea Institute of Radiological And Medical Sciences (KIRAMS), to measure the beam properties i.e. position, size and intensity, we have studied using scintillating screen monitor and the imaging analysis method. The beam properties can be inferred by measuring the visible light from the scintillation screen when the charged particle passing through. The resulting photon emission represents the two-dimensional beam distribution and can be recorded by a standard optical device, a charge-coupled-device (CCD) camera. The scintillating screen provides many advantages, such as a high resolution of beam profile,a direct intercepting method to observe beam profiles, and a simple structure etc. For the high energy beam transport (HEBT) line of KHIMA, a prototype beam profile monitoring system was manufactured and tested in MC50 cyclotron facility at KIRAMS. Through the preliminary experimental results, we checked and evaluated the beam position, size and intensity by using a developed image analysis program.

FABRICATION OF SCINTILLATION SCREEN MONITOR

Hardware

As shown in Fig. 1, the scintillation screen monitoring system consists of a very thin phosphor screen and CCD camera. The prototype system used a gadolinium sulphate oxide doped with Terbium (Gd_2O_2S:Tb) phosphor screen for convert the proton beam path to visible light [1]. And, a high spatial resolution CCD camera (type: 659 × 494 pixels, H:0.169mm/pixel, V:0.14mm/pixel, model: acA640-90gm, Basler, Germany) was adopted to record the emitted light the scintillation screen.

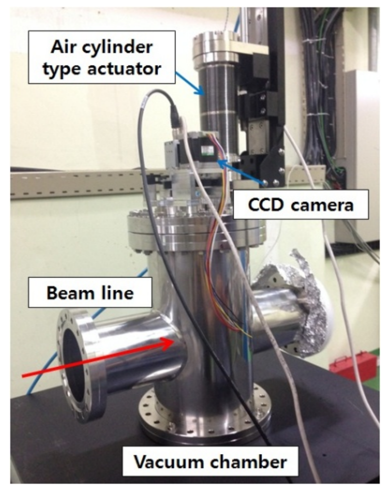

Figure 1: Photograph of the 2D beam imaging system.

The CCD camera was located perpendicularly to the beam axis, and the 100 mm diameter scintillation screen was mounted on the holder 45 degree tilted with respect to the beam axis. The 2 dimensional beam profiles display on the computer screen, and can be stored by the LabVIEW®-based data acquisition program [2,3]. The schematic drawing of the 2D beam imaging system is shown in Fig. 2.

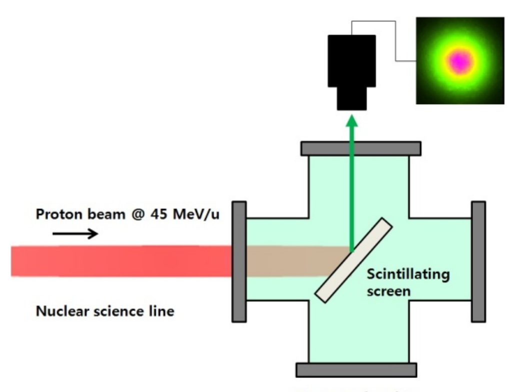

Figure 2: Experimental setup of 2D beam imaging.

*Work supported by KIRAMS
#synoh@kirams.re.kr

2D Beam Image Processing Software

The beam profile and position were determined by a series of image processing. The work flow was shown in Fig. 3. The detailed image processing steps follow as:

1) An image was taken based on an appropriate exposure time and the CCD gain condition.

2) A median filter removes the noise from the CCD.

3) The image distortion by 45 degree tilting scintillation screen was corrected for the horizontal and vertical direction.

The first region of interests (ROI) is selected to remove unnecessary reflected image by the structure of scintillation monitor. The size of the 1st ROI is limited by the size of the scintillation screen. After the noise removal from the 1st ROI, the FWHM of the beam is calculated. And the 2nd ROI which is doubled area of FWHM is selected to remove the noise from the periphery. The 2nd ROI selection process applies dynamically in response to the measured beam profile [4].

After noise removal, the center of mass algorithm calculates the beam center. It calculates the partial sum of intensities for each 1D line projection profile and 2D intensity profile in order to obtain the correct beam size even if the entering beam is non Gaussian distribution. Depending on the purpose of beam, it is required the beam current confirmation for the appropriate irradiation.

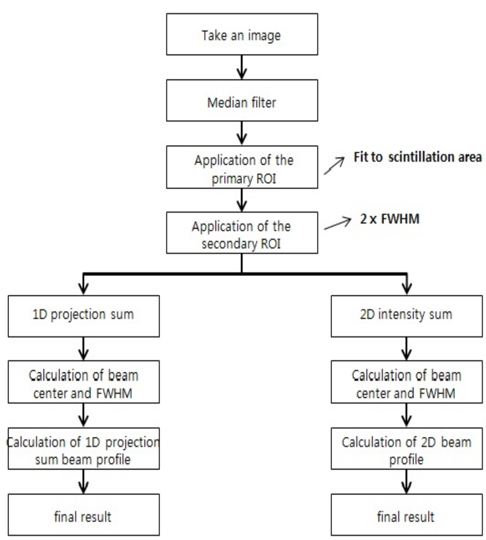

Figure 3: The flow chart of image processing.

The HD-V2 GaF film, which has no electrical noise effect and distortion free, was used to verify the profile image from CCD camera. A piece of GaF film was attached at the entrance of the vacuum chamber and installed in MC50 nuclear science beam line. The 45MeV proton beam was irradiated for 1 minute 30 seconds using100nA beam current. In case of HD-V2 GaF film, the green image components among the RGB show linearity for the incoming proton beam. So, we have selected the green intensity through the image analysis and applied for the beam property calculations as shown in Fig. 3. Figure 4 shows the obtained image from the GaF film.

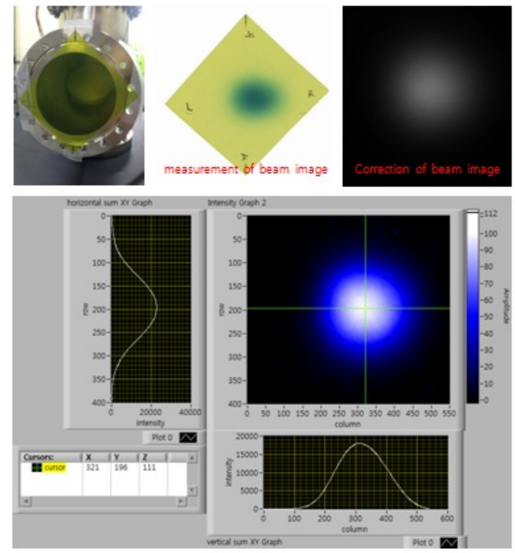

Figure 4: Measured beam profile using by GaF film at vacuum chamber entrance.

RESULT

Comparing GaF Film and P43 Screen

To compare the beam sizes from the GaF film and the scintillation screen results, the beam sizes were normalized for both cases. Also, in order to evaluate the CCD background noise, the original image and the image after removing background noise were compared. Referentially, CCD dark noise can be removed by subtracting beam-off image. Background noise removal method is subtracting the average value by selecting a number of points of the border of 2nd ROI from the original beam intensity.

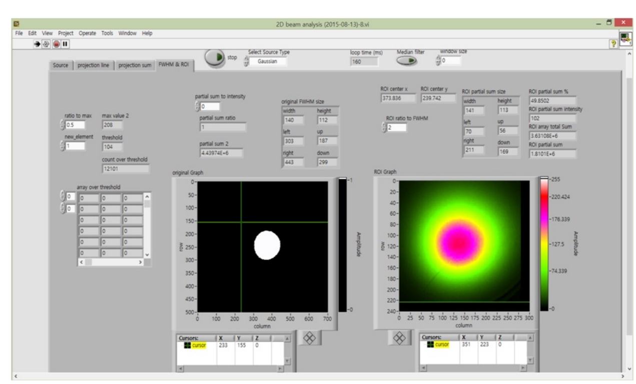

Figure 5: Capture of the beam profile analysis program.

Figure 5 shows a snapshot of the analysis program. First, the horizontal and the vertical beam sizes are calculated from the CCD image, which averaged 10 frames within 2 seconds. For the 1D projection sum profile, the 68 % beam size of total intensity is as follows. The beam size is 20.3 and 25.18 mm for vertical and horizontal directions.

ISBN 978-3-95450-176-2

Corresponding to 98% of the total beam intensity (for Gaussian distribution 2sigma is 95%), the vertical and horizontal beam size were 40.88 mm and 50.02 mm. For the 2D intensity profile, the beam size of 68% of total intensity is 28.98 mm and 36.17 mm for vertical and horizontal

The beam center at the 1st ROI is (8.45 mm, 2.1mm) and the 2nd ROI is (9.13 mm, 1.82 mm). As a result, there was little difference on the beam center calculation between 1st and 2nd ROI.

In case of CCD images, the beam size difference between the background noise subtraction image and the normal image shows less than 1.35mm difference. In case of the beam center position, the difference shows less than 0.5 mm.

During the analysis of the GaF film result, the median filter applied for the beam profile calculation. And, the Table 1 shows the comparison between the CCD and the GaF film analysis results.

Table 1: Comparing GaF Film and P43 Screen

Material		Name		Horizontal (mm)	Vertical (mm)
P43 screen	1st ROI	Beam center position		8.45	2.1
		1D profile	Beam size (68%)	25.18	20.30
			Beam size (95%)	50.02	40.88
		FWHM		28.73	22.82
	2nd ROI	2D profile	Beam size (68%)	36.17	28.98
GaF film	1st ROI	Beam center position		8.62	0.68
		1D profile	Beam size (68%)	26.03	20.62
			Beam size (95%)	48.17	38.70
		FWHM		26.87	34.65
	2nd ROI	2D profile	Beam size (68%)	39.55	31.27

As a result, the 68% beam size of total intensity at the 1D profile, the difference between the CCD and GaF film results shows below 1mm for vertical and horizontal direction. And for the 95% beam size case, the difference shows below 2mm for both directions. And for the 2D intensity profile, the beam size from the GaF film is bigger by 3.4mm for horizontal and 2.3 mm for vertical. It would be required more analysis on CCD intensity profile calculation.

To measure the beam position accuracy, the monitor was placed at several different positions and obtained the each beam profile. As shown in Fig. 6, the beam is passing through the collimator of 3.5 mm diameter and the beam position was measured while moving 20 mm for horizontal direction and 10mm for vertical direction. The beam position measurement results were summarized in Table 2.

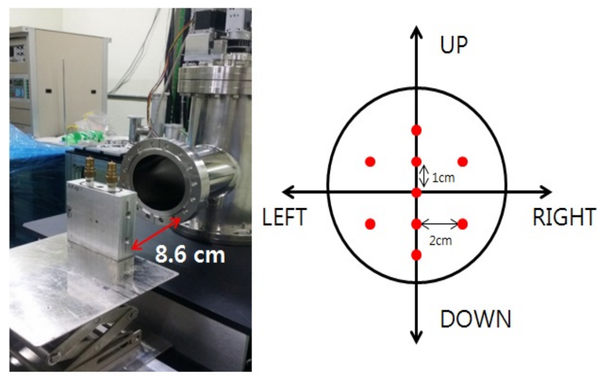

Figure 6: Scanning of beam position using the collimator.

Table 2: The Result of the Beam Position

Move (mm)		Measurement (mm)	
X	Y	X	Y
0	10	0.075	10.01
0	0	0.00	0.00
0	-10	0.078	-9.35
-20	10	-20.30	10.01
-20	-10	-20.04	-10.26
20	10	20.01	9.77
20	-10	20.36	-9.93

CONCLUSION

We have manufactured and tested a prototype beam profile monitoring system at KIRAMS. In order to determine the beam profile measured by the CCD, we compared with the one measured at the vacuum chamber entrance GaFfilm. In case of beam size measurement, the CCD image without background noise reduction was closer to the GaF film result. The beam size difference between the CCD and GaF film results could be generated by their physical position difference. The P43 scintillation screen is located in 173 mm beyond the GaF flim. In case of beam position measurement, the real beam center position did not correctly match the center of the beam that is measured by the method of the center of mass.

ISBN 978-3-95450-176-2

Because the measurement of the beam position at a periphery was affected by the beam cut due to the scintillation screen size of 100mm diameter. The designed scintillation screen monitor and the analysis program have featured on selecting the 2nd ROI in real time for moving beam center. When the beam size is big enough, the center of beam can be calculated correctly using only the 1st ROI because there is little noise from CCD. But when the beam size is small, the 2nd ROI would be required to calculate the center of beam correctly. We could calculate the real beam size (Position) of a certain percent of the total intensity using actual the 2D profile data without graph fitting. In the future analyzing the beam image of CCD and GaF film will be done to more accurately correct the cause of the differences in beam size and the beam position.

ACKNOWLEDGMENT

This work was supported by the National Research Foundation of Korea (NRF) grant funded by the Korea government (MSIP) (no. NRF-2014M2C3A1029534). And this experiment conducted at the MC50 cyclotron facility operated by KIRAMS, supported by the National R&D Program through the Korea Institute of Radiological and Medical Sciences funded by the Ministry of Science, ICT & Future Planning. (No.1711021909).

REFERENCES

[1] P. Forck et al., "Scintillation screen investigations for high energy heavy ion beams at GSI", MOPD53, DIPAC 2011, Hamburg, Germany (2011)

[2] A. Peters et al., "2D-CHARACTERIZATION OF ION BEAMS USING VIEWING SCREENS", THPRI057, EPAC 2002, Paris, France(2002)

[3] K. Mizushima et al., "Beam spot measurement using a phosphor screen for carbon-ion therapy at NIRS", MOPB78, IBIC 2012, Tsukuba, Japan(2012)

[4] N. Saotome et al., "Development of screen beam-profile-monitor system for high-energy beam-transport line at the HIMAC", TH6REP001, PAC09, Vancouver, Canada (2009)

ISBN 978-3-95450-176-2

INTEGRATION OF THE DIAMOND TRANSVERSE MULTIBUNCH FEEDBACK SYSTEM AT ALBA

A. Olmos, U. Iriso, J. Moldes, F. Pérez, ALBA-CELLS, Cerdanyola, Spain
M. Abbott, G. Rehm, I. Uzun, Diamond Light Source, Oxfordshire, UK

Abstract

A Transverse Multi-Bunch Feedback system (TMBF) has been commissioned at the ALBA storage ring for stabilization of the beam instabilities. The system is based on the Libera Bunch-By-Bunch electronics, controlled using a specific software developed at Diamond Light Source. This system refurbishes the existing FPGA code to include several features for machine studies, like fast and precise tune measurements using a Phase Locked Loop, sequences of grow-damp experiments that allow measuring damping rates on a mode-by-mode basis, and precise bunch cleaning. We describe the TMBF system and the integration of the control software into the ALBA machine. We show examples of beam stabilization and machine studies using this system.

INTRODUCTION

Transverse betatron oscillations associated with coupled-bunch instabilities limit the machine performance in current synchrotron light sources. The TMBF system is designed to cure these instabilities by using an active feedback system based on sensors capable of detecting the beam motion, fast FPGA processors to calculate the motion correction, and actuators that apply the correction to the beam.

At ALBA, we have commissioned a TMBF system based on the Libera Bunch-By-Bunch electronics [1] provided by Instrumentation Technologies (ITech), controlled using the firmware and software developed at Diamond Light Source (DLS) [2]. Since 2007, DLS has been developing functionality beyond the pure feedback action, and ALBA decided to profit from this experience.

This paper describes the ALBA TMBF system, the integration of the control system from DLS to ALBA, and the performance and first results with it.

SYSTEM OVERVIEW

The block diagram of the ALBA TMBF is shown in Fig. 1. The signal coming from the BPM buttons is sent to the in-house Hybrid combiner designed to work around 1.5 GHz (3rd harmonic of the RF frequency) to maximize the transfer function. The Hybrid combines the four BPM signals to obtain the Horizontal, Vertical and Longitudinal (not used for the time being) components. Following to the Hybrid module, the RF FrontEnd, also by ITech, performs an amplitude and phase demodulation of the wideband components to the required working frequency of the following electronics.

The Libera Bunch-by-Bunch unit is in charge of the detection of beam instabilities and the calculation of the corresponding correcting action (kick). Correct synchronization with bunches is accomplished by proper locking to 500 MHz RF clock, usage of timing signals from ALBA timing Event Receivers (EVR) and phase matching of all critical cables down to the picosecond range. Following to the Libera electronics, 180° splitters provide the drive for the 100 W / 50 dB / 250 MHz amplifiers by IFI. Signals from the amplifiers are sent through phase-matched cables to the feedback kickers (FFK) to act on the corresponding bunches. Forward signals out of the kickers are sent out of the tunnel for diagnostics purposes.

We have faced a problem on the amplifiers' phase response. While their 50 dB gain stays quite flat up to their higher working frequency (250 MHz), the amplifiers phase response starts degrading around 200 MHz, as it is shown in Fig. 2 and Fig. 3. The effect of such amplifier imperfection is that when the system attempts to act on a particular bunch (while running the feedback, doing bunch cleaning etc.), it can happen that it also affects the neighbor bunches. In the future, we plan to change our amplifiers.

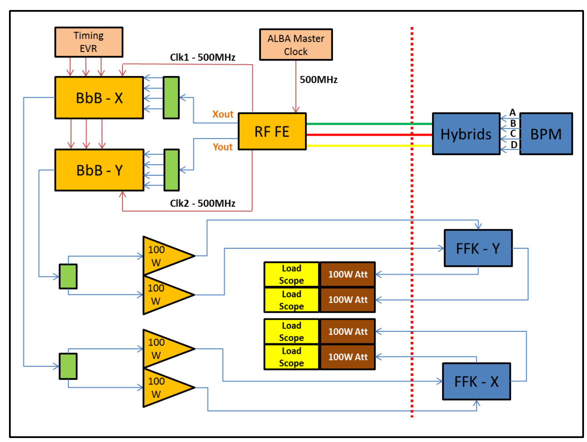

Figure 1: Schematic of the TMBF.

CONTROL SOFTWARE

DLS developed its own FPGA implementation to be run in the Libera Bunch-by-Bunch, replacing the one provided by factory. DLS also developed an EPICS driver for controlling the system, including an EPICS IOC meant to be run inside the unit, a user interface based on Extensible Display Manager (EDM) together with python and Matlab scripts and some other software utilities [2–4]. Since ALBA uses Tango as machine control system, we installed EPICS Base on some selected machines for running the user EDM. Great effort has been done by DLS to prepare a working software infrastructure to adapt all EPICS developments to the ALBA environment, including also the migration of the whole FPGA code from System Verilog to VHDL languages.

ISBN 978-3-95450-176-2

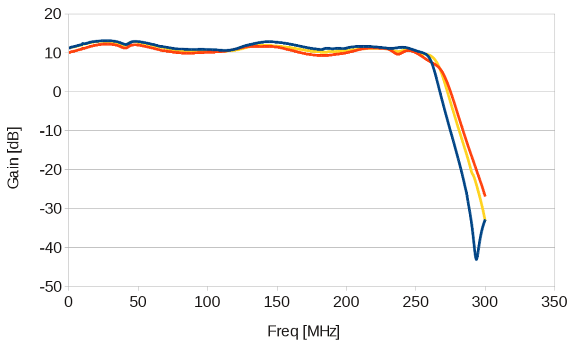

Figure 2: Gain response of three IFI amplifiers. Measurement was done using a 40dB attenuator, so the actual amplifiers gain was around the specified 50dB.

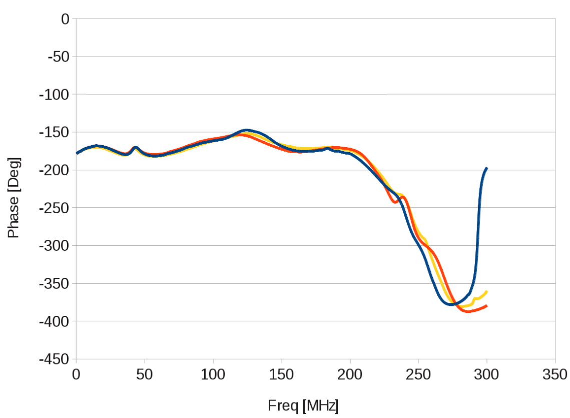

Figure 3: Phase response of three IFI amplifiers. Clear degradation is observed from 200MHz on.

Next steps regarding the interfacing of the TMBF will be the integration of the EPICS controls into the ALBA Tango system by the use of the so-called *cothread* binding [5].

In addition to the instabilities damping capabilities, which is the main application of the system, the control software includes several features for machine studies [2]:

- Frequency response compensation using and input (ADC) and output (DAC) gain pre-emphasis with a 3 point FIR.
- Program sequencing: This allows to apply different control parameters at the same time as data acquisition.
- Tune detection and fast tune tracking via Phase Locked Loop (PLL) excitation of either one or many bunches.
- Concurrent sweep tune measurements on up to four bunches.
- Separate feedback parameters for individual bunches (useful for hybrid filling patterns).

TMBF COMMISSIONING

Due to some problems in the power amplifiers, for the time being we have only commissioned the TMBF in the vertical plane. For a proper TMBF performance, the phase/delay match throughout the different TMBF components and cables must be carefully checked. This is particularly sensitive in the Hybrid combiner, because phase match tolerances at 1.5 GHz are quite stringent: for a 10° tolerance, this is equivalent to cable lengths in the order of 10 mm.

Figure 4 shows both the input pulse and the beam passage as seen by one of the electrodes in the vertical kicker. In order to synchronize the bunch passage with the TMBF pulse, we added a 1 ns length cable upstream the amplifier input. Other cable studies to optimize the TMBF performance are shown in Ref. [6].

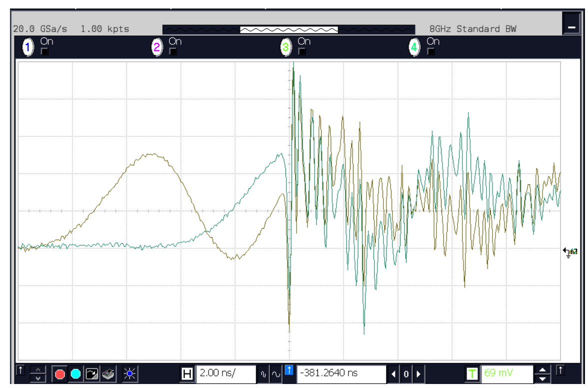

Figure 4: TMBF pulse and bunch passage (high frequency signal at t=0) for the original case (brown trace) and after adding 1 ns length cable (blue trace). Other 4 ns shift (i.e., two buckets) is done using the TMBF GUI.

Closing the Loop

Configuration of the different subsystems to close the feedback loop started with the proper gain and phase setting of the RF FrontEnd to have the highest components levels at Libera Bunch-by-Bunch inputs. Then, in order to enhance the possible beam instabilities, we decreased the vertical chromaticity of the uniform filled beam (440 buckets out of 448) to almost 0. As expected, the vertical instability started at around 40 mA due to Resistive Wall (RW), consistent with studies at [7]. At this point, the injection was halted to find the proper feedback phase that closes the loop, which could be seen by a reduction in the beam size. Finally, we adjusted the loop gain, the injection was resumed and we could inject up to 110 mA keeping the beam instabilities under control (see Fig. 5).

TMBF PERFORMANCE

Figure 6 shows a pinhole image with the TMBF OFF, at an intermediate gain of -42 dB, and after fully correction at 0 dB. Currently, with TMBF OFF, to avoid beam instabilities we are obliged to operate the machine at vertical chromaticity ξ_V ~3.5, and use an odd filling pattern in which we fill the machine with 10 trains of 32 bunches each spaced by gaps of 24 ns (in total, 320bunches).

ISBN 978-3-95450-176-2

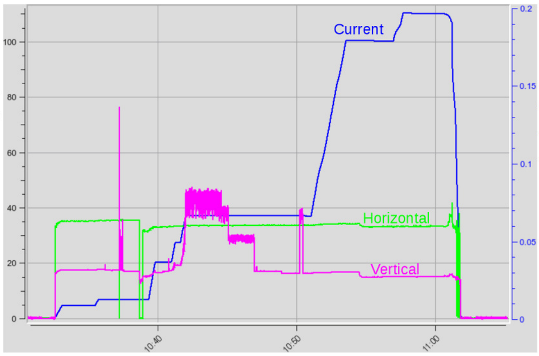

Figure 5: Injection up to 110 mA with vertical $\xi_V \approx 0$. The beam becomes unstable when reaching 40mA and the vertical beam size (pink trace) increases from 28 to 70 μm. Instabilities are next damped by switching the TMBF ON.

With the TMBF ON, we can fill the machine with $\xi_V \sim 0$ and use an almost uniform filling pattern, increasing the number of bunches from 320 until 440. Thus, the ALBA performance is improved because the injection efficiency improves and the lifetime increases by about 25%. So far, the TMBF has been left running for 8 h tests without problems during machine shifts, and it is expected to start operating in users mode in September 2015. Meanwhile, other machine tests have been also carried out.

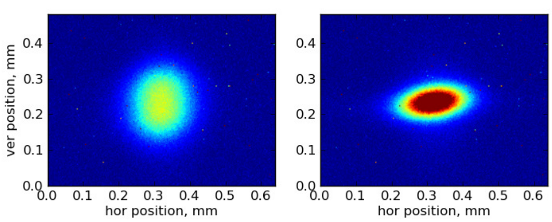

Figure 6: Beam image with TMBF Off (left) and On (right).

Mode Damping Scan

One of the TMBF features allows to program sequences that apply different control parameters at the same time as data acquisition. This is used to measure the growth rates of the individual multi-bunch modes, and to assess the most dangerous modes for ALBA.

We program a "super-sequence" that starts from an unstable beam, which is stabilized with the TMBF. We then excite mode "m" using a Numerically Controlled Oscillator (NCO), and we measure its growth time. We then switch it back On and measure its damping time as well. The sequence is then repeated for mode "m+1" and a full characterization spans up to mode 448. The "super-sequence" is also repeated with the TMBF Off (unstable beam) and the results are shown in Fig. 7, where one can see (blue trace) that the most unstable modes (with positive growth rates) are modes between [440,..., 447] (or equivalent, [-1, ... -7]), which indicates the presence of RW instabilities. On the other hand, there also exists mode 324 (or m=-124), which needs further investigations. In any case, all modes are efficiently damped with the TMBF On (at least for these beam settings, 100 mA and $\xi_V \sim 0$).

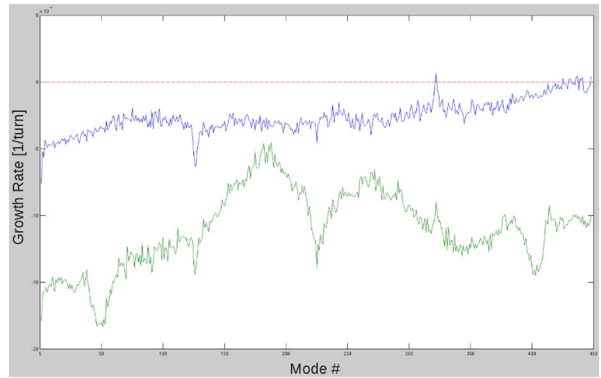

Figure 7: Growth rate for the 448 modes with TMBF On (green) and Off (blue) for a beam of 100 mA and $\xi_V \sim 0$.

Tune Measurements

Tune measurements can be done in two ways with the TMBF: using the classical method of sweep excitation and detection of one (or many) bunches, or using a tune tracking employing a PLL. This method excites one (or many) bunches using the NCO, detects the phase of the bunches relative to the excitation, and feeds it back through a proportional-integral controller to the NCO frequency. This allows to measure the tune with a precision that can go down to 10^{-5}.

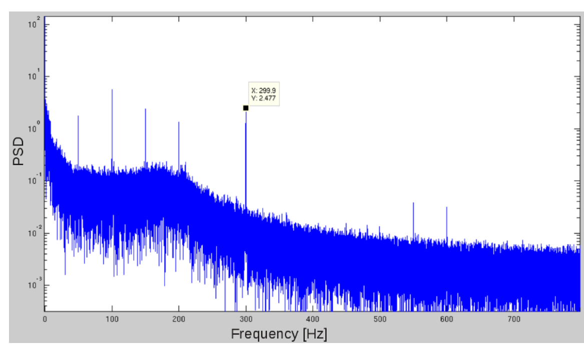

Figure 8: Tune Jitter measured with the fast tune tracking.

The tune measurement rate depends on the number of turns to detect the beam phase, which is configurable and typically last for 100 or 200 turns. The buffer that stores this tune measurement can be up to 4096 samples, but it can be read out every time it is updated. Using this capability, the TMBF allows to monitor the tune in long terms and thus monitor, for example, the tune jitter with high precision: Figure 8 shows the spectral density obtained after monitoring the vertical betatron tune during 70 s every 200 turns. One can see that most of the tune jitter is at low frequencies (below 10 Hz), but there also exists peaks at 50 Hz and its harmonics (particularly, the 300 Hz corresponding the power supplies).

ISBN 978-3-95450-176-2

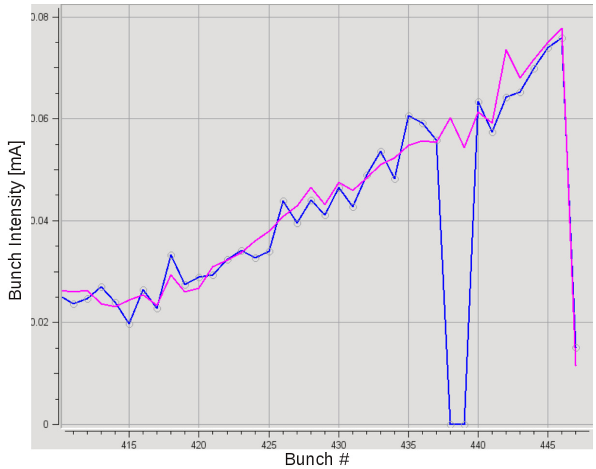

Figure 9: Bunch intensity for buckets between 410 and 448 before (pink trace) and after bunch cleaning (blue trace).

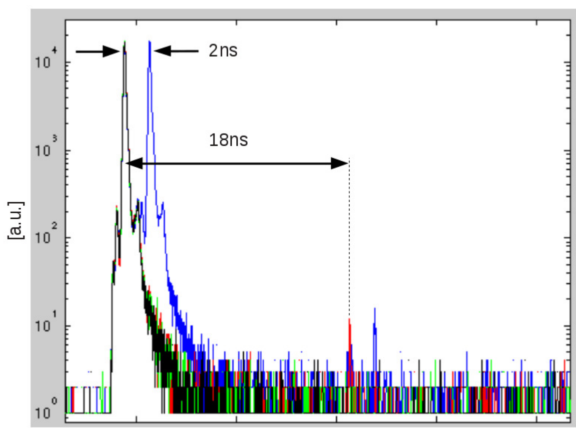

Figure 10: Bunch intensity (in arbitrary units) as measured with the photon counting. Initially, the machine was filled with two consecutive bunches (blue trace), and we noted that two more bunches were filled 18 ns later. We then proceed to kill the different bunches one by one (red and green traces), until we left the machine with only one bunch (black trace).

Bunch Cleaning

Bunch cleaning is performed by exciting the target bunch with a backwards frequency sweep around the vertical betatron tune, and slightly closing the vertical scraper from the nominal position (9.5 mm gap) to 7 mm.

A first attempt to kill one bunch is shown in Fig. 9, where the target bunch was initially bunch 438. However, by comparing the traces before (pink) and after (blue), actually two bunches were killed. This is a consequence of the bad phase response of the amplifiers (see Fig. 3), which spreads the single kick produced by the Libera Bunch-by-Bunch to actually two bunches.

Nevertheless, we could see by filling the ring with two consecutive bunches, that optimum settings can be achieved to kill the second bunch (see Fig. 10). Moreover, this experiment allowed us to realize that our Linac produces a parasitic bunch after 18 ns from the target buckets whose purity is about 10^{-3} (from reasons yet to be understood). However, by using the TMBF, we were able to clean also these parasitic bunches and finally leave the machine with a pure single bunch (black trace).

SUMMARY

The implementation of the DLS TMBF system at ALBA has been demonstrated, both in terms of software integration and feedback capabilities. Moreover, extra features have been also tested and proved to be excellent tools for machine studies. In the future, we plan to slightly change our TMBF schematic to add high power splitters after the amplifiers so only one amplifier per plane will be needed. The commissioning of the Horizontal plane and the final integration of the TMBF into the ALBA Tango control system are also to be done now that we have proved that the system behaves as expected.

ACKNOWLEDGMENTS

We would like to acknowledge M. Álvarez for his technical support on the RF measurements of the different system devices.

REFERENCES

[1] Libera Bunch-by-Bunch, Instrumentation Technologies. http://www.i-tech.si

[2] G. Rehm, M.G. Abbott, A.F. Morgan, *New features and measurements using the upgraded TMBF at Diamond*, Proc. of IBIC'14, Monterey (USA).

[3] A.F. Morgan, G. Rehm, I. Uzun, *Performance and features of the Diamond TMBF system*, Proc. of EPAC08, Genoa (Italy).

[4] M.G. Abbott, G. Rehm, I.S. Uzun, *Capability Upgrade of the Diamond Transverse Multibunch Feedback*, Proc. of IBIC13, Oxford (UK).

[5] http://controls.diamond.ac.uk/downloads/python/cothread/

[6] M. Alvarez and U. Iriso, *SR FFK CABLES STUDY*, ALBA Internal Report AAD-SRDIFFK-TR-0002 (2012).

[7] T. Guenzel, *Impedance and instabilities for ALBA*, Proc. of EPAC08, Genova (Italy).

ISBN 978-3-95450-176-2

ELECTROSTATIC FINITE-ELEMENT CODE TO STUDY GEOMETRICAL NONLINEAR EFFECTS OF BPMS IN 2D

A. A. Nosych, U. Iriso, ALBA-CELLS, Barcelona, Spain
J. Olle, UAB, Barcelona, Spain

Abstract

We have developed a 2D finite element-based software for Matlab to study non-resonant effects in BPMs of arbitrary geometry, in particular the geometric nonlinearities. The developed code called *BpmLab* utilizes an open-source tetrahedral mesh generator *DistMesh*, combined with a short implementation of FEM with linear basis functions to find the electrostatic field distribution for boundary electric potential excitation. The BPM response as a function of beam position is calculated in a single simulation for all beam positions using the potential ratios, according to the Green's reciprocity theorem. The code offers ways to correct the geometrical nonlinear distortion, either by polynomials or by direct inversion of the electrode signals through numerical optimization. This work is an overview of the *BpmLab* capabilities to date, including its extensive benchmarking and validation against other methods.

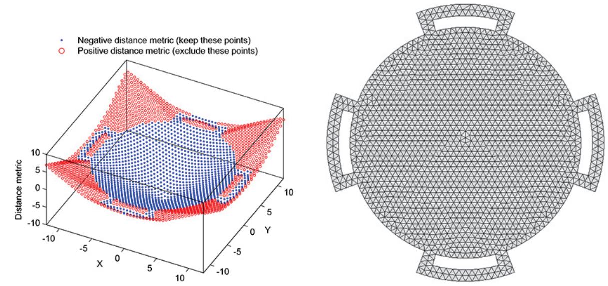

(a) Modeling the BPM geometry by metric functions prior to triangular meshing.

(b) Optimized equilateral Delaunay mesh of the BPM's vacuum interior, generated by *DistMesh*.

Figure 1: Modeling the pilot-BPM in *BpmLab* by combining a circle with arcs as functions of radii and internal/orientation angles.

INTRODUCTION

At the initial design stage of any beam position monitor (BPM) lies its numerical characterization and optimization to fit the machine requirements. The common nowadays tools for electromagnetic (EM) simulations are usually an overkill for BPM simulations: they are either expensive (CST, Ansys, GdfidL), or free but complex (ACE3P, POISSON), requiring users to possess specific knowledge of geometrical modeling in 2D/3D and the tool itself. However, BPMs used in accelerators with ultra-relativistic beams are usually designed to be resonance-free and their position characteristic to be independent from the accelerator's operating frequency. Hence, the numerical characterization of a BPM does not need to be complicated and 2D approximations can be made to simulate the behavior of most BPM types and provide their optimization.

At ALBA, characterization of storage ring and booster BPMs has previously been done with the 2D boundary element method (BEM) [1, 2], and lately cross-checked with ACE3P [3]. However, though sufficient for ALBA's needs, the BEM code was limited to only two simple BPM geometries, while using the 3D time domain solver of ACE3P is rather complicated for such tasks.

The electrostatic (ES) approach to numerical BPM characterization is not new and has been used for over a decade in various accelerator laboratories, e.g. SLAC [4], CESR [5] and FNPL [6]. However, together with post-processing, this approach usually requires extra effort of additional software to get the final results.

Matlab is, perhaps, the most common tool for mathematics and data analysis in the accelerator community, with its mighty Middle Layer [7] used in the control systems of a number of accelerators, including ALBA. Thanks to a vast amount of built-in and open-source code solutions offered by Matlab, we have developed *BpmLab*: a simplistic yet powerful code for electrostatic analysis of BPMs of arbitrary geometry and free electrode arrangement in 2D.

METHODOLOGY

Some functionality, mentioned in this work, already exists in Matlab to some extent as parts of paid toolboxes. Our intention, however, is to create a free and easy to use tool, while bringing some novelty to the table.

FEM to Solve Laplace's Equation

In order to solve Poisson's equation we have used a short numerical implementation of Laplace's equation solver in 2D with mixed (Dirichlet + Neumann) boundary conditions for unstructured grids with linear triangular or quadrilateral elements [8]. Here, the problem is solved employing the finite element method (FEM) using the standard Galerkin discretization scheme. The FEM solver calculates the electrostatic potential value in each mesh node based on the boundary conditions and any volume forces, if they exist.

Meshing

For meshing we are using *DistMesh* [9], which is a simple Matlab code for generating constrained equilateral Delaunay meshes with node coordinates optimization by a force-based smoothing procedure. Here the geometry specification is done by *signed distance functions*, which give the shortest distance from every node to the boundary of the domain. The sign is negative inside the region and positive outside,

ISBN 978-3-95450-176-2

Fig. 1(a), and tells the algorithm which nodes to exclude from the final mesh, Fig. 1(b).

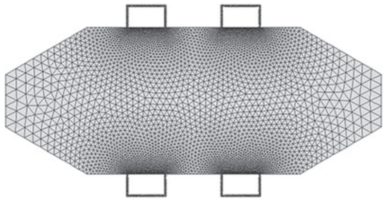

Figure 2: Meshed model of the ALBA storage ring BPM, whose optimized non-uniform Delaunay mesh consists of 8409 triangles on 4558 nodes.

Combining the FEM electrostatic solver with *DistMesh* opens plenty of possibilities for 2D EM modeling, in particular useful for beam instrumentation engineering.

For the moment, we are omitting the Neumann boundary conditions and quadrilateral mesh elements, but focus on fine-tuning the triangular mesh with Dirichlet-type boundaries. We have modified the FEM and *DistMesh* codes and improved their capabilities, e.g. by adding the manual mesh density control in fine geometrical areas (e.g. around the electrodes of ALBA BPM in Fig. 2), the boundary node search for potentials assignment, and the ability to accept any function f as the source of electrostatic field (sometimes also called *volume force* or *space charge*).

Convergence

In order to test the basic reliability of the FEM solver we check convergence of several parameters as functions of mesh edge size. For analytic shapes the error norms L_1 (L_2) are calculated by taking length of vectors whose components are the difference (squared difference) between analytic and FEM solutions in the mesh nodes.

Additionally, a quantity proportional to the system's stored electrostatic energy is calculated, which matches the theoretical result for analytical shapes, and estimates convergence for more complex geometries:

$$\varepsilon = \frac{1}{2}\epsilon_0 \int_V E^2 dV \approx \frac{1}{2}\sum_t {E_t}^2 A_t \text{ [arb. units]} \qquad (1)$$

where $\epsilon_0 = 1$ and E^2 is the squared norm of electric field. In Eq. (1) the label t is used to indicate the triangular element we are on and A_t corresponds to its area.

Consider solving the Poisson's equation $-\nabla^2\phi = f$ for each of the two following analytic unit-sized shapes with grounded Dirichlet boundary conditions, which have known analytic solutions:

1) Circle S_1 with radius $R = 0.5$:

$$\begin{cases} \phi_{xx} + \phi_{yy} = -4, & x^2 + y^2 < R^2 \\ \phi = 0, & x^2 + y^2 = R^2 \end{cases} \qquad (2)$$

Solution: $\phi(x, y) = R^2 - x^2 - y^2$.

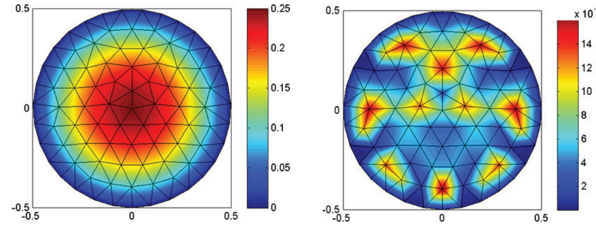

(a) FEM solution on a circle meshed with 145 triangles on 89 nodes.

(b) Difference between FEM and the exact solution, Eq. (2).

Figure 3: Comparison between the FEM and the exact solution of the Poisson's equation for the unit circle shape.

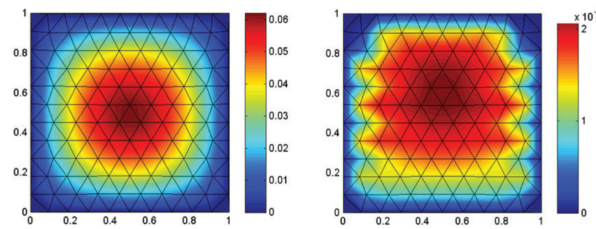

(a) FEM solution on a square meshed with 211 triangles on 128 nodes.

(b) Difference between FEM and the exact solution, Eq. (3).

Figure 4: Comparison between the FEM and the exact solution of the Poisson's equation for the unit square shape.

2) Square S_2 with side length $a = 1$:

$$\begin{cases} -\nabla^2\phi = 2x(a - x) + 2y(a - y), & (x, y) \in S_2 \backslash \Omega S_2 \\ \phi = 0, & (x, y) \in \Omega S_2 \end{cases} \qquad (3)$$

Solution: $\phi(x, y) = xy(a - x)(a - y)$.

The exact solutions were compared against the ones obtained with the FEM solver achieving excellent accuracy of under 1 mV even for scarce mesh, Figs. 3 and 4.

Plotting the L_1 and L_2 norms as functions of the decreasing mesh size (thus, the increasing number of nodes), reveals an expected converging trend for norms of S_1 and S_2, Fig. 5, and an interesting behavior of the norms of S_2 which appear smoother. This is because a square is much better approximated by triangles than a circle.

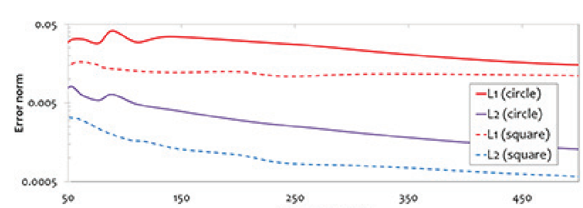

Figure 5: Error norms L_1 and L_2 for the circle and square as functions of the number of nodes.

ISBN 978-3-95450-176-2

SIMULATIONS AND BENCHMARKING

Green's Reciprocity Theorem

Instead of simulating a beam sweep for multiple beam positions, as common with 3D time domain EM solvers in application to BPM modeling, the ES approach offers a similar outcome by a much faster procedure offered by the Green's reciprocity theorem (GRT): obtaining the electrode signals for all beam positions in a single calculation.

In the specific case that we are interested in, GRT states that the charge induced on an electrode surface q_e due to a test charge q at (x_0, y_0) position is proportional to the potential ϕ at that same position when the test charge is absent and the electrode is set to a potential V_0, see [5]:

$$q_e V_0 = -q\phi(x_0, y_0) \tag{4}$$

Therefore, $\phi(x_0, y_0)$ is the solution to the problem of calculating the signal of an electrode, up to a multiplicative constant, as a function of the charge location. This constant, q_e in Eq. (4), is of no importance because we later compute the normalized ratio of potentials, which is equivalent to the normalized ratio of electrode signals. The problem comes down to computing $\phi_i(x, y)$ for each electrode $i = 1..4$ for every mesh node inside the chamber.

We test and validate the developed codes on a 2D model of a showcase BPM labeled *pilot-BPM*. It has 1 mm thick electrodes spanning $\alpha = 30^{\text{o}}$ each, mounted flush in a $0°/90°$ orthogonal arrangement in the circular vacuum chamber of radius $R = 10$ mm and gap of 1 mm.

In practice, the application of GRT comes down to exciting one electrode with non-zero voltage and grounding the others, including the vacuum chamber. The resulting potential $\phi_1(x, y)$ and mesh is then rotated/mirrored to get $\phi_{2,3,4}(x, y)$, as illustrated with the pilot-BPM in Fig. 6. Potential values beyond the mesh nodes are found by linear interpolation which is sufficient due to working with linear finite elements.

BpmLab offers several standard *difference over sum* (DOS) treatments of BPM signals, which can be applied to a given BPM geometry according to its electrode arrangement.

In particular, the normalized "raw" position characteristic for the circular pilot-BPM is calculated conventionally as

$$x_{\text{raw}} = \frac{\phi_1 - \phi_2}{\phi_1 + \phi_2}\,, \quad y_{\text{raw}} = \frac{\phi_3 - \phi_4}{\phi_3 + \phi_4} \tag{5}$$

Combining together the potentials $\phi_i(x, y)$ for the pilot-BPM with Eq. (5), the normalized horizontal and vertical beam positions in the locations of mesh nodes are obtained, Fig. 7(a). From here they can be interpolated on a rectangular grid and calibrated to mm by scaling factors $k_{x,y}$ which, for circular beam pipes, can be simply approximated by $k_{x,y} = R/2$, see [10].

Computing the 29×29-point beam position map (±7mm, step of 0.5 mm) for the pilot-BPM results in a typical "pincushion" characteristic map, Fig. 7(b).

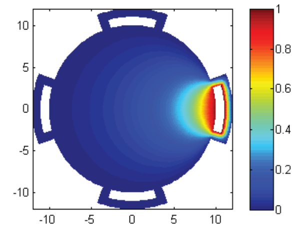

(a) Original calculation of $\phi_1(x, y)$ by exciting the right electrode to 1 volt.

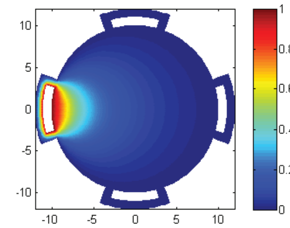

(b) Rotating $\phi_1(x, y)$ by 180° to obtain $\phi_2(x, y)$.

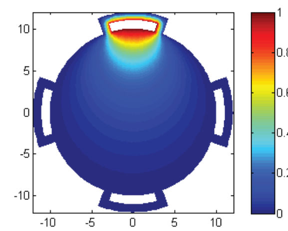

(c) Rotating $\phi_1(x, y)$ by 90° to obtain $\phi_3(x, y)$.

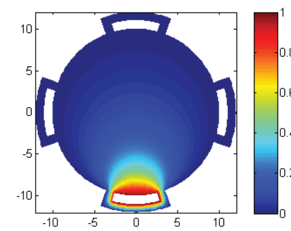

(d) Rotating $\phi_1(x, y)$ by 270° to obtain $\phi_4(x, y)$.

Figure 6: One electrostatic solution rotated 3 times to emulate 3 other excitations.

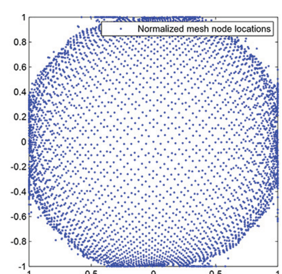

(a) Normalized DOS ratios of $\phi_{1..4}$ calculated in mesh nodes.

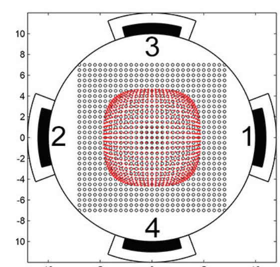

(b) Interpolated and calibrated beam position map.

Figure 7: Simulating BPM response for the pilot-BPM: blue dots are the normalized DOS values in node locations, black dots are the true beam positions, and red ones form the nonlinear response map.

Validation Against Other Methods

It is important to validate the results obtained by *BpmLab* with the results obtained by other available methods and tools. The pilot-BPM geometry was simulated by each of the following methods, and differences between position maps, treated by Eq. (5), are shown.

a) ***BpmLab* versus the Wall Current Method (WCM).** For BPMs mounted in circular vacuum chambers the sensitivity function can be estimated analytically by integrating the wall current distribution induced on an electrode due to a line-charge as a function of (x_0, y_0, α, R), [10]. The difference between the beam position maps calculated by *BpmLab* and WCM for the pilot-BPM is below 30 μm in most of the map region except its corners, Fig. 8 (a).

ISBN 978-3-95450-176-2

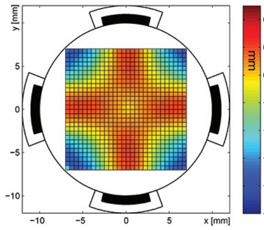

(a) *BpmLab* versus the Wall Current Method.

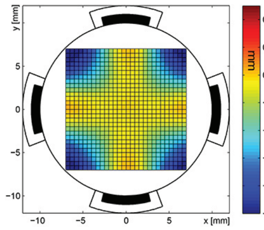

(b) *BpmLab* versus the Boundary Element Method.

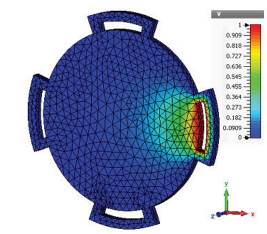

(c) Electrostatic 3D simulation by CST of 1 mm "slice" of the BPM.

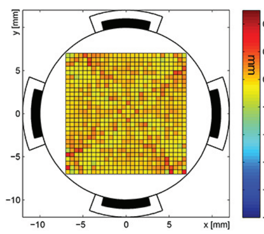

(d) *BpmLab* versus the Electrostatic solver of CST ES.

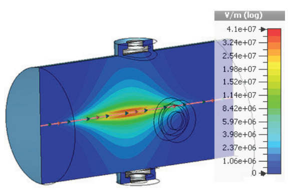

(e) A snapshot in time of the 3D Wakefield simulation by CST PS.

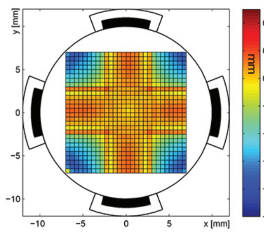

(f) *BpmLab* versus the Wakefield solver of CST PS.

Figure 8: Differences between beam position maps of the pilot-BPM, calculated by *BpmLab* and other methods.

b) ***BpmLab* versus the Boundary Element Method (BEM).** BEM is based on the numerical solution of the 2D electrostatic problem of finding the induced charge on the *boundary* of the domain containing some charge $\rho(x_0, y_0)$ that represents the relativistic beam. The BEM solver available at ALBA [2] shows mainly a 20 μm difference between the response map calculated by *BpmLab*, Fig. 8 (b).

c) *BpmLab* versus the CST Electrostatic solver. Potential excitation of the right electrode to 1 volt is simulated by the Electrostatic solver of CST in Fig. 8(c). After post-processing comparing the maps calculated with CST ES and *BpmLab* show that they essentially overlap with under 10 μm difference, Fig. 8(d).

d) *BpmLab* versus the CST Wakefield solver. Finally, the pilot-BPM was simulated and mapped with the time domain wakefield solver of CST Particle Studio, Fig. 8(e). The 3D model consisted of 200k hexahedral mesh cells; the beam scan was modeled by a single Gaussian relativistic bunch (σ_τ = 5 mm, $Q = 10^{-8}$ C) traveling for 500 ps (80 mm) of wake length. The resulting difference with the response map calculated by *BpmLab* is mainly below 30 μm, Fig. 8(f).

NONLINEARITY CORRECTIONS

Nonlinear distortion of the BPM response can be an issue, especially when large beam offsets are foreseen. Correction of such nonlinearities is integrated into *BpmLab* through:

1) calculation of polynomial coefficients of a non linear fit of two normalized quantities, x_{raw}, y_{raw}, derived from potentials $\phi_{1..4}$. These polynomials allow accurate real-time reconstruction of the transverse beam position taking into account the coupling between electrodes [10, 11]. Low-power polynomials are often sufficient for good precision: Fig. 9 shows the result of applying a 9$^{\mathrm{th}}$ order 2D polynomial to correct the DOS distortion of the pilot-BPM in Fig. 7(b).

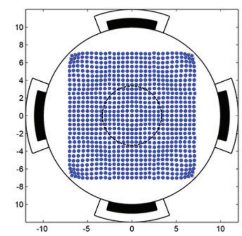

(a) Corrected map.

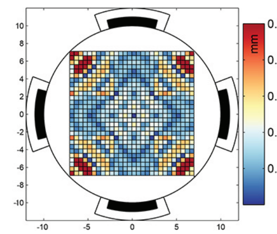

(b) Error of correction in mm.

Figure 9: Response map of the pilot-BPM, corrected by the 9$^{\mathrm{th}}$ order 2D polynomial.

2) direct inversion of the electrode voltages to corresponding beam position using the model behavior of a certain BPM. This procedure is intended for offline post-processing through iterative numerical optimization [5], [11], [12] and promises much more precision over polynomial fits.

This algorithm is implemented in *BpmLab* for an arbitrary 4-electrode BPM geometry. The BPM characteristic is modeled by a set of calculated potentials $\varphi_{i,i=1..4}$ on a non-uniformly distributed array of triangular mesh nodes.

Briefly, to invert a set of voltages $V_{i,i=1..4}$ to the unique beam position inducing them, the following target function is minimized

$$f(x,y) = f_{\mathrm{h}}^2(x,y) + f_{\mathrm{v}}^2(x,y) \to \min\,, \qquad (6)$$

where

$$f_{\mathrm{h}}(x,y) = \frac{\Delta_{\mathrm{h}}\phi(x,y)}{\Sigma_{\mathrm{h}}\phi(x,y)} - \frac{\Delta_{\mathrm{h}}V}{\Sigma_{\mathrm{h}}V} \qquad (7)$$

and a similar expression for $f_{\mathrm{v}}(x,y)$.

To minimize the target function (6) the *gradient descent method* (GDM) is used, which presupposes that the gradient of the function can be computed numerically or analytically. The DOS ratios of ϕ and V in Eq. (7) follow the particular DOS convention, e.g. Eq. 5.

The search starts at a certain starting point (x_0, y_0) and, as many times as needed, moves from (x_i, y_i) to (x_{i+1}, y_{i+1}) by minimizing along the line in the direction of the local downhill gradient, expressed analytically:

ISBN 978-3-95450-176-2

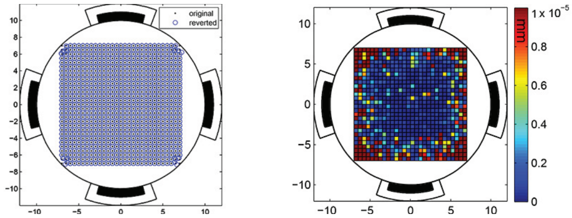

(a) Corrected map. (b) Error of correction.

Figure 10: Correction based on voltage inversion through optimization. Here the self-generated BPM signals are used for backward convergence test of the FEM method.

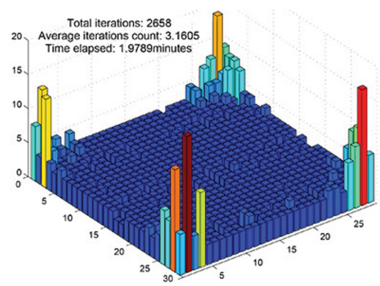

Figure 11: Amount of iterations (represented in bar height and color) it took to invert 4×841 sets of self-generated signals back to 841 beam positions.

$$\nabla f(x_i, y_i) = \left[\frac{\partial f(x_i, y_i)}{\partial x}; \frac{\partial f(x_i, y_i)}{\partial y} \right]. \quad (8)$$

The starting point is found by yet another minor optimization routine: *the nearest node search*, which looks for the node for which the normalized $(x_{\mathrm{raw}}, y_{\mathrm{raw}})$ of the potentials resemble the corresponding ratio of the voltages.

Assuming that ϕ_i are piece-wise planar functions over the triangulated region, the partial derivatives of $\partial\phi_i$ implied in (8) are found numerically in every node as first order approximations.

The inversion procedure was tested for backward convergence on the FEM model of the pilot-BPM using self-generated signals on a square grid of beam positions. It has shown excellent beam position recovery, Fig. 10(a), with machine precision, Fig. 10(b). The inversion process took under 2 minutes for 29×29 map points taking 3 iterations on average to reach the optimum for each position, Fig. 11.

We have also made an attempt to restore the beam position map based on voltages, generated by the CST Wakefield solver for same map parameters, which resulted in achieving $< 50\mu$m accuracy across most part of the map, Figs. 12.

ACKNOWLEDGMENTS

The authors would like to thank M. Wendt and G. Rehm for inspiration and time spent in fruitful discussions.

CONCLUSION

We have created a functional tool to ease the process of BPM modeling for the Matlab platform. Performing a single electrostatic simulation on a modern desktop PC takes negligible amount of time for a meshed BPM model with some 10k nodes, so characterizing BPMs becomes a fast seamless task. The code offers ways to correct for the non-linear geometrical distortion effect via polynomials, or by voltage inversion through numerical optimization, naturally using the mesh properties.

BpmLab has been extensively benchmarked against a number of other methods and commercial tools. It has shown to be computationally quick and easily adjustable to any BPM geometry, assuring its precise meshing and reliable results.

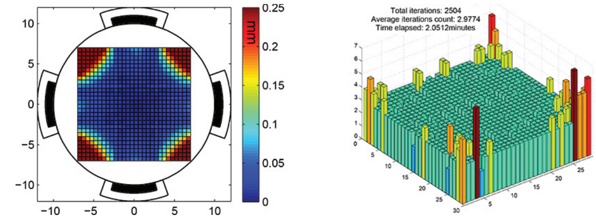

(a) Corrected map. (b) Inversion iterations.

Figure 12: Correction based on voltage inversion, performed on voltages simulated with the Wakefield solver of CST PS.

REFERENCES

[1] A. Stella, "Analysis of the Dafne beam position monitor with a boundary element method", *Dafne Tech. Note*, **CD-10** (1997).

[2] A. Olmos et al., "Matlab code for BPM button geometry computation", *Proc. DIPAC-2007*, pp. 186-188 (2007).

[3] A. A. Nosych et al, "Overview of the geometrical non-linear effects of button BPMs and methodology for their efficient suppression", *Proc. IBIC'14* (2014).

[4] S. R. Smith, "Beam position monitor engineering", **SLAC-PUB-7244** (1996).

[5] R. W. Helms, G. H. Hoffstaetter, "Orbit and optics improvement by evaluating the nonlinear BPM response in the Cornell Electron Storage Ring", *Phys. Rev. ST AB*, vol. **8**, issue **6** (2005).

[6] P. Piot, "Evaluation and correction of nonlinear effects in FNPL BPM", *FERMI Note* (2005).

[7] G. Portmann et al., "Middle Layer Software Manual for Accelerator Physics", *LBNL Internal Report*, **LSAP-302** (2005).

[8] J. Alberty, C. Carstensen, S. A. Funken, "Remarks around 50 lines of Matlab: short finite element implementation", *Numerical Algorithms* **20**, 117-137 (1999).

[9] P.-O. Persson, G. Strang, "A Simple Mesh Generator in MATLAB", *SIAM Review*, Volume **46 (2),** pp. 329-345 (2004).

[10] A. A. Nosych, M. Wendt, "Analysis of Geometric Nonlinearities of LHC BPMs by 2D and 3D Electromagnetic Simulations", *PRST-AB* (submitted).

[11] R. Bartolini, J. Rowland, "Geometric nonlinearities of a four buttons BPM", *DLS Int. Rep.* **No. AP-SRREP-0174** (2010).

[12] N. Hubert, B. Beranger, L. S. Nadolski, "BPM data correction at Soleil", *Proceedings of IPAC'14* (2014).

ISBN 978-3-95450-176-2

MEASUREMENTS AND CALIBRATION OF THE STRIPLINE BPM FOR THE ELI-NP FACILITY WITH THE STRETCHED WIRE METHOD

A. A. Nosych, U. Iriso, A. Olmos, A. Crisol, C. Colldelram, ALBA-CELLS, Barcelona, Spain
F. Cioeta, A. Falone, A. Ghigo, M. Serio, A. Stella, INFN/LNF, Frascati, Italy
A. Mostacci, Rome University, Rome, Italy

Abstract

A methodology has been developed to perform electrical characterization of the stripline BPMs for the future Gamma Beam System of ELI Nuclear Physics facility in Romania. Several prototype units are extensively benchmarked and the results are presented in this paper. The BPM sensitivity function is determined using a uniquely designed motorized test bench with a stretched wire to measure the BPM response map. Here, the BPM feedthroughs are connected to Libera Brilliance electronics and the wire is fed by continuous wave signal, while the two software-controlled motors provide horizontal and vertical motion of the BPM around the wire. The electrical offset is obtained using S-parameter measurements with a Network Analyzer (via the "Lambertson" method) and is referenced to the mechanical offset.

INTRODUCTION

The future Extreme Light Infrastructure Nuclear Physics (ELI-NP) facility will be located in Bucharest (Romania), and will be dedicated to the study of secondary light sources and attosecond pulses. This will be done by the Gamma Beam System (GBS) consisting of a 90 m long Linac producing a 700 MeV electron beam, whose main characteristics are listed in Table 1.

Table 1: Main Characteristics of the ELI-NP Linac

Number of bunches	32
Bunch spacing	16 ns
Charge/bunch	[25–400] pC
Bunch size, σ_x	100-200 µm
Bunch size, σ_y	100-200 µm
Bunch length, σ_z	3–4 ps

The stripline BPMs for the GBS of ELI-NP have been originally designed by the Accelerator division of INFN/LNF in Frascati (Rome), and are being manufactured by the company *Comeb*. After production, the BPM units are shipped to ALBA for electrical characterization and alignment measurements. In total there will be 32 BPM units, all of them $\lambda/4$ stripline type working at ~500 MHz, shorted on the downstream port. Figure 1 shows a schematic drawing and a model of the stripline, including the port naming convention used throughout all measurements.

This document describes the methodology followed to characterize the stripline BPMs. This is done in two ways: first, the so-called electrical offset is obtained (x_e, y_e) using the well-known Lambertson method [1, 2], which is used to analyze the asymmetries among BPM electrodes.

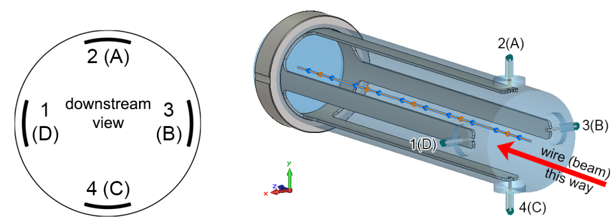

(a) cross-section. (b) 3D BPM Model.

Figure 1: Naming convention and 3D BPM Model.

Next, we emulate the wire scan by scanning the BPM transversely around the stretched wire, Fig. 2, to obtain the sensitivity factors k_x, k_y and the mechanical offset (x_w, y_w). These offsets, referenced with respect to BPM's fiducial points, are due to all possible mechanical effects and they will be taken into account when installing the BPM units in the GBS Linac oF ELI-NP facility.

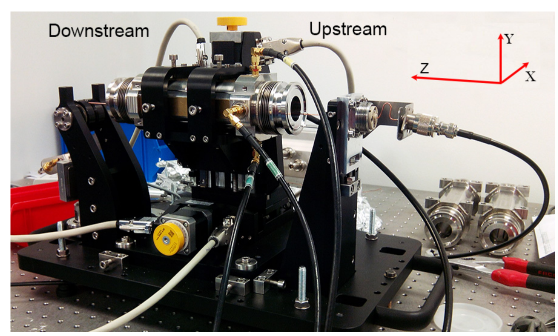

Figure 2: Photo of the BPM and the test bench in the lab.

ELECTRICAL CHARACTERIZATION

The beam position (x_b, y_b) in a symmetric BPM mounted in a circular chamber is obtained from the classical difference over sum (DOS) expression for the electrode signals $V_{1..4}$ with removed offset:

$$x_b = k_x \times \frac{V_3 - V_1}{V_3 + V_1} - x_{\text{offset}} \quad (1)$$

$$y_b = k_y \times \frac{V_2 - V_4}{V_2 + V_4} - y_{\text{offset}} \quad (2)$$

Lambertson Method

The BPM electrical center is defined as the position where $V_3 - V_1 = V_2 - V_4 = 0$, and it corresponds to the deviation (x_e, y_e) from the BPM geometrical origin (mechanical center). Its measurement does not require a BPM precisely

ISBN 978-3-95450-176-2

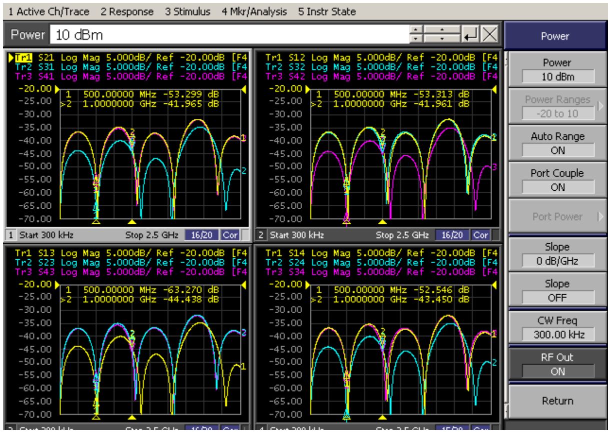

Figure 3: Sample snapshot of the S-parameter measurement by a Network Analyzer.

positioned on a test bench due to an external calibration method developed by D. Lambertson [1, 2].

This method uses the coupling between buttons/electrodes to determine the gain factors of each electrode; the ratios between gain factors then provide the difference between the mechanical and electrical centers. It has previously been applied to measure electrical offsets of the ALBA Booster BPMs with 6 µm precision at fixed 500 MHz [3].

Each BPM electrode has an associated gain factor g which causes the difference between the mechanical and electrical center of a BPM. Based on differences between the gain factors we can obtain the electrical center with respect to the mechanical one:

$$x_e = k_x \times \frac{g_3 - g_1}{g_3 + g_1}\ ,\quad y_e = k_y \times \frac{g_2 - g_4}{g_2 + g_4} \tag{3}$$

The normalized coupled voltage between two electrodes i (excited) and j (detected) is given by:

$$V_{ij} = 2 \cdot 50 \cdot G_{ij} g_i g_j . \tag{4}$$

where $G_{ij} = G_{ji}$ are the capacitive coupling coefficients.

From the asymmetries between the electrodes, the gain factors $g_{i,j}$ can be obtained from the three alternative combinations of the measured V_{ij}, e.g. for g_1, this is:

$$\begin{aligned} 2 * 50 * g_1^2 = \frac{V_{21} V_{14}}{V_{42}} \times \frac{G_{13}}{G_{12} G_{23}} &= \\ = \frac{V_{12} V_{31}}{V_{32}} \times \frac{G_{23}}{G_{12} G_{13}} &= \\ = \frac{V_{41} V_{31}}{V_{43}} \times \frac{G_{12}}{G_{23} G_{13}} & \end{aligned} \tag{5}$$

and 3 more similar triplet sets for $g_{2,3,4}$. Since we are interested in the ratios of gain factors (Eq. (3), the values of $G_{\mathrm{i,j}}$ are not needed. Solving Eq. (5) and using Eq. (3) provides 3 different pairs of solutions $(x_{\mathrm{e(a,b,c)}}, y_{\mathrm{e(a,b,c)}})$ for each offset, whose good or bad agreement has to do with the quality of the geometrical symmetry of electrode strips.

In practice, the BPM electrical offset is obtained by measuring S-parameters of the 4 electrodes with a Network Analyzer (NA). In this case, we use the 4-port NA (*Agilent E5071B*, 300 kHz – 8.5 GHz). The NA output signal is injected through one electrode and the S-parameters of the other electrodes are measured, which correspond to the elements of the 4x4 scattering matrix (or S-matrix). A snapshot of one full measurement is shown in Fig. 3. Ideally the reflection coefficients should be zero and the transmission ones, $S_{\mathrm{ij}} = S_{\mathrm{ji}}$, symmetric.

The normalized voltage V_{ij} in Eq. (4) is equal to the transmission coefficient S_{ij}. The final calculation formula for the horizontal electrical offset, includes transformation from dB to linear S-parameter readings:

$$x_e = k_x \frac{\sqrt{10^{S_{\mathrm{x,ijm}}/20}} - \sqrt{10^{S_{\mathrm{x,npq}}/20}}}{\sqrt{10^{S_{\mathrm{x,ijm}}/20}} + \sqrt{10^{S_{\mathrm{x,npq}}/20}}} \tag{6}$$

and a similar one for y_e, where $S_{\mathrm{xy,ijm}}$ and $S_{\mathrm{xy,npq}}$ are combinations of S-parameter triplets originating from Eq. (5), which also depend on the solution of g_i used.

Finally, three variants of the offsets labeled (a), (b) and (c), e.g. $(x_{e(\mathrm{a})}, y_{e(\mathrm{a})})$) are using the corresponding sets of S-parameter triplets for x and y:

$$\text{(a)} \begin{cases} S_{x,\mathrm{ijm}} = S_{32} + S_{42} - S_{43} \\ S_{x,\mathrm{npq}} = S_{14} + S_{42} - S_{21} \end{cases}$$

$$\text{and} \begin{cases} S_{y,\mathrm{ijm}} = S_{41} + S_{31} - S_{43} \\ S_{y,\mathrm{npq}} = S_{32} + S_{31} - S_{21} \end{cases} , \tag{7}$$

$$\text{(b)} \begin{cases} S_{x,\mathrm{ijm}} = S_{43} + S_{42} - S_{32} \\ S_{x,\mathrm{npq}} = S_{21} + S_{42} - S_{14} \end{cases}$$

$$\text{and} \begin{cases} S_{y,\mathrm{ijm}} = S_{41} + S_{31} - S_{43} \\ S_{y,\mathrm{npq}} = S_{32} + S_{31} - S_{21} \end{cases} , \tag{8}$$

$$\text{(c)} \begin{cases} S_{x,\mathrm{ijm}} = S_{43} + S_{14} - S_{31} \\ S_{x,\mathrm{npq}} = S_{21} + S_{32} - S_{31} \end{cases}$$

$$\text{and} \begin{cases} S_{y,\mathrm{ijm}} = S_{21} + S_{14} - S_{42} \\ S_{y,\mathrm{npq}} = S_{32} + S_{43} - S_{42} \end{cases} . \tag{9}$$

Results

As an example, Fig. 4 shows the offset for a range of frequencies calculated by Eq. (6) for $x_{e(\mathrm{a})}$. Similar results are found for the vertical plane. The periodic notches are due to the electrode geometry and excitation system (excitation via one electrode, measuring on the others). This is in agreement with the CST simulations shown in Fig. 5, which compares the case in which the excitation is done via one electrode or through the wire. Note that when the excitation is done via one electrode (red), the notches occur at around 500 MHz, in agreement with Fig. 3. However, in the real case with an electron beam the notches are displaced to around 1 GHz.

Originally the "Lambertson" offset measurement is intended to be done at some fixed frequency; however, due

ISBN 978-3-95450-176-2

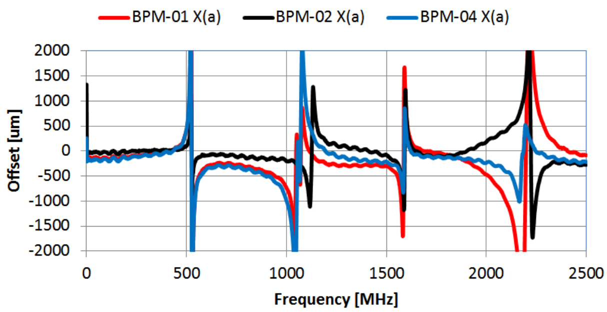

Figure 4: Horizontal electrical offset type $x_{e(a)}$.

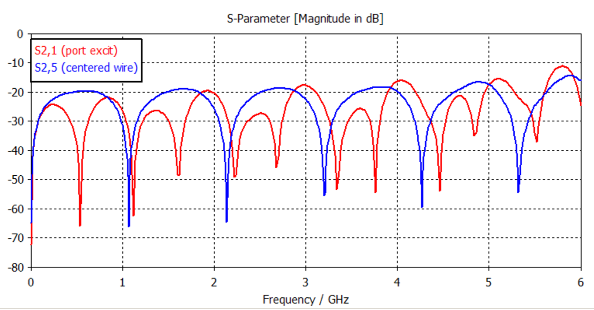

Figure 5: CST simulations exciting one electrode (red) or the wire (blue).

to aforementioned reasons, the measured offsets of the 3 striplines do not show a flat behavior at their working frequency, but rather a notch (see the zoom in Fig. 6). It therefore makes sense to take an average value for offsets in both planes between [20-200] MHz. This is shown in Table 2 for the three GBS BPMs measured so far. The electrical offsets are shown with margins taking into account the different S-parameter triplets (Eqs. (7), (8) and (9)).

The electrical offset measured this way is not affected by any systematic error due to the test bench or BPM positioning in space. However, this offset can not be compared directly with the one obtained by wire scans, because the mechanical offset measured by the wire scan is a combination of the offsets due to cable differences, reading electronics and geometrical imperfections of the BPM.

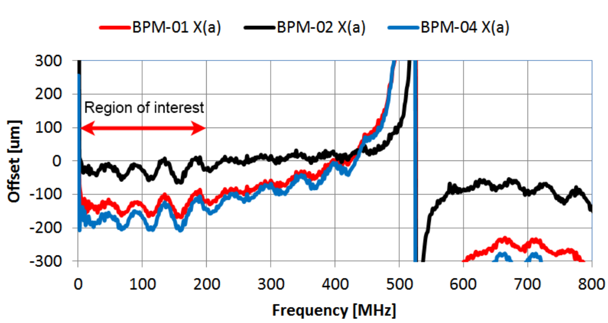

Figure 6: Horizontal electrical offset type $x_{e(a)}$ (zoom).

Table 2: Electrical Offsets Measured Using the External "Lambertson" Method

	x_e, µm	y_e, µm
BPM-01	132 ± 0	-238 ± 8.5
BPM-02	25 ± 0.15	-134 ± 10.4
BPM-04	165 ± 0.7	-157 ± 10

WIRE SCAN CHARACTERIZATION

The mechanical characterization is done via wire scanning the BPM units. The equipment and connectivity schematic is shown in Fig. 7. The BPM is placed on a test bench and a wire is pulled through its theoretical center using fiducials or other reference points/surfaces. The wire is fed by an RF signal generator and is terminated by 50 Ω at the other end. The signal, caught by the BPM electrodes, is read by *Libera Brilliance* electronics. The wire scan is done by moving the BPM in the horizontal and vertical directions using the motors in the test stand, controlled by a standard IcePap motor controller from a remote PC.

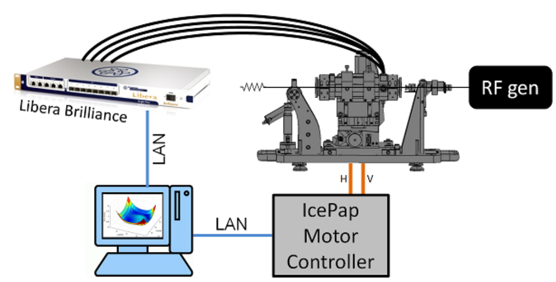

Figure 7: Schematic of lab setup and equipment connectivity for wire scanning the BPMs.

Test Bench for Wire Mapping

The ALBA engineering department has designed an ad-hoc test bench to mechanically hold the stripline BPMs for stretched wire measurements. The bench is equipped with two motors (*Micos Linear Stage LS-120*) with unidirectional repeatability of 0.1 µm for horizontal and vertical movement. The test bench ensures reproducibility of within 20 µm between BPM-to-BPM measurements. Figure 8 shows a complete 3D model of a BPM mounted on the test bench; a photo of the setup is shown in Fig. 2.

As a compromise between stress and conductivity, the wire material is chosen to be copper of 1 mm in diameter. The wire tension is controlled by the force gauge at nominal force of 120 N to minimize contribution of the sag effect on measurements. For reference, the sag values in the mid-wire position for various tension, calculated by the catenary equation, are shown in Table 3.

Table 3: Sag Value in the Mid-Wire Position

Force, N	94	100	120
Deviation, µm	8.2	7.0	6.4

ISBN 978-3-95450-176-2

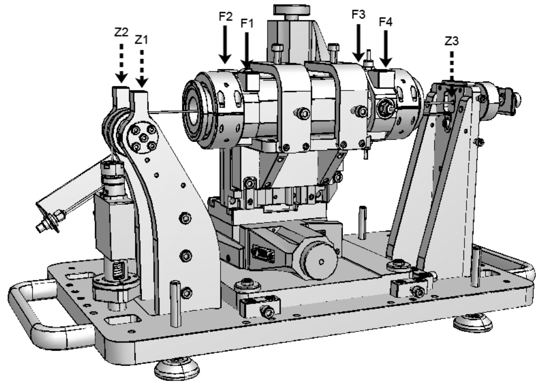

Figure 8: A complete 3D model of the test bench for ELI BPM measurements.

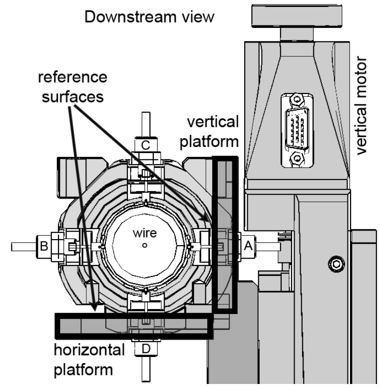

Figure 10: Positioning a BPM on an L-shaped platform by touching it with 2 reference surfaces.

Fiducial Measurements

Although the test bench ensures acceptable reproducibility of 20 µm, we have observed several mechanical issues that limit our precision to much larger values. Firstly, the BPM fiducials, labeled F1…F4 in Fig. 8 are often out of tolerances in both planes from the manufacturing criteria provided by factory certificates. As an example, Fig. 9 shows the deviations of fiducial planes as measured by the factory and by the ALBA alignment group for the vertical plane. While we generally measure slightly larger fiducial offsets, in some cases it reaches a 200 µm, and even 500 µm mismatch with respect to factory measurements.

Secondly, the diameters of some fiducial holes are out of tolerances, e.g. the 8 mm slot where the spherical mounted reflector (SMR) of the laser tracker is placed is sometimes larger by +100–200 µm (up to +400 µm in one case) with respect to +20 µm specified by the BPM drawings. This means that the horizontal position of the SMR alone can have a significant displacement.

Since its is not straightforward to align a BPM with respect to the wire by using BPM's fiducials, all BPMs are positioned on the test bench for wire mapping according to an established procedure:

a) The stretched wire is considered as the nominal zero position, referenced by the three fiducials on the test bench (Z1, Z2 and Z3, as indicated by dashed arrows in Fig. 8).

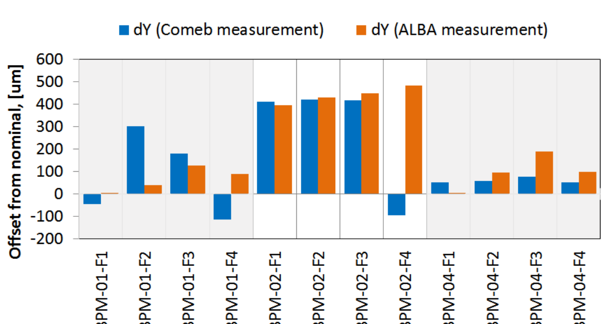

Figure 9: Fiducial position deviations from nominal in Y.

b) A BPM is placed on an L-shaped platform touching it with its two reference surfaces (bottom and right side walls), Fig. 10. The geometrical positions of the planes, manufactured with 20 µm precision, is known from the drawings with respect to BPM's origin. The pitch (20 µm in the horizontal plane) and yaw (10 µm in the vertical plane) errors of the platform are also measured.

c) The L-platform, controlled by the motors, is placed such that its position with respect to the wire resembles the nominal distances from the BPM side walls to its center. This platform's position (motor settings) is defined as the *homing position*, meaning the wire here is at $(x, y) = [0, 0]$ which is same for all BPMs.

d) When the BPM is positioned on the platform its fiducial positions are measured with the laser tracker with respect to the stretched wire. Any tilt, yaw or roll imperfection of the particular BPM is encoded in its fiducial coordinates with respect to the stretched wire.

e) After these considerations and measurements the BPM is mapped.

Wire Mapping

Wire mapping is done by exciting the wire to a continuous wave excitation of 499.654 MHz and moving the motors to scan the BPM around the wire. The motor positions are then translated into wire movements. The electrode voltages are read by the Libera with averaging over 1024 samples and processed by DOS equations with $k_x = k_y = 10$:

$$x_{\text{bpm}} = k_x \times \frac{V_3 - V_1}{V_3 + V_1} \tag{10}$$

$$y_{\text{bpm}} = k_y \times \frac{V_2 - V_4}{V_2 + V_4} \tag{11}$$

Figure 11 shows the result of wire scanning of one of the first BPM units, including the error map defined as absolute distance between the measured and actual wire positions. The measured map offset (x_w, y_w) is relative to the wire at its homing position. It includes the mechanical and the "Lambertson" electrical offsets, hence $x_{\text{offset}} = x_w$ and $y_{\text{offset}} = y_w$.

ISBN 978-3-95450-176-2

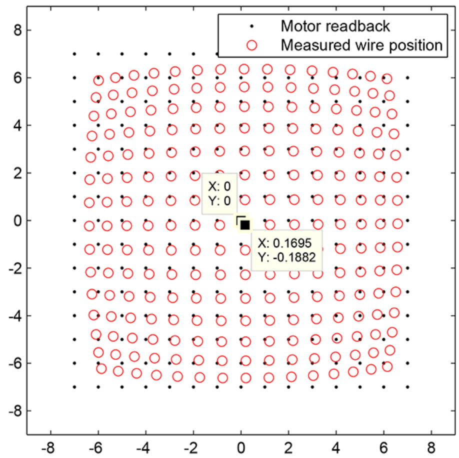

(a) BPM response map measured by wire scanning within ±7 mm. The central point corresponds to the wire homing position (0, 0). Its electrode readings correspond to the mechanical offset of the BPM.

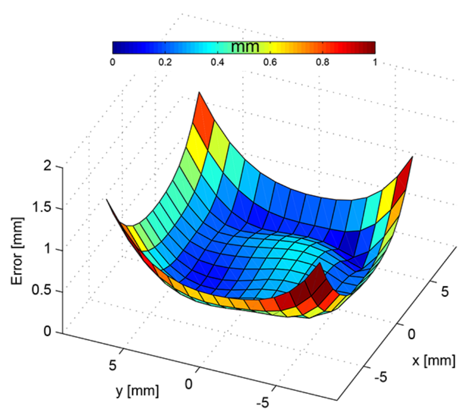

(b) Error of the response map in mm with respect to motor read-back positions.

Figure 11: Wire mapping the BPM-02 of the ELI-NP.

The repeatability of wire scans was also checked by measuring the map center with respect to the homing position by repeating the dismount-mount cycle of same BPM several times. This way the map center was usually measured within 50 µm in both X and Y for all BPMs.

Results

Table 4 lists the results of the offsets measured by wire scanning. These values include both the electrical offsets, shown in Tab 2, and mechanical manufacturing imperfections. Besides, while the theoretical value of $k_{x,y} = 10$, its

Table 4: Offsets Measured Using the Wire Scan

	k_x	k_y	x_w, µm	y_w, µm
BPM-01	9.57	9.51	146 ± 39	−19 ± 16
BPM-02	9.47	9.45	114 ± 14	−210 ± 48
BPM-04	9.57	9.54	256 ± 16	−139 ± 34

values, measured in 3 × 3 points within ±1 mm, are also shown.

CONCLUSIONS

Using different techniques, we have measured the electrical and the mechanical offsets of several BPM units for the future Gamma Beam System of the ELI Nuclear Physics facility.

For the electrical offset an external calibration, called the "Lambertson" method, was applied, estimating the geometrical asymmetry of the stripline electrodes. For measuring the mechanical offset and the sensitivity factors of the BPMs we have designed and built a motorized test bench for wire mapping the BPM units. The obtained sensitivity factors have shown to be smaller than their theoretical value. Fiducial coordinates of the BPM units were also measured with the laser tracker and found to be significantly different from the factory-provided values.

The mechanical offsets, referenced with respect to BPM's fiducial points, are due to all possible mechanical effects and they will be taken into account when installing the BPM units in the GBS Linac oF ELI-NP facility.

ACKNOWLEDGEMENTS

We would like to thank the alignment team of ALBA, M. Llonch and J. Landera for their time and extensive alignment measurements.

REFERENCES

[1] G.R. Lambertson, "Calibration of Position Electrodes using external measurements", LSAP Note-5, LBL, 1987.

[2] Y. Chung, G. Decker, "Offset calibration of the Beam Position Monitor Using External Means", Proc. of 1991 Acc. Instrum. Workshop.

[3] A. Olmos, M. Alvarez and F. Perez, "Beam position monitors characterization for ALBA", TUPSM075, Proceedings of BIW10, 2010.

ISBN 978-3-95450-176-2

LIMITATIONS AND SOLUTIONS OF BEAM SIZE MEASUREMENTS VIA INTERFEROMETRY AT ALBA

L. Torino, U. Iriso, ALBA-CELLS, Cerdanyola del Vallès, Spain

Abstract

The interferometry beamline at ALBA had several limitations which have been overcome over the past years until currently, beam size measurements are successfully performed using this technique. The main limitation has been related to vibrations in the light wavefront transportation along the beamline. Several counter-measures have been taken to overcome these limitations, related both to the software analysis and the mechanical setup, where the conventional double slit system is substituted by a double pinhole in order to obtain more light and a better interferogram. This report describes the current interferometry setup at ALBA, and show some results.

INTRODUCTION

After two years, interferometry is a reliable technique to measure the beam size at the ALBA storage ring. The diagnostic beamline Xanadu has been updated, analyzed and optimized to achieve good horizontal and vertical results using the this technique [1].

The main parameters related with the beam size and the synchrotron radiation characteristics are listed in Table 1.

Table 1: ALBA Lattice Parameters

	x	y
β	0.299 m	25.08 m
Dispersion	0.04 m	0 m
Energy spread	0.001 01	
Emittance	4.6 nm	0.023 nm
Beam size	53.6 µm	23.9 µm

Several limitations due to the beamline layout have been overcome theoretically and practically. In this report the limitations and the solutions applied are described, and the results for both horizontal and vertical beam size measurements are presented.

MAIN LIMITATIONS

ALBA diagnostic beamline, Xanadu [2], takes the synchrotron radiation from a bending magnet. The light is selected by a photon shutter located at 1.684 m from the source point with an aperture of ±3.2 mm in the horizontal plane and ±5.5 mm in the vertical. After the shutter the light travels for roughly 7 m where a $\frac{\lambda}{8}$ mirror extracts only the upper lobe of the visible radiation. The mirror is motorized and approaches the orbit plane (where the majority of the x-rays are concentrated) up to a distance of 7 mm, in order to maintain the heat load low. The radiation is extracted through a vacuum window $\left(\frac{\lambda}{10}\right)$ and transported outside the tunnel in the experimental hutch through an optical path of 7 mirrors (Thorlabs, 4 ", $\frac{\lambda}{10}$). The mirrors are located "in-air".

The full beamline had been updated in 2014. The improvements of the quality of the in-vacuum mirror, of the extraction window and of all the mirrors of the optical path, already gave the possibility to obtain some preliminary results, as presented in [3].

In any case, the layout of the beamline still presents two mayor limitations.

Diffraction

The footprint of the light reaching Xanadu is strongly affected from Fraunhofer diffraction [4]. The effect is due to the first horizontal cut of the light performed from the photon shutter (vertical strips), and the vertical one due to the extraction mirror (horizontal strips). An SRW [5] simulation of the footprint is shown in Fig. 1.

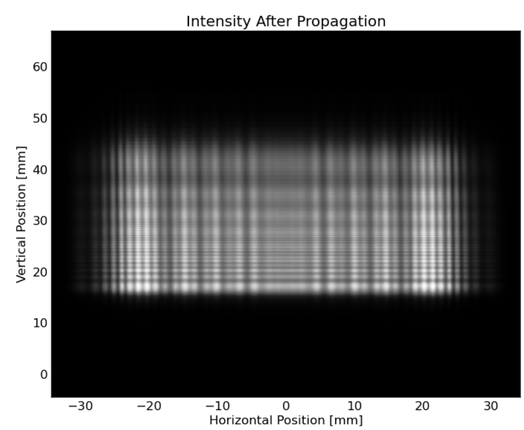

Figure 1: SRW simulation of the footprint reaching Xanadu diagnostic beamline.

When trying to perform interferometry, the use of long rectangular slits allows the selection of a large number of Fraunhofer fringes. The relative phase of these fringes is not necessarily the same and this provokes a modification in the interferogram that leads to a loss of contrast. A solution to this problem was found by using pinholes instead of slits, and adapting the theoretical formula describing the interferogram for this setup.

Vibrations

The second limitation is due to the fact that almost the whole beamline is in-air. This originates vibration in the optical components, which are sensible to air turbulence. This effect provokes changes in the interferogram characteristics and a rigid displacement of the centroid of the image.

ISBN 978-3-95450-176-2

Using an exposure time of 100 µs, and a fast acquisition camera working at 50 Hz, it was possible to reconstruct the spectrum of the vibration following the displacement of the interferogram centroid. The result of the FFT of the displacement in the horizontal (red) and vertical (blue) direction with respect to time is shown in Fig. 2: vertical vibration looks much more problemtic and major peaks are present at 10 and 14 Hz.

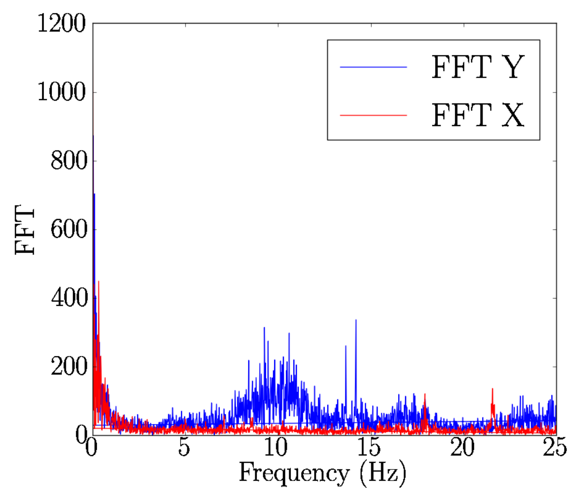

Figure 2: FFT of the displacement of the centroid of the interferogram in the horizontal (red) and vertical (blue) direction.

The problem can be reduced by lowering the exposure time of the CCD camera during the image acquisition. On the other hand, this decreases the quantity of light reaching the CCD sensor and the interferogram might be not clear enough the measure.

To overcome this problem, a dedicated algorithm was implemented to match more images together to improve the dynamic range of the measurement.

INTERFEROMETRY USING PINHOLES

The standard interferometry set-up in Accelerator physics is composed by a double slit system, as introduced by T. Mitsuhashi [1, 6]. Replacing the slits with pinholes forces to an adjustment of the formula, used by Mitsuhashi to fit the results.

The envelope of the interferogram is given by the Fourier transform of the shape of the aperture generating the interference [4, 7]. In the Mitsuhashi formula the envelope is parametrized by a sinc(x), being this the Fourier transform of a rectangle. In the case of pinhole the resulting function is a Bessel function of the first type J_1 and the formula for the interferogram becomes:

$$I = I_0 \left\{ \frac{\mathrm{J}_1\left(\frac{2\pi a x}{\lambda f}\right)}{\left(\frac{2\pi a x}{\lambda f}\right)} \right\}^2 \times \left\{ 1 + V \cos\left(\frac{2\pi D x}{\lambda f}\right) \right\}, \quad (1)$$

where I_0 is the intensity of the interferogram, a is half diameter of the pinhole, f is the focal distance of the optical system used, λ is the radiation wavelength, V is the visibility $\left(\simeq \frac{I_{Max}-I_{min}}{I_{Max}+I_{min}}\right)$, and D is the distance between the pinhole centers. Obtaining V from the fit, and using the distance between the source point and the pinholes, L, the beam size is computed as:

$$\sigma = \frac{\lambda L}{\pi D} \sqrt{\frac{1}{2} \ln \frac{1}{V}}. \quad (2)$$

The use of pinholes instead of slits makes the alignment easier, and allows to select more uniform zones of the footprint. As a consequence, less Fraunhofer fringes are selected, and the contrast of the interferometry results improves.

For this reason the ALBA experimental set-up is composed by a double pinhole system. The diameter of the pinholes is 3 mm (good results were obtained with pinholes up to ≃ 6 mm), and the separation between them is 16 mm (or larger if using larger pinholes).

CCD EXPOSURE TIME

An intuitive and convenient way to reduce the effect due to the beamline vibrations and the air turbulences is the reduction of the exposure time of the CCD camera, which reduces the number of oscillations during the image acquisition (as well as the superposition of artificially shifted interferograms).

This behavior is well summarized in the plot in Fig. 3. The plot shows the results for the horizontal and vertical beam size, taken in the same conditions at different exposure times.

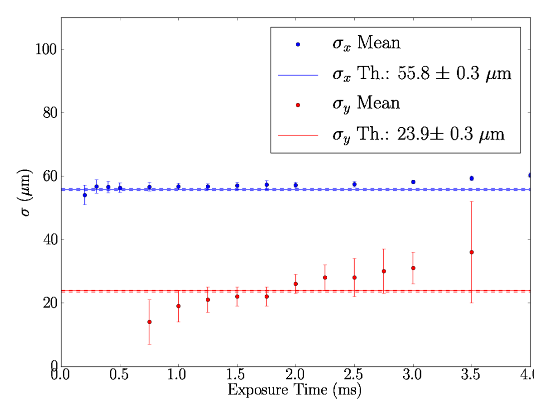

Figure 3: Horizontal (blue) and vertical beam size as a function of the exposure time. Solid lines represent the expected value. Error bars corresponds to statistical measurement fluctuations.

In general, for low exposure time, the measured beam size is smaller with respect to the expected, and the statistical error bar is quite big since the fit is not able to properly reconstruct the image. At high exposure time the measured beam size is larger with respect to the theoretical one, since several shifted interferogram are summed up during the long acquisition time, affecting the contrast. The effect is much

ISBN 978-3-95450-176-2

more evident for the vertical measurements with respect to the horizontal, this is mainly due to two reasons. First the horizontal beam size is almost double of the vertical, therefore the expected visibility for the horizontal measurements is smaller and does not require such a high contrast for the images. Second, the vibration of the optical path due to the Xanadu layout are much stronger in the vertical direction (as shown in Fig. 2).

The reasonable choice for the exposure time is to be chosen among the ones in the plateau in Fig. 3, where the image distortion due to vibrations is minimized. For this reason, the usual exposure time set for beam size measurements is 1.5 ms.

HORIZONTAL BEAM SIZE MEASURE

An example of interferogram for horizontal beam size measurements is shown in Fig. 4. To obtain the final result, the projection of the central part (10 rows) of the interferogram is fitted using Eq. (1). The resulting visibility is then plugged in Eq. (2) and the beam size is obtained.

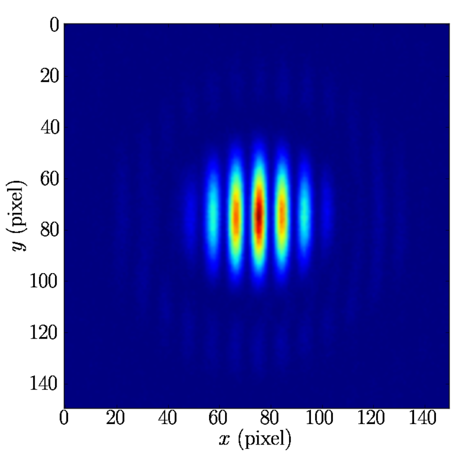

Figure 4: Horizontal Interferogram.

An alternative way to measure the beam size with the interferometer technique is to perform a scan of the distance between the pinholes, D. This parameter is indeed the Fourier conjugate of the beam size: inverting Eq. (2) one obtains:

$$V = e^{-2\pi \frac{\sigma^2 D^2}{\lambda^2 L^2}}. \quad (3)$$

Considering the visibility as a function of D the expected result is a Gaussian. Fitting the results letting the beam size as a free parameter, it is possible to obtain σ.

Depth of Field

It is interesting to study with this method the effects of the Depth of Field due to the photon shutter aperture (±1.9 mrad). Because this aperture, the light reaching Xanadu is creating a blurring of the image due to the curvature of the trajectory. The bending radius of the magnet producing the radiation is 7.05 m, that leads to blurring of ±13 µm. This incoherent effect can be observed when measuring the horizontal beam size using the pinholes distance scan.

Figure 5 shows the visibility as a function of the distance between the pinholes. The data (red dots) are fitted with a Gaussian that take into account the effect of the Depth of Field:

$$V = e^{-2\pi \frac{\sigma^2 D^2}{\lambda^2 L^2} + \sigma^2_{DoF}}. \quad (4)$$

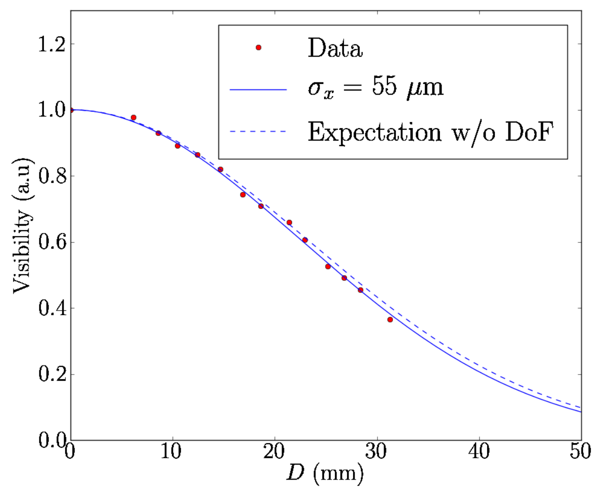

Figure 5: Visibility as a function of the distance between pinholes.

The solid line is the result of the fit using Eq. (4) and fixing σ_{DoF} =26 µm. The dashed line is the theoretical curve (Eq. (3)) without the effects of the depth of field, and using as σ the result of the previous fit. The fit is providing the expected results for the horizontal beam size. This shows that the depth of field must be taken into account when performing this measurements.

Vertical beam size measures are not affected by this effect since the light is not coming from the orbit plane.

VERTICAL BEAM SIZE MEASURE

The limitations of Xanadu beamline were mostly affecting the vertical beam size measure, but thanks to to the adjustments it is now possible to achieve reliable results.

Coupling Scan

To prove that the vertical interferometry beam size measurements are effective, scans of the beam coupling are performed. Varying the current in the skew magnets, the beam coupling varies as well as the vertical beam size.

Vertical beam size measurements are performed for several couplings and the results are compared to the one obtained with the x-rays pinhole. The pinhole and the Xanadu beamline take the synchrotron radiation from the two consecutive dipoles, at different locations inside the magnet. During normal operations, as well as during the coupling

ISBN 978-3-95450-176-2

scan, the vertical and the horizontal beam size differs one from the other of a few μm.

As an example, in Fig. 6, the vertical beam size of the pinhole (in blue) and of the interferometry (in red) are plotted as a function of the beam coupling.

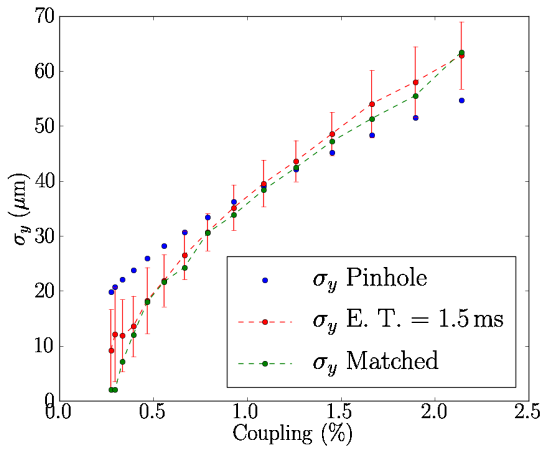

Figure 6: Vertical beam size measured with the pinhole (blue), with the interferometry (red), and interferometry with the application of the matching algorithm, as a function of the coupling.

The interferometry measurements follow nicely the one of the pinhole when the coupling is varying. Several coupling scans were performed and in all the cases the two curves intercept each other around a coupling of 1.2%. The ALBA operation coupling is around 0.5% and, as expected, the interferometry beam size is smaller with respect the pinhole one. After the 1.2% coupling the interferometry measurements are larger with respect to the one of the pinhole.

Results of these tests prove the effectiveness of the interferometry measurements performed at ALBA.

Matching Algorithm

In order to keep the exposure time as low as possible, an algorithm to superimpose several interferograms was implemented in Python.

The experimental set-up is the same that the one described in previous case. The exposure time was set to 100 μs, the minimum given by the CCD, and data were acquired for 1 minute at 50 Hz to obtain 3000 interferograms.

The raw interferogram at 100 μs of exposure time is presented in Fig. 9a. Data are very noisy and it is not possible to obtain a good result by fitting.

The algorithm takes the first interferogram acquired as reference, computes the correlations between this and the others, and shifts them of the resulting quantity. Figure 7 presents the horizontal and vertical distances the interferograms needed to be shifted in order to be matched with the reference.

The images are shifted until the interferograms can all be superimposed with the proper centroid match.

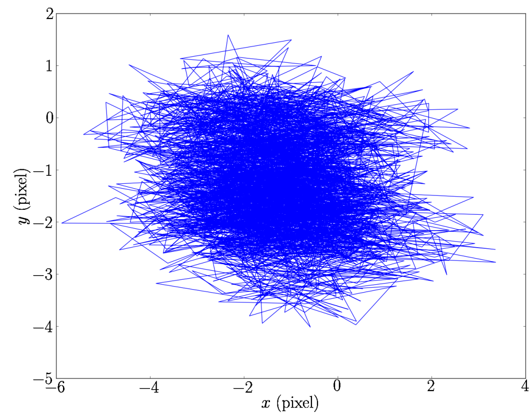

Figure 7: Distribution of the shifts to be applied to match the images.

The data analysis is done considering the projection of the centrals columns of the interferogram. Figure 8 shows the 3000 projections without (blue) and with (red) the application of the matching algorithm.

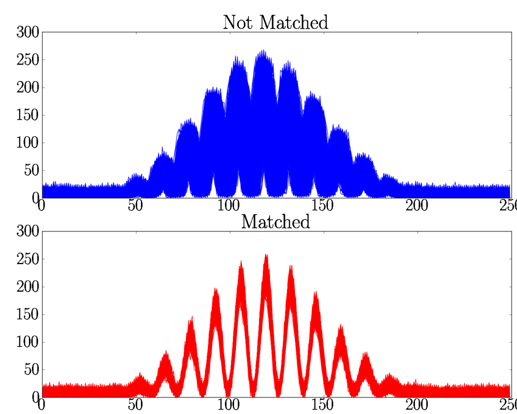

Figure 8: Plot of the 3000 projections without (blue) and with (red) the application of the matching algorithm.

It is clear that summing the projections without the application of the algorithm leads to a loss of contrast and a consequent reduction of the visibility, while for the projections of the matched images the effect is strongly reduced.

The interferogram as sum of the unmatched images is presented in Fig. 9b. The result of the fit provides a larger beam size because of the loss of contrast. The result obtained by applying the algorithm is shown in Fig. 9c. The matching algorithm improves both dynamic range and contrast of the final interferogram.

In order to prove the algorithm performance a coupling scan was carried out and the matching algorithm was applied to reconstruct the interferograms at different coupling.

Green dots in Fig. 6 present the beam size using the matching algorithm. Also in this case the obtained values are consistent.

ISBN 978-3-95450-176-2

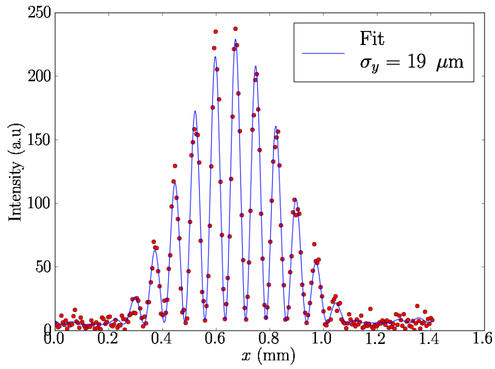

(a) *Single acquisition.*

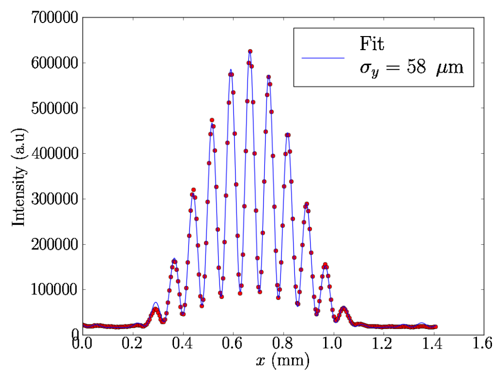

(b) *Not matched.*

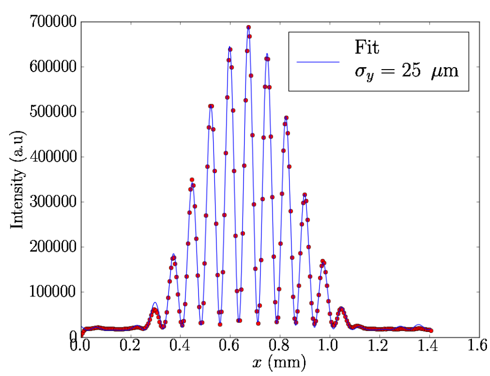

(c) *Matched.*

Figure 9: Fit of the interferograms for different acquisition methods.

CONCLUSION

After a period of commissioning the beam size measurements using interferometry are finally fully reliable at ALBA. The use of pinholes instead of slits reduced the loss of contrast due to the Fraunhofer diffraction. Measurements showed that it is possible to balance the loss of contrast due to vibrations and the low dynamic range of the camera, by reducing the exposure time of the image acquisition accordingly.

It was possible to study the effect of the incoherent depth of field on the horizontal beam size measurements analyzing the visibility distribution as a function of the pinholes separation. On the other hand the efficiency of vertical beam size measurements was proved performing coupling scans and verifying that interferometry was able to reproduce the result of the pinhole. Finally an algorithm was developed in order to match images displaced by vibration acquired at very low exposure times. Also in this case coupling scans were performed to prove the goodness of the algorithm.

ACKNOWLEDGMENT

This work owns a lot to J. Nicolás for the enlightening discussions on optics. Thanks also to S. Blanch for the development of the fast acquisition software of the CCD camera and all the technical staff of ALBA.

This project is funded by the European Union within the oPAC network under contract PITN-GA-2011-289485.

REFERENCES

[1] T. Mitsuhashi, “SR Monitor – Special topics”, BIW2012, Newport, April 2012, TUAP02 (2012)

[2] U. Iriso et al., “Diagnostics during the ALBA SR commissioning”, DIPAC-2011, Hamburg, May 2011, TUOA02 (2011)

[3] L. Torino et al., “Beam Size Measurements using Synchrotron Radiation Interferometry at ALBA”, IBIC-2014, Monterey, September 2014, TUPF23 (2014)

[4] M. Born and E. Wolf, *Principles of Optics, 7th edition*, (Cambridge University press, 2006)

[5] O. Chubar et al., “Accurate and Efficien Computation of Synchrotron Radiation in the Near Field Region”, EPAC-1998, Stockholm, June 1998, 1177 (1998)

[6] T. Mitsuhashi, “Measurement of small transverse beam size using interferometry”, DIPAC’2001, Grenoble, May 2001, IT06 (2001)

[7] A. Glindemann, “Introduction to Spatial Interferometry” `https://www.eso.org/sci/facilities/paranal/telescopes/vlti/tuto/tutorial_spatial_interferometry.pdf`

DESIGN OF A NEW SUPER-HETERODYNE MICROTCA.4 BPM AND LLRF REAR TRANSITION MODULE (RTM) FOR THE EUROPEAN SPALLATION SOURCE

A. Young, SLAC, California, USA
H. Hassanzadegan, ESS, Lund, Sweden

Abstract

The 5 MW European Spallation Source (ESS) is a long pulsed source based on a high power superconducting LINAC. In order to achieve this high level of performance, the beam position measurement system needs to measure the beam position, phase and intensity in all foreseen beam modes with a pulse rate of 14 Hz, duration of 2.86 ms and amplitude ranging from 5 mA to 62.5 mA. We have designed a general purpose Beam Position Monitor (BPM) front-end electronics that has a dynamic range of 70dB. The front-end uses the MicroTCA (Micro Telecommunication Computing Architecture) for physics platform that consists of a 16-bit 125 MSPS ADC module (SIS8300L/2 from Struck) that uses the Zone 3 A1.1 classification for the RTM. This paper will discuss the design of this new RTM that includes eight channels of super-heterodyne receivers, two channels of DC-coupled inputs to measure klystron voltage and current, one vector modulator that modulates the LLRF output. The RTM communicates with the AMC FPGA using a QSPI interface over the zone 3 connection.

INTRODUCTION

The Beam Position Monitor (BPM) system of the ESS linac will use BPM sensors of different sizes and types. It is planned to use small-aperture stripline BPMs in the low-energy linac including the Medium Energy Beam Transport (MEBT) and Drift Tube Linac (DTL) sections. The BPMs of the cold linac including the Spoke, Elliptical and the downstream sections such as LogLeg, Dumpline and Accelerator-to-Target (A2T) may be of electrostatic button or stripline type. These two types are currently being studied in terms of performance, cost, space requirements etc. before a decision will be eventually taken on which type to use.

Most of the BPMs will belong to the Linac Warm Units (LWUs) that will be installed in between each two successive cryomodules. The LWU will include two quadrupoles, and in the current design, there is a BPM close to each quadrupole [1]. The BPM number per LWU may however be decreased to one in the next revisions that is mainly due to space limitations. The other alternative would be to use two longitudinally-short BPMs with welded feedthroughs to resolve the space limitation issue.

In order to minimize potential disturbances from nearby RF sources, BPM signal processing will be done at opposite frequency with respect to RF. This means the second harmonic (i.e. 704.42 MHz) of the BPM signal will be processed in the Spoke and upstream sections while the fundamental harmonic (i.e. 352.21 MHz) will be processed in the sections downstream to the Spokes. A direct consequence of this is that for beam phase measurements, the BPM and Low Level Radio Frequency (LLRF) systems will need phase reference signals with opposite frequencies.

The BPMs need to have an overall accuracy of +/-200 um and a resolution of 20 um with the nominal beam current of 62.5 mA and pulse width of 2.86 ms. The BPMs also need to successfully measure the beam position (possibly with a lower S/N ratio) under off-optimal conditions such as with a debunched [2] and low-current beam of 6.25 mA and pulse width of 10 us that is foreseen for linac commissioning. Calculations show that under the worst-case scenario, the BPM voltage with the off-optimal beam can be lower than the nominal voltage by three orders of magnitude.

The BPM button voltage is expected to decrease to less than one-half from the beginning to the end of the linac [1]. This is due to the beam velocity increase and the changes in the BPM size and type. Despite these voltage level variations, the electronics of all the BPMs will be based on the "ESS centralized design". The BPM electronics and firmware of the low-energy linac will however be slightly different from those of the high-energy linac because of the RF frequency jump at the end of the Spoke section.

The BPMs will also be used to measure the absolute and relative beam phase. The phase information will be needed for RF tuning as well as beam energy measurements based on the beam Time Of Flight (TOF).

As the LLRF and BPM systems have somewhat similar requirements, an effort is being made to maximize synergy by using same/similar electronics and firmware for both systems.

ESS BPM/LLRF FRONT-END REQUIREMENTS

Both the BPM and LLRF front-end designs are based on down-mixing to Intermediate Frequency (IF) and sampling in In-phase / Quadrature-phase (I/Q) or near-IQ to measure the amplitude and phase of the RF input signal. These signals will then be FPGA processed to calculate the beam position, phase and intensity (BPM system) or to control/regulate the cavity voltage (LLRF system). A clock frequency of 88.0525 MHz (this is one-

ISBN 978-3-95450-176-2

forth of the bunch frequency and it is locked to RF) is already available from the ESS timing system. Therefore, for I/Q sampling, the IF frequency needs to be 22.013125 MHz. With respect to near-IQ sampling, a clock frequency of 110.065625 MHz may be used at later stages of the development.

The ADC clock and the LO for down-mixing will be generated and synchronized to RF using a new MTCA.4 module that is currently under detailed design. The LO generator, the RTM and the digitizer will be all hosted by the same MTCA.4 crate.

Both the BPM and LLRF designs are based on a RTM/digitizer with 10 ADC input channels. In the case of BPMs, 9 AC-coupled inputs will be needed to measure signals from two successive BPMs, being 8 for the electrode signals plus one for the phase reference. In the LLRF case, 8 AC-coupled inputs will be needed to measure the cavity/waveguide field in each RF plant, and 2 DC-coupled inputs will be needed to measure the modulator current and voltage. Moreover, the LLRF will need one Vector Modulator (VM) output on the RTM to control the RF amplifier.

The RF input channels need to be optimized for 352.21 MHz or 704.42 MHz depending on location in the linac.

As there is a possibility that the final BPM/LLRF systems will use a combination of off-the-shelf and custom-made RTMs, care should be taken to have -to the extent possible- same connectors on both RTM types. That will then facilitate RTM connection to other modules and reduce cost as well. Also, the input voltage range of the two RTM types need to be similar. Assuming that the RTM is configured for 0 dB net gain/attenuation, then the maximum input needs to be about +/- 1 V_{peak} (i.e. 10 dBm).

The overall gain/attenuation of the front-end card needs to be controlled over a wide range of typically larger than 30 dB. This is mainly to adapt the BPM voltage level to the ADC input range. Also, in order to improve the S/N ratio with a weak BPM signal, it might be useful to amplify the electrode voltage before the mixer, because the mixer has a large Noise Figure of 16 dB.

Both the BPM and LLRF systems have stringent requirements on S/N ratio. Current version of the LLRF requirements mandates that the amplitude and phase of the RF voltage in the superconducting cavities be stabilized to 0.1% and 0.1 degree over the pulse length (these stability requirements are 0.2% and 0.2 degree with the normal-conducting cavities). Also, in the BPM case, the position and phase need to be measured with a resolution of 20 um and 0.2 degree respectively. In order to achieve these, the S/N ratio and the channel-to-channel isolation need to be better than 70 dB.

Shafer equations [3] have been used to calculate the button voltage. This is estimated at 170 mV_{peak} at high energy with the nominal beam being at the centre of the beam pipe. Considering cable attenuation, thermal noise and the RTM noise figure, the expected S/N ratio at the input of the digitizer is about 67 dB at 352 MHz. Using Eq. 1, the resultant BPM resolution will be about 10 um that meets the requirements.

$$\sigma_X = \frac{b}{2} \cdot \frac{\sqrt{2}\sigma_V}{2V} = \frac{b}{2\sqrt{2}} \cdot \frac{1}{\sqrt{SNR}} \qquad (1)$$

Also, it is foreseen to provide the BPM/LLRF electronics with clean LO, phase reference and clock signals. Additive jitter (10 Hz – 10 MHz) of these signals will be significantly better than 1 ps.

SUPER-HETERODYNE RTM DESIGN

Super-heterodyne RTM design as illustrated in Fig. 1. The design of the super-heterodyne was chosen because the ADC input bandwidth would attenuate the 352MHz by 10dB thus effecting the signal to noise ratio. The super-heterodyne circuit uses two programmable attenuator one to prevent saturation at the input and a second attenuator after the amplifier to prevent saturation of the mixer. The output of the mixer is converted to single ended to amplify the signal and filter mixing harmonics. The specification of the LTC5577 requires that the heterodyne be a “High-Side” mixer. This means that the f_{lo} is greater than $f_{rf.}$ [4]. This mixer has a broad range of operating frequencies (300MHz -6GHz). To insure that the mixer appears to be 50 ohms at 352MHz a matching circuit for the RF has been carefully tuned. The output of the mixer is a 100 ohms differential. A 2:1 transformer was added to provide gain and IF filtering. An ADC matching circuit was added to provide known impedance over the zone 3 connection. The design of the LO distribution is a simple design using 90^0 hybrids. This was done so that any reflection would be terminated in the isolation port. In the next version a full PLL circuit would be added to derive the LO from the master RF.

To communicate with the RTM a QSPI interface was chosen to provide good noise isolation and an easy way to write and read back attenuator, board health and switch values. This interface has been used on the Pohang, LCLS BPM system [5]. Figure 2 shows a photo of the fabricated RTM.

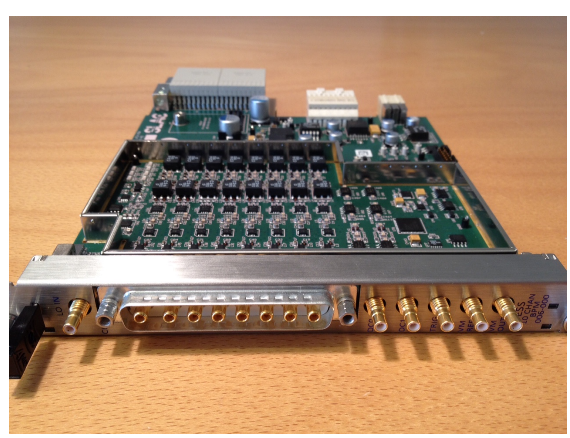

Figure 2: Photo of the RTM.

ISBN 978-3-95450-176-2

RTM TEST PLAN

As the 352 MHz super-heterodyne RTM is a new and complex design, it may need to go through a test procedure before it is installed in a crate that is populated with other modules and used for some RF signal measurements. The RTM was designed with a way to test some active components (power supplies, opamps, amplifiers) by using a header to supply 12V. This will also be used to measure the current of the board and calculate power of the module. The test procedure should typically start with checking the power lines and also verifying that the design and manufacturing is free from any errors.

The parameters that are of significant importance for both BPM and LLRF include those that have a large influence on resolution and accuracy. This includes ex. S/N ratio, channel-to-channel cross-talk, and third-order intercept using two-tone measurement technique. These measurements check dynamic range, noise from adjacent channels, and linearity and temperature dependencies on each channel. Also, it is important to make sure that the RTM can be successfully operated within its attenuation range, and the LO, clock and trigger sources configured as desired. In order to verify these, an FPGA code and a software driver will be needed. These are basically to control the two on-board attenuators as well the RF switches.

It is also foreseen to test the RTM later on a BPM test bench that is already available at ESS. An RF signal generator will then be used to generate a 352.21 MHz sinusoidal current going through a wire that will emulate the beam. The induced voltages on a prototype BPM will then be band-pass filtered and fed into the RTM. These signals will get down-mixed to 22 MHz in the RTM, and then digitized and FPGA processed in the digitizer card to calculate position, phase and intensity.

Similar tests will be done in parallel by the LLRF group using a LLRF prototype connected to a mock-up pillbox cavity.

FUTURE RTM MODIFICATIONS

Due to the RF frequency jump at the end of the Spoke section, and as the BPM and LLRF requirements are slightly different, 4 variants of the RTM will be ideally needed for the ESS linac. These are summarized in Table 1 (current design is variant 3).

Table 1: Summary of BPM/LLRF RTM requirements

	Var.	Freq. [MHz]	No. of AC inputs	No. of DC inputs	No. of VM outputs
BPM	1	352	10	0	0
	2	704	10	0	0
LLRF	3	352	8	2	1
	4	704	8	2	1

After the performance of the current RTM has been verified, a decision may be taken to proceed with the other variants as well.

SUMMARY AND OUTLOOK

Over the past two years, SLAC and ESS Beam Instrumentation group have made a successful collaboration to design a new super-heterodyne front-end RTM for the ESS BPM and LLRF systems. The design has been done by SLAC based on the ESS requirements. A pre-series of the RTM has recently become available, and preliminary tests are being planned before using the RTM for RF signal measurements on BPM and LLRF systems. The current RTM is in principle an ideal choice for the LLRF systems of the low-energy linac in terms of frequency and the number of the AC- and DC-coupled input and vector modulator output ports. After the RTM performance has been successfully verified in practice, a decision may be taken to go ahead with other RTM variants, thus fulfilling both the BPM and LLRF requirements in the low-energy as well as the high-energy linac.

REFERENCES

[1] H. Hassanzadegan et. al., THPME166, proc. IPAC2014
[2] H. Hassanzadegan et. al., TUPC13, proc. IBIC2013
[3] R. Shafer, Beam Position Monitoring, Los Alamos National Laboratory, 1990
[4] Linear Technology datasheet http://cds.linear.com/docs/en/datasheet/5577f.pdf
[5] C. Xu et. al., WEPD17, proc. IBIC2014

ISBN 978-3-95450-176-2

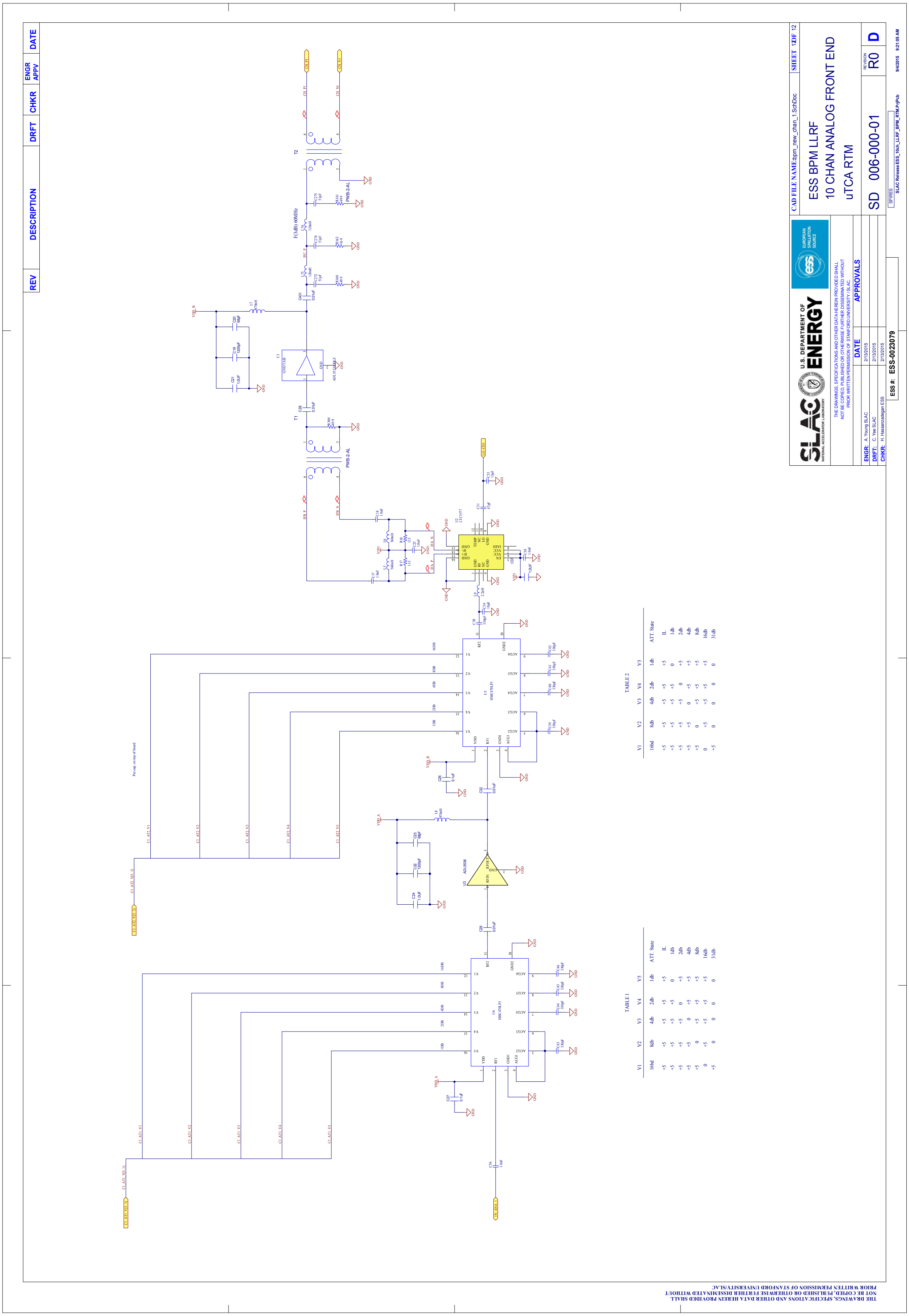

Figure 1: Super-heterodyne circuit.

WIRE SCANNERS AND VIBRATIONS – MODELS AND MEASUREMENTS

Juan Herranz[123], Bernd Dehning[1], Ewald Effinger[1], Jonathan Emery[1], Ana Guerrero[1]
Carlos Pereira[1], Ana Barjau[2]
[1]CERN, Geneva, Switzerland
[2]Universitat Politécnica de Catalunya, Barcelona, Spain
[3]Proactive Research and Development, Barcelona, Spain

Abstract

The new fast wire scanner foreseen to measure small emittance beams throughout the LHC injector chain will have a wire travelling at a speed of up to 20 m.s^{-1}, with a requested wire position measurement accuracy in the order of a few microns. The vibration of the thin carbon wires used has been identified as one of the major error sources on the wire position accuracy. One of the most challenging and innovative developments in this project has been the work to quantify the effect of wire vibrations and fork deformation. The measurement strategy for the former is based on the piezo resistive effect of the wire itself, while the deflection of the fork supporting the wire has been measured by semiconductor strain gauges. Dynamic models of the wire and fork have been created to predict the behaviour of the fork-wire assembly and will be used for its optimisation. This contribution will discuss the measurement setup and the model development as well as their comparison. In addition it will show that this technology can easily be implemented in current operating devices without major modifications.

INTRODUCTION

A wire scanner is an electro-mechanical device which measures the transverse beam profile in a particle accelerator by means of a thin wire moving rapidly across the beam [1]. The intersection of the wire and the beam generates a cascade of secondary particles. Those particles are intercepted by a scintillator, coupled with a photomultiplier, which measures the intensity of the light generated by the crossing particles (Fig. 1). The wire position is typically measured with a precision rotary potentiometer. By synchronising the digitised potentiometer and the scintillator photomultiplier signals it is then possible to reconstruct the transverse beam profile.

In order for the wire to reach a suitable speed when it crosses the beam, the actuator has to provide a motion which consists of an acceleration phase, a constant speed plateau and a deceleration phase (Fig. 2).

The peak acceleration values will vary depending on the peak speed required, the length of the fork, the angular travel available for the complete motion and the motion pattern parameters.

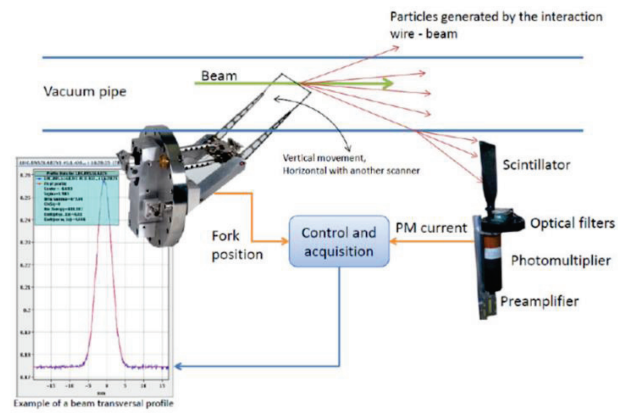

Figure 1: Schematic of the wire scanner instrument.

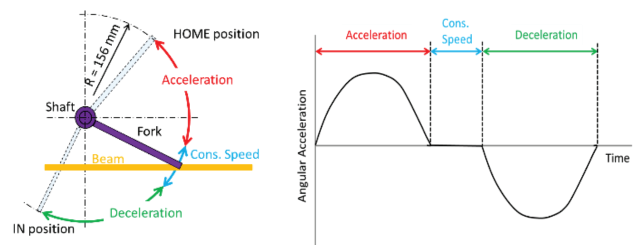

Figure 2: Typical scan cycle (left) and motion pattern (right).

The strong initial acceleration required induces deflections and vibrations in the mechanics (shaft, fork and wire), which result in discrepancies between the true position of the wire midpoint (P) and the position measured by the angular sensor (R) (Fig. 3) [2]. Due to the variation in the acceleration, these deflections cause oscillations, thus increasing the uncertainty of the wire position even further [3].

ISBN 978-3-95450-176-2

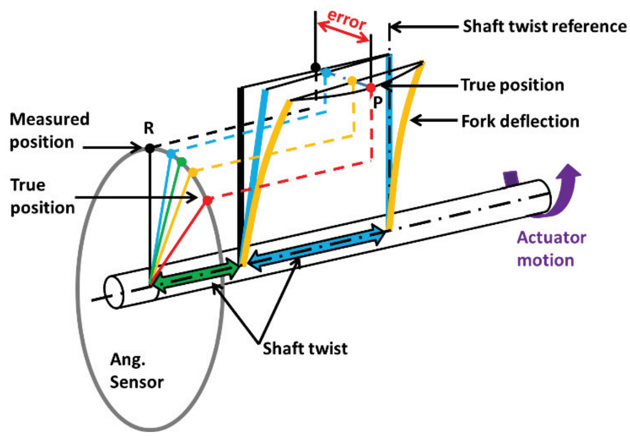

Figure 3: Typical deflections on a conceptual wire scanner instrument.

For the new CERN wire scanner the specified position accuracy is 2 μm (see Table 1 for the complete list of requirements). A new wire scanner design has therefore been developed which improves the performance of the existing device, overcoming many of its drawbacks [4]. However, acting only at the level of the design would not guarantee that the requirements would be met. A specific system for vibration measurement was therefore developed to allow the motion of the scanner to be optimizing for the final device.

Table 1: Requirements and Performances, New CERN Vacuum Wire Scanner

Peak speed	20 m/s
Fork length	156 mm
Peak angular speed	128.20 rad/s
Peak angular acceleration	6700 - 10000 rad/s^2
Tangential acceleration	95 – 159 g
Normal acceleration	260 g
Position accuracy	2 μm

VIBRATION MEASUREMENT SETUP

The vibration measurement system was developed using one of the existing proton synchrotron (PS) fast wire scanners. The fork of the scanner was equipped with high sensitivity semiconductor strain gauges, strategically located in different regions of the fork in order to record its dynamic deflection during the scan. Fig. 4 shows the location of the strain gauges. Gauges G4 and G8 mainly sensitive to the twist of the shaft; gauges G2, G3, G6 and G7 are sensitive to the deflections in X direction (transversal deflections); and gauges G1 and G5 are sensitive to the deflections in the Z direction (longitudinal deflections) (Fig. 5).

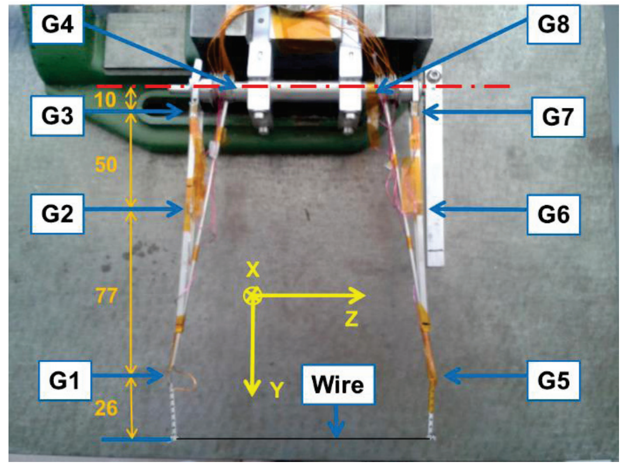

Figure 4: Gauge locations on the fork.

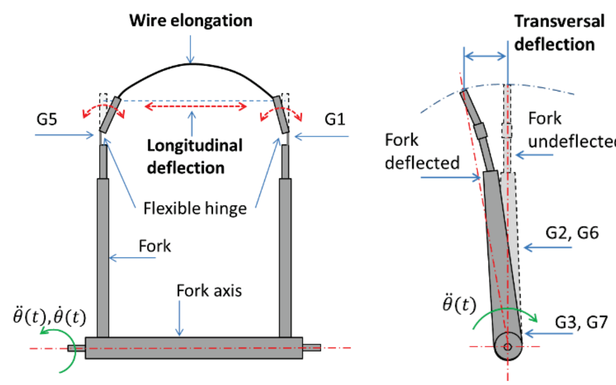

Figure 5: Schematics of the measurable parameters.

An electronic circuit based on a Wheatstone bridge and an amplifier was developed to measure the strain gauges and wire resistance variations. The amplified voltages produced were read-out using an oscilloscope. This acquisition system also records the angular position of the fork by means of the angular sensor of the actuator (Fig. 6).

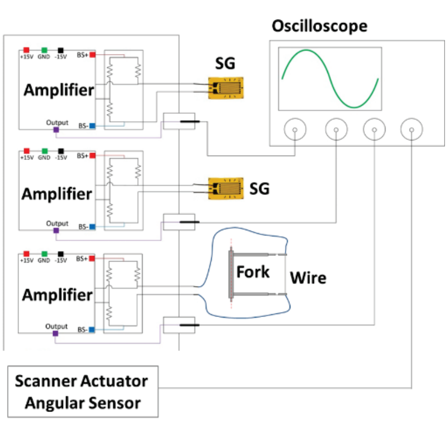

Figure 6: Schematics of the data acquisition system.

An accurate calibration is required in order to quantify the X and Z deflections of the fork arms and the wire elongation from the measurement of the voltage variations recorded by the acquisition system. The strain

ISBN 978-3-95450-176-2

gauges were calibrated using both experimental measurements and finite element analysis (FE) models. The calibration factors for the strain gauges and the wire can be seen in Table 2.

Table 2: Calibration Factors

Sensor	Factor [mm/V]	Measured parameter
G1	0.140	Tip longitudinal deflection
G2	1.329	Tip transversal deflection
G3	0.652	Tip transversal deflection
G5	-0.158	Tip longitudinal deflection
G6	1.329	Tip transversal deflection
G7	0.652	Tip transversal deflection
wire	-0.350	Wire elongation

MODELS

A modal analysis of the fork-wire system has been performed through an FE model. The first two natural vibrational modes associated with the Z-deflection of the fork are shown in Fig. 7. The first Z-mode has a frequency of 151 Hz corresponding to the symmetrical Z-deflection of the fork tips (SZ-mode). In this case, the wire maintains a constant length.

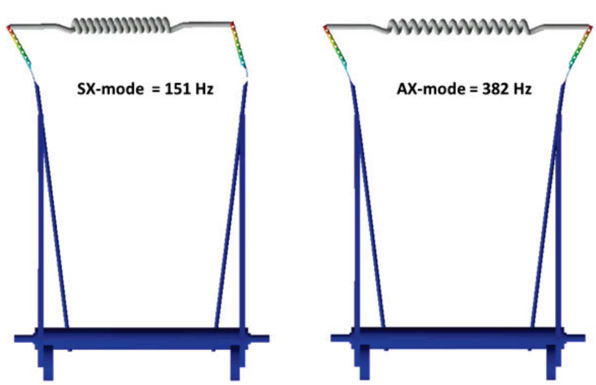

Figure 7: Symmetric (left) and Antisymmetric (right) Z-modes of vibration obtained through the modal analysis performed with ANSYS.

The second Z-mode is located at 382 Hz and corresponding to an asymmetrical Z-deflection of the tips (AZ-mode). This mode may lead to an instability of the wire generating parametrically-driven transverse oscillations.

RESULTS

The Fast Fourier Transform (FFT) performed on the signal of G1 and G5 (Fig. 8) clearly show the two frequencies which correspond to the first and second natural modes of the fork-wire system (~150 Hz and ~400 Hz).

Figure 9 shows the FFT performed on the wire signal. Only the second mode at ~400 Hz appears, as the first mode at ~150 Hz does not provoke wire elongation.

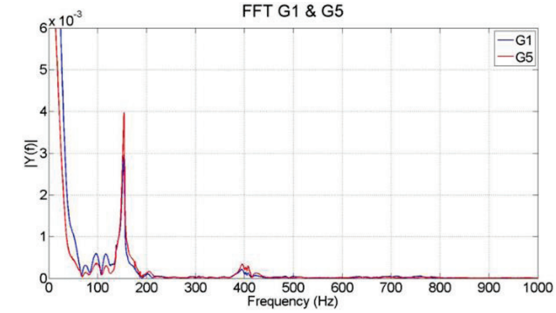

Figure 8: Frequency spectrum of the G1 and G5 signals.

The wire length (Sm) is calculated form the wire electrical tension variations and the wire elongation calibration factor. The distance between tips (Lm) is calculate from the electrical tension variation of gauges G1, G5 and their respective calibration factors. The values of Lm and Sm show the same trend (Fig. 10).

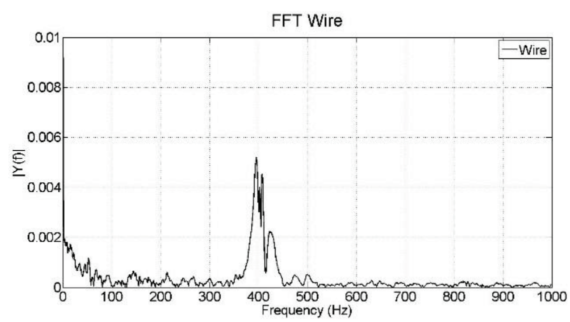

Figure 9: Frequency spectrum of the wire elongation.

The transversal gauges measurement with their respective calibration factors allows the quantification of the fork transversal displacement which is on the range 0.5 mm (Fig. 11). Wire transversal displacement estimated from the values of Sm and Lm are in the range of 10 um.

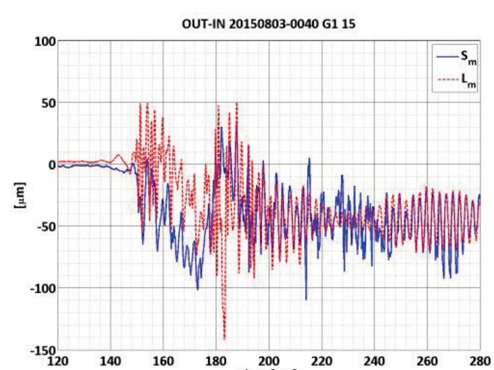

Figure 10: Comparison between wire elongation and tips separation. Motion occurs from ~ 135 to 185 ms.

The conceptual design of the PS fork, because of the flexible hinges feature, is prone to vibrate at relatively low frequencies with important amplitudes (~150 Hz and 0.6 mm for the SZ-mode, ~400 Hz and 0.1 mm for the AZ-mode), although this vibrations are in the wire longitudinal direction, which in essence would not affect

ISBN 978-3-95450-176-2

the measurement accuracy, parametric vibration can appear depending on the wire initial tension. This parametric vibrations, under the inertial forces, results in significant transversal wire oscillation, which would greatly affect the accuracy of the measurement. This transversal oscillation could even cause wire to break.

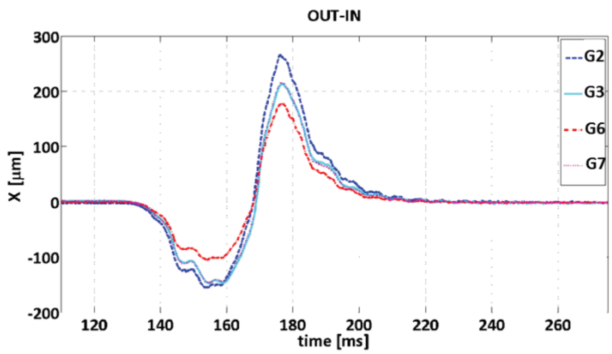

Figure 11: Tip transversal displacement results from gauges G2, G3, G6 and G7. Motion occurs from ~ 135 to 185 ms.

The oscillations of the kinematic chain, which link the actuator and the fork shaft, induce traversal oscillations on the fork tips which directly affect the measurement accuracy. This oscillations and the play of this kinematic chain disrupt the actuator control system performances and consequently the accuracy of measurement.

CONCLUSION

A vibration measurement system has been developed and tested for use with CERN wire scanners. The results show that this system allows the vibrational behaviour of the wire and fork to be clearly visualised.

A hybrid calibration procedure using experimental measurements and FE calculations has been developed in order to overcome the difficulty of calibration under a dynamic and nonlinear acceleration field.

It has also been proven that measurements based on the piezo-resistive effect of the wire provide consistent information allowing the vibrational behaviour of such a system to be determined. Such system can easily be implemented in existing wire scanner devices as only an additional external signal measurement system is required. This implementation would provide valuable information about the device vibrational behaviour. This information can be combined with the profile measurement in order to apply suitable experimental correction factors to the measurement. Additionally monitoring the wire vibrations along the scanner live time, allows to evaluate the aging of the system (especially wire, fork and bearings) and prevent unexpected failures. Vibration monitoring also would serve as an indicator to modify initial motion pattern parameters according to the wear or aging of the system and therefore minimize the wire position uncertainty. Also any unexpected change on the wire configuration (like a tension variation) would be easy detected and corrective actions could be applied.

For the first time the piezo resistive effect is used for wire vibrations measurements during the scan.

As a general conclusion, this work suggests that the use of a rigid fork is preferable to a flexible one, to avoid the risk of generating high wire amplitudes associated with a possible parametric resonance. This should be taken into account when designing the new scanner.

Future work will be focused on the implementation of the vibrational measurement system in the new wire scanner design. More accurate models will also be developed to verify the hypothesis of parametric excitation in the wire oscillations.

RFERENCES

[1] Proposal of PhD thesis: Minimisation of the wire position uncertainties of the new CERN vacuum wire scanner - https://edms.cern.ch/document/1398456/1

[2] Mechanical aspects important for determining the final wire position accuracy on the New Vacuum Wire Scanner. https://edms.cern.ch/document/1311456/1

[3] CERN Vacuum Wire Scanner Mechanical Challenge https://edms.cern.ch/document/1404907/1

[4] Design of a High-Precision Fast Wire Scanner for The SPS at CERN, N.Chritin, B.Dehning, J.Emery, J.Herranz Alvarez, M.Koujili, S.Samuelsson, J.Sirvent Blasco, R.Veness. http://ibic12.kek.jp/prepress/papers/mopb79.pdf

ISBN 978-3-95450-176-2

HIGH DYNAMIC RANGE DIAMOND DETECTOR READOUT SYSTEM FOR THE CERN'S BEAM WIRE SCANNERS UPGRADE PROGRAM

J.L. Sirvent#, B. Dehning, J. Emery, CERN, Geneva, Switzerland
A. Dieguez, Universitat de Barcelona, Barcelona, Spain

Abstract

A secondary particle shower acquisition system is under design for the upgrade of CERN's beam wire scanners. The system needs to be capable of performing bunch by bunch synchronous measurements with an integration time of 25 ns and to cope with signal variations of up to 6 orders of magnitude. The whole dynamic range should be covered by the acquisition system with a single configuration and should have no tuneable parameters. The secondary particles are detected using a polycrystalline diamond detector with the signal digitization performed nearby with a custom front-end system, designed to resist a total ionising radiation dose up to 1 kGy in 10 years. The digital data transmission, front-end synchronization and control are performed through a bidirectional optical link operating at 4.8 Gbps using CERN's GBT protocol. For the digitization, two radiation tolerant integrator ASICs (ICECAL and QIE10) are under study.

INTRODUCTION

A beam wire scan is an interceptive method for transverse beam profile measurements. The working principle of wire scanners consists on the passage of a very thin carbon wire (~30um) through the particle beam. The secondary particle shower generated by the beam/wire interaction, is detected outside of the beam pipe and transformed into an electrical current proportional to the loss intensity. The beam profile is reconstructed by plotting the loss intensity versus the wire position. Using the measurements from these devices the beam is determined, allowing calculation of the beam emittance, an important parameter for optimising collider's luminosity.

The Beam Wire Scanners Upgrade Program

The CERN accelerator complex currently has 32 installed beam wire scanner systems of different architectures located along the injector chain and in the Large Hadron Collider (LHC) itself. In terms of mechanics, these systems share some common characteristics, such as the transfer of the motor movement from air to vacuum through bellows. These bellows have a limited lifetime and have compromised accelerator operation in the past trough the appearance of vacuum leaks. In addition, the use of complex mechanics leads to mechanical play that reduces the systems accuracy and hence measurement performance. The current scan speeds are also limited and do not allow the measurement of high intensity beams due to wire sublimation [1].

jsirvent@cern.ch

The development of a new scanner type is motivated by all the above mentioned issues and the need to measure smaller beam sizes at higher beam intensities in the future. The basic concept is to combine a high scan velocity, nominally $20ms^{-1}$ to avoid wire damage, with an accurate and direct wire position determination avoiding bellows and any lever arm mechanism. The specified beam profile measurement accuracy is set to 2µm. The upgraded system, common for the CERN PSB, PS, SPS and LHC, is therefore based on an in-vacuum motor rotor, with the stator outside, avoiding the use of bellows, and incorporating an optical position sensor for accurate position determination [2] (see Figure 1).

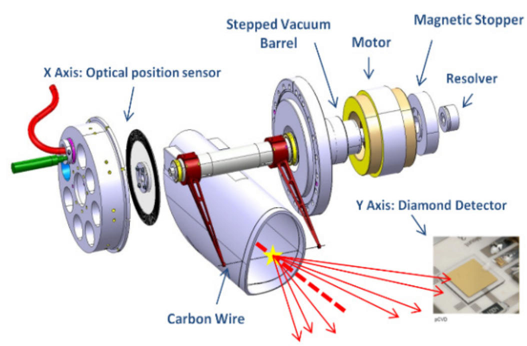

Figure 1: Upgraded Beam Wire Scanner Design.

Secondary Shower Acquisition System Upgrade

Presently, the secondary particle showers from operational beam wire scanners are detected by a scintillator. The light produced transits a wheel of selectable optical filters, after, it is detected using a photo multiplier tube (PMT) that transforms the optical signal into a current. A current-to-voltage, transimpedance, amplifier is used to drive this signal over CK50 coaxial cables of up to 250m, to surface buildings where the digitization is performed. To reach a suitable resolution, this architecture obliges the accelerator operators to set-up the system, selecting a suitable combination of PMT gain and optical filter, according to the beam characteristics. On these systems the dynamic range is limited by the pre-amplifier, sometimes the Gaussian tails of the beam profile are too much shadowed by noise, and in some cases PMT saturation effect can lead to incorrect measurements [3].

The upgraded secondary shower acquisition system aims to use 500um thick polycrystalline chemical vapour deposition (pCVD) diamond as detector. This requires new acquisition electronics which need to cover the high dynamic range of the diamond detector without tuneable parameters, while also providing very low noise

ISBN 978-3-95450-176-2

measurements. The design of such system must be compatible with any CERN accelerator and beam wire scanner location.

DIAMOND DETECTORS AS BEAM PROFILE MONITORS

Diamond detectors are solid state ionization chambers. When applying a bias voltage on its electrodes, the passage of charged particles through the diamond bulk generate a current on the detector proportional to the deposited energy, and therefore to the number of particles that cross the material. These detectors have been deeply studied and characterized in terms of temporal resolution, radiation hardness and linearity by the RD42 collaboration at CERN [4], and successfully implemented as beam loss monitors [5].

Analogue Front-End Tests with Alpha Particles

An analog front-end was prepared and tested with an alpha source (^{241}Am). In order to drive the signal along 50 Ohm coaxial cables, the current signal from the detector is transformed into a voltage by a fast transimpedance amplifier, based on the THS3001 high slew rate operational amplifier. Input and output impedances are matched to 50 Ohm as shown in Figure 4.

The signal from the amplifier, produced by alpha particles crossing the detector, was sampled with a LeCroy oscilloscope at 5GSps with 50 Ohm input impedance. With the pCVD diamond detector biased at -700V, the front-end produced pulses of 4.5mV of amplitude with an approximate duration of 8ns (FWHM) and a little undershoot. The small undershoot due to the amplifier response was recovered in around 13ns, as shown in Figure 2. This is more than adequate to reach the 25ns resolution with no signal pile-up.

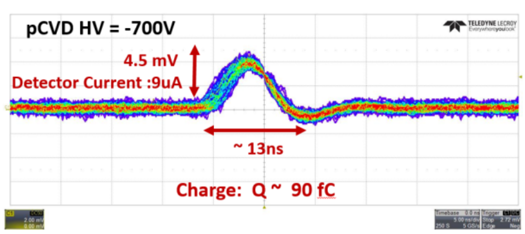

Figure 2: Signal from pCVD Diamond Detector after a transimpedance amplifier based on THS3001.

The charge created in the detector by a single alpha particle is around 90fC, and can be determined by integrating the detector current over the pulse duration. The detector current with this configuration can be easily calculated using the transimpedance amplifier transfer function, as shown on equation 1:

$$I_d(A) = 2V_o\,/Rf \qquad (1)$$

Where I_d is the detector current, V_o is the signal amplitude in 50 Ohm and R_f is the feedback resistor used on the amplifier (1KOhm in this test).

Tests with Beam Wire Scanners

The analog front-end has been installed in the Long Straight Section 5 (LSS5) of the SPS accelerator, at approximately 1.6m from an operational linear wire scanner (BWS51731), and just in front of the original scintillation detector. See Figure 3.

Figure 3: Test Set-up on the SPS accelerator.

Measurements from the analogue front-end were recorded with an oscilloscope on the surface, using 80m of CK50 coaxial cable for signal transmission. A simplified electrical model of the set-up is shown on Figure 4.

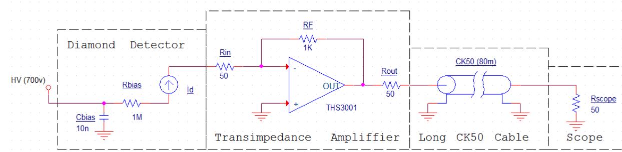

Figure 4: Simplified set-up for evaluating a pCVD diamond detector for beam profile monitoring.

The linear beam wire scanner mechanics in the SPS have a scan speed limited to 1ms^{-1}. To avoid wire sublimation, the beam used on the machine for these tests was an LHC pilot beam. The test conditions are summarized in Table 1.

Table 1: Testing Conditions

Attribute	Value
Scan Speed	1 ms^{-1}
Carbon Wire Diameter	30 um
SPS User	LHC Pilot
Bunches in the SPS Ring	1
Protons per bunch	1e^{10} protons
Bunch Length (4 Sigma)	4 ns
SPS Revolution Period	23 us
Energy	450 GeV

During the test, the bunch clock as well as the turn clock were sampled and used as a timing reference for the data processing. A Matlab script was used to perform a digital bunch integral with a duration of 25ns on every turn. The detector signal is shown in blue and the integrals as green markers on F5 top. The scan speed information, taken from the database, is then used to change the x-axis from the temporal to the spatial domain. Once this is done, a Gaussian fit is performed to

ISBN 978-3-95450-176-2

determine transversal bunch size (middle chart). For comparison, the profile measured with the operational system is shown in the bottom plot of Figure 5.

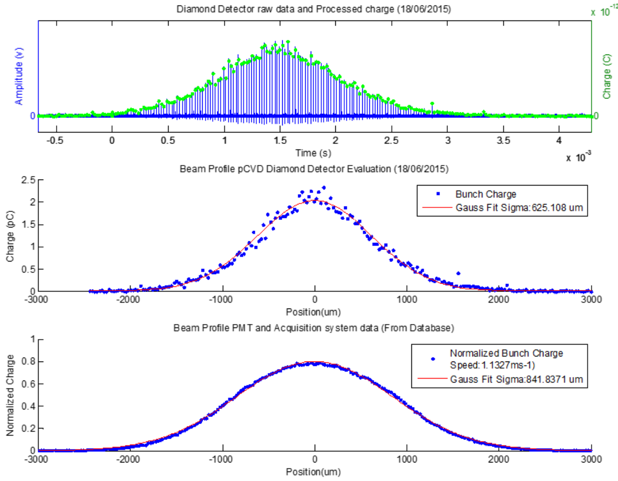

Figure 5: Signal amplitude of secondary shower intensities as a function of time and position. Top: pCVD Diamond detector measurements versus time. Middle: pCVD diamond detector integrals versus position. Bottom: Scintillator/PMT detector measurements versus position.

A couple of interesting effects can be observed comparing the middle and bottom plots of Figure 5:

- ***Spread of detector signals***: The measured signals on both detectors (pCVD and scintillator/PMT) are parameterized with a Gaussian distribution. It can be observed that the residuals variation is larger for the pCVD compared to the scintillator/PMT assembly. The higher variation shown by the diamond detector signal could be a statistical effect related to the random distribution of the secondary particle cone produced by beam-wire interaction, and the small size of the detector ($1cm^2$). With the scintillator covering a larger area, the effect of particle number fluctuation in the final signal is much lower compared to the pCVD detector.
- ***Profile width determination:*** The sigma values of the Gaussian parametrization for the pCVD detector is a 27% smaller than for scintillator/PMT setup. The reason of such beam profile difference remains unknown, and further studies are needed to understand this effect.

In total, 9 scans were done. A summary of the profile parameters are shown on Table 2, including the least-squares error (SSE) of both fits once normalized for comparison.

Table 2: Profile Measurements Summary

System	Mean Sigma	Std. Dev	SSE
Diamond	613.0 um	12.4 um	0.233
Scintillator	839.7 um	1.9 um	0.072

Although the sources of such differences remain unclear, they do not seem to be related to an effect of the electronics or the processing algorithm. To study such effects, a different set-up is scheduled to be installed at the same location with two diamond detectors placed above and below the beam pipe.

SECONDARY SHOWER ACQUISITION SYSTEM ARCHITECTURE

The implemented system architecture is shown in Figure 6. A previous article describes the motivation behind the architecture choice [6]. A custom radiation tolerant front-end will be placed in the tunnel at ~10m from the diamond detector. The front-end will perform charge integrations at 40MHz, synchronous with the beam and with a very high dynamic range. The digital data will be sent through a dual single mode optical fibre using CERN's GBT protocol at 4.8Gbps to the back-end electronics [7]. The front-end synchronization, data transmission and control is performed through the optical link. For the back-end system, the CERN custom designed VME FMC Carrier board (VFC) will be used to manage the data processing and storage. On the VFC, one Small Form-Factor Pluggable (SFP+) transceiver is needed per system, allowing up to 4 front-ends to be controlled with a single VFC.

Front-End Design

For the detector readout, two integrator ASIC candidates are being evaluated, ICECAL [8], and QIE10 [9]. Their main specifications are summarized on Table 3.

Table 3: Diamond Detector Readout ASIC Candidates

Feature	QIE10	ICECAL
Dynamic Range	3.2fC-340pC (1e5)	4fC-16pC (1e3)
Integration Window	25ns (40Mhz)	
Channels per ASIC	1	3
Input Impedance	50 Ohms	
Dead-timeless	Yes	
Number of Bits	8	12 *
Quantification Error	~1%	<<1% *
Linearity Error	~1% (Log)	<1% *
TDC Capability	Yes	No
Max TID	~0.5kGy *	***
ASIC Technology	AMS SiGe BICMOS 0.35um	
Designer Entity	Fermilab	U. Barcelona

* ADC Dependent
** Early characterization, further tests will be done
*** Not yet characterized.

ISBN 978-3-95450-176-2

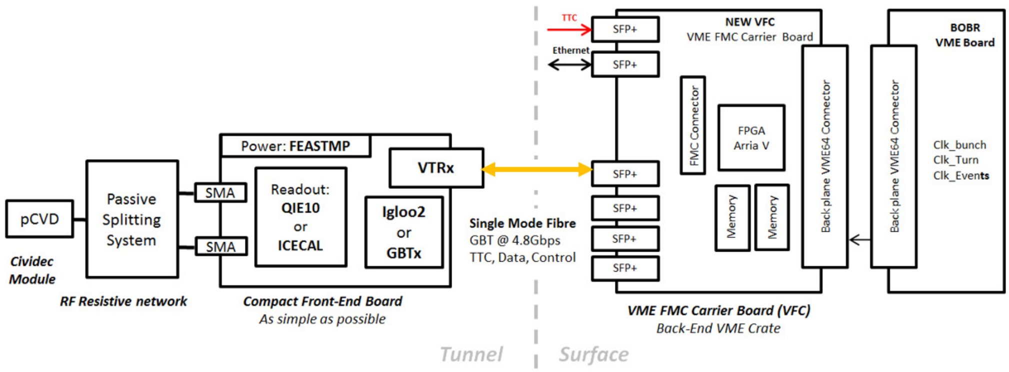

Figure 6: Upgraded secondary shower acquisition system architecture.

For fast evaluation, not only under laboratory conditions but also for tunnel operation, the digital front-end was designed in a modular way. The Igloo2 UMd Mezzanine from the CERN CMS collaboration [10] is used as a digital motherboard, responsible for driving the optical link. This board features an Igloo2 Flash-based FPGA with the GBT protocol implemented on its firmware and a versatile link transceiver (VTRx).

Independent mezzanine boards for each of the two readout ASIC candidates were designed to be attached to the motherboard through a SAMTEC connector. The two front-end versions are shown in Figure 7. All the components used on these boards have already been characterized under radiation by collaborators.

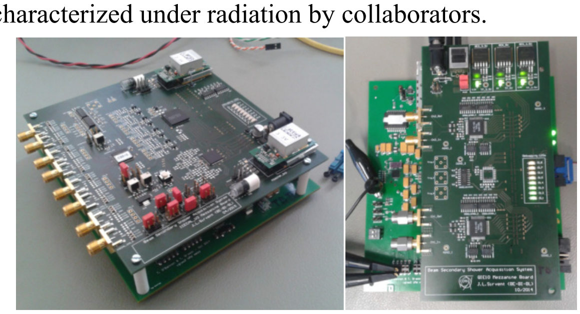

Figure 7: F.E. versions (Left: ICECAL, Right: QIE10).

In order to reach the 1e6 dynamic range of the specifications, the signal from the diamond detector will be split into several channels with different gain/attenuation. These signals will be sampled in parallel on the front-end and processed in parallel on the back-end to reconstruct the beam profile.

QIE10 Front-End Version Studies

A full prototype set-up was used for the first measurements with the QIE10 front-end. Due to unavailability of the CERN-VFC board at the time of the tests, an Igloo2 development kit was used as back-end system. For complete operation, an SMA to SFP+ module and a custom clock conditioning circuit, including programmable delay lines, were attached to this kit.

On this prototype system, the front-end is continuously sampling and sending data to the back-end system in synchronism with the accelerator bunch clock. When the back-end receives a trigger signal, the optical link data is temporally stored on a 512MB LPDDR memory using 64 bits words. The 64 bits data frames contain: bunch ID, Turn ID, data and status bits. A PC connected to the back-end system, through UART and with a custom user application, provides feedback on the optical link status, allows the user to perform the control of the front-end over the link and recovers the data from the LPDDR memory for analysis. This application also controls a Keithley 6430 sub-FemtoAmp current source through a general purpose instrumentation bus (GPIB). The complete set-up for laboratory tests is shown in Figure 8.

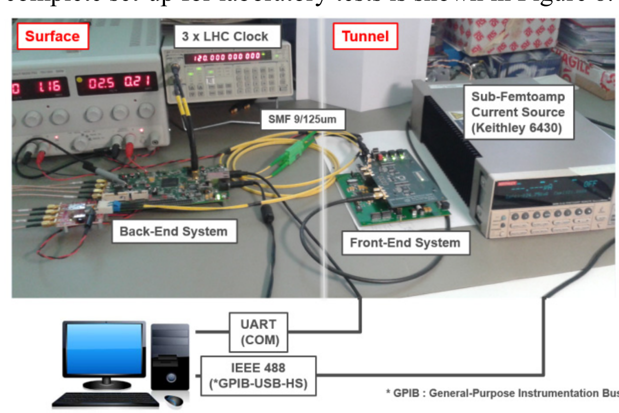

Figure 8: Laboratory tests set-up.

QIE10 is a charge integrator and digitalization ASIC able to cover a dynamic range of 1e5 with 8 bits encoding. Its logarithmic charge encoding algorithm contains 16 sensitivity levels, which are divided in 4 ranges. Its 8 bits digital data format contains 6 bits for mantissa and 2 for range. The QIE10 uses 4 different internal capacitors, highlighter later as CIDx in different colours, to achieve integrations every 25ns, with each integrator channel requiring 100ns to process its 25ns integral. In order to check the QIE10 response, logarithmic sweeps were performed with the Keithley current source. Temporal windows of 25us (1000 samples at 40 MHz) were taken for each current increment, then, the value of each CID was averaged. The data measured was compared with the ASIC nominal logarithmic parametrisation to check any possible deviation, as shown in Figure 9.

ISBN 978-3-95450-176-2

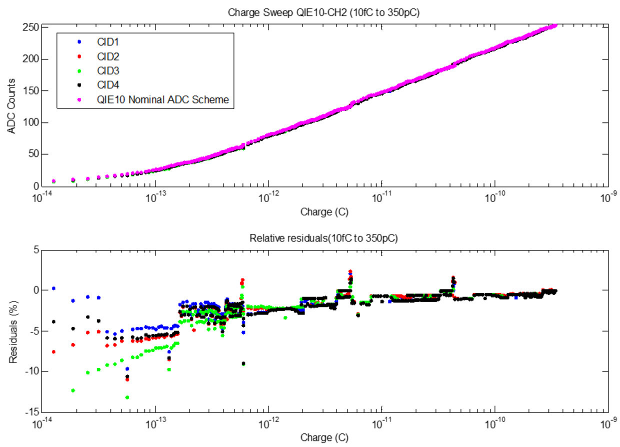

Figure 9: QIE10 response to a logarithmic current sweep (top) and relative residuals from nominal response (bottom).

The top plot of Figure 9 shows the QIE10 ADC values which represent the input charge, while the lower plot shows the residual error. Clearly visible is the logarithmic behaviour of the QIE10 and the 4 ranges in which the ASIC splits its dynamic range (seen as little spikes in the residual error). The measured values in our prototypes show a good agreement with respect to the ASIC nominal ADC response, remaining below 5% of difference, except for a small part of the first range. All the integrator capacitors (CIDs) show a similar response.

The check of the 16 sensitivity levels (4 per range) are shown in Fig. 10, with the charge versus mantissa value plotted. The slope of the linear fits performed in each sub-range shows the sensitivity levels.

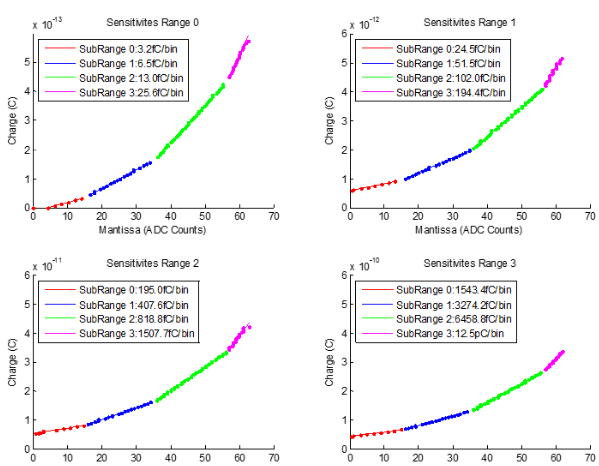

Figure 10: QIE10 Sensitivity levels.

Both of the QIE10 ASICs contained on the front-end board show a similar behaviour, the data collected during these studies will be used later for calibration. The tests have shown that the complete front-end performs according to specification, which qualifies the electronics in terms of functionality and accuracy for installation in the SPS tunnel for further testing.

CONCLUSION

Diamond detectors have been shown to be a promising solution for secondary particle detection in combination with wire scanners to determine the transverse beam size. Further investigations are required to understand the 27% difference of the beam profile measured with such detectors with respect to the standard scintillator/PMT system. The larger fluctuation of the diamond based system will be addressed with a second test set-up using more detectors.

The digital readout electronics system has been fully tested under laboratory conditions demonstrating the specified performance of the QIE10 readout ASIC. The measured signals are showing a remaining systematic error of maximum 5% respect to the nominal ASIC response. The QIE10 front-end will be installed in the SPS tunnel and its performance tested under operational conditions.

REFERENCES

[1] M. Sapinski et al., Carbon fiber damage in particle beam, Proc. of HB2010, Morschach, Switzerland, pp. 231-234, (2010). http://jacow.org/.

[2] J. Emery et al., "A fast and accurate wire scanner instrument for the CERN accelerators to cope with high environmental constraints and increasing availability demand", Proc. of IEEE Multi-conference on Systems and Control, Antibes, France (2014)

[3] M. Kuhn et al., Investigations of the LHC emittance blow-up during the 2012 proton run, Proc of IPAC2013, Shangai, China, pp. 1394-1396, (2013), http://jacow.org/.

[4] CERN RD-42 collaboration. "CVD diamond radiation detector development". http://rd42.web.cern.ch/rd42/.

[5] E. Griesmayer et al., A fast CVD diamond beam loss monitor for LHC, Proc. of DIPAC2011, Hamburg, Germany, pp. 143-145, (2011), http://jacow.org/.

[6] J.L. Sirvent et al., "Secondary particle acquisition system for the CERN beam wire scanners upgrade". Journal of Instrumentation, 10, C04021 (2015).

[7] The GBT Project, "Radiation Hard Optical Link". https://espace.cern.ch/GBT-Project/

[8] E. Picatoste et al., "Low noise 4-channel front end ASIC with on-chip DDL for the Upgrade of the LHCb Calorimeter". Journal of Instrumentation, 10, C04017 (2015).

[9] A. Baumbaugh et al., "QIE10: a new front-end custom integrated circuit for high-rate experiments". Journal of Instrumentation, 9, C01062 (2014).

[10] S. Goadhouse, et al., "The CMS HCAL FEE Control Module" TWEPP14, Aix-en-Provence, France. September 2014.

ISBN 978-3-95450-176-2

ELECTROMAGNETIC FIELD PRE-ALIGNMENT OF THE COMPACT LINEAR COLLIDER (CLIC) ACCELERATING STRUCTURE WITH HELP OF WAKEFIELD MONITOR SIGNALS

N. Galindo Munoz, N. Catalan Lasheras, S. Zorzetti, M. Wendt, CERN, Geneva, Switzerland
A. Faus Golfe, IFIC, Valencia, Spain;
V. Boria Esbert, Polytechnical University of Valencia, Valencia, Spain

Abstract

The CLIC project, currently under study at CERN is an electron-positron collider at 3 TeV centre-of-mass energy and luminosity of $2*10^{34}\,cm^{-2}s^{-1}$. Achieving such luminosity requires a beam dimension of 1 nm in the vertical plane and high beam stability. The TD24 is a traveling wave structure operating at 12 GHz designed to reach 100 MV/m at constant gradient. It consists of two coupling cells and 24 disks. The RF is coupled from cell to cell though an iris of 5.5 mm. To minimize the occurrence of wake-fields and minimize the emittance growth $\Delta\varepsilon_y$ below 5%, the pre-alignment precision of the electrical centre of the accelerating structure (AS) on its support has to be better than 7 µm. Following, the AS is actively aligned with beam using the wakefield monitor (WFM) signals, with a resolution of 3.5 µm. A test bench for laboratory measurements has been designed and exploits the asymmetry created by RF scattering parameters by an off-centre conductive wire, stretched to locate the electromagnetic centre of the AS. Simulations and preliminary measurement results are presented.

INTRODUCTION

The study that concerns this paper is part of a project founded by the European Commission under the name of PACMAN* [1] (Particle Accelerator Component's Metrology and Alignment in the Nanometre scale). The status of this project is presented in these proceedings [2].

The CLIC (Compact Linear Collider) [3] [4] accelerator currently under study at CERN, aims to collide electrons and positrons with vertical beam sizes of 1 nm and an emittance growth budget $\Delta\varepsilon_y$ of less than 5%. To preserve the emittance at the main linac at CLIC, very tight micrometric tolerances are required concerning the position of the components focusing (Quadrupole), accelerating (Accelerating Structure, AS) and detecting (Beam Position Monitor, BPM) the beam over a distance of several hundreds of meters, all along the accelerator.

The accelerating structure TD24 shown in Figure 1 is a traveling wave structure designed for high constant gradient of 100MV/m for compact acceleration required at CLIC. It consists of two coupling cells and twenty-four accelerating cells (see Figure 2) whose iris dimensions decrease gradually in order to compensate the energy given to the beam and ensure constant accelerating gradient. Very precise machining and nanometric tolerances are achieved and demonstrated during the fabrication process of the disks forming the structure. These disks are stacked and assembled by diffusion bonding. The full assembly and bonding process may lead to a geometric deformation of the structure whose tolerances have been established to be less than 1 µm in the case of errors of the iris shape, 5 µm for disk-to-disk misalignment, and a maximum tilt error of 140 µrad.

Figure 1: The TD24 accelerating structure.

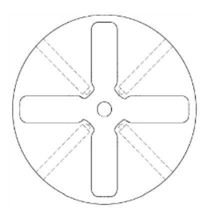

Figure 2: One of the disks of the AS.

The AS is feed in the first coupling cell with a 12 GHz radiofrequency (RF) signal that is coupled from cell to cell through an iris with a mean aperture of approximately 5.5 mm. With such small apertures, the alignment of the electrical centre of each cell in the accelerating structure with respect to the beam axis is extremely important to avoid the excitation of wake-fields. In particular transverse wake-fields might lead to beam instabilities, incoherent transverse kicks in following bunches, and an effective increase of the emittance, which results in a decrease of the luminosity of the collider.

Four waveguides with a cut-off frequency of 15 GHz are installed at the end of every cell in order to extract the high order modes (HOM) without distorting the

*The PACMAN project is funded by the European Union's 7th Framework Programme under Grant Agreement no. 606839

ISBN 978-3-95450-176-2

accelerating mode. Each waveguide is terminated with SiC damping material to absorb the HOMs energy. The middle cell of the AS, prior to the absorber, is equipped with four bent waveguides called Wakefield Monitors (WFM), each has two RF pick-ups attached to extract the main TE and TM mode signals (18 & 24 GHz) for measuring the misalignment with beam [5] [6]. Beam dynamics simulations estimate a resolution requirement of 3.5 μm of the beam-based WFM system, in order to efficiently minimize the emittance growth along the linac. In a similar way, the minimization of the wakefield effects require a cell-to-cell alignment error below 5 μm, and a positioning of the structure in its support within 7 μm.

This work aims to measure these quantities in a laboratory environment, without using the particle beam, to the required level of precision:

- Find the electromagnetic mean axis of the AS and locate the external references (fiducials) on the structure with an accuracy better than 7 μm.
- Demonstrate the required resolution of the WFM in a laboratory environment.
- Measure the disk-to-disk misalignment and propose a method to be applied during the assembly of the structure.

In this paper we present a stretched-wire based method, together with first preliminary measurements which promises to achieve a precise pre-alignment of the AS on its electromagnetic, i.e. dipole mode properties.

MEASURING PRINCIPLE

We use the lowest order dipole eigenmodes to detect the position of a wire inside the accelerating structure. Exciting a dipole mode in presence of a conductive wire near the centre of the iris will perturb the dipole field, in our case at at 18 GHz, and hence alter the transmission between the different ports as measured by a vector network analyzer (VNA). If the wire is precisely moved to the electromagnetic center of the iris, this perturbation is minimized. The tilt of the wire is corrected through the repetition of the method in the first and in the last cell of the structure.

A model of the AS (see Figure 3) is simulated in ANSYS HFSS to find out the sensitivity of the response to the position of the wire and the expected resolution, the influence of the thickness of the wire and the response dependence to tilts.

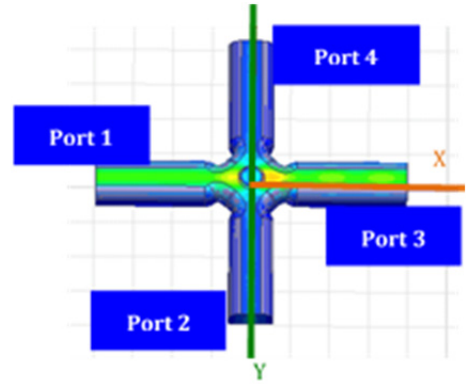

Figure 3: Dipole mode excitation at port 1 in the middle cell.

Different radios of the wire made of different materials were studied in order to select the one that best fits the resolution required for laboratory measurements. The results show, a conductive (metallic) wire is more sensitive to the perturbation created by the wire than a dielectric one; and a 0.1 mm diameter Be-Cu wire is a good compromise between sensitivity and mechanical handling of the wire as experienced by other members of the team. The mechanical and optical characterization of the wire is the subject of another PACMAN work package.

We found, the highest sensitivity to a horizontal movement of the wire is detected as magnitude difference between ports 2 and 4 while applying the RF signal to port 1, see Figure 3. This result is shown in Figure 4. As expected, a minimum of the difference S21-S41 is found when the wire is in the centre of the dipole mode. The minimum step found with simulations is 1 μm taking into account the 0.01 dB value of uncertainty expected from the VNA.

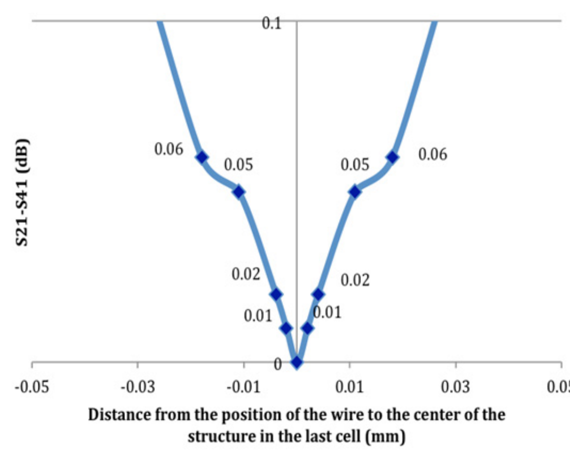

Figure 4: S12-S14 (dB) with respect of the position of the wire.

ISBN 978-3-95450-176-2

TEST BENCH

A test bench [7] shown in Figure 5 is designed for accurate positioning of the wire wrt. to the AS, to demonstrate 1 µm resolution. It consists out of:

- An active-stabilized optical table to reduce external vertical and horizontal vibrations by 85% or more (above 5 Hz), and by greater than 95% (above 10 Hz), having a flatness of ± 0.1 mm over 600 mm square, and a load capacity of 590 kg.
- A remote controlled hexapod to precisely position the AS. The hexapod offers precise movements of 0.25 µm in six degrees of freedom with a maximum load capacity of 20 kg. The repeatability and precision of the movement was carefully verified with a Leitz Coordinate Measuring Machine (CMM), having an uncertainty of 0.3 + (L/1000) µm.
- Two supports that host a fixed and stretched Be-Cu wire of 0.1 mm of diameter.
- A VNA with a frequency range from 10 MHz to 50 GHz.
- A PXI controller running a LabVIEW program to control the motion of the hexapod and performing automatic measurements with the VNA.

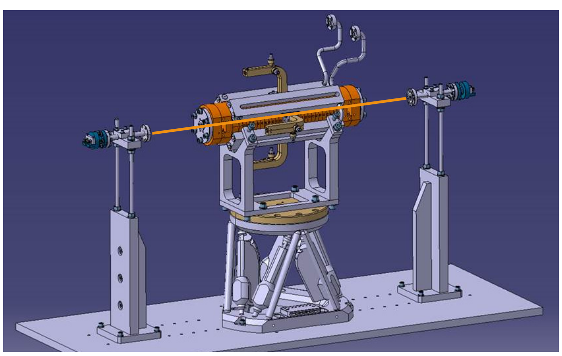

Figure 5: Test bench for accurate positioning of the wire.

FIRST RESULTS

Measurements in an existing vertical test bench without micrometric location were performed in order to validate the principle given by simulations. The bench is shown in Figure 6 and is formed by a marble table with a metal support where the AS is placed vertically. Other elements are a stepper motor with a wire support, a small weight of 0.2 kg for wire straightening using gravity, a 0,1 mm diameter Be-Cu wire, and a four-port VNA with a frequency range from 10 MHz to 24 GHz. The error of the positioning of the wire is ± 0.1 mm and the uncertainty on the VNA measurements is 0.01 dB. The RF ports are defined by the WFM, RF loads have not been installed in the cells for this initial measurement.

The position of the wire was fixed in the center of the last disk, while it was displaced along the cross section axes in the last disk. The results are plotted in Figure 7. The four traces represent four-port S-parameter measurements, with an excitation at each port, as shown in Figure 4. The differences of those traces might due to mechanical asymmetries, e.g. internal deformation of the structure after bonding, the non-perfect assembly of the WFM, and the uncertainty of the wire position.

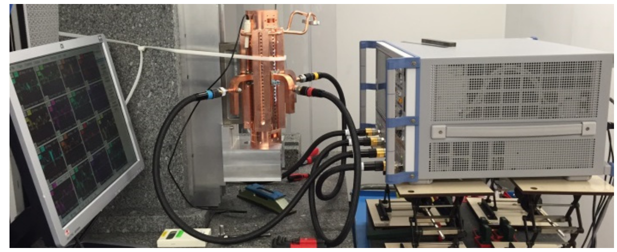

Figure 6: Vertical test bench for a proof of principle.

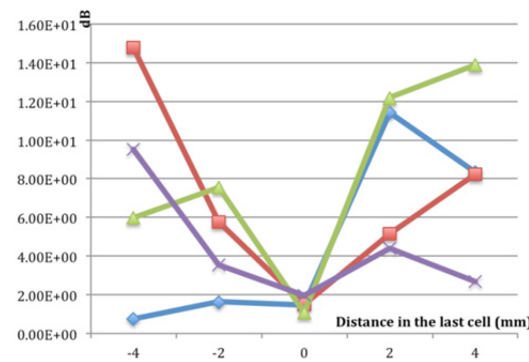

Figure 7: Transmission measurements through ports defined at WFM for different tilts of the wire measured in the last cell in absolute distance.

Figure 8 shows the difference between measurements and simulations to demonstrate the proof-of-principle. It validates a sufficient agreement on course wire displacements. For the final bench setup as shown in Figure 5, we expect results to follow the predicted shape as computed with ANSYS HFSS.

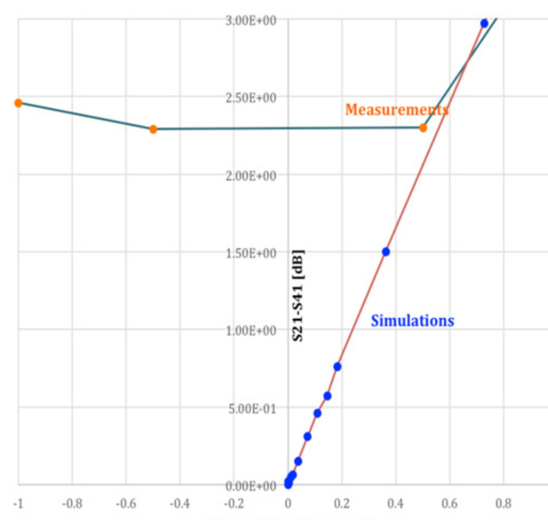

Figure 8: Measurement and simulation results for different tilts of the wire in the middle cell measured in absolute distance in the last cell.

ISBN 978-3-95450-176-2

DETAILS ON MEASUREMENT ACTIVITIES

The current activities focus on the development of the best algorithm using a LabVIEW program to perform automatized, two-dimensional measurements in a test bench with micron-accurate positioning.

Precision stretched-wire measurements utilizing the designed test bench are in preparation, and include the following aspects:

Tapered WFM WG Design to Demonstrate the Resolution of the WFM and the Requirements and Fiducialisation of the AS

The WFMs are originally designed to detect parts of the energy of the higher order modes (HOM) propagating to the absorption loads, helping to actively align the AS with the beam. However, RF measurements show considerable reflections when the WFMs were used to detect input power signals. A solution based on a tapered transition between the middle cell and the VNA (see Figure 9) is proposed to improve the signal quality, measured by the VNA, The design was optimized for the range of frequencies of interest (15-20 GHz), and shows the value of the reflection coefficient S_{11} below -40 dB, as shown in Figure 10.

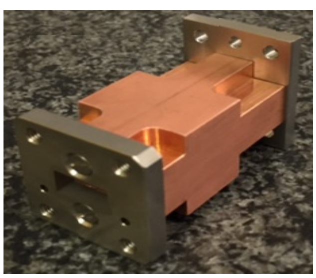

Figure 9: Middle-cell taper to standard waveguide WR-51.

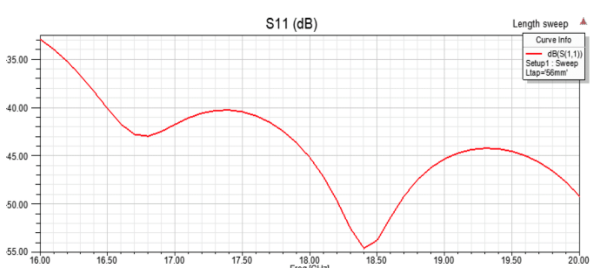

Figure 10: S_{11} (dB) for the designed taper.

Disk to Disk Misalignment Measurement

We plan to use the existing holes at the end of the damping waveguides, whose initial purpose lies on improving vacuum pumping, to host small feedthroughs as shown in Figure 11. In this way we will be able to measure the centre of the cell in a similar way as with the WFM, and establish a handle to analyze the disk-to-disk misalignment on this structure. This could be used as an intermediate acceptance tests during structure manufacturing.

Figure 11: SMA connector for a disk to disk misalignment measurement.

Use of NI-PXI Technology

The control of the hexapod movement and acquisition are currently performed via a LabVIEW software. We are investigating the possibility to extend the 4-port VNA to twelve ports using a switching network using PCI eXtensions for Instrumentation (PXI) (see Figure 12). In this way, we could correct the tilt of the wire. Ports are defined at the first cell, the WFM and the last cell of the AS. NI-PXI modules might also replace the initial VNA setup in order to perform non-linear measurements.

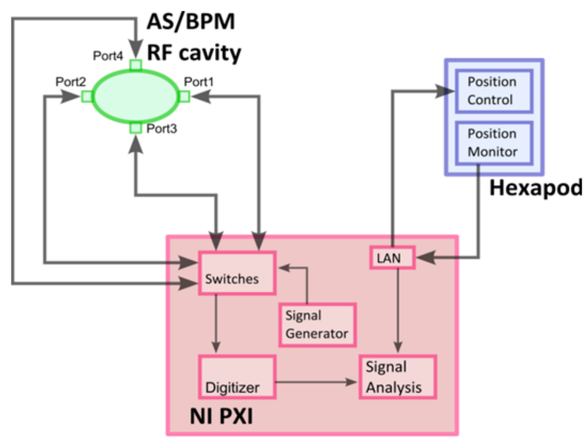

Figure 12: Flux diagram of the system.

CONCLUSIONS

Initial WFM measurements performed on a 12 GHz CLIC accelerating structure demonstrate qualitatively the feasibility of a stretched-wire method to locate the electromagnetic centre of the middle cell of the AS. Still, a long, challenging way is ahead to fiducialise the accelerating structure with an accuracy of less than 7 µm.

ACKNOWLEDGMENTS

Special thanks to the European Commission for making the PACMAN project be possible; to the PACMAN team; to my technical and academic supervisors; to National Instruments Hungary for the technical and personal support during my three-month secondment, in particular: B. Barabas, P. Nemeti, L. Abraham and E. Kun; and to my colleagues at CLIC: A. Grudiev, W. Wuensch, A. Solodko, A. Olydnin, S. Lebet, D. Glaude, R. Wegner, L. Navarro and W. Farabolini.

ISBN 978-3-95450-176-2

REFERENCES

[1] PACMAN website: http://pacman.web.cern.ch/.
[2] K. Artoos et al., "Status of PACMAN project", these proceedings, IBIC, Melbourne, Australia (2015).
[3] CLIC study website: http://clic-study.web.cern.ch/
[4] CLIC CDR, "A multi-TeV linear collider based on CLIC technology: CLIC Conceptual Design Report", edited by M. Aicheler, P. Burrows, M. Draper, T. Garvey, P. Lebrun, K. Peach, N. Phinney, H. Schmickler, D. Schulte and N. Toge, CERN-2012-007.
[5] F. Peauger et al., "Wakefield monitor development of CLIC accelerating structure", Proceeding of Linear Accelerator Conference LINAC2010, Tsukuba, Japan.
[6] R. L. Lillestol et al., "Wakefield monitor experiments with X-Band accelerating structures, IPAC 2015.
[7] S. Zorzetti et al., "Design of the 15 GHz BPM test bench for the CLIC test facility to perform precise stretched-wire RF measurements", Measurement Science and Technology, July 2015.

ISBN 978-3-95450-176-2

DESIGN OF A LASER-BASED PROFILE MONITOR FOR LINAC4 COMMISSIONING AT 50 MeV AND 100 MeV

T. Hofmann*, E. Bravin, U. Raich, F. Roncarolo, CERN, Geneva, Switzerland
S. Gibson, A. Bosco, G. Boorman
John Adams Institute at Royal Holloway, University of London, Egham, United Kingdom
E. Griesmayer, CIVIDEC Instrumentation, Vienna

Abstract

A laser-based profile monitor has been designed for commissioning of CERN's LINAC4 accelerator at 50 MeV and 100 MeV, as part of the development of a non-destructive profile and emittance monitor foreseen for the final 160 MeV beam. The system is based on a low power laser which is scanned through the H^- beam. Electrons, which are photo-detached from the ions by the laser, are deflected by a steerer magnet and measured by a diamond detector. The custom designed diamond detector is tailored to minimize the disturbance due to the electromagnetic field of the passing main beam. The laser source will be installed in the LINAC4 Klystron gallery located 75 m away from the profile station and an optical fiber will transport the laser to the tunnel. The laser propagation for different pulse length and peak power values was characterized with laboratory tests with such a long fiber. In this paper we describe the overall design, focusing on key elements such as the fiber-based laser transport and the electron detection with the diamond detector.

INTRODUCTION

As the LINAC4 construction advances, its commissioning is taking place in stages at different beam energies, as indicated in Fig. 1. So far, all the accelerator's equipment and the beam parameters have been validated up to the exit of the first DTL tank (12 MeV).

The conventional techniques which are foreseen to measure the beam profile and transverse emittance, like SEM-grids or wire-scanners, are all destructive or at least invasive with respect to the ion beam.

During the 3 MeV and 12 MeV commissioning, a non-invasive laser system was successfully operated to measure the vertical emittance of the H^- beam, by collecting the neutralized H^0 atoms [1–3].

The next two stages of the LINAC4 commissioning will be used to check the performance of a modified version of the laser-based instrument. The system will be part of a diagnostics test bench that will be temporarily installed after the last DTL cavity (50 MeV) and then moved after last CCDTL cavity (100 MeV).

For these development stages, the system will be setup for measurements in the vertical plane only, with the aim of demonstrating the ion beam profile reconstruction by collecting the electrons that are photo-detached during the laser scan [4].

* thomas.hofmann@cern.ch

The main novelty of our system with respect to those in other facilities [5,6] will be the use of a relatively low power laser and of a fast diamond detector as electron collector.

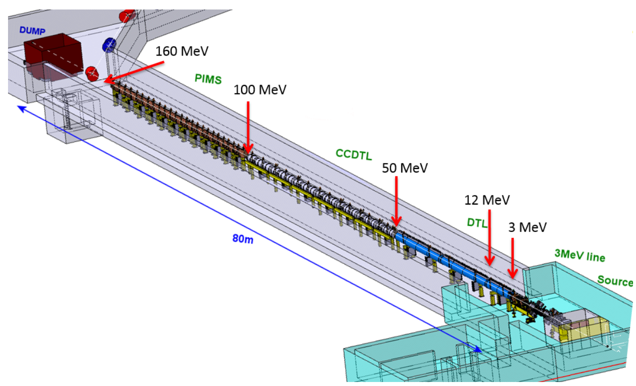

Figure 1: LINAC4 facility indicating the beam energy that will be reached during the different commissioning stages. The laser stripping system has already been tested at 3 MeV and 12 MeV periods and is presently setup for 50 MeV and 100 MeV before being permanently installed at 160 MeV.

CONCEPTUAL DESIGN

The conceptual and mechanical design of the system is shown in Fig. 2. Since in our application the laser beam is relatively small with respect to the H^- beam size, the vertical position of the liberated electrons is well defined and counting the stripped electrons as function of the laser position during a scan allows the beam profile to be reconstructed. A dipole magnet located just after the laser interaction point (IP) is used to extract the electrons toward the diamond detector designed to integrate the electron signal. Due to the much lower energy of the stripped electrons with respect to the H^- ions, the magnetic field necessary to extract the electrons has a very weak effect on the main beam.

As the detachment cross section is small and during a linac pulse only a tiny H^- beamlet is traversed by the laser, less than 10^8 H^- ions per linac pulse are neutralized (i.e. lost). Compared with the total pulse charge of 10^{14} for the nominal beam current (40 mA), this technique can therefore be considered as non-invasive.

LASER DELIVERY, TRANSPORT AND FOCUSING

The selected fiber-laser (V-Gen VPFL-ISP-1-40-50) operates at a wavelength of 1064 nm, with kilowatt peak powers

ISBN 978-3-95450-176-2

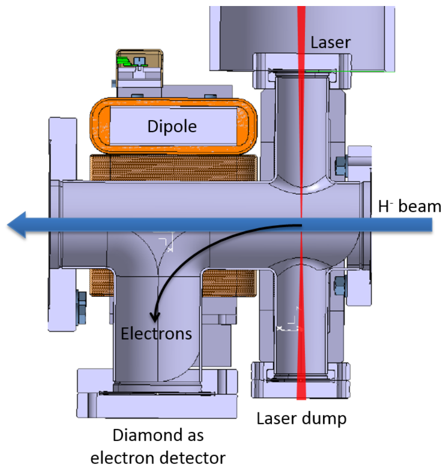

Figure 2: Conceptual design of the laser profile monitor.

and pulse-lengths variable from 1 ns to 300 ns. This is significantly different from existing systems [6, 7], based on q-switched Nd-YAG lasers with peak powers 3 orders of magnitude higher.

The low peak-power facilitates the laser operation/safety measures and allows the laser to be transported from its location in the klystron gallery to the interaction point (IP) by means of a large-mode-area (LMA) optical fiber [8]. This represents a distance of 20 m to the final position at 160 MeV and 75 m to the 50 MeV area (see Fig. 1). This technique greatly reduces the complexity of the transport system and thus provides a reliable solution with minimal maintenance. The remaining challenges are the high power densities at the end-facets [9] and non-linear effects in the fiber, which limits the transmitted peak power [10].

The optical setup to focus the laser to the IP consists of collimation and focusing optics which are mounted on a vertical stage to scan the laser across the H^- beam. Furthermore an optical path to characterise the laser pulse shape and M^2 is added. More details can be found in [1].

75 m Fiber Transmission

Looking into theory, Stimulated Brillouin Scattering (SBS) is the dominant non-linear effect, limiting the transmission through the fiber. This effect increases with the length of the fiber and acts above a certain peak power threshold, causing Stokes-shifted back-reflections due to spontaneous light scattering at thermal phonons. The threshold peak power is defined in [10] as,

$$P_{B,th} = C_{B,th} \frac{1}{\gamma_B L_{eff}} \qquad (1)$$

where $C_{B,th}$ is the critical factor, γ_B is the fiber-specific Brillouin coefficient and L_{eff} the fiber length. Moreover, SBS also depends on the spectral width of the stimulating laser pulse. For shorter pulses corresponding to wider spectra the effect is less dominant. As $C_{B,th}$ and γ_B is not known for the LMA fiber, a test in the laboratory was performed to characterize the laser transmission

Figure 3 shows the pulse shape before and after the fiber transmission for different pulse energies. The pulses after transmission are clearly delayed by 375 ns, which corresponds to the light propagation along 75 m. Distortions in pulse shape and pulse width cannot be observed even for peak powers above 2 kW.

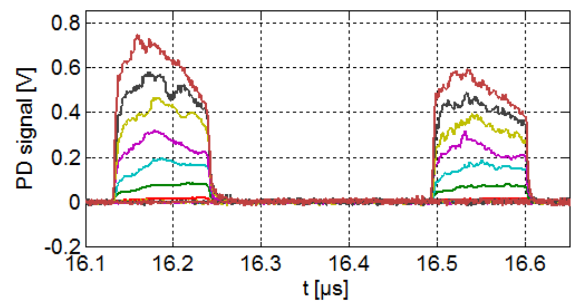

Figure 3: Laser pulses with different energies before (left) and after fiber (right).

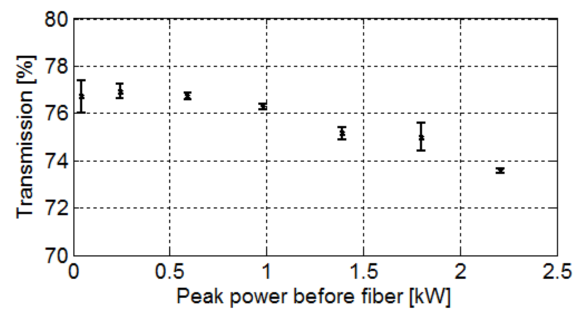

Figure 4: Laser transmission through the 75m large-mode-area (LMA) optical fiber.

By using an energy meter with a large surface detector, the overall transmission of the laser pulses could also be measured for different peak powers. The plot in Fig. 4 shows a transmission above 75% below 1 kW peak power and slightly lower transmission for higher pulse peak powers. The tests were not continued beyond the 2 kW level, in order not to damage the fiber end-facets before the actual beam measurements. The experiences gained during the measurement campaigns at 3 MeV and 12 MeV [1, 2] makes us confident that sufficient electron stripping can be achieved with laser peak powers below 1 kW. Measurements with 5 ns, 10 ns and 30 ns pulse lengths confirmed the high transmission for similar high peak powers.

After these laboratory tests we concluded that the fiber transmission with peak powers below 2 kW works very reliably and is not significantly affected by SBS.

Another challenge for kilowatt fiber transmission is the coupling into the fiber core. The LMA-fiber we are using has a 20 µm core diameter, which can lead to power densities of more than 100 J/cm^2. In this regime ablation can take place and damage the end-facet [9].

To handle this problem, fiber connectors with inserted end-caps were chosen. As illustrated in Fig. 5, the core material is expanded into the cladding area. In this way,

ISBN 978-3-95450-176-2

the laser must be focused inside the fiber to maximise the transmission, which means that the power density at the fiber surface is greatly reduced.

Using this technique no issues with burned end-facets were observed, in contrast to what occurred during the measurements with the LINAC4 3 MeV beam, when the fiber was not equipped with end-cap connectors.

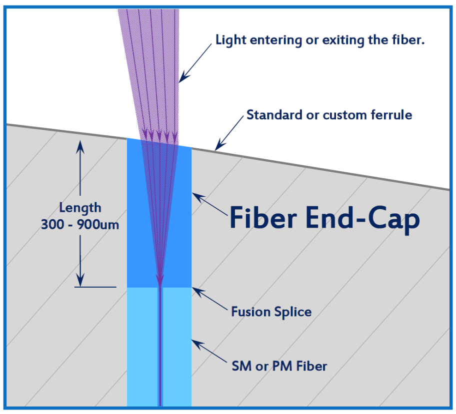

Figure 5: Principle of end-cap fiber facet [11].

ELECTRON MONITORING

As shown in Fig. 2, the dipole magnetic field guides the detached electrons from the main H^- beam axis into a T-shaped vacuum chamber hosting the diamond detector. In this section the magnet and detector design will be described.

Electron Deflector

The electrons kinetic energy is only 27 keV, as can be derived from the 50 MeV H^- energy and the proton to electron mass ratio. These low energy electrons can be deflected by 90° with an integrated field of only 0.9 mTm.

Steerer magnets used routinely at LINAC4 can provide up to 3.5 mTm integrated field. We therefore decided to modify one of these steerer magnets as a simple and cost-effective solution. By removing the magnet coil on the T-chamber side, the steerer acts as a C-shaped magnet with the remaining coil powered to create the field.

To predict the electron trajectories in the modified steerer field, a magnetic field-map was created. In Fig. 6 the B-field in the Y-plane is plotted. The trajectories for the stripped electrons were simulated using as input the beam dynamics data in the plane of the laser interaction (X = 0 mm; Z = -83 mm) and the magnetic vector-field. In addition to the Lorentz force, space charge effects of the main H^- beam and synchrotron radiation was taken into account but had no significant effects on the paths of the electrons.

In Fig. 6 the black curve represents the 3-sigma envelope of the electron trajectory when powering the magnet coil with a current of 4.7 A. The dark blue bar at Z = -60 mm represents a shielding which surrounds the beam-pipe between laser IP and steerer magnet. The shielding outside the vacuum chamber was designed to modify the magnetic field lines in order to avoid electrons being deflected too early after the stripping process and subsequently hitting the wall of the beam-pipe before reaching the extraction channel towards the electron monitor.

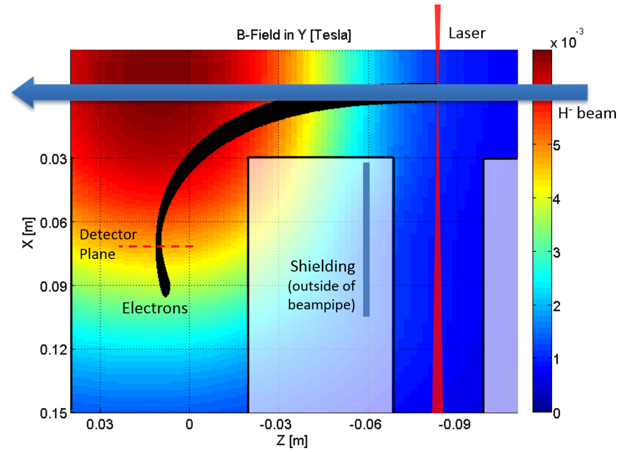

Figure 6: Magnetic field map (in Tesla) and electron trajectories (black) from the laser interaction point to the diamond detector. White areas are outside of beam-pipe.

Figure 7 visualizes an overlay of electron distributions, generated during the laser scanning process, arriving at X = 72 mm. It represents the superposition of the stripped electrons at each laser position during the vertical laser-scan. For one laser position, the width of the distribution in the Y-plane would be less than 1 mm. The detector position X = 72 mm was chosen, as this is the focal point generated by the weak focusing of the dipole.

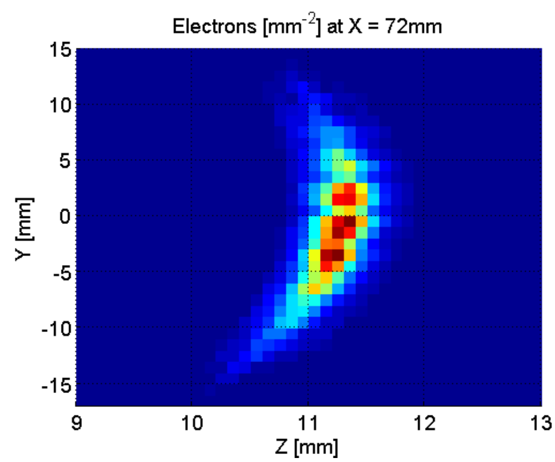

Figure 7: Expected electrons distribution at the detector plane, accounting for all laser positions during a scan.

Diamond Detector

A laser pulse with 100 µJ pulse-energy and 100 ns pulse-length is expected to detach approx. $5 \cdot 10^5$ electrons from the atomic cores. The detection of such a small number of low energy electrons (E_{kin} =27 keV) required the design

ISBN 978-3-95450-176-2

of a high sensitivity and fast (to cope with the short laser pulses) detector.

After considering various options, it was decided to design and fabricate a single-crystal chemical vapor deposition (sCVD) diamond detector, capable of providing a fast response, high sensitivity and radiation hardness. A picture of the detector that was recently installed in the laser profile meter tank assembly is shown in Fig. 8.

The front electrode of the detector facing the electron beamlet is bonded to ground potential all around its perimeter to avoid electro-magnetic disturbance from the main H^- beam passing just 72 mm away from the detector.

Due to the low range of the electrons (6 µm in diamond) this front electrode must be as thin as possible in order to minimize energy loss. Table 1 lists the front electrode layer materials and associated energy loss. In summary, 3.2 keV of the electron‘s energy is absorbed in the electrode layers while 23.8 keV is left to create a signal in the diamond bulk.

Table 1: Diamond Detector Layer Composition

Layer	Thickness	Energy Loss of e^-
Gold	250 nm	2.3 keV
Platin	120 nm	0.7 keV
Titan	100 nm	0.2 keV
Diamond	500 µm	23.8 keV

The electron signal generation and read out is sketched in Fig. 9. The 23.8 keV energy deposition creates electron hole pairs, each requiring 13 eV (diamond’s generation energy). This means that a charge of $1.5 \cdot 10^{-10}$ C is created for the $5 \cdot 10^{-5}$ electrons generated by each laser pulse, which can then be read out via the applied bias of 500 V. Due to the single crystal diamond material, no internal losses are expected. The charge is then amplified and converted to a voltage signal that can be digitized by a 1 GSps Analog-to-Digital-converter (ADC). A filter circuit, included in the preamplifier, was designed to separate the high-frequency signal of the laser pulses from low-frequency background

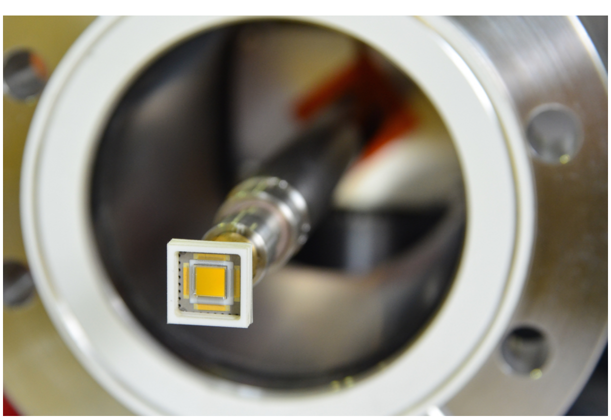

Figure 8: sCVD diamond detector [12] mounted on the actuator that is part of the laser monitor assembly for the 50 MeV experiment.

(e.g. electrons from beam-gas ionization occurring in the drift space upstream the laser IP).

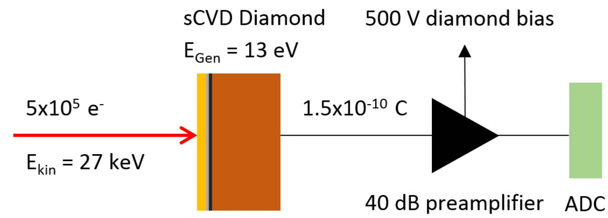

Figure 9: Signal creation and readout of the diamond detector.

In order to achieve the detector bandwidth required to resolve the laser pulses, it was decided to produce a detector with a relatively small surface (4 mm x 4 mm) to avoid parasitic capacitances. This feature also minimizes electromagnetic coupling and background due to residual gas stripping [1].

In order to ensure the collection of all electrons during a scan (see Fig. 7) with such a small detector, the diamond is mounted on an actuator that will be moved in synchronism with the laser. As the laser width is approx. 150 µm, the electron beamlet will be spread out less than one millimeter in the Y-plane of the detector. Therefore no electrons missing the diamond detector are expected.

SUMMARY AND OUTLOOK

A system for non-destructive vertical profile measurements for the LINAC4 H^- beam has been designed. The laser system consists of a pulsed laser-source, a 75 m long fiber-based laser transport line, a scanning and diagnostics assembly and a laser energy meter functioning as a laser dump. Tests of the laser delivery with a 75 m fiber have been performed and the results are very promising.

The liberated electrons will be deflected by a modified steerer magnet, with the electron trajectory optimization and the dimensioning of the detector supported by a set of dedicated electron tracking simulations accounting for space charge effects.

A sCVD diamond detector was chosen as electron collector. The monitor design was based on studies to optimize signal formation and electromagnetic shielding. It was decided to move the detector vertically synchronous with the laser to achieve a compact design with a fast response.

Figure 10 shows a picture of the system installed at LINAC4, as part of the 50/100 MeV test bench. According to the present LINAC4 schedule, first beam tests at an energy of 50 MeV are foreseen in October 2015. The next tests at 100 MeV will take place in early 2016 and will be used to gain more experience in operating the novel profile-meter to feed-in to the design of the final system. This final system will be installed permanently at the LINAC4 top energy of 160 MeV and will be designed to monitor both horizontal and vertical transverse profiles (via electron monitoring) and the transverse emittances (via H^0 monitoring).

ISBN 978-3-95450-176-2

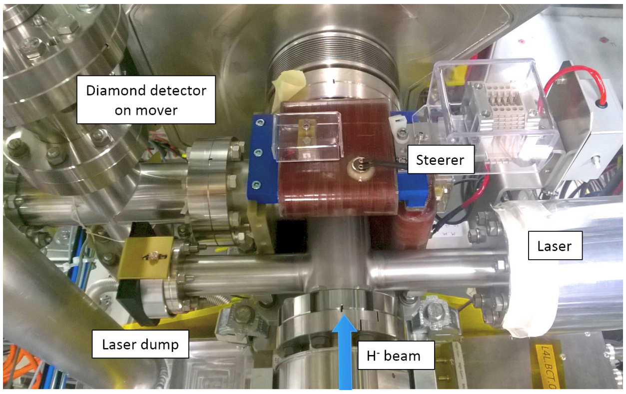

Figure 10: Installed system at the LINAC4 diagnostic test-bench.

ACKNOWLEDGEMENTS

We acknowledge the support of the Marie Curie Network LA^{3}NET which is funded by the European Commission under Grant Agreement Number GA-ITN-2011-289191.

In addition we would like to thank A. Vorozhtsov and J. Bauche for providing and commissioning of the steerer magnet and generating a magnetic field map as well as the LINAC4 commissioning team for giving us the opportunity to test our novel instrument.

REFERENCES

[1] T. Hofmann et al., “Demonstration of a Laserwire Emittance Scanner for the CERN LINAC4 H-. Beam”, to be submitted to Phys. Rev. ST, Accelerators and Beams, Preprint: arXiv:1508.05750

[2] T. Hofmann et al., “Experimental results of the laserwire emittance scanner for LINAC4 at CERN” Proceedings of Laser Applications at Accelerators Conference 2015, Mallorca, Spain

[3] S. Gibson et al., "A fibre coupled, lowpower laserwire emittance scanner at CERN LINAC4", Proceedings of IPAC2014, Dresden, Germany

[4] J.T. Broad, W.P. Reinhardt,"One- and two-electron photoejection from H^- : A multichannel J-matrix calculation", Physics Review A 14, 2159 (1976)

[5] R. Connolly et al., “A laser-wire beam-energy and beam-profile monitor at the BNL LINAC”, MOP194, Proceedings of 2011 PAC, New York, NY, USA

[6] Y. Liu et al., "Laser wire beam profile monitor in the spallation neutron source (SNS) superconducting linac", Nucl. Instr. and Meth. in Phys. Res. section A 612, 241, (2010).

[7] W.B. Cottingame, G.P. Boicourt, J.H. Cortez, W.W. Higgins, O.R. Sander, D.P. Sandoval, "Noninterceptive techniques for the measurement of longitudinal parameters for thr intense H^- beams" IEEE Trans. Nucl. Sci., NS-32(5):1871-1873, 1985.

[8] Datasheet, "20/130 Passive LMA Double Clad Fiber", www.nufern.com

[9] G. Mann et al., "Nanosecond laser damage resistance of differently prepared semi-finished parts of optical multimode fibers", Applied Surface Science 254, pp.1096-1100 (2007)

[10] Rainer Engelbrecht, "Nichtlineare Faseroptik - Grundlagen und Anwendungsbeispiele", Springer, 2014

[11] Coastal Connections, www.coastalconnections.biz, California, USA

[12] CIVIDEC Instrumentation GmbH, www.cividec.at, Austria

ISBN 978-3-95450-176-2

TRANSVERSE RIGID DIPOLE AND INTRA-BUNCH OSCILLATION DETECTION USING THE TRANSVERSE FEEDBACK BEAM POSITION DETECTION SCHEME IN SPS AND LHC

W. Hofle, G. Kotzian, D. Valuch, CERN, Geneva, Switzerland

Abstract

The LHC and SPS transverse dampers use beam position electronics with I,Q detection at 400 MHz and 200 MHz, of the sum and difference signals from a strip-line pick-up. Digitization is performed to give synchronous bunch-by-bunch data at the rate of 40 MHz corresponding to the bunch spacing of 25 ns. A performance in the μm range is achieved with beams in LHC and has contributed to the high performance of the essential transverse feedback during the LHC run 1. In the present paper we review the systems deployed and their performance as well as the potential of the I,Q detection to also detect intra-bunch motion. The principle is illustrated using data from LHC injection tests in which intra-bunch motion is expected and has been observed due to electron cloud instabilities. The potential use of this signal to drive a transverse intra-bunch feedback system is outlined.

INTRODUCTION

The CERN LHC transverse feedback system, fully commissioned in 2010 [1] uses strip-line beam position monitors to detect bunch oscillations [2] around the closed orbit and provides feedback to damp these oscillations and keep the beam stable. Kickers operate in baseband and cover betatron frequencies up to 20 MHz, half the bunch repetition frequency to be able to damp all coupled bunch dipole oscillations. The power system of the LHC transverse feedback system uses the same technology as used in the CERN SPS transverse feedback system having operated for many years. Kickers use the electric field only with kicker plates ranging from 1.5 m length to 2.4 m length (1.5 m for the LHC and the SPS vertical systems and 2.4 m for the SPS horizontal systems) driven by tetrode tube amplifiers directly installed in the accelerator tunnel under the kicker structure. The SPS transverse feedback system has been upgraded during the long shutdown 1 (LS1, 2013-2014) as part of the LHC Injector Upgrade Project (LIU) [3] to use the same analogue and digital signal processing techniques as already used successfully since 2010 in the LHC.

In the following we describe the signal processing, analogue and digital, used to compute the bunch position (symmetric mode component) as well as the headtail oscillation amplitude (asymmetric mode component).

POSITION DETECTION IN THE SPS AND LHC TRANSVERSE DAMPERS

The stripline pick-ups are optimized in length to have the maximum response around the RF frequency of the main RF system in these accelerators, 400 MHz in case of the LHC and 200 MHz in the SPS case. The SPS system also includes a variant of hardware for the doublet scrubbing beam, a beam that is split at SPS injection to form two bunches spaced 5 ns every 25 ns [3]. The hardware dedicated to this type of beam takes the beam-pick-up signal at a band centered around 40 MHz directly sampling it with 120 MS/s without analogue down conversion. This ensures proper operation during the splitting process.

LHC Transverse Damper (ADT)

The LHC pick-up signal processing scheme [2] is depicted in Fig. 1. The signals from the strip-line pick-up plates pass through a hybrid and both the sum signal (proportional to bunch intensity) and the delta signal (difference of PU plates, proportional to bunch intensity and position) are taken into account in the further processing. A band-pass filter selects the frequency components around the RF frequency of 400 MHz. The filter is shaped to give in time domain a burst of nine pulses from each bunch, at 400 MHz. Each of the signal bursts from the individual bunches is then separated by one RF period, 2.5 ns , for the canonical bunch spacing of 25 ns. After analogue down conversion a 15 ns to 20 ns wide pulse is obtained that is sampled synchronously using a 40 MHz sampling clock. Digitization is done with a 16 bit ADC and four numerical values are obtained for each bunch, the in-phase (I) and quadrature components (Q) — with respect to the RF frequency — of the Σ and Δ signals.

Within an FPGA the absolute value of the bunch position can be calculated by division of the magnitude of the (I, Q) vector of the Δ and Σ signals

$$x = \frac{\sqrt{\Delta_\mathrm{I}^2 + \Delta_\mathrm{Q}^2}}{\sqrt{\Sigma_\mathrm{I}^2 + \Sigma_\mathrm{Q}^2}} c_\mathrm{cal} \,. \tag{1}$$

The sign for the beam position has to be correctly chosen and depends on the exact phasing of the beam RF signal with the 400 MHz reference RF used for the demodulation. A calibration factor ($\mathrm{mm}/\mathrm{counts}_\mathrm{ADC}$) is determined when the damper is set-up using the orbit measurement system and making closed orbit bumps at the location of the damper pick-ups. In practice, on the FPGA in the damper feedback system, a different algorithm is used to compute the normalised position which takes into account the measured angle between sum and delta signal with respect to the (I,Q) coordinates defined by the 400 MHz RF. This algorithm is using the relation

$$\frac{\Delta_\mathrm{I}\Sigma_\mathrm{I} + \Delta_\mathrm{Q}\Sigma_\mathrm{Q}}{\Sigma_\mathrm{I}^2 + \Sigma_\mathrm{Q}^2} = \frac{|\Delta|}{|\Sigma|}\cos(\phi_\Delta - \phi_\Sigma) \tag{2}$$

ISBN 978-3-95450-176-2

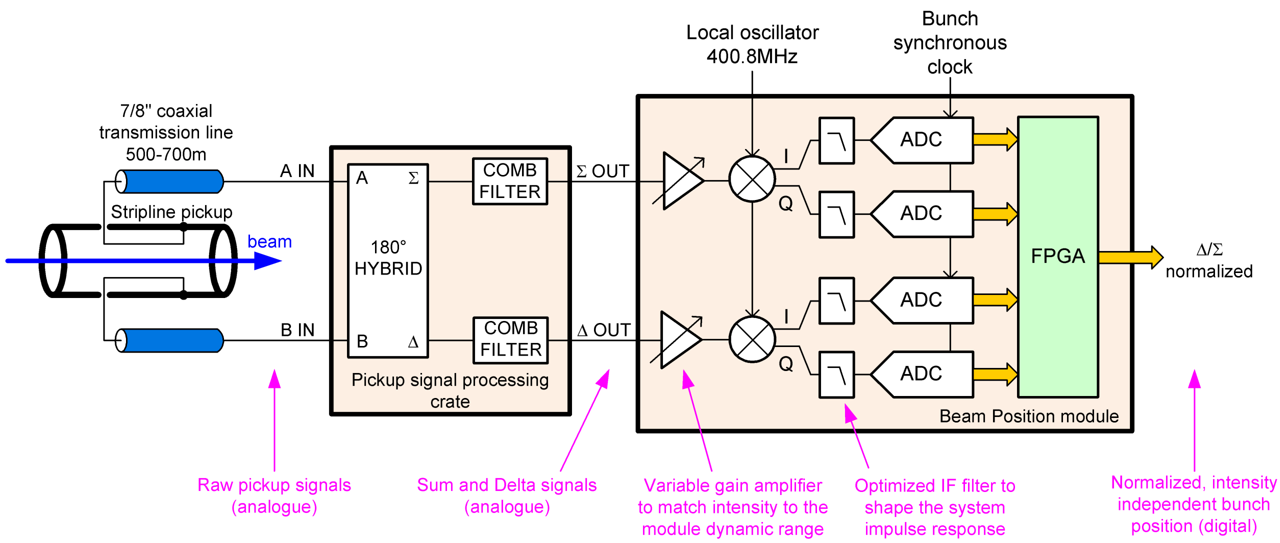

Figure 1: Pick-up front-end processing for LHC transverse feedback system (ADT).

where ϕ_Δ and ϕ_Σ are the phases of the delta and sum signals with respect to the RF signal at the mixer. It can be seen that, if the signals are aligned on the mixers (Δ and Σ vectors parallel in (I,Q) space) the expression yields readily the normalised beam position with the sign coded in the difference angle between sum and delta $\Delta\phi = \phi_\Delta - \phi_\Sigma$. In this case, $\Delta\phi$ is 0 for positive position and π for negative positions as calibrated by comparison with the orbit system. In practice the vectorial alignment of the sum and delta signals is not done in the analog domain, but digitally by applying a standard rotation matrix to the Δ signal

$$\begin{pmatrix}\Delta_I\\ \Delta_Q\end{pmatrix} = \begin{pmatrix}\cos\psi & -\sin\psi\\ \sin\psi & \cos\psi\end{pmatrix}\begin{pmatrix}\Delta'_I\\ \Delta'_Q\end{pmatrix} \tag{3}$$

where ψ is the required rotation angle to align sum and delta signals correctly in the (I,Q) space and the dashes apply to the raw digitized delta I and Q components. The angles ψ for each pick-up are determined during a beam-based calibration.

Provided both channels, sum (Σ) and difference signal (Δ) are equal in transmission characteristics from the pick-up through the hybrid and amplification chain as well as the down conversion, the resultant position is independent of both bunch intensity and bunch length. This is still true for a bunch with an asymmetric longitudinal shape as can be the case in the double harmonic system of the SPS with 200 MHz and 800 MHz RF. If bunches oscillate longitudinally the difference phase $\phi_\Delta - \phi_\Sigma$ remains equal and the computed bunch position is not affected by this oscillation.

SPS Transverse Damper

Within the SPS-LIU Project the lowlevel system of the SPS transverse damper was upgraded [3] and the system fitted with dedicated pick-ups and processing matched to the requirements of the specific beams. In total the upgrade is foreseeing four parallel signal processing paths, one for the fixed target beam (5 ns bunch spacing) using electrostatic pick-ups, and three for the LHC type beams using signals from two strip-line coupler pick-ups.

The three systems for the LHC type beams serve the standard LHC proton beams with a bunch spacing of a multiple of 25 ns, the special scrubbing doublet beam with two bunchlets spaced by 5 ns every 25 ns, and a special set of electronics foreseen for the LHC ion beam injection damping with unique requirements for the clocking scheme due to the FSK modulation of the RF [3].

Three out of the four transverse damper lowlevel systems for the SPS transverse damper were completed in long shutdown 1 (LS1) — all but the system foreseen for ions, which is still under development. All beams were re-commissioned in 2014/2015 with the SPS system now offering similar diagnostics for instabilities as the LHC transverse feedback system since 2010.

In the case of the SPS system a sampling frequency of 120 MHz was chosen at 16 bit, using a Dual ADC from Linear Technology (LTC 2185). The sampling is synchronous with the bunch repetition frequency of 40 MHz and allows two samples to be placed on the pulse from a single bunch meant to enhancing the signal/noise ratio. The choice of sampling rate also allows direct digitization of the RF signal for the scrubbing doublet beam from a band at 40 MHz.

The fact that the Δ signal is proportional to the bunch longitudinal profile and the bunch oscillation pattern can be viewed as a mixing process. This is illustrated in Fig. 2 for a symmtric osillation $x(t) = \cos(2\pi f t)$ at $f = 1$ GHz, on a guassian bunch with $4\sigma = 1.5$ ns. The resultant spectrum is the convolution of the complex spectra and also depicted in Fig. 2. The detected beam position will depend on the value of this spectrum at 400 MHz in the LHC case, the frequency of detection used for the transverse feedback system. For a given bunch profile $\lambda(t)$ we can now plot the sensitivity of the detected position on the intra-bunch frequency and

ISBN 978-3-95450-176-2

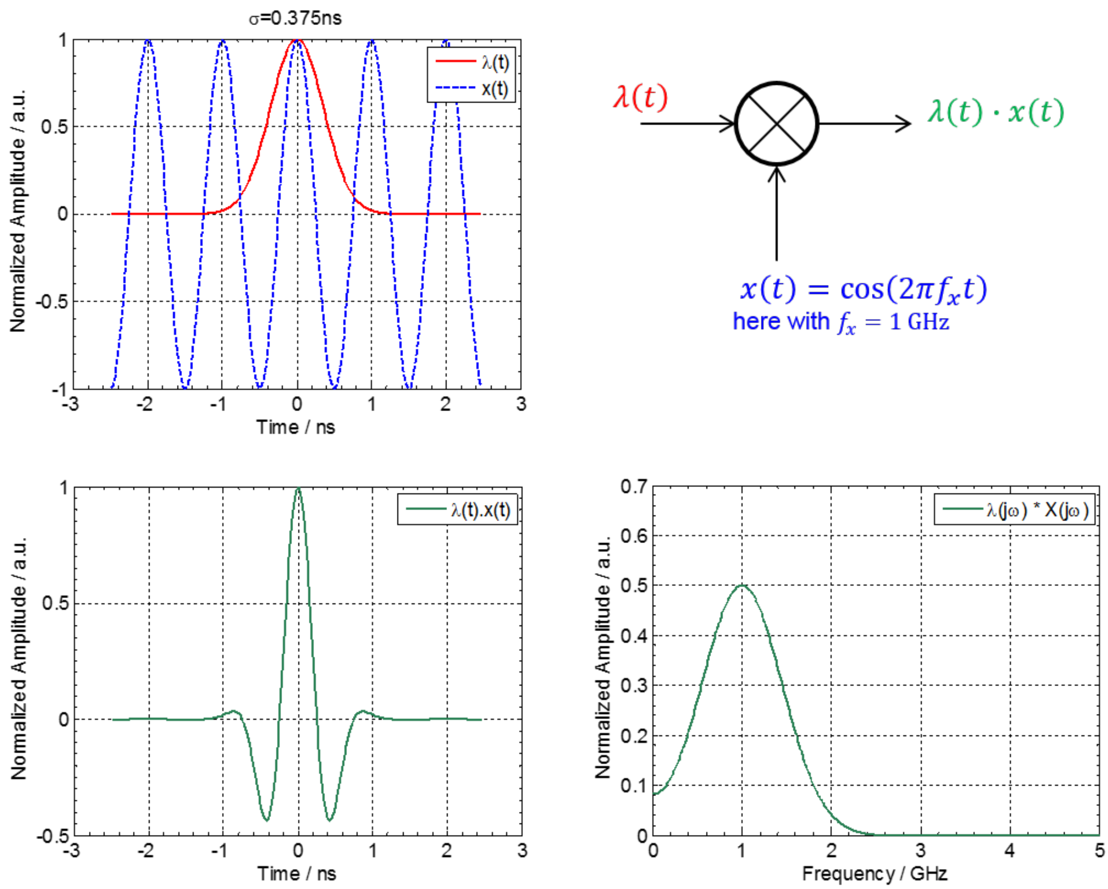

Figure 2: Illustration of internal bunch oscillation pattern multiplied by bunch shape function (top) with resulting time domain pick-up Δ signal and spectrum (bottom).

compare it with the average weighted bunch position (see Fig. 4).

$$\bar{x} = \int_{\text{bucket}} x(t)\lambda(t)\mathrm{d}t \ . \tag{4}$$

SENSITIVITY TO INTRA BUNCH MOTION

In the presence of intra-bunch transverse motion the 400 MHz component of the transverse signal will carry information of this oscillation in its amplitude and phase when compared to the 400 MHz component of the longitudinal signal. This fact is explored in the Multiband-Instability-Monitor being developed at CERN [4]. In this monitor system a bank of band-pass filtered spaced in frequency at the inverse of the bucket-length is used to track down in which frequency range instability occurs. The combination of direct diode detection from the BBQ system [5] is combined to give a very sensitive instrument that can indicate that beam instability occurs in a certain range of frequencies within a multi-bunch beam. However, using gating on the BBQ type of detector reduces its signal-to-noise ratio that can be achieved, making it difficult to track down within a bunch train the instability to a specific bunch. The scheme proposed here in this paper overcomes this limitation and is well adapted to diagnose intra-bunch motion on a bunch-by-bunch basis.

Rigid Dipole Oscillation and Symmetric Component

Taking an actual, non-gaussian profile, as has been measured for LHC with notches in the spectra at 1.5 GHz [6] can reveal some subtleties in the following example of the spectrum of Fig. 3 approximating the LHC spectra of LHC Run 1 [6]. The spectral sensitivity of the detected oscillation for this spectrum is shown in Fig. 4. For a rigid dipole oscillation ($f = 0$) the algorithm (1) exactly gives the average bunch position. For higher symmetric oscillations within the bunch the algorithm used in the feedback gives a signal slightly larger for this type of bunch shape. At 1.5 GHz, the first zero in the spectrum the sign changes for the computed position. This means if an oscillation develops at such a high frequency the feedback system does no longer damp directly the oscillation of the average bunch position that results from this oscillation. However, as the beam then will coherently oscillate also in baseband where a large feedback gain is available this phenomenon is not expected to lead to instability but thought to merely represent an additional mechanism that injects noise into the system.

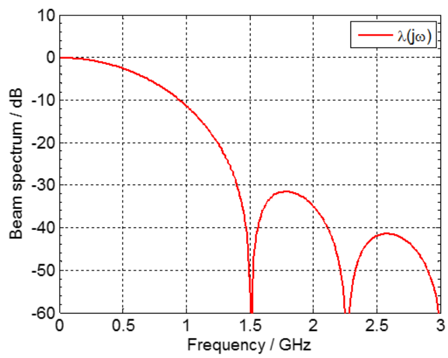

Figure 3: Approximated spectrum of bunch from LHC run 1 [6].

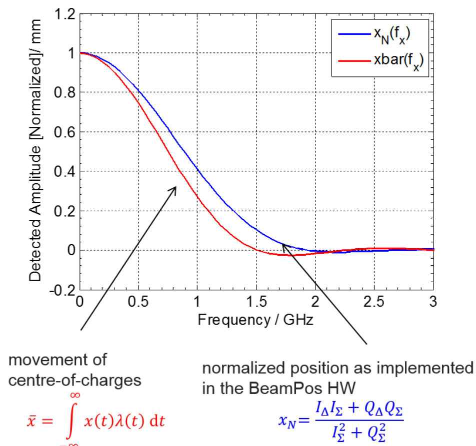

Figure 4: Computed bunch position for symmetric component of oscillation within bunch compared to bunch position weighted with line density.

Headtail Oscillation and Asymmetric Component

The I and Q components of Σ and Δ can be combined in a different way to give a single quantity indicating the presence of asymmetric oscillations within the bunch. Again the sensitivity of this cross term

$$x_{\mathrm{HT}} = \frac{\Delta_{\mathrm{Q}}\Sigma_{\mathrm{I}} - \Delta_{\mathrm{I}}\Sigma_{\mathrm{Q}}}{\Sigma_{\mathrm{I}}^2 + \Sigma_{\mathrm{Q}}^2} \tag{5}$$

can be computed as a function of frequency (Fig. 5).

Equation (5) assumes correct alignment in (I, Q) space. Using 400 MHz for the down conversion as in the LHC shows a broad range of frequencies up to close to 2 GHz that the algorithm is sensitive to. Since this quantity x_{HT} can be computed on a bunch-by-bunch basis, this presents an excellent possibility to diagnose intra-bunch headtail oscillations pointing to the unstable bunches in a train. Deploying this type of detection scheme on the Multi-Band-Instability Monitor would add additional possibilities to track down the frequency band of instability.

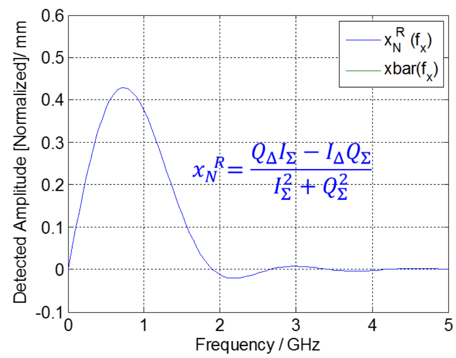

Figure 5: Computed bunch position for asymmetric component of oscillation within bunch; the weighted position for an asymmetric oscillation is always zero for a symmetric line density.

EXAMPLE FROM BEAM OPERATION

Trains of 48 bunches with 25 ns bunch spacing were for the first time injected into LHC in run 1 in 2011. As an example we will show results from a particular beam dump on August 26, 2011 with transverse feedback off. Following injection a transverse instability developed, interpreted as being driven by the electron effect [7, 8]. The data from the postmortem system of the LHC transverse damper for this dump were already analyzed in depth with respect to the rigid bunch motion using Eq. (1) [7]. Applying the algorithm (5) to the raw data reveals that in addition to the rigid bunch dipole oscillation there is also a headtail oscillation present. The two oscillation patterns dipole and headtail, are compared with their bunch-by-bunch amplitudes plotted in Fig. 6. Shown are the injected batch of 48 bunches for the last 73 turns before the beam dump. Clearly the instability, both rigid dipole and headtail develop along the batch and are similar in order of magnitude.

POTENTIAL OF HEADTAIL SIGNAL FOR USE IN A FEEDBACK SYSTEM

The headtail signal has a potential to be used in a feedback system. Similar to the approach of the SPS High Bandwidth Transvserse Feedback system [9], the signal could drive a kicker to damp the oscillation. Up-conversion to the RF frequency is needed as well as a signal processing that creates a signal in quadrature to the oscillation which can be achieved by digital processing using FIR filters similar to the standard coupled bunch feedbacks used at CERN. The up-conversion will create a signal that varies across the bunch and can drive a set of wideband kickers. The technique is particularly interesting for LHC where the shorter bunch length may limit the use of direct digitization of the signal. Moreover, resolution is more important for LHC where keeping noise levels low in any operating transverse feedback system is of great importance. The sampling in baseband of the proposed system offers the advantage of a large number of bit available

ISBN 978-3-95450-176-2

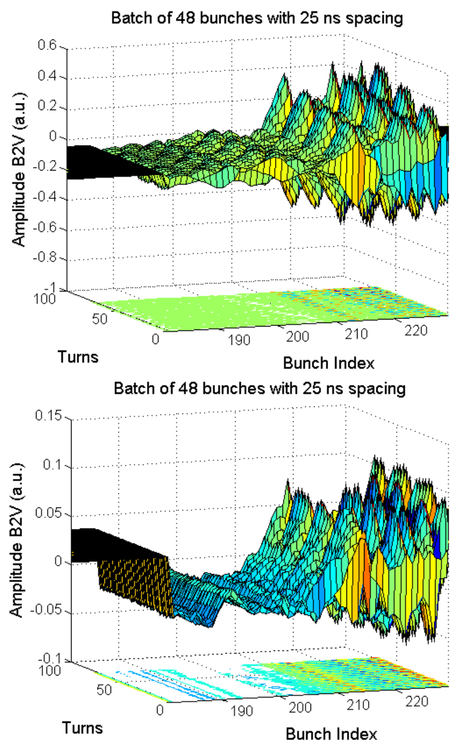

Figure 6: Symmetric (top) [7,8] and asymmetric (headtail, bottom) bunch oscillation pattern along batch before beam dump; LHC, 26.08.2011, transverse feedback off.

compared to direct sampling of the GHz analog signals and consequently a better resolution.

SUMMARY AND CONCLUSION

We have shown how in addition to the bunch position headtail oscillations can be detected using the existing hardware of the LHC and upgraded SPS transverse dampers. The method is promising as it can point to instabilities within a bunch train and identify which bunches are unstable. The potential use of the headtail signal to drive a feedback system to damp the fundamental lowest order asymmetric mode within a bunch has been outlined and represents a promising path to follow in simulation and experiment.

REFERENCES

[1] W. Höfle, G. Kotzian, M. Schokker, D. Valuch, *LHC Damper Beam Commissioning in 2010*, IPAC'11, San Sebastian, September 2011, MOPO012, (2011).

[2] P. Baudrenghien, D. Valuch, *Beam phase measurement and transverse position measurement module for the LHC*, LLRF07 Workshop, October 2007, Knoxville TN, USA (2007); CERN EDMS document 929563, CERN, Geneva, `https://edms.cern.ch/file/929563/1/llrf07_poster.pdf`, (2007).

[3] J. Coupard et al. (Ed.), *LHC Injectors Upgrade, Technical Design Report - Vol. 1: Protons*, CERN-ACC-2014-0337, CERN, Geneva, Switzerland, (2014).

[4] R. Steinhagen, M. J. Boland, T. G. Lucas, *A Multiband-Instability-Monitor for High-Frequency Intra-Bunch Beam Diagnostics*, IBIC'13, Oxford, September 2013, TUBL3, (2013).

[5] M. Gasior and R. Jones, *The Principle and First Results of Betatron Tune Measurement by Direct Diode Detection*, LHC-Project-Report-853, CERN, Geneva, Switzerland, (2005).

[6] B. Salvant et al., *Update on Beam Induced RF Heating in the LHC*, IPAC'13, May 2013, TUPME032, (2013).

[7] H. Bartosik, W. Höfle, *Analysis of bunch by bunch oscillation with bunch trains at injection into LHC at 25 ns bunch spacing*, CERN-ATS-Note-2012-027 MD (LHC), CERN, Geneva (2012).

[8] H. Bartosik, W. Höfle, G. Iadarola, Y. Papaphilippou, G. Rumolo, *Benchmarking Headtail with Electron Cloud Instabilities observed in the LHC*, Ecloud'12, La Biodola, Isola d'Elba, June 2012, CERN-2013-002, p. 211-217.

[9] J. Fox et al., *Wideband Vertical Intra-bunch Feedback at the SPS - Technology Development, Recent Accelerator Measurements and Next Steps*, presented at IBIC'15, Melbourne, Australia, Sep 2015, paper WECLA04, *These Proceedings*.

ISBN 978-3-95450-176-2

DEVELOPMENT OF A VERSATILE OTR-ODR STATION FOR FUTURE LINEAR COLLIDERS.

R. Kieffer, T. Lefevre, S. Mazzoni, CERN, Geneva, Switzerland
L. Bobb, Diamond Light Source, Oxfordshire, UK
M. Bergamaschi, P. Karataev, T. Aumeyr, JAI, Egham, Royal Holloway, Univ. of London, Surrey, UK
M. Billing, J. Conway, J. Shanks, Cornell University, CLASSE, Ithaca, NY, USA
N. Terunuma, KEK, Tsukuba, Japan

Abstract

In order to study the feasibility of Optical Transition (OTR) and Diffraction (ODR) Radiation based profile measurement for the future electron-positron linear colliders (ILC, CLIC) a new dedicated instrument is under development at CERN to be installed in the Accelerator Test Facility 2 (ATF2) at KEK in fall 2015. To optimize sensitivity to micron and sub-micron beam sizes, we plan to observe ODR/OTR in the visible-UV wavelength range, down to approximately 150 nm. In this paper, we will present the status of the project with a focus on the target development which is one of the most critical aspects of the design.

INTRODUCTION

OTR beam imaging systems are widely used to measure the transverse properties of a particle beam. Recently, sub-micron beam size measurements have been reported on the ATF2 extraction beam line by measuring the visibility of the OTR point spread function [1–3]. However, as OTR occurs where a particle beam crosses a boundary between two different dielectric media, e.g. a Si target, the measurement is strongly invasive. An OTR target will withstand a single bunch but will get quickly damaged when using longer bunch trains as foreseen in linear colliders. A non-interceptive alternative for high power beams would be to replace the solid target by a slit, which will emit ODR. The Coulomb field induced by the beam generates polarisation currents on the slit edges that in turn give rise to radiation [4]. Similarly to OTR, Diffraction radiation will be emitted both in the backward (BDR) and forward (FDR) direction. Beam size information is retrieved from the far-field angular distribution of ODR. Experiments using ODR were performed in 2004 [5] measuring beam sizes as small as 14 microns. Since then ODR has been developed further [6] to provide online transverse beam size monitoring. Further improvements in resolution can be achieved by a careful optical design as well as the observation of DR at smaller wavelength down to 150 nm. In 2010, an experimental test program [7] was initiated aiming at developing the DR slit technology and possibly demonstrating resolution down to few microns.

In this paper, a combined Optical Transition Radiation (OTR) and Diffraction Radiation (ODR) monitor is being proposed to measure the ultra-small emittance of beams generated in damping rings. The latest results on slit development tested at Cornell are also discussed.

THE ODR/OTR STATION FOR ATF2

The Accelerator Test Facility 2 (ATF2) at KEK extracts a 1.28 GeV electron beam from the low-emittance damping ring of ATF, which can be focussed to a sub-micron vertical beam size [8], making it an ideal test facility for high resolution beam size studies. The first phase of the experiment will be dedicated to the OTR Point Spread Function (PSF) and ODR/OTR angular measurements in the visible range. At a later time, the setup will be upgraded with a UV ODR line to further improve optical resolution.

Description of the Setup

The station, as depicted in Fig. 1, will be composed of a mirrored target and a set of two masks (horizontal, vertical) in order to shield the target from synchrotron radiation. Mask and targets can be inserted and removed one by one with micrometer precision actuators. Two UV-compatible view ports sitting at 40 and 90 degrees with respect to the beam axis will be used to extract the light from the tank.

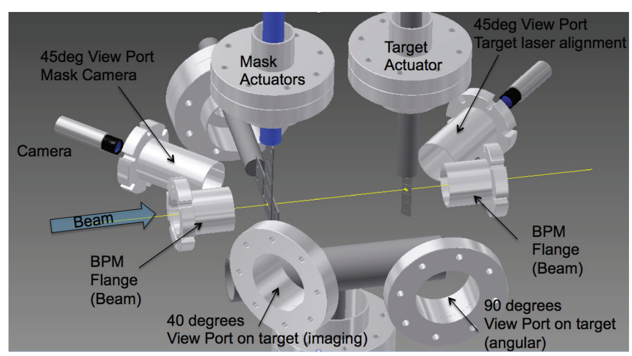

Figure 1: Sketch of the ODR-OTR station.

The OTR Optical Line

OTR will be used to measure single bunch, sub-micron beam size using the PSF visibility technique [2]. The optical line has been designed with the help of optical simulations performed with ZEMAX. [9] A two-lens system has been adopted, with a short (f = 15 mm) focal objective lens installed on the target holder producing an intermediate image that is conjugated to the camera sensor plane by means of a relay lens. This configuration allows a high magnification factor of up to M = 12 with a 4.6 mm PSF

ISBN 978-3-95450-176-2

peak separation in the intermediate image (see Fig. 2).

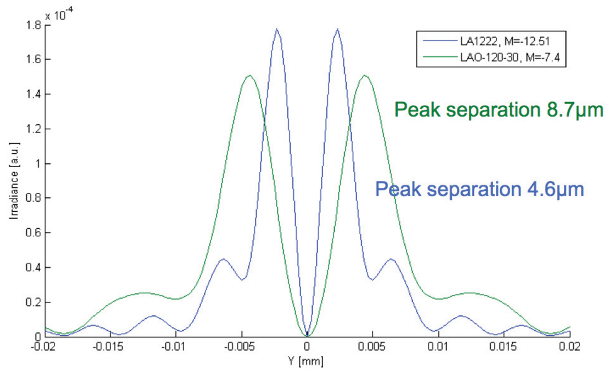

Figure 2: Zemax simulation of the expected OTR PSF for a selection of commercial lenses.

The target holder can be displaced with respect to the beam within micron step resolution (see Fig. 3). This allows the distance between source and first lens to be controlled, therefore changing the overall magnification. After bandpass and polarisation filters, the intermediate image is then imaged onto the camera (a pco edge 4.2 sCMOS) through a macro photo lens (Nikkor 40 mm f/2.8).

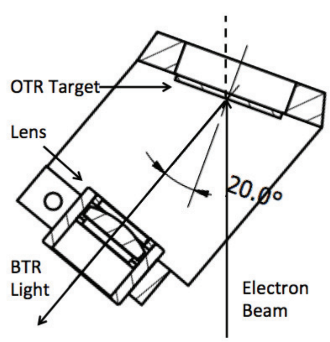

Figure 3: Sketch of the target holder in OTR position.

The ODR Setup

As mentioned before, ODR beam size measurements are derived from the reduction in visibility of the projected vertical polarisation component (PVPC) [5] of the far field angular distribution. This is achieved by placing the imaging sensor in the back focal plane of a lens. A 2 inch diameter lens of f=500 mm was chosen, allowing an approximate angular magnification of 12 μrad. The ODR target accommodates multiple slits of width d ranging from 200 to 25 μm. This ensures that DR is generated even for micrometer size beams both in the visible and UV, given that the condition $d \leq \lambda\gamma/2\pi$ holds even at $\lambda = 150$ nm for the smallest slit width. The challenging production of such a target due to the stringent requirements on surface co-planarity and slit edge roughness will be discussed in the following paragraphs.

OPTIMISATION OF THE SIGNAL TO NOISE RATIO

The design of the ODR target capitalizes on a series of ODR test runs performed at the Cornell Electron Storage Ring (CESR) test accelerator. The main noise contribution that was encountered is the synchrotron radiation (SR) emitted in bending magnets upstream the target. For ODR observation, the SR contribution can be almost equal to the ODR. Even if the SR is reduced to a much smaller amount on linear machines, such as in ATF2, it is still a source of noise that must be reduced to perform precise ODR measurements. To overcome this difficulty, two complementary approaches have been investigated and tested at CESR [6].

Synchrotron Radiation Shielding Mask

A shielding mask can be used to get rid of a part of the SR, as first suggested in [5]. In the CESR ODR experiment, a silicon carbide shielding mask was installed 15.5 mm upstream a target made of Suprasil fused silica glass with an aluminium and chromium coating to enhance specular reflection, (Fig. 4). While blocking part of the SR background, the mask is itself a new source of FDR, which will interfere with the BDR emitted from the target slit.

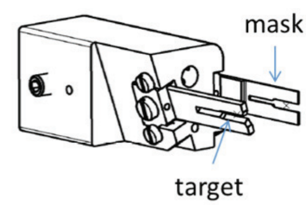

Figure 4: Isomeric view of the mask and target assembly.

Since the ODR angular distribution corresponds to the interference pattern of both FDR and BDR sources, the ratio between target and mask aperture will have a strong impact on the observed pattern. To probe this effect and evaluate the strength of this technique, a few target and mask apertures were tested on the CESR ODR setup. For the "mask:slit" ratio 4:1 shown in Fig. 5, the poor quality of the angular sides lobes is expected to be due to the interference of ODR with SR. The best signal to noise ratio was obtained using the ratio 2:1 for a 0.5 mm slit. This can be seen in Fig. 6 where the interference pattern has been fitted successfully with the theoretical model from [6] to extract the beam offset of 120 μm with respect to the slit centre, thanks to the SR shielding mask.

Reduction of Mirrored Surfaces

While imaging the target as seen in Fig. 7, we noticed that only a small part of the target is actually used in order to produce ODR light, while SR is reflected from the entire surface. To further improve the SR noise contribution, the targets have been modified to limit the highly reflective aluminium coated surfaces to small areas close to the edge that generates ODR, the light yield being proportional to the surface reflectivity.

ISBN 978-3-95450-176-2

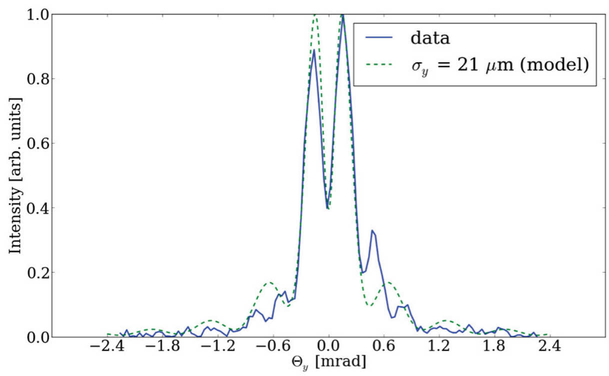

Figure 5: Angular distribution (4 mm mask : 1 mm target - Ratio: 4:1) fitted with ODR model (i. e. no interference).

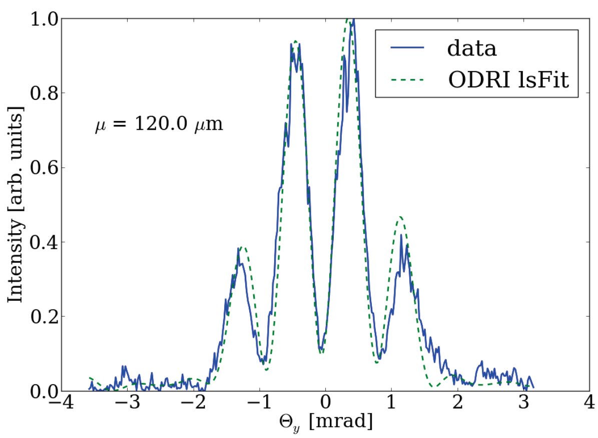

Figure 6: Angular distribution (1 mm mask : 0.5 mm target - Ratio: 2:1) fitted with ODRI model (i. e. interference between mask FDR and target BDR).

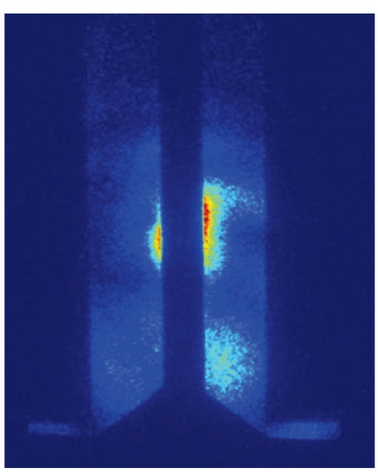

Figure 7: Imaging of the ODR target.

As the target substrate is made of glass, partial light reflection could still occur on non-coated surfaces. Multiple tests have been carried out to find the optimum way to further reduce the reflectivity around the ODR mirrors. Several samples were processed and their reflectivity spectra measured using an integrating sphere (see Fig. 8).

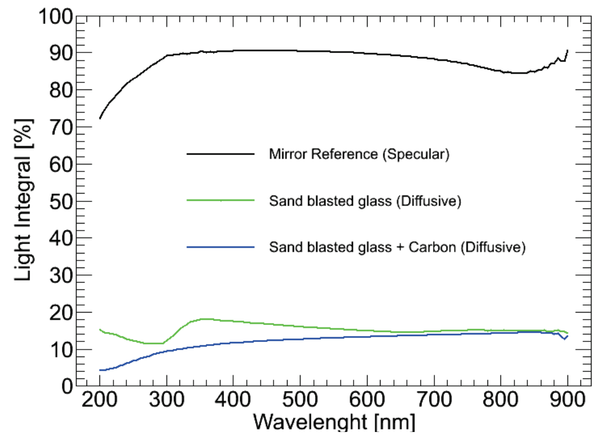

Figure 8: Reflectivity measurement, using an integrating sphere.

Micro sand blasting appears to be the most efficient technique to get a factor 6 attenuation of the reflectivity, including both specular and diffuse light. Carbon sputtering was also tried after sand-blasting. It seems to improve further the attenuation in the blue range but as it adds some complexity in the overall manufacturing process, and therefore we have not produced and tested a carbon coated target. If we scale the measured diffused power from the integrating sphere to the optical setup aperture, we obtain an attenuation factor of approximately 100 due to the fact that most of the light diffused by the sand blasted regions is not collected by the optical system.

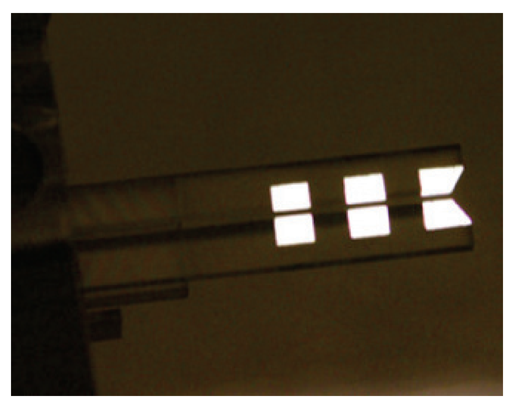

Figure 9: Reprocessed target, slit size 0.5mm, mirrors surface (2.5×4 mm^2).

A new target with three ODR mirrors (shown in Fig. 9) was tested in April 2015 at CESR. The ratio between SR and DR light was measured using angular domain images where SR and DR distributions are easily identified. Figure 10 shows their relative intensity as a function of the beam position along the slit. The SR light contribution increases as the slit is inserted further in, since the amount of SR reflected by the first two mirrored areas will contribute to the total amount of SR detected.

ISBN 978-3-95450-176-2

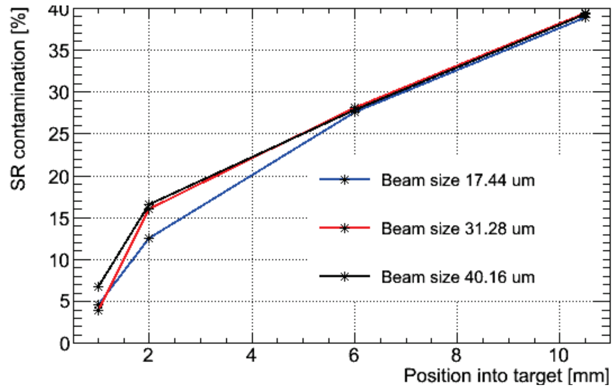

Figure 10: SR contamination in the angular domain for the three mirrors position inserting the target.

TARGET MANUFACTURING

In order to improve the sensitivity of the ODR measurement for micron-size beams, the slit must be small enough for an appreciable light yield. For the range of beam sizes and observation wavelengths considered (approximately 600 to 150 nm), slits as small as 25 μm will be required. The planarity between the two slit edges needs to be better than a tenth of the observation wavelengths (< 20 nm). For the production of such a critical element, two alternative methods are being investigated. The first one makes use of the molecular adhesion between polished glass or silicon parts (see Fig. 11, top part) that are individually machined before adhesion. This technique was used successfully to produce the targets used for the CESR tests, where a co-planarity better than 20 nm was achieved.

Alternatively, chemical etching of a monocrystalline silicon wafer is being tested in the CMI-Center of MicroNano Technology at the Ecole Polytechnique Federale de Lausanne. The slit production is based on chemical anisotropic etching of the silicon (KOH etch). To ensure the best slit quality with high precision width, the photolithographic mask pattern to be chemically etched is aligned with the crystalline plane of the wafer within 0.1 degree. The process makes use of the anisotropic etching properties in order to etch through the wafer thickness from the back-side. The challenge is to obtain the desired aperture when the etching reaches through. At the time of writing, the first test sample is being produced to validate the technique. It consists of a series of slits increasing in sizes with steps of 50 μm. The planarity measurement of this sample will be the next step to validate the fabrication process.

CONCLUSION AND OUTLOOK

The OTR-ODR station to be tested on ATF2 is under development at CERN. Dedicated side experiments are conducted in order to optimise the target geometry and design. The mechanical drawings of the experimental system are now completed, and the vacuum tank is being produced by the CERN workshop. The target development is still on going. The experiment will be fully assembled and its functionalities tested at CERN in fall 2015. It is scheduled to finalise the installation on the KEK-ATF2 beamline by April 2016.

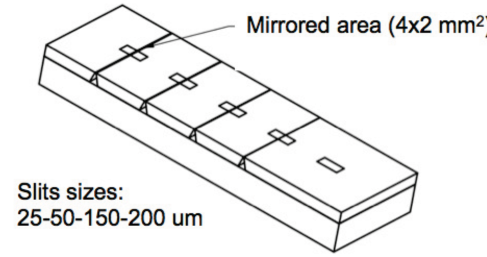

(a)

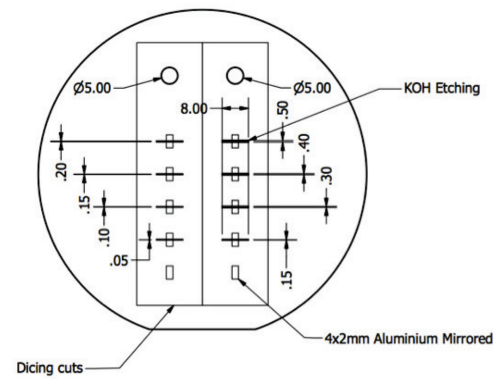

(b)

Figure 11: Molecular adhesion target (a) and chemical etching of silicon wafers (b).

REFERENCES

[1] P. Karataev et al., "First observation of the Point Spread function of optical transition radiation", Phys. Rev. Let. **107**, 174801 (2011)

[2] K. Kruchinin, et al., "Sub-micrometer transverse Beam size diagnostics using optical transition radiation", J. Phys. Conf. Ser. **517**, 012011 (2014)

[3] B. Bolzon et al., "Very High Resolution OTR Imaging System: Comparison Between Simulations and Experiment", Phys. Rev. ST Accel. Beams **18**, 082903 (2015)

[4] A. P. Potylitsyn et al., *Diffraction Radiation from Relativistic Particles*, (Springer, Berlin Heidelberg, 2010)

[5] P. Karataev, et al. “Beam-size measurement with Optical Diffraction Radiation at KEK Accelerator Test Facility”, Phys. Rev. Lett. **93**, 244802 (2004)

[6] A. Cianchi, et al., "Nonintercepting electron beam size monitor using optical diffraction radiation interference", Phys. Rev. ST Accel. Beams **14**, 102803 (2011)

[7] L. Bobb, et al., "Vertical Beam Size Measurement at CESRTA Using Diffraction Radiation", in Proceedings of the 3rd International Beam Instrumentation Conference, Monterey, CA, (2014), MOPF14

[8] ATF2 Collaboration, "ATF2 Proposal", KEK report-2005-2

[9] ZEMAX user’s manual, 2013.

ISBN 978-3-95450-176-2

A NEW ORBIT SYSTEM FOR THE CERN ANTIPROTON DECELERATOR

R. Marco-Hernández, M.E Angoletta, M. Ludwig, J.C. Molendijk, F. Pedersen, R. Ruffieux, J. Sánchez-Quesada, L. Søby, CERN, Geneva, Switzerland

Abstract

This contribution will describe the new orbit system foreseen for the Antiproton Decelerator (AD) located at CERN. The AD decelerates antiprotons from 3.57 GeV/c down to 100 MeV/c, with an intensity ranging from 1×10^7 to 5×10^7 particles. The orbit system developed is based on 34 horizontal and 29 vertical electrostatic beam position monitors (BPMs) fitted with existing low noise front-end amplifiers. After amplification, the BPM signals will be digitized and down-mixed to baseband, decimated and filtered before computation to extract the position. The digital acquisition part of the orbit measurement system is based on the VME Switched Serial (VXS) enhancement of the VME64x standard and includes VITA57 standard FPGA Mezzanine Cards (FMC). The system is foreseen to measure complete orbits every 2.5 ms with a resolution of 0.1 mm.

INTRODUCTION

The AD ring [1] is a synchrotron where ~$3\text{x}10^7$ antiprotons produced from a production target are injected at 3.57 GeV/c. After RF manipulation and stochastic cooling, the beam is decelerated in several stages involving additional stochastic cooling, electron cooling and RF manipulation, before the antiprotons are extracted at 100 MeV/c. The AD revolution frequency varies from 1.59 MHz down to 174.5 kHz during the deceleration cycle. Fig. 1 shows a schematic view of the AD deceleration cycle and the essentials of its operation.

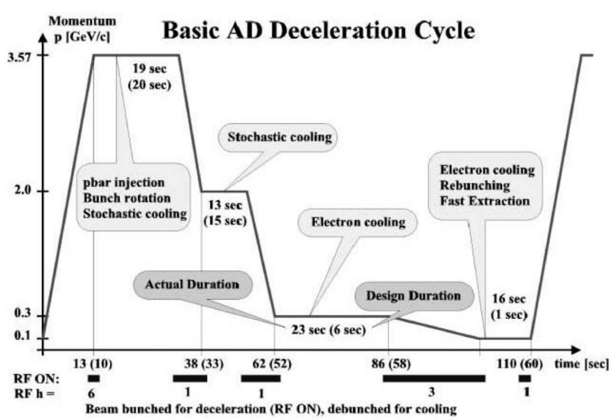

Figure 1: Basic AD deceleration cycle.

The present AD orbit system [2] has a limited performance in terms of time resolution since it is a multiplexed system acquiring signals from one BPM at a time. This allows for a complete orbit measurement only every 1.2 seconds. The new requirement of orbit measurements on the deceleration ramps involves moving to a parallel system where each BPM signal has its own analogue to digital converter (ADC) channel.

The new beam position system will use the same 63 BPMs as well as the head amplifiers of the present system, but with the reception amplifiers, the digital acquisition system as well as the front-end software totally updated.

The aim for the new system is to measure complete orbits every 2.5 ms with a resolution of 0.1 mm.

FRONT-END ELECTRONICS

Beam Position Monitors

The new orbit system acquires the signals from 34 horizonal and 29 vertical electrostatic BPMs. The sigma (Σ) signal is provided by a specific annular electrode while the delta (Δ) signals are derived from two semi-sinusoidal electrodes. The Δ signal level in the electrodes for $1\text{x}10^7$ particles is 4.2 μVp with a BPM differential sensitivity of 0.1 μVp/mm.

Head Amplifiers

The existing head amplifiers [2], placed close to the BPMs around the AD ring, will be also used in the AD new orbit system. These amplifiers have an equivalent input noise of 0.6 nV/√Hz for the Δ inputs, which is low enough to fulfil the 0.1 mm resolution requirement. In order to have this low input noise level, they feature a differential amplifier of 2 times 6 parallel Junction Field Effect Transistors (JFETs). The gain for the Δ outputs can be selected (47 dB or 20 dB) by means of a Transitor-Transistor Logic (TTL) digital control signal. The bandwidth for the high gain setting, which will be used in the new system, is 10 kHz – 20 MHz and the CMRR is better than 66 dB below 10 MHz. The head amplifiers have differential delta and sigma outputs which are transmitted from the AD ring to the AD control room. An analogue calibration input signal and two TTL digital control signals are implemented to simulate the maximum positive/negative beam displacement as well as a centred beam for calibration purposes.

Reception Amplifiers

New reception amplifiers, placed close to the digital acquisition system in the AD control room, have been designed to transform the differential signals coming from the head amplifiers to single ended signals and transmit them to the ADCs of the digital acquisition system. Two differential amplifiers with a 0 dB gain and a bandwidth of 560 Hz-80 MHz have been implemented for the sigma and delta signals.

ISBN 978-3-95450-176-2

ORBIT MEASUREMENTS

The analogue front-end electronics will deliver RF difference and sum signals for each BPM, i.e. 126 signals, which must be digitized and down converted to baseband for position calculations. The measurements will be carried out using the first harmonic of the f_{REV}, or the second harmonic in case of RF induced interference (EMI). Digital down conversion using the selected harmonic as local oscillator permits continuous position measurements during the whole deceleration cycle, whenever the beam is bunched. After low pass filtering and decimation of the complex I/Q data the positions are calculated (in mm) according to Eq.1.

$$Pos(t) = k \cdot \left(\frac{1}{\frac{\Delta}{\Sigma}_{cal}} \right) \cdot \left(\mathrm{Re}\left\{ \frac{I_\Delta(t) + jQ_\Delta(t)}{I_\Sigma(t) + jQ_\Sigma(t)} \right\} - \frac{\Delta}{\Sigma}_{zero} \right) + BPM_{off} . \quad (1)$$

k being the BPM sensitivity, BPM_{off} the total BPM offset Δ/Σ_{cal} the calibration slope calculated from calibration data and Δ/Σ_{zero} the offset obtained from calibration data.

The digital acquisition system includes a calibration procedure to obtain the calibration parameters required in equation (1). Three consecutive calibration acquisitions, simulating the maximum positive and negative beam displacements and a centred beam are performed to get three different values of the Δ over Σ signal for each BPM. In each calibration acquisition the system averages 522540 samples of the acquired Δ over Σ signal for each BPM. The calibration offset value (Δ/Σ_{zero}) for each BPM will be directly the averaged calibration value obtained for a centred beam (Δ/Σ_{zero}) while the calibration slope (Δ/Σ_{cal}) for each BPM will be given by Eq. 2.

$$\frac{\Delta}{\Sigma}_{cal} = \frac{\frac{\Delta}{\Sigma}_{pos} - \frac{\Delta}{\Sigma}_{neg}}{2} . \quad (2)$$

Being Δ/Σ_{pos} and Δ/Σ_{neg} the averaged calibration values obtained for the maximum positive and maximum negative beam displacements respectively.

DIGITAL ACQUISITION SYSTEM

System Layout

The new digital acquisition system is based on an in-house (CERN RF Group) developed hardware family [3]. This hardware family follows the VME Switched Serial (VXS) [4] enhancement of the VME64x standard, which supports switched serial transmission over a new high-speed P0 connector. For the daughter boards, the VITA57 standard FPGA Mezzanine Card (FMC) [5] is used.

Two different VXS-VME crates will be used to group the digitization of the horizontal and vertical BPM signals. In the horizontal crate, there will be nine VXS-DSP-FMC carriers, one holding a FMC-MDDS (FMC Master Direct Digital Synthesizer) and a FMC-ADC (FMC Analogue to Digital Converter) board and the rest holding two FMC-ADC boards. A timing module (CTRV) will provide all the triggers related to the AD cycle. The vertical crate will have a similar configuration. The digital acquisition system block diagram can be seen in Fig. 2.

The digitization of the BPM signals, at the FMC-ADC boards, and generation of the calibration analogue signals, at the FMC-SDDS board, as well as the associated low-level signal processing, at the FPGAs, is driven by a common RF clock which is a programmable higher harmonic of the AD revolution frequency (f_{REV}). A TAG pulsed signal marks the revolution frequency and synchronises all boards in the system. The RF clock and TAG signals will be generated from the revolution frequency by an FMC-MDDS board. The revolution frequency value will be calculated during the AD cycle by the Digital Signal Processor (DSP) of the VXS-DSP-FMC Carrier M1 from the value of the magnetic field of the main dipoles, the evolution of which is provided via a train of two pulsed signals (BUP and BDOWN).

VXS Switch Board

The VXS Switch board is used to interconnect the VXS-DSP-FMC Carrier boards via full-duplex Giga-bit serial links by means of the VXS transmission. Each VXS crate will contain two VXS Switch boards (positioned at a star-point) allowing the routing of a total of eight full-duplex links of up to 3.125 Gbit/s between any payload slot. In both crates, one VXS Switch boards will be used to distribute the RF clock and TAG signal through each VME-VXS crate and between crates. The other VXS Switch board will be used for the communication among VXS-DSP-FMC carriers by means of the VXS fabric through the VME-VXS crate and between crates. Optical fibres will connect the VXS switches of both crates.

VXS-DSP-FMC Carriers

The VXS-DSP-FMC carrier accommodates a Digital Signal Processor (DSP) ADSP-21368 and two Xilinx Virtex 5 Field Programmable Gate Arrays (FPGAs), known as the Main FPGA (XC5VLX110T) and FMC FPGA (XC5VSX95T). In order to distribute the RF clock and TAG signals, there are two dedicated full-duplex VXS channels from each VXS-DSP-FMC carrier routed to one of the VXS Switch boards. The other six full-duplex VXS channels, combined to form three 32 bit data paths, are used to transfer 10b8b-encoded data between VXS-DSP-FMC carriers at a raw link rate of 2 Gbit/s or 100 MSPS (32 bit). Each VXS-DSP-FMC carrier can host up to two FMC daughter boards with a high-pin count format. The VXS-DSP-FMC carrier also includes several memory banks for observation purposes. In particular, two, 4Mx18 bit banks that are clocked at 100 MHz and two 1Mx4x18 bit banks that are clocked at the RF frequency.

ISBN 978-3-95450-176-2

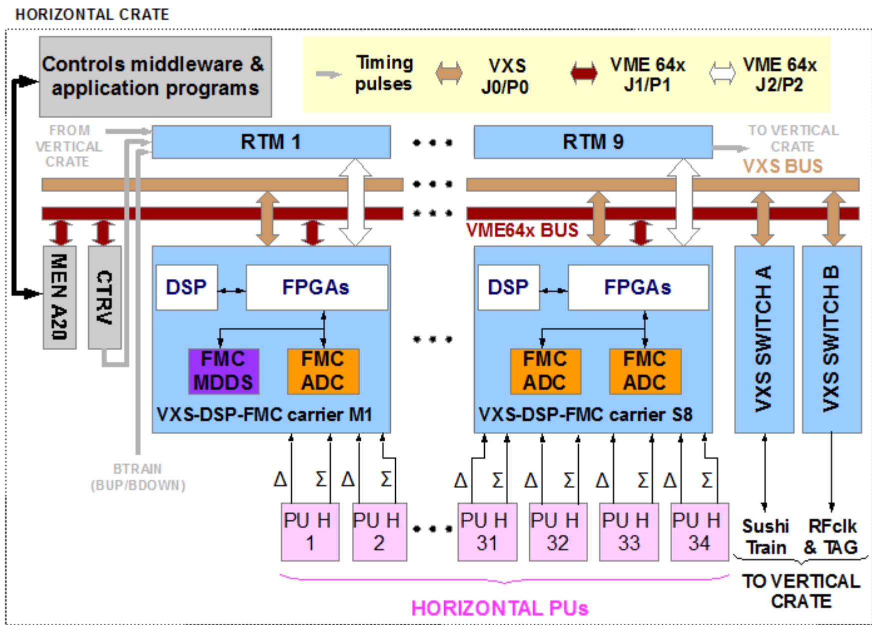

Figure 2: Digital acquisition system block diagram (horizontal crate). MDDS: Master DDS FMC board. ADC: Analogue-to-Digital FMC board. RTM: Rear Transition Module. CTRV: Timing Receiver Module. Men A20: master VME board. PU H: Horizontal transverse Pick-Up.

Rear Transition Modules (RTM)

There is a Rear Transition Module (RTM) connected to each VXS-DSP-FMC carrier through the J2/P2 connector. It carries all major secondary power supplies needed by the VXS-DSP-FMC carrier. The RTM front panel provides sixteen digital inputs and eight digital outputs, directly interfaced to the Main FPGA using stacked LEMO 00 connectors. The digital inputs can be configured as high impedance or TTL 50 Ohm. These digital inputs/outputs will be used to connect the trigger signals generated by the timing module, e.g. the start and end of the AD cycle, as well as to implement the timing and interlock wired daisy chains required by the system.

FMC-MDDS Daughter Board

The FMC-MDDS board generates the RF clock and the TAG synchronization signals. The RF clock can range from 62.5 MHz to 125 MHz at any revolution frequency harmonic from 1 to 1023. It needs a 10 MHz input reference clock to operate. Two independent channels are synchronized to the same input reference. The board includes a 32 bit direct digital synthesizer core (AD9858) with 232 mHz frequency resolution. It also features the possibility of distributing the RF clock and TAG signal either through VXS switch or a front panel eSATA connector.

FMC-SDDS Daughter Board

The FMC-SDDS is used to generate the analogue calibration signals required by the head amplifiers. This board is based on an AD9747 DAC and allows four independent digital-to-analogue conversion channels with 16 bits resolution and a programmable gain switching of 18 dB. The output is DC coupled, with a 40 MHz analogue bandwidth and a full scale, peak output voltage of 3.6 V. The sampling rate of the DAC mezzanine can go up to 250 MSPS.

FMC-ADC Daughter Board

The FMC-ADC board is used to digitize the BPM delta and sigma signals. It has four independent DC coupled channels, with an input signal range of ±1V over 50 ohms. Two dual, 16 bit ADCs (AD9286) with a sampling rate up to 125 MSPS are used for digitizing the input signals. The bandwidth of each channel is limited to 40 MHz. The gain of each input channel is selectable, 0 dB or 18 dB, with DC offset compensation performed automatically. The signal to noise ratio is better than 70 dB which is equivalent to 12.5 bits of resolution.

FPGA Firmware

The Main FPGA firmware implements the essential infrastructure for the system communication and data exchange. It includes the following communication channels:

- VME64x (A32/D32 + A32/D64 MBLT).
- DSP (A16/D32).
- VXS full-duplex dual 32 bit link with a transfer rate of 100 MHz (carrier-to-carrier).
- Communication and data exchange with the FMC FPGA (full-duplex 32 bit Gigabit links).
- Different I2C links to control the RTM or the VXS Switch boards.

The communication architecture is configured so that no arbitration is required on any of the link or bus interfaces in order to have a simpler and more reliable system. The

ISBN 978-3-95450-176-2

Main FPGA firmware also implements other useful blocks such as:

- a dual, 128 channel timing generator.
- 16 channel, 32 bit x 1024 vector function generators.
- 48 channel, 32-bit x 2048 programmable digital signal observation.

The Main FPGA firmware allows for remote updating of the FPGA and DSP software. Finally, numerous diagnostics functions are available. The main FPGA firmware will be the same for all boards and the capabilities will be enabled or disabled depending on the desired board functionality.

The FMC FPGA firmware implements the custom FMC hardware control and data treatment. Digital signal observation is also possible via configurable buffers clocked at the RF clock and located in the fast memory on the VXS-DSP-FMC Carrier board. The firmware code in the FMC FPGA is tailored to the specific FMC hardware via the instantiation of FMC IP cores, i.e. each daughter board is complemented by an FPGA IP core running on the FMC FPGA. These IP Cores are developed in independent version-controlled libraries through a collaborative design while the FMC FPGA common firmware is held in a separate library. The FMC FPGA firmware instantiates the corresponding IP cores in each slot.

The ensemble of FMC daughter board and corresponding IP core implements the functionality of a FMC-MDDS, FMC-DDC or a FMC-SDDS. The MDDS generates a clock that clocks all daughter boards at a high f_{REV} harmonic. The TAG signal phase synchronises all FMC-DDC and FMC-SDDS channels in the system.

The FMC-SDDS generates RF analogue signals of programmable f_{REV} harmonic and phase. Data acquisition and control are carried out in I/Q coordinates.

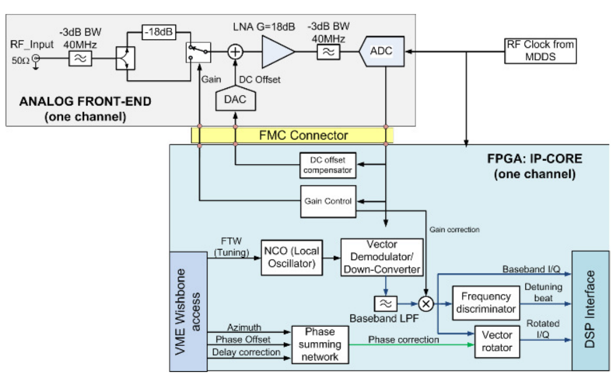

Figure 3: FMC-ADC board hardware and DDC firmware.

The FMC-DDC (Fig. 3) performs digitization, down-conversion, low-pass filtering and decimation. The digital down converter is a homodyne receiver that converts the selected beam revolution harmonic into a baseband I/Q signal. The ADC sampling clock and the local oscillator are locked to the RF clock, so the local oscillator frequency and phase is controlled to select the required beam revolution harmonic. A baseband low pass filtering and a decimation stage have been implemented by means of a first order Cascaded Integrator Comb (CIC) filter. The decimation factor and the differential delay of the CIC filter can be modified. The phase of the down-converted I/Q signal can be varied so as to compensate the beam time of flight and cable delay differences of each input channel.

DSP Firmware

The DSP firmware is developed in C code as an interrupt driven finite state machine. It implements the core data treatment and system control, such as the acquisition and data processing from the FMC-DDCs and the on-line control of all the FMC daughter boards. The DSP firmware will depend entirely on the functionality of the VXS-DSP-FMC carrier hosting the DSP itself and will allow full system customisation.

The DSP firmware of the M1 VXS-FMC-DSP carrier controls the FMC-MDDS operation and acquires data from two horizontal BPMs via the FMC-DDC daughter board. This DSP firmware also calculates the revolution frequency during the AD cycle from the value of the main dipoles magnetic field. The hand-shaking via VXS communication to synchronize all the FMC-DDC daughter boards is also controlled by the M1 DSP firmware.

The DSP firmware of the M2 VXS-FMC-DSP carrier controls the FMC-SDDS operation for the calibration and acquires data from two vertical BPMs by means of an FMC-DDC daughter board.

The DSP firmware of the other VXS-FMC-DSP carriers (S1 to S15) is configured to acquire data from 4 BPMs using two FMC-DDC daughter boards per carrier.

SOFTWARE

Specific real-time and communication software running in the dedicated VME crates is needed in order to perform data post-processing, calibration runs, real-time control following machine timing and to ensure a seamless integration of the measurement into the AD operational control system. The standard CERN software framework (FESA: Front End Software Architecture) [6] is used for running the new AD orbit system. This implementation will allow for easy porting to the ELENA (Extra Low ENergy Antiproton) machine, currently under construction and foreseen to use the same orbit system.

SYSTEM STATUS AND TESTS

Most of the hardware required for the system is already produced, tested and installed, with the exception of the FMC-ADC boards. The current version of the FMC-ADC daughter boards was found to be too noisy for the system. The noise density level of the FMC-ADC board must be lower than 20 nV/√Hz for the BPM Δ input signals while, in the current version of the FMC-ADC board, it was found to have noise peaks of up to 45 nV/√Hz in the bandwidth of interest (174.5 kHz - 1.59 MHz). These peaks were due to the switching frequency of the on-board DC-DC converters used to generate the ±5V and 1.8V power supply levels. It was therefore decided to redesign the FMC-ADC board to have AC coupling inputs in order to

ISBN 978-3-95450-176-2

require only positive power supply levels (10V and 1.8V) generated with linear regulators. Preliminary results measured with a prototype show that the maximum noise density level for the FMC-ADC AC coupled version is well below 10 nV/√Hz.

The DSP firmware for each VXS-DSP-FMC carrier is already developed. The FPGA firmware has been upgraded in order to allow communication of up to 32 VXS-DSP-FMC carriers via the VXS. Other minor changes have also been included to be able to read out the BPM position data continuously during the whole AD cycle.

The specifications for the software have been written and the final software is currently being developed. For the initial system tests, different scripts based on Python have been developed to mimic the final software.

An initial version of the system with only the M1 VXS-DSP-FMC carrier without VXS communication was tested in December of 2014 in AD as proof of concept of the system, with data from two BPMs acquired successfully.

A second version of the system is currently being tested in AD with beam. It consists of a VXS-VME crate holding the M1 VXS-DSP-FMC carrier, the M2 VXS-DSP-FMC carrier, another six (S1-S6) slave VXS-DSP-FMC carriers and a CTRV timing module. The aim is to acquire data from all vertical BPMs and test all the features of the final system (VXS communication, calibration procedure, etc.) in real conditions. For this test, the noisier DC-coupled version of the FMC-DDC boards will be used until the new AC-coupled FMC-DDC boards are available.

Fig. 4 shows the position measurement for a vertical BPM during the first flat top and deceleration ramp in the AD cycle (3.57-2 GeV/c). It can be seen that a position signal with a resolution better than 0.1 mm is obtained from 35 s onwards, corresponding to the time when the beam is bunched (it being debunched for stochastic cooling beforehand).

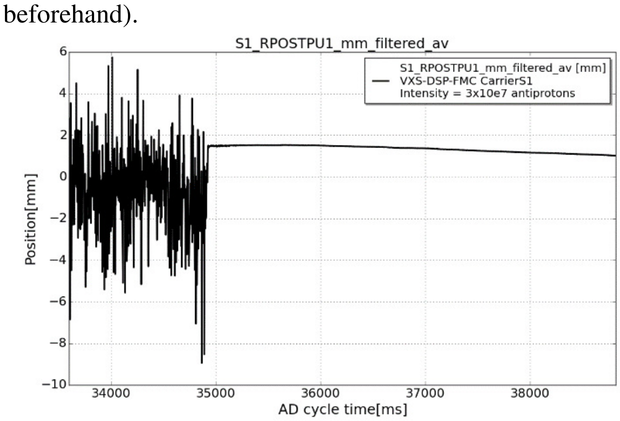

Figure 4: Position measurement for a vertical BPM acquired with the S1 VXS-DSP-FMC carrier during the first flat top and deceleration ramp in the AD cycle.

Fig. 5 shows the position measurement for the vertical plane of all BPMs during the first flat top. The green line corresponds to the current orbit system and the blue line to the prototype version of the new orbit system being tested. The discrepancies between both systems are currently being investigated.

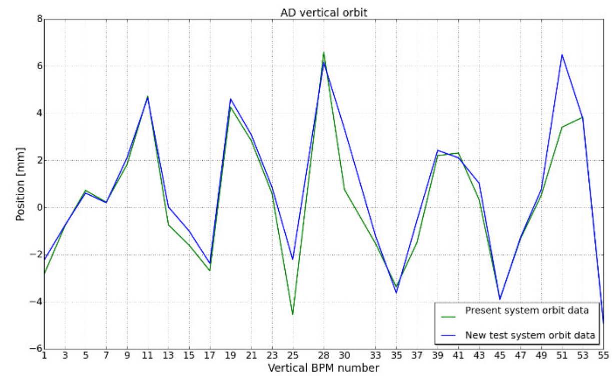

Figure 5: Position measurement all vertical BPMs acquired during the first AD flat top (at 35.77 s) with the current orbit system (green line) and the prototype version of new orbit system (blue line).

The final AD orbit measurement system is foreseen to be commissioned by the end of 2015.

CONCLUSION

The design of the new orbit system for AD has been presented. It will use the same 63 BPMs and the head amplifiers than the current orbit system. A new digital acquisition system based on in-house developed hardware will digitize and process the BPM signals to obtain an orbit measurement with a resolution of 0.1 mm every 2.55 ms. The 17 VXS-DSP-FMC carriers and the 34 FMC daughter boards used will be accommodated in two VME-VXS crates for acquiring the horizontal and the vertical BPM signals. The majority of the hardware is already produced and tested, with a new low noise FMC-ADC board under development. Tests with a prototype version of the final orbit system are currently being carried out with beam in the AD, with the final orbit system foreseen to be commissioned by the end of 2015.

REFERENCES

[1] S. Baird et al., “The Antiproton Decelerator: AD”, Proc. of PAC 1997, Vancouver, Canada (1997).
[2] M. Le Gras, L. Soby and D. J. Williams, “The Closed Orbit Measurement System for the CERN Antiproton Decelerator antiproton decelerator: AD”, Proc. of DIPAC 1999, Chester, UK (1999).
[3] M. E. Angoletta et al., “A Leading-Edge Hardware Family for Diagnostics Applications and Low-Level RF in CERN’s ELENA Ring”, IBIC 2013, Oxford, UK, September 2013, TUPF28, p. 575-578; http://www.JACoW.org.
[4] VITA website: http://www.vita.com/vxs.html.
[5] VITA website: http://www.vita.com/fmc.html.
[6] M. Arruat et al., “Front-End Software Architecture”, Proc. of 11th International Conference on Accelerator and Large Experimental Physics Control Systems, Knoxville, TN, USA, October 2007, p. 310.

ISBN 978-3-95450-176-2

DEVELOPMENT OF AN IONIZATION PROFILE MONITOR BASED ON A PIXEL DETECTOR FOR THE CERN PROTON SYNCHROTRON

D. Bodart[1], B. Dehning[1], S. Levasseur[1], P. Pacholek[1], A. Rakai[1], M. Sapinski[1], K. Satou[1,2], G. Schneider[1], D. Steyart[1], and J.W. Storey[1]

[1]CERN, Geneva, Switzerland
[2]Accelerator Laboratory, KEK, Oho, Tsukuba, Ibaaraki, Japan

Abstract

The transverse emittance measurement in the CERN Proton Synchrotron (CPS) is currently performed using fast rotational wire scanners. These scanners cannot provide continuous bunch-by-bunch measurements and the expected future increase of the beam brightness will lead to an accelerated sublimation of the wire. A novel Ionization Profile Monitor (IPM) is currently under development to cope with these challenges. The readout of this device will be based on a hybrid silicon pixel detector with a Timepix3 readout chip. Pixel detectors are sensitive to single electrons therefore eliminating the need for traditional Multi-Channel Plates, which suffer from aging phenomena. The early digitization of the signal will reduce the susceptibility of the readout system to electromagnetic interference, while the time resolution of the Timepix3 allows for bunch-by-bunch measurements. Due to the small length of the detector a new simplified ion trap has been designed. The guiding field will be provided by a new self-compensating magnet. It is foreseen to test a prototype version of the device with beam in 2016.

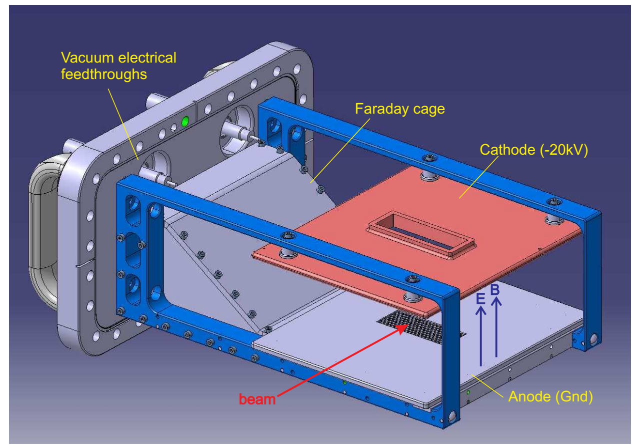

Figure 1: Design of the new non-destructive transverse beam profile monitor for the CPS. Ionization electrons are accelerated by a 270 kV/m electric field towards the pixel detector, which is located at the ground electrode just beneath a honeycomb shield. To suppress any beam induced electromagnetic effects the pixel detector and readout electronics are located in a Faraday cage.

INTRODUCTION

A fast non-destructive transverse profile monitor is currently under development for the CERN Proton Synchrotron (CPS) which is based on the ionization of rest gas molecules by high energy beam particles. The transverse beam profile is inferred from the distribution of ionization electrons which is measured by accelerating the electrons onto an imaging detector consisting of a pixelated p-on-n silicon sensor bonded to a Timepix3 readout chip. The fast sampling and readout speed of the Timepix3 will facilitate bunch-by-bunch measurement of the beam profile. A 0.2 T magnetic field parallel to the electric field will maintain the transverse position of the ionization electrons during the passage of the electrons to the imaging detector. The main elements of the design are shown in Fig. 1. Initial studies of the electron rates for various types of beams expected in the PS together with proposed modes of data acquisition are presented in [1]. Here the final design of the prototype device is presented.

HYBRID PIXEL DETECTOR

Ionization profile monitors typically amplify the ionization signal electrons or ions by means of Micro Channel Plates (MCPs). Charge from the MCP is then either readout optically by means of a phosphor screen and camera [2, 3] or directly using arrays of narrow anodes [4, 5]. A common problem for MCP based systems is the inhomogeneous degradation of the MCP gain and limited lifetime. In recent years hybrid pixel detectors, which consist of a pixelated silicon sensor bump bonded to a pixelated readout chip, have become widely used in many high energy physics and medical imaging applications. By removing the metalization usually applied to the surface of a silicon sensor, hybrid pixel detectors become sensitive to single electrons with an energy of at least 3.6 keV. As an imaging detector for IPMs hybrid pixel detectors offer a number of advantages, namely: trigger-less readout, high spatial and time resolution, early digitization, radiation hardness and removing the requirement for additional amplification stages.

The imaging detector for the CPS IPM is based on the Timepix3 hybrid pixel detector readout chip, which has been developed in the framework of the Medipix3 collaboration [6, 7]. Timepix3 consists of a pixel matrix of 256×256 square pixels with a pitch of 55 μm, covering an area of $14 \times 14\,\mathrm{mm}^2$. The trigger-less readout allows for a sustained hit-rate of up to 40 Mhits/cm^2/s and has a minimum time resolution of 1.562 ns. To detect electrons the Timepix3 will

ISBN 978-3-95450-176-2

be bump bonded to a 100 µm thick p-on-n silicon sensor. The metalization layer on the backside of the sensor is removed and the depth of the n+ layer is minimized in order to improve the detection efficiency of the ionization electrons.

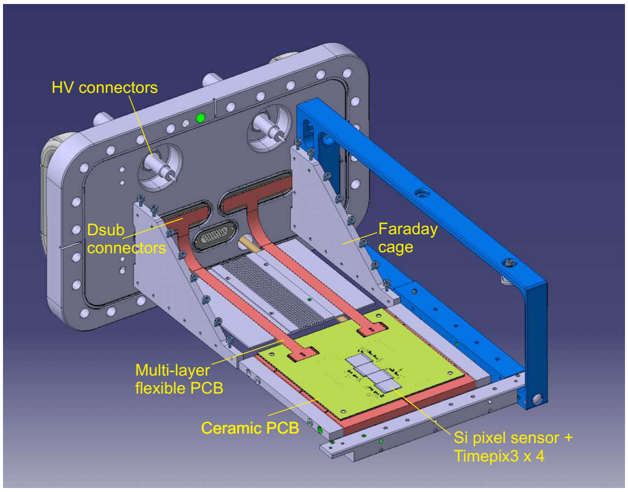

Figure 2: Hybrid pixel detector imaging system based on the Timepix3 readout chip.

The design for the CPS IPM Timepix3 based imaging detector is shown in Fig. 2. The imaging detector, covering a total area of 5.6 cm × 1.4 cm, will consist of four hybrid pixel detectors aligned transverse to the direction of the beam. The environment in which the pixel detector must operate is very challenging: it must operate inside the CPS ultra-high vacuum (10^{-9} mbar), in a 10 kGy/yr radiation area and be tolerant to electromagnetic interference caused by the beam. Furthermore, the system must be sufficiently robust to run reliably for the duration of the annual injector program. To ensure compatibility with the ultra high vacuum environment a complete readout system for the Timepix3 has been designed which is optimized for low out-gassing characteristics. The pixel detectors themselves are mounted on a 300 µm thick ceramic PCB. Multi-layer flexible PCBs provide the link between the ceramic PCB and sub-D connectors on the electrical feedthrough. A Faraday cage is used to shield all elements of the readout electronics from electromagnetic interference from the beam. The radiation tolerance of the Timepix3 chip is expected to be high; the Medipix3 hybrid pixel detector is based on the same 130 nm CMOS technology as the Timepix3 and has been measured to be operating well after 4.6 MGy [8].

The readout architecture for the IPM imaging detector is shown in Fig. 3. A front-end readout board, mounted on the air side of the vacuum feed-through, provides the power and control signals for the Timepix3 chips. It is also responsible for transmitting the 32×640 MB/s data outputs of the 4 × Timepix3 chips via radiation hard optical transceivers to the back-end readout electronics located in a non-radiation environment. The data acquisition and bunch-by-bunch reconstruction will be done by an FPGA based system. Synchronization to the CPS bunch structure will

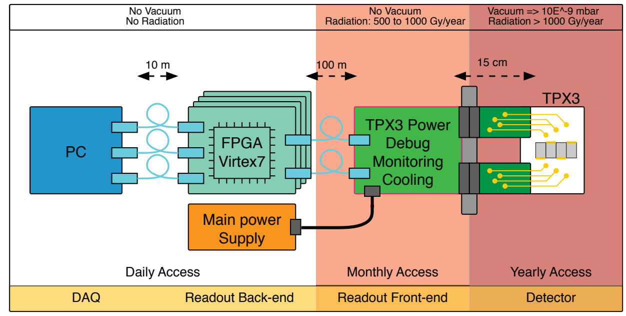

Figure 3: Readout architecture for the hybrid pixel detector.

follow the procedure developed for the CPS trajectory measurement system [9].

Cooling

The silicon sensors will be exposed to radiation levels of several tens of kGy per year. A cooling system has been designed to cool the sensors to below 0°C. This serves two purposes: firstly, to remove the 12 W of heat produced by the Timepix3 chips and secondly, to improve the radiation hardness of the sensors. Operating the sensors at 0°C rather than room temperature will reduce the radiation induced increase in leakage current by two orders of magnitude and increase the reverse annealing time constant from one to fifteen years [10].

In the first design cooling was performed with Peltier elements, which on further investigation were found to be unsuitable due the presence of Bismuth which upon interaction with neutrons transmutates to Polonium. The final design is based on liquid cooling a copper plate that is soldered to the Ceramic PCB holding the hybrid pixel detectors. The ceramic PCB has a very good thermal conductivity (24 W/mK, about 50 times more than a standard PCB) and thermal simulations show that the coolant temperature needed to keep the copper plate below 0°C is between −2°C and −8°C.

FIELD CAGE DESIGN

The IPM field cage, shown in Fig. 1, is required to:

- provide an electric field to accelerate ionization electrons onto the hybrid pixel detector, with sufficient homogeneity as to not distort the original transverse position of the ionization electron.
- shield the pixel detector from electrons produced by the interaction of the ionization ions with the cathode.
- provide a path for the beam mirror current.
- shield the readout electronics from electromagnetic interference from the beam.

The field cage is made of two flat parallel electrodes: an upper cathode held at a potential of −20 kV and a lower anode which is grounded. The hybrid pixel detectors are located at the anode below a honeycomb shield which protects the chips from electromagnetic interference from the beam, while also providing high transparency for the passage of the ionization electrons.

ISBN 978-3-95450-176-2

Ion Trap

The ionization process produces ions in addition to the electrons used to measure the beam profile. The ions will accelerate towards the cathode and impact the electrode surface with sufficient kinetic energy to cause the emission of secondary electrons. These electrons the transverse position of which are distorted compared to the original ionization electron, will accelerate back towards the anode and can be a potentially significant source of background electrons for the imaging detector system. The problem of background electrons for the Timepix3 pixel detector is particularly acute since the sustained readout rate is limited to 40 Mhits/cm^2/s.

In order to remove these background electrons, a wire mesh is typically located just below the cathode with a slightly higher potential than the cathode itself. Secondary electrons emitted from the cathode are stopped by the potential barrier between the cathode and the wire mesh and are thus unable to reach the detector. However, the wire grid itself can also be a source of background electrons due to either electron emission caused by beam induced heating of the wire or emission of secondary electrons due to the impact of the ion on the wire grid. To remove these additional sources of background electrons a simplified scheme has been devised which dispenses with the wire grid. In this *ion trap* scheme a slit is created in the cathode directly above and with dimensions similar to the imaging detector plane. The slit allows ions to pass through the cathode and to be directed by electric fields lines onto the back of the cathode where the secondary electrons will find no path back to the pixel detector. The wire grid and ion trap schemes are illustrated in Fig. 4. Simulations of the ionization electron trajectories in the presence of the ion trap demonstrate negligible distortion of the transverse beam profile.

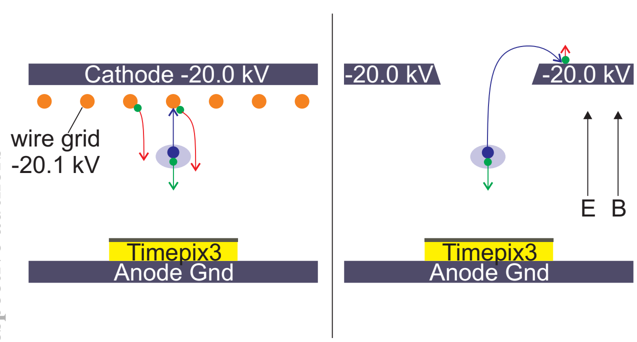

Figure 4: Schemes to prevent ion induced secondary electrons from reaching the pixel detector. Left: A wire grid based scheme forms a potential barrier for electrons between the cathode and wire grid, but the grid itself is a source of background electrons. Right: Ion trap scheme to prevent secondary electrons reaching the pixel detector, which does not require a wire grid structure.

Side Electrodes

Side electrodes are typically used to increase the uniformity of the electric field and therefore decrease the distortion of the transverse beam profile. Simulations have been performed to optimize the number and shape of the side electrodes in the presence of the 0.2 T magnetic field. Fig. 5 shows the standard deviation of an electron distribution on the imaging detection surface for point sources at different transverse distances from the beam center for the case of a field cage with 0 and 3 side electrodes. The simulation shows that at up-to ±28 mm from the center of the beam there is negligible difference between the 0 and 3 side electrode designs. Based upon this simulation no side electrodes are included in the field cage design, which simplifies both the construction and assembly of the field cage.

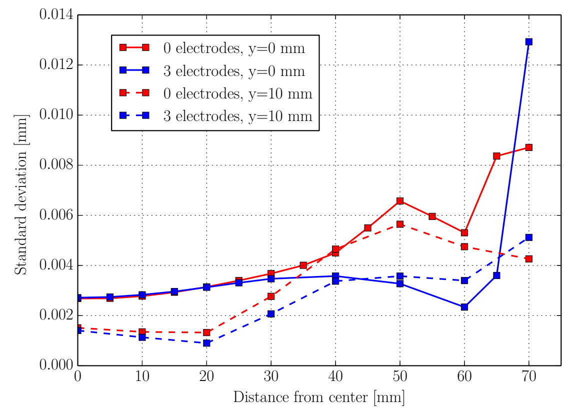

Figure 5: Simulation of the effect of side electrodes on the trajectory of electrons. Initial electrons are a point source produced in the middle between the two electrodes (y=0 mm) and 10 mm higher.

Simulation of Beam Space Charge Effect

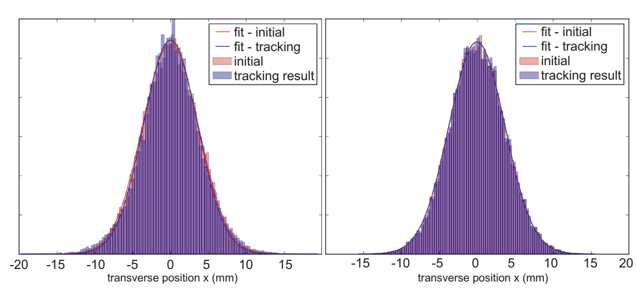

Figure 6: Initial and reconstructed beam profiles without magnetic field (left) and with a 0.2 T magnetic field (right).

The magnetic field should be strong enough to ensure that the electron gyration radius is much smaller than the beam size. The gyroradius depends on the initial velocity of the electron; which is determined by the ionization process and the kick given to the electron by the space charge of the beam. A simulation of the beam space charge effect on the reconstructed beam profile has been performed. The simulated reconstructed profile for a standard 25 ns LHC beam in the PS (1.33×10^{11} protons per bunch, extraction energy =

ISBN 978-3-95450-176-2

25 GeV, beam width: σ_x = 3.7mm, σ_y = 1.4mm) is shown in Fig. 6 for an IPM with no magnetic field and a 0.2 T magnetic field. Without the magnetic field the systematic error on the reconstructed beam profile width is 2.6%; while the error with the 0.2 T magnetic field is 0.03%. Details of this simulation will be the subject of a forthcoming publication.

MAGNET

A novel magnet is designed to provide a 0.2 T magnetic field in the detector region (x=50 mm long, y=84 mm gap, z=50 mm width) with a field homogeneity of less than 1×10^{-3}. The magnet design is illustrated in Fig. 7.The magnet provides the field for the detector and the canceling field that brings the beam particles back in orbit. Both functions are integrated into a single magnet and ensures that the integrated magnetic field along the beam axis is equal to zero. Lattice correctors installed around the accelerator ring will compensate the 0.5 mm shift of the beam in the transverse plane. The magnet fits within the available space of the available straight section of 850 mm. The design allows direct access to the detector and the magnet can be removed from its position directly.

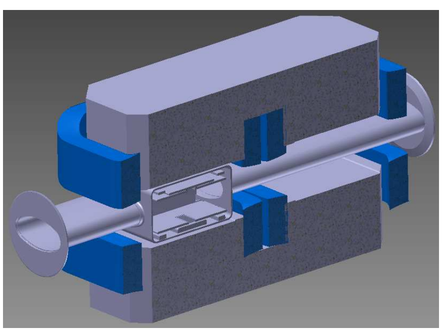

Figure 7: A single magnet provides both the field for the IPM and the corrector field.

CONCLUSIONS

The new Ionization Profile Monitor for the CERN Proton Synchrotron will use, for the first time in an IPM, a hybrid silicon pixel detector as the imaging detector for the ionization electrons. The application of this technology to the ultra-high vacuum, high radiation, and electromagnetic environment of the CPS is very challenging but offers the prospect of fast bunch-by-bunch measurement in a compact design, without the need for additional electron amplification stages. Detailed simulations of the IPM field cage have been used to develop a field cage design without side electrodes and an ion trap that dispenses with the need for a wire grid. A prototype version of the design will be tested in the CPS in 2016.

ACKNOWLEDGMENTS

The authors would like to thank James Zagel, and Randy Thurman-Keup from FNAL, Michiko Minty and Roger Connolly from BNL, Andreas Jannson from ESS and Tino Giacomini from GSI for sharing their experience and detailed designs of Ionization Profile Monitors. Thanks also to Michael Campbell, Xavier Llopart, Jerome Alozy and other colleagues from the CERN microelectronics group, who designed the Timepix3, and also to Jan Vissier and Bas van der Heijden from NIKHEF who prepared the FPGA board and firmware.

REFERENCES

[1] O. Keller, B. Dehning, S. Levasseur, M. Sapinski, Feasibility Study of a Novel, Fast Read-out System for an Ionization Profile Monitor Based on a Hybrid Pixel Detector, proceedings of HB2014, MOPAB41.

[2] M. Sapinski et al., The First Experience with LHC Beam Gas Ionization Monitor, proceedings of IBIC12, TUPB61.

[3] T. Giacomini et al., Ionization Profile Monitors at GSI, proceedings DIPAC2011, TUPD51.

[4] A. Jansson et al., The Tevatron Ionization Profile Monitors, AIP Conf. Proc. 868, 159 (2006).

[5] R. Connolly et al., Residual-Gas-Ionization Beam Profile Monitors in RHIC, preceedings of BIW10, TUPSM010.

[6] T. Poikela et al., Timepix3: a 65K channel hybrid pixel readout chip with simultaneous ToA/ToT and sparse readout, 2014 JINST 9 C05013.

[7] MEDIPIX3 collaboration, http://www.cern.ch/medipix.

[8] R. Plackett et al., Measurement of radiation damage to 130 nm Hybrid pixel detector readout chips, TWEPP 2009, Paris, 2009.

[9] J.M. Belleman, A New Trajectory Measurement System for the CERN Proton Synchrotron, proceedings of DIPAC2005.

[10] Z. Li, Radiation hardness/tolerance of Si sensors/detectors for nuclear and high energy physics experiments, proceedings of PIXEL Int. Workshop, Carmel, CA, 2002.

ISBN 978-3-95450-176-2

DEVELOPMENT AND TEST OF HIGH RESOLUTION CAVITY BPMS FOR THE CLIC MAIN BEAM LINAC*

J. R. Towler†, T. Lefevre, M. Wendt, CERN, Geneva, Switzerland
S. T. Boogert, A. Lyapin, JAI, Egham, UK
B. Fellenz, Fermilab, Batavia, USA

Abstract

The main beam of the Compact LInear Collider (CLIC) requires the beam trajectory to be measured with 50 nm spatial resolution. It also requires a time resolution capable of making position measurements of the head and tail of the 156 ns long CLIC bunch train, for use in dispersion free steering based on an energy chirp applied along the train. For this purpose, a stainless steel 15 GHz cavity BPM prototype has been manufactured, installed at the CLIC Test Facility (CTF3) and tested with beam. An improved design has been fabricated from copper. We discuss results from the two types of the prototype pickups, both from laboratory tests and from beam tests. We also cover the development of the new downconverter electronics.

INTRODUCTION

CLIC is a proposed next generation linear collider which will have a center of mass energy of 3 TeV. The main linac is 40 km long and the beam delivery system (BDS) is 10 km long in total. Over this distance, a precise, reproducible measurement of the beam trajectory is mandatory with almost 4800 BPMs will be needed to achieve this goal [1]. The BPMs are required to have a spatial resolution of 50 nm and are also required to make multiple measurements along the 156 ns bunch train. This is necessary to distinguish the beam displacement along the energy-chirped bunch train on a dispersive trajectory.

A new system of three prototype copper cavity BPMs have been manufactured and installed in the main beam of the Two Beam Test Stand (TBTS) at the CLIC Test Facility (CTF3). One of these BPMs is shown in Figure 1. The BPMs consist of a cylindrical pillbox position cavity with waveguides which strongly coupled to the two polarisations of the first order dipole mode (TM_{110}). The BPM is also equipped with a reentrant reference cav- ity, for coupling to the first order monopole mode (TM_{010}). These modes are excited at 15 GHz, as this is a harmonic of the 1.5 GHz bunching frequency allowing signals from each bunch to add constructively and dominate signals from other modes. The chosen harmonic frequency is sufficiently high, to ensure a high shunt impedance, i.e. high position sensitivity, while staying well below the fundamental TM_{01} beampipe cutoff frequency of 29 GHz. The bunch spacing used at CTF3 differs from that proposed for CLIC where the final bunch spacing frequency will be 2 GHz. A cavity with a dipole frequency of 14 GHz is therefore foreseen to be used.

* Computing time with ACE3P provided by US DOE at NERSC
† jack.towler@cern.ch

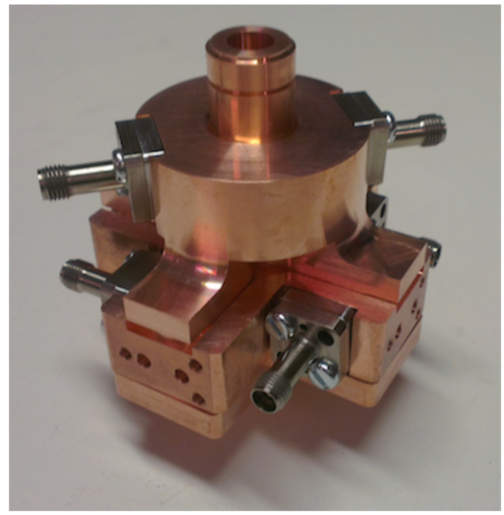

Figure 1: Prototype copper CLIC cavity BPM.

The signal amplitude of the TM_{110} dipole mode, excited in the position cavity by a displaced beam, is directly proportional to beam offset and charge for small offsets [2]while the amplitude of the (TM_{010}) monopole mode is directly proportional to the beam charge, but independent of the beam offset. The (TM_{010}) monopole mode can therefore be used to normalise signals from the position cavity, and used as a phase reference to indicate the sign of the beam position and for rejection of the trajectory and bunch tilt signals.

BPM OVERVIEW

During 2013 and 2014, a stainless steel cavity BPM was tested at CTF3 which performed well, but could benefit from a few im- provements [3]. These improvements were taken into account and incorporated into a new design [4]. The old design had a low Q factor of 250, which gave a higher time resolution than required but the position resolution suffered as a result. To improve this, simulations were performed to optimise the Q value. Copper was finally chosen as the material for the new design, to give the best position resolution while maintaining a temporal resolution within the specification. New feedthrough antennas were also designed to remove the necessity of tuning the distance between the antenna and the opposite waveguide wall. The geometry of the reference cavity then had to be slightly modified to compensate the change in resonant frequency and Q value caused by the new feedthroughs. The geometry of the position cavity remained unchanged.

ISBN 978-3-95450-176-2

The manufacture of the copper cavity BPMs proved troublesome, as it took three attempts before the key internal dimensions stayed within our specified tolerances. Parts for five BPMs were manufactured in total, so the pieces for the three BPMs to be installed in CTF3 were selected from the pieces with the most suitable dimensions. Four of the cavity BPMs were brazed and the remaining parts for a fifth pickup were left unbrazed. The best three BPMs, based on the results of bench tests in the laboratory, were selected for installation and the fourth is being used to study the high precision alignment of CLIC quadrupole magnets [5]. Tables 1 and 2 show laboratory measurements of the Q factors and resonant frequencies of the reference and position cavities respectively. The naming of the cavities was arbitrarily chosen during the brazing process.

Table 1: Q Values and Resonant Frequencies of the Copper Reference Cavities after Brazing

BPM	Q_0	Q_{ext}	Q_L	f_0 /GHz
A	1235	2156	790	15.310
B	1133	1851	705	15.182
C	1212	1885	740	15.265
D	1161	1762	705	15.327

Table 2: Q Values, Cross Couplings and Resonant Frequencies of the Copper Position Cavities after Brazing

BPM	Q_0	Q_{ext}	Q_L	Cross-Talk /dB	f_0 /GHz
A	1362	2236	866	-27.0	14.981
B	1338	2341	876	-35.0	14.980
C	1218	2725	866	-40.9	14.987
D	1259	2110	814	-33.9	14.983

From these results it can be seen that the frequency of the reference cavity is on average ~300 MHz greater than the expected value of 15 GHz. There is also a large spread in the resonant frequency of the three cavities, indicating that something had been overlooked when redesigning the cavity. Clearly, the frequency is sensitive to something not covered by our specified tolerances and an investigation is underway to look into the cause of this sensitivity. The new feedthrough antennas are a likely candidate as they are very fragile and easily misaligned, with both the Q value and frequency sensitive to this misalignment. However, both laboratory measurements and simulation showed the sensitivity is not high enough to explain the 300 MHz discrepancy. The frequency difference is apparent in the traces shown in Figure 2. The loaded Q factors of both cavities are also greater than the expected value. The temporal resolution of the prototypes is higher than the design value of 50 ns. However, the CLIC specification requires multiple measurements to be made along the 156 ns bunch train, which is still possible with these Q factors. The position cavity central frequencies, though not exactly at 15 GHz are all closer than the 30 MHz bandwidth of the cavities. The cross-couplings between horizontal and vertical plane are sufficiently low for all BPMs. BPMs B, C and D were chosen to be installed based on these values and the frequency of the position cavities. Cavity C was chosen to be the central BPM as it has the lowest cross-talk and a resonant frequency closest to 15 GHz.

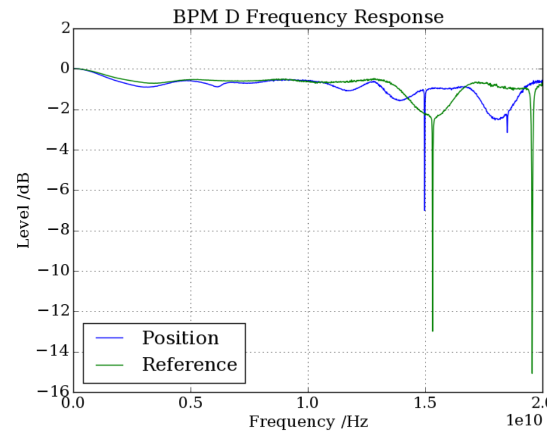

Figure 2: Frequency response of position and reference cavity of BPM D.

SYSTEM OVERVIEW

Originally three copper BPMs were to be installed at CTF3 with three channels on each connected to one electronics module: one for the reference and two for horizontal and vertical measurement. However, the narrow bandwidth of the downconversion scheme and the use of a single Local Oscillator (LO) per electronics module did not allow for simultaneous processing of signals differing by 300 MHz in frequency. The first stainless steel prototype BPM was therefore reused as a suitable reference cavity, and located upstream of the three new copper BPMs. It was then possible to process this with the same electronics module as for the position signals of the copper BPMs with no need for LO frequency alterations. The stainless steel pickup is seen in the front attached to the first copper BPM of the installation shown in Figure 3 with a schematic layout of the new system is shown in Figure 4.

Each of the BPMs is seated on translation stages which move the BPM horizontally and vertically, used for centring the bEach of the BPMs is mounted on translation stages which allow the BPM to move both horizontally and vertically, and are used for centering the beam within the BPMs and position calibration. Additionally, there is an optical transition ra- diation screen downstream of the setup which is useful for steering the beam through the BPMs. The outputs of the BPMs are connected with short coaxial cables to the downconverter electronics which are located in the accelerator tunnel just below the beam line. The LO signal for the mixers and a calibration signal are generated by two RF signal sources upstairs in the klystron gallery. These feed PLL

ISBN 978-3-95450-176-2

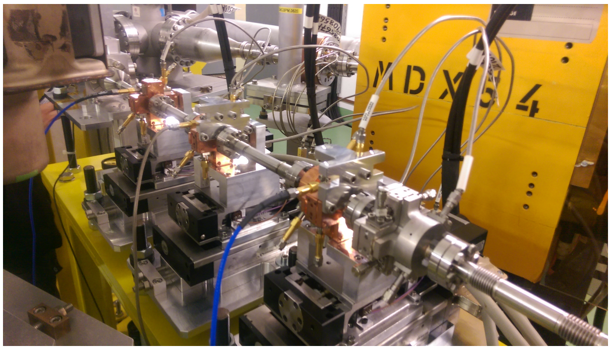

Figure 3: Photo of the new system installed in CTF3.

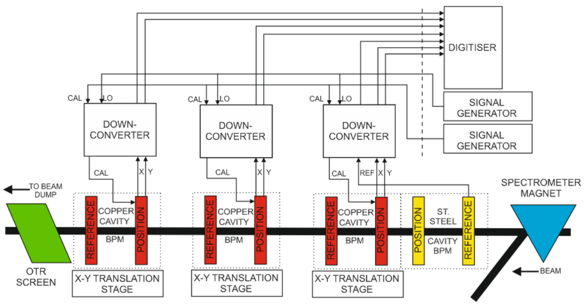

Figure 4: Layout of the new BPM system in CTF3.

controlled RF multipliers (64x) in the electronic modules. The frequency of the LO signal is 235.546875 MHz, which is multiplied by 64 to 15.075 GHz so that 15 GHz signals are downconverted to 75 MHz. A second, gain monitoring signal is derived from 234.375 MHz to give a second 15 GHz signal that can be connected to the unused cavity ports for debugging and online gain monitoring. In the current setup there are 7 electronics outputs delivering the downconverted signals to the gallery, where they are acquired by a set of new 12-bit 250 MS/s digitizers. Ideally, a better resolution digitiser should have been used, but the selected unit was the only suitable card readily supported by CERN's control system.

Downconverter Electronics

There are three downconverter electronic units, designed and manufactured at FermiLab, each with three downconverter boards, one LO board and one calibration signal board. A schematic of one of the downconverter channels with LO and calibration signal is shown in Figure 5.

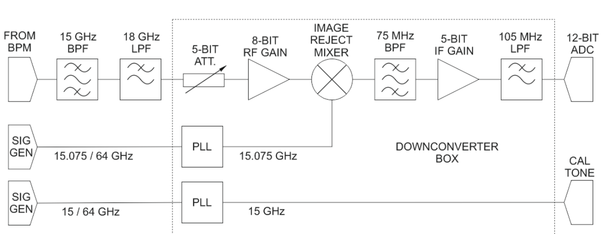

Figure 5: Schematic of one channel of the new downconverter electronics.

The electronics have several improvements over the system used in the previous installation. They include the a 5-bit attenuation and 8-bit gain control in the RF section and a 5-bit gain control in the IF section after downconversion. This provides the user with the ability to optimise the intensity of the analog beam signal throughout the acquisition chain, allowing maximum resolution to be achieved without saturation. The 75 MHz bandpass filter in the IF stage was designed specifically for this system. It has an 18 MHz bandwidth, such that the electronics define the overall bandwidth of the systems and the associated time domain waveform, rather than the individual cavities, which was not the case for the old prototype electronics. The addition of a calibration signal is also useful for remote testing of the electronics without the beam present.

As the variable gain controls were known to be non-linear and to differ between channels, an investigation into the electronics took place where the gains of each of the available nine channels were measured for various gain and attenuation settings. The dynamic range was also measured for one downconverter channel, with various settings. For the calibration of the beam position the overall gain for each individual electronics channel is critical and needs to be precisely measured. The measured gain of each channel is applied to the corresponding signals from the cavity to accurately calculate the actual signal level.

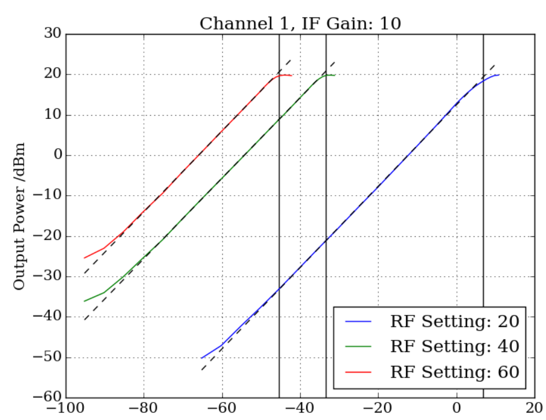

Figure 6: Compression measurements of a single channel of the electronics at various gain settings.

From the investigation, it was observed that increasing the RF gain setting above 60 does not result in any meaningful increase in the measured gain, while when it is set below 10, changing the attenuation setting has little effect on the gain. For the IF gain setting, when it is set to its maximum value of 19, the dynamic range is so small that it is quite unsuitable for beam measurements. From this investigation we decided upon using RF gain settings of 20 to 40 and IF gain settings of 0 to 10. These decisions were also backed up by the measurements of the 1 dB compression points at each setting. Table 3 shows these measurements for one channel and Figure 6 shows a few example curves at differ-

ISBN 978-3-95450-176-2

ent gain settings. At higher gains the compression threshold is inherently lower, and so is the range of measurable offsets. A nominal dynamic range of 80 dB is available at the chosen gain settings for initial CTF3 measurements. Future improvements are already foreseen to the system resulting in progress towards higher gains and respectively higher position resolution. This is nevertheless subject to the noise behaviour at different gain settings, which is currently being evaluated.

Table 3: Measured 1-dB Compression Points of a Single Downconverter Channel at Various Gain Settings

RF Gain Setting	0 IF Gain Setting P1dB /dBm	10 IF Gain Setting P1dB /dBm	19 IF Gain Setting P1dB /dBm
20	7.65	7.4	-0.4
30	-7.71	-16.98	-25.83
40	-24.42	-33.47	-42.25
50	-33.19	-41.90	-50.97
60	-36.72	-45.43	-54.34

BEAM TESTS

After the BPMs were installed, the first beam tests began in July. It quickly became apparent that it was difficult to centre the beam horizontally in the first BPM. This was due to the poor initial horizontal alignment. As a result, only the vertical scans taken so far are of interest for for resolution and position measurements.

Due to the limited bandwidth of the electronics, the digital downconversion and sampling of the signals had to be modified from the initial method, and as no optimum set of parameters has yet been found to allow resolution measurements. However, the position sensitivity of the copper cavities has been measured. Figure 7 shows an example plot of these sensitivity measurements. The charge sensitivity of the reference cavity has been studied before [3] and the results of this study where used as to normalise the signals for the position sensitivity measurement. These measurements were taken by scanning the translation stages in steps and taking several measurements at each step, normalising and then averaging.

A summary table of the sensitivity values taken from these measurements is shown in Table 4. The sensitivity values were taken calculated using the measured resonant frequencies and Q factors taken from Table 2 and the simulated value for the normalised shunt impedance R/Q (3.27 Ω/mm).

The high external Q of the dipole cavities decreases the potential position sensitivity. Combining these measurements with the gains measured during the lab tests the predicted sensitivities match well with those measured with beam.

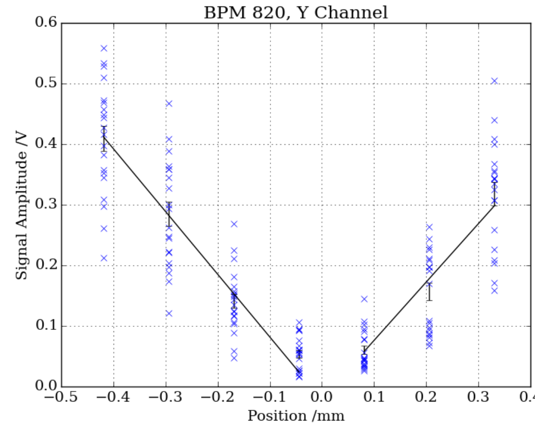

Figure 7: An example of a dipole cavity position sensitivity plot.

Table 4: Summary of Position Sensitivity Values Taken from the Measurements in the Vertical Axis

BPM	Measured Sensitivity $/VnC^{-1}$	Predicted Sensitivity $/VnC^{-1}$
810	8.3 ± 0.5	8.79
820	8.1 ± 0.6	8.16
830	9.5 ± 0.6	9.27

SUMMARY AND OUTLOOK

Redesigned cavity BPMs for possible future use on CLIC are currently being tested at CTF3. The position cavity operates with a resonant frequency and Q factor close to the desired values. However, the reference cavity does not have the desired frequency and there is also a spread of almost 150 MHz in these offset frequencies between BPMs. The cause of this is currently being investigated. The high external Q of the position cavities gives a reduced beam position sensitivity of ∼9 /VnC^{-1} which has been verified with beam data.

Although initial beam tests have been made with these new BPMs, the main goals are still to be achieved. The first of these goals is to determine the position resolution of these BPMs. The analysis of the current beam data for vertical resolution and then new data needs to be taken for the horizontal position resolutions. Then, ultimately the position resolution and temporal resolution need to be demonstrated simultaneously. To achieve this, an energy chirp will need to be applied to the CALIFES beam at CTF3 and multiple measurements made along the CLIC-like bunch train. Additionally, some consideration needs to be given to the wakefield effects of the cavity. This will be investigated through simulations and comparison with the theoretical analysis.

ISBN 978-3-95450-176-2

REFERENCES

[1] T. Lefevre et al., "Overview of the CLIC Beam Instrumentation", IPAC2011, San Sebastián, Spain, 2011, TUPC139, http://accelconf.web.cern.ch/accelconf/IPAC2011/papers/tupc139.pdf

[2] S. Walston et al., "Performance of a High Resolution Cavity Beam Position Monitor System," Nucl. Instrum. Meth. Phys. Res. A 578 (2007) 1-22.

[3] F.J. Cullinan et al., "First Beam Tests of a Prototype Beam Position Monitor for the CLIC Main Beam", IBIC2013, Oxford, UK, 2013, TUPC19, http://accelconf.web.cern.ch/AccelConf/ibic2013/papers/tupc19.pdf

[4] J.R. Towler et al., "Technologies and R&D for a High Resolution Cavity BPM for the CLIC Main Beam", IBIC2013, Oxford, UK, 2013, TUPC20, http://accelconf.web.cern.ch/AccelConf/ibic2013/papers/tupc20.pdf

[5] S. Zorzetti et al., "Stretched-Wire Techniques and Measurements for the Alignment of a 15GHz RF-BPM for CLIC", presented at IBIC'15, Melbourne, Australia, Sep 2015, paper TUPB063, these proceedings.

ISBN 978-3-95450-176-2

EXPERIENCE FROM THE CONSTRUCTION OF A NEW FAST WIRE SCANNER PROTOTYPE FOR THE CERN- SPS AND ITS OPTIMISATION FOR INSTALLATION IN THE CERN-PS BOOSTER

R.Veness, W.Andreazza, N.Chritin, B.Dehning, J.Emery, D.Gudkov, J.Herranz Alvarez, P.Magagnin, E.Piselli, CERN, Geneva, Switzerland
S.Samuelsson, CERN, Geneva, Switzerland, on secondment from Chalmers University of Technology, Gothenburg, Sweden

Abstract

A new design of wire scanner is under development for the LHC Injector Upgrade project at CERN. A prototype has been designed, built and installed in the SPS accelerator to test the concept in an operational environment. New technology has been developed and qualified for in-vacuum motor and structural components using 3D metal additive machining. This paper will describe the technology developed for this scanner and the test results to date.

This prototype has recently been re-optimised to fit in the limited space available in the PS Booster rings. This design will also be presented.

INTRODUCTION

The LHC Injector Upgrades (LIU) project at CERN [1] covers a wide range of changes to the LHC pre-injectors (LINAC, PS Booster, PS and SPS) to optimise beam emittance and intensity for the future upgrade of the LHC. These improvements will require new beam instrumentation, including transverse profile monitoring for the smaller, brighter beams in all injectors. LIU is scheduled for completion during the next long machine shutdown in 2019-20.

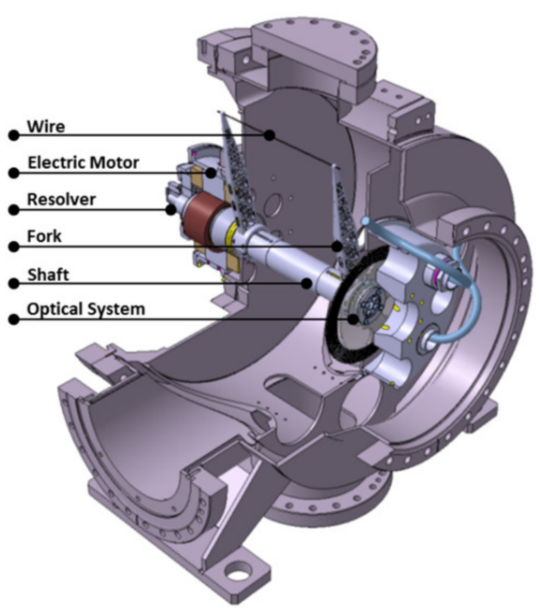

Figure 1: Beam wire scanner for SPS, general view.

A new wire scanner concept, based around an in-vacuum motor rotor is under development [2] to fulfil the LIU requirements. Prototypes have been built, with one installed in the SPS to test performance in an accelerator and the other used for laboratory development and testing. Figure 1 shows a cut away view of the scanner and vacuum tank with the main components labelled.

The PS Booster (PSB) presents the greatest challenge for integration as beams circulate in 4 superimposed concentric rings, with only 360 mm between their centres. The next step in the development is therefore to adapt the SPS prototype concept such that it can be installed in the PSB.

MOTOR SELECTION

Requirements

The conceptual design of the beam wire scanner (BWS) uses a frameless electrical motor with the rotor operating in vacuum and stator at atmosphere pressure. The most appropriate type for such applications is a frameless permanent magnet synchronous motor [1].

The device should provide sufficient torque to accelerate the wire to 20 ms^{-1} following the accelerating profile shown in Fig. 2 [3].

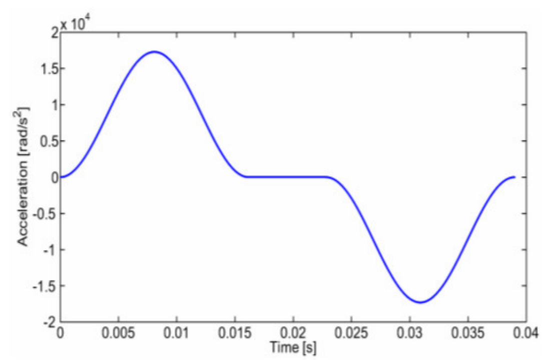

Figure 2: Acceleration profile.

The maximum value of the acceleration is α = 15711 rad.s^{-2} from which the required torque can be calculated using Newton's 2nd law:

$$T = J_{total} \times \alpha.$$

where J_{total} is the sum of moments of inertia of the load and rotor:

$$J_{total} = J_{load} + J_{rotor}$$

ISBN 978-3-95450-176-2

J_{load} is the sum of moments of inertia for all components moved by motor, including the shaft, forks, magnetic brake rotor, optical disk, and bearings. This value for the current BWS design is 8.6×10^{-4} kg.m^2. J_{rotor} is the moment of inertia of the motor rotor itself, with a value that depends on the selected motor.

Selection

According to current plans, the expected number of motors will not exceed 40 units at the current development phase. However the motor should be available for purchase during the whole lifecycle of the instrument which can exceed 20 years. Hence it was decided to search for a suitable commercial product.

For wire scanner operation the required torque should not exceed peak torque of the motor, i. e. maximum torque the motor can generate for the short periods of time, for example acceleration or deceleration.

A motor with high peak torque and low inertia rotor relatively (compared with other available options) was preselected for detailed study. This model has a rotor with a moment of inertia $J_{rotor} = 1.28 \times 10^{-3}$ kg.m^2 and peak torque 55 Nm. Even this low inertia motor represents some 60% of J_{total}, making motor selection crucial to an optimised instrument design.

The required torque for this case can be calculated using the equation below :

$$T = J_{total} \times \alpha = 31.56\ Nm,$$

which is around 1.75 times less than the specified peak torque for the selected motor. Hence once customised for UHV applications, it was suitable for installation and operation of the BWS instrument to provide the required torque with significant margin.

Customisation

Standard solutions available on the market are usually not vacuum compatible so the company was requested to perform a customisation of the standard product in order to fulfil the BWS requirements. Vacuum compatibility implies no use of glues, epoxies or other adhesives normally utilized by manufacturers for fixing the permanent magnets to the rotor body. An alternative fixation method like holding them using a thin-walled metallic sleeve (rotor banding) or sliding them into pre-machined wedge-shaped slots on the rotor frame was therefore requested.

Another customisation requested was optimisation of the radial air gap between the external diameter of the rotor and internal diameter of the stator. This value needed to be large enough to allow room for the vacuum chamber with a wall thickness 0.3 mm.

For the permanent magnet material, the best choice for this application is Sm_2Co_{17} as it has a Curie temperature above 250 ^{0}C allowing bakeout for achieving ultra-high vacuum (UHV). Furthermore this material is less sensitive to radiation [2].

All the requirements mentioned above were taken into account and implemented to the selected standard model by the supplier during the customisation phase. Being one of the core company products it is hoped that this type of motor will remain available for purchase in the coming years.

DESIGN AND MANUFACTURE OF FORKS

The forks serve to support the wire under tension while it is moved across the beam by the rotation of the shaft. Their design is therefore very important for the final performance. They must be rigid enough to keep the wire under tension in the plane parallel to the shaft and minimise deformation or vibration due to acceleration in the plane perpendicular to the shaft. They must also be optimised to minimise the inertial load on the motor during acceleration and deceleration of the wire.

As these requirements were readily quantifiable and the base geometry rather simple, it was a good candidate for automated topological optimisation. A number of commercially available software tools were used to make firstly 2D then 3D optimisation of the fork shape, iteratively removing material to converge towards an optimum for the given loads and displacement maxima [4].

The topology proposed by this optimisation was then implemented in the ANSYS finite element package and refined to conform to requirements of stiffness and vibration modes.

The resulting 3D model was then adapted for manufacture by laser-sintered 3D additive machining which imposes some constraints on the geometry. Forks were produced in one piece from titanium (TiAlV6) powder with a wall thickness of 0.4 mm by a specialist manufacturer with precision details post-machined at CERN.

Images from the four stages of the process: optimisation; analysis; 3D manufacture and post-machined structure are shown in figure 3.

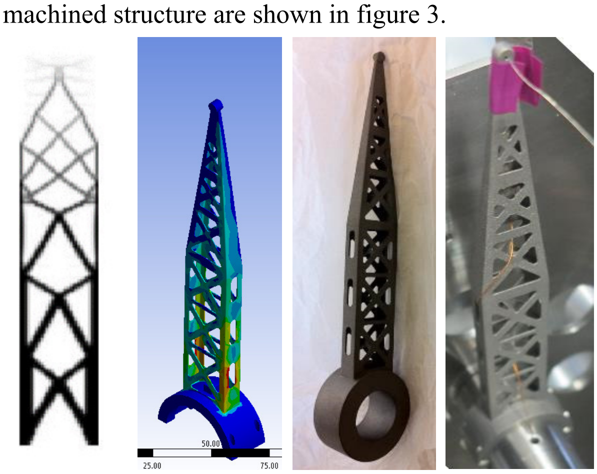

Figure 3: Design and manufacture process of forks.

ISBN 978-3-95450-176-2

QUALIFICATION OF MATERIALS FOR VACUUM

The wire scanner will operate in a UHV environment requiring all of the in-vacuum parts of the instrument to be UHV compatible.

A measurement campaign was performed to measure and qualify each component as well as the fully-assembled instrument. Special attention was given to components that are not normally used for UHV applications.

The residual gas analysis and outgassing rate measurements of the samarium cobalt permanent magnets, three type of bearings (metallic, hybrid and fully ceramic), optical fibres and optical components showed that they are all UHV- compatible and can thus be used in an accelerator environment.

Once the wire scanner prototype was ready and fully assembled a final measurement to check the vacuum compatibility was performed. This last test showed a much higher outgassing rate (not expected after the individual component measurements). This is suspected to be due to Kapton cables used to measure wire resistance or some contamination during the final assembly. Further tests are in progress.

An additional vacuum pump was added onto the instrument tank (a flange was already planned for such a device) to reach the required vacuum pressure.

PROTOTYPE VALIDATION PRIOR TO INSTALLATION

The functional validation of the prototypes and first actuator performance checks were performed on a dedicated test bench. This bench uses a control prototyping system called DSpace, based on MatLab/Simulink tools to design and validate the future motion control architecture and optimise its parameters for optimal performance. It was first used in [5] and then redesigned and optimized recently in [6].

Multiple mechanical configurations have been tested and compared against each other to provide an in-depth understanding of the dynamic behaviour of the scanner. This setup allows fine tuning of system parameters using the final assembly to achieve the required performance. Using the angular sensor of the motor control to measure the angular position of the shaft showed that the nominal speed and expected position are reproduced consistently. Figure 4 shows the position of the scanner prototype as the shaft rotates by π radians to the 'in' position and then back to the 'out' position over a very rapid 0.3 second cycle. This graph consists of 6 repeated in-out cycles superimposed on the same graph. Figure 5 shows the speed of the shaft, calculated by on-line processing using Kalman filtering techniques, also with 6 cycles superimposed. The position and speed can be seen to be very reproducible but not completely flat at maximum speed. Further optimisation of system parameters is foreseen to improve this issue.

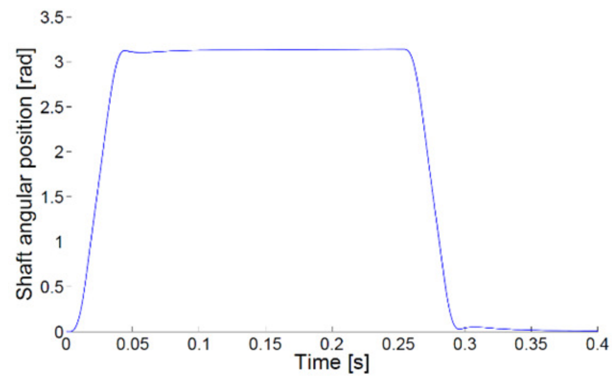

Figure 4: Shaft position with 6 superimposed scan cycles.

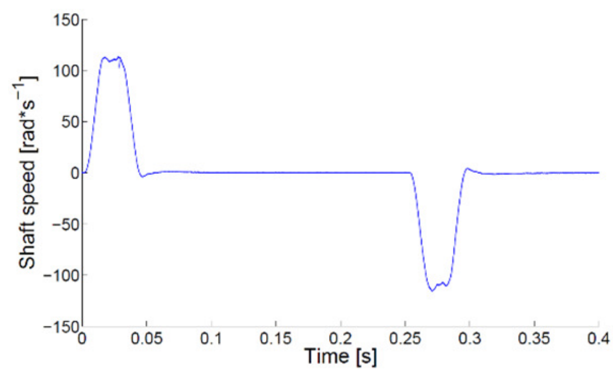

Figure 5: Shaft speed with 6 superimposed scan cycles.

Following this first phase, more than 70'000 cycles have been run to verify the stability of the movement cycle over extended periods of use. Preliminary results have shown a good stability even with a demanding cycle rate as short as one scan every 3 seconds. These very encouraging results give confidence for the expected performance of the scanner installed in the SPS accelerator.

This cyclic testing has also served as a preliminary validation of the moving mechanical components (bearings, forks, and shaft) which showed no sign of wear or damage, with the exception of some colouring of the bearings which is under investigation.

PROTOTYPE INSTALLATION AND TESTING IN THE SPS MACHINE

The prototype was integrated into the SPS LSS5 where a suitable space was available with low activation levels, easy access and appropriate beam size.

The beam wire scanner tank was installed and aligned in May 2014, during the long accelerator stop with the instrument itself installed during a shorter stop in January 2015.

The first functional testing of the scanner in the SPS accelerator is foreseen to take place before the end of 2015 with custom electronics as described in [7] instead of the development platform used on test the benches.

ISBN 978-3-95450-176-2

OPTIMISING THE DESIGN FOR THE PSB

The PS Booster ring is composed of four vertically stacked synchrotron beamlines that currently receives a proton beam at 50 MeV from the LINAC 2, and accelerates it up to 1.4 GeV before injecting it into the PS. LIU will increase these energies to 160 MeV injection into the PSB from the new LINAC4 and 2 GeV from PSB to an upgraded PS.

These four rings are stacked with an inter-axis distance of 360 mm, and have a beam aperture of 80 mm x 120 mm. This configuration, together with a longitudinal available space of 1000 mm for fitting a total of eight wire scanners, represents a major design constraint. The original design for the SPS has therefore been modified to fit in the limited available space.

The conceptual phase aimed to have the same design for horizontal and vertical wire scanner, using standard components with access to all instruments from the passage side of the ring, to allow easy maintenance.

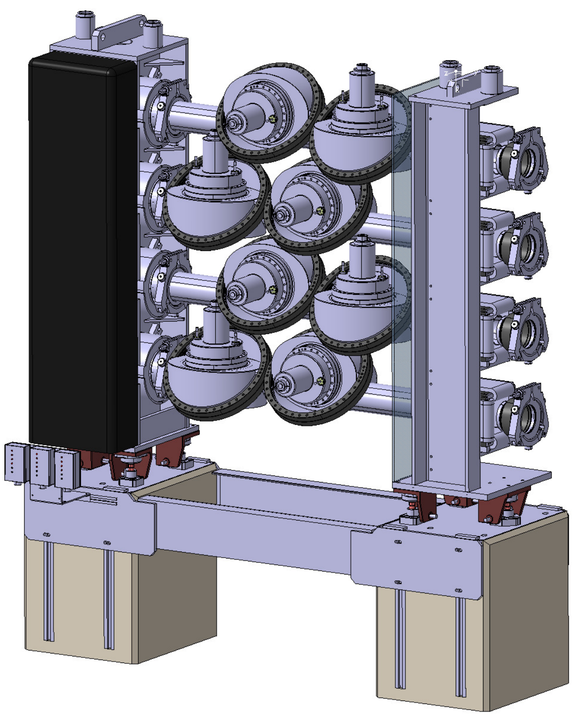

Figure 6: Possible BWS integration in the Booster.

The precisely machined drum used in the SPS design has been removed, making the shaft cantilevered. The optical system is shifted close to the motor and the shaft re-optimised in order to increase its stiffness while reducing the inertia. Stainless steel has been retained as the shaft material to maximise the ratio of shear modulus to mass density while still keeping the possibility to bake out the system.

The position of the optical sensors requires a large optical disc, which, if made out of glass would need custom manufacture, as well as being rather fragile under the extremely high acceleration of the system. Therefore, a metallic optical disc is under development in collaboration with Dundee University, UK.

The thickness of the vacuum chamber required between stator and the rotor has been optimised to 0.3 mm in order to integrate a commercial motor whilst remaining practical to manufacture.

However, despite these modification, integration is extremely problematic, as shown in Figure 6. The possibility of putting H and V scanners in different sectors of the machine is under investigation, which would make more space available and also allow for simultaneous scans in both planes.

CONCLUSIONS AND NEXT STEPS

Two prototype wire scanners based on an in-vacuum, directly coupled motor have been designed and built, with one installed for test in the SPS accelerator. Preliminary testing in the lab has validated the mechanics, control system and performance, with more than 70’000 scans successfully completed.

Modification to this design allowing for integration in the PSB is now in progress.

Production of a small prototype series is expected to start in early 2016, with installation in the PSB in early 2017, during a machine technical stop.

LIU will require a total of 18 of these new scanners to be installed across the injector complex during the period 2019-2020. A robust and cost-effective engineering of both mechanics and control system will therefore be required before series production.

REFERENCES

[1] K. Hanke et al. “Status of the LIU project at CERN”, Proc. IPAC 2014, Dresden, Germany.

[2] R.Veness et al. “Design of a high-precision fast wire scanner for the SPS at CERN”, Proc. IBIC 2012, Tsukuba, Japan.

[3] M. Koujili “Design and construction of a new actuator for the LHC Wire Scanner”, PhD thesis in Electrical Engineering.

[4] S.Samuelsson. ‘Mechanical optimisation of a high-precision fast wirescanner at CERN’. CERN-THESIS-2013-112.

[5] C. Grosjean, “Motor and Break Design for the Wire Scanner”, Bachelor thesis, Heig-vd, Yverdon-les-bains, 2014, CERN EDMS 1416824.

[6] M. Macchini, “Motion control design of a PMSM and FPGA implementation for the Beam Wire Scanner at CERN”, Master thesis, University of Pisa, 2015, CERN-THESIS-2015-055.

[7] J. Emery, “Beam Scanner Control, Monitoring and Supplies”, Engineering specification, CERN EDMS No 1318827.

ISBN 978-3-95450-176-2

STATUS OF THE PACMAN PROJECT

K. Artoos, M. Buzio, D. Caiazza, N. Catalan Lasheras, A. Cherif, I. Doytchinov, J-F. Fuchs, A. Gaddi, N. Galindo Munoz, J-C. Gayde, S. W. Kamugasa, H. Mainaud Durand, M. Modena, P. Novotny, S. Russenschuck, C. Sanz, G. Severino, D. Tshilumba, V. Vlachakis, M. Wendt, S. Zorzetti, CERN, Geneva, Switzerland

Abstract

PACMAN*, a study on Particle Accelerator Components' Metrology and Alignment to the Nanometre scale, is an Innovative Doctoral Programme, funded by the European Commission, hosted by CERN, providing a high quality training to 10 Early Stage Researchers (ESR) working towards a PhD. It is a multi-disciplinary project covering diverse fields such as beam instrumentation, magnetic measurements, metrology, high accuracy alignment and high precision mechanics. The objective of the PACMAN project is to propose new methods allowing the determination of the reference axis of accelerator components w.r.t. external alignment targets (fiducialisation process). A test bench, using components of the Compact LInear Collider (CLIC) study, will demonstrate the feasibility of the solutions developed and that a micrometric accuracy of their fiducialisation process can be reached. The results of this study, which has started in September 2013, are detailed. They concern the methods developed using a stretched wire to determine: the magnetic axis of small aperture magnets, the electrical centre of a 15 GHz Radio Frequency-Beam Position Monitor (RF-BPM) and the electro-magnetic axis of an accelerating cavity. They integrate also the solutions carried out to measure the position of the wire w.r.t. the external alignment targets. Other systems developed in the frame of the project are also taken into account: a nano-positioning system to validate the nanometric resolution of the BPM and a dedicated seismic sensor to characterize the environment during the measurements.

INTRODUCTION

The preservation of the emittance is a key issue for the next generation of linear colliders, and more particularly for CLIC [1], that will have nanometric beams size at the collision point. To reach such objectives, a strategy of alignment was proposed in the Conceptual Design Report of the CLIC study edited 3 years ago, consisting among others of a high accuracy and active pre-alignment of the components [2]. The aim of the PACMAN project [3] is to improve the pre-alignment accuracy of the major components of the CLIC main linac: 15 GHz RF-BPM, Accelerating Structures (AS) and quadrupole magnets along the main beam. This will be achieved by developing new methods and tools addressing several steps of pre-alignment simultaneously, using a stretched wire acting as a reference to fiducialise the components in the accurate environment of a 3D Coordinate Measuring Machine (CMM) [4].

The tools and methods developed will be then validated on a final bench to demonstrate their feasibility, before being extrapolated on other projects.

This paper reviews first the requirements concerning the pre-alignment of the CLIC study and the improvements in term of accuracy targeted by the PACMAN project. It then presents the objectives and first results obtained, concerning the determination of the reference axis of components using a stretched wire, the means to determine the position of this wire acting as a reference of alignment, and the alternative studies undertaken to achieve such a goal.

CLIC PRE-ALIGNMENT REQUIREMENTS AND PACMAN

The requirements concerning the pre-alignment of the three types of main component: BPM, AS and quadrupoles, are beyond the actual state-of-the-art. For a sliding window of 200 m, the standard deviations of the transverse position of the reference axis of each component (magnetic axis for a quadrupole, electric axis for a BPM and electro-magnetic axis for an AS) w.r.t. a straight line fit must be less than 14 µm for AS and BPM and less than 17 µm for quadrupoles [2].

Taking into account the number of components to be pre-aligned (more than 4000 BPM and quadrupoles, more than 60000 AS) and the very tight tolerances required, an active pre-alignment will be implemented. The position of the components, more precisely the position of their supports, will be determined continuously by alignment sensors, and re-adjusted by actuators. To ease the process, several components will be assembled on the same support: 4 AS per girder support, 1 BPM coupled with 1 quadrupole. This assembly step will occur after the determination of the reference axis of the components w.r.t. external alignment targets (fiducialisation). Then, the position of the pre-alignment sensors interface will be determined in the referential frame of the assembly support. Once the assembly support is installed in the tunnel, the pre-alignment sensors are plugged on their interface; measurements w.r.t. a straight reference line are carried out. Combining all the above-cited measurements, the position of the reference axis of each component can finally be deduced in the global coordinate system of the tunnel

The PACMAN project aims at combining at the same time the fiducialisation and the assembly steps, in the

*The PACMAN project is funded by the European Union's 7th Framework Programme under Grant Agreement no. 606839

ISBN 978-3-95450-176-2

environment of one of the most accurate 3D CMM of the world, in use at CERN: the Leitz Infinity CMM, with a Maximum Permissible Error (MPE) of 0.3 µm + 1 µm/m. The 10 researchers (ESR) working towards a PhD will collaborate to propose and validate different methods and tools related to metrology.

The first objective of the project was to choose a common wire compatible with all the different types of measurements to be performed. A Copper Beryllium wire with a diameter of 0.1 mm has been retained and its characterization has been performed successfully by ESR1.1 concerning the following parameters: electrical resistivity, micro hardness, linear mass, diameter, variation of the roughness fulfil the initial requirements, with only one criteria which is not fulfilled: the form error [5]. The form error will be determined in-situ during the process of measurement of the wire.

The methods developed to determine the reference axis of components using this wire as well as the first results obtained are detailed in the next chapter.

DETERMINATION OF A REFERENCE AXIS USING A STRETCHED WIRE

Determination of the Magnetic Axis of a Small Aperture Quadrupole Using a Stretched Wire (ESR 2.1)

Two methods can be considered to determine the magnetic axis of a quadrupole using a stretched wire:

- The single stretched wire method. Based on magnetic flux variation, it consists of displacing the wire by moving its extremities and measuring the voltage induced across the wire loop,
- The vibrating-wire method. The wire is fed by an alternating current and placed in magnetic fields. The measurement of its vibration amplitudes and phases will lead to the determination of the magnetic axis, knowing that this one is located at the minimum amplitude [6].

A comparative study has been carried out between both methods, demonstrating their compatibility and a higher accuracy for the vibrating-wire method. Also a repeatability 30 times better (3-4 µm) was observed, combined with a good sensitivity at low integrated strength. One of the major issues of the vibrating wire method is that background magnetic fields such as the Earth's magnetic field must be compensated. A correction procedure has been developed, suitable for strength adjustable magnets and for non-homogeneous field distribution [7].

An uncertainty analysis of the vibrating wire method is under way in order to identify the parameters with the biggest contribution and to optimize the performance from the repeatability and sensitivity point of view.

Determination of the Electrical Centre of a BPM Using a Stretched Wire (ESR 4.1)

Two methods have been studied to determine the electrical axis of a BPM using a stretched wire, first by simulations, then on a dedicated bench:

- The signal excitation method. A 15 GHz signal is fed on a conductive stretched wire, creating an excitation in a similar way to the beam. A scan of the cavity is carried out to find the electrical centre by small transverse displacements of the wire inside the BPM.
- The perturbation analysis method. The stretched wire is used in that case as a perturbation target. The cavity BPM is excited via one of the lateral waveguides and the output signal is analysed on one of the other later waveguides (opposite or adjacent). The minimum perturbations are observed when the wire is located at the centre of the cavity.

Simulations showed a higher sensitivity around the electrical centre for the signal excitation method but an easier integration for the perturbation analysis method: no RF impedance matching is needed, which means no coaxial line consisting of the wire and its beam pipe. A beam pipe would hide the wire and prevent the measurement of its location using a 3D CMM [8].

A dedicated bench has been put in place, for which the 5 Degrees of Freedom (DOF) displacements performed by a hexapod are taken as reference. The hexapod has been validated using Leitz Infinity CMM, confirming a bi-direction repeatability below 4 µm, as claimed by the manufacturer, for a load capacity of 5 kg. The measurements performed with the bench fit with the simulated ones and show a repeatability of the order of 1 µm in the determination of the centre using the perturbation analysis method [9].

Determination of the Electromagnetic Axis of AS (ESR 4.2)

Similarly to the BPM case, the perturbation analysis method has been chosen: the wire is displaced while the transmission of power is measured between ports. Extensive simulations using the HFSS software and measurements on a vertical test bench using a vector network analyser showed that a resolution of 1 µm could be reached with an error of 0.01 dB in the determination of the electromagnetic axis [10]. It still needs to be proven that this accuracy is maintained when connecting the actual wake field monitor and acquisition electronics to the accelerating structure instead of the optimised tapers designed for fiducialisation purposes.

This method can be extended to the measurement of the position of the wire from all the cells inserting special feed-throughs and thus verify the cell-to-cell misalignment

ISBN 978-3-95450-176-2

achieved during manufacturing of the structure (tolerance of ± 5 µm).

Once the wire is located at the reference axis of each component, its position will have to be measured w.r.t. the alignment targets and pre-alignment sensors interfaces. Three methods are considered in the next chapter for such an objective.

DETERMINATION OF THE POSITION OF THE STRETCHED WIRE USED AS REFERENCE

With the Leitz Infinity CMM (ESR 1.1)

Two challenges must be overcome to use the Leitz Infinity CMM to measure the position of the stretched wire w.r.t the alignment sensor interfaces. First, such a CMM is not able currently to perform non-contact measurements of the wire. "Off the shelf" sensors able to perform such a performance have been identified and will be tested on a dedicated bench, before being integrated on the CMM measurement head and calibrated. Second, the measurement head will have to be compatible with magnetic fields. First tests performed at Hexagon Metrology have shown that the impact of magnetic fields was not negligible at the level of the measurement head [11] when contact measurements were performed. However, when the measurement head is blocked, e.g. in case of non-contact measurements to the wire, the impact of magnetic fields was proven negligible.

With an Alternative Based on FSI Measurements and Micro-Triangulation (ESR 1.2, ESR 1.3)

The use of a combination of high accuracy angular measurements provided by the micro-triangulation system and absolute distances provided by a Frequency Scanning Interferometry (FSI) system represents an alternative to CMM measurements to measure the position of a stretched wire, with the advantage of being portable solutions, able to be used in the accelerator tunnel, during the installation of the equipment [12].

The Absolute Multiline system, manufactured by Etalon AG, is the only commercialised FSI system in the world. The first objective is to establish the 3D position of the FSI optical fibre tip from the exterior. A prototype of station consisting of an aluminium sphere with a diameter of 38.1 mm has been manufactured, in which the FSI collimator is centred. A modus operandi close to the Electronic Distance Measurement calibrations has been put in place in order to determine the centring offset of the collimator, within a few micrometres. Second objective is to adapt such a system for multilateration measurements, e.g. to measure distances to several points from a single point. Concerning the alignment targets, several types of spheres are under study, particularly glass spheres with a refraction index close to 2, able to be measured from different stations. The theoretical trajectory of the beam inside the glass sphere is under study with the help of the University of Liberec, the key point being the intensity of the return signal that must be strong enough to be analysed. To measure several targets from one station, one option under study is to install the station on displacement stages; the design and calibration of such solution is under study.

Concerning micro-triangulation, an inventory of all the hardware and software upgrades to be performed on the QDaedalus system has been carried out. The challenge concerns the detection of the wire, using image processing techniques, and the reconstruction of its catenary shape, using angles from several theodolites to arbitrary, non-identical and non-materialized points of the wire. The first tests performed at ETH Zürich show that it is possible to detect the common Copper Beryllium wire from a distance of 2 m, to extract the edges with 0.1 pixels precision, and to estimate the local axis within a few micrometres. The method and associated algorithms to reconstruct the wire over its all length remain to be implemented.

Once the position of the wire is determined, additional studies are foreseen to determine the resolution of the BPM developed, using a nano-positioning system foreseen for CLIC to displace the BPM w.r.t the wire, and seismic sensors to characterize the environment of measurements. These two additional studies are detailed in the next chapter, as well as the development of an alternative method to determine the magnetic axis of small aperture magnets.

ADDITIONAL STUDIES

Characterization of the Environment (ESR3.2)

One of the goals of the PACMAN project is to demonstrate the nanometric resolution of the 15 GHz RF-BPM, in the final PACMAN test setup. Such tight measurements will imply a very good knowledge and characterization of the vibration sources of the environment of measurement. This will be performed by a seismic sensor installed on the quadrupole, fulfilling the following requirements: a bandwidth comprised between 0.1 Hz and 200 Hz, a resolution below 0.1 nm at 1 Hz, a dynamic range above 80 dB, a compact size to be hosted on top of the quadrupole, not sensitive to stray magnetic fields. An inventory of "off the shelf" sensors was carried out. The behaviour of accelerometers, force balanced optical accelerometers, seismometers, geophones, has been simulated with Matlab and Simulink software; the seismic sensors have been compared according to different parameters: sensitivity, bandwidth and noise level. Dedicated procedures of acquisition and control have been put in place to start the sensors characterization.

A Long Range Nano-positioning System(ESR3.3)

A full mechanical system has been designed, manufactured and assembled for vibration isolation and nanometric positioning purposes for the quadrupole [13] but presented low eigen modes, below 50 Hz while the objective is to have frequency modes above 100 Hz. The low modes have been identified by a Finite Element Analysis showing that gluing rather than bolting the components of the assembly leads to a maximum reduction

ISBN 978-3-95450-176-2

of eigen frequencies of 8.5% (compared to 40% for the bolting). A re-design of the bedplates of the system is under way, and the current nano-positioning will be upgraded to be used for the final PACMAN bench.

In parallel, the study and development of long range actuators are under way, cumulating two functions: nanometric displacements over a long stroke, in order to allow nanometric positioning (nanometric displacements over a few micrometres) and pre-alignment adjustment (micrometric displacements over a few millimetres) of the quadrupole. Different options are under study to realize high stiffness load/long range actuators: the use of linear piezo-motors or a hybrid actuator, e.g. a combination of stepper motors with piezo stacks.

An Alternative to Determine the Magnetic Axis of Small Aperture Magnets (ESR 2.2)

An alternative to the stretched wire method based on Printed Circuit Board (PCB) rotating coil is proposed to determine the magnetic axis of small aperture quadrupoles and measure some key parameters as magnet field harmonics, main field direction and integral field gradient [13-14]. The development of small rotating coils raises several issues: the dimensions must be reduced without losing sensitivity, a compromise must be found concerning the design of the shaft between its stiffness and its radius, new technology and materials are needed for small shafts and PCB coil process needs to be improved. A new design of PCB and shaft is under way, taking into account all these parameters. A bench to perform such measurements is also under study. It will integrate better bearings around the shaft to achieve smaller vibration amplitudes and torsion. The location of encoders and motors will be optimized as well as the bearing assembly setup. Two calibration procedures have been studied: the classical calibration and the in-situ calibration [15].

Measurement Using Budget for Future Particle Accelerators Alignment Bench (ESR3.1)

A measurement uncertainty of the final PACMAN bench of 7 μm is targeted. The identification of the sources of errors is nearly completed. This will allow the determination of a complete budget of errors for the final bench.

CONCLUSION

The 10 PACMAN PhD students started working on their subject more than one year ago. After a familiarization phase, consisting of intensive training, discussions with experts and reading to prepare their literature review, as well as simulations and tests to determine the best methods and tools, the students have started validating their solutions on dedicated benches. A common 0.1 mm diameter Copper Beryllium wire, considered as reference of alignment, has been chosen for the whole project and characterized successfully. The first results presented in that paper are more than promising, confirming that a new way of pre-aligning components such as BPM, AS and quadrupoles, more accurate and less time-consuming than the current methods in use, will soon be demonstrated.

REFERENCES

[1] CLIC study website: http://clic-study.web.cern.ch/

[2] CLIC CDR, “A multi-TeV linear collider based on CLIC technology: CLIC Conceptual Design Report”, edited by M. Aicheler, P. Burrows, M. Draper, T. Garvey, P. Lebrun, K. Peach, N. Phinney, H. Schmickler, D. Schulte and N. Toge, CERN-2012-007

[3] PACMAN website: http://pacman.web.cern.ch/

[4] N. Catalan Lasheras et al., « Measuring and aligning accelerator components to the nanometre scale », IPAC 2014, Dresden, Germany, June 2014

[5] C. Sanz et al., “Characterization and measurement to the sub-micron scale of a reference wire position”, CIM 2015, Paris, France, Sept.2015

[6] D. Caiazza et al., “challenges in measuring the longitudinal field profile of a magnet by a vibrating wire”, 20th IMEKO TC4 International Symposium, Benevento, Italy, September 2014

[7] D. Caiazza et al., “Performance of the stretched and vibrating wire techniques and correction of background fields in locating quadrupole magnetic axes”, XXI IMEKO World Congress, Prague, Czech Republic, September 2015

[8] S. Zorzetti et al., “Design of the 15 GHz BPM test bench for the CLIC test facility to perform precise stretched-wire RF measurements, July 2015, IOP Science, Measurement science & technology, Volume 26, Number 9

[9] S. Zorzetti et al., “Stretched-wire techniques and measurements for the alignment of a 15 GHz RF-BPM for CLIC”, these proceedings, IBIC 2015, Melbourne, Australia.

[10] N. Galindo Munoz et al., "Electromagnetic field alignment of the Compact Linear Collider (CLIC) Accelerating Structure with help of wakefield monitor signals", these proceedings, IBIC 2015, Melbourne, Australia.

[11] C. Sanz et al., “New potential for the Leitz Infinity Coordinate Measuring Machine”, EUSPEN’s 15th International Conference and Exhibition, Leuven, Belgium, June 2015

[12] S. W. Kamugasa, V. Vlachakis, “PACMAN study of FSI and micro-triangulation for the pre-alignment of CLIC”, IWAA 2014, Beijing, China, October 2014

[13] S. Janssens et al., “Stabilization and precision pointing quadrupole magnets in the Compact Linear Collider (CLIC)”, PhD thesis, University of Amsterdam, January 2014, CERN-THESIS-2015-004

[14] S. Sanfilippo et al., “Small-diameter rotating coils for field quality measurements in quadrupole magnets, 20th IMEKO TC4 International Symposium, Benevento, Italy, September 2014

[15] G. Severino et al, “Calibrating the sensing-coil radius by feed-down from a harmonic reference”, 20th IMEKO TC4 International Symposium, Benevento, Italy, September 2014.

ISBN 978-3-95450-176-2

STRETCHED-WIRE TECHNIQUES AND MEASUREMENTS FOR THE ALIGNMENT OF A 15GHz RF-BPM FOR CLIC*

S. Zorzetti†, N. Galindo Munoz, M. Wendt, CERN, Geneva, Switzerland
L. Fanucci, Universitá di Pisa, Pisa, Italy

Abstract

For the Compact LInear Collider (CLIC) project at CERN, maintaining low emittance beams, as they are transported along the two independent 10-20 km long main linacs, is crucial. The beam trajectory therefore has to be very well aligned to the magnetic centre of the quadrupole magnets. A series of microwave cavity beam position monitors (BPM) is foreseen to detect the position of the beam along the main linacs to precisely monitor the beam trajectory in the circular beam pipe of only 8 mm diameter. The PACMAN project aims to demonstrate the pre-alignment of the magnetic field of a main CLIC quadrupole with the electro-magnetic centre of a 15 GHz RF-BPM to the required sub-micron accuracy. This paper focuses on stretched-wire measurements of a CLIC Test Facility (CTF) cavity BPM, to locate its electrical centre. Details of two measurement methods are discussed: RF signal excitation of the wire and analysis of RF signal transfer through the slot-coupled waveguides of the cavity, using the stretched wire as a passive target. This contribution will present the theory behind these measurements, their electromagnetic analysis and first, preliminary experimental results.

INTRODUCTION

To preserve the transverse emittance along the CLIC main linacs, the beam orbit needs to be steered with sub-μm accuracy and reproducibility along an optimal trajectory close to the electromagnetic center of the quadrupole magnets. This trajectory is foreseen to be measured using approximately 4800 high resolution cavity BPMs [1], located at each quadrupole along the beamline. At the CLIC Test Facility (CTF) a set of three cavity BPMs are currently under investigation. The PACMAN project [2] focuses on the study of the pre-alignment between the Main Beam Quadrupole (MBQ) and the resonant cavity Beam Position Monitor (RF-BPM). The pre-alignment methodology consist of characterizing the single components on separate test benches, integrating them on a dedicated support, aligning their respective electro-magnetic centres with stretched-wire measurement techniques.This paper summarizes the current status of the dedicated test stand and measurement setup for the cavity BPM.

* The PACMAN project is funded by the European Union's Seventh Framework Programme for research, technological development and demonstration under grant agreement no. 606839.

† silvia.zorzetti@cern.ch

CLIC RF-BPM

The CLIC RF-BPM consist of a resonant cavity coupled to four lateral waveguide slots with the signal picked up through coaxial connectors (*Fig. 1*) [3].

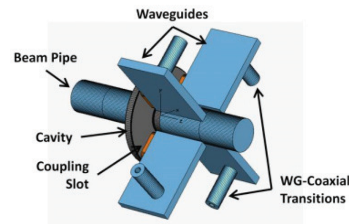

Figure 1: CLIC RF-BPM.

The fundamental mode of the cavity is a TM monopole mode at $\sim 11GHz$, with the TM dipole mode at $\sim 15GHz$. The lateral waveguides act as a high pass filter, suppressing the monopole mode while allowing the dipole mode to pass. Ideally, when the particle beam is centred into the RF cavity, the signal is zero, as the electric field of the dipole mode vanishes. In reality, because of mechanical imperfections, the electrical centre may not match the geometrical centre. The main task of the BPM test bench is therefore to accurately locate the electrical center.

MEASUREMENT METHODS

Two measurements methods have been identified, both using a conductive stretched-wire[1].

Signal Excitation

By means of a coaxial line the signal is propagated from the signal launcher to the BPM cavity. The wire is excited with a continuous sinewave at 15GHz and the BPM signal picked up through the lateral waveguides. With this method we are able to simulate the BPM behaviour as if it were excited by a particle beam (*Fig.*2).

To ensure a good transmission coefficient and to minimize reflections a hybrid PCB-coaxial transformer, operating at 15GHz, has been designed to launch the RF signal and to terminate the coaxial line configuration (*Fig.*3).

As the wire is excited and moved in the transverse plane of the BPM cavity, the signal picked up by one of the slot coupled waveguides is proportional to the electric field of the dipole eigenmode. When the wire is located in the centre of the cavity, the output signal is at a minimum.

The Slater theorem describes the dipole eigenfrequency shift in an RF cavity due to a metallic or dielectric perturbation,

[1] Cu-Be wire, $0.1mm$ diameter.

ISBN 978-3-95450-176-2

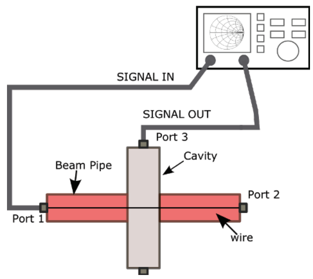

Figure 2: Signal excitation method setup.

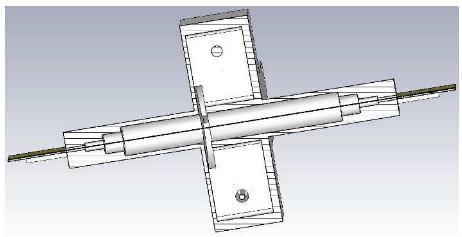

Figure 3: Model of the CLIC BPM Test Bench, including coaxial lines, terminations and signal launchers.

in this case the wire itself, which depends on its position. Because of this effect the linear zone of movement for a wire excited at a fixed frequency is reduced to $\sim \pm 300\mu m$, narrower than expected ($\sim \pm 500\mu m$). The final setup will have the BPM and the quadrupole rigidity mounted together, with their electromagnetic centres falling into the BPM linear range, to acquire a linear response with respect when the wire is in proximity of the quadrupole magnetic centre.

Perturbation Analysis

With this technique, the RF cavity BPM is excited by feeding a continuous sinewave at 15GHz through one of the four lateral waveguides, while looking at the signal picked up by the opposite or adjacent waveguide (*Fig*.4).

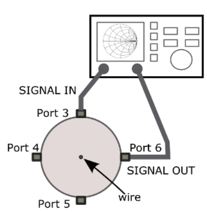

Figure 4: Perturbation analysis method setup.

The conductive wire represents a passive target, coupling with the electric field and draining power according to the amplitude of the field at that location. When the wire is located in the electrical center, the dipole E-field component is at a minimum, thus the power transmission between opposite waveguides is maximum.

On the other hand, the power transmission between adjacent waveguides is close to zero, as the RF-BPM has been designed to minimize the cross-talk between horizontal and vertical waveguides.

The plot *Fig*.5 compares the signals picked up by different waveguides, when the wire is excited ($|S31|$) and when the cavity is excited by the lateral waveguides: $|S43|$ referring to signal picked up by the adjacent port and $|S53|$ to the signal picked up by the opposite waveguides. From this plot we can anticipate a lower sensitivity around the electrical centre for the *perturbation analysis* method, as we are looking for maxima and minima rather than for a zero crossing slope. Nevertheless for integration purposes with the magnet and for allowing the metrology instrumentation to detect the position of the wire, the *perturbation analysis* is the preferred method for the final PACMAN test bench. In addition, the mechanics required for the coaxial line, necessary to transport the RF signal from the signal launcher to the cavity, would not allow a precise localisation of the wire with the *signal excitation* method.

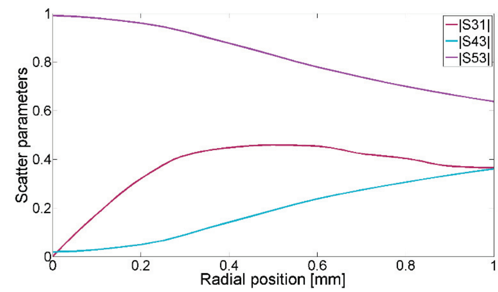

Figure 5: Equivalent E-field with respect to the wire's position performing measurements with the *signal excitation* method ($|S31|$) and to the *perturbation analysis* method ($|S43|$ adjacent waveguides and $|S53|$ opposite waveguides).

To more accurately locate the electrical center phase measurements may help. The plots in *Fig*.6 shows the phase jump when the signal is picked up from the adjacent port ($\angle S43$) in the *perturbation analysis* method, which is not in present on a same-axis measurement($\angle S53$) when looking to opposite waveguides.

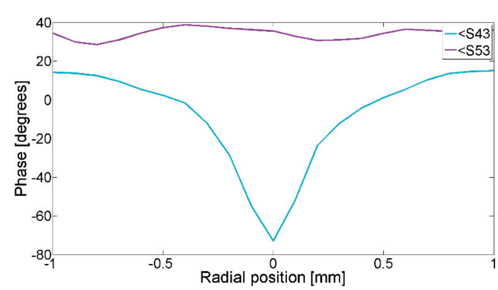

Figure 6: *Perturbation analysis* technique, phase measurements.

BPM TEST STAND

The BPM is mounted on a six-axis translation stage (hexapod), and moved with respect to a stretched wire. PXI technology from *National Instruments* is used to control the hexapod, to generate signals and acquire the response from

ISBN 978-3-95450-176-2

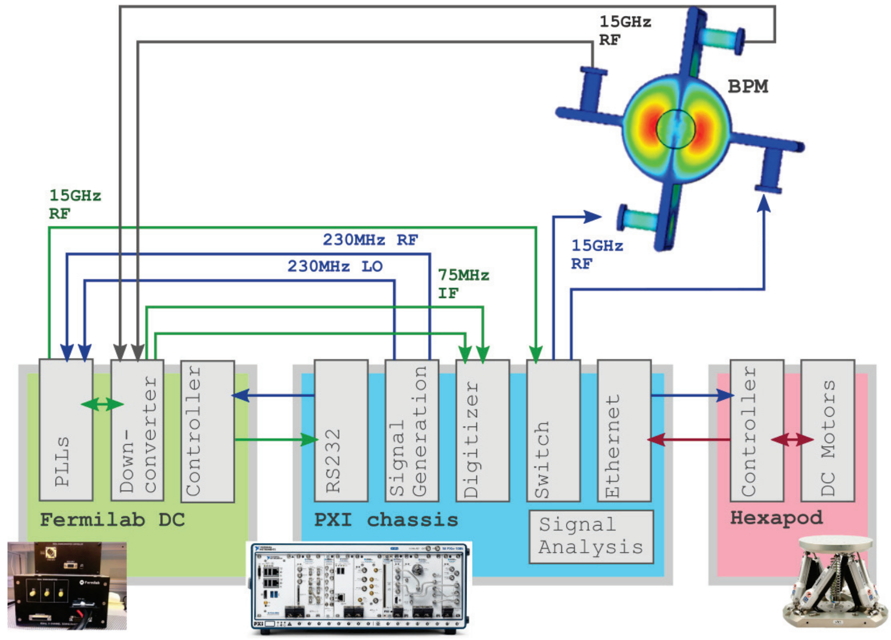

Figure 7: BPM Test Bench Block Diagram.

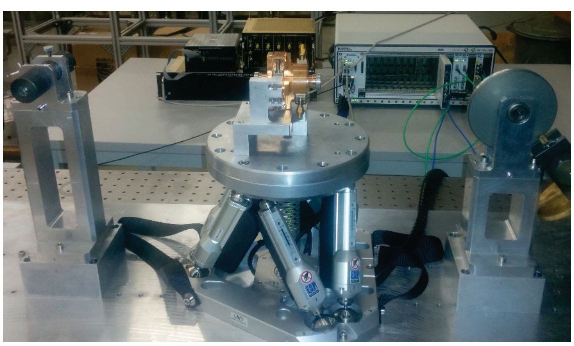

Figure 8: BPM Test Bench.

the BPM. A downconverter, which includes PLLs for RF and LO signal generation, is provided by *Fermilab* (US). It is used to downconvert the 15GHz signal to Intermediate Frequency (IF) of $75MHz$. A block diagram of the BPM test stand is presented in *Fig.*7, while a picture of the setup is shown in *Fig.*8.

Hexapod

The Hexapod[2] is a 6 Degrees of Freedom (DOF) translation stage with sub-micrometric resolution[3]. It has been validated with a *Leitz* Coordinate Motion Machine (CMM)[4]. Four spherical targets were mounted on the hexapod plate with the CMM sensor detecting the 3D position of each of those targets. The position of the device is determined by interpolating a plane between three of the four targets, projecting the fourth one onto the same plane and finding the mid-point.

In particular, the repeatability of the instrument was tested. The *uni-directional repeatability* is defined as the ability of the instrument to achieve a given position by attempting from a single direction, the *bi-directional repeatability* as the ability of the instrument to achieve a given position by attempting from different directions [4].

The results plotted in *Fig.*9 [5] refer to the movement of the hexapod on the z-axis[6] with a step size of $5\mu m$.

While the uni-directional repeatability specification has been confirmed (the error is estimated as $0.25\mu m$, which corresponds to the CMM uncertainty), the hexapod failed the test on the the bi-directional repeatability, as it is above $2\mu m$. Though the backlash effect can be compensated from the repeatable behaviour of the hexapod around the same trace.

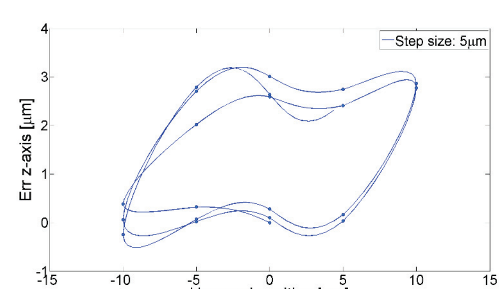

Figure 9: Hexapod validation result: hysteresis and repeatability evaluation on the z-axis.

[2] HXP100-MECA from *Newport*.
[3] (X,Y,Z) Minimum step size: $(0.5, 0.5, 0.25)\mu m$;
(X,Y,Z) Bi-directional repeatability: $(4, 4, 2)\mu m$.
[4] CMM uncertanty of $\pm(0.3\mu m + L/1000)$, where L is the dimension od the odject under test in mm

[5] Load on the support: 5Kg.
[6] The x-y plane is parallel to the hexapod plate, the z-axis or vertical axis is orthogonal to the x-y plane

ISBN 978-3-95450-176-2

Exploiting the good uni-directional repeatability, the measurement strategy was to scan the BPM cavity from a given starting point, moving on a single axis, then to reset the hexapod and scan a parallel line in the same direction.

Downconverter

The downconverter unit designed by *Fermilab*, also used for the cavity BPM studies at CTF, serves as the signal source and RF analogue signal processing unit. Two PLLs multiply the $\sim 230MHz$ Local Oscillation (LO) and RF signals, generated by the *National Instruments* PXI RF generators, 64 times to $15.075GHz$ and $15.000GHz$ respectively. The $15.000GHz$ signal feeds the cavity BPM port via the RF switch, while the $15.075GHz$ LO signal feeds a mixer, which downconverts the RF signal to $75MHz$. The RF and IF stages of each of the three downconverter channels are equipped with variable gain and attenuation, delivering an overall dynamic range of $80dB$ [5].

National Instruments PXI and Controls

The PXI technology from *National Instruments* is used to control the downconverter and perform signal generation, acquisition and processing; while a switch board is used extend the measurement to four ports. A LabVIEW interface (*Fig.*10) acquires the RF data and controls and monitors the hexapod movements.

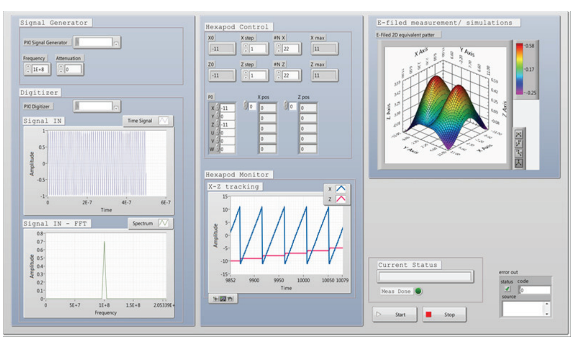

Figure 10: LabVIEW interface, in this version the E-field is rebuilt by simulations.

The LabVIEW coontrol software is composed of three main items:

- **PXI Hardware control**
  The electronic boards are controlled inside the PXI chassis. The signal is generated with user-configurable parameters. The IF signal from the downconverter is digitized and analyzed in the frequency domain.

- **Hexapod controller**
  The hexapod is controlled through an Ethernet connection. The interface allows setting the starting point and the step-size in the two scanning dimensions.

- **Signal analysis**
  The IF signals are analysed and a quantity equivalent to the E-field component is visualized in a 3D graph with respect to the wire x-y position, with the third dimension being the measured amplitude of the electric-field component.

EQUIVALENT E-FIELD PATTERN RECONSTRUCTION

Employing the hardware and software systems presented in the previous section, the RF-BPM cavity was scanned using the wire as a probe while the dipolemode intensity chart was recorded (*Fig.*5).

The initial measurements have been carried out with the *perturbation analysis* setup, considering only transmission between opposite waveguides; further phase measurements between adjacent waveguides are foreseen. As the PXI electronics was not yet available only a limited number of samples could be taken, which underlines the necessity for having an automatic test bench. The scan starts with a wide step-size of the hexapod, which decreases to smaller steps when approaching to the electrical center. *Figg.*11a to 11c show the progression from a step-size of $500\mu m$ to $20\mu m$.

A transverse cut of the intensity diagram in *Fig.*11c is displayed in *Fig.*12, showing a gradient around the electrical centre of $0.59mdB/\mu m$. The aim is now to increase this resolution by refining the measurement method.

Resolution and Repeatability Studies

Studies on the BPM resolution and repeatability have also been undertaken with the goal of demonstrating a nanometric resolution, anticipated as $50nm$ by simulations and not yet proved.

*Fig.*13 plots the resolution and bi-directional repeatability results demonstrated so far. Starting from a given point approaching the electrical centre, one position has been recorded ($P0$ in the graph); moving on a single $1\mu m$ step on the x-axis ($P0 - 1\mu m$) a $10mdB/\mu m$ resolution has been proved, obtaining a $\sim 2.5mdB$ bi-directional repeatability by moving a same step size on the same axis in opposite direction($P0 + 1\mu m$).

CONCLUSION

The BPM test bench has been studied and several measurement methods, promising different resolution and sensitivity, have been identified. Results achieved so far are encouraging and we look forward to progress on this path, with the aim of testing all the identified measurements methods, to compare their precision in the location of the electrical centre and proving the nanometric resolution of the RF-BPM.

ACKNOWLEDGMENT

My sincere thanks go to the NI team which followed me during my secondment at National Instruments in Hungary, in particular Botond Barabas, Erika Kun, and Peter Nemeti. I would also like to thank Nathan Eddy and Brian J. Fellenz from Fermilab for the work on the RF downconverter unit.

ISBN 978-3-95450-176-2

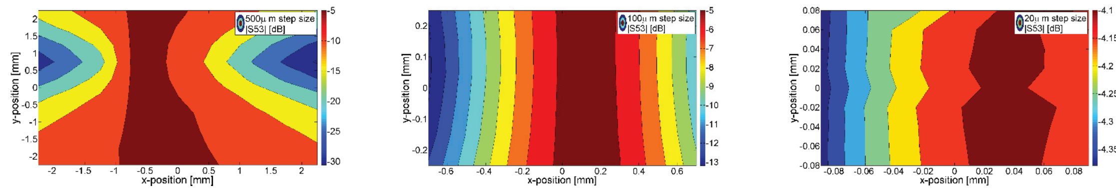

(a) Step size: $500\mu m$ (b) Step size: $100\mu m$ (c) Step size: $20\mu m$

Figure 11: E-filed pattern reconstruction by RF measurements in the area of the electrical center of the RF-BPM.

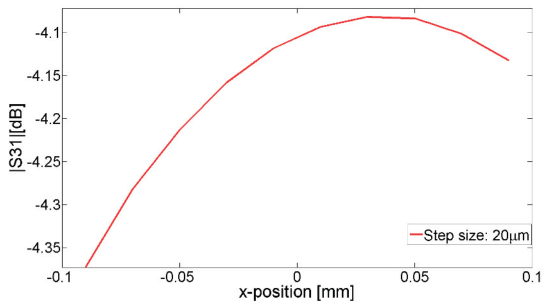

Figure 12: Transverse cut of *Fig.*11c, $20\mu m$ step size.

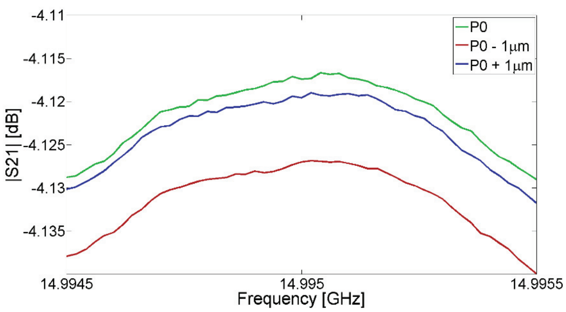

Figure 13: $1\mu m$ resolution results.

REFERENCES

[1] H. Schmickler et al., *Submicron multi-bunch BPM for CLIC*, FERMILAB-CONF-10-292-AD.

[2] H. Mainaud Durand et al., “Status of the PACMAN project”, *these proceedings*, IBIC’ 15, Melbourne, Asutralia (2015).

[3] N. Chritin et al. *A high resolution cavity BPM for the CLIC Test Facility*. FERMILAB-CONF-10-291.

[4] Newport website: `http://www.newport.com/Motion-Basics-and-Standards/140230/1033/content.aspx`

[5] J. R. Towler et al., "Development and Test of High Resolution Cavity BPMs for the CLIC Main Beam", *these proceedings*, IBIC’ 15, Melbourne, Australia (2015).

ISBN 978-3-95450-176-2

STATUS OF THE EUROPEAN XFEL TRANSVERSE INTRA BUNCH TRAIN FEEDBACK SYSTEM

Boris Keil, Raphael Baldinger, Robin Ditter, Mathias Gloor, Waldemar Koprek, Fabio Marcellini, Goran Marinkovic, Markus Roggli, Martin Rohrer, Markus Stadler, Daniel Marco Treyer (Paul Scherrer Institute, Villigen, Switzerland)*

Abstract

The European XFEL (E-XFEL) will have a transverse intra bunch train feedback system (IBFB) that is capable of correcting the beam position of individual bunches in the ~650us long bunch train, with a minimal bunch spacing of 222ns. The IBFB measures the beam positions with high-resolution cavity BPMs, and corrects the position of each bunch via stripline kicker magnets driven by class AB solid-state RF power amplifiers. The production of the IBFB BPM pickups is finished, and a pre-series version of the low-latency BPM electronics, including firmware and software, has been successfully tested with beam. After successful production and tests of prototypes, the series production of IBFB kicker magnets and RF power amplifiers is in progress. The IBFB feedback electronics hardware development is mainly finished, while firmware and software development is still ongoing. This report summarizes the latest design status and test results of the different IBFB system components.

IBFB SYSTEM OVERVIEW

Figure 1 shows the layout of the IBFB. The core of the system is located just upstream of the E-XFEL beam distribution kicker system and downstream of the collimation area. Four cavity BPMs (CBPMs) downstream of the IBFB ("downstream BPMs") are used to implement a fast feedback loop, where two vertical and two horizontal stripline kickers can apply individual kicks to each bunch in order to correct the beam trajectory at the downstream BPMs to the desired position. A feedback loop latency of ~1µs is expected to be sufficient to damp all relevant perturbations.

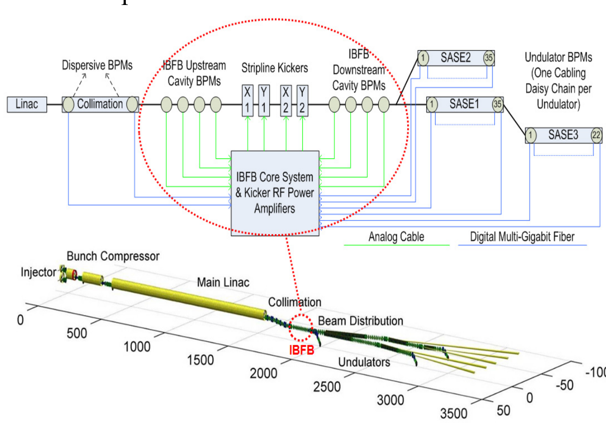

Figure 1: IBFB System.

* This work was partially funded by the Swiss State Secretariat for Education, Research and Innovation SERI.

The necessary kick amplitudes are calculated by an FPGA board that receives the beam position data from the CBPM electronics via fast fiber optic links. The FPGA board applies the kicks via two digital-to-analog converter (DAC) mezzanines with four 16-bit 500MSPS DACs each. In order to apply corrective kicks to each bunch, the DAC mezzanines generate suitable output waveforms that are amplified by pulsed solid-state RF power amplifiers driving the stripline kicker magnets. Each stripline kicker has two amplifiers for driving its two opposite strips in push-pull mode, i.e. with opposite voltages.

Four CBPMs upstream of the kickers ("upstream BPMs") are used by the IBFB to predict the beam position at the downstream BPMs from the upstream BPM readings and DAC set values. This enables the IBFB e.g. to detect failures or drifts of the RF power amplifiers, variations of the beam energy, or to check and adjust the IBFB timing.

The IBFB also receives the data of a dispersive CBPM in the collimator section (for beam energy measurement and kicker scaling factor adjustment) as well as data from all undulator CBPMs via digital multi-gigabit fiber optic links. In order to reduce the amount of cables, the undulator CBPMs of each of the three initial undulators (SASE1, SASE2, SASE3) are connected in a daisy chain, where only the first and last CBPM electronics of each chain is connected to the IBFB core system via single-mode fiber optic cables up to 1km length. When the first bunches of the E-XFEL bunch train (with up to 650µs train length and down to 222ns bunch spacing) arrive at the IBFB, it first corrects the trajectory using only downstream BPM data. As soon as the first undulator CBPM data is received by the IBFB, it fine-tunes the beam trajectory (if necessary), such that the following bunches reach the desired beam position in the undulators. Due to the long distance from IBFB to undulator CBPMs, the resulting latency of this correction is 4 to 10µs, depending on undulator and BPM location. However, the beam trajectory perturbations that occur between IBFB and undulators are expected to be either low-frequent (e.g. quadrupole magnet vibrations) or predictable, therefore it is sufficient to do this fine-tuning of the undulator beam trajectory once at the beginning of the bunch train, and then with a low correction bandwidth for the remaining part of the bunch train, in combination with the above mentioned fast (low-latency) feedback loop based on BPMs near the IBFB. In addition to this feedback-based correction, the IBFB will also perform an

ISBN 978-3-95450-176-2

adaptive feed-forward correction of the beam positions, by predicting perturbations that are reproducible or varying slowly from bunch train to bunch train, such that the feedback loop only has to correct the unpredictable perturbations.

BEAM POSITION MONITORS

The performance requirements to the IBFB BPMs are identical to the requirements of the undulator BPMs [2], i.e. <1µm resolution and weekly drift at 100-1000pC and ±0.5mm range, with the exception that the latency of the BPM electronics must be so small that an overall feedback loop latency of ~1µs can be achieved. It should be noted that the electronics of all E-XFEL cavity BPMs will have the required low latency, thus allowing to use also cavity BPMs in undulators and transfer lines for intra bunch train corrections.

Figure 2: E-XFEL cavity BPM electronics (MBU = Modular BPM electronics), with two cavity BPM RF front-ends (RFFEs, top) and FPGA carrier board with two ADC mezzanines (bottom) [2].

The high-resolution BPMs in E-XFEL have two types of 3.3GHz dual-resonator cavity BPM pickups: One type with 10mm aperture used in the undulator intersections, and one with 40.5mm aperture used in the warm beam transfer lines, including the CBPMs of the IBFB core system. All these CBPMs have basically the same electronics, firmware and software. However, since the 40.5mm CBPMs have a position cavity sensitivity (in units of V/mm/nC) and Q factor comparable to the 10mm CBPMs, their position cavity signal may be up to four times higher for the same beam charge when the beam is close to the aperture limit. Therefore the non-IBFB CBPMs have additional attenuators at their RF front-end (RFFE) inputs, where the necessary attenuation to protect the RFFE from overvoltage is still low enough to reach their specified single-bunch position RMS noise of <10µm RMS for a measurement range of ±10mm. The 40.5mm BPMs used by the IBFB core system for the ultra-fast feedback loop require a resolution <1µm RMS for a desired range of ±1mm. Therefore their RFFEs do not have additional attenuators, but a special input protection circuit that clips the input signals when they reach a certain voltage. The IBFB CBPMs also determine the bunch charge range where the IBFB can be used. At very low bunch charge, the noise of the BPMs scales inversely with the bunch charge, and so does the noise modulated by the IBFB onto the beam (for fixed settings of the feedback parameters).

Although the E-XFEL IBFB and undulator cavity BPMs have been specified to reach <1µm RMS noise only between 100pC and 1000pC, PSI designed the BPM electronics to reach this performance also for much lower charge down to about 20pC (see Figure 3). Moreover, the noise modulated by the IBFB onto the beam can be reduced if necessary by changing the feedback algorithm parameters to reduce the feedback loop bandwidth. However, this will of course also lower the frequency up to which random perturbations can be corrected, and reduce the correction efficiency at lower frequencies. Therefore the IBFB will allow to adjust the feedback algorithm settings to the bunch charge, either manually or automatically by measuring the bunch charge with the IBFB BPMs and adjusting the feedback algorithm parameters accordingly.

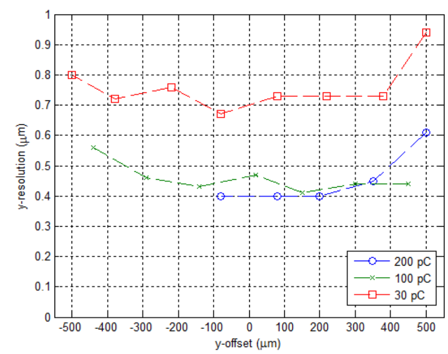

Figure 3: Position resolution (RMS noise) of E-XFEL cavity BPM, measured by correlating data of several BPMs, for different bunch charges [3].

KICKERS

E-XFEL has a variety of random and reproducible beam trajectory perturbation sources, where a conservative estimate predicts worse-case beam trajectory perturbations of about ±100µm (assuming 20m beta function) [1]. For 17.5GeV beam energy, this corresponds to kick angles of ±3.5µrad (for the same beta function at the kickers). Although the beta functions and betatron phase advance at the locations of the kickers have been optimized to reduce the required kick strength, we still decided to install a baseline kicker system that provides about ±4µrad kick angle at 17.5GeV. In order to reach this value, we designed 2.2m long (flange-to-flange) stripline kickers with 2m effective strip length (for a 40.5mm aperture beam pipe), driven by pulsed RF power amplifiers with a specified linear power of >2kW.

Stripline Kickers

Figure 4 shows a longitudinal cut through an IBFB kicker. Only about 30% of the overall length (that is 2.2m flange-to-flange) is visible in the figure. The RF power amplifier signals enter the kicker at the left side via two N-type connectors that are attached to the opposing strips via flexible bellows (shown in Figure 5, right photo) to allow relative movement of strips and outer vessel due to thermal expansion and contraction.

ISBN 978-3-95450-176-2

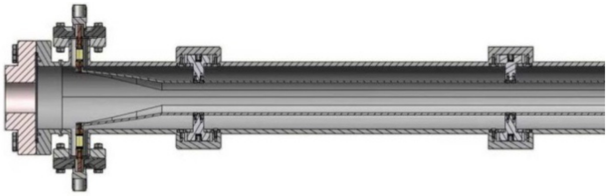

Figure 4: IBFB stripline kicker cross section (only 1/3rd of the kicker shown).

Each of the two conductive strips inside the vessel is held in place via five ceramic spacers with equal distance (only two visible in Figure 4), where the center spacer has a fixed position, while the other four can slide longitudinally (see Figure 5, middle photo). This avoids mechanical stress and risk of cracks of the ceramics during assembly and vacuum bake-out. The kicker vessel and strips are made from aluminum, which reduces the weight and allows easier and more cost-efficient machining. The vacuum flanges at both ends are made from stainless steel. Rather than using the expensive explosion-bonding technique to connect steel to aluminum, a special second gasket between the aluminum kicker body and steel end flange pieces is used. This cost-efficient solution had already been employed successfully for UHV beam pipes at other accelerator labs. Figure 5 shows a kicker prototype during production at the company.

Figure 5: IBFB kicker magnet during assembly. Left: Kicker magnet without end flanges. Middle: Sliding ceramic spacer (white) allows relative movement of strip and outer vessel. Right: Flexible RF feed-through at end of strip.

Figure 6 shows the reflection at the kicker input in dB as a function of the drive signal frequency. Figure 7 shows the impedance of the stripline kicker as a function of the longitudinal coordinate (blue: measurement, red: simulation). The positive peaks at the very left and right are caused by a small impedance mismatch of the input and output port at both ends of the kicker. The five negative peaks in between are caused by the five ceramic pieces that hold the strips in position. The positive peak at 1.25m is caused by a flange for a vacuum pump in the kicker vessel. Figure 8 shows one of the four IBFB series version kickers during the vacuum acceptance test at PSI. The produced kickers passed all acceptance tests and are now ready for installation in the E-XFEL tunnel.

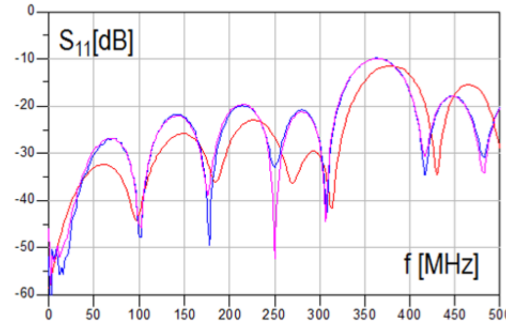

Figure 6: Measured reflection S11[dB] (blue: port 1, pink: port 2) and simulated reflection (red) of IBFB prototype kicker vs. frequency.

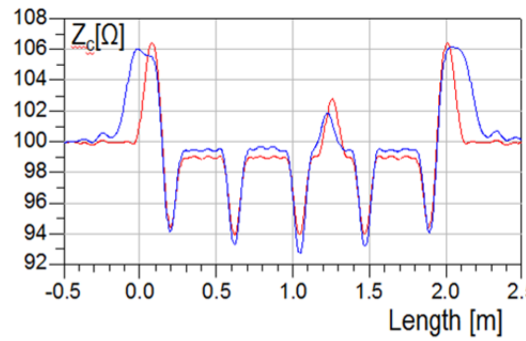

Figure 7: Kicker impedance as function of longitudinal position (red: simulation, blue: measurement).

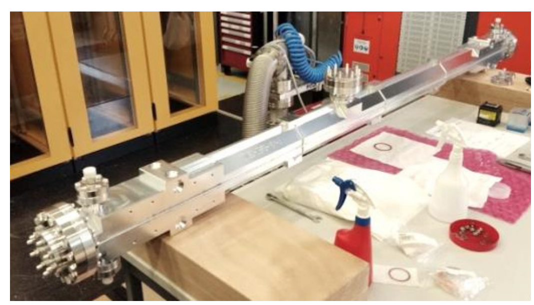

Figure 8: IBFB kicker magnet during vacuum acceptance test at PSI.

RF POWER AMPLIFIERS

Since E-XFEL has bunch trains with up to ~650µs length and typically 10Hz (max. 25Hz) repetition rate, the IBFB kicker system uses pulsed amplifiers with ~1ms maximum pulse length, 25Hz max. repetition rate, and ~3% duty cycle. Suitable commercially available kW-range solid-state power amplifiers that meet the IBFB requirements are commonly used e.g. for radar and MRI systems. After an extensive market study, PSI purchased two prototypes from the company TOMCO in 2012. These prototypes are based on an already existing commercially available amplifier model, but were modified by the manufacturer to improve the MTBF. Modifications include a redundant main power supply as well as redundant amplifier sub-modules, where the amplifier can continue to operate even if one of the redundant components fails.

ISBN 978-3-95450-176-2

Figure 9: Two IBFB RF Power Amplifiers.

Figure 10 is a plot of output power vs. input power of the amplifier, measured at PSI for one of the purchased prototypes. Both the linearity and the maximum power are better than specified by PSI (we measured 6kW, compared to a specification of 2kW linear and 3kW saturated), as well as the droop (i.e. deviation of the power from an ideal flat top for constant input power) shown in Figure 11. The measured amplifier latency is <35ns, compared to a specification of <50ns. Figure 12 shows the frequency response of the amplifier measured at PSI, Figure 13 the output signal response to a rectangular input signal pulse. Obviously, such an output signal is not well suited for the IBFB, since significant ringing of the output signal causes undesired kicks of the following bunches (with 222ns minimal bunch spacing in E-XFEL).

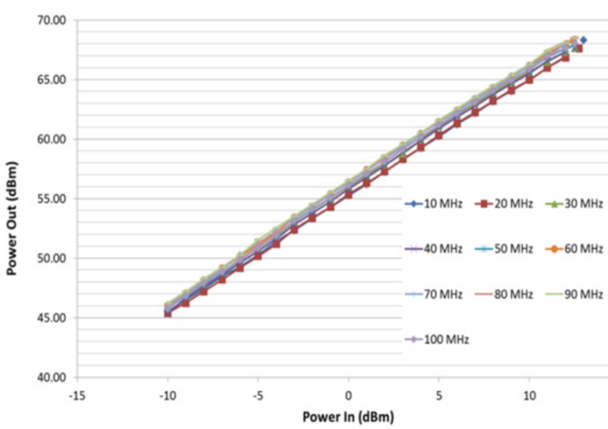

Figure 10: Output power vs. input power of the IBFB RF power amplifier, for different frequencies.

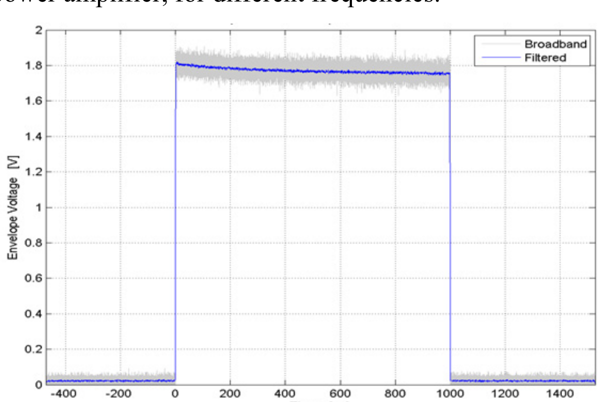

Figure 11: Output voltage of the IBFB power amplifier vs. time for constant input power.

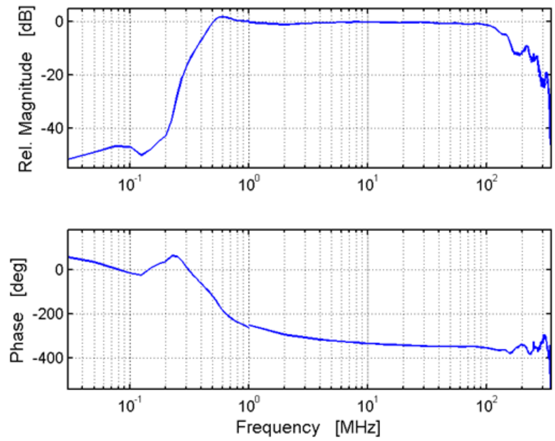

Figure 12: Frequency response of the IBFB power amplifier.

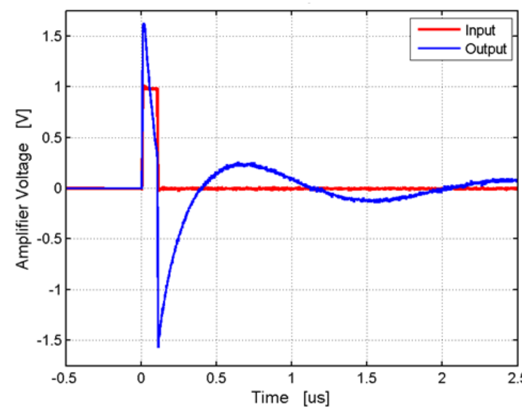

Figure 13: Output signal (blue) of the IBFB power amplifier for a rectangular input signal pulse (red), with undesired ringing after the pulse.

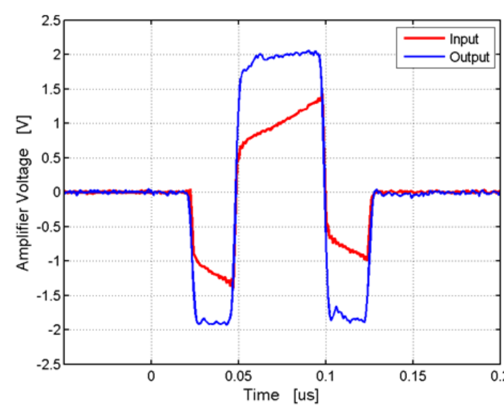

Figure 14: Optimization of output signal (nearly ideal flat top, no post-pulse ringing), by optimized input signal shape.

As shown in Figure 14, we managed to generate a practically optimal output waveform with a nearly flat top, by introducing suitable slopes a DC-free symmetric amplifier input waveform. By using such waveforms, the IBFB will be able to apply well-defined arbitrary kicks to each electron bunch, where the kick angle is insensitive against arrival time and phase drift, with minimal disturbances for the following bunches.

ISBN 978-3-95450-176-2

FEEDBACK ELECTRONICS

Figure 15 shows the IBFB system core electronics, consisting of two FPGA boards (“GPAC” = Generic PSI ADC Carrier) also used by the E-XFEL BPM system. The FPGA board on the left side of Figure 15 performs the actual feedback and feed-forward algorithm (using a combination of FPGA firmware and software in the embedded processor of the FPGA). The board applies the calculated corrective kicks via two DAC mezzanines with four 16-bit 500MSPS DAC channels each. The DACs are synchronized to the accelerator bunch repetition rate and allow to generate suitable waveforms that drive the power amplifiers of the kicker magnets (within the bandwidth limits of the amplifiers). The power amplifiers also have a fast gate input that is controlled by dedicated (coaxial) output signals of the DAC mezzanine boards, thus allowing the IBFB core electronics to enable and disable the amplifiers beam-synchronously. The FPGA board on the right side of Figure 15 monitors the output signals of the kickers and of the RF power amplifiers via two 8-channel 12-bit 500MSample/s ADC mezzanines with bunch-synchronous clocks, thus allowing to detect drifts and malfunctions, e.g. the failure of one of the two operational RF power amplifier modules in the amplifier. The FPGA board also has a digital interface to the kicker amplifiers that allows e.g. to monitor their health status or enable/disable internal amplifier power modules, including the possibility to switch over to a redundant spare amplifier module if one of the two operational power modules fails.

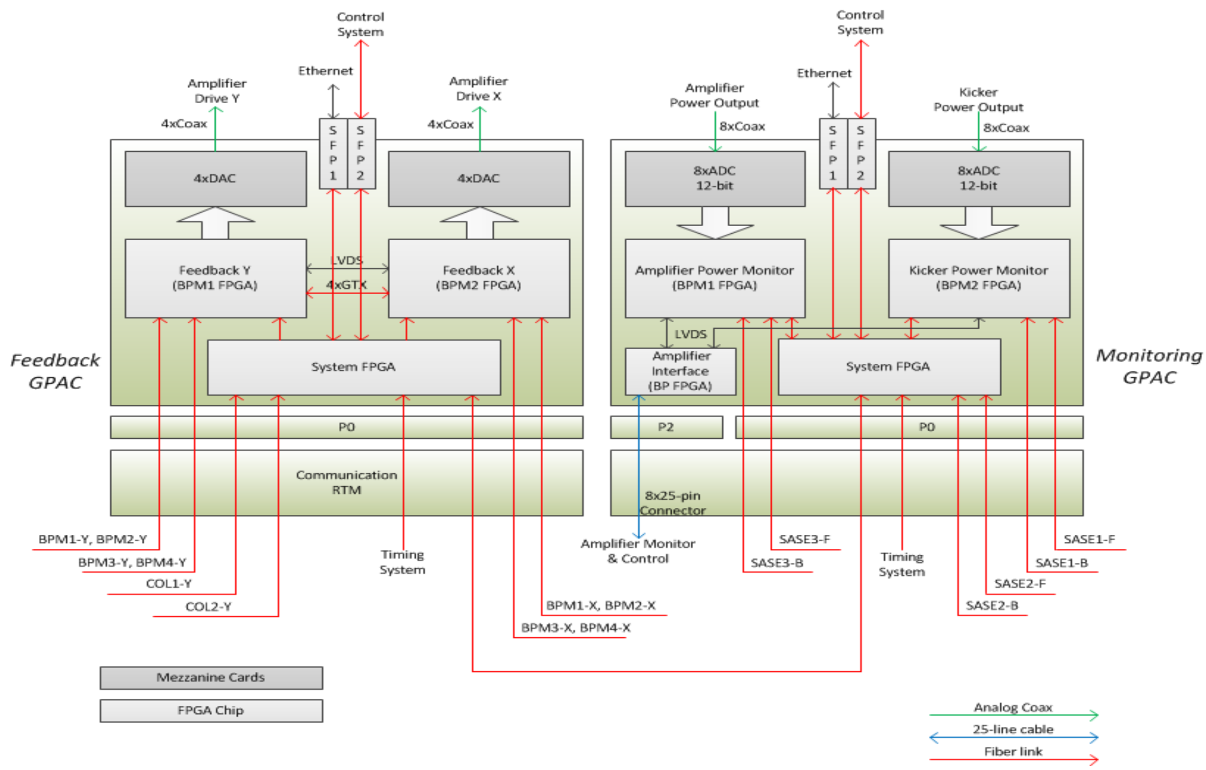

Figure 15: IBFB Feedback Electronics.

SUMMARY AND OUTLOOK

The production of the IBFB kickers and other hardware components is nearly finished, with installation in the E-XFEL tunnel in Q1/2016. The IBFB will be ready for beam operation mid-2016, including software/firmware where the implementation is still ongoing. First beam at the IBFB is expected in the 2nd half of 2016. Although the IBFB kicker system allows to correct the presently expected maximum trajectory perturbations, space for additional four kicker magnets is reserved, thus allowing to double the kick angle if necessary. In addition to beam trajectory correction, the IBFB can also be used for other purposes, e.g. 2-color FEL operation, where the IBFB applies a controlled kick to each bunch, such that it lases only in the first or only in the 2nd half of the undulator line (using a suitable DC kicker in the middle of the line), where both halves are tuned to different wavelengths.

REFERENCES

[1] B. Keil et al., “Design Status of the European X-FEL Transverse Intra Bunch Train Feedback”, Proc. IBIC’12, Tsukuba, Japan, 2012, http://www.jacow.org/.

[2] B. Keil et al., *“The European XFEL Beam Position Monitor System”*, Proc. IPAC’10, Kyoto, Japan, 2010, http://jacow.org/.

[3] M. Stadler et al., *“Low-Q Cavity BPM Electronics for E-XFEL, FLASH-II and SwissFEL”*, Proc. IBIC’14, Monterey, USA, 2014, http://jacow.org/.

ISBN 978-3-95450-176-2

STATUS OF THE SwissFEL BPM SYSTEM

Boris Keil, Raphael Baldinger, Robin Ditter, Daniel Engeler, Waldemar Koprek, Reinhold Kramert, Alessandro Malatesta, Fabio Marcellini, Goran Marinkovic, Markus Roggli, Martin Rohrer, Markus Stadler, Paul Scherrer Institute, Villigen, Switzerland

Abstract

SwissFEL is a 5.8GeV free electron laser facility presently under construction at PSI. The electron beam position will be measured by three types of cavity beam position monitors (CBPMs). For the injector, linac and beam transfer lines, low-Q 3.3GHz cavity BPMs with 38mm and 16mm aperture (CBPM38 and CBPM16) will be used to measure the position and charge of two bunches with 28ns spacing individually. A fast kicker system distributes each bunch to a different undulator line, where 4.9GHz high-Q cavity BPMs with 8mm aperture (CBPM8) are used in the undulator intersections. The production of the CBPM38 pickups is finished, while the CBPM16 production is in progress. For CBPM8, a prototype pickup has been successfully tested, and a 2nd pre-series prototype with reduced dark-current sensitivity is currently in production. The development of the common 3.3GHz CBPM electronics for CBPM38 and CBPM16 is finished, while the CBPM8 electronics is currently in the prototyping phase. This paper gives an overview of the present pickup, electronics, firmware and software design and production status, including test results and methods to control and maintain the quality during series production.

INTRODUCTION

Table 1 lists the quantities and requirements for the SwissFEL BPMs [1]. CBPM38 pickups [2] are only installed at a few locations where a larger aperture is needed, e.g. at the beam distribution kicker, in beam dumps, or bunch compressor arms. The CBPM16 pickups [2] are used in most parts of the accelerator, except for the undulator intersections where the high-Q CBPM8 pickups [3] will provide higher (sub-micron) resolution and drift as required for the alignment and control of the electron-photon beam overlap in the undulators.

Table 1: SwissFEL BPM Quantities and Requirements

	CBPM38	CBPM16	CBPM8
Quantity*	7	114	51
Usage	Linac, Transfer Lines		Undulat.
Aperture	38mm	16m	8mm
Position Range	±10mm	±5mm	±1mm
Position Noise	<10µm*	<5µm*	<1µm**
Pos. Drift/Week	<10µm	<5µm	<1µm
Charge Noise	<0.1%***		
Charge Range	10-200pC		
#Bunches/Train	1-3		1
Bunch Spacing	28ns		10ms

* Within 30% of the position range
** Within 50% of the position range
*** Or 30fC, whatever is larger

Beam Energy Measurement

The CBPM16 and CBPM38 are also used at dispersive locations for beam energy measurement, e.g. in the arms of the bunch compressors between 1st and 2nd (as well as 3rd and 4th) dipole, or downstream of beam dump dipoles. For an expected position resolution of <1µm, the corresponding energy resolution is typically <2E-5.

Bunch Charge and Beam Loss Measurement

Like in the SwissFEL injector test facility (SITF), high-resolution charge measurements in SwissFEL will mainly rely on CBPMs since they provide higher resolution than dedicated charge monitors (ICTs, wall current monitors, etc.). CBPM16 prototypes achieved <0.07% relative resolution at high charge and <8fC absolute resolution at very low charge [1]. Since the pre-calibration of the CBPMs in the lab only provides ~10% scaling factor error for the charge, the CBPMs will be cross-calibrated with beam against dedicated charge monitors to achieve better absolute accuracy of ~1%.

BPM PICKUP DESIGN

All SwissFEL BPMs are cavity BPMs with two resonators. The so-called reference resonator has one (CBPM16, CBPM8) or two (CBPM38) standard couplers to measure the charge using the TM_{010} mode, while the position resonator has four couplers, using TM_{010} mode-suppressing waveguides to obtain the product of position and charge via the TM_{110} mode. By using the same working mode frequency for both resonators, undesired frequency-dependent drifts of the symmetrically designed BPM electronics are minimized. Both resonators also have the same loaded quality factor Q_L to obtain symmetric waveforms for minimal arrival time dependency of the CBPM electronics.

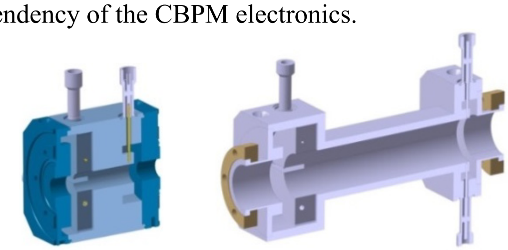

Figure 1: SwissFEL CBPM16 pickup (left) and CBPM38 pickup (right).

The CBPM16 and CBPM38 pickups are based on a SACLA design [4] that was also adopted for the E-XFEL [5][6]. For SwissFEL we did systematic simulation scans of all relevant pickup dimensions in order to achieve high resolution at low charge, and we also optimized the

ISBN 978-3-95450-176-2

design and production for lowest costs while maintaining high quality. The CBPM16 and CBPM38 pickups are made of stainless steel (like SCACLA and E-XFEL pickups), while the CBPM8 has a new high-Q design consisting of a massive copper core brazed into an outer hull of stainless steel.

Table 2: CBPM Frequencies and Quality Factors

	CBPM38	CBPM16	CPBM8
Frequency	3.2844GHz		4.9266GHz
Q_L	40	40	1000

Choice of BPM Frequency and Quality Factor

The comparatively low bunch charge of SwissFEL motivates a high working mode frequency, since the theoretical resolution limit of CBPMs (neglecting cable losses and reflections) improves with higher frequencies. On the other hand, we wanted to simplify the electronics design, and keep phase drift effects (that increase with frequency) and cables losses reasonably low, where the BPM electronics will be completely installed outside the SwissFEL tunnel, with typical cable lengths in the order of 15-25m, suggesting a frequency below 6GHz. Moreover, the CBPM frequencies should not be too close to the frequencies of S-band and C-band structures to minimize possible interference noise. Finally, the working mode frequency of the pickups should stay well below the beam-pipe cut-off (i.e. <4GHz for CBPM38), and we wanted to use the same electronics for CBPM16 and CBPM38, while maximizing synergies with the E-XFEL cavity BPM electronics working at 3.3GHz. As a result, we chose 3.2844GHz for CBPM16 and CBPM38, and 4.9266GHz for CBPM8. Choosing e.g. 6.5GHz for the CBPM8 working mode frequency would not have led to a significant resolution improvement (while increasing drift effects and design effort), since the theoretical low-charge resolution improvement (relative to 4.9622GHz) is practically eliminated by increased cable losses and reflections.

For the CBPM38 and CBPM16, the chosen Q_L value of ~40 is low enough to simplify the digital bunch-to-bunch crosstalk suppression (the pickup signal of the 1st bunch has decayed to ~0.07% when the 2nd bunch arrives), but still large enough to allow easy sampling of the ~20ns long RFFE output pulse (that is not much longer than the pickup pulse). For the CBPM8, we decided to go from stainless steel to a copper resonator, which allowed to increase the Q_L from ~300 [1] to ~1000 without having significant resistive losses that were already ~15% for the stainless steel version, thus not compromising the resolution at very low charge. The higher Q_L simplifies the electronics design that uses mixing to an IF rather than mixing to baseband like for CBPM16 and CBPM38, and the ratio of range to resolution is also increased.

Dark Current Considerations

Table 2 shows the frequencies of the SwissFEL S-band and C-band accelerating structures and BPMs, as well as the multiplication factors for the 142.8MHz SwissFEL machine reference clock that are needed to obtain these frequencies. Since the smallest common multiple of S-band and C-band RF period is 7ns (i.e. the reference clock period), only every 7ns a dark current bunch manages to reach the undulators, while all other dark current bunches (bunched with the S-band RF gun frequency) are accelerated to the wrong energy and thus get lost in collimators upstream of the undulators. In order to avoid that the dark current excites the undulator CBPM8 pickups, we decided to increase the pickup frequency from 34 to 34.5 times the reference clock, such that the RF signals from adjacent dark current bunches interfere destructively in the CBPM8 pickups. For the less critical low-Q CBPM16 and CBPM38 pickups, we use an integer multiple of the reference clock as working mode frequency.

Table 3: SwissFEL RF Frequencies and Multiplication factors for the 142.8MHz Machine Reference Clock

System	Frequency	Ref Clock Multiplier
S-Band Injector	2.9988 GHz	21
C-Band Linac	5.712 GHz	40
CBPM16/38	3.2844 GHz	23
CBPM8	4.9266 GHz	34.5

BPM PICKUP PRODUCTION

RF Feedthroughs

For the SITF stripline BPMs, we designed RF feedthroughs in collaboration with a Swiss company (BC-Tech AG, http://www.bctech.ch) that produces them for us, for a fraction of the price of similar commercially available multi-GHz RF feedthroughs that we had purchased so far. The quality control of the feedthroughs at the company includes measurements of all mechanical dimensions, leak tests and electrical tests for every feedthrough. In addition, we did S-parameter measurements of all feedthroughs (see Figure 2), and high-temperature cycling test of samples with leak tests at high and low temperature at PSI. Figure 3 shows histograms of the S11 parameter measurements for the 1300 feedthroughs we have produced so far, excluding a smaller pre-series where we tuned and optimized the design and production process.

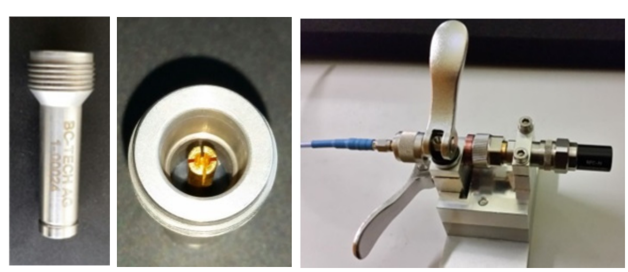

Figure 2: SwissFEL RF feedthrough (left, middle) with test adapter (right) that uses a standard APCN-7 adapter and 50Ω broadband load.

ISBN 978-3-95450-176-2

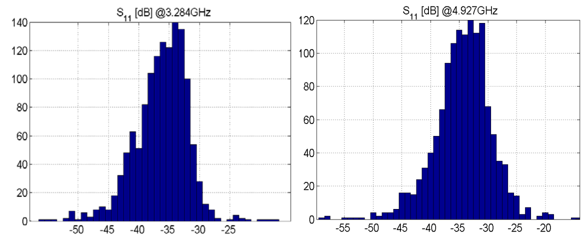

Figure 3: Histograms of measured S11 of the 1300 SwissFEL CBPM RF feedthroughs, for 3.2844 GHz (left) and 4.9266 GHz (right).

In order to keep the influence of the feedthroughs on the pickup RF parameters reasonably low, we defined a minimum requirement for S11 of <-25dB, aiming at typical values of <-30dB. As shown in the figures, this goal was reached for nearly all feedthroughs. Due to the low production costs, we produced more feedthroughs than we needed, thus allowing to sort out a smaller number with suboptimal performance.

Pickup Production RF Measurements

The body of the CBPM16 and CBPM38 pickups consists of three parts (see Figure 1 for CBPM16, parts colored differently) that are brazed together before the RF feedthroughs are welded to the body. The body parts are machined by an external company and then brazed and welded at PSI. The mechanical tolerances of the pickups were defined such that they reach the desired RF parameters while keeping the production reasonably simple and cost efficient. In addition to checks of all relevant mechanical dimensions of the body parts by the company, we also measured the pickup frequencies and Q_L before and after brazing. Before brazing, a special holder pressed the body parts and feedthroughs together such that they had sufficient and reproducible contact.

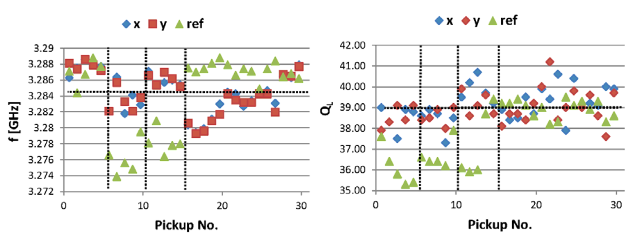

Figure 4: Frequency (left) and Q_L (right) of brazed CBPM16 pickups. Pickups no. 1-15 are a pre-series from 3 companies, no. 16-30 are the first batch of the SwissFEL series production.

Figure 4 shows the measured frequencies of the 15 pre-series CBPM16 pickups and the first batch of 15 series pickups, produced by the company that also made pre-series pickups no. 11-15. For the series, we empirically changed the reference cavity dimensions, intending to correct a small systematic deviation of the reference cavity frequency and Q_L in the pre-series. While we initially aimed at Q_L=40, we re-defined the nominal value to 39 for the series, since our main goal is to get the same Q_L (and frequency) for position and reference cavity, while the absolute value is less critical.

Table 4: Measured average position cavity (X,Y) and reference cavity (R) frequency and Q_L of 30 CBPM16 pickups before and after brazing/welding.

CBPM16	Before	After	Average
	Brazing/Welding		Difference
f_X [MHz]	3282.6	3284.6	2.0
f_Y [MHz]	3282.1	3284.5	2.3
f_R [MHz]	3282.5	3283.8	1.3
$Q_{L,X}$	39.06	39.11	0.05
$Q_{L,Y}$	39.03	38.92	-0.12
$Q_{L,R}$	36.42	37.80	1.39

Table 4 shows that the brazing led to an average increase of only 2.0MHz and 2.3MHz for the position cavity, and 1.3MHz for the reference cavity. We empirically optimized the frequency and Q_L to be close to the nominal value after brazing, and used the measured shifts to predict these values from the pre-brazing measurements. Figure 5 shows the difference of the frequency and Q_L of reference and position cavity (using the average of horizontal plane X and vertical plane Y for the position cavity). The values were measured before and after brazing/welding of the feedthrough parts. Especially for no. 11-30 (produced by the same company), the difference between pre- and post-brazing/welding measurement is rather small.

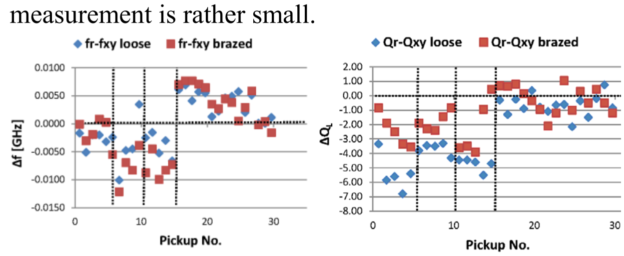

Figure 5: Difference of CBPM16 reference and position cavity frequency (left) and Q_L (right) before and after brazing/welding of the pickup parts.

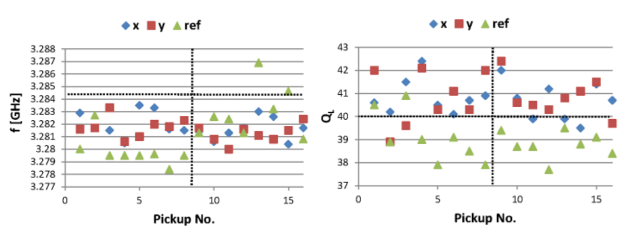

Figure 6: Frequency (left) and Q_L (right) of CBPM38 pickups.

Table 5: Average position cavity (X,Y) and reference cavity (R) frequency and Q_L of 16 CBPM38 pickups before and after brazing/welding

CBPM38	Before	After	Average
	Brazing/Welding		Difference
f_X [MHz]	3280.2	3281.8	1.7
f_Y [MHz]	3280.3	3281.5	1.2
f_R [MHz]	3280.0	3281.4	1.4
$Q_{L,X}$	42.9	40.8	-2.1
$Q_{L,Y}$	42.3	40.8	-1.5
$Q_{L,R}$	37.7	39	1.3

ISBN 978-3-95450-176-2

Figure 6, Table 5 and Figure 7 show the respective RF parameter measurement results for the 16 CBPM38 pickups. Pickup no. 1-8 was a pre-series produced for KIT/FLUTE [7], no. 9-16 for SwissFEL.

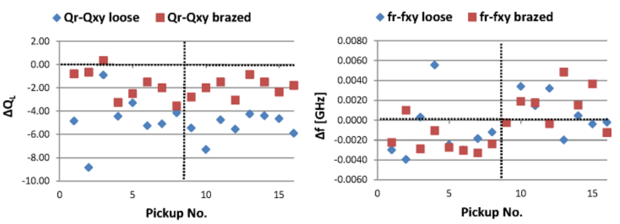

Figure 7: Difference of CBPM38 reference and position cavity frequency (left) and Q_L (right) before and after brazing/welding of the pickup parts.

Mechanical Supports

For cost reasons, all CBPM8 pickups and most CBPM16 pickups have mechanical supports where the position and angle of the pickup can only be adjusted manually via shimming plates with ~10µm position and 100µrad angle uncertainty for relative adjustments.

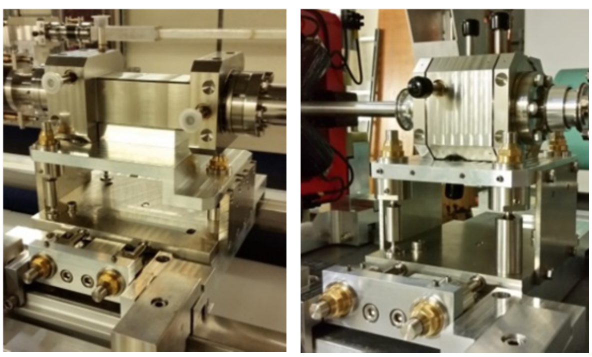

Figure 8: CBPM38 (left) and CBPM16 pickup (right) with manually adjustable supports.

Some CBPM16 where the performance (affected by angle misalignment) is critical and all CBPM38 have supports that are manually adjustable via differential screws with <2µm position and <20um (CBPM16) or <8µm (CBPM38) angle uncertainty. As already discussed in [8], this is sufficient to achieve the desired performance. In addition, the CBPM8 and their adjacent quadrupoles can be moved with a common motorized 2D mover system.

The SwissFEL building is now mainly finished, but not yet clean enough to install girders and diagnostics components in the accelerator tunnel. In order to reduce the installation time, BPMs and other components are currently pre-installed in other PSI buildings (where the photos in Figure 8 were taken) on their girders and then aligned relative to the girder. Then the complete girder with its components will be moved into the SwissFEL tunnel when it is ready and aligned relative to the tunnel reference system. When moving the girder with sufficient care, this should result in an acceptable alignment of all components relative to the beam, with the possibility of laser tracker and/or beam based re-alignment where necessary.

BPM ELECTRONICS

The SwissFEL BPM system is a modular design, consisting of a customized crate (MBU = Modular BPM Unit), where 2-4 RF front-ends and a digital carrier FPGA board with two ADC mezzanines (6 channel 16bit 160MSPS each) can be inserted from the front side. At the rear side, there are additional slots for a modular redundant power supply supporting intelligent power and temperature management, interlock board, and communication board with SFP+ transceivers and other inputs for feedback, optical (multi-gigabit) or copper cable based timing system signals, and control system interface (supporting Ethernet, PCIe, or custom multi-gigabit fiber optic link protocols).

Figure 9: Modular BPM unit, with two cavity BPM RFFEs (top) and FPGA carrier board with two ADC mezzanines (bottom).

Integrated Timing System Interface

The MBU does not require a dedicated interface board to the (MicroResearch) timing system of SwissFEL (or E-XFEL that uses a different timing protocol). Instead, it decodes the digital multi-gigabit stream of the timing system directly in one of the FPGAs of the digitizer board in the MBU using firmware developed at PSI.

CBPM16/CBPM38 Electronics

As already described in ref [9], CBPM16 and CBPM38 have a common BPM electronics based on an RFFE with IQ downconversion of the pickup signals to baseband.

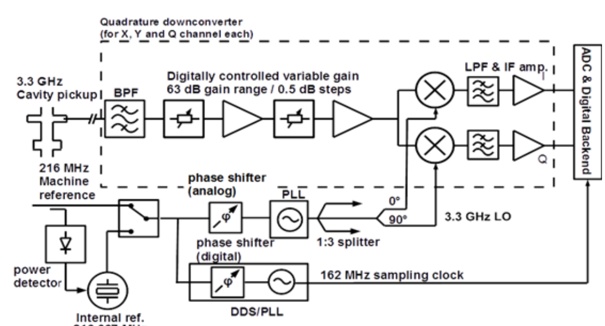

Figure 10: Simplified schematic of CBPM16/CBPM38 CBPM RFFE electronics, showing only one of its three input channels (one reference and two position signal channels).

ISBN 978-3-95450-176-2

The differential RFFE output signal pulses of ~20ns length are sampled at the top with differential ADCs (employing baseline subtraction) and then processed by the FPGA carrier board to obtain position and charge, already in physical units as required for fast beam-based feedbacks. The FPGA board also controls various parameters of the fully programmable RFFE, performing ADC and LO clock phase feedbacks to keep the ADC clock phase and IQ phase constant, thus making sure the RFFE output pulses are always sampled at the top.

CBPM8 Electronics

In contrast to the CBPM16/38 electronics, the CBPM8 RFFE (shown in Figure 11) has only one mixer for each of the three pickup signals, and converts the signals to an IF frequency of 133MHz rather than to baseband.

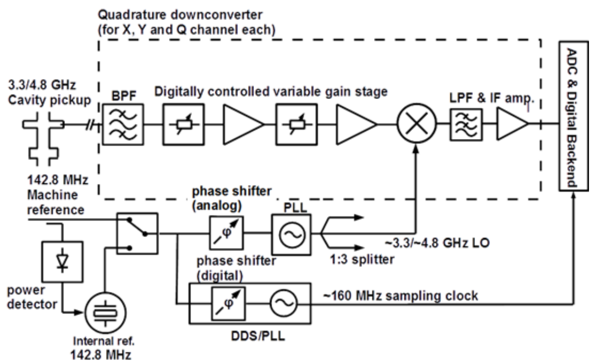

Figure 11: Simplified schematics of CBPM8 RFFE electronics, showing only one of its three input channels.

The electronics thus needs only three ADC channels per RFFE, and can use the same ADC board as the low-Q CBPMs. With 160MSPS sampling rate, the 16-bit ADCs convert the IF to a 27MHz signal that is digitally downconverted by the FPGA board to obtain position and charge via Cartesian-to-polar conversion and suitable filter and detector algorithms. Figure 12 shows a conservative estimate for the CBPM8 position resolution as a function of charge, assuming that a comparatively simple algorithm for the position calculation is used (based on matched filters and top sampling). For the maximum bunch charge of 200pC, <100nm resolution at ±200µm dynamic range is feasible, while the resolution at 10pC is still expected to be <1µm (for ±1mm range).

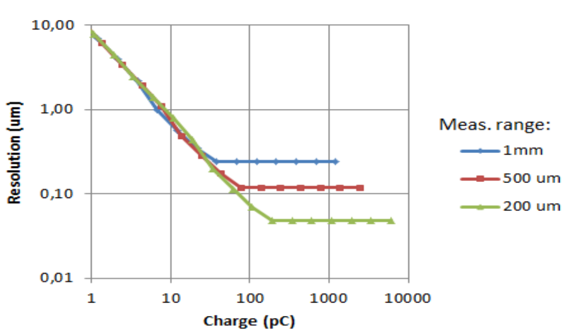

Figure 12: Estimated position resolution vs. bunch charge of the CBPM8 system for different measurement ranges.

While the CBPM16/38 electronics has already been tested with beam [1], the first CBPM8 RFFE is presently in production, with prototype tests at the SLS linac scheduled for end 2015.

SUMMARY AND CONCLUSION

The SwissFEL CBPM pickup production is in progress. The very cost-efficient RF feedthroughs and pickups produced so far have rather low RF parameter variations, ensured by constant quality control and monitoring during the production. By doing the most critical brazing and welding process in house, we so far managed to avoid any quality problems. For the CBPM electronics, we will soon start a pre-series production for the SwissFEL injector to be commissioned with beam in 3/2016, followed by series production and commissioning of the complete SwissFEL linac and undulators with beam in Q4/2016.

ACKNOWLEDGEMENTS

The authors gratefully acknowledge the support of RF tests and measurement data processing by D. Treyer, as well as the support of mechanical design, brazing and welding of BPM pickups by the mechanical construction department and workshop at PSI.

REFERENCES

[1] B. Keil et al., *"Design of the SwissFEL BPM System"*, Proc. IBIC'13, Oxford, UK, 2013, http://jacow.org/.

[2] F. Marcellini et al., "*Design of Cavity BPM Pickups for SwissFEL*", Proc. IBIC'12, Tsukuba, Japan, 2012, http://jacow.org/.

[3] M. Stadler et al., *"Development of the SwissFEL Undulator BPM System"*, Proc. IBIC'14, Monterey, CA, USA, 2014, http://jacow.org/.

[4] H. Maesaka et al., "*Development of RF cavity BPM of XFEL/SPRING-8*", Proc. DIPAC'09, Basel, Switzerland, 2009, http://jacow.org/.

[5] D. Lipka et al., *"Development of Cavity BPM for the European XFEL"*, Proc. Linac'10, Tsukuba, Japan, 2010, http://jacow.org/.

[6] B. Keil et al., *"The European XFEL Beam Position Monitor System"*, Proc. IPAC'10, Kyoto, Japan, 2010, http://jacow.org/.

[7] M.J. Nasse et al., *"Status of the Accelerator Physics Test Facility FLUTE"*, Proc. IPAC'15, Richmond, VA, USA, 2015, http://jacow.org/.

[8] B. Keil et al., *"Beam-Based Calibration and Performance Optimization of Cavity BPMs for SwissFEL, E-XFEL and FLASH2"*, Proc. IBIC'14, Monterey, USA, 2014, http://jacow.org/.

[9] M. Stadler et al., *"Low-Q Cavity BPM Electronics for E-XFEL, FLASH-II and SwissFEL"*, Proc. IBIC'14, Monterey, USA, 2014, http://jacow.org/.

ISBN 978-3-95450-176-2

PRELIMINARY TEST OF THE BUNCH-BY-BUNCH TRANSVERSE FEEDBACK SYSTEM FOR TPS STORAGE RING

Y.S. Cheng, H.P. Hsueh, K.H. Hu, C.Y. Liao, S.Y. Hsu, P.C. Chiu, K.T. Hsu#
NSRRC, Hsinchu 30076, Taiwan

Abstract

Commissioning of the Taiwan Photon Source (TPS) is in progress and divided into two phases. The storage ring equips with two five-cell PETRA RF cavities and without insertion devices installed for Phase-I commission to confirm correctness of everything, to do preliminary vacuum clearing, and wait available of cryogenic system available. After finished the Phase-I commissioning in March, 2015, installation of two superconducting RF cavities and 10 sets of insertion devices are ongoing. The commissioning is planned to start around in August. There is a prototype vertical stripline kicker installed in 2014. One horizontal stripline kicker and two vertical stripline kickers were installed in May. Commercial available feedback processor was selected for the feedback system integration. Preliminary feedback loop closed have been tested during Phase-I beam commissioning in early 2015 with prototype vertical kicker. Beam commissioning with new kickers is scheduled when beam stored in Phase-II beam commissioning which will started soon. Final check before beam test is under way.

INTRODUCTION

The NSRRC campus host two synchrotron light source, one is a 1.5 GeV Taiwan Light Source (TLS), and the other is 3 GeV TPS. The TPS was started Phase-I commissioning without IDs and superconducting RF system recently [1]. Phase-II commissioning is started from mid September 2015 with 10 sets of IDs and two KEKB-type superconducting RF modules. Analogue type transverse feedback system for TLS is operated since 1996 [2]. The system convert to FPGA based feedback system in during 2004~2005 for transverse as well as longitudinal planes by using SPring-8 feedback processors [3]. Transverse coupled-bunch instability, caused by the resistive wall impedance and fast ion will deteriorate beam quality. Bunch-by-bunch feedback will suppress various transverse instabilities to ensure TPS will achieve its design goals. The TPS project adopts EPICS toolkits as control system frameworks. To simplify system integration, it was decided to adopt EPICS embedded feedback processor iGp/iGp12 from Dimtel [4] for BBF system for TLS and TPS. First system by use iGp was put into operation in 2009 [5] at TLS. Two transverse loops and one longitudinal feedback loop were convert to iGP12 based system around 2010~2011 at TLS [6]. The TPS system are commissioning in 2015 by using latest revision gateware (FPGA code).

Stored beam current reach more than 100 mA in multi-bunch operation with two five-cell PETRA cavities are expected. Strong synchrotron dipole motion is onset around 30 mA. This strong motion limit maximum stored beam current less than 50 mA. RF experts found that the bandwidth of the RF amplitude feedback loop is too large such that a synchrotron sideband entered the loop in March 26. After cure the problem and increasing the chromaticity, beam stored more than 100 mA soon just before April shutdown. Threshold current for the longitudinal instability appeared at 82 mA. Longitudinal instability will be not a problem after replacement of the five-cell PETRA cavities with SRF in Phase-II commissioning.

Phase-I commissioning of the vertical loop with prototype kicker is performed in mid January 2015. Beam commissioning with new kickers is scheduled when beam stored in Phase-II beam commissioning is scheduled in the last quarter of 2015.

TRANSVERSE KICKERS

In order to suppress coupled-bunch instabilities effectively, transverse kickers with higher shunt impedance are desirable especially in vertical plane. However, due to limited manpower available during the final phase of installation, one simple prototype kicker was implemented and installed at diagnostics straight in June 2004. Only this kicker was available for Phase-I commissioning. Shunt impedance of this kicker at lower frequency is less than 5 k. Drawing and installation photo of this prototype vertical kicker is shown in Fig. 1.

Two new vertical kickers and one new horizontal kicker were designed, fabricated, and installed during April to July, 2015 shutdown. Concept of these kickers is derives from the design of PSI/SLS [7] and adapt to fit vacuum duct of TPS at ID straight. Optimization of geometry and shunt impedance was done by SUPERFISH 2D codes. Length of the electrode is 300 mm. Shunt impedance at low frequency is about more than 50 k for vertical and horizontal kicker respectively. Detailed analysis of the impedance, absorption power is underway. About 10 time large than the prototype, and almost factor of 3 times kick voltage will produce than the prototype when the same driven power level. Perspective drawing and installation at the storage ring are shown in Fig. 2. Original, all transverse kickers were planned to install at one dedicated diagnostics straight. However, to save space to accommodate one more insertion devices, decision was made in March 2015 that all kickers install at upstream of in-vacuum undulator (IU22) at three 7 m

#kuotung@nsrrc.org.tw

ISBN 978-3-95450-176-2

long insertion devices straights. This prevents the option to install all feedback electronics at the same site. The Horizontal kicker is installed at upstream of SR03 (SRnn consist of upstream ID straight and following lattice cell #nn in the name convention of TPS vacuum system), two vertical kickers are installed at upstream of SR11 and SR12 exit. Three sets of 3 m long in-vacuum undulator were installed at that location.

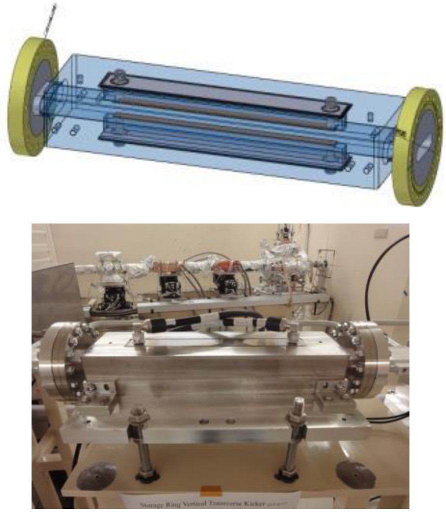

Figure 1: Perspective view (above) and installation picture at diagnostic straight (below) of the prototype vertical kicker.

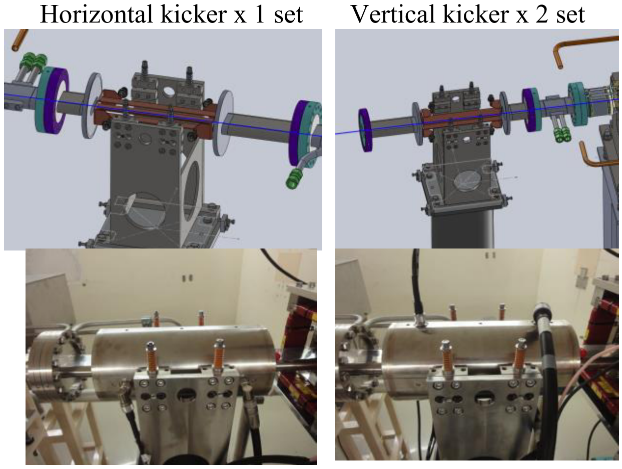

Figure 2: Perspective drawing of transverse kickers (upper) and install at upstream of three 7 m straight which in-vacuum undulators located (lower).

FEEDBACK ELECTRONICS

Feedback electronics of bunch-by-bunch include feedback functionality, such as housekeeping, filter design, timing adjustment, feedback, data capture, etc. It supports bunch oscillation data capture for analysis to deduce rich beam information, tune measurement, bunch clearing, beam excitation, etc. Features of the planned system include the latest high dynamic range ADC/DAC (12 bits), high performance FPGA, flexible signal processing chains, flexible filter design, bunch feedback, tune measurement, bunch cleaning, various beam excitation scheme, flexible connectivity, and seamless integration with the control system. An on-line control interface to operate feedback system and off-line analysis tools should be included.

Commercial feedback processor with EPICS IOC embed are used. This option is simply system integration efforts. A functional block diagram of the bunch-by-bunch feedback system will delivery for TPS is shown as Fig. 3 for horizontal feedback loop and Fig. 4 for two vertical feedback loops. Frontend for the horizontal is plane is Libera Bunch-by-Bunch Front End [8] is use. Dimtel Bunch-by-bunch Front/Back End FBE-LT [4] is used for vertical plane. Commercial feedback processor iGp12 are selected for three feedback loops. Three iGp12s already serve for the transverse as well as longitudinal feedback loops for the existed 1.5 GeV Taiwan Light Source for several years already [6].

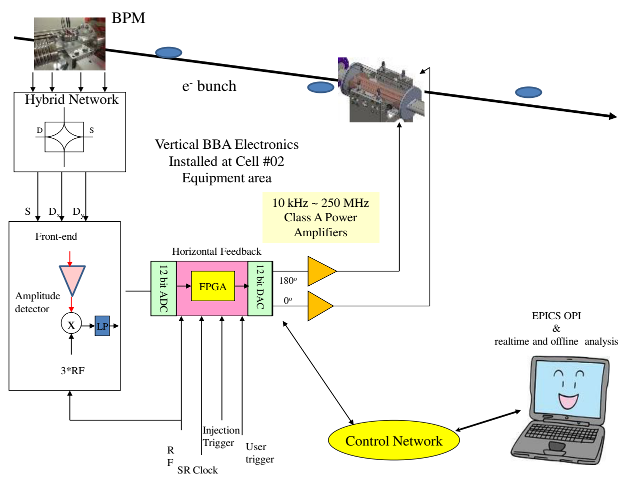

Figure 3: Configuration of the horizontal bunch-by-bunch feedback loop.

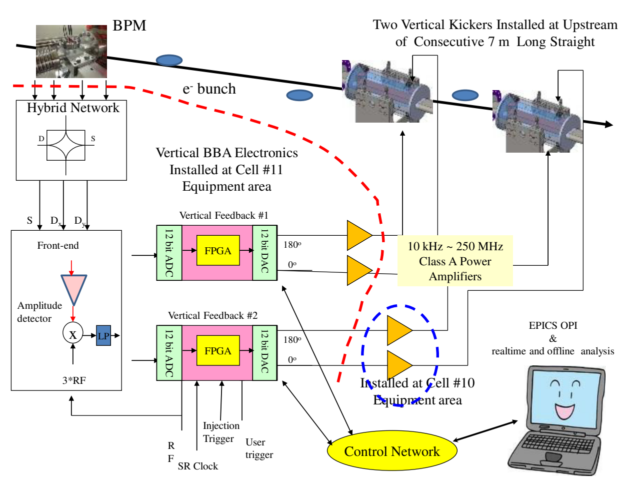

Figure 4: Configuration of the vertical bunch-by-bunch feedback loops.

ISBN 978-3-95450-176-2

PHASE-I COMMISSIONING

Loop closed of the prototype vertical feedback loop was done in January 14 to check functionalities of the system. However, due to very strong synchrotron oscillation existed, a lot of efforts devote to study try to dig out the problem, no much efforts to do for feedbacks before problem was identified and solved in late March. Various measurements [9] are possible just a few days before machine shutdown in April. Transverse instability threshold is around 30 mA when near zero chromaticity. The vertical instability in vertical plane was damped by the bunch by bunch-by-bunch feedback loop.

Feedback Functionality

Vertical beam blow up due to vertical instability at stored beam current 98 mA shown in Fig. 5(a). After feedback loop engage, instability is suppressed as shown in Fig. 5(b). Beam spectrum show that the betatron sidebands are suppressed by the feedback loops as shown in Fig. 6.

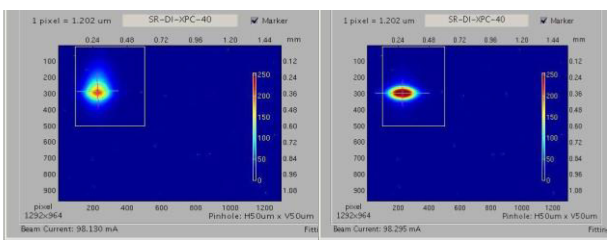

(a) Feedback “Off” (b) Feedback “On”

Figure 5: Beam profile observed by pinhole camera when vertical instability appeared (a) and instability suppressed by the bunch-by-bunch feedback loop (b).

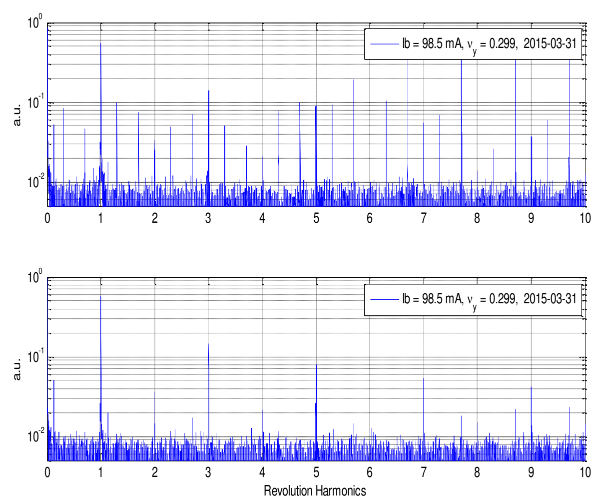

Figure 6: Vertical betatron sideband (above) suppressed by the feedback loop (below).

Grow-Damp Measurement

Grow/damp experimental for vertical plane was performed during test session. Fig. 7 shows that the experimental perform at stored beam current 98.5 mA. Growth rate is in the order of 0.2 ms^{-1}, while 10 ms^{-1} damping rate ensure beam is stable.

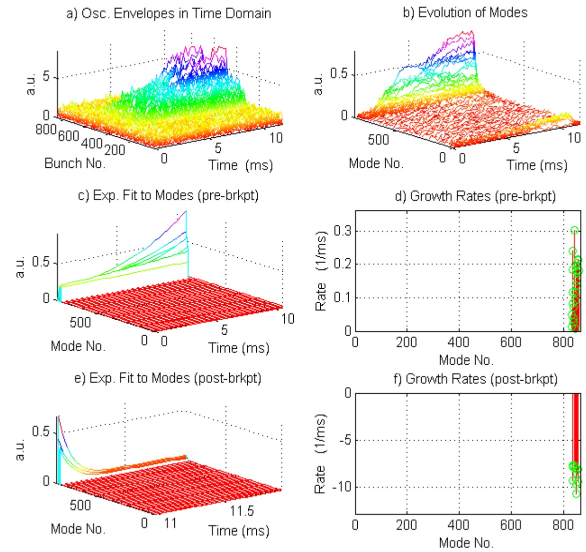

Figure 7: Grow/damp experiment of vertical plan at beam current 98.5 mA. Resistive-wall and fast ions are major sources of instability.

Instability in Horizontal Plane

Horizontal instability is onset around 70 mA also. Strength is weak than vertical plane. Evolution of envelop and modal spectrum of the horizontal plane are shown in Fig. 8. Most prominent modes with mode number are large than 800. There are peaks within the modal spectrum. Resistive-wall and fast ion related instability might major contribution the horizontal instability. Rich betatron sidebands in beam spectrum is shown in Fig. 9.

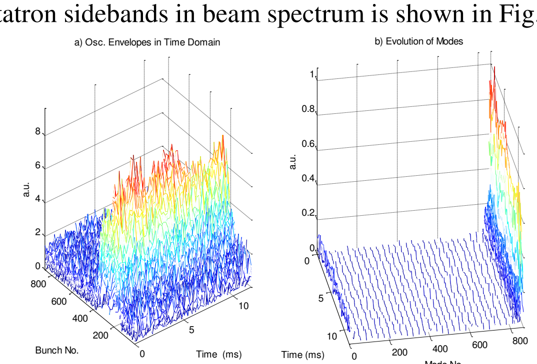

Figure 8: Oscillation envelope and modal spectrum at 93.274 mA.

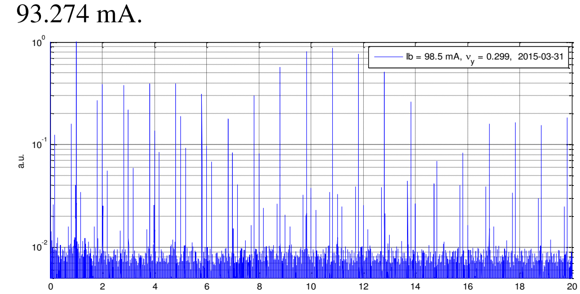

Figure 9: Rich betatron sidebands in beam spectrum of horizontal plane.

ISBN 978-3-95450-176-2

Longitudinal Motion

Strong longitudinal was observed when current large than 20 mA which limited stored beam current around 50 mA maximum. Streak camera observed the oscillation amplitude can be large than 350 psec (peak-to-peak), it corresponding to about +/- 30 RF degree. The problem was identified by RF experts and solved in March 26, 2015. Large zero mode oscillation come from wrong parameters setting of the amplitude loop of the low level RF system. After problem cured on March 26, the beam can store up to 100 mA soon before shutdown started from April. Typical behaviour in longitudinal plane is shown in Fig. 10. Strong in-phase synchrotron motion and a strong mode 800 for all stored bunches were observed. The mode 800 might cause by the TM_{021} high order mode of five-cell PETRA cavity [10]. Fig. 11 compare the longitudinal modal spectrum, strong mode zero oscillation at lower current. After problem of feedback loop solved, mode zero motion is negligible compare to the instability driven by the TEM_{021} high order mode of RF cavity near mode 800. Threshold current is near 82 mA.

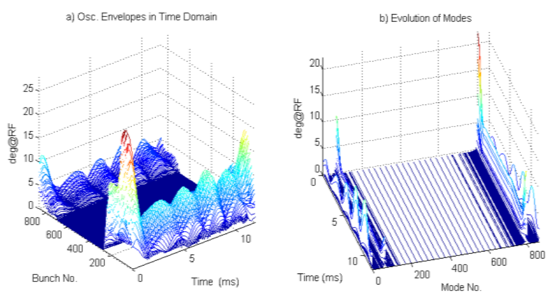

Figure 10: Evolution of longitudinal oscillation envelope and modes at 92 mA. Threshold current is about 82 mA.

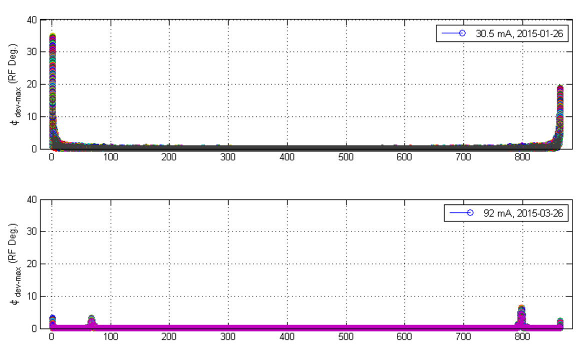

Figure 11: Comparison of modal spectrum before RF fixed its amplitude loop at stored beam current 30 mA before (a) and 92 mA after (b).

Single Bunch Transfer Function

Current version of gateware support single bunch excitation and data capture functionality. Sweep the excitation frequency and demodulated beam signal quadrature can be deduced transfer function. Fig. 12 shows a transfer function measurement for selected bunch in a bunch train in multi-bunch mode. Study transfer function a function of single bunch current is planned after beam available.

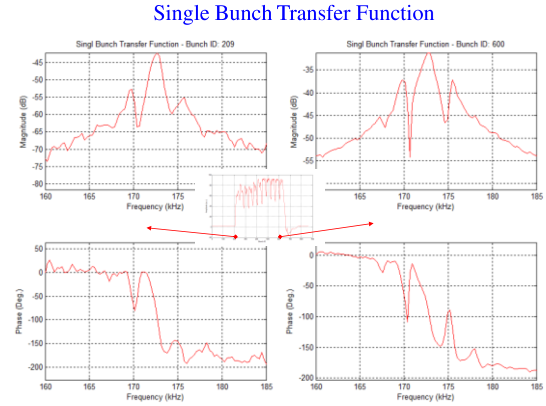

Figure 12: Individual bunch transfer function in multi-bunch fill mode at 93 mA.

Bunch Cleaning

Single bunch beam is used to measurement bunch length versus beam current during the Phase-I commissioning. However, high purity single bunch beam from Linac not always available during the study. Impurity can be a few percents to a few tens of percents. Bunch cleaning functionality have been applied continuously to keep population of the satellite bunches small than the main bunch more than 10^{-4} even the system is still no optimized. Fig. 13 is a snapshot during the bunch cleaning process in proceeding.

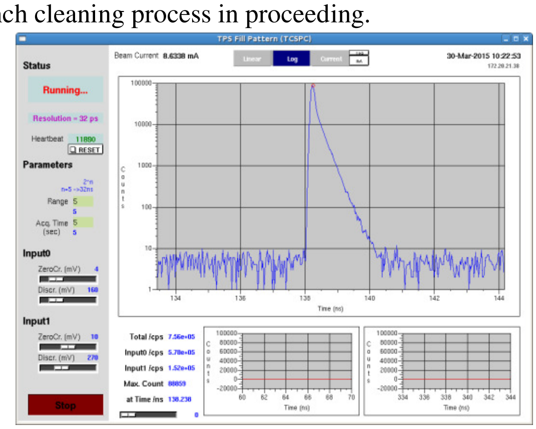

Figure 13: Single bunch impurity is achieved more than $10^{-4}$by bunch cleaning process.

PREPARTION FOR PHASE-II COMMISSIONING

During April to August shutdown, all feedback kickers were installed. Electronics installation and interconnectivity are done before September. Horizontal kicker is installed at upstream of the straight SR03, two vertical kickers were installed at the upstream of straight of cell SR11, and SR12 respectively. In-vacuum insertion devices installed during the shutdown, three kickers are installed accompany with these installation to minimize various efforts. Feedback electronics is installed also as shown in Fig. 14 are installed at nearby equipment areas.

Investigate instabilities modes and ion effects are plans. The commissioning schedule of SRF and ten IDs is scheduled in September 2015. Superconducting RF

ISBN 978-3-95450-176-2

system need more time to ensure everything are correctness, the possible commissioning schedule of the bunch-by-bunch feedback system will be possible in the 4th quarter of 2015.

Cell 02 Equipment Area | Cell 10 Equipment Area | Cell 11 Equipment Area

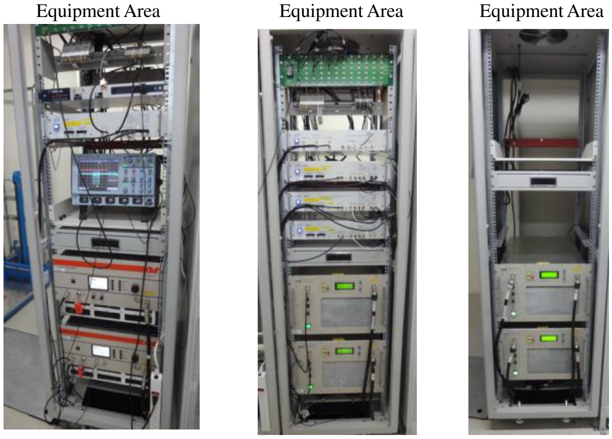

Horizontal BBF & PA | Vertical BBF & PA for Kicker 2 | PA for Kicker 1

Figure 14: Photos of the installed feedback electronics.

SUMMARY

Preliminary test of the bunch-by-bunch system were performed in early 2015 during Phase-I commissioning of the TPS. Resistive wall induced instability was observed for stored beam current up to 100 mA. All components for Phase-II commissioning were prepared. The system is ready for further study soon. Experiences gain during the test will useful to help future optimization.

ACKNOWLEDGEMENT

Thanks for the help from T. Nakamura of RIKEN/Spring-8 to introduce FPGA based BBF technology for TLS. Many technical discussions with Dmitry of Dimtel are fruitful. Encourage from Prof. J. H. Wang of USTC/NSRL during last decade are highly appreciated. Helps from vacuum group are crucial for their high efficiency to implement current version of kickers in the second quarter of 2015 which is impossible to achieve if contract to vendor within such short period. In-house made kickers option is also relax pressure due to limited budget available.

REFERENCES

[1] C. C. Kuo, et al., "Commissioning Results of Taiwan Photon Source", IPAC2015, Richmond, VA, USA, May 2015.

[2] K. T. Hsu, et al., "Performance of the Transverse Coupled-Bunch Feedback System in the SRRC", EPAC96, Barcelona, Spain. 10 to 14 June 1996.

[3] K. H. Hu, et al., "Commissioning of FPGA-based Transverse and Longitudinal Bunch-by-Bunch Feedback System for the TLS", AIP Conf. Proc. 868, 179 (2006); http://dx.doi.org/10.1063/1.2401403.

[4] Dimtel, Inc., http://www.dimtel.com.

[5] C. H. Kuo, et al., "Diagnostics Update of the Taiwan Light Source", BIW2010

[6] C. H. Kuo, et al., "New Bunch-by-Bunch Feedback System for the TLS", DIPAC2011.

[7] D. Micha, et al., "Current Status of the ELETTRA/SLS Transverse Multi Bunch Feedback", Proceedings of EPAC 2000, Vienna, Austria.

[8] Instrumentation Technologies: http://www.i-tech.si

[9] J. H. Wang, "Coupled bunch instabilities measurement and suppression", in Chinese, ISBN: 978-7-03-041478-6, China Science Publishing & Media Ltd. 2014, Beijing, China.

[10] F. Hinterkeuser, "Störkörpermessung an einem PETRA-Resonator", Bachelorarbeit in Physik, http://www-elsa.physik.uni-bonn.de/Publikationen/texte/hinterkeuser_bachelor.pdf, July 2013.

ISBN 978-3-95450-176-2

SYNCHROTRON RADIATION MEASUREMENT AT TAIWAN PHOTON SOURCE

C.Y. Liao#, C.Y. Wu, Y.S. Chen, P.C. Chiu, C.K. Kuan, H.P. Hsueh, S.Y. Hsu, K.H. Hu, K.T. Hsu
NSRRC, Hsinchu 30076, Taiwan

Abstract

The synchrotron radiation light produced from a dipole magnet is widely used to characterize beam parameters in synchrotron light source (photon synchrotron). The synchrotron radiation monitor (SRM) systems were implemented for the booster synchrotron and the storage ring at Taiwan Photon Source (TPS). The beam parameters of the booster were recorded during the energy ramping process through the CCD camera and streak camera. The beam size measurement and beam behavior observed of the storage ring were performed by X-ray pinhole camera and streak camera respectability. The results are summarized in this report.

INTRODUCTION

The Taiwan Photon Source (TPS) with low emittance and high photon brightness is a state-of-the-art synchrotron radiation facility. The TPS accelerator consists of a 150 MeV S-band linear accelerator (LINAC) system, linac to booster transfer line (LTB), 0.15–3 GeV booster synchrotron, booster to storage ring transfer line (BTS), and 3 GeV storage ring. The storage ring consists of 518.4 m circumference and 24 DBA lattice cells with 6-fold symmetry [1]. The TPS commissioning is divide into two phases. Phase-I commissioning, two 5-cells Petra cavities without insertion device was done in the first quarter of 2015. Phase-II commissioning will start in the third quarter of 2015 with two superconducting RF cavities and 10 sets of insertion devices.

The SRM play an important role during the Phase-I beam commissioning, which is designed for the booster synchrotron and storage ring of the TPS. Synchrotron radiation generated from a dipole bending magnet serves to characterize energy ramping process for the booster synchrotron. In the storage ring, SRM is used to characterize beam size by x-ray pinhole camera, bunch length and longitudinal dynamics by streak camera, and fill pattern by photon counting technique. The outline of design and preliminary beam test results are presented in this report.

SYSTEM DESIGN

Synchrotron Radiation Monitor for Booster

Synchrotron radiation light from a bending magnet is guided to outside of shield wall via a four-piece adjustable mirror. The light is focus by a lens with 1 m focal length. A band-pass filter is insert before the GigE Vision camera. The camera trigger is synchronized with the booster ramping trigger; change delay time will change the energy point of observation. This synchrotron radiation diagnostic port is located at downstream of the booster injection section, so it can used to observe linac beam and booster stored beam with streak camera. Setup for the CCD camera and streak camera is shown in Fig. 1.

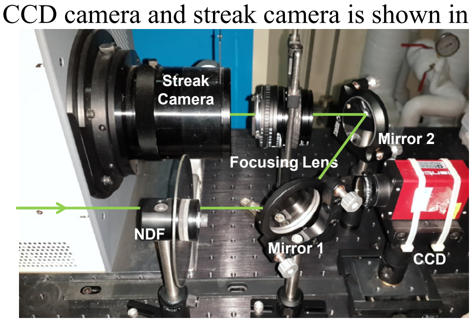

Figure 1: Optical layout of SRM measurement for booster synchrotron. The synchrotron light leads to the wall via a four-piece adjustable mirror and a lens (which are not shown here) then through a band-pass filter and additional two mirrors and focusing lens, finally to the streak camera system. Without the mirror 1, the synchrotron light is guided to the CCD camera.

Diagnostics Beamline for Storage Ring

There is a dedicated beamline for photon diagnostics at the TPS storage ring utilized visible light and X-ray of the synchrotron radiation. The diagnostics devices and its functionality are summary in Table 1. The X-ray pinhole camera is used for imaging the electron beam from bending magnet for the beam size and emittance measurements. It offers the required resolution and the dynamic range to measure the electron beam size accurately at all beam currents. The visible light of synchrotron radiation coming out of the tunnel was design for streak camera, interferometer and fill pattern measurements, as shown in Fig. 2.

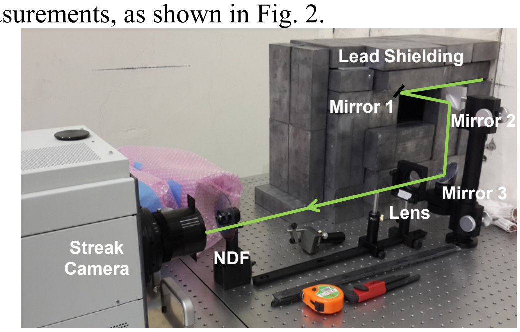

Figure 2: Temporary optical layout of SRM measurement for storage ring. The visible light of synchrotron radiation leads out of the tunnel, then through three mirrors, Lens, and band-pass filter, finally to the streak camera system.

#liao.cy@nsrrc.org.tw

ISBN 978-3-95450-176-2

Table 1: The Monitors of Diagnostics Devices for SR

Monitor	Beam parameters
X-ray	
Pinhole camera	Beam size and emittance
TCSPC[a]/APD[b]	Filling pattern and purity of isolated bunch
Visible light	
Interferometer	Beam size
Gated camera	Beam size
Streak camera	Bunch length, Longitudinal and transverse dynamic
TCSPC/APD/ MCP[c] PMT[d]	Filling pattern and purity of isolated bunch

[a] Time-correlated single photon counting
[b] Avalanche photodiodes
[c] Microchannel plates
[d] Photomultiplier tubes

SRM OF BOOSTER SYNCHROTRON

The beam size of the electron vary during the booster energy ramping from 150 MeV to 3 GeV, as shown in Fig. 3.

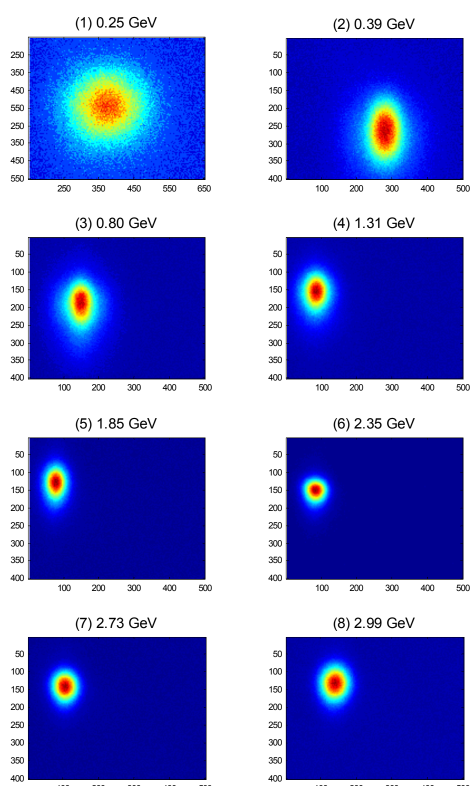

Figure 3: TPS booster synchrotron radiation profiles at varied energy during energy ramping, one pixel corresponding to 9 μm.

The beam size in both axes decreases when the energy increases due to radiation damping clearly, as shown in Fig. 4(a). This result is agree with the design [2]. The beam center position also change around 3.5 mm during the energy ramping as shown in Fig. 4(b) which are confirmed by the ramping orbit measurement BPM [3].

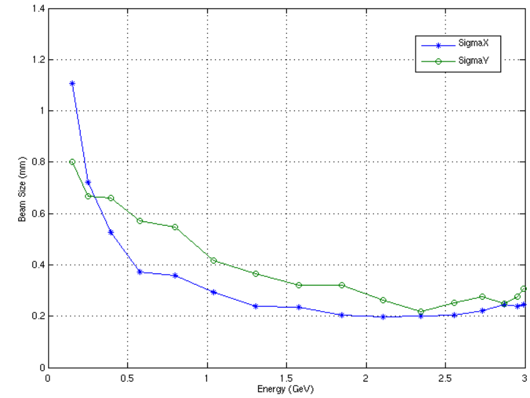

(a)

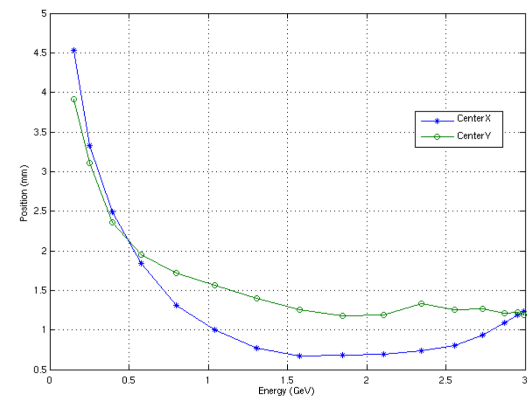

(b)

Figure 4: SRM measured of booster synchrotron during energy ramping from 150 MeV to 3 GeV, the variation of (a) beam size and (b) beam center position.

X-RAY PINHOLE OF STORAGE RING

Resolution Measurement

The in situ resolution of the X-ray pinhole camera was analysed by using the sharp edge from a Tungsten bar which mounted in front of the fluorescent screen. Fitting a complementary error function (see Eq. 1) to the edge image, the system resolution can be deduced to be about 5 μm [4].

$$BG(X) = a_0 \cdot erfc\left(\frac{(a_1 - X)}{a_2}\right) + a_3, \quad (1)$$

where *BG* is measured background intensity as a function of *X* position, a_0 is half-magnitude of the step, a_1 is location of the step, $(2\sqrt{\ln 2})a_2$ is the full width at half maximum (FWHM) of the Gaussian used to compute the complementary error function and a_3 is a constant offset.

Beam Size Measurement

The X-ray pinhole camera is used to measure the beam size. The beam size versus beam current in single bunch mode as shown in Fig. 5. In low current (0.2 mA), the beam size around ~38 μm in horizontal and ~19 μm in

ISBN 978-3-95450-176-2

vertical. When the storage beam current increases, the beam size of the horizontal axis also increases, but the vertical axis is no significant change. The CCD exposure time is reduced (~10 ms) to avoid the measurement error caused by the beam oscillation due to mechanical vibration.

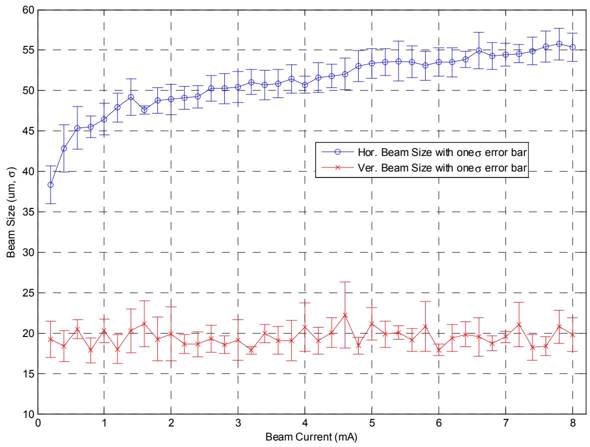

Figure 5: Plot of beam size measurement by X-ray pinhole camera in horizontal and vertical direction versus beam current under single bunch mode.

STREAK CAMERA MEASUREMENT

The streak camera is widely used in accelerator system for longitudinal as well as transverse dynamics study. A dual sweep streak camera (Model C10910, Hamamatsu Photonics) with one fast, one slow and two frequency of synchroscan sweep unit is used to perform temporal/longitudinal measurements on the beam at TPS. The commissioning of this streak camera was summary in previous report [5]. The streak camera for synchrotron light measurement on the TPS storage ring includes bunch length, longitudinal instability, and bunch length vs. bunch current up to now.

Injection Point and Energy Ramping of Booster

The TPS linac system consists e-gun, a 500 MHz subharmonic prebuncher (SPB), a 2998 MHz buncher and three 2998 accelerator linacs to producing 150 MeV electron beam. Electron gun have two operation mode, one is multi-bunch mode which electron beam generated by the 500 MHz modulated pulser, the other is single bunch mode which is generated by an avalanche transistor based pulser with base width less than 2 nsec. To produce pure single bunch at booster synchrotron should optimized timing setting and SPB setting [6]. Usually there will produced two to six s-band bucket dependent on tuning of the SPB and timing of e-gun pulser. For an optimized setting, the s-band bunch consists one main bunch and two small consecutive bunches before and after the main bunch. The synchrotron diagnostic port is located at the injection of booster synchrotron, it is possible to observed synchrotron radiation produce by linac beam. Figure 6 shown that three individual bunches with 333 psec separation are injected to the booster synchrotron. Following a beam capture process in the booster. The intensity indicated three bunches have difference population. Further study is needed and is planned to understand behind physics. This might provide an alternative tools for linac and injection tuning of the booster synchrotron. After beam injected to the booster, the SRM capture the ramping process as shown in Fig. 7. Measured bunch length around 17 psec (1 σ) at the setting of measure time. The bunch length and bunch phase are changing during the process, shown in Fig. 8.

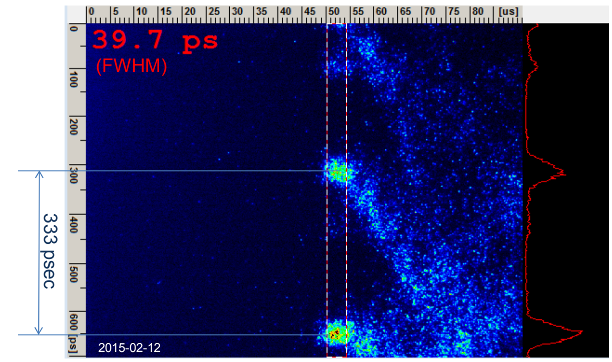

Figure 6: Injection point of at booster under single bunch mode, the bunch length ~17 ps (1 σ), vertical time scale = 700 ps, horizontal time scale = 90 μs.

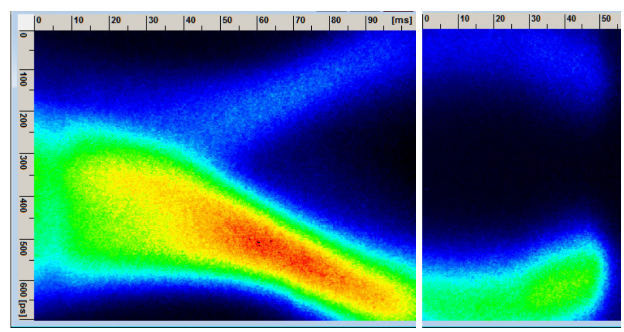

Figure 7: Bunch length as shrink during booster energy ramping observed by streak camera, vertical time scale = 700 ps, time scale for horizontal is millisecond.

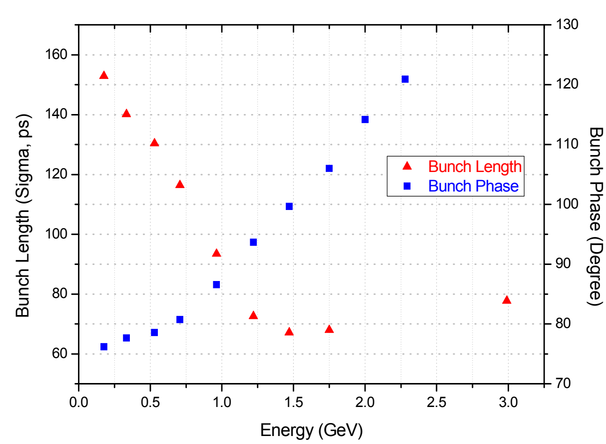

Figure 8: Bunch length and phase variation during the energy ramping process. Bunch length changes around 85 psec, bunch phase change around 45 degree.

ISBN 978-3-95450-176-2

Bunch Length Measurement of Storage Beam

The 250 MHz synchroscan unit is used for the bunch length measurement. The bunch length of the TPS storage ring is around 11.4 psec (sigma) in low current (~0.2 mA) single bunch mode [7]. When the current is increased, resistive-wall impedance contributed RF potential-well distortion as shown in Fig. 9. The Fig. 10 shows the bunch length as function of stored beam current at RF gap voltage 2.4 MV. The curve is fitted with Zotter's potential-well distortion cubic equation, longitudinal broadband impedance of $|Z/n|=0.12\ \Omega$ is deduced [7].

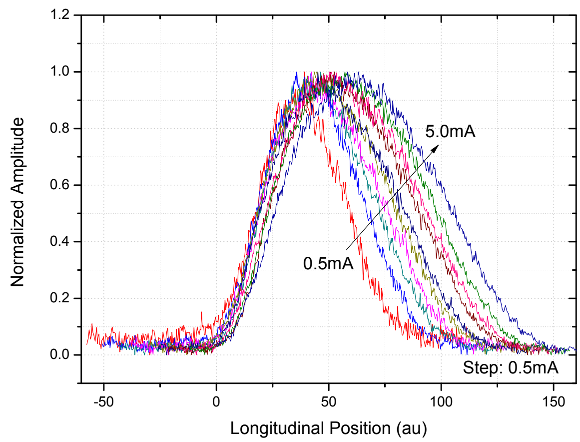

Figure 9: Single bunch profile distortion as function of beam current.

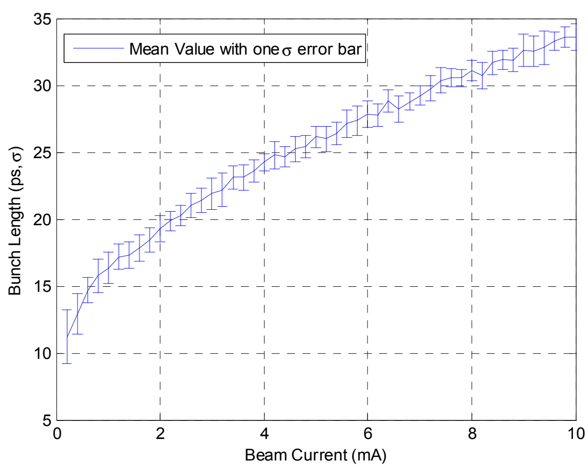

Figure 10: The relative relationship between the beam current and bunch length under the single bunch mode.

Longitudinal Instability

In the TPS commissioning beginning, there are many type of longitudinal beam motion (phase information) was observed by streak camera using the synchroscan unit (operate at 250 MHz) with dual-sweep unit, as shown in Fig. 11. The more stable situation is achieved through the concerted efforts of all groups, most of the longitudinal beam motion in the low current can be eliminated. However, there is a significant longitudinal motion occurs occasionally when beam current greater than a certain threshold value (~80 mA) in multi-bunch filled. The width of the streak trace growth up to around 144 psec (FWHM) which composed bunch length and energy oscillation amplitude, as shown in Fig. 12.

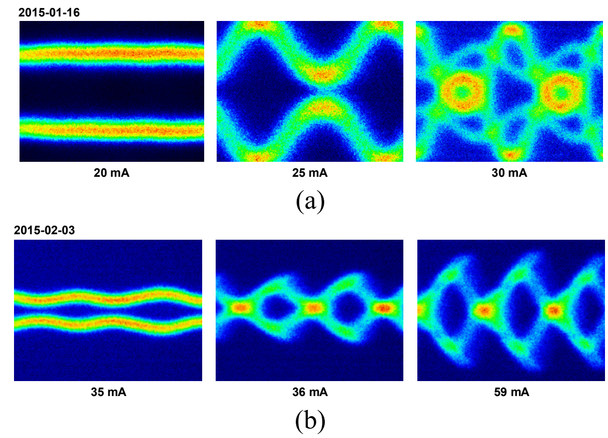

Figure 11: Longitudinal instability behavior of the stored beam observed by streak camera in TPS commissioning before amplitude feedback loop problem of RF system was identified. Both cases with difference chromaticity setting. (a) Stored beam current increase from 20 mA to 30 mA, (b) from 35 mA to 59 mA. Vertical time scale = 700 ps, horizontal time scale = 1 ms.

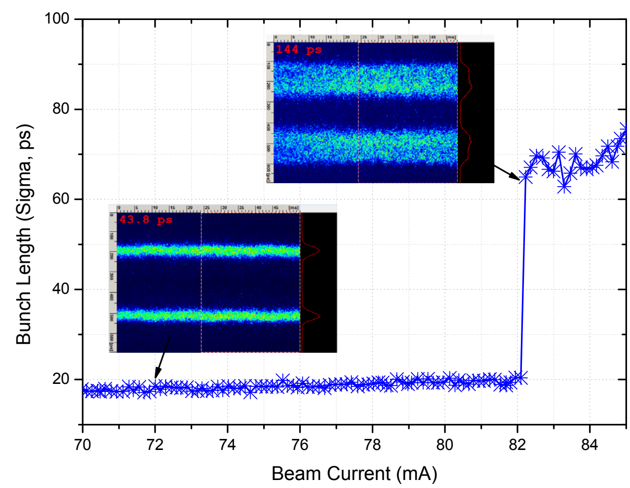

Figure 12: Longitudinal instability onset at 82 mA is indicated by the trace width of the streak camera increase in multi-bunch mode. Bunch length can measure before by the trace width below instability threshold. However, it failed after instability appeared.

FILL PATTERN MEASUREMENT

The time-correlated single-photon counting (TCSPC) technique is installed and used for fill pattern measurement from the synchrotron radiation in storage ring. It provides high dynamic range measurement with picosecond time accuracy high dynamic ranges. Typical stored single bunch beam at the storage ring is shown in Fig. 13(a) if linac parameters not optimized and special care. One main bunch accompany two satellite bunches existed. To obtain a pure single bunch beam, bunch cleaning by bunch-by-bunch feedback system is applied. It can keep bunch purity around 10^{-5} (5 sec accumulation of TCSPC counter) shown in Fig. 13(b) easily.

ISBN 978-3-95450-176-2

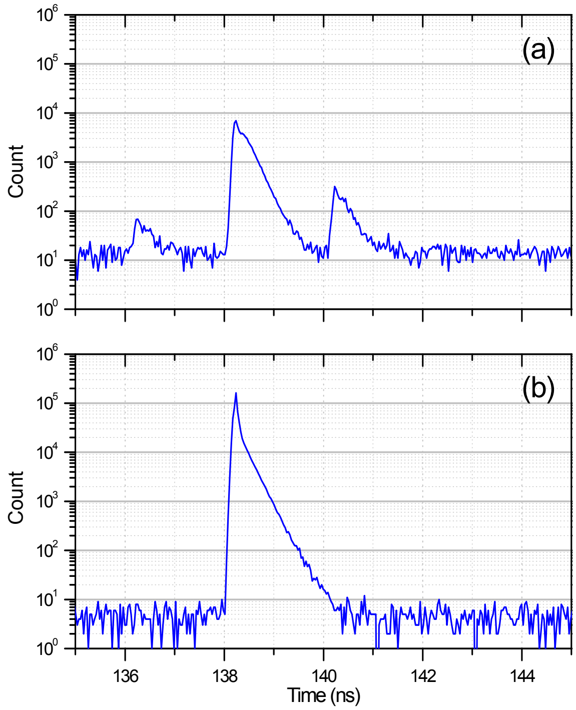

Figure 13: Single bunch purity measurement by TCSPC technique (5 sec accumulation), (a) before and (b) after bunch cleaning applied.

CONCLUSIONS

The synchrotron radiation monitor systems were designed, implemented and test for the booster synchrotron and storage ring during the Phase-I beam commissioning of TPS. It plays an important role for beam parameters measurement. Improvement is underway, preparation for Phase-II commissioning is in proceeding.

REFERENCES

[1] *TPS Design Handbook*, version 16, June 2009.

[2] H. J. Tsai, et al., "Hardware Improvements and Beam Commissioning of the Booster Ring in Taiwan Photon Source", TUPJE053, IPAC'15, Richmond, USA (2015).

[3] P. C. Chiu, et al., "Commissioning of BPM System for the TPS Project", TUPB067, IPAC'15, Melbourne, Australia (2015).

[4] C. Y. Liao, et al., "Preliminary Beam Test of Synchrotron Radiation Monitoring System at Taiwan Photon Source", Proceedings of IPAC'15, MOPTY074, Richmond, USA (2015).

[5] C. Y. Liao, et al., "Commissioning of a New Streak Camera at TLS for TPS Project", Proceedings of IBIC'13, MOPC39, Oxford, UK (2013).

[6] K. L. Tsai, et al., "Beam Line Design and Beam Measurement for TPS Linac", Proceeding of IPAC'11, WEPC038, San Sebastian, Spain (2011).

[7] C. C. Kuo, et al., "Commissioning of the Taiwan Photon Source", TUXC3, IPAC'15, Richmond, USA (2015).

ISBN 978-3-95450-176-2

COMMISSIONING OF BPM SYSTEM FOR THE TPS PROJECT

P. C. Chiu, K. H. Hu, C. H. Kuo, C. H. Huang, Demi Lee, Y. S. Cheng, K. T. Hsu
NSRRC, Hsinchu 30076, Taiwan

Abstract

Taiwan Photon Source (TPS) is a newly constructed 3-GeV synchrotron light source which ground breaking began February 2010. Its Booster beam commissioning and hardware improvement started at August 2014 and ramped to 3 GeV successfully in December 16 2014. Soon the stored beam in the storage ring had achieved 5 mA in December 31[1][2]. The BPM electronics Libera Brilliance+ [3][4] are adopted for booster and storage ring of TPS. The provided BPM data is useful for beam commissioning where it can be used to measure beam position, rough beam intensity along the longitudinal position and also for tune measurement. This report summarizes BPM commissioning and measurement during beam commissioning.

INTRODUCTION

The TPS is a state-of-the-art synchrotron radiation facility featuring ultra-high photon brightness with extremely low emittance [5]. The TPS accelerator complex consists of a 150 MeV S-band linac, linac to booster transfer line (LTB), 0.15–3 GeV booster synchrotron, booster to storage ring transfer line (BTS), and 3 GeV storage ring. The Storage Ring's circumference is 518.4 meters with 24 DBA lattice and 6-fold symmetry; the booster has 6 FODO cells and its circumference is 496.8 meters. The booster and the storage ring share the same tunnel in a concentric fashion. During 4 years of construction period, civil constructions had been completed in early 2013.

At September 2014, booster BPM commissioning had committed with beam commissioning. After some hardware improvement such as power supply tuning, chamber and magnet re-alignment, demagnetization of chamber, kicker and septum improving and etc., booster had achieved beam ramped to 3 GeV at December 16 2014. Later, after improving field leakage of Booster extraction DC septum, we had a 5-mA stored beam on Dec. 31 2014. Diagnostic system played a helpful role to provided beam profile and information to improve or tune subsystem to make progress quickly during beam commissioning. This report will focus on the BPM related environment, functionalities and measurement.

BPM FUNCTIONALITIES AND COMMISSIONING

The TPS storage ring is divided into 24 cells and there are 7 BPMs per cell; the booster ring has six cells where each cell is equipped with 10 BPMs. Booster button BPM shapes 35x20 mm elliptical and button diameter 10.7 mm. The calibration factor Kx and Ky is 8.25 and 9.66 mm respectively. There are two kinds of BPM for storage ring as Fig. 1 shown: one is standard button BPM shapes 68x30 mm elliptical and diameter 7.4 mm at arc section; the other is primary BPM shapes 64x16 mm racetrack and diameter 7.4 mm at straight line. The calibration factor Kx/Ky is 13.8/12.73 and 6.58/8.89 mm for standard and primary BPM respectively.

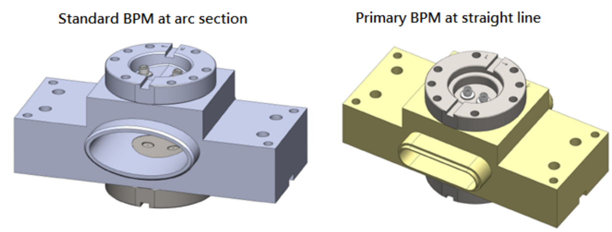

Figure 1: Mechanical drawings of standard type and primary type BPM for TPS storage ring.

The conceptual functional block diagram of the BPM electronics is shown in Fig. 2. It will provide several data type for different application. ADC and TBT data is acquired on demand by trigger; 10 Hz slow data is for DC average orbit and 10 kHz fast data could be applied for booster ramping orbit or fast orbit feedback application. It is also embedded with EPICS IOC for control, monitor and configuration. The timing AMC module would provide functionalities of synchronization, trigger, interlock and post-mortem. To support operation of the BPM electronics, functionalities like cold start, shutdown, housing, control system interface should meet the requirements. The delivered units also had been performed functionality and performance test to ensure compliance with this specification.

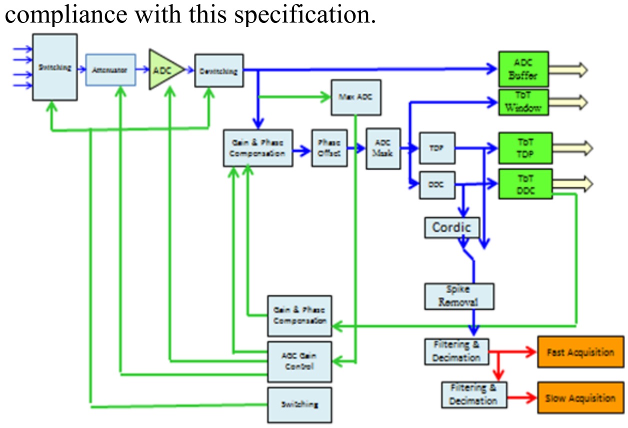

Figure 2: BPM platform functional block diagram.

At September, the first turn of the booster beam had achieved soon after correctors steering. There are only

ISBN 978-3-95450-176-2

few buttons of BPM found to have contact problems quickly by observing ADC data with extremely low count compared to other buttons. The real BPM calibration factor was agreed with the designed values by measuring and comparing the optical function of machine model. The first turn and accumulated beam of the storage ring soon obtained without correctors after injection started. It was also found that there are some cabling problems during machine measurement and optimization. Button B and C of two BPMs were cross connected. The cables of BPM 24_4 and 24_6 were also in wrong order. Besides, the LOCO fitting for BPM calibration factor showed that there were three primary BPMs which sensitivity Kx/Ky were almost only the half as shown in Fig 3. It was caused by incorrect settings of sensitivity factor of these three BPMs. Primary BPM are generally installed at straight line for normal ID. However, vertical beam duct height enlarge rather than reduce to transition to large aperture of vacuum duct of SRF modules. Therefore, standard BPMs are installed rather than primary BPMs installed at these sites.

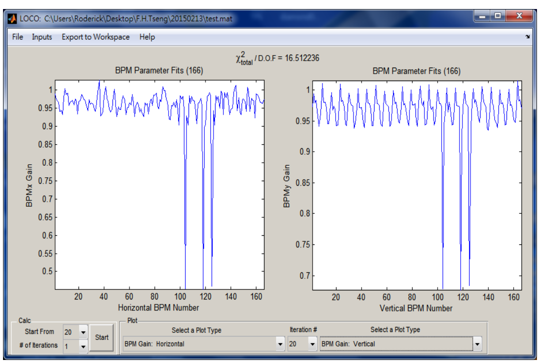

Figure 3: BPM calibration factor fitting results for LOCO. There are three BPM that should be primary BPM but actually standard BPM.

BOOSTER BPM MEASUREMENT

There are 60 sets of phase-trimmed 0.240" form polyethylene coaxial cables connected between the buttons and BPM electronics for booster. The trimmed BPM cables have the phase difference less than ±3° and attenuation difference less than 0.1 dB. Different BPM data flow will be demonstrated for different applications in this section.

ADC Raw Data

The ADC raw data is useful for checking the timing of the beam and beam property especially in the first turn. The phase delay due to time difference when beam travel pass the buttons along the ring could align by ADC clock offset. Fig. 4(a) shows that the first beam passing through the injection septum and kicker and arriving the 1st BPM of the booster ring when beam first steered pass through; (b) ADC data as the beam had stored in the booster.

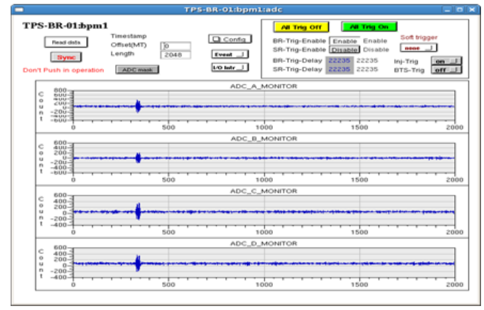

(a)

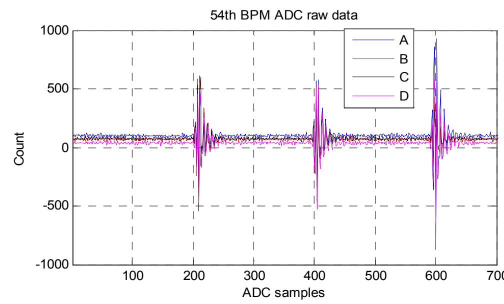

(b)

Figure 4: (a) The ADC data when beam passes through the 1st BPM of the booster synchrotron on the first day of Booster commissioning. (b) The ADC data as the beam had stored in the booster.

First-turn Application

BPM electronics provides single pass mode for calculating first turn trajectory from ADC data. However, vast beam losses and ADC DC offset up to 100 count will result in worsen signal to noise ratio and position calculation offset error. Therefore, a soft IOC would be applied to acquire more precise first turn trajectory from ADC raw minus DC offset. Fig. 4 shows the first turn orbit trajectory and sum along 60 BPMs. Horizontal trajectory shapes like dispersion function due to energy drift from Linac modulator.

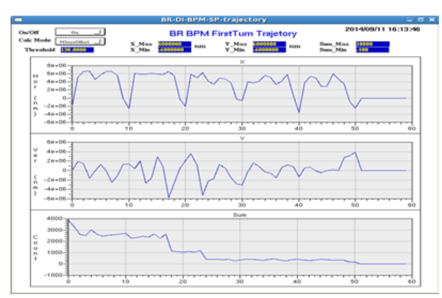

Figure 5: First turn horizontal, vertical trajectory and sum along 60 BPMs of booster.

Slow & Fast Orbit Data

The BPM electronics also provide 10 Hz slow and 10 kHz fast position data to measure average stored beam orbit. Figure 6 shows the FA orbit variation for DC and AC mode respectively. At DC mode, 60 Hz orbit

ISBN 978-3-95450-176-2

perturbation is clearly observed mainly from quadrupole power supply ripple. Horizontal phase advance between adjacent BPMs is around $\pi/4$. Resolution of BPM is gradually deteriorated after 120 msec due to beam loss. At AC mode, close orbit variation during ramping could be around 6 mm in horizontal and 2 mm in vertical. The variations in horizontal during the first thousands of turns are especially large due to the synchrotron motion.

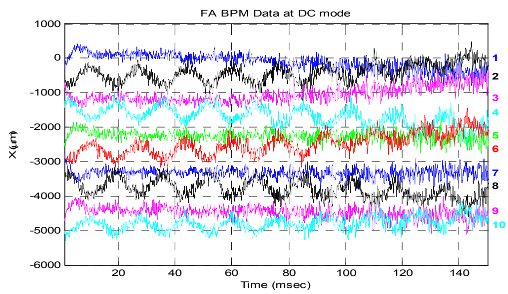

(a)

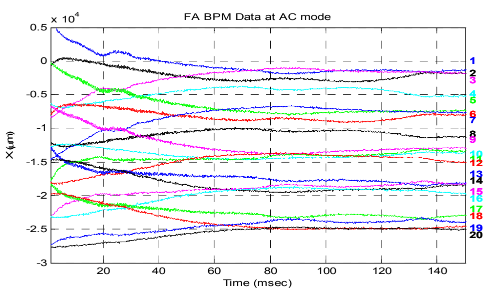

(b)

Figure 6: (a) DC mode Orbit. (b) AC mode Orbit.

Turn by Turn Application

DDC (Digital Down Converter) and TDP (Time Domain Processing) Turn-by-turn data are both provided and the resolution could achieve around 150 um at 0.5 mA. The BPM TBT data could be applied to extract tune as Fig. 7 shown as well as calculate optical function such as beta and dispersion. To use TDP properly, phase offset should be adjusted by beam according ADC data. Compared to DDC, TDP could well resolve tune due to clear and no smear TBT data as Fig. 8 which shows the spectrogram of DDC and TDP data respectively.

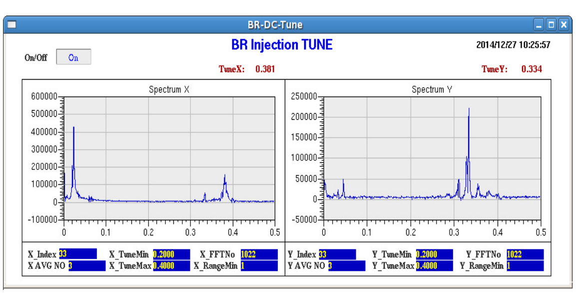

Figure 7: Booster injection tune extracted from BPM TBT data at injection time.

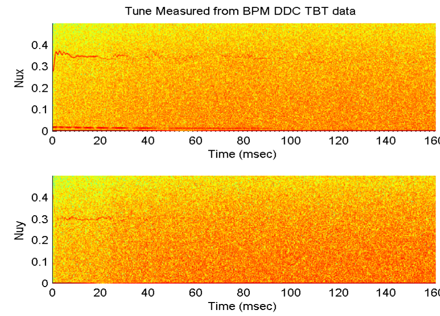

(a)

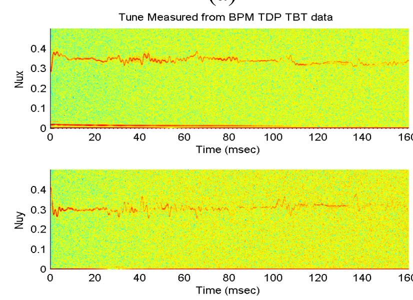

(b)

Figure 8: (a) Tune extracted from BPM DDC TBT data during booster ramping (b) Tune extracted from BPM TDP TBT data.

STORAGE RING BPM MEASUREMENT

There are many similar applications and commissioning process with Booster and Storage Ring such as ADC data, first-turn application and tune measurement. The phase offset for each BPM is also set according to ADC data. Turn-by-turn and FA BPM data will be focused in this section.

Turn-by-turn Data

After beam stored, the beam current had achieved 50 mA in March 2015 with vacuum pressure dropped. However, it was hardly continuously accumulated and beam trip happened. It was later verified that synchrotron motion is the major reason due to RF feedback loop resonance. The BPM turn-by-turn data observed that the synchrotron motion make horizontal position vibration at same phase as Fig 9 shown and it became stronger as beam current increased.

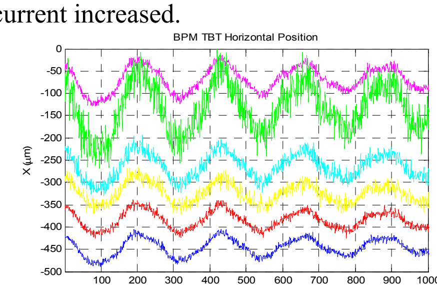

Figure 9: Horizontal TBT data. The synchrotron motion's amplitude for each BPM is proportional to its dispersion.

ISBN 978-3-95450-176-2

TBT data is also applied to extract tune in the storage ring. Besides injection kickers, the horizontal and vertical pingers are used to excite beam motion in two planes respectively. Timing for trigger of BPM, kickers and pingers are controlled by event system. Fig. 10 shows the real time tune display page. The chosen BPM, average number, FFT length and etc. could be selected according to different condition and requirement.

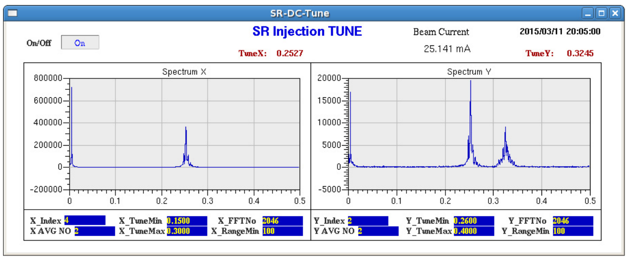

Figure 10: Storage ring tune extracted from BPM TBT data where beam are excited by pingers.

FA Data

10 kHz FA data could be provided to analyse transient motion, orbit stability as well as applied for fast orbit feedback. Fig. 11 shows orbit turbulence due to field leakage of septum during injection. The synchrotron motion around 2 kHz could be also observed.

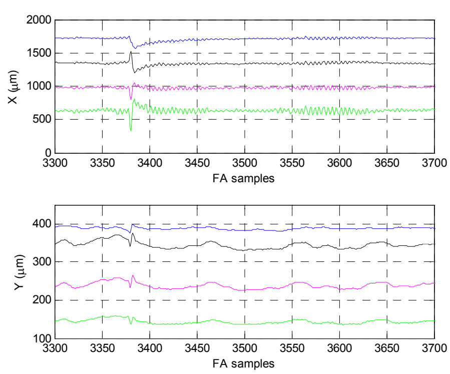

Figure 11: Horizontal & vertical FA position data during injection. The septum filed leakage cause horizontal orbit distortion 100 um.

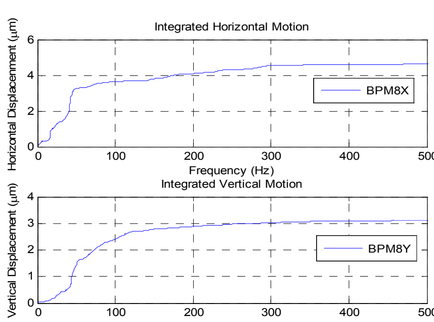

Figure 12: Horizontal and vertical integrated PSD.

According to BPM spectrum from FA data, 29 Hz noise was found the dominant noise source induced from turbo-pump motor. Booster extraction at 3 Hz repetition rate also makes 3 Hz noise observed. Besides, water flow also causes wide band vibration from 30 to 70 Hz. Fig. 12 shows the integrated PSD for the horizontal and vertical planes. Efforts to eliminate the noise source will be undertaken in the future.

Moreover, BPM FA data of the storage ring are also used for interlock safety for position and angle. BPM electronics itself provide position interlock functionalities. Another dedicated IOC is adopted to calculate all angles between different BPM from streaming in FA data through Gigabit Ethernet and activates interlock. Fig. 13 shows BPM angle interlock display and control page.

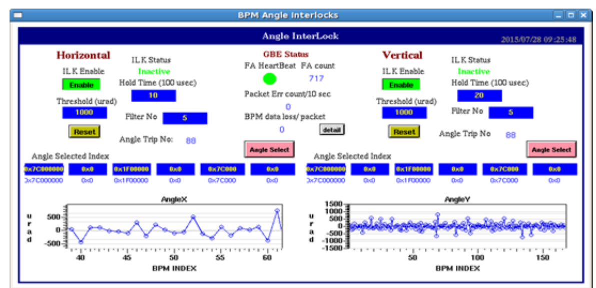

Figure 13: BPM angle interlock display and control page.

CURRENT STATUS

Final BPM system test and beam commissioning for TPS had started at the same time in September 2014 and completed at December 31. BPM functionalities and performance for the booster and storage ring have been exercised with beam during last several months. Supporting tools of software have been continuously revised and developed. Now the optimization of injection efficiency is still required further improvement [1]. The diagnostic tools especially BPM system provide quite a lot of information during commissioning as well as future optimization.

ACKNOWLEDGEMENT

Thanks for the help form H. J. Tsai, Y. T. Chang, and Demi Lee. The authors appreciate help from staffs of I-Tech for brainstorming and discussion.

REFERENCES

[1] H. J. Tsai et al., "Hardware Improvements and Beam Commissioning of the Booster Ring in Taiwan Photon Source", IPAC2015, Richmond, VA, USA, May 2015.
[2] C. C. Kuo et al., "Commissioning Results of Taiwan Photon Source", IPAC2015, Richmond, VA, USA, May 2015.
[3] Instrumentation Technologies, http://www.i-tech.si
[4] P. C. Chiu, et. al., "TPS BPM electronics Performance measurement and statistics", IBIC 2012, Tsukuba, Japan.
[5] TPS Design Handbook, version 16, June 2009.

ISBN 978-3-95450-176-2

BEAM CHARACTERISATION USING LASER SELF-MIXING*

A.S. Alexandrova#, C.P. Welsch, Cockcroft Institute and The University of Liverpool, UK

Abstract

Non-destructive beam diagnostics are highly desirable for essentially any accelerator or storage ring. This concerns the characterization of the primary beam itself, but also for example of atom and molecular jets that are crossed with the primary beam as experimental targets or for diagnostics purposes. A laser feedback interferometer based on the optical self-mixing effect provides a low - cost, robust, compact and non-invasive sensor for velocity, displacement and density measurements of various targets. This contribution presents results from theoretical and experimental studies into the factors influencing the performance and accuracy of this sensor. Parameters that have been assessed include the target velocity, the size of scattering particles, their density, type and scattering properties.

INTRODUCTION

Gaseous targets and gas jets have many applications in different fields of accelerator physics. A curtain shaped gas-jet is used as a non-destructive beam profile monitor for various types of the particle beams [1-2]. The beam profile monitor is based on the ionisation of the gas jet when it interacts with the beam resulting in 2-dimensional profile picture. Gas jets are used as a source of a laser induced plasma in laser-plasma acceleration experiments [3]. Supersonic gas jets in various configurations are used for the production and spectroscopy of radioactive isotopes [4]. The increasing importance of gas jets means that their characterisation is essential and a sensor is required to obtain information about the velocity, the density and the temperature. The laser self-mixing (SM) sensor is proposed as easy integratable, compact and cheap device for such purposes [5-7].

A laser velocimeter is under development in the QUASAR Group at the Cockcroft Institute/University of Liverpool, UK for the purposes of measuring the velocities of gas jets. The gas jet consists of neutral molecules, such as argon, nitrogen or helium, and forms a curtain of 1-20 mm diameter. Molecules move uniformly with a velocity which can vary from 100 m/s to 2000 m/s. The density of the gas jet depends on the pressure in the vacuum chamber and is expected to be in the range of 10^9–10^{12} particles/cm^3 [1-2]. An SM sensor is expected to measure the flow of gas jets with these parameters. It has been successfully used for characterising velocities of solid targets up to 100 m/s [8], and for some fluids up to 1 m/s [9]. The scattering of light off gas jets and off the seeding particles, which are added to improve the SM signal, directly influences the performance and accuracy of the results.

*Work supported by the European Commission: GA-ITN-2011-289191
#a.alexandrova@liverpool.ac.

THEORY AND METHODOLOGY

The self-mixing phenomenon is based on the coupling of laser light reflected or scattered off a moving target back into the cavity and interacting with the light inside the laser cavity. The backscattered light's wavelength is shifted due to the Doppler effect and the intensity of the backscattered light depends on the particulars of the target i.e. optical properties etc. The here-presented sensor is based on the SM effect in semiconductor lasers. The detection system includes a photodiode (PD), which is part of the commercially available laser diode. The SM phenomenon influences both the wavelength of the light and its power fluctuation. The interaction within the cavity causes backscattered light to be amplified, so the sensor doesn't require powerful light and there is no need for a complex optical system.

Scattering Theory of Light off Various Targets: Expected Spectrum

The distribution function of an electro-magnetic field scattering off a target is expected to be Gaussian [10], independent on the properties of the scattering media and the character of its motion. However, if the amount of illuminated scatters is large enough and their movements are correlated, the resulting function depends on the type of motion of the scatters. For example, the spectrum of scattered light is a Lorentzian function when a large amount of particles undergoes Brownian motion [11]. The process of scattering off a target or group of particles is a complicated process which requires different considerations depending on the nature of the particle.

1. If the light scatters from density fluctuations in a medium, there is a finite correlation between different coherent volumes [12].
2. If the light scatters form a rotating target, the motion of the scatters can vary from fully correlated to completely uncorrelated. It can be assumed that different parts of the rotating target are indifferent from each other. At the same time, the motion of the scatters can be characterised by the distribution of the velocities of the delta-function with the velocity of the centre of the light focus point [13].
3. If the light scatters off a moving flow with a specific velocity, the scatters are independent from each other. However, the flow can be characterised with a velocity distribution within an illuminated volume. Hence, the spectrum should be similar to the second case taking into account the velocity distribution.

The spectrum is to be calculated first for the rotating target with the velocity distribution of delta-function, and to be modified in more difficult case. The theoretical spectrum of the light scattered off a rotating ground glass has been analysed [14]. Assuming the size of the light

ISBN 978-3-95450-176-2

beam σ was focused by the lens with focus f on the target where the spot has size A, and that the target is located at a distance z, which is very close to the focus plane, then the spectrum of the signal is Gaussian:

$$\mathrm{I}(\omega) = I_0 \frac{1}{A} \frac{N}{v / w_0} \exp\left(-\frac{(\omega-\omega_0)^2}{2v^2 / w_0^2}\right) \tag{1}$$

Hence, the spectrum has a peak at the frequency centred on around the frequency of the incident light ω_0 and is broadened proportionally to the velocity υ of the target and inversely proportional to the beam waist radius w_0. The Gaussian peak and its broadening are independent on the distance to the object. The amplitude of the scattered spectrum is inversely proportional to the velocity of the target and inversely proportional to the illuminated area of the target. The illuminated area A can be calculated based on the beam radius. Hence, the amplitude of the scattered light increases with a decreasing size of the beam waist, and increases with an increasing amount of scattered centres N.

Broadening of the spectrum means that there are additional components added to the spectrum, so effectively speaking light is Doppler-shifted over many frequencies. They appear due to the roughness of the surface, i.e. 3D-dimention of the surface.

The discussion above was correct for the case of the light beam perpendicular to the target. Now, taking into the account the non-zero angle between the velocity vector and the wavelength vector, i.e. $\boldsymbol{k}\cdot\boldsymbol{\upsilon}$, a similar equation can be found for this case.

The geometry of a self-mixing experiment for the case of a rotating wheel is shown in Fig. 1a. The wavelength vector $\boldsymbol{k}$ is related to the wavelength by $\boldsymbol{k}=\boldsymbol{n}2\pi/\lambda$, where **n** is the unit vector in the direction of the light propagation. In the geometry presented in the figure $\boldsymbol{k}\cdot\boldsymbol{\upsilon} = k\upsilon\cos\alpha$. This will lead to a shift in the main frequency ω_0. As it was mention earlier, broadening of light when incident perpendicular to the target appears due to the roughness of the surface in that plain. Hence in the case of an inclined target, the broadening is proportional not to the whole component of the velocity, but to the component perpendicular to the **k** vector, i.e.to $\upsilon\sin\alpha$ in the geometry in Fig. 1. In the general case, it can be written as $|\boldsymbol{n}\times\boldsymbol{\upsilon}|$. The integral leads to a similar expression to Eq. 1 with a difference in the central frequency of the spectrum and broadening component:

$$\mathrm{I}(\omega) = I_0 \frac{1}{A} \frac{N}{|\, n\times v\,| / w_0} \exp\left(-\frac{(\omega-(\omega_0+kv))^2}{2(|\, n\times v\,|)^2 / w_0^2}\right) \tag{2}$$

In the case of the self-mixing technique, the beating of the optical power has a frequency proportional to the shift in the wavelength of the scattered/reflected light. Hence the spectrum of the SM signal is described by Eq. 2, so the peak is proportional to the Doppler shift and broadened according to these formulas.

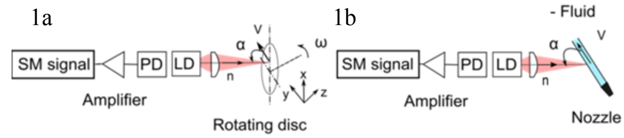

Figure 1: The set-up of SM sensor used for velocity measurements with a fluid as a target. The SM set-up contains a laser diode (LD) with light focused onto a target at an angle α from the normal of the target surface. A photodiode (PD) takes the role of a detector of the SM modulated light, the signal from which is converted into the voltage signal by a transimperdance amplifier. 1a) A rotating disc target, which was used for the theoretical study into the spectrum which can be obtain from the SM sensor. 1b) A fluid target, the parameters of which are under the scope of this contribution, such as velocity $\boldsymbol{\upsilon}$, the concentration of seeders.

The described spectrum of the SM signal is based on the interaction of the electric field of the incident light with the surface which has roughness, which causes a distortion of the field scattered/reflected from the surface with some unevenness. The same principal can be applied to liquids since the fluid can be seen as 3D object for the laser beam.

The amount of backscattered light can be defined based on scattering theory. The solid target is assumed to scatter light evenly in all direction in a solid angle (0, π). Any type of flow has some centre from which the scattering process can occur. This can be particles, density fluctuations, or temperature fluctuations, which leads to a cross-section distribution of amplitudes over a range of scattering angles.

Expected Backscattered Light from Gas Jets

An estimation of the expected backscattered light may be found from Rayleigh scattering theory [15]. If laser light with power P_0 incident on the gas-jets, with constituent particles with diameter d and particle density N, will scatter light with optical power P_{det} within a solid angle ΔΩ, which is defined by the optics of the sensor:

$$P_{\mathrm{det}} = P_0 \eta N z_d \cdot \Delta\Omega \cdot \frac{9\pi^2}{\lambda^4} \cdot d^6$$

where η is the optics collection efficiency and z_d is the depth of the measurement volume. The power attenuation based on this formula for gas-jet parameters, assuming a size of scatter 0.1 nm and a gas jet density of 10^{12} molecules/cm^3 is around -240 dB. The minimum level of feedback is -90 dB for a SM sensor [7].To bring the attenuation level closer to the required value, seeding with the additional particles of at least 10 nm diameter is necessary.

Choice of Seeders

Different types of scattering particles could be used for the self-mixing technique. Since the main interest of this

ISBN 978-3-95450-176-2

work is to measure high velocities up to 2000 m/s including gases, there is a need to find the most efficient seeding particles or material to obtain the required level of feedback for efficient operation of the SM sensor.

The geometry of the SM sensor is such that the light, which is coupling back into the cavity, is always backscattered light unless there is a modification of the system.

A number of experiments of a similar nature of light interaction were performed for PIV (Particle Imaging Velocimetry), the initial range/choice of the materials for the SM sensor can be taken directly from there. Moreover, there are a few works [5-7] within the SM field to get an idea of which seeders have already worked successfully for SM velocity measurements.

PIV is based on analysing the net displacement of moving particles. In this technique, the flow is seeded with tracer particles, which scatters the light. A laser light sheet, which is formed by a cylindrical lens, illuminates the region of interest. The picture of scattering light is visualized. If the tracer particles are assumed to follow faithfully to the flow, a statement can be made on the average velocity of the flow. Hence, substantial research has been performed into seeding materials and seeding techniques for PIV application [16]. The main seeding materials and their sizes are presented in Table 1. The range of materials which were used for seeding both liquids and gases, are presented among which both liquid and solid types of seeders were used.

Table 1: Seeding Material for Liquid and Gas Flows in PIV Measurements. [16]

Type	Material	D for liquid flows, µm	D for gas flows, µm
Solid	Polystyrene	10-100	0.5-10
	Alumina Al_2O_3	2-7	0.2-5
	Titania TiO_2		0.1-5
	Carbon dioxide CO_2		5-15
	Glass spheres	10-100	0.2-3
	Granules for synthetic coatings	10-500	10-50
	Dioctylphathalate		1-10
Liquid	Different oils	50-500	0.5-10
	Diethylhexylsebacate		0.5-1.5
	Helium-filled soap bubbles		1000-3000
Gases	Oxygen bubbles	50-1000	

Generally, the scattering efficiency function strongly depends on the refractive index of the seeders and surrounding area, the size, shape and orientation of particles and the observation angle. Along with this the scattering efficiency is a function of the ratio of the refractive index of the seeders and surrounding area [13]. The refractive index of air is considerably less than that of water, so the amount of light scattered off the small particles of the same size in air is at least one order of magnitude more than in the water. As a result, the size of the seeders can be smaller for velocimetry of gases, and vice versa, for water flow measurement, a larger size of particles has to be used for a sufficient amount of scattered light. This can be seen in the Table 1.

The nature of gases and analysis of the experiments using different technique for the mapping the velocities shows that other materials can give promising level of the backscattered light for the SM sensor.

As it was mentioned, the self-mixing technique is used not only for displacement measurements, but also for velocity detection of solid and liquid targets. The SM fluid velocity measurements were mainly aimed at biological applications such as blood characterisation [5] and molecular dynamic [6]. Milk and polystyrene (latex) spheres were mostly used for seeding the water.

The size of polystyrene in SM experiments varies from 110 nm up to 1.23 µm, compared to the size of the polystyrene seeders used in fluid PIV experiments of 10 µm to 100 µm. SM system for velocity detection is more sensitive to scattered light, so smaller particles can be used for the velocimetry. The main and easy-to-use seeders are milk. The velocity measurements demonstrated in recent published papers do not exceed 15 cm/s for milk as seeders, 17 cm/s with polystyrene spheres as seeders of 1.23 µm size (and with lower velocities in case of the smaller sizes of the seeders), and up to 35 cm/s for the blood measurements for very high concentration and without reference verification of the experimental results.

EXPERIMENTS WITH FLUIDS

To measure the velocity of liquids, an experimental set-up was established in order to compare the influence of different parameter from analytical solutions for spectrum of the SM velocimeter with the experimental results.

The experimental set-up of the SM sensor for the measurement of the velocities of the liquids is presented in Fig. 1b. The light from LD was focused using a lens on to the fluid target at an angle of α=75°. The backscattered light from the target was coupled back into the cavity using the same lens. The signal was measured by PD and a transimperdance amplifier.

The frequency of each SM signal is expected to be proportional to the projection of the velocity of the laser light axis according to the Doppler shift and broadened according to Eq. 2. The Doppler shift of the periodic optical power fluctuation measured with PD and the amplifier is equal to $(2\upsilon\cos\alpha)/\lambda$. In the here-presented set-up, the LD of 650 nm wavelength was used. The data analysis based on the Fast Fourier Transformation allows the spectrum of the signal to be obtained, which is compared with spectrums theoretically obtained before.

ISBN 978-3-95450-176-2

The constant velocity of the fluid was achieved by using a pump with variable flow rate and discharged from the tube. The pump rates were used such that the fluid did not enter the chaotic regime allowing a stable and measurable reference velocity of the water stream. The experimental set-up was constructed in such way that different parameters can be varied. The velocity of the fluid can reach up to 3 m/s without entering the chaotic regime. The seeding material parameters were changed such as the material itself (milk, titanium dioxide) and the size of the seeders (5 µm, 1 µm, 150 nm, 21 nm) without changing the viscosity of the fluid. Based on the analysis above and taking into the account the PIV experiments, the experiments were performed with following seeders:

- Milk: 5 µm;
- Titanium dioxide TiO_2: 1 µm; 150nm; 21 nm.

The Effect of Varying the Velocity of the Laminar Flow

The variation of the velocity of the target directly influences on not only the value of the Doppler shift in the wavelength, but also the amplitude of the peak of the signal spectrum and its bandwidth. The spectrum of SM signal obtained in the experiments when the velocity of the flow was varied is presented in Fig. 2. When the velocity was increased, the peak amplitude decreased and its full width at half maximum (FWHM) increased proportionally. It agrees well with theory described earlier by Eq. 2.

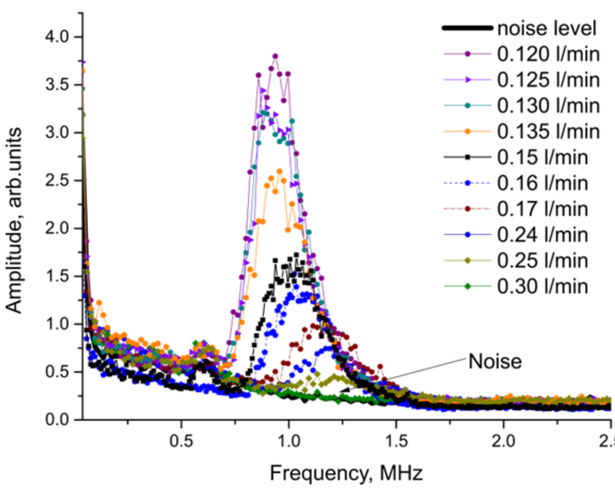

Figure 2: The experimental results of the velocity measurements of the flow of water: the spectrum of the self-mixing signal at different pump rates. The liquid was seeded with titanium dioxide TiO_2 with a 1 µm diameter. The velocity of liquid was varied from 1.0 m/s to 1.5 m/s. The amplitude of the spectrum peak decreases steadily with increasing velocity.

Varying the Concentration of Seeding Materials

The concentration of the seeders is responsible for the amount of light being backscattered into the cavity. Varying concentrations of different seeder sizes was under study to see the influence on both the amplitude of the spectrum peak and its bandwidth.

Figure 3 presents the results of the experiments obtained when the concentration of the seeders TiO_2 in this case varied from 0.03 wt% to 3.4 wt% (wt% is percentage by weight which can be defined as relation of the weight of the seeders to the weight of the solution multiplied by 100%) in the water. The amplitude of the spectrum peak obtained from the SM signal is averaged over 100 measurements from the signal from the fluid. Figure 3 shows the dependence of the peak amplitude on the concentration of the TiO_2 particle of 1 µm in diameter by the round white dots, 150 nm in diameter by the square dots, and 21 nm in diameter by the grey triangular dots. The trend of the plots, shown by the blue lines, has exactly the same character for the various sizes of seeders with different amplitudes.

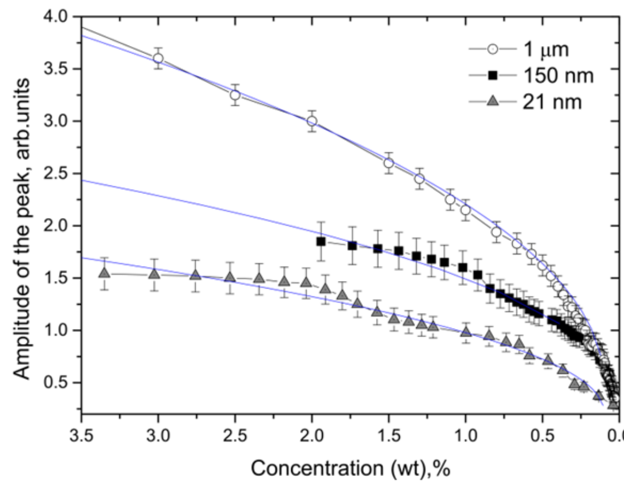

Figure 3: The experimental influence of the concentration of TiO_2 seeders in the flow of water on the spectrum of the self-mixing signal with a fixed flow velocity (at 1.3 m/s). The obtained result for seeders a 1 µm diameter are shown by round white dots, 150 nm diameter by the black square dots, and 21 nm by the grey triangular dots. The concentration of the seeder was varied in the experiments in the range of 3.4 wt% to 0.03 wt%. The amplitude of the spectrum peak decreases steadily with decreasing concentration.

According to the experimental results for the different size of seeding material, the amplitude of the peak increases for higher concentrations. The FWHM does not depend on the concentration of the seeders and remains constant in the case of fixed flow velocity for all experiments, which is predicted by Eq. 2. The measured velocity of the fluids agreed with the reference velocity with better than 3% precision.

The Effect of Varying the Size of Seeding Materials

According to theory, the amplitude of the peak of the spectrum should be proportional to the number of seeders

ISBN 978-3-95450-176-2

in the flow, i.e. to the concentration. However, Fig. 3 shows the dependence of the concentration on the amplitude of the peak for the same type of seeders (TiO_2) of different size. The peak amplitude of the spectrum is higher for the 1 µm diameter compared to 150 nm and to 21 nm. The amount of backscattered light strongly depends on the size of the particles, when the size of the scatters is of the same order of the wavelength of the scattered light When the size of the seeding particles was 5 µm it was observed that the amplitude of the peaks was lower as well [9].

The Effect of Varying the Optical Properties of Seeding Materials

During experiments, different types of seeders were used. As it has been shown before [17], the velocity of the fluid directly influences the amplitude of the peak, which decreases with increasing velocity. Hence, after some velocities, it is impossible to detect a signal. Using the same geometry of the set-up, velocities up to 100 m/s were measured when the white paper was used as a target [8]. Switching to fluids, the limit of the detected velocity increased dramatically. In experiments with milk as seeders, a velocity up to 20 cm/s was measured [9]. Using titanium dioxide as a seeding material makes it possible for velocities up to 1.5 m/s to be measured with the same or even lower level of the concentration as milk.

CONCLUSION

This study has been focussed on the optimisation of a SM sensor to measure the velocity of gas jet based beam profile monitors. A theoretical investigation into the spectrum expected for such a sensor has been presented together with a calculation of the expected level of backscattered signal from a gas jet. A range of different seeding materials added to a water flow was investigated, and such parameters as velocity, reflectivity, and concentration of the seeders in the fluid were under study. The laboratory experiments with TiO_2 with different diameters (1 µm, 150 nm, 21 nm) showed the dependence of the peak spectrum amplitude from the concentration of seeders with a minimum concentration of 0.03 wt% still being possible to measure velocities with better than 3% accuracy. Using the same type of seeders for the gas jet is currently under investigation since it should improve the SM signal even more than liquids.

ACKNOWLEDGMENT

Work supported within LA3NET which is funded by the European Commission under grant agreement no 289191; HGF and GSI under contract VHNG328 and STFC under the Cockcroft Institute Core Grant No.ST/G008248/1

We would like to thank Dr. Massimiliano Putignano for his initial help with the project, Prof. Gaetano Scamarcio and his group from the University of Bari for their support with understanding of the SM technique, Dr Ralph Fiorito and Lee Devlin for useful discussions.

REFERENCES

[1] V. Tzoganis et al., "Gas dynamics considerations in a non-invasive profile monitor for charged particle beams." Vacuum, 109-0, p 417-424(2014).
[2] V. Tzoganis et al., "A non-invasive beam profile monitor for charged particle beams." Applied Physics Letters, 104-20, p 204104 (2014).
[3] D. Kaganovich et al., "Shaping gas jet plasma density profile by laser generated shock waves." Journal of Applied Physics, 116-1, p. 013304-1 (2014).
[4] Yu. Kudryavtsev et al., "The in-gas-jet laser ion source: Resonance ionization spectroscopy of radioactive atoms in supersonic gas jets." Nucl. Instrum. Meth. B 297, p 7-22 (2013).
[5] M. Norgia et al., "Self-mixing laser Doppler spectra of extracorporeal blood flow: a theoretical and experimental study." IEEE Sens. J. 12 (3), p 552 – 557 (2012).
[6] K. Otsuka, "Self-mixing thin-slice solid-state laser metrology. " Sensors, 11, (2), p 22195 –2245 (2011).
[7] T. Bosch at al., "Optical feedback interferometry for sensing application. " Opt. Eng.. 40 (1), p. 20–27 (2001).
[8] A. S. Alexandrova et al., "Self-mixing diode laser interferometry for velocity measurements of different targets." SPIE Photonics Europe. International Society for Optics and Photonics, pp. 91412C-91412C (2014).
[9] A. S. Alexandrova et al., "Laser diode self-mixing interferometry for velocity measurements." Optical Engineering, 54.3, p 034104 (2015).
[10] W. Martienssen, E. Spiller, "Coherence and Fluctuations in Light Beams." Am. J. Phys. 32, 919 (1964).
[11] F. T. Arecchi et al., "Scattering of Coherent Light by a Statistical Medium." Phys. Rev. 163, 186 (1967).
[12] G. B. Benedek, *Brandeis Sumnmer Institute in Theoretical Physics* (Gordon and Breach, New York, 1968).)
[13] F. T. Arecchi, *Quantuin Optics,* edited by R. J. Glauber (Academic, New York, 1970).
[14] L. E. Estes et al., "Scattering of Light from a Rotating Ground Glass." J. Opt. Soc. Am. 61, p 1301-1306 (1971).
[15] R. B. Miles et al., "Laser Rayleigh scattering." Meas. Sci. Technol. 12.5 (2001) 33.
[16] M. Raffel et al., *Particle Image Velocimetry: A Practical Guide* (Springer, Germany, 2007).
[17] A. S. Alexandrova, C. P. Welsch, "Laser diode self-mixing technique for liquid velocimetry." LA3NET2015, Int. Conf. on Laser Appl. at Accelerators, Mallorca, Spain (2015).

ISBN 978-3-95450-176-2

SIMULATIONS OF THE FETS LASER DIAGNOSTIC

A. Kurup, J. Pozimski, P. Savage, Imperial College London, UK
S. M. Gibson, K. Kruchinin, Royal Holloway, University of London, UK
A. Letchford, Science and Technology Facilities Council, Rutherford Appleton Laboratory, UK

Abstract

The Front-End Test Stand (FETS) aims to demonstrate clean chopping of a 60mA, 3MeV H- ion beam. Such high beam intensities require unconventional emittance and profile measuring devices such as the laserwire system that will be used on FETS.

A laser is used to neutralise part of the H- ion beam. The main beam is then separated from the stripped beam by using a dipole magnet. This paper presents tracking results of the laser diagnostic lattice using a simulated field map of an existing dipole magnet and investigates the possibility of laser stripping upstream of the dipole.

INTRODUCTION

The Front End Test Stand is an R&D project at the Rutherford Appleton Laboratory (RAL) with the aim to demonstrate a high power (60 mA, 3 MeV with 50 pps and 10 % duty cycle), fast chopped H- ion beam [1]. FETS consists of a high brightness ion source [2] and a magnetic three solenoid LEBT [3], both of which are operational, see Figure 1. The 4-vane 324MHz radio frequency quadrupole [4],

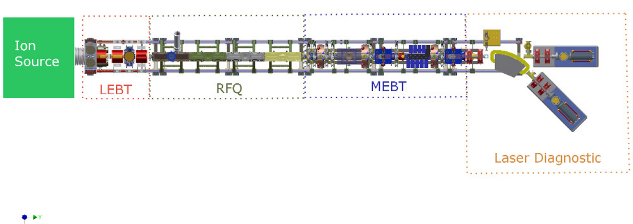

Figure 1: Layout of the Front End Test Stand.

which accelerates the beam from 65KeV to 3 MeV is manufactured and will be assembled and tested in the following months. Downstream of the RFQ is the medium energy beam transport (MEBT) [5], containing a high speed beam chopper [6] and non-destructive photo-detachment diagnostics. The MEBT is in the design phase; with the particle dynamics design finished and the transition to the mechanical design started. The diagnostics of high power particle beams is difficult, due to the power deposition on diagnostics elements by the beam, so non-invasive instrumentation is highly desirable. The laserwire emittance scanner is based on a photo-detachment process, utilizing the neutralized particles produced in the interaction between laser and H- beam for beam diagnostics purposes. The principle is appropriate to determine the transversal beam density distribution, as well as the transversal and longitudinal beam emittance downstream of the RFQ.

Previous studies of the FETS laserwire, see [7] and [8], were done with the laser stripping taking place within the dipole magnet to provide separation between neutrals within the beam and the H^0 particles produced by the laser interaction. The plan was to use a custom-built large aperture magnet and a vacuum vessel with three exit ports to allow scanning the laser over a distance of 40 mm to provide good emittance resolution. Since then it has been decided to use an existing dipole magnet and vacuum vessel and to investigate the possibility of stripping outside of the dipole magnet.

A model of the magnet was made to generate a field map which was then used to perform particle tracking simulations, including space charge effects, using General Particle Tracer (GPT) [9]. The aim was to adjust the optics of the laserwire quadrupoles to transport the beam but keeping the beam size large (around ±20 mm) at the stripping location in order to get good resolution at the detector and to have as large a beam size as possible on the dumps to keep the power density in the dumps as low as possible. The following sections give details of the magnet simulation and the tracking results for the quadrupole configuration that gives the required beam parameters at the stripping location and the subsequent transport of the stripped and unstripped beams to their respective dumps.

DIPOLE FIELD SIMULATION

The existing dipole magnet, see Figure 2, was modelled using CST Studio [10] to produce a magnetic field map that was used in the particle tracking simulations. Measurements of the yoke and coils were made and a 3D model of the magnet, see Figure 3. Here the magnet requires flipping to get a bend in the negative direction and will require mounting the existing magnet upside down. However, for the purposes of these simulations, this will not have any effect on the outcomes of the simulation results so the magnet was used in its current orientation. A 3D field map was generated using 100 A excitation current in the coils which gave 0.2475 T in the centre of the magnet. Figure 4 is a plot of the on-axis vertical field and shows that the fringe fields extend up to 300 mm from the entrance and exit faces of the magnet. Tracking a 3 MeV H^- ion, and ensuring it is on-axis at the entrance and exit faces, requires scaling the field by 0.894 to take into account the longer effective magnetic length due to the fringe fields.

The full 3D field map from this simulation was used in the tracking simulations described in the following section.

ISBN 978-3-95450-176-2

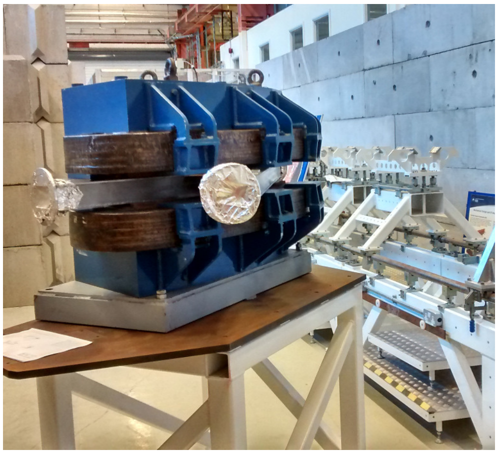

Figure 2: Picture of the existing dipole that can be used for the laserwire beam line.

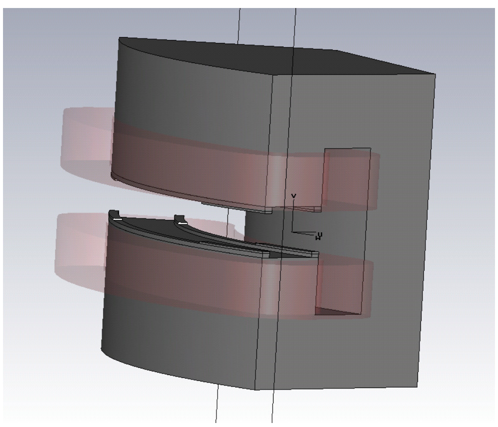

Figure 3: 3D model of the magnet in CST Studio.

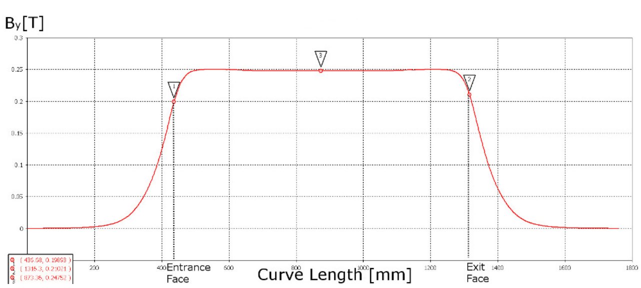

Figure 4: On-axis field from the CST Studio simulation. The markers indicate the field at: 1) the entrance face; 2) the exit face; 3) the centre of the magnet.

PARTICLE TRACKING SIMULATIONS

The main aim of these simulations was to demonstrate the feasibility of using the existing dipole and to perform stripping upstream of the dipole. Figure 5 shows the CAD drawing of the laserwire lattice, the main components being the 45° sector-bend dipole magnet, the six quadrupole magnets (two upstream and two downstream in each direction), the laser feedthrough and the beam dumps. The beam at the exit of the RFQ (10k particles) was tracked through the final version of the MEBT lattice (using the latest fields maps

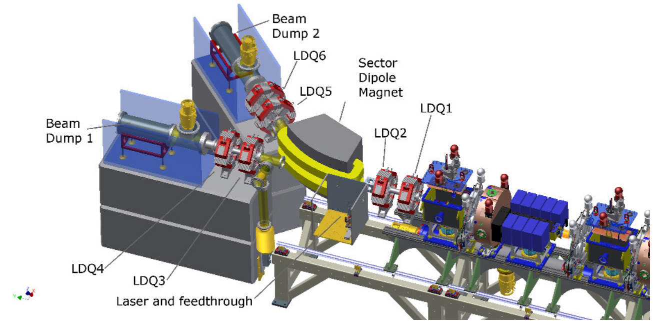

Figure 5: CAD model of the laserwire lattice showing the six quadrupoles (LDQn), the 45° sector-bend dipole magnet, the laser feedthrough and the beam dumps.

for the quadrupole magnets and rebunching cavities) to the location 4.4m downstream of the RFQ exit, which is the start of the laserwire lattice. The beam distribution at this location, see Figure 6, was used as the input beam for the laserwire lattice. Tracking of particles through the laserwire lattice was done in three separate stages: tracking of the H^- ion beam with the dipole switched off (this is the normal operating mode); with the dipole switched on and tracking H^- ions through to dump 2; and taking the beam distribution at the stripping location and drifting it (i.e. track with zero charge to simulate H^0) to dump 1.

The positions of the first two quadrupole magnets in the laser diagnostic beam line were adjusted such that there is no overlap of the magnets' fringe fields and to have a region of zero magnetic field before the dipole where laser stripping can take place. To get the best resolution at the detector it is better to have a beam size close to the maximum size of the detector. So the quadrupole strengths were adjusted to give a beam size around 40 mm in diameter at the detector location while ensuring the beam envelope stays within the aperture of the quadrupole magnets, i.e. ±30 mm and is large over the length of the beam dumps. The chosen set of quadrupole settings transports the beam without going through focal points and so a large beam size is maintained throughout the lattice. Figure 7 shows the trajectories in the x-z and y-z planes of the particles with the dipole switched off. This is the normal operating mode with the full beam going through to dump 1. The density profile of the beam at dump 1, see Figure 8, shows that the beam is well spread out.

With the dipole on the beam is deflected to dump 2. Figure 9 shows the trajectories in the x-z and y-z planes for the beam when the dipole is on. The bottom two plots are in the coordinate system of the exit face of the magnet (i.e. the z-axis is perpendicular to the exit face) and give a clearer indication of the beam envelope through LDQ3, LDQ4 and dump 2.

The density of the beam at dump 2, see Figure 10, shows the beam is well spread out but shows some distortion, which is currently under investigation.

The particle distribution is read out at the stripping location, which is 300 mm before the entrance face of the dipole,

ISBN 978-3-95450-176-2

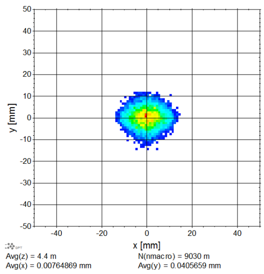

(a) Transverse profile

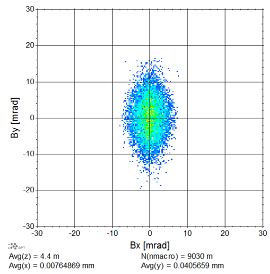

(b) Transverse divergences

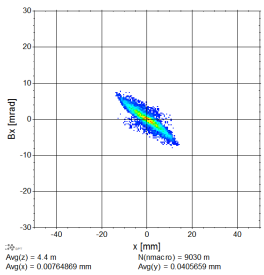

(c) x Emittance

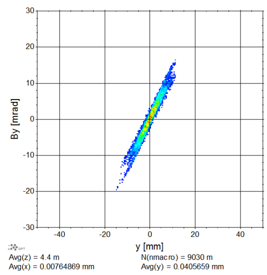

(d) y Emittance

Figure 6: Phase space distrbution of the input beam used in the tracking simulations.

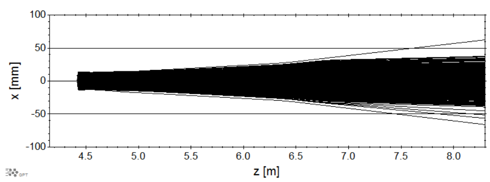

(a) x-z plane

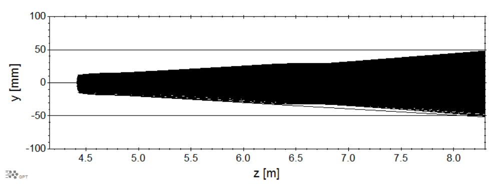

(b) y-z plane

Figure 7: Particle trajectories with the dipole switched off.

see Figure 11. The charge is set to zero for this particle distribution. These are then drifted (using the mass of the H^0) to the detector location, see Figures 12.

CONCLUSION

The simulation results show that the existing dipole is suitable for use as the bending magnet for the FETS laserwire emittance measurement device. The quadrupole settings have been adjusted to provide the required beam parameters at the stripping location in order to give good coverage over the full area of the detector, thus maximising the measurement resolution. The laserwire lattice has the flexibility to test different methods for the emittance measurement, including the options to scan the laser outside of the dipole field and in all transverse directions. Further work will focus on defining the set of measurements to be performed with

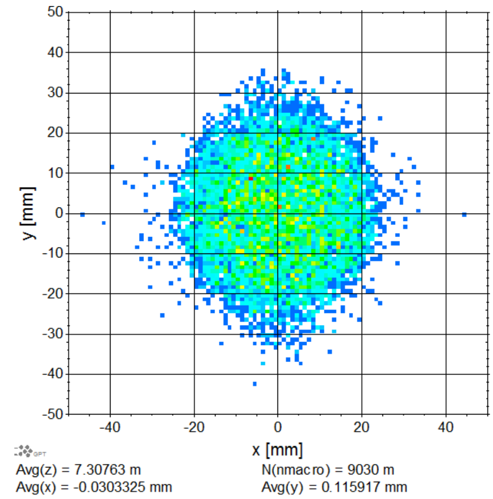

(a) x-y profile

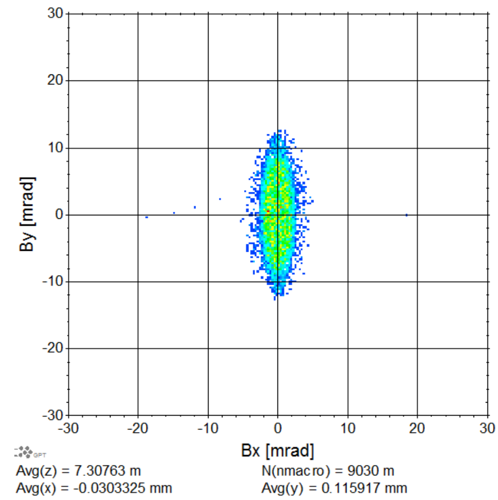

(b) x-y divergences

Figure 8: Beam at the entrance face of dump 1.

this configuration and investigate the best emittance resolution achievable by using different laser configurations and detectors.

ACKNOWLEDGMENT

The authors would like to thank Scott Lawrie for the quadrupole field map and Morteza Aslaninejad for the MEBT simulation and assistance with GPT.

ISBN 978-3-95450-176-2

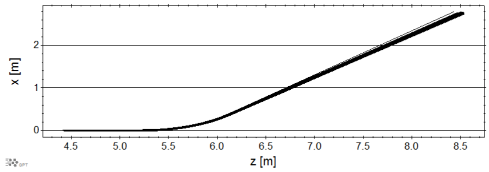

(a) x-z plane

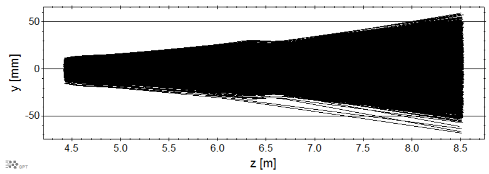

(b) y-z plane

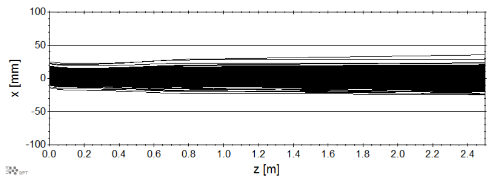

(c) x-z plane in the coordinate system of the exit face of the dipole.

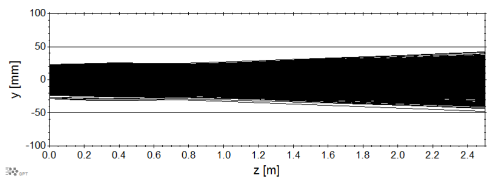

(d) y-z plane in the coordinate system of the exit face of the dipole.

Figure 9: Particle trajectories with the dipole switched on.

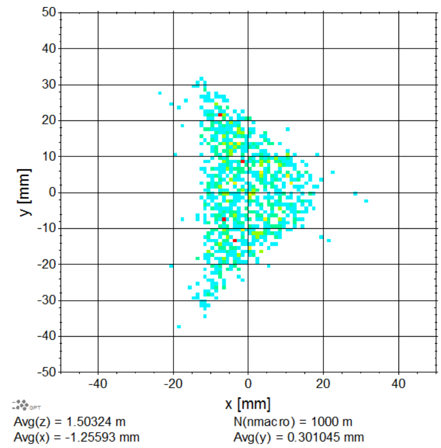

(a) x-y profile

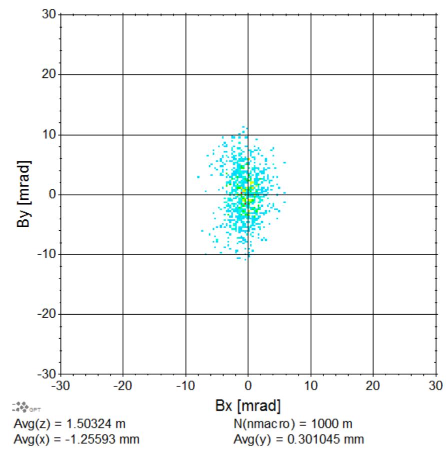

(b) x-y divergences

Figure 10: Beam at the entrance face of dump 2.

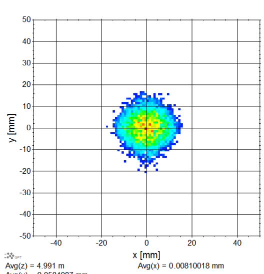

(a) Transverse profile

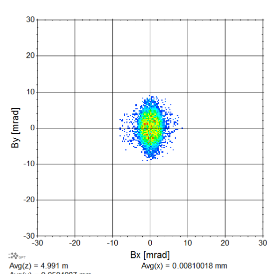

(b) Transverse divergences

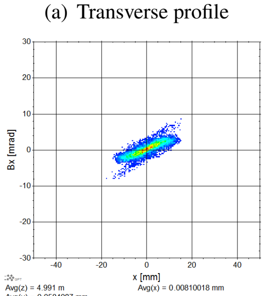

(c) x Emittance

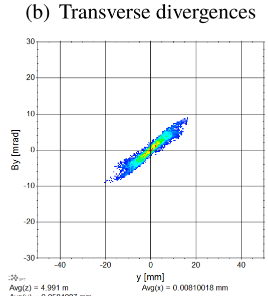

(d) y Emittance

Figure 11: Phase space distrbution of the stripped beam used as the input beam for tracking neutrals to the detector.

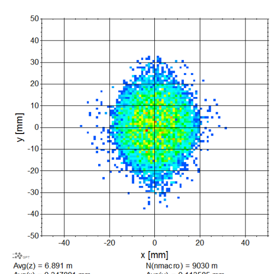

(a) Transverse profile

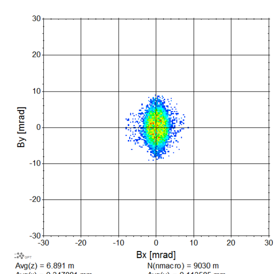

(b) Transverse divergences

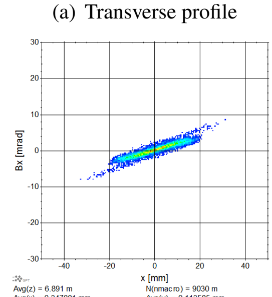

(c) x Emittance

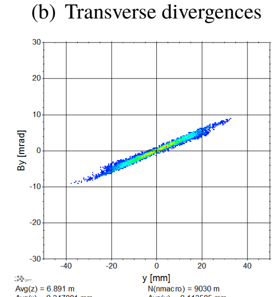

(d) y Emittance

Figure 12: Phase space distrbution of the beam of neutrals at the detector location.

ISBN 978-3-95450-176-2

REFERENCES

[1] "Status of the FETS project", A. Letchford et al, LINAC 14, Geneva (2014)

[2] "Extracting a High Current Long Pulse Hminus Beam for FETS", D. C. Faircloth et al., IPAC 14, Dresden, Germany (2014)

[3] "Performance of the Low Energy Beam Transport at the RAL Front End Test Stand", J. Back et al., IPAC 14, Dresden, Germany (2014)

[4] "Production of the FETS RFQ", P. Savage et al, IPAC 13, Shanghai (2013)

[5] "Lattice and Component Design for the Front End Test Stand MEBT at RAL", M. Aslaninejad et al., IPAC 14, Dresden, Germany (2014)

[6] "A Two Stage Fast Beam Chopper for Next Generation High Power Proton Drivers", M. Clarke-Gayther, IPAC 11, San Sebastian (2011)

[7] "Particle Tracking for the FETS Laserwire Emittance Scanner", J. Pozimski, S. Gibson, IBIC 2013, Oxford (2013)

[8] "Simulation results of the FETS laserwire emittance scanner", K.O. Kruchinin, et al., Proc. IPAC 14, Dresden, Germany (2014)

[9] Pulsar Physics, http://www.pulsar.nl/gpt.

[10] CST STUDIO SUITE, https://www.cst.com

ISBN 978-3-95450-176-2

CHARACTERISING THE SIGNAL PROCESSING SYSTEM FOR BEAM POSITION MONITORS AT THE FRONT END TEST STAND*

G. Boorman#, S.M. Gibson, N. Rajaeifar, RHUL, London, UK
J. Pozimski, Imperial College, London, UK
S. Jolly, University College, London, UK
S.R. Lawrie, A.P. Letchford, STFC/RAL, Oxfordshire, UK
J.D. Gale, University of Sussex, UK

Abstract

A number of beam position monitors (BPM) are being installed at the Front End Test Stand (FETS) H^- ion source at the Rutherford Appleton Laboratory, UK, as part of the 3 MeV medium energy beam transport. The FETS ion source delivers pulses up to 2 ms long at a rate up to 50 Hz and a maximum current of 60 mA, with a 324 MHz micro-bunch structure imposed by the frequency of the FETS RF acceleration cavity. The response of an in-house designed button BPM has been simulated and then characterised on a wire-based test-rig and the results are presented. The output from a custom algorithm running on a commercial PXI-based FPGA signal processing system is evaluated using test signals from both a function generator and the BPM in the test-rig, to verify the speed and precision of the processing algorithm. The processing system can determine the beam position in eight BPMs, with a precision of better than 20 µm, within one microsecond of the signal sampling being completed.

FETS BPMS

Eight BPMs are being installed in the FETS medium energy beam transport (MEBT) after the radio-frequency quadrupole (RFQ). Six of the BPMs are in-house designed button BPMs that have been described previously, along with a description of the wire-rig [1]. The remaining two BPMs are strip-line types that are manufactured to a design from the LINAC4 group at CERN, Geneva [2]. The prototype button BPM was originally tested using a wire-rig (Fig. 1), with the output from the electrodes being acquired by a four-channel oscilloscope, the data then being read and analysed to produce a wire position in the *x* and *y* axes.

The beam (or wire) position in X and Y is given by Eqn. 1 and 2, where V_{right}, V_{left}, V_{up} and V_{down} are the voltages as measured on the right, left, up and down electrodes respectively. The constants S_x and S_y are the sensitivities for the relevant axes, d_x and d_y are the relevant position offsets.

$$Position_x = \frac{1}{S_x} * \frac{V_{right} - V_{left}}{V_{right} + V_{left}} + d_x \quad (1)$$

$$Position_y = \frac{1}{S_y} * \frac{V_{up} - V_{down}}{V_{up} + V_{down}} + d_y \quad (2)$$

G.Boorman@rhul.ac.uk

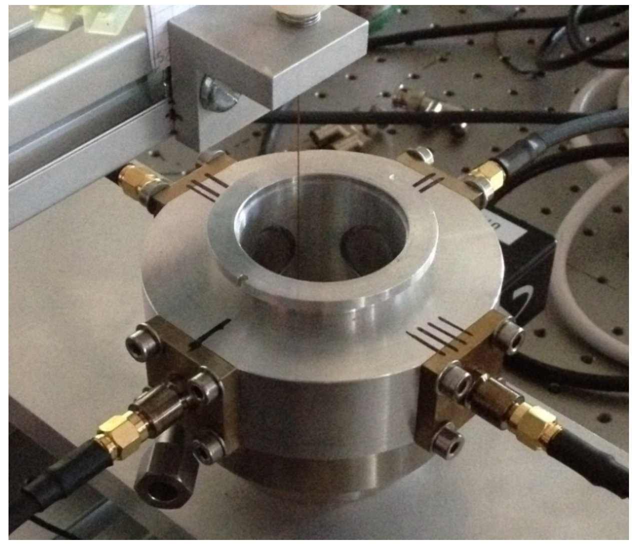

Figure 1: Prototype button BPM on the wire-rig system.

Beam Position Requirements

The ion beam rms width varies as it traverses the MEBT, varying from around 1 mm to about 20 mm. The beam position is required to be known to a precision of better than 100 µm. The beam position during the rising edge of the macro-pulse moves around, due to the stabilisation time of both the pulsed ion source extraction voltage and the space charge compensation, so several position samples of the beam must be taken during this 50 µs period [3]. The position calculation must be completed within 1 µs to avoid result pile-up in the FPGA position-calculation section. The BPM is tested on the wire-rig, and the position calculated using the FPGA, to establish the constants S_x and S_y and the accuracy of each constant.

BEAM POSITION MEASUREMENT

The signal from each BPM electrode is down-mixed, using a single stage mixer, from 324 MHz to 10.125 MHz intermediate frequency (IF), using a local oscillator (LO) frequency of 313.875 MHz. The electronics used is based on a design used by the BPM development group working on the LINAC4 H^- accelerator at CERN. The output filter has been adjusted to take into account the different IF values.

Wire-rig and Ion Beam Signal Levels

The electronics has digitally-controlled amplifiers and attenuators before the mixer, and again after the low-pass

ISBN 978-3-95450-176-2

filter. The resulting IF signal is amplified and filtered, with a maximum output level of 2 V_{p-p}. The simulated signal level from one electrode, with a 0.35 mm diameter wire in the centre of the BPM, is around 5.5 mV_{p-p} (≈ -40 dBm), rising/falling by a factor 1.126 when the beam is moved six millimetres towards and away from an electrode, as shown in Fig. 2.

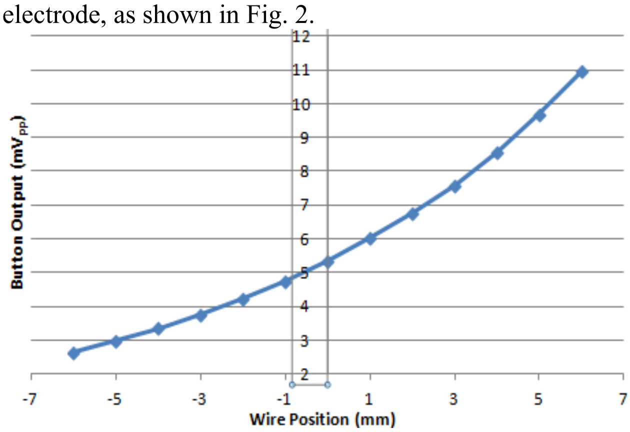

Figure 2: Simulated electrode signal level for a ø0.35 mm wire moving between -6 mm and +6 mm in the BPM.

The BPM electrode output from a macro-pulse of a centrally-positioned, 3 MeV beam at 60 mA has been calculated to be about 350 mV_{p-p} (≈ -5 dBm). The electronics has sufficient adjustment range to allow both testing using the wire-rig and operation with a real ion beam, allowing a maximum output level of 1V_{p-p} for the largest expected electrode signal. The displacement factor has been measured to be the same for both *x* and *y* axes, within the accuracy required.

Signal acquisition and IQ sampling

Since the beam position causes the electrode signal to only vary in amplitude and not frequency, the signal can be sampled at exactly four times the IF to obtain the signal amplitude, rather than many times per cycle. The sample rate is therefore 40.5 MS/s, which can be locked, using integer multiples and divisors, to the RF of 324 MHz and the LO of 313.875 MHz. The IQ sampling is shown Fig. 3.

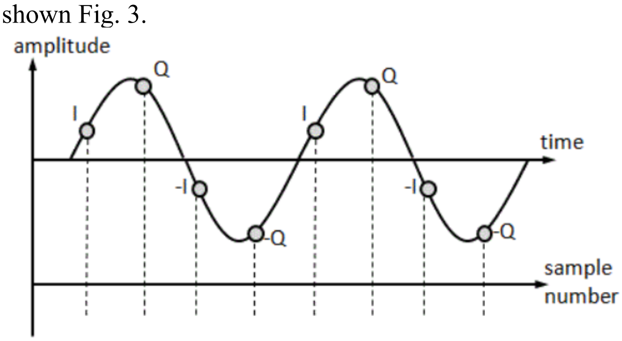

Figure 3: IQ sampling.

The amplitude and phase of the sampled signal is given by Eqn. 3 to 6. The peak amplitude for the positive and negative halves of the cycle are calculated independently allowing any possible offset to be assessed. The phase can be used to determine the time-of-flight between successive BPMs in the MEBT.

$$V_{peak+} = \sqrt{I^2 + Q^2} \tag{3}$$

$$V_{peak-} = \sqrt{-I^2 + -Q^2} \tag{4}$$

$$\phi_+ = tan^{-1}\left({}^{Q}/_{I}\right) \tag{5}$$

$$\phi_- = tan^{-1}\left({}^{-Q}/_{-I}\right) \tag{6}$$

The BPM and electronics noise contribution is negligible to the required BPM position resolution.

DIGITIZER AND FPGA

A PXI-based FPGA card and a digitizer FPGA adaptor module (FAM), both manufactured by National Instruments (NI), are used for determining the beam position and phase using the mixed-down signals from the BPM electrodes. The specifications for the FPGA card, model PXI-7954R, and the digitizer FAM, model NI-5752, can be found in [4, 5]. The FPGA is used in a co-processing mode, which reduces the data load on the PXI chassis backplane and associated RT controller. Other beam-line instrumentation (beam current toroids and Laserwire), as well as the MEBT re-buncher cavity-control FPGA cards, will be added to the PXI chassis [6].

FPGA Programming

The PXI-7954R belongs to the Flex-RIO family of NI FPGA cards and contains a Xilinx Virtex-5 LX110 FPGA. During the BPM processing development phase, the PXI controller ran LabVIEW to enable fast debugging, but will be running LabVIEW Real-Time when the FETS beam-line starts, and will be responsible for control of the other beam-line diagnostics [6]. The position data is streamed from the FPGA card to the PXI controller using one DMA channel. The FPGA code is written in LabVIEW and uses the Xilinx compiler built in to the LabVIEW FPGA Module for code compilation and fitting. The code uses the default 40 MHz clock domain when running on the FPGA. The PXI-7954R and Digitizer FAM are shown in Fig. 4.

The processing code was initially simulated to see what size and speed of FPGA would be required to calculate the positions for eight BPMs, before a decision was taken on which FPGA card to use. The final code takes about 30% of the available FPGA resources, which allows sufficient headroom for further development.

Digitizer FAM

The NI-5752 is a 32-channel, 12-bit, simultaneously-sampled 50 MS/s digitizer module that attaches to, and is directly controlled by, a Flex-RIO FPGA card. Each of the 32 channels is connected to one channel of BPM electrode/electronics, with the channels sampled at 40.5 MS/s. Each digitizer channel signal should be in the range -1 V to +1 V. Signals a small amount outside this

ISBN 978-3-95450-176-2

range will be clamped, but large signals may destroy the device, so the mixer electronics is clamped to ±1 V to ensure damage is avoided.

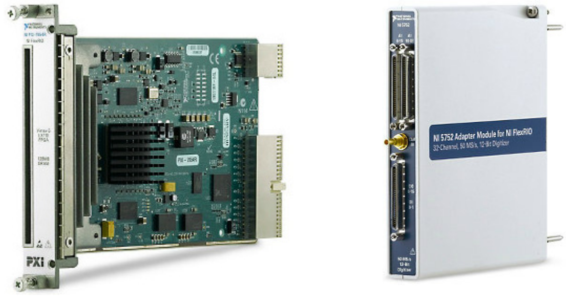

Figure 4: PXI-7954R FPGA card and NI-5752 Digitizer Adaptor Module.

Processing Method

At the start of the macro-pulse a synchronisation pulse starts the FPGA-controlled digitizer acquisition. At each rising edge of the sample clock, the sampled channel data is added to one of four FPGA accumulators, labelled I, Q, -I and –Q, on a round-robin basis. After 1024 sample clock edges (time), the accumulator result data is right-shifted by eight bits, equivalent to dividing each accumulator by 2^8 (256), and the resulting accumulator mean put into FIFOs ready for further processing.

Each output from the total of 128 means now has identical, parallel processing performed. Each mean is squared by multiplying with itself, added to its 'partner' squared mean (eg add BPM1 I^2 to Q^2, $-I^2$ to $-Q^2$ etc), and the square-root of the resulting sum it calculated. The square-root results from opposite pairs of BPM electrodes are then divided to obtain a position ratio. The ratio is scaled by the relevant sensitivity factor, which has previously been loaded into a look-up-tale (LUT). The resulting beam positions for both the positive and negative parts for each axis of all the BPMs is then DMA'd to the PXI host controller for distribution to BPM position client software. For phase of the BPM signal is calculated by taking the arctangent of Q/I and –Q/-I.

Position Calculation Time

The LabVIEW FPGA module has a set of functions, from the *high-throughput maths* palette, allowing deterministic operation on fixed-point numbers running on FPGA targets. Each function can be configured to accept a fixed-point number as input, and convert it if necessary, within the same clock cycle. Handshaking is used between functions to indicate when an operation has completed.

The multiplication and addition functions are all 'single-cycle' operations, meaning they take one clock cycle. One clock cycle for a 40 MHz clock is 25 ns. The number of clock cycles taken to perform square-root, division and arctangent functions is the number of bits describing the number which is being operated on.

To minimize the time taken for the bit-length dependent operations, each number is described using fixed-point representation, the number of bits being sufficient to express the largest value that can occur. The digitizer interface reads out 256 12-bit numbers thus requiring 20 bits. After squaring and summing the $I^2 + Q^2$ value is described by 41 bits, but the output from square-root function is just 21 bits, and therefore requires 21 clock cycles, totalling 525 ns. The division of two 21-bit numbers requires 22 bits to describe its output, taking 550 ns. The beam position can therefore be calculated in 46 clock cycles, or 1.15 µs using a 40 MHz clock.

Calculation Optimisation

There are several optimisations for the code and compilation parameters that can be made to reduce the position calculation time. The first is to increase the clock rate from 40 MHz for the functions taking the most clock cycles, namely the square-root and division operations. But increasing the clock rate makes the logic more difficult to fit into the FPGA, and a lot of the functions have been optimised for fitting using a 25 ns cycle time. Nevertheless a compilation has been completed using a 45 MHz clock, reducing the position calculation time by around 10%

A further improvement in calculation time can be obtained by reducing the number of samples required for the mean, hence decreasing the number of bits that are necessary. The subsequent division and square-root functions will operate on a reduced number of bits, reducing the amount of clock cycles required. A reduced number of digitizer samples being used for the mean calculation means that more beam positions can be calculated during the macro-pulse. Table 1 summarises the beam sampling time, or interval between successive position determinations, and the corresponding number of clock cycles required for the calculation. The minimum sampling interval is 1.58 µs to avoid calculation pile-up.

Table 1: Number of clock cycles required to calculate beam position for different sampling intervals

Sampling Interval (µs)	Number of clock cycles	Processing time at 40 MHz (µs)
25.28	46	1.15
12.64	44	1.10
6.32	42	1.05
3.16	40	1.00
1.58	38	0.95
0.79	36	0.90

A further decrease in processing time can be achieved by pipelining some of the high-throughput functions, meaning a subsequent calculation, or calculations, can be started before the previous calculation has finished.

BPM SYSTEM CHARACTERISATION

Calibration of the prototype BPM has been performed, firstly to check the function of the wire-rig apparatus,

ISBN 978-3-95450-176-2

BPM and the electronics, but primarily to measure the sensitivity constants, S_x and S_y. The results obtained when using the button electrode outputs were read directly by a four-channel, 8-bit, 2 GS/s oscilloscope showed large errors, since the quantisation noise is significant in the unamplified electrode signal of just a few mV.

The results from a single wire-rig measurement, using the down-mix electronics and the FPGA position calculation are shown in Fig. 5. The error for both x and y axes is less than 20 µm, a factor five better than the positional requirements. Further measurements indicate the linear region extends to around 4 mm from the BPM centre, maintaining a position error within 20 µm, which is in good agreement with the simulated value.

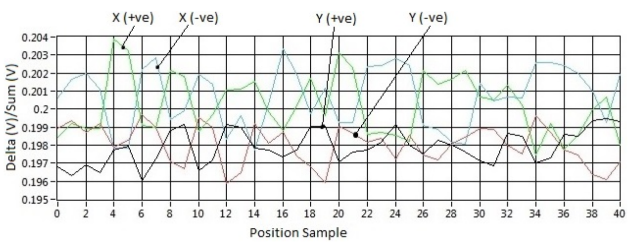

Figure 5: Measured wire position for *x* and *y* axes, for both positive and negative amplitudes.

There is a small discrepancy between the calculated, simulated and measured sensitivities. The simulated sensitivity axis is 1.03±0.02 dB/mm compared with a measured sensitivity of 0.81±0.14 dB/mm. The calculated sensitivity, using the formula in [7], for the FETS button BPM of 40 mm internal diameter and a button of azimuthal diameter 47˚, is 1.67 dB/mm. The sensitivities are summarised in Table 2. The wire-rig and simulated sensitivities are in good agreement. The calculated sensitivity is somewhat higher than the simulated value, but the higher order terms have been neglected in the calculation.

Table 2: Summary of sensitivity values for different calculation methods

Calculation Method	Sensitivity (dB/mm)	Ratio	Difference wrt Simulation
Simulation	1.03	1.126	0%
Wire rig	0.81	1.098	-2.5%
Calculated	1.67	1.212	+7.6%

BPM INSTALLATION

The eight production button BPMs have now been manufactured, albeit with a slight misalignment between the axis of each electrode and their respective mounting holes, as shown in Fig. N. Rotating a BPM in its port by 180˚ reduces the axial misalignment to 0.1 mm with respect to the BPM axis. It is expected that a very small 'tilt' to the measured beam position will be apparent, although this can be corrected by rotating the BPM a slight amount during installation.

The wire position has been read from the LabVIEW real-time controller, to which the calculated BPM positions have been channelled from the FPGA, using network-published shared variables. The network loading passing position data to the BPM viewer client was negligible, and there was no pile-up of data in the RT controller, network or client. The beam position as measured by each BPM will be recorded, along with other beam-line diagnostic data, to monitor and improve the ion-source and beam-line performance.

CONCLUSION

The FPGA and digitizer FAM, along with the associated LabVIEW code, have proved to be part of a very effective beam position measuring system. The requirement for a readout position resolution of 100 µm was exceeded by a factor of five when testing the BPM on the wire-rig, and the total processing time of 1 us allows for a large number of samples during a beam macro-pulse. By using faster clocks for some of the FPGA calculation functions, reducing the sampling interval and more efficient pipelining of functions it is estimated the calculation time can be reduced by around 50%.

The simulated and measured wire positions are in good agreement, and it is expected this agreement will extend to the actual beam position. Further characterisation of all the BPMs to be installed in the beam-line is currently taking place, and additional development of the wire-rig will also occur.

ACKNOWLEDGMENT

We gratefully acknowledge assistance from the LINAC4 group at CERN with the down-conversion electronics.

REFERENCES

[1] G. Boorman et al, "Development of a BPM System using a Commercial FPGA Card and Digitizer Adaptor Module for FETS", Proc. IPAC 2014, THPME186, Dresden, Germany
[2] J. Tan et al, "Commissioning of the CERN LINAC4 BPM System with 50 MeV Proton Beams", Proc. IPAC 2013, MOPWA37, Shanghai, China
[3] J. Pozimski et al, "Investigation of Space Charge Compensation at FETS", Proc. IPAC 2013, THPWA042, Shanghai, China, 2013
[4] http://www.ni.com/datasheet/pdf/en/ds-366.pdf
[5] http://www.ni.com/pdf/manuals/373035b.pdf
[6] G. Boorman et al, "Beam-Line Diagnostics at the Front End Test Stand (FETS), Rutherford Appleton Laboratory, Oxfordshire, UK", Proc. IBIC 2013, TUPC26, Oxford, UK
[7] R.E. Shafer, Proc. Beam Instrumentation Workshop BIW 92, Berkeley, USA, p. 34 (1992)

ISBN 978-3-95450-176-2

DEVELOPMENT OF A SUPERSONIC GAS JET BEAM PROFILE MONITOR

H. Zhang[1,#], V. Tzoganis[1,2], A. Jeff[1,3], C.P. Welsch[1]
[1]Cockcroft Institute and The University of Liverpool, Warrington, WA44AD, UK
[2]RIKEN, Nishina center, Wako-chi, Japan
[3]CERN, Geneva, Switzerland

Abstract

A supersonic gas jet beam profile monitor has been developed by the QUASAR Group at the Cockcroft Institute, UK. It creates a 45 degree supersonic gas curtain to interact with the primary beam, and then collect the generated ions to measure the transverse profiles of the primary beam. The gas curtain functions as a non-interceptive screen, which allows us to insert it into high energy, high luminosity and high power beams without worrying about the damage that normal screen would suffer.

Recently, a new movable gauge module has been implemented in the test stand. The purpose is to investigate the gas curtain density distribution in order to understand the jet better. In this contribution, we will briefly discuss the monitor and focus on the gas curtain measurement with the newly installed movable gauge module.

INTRODUCTION

For almost every particle accelerator used contemporarily, beam profile monitors are an essential tool to diagnose the characteristics of the particle beam such as beam centroids, sizes and emittance. Many methods have been widely used for many years, for example scintillating screens, wire scanners, optical transition radiation, synchrotron radiation and laser wire. Each method has its own benefits and specific parameter space over which it can be applied. Nowadays, for the next generation of high energy, high brightness and high power beams such as the High Luminosity Large Hadron Collider upgrade [1] and the European Spallation Source [2], new methods are required in order to survive the destructive nature of the beams. In addition, low-energy, low-intensity beams of exotic particles such as the proposed Facility for Antiproton and Ion Research (FAIR) [3] require new non-interceptive methods to minimize the influence of monitoring on the beam.

Previously, residual gas Ionization Profile Monitors (IPM) [4] and Beam Induced Fluorescence profile monitors (BIF) [5] have been used in these situations due to their non-invasive properties. However, for both methods, the measurement is usually in one dimension, which means two monitors are required for horizontal and vertical profile measurement. Since both methods rely on the residual gas density or pressure, accelerators operating in ultra-high vacuum will require a stable beam for long periods of time to accumulate sufficient signal. Normally, the BIF method requires much more time for integration under the same vacuum condition than the IPM method, but the latter can have poorer spatial resolution due to the ionization and collecting process; about 1.0 mm rms for positive ions and 4.0 mm rms for electrons has been reported by J. Krider [4] in one of the setup in Fermi National Accelerator Laboratory. A hydrogen jet [6] was also used to create a pressure bump in Brookhaven National Laboratory to diagnose their proton beam but the measurement was still limited to one dimension due to the large thickness of the jet.

Based on these gas-based methods, at the Cockcroft Institute we have developed a beam profile monitor using a thin supersonic gas jet [7,8]. In this paper, we will give a brief overview of the experimental setup and measurement principle. Together with the newly installed moveable gauge module, we will discuss the supersonic gas jet properties and the related resolution for this monitor.

EXPERIMENTAL SETUP

The whole setup of this monitor is shown in Fig. 1. In order to produce a supersonic gas jet, a 30 μm diameter nozzle was used in the nozzle chamber. Using a differential pumping technique, gas can flow through the nozzle from the gas cylinder with a high stagnation pressure (1-10 bars) to the low pressure area, the nozzle chamber (about 10^{-3} to 10^{-4} mbar in the pulsed operation). With such a large pressure decline, the gas enters the nozzle chamber without the sense of boundary condition and expands freely until a Mach disk is formed [9]. In this process, gas flow reaches a supersonic speed inside the Mach disk and then returns to a subsonic speed very quickly after the Mach disk. A conical skimmer (180 μm in diameter) is placed a short distance after the nozzle to accept the supersonic flow and collimate the flow. From the formula in [10], the distance between the nozzle exit and the Mach disk is proportional to the square root of the ratio of this stagnation pressure and nozzle chamber pressure. For our case it can be in the range of several tens mm. A 3D translation stage is attached to the nozzle to align the nozzle with skimmer as well as modifying the nozzle-skimmer distance to make sure the gas flow expands to supersonic speed and the Mach disk is not

#hao.zhang@cockcroft.ac.uk

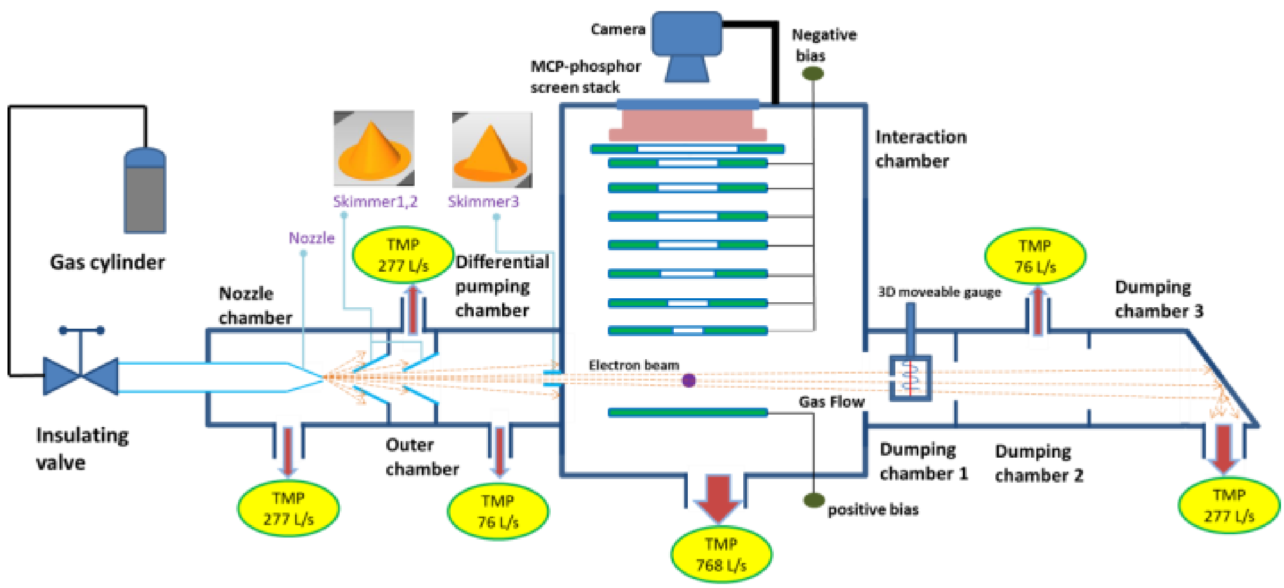

Figure 1: Schematic of the experimental setup

reached when the flow is collimated by the first skimmer. The gas loading is controlled by a pulsed valve with a sharp opening time on the millisecond level [10]. The formed supersonic gas jet is further collimated by a second conical skimmer (400 µm in diameter) which is positioned 25 mm from the first skimmer before the differential pumping chamber. The final collimation is done by a rectangular skimmer rotated by 45 degree with respect to the measured beam and placed at 325 mm from the first skimmer and before the interaction chamber. The jet is collimated as 45 degree screen in order to allow two-dimensional measurement. Two sizes of this third skimmer have been tested, 7.2×1.8 mm^2 and 4.0x0.4 mm^2. In normal operation the jet flows mostly across the interaction chamber and into the dumping chambers where it is pumped out by two turbo molecular pumps. In that way, the vacuum condition in the interaction chamber can be minimally affected.

Inside the interaction chamber a 3.5 keV electron beam was created and propagate perpendicular to the flow of the supersonic gas jet curtain. When collisions occur between the electron beam and the gas jet, the gas molecules will be ionized and then the produced ions will be accelerated by an external static electrical field. The field is generated by a series of hollow metallic electrodes biased at different potential levels to create a 12 kV/m potential gradient. After that, a Micro-channel plates and phosphor screen stack is implemented to amplify the ion signal and convert the signal to scintillating light which can be viewed by a CCD camera.

EXPERIMENTAL RESULTS FROM DIFFERENT THICKNESS JET CURTAIN

Previously, a larger third skimmer (7.2×1.8 mm^2) was used for preliminary tests as shown in Fig. 2. Since the size is relatively large, it makes the alignment relatively simple. In Fig. 3, we see images from both the gas jet and residual gas. The image from the gas jet is much brighter than that from the residual gas due to its higher localized density which increases the possibility for collisions to occur.

The Gaussian fit from the point of the maximum intensity gives a spot size of $\sigma_x = 0.42 \pm 0.02$ mm, $\sigma_y = 1.23 \pm 0.03$ mm for the gas jet image and $\sigma_x = 1.01 \pm 0.07$ mm for the residual gas image. The error here or for later Gaussian fit only shows the statistical error of the Gaussian fit with a 95% confidence bound, without considering the real resolution. The smaller size measured from the gas jet ions in the x direction is due to the smaller thermal spread of gas jet molecules compared with the residual gas, which is due to the low temperature characteristics of the supersonic gas jet. Normally the temperature of the supersonic gas jet is as low as few tens of degrees Kelvin. Along the y-axis, since residual gas fills the whole chamber, the image from the residual gas is limited only by the boundary of the metallic plates used to generate the extraction field. The increased brightness close to the edge illustrates the nonlinearity of the electric field close to the plates, which could degrade the resolution the monitor if the collision between the jet and electron beam happens near the fringe of the electric field. Another factor which affects the resolution particularly in the y axis is the thickness of the jet. For the jet curtain, since the larger skimmer is used, the thickness of the jet is at least $1.8/\sin(45^\circ) = 2.5$ mm, which is much larger than the electron beam. In practice there is also an expansion of the jet after the final skimmer until the interaction point, so the thickness will be even larger. If we assume the measured beam size in y-axis will be the true size plus the jet thickness and regard the beam is equal sized in x and y axis, we can estimate roughly the jet thickness from the measurement. This assumption could be confirmed by an insertable phosphor screen directly measuring the electron beam which gives an approximately round beam shape. If we also assume the jet distribution is Gaussian.

ISBN 978-3-95450-176-2

We can calculate the jet thickness (RMS size) as $\sigma_y - \sigma_x$, we get a value about 0.81 mm. Notice the RMS jet thickness at the third skimmer is $2.5/2\sqrt{3}$ = 0.72 mm (uniform distribution assume here, which is most likely happen after the collimation). There is a 12.5% growth of the thickness.

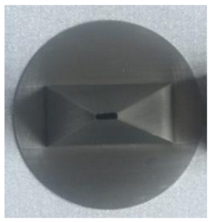

Figure 2: Picture of the previously used third skimmer with sizes 7.2×1.8 mm^2.

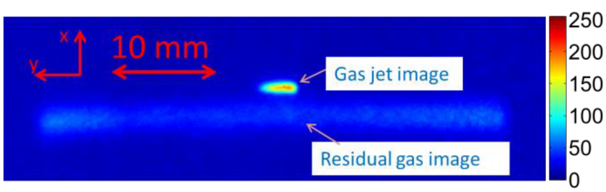

Figure 3: Images of the electron beam from both gas jet (larger size third skimmer) and residual gas.

Recently, a smaller rectangular skimmer (4×0.4 mm^2) has been installed to replace the larger size third skimmer as shown in Fig. 4. Although the alignment for this skimmer is more difficult, the curtain thickness can be considerably reduced. This will give a better resolution in the y axis which should allow a true 2-dimensional beam profile to be measured. As seen from the figure, the rotation angle is 32 degree due to limitations of the current mounting system. Fig. 5 is an example of this measurement with the same electron beam source. Note that some camera settings such as shutter time and gain have been changed to get a better image and the focus in the electron gun was also slightly changed thus measurements cannot be directly compared to each other. The Gaussian fit from the point of the maximum intensity gives a beam size σ_x = 0.56 ± 0.02 mm, σ_y = 0.53 ± 0.03 mm for the gas jet image and σ_x = 1.52 ± 0.07 mm for the residual gas image. For this measurement, since the beam size is comparable to the jet thickness (0.4/sin(32˚) = 0.75 mm), the previous assumption used to calculate the jet thickness is no longer applicable. Thus a detailed scan of the jet itself needs to be done using another method.

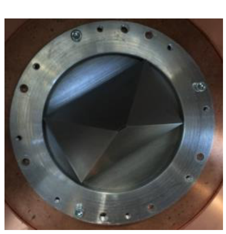

Figure 4: Picture of the newly third skimmer with sizes 4.0×0.4 mm^2.

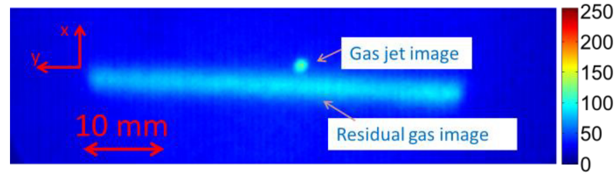

Figure 5: Images of the electron beam from both gas jet (smaller size third skimmer) and residual gas.

GAS JET DENSITY DISTRIBUTION MEASUREMENT

In order to understand the distribution of the gas jet curtain with the smaller skimmer, a moveable gauge module has been recently installed inside the first dumping chamber as shown in Fig. 1. The compression gauge concept [11] is used where the gauge is closed inside a small tube, with only a 2 mm slit open to accept the jet. The schematic of the compression gauge is shown in Fig. 6. Compared with a through gauge system, where there is no such closed tube, the surrounding pressure built up by the rest of the jet will not affect the measurement much. Here, we use a Granville-Phillips Series 274 Nude Bayard-Alpert Gauge. The whole module is attached to a 3D translation stage outside the vacuum chamber. The measured signal will be a time integration of the jet entering through the slit, and this signal will be amplified by a pico-ampere meter and then collected by a scope.

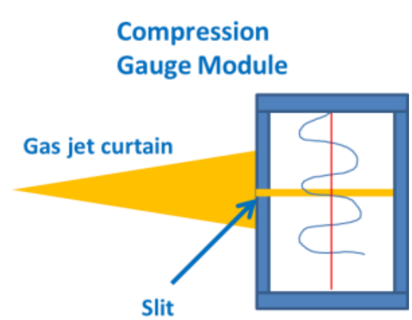

Figure 6: The schematic of the compression ion gauge module.

A typical measurement of the gas jet curtain from this gauge module is shown in Fig. 7. In the figure, the red curve indicates the trigger for pulse valve opening. The pulse width is 1.50 s. The blue curve represent the case when partial of the jet enters the compression gauge module through the slit, while the purple one shows the case that there is no jet entering the slit and the pressure bump is from the overall pressure change due to the jet flowing into the first dump chamber. Notice that in order to compare the two cases, the pressure curve shown here is the original pressure curve offset by the base pressure or the static pressure. It is clear that when there is a jet into the gauge module, the pressure rise follows the trigger immediately, because of the supersonic property of the jet; otherwise, the pressure rises more slowly.

ISBN 978-3-95450-176-2

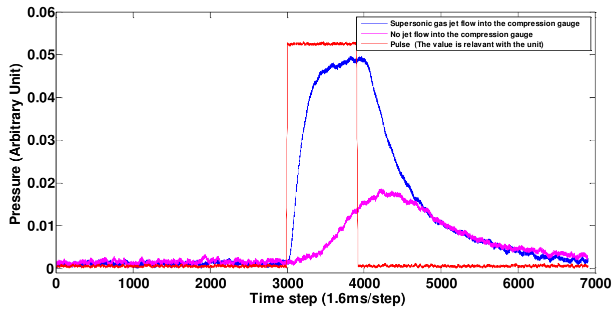

Figure 7: Measured pressure change of the moveable ion gauge.

Following the same procedure, we did a vertical scan across the gas jet. Pressure curves related to different vertical positions of the gauge are plotted in Fig. 8. For each curve, we acquire the maximum pressure and plot them in Fig. 9 against vertical position, thus giving a vertical distribution of the gas jet curtain. It can be seen that this distribution has a Gaussian shape, and a Gaussian fit shows that the gas curtain vertical distribution has RMS size of 1.01 ± 0.07 mm (one sigma), and the FWHM is 2.38 ± 0.17 mm. Considering that the vertical size of the skimmer is 4*sin(32°) = 2.12 mm, the collimated jet at this location will most likely be uniform and thus the RMS vertical size can be calculated as $2.12/2\sqrt{3}$ = 0.61 mm. Then the expansion of the curtain in vertical dimension over a long distance, i.e. from the 3rd skimmer to the moveable gauge which is about 560 mm, is rather small. This indicates that the jet is well collimated by the series of skimmers. By assuming the expansion is linear, we can obtain the vertical size of the jet.

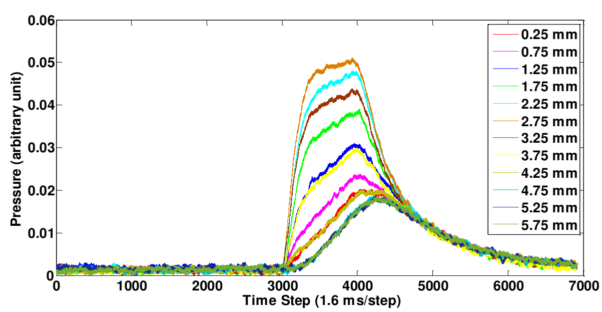

Figure 8: A vertical pressure scan of the gas jet from the moveable gauge module. Plots show the pressure curve at a few selected gauge positions.

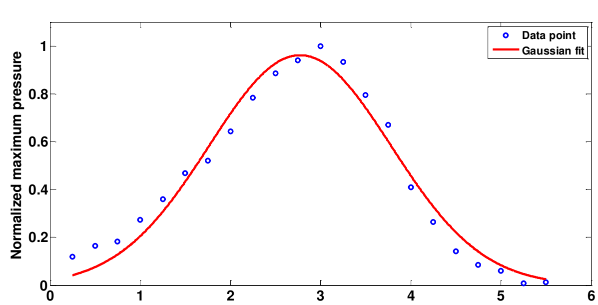

Figure 9: A vertical density distribution at the first dumping chamber.

To investigate the gas dynamics of the jet, we vary the distance between the nozzle and the first skimmer. Two measurements are made at each position: the jet pressure is measured with the moveable gauge module and the peak intensity from the gas jet image. The input pressure from the gas cylinder is kept at 5 bars and the pulse duration is kept at 1.5 seconds. For the jet pressure measurement we set the slit of the gauge module at the vertical position where the maximum density of the jet is achieved. Each data point represents the pressure rise for a specific nozzle skimmer distance as shown in Fig. 10. We can see that the pressure decays exponentially with a distance constant of about 3.76 mm. This decay is similar to the decay in gas density. Based on theory we assume that a pressure drop to one thousandth of the initial level indicates the position of the Mach disk, the latter is located at about 25.8 mm for the stagnation pressure.

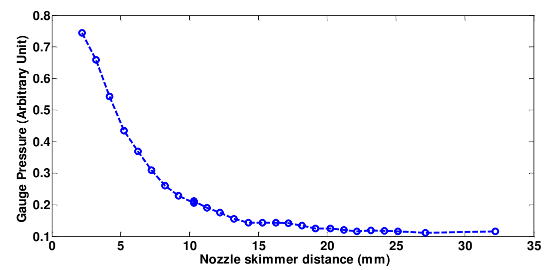

Figure 10: Plot of sampled supersonic jet pressure measured at the first dump chamber by the moveable gauge module versus nozzle to first skimmer distance.

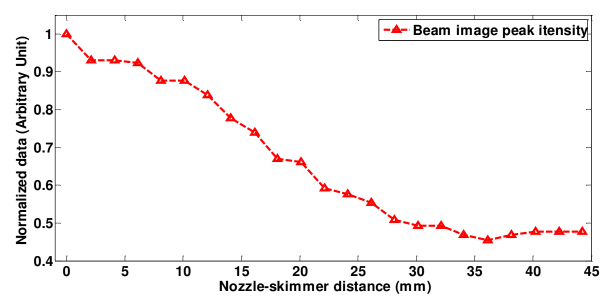

Figure 11: Plot of Peak intensity of the image from gas jet versus the nozzle to first skimmer distance.

From the peak intensity of the gas jet image with respect to the nozzle skimmer distance shown in Fig. 11, we see a quasi-linear decay of peak intensity and the Mach disk location should be larger than 30.0 mm. The formula describing the Mach disc [9]

$$X_M = 0.67 * d * \sqrt{\frac{P_0}{P_a}}$$

where X_M is the Mach disk location, d is the nozzle diameter (30 μm), P_0 is the stagnation pressure (5 bars), P_a is the boundary pressure inside the nozzle chamber (1.0e-3 mbar), then yields X_M = 45.0 mm. The measured Mach disk location is smaller than the theoretical value

ISBN 978-3-95450-176-2

because the theory does not include the skimmer itself which partially reflects the pressure wave and thus reduces the Mach disk distance.

CONCLUSION

In this paper we discussed recent progress on the supersonic gas-jet beam profile monitor. With a new third skimmer added the resolution in the y axis was greatly improved and allowed 2D measurement at the same time. A newly installed moveable ion gauge module opens the door for a detailed analysis of the factors affecting the resolution of this monitor, as well as a better understanding of the supersonic jet formation and dynamics.

Future developments will include a full 3D measurement of the jet, especially scans to study the thickness of the jet as a function of geometrical and thermodynamic parameters. These are key factors determining the achievable monitor resolution. Detailed comparison with the results from gas fluid simulations will then allow to benchmark simulation results and help to future improve the existing design for specific applications.

ACKNOWLEDGMENT

This work is supported by the Helmholtz Association under contract VH-NG-328, the European Union's Seventh Framework Programme for research, technological development and demonstration under grant agreement no 215080 and the STFC Cockcroft core grant No. ST/G008248/1.

REFERENCES

[1] R. Jones, E. Bravin, B. Dehning, T.Lefevre and H. Schmickler, 'Beam instrumentation and diagnostics for high luminosity LHC', *Proc. IPAC*, TUAC1, Richmond, VA, USA, 2015.

[2] A. Jansson, C. Böhme, B. Cheymol, H. Hassanzadegan, T. Shea and L. Tchelidze, 'Beam diagnostics for ESS', *Proc. IPAC*, New Orleans, Louisiana, USA, 2012.

[3] A. Peters and P. Forck, 'Beam diagnostics challenges in the FAIR project at GSI', *AIP Conf. Proc. 868*, 98 2006.

[4] J. Krider, 'Residual gas beam profile monitor', Nucl. Instrum. Methods Phys. Res., Sect. A, 278 (3),660-663, 1989.

[5] P.Forck, C. Andre, F. Becker R. Haseitl, and B. Walasek-Hohne, 'Beam induced fluorescence profile monitor developments', Proc. HB2012, WEO1C03 Morschach, Switzerland.

[6] T. Tsang, S. Bellavia, R. Connolly, D. Gassner, Y. Makdisi, M. Minty, T. Russo, P. Thieberger, D. Trbojevic, and A. Zelenski, "Optical beam profile monitor at the RHIC polarized hydrogen jet", *Proc. PAC09*, TH5RFP019, Vancouver, BC, Canada

[7] V. Tzoganis, C. P. Welsch, 'A non-invasive beam profile monitor for charged particle beams', Applied Physics Letters 104, 204104 (2014).

[8] V. Tzoganis, A. Jeff, C. P. Welsch, 'Gas dynamics considerations in a non-invasive profile monitor for charged particle beams', *VACUUM*, 109, pp. 417-424, 2014.

[9] H. Pauly, 'Atom, Molecule, and Cluster Beams I', Taylor & Francis, Berlin, 2000.

[10] H. Zhang, V. Tzoganis, A. Jeff, C. Welsch 'Development of a supersonic gas-jet monitor to measure beam profile non-destructively', *Proc. IPAC*, MOPWI006, Richmond, VA, USA, 2015.

[11] Y. Hashimoto, Y. Hori, T. Toyama, T. Fujisawa, T. Murakami, K. Noda, D. Ohsawa, 'Development of a Beam Profile Monitor using a Nitrogen-Molecular Jet for the J-PARC MR', *Proc. IBIC*, WEPF17, Oxford, UK, 2013.

INSTALLATION STATUS OF THE ELECTRON BEAM PROFILER FOR THE FERMILAB MAIN INJECTOR*

R. Thurman-Keup#, M. Alvarez, J. Fitzgerald, C. Lundberg, P. Prieto, M. Roberts, J. Zagel,
FNAL, Batavia, IL 60510, USA
W. Blokland, ORNL, Oak Ridge, TN 37831, USA

Abstract

The planned neutrino program at Fermilab requires large proton beam intensities in excess of 2 MW. Measuring the transverse profiles of these high intensity beams is challenging and often depends on non-invasive techniques. One such technique involves measuring the deflection of a probe beam of electrons with a trajectory perpendicular to the proton beam. A device such as this is already in use at the Spallation Neutron Source at ORNL and the installation of a similar device is underway in the Main Injector at Fermilab. The present installation status of the electron beam profiler for the Main Injector will be discussed together with some simulations and test stand results.

INTRODUCTION

Traditional techniques for measuring the transverse profile of proton beams typically involve the insertion of a physical object into the path of the proton beam. Flying wires for instance in the case of circulating beams, or secondary emission devices for single pass beamlines. With increasing intensities, these techniques become difficult, if not impossible. A number of alternatives exist including ionization profile monitors, gas fluorescence monitors, and the subject of this report, electron beam profile monitors.

The use of a probe beam of charged particles to determine a charge distribution has been around since at least the early 1970's (see [1] for references to previous devices). The most recent incarnation of this technique is a profile monitor in the accumulator ring at SNS [2].

An Electron Beam Profiler (EBP) has been constructed at Fermilab and has been installed in the Main Injector (MI). The MI is a proton synchrotron that can accelerate protons from 8 GeV to 120 GeV for use by a number of neutrino experiments, and eventually several muon-based experiments. The protons are bunched at 53 MHz with a typical rms bunch length of 1-2 ns. In this report we discuss the design and installation of the EBP and present some studies of the electron beam and simulation results for the anticipated measurement technique.

THEORY

The principle behind the EBP is electromagnetic deflection of the probe beam by the target beam under study (Fig. 1).

*Operated by Fermi Research Alliance, LLC under Contract No. De-AC02-07CH11359 with the United States Department of Energy.
#keup@fnal.gov

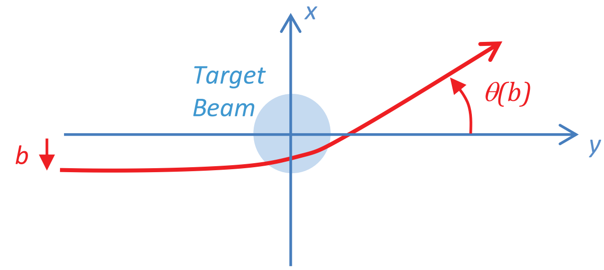

Figure 1: Probe beam deflection (red) for some impact parameter b.

If one assumes a target beam with $\gamma \gg 1$, no magnetic field, and $\rho \neq f(z)$, then the force on a probe particle is

$$\vec{F}(\vec{r}) \propto \int d^2\vec{r}'\rho(\vec{r}')\frac{(\vec{r}-\vec{r}')}{|\vec{r}-\vec{r}'|^2}$$

and the change in momentum is

$$\Delta\vec{p} = \int_{-\infty}^{\infty} dt\ \vec{F}\big(\vec{r}(t)\big)$$

For small deflections, $\vec{r} \approx \{b, vt\}$, and the change in momentum is

$$\Delta\vec{p} \propto \int_{-\infty}^{\infty} dx' \int_{-\infty}^{\infty} dy'\ \rho(x',y') \cdot \int_{-\infty}^{\infty} dt\ \frac{\{b-x', vt-y'\}}{(b-x')^2+(vt-y')^2}$$

where $\{\}$ indicates a vector. For small deflections, $\vec{p} \approx \{0, p\}$ and the deflection is $\theta \approx \frac{|\Delta\vec{p}|}{|\vec{p}|}$. The integral over time can be written as $\mathrm{sgn}(b - x')$ leading to an equation for the deflection

$$\theta(b) \propto \int_{-\infty}^{\infty} dx' \int_{-\infty}^{\infty} dy'\,\rho(x',y')\,\mathrm{sgn}(b-x')$$

where $\mathrm{sgn}(x) = -1$ for $x < 0$ and $+1$ for $x \geq 0$.

If one takes the derivative of $\theta(b)$ with respect to b, the sgn function becomes $\delta(b-x')$ leading to

$$\frac{d\theta(b)}{db} \propto \int_{-\infty}^{\infty} dy'\,\rho(b,y')$$

which is the profile of the charge distribution of the beam. Thus for a Gaussian beam, this would be a Gaussian distribution and the original deflection angle would be the error function, $\mathrm{erf}(b)$. This of course is true only to the extent that the above assumptions are valid.

EXPERIMENTAL PROCEDURE

There are a number of techniques for obtaining $\theta(b)$. A fast scan of the electron beam diagonally through the

ISBN 978-3-95450-176-2

proton bunch can in principle achieve a measurement in one pass of the bunch. This requires a deflection of the electron beam in a period that is much shorter than the proton bunch. For the MI, this would be sub-nanosecond and may be difficult to achieve.

A second method involves slowly stepping the electron beam through the proton beam and recording a deflection value on each turn of the proton bunch (Fig. 2). In this method the electron beam is stationary each time the proton bunch passes, and then is moved to the next impact parameter.

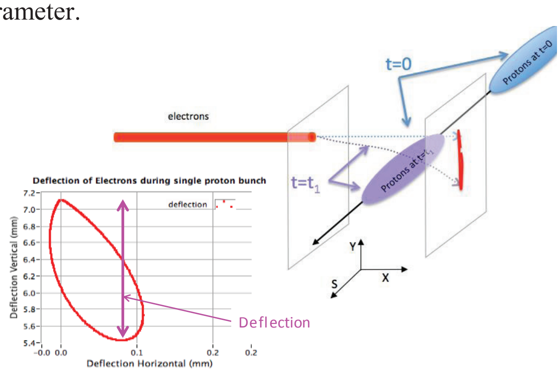

Figure 2: Trajectory followed by a stationary electron beam as the proton bunch passes by. There is some deflection along the proton beam direction due to the magnetic field of the proton beam, but it is much smaller than the deflection transverse to the proton beam.

A variation on the slow scan is to scan quickly along the proton beam direction and slowly transverse to the beam (Fig. 3). The fast scan along the proton beam has a duration similar to the bunch length and allows one to obtain a measurement of the longitudinal beam structure. This longitudinal information can be compared to other instruments and used as a check of the scanning procedure. Additionally, since it is effectively the deflection as a function of longitudinal position within the bunch, it would in principle allow a measurement of the slice profile. At the very least one should be able to obtain head-tail differences.

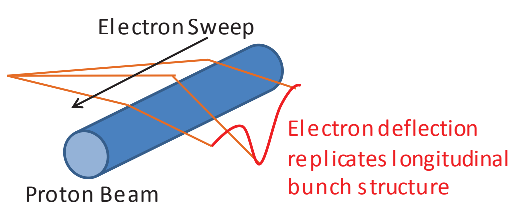

Figure 3: Deflection when the electron beam is scanned along the direction of the proton bunch with duration similar to the bunch structure.

APPARATUS

The device (Fig. 4) that was constructed for the MI consists of the EGH-6210 electron gun from Kimball Physics, followed by a cylindrical, parallel-plate electrostatic deflector, and terminating in a phosphor screen.

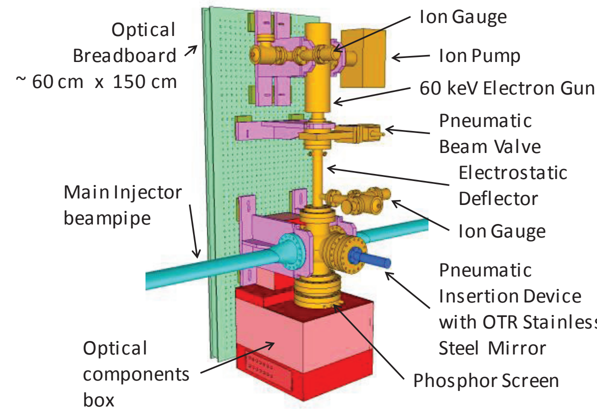

Figure 4: Model of the EBP showing the main components.

The gun (Fig. 5) is a 60 keV, 6 mA, thermionic gun with a LaB_6 cathode, that can be gated from 2 µs to DC at a 1 kHz rate. The gun contains a focusing solenoid and four independent magnet poles for steering/focusing. The minimum working spot size is <100 µm. The electrostatic deflector (Fig. 5) contains 4 cylindrical plates that are 15 cm long and separated by ~2.5 cm. Following the electrostatic deflector is the intersection with the proton beamline. There is a pneumatic actuator at this point with a stainless steel mirror for generating optical transition radiation (OTR) to be used in calibrating the electron beam.

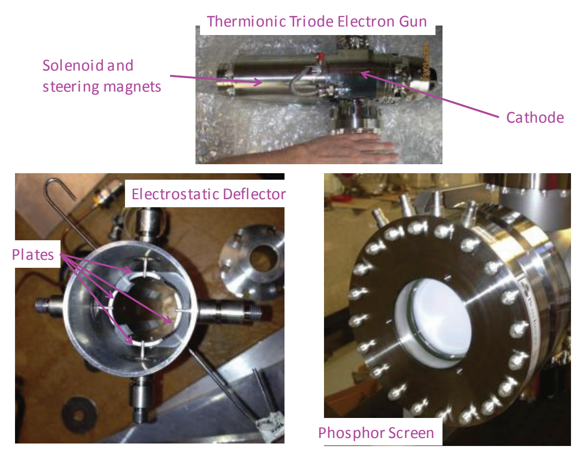

Figure 5: Left) Inside view of the electrostatic deflector showing the cylindrical parallel plates. Right) Phosphor screen mounted in an 8 in conflat flange. A drain wire is attached between the screen and one of the SHV connectors.

After the proton beam intersection there is a phosphor screen from Beam Imaging Systems (Fig. 5). It is composed of P47 (Y_2SiO_5:Ce3+) with an emission wavelength of 400 nm, a decay time of ~60 ns and a quantum yield of 0.055 photons/eV/electron. The phosphor screen has a thin conductive coating with a drain wire attached.

Both the OTR and the phosphor screen are imaged by a single intensified camera system (Fig. 6, 7). The source is

ISBN 978-3-95450-176-2

chosen by a mirror on a moving stage. Each source traverses a two-lens system plus optional neutral density filters or polarizers before entering the image intensifier (Hamamatsu V6887U-02). The output of the intensifier is imaged by a Megarad CID camera from Thermo-electron (now Thermo Scientific) with a C-mount lens.

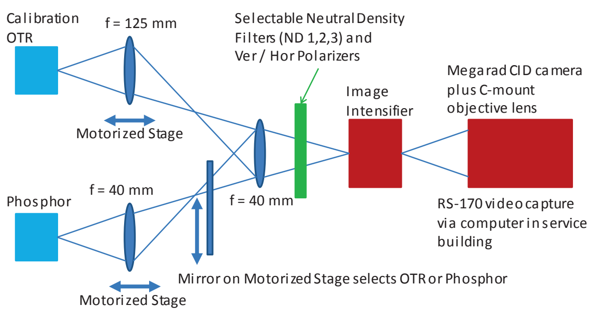

Figure 6: Optical paths followed by the OTR light and the phosphor screen light. Of the two lenses in each path, one is shared.

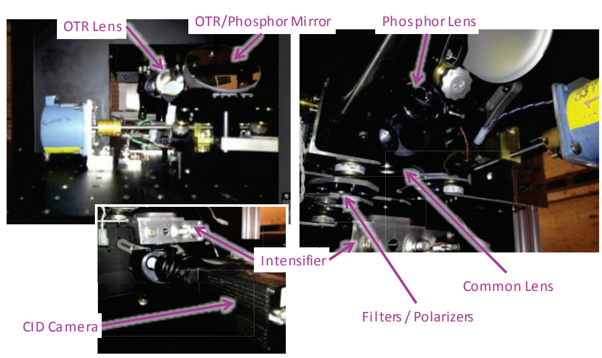

Figure 7: Optical components mounted inside box. The top left picture is looking vertically along the OTR line. The top right picture shows the phosphor path.

TEST RESULTS

A test stand was setup to measure beam characteristics of the electron gun (Fig. 8). It consisted of a pair of screens used to measure the spot size and divergence to verify the manufacturer's specifications and for use in the simulation.

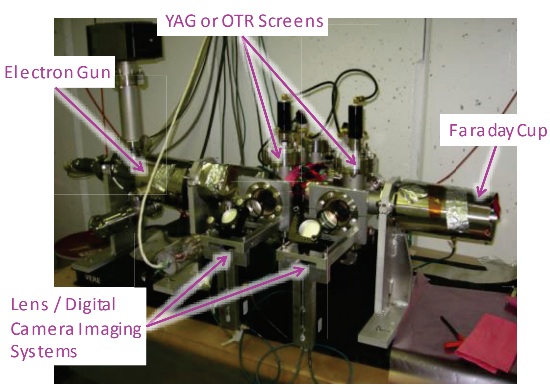

Figure 8: Test stand for measuring beam parameters.

The beam measurements were carried out using the solenoidal magnet in the gun to focus the beam at the first screen, allowing a measurement of the emittance of the electron beam (Fig. 9). Though initial tests were done at 50 keV, the intensity of the MI beam will require an electron energy of around 15 keV.

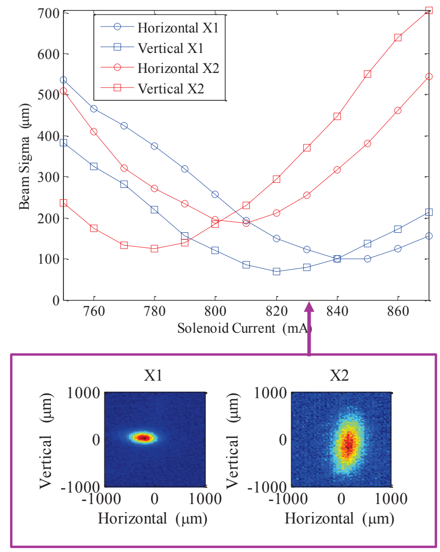

Figure 9: Horizontal and vertical rms beam sizes at the first (blue) and second (red) crosses in the test stand. The measurements are from OTR taken at ~50 keV and 1 mA beam current onto the stainless steel mirrors.

SIMULATIONS

Electron Beam

Simulations of the electron beam were developed both at SNS and Fermilab. The SNS calculations (Fig. 10) showed that the measured profile was within 2% of the actual profile. This simulation was based on the slow stepping method and utilized a pencil beam of electrons.

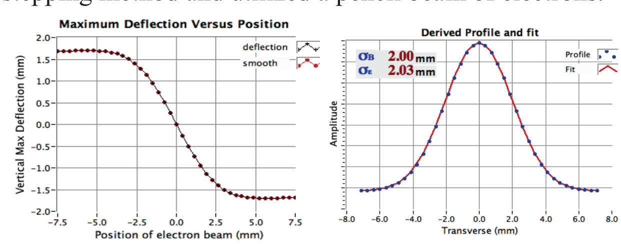

Figure 10: Deflection plot of pencil electron beam, and the derivative of it, showing agreement to better than 2%.

At Fermilab, an electron beam simulation was developed in MATLAB to track electrons through the deflector and proton beam to the phosphor screen. The simulation starts with the measured emittance of the electron gun and propagates the beam through a 2-D calculation of the deflector electric field and through the 3-D electric and magnetic fields of a proton bunch. The time dependence of the deflector field is handled by a linear scaling of the fields. The time dependence of the proton bunch position however, is fully accounted for in evaluating the fields at a given point in time. This

ISBN 978-3-95450-176-2

simulation was focused on using fast sweeps along the proton direction while slowly stepping through the proton beam. Some results of this simulation are shown in Fig. 11.

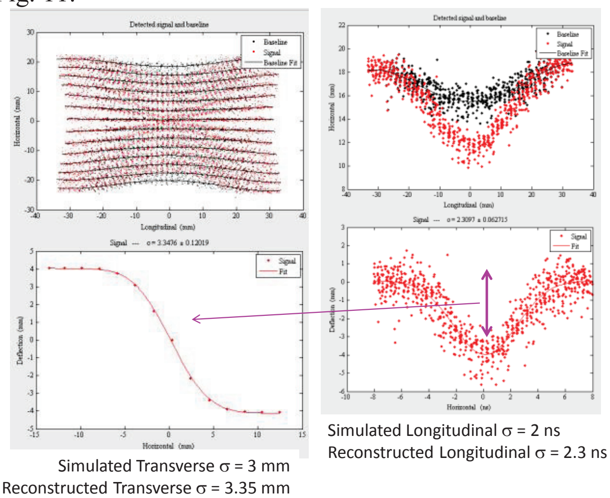

Figure 11: Simulated deflection data for varying impact parameters. The black points are baseline deflections with no beam. They result from the non-uniform deflector field. Each point represents a single electron with the random spread given by the measured emittance.

External Magnetic Fields

External magnetic fields are a serious problem for low energy electron beams. From calculations, a 2 G transverse field will deflect the 15 keV electron beam by 100 mm from gun to phosphor screen. This makes the device inoperable. Figure 17 shows the magnetic fields from the MI magnet busses which are located ~50 cm from the electron beam. The busses run in pairs to mostly cancel the magnetic fields, but there are still low levels remaining. A CST calculation was done to assess the effectiveness of mumetal shielding (Fig. 12).

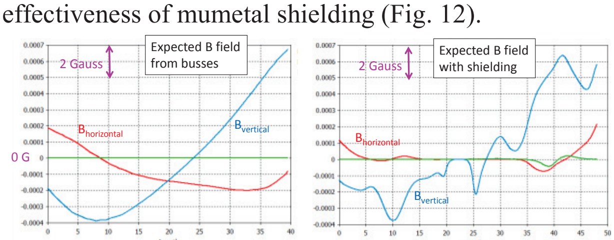

Figure 12: CST simulations of magnetic field from magnet busses along the line of the electron beam. The horizontal component is most important as the electron beam is vertical. Left) The expected dipole field from the magnet busses. Right) The expected field with three layers of mumetal shielding.

The simulation and bench tests both indicated that three layers should be sufficient to eliminate most of the fields. The layers of mumetal were wrapped around the various sections of the EBP separated by welding cloth (Fig. 13). If the mumetal does not work sufficiently, further shielding of the busses may be required.

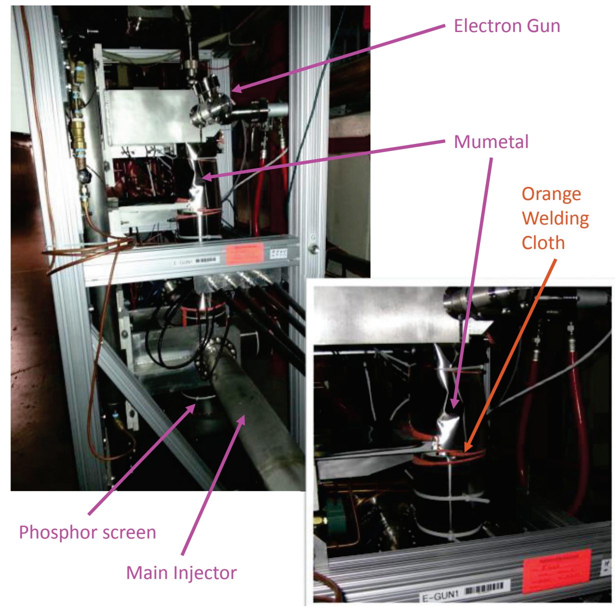

Figure 13: View of the electron beamline showing the mumetal covering.

INSTALLATION

The EBP was installed in the MI during the 2014 shutdown (Fig. 14). The location is near the end of a straight section just upstream of a horizontal defocussing quadrupole (Q622). The expected horizontal rms beam size at this location is several millimetres.

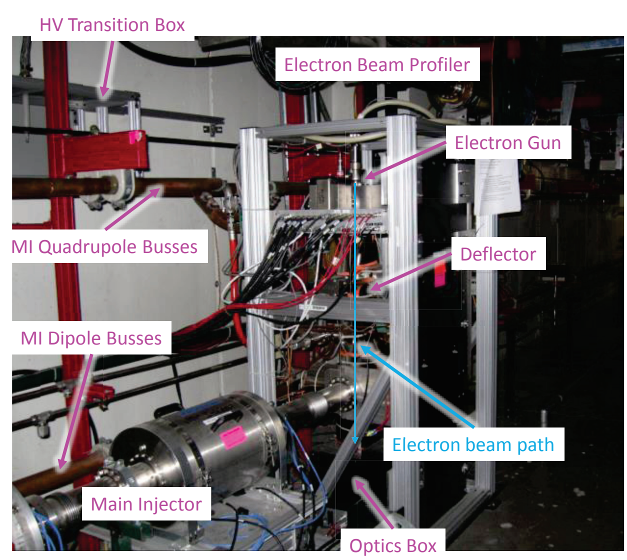

Figure 14: EBP installed in the end of a straight section in the MI. One can see the close proximity to the magnet busses.

Since the installation, effort has been underway to construct the HV transition boxes (Fig. 15, 16) that connect the commercial cables both from the controller in the service building and the gun in the tunnel, to the RG 220 cables that run from the service building to the tunnel.

ISBN 978-3-95450-176-2

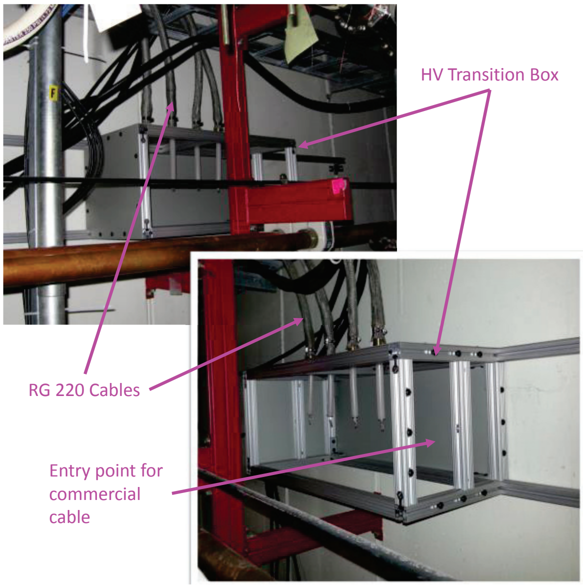

Figure 15: HV transition box in the tunnel. The cables entering from the top are the RG220 cables The commercial cable to the gun will exit from the side panel.

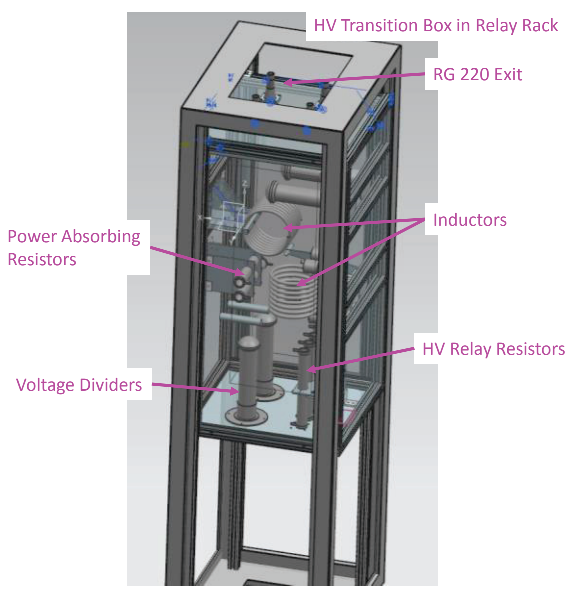

Figure 16: HV Transition box in the service building. This box contains HV relays connected to the safety interlock system, and power absorbers to handle the stored energy in the RG 220 cables.

ACKNOWLEDGMENT

The authors would like to acknowledge the help of the Main Injector, Mechanical Support, Electrical Engineering, and Instrumentation departments for all their assistance in the construction and installation of this device.

The choice of RG 220 cables was driven by two facts: the desire to use the commercial controller which limited the resistance of the cables connecting the cathode; and the availability of the RG 220 cables which were left over from the antiproton kicker magnets.

The service building transition box has a number of HV protection and interlock features as seen in the schematic in Fig. 17. Each of the 4 connections to the gun (2 cathode connections, 1 triode gate, 1 HV reference labelled Vgun in the schematic) have an interlock relay to ground for safety. The gate and HV reference connections also have inductors and resistors in series to protect the controller from the stored energy in the ~80 m cables.

The transition box in the tunnel simply makes the connections between the RG 220 and the commercial cable and has no electrical elements.

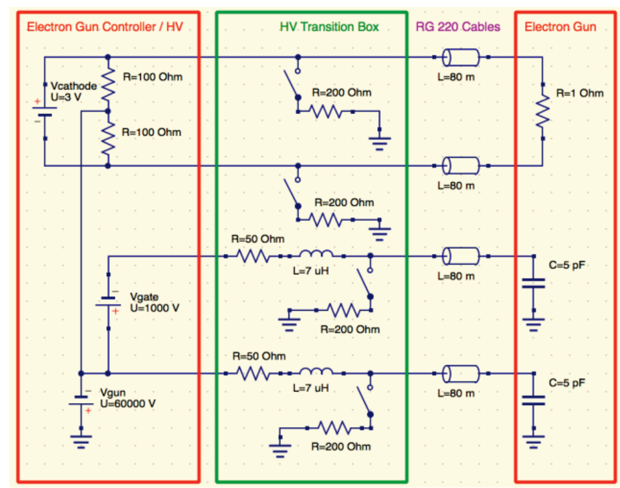

Figure 17: Schematic of HV connections to the electron gun.

SUMMARY

The EBP has been installed in the MI tunnel with mumetal shielding surrounding the electron beamline. The HV transition boxes are in the process of being assembled with the goal of all work in the tunnel being completed before the end of the current shutdown. Initial turn on of the system is planned for early 2016.

REFERENCES

[1] R. Thurman-Keup et al., “Electron Beam Profiler for the Fermilab Main Injector”, IBIC’14, Monterey, September 2014.

[2] W. Blokland, S. Cousineau, “A Non-Destructive Profile Monitor for High Intensity Beams”, PAC’11, New York, March 2011.

ISBN 978-3-95450-176-2

SIGNAL PROCESSING ALGORITHM FOR BEAM POSITION AND PHASE MONITORS AT LANSCE

R. C. McCrady, H. A. Watkins, Los Alamos National Laboratory, Los Alamos, NM 87545 U.S.A

Abstract

The new beam position and phase monitors at LANSCE measure the phase of the beam relative to a reference signal from the master reference oscillator. Because of the various beam pulse formats used at LANSCE the algorithm needs to be flexible and to work well with short bursts of signals. We have developed an algorithm that provides phase resolution of better than 0.25 degrees with signal bursts one microsecond long, and also allows measurement of bursts as short as 100 nanoseconds. For beam position measurements flexibility took priority over precision; the processing scheme provides precision of less than 0.1 mm. In this paper we will present the principles of the algorithm and results of measurements.

INTRODUCTION

We are preparing to install beam position and Phase Monitors (BPPMs) in the linac at the Los Alamos Neutron Science Center (LANSCE.) The transducers are 4-electrode shorted-stripline detectors; the 201.25MHz signals from the electrodes are sampled at 240 Msamples/second, along with a 201.25MHz reference signal. These sample streams are processed using a custom algorithm in a field-programmable gate array (FPGA) to provide both the position of the beam and the phase (arrival time) with respect to the reference signal.

The signal-processing algorithm was developed to provide good precision for the phase measurement, as this is used for the Δt turn-on process [1] for the linac, where the energy of the proton beam can be inferred using phase measurements at two BPPMs. Another feature of the algorithm is its ability to provide good measurements using short bursts of beam signals. This is important because the LANSCE linac provides beams with various pulse formats to several user facilities.

In the following sections the algorithm is described.

THE ALGORITHM

The algorithm can be thought of as a fit of a sinusoid to the data. That is, an amplitude, phase, and DC offset that best fit the data are determined using a linear fitting process.

The i^{th} data sample of an electrode signal is:

$$y_i = A\cos(wi+\phi)+y_{DC} \tag{1}$$

A and ϕ are the signal amplitude and phase, y_{DC} is the DC offset, and w is the phase advance of the RF waveform per sample interval:

$$w = 2\pi f_{RF} \div f_{sample}.$$

In order to make the fit linear in the fit parameters, Eq. 1 can be written as:

$$\begin{gathered} y_i = a\cos(wi)+b\sin(wi)+y_{DC} \\ \text{where } A^2 = a^2+b^2 \text{ and } \tan\phi = b/a \end{gathered} \tag{2}$$

To keep the notation compact, the series of N samples to be analyzed can be denoted by:

$$\vec{y} = a\vec{c}+b\vec{s}+y_{DC}\vec{u} \tag{3}$$

where $\vec{c}$ is the series of values of cos(wi), $\vec{s}$ is the series of values of sin(wi), and all elements of $\vec{u}$ are one. Each of these vectors has N elements.

Now equation 3 can be multiplied by each vector, $\vec{c}$, $\vec{s}$ and $\vec{u}$:

$$\begin{aligned} \vec{c}\cdot\vec{y} &= a\vec{c}\cdot\vec{c}+b\vec{c}\cdot\vec{s}+y_{DC}\vec{c}\cdot\vec{u} \\ \vec{s}\cdot\vec{y} &= a\vec{s}\cdot\vec{c}+b\vec{s}\cdot\vec{s}+y_{DC}\vec{s}\cdot\vec{u} \\ \vec{u}\cdot\vec{y} &= a\vec{u}\cdot\vec{c}+b\vec{u}\cdot\vec{s}+y_{DC}\vec{u}\cdot\vec{u} \end{aligned} \tag{4}$$

Note that each vector dot product is a scalar number. The entire data series to analyse is now represented by 9 numbers (because some of the dot products appear twice in Eq. 4.) Equations 4 can be written in matrix form:

$$\begin{pmatrix} \vec{c}\cdot\vec{y} \\ \vec{s}\cdot\vec{y} \\ \vec{u}\cdot\vec{y} \end{pmatrix} = \begin{pmatrix} \vec{c}\cdot\vec{c} & \vec{c}\cdot\vec{s} & \vec{c}\cdot\vec{u} \\ \vec{s}\cdot\vec{c} & \vec{s}\cdot\vec{s} & \vec{s}\cdot\vec{u} \\ \vec{u}\cdot\vec{c} & \vec{u}\cdot\vec{s} & \vec{u}\cdot\vec{u} \end{pmatrix} \begin{pmatrix} a \\ b \\ y_{DC} \end{pmatrix} \tag{5}$$

Now all that needs to be done is to invert the matrix in Eq. 5 and multiply the inverse onto the vector on the left-hand side. This will determine the 3 quantities to be fit.

The Vectors of Sines and Cosines

Because the frequencies of the RF and sampling are known, one could in principle compute $\vec{c}$ and $\vec{s}$. We found, however, that slight drifts of the sampling frequency caused problems with the stability of the phase

ISBN 978-3-95450-176-2

measurements, especially with long records (series of data.)

Instead, the stream of samples of the reference signal can be used as the source of $\vec{C}$ and $\vec{S}$. The vector of cosines is taken directly from the reference samples: $c_i = r_i$ where r_i is the i^{th} sample of the reference signal.

To generate the vector of sines, two consecutive samples of the reference are used:

$$s_i = \frac{r_{i-1} - r_i \cos w}{\sin w} .$$

(This can be thought of as a two-tap 90° phase shift FIR filter.)

One advantage of using the reference signal as the source of the fitting model is that the phase of the beam signal is measured directly with respect to the reference. If the beam signal and reference were fitted separately, one would then need to subtract the two phases and deal with phase-wrap issues to get an answer.

IMPLEMENTATION

The dot products in Eq. 5 are computed as data samples stream into the FPGA. The 16-bit samples are multiplied and accumulated and, when the end of an analysis record is reached, the accumulated sums are clocked into registers. This enables the accumulators to begin processing the next record as further analysis steps are executed.

In order to provide the numerical dynamic range necessary to accommodate the wide range of signal strengths and record lengths that we anticipate, much of the algorithm is implemented using floating-point arithmetic. The integer dot products are converted to floating-point representation and the matrix inversion is carried out by expansion of cofactors [2]. The inverse matrix is used to determine the fit parameters. These parameters are converted to amplitude and phase according to Eq. 2. Finally the amplitude, phase, and DC offset are converted back to integers and communicated to the external data system.

This algorithm is rather expensive in terms of FPGA fabric, especially multiplier blocks. The benefits in terms of versatility and precision of the algorithm justify this cost.

PERFORMANCE

One advantage of this approach over algorithms based on Fourier transforms (such as the Goertzel algorithm [3]) is its ability to operate stably on short records. As is typical with these techniques, short records with produce ringing effects in the frequency domain. In particular the measured phase using the Goertzel algorithm depends on the record length, while the fitting algorithm shows no such systematic dependence.

The algorithm presented here works well on beam pulses <100ns long; this is beneficial for us, as such short pulses are frequently used during linac tune-up and for delivery to one of our user facilities.

This system has shown phase resolution of better than 0.25°, meeting our requirement for the Δt turn-on procedure.

We have performed in-situ measurements on this system in order to ensure that the system was characterized in the environment in which it will operate. To perform the tests, we drove one electrode of a transducer with 201.25MHz RF, and picked up the signal on two other electrodes. We used record lengths of 100 samples (400ns.) We used a variety of signal strengths, and found that with signals of ±200 ADC counts the phase resolution was better than 0.1° and the position resolution was better than 20μm.

SUMMARY

The algorithm described above measures the amplitude and phase of a beam-induced signal with respect to a reference signal by using the reference signal as the fit function. This method works well with a wide range of record lengths and signal strengths.

REFERENCES

[1] K. Crandall, et al, "The Δt turn-on procedure," Proceedings of the 1972 proton linear accelerator conference, October 1972, p. 122,

[2] G. Strang, "Linear Algebra and Its Applications," Academic Press, New York, 1980.

[3] P. Sysel and P. Rajmic, "Goertzel algorithm generalized to non-integer multiples of fundamental frequency," Journal on Advances in Signal Processing **2012**: 56 (2012).

ISBN 978-3-95450-176-2

LANSCE 1L HARP DATA ACQUISITION SYSTEM UPGRADE: FIRST RESULTS*

J. Sedillo, D. Martinez, J. Nguyen, LANL, Los Alamos, NM 87545 USA

Abstract

Efforts applied toward the upgrade of the LANSCE 1L harp beam diagnostic data acquisition system have completed with the system's successful deployment in late December 2014. Leveraging the principle of secondary electron emission, the data acquisition system measures the particle beam-induced, negative charge-loss response of a statically-located, harp-style, beam diagnostic sensor. The harp's sense wires span two orthogonal planes, transversely oriented with the beam's direction of travel resulting in two orthogonal profiles. The profile data provided by this beam diagnostic system allows LANSCE operators to measure the particle beam's transverse properties prior to reaching its final destination: the 1L target. Details will be provided with respect to the system's final hardware architecture, the system's theoretical beam response model, and the system's measured beam response.

INTRODUCTION

Shown in Fig. 1, the 1L harp is a fixed-position beam diagnostic sensor for measurement of the beam's transverse profiles immediately prior to impingement on the 1L target. The sensor is composed of three planes of silicon-carbide (SiC) fibers; two sense planes for measuring horizontal and vertical beam profiles, and a bias plane for absorption of secondary electrons. Each sense plane is composed of seventeen sense fibers spaced at 6 mm intervals. All fibers connect to individual 10 pF capacitors at one end and a cable plant at the other end for signal transmission to the data acquisition system [1].

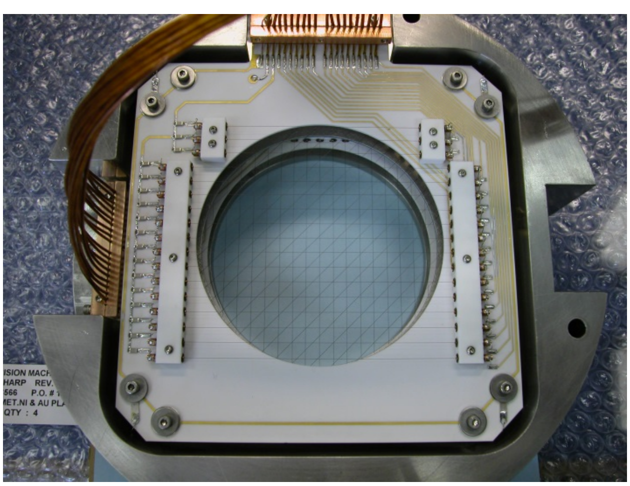

Figure1: 1L harp sensor.

*Funded under the auspices of the US Department of Energy. Contract DE-AC52-06NA25396.

PRINCIPLE OF OPERATION

The 1L harp operates on the principle of secondary electron emission resulting from the interaction of the particle beam with the harp's sense fibers. As the high-energy (800 MeV) H+ particle beam passes through the fiber, electrons from the material are forcefully removed from the fiber's surface into free space, leaving a positive charge gain within the fiber. The positive voltage resulting from the fiber's loss of electrons attracts a flow of electron current from the signal conditioning circuit to the fiber, neutralizing the charge difference. This current and its associated net charge are transformed by the signal conditioning circuitry into a voltage signal proportionally related to the charge. Since the particle beam's transverse particle density is generally Gaussian, each fiber in the plane receives a different amount of beam flux. This beam flux translates into secondary electron emission differences resulting in charge differences at the signal conditioning circuitry and finally a voltage difference at the analog-to-digital converter (ADC) dedicated to each fiber. Plotting the resulting voltages as a function of the fiber's relative position creates a Gaussian profile corresponding to the beam's transverse particle density. General beam and 1L harp parameters are listed in Table 1.

Table 1: 1L Harp and Beam Properties

Beam Property	Value
Beam species	H+
Beam energy	800 MeV
Longitudinal current profile	Triangular
Pulse duration	300 ns
Peak current	33.3 A
Bunch charge	5 μCoulombs
Beam Transverse σ	12.5 mm
Sensor Material	Silicon-Carbide Fiber (SiC)
Sensor Diameter	0.079 mm

BEAM RESPONSE MODEL

In order to model the particle beam's electrical effect on the fibers, the following mathematical tools and theories were employed:

- The Bethe-Bloch stopping power formula [2].

ISBN 978-3-95450-176-2

- Error function for Gaussian integral calculation.
- Sternglass secondary emission yield formula.
- TI ACF2101 electrical response model.

Beam Energy Loss in Silicon-Carbide

The Bethe-Bloch formula describes a beam particle's rate of energy loss per unit distance as it travels through a stopping medium. The formula employed is shown in equation 1. While the stopping material and beam properties required for this calculation are listed in Table 2.

$$-\frac{dE}{dx} = 4\pi N_A r_e^2 m_e c^2 \rho \frac{Zq^2}{A\beta^2}\left[\ln\left(\frac{W_{\max}}{I} - \beta^2\right)\right] \quad (1)$$

$$\mathrm{W}_{\max} = 2m_e c^2 (\gamma\beta)^2 \quad (2)$$

Table 2: Bethe-Bloch Parameters for the 1L Harp

Parameter	Value
N_A	6.02×10^{23}
r_e, electron radius	2.818×10^{-13} cm
$m_e c^2$, electron rest energy	0.511 MeV
ρ, density of SiC	$3.21\ \frac{\mathrm{g}}{\mathrm{cm}^3}$
Z, combined atomic number of Si and C	20
q, charge of a proton	+1
A, combined atomic mass of Si and C	40.1
β, beam velocity ratio relative to speed of light	0.84
γ, beam Lorentz factor	1.85
E_{beam}, beam energy	800 MeV
$m_o c^2$, proton rest mass	938 MeV
W_{max}, maximum energy transfer	2.49
I, ionization potential of SiC [3]	180×10^{-6} MeV

Combining the parameters of Table 2 with equation 1 results in an expected beam energy loss rate or $-\frac{dE}{dx}$ of 6.12 MeV/cm as it travels through a silicon-carbide fiber.

Beam Flux Through a Harp Fiber

A particle beam with a Gaussian, transverse particle/charge density, ideally centered on a thin fiber will provide the maximum amount of particle flux through that fiber. Calculating the particle charge intercepted by the fiber is accomplished by evaluating equation 3, where the Gaussian charge density function is evaluated over the diameter of the wire with a beam of assumed mean position of $\mu = 0$ [5].

$$\mathrm{Q}_{\mathrm{i,ratio}}(r,\sigma) = \int_{-r}^{r} \frac{1}{\sigma\sqrt{2\pi}} e^{\left(\frac{-x^2}{2\sigma^2}\right)} dx = erf\left(\frac{r}{\sigma\sqrt{2}}\right) \quad (3)$$

Evaluating equation 3 with the relevant parameters of Table 1 (i.e. $\mathrm{r} = \frac{0.079}{2}, \sigma = 12.5$) results in $\mathrm{Q}_{\mathrm{i,ratio}} = 0.0025$, or approximately 0.25% of the beam will be intercepted by a fiber placed at beam center. With a bunch charge of 5 micro-coulombs, a 0.25% flux translates to an intercepted charge of 12.6 nano-coulombs.

Since the beam passes through the fiber with relatively low energy loss, the particle flux is enhanced by the particles emerging from the downstream-side of the fiber. Furthermore, since the fiber has a circular cross-section, a geometrical flux-enhancing feature should be considered. This is accomplished by multiplying the charge flux obtained by π since the flux encounters the entire perimeter of the circular fiber. Accounting for this results in an "effective" intercepted charge of 39.6 nano-coulombs.

Secondary Electron Yield Ratio

Knowledge of the stopping power allows for the calculation of the secondary electron yield, Y, per incident beam particle. A formula that models this phenomenon is defined by equation 4 and is known as the Sternglass Theory [4].

$$\mathrm{Y} = \frac{Pd_s}{E^*}\frac{dE}{dx} \quad (4)$$

Table 3 lists the parameters and values suggested by Sternglass along with the energy loss value calculated earlier.

Table 3: Sternglass Parameters for 1L Harp

Parameter	Value
P, probability of electron escape	0.5
d_s, average electron depth	1 nm
E^*, average kinetic energy lost by incident beam particles	25 eV
$\frac{dE}{dx}$, Bethe-Bloch result	6.12 MeV/cm

ISBN 978-3-95450-176-2

Combining the parameters in table 3 with equation 4 results in a yield ratio, Y, of 0.0122 electrons per incident proton.

Knowledge of the effective charge and the yield ratio leads to the determination of charge loss due to secondary emission. Multiplying the effective intercepted charge (39.6 nano-coulombs) by the yield ratio Y (0.0122) results in a maximum expected negative charge loss of 484 pico-coulombs.

ACF2101 Integrator Response

With the expected charge loss determined, it now becomes possible to determine the response of the integrator circuitry. The integrator utilized in the 1L Harp is the Texas Instruments (TI) ACF2101 chip. The integrator circuits of this chip have the behavioral model described by equation 5 [6].

$$V_{out}(t) = \frac{-1}{100 \times 10^{-12}} \int_0^t I(\tau) d\tau = \frac{-Q(t)}{100 \times 10^{-12}} \qquad (5)$$

Substituting the 484 pico-coulomb value into equation 5 results in an integrated response of -4.84 volts. The outputs of the integrators are then digitized by the system's ADCs and negated to positive values prior to profile assembly.

SYSTEM HARDWARE

Beam Signal Conditioning Subsystem/Analog Front End (AFE)

Each ACF2101 integrated circuit features dual, independent integrators with on-die capacitors and multiplexing circuitry for integration, select, reset, and hold operations. Set at 100 pF, the on-die capacitor is capable of measuring up to 1 nano-coulomb of positive charge before the integrator saturates [6]. Beam integration time is variable and can be set by the control logic signals applied to the ACF2101. Additionally, the state of integration is reset after the measurement has been made to prevent interference to subsequent pulse

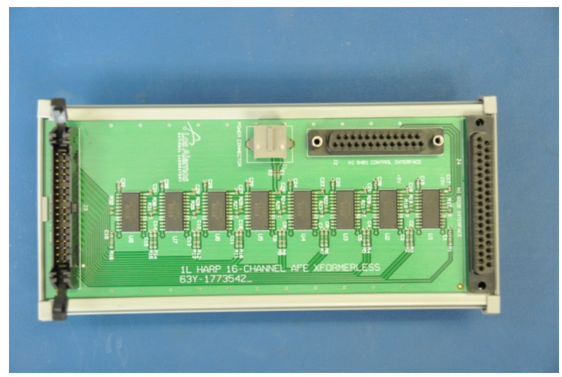

Figure 2: 16-Channel AFE.

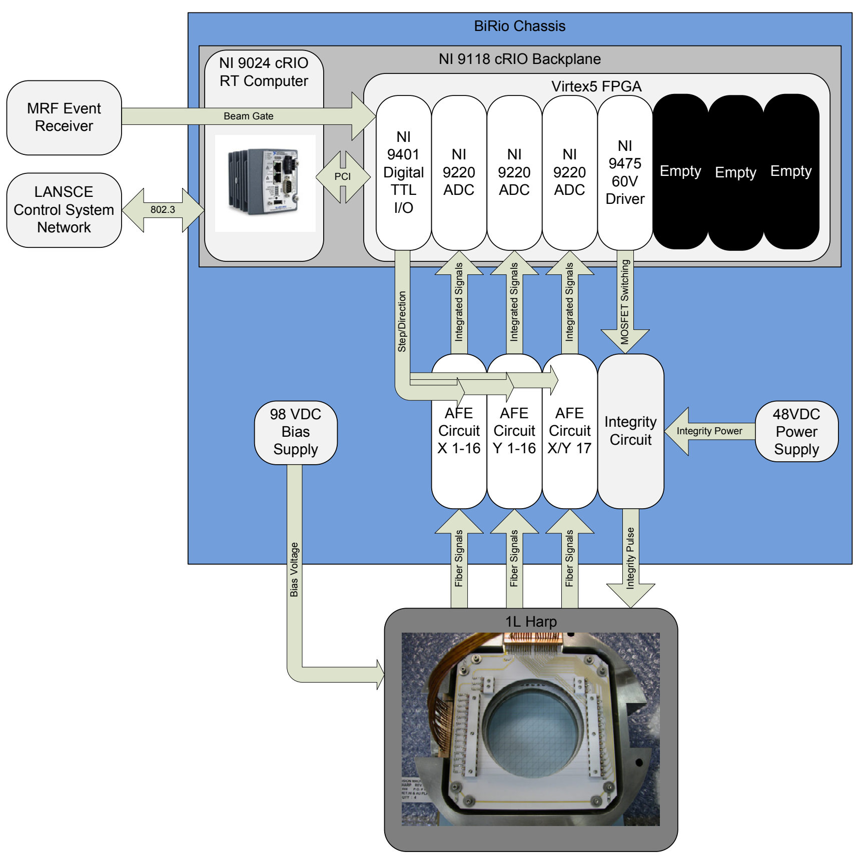

Figure 3: 1L Harp data acquisition system hardware diagram.

ISBN 978-3-95450-176-2

measurements. The final value of each signal's integration is applied to the beam profile for observation. Figure 2 shows one of the system's three AFE circuits. Each board contains eight ACF2101 integrators for processing sixteen channels. Connections to the AFE board include the Harp sensor interface shown on the left of the board, a power connector shown on the top-center, a control connection to the right of the power connector, and the output connector to the ADC on the right.

Data Acquisition System/ EPICS IOC

The overall data acquisition hardware unit (Fig. 3) is composed of a National Instruments CompactRIO computer system with interfaces to the three AFE boards and one integrity board housed within a rack-mountable BiRIO chassis. Logic signals for beam synchronization and ACF2101 control interface to the compactRIO through one NI-9401 10 MHz, 5V TTL logic module. Signals generated by the ACF2101's are digitized by three NI-9220 16-channel, 100kHz, +/-10V ADC modules. Finally, one NI-9475 60V-source module is incorporated for integrity pulse generation. Additional circuitry includes a 100V power supply for the harp bias plane.

Integrity Subsystem

As beam-induced sensor damage is a common mode of failure with harp diagnostics, a fiber integrity subsystem has been incorporated for monitoring the continuity of the fibers. This is accomplished by sending a 48 volt, square pulse to the 10 pF capacitor-end of the fibers. The 10 pF capacitors are applied in series to each wire at the harp and function to AC-couple the 48 volt pulse to the fiber. As the pulse translates through the capacitor-fiber circuit, it is attenuated to a signal on the order of 20 mV with an expected charge displacement of 480 pico-coulombs. Measurement of this signal occurs in the same manner as the beam signal; via charge integration. Through this method, an acceptable integrity signal can be read as -4.8 Volts by the ADCs.

SYSTEM SOFTWARE

FPGA Software Architecture

Harp data acquisition starts with the compactRIO's FPGA and its associated I/O modules. The FPGA program consists of two parallel operations (Fig. 4). The first of these simultaneously monitors the beam synchronization/gate pulse and applies the control signals for all ACF2101 integrators via the NI-9401 module. Since the gate pulse has a narrow, 300 ns pulse width, the NI-9401 must sample at its fastest operating rate of 10 MHz to achieve 2-3 samples per pulse. When the gate has been detected by this process, an internal flag is set, signalling the second parallel process. The primary purpose of the second process is to continuously sample the wire signals at the maximum ADC sampling rate. Once notified of a gate, this process will save the set number (typically 2) of pre-gate, rising-edge samples and

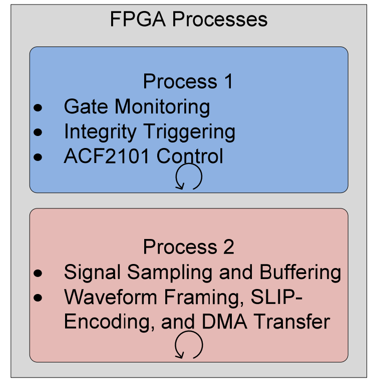

Figure 4: The compactRIO FPGA program architecture.

acquire a set amount (typically 8) of post-gate, rising-edge samples across all 34-channels. These samples are temporarily stored in block memory until all samples have been obtained. Once all prescribed samples have been stored in block memory, their data is framed via SLIP (Serial Line Internet Protocol) encoding, a SLIP-encoded trailer frame is appended, and the data is transferred to the DMA (Direct Memory Access) buffer for retrieval by the compactRIO's Real-Time (RT) computer. Data transferred to the RT process consists of 34, 10-sample arrays representing all waveform data obtained from all sense wires from one, 300 ns beam pulse. Since the waveform data generally represents a monotonic function due to the charge integration process, the final values of the waveforms represent the total accumulated charge for those channels and therefore are used to compose the transverse profile of interest.

Integrity Process

The integrity process operates in a similar manner as that of the beam data acquisition process. Subtle differences include the manner in which the integrity process is triggered and how the integrity data is differentiated from beam data as it is transferred through the DMA channel. Since beam signals are characterized by a 20 Hz pulse rate with a 150 µs-long width, an opportunity for triggering an integrity acquisition presents itself within the remaining ~49 ms of dead signal time. Process 1, mentioned previously in the beam data acquisition process, derives a virtual gate signal for process 2 by calculating the period of the last beam gate cycle, and then adding half of that period to the time the next beam gate is expected to occur. This permits the integrity process to be interleaved with the gate signalling, resulting in an interference-free analysis of wire continuity.

RT Software Architecture

The compactRIO RT computer utilizes a low-priority process for EPICS client interaction and a real-time (RT) process for deterministically extracting waveforms from the DMA channel as shown in Fig. 5. The data stream extracted from the DMA channel is reframed and SLIP-decoded for transfer to an appropriate analysis routine. In this way beam data is averaged and presented to EPICS

ISBN 978-3-95450-176-2

variables for operator display while integrity waveforms are compared with threshold values for wire continuity checking.

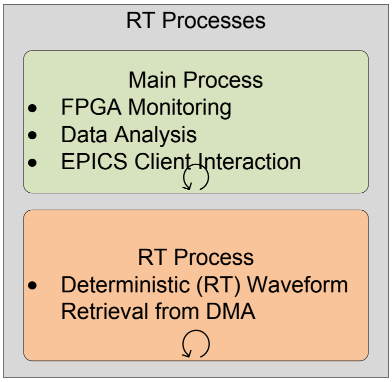

Figure 5: The compactRIO RT program architecture.

SYSTEM PERFORMANCE

Raw beam profiles obtained by the 1L harp system are represented by the red lines in Figs 6 and 7 for the horizontal and vertical planes, respectively. The horizontal profile data indicates a peak intensity level of 3.9 volts, and a standard deviation of 11.48 mm. The vertical profile suffers from a damaged wire at the -12 mm position, causing the Gaussian fit to report an inaccurate standard deviation. From the data it is evident that the particle beam has an elliptical profile with the horizontal axis having the most focused transverse profile and is thus the best profile to compare with the model. Comparing this peak intensity level to the model-predicted level of 4.84 volts indicates a model error of about 19.4%.

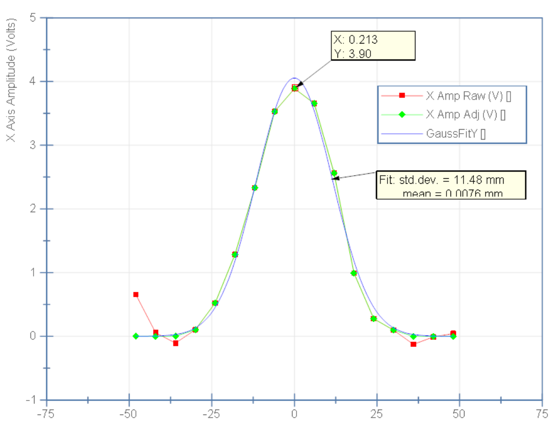

Figure 6: Horizontal profile.

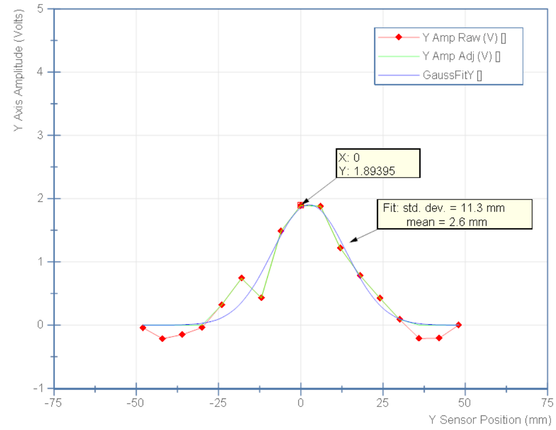

Figure 7: Vertical profile.

CONCLUSION

The model utilized yields a sufficient result for approximating the 1L harp system's electrical exposure to the beam-induced, secondary electron emission and has allowed for predicted signal levels that remain within the system's dynamic range. As for the data acquisition system itself, the compactRIO-based controller and its associated electronics have proven to be a suitable EPICS IOC for obtaining transverse profile measurements from harp diagnostic sensors.

REFERENCES

[1] J.D. Gilpatrick et al.,"LANSCE Harp Upgrade: Analysis, Design, Fabrication, and Installation," TUPSM014, BIW'10, Santa Fe, May 2010: http://www.JACoW.org
[2] W.D. Loveland et al. *Modern Nuclear Chemistry*, (Hoboken: John Wiley & Sons, 2006), 502.
[3] Y. Zhang, et al., "Electronic Stopping Powers in Silicon Carbide," Physical Review B 69, 205201 (2004).
[4] M. Plum, "Interceptive Beam Diagnostics – Signal Creation and Materials Interactions," CP732, BIW '04, Knoxville, May 2004: http://www.JACoW.org
[5] B. Van Zeghbroeck, "Principles of Semiconductor Devices," http://ecee.colorado.edu/~bart/book/gaussian.htm
[6] ACF2101 Data Sheet. www.ti.com/product/acf2101

ISBN 978-3-95450-176-2

PERFORMANCE OF THE NEW FAST WIRE SCANNER AT THE LCLS*

P. Krejcik#, M. Campell, M. D'Ewart, H. Loos, K. Luchini, SLAC, Menlo Park, CA 94306, USA

Abstract

A new fast wire scanner based on a linear dc servo motor acting through dual bellows has been developed at SLAC. After successful beam testing at LCLS we are now replacing all the old style stepping motor driven scanners with the new type. The fast scanner design allows full emittance scans to be completed in seconds rather than minutes as before, facilitating speedier tuning of the accelerator. The low vibration design allows for wire speeds up to 1 m/s, making it also suitable for use in the new LCLS-II machine where high wire speeds are essential to prevent wire breakage from the high power electron beam with a 1 MHz repetition rate. The wire scanner design is presented along with beam measurements demonstrating its performance.

INTRODUCTION

The measurement and optimization of transverse emittances in the Linac Coherent Light Source (LCLS) accelerator relies on beam size measurements performed throughout the machine using wire scanners[1]. Beam profile monitors using OTR screens have proved to be unreliable because of the dominance of COTR effects arising from the very short bunches employed at LCLS. The original SLAC wire scanners, originally intended as a backup measurement for the profile monitors, are fairly slow in operation so that a complete emittance measurement may take several minutes of beam time. This early design is based on a stepper motor and ball screw system driving a cantilevered fork at 45° through the beam[2]. The motor speed must be intentionally kept low for measurements of the LCLS beam in order to minimize vibration.

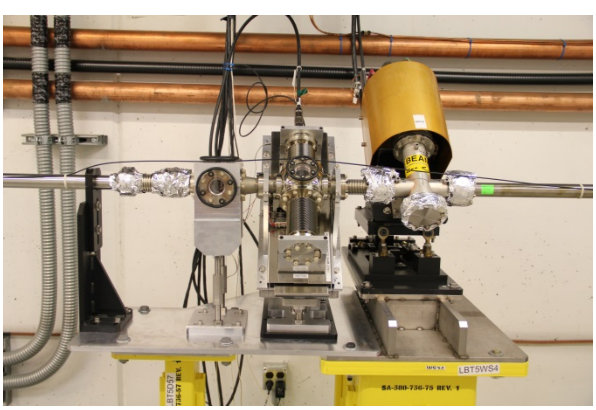

Figure 1: A section of the linac-to-undulator beam line in the LCLS with the new Fast Wire Scanner (middle) installed next to an old style scanner (right).

* This work was supported by Department of Energy Contract No. DE-AC0276SF00515

#pkr@slac.stanford.edu

The need to reduce the accelerator tuning time has motivated us to develop a new wire scanner with higher speeds and minimum vibration. The first of the new fast wire scanners was installed in the linac-to-undulator beam line of the LCLS, shown in Fig. 1, where it could be tested alongside the old style wire scanner.

The advent of the LCLS-II project at SLAC has also resulted in the need for a wire scanner that can move at speeds sufficient to prevent wire destruction during CW beam operation.

For the nominal LCLS-II beam parameters of 100 pC charge per bunch, a transverse emittance of 0.5 μm, and a bunch repetition rate of 0.6 MHz the minimum wire speed to avoid damage is calculated to be 0.34 ms^{-1}.

DESIGN FEATURES

The wires themselves are mounted on an interchangeable card that typically holds an x, y and u (at 45° to the beam axes) wire. The card is moved by a carriage assembly at 45° to the beam axis so that the horizontal, vertical and skew transverse profiles of the beam are measured sequentially. The carriage acts through dual vacuum bellows so that there is no opposing vacuum force for the motor. The carriage moves smoothly on a linear slide that is integrated into the commercially supplied dc linear servo motor assembly [3].

Vibration is minimized in this design since little force is required to move the carriage and the wire card is held at both ends rather than cantilevered as in the old design.

The motor servo control uses an integrated position encoder that allows the motion to be accelerated smoothly to scanning speed and slowed down again within across the total range of travel of 50 mm.

A second external position encoder reads the exact position of the wire with sub-micron resolution at the time of each beam trigger. With this approach the exact position of the wire does not have to be programmed during the scan since we can correlate the signal with the actual measured wire position. This external position encoder is connected to the Beam Synchronous Acquisition (BSA) system in the LCLS controls to seamlessly integrate the data collection during measurements.

The wire scanner assembly mounted on its 45° motion stage is shown in Fig. 2. The at-rest position is down most, against the stops, where no motor holding current is required. A scan of all 3 wire planes can be done in a single upward motion of the scanner before returning to the downward rest position and takes just a couple of seconds. The peak motor current during acceleration for such a scan is of the order of 10 amperes.

The magnetic field generated by the motor drawing this peak current can perturb the electron beam so we placed mu-metal shielding around the motor stage to virtually

ISBN 978-3-95450-176-2

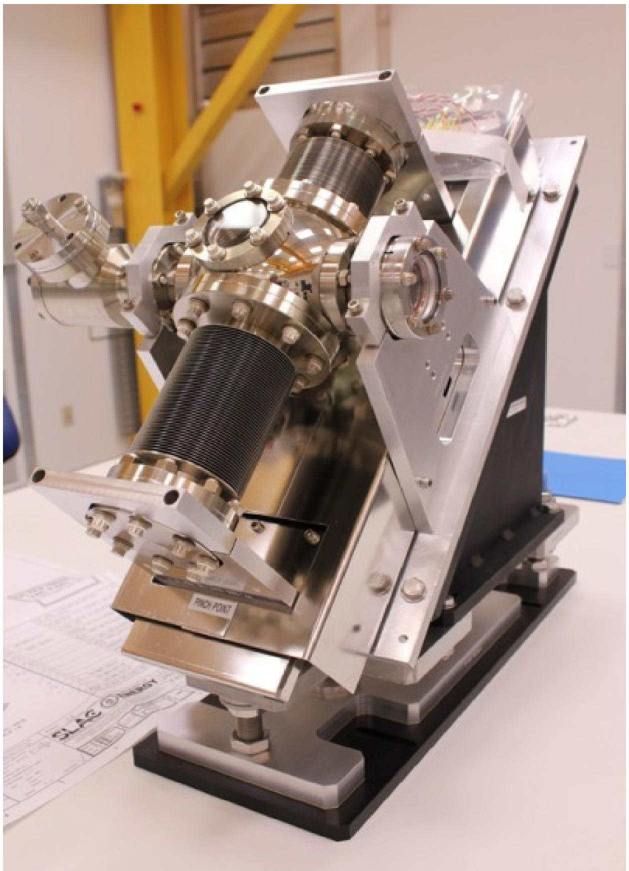

Figure 2: The wire scanner mounted on its 45° motion assembly.

eliminate stray magnetic fields. The linear motor with the shielding removed is shown in Fig. 3.

The mechanical sub-assemblies for the wire scanner are shown in Fig. 4, and the wire card showing details of the arrangement of the x, y and u wires is shown in Fig. 5. Note that in different locations we equip the card with wires of different materials and thicknesses according to how great a beam loss signal we wish to generate. The wires may typically range from 10 µm carbon filaments to 30 µm tungsten wire.

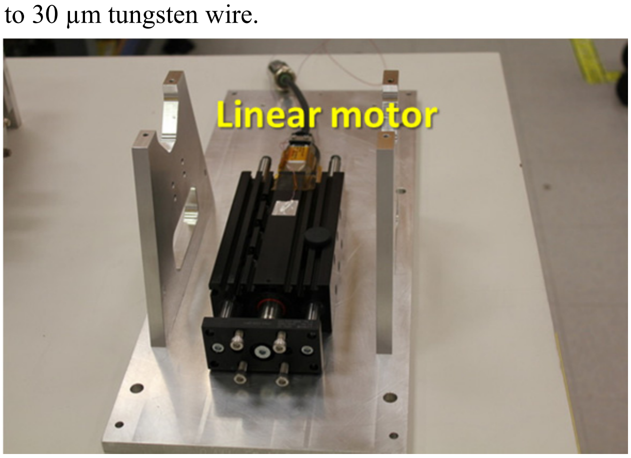

Figure 3: Linear motor slide assembly with magnetic shielding removed.

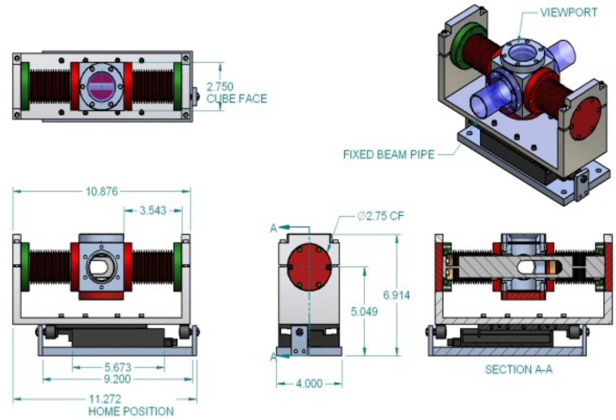

Figure 4: Mechanical sub-assemblies of the wire scanner.

CONTROL SYSTEM

The wire scanner is integrated into the existing LCLS control system and beam synchronous acquisition data gathering system. The linear motor is powered by a remote power unit located outside of the tunnel. This Linmot power unit also provides the dc servo control of the unit. The motor servo is a PID feedback controller where the PID coefficients can be remotely optimized for a given installation. The PID coefficients typically depend on the mass, spring forces and cable lengths. The Linmot power unit is interfaced to the EPICS control system via a MAXv module as shown in Fig. 6. The MAXv module also interfaces to the external position encoder used to record the wire position during the scans. The MAXv module is installed in a VME crate where it communicates with an EPICS IOC module and the timing module.

A Beckhoff controller interfaces the limit switches to the control system that confirm when the scanner is at the end of its range of travel.

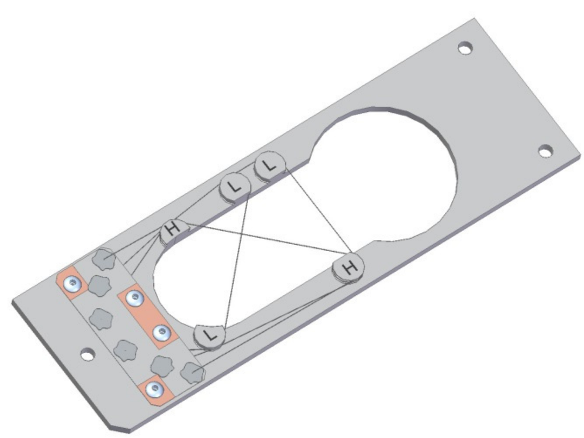

Figure 5: Wire card assembly showing how the x, y and u wires are mounted.

ISBN 978-3-95450-176-2

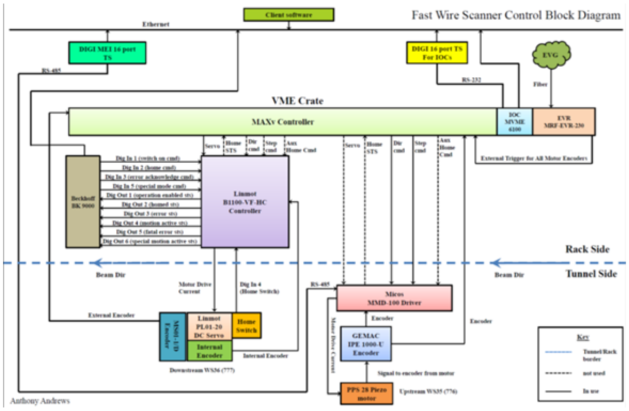

Figure 6: Block diagram of the wire scanner control system.

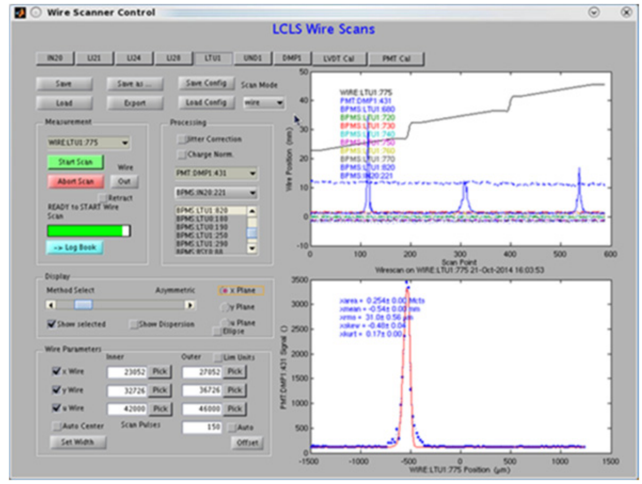

Figure 7: Snapshot of the wire scan graphical user interface showing x, y, and u wire scan signals during a single sweep (top right) and an individual wire scan plotted versus measured wire position (bottom right).

BEAM MEASUREMENTS

A wire scan measurement can be initiated from the graphical user interface (GUI), shown in Fig. 7, or from an automated script. The scan ranges are set via EPICS Process Variables (PVs) visible on the GUI and can be set to scan all 3 wires or any single wire.

The top right pane in Fig. 7 shows the result of all 3 wires scanned consecutively, plotted as a function of sample number (or time). The 3 peaks in the beam loss signal indicate the beam intercepting each wire. The position encoder signal is also plotted as a function of time where one can see the wire accelerate and then slow down to scan through the beam core. The optimum wire speed is calculated according to the actual rate of the beam so that one always gets a reasonable number of measurement points across the beam to enable a Gaussian or asymmetric Gaussian curve to be fitted. The fitted beam width is then used in subsequent emittance measurement calculations.

The measured data points in an individual scan show no horizontal deviation from the fitted curve which indicates that there is no measurable vibration of the scanner assembly.

REFERENCES

[1] Emma, P. et al. “First lasing and operation of an angstrom-wavelength free-electron laser.” Nat. Photon. 4, 641–647 (2010).

[2] M.C. Ross, et.al., “Wire Scanners for Beam Size and Emittance Measurement at the SLC”, Proceedings of the 1991 IEEE Particle Accelerator Conference, p.1201, May 1991.

[3] http://www.linmot-usa.com/

ISBN 978-3-95450-176-2

CHERENKOV CONVERTER FOR LARGE DYNAMIC RANGE, HIGH SENSITIVITY DETECTORS FOR USE ON WIRE-SCANNERS*

J. F. Gubeli, P. Evtushenko
Thomas Jefferson National Accelerator Facility, Newport News, VA 23606, USA

Abstract

We are developing a wire-scanner with a dynamic range of 1e+6 or larger. In addition to the large dynamic range (LDR), high sensitivity is very desirable so that measurements can be made with a small amount of beam or small duty cycle beam. This high sensitivity requirement makes photo multiplier tubes (PMT) the preferred detector. Low dark current PMTs have maximum quantum efficiency in the visible wavelength range. We describe a converter where Cherenkov radiation (CR) is used to generate visible photons from electrons and positrons that are present due to wire-beam interaction. Also described is an optical system that collects and couples the CR into an optical fiber that delivers the visible photons to the PMT outside of the accelerator area, reducing background. The high directivity of the CR is used in a way that, when CR in the radiating medium is generated by particles not directed from the wire-beam interaction point to the converter, the CR is not coupled into the optical fiber and therefore does not create background for the wire-scanner measurements. Sensitivities to the refractive index of the radiating medium, alignment and mechanical tolerances are also presented.

INTRODUCTION

Particle accelerators have been using wire scanners as a valuable diagnostic tool to measure the spatial extent of their beam for many years. Several methods of determining the beam profile have been used, including measuring the induced current on the wires [1], by collecting the optical transition radiation [2] or by the use of scintillators [3]. We are developing a wire scanner that utilizes the shower of charged particles generated by the scattered electrons from the wire-beam interaction that impinge on the beam tube. We describe a method of converting these particles to photons by use of Cherenkov radiation and measuring the photons with a photomultiplier tube.

CHERENKOV RADIATION

Cherenkov radiation is electromagnetic radiation created when charged particles travel through an electrically polarizable medium faster than phase velocity of light in that medium. The threshold velocity of a particle to generate Cherenkov radiation is $\nu_n < \nu_p$ where ν_n is the phase velocity of light in a medium ($\nu_n = c/n$) and ν_p is the velocity of the charged particle. The velocity of an electron can be derived from the relativistic kinetic energy equation $E_k = (\gamma - 1)\, mc^2$ where $\gamma = (1 - \beta^2)^{-0.5}$ and $\beta = \nu_p/c$.

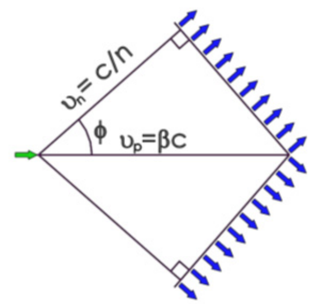

Figure 1: Cherenkov radiation geometry.

Cherenkov radiation is emitted in a cone where the angle is related to the velocities as $\cos\phi = (n\beta)^{-1}$ (Fig. 1). By solving for β in the relativistic kinetic energy equation, we can describe the emitted center wavelength angle as a function of n and E_k (MeV), equation 1.

$$\phi\left(E_k, n\right) := \mathrm{acos}\left(\frac{1}{n \cdot \frac{\sqrt{E_k^{\,2} + 2 \cdot E_o \cdot E_k}}{E_k + E_o}}\right) \tag{1}$$

The Frank-Tamm formula describes the number of Cherenkov photons generated per angle and per wavelength of the generated photon [4], equation 2. The right side of this equation S_{CR} is a measure of the spectral distribution of the emitted photons.

$$\frac{d^2N}{d\Omega d\lambda} = S_{CR} = \left(\frac{\alpha \cdot n(\lambda) \cdot L^2}{\lambda^3}\right) \cdot \sin(\theta)^2 \cdot \left(\frac{\sin(k \cdot \pi)}{k \cdot \pi}\right)^2 \tag{2}$$

$$k = \frac{L}{\beta \cdot \lambda} \cdot (1 - \beta \cdot n(\lambda) \cdot \cos(\theta)) \tag{3}$$

CHERENKOV GENERATION CELL

The Cherenkov generation cell for this experiment consists of a 100 mm long water cell with a thin aluminium input window and a quartz output window (Fig. 2). For an index of refraction of 1.337, the phase velocity of light in water is ν_n = 0.748c. To generate Cherenkov radiation, the minimum energy of an electron/positron traveling in water must be greater than 0.259 MeV.

*Work supported by US DOE Office of Basic Energy Sciences early career program; DOE award number FWP#JLAB-BES11-05

ISBN 978-3-95450-176-2

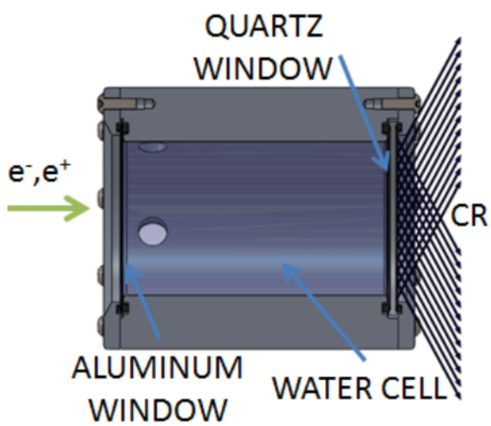

Figure 2: Cherenkov generation cell.

The photon angle leaving the generation cell can be determined by applying Snell's Law, $\sin(\phi_w)n_w = \sin(\phi_q)n_q = \sin(\phi_a)n_a$ for water, quartz and air. The equality allows the index of the quartz window to be ignored as long as the angle of incident doesn't exceed the critical angle $\theta_c = \mathrm{asin}(n_2/n_1)$. Substituting this equality into equation 1 results in an expression of the photon exit angle as a function of the energy of the charged particle (MeV) and the index of refraction of water, equation 4.

$$\phi(E_k, n) := \mathrm{acos}\left(\frac{1}{n \cdot \frac{\sqrt{E_k^2 + 2 \cdot E_o \cdot E_k}}{E_k + E_o}}\right) \tag{4}$$

The plot of Fig. 3 shows that the change in the exit angle is negligible with particle energy in excess of 20MeV.

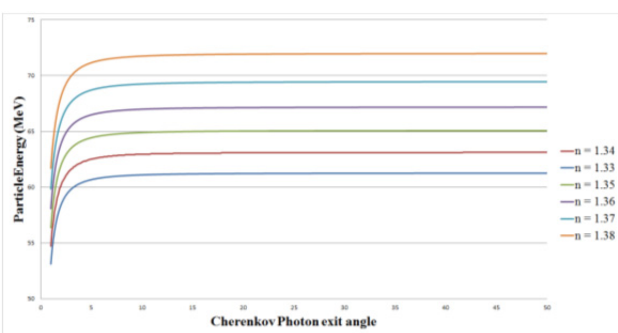

Figure 3: Plot of the cell exit angles as a function of energy and refractive index.

This plot varies the index of refraction of water [5-7] with wavelengths between 250nm and 600nm and temperatures 19°C to 24°C. The cell exit angle for this range of n at high particle energy goes from 61.7° at longer wavelengths to 71.5° at shorter wavelengths.

The spectral distribution of the radiation leaving the cell is obtained by substituting the angular relationship of the generation angle to that of the angle leaving the cell in equation 3 by use of Snell's Law. The plot of Fig. 4 is the normalized spectral distribution of the photons leaving a 20°C cell generated by 20MeV particles. The number of photons generated by the 100mm long cell per electron ranges from ~700 at 250nm to ~100 at 600nm (Fig. 5). The number of photons can be as large as 700 x 6.25e8 for 100pC electron bunch charges.

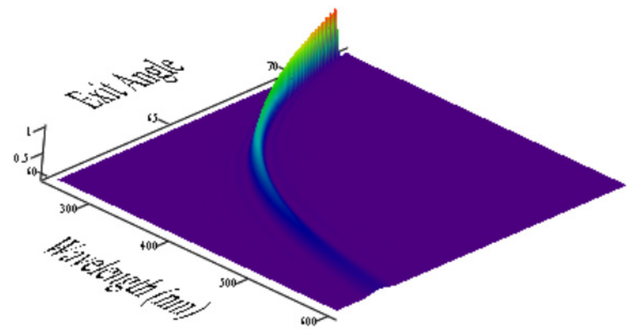

Figure 4: Normalized spectral distribution of the emitted photons leaving the generation cell.

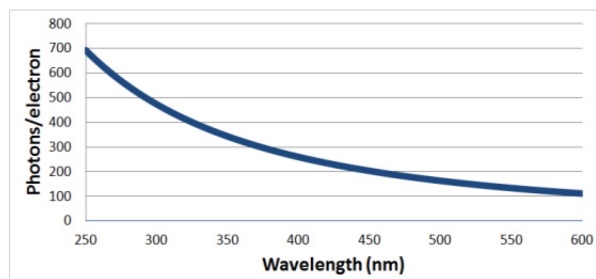

Figure 5: Number of photons per electron produced in a 100mm long water cell.

OPTICAL DESIGN / SIGNAL PROCESSING

The design specifications for the optical design are to first collimate the Cherenkov radiation leaving the generation cell, then to focus the light in to an optical fiber. The fiber would then transport the light to a photomultiplier tube located outside the radiation environment to increase the signal to noise ratio. This design also requires that the angular acceptance of the fiber coupling be small to ensure that only particles generated by the wire-beam interaction would be detected. The two factors that vary the angular trajectory of the generated photons in a water cell are the charged particle energy and the index of refraction. As the energy of the accelerator that we would use to test this system was well above 20MeV, causing little variation to the emitted photon angle, we looked at narrowing down which index of refraction the system would accept. The index of refraction of water changes slowly with small changes in temperature and pressure making the largest consideration the wavelength. The wavelength was

ISBN 978-3-95450-176-2

chosen that would maximize the number of Cherenkov photons generated, minimize the attenuation in water and in the fiber and maximize the sensitivity of the photomultiplier [8]. We used 350nm as our target wavelength and thus 65^{o} as the angle for the emitted photons.

The photons exiting the Cherenkov generation cell are first reflected off a cylindrical mirror to a conical mirror with a cone angle of 32.5^{o} (65^{o}/2). An off-axis parabolic mirror is used to focus the photons into a 600µm diameter optical fiber. A three-armed support structure with a small cross-sectional area in the photon direction maintains the alignment of these two optics to the generation cell (Fig. 6). The cell as well as the cylindrical and conical mirrors are made of 7075-T6 to facilitate a mirror polish.

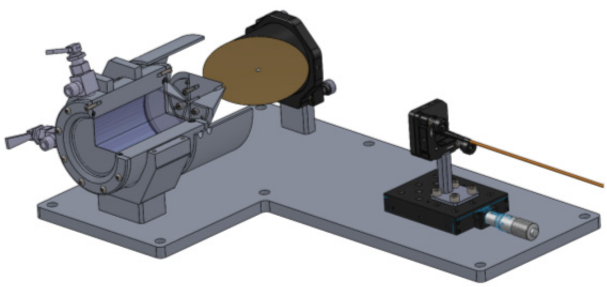

Figure 6: Cherenkov assembly.

This all-reflective layout was chosen for its wavelength independence. A raytrace was performed with 150,000 source rays generated by creating 100 sets of cones of 1,500 radially symmetric rays each. A 1mm diameter mask was created at the plane of the fiber input to display the irradiance map of the raytrace. All of the incident flux was captured by a 600µm disk with the charged particles striking generation cell normal to the entrance. A small misalignment of 0.35mrad will result in a 35% loss of detected signal (Fig. 7). This optical design is intentionally sensitive to the angle on incidence (AOI) of the charged particles to the generation cell. This sensitivity ensures that only the Cherenkov photons created by particles from the wire-beam interaction are captured. An AOI of 0.4 mrad will result in a 50% loss of signal (Fig. 8).

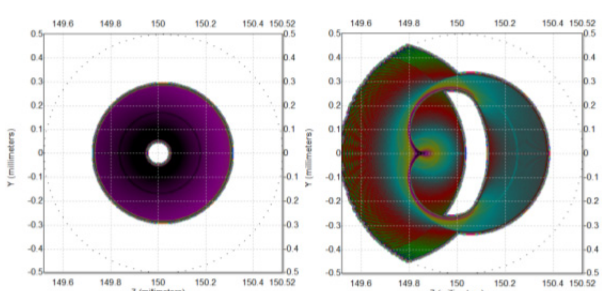

Figure 7: Irradiance map on the plane of the fiber input. Left image for charged particles aligned to the generation cell, right image charged particles misaligned by 0.35mrad.

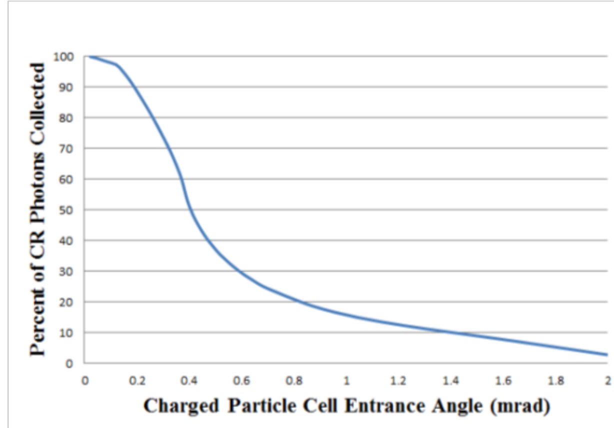

Figure 8: Percentage of Cherenkov photons coupled into the optical fiber as the angle of the charged particles move off the axis of the generation cell.

The optical fiber transports the collected photons outside of the beam accelerator to a PMT. Placing the PMT outside of the beam accelerator reduces the risk of environmental electrons striking a dynode and contributing to both signal and background. The PMT's negative output current is sent to a current mirror that first inverts then makes multiple "copies" of this current [9]. The current mirrors are sent to gated integrators (GI) (Fig. 9) at 100% and 1% of the PMT current and then digitized with a 16-bit ADC at 4 MS/s. The arrangement of these two GI's combined with the PMT allows for dynamic ranges of 10^{8} to be reached.

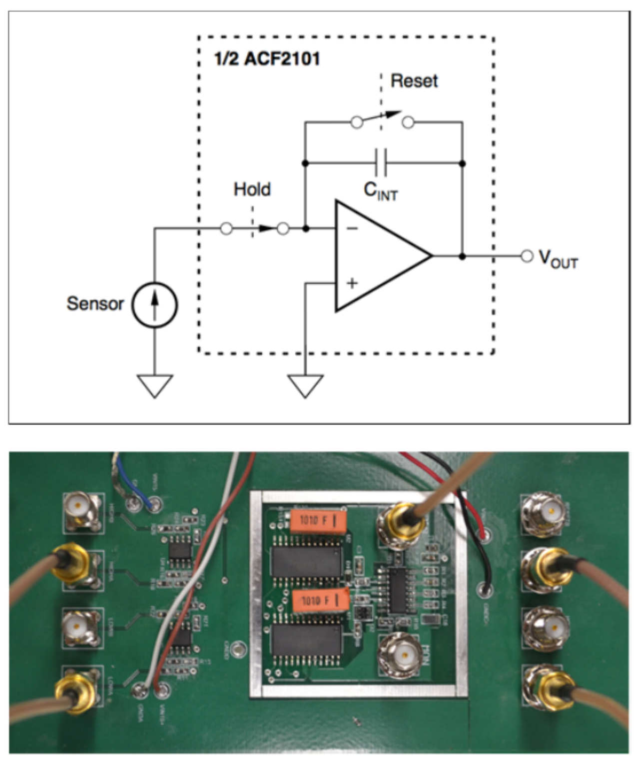

Figure 9: Gated Integrator circuit and board.

ISBN 978-3-95450-176-2

CONCLUSION

We have presented a method to measure the beam profile using Cherenkov radiation of charged particles generated by wire-beam interaction. A 100mm long water cell is used as the Cherenkov generation medium converting charged particles of 20MeV and larger to 350nm photons that are focused on an optical fiber. Due to the small angular acceptance of the optical system, only those electrons entering the generation cell parallel to the axis of the cell are captured. A PMT coupled with two gated integrators will allow measurements of low duty cycle beams with a dynamic range of 10^8.

REFERENCES

[1] M.C. Ross et al., “Experience with wire scanners at SLC”, SLAC-PUB-6014.

[2] P. Elmfors et al., “Wire-scanners in low energy accelerators”, NIM A 396 (1997) 13-22.

[3] H. Grabosch et al., “Test of a wire scanner in the diagnostic section of PITZ”, Proc. FEL, Novosibirsk, Russia (2007).

[4] C. Grupen, “Teilchendetektoren”, BI-Wiss.-Verl., 1993.

[5] S. Kedenburg et al., “Linear refractive index and absorption measurements of nonlinear optical liquids in the visible and near-infrared spectral region”, Opt. Mat. Express 2, (2012), p. 1588-1611.

[6] M. Daimon et al., “Measurement of the refractive index of distilled water from the near-infrared region to the ultraviolet region”, Appl. Opt. 46, (2007), p. 3811-3820.

[7] G. M. Hale et al., “Optical Constants of Water in the 200-nm to 200-µm Wavelength Region”, Appl. Opt. 12, (1973), p. 555-563.

[8] Hamamatsu preliminary data, “Photomultiplier Tube R7378A”, TPMH1288E01 (2004) [http://www.hamamatsu.com/resources/pdf/etd/R7378A_TPMH1288E.pdf].

[9] P. Evtushenko et al., “Design of Wire-Scanner (electronics) for Large Dynamic Range Beam Profile Measurements”, Poster IBIC 2014, Monterey, CA, USA (2014).

ISBN 978-3-95450-176-2

MULTI-DIAGNOSTIC TRANSVERSE PROFILE MONITOR CHAMBER FOR EXTREME ULTRAVIOLET LITHOGRAPHY*

T. Campese#, R. Agustsson, M. A. Harrison, B. Jacobson, A. Murokh, A. Ovodenko, M. Ruelas, H. L. To, RadiaBeam Technologies, Santa Monica, CA 90404, USA
M. Fedurin, I. Pogorelsky, T. Shaftan, Brookhaven National Lab, Upton, NY 11973, USA

Abstract

RadiaBeam Technologies has developed a compact transverse beam profile measurement system for the Extreme Ultraviolet Lithography (EUL) experiment at the Brookhaven National Laboratory-Accelerator Test Facility (BNL-ATF). The EUL experiment requires fine e-beam and laser alignment across multiple passes. To accomplish this, the system consists of four profile monitor diagnostics: Interaction Point (IP), upstream, downstream, and a sub-micron resolution diagnostic 11.5 mm downstream of the IP. Care was taken in the design to minimize footprint, avoid possible diagnostic collisions, and maximize ease of assembly and alignment. This paper will review the requirements for the dimensional and optical constraints and solutions for this experiment.

INTRODUCTION

Extreme ultraviolet sources in the 7-15 nm range are needed for next-generation integrated circuit fabrication [1]. High quality sources in this range are large and cumbersome and therefore difficult to implement in an industrial setting. Inverse Compton Scattering (ICS) sources, such as the proof-of-concept EUL experiment at BNL-ATF, promise a smaller footprint per photon. In this scheme, a recirculated pulsed CO_2 laser is collided head-on with a 60-MeV electron beam, producing a higher-energy 13-nm photon. Both the laser and electron beam are focused to 50 µm or less at the IP with a minimized electron beam spot size of 22 µm measured.

CHAMBER DESIGN

Four different beam diagnostics are needed to monitor a 50-µm RMS beam size at the IP. They need to fit between two opposing, off-axis parabolic mirrors arranged equidistant from the IP focus which are used to focus and re-collimate the laser. The required separation distance is 120 cm, which caused a particularly challenging limitation for fitting in so many diagnostics. The parabolic mirrors are placed inside larger chambers upstream and downstream of the multi-diagnostic assembly. These three chambers are kept separate for ease of installation and serviceability in the experimental hall (see Figure 1).

Dual Position Profile Monitors

To monitor the transverse profile of the beam, both cerium-doped yttrium aluminum garnet (YAG:Ce) crystals and aluminum-coated silicon wafers are used as optical transition radiation (OTR) screens and are placed in the upstream and downstream profile monitors. Both the OTR and YAG screens are 100 µm thick and placed perpendicular to the electron beam on a multi-position pneumatic actuator. Each screen is backed by a 45° turning mirror (an aluminized silicon water) and viewed by CCD cameras through viewports, allowing for uniform magnification across the screen surface. These upstream and downstream profile monitors are mounted on pneumatic actuators to allow for high (25 µm) repeatability and fast extraction from the beam path (see Figure 2 and Table 1).

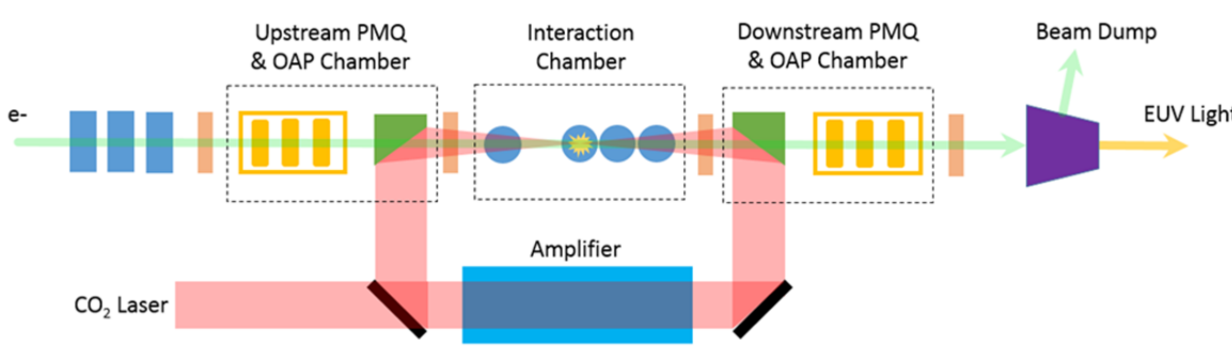

Figure 1: Full EUL Experiment including upstream quadrupole triplet (blue) and steering magnets (Orange).

*Work supported by DOE SBIR Grant No DE-SC0007703
#campese@radiabeam.com

Germanium Target and Pinholes

A 500-µm thick germanium OTR target is installed at the IP at a 45-degree angle to align the CO_2 laser. In addition, germanium was chosen to synchronize the electron and CO_2 beam. The 10.6 µm wavelength normally passes through the germanium. However, the passing electron beam produces a plasma at the germanium surface that the 10.6 µm radiation cannot penetrate. Measuring the reflected CO_2 laser power and adjusting a delay stage allows synchronization of the CO_2 laser and electron beam. Below the germanium wafer, a pinhole array is mounted perpendicular to the beam for precise alignment. The pinhole array is made of 1-mm thick tungsten and contains five pinholes of progressively decreasing diameter: 500 µm, 350 µm, 250 µm, 225 µm, and 200 µm. The laser and electron beam trajectory are passed through progressively smaller pinholes while transmission is monitored, allowing a straightforward method of alignment.

The pinhole array is adjustable in three dimensions (insertion, horizontal, and tilt) so that the pinhole array can be aligned to the ideal orbit defined by the permanent magnet triplet. A stepper motor actuator controls the insertion position while also allowing cycling through the different pinholes. Horizontal motion is adjustable using a manual micrometer mounted to a commercially available gimbal. The gimbal was modified in-house to fit the tight space requirements of this experiment.

The tilt motion is controlled by a fine adjustment screw mounted in a locking sleeve. This linear shift provides the fine positioning required to align the pinholes to the beam axis with a resolution of 1 µm. Although tilt motion is available, it was not used since the motion is not gimbaled about the beam and therefore couples to vertical (insertion) position.

Once the CO_2 and electron beam are aligned to the largest pinhole, the next smaller pinhole is inserted, thus increasing the alignment accuracy.

Table 1: Diagnostic Type, Location, and Purpose

Type	Distance from IP	Purpose
YAG & OTR target	85.7 mm upstream	Measure transverse profile
Germanium target & Pinholes	IP	CO_2 laser optics and e-beam positioning
High Resolution OTR target	11.5 mm downstream	Sub-micron transverse profile measurement
YAG & OTR target	85.7 mm downstream	Measure transverse profile

High-Resolution Profile Monitor

The high-resolution profile monitor consists of an OTR target mounted at 45 degrees to the beam, a 10x magnifying in-vacuum microscope objective (NA = 0.25), a re-entrant style viewport, and out-of-vacuum imaging optics mounted inside the viewport tube. This profile monitor is used to view spot sizes in the range of 50-75 µm with a resolution of approximately 1 µm/pixel [2].

The high-resolution profile monitor is pneumatically actuated on a linear shift mechanism. The linear shift allows for rigid insertion of the precisely aligned optics and screen. The high-magnification optics are mounted inside a re-entrant viewport and move along with the diagnostic.

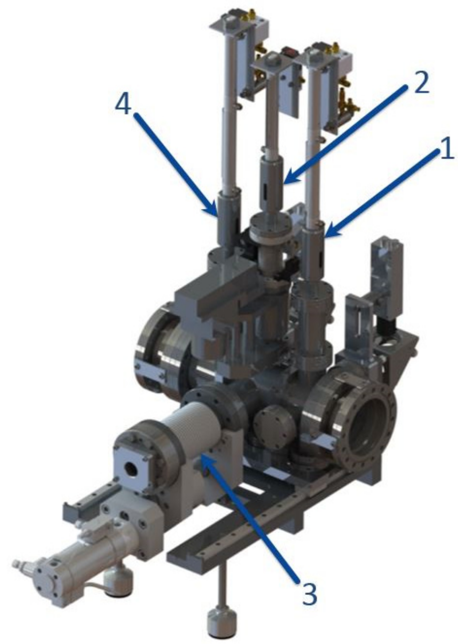

Figure 2: The beamline placement of the diagnostics reference in Table 1. (1) YAG & OTR screen, (2) germanium & pinholes, (3) high-resolution OTR screen, and (4) YAG & OTR screen.

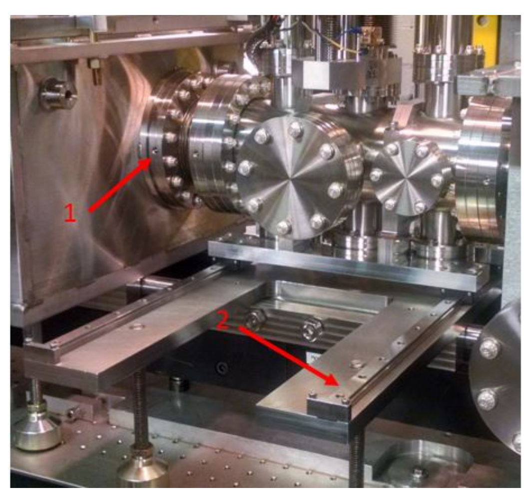

Figure 3: (1) Bellows and (2) rail system for ease of maintenance. This picture shows the assembly without the high-resolution profile monitor connected.

ISBN 978-3-95450-176-2

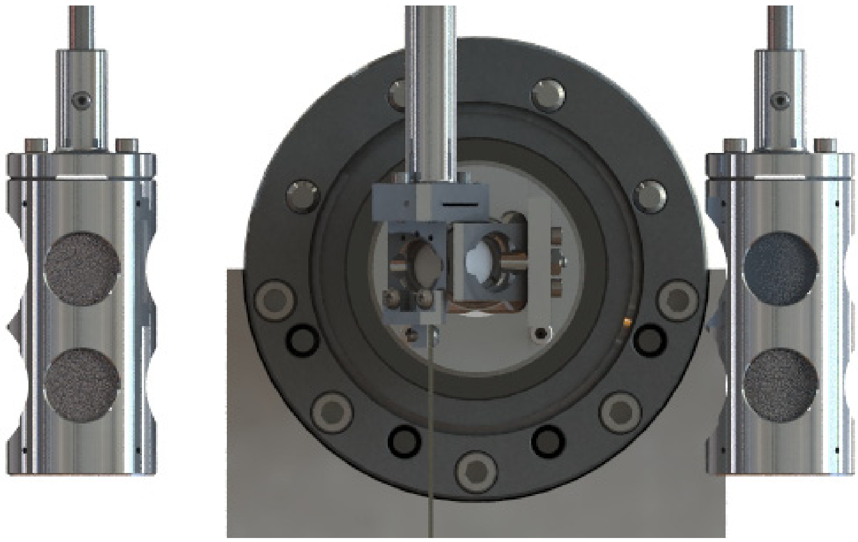

Figure 4: Collision is avoided when the YAGs, Germanium wafer, and High Resolution OTR screen are inserted at the same time.

Serviceability

The high power density of the EUL system will likely require the scintillators, OTR targets and pinholes to be replaced at regular intervals. In order to make this process quick and easy, the multi-diagnostic chamber mates to the beamline using two 6.00" Conflat (CF) flange-mounted bellows. The flanges have four tapped holes around the perimeter to allow for tabs to be secured. When it came time to remove the multi-diagnostic chamber from the beamline, the CF flange was disconnected from the chambers upstream and downstream and the bellows were locked in a compressed position using the tabs and bolts. These tabs both secure and support the bellows during removal for servicing.

The entire multi-diagnostic chamber is mounted on a moving rail system, as seen in Figure 3, which allows the user to easily slide the assembly out of the beamline. The rails provide smooth motion and high repeatability to ensure that minimal realignment is needed once the assembly is reattached to the beamline. The rail carriages are then locked in place to prevent movement during the experiment.

Each insertable diagnostic is removable via a single CF flange connection. Once the diagnostic sub-assembly has been removed, the YAGs and OTR screens are replaceable by removing a single lens mount retaining ring from each holder position. This allows for quick and easy changing of all of the diagnostic components [3].

Cameras

A CCD camera is mounted to each viewport using a custom mounting bracket. These brackets allow for each camera assembly to be mountable using two bolts and two off-the-shelf alignment rods. This makes the multi-diagnostic chamber compatible with commercially available cage plate optical assemblies (see Figure 4). All three analog cameras mounted to the side of the chamber have a 768 (H) x 493 (V) active pixel resolution with a 2/3 inch sensor format.

The high-resolution profile monitor is observed using a 100 mm focal length lens and a UV sensitive CCD camera with an observation wave length of 350 nm. This GigE Vision camera has a ½ inch sensor format and GigE data transfer interface. The resulting field of view in the image obtained is 1.3 mm x 1.0 mm.

CONCLUSION

The single pass experiment was run earlier this year and was a success. The first x-rays were obtained using this compact system on June 4th, 2015 [4]. Further tests are scheduled to be performed later this year to obtain multi-pass data.

ACKNOWLEDGMENT

The authors would like to thank the staff at BNL-ATF for their expertise and the operation of their facilities. Work is supported by DOE SBIR Grant No. DE-SC0007703.

REFERENCES

[1] A. Murokh, "Inverse Compton Source for Extreme Ultraviolet Lithography", DOE Phase II Proposal, December 2012

[2] B. Jacobson, "Test of high-resolution deep ultraviolet imaging system for transverse beam diagnostics at BNL-ATF", BNL Newsletter, Upton, NY, 2014

[3] M. Ruelas et al, "Commercially Available Transverse Profile Monitors, the IBIS", MOP239, NPAC'11, New York, NY, March 2011; http://accelconf.web.cern.ch/AccelConf/PAC2011/papers/mop239.pdf

[4] A. Murokh, Private Communication, June 2015

Observation of Ion-induced Instabilities at NSLS2 Storage Ring*

Weixing Cheng#, Yongjun Li, Boris Podobedov
NSLS-II, Brookhaven National Laboratory, Upton, NY 11973

Abstract

NSLS2 storage ring has been commissioned and is open for user operations. At relatively low beam current (~ 25mA) multi-bunch fills, ion-induced instabilities have been observed. For the present user operations, 150mA of total beam current is filled in ~1000 bunches, fast ion is the dominant instability at the NSLS2 storage ring. Although the ion-induced dipole motions can be suppressed using bunch by bunch (BxB) feedback system and it is expected to decrease in severity as the vacuum conditioning progresses further, a thorough understanding and characterization of this effect is still important, especially in preparation to the future 500mA operations. A number of ion instability related studies, mostly parasitic to other machine activities, have been carried out at various fill patterns and beam currents. Preliminary measurement results are reported in this paper.

INTRODUCTION

Residual gas in the vacuum chamber will be ionized by high energy beam. Ions will be trapped by the beam potential and cause ion related instabilities. Conventional ion trapping can be easily cured with empty buckets. However fast-ion instability during the single pass of bunch train will be strong in the low-emittance high current ring like NSLS2. NSLS2 is an advanced third generation light source recently constructed at Brookhaven National Laboratory. Weak dipoles and three damping wigglers are used to decrease the horizontal emittance from 2nm.rad (bare lattice, no insertion devices) to < 1nm.rad (with 3 DWs). Vertical emittance has been measured to be less than 8pm.rad [1].

Even with ion-clean gap, another kind of ion instabilities could happen in small emittance high current storage rings, called "Fast" ion instability. Fast ion instability has been considered to be important for the NSLS2 storage ring and was investigated at design stage of the machine [2]. Transverse BxB feedback has been designed, constructed and commissioned to cure the fast ion and other coupled bunch instabilities [3].

Theory of fast-ion instability and early observations were reported almost 20-years ago [4-6]. As the recent machine development push to lower emittance and high current, fast-ion instability is getting severe for modern light sources and colliders. More recent observations on newly constructed light sources can be found, for example [7-9].

Fast ion instability will be affected by vacuum pressure, chromaticity and coupling. As vertical beam sizes are smaller than horizontal sizes, ion instability is usual dominant in vertical plane and it's expected to be worse at improved coupling. With three DWs, NSLS2 storage ring horizontal emittance is half of bare lattice, this may change the fast ion growth rate. Close the IVUs may have elevated localized vacuum pressure which will in turn makes the fast ion easier to accumulate. Unfortunately, there was not much machine study time allocated to investigate fast ion behaviors at various machine conditions. Most of the observations reported here were parasitic to other studies, not insertion devices were closed and chromaticity was at nominal value of +2/+2 if not specified. We would like to have further systematic study of the issue in the future, to understand the fast ion behavior with different vacuum condition, chromaticity, coupling and insertion devices.

FAST ION INSTABILITY OBSERVATION

During early commissioning stage of NSLS2 storage ring, fast ion instability was first observed at about 10mA filled in 500 bunches during BxB feedback commissioning. Preliminary observations have been reported in [3].

More recently a study was done at fixed, 1000-bunch and approximately uniform fill pattern while varying the total beam current. Specifically, there were 17mA, 31mA, 46mA, 100mA and higher total beam current evenly distributed in ~1000 bunches. Fill patterns of the first three data sets (17mA, 31mA and 46mA) were well controlled to minimize the bunch to bunch current variation. Rising/falling edges of the bunch train were trimmed to have a uniform bunch train. Figure 1 gives the measured bunch to bunch current at 46mA. Details on how to measure the bunch to bunch fill pattern can be found in [10]. 100mA and other higher current fill patterns had somewhat larger bunch to bunch current variation, edge bunches were not trimmed as these observations were parasitic to other studies.

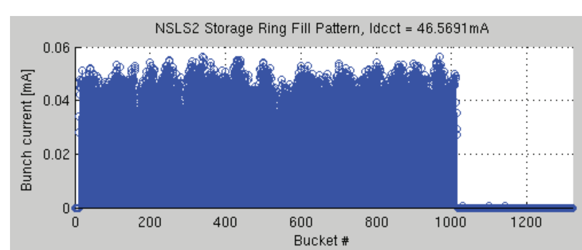

Figure 1: Bunch to bunch current measured at 46mA, machine was filled from bucket #1 to #1020. Rise/falling edge buckets were trimmed, only bunches #11 to #1005 were kept.

With injector set to multi-bunch fill with 20 bunch-train, storage ring was filled with 50% overlap (10 buckets) from shot to shot. After knocking out the head/tail bunches, bunch to bunch current variation shown in Fig 1 was ~ 3.7uA RMS with mean bunch current at 46.4uA. Relative bunch to bunch current

*Work supported by DOE contract No: DE-AC02-98CH10886
#chengwx@bnl.gov

ISBN 978-3-95450-176-2

variation was ~8% which can be further improved at higher total beam current fill.

With the transverse BxB feedback switched ON, both horizontal and vertical instabilities were suppressed. There was no betatron motion sidebands observed on the button BPM spectrum. It was possible to switch OFF the feedback system at 46mA without losing the beam. Measured horizontal and vertical beam sizes from the x-ray pinhole camera were increased, as shown in Fig. 2. Top two x-ray pinhole camera images were captured with and w/o BxB feedback, camera exposure time was fixed at 2 seconds. As feedback switched OFF, x-ray pinhole profile saw spread out and fitted beam sizes were increased on both horizontal and vertical plane. Bottom plot in the figure shows history of horizontal and vertical beam sizes measured from the x-ray pinhole camera. When horizontal feedback was turned OFF, horizontal beam sizes jumped from ~102um to 160um. Vertical beam sizes increased from ~ 58um to 120um. Beam sizes were fitted to a one-dimensional Gaussian function. Note that even with BxB feedback ON, there was large coupling during the shift, that's why there x-ray profile was tilted. When horizontal feedback was turned OFF, vertical beam sizes saw small increases as well, this is another indication of x/y coupling.

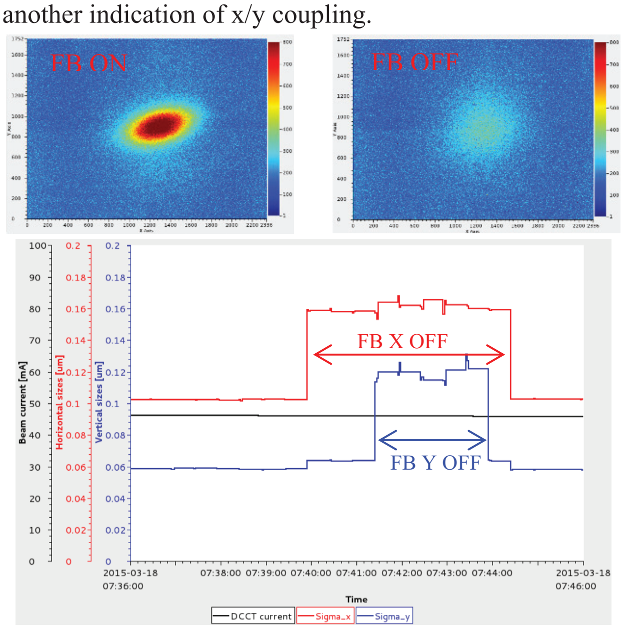

Figure 2: (Top) two x-ray pinhole camera images captured with and w/o BxB feedback separately. (Bottom) history plot of x-ray pinhole camera measured beam sizes.

Beam motion spectrum was measured with BxB feedback gated OFF for a short period of time (growth damp measurement). Most unstable mode(s) will appear during the period without feedback. Figure. 3 is an example of such kind of measurement using Tektonic FFT spectrum analyzer, vertical BxB feedback was OFF for 20ms, spectrum analyzer was external triggerrf on the same signal to gate OFF the feedback. Cnetre frequency of the spectrum analyzer was at Frf + 6*Frev to see the most unstable mode (-6). As can be seen, vertical betatron sidebands (~100kHz away from the center) started to grow before it was suppressed as feedback switched back ON. Spectrum around Frf was checked and no apparent betatron sidebands appear during the period w/o feedback. This means the instability with fastest growth rate was not due to resistive wall. Most unstable mode(s) vary at different storage current which is another evidence of ion induced instabilities, as ion frequency increases at higher current, described in Eq. (1).

$$\omega_{ion} = 2\pi f_{ion} = \left[\frac{2N_b r_p c}{A\sigma_{x,y}\left(\sigma_x + \sigma_y\right)T_b} \right]^{1/2} \tag{1}$$

Where N_b the number of electrons per bunch, T_b the bunch separation period, r_p the classical proton radius, A the atomic mass number of the ion and $\sigma_{x,y}$ the horizontal and vertical beam sizes.

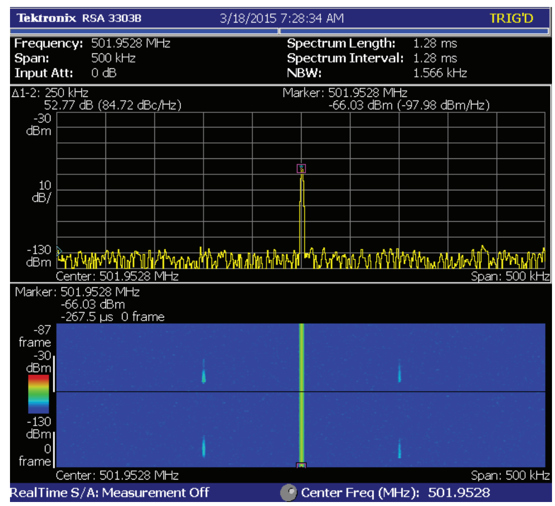

Figure 3: FFT spectrum while vertical BxB feedback was gated OFF for 20ms. Center frequency of the SA was set to be at Frf + 6*Frev. Vertical betatron sidebands grew at around 100kHz and suppressed once the feedback was switched back ON.

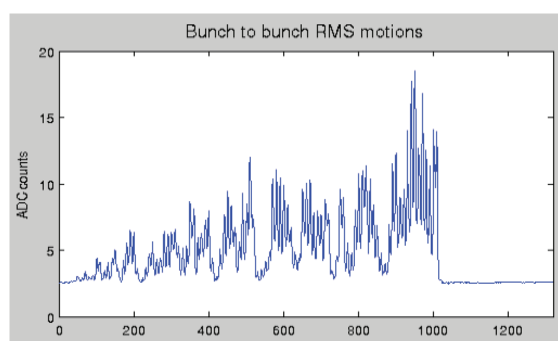

Figure 4: Bunch to bunch RMS motions along the 1000-bunch train with vertical feedback gated OFF for 20ms. Beam was filled to 46mA with all insertion devices gap closed.

Bunch by bunch position data from the feedback system is useful to determine how the bunch oscillation was developed with feedback OFF and ON transient. Fig. 4 gives an example of bunch to bunch motions collecting at 46mA filled in 1000 bunches, all insertion devices gap

ISBN 978-3-95450-176-2

closed. Vertical feedback was turned OFF for 20ms while horizontal feedback was ON all the time. From turn by turn position information, RMS motion of individual bunches along the bunch train can be calculated. As can been seen in the figure, starting from bunch #100, vertical position oscillations were growing along the bunch train, which is a typical behavior of a fast ion-instability. Therefore even with four IVUs gap closed the fast ion is still the most unstable instability presently dominates over the resistive wall. However, as more IVUs are installed in the ring, resistive wall instability may get stronger, while ion-related effects are expected to get weaker with further vacuum conditioning.

From bunch by bunch data acquired during the gated OFF period, unstable mode analysis reveals how the ion frequency varied at different storage current. Unstable mode amplitude is defined as sideband amplitude when it appears at $p{*}F_{rf} + m{*}F_{rev} + f_{x,y}$ appear, where m is called mode number ($m = 0,1,\ldots 1319$, $p = 0,1,2,\ldots$). Fig. 5 gives the averaged unstable modes amplitudes measured in March 2015, when a 1000-bunch train was filled with different amounts of total beam current. As can be seen, as total beam current increasing, unstable modes are shifting to higher frequencies which mean higher ion frequencies.

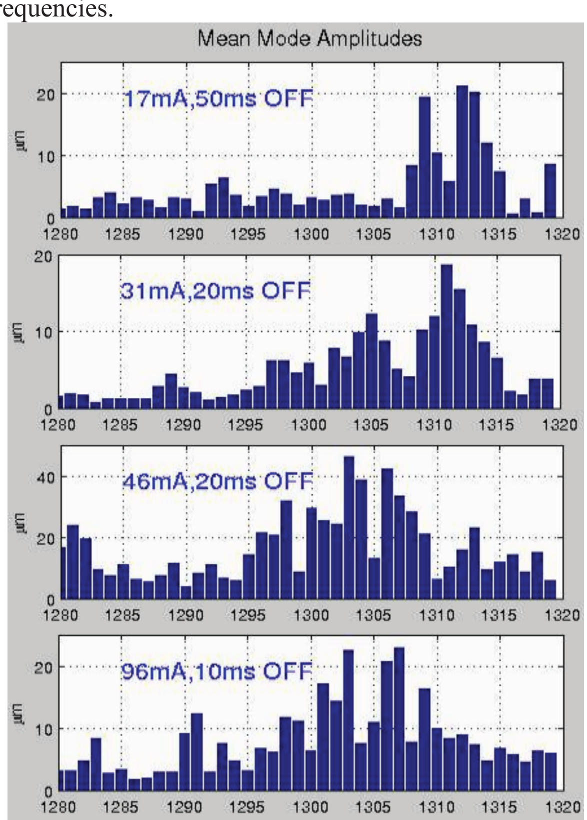

Figure 5: Averaged unstable mode amplitudes at different total beam current. Machine was filled with ~1000 bunches with small bunch to bunch current variations. BxB feedback was switched OFF for short period of time to allow most unstable modes grow.

96mA result in the figure was filled to 1000 bunch train as well, fill pattern was not well controlled as the first three fills at 17mA, 31mA and 46mA. That's probably the reason unstable modes didn't continue to higher frequencies. After months of high current user operation, storage ring vacuum condition was improved. Fill the ring to similar 100mA 80% fill (~1000 bunches), averaged vacuum pressure was improved from 3 nTorr (Mar 2015) to 2.2 nTorr (Aug 2015). Similar analysis was applied to data collected in August, ion instability growth rate was not as fast but unstable mode hump around 1300 (-10) is still obvious.

CHROMATICITY EFFECT

During studies with high chromaticity of +7/+7, up to 100mA of beam current was stored in the ring with bunch-by-bunch feedback off. No apparent instabilities were observed from BPM turn-by-turn data. Using FFT spectrum analyzer measuring button BPM spectrum, there were unstable modes observed at 100mA 80% fill, most unstable modes were -8 horizontally (stronger sideband at $p{*}F_{rf} + 8{*}F_{rev} - f_x$, which is the same sideband as $p{*}F_{rf} + 1312{*}F_{rev} + f_x$) and -12 vertically (stronger sideband at $p{*}F_{rf} + 12{*}F_{rev} - f_y$).

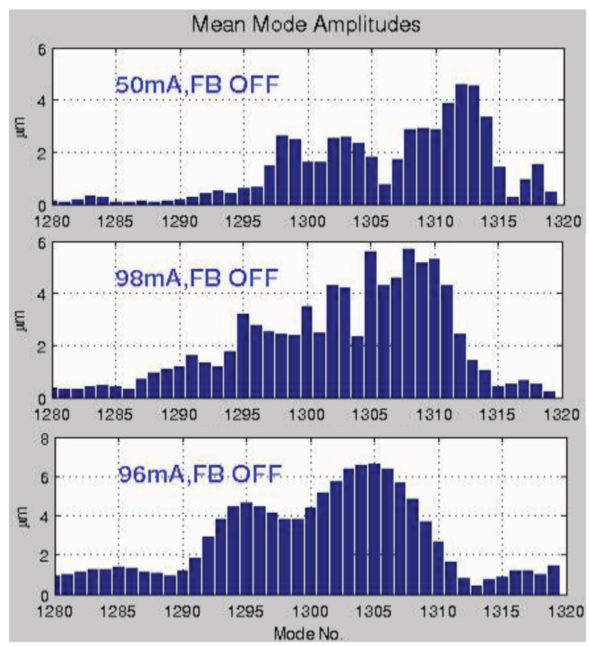

Figure 6: Average unstable mode amplitudes measured with high chromaticity +7/+7. BxB was OFF, there were unstable modes observed.

Similar to Fig. 5, mode analysis of bunch by bunch feedback data tells what the most unstable modes at high chromaticity were. Fig. 6 compares the unstable modes at different currents and filling patterns. The first two plots have the same 1000-bunch (80%) fill with total current at 50mA and 98mA. As the beam current roughly doubled, the most unstable mode shifts from -8 to -12 which agrees with Eq. (1). The third plot shows the 100mA 50% fill (660 bunches), and as compared to the middle plot with the same total current, the ion frequency is even shifted to higher values (the most unstable mode is at -15), which is expected as per-bunch intensity is 60% higher.

ISBN 978-3-95450-176-2

BETATRON TUNE SHIFT

Single bunch spectrum can be measured to determine the bunch betatron oscillation frequency and amplitude. BxB feedback was configured to have feedback OFF for the bunch under measurement while keeping the rest of bunches stable with feedback ON. By scanning the single bunch under measurement along the bunch train, betatron oscillation frequency/amplitude of bunch to bunch can be measured.

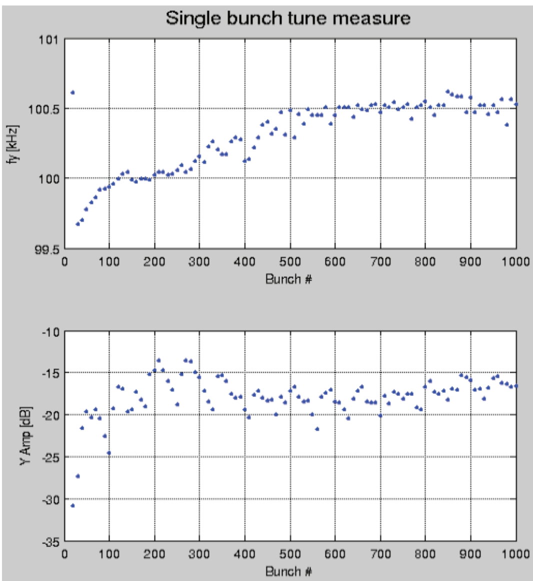

Figure 7: Single bunch vertical tune and amplitude measurement along a 1000-bunch train. BxB feedback was switched OFF one bunch at a time to see the betatron motion of that particular bunch.

Figure 7 gives the result of vertical plane single bunch spectrum with 100mA filled in ~1000 bunches, all insertion devices (3 DWs + 1 EPU + 4 IVUs) had gap closed. Switch OFF the feedback for one bunch at a time, from bucket 20 to 1000, with 10 buckets steps. No excitation was needed to see the betatron sideband of the bunch without feedback. During the data collection, total beam current was maintained at around 95mA, 1000 bunches had more or less even fill pattern. It's clear that the vertical betatron frequency increases along the bunch train and eventually reach to flat for tail bunches. There was ~ 800Hz difference between the head and tail bunches. Bunch oscillation amplitude saturated at bunch #200. Notice the first data point was not accurate as the betatron oscillation amplitude was too low. Horizontally, there was no clear betatron sideband observed on the spectrum while turning OFF feedback for one particular bunch, which is consistent with our expectations for fast-ion instability.

At another time, the same measurement was performed at 150mA fill with all insertion device gaps open. Single bunch betatron frequency was increasing for the first ~200 bunch and reached equilibrium after that. This increase of vertical betatron oscillation frequency and amplitude is likely due to ion accumulation along the bunch train.

As a step for future study, a probe single bunch may be filled at different locations after the bunch train, measuring the probe bunch tune and amplitude will tell how the ions escape in the empty gap.

BUNCH TO BUNCH LIFETIME

Bunch to bunch current is measured using button BPM SUM signal in NSLS2 storage ring [10]. Lifetime of individual bunches can be measured from history of bunch to bunch current data.

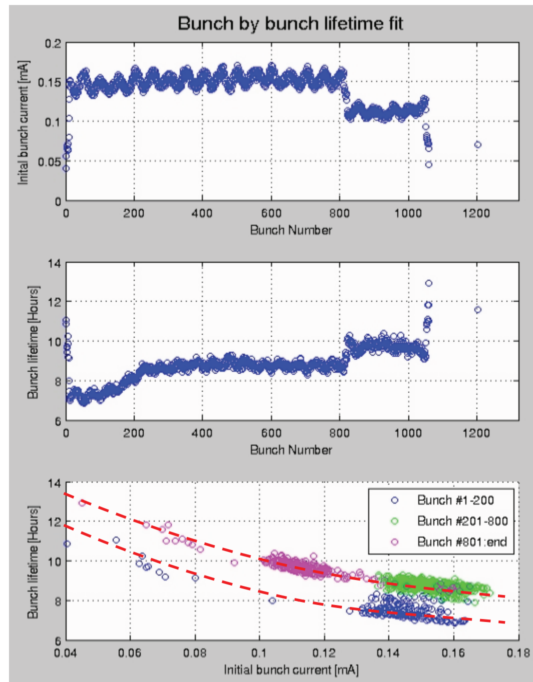

Figure 8: Bunch to bunch lifetime fitted from fill pattern monitor. First 200 bunches in the 1000-bunch train reside in a lower lifetime band.

It has been noticed that bunch to bunch lifetime varies, depends on the locations of the bunch. Fig. 8 is an example of measured bunch lifetime during 150mA user operation. An 80% fill long bunch train was filled, plus a camshaft single bunch at bucket 1200. Initial fill pattern is shown on the top, first 800 bunches had high bunch current as injection stopped there when 150mA total beam current reached. Bunch lifetime was fitted from 30 minutes of bunch to bunch current. As expected, bunches after 800 have longer lifetime due to smaller bunch charges. It's interesting to point out that first 200 bunches lifetime was gradually increased (middle plot), even though the first 800 bunches had more or less same bunch current. While plotting the bunch lifetime vs. bunch current, there were two clear bands, as shown in the bottom plot. Head bunches reside in the lower lifetime band (blue circles) and rest of bunches had longer lifetime.

Lifetime difference of head bunches seems correlated to the single bunch tune measurement and bunch RMS motion along the train. BxB feedback system was turned ON all the time during 150mA operation. There was no dipole motions observed with the feedback ON. As ions

ISBN 978-3-95450-176-2

are still accumulated along the bunch train, it is believed interaction of ion cloud with electron beam may cause beam sizes increase along the bunch train which in turn increases the Touschek lifetime. There is no direct observation of beam sizes with different length of bunch train which can be studies when the tools are prepared.

STREAK CAMERA OBSERVATIONS

Streak camera has been configured to observe the longitudinal and vertical (y-z) profile, when single bunch and multi-bunch instabilities appear [11]. Using slow sweep module, the streak camera can see y-z image of bunches along the bunch train.

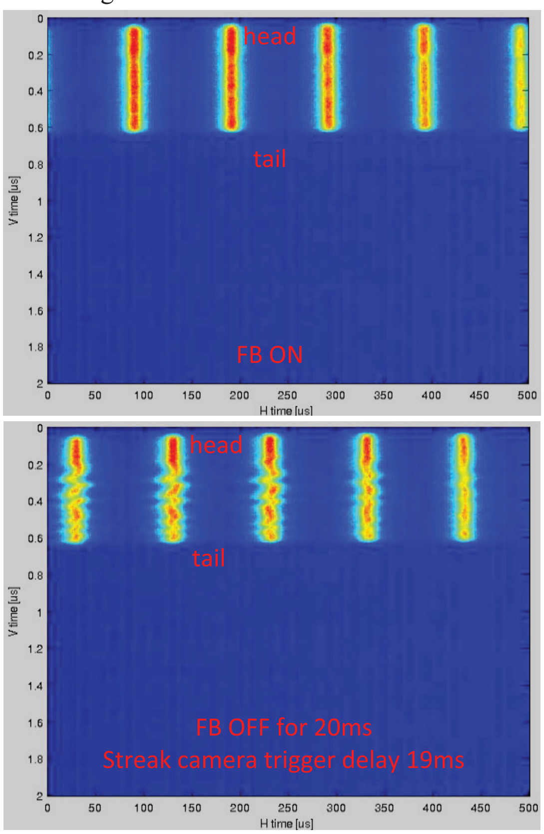

Figure 9: Dual sweep streak camera image using slow sweep module. (Top) with BxB feedback ON, there was no instability observed on the streak camera y-z image. (Bottom) with feedback turned OFF for 20ms, and streak camera trigger delay adjusted to see 19ms after the feedback OFF, bunches after #100 show vertical motions on the streak camera image.

Streak camera images have been saved with different length bunch train filled in the ring. When BxB feedback was kept ON, there were no vertical dipole instabilities. Turn to turn profile is like the image shown in Fig. 9 upper plot. There was 300 bunches filled in the ring with total current ~63mA. Streak camera was operating in dual sweep mode, vertical sweep time was set to 2µs to see one turn profile of stored multi bunches, sweeping clock was adjusted to 10kHz period. Horizontal sweep time was at 500µs to see five turns of profile with 100µs separation. Each vertical strip in the figure is one turn image, head bunches are at the top. It's worth to point out that differation limit of SLM direct image is limited to ~60 µm. It's not possible to measure vertical beam sizes from the streak camera image.

To see the fast ion introduced dipole motions, vertical BxB feedback was gated OFF for 20ms and streak camera horizontal trigger delay was adjusted to see the turn to turn profiles at 19ms after feedback OFF. As shown in the bottom image, the head bunches were still stable while the tail bunches (> bunch #100) were executing some dipole motions.

SUMMARY

Fast ion instability has been observed at NSLS2 storage ring at different vacuum conditions, beam current, filling pattern, chromaticity and insertion devices. Unstable modes tend to move to higher frequency at higher bunch current, due to increased ion frequencies. As beam sizes along the ring vary a lot, ion frequency and induced instabilities typically have a broadband hump. Further systematic studies at different emittance and coupling will help to understand the observations better. This will in turn help to operate the machine stably and reliably at high current and lower emittance.

Our measurements of single bunch tune, bunch to bunch tune shift and lifetime increase along the bunch train, as well as vertical oscillation developing along the train captured with the streak camera all show that thee leading 100-200 bunches behave quite differently. Bunches after that are likely seeing ion effects.

REFERENCES

[1] F. Willeke, "Commissioning of NSLS-II", IPAC'2015

[2] G. Stupakov, L. Wang, "Fast Ion Instability in the NSLS-II", unpublished.

[3] W. Cheng, et. al., "Commissioning of Bunch-by-bunch Feedback System for NSLS2 Storage Ring", IBIC'2014

[4] T. Raubenheimer and F. Zimmermann, "Fast beam-ion instability I. Linear theory and simulations", Phys. Rev. E52, No. 5, 5487 (1995)

[5] G.Stupakov, T. Raubenheimer, F. Zimmermann, "Fast beam-ion instability II. Effect of ion decoherence", Phys, Rev. E52, 5499 (1995)

[6] J. Byrd et al., "First Observations of a Fast Beam-Ion Instability", Phys. Rev. Lett. 79, 79 (1997)

[7] B. Jiang et al., "Investigation of fast ion instability in SSRF", Nulc. Inst. Meth. A, Vol. 614, 331 (2010)

[8] R. Nagaoka et al., "Fast Beam-ion Instability Observations at SOLEIL", IPAC'2010

[9] L. Wang et al., "Beam ion instability: Measurement, analysis, and simulation", PRST-AB, 16, 104402 (2013)

[10] W. Cheng et al., "NSLS2 Fill Pattern Monitor and Control", this proceeding.

[11] W. Cheng et al., "Longitudinal Bunch Profile Measurement at NSLS2 Storage Ring", this proceeding.

ISBN 978-3-95450-176-2

FIRST LHC EMITTANCE MEASUREMENTS AT 6.5 TeV

M. Kuhn[1,2], F. Antoniou[1], E. Bravin[1], B. Dehning[1], J. Emery[1], V. Kain[1],
A. Langner[1,2], Y. Papaphilippou[1], E. Piselli[1], G. Trad[1]
[1]CERN, Geneva, Switzerland [2]University of Hamburg, Germany

Abstract

During LHC Run 1 significant transverse emittance growth through the LHC cycle was observed. Measurements indicated most of the blow-up to occur during the injection plateau and the ramp. Intra beam scattering was one of the main drivers of emittance growth. However, finding a good wire scanner working point was difficult. Photomultiplier saturation added uncertainty on all measurements. A large discrepancy between emittances from wire scanners and luminosity was discovered but not solved. During Long Shutdown 1 the wire scanner system was upgraded with new photomultipliers. In April 2015 the LHC re-started with collision energy of 6.5 TeV per beam. This paper presents the first transverse emittance measurements through the LHC Run 2 cycle with low beam intensity. Comparisons with data from the synchrotron light monitors and the LHC experiments will be discussed and results summarized. In addition, a thorough study of wire scanner photomultiplier saturation will be presented. Finally, the emittance growth results will be compared to intra beam scattering simulations.

INTRODUCTION

In 2012 the LHC was operated with high brightness beams with beam parameters pushed to their limits for outstanding luminosity production. With a bunch spacing of 50 ns the LHC was filled for physics with 1374 bunches per ring, containing up to 1.7×10^{11} protons per bunch (ppb) with transverse emittances as small as 1.5 µm at injection. However, the high brightness could not be preserved during the LHC cycle. Measurements in 2012 revealed a transverse emittance blow-up of about 0.4 to 0.9 µm from injection into the LHC to the start of collisions [1].

At the start of Run 2 in 2015 the LHC is operated with beams of reduced brightness. The beam parameters of the 2015 early physics beams as well as the nominal parameters are listed in Table 1. During the first phase of commissioning and intensity ramp-up measurements indicate less total blow-up than in 2015. This paper summarizes the results of beam size measurement accuracy with the LHC wire scanners and emittance growth through the LHC cycle.

LHC Wire Scanner Intensity Limitations

The LHC wire scanners are equipped with a 36 µm thick carbon wire attached to a linearly moving fork [2]. The wire crosses the beam at a constant speed of 1 m/s. For each measurement the beam profile is scanned twice as the wire passes through the beam with in and out scan. In this paper only the average beam size obtained from in and out scan is used and the error from averaging is included in the results.

Table 1: LHC Design and Early 2015 Run Configurations

	Design	Early 2015
Total number bunches per beam	2808	3 – 458
Bunch spacing [ns]	25	25 and 50
Mean bunch length [ns]	1.3	1.2
Bunch intensity [10^{11} protons]	1.15	1.0 – 1.2
Injection energy [GeV]	450	450
Emittance at injection [µm]	3.5	1.5 – 3.0
Collision energy per beam [TeV]	7	6.5
Emittance at collision [µm]	3.75	1.5 – 4.0
β^* at ATLAS/CMS [m]	0.55	0.8

The LHC wire scanners can only be used with a small fraction of the total nominal intensity per ring due to wire heating. The carbon wire should be able to take 2–3×10^{13} charges/mm before sublimating. The close-by LHC superconducting magnets limit the maximum scan intensity further, to 5×10^{12} charges/mm [2], because the particle showers produced by the wire passing through the beam can quench the magnets. This limit corresponds to about 240 bunches per beam ($2.7\times10^{13}p$), less than one injected nominal batch (288 bunches). At 6.5 TeV flattop energy scans were possible with up to two nominal bunches ($2.3\times10^{11}p$). The flattop limit has recently been redefined to $1.6\times10^{12}p$ after the first experience at 6.5 TeV.

The emittance evolution of high intensity physics fills cannot be measured with the LHC wire scanners. The synchrotron light telescope (BSRT) is used for that purpose. The BSRT absolute beam size measurement is obtained from a cross-calibration with wire scanners. Also, the wire scanner is currently the only operational device that can accurately measure beam sizes through the LHC energy ramp. Low intensity test fills during the commissioning phase are used for the calibration of the emittance measuring instruments and emittance preservation studies.

RUN 2 LHC WIRE SCANNER ACCURACY

The obtainable emittance measurement accuracy for a wire scanner at location with no dispersion depends on the accuracy of the optics knowledge (β) and measurement error ($\Delta\beta$) as well as on the beam size measurement accuracy ($\Delta\sigma$) of the given device:

$$\frac{\Delta\varepsilon}{\varepsilon} = \sqrt{\left(2\frac{\Delta\sigma}{\sigma}\right)^2 + \left(\frac{\Delta\beta}{\beta}\right)^2} \quad (1)$$

A large contribution to the wire scanner beam size accuracy derives from the wire position measurement precision and the position measurement calibration. The precision

ISBN 978-3-95450-176-2

of the position measurement potentiometer is estimated to be 50 µm. The position measurement calibration was verified with beam by an orbit bump scan at the wire scanner location.

The wire scanner shower product is amplified by a photomultiplier (PM). The amplification settings (gain and filter) can alter the obtained beam profile. During LHC Run 1 a strong dependence of PM settings on the measured beam size was observed [1]. Therefore the optimum PM working point has to be established.

Wire Position Measurement Calibration

While the centre of the beam was shifted locally at the scanners, wire scans were triggered to determine the accuracy of the position measurement of the wire scanners. The orbit at the wire scanner is extrapolated from beam position measurements with the LHC orbit system and compared to the mean position obtained from a Gaussian fit to the measured wire scanner beam profile. Measurements at 450 GeV and 6.5 TeV are consistent. As an example the calibration results of scanner B2V1 are shown in Fig. 1. The slope of the linear fit shows a 3.3 % calibration error for this wire scanner. The results in terms of emittance for all operational wire scanners are listed in Table 2. Another set of orbit bump scans is foreseen for the near future to check reproducibility. For the time being measurement results in this paper do not include a calibration error.

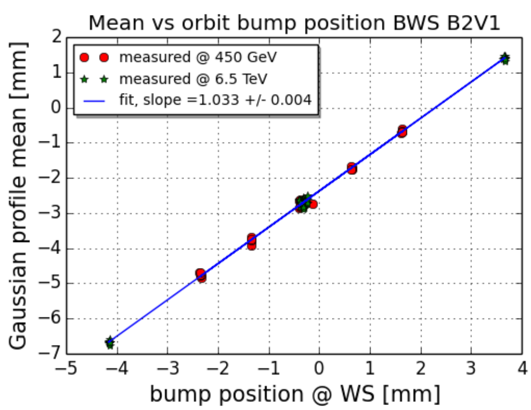

Figure 1: Gaussian profile mean of beam 2 vertical measured with wire scanner at different orbit bumps at 450 GeV (red) and 6.5 TeV (green), Fill 3644 (April 24, 2015). A linear fit (blue) is applied.

All wire scanner measurements show a large beam size measurement spread from scan to scan which depends on the scanner and the energy, see Fig. 2 and Fig. 3. Table 2 summarizes the emittance measurement precision with the different wire scanners according to the current knowledge. The LHC Run 2 optics at the transverse profile monitors have been measured with the k-modulation method at 450 GeV injection energy [3] and with the turn-by-turn BPM phase advance method at 6.5 TeV flattop energy, before and after the 80 cm β^* squeeze. The β function accuracy at the wire scanners is better than 3 %.

Photomultiplier Working Point Investigations

To find the optimum working point of the wire scanners, measurements with all available PM gain and filter setting combinations were performed. Figure 2 shows the measurement results for scanner B2V1 at 450 GeV. Bunches with different beam sizes were injected into the LHC. The beam size evolution is plotted over time with the applied gain and filter settings. To remove the natural emittance growth at the injection plateau, scans with a fixed reference settings were done after each settings change and fitted assuming an exponential function. Figure 4 then shows measured beam sizes minus the fitted growth. In addition, the results of measurements with same gain and filter settings are averaged to one data point. At 450 GeV no sign of PM saturation could be detected. Moreover, all combinations of settings below ADC saturation result in reasonable profiles. Similar results were obtained for the other wire scanners.

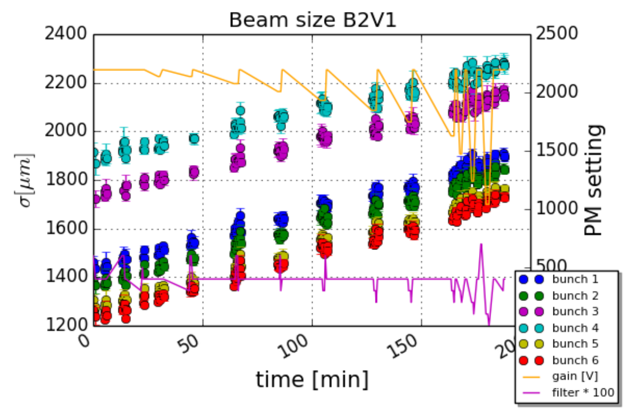

Figure 2: Beam 2 vertical beam size of six single bunches from wire scans at 450 GeV, Fill 3808 (May 31, 2015). The PM voltage (orange) and filter (purple) are displayed.

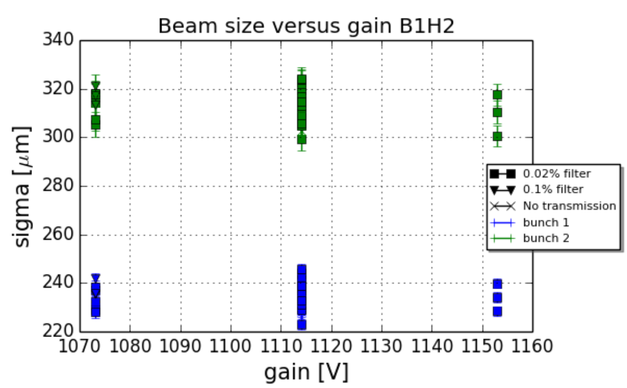

Figure 3: Beam 1 horizontal beam size of two single bunches from wire scans at 6.5 TeV, Fill 3809 (June 1, 2015), as a function of the applied PM voltage. The different PM filters are marked.

Measurements at 6.5 TeV were more difficult because the possible range of PM settings is much smaller than at 450 GeV. Nevertheless, also at flattop energy no PM saturation can be seen, see Fig. 3.

Investigations during Run 1 showed significant dependency of measured beam size on PM settings. The upgrade

ISBN 978-3-95450-176-2

Table 2: LHC Run 2 Wire Scanner Emittance Calibration Error ($\Delta\varepsilon_{cal}$), Typical Emittance Measurement Spread of Four Consecutive Measurements at 450 GeV ($\Delta\varepsilon_{inj}$) and 6.5 TeV ($\Delta\varepsilon_{top}$), and β Function Measurement Results.

Scanner	$\Delta\varepsilon_{cal}$ [%]	$\Delta\varepsilon_{inj}$ [%]	$\Delta\varepsilon_{top}$ [%]	β_{inj} [m]	β_{top} [m]	$\beta_{squeeze}$ [m]
B1H2	+7.2	25	20	194.0 ± 0.8	196.8 ± 1.4	209.0 ± 5.0
B1V2	-5.2	20	10	363.3 ± 1.8	369.0 ± 3.0	366.0 ± 4.0
B2H1	+9.0	25	15	192.0 ± 0.7	193.8 ± 1.1	196.0 ± 3.0
B2V1	+6.6	15	10	410.7 ± 2.3	396.0 ± 3.0	404.0 ± 5.0

of the LHC wire scanners during Long Shutdown 1 could explain the improved situation. One broken PM has been replaced (beam 2) and power supply schematics have been upgraded. Also the PM gain dependency on light intensity has been reduced.

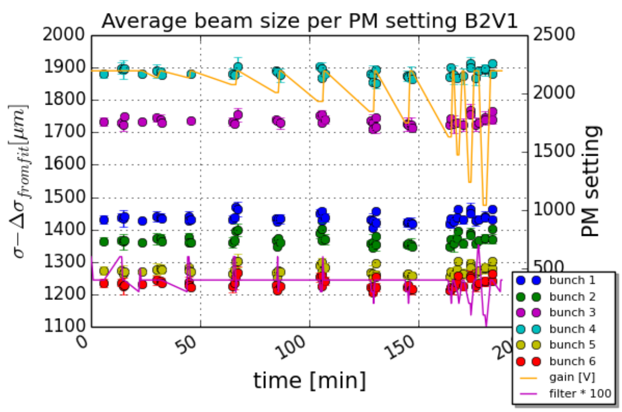

Figure 4: Average beam 2 vertical beam size per PM setting minus growth from exponential fit of six single bunches from wire scans at 450 GeV, Fill 3808 (May 31, 2015). The PM voltage (orange) and filter (purple) are displayed.

FIRST EMITTANCE MEASUREMENTS

The emittance evolution through the different parts of the LHC cycle has been studied during the LHC commissioning phase for 30 low intensity fills. As an example Fill 4287 was analysed in detail through the cycle with the following phases:

- Injection process from SPS to LHC
- 450 GeV injection plateau (~ 30 min)
- Ramp from 450 GeV to 6.5 TeV (20.2 min)
- Change to collision tunes and β^* squeeze from 11 m to 80 cm in ATLAS/CMS (12.5 min)

During Fill 4284 three bunches were injected into the LHC with different initial emittances, intensities ($0.6 - 1.1 \times 10^{11}\,ppb$) and bunch lengths (1.0 – 1.25 ns). An overview of the measured emittances through the cycle can be found in Fig. 5.

The total measured and simulated emittance growth through the LHC cycle of bunch 3 is enumerated in Table 3. The emittance at SPS extraction of bunch 3 measured with wire scanners was 1.9 µm in the horizontal plane and 1.5 µm in the vertical plane. The procedure was repeated during many fills. No emittance growth could be observed during the transfer from SPS to LHC within measurement accuracy.

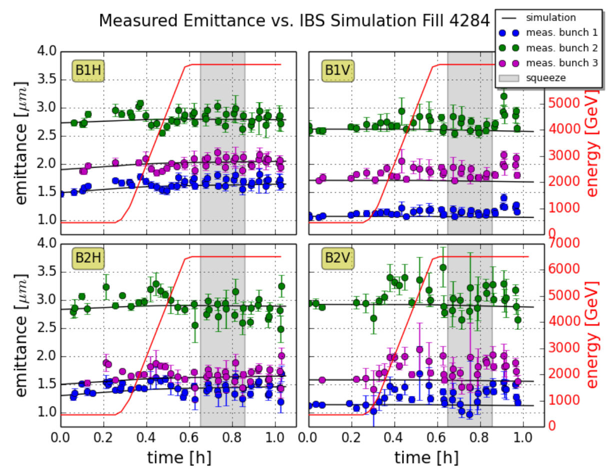

Figure 5: Emittance from wire scans of three single bunches during the LHC cycle, Fill 4284 (August 28, 2015), with IBS simulations (black). The energy (red) and β^* squeeze (grey) are displayed.

Table 3: Emittance Blow-up from Injection (0) to End of Squeeze (1), Fill 4284 Bunch 3, and Simulated Growth (sim)

	ε_0 [µm]	ε_1 [µm]	$\Delta\varepsilon$ [µm]	$\Delta\varepsilon/\varepsilon$	$\Delta\varepsilon/\varepsilon_{sim}$
B1H	1.90	2.08	0.18	0.09	0.08
B1V	1.71	2.04	0.33	0.19	−0.02
B2H	1.50	1.65	0.15	0.10	0.10
B2V	1.58	1.95	0.37	0.23	−0.02

IBS at the Injection Plateau

The emittance growth during the injection plateau depends on the initial beam parameters. Intra beam scattering (IBS) is the major cause for horizontal emittance blow-up at low energies. An IBS simulation with MADX [4] is shown in Fig. 5. The simulated growth is compared to the measured emittances. For all planes the growth at 450 GeV is fairly well predicted. Despite the large emittance spread, the mean measured horizontal growth matches the simulated values.

Emittance Growth During the LHC Ramp

Measured β functions for the 2015 energy ramp are not yet available. Non-physically growing and shrinking emittances in all planes can be observed, see Fig. 6, as was

ISBN 978-3-95450-176-2

already the case during LHC Run 1. This was due to the non-monotonically changing β functions during the ramp. IBS simulations with these parameters suggest less than 0.05 µm (3 %) horizontal emittance blow-up during the ramp, which is within the measurement accuracy and consistent with measurements. Vertical emittances experience an emittance blow-up of about 0.1 – 0.3 µm (10 – 20 %), which cannot be reproduced with IBS simulations.

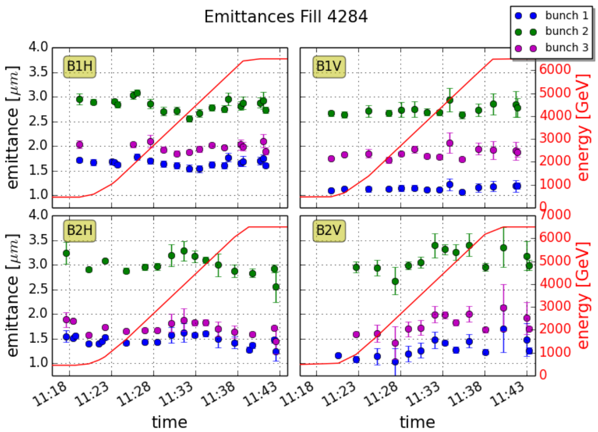

Figure 6: Emittance from wire scans of three bunches during the energy ramp to 6.5 TeV for Fill 4284. The energy (red) is displayed.

Emittance Preservation During the Squeeze

Within measurement accuracy the emittances are conserved during the β^* squeeze, see BSRT measurements in Fig. 7. This result is reproducible and has also been confirmed with wire scanner measurements. BSRT emittances are averaged over several hundred measurements. Beam 1 horizontal always shows large statistical fluctuations from measurement to measurement.

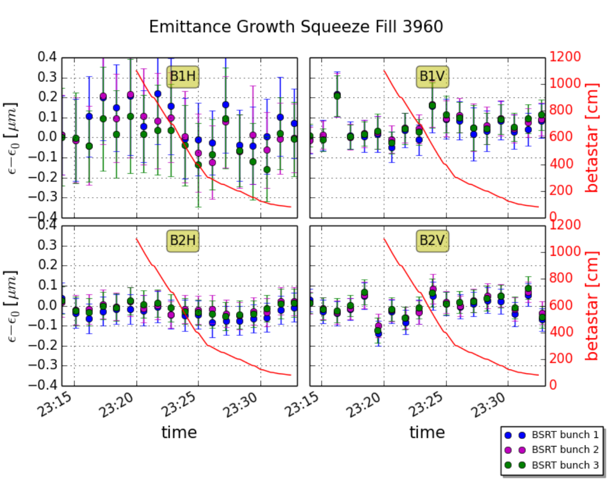

Figure 7: Emittance from BSRT measurements of three single bunches during the tune change at 6.5 TeV and the β^* squeeze to 80 cm in ATLAS/CMS, Fill 3960 (July 4, 2015). The β^* value (red) is displayed.

Emittance at the Start of Collisions

During head-on collisions it is possible to derive emittance from luminosity and directly compare it to the convoluted emittance from simultaneous wire scans during low intensity fills. The method assumes identical Gaussian shaped and perfectly aligned beams. During collisions of Fill 3954 the convoluted emittance from wire scans is compared to emittance from ATLAS and CMS luminosity, see Table 4. The values are taken after the interaction points have been optimized. ATLAS and wire scan emittances at collision agree within measurement uncertainties. However, the luminosity is not yet calibrated. According to experts the luminosity in both experiments is currently low by 10 % with an uncertainty of ± 10 %. The measured β^* values are used. They have been measured with k-modulation with 1 % uncertainty [3]. The crossing angle is known within an uncertainty of ±5 %. Due to a controlled longitudinal RF blow-up of the bunches at 6.5 TeV the longitudinal bunch shape becomes non Gaussian. However, the LHC Beam Quality Monitor (BQM) publishes a 4σ bunch length value based on the Full-Width-Half-Maximum algorithm assuming Gaussian bunch profiles. This results in an estimated bunch length error of ±1 cm [5]. If the measured bunch length is for instance 0.09 m (= 1.2 ns), the real bunch length is rather 1.1 ns. This would result in a 0.1 µm larger emittance.

The large discrepancy between emittance from luminosity and wire scanner as found during Run 1 is not apparent any more during Run 2. A possible explanation is the better understanding of the wire scanners. The total convoluted emittance blow-up through the cycle is 10 % from wire scanners and 20 % from luminosity for single bunches.

Table 4: Comparison Convoluted Emittance from Wire Scans and Luminosity for Fill 3954

	Wire Scan	**ATLAS**
$\varepsilon_{injection}$ [µm]	2.51 ± 0.10	No measurement.
$\varepsilon_{collision}$ [µm]	2.75 ± 0.20	2.97 ± 0.36
$\Delta\varepsilon$ [µm]	0.24 ± 0.22 (10 %)	0.46 ± 0.37 (19 %)

Radiation Damping at 6.5 TeV

At high energies protons circulating in the LHC emit enough synchrotron radiation to modify the beam parameters. This effect counteracts IBS and could be observed for the first time during LHC Run 2. Synchrotron radiation damping slowly reduces the vertical emittance at 6.5 TeV, see Fig. 8. The LHC emittance damping time is about 32 hours at 6.5 TeV. The emittance evolution due to radiation damping was simulated with the MADX IBS module and also displayed in Fig. 8. The simulation predicts slightly faster vertical emittance decrease than measured due to emittance growth from proton collisions and other beam-beam effects not included in the simulation.

ISBN 978-3-95450-176-2

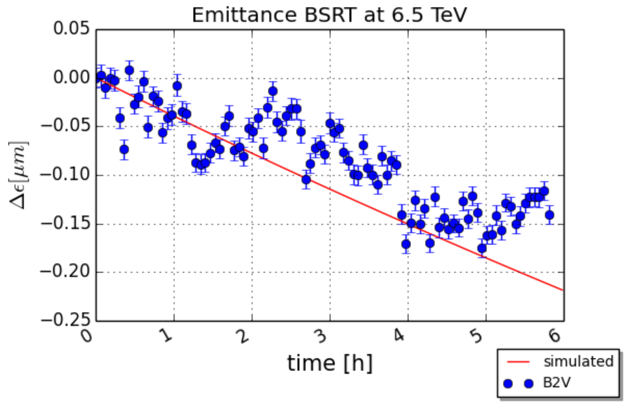

Figure 8: BSRT measurements of beam 2 vertical emittance during collisions of Fill 3988 (July 12, 2015) compared to simulations.

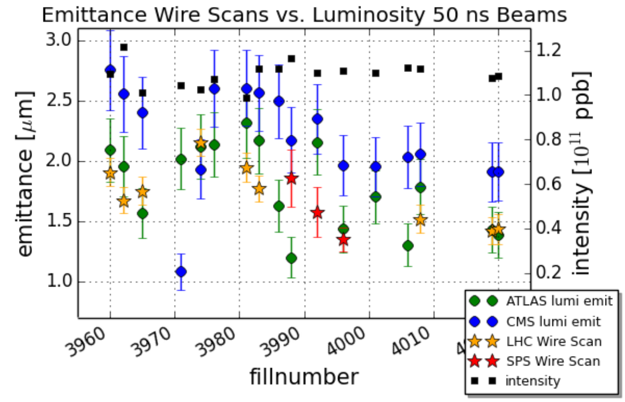

Figure 9: Emittance of 50 ns beams from ATLAS (green) and CMS (blue) luminosity at the start of collisions compared to the convoluted emittance at LHC injection (orange) or SPS extraction (red) measured with wire scanners.

PERFORMANCE OF THE LHC

Wire scanner measurements of low intensity fills can only give an indication of emittance blow-up during the various phases of the LHC cycle. High intensity effects have to be added. To understand the emittance evolution for LHC physics fills, the transverse emittance at the end of the cycle is derived from ATLAS and CMS luminosity. The emittance of the first injected batch at the start of the cycle can be measured at SPS extraction and LHC injection with wire scanners. For the intensity ramp-up in 2015 with 50 ns beams an overview of all physics fills can be seen in Fig. 9. Overall, the emittance blow-up is much smaller than during Run 1 (10 % average growth). Emittances of the 25 ns physics beams during the intensity ramp-up in 2015 show a large blow-up from injection to start of collisions, see Fig. 10, but improving over time (25 % for the most recent fills). Possible sources are electron cloud effects and beam instabilities.

Emittance measurements with the BSRT are unfortunately not useful for a short time frame and many bunches due to a long integration time. Only three to four bunch profiles per second can be obtained.

CONCLUSION

Good progress was made in understanding the wire scanner (and BSRT) emittance measurements for LHC Run 2. In general, the profile monitors are in a better shape than during Run 1. The wire scanner calibration could be verified and no PM saturation effects could be detected. Horizontal emittance growth during the entire LHC cycle can be matched with IBS simulations. Small growth in the vertical planes was measured and is not yet understood. For the first time, synchrotron radiation damping of protons at 6.5 TeV was observed. With the still not fully calibrated luminosity data, emittances from wire scans and ATLAS luminosity agree within measurement uncertainties. ATLAS luminosity measurements of 50 ns beams in 2015 indicate small growth through the cycle. However, large emittance blow-up

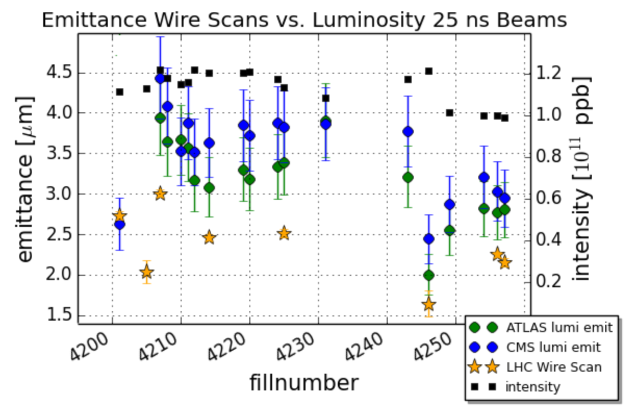

Figure 10: Emittance of 25 ns beams from ATLAS (green) and CMS (blue) luminosity at the start of collisions compared to the convoluted emittance at LHC injection measured with wire scanners (orange).

of 25 ns beams during the cycle could be measured. The electron cloud effect is not fully under control and beam instabilities degrade beam quality.

REFERENCES

[1] M. Kuhn, “Emittance Preservation at the LHC,” Master Thesis, University of Hamburg/CERN, Geneva, Switzerland 2013.

[2] M. Sapinski, “Beam Interaction with Thin Materials: Heat Deposition, Cooling Phenomena and Damage Limits,” BIW2012, Newport News, Virginia, USA, April 2012.

[3] M. Kuhn, “First K-Modulation Measurements in the LHC during Run 2,” presented at IBIC’15, Melbourne, Australia, Sep 2015, paper MOPB046, these proceedings.

[4] http://mad.web.cern.ch/mad/

[5] M. Hostettler, “Observations from OP extended luminosity scans,” LBOC Meeting No 44, CERN, Geneva, Switzerland, July 28, 2015.

ISBN 978-3-95450-176-2

BEAM LOSS MONITORING FOR DEMANDING ENVIRONMENTS

E. B. Holzer*, CERN, Geneva, Switzerland

Abstract

Beam Loss Monitoring (BLM) is a key protection system for machines using beams with damage potential and is an essential beam diagnostic tool for any machine. All BLM systems are based on the observation of secondary particle showers originating from escaping beam particles. With ever higher beam energies and intensities, the loss of even a tiny fraction of the beam can lead to damage or, in the case of superconducting machines, quenches. Losses also lead to material aging and activation and should therefore be well controlled and reduced to a minimum. The ideal BLM system would have full machine coverage and the capability to accurately quantify the number of lost beam particles from the measured secondary shower. Position and time resolution, dynamic range, noise levels and radiation hardness all have to be considered, while at the same time optimizing the system for reliability, availability and maintainability. This contribution will focus on design choices for BLM systems operating in demanding environments, with a special emphasis on measuring particle losses in the presence of synchrotron radiation and other background sources.

INTRODUCTION

A Beam Loss Monitoring (BLM) system has three main roles: provide protection against beam induced damage or quench, provide a diagnostics tool for the operation and commissioning of the machine, and keep the activation levels low. When beam particles in an accelerator or a transfer line deviate from the ideal trajectory, they eventually hit the vacuum chamber walls or beamline components and generate secondary particle showers. If their energy is high enough to penetrate, these secondaries can be measured outside of the machine by a BLM system. Hence, for all but the very lowest energy machines, beam loss monitoring is an essential beam diagnostics tool. It applications include: beam steering in linear machines, by minimizing the losses along the line; diagnostic of failure scenarios; search for aperture restrictions or erroneous machine elements causing local losses.

It is important to minimize beam losses even if they are not immediately compromising the machine structure, as they lead to aging of the materials and to activation. Radiation levels have to be kept as low as possible to limit human exposure during maintenance and repair work and to reduce the amount and activation levels of radioactive material at the end of the machine life-cycle. Collimation systems play an important role in this respect. They concentrate the unavoidable losses in comparatively short regions and, in the ideal case, can keep the rest of the machine virtually loss free. The importance of beam collimation increases at very high beam intensities and energies, where uncontrolled losses of even the beam halo have to be avoided.

The first part of the paper will discuss general design considerations for a BLM system with a focus on machines with damage potential, on regions of high radiation levels and on physically large machines. Machine protection, the coverage of loss scenarios and the system dependability will be discussed, as well as the possibility to resolve the position, the magnitude and the time structure of the losses. The second part of the paper discusses background sources to the beam loss measurement. These can limit the sensitivity, reduce the dynamic range and even compromise the machine protection functionality. Showers from distant beam losses, radiation from accelerating structures and background due to synchrotron radiation are reviewed. Throughout the paper examples will be given mostly of recent and current developments to cope with the challenges of future machines.

BLM FOR MACHINE PROTECTION

Where the beam has the potential to damage accelerator structures or to cause quenches in superconductive machines, by far the most demanding role of the BLM system is machine protection. On October 9, 2015 the record level of 200 MJ of stored energy per beam was surpassed with 6.5 TeV beams in the LHC as part of the intensity ramp-up. 362 MJ per beam is envisaged at the design beam energy of 7 TeV and nominal beam intensity. Already one LHC pilot bunch of 5×10^9 protons is close to the damage limit at 7 TeV. At HL-LHC (High Luminosity LHC), a major upgrade of the LHC planned for 2023, it is foreseen that the energy of one beam will reach 694 MJ, and even 8 GJ is envisaged for FCC-hh (Future Circular hadron Collider). Besides the beams, the enormous amount of 10 GJ will be contained in the LHC magnets at 7 TeV. This corresponds to 2.4 ton of TNT. If even a small fraction of this energy is released in an uncontrolled way massive damage could result.

In the design of the CLIC (Compact Linear Collider) two beam module, a low energy (2.4 GeV) and high current (100 A) electron drive beam is decelerated and the extracted power is transferred to a high energy (1.5 TeV) and low current (1.2 A) electron or positron main beam. The nominal beam power is large, 72 MW and 14 MW for the drive and the main beam respectively. Losses from either beam can have severe consequences. The most critical beam quantities are the high intensity for the drive beam and the high energy and small emittance for the main beam.

A powerful machine protection system is vital for all machines with damage potential and constitutes an integral part of the machine design. The BLM system is one of its key components. When losses exceed threshold values on any one of the 3600 loss detectors at the LHC, the beam is safely aborted. The thresholds depend on the detector location, the

* barbara.holzer@cern.ch

ISBN 978-3-95450-176-2

beam energy and the duration of the loss (in a range of 40 µs – 84 s), resulting in a total of about 1.5 million threshold values which span up to eight orders of magnitude. The CLIC machine protection is based on a 'next cycle permit': A subsequent injection is inhibited, when the onset of a potentially dangerous loss is detected.

A dependability analysis comprising reliability, availability, maintainability and safety is required for the design of a machine protection system. This analysis yields the allowed budgets for the BLM system in terms of: probability of component damage due to malfunction; downtime due to false alarms; and downtime due to maintenance. There is an inherent conflict between these budgets. By reducing the damage probability (hence increasing the protection) the machine availability will go down due to increased numbers of false dumps and maintenance time.

DETECTOR CHOICE AND DISTRIBUTION

BLM systems employ either a number of individual, localized particle detectors (e. g. pin diodes, short ionization chambers) installed at likely loss locations such as aperture limitations, or long distributed detectors (e. g. fibers, RF cables) covering the whole beamline.

Individual, Short Particle Detectors

Typical locations for loss monitors include: quadrupoles; collimators, scrapers and masks; stripping or charge exchange foils; aperture restrictions for dispersive particles; beam dump regions; injection and extraction regions; beam diagnostics posing an aperture restriction e. g. mirrors, or utilizing gas injection.

For the best time resolution, a very small detector is required. Diamond BLMs at selected locations in the LHC have a time resolution of a few ns and give a one turn bunch-by-bunch loss measurement [1, 2]. Experience at the LHC shows that a significant localized loss anywhere in the machine leads to losses at the primary collimators as well. Hence, the time structure of the loss can be resolved by just a few high resolution BLMs at the collimators [3].

Small crystal Cherenkov detectors coupled to fast photon sensors have the potential to achieve even higher time resolution. Since Cherenkov light emission is a prompt process, the time resolution is governed by the size and the refractive index of the radiator and the photon sensor performance. With current sensor technologies, which in the sensitivity range of interest approach the 100 ps range, intra-bunch loss measurements at the LHC should be feasible.

The position resolution is given, in general, by the distance between the installed detectors. For the same magnitude of loss (same number of lost beam particles), the measured signal varies strongly with the distance from the detector. For the LHC it has been simulated that this can easily reach a factor of ten for only one meter. If, however, the loss is visible on several detectors, a much more precise loss location and magnitude can be determined with the help of detailed shower simulations [4]: FLUKA [5, 6] simulations based on detailed models of the LHC have been estimated to determine the position of losses caused by beam-dust particle interactions to within ± 1 m and the number of inelastic proton-nucleus interaction in the event to within a factor of 2. The analysis of LHC magnet quenches during Run1 showed that, with good knowledge of initial conditions and sufficient data for validation, particle-tracking and particle-shower simulations provide, in the best cases, 20 % agreement of magnet model predicted quench levels with BLM signals in the region of peak losses [7]. For well known impact location and conditions (e. g. at a collimator or charge exchange foil) a conversion factor from BLM signal to impacting particles can be determined by measurement and/or simulation.

But all loss locations can not necessarily be predicted at the design stage. At the LHC, about one third of the BLMs had to be relocated between Run1 and Run2, 2013–2014, to cover the circumference of the machine more uniformly. During beam operation previously unconsidered beam losses, dubbed 'UFO' losses, had appeared in high numbers all along the machine, also in the cold dipole magnets which had not been equipped with BLMs during Run1. These losses are believed to be caused by interactions of the beam with dust particles. At the 2015 LHC energy of 6.5 TeV they can quench a magnet. During Run1 no magnet quench due to an UFO event occurred. Less heat was deposited in the coils due to the lower beam energy, and the lower magnetic field meant a higher margin for coil heating. The BLM thresholds during Run1 were set conservatively at one third of the assumed quench level. In 2015, the thresholds were set right at the quench level as calculated and measured during quench test campaigns for arc and dispersion suppressor magnets. Three UFO induced quenches and nine BLM protection dumps without quench occurred till October 4, 2015 in these regions . The now better longitudinal coverage due to BLM relocation allowed to increase the beam abort thresholds by a factor of 30, as the variation in measured BLM signal at the magnet quench level due to position variations is reduced.

Distributed, Long Particle Detectors

Long, distributed loss detectors avoid holes in the coverage. They are of particular interest for large machines and for beams of high damage potential. The number of monitors and readout channels is significantly reduced, lowering the cost and easing the dependability requirements for the individual channel. Examples are long ionization chambers (e. g. gas filled coaxial RF cables), scintillator fibers and detection based on the Cherenkov effect in optical quartz fibers. They have successfully been employed on many machines for qualitative loss measurements.

BLM systems based on optical fibers have become increasingly popular in recent years in particular for electron machines that produce high levels of synchrotron radiation, see for example [8–11]. Beam loss induced high energy charged particles crossing an optical fiber generate Cherenkov light that is partially trapped and transported to the end, where a

ISBN 978-3-95450-176-2

photon sensor converts it into an electrical signal. The fibers are small, insensitive to photons and electromagnetic fields and can be adapted to a wide dose range by choosing appropriate combinations of fiber and readout. The measurement of the total dose deposited in the fiber, typically proportional to the amount of beam losses, requires full understanding of the system: Light generation and propagation, attenuation effects, optical coupling efficiencies and response of the photon sensor. Moreover, the aging of optical fibers in different irradiation conditions needs to be investigated and corrected by calibration. One fiber can cover up to approximately 100 m of beam line with a single detector, the range being limited by attenuation in the fiber. A time resolution of about 1 ns can be achieved and single bunch position resolutions down to 50 cm have been reported [10]. Because of attenuation effects the measured signal height and the loss location (distance to the photo-detector) are coupled. For short beams the loss magnitude can be determined by applying an appropriate calibration. To be able to use fiber loss detectors for machine protection, further R&D work is required, in particular for absolute loss measurements and for position and time resolution of long bunch trains.

A straight forward absolute longitudinal position and time measurement can be achieved with long detectors whenever the combination of bunch spacing, beam velocity, detector length and traveling time of the signal to the readout combines in a way that the loss signal of individual bunches never overlap at the readout, wherever the loss occurs along the detector. For long bunch trains this will, in general, not be the case any more. Time, position and loss magnitude information are coupled, and the reduced number of readout channels means that a general unfolding is not possible. Combination with a small detector with high time resolution measurement could help to recover also the position information. But most of the losses encountered during the life-time of a machine will be among a set of, eventually, well known loss scenarios. Once the scenarios are studied and cataloged it should be possible to analyze automatically the type and magnitude of the loss, recovering at the same time the position and time information. In a similar way, once the UFO loss pattern at the LHC was understood, it was possible to automatically detect these type of losses by combining the information from several monitors (locally and at the collimation) for online monitoring and statistical analysis.

Simulation studies of 100 m long Cherenkov fibers have shown a longitudinal resolution of 1 m and a time resolution of about 1 ns for the starting point of individual loss locations affecting all bunches in a long beam [12, 13]. First results from measurements at the Australian Synchrotron and the CLIC Test Facility (CTF3) indicate the feasibility of a position measurement for such loss scenarios with a resolution below 2 m [14].

MACHINE SIZE AND RADIATION

Physically large machines (like LHC, ILC, CLIC, FCC, SppC) pose considerable challenges for the BLM system already by their size alone. If localized detectors are chosen, their number increases in proportion to the number of optics cells. The cost increases, but also system maintenance and availability become increasingly challenging. More measurement data is produced, which needs to be extracted, logged, monitored, analyzed and made available for various online and offline applications. To keep electromagnetic interferences small, and considering the long distances involved, the front-end read-out electronics will in general be positioned in the accelerator tunnel, as close to the detector as feasible. In this case it has to be radiation tolerant, which considerably complicates design and production. Radiation certified components are often not available, therefore the radiation hardness has to be tested with particle beams. It is important to note, that only components from the same batch as the ones tested can be considered to have the corresponding radiation tolerance. Production details often change from batch to batch, influencing the susceptibility to radiation.

Example: Radiation Tolerant BLM ASIC

The LHC BLM front-end electronics is verified to be radiation tolerant up to 500 Gy. This is sufficient for the virtually loss free arcs even for the HL-LHC upgrade, where the electronics is placed in the vicinity of the detectors underneath the quadrupole magnets. The front-end electronics of the higher radiation dispersion suppressors and straight sections is placed up to 300–800 m away in radiation shielded locations. The long cables lead to increased noise levels, which are in some cases reaching the required beam abort levels for quench protection at 7 TeV. Development is ongoing to implement the front-end electronics in a radiation hard Application Specific Integrated Circuit (ASIC) [15, 16]. Again based on current-to-frequency conversion, it is packaged in a compact and radiation tolerant form. The plan is to install it directly on the ionization chamber, inside the so called electric box, which houses high voltage filtering. The integration time remains 40 µs. The dynamic range increases to 120 dB (40 fC – 42 nC) and it will newly operate with positive and negative input currents. The radiation tolerance up to 100 kGy has been verified using X-rays of 20 keV peak energy.

To transport the signal to the surface requires low noise, low loss signal transmission. Optical signal transmission and, in general, optical diagnostic techniques are preferable under such conditions.

BACKGROUND FROM DISTANT BEAM LOSSES

Collimation regions, the vicinity of the interaction points, regions of beam injection and beam extraction have particularly high levels of radiation. This poses a problem for beam loss monitoring, as a typical loss monitor cannot distinguish

ISBN 978-3-95450-176-2

between a beam loss and other sources of radiation. These additional radiation sources are often generated by beam losses further upstream (e. g. by collimation or scraping), losses from another beam line (injection or extraction lines, opposite beam in particle colliders), or by beam-beam collision products from interaction points. Critical regions in the LHC are the injection regions, which see losses from the injection line collimators; the collimation regions, which see losses from several collimators from the same beam and the opposite beam; and the insertion region triplet magnets, which are exposed to high radiation levels from collision debris.

Example: The CLIC Two-Beam Module

A particular case is the CLIC main linac, where the drive beam and the main beam run in parallel just 65 cm apart. The energy ranges from 2.37 to 0.237 GeV in the drive beam, and from 9 to 1500 GeV in the main beam. Beam dynamics considerations impose the total losses to be no more than 10^{-3} of the respective total beam intensity along the 20 km main linac as well as along each drive beam decelerator section. Otherwise, luminosity losses from beam loading variations would become intolerably high. Due to the large differences in beam intensity and energy the signal of the maximum acceptable loss of the main beam is up to two orders of magnitude below the signal of the maximum acceptable loss of the drive beam in the same two-beam module, for detector positions close to the respective quadrupole [17]. Due to the vicinity of the two beams, it is not obvious how to measure a main beam loss in the presence of a drive beam loss. For machine protection purpose that is actually not a problem, as simulations have shown that dangerous beam losses will be detected in any case.

An experiment was set up at the two-beam module of CTF3 to address the question of distinguishing the origin of the loss using Little Ionization Chambers (LIC), a shortened version of the LHC-type ionization chamber with only one signal electrode, and Cherenkov fiber detectors [18]. A first, limited measurement period showed losses on one beam leading to signals in the detectors on the other side of the two-beam module of 1–5 % of the signals on the side affected by losses. More systematic measurements will be performed.

Example: Cryogenic BLM for HL-LHC

Conventional loss detectors are installed on the outside of the magnets. At the LHC, the ionization chambers are located outside of the magnet cryostat, far from the superconducting coils. With the magnet yoke and the cryostat material in between, they can only measure the tails of the beam loss induced shower which heats the coils. The dose at the sensitive superconductor coil is much higher than the dose at the detector. The opposite is true for any background radiation from outside of the magnet: The cryostat and yoke now shield the coil and the dose to the detector will be higher than the dose to the coil. This effect can seriously hamper the loss measurement and compromise the quench protection.

The insertion region triplet magnets focus the beams on the interaction point. They are particularly challenging magnets, due to the high gradient of 215 T/m [19], their wide aperture and their exposure to a high radiation dose just 23 meters from the interaction point.

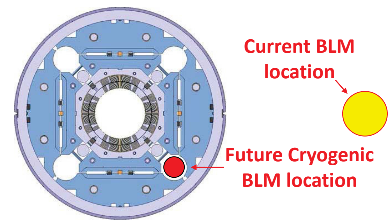

Figure 1: Cross section of the triplet magnet (MQXF) foreseen for HL-LHC, indicating the current BLM placement and the possible location of a cryogenic BLM [20].

For the HL-LHC upgrade it is foreseen to install loss detectors inside the new triplet magnets in super-fluid helium, see Fig. 1. Much closer to the loss location and shielded from other radiation sources, quench protection can be assured even in particularly high radiation areas. The system challenges include: operation of the detector in liquid helium at 1.9 K with a total radiation dose of 2 MGy during 20 years without access to the cold part of the system; a magnetic field of 2 T; fast pressure rise in case of magnet quench from 1.1 bar to 20 bar; a linear response in the range of 0.1 to 10 mGy/s; and the possibility to reliably predict and correct for radiation induced response degradation. The installation inside of the cryostat calls for very high dependability of the systems. Three different technologies are being investigated at CERN: liquid helium, silicon detectors and single crystal Chemical Vapour Deposition (scCVD) diamond detectors. The operation at such extreme conditions has not been previously attempted. Therefore, an extensive measurement program is being carried out at CERN since 2011 [20–22].

The liquid helium detector prototypes [21] were parallel plate ionization chambers, similar in design to the LHC-type ionization chamber, but smaller and with a plate distance of 1–3 mm. They can use directly the magnet cooling helium as ionization medium. With a full metal and ceramics design and the ionization medium being continuously flushed, this detector is intrinsically radiation hard. The detectors were tested at 1.8 and 4.2 K and up to 400 V/mm. The test measurements were promising, but not fully conclusive. In any case, the time resolution is limited by the low charge mobility in the order of 8–10 mm^2/Vs at 1.8 K [23], which is seven orders of magnitude smaller than the charge mobility in silicon at this temperature. The detector can not protect against losses which are faster than 180 µs. Hence it is too slow for the protection of the triplet magnets.

The behavior of the solid state detectors has been classified in terms of: detector sensitivity, leakage current, signal speed, signal shape, and radiation induced degradation of these parameters; and the dependency of the above on temperature, temperature cycling, bias voltage and dose rate. A variety of silicon and scCVD diamond detectors from differ-

ISBN 978-3-95450-176-2

ent manufacturers and with varying designs are investigated. The FWHM signal from a MIP (Minimum Ionizing Particle) at 1.9 K is 2.5 ± 0.7 and 3.6 ± 0.8 ns for silicon and diamond detectors respectively. This allows for bunch-by-bunch loss measurements. It could be shown that both materials can operate at 1.9 K and after irradiation of 2 MGy [22]. At liquid helium temperatures, the major downside of silicon compared to diamond, namely its high leakage current, disappears. The leakage current of an irradiated silicon detector remains below 100 pA at 400 V, even under forward bias. Figure 2 shows results for a 500 µm thick diamond with an active area of 22 mm^2 and gold metallization and a 300 µm p$^+$-n-n$^+$ silicon with an active area of 23 mm^2, aluminum metallization and a resistivity of 10 kΩ cm and 500 kΩ cm respectively. For low doses the sensitivity of the silicon is higher, but for high doses the diamond detectors give higher signals. With a decrease by a factor of 14 ± 3, the diamond shows the lowest signal degradation for a dose of 2 MGy. The expected signal degradation for silicon is of a factor of 25 ± 5. For absolute loss measurement and for machine protection, in any case, it is essential to establish a calibration method.

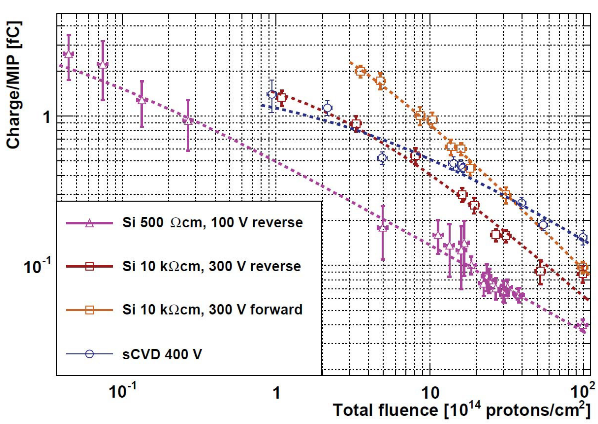

Figure 2: Radiation induced degradation of silicon and diamond detectors for a dose corresponding to 20 year of LHC operation in the triplet magnets [21].

Cryogenic BLMs were installed at the LHC to test the validity of the set-up and the long term behavior in the machine environment [24]. Two dipole magnets were equipped with four detectors each (one 500 µm scCVD diamond, one 100 µm silicon and two 300 µm silicon detectors) mounted right against the outside of the cold mass in the insulation vacuum of the cryostat. The temperature at this location is about 20 K. First loss measurements are expected at the end of 2015.

New 11 T dipole magnets are considered for selected locations in the LHC dispersion suppressors as part of an upgrade of the collimation system [25]. If this option is chosen, they could be equipped with cryogenic BLMs inside the magnet cold mass, and would allow for the first measurements in 1.9 K liquid helium in the LHC machine.

BACKGROUND FROM ACCELERATING STRUCTURES

Potential sources of background generated by high gradient accelerating structures are due to dark current and voltage breakdown. Dark currents are electrons which are released from internal surfaces by electron field emission and then accelerated, generating X-rays and secondary showers when they impinge on cavity walls or other beamline components. Besides RF accelerating structures, particle sources emit dark currents as well. Voltage breakdown refers to an internal discharge in the RF cavity, creating an electric arc. It is accompanied by a high emission of X-rays and electrons. In the case of the CLIC two beam module a breakdown current on the order of 100 A can occur in the main beam structure [17]. Not only do these effects limit the possibility to measure primary beam losses, they have a negative impact on the performance of the accelerator: They reduce the beam stability and/or availability, lead to component heating and radiation aging, and can result in quenches in superconducting structures. Beam loss monitors can also be employed to measure such events which are a priori not associated with beam losses, but which can easily trigger additional beam losses.

Example: CLIC Main Linac Cavity

An optical fiber Cherenkov loss monitor coupled to Multi-Pixel Photon Counter (MPPC) readout has been installed at an experiment of the CLIC Test Facility (CTF3), where a dedicated study of the performance of a loaded and unloaded CLIC accelerating structure is ongoing. The aim is to study the sensitivity limitations of the beam loss measurements and the feasibility to use such a system for RF cavity diagnostics [26]. A 900 µm core radius Cherenkov fiber was exposed over 30 cm at a distance of 2.5 cm from the structure. It was shown that both dark current and breakdown induced signals in the absence of electron beam are well within the measurement range. They have been measured as a function of cavity input power in a range of 22 MW to 34 MW and extrapolated to the nominal 40 MW and 60 MW for unloaded and loaded main beam RF structures respectively. The signals increase exponentially with the cavity input power, the dark current signal increasing much more strongly than the signal from breakdown, see Fig. 3. The extrapolation to 40 MW yields 2.2×10^5 and 5.7×10^6 detected Cherenkov photons for dark current and for RF breakdown respectively in a fiber volume of 0.76 cm^3. This indicates a very high electron background in the close vicinity of the accelerating structure and will reduce the sensitivity to low beam losses.

Example: Cryogenic Loss Monitors at Fermilab

Cryogenic Loss Monitors (CLM) [27] have been developed for Fermilab's Advanced Superconducting Test Accelerator (ASTA), a test facility for ILC-type superconducting RF acceleration structures. The purpose of the CLM is the measurement of beam losses and in particular of RF dark current induced losses. The coaxial design ionization chambers

ISBN 978-3-95450-176-2

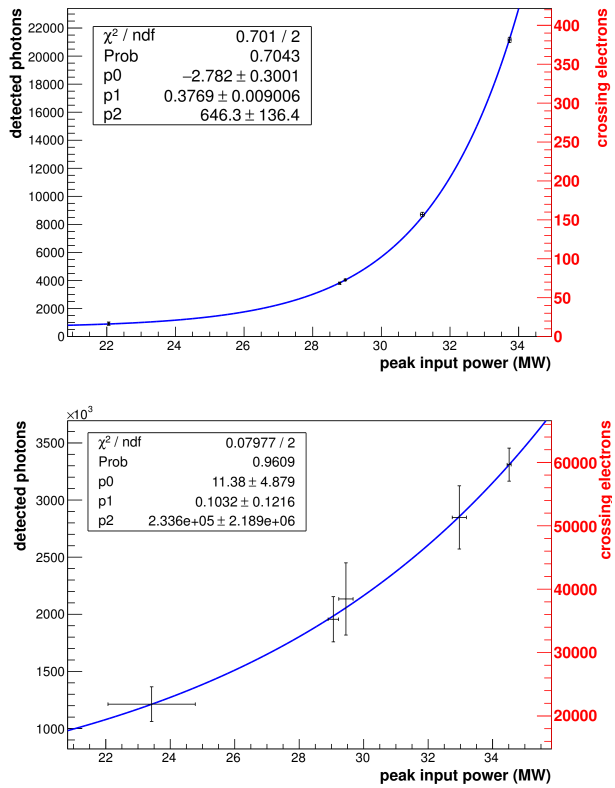

Figure 3: Signal in an optical fiber as a function of cavity input power for electron field emission (top) and RF breakdown (bottom) in number of photons detected (left y-axis). The right y-axis is an estimate of the number of electrons with $\beta = 1$ that will give the respective signal when crossing the fiber detector [26].

are filled with 120 cm^3 helium gas at a pressure of 1–1.5 bar. They can operate down to 5 K (and up to 350 K); as helium-4 becomes liquid below 5 K, the detectors cannot be operated at lower temperatures. The chambers are designed to be installed inside the cryomodules of RF structures and to measure dose rates of up to 300 Gy/hour with a sensitivity of approximately 0.19 nA/(Gy/hour). Dark current measurements at the A0-photo-injector test accelerator and the Horizontal Test Stand (HTS) were reported [27].

BACKGROUND FROM SYNCHROTRON RADIATION

Example: Simulation Study Comparing Different Detectors

A FLUKA simulation study was conducted recently on the sensitivity limitation of beam loss measurement in the CLIC damping ring arcs due to synchrotron light from the bending magnets [28]. The damping rings are required to reduce the transverse emittance of the electron and positron beams by synchrotron radiation damping in the superconducting wiggler magnets (2.5 T) installed in the two straight sections. The parameters of the simulation are: 2.86 GeV electron beam energy, 200 mA current, bending field of 1 T, critical energy of the synchrotron radiation of 5.4 keV. These parameters are very similar to several existing synchrotron light sources, e. g. the Australian Synchrotron, where several test measurement campaigns for CLIC BLM have been carried out.

The worst case for synchrotron radiation background from the dipoles was investigated using a simplified geometry [28]. Typical detector types were placed close to the beamline (10 cm and 40 cm) at the location of the maximum radiation, without any shielding. LHC-type ionization chambers [29, 30], NE102 plastic scintillators ($25 \times 16 \times 2$ cm^3) coupled to a photomultiplier tube with a gain of 10^4, silicon PIN diodes in current mode with an area of 1 cm^2 and a depletion layer of 100 µm, and small Cherenkov crystals with a volume of 1 cm^3 coupled to either a photomultiplier tube with a gain of 10^4 or an SiPM (Silicon Photomultiplier) with a gain of 10^5 were investigated. As the spectrum is not hard enough to produce electrons above the Cherenkov threshold in quartz (about 190 keV), the Cherenkov detectors are insensitive to the synchrotron radiation induced charged particle showers. Preliminary results yield, at 10 cm distance from the beampipe, currents of 80 pA, 64 µA, and 300 pA for the ionization chamber, the scintillator, and the PIN diode respectively. For the PIN diode this value is smaller than its typical dark current. The other two detectors will be able to measure the synchrotron radiation, at least when placed favorably, as in this simulation. The detector response to electron beam loss was simulated as well. For reasons of comparison the electron loss location simulated is also at the end of an arc dipole.

Figure 4 shows the resulting sensitivity limits for measuring beam losses. In red are typical values (upper and lower range) for the dark current of the respective detectors expressed in beam loss rates using the FLUKA results. They indicate the lower end of the dynamic range for measuring electron beam losses for the PIN diode and the Cherenkov crystal. Indicated in green are the beam loss rates which cannot be measured (at these locations), as their loss signal is below the signal from the synchrotron radiation. For ionization chambers and scintillators they determine the lower limit of measurable loss rates. The lowest detection limit for losses is that of the ionization chamber with 1.2×10^7 e$^-$/s. The Cherenkov counter (assuming charge multiplication at the lower end of the dark current range) and scintillator have very similar limits with 4×10^7 e$^-$/s and 3.7×10^7 e$^-$/s respectively. It is interesting to note that in this radiation field the advantage of the Cherenkov counter of being insensitive to photons is counteracted by its low sensitivity and by choosing a very small crystal size. The sensitivity limit of the Cherenkov detector decreases linearly with the increase in crystal size (not accounting for reduction in light collection efficiency, nor attenuation), as the dark current is dominated by the photon detector. At the same size as the scintillator (800 cm^3), for example in the form of a quartz rod, beam loss rates down to 5×10^4 e$^-$/s could be measured. The CLIC conceptual design report [17] specifies that the

ISBN 978-3-95450-176-2

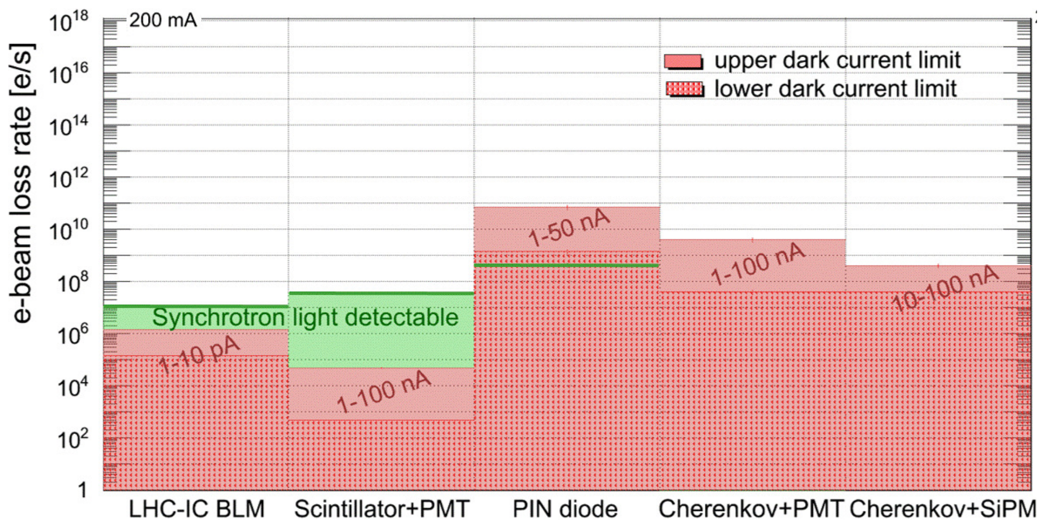

Figure 4: Worst case estimate of detector sensitivity to beam losses in the CLIC damping ring arcs based on FLUKA simulations [28].

BLM system in the damping rings should be able to measure loss rates of 2×10^7 e^-/s per meter. In the arcs, a Cherenkov crystal of a few cm^3 should be able to achieve this. An ionization chamber would have to be carefully positioned outside of the synchrotron radiation. In any case, exposure to synchrotron radiation should be kept low to limit radiation aging by positioning the monitors in low background regions and/or by shielding of the monitors.

Loss measurements with optical fibers at the Australian Synchrotron in the presence of synchrotron radiation have shown a sensitivity down to about 1×10^4 electrons lost in a single location using MPPC (Multi-Pixel Photon Counter) as photon detectors, and a dynamic range of 10^5 when combining MPPC at low count rate with photomultiplier readout at high count rate [31].

Example: HERA PIN Diodes

PIN diodes, albeit in counting mode, have been used very successfully in much harder synchrotron radiation backgrounds for loss measurements. The HERA machine at DESY collided protons at 920 GeV/c (from a superconducting 6.3 km proton ring) with 30 GeV/c electrons (positrons). Dual PIN diodes (mounted face-to-face) in coincidence counting mode were developed to measure proton beam losses and to provide quench protection in the presence of synchrotron radiation with a critical energy of 88 keV at a dose rate of about 10^4 Gy/year from the counter-circulating electron beam [32, 33]. The efficiency to detect a charged particle in coincidence mode was shown to be still above 30 % (compared to 70 % for a single diode). A synchrotron photon, on the other hand, only generates a signal in one of the diodes, mostly due to photoelectric absorption and due to Compton scattering for the higher photon energies. Coincidence counts due to synchrotron radiation can occur either statistically (due to high photon flux) or if the created electron has an energy high enough to reach the second diode. The detection efficiency of photons in coincidence mode has been reported as 3.5×10^{-5}, which means excellent suppression. Lead shielding had to be applied in addition to reduce the photon count rate. The maximum count rate of 10.4 MHz corresponded to the proton bunch spacing of 96 ns. The integration time was 5.2 ms; the time resolution is limited by the relatively low count rate. A wide dynamic range of up to 10^9 was achieved as well as a good calibration. The measured beam lifetime by current decay and by beam losses agreed to within a factor of 2.

The dual coincidence counting PIN diodes were also used for loss measurements at the HERA electron ring. Here, an additional thin layer of metal between the two diodes was applied to absorb electrons created by the photons, and further reduce the background. In the meantime these detectors are commercially available, and have been/are used by several machines.

ACKNOWLEDGMENT

The numerous contributions from various colleagues and laboratories are gratefully acknowledged. I wish to thank in particular Sanja Damjanovic and Eduardo Nebot Del Busto for their valuable input and support.

REFERENCES

[1] B. Dehning et al., "Test of a Diamond Detector Using Unbunched Beam Halo Particles", CERN-ATS-2010-027.

[2] E. Effinger et al., "A prototype readout system for the Diamond Beam Loss Monitors at LHC", IBIC 2013, Oxford, UK, MOPC45.

[3] E. Griesmayer et al., "A Fast CVD Diamond Beam Loss Monitor for LHC", Conf. Proc. C11-05-16.4 (2011), MOPD41, DIPAC 2011, Hamburg, Germany.

[4] A. Lechner et al., "Post-LS1-BLM Thresholds for the LHC Arcs," to be published in the Proc. of the Workshop on Beam Induced Quenches BIQ, CERN, Geneva, Switzerland (2014).

ISBN 978-3-95450-176-2

[5] G. Battistoni et al., "The FLUKA code: Description and Benchmarking", Proc. of the Hadronic Shower Simulation Workshop 2006, Fermilab, Batavia, USA, AIP Conference Proceeding 896, 31-49, (2007).

[6] A. Fassò et al., "FLUKA: a multi-particle transport code", CERN-2005-10 (2005), INFN/TC-05/11, SLAC-R-773.

[7] B. Auchmann et al., "Testing Beam-Induced Quench Levels of LHC Superconducting Magnets," Phys. Rev. S. T. A. B. **18** (2015) 061002 [arXiv:1502.05261 [physics.acc-ph]].

[8] T. Obina, Y. Yano, "Optical fibre based Beam Loss Monitoring for electron storage rings", IBIC 2013, Oxford, UK.

[9] X.-M. Maréchal, Y. Asano, T. Itoga, "Design, development, and operation of a fiber-based Cherenkov beam loss monitor at the SPring-8 Angstrom Compact Free Electron Laser", Nucl. Instrum. Meth. A **673** (2012) 32.

[10] L. Fröhlich et al., "Instrumentation for Machine Protection at FERMI@ELETTRA," DIPAC 2011, Hamburg, Germany.

[11] F. Wulf, M. Körfer, "Beam Loss and Beam Profile Monitoring with Optical Fibers," DIPAC 2009, Basel, Switzerland.

[12] J. W. van Hoorne, "Cherenkov Fibers for Beam Loss Monitoring at the CLIC Two Beam Module," CERN-THESIS-2012-112.

[13] M. Zingl, "Longitudinal Resolution of Cherenkov Fibers – Loss Simulations and Signal Calculation for the CLIC Drive Beam Decelerator", unpublished report.

[14] E. Nebot et al., "Position Resolution of Optical Fibre-Based Beam Loss Monitors Using Long Electron Pulses", IBIC 2015, Melbourne, Australia, WEBLA03, *these proceedings.*

[15] G. Venturini et al., "A 120 dB dynamic-range radiation-tolerant charge-to-digital converter for radiation monitoring" Microelectronics Journal 44 (2013) 1302-1308.

[16] G. Venturini et al., "Characterization of a Wide Dynamic-Range, Radiation-Tolerant Charge-Digitizer ASIC for Monitoring of Beam Losses," IBIC 2012, Tsukuba, Japan, MOPA12.

[17] M. Aicheler et al., "A Multi-TeV Linear Collider Based on CLIC Technology : CLIC Conceptual Design Report," CERN-2012-007, SLAC-R-985, KEK-Report-2012-1, PSI-12-01, JAI-2012-001.

[18] M. Kastriotou et al., "BLM Crosstalk Studies at the CLIC Two-Beam Module," IBIC 2015, Melbourne, Australia, MOPB045, *these proceedings.*

[19] O. S. Bruning et al., "LHC Design Report Vol.1: The LHC Main Ring," CERN-2004-003-V1.

[20] M. R. Bartosik et al., "Cryogenic Beam Loss Monitors for the Superconducting Magnets of the LHC," IBIC 2014, Monterey, USA; CERN-BE-2014-009.

[21] C. Kurfürst, "Cryogenic Beam Loss Monitoring for the LHC", CERN-THESIS-2013-232.

[22] C. Kurfürst et al., "In situ radiation test of silicon and diamond detectors operating in superfluid helium and developed for beam loss monitoring," Nucl. Instrum. Meth. A **782** (2015) 149.

[23] A. F. Borghesani, *Ions and Electrons in Liquid Helium,* Print ISBN-13: 9780199213603, Oxford Science Publications (2007); DOI:10.1093/acprof:oso/9780199213603.001.0001 Oxford Scholarship Online (2008).

[24] M. R. Bartosik et al., "Cryogenic Beam Loss Monitors for the Superconducting Magnets of the LHC," IBIC 2015, Melbourne, Australia, MOPB042, *these proceedings.*

[25] N. Andreev et al., "Design and Fabrication of a Single-Aperture 11T Nb_3Sn Dipole Model for LHC Upgrades," IEEE Trans. Appl. Supercond. **22** (2012) 3, 4001705.

[26] M. Kastriotou, "RF cavity induced sensitivity limitations on Beam Loss Monitors," LA3NET 2015, Phys. Procedia (2015) accepted.

[27] A. Warner, J. Wu, "Cryogenic loss monitors with FPGA TDC signal processing," Phys. Procedia **37** (2012) 2031.

[28] S. Damjanovic, to be published.

[29] E. B. Holzer et al., "Development, Production and Testing of 4500 Beam Loss Monitors," EPAC 2008, Genoa, Italy, Conf. Proc. C **0806233** (2008) TUPC037; CERN-AB-2008-054.

[30] E. B. Holzer et al., "Beam loss monitoring system for the LHC," NSS 2005, IEEE Transactions on Nuclear Science, Vol. 53 (2006) p.1052; CERN-AB-2006-009.

[31] E. Nebot et al., "Measurement of Beam Losses Using Optical Fibers at the Australian Synchrotron", IBIC 2014, Monterey, USA.

[32] K. Wittenburg, "The PIN-diode beam loss monitor system at HERA," BIW 2000, Cambridge, Massachusetts, USA; DESY-HERA-00-03.

[33] K. Wittenburg, "Preservation of beam loss induced quenches, beam lifetime and beam loss measurements with the HERAp beam-loss-monitor," Nucl. Instrum. Meth. A **345** (1994), 226.

ISBN 978-3-95450-176-2

DEVELOPMENT OF THE BEAM LOSS MONITOR FOR BEAM HALO MEASUREMENT IN THE J-PARC RCS

M. Yoshimoto#, H. Harada, K. Okabe, M. Kinsho,
J-PARC, JAEA, Tokai, Ibaraki, 319-1195, Japan

Abstract

In the J-PARC RCS, transverse beam profiles including both the beam core and halo at extraction beam transport line (3NBT) were measured by using a combination with a wire scanner type beam scraper and some beam loss monitors (BLMs). Our final goal of this halo monitor is to measure the intra-bunch beam halo of extracted two bunches from the RCS. Thus the plastic scintillator and photomultiplier (PMT) assemblages were adopted as the BLMs with quick time response. However, we found that the BLMs detected not only the radiation from the wire but also reflected one from other devices and wall. Therefore we tried to develop new-type BLMs, which are scintillation-type BLM of lead glass and Cherenkov-type BLM of quartz or UV acrylic. In this presentation, we will report on the overview and experimental results of the new-type BLMs together with the outline of halo monitor system.

INTRODUCTION

The 3-GeV Rapid Cycling Synchrotron (RCS) of the Japan Proton Accelerator Research Complex (J-PARC) is a MW class of high intensity proton accelerator [1]. In addition, the RCS has two functions as a proton driver for neutron/muon production at the Material and Life science experimental Facility (MLF) and as a booster of the 50-GeV Main Ring synchrotron (MR) injection. To provide such a high power proton beam for the MR with small injection beam loss or for the MLF with broad range and uniformity irradiation to the target using the octupole magnet [2], it is required to improve the extraction beam quality, namely to achieve the Low-Halo and High-Intensity beam by finer beam tuning in the RCS [3]. Therefore the measurement of the transverse beam profile including both of the beam core and the beam halo is one of the key issues for the high power beam operation in the RCS. Thus a new beam halo monitor was developed and installed at the 3GeV-RCS to Neutron source Beam Transport (3NBT) line as shown in Fig. 1 and Fig. 2 [4]. This new beam halo monitor was constructed by combining a wire scanner type beam scraper and some beam loss monitors (BLMs). The transverse beam profile including the beam core and beam halo can be reconstructed with the halo monitor. On the other hand, our final goal of the halo monitor is to measure not only the transverse beam halo but also the intra-bunch beam halo of the extracted two bunches from the RCS. However the beam experiments made clear that there are some issues for the intra-bunch beam halo measurement.

In this paper, we report the transverse beam halo measurement with the new beam halo monitor. In addition, we introduce the new BLMs which were developed for intra-bunch beam halo measurement.

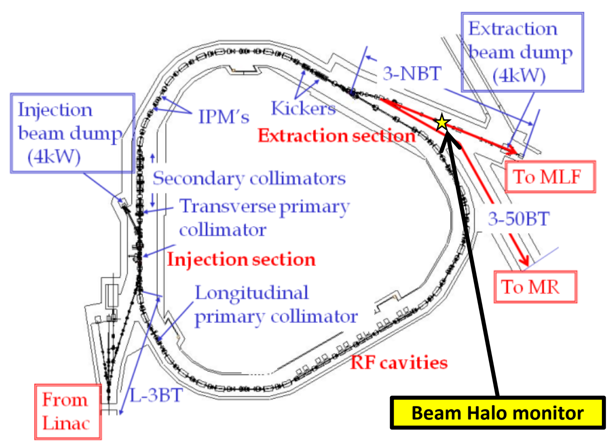

Figure 1: Top view of the RCS and location of the beam halo monitor installation.

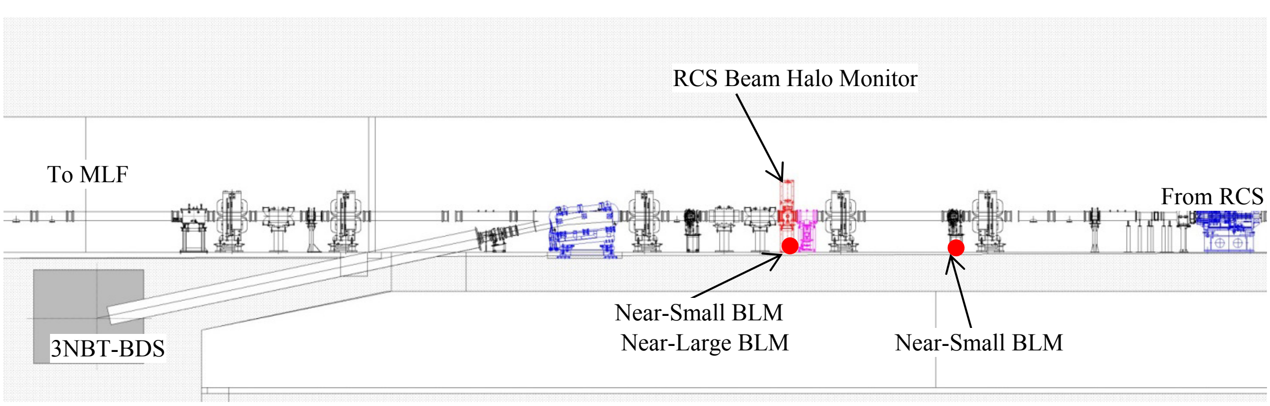

Figure 2: Side view of the 3NBT line and location of the beam halo monitor installation.

ISBN 978-3-95450-176-2

TRANSVERSE BEAM HALO MEASUREMENT

Measurement Principle

The new beam halo monitor was constructed by combining a wire scanner type beam scraper and some BLMs as shown in Fig. 3. Popular wire beam profile monitor detects the secondary electron emitted from the wire due to irradiate the beam. In this case, the wire signal should be disturbed by the floating electrons in the vacuum chamber. Moreover it is difficult to achieve a wide dynamic range for the beam halo measurement by using only the electric circuits. In contrast, our monitor detects the radiation in order to suppress the signal disturbance due to floating electrons. And more the ultra-wide dynamic range can be achieved by using the several BLMs with the different sensitivities.

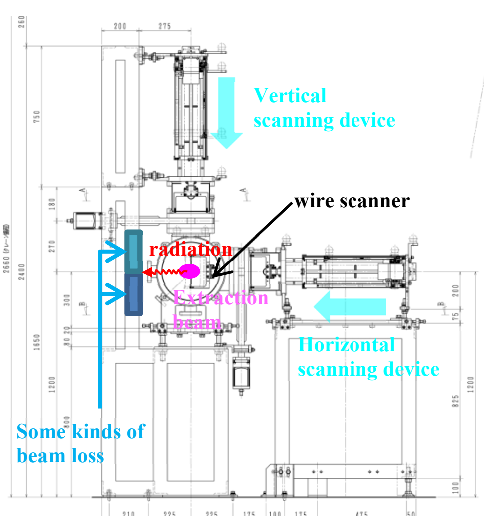

Figure 3: Schematic diagram of the new beam halo monitor.

Scintillator type BLMs (S-BLMs) are adopted for the halo monitor because they have good time responsiveness. We chose a common photomultiplier tube (PMT). And we controlled the sensitivities of the S-BLM by changing the volume size of the plastic scintillator or the distance from the wire scanner to the S-BLM. For the first trial test, two kinds of S-BLM were assembled. One is the small plastic scintillator type as shown in Fig. 4, and the other is the large plastic scintillator type in Fig. 5. The small type S-BLM has a light guide for a support of the thin plastic scintillator. Two large type S-BLMs were assembled. One wsa installed close to the wire scanner together with the small type S-BLM as shown in Fig. 2. The other was installed upstream of about 5m away from the wire scanner. The aim of the near large type S-BLM is a high sensitivity detector to measure beam halo elements. And the aim of both the near small type and the far large type S-BLMs are a low sensitivity detectors to measure beam core elements.

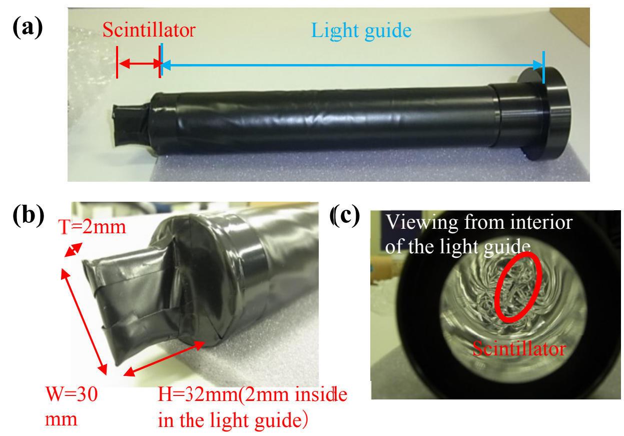

Figure 4: Photographs of the Small Scintillator type BLM. It has a light guide for a support of the thin plastic scintillator.

Figure 5: Photograph of the Large Scintillator type BLMs.

Reconstruction of the Transverse Beam Profile

In this system, BLMs can detect the only radiations caused by hitting the beam into the wire scanner. Thus BLMs signal should be proportional to the number of the hitting particles. Calibration formula ($N_{particle}$ / S_{BLM}) for each BLM can be obtained by using the matched beam intensity with the each sensitivity [4].

After completing each calibration curve acquiring, we demonstrated the transverse beam profile reconstruction with the new halo monitor. In this first trial beam test, the output beam power was 340kW equivalent. All PMTs were excited by a common power supply and the high voltage was fixed on -1kV. Fig. 6 shows the experimental result. Fig. 6 (a) shows the scanning raw data with three beam loss monitors and (b) shows the reconstructed profiles. Only by using each sensitivity calibration formula, we can reconstruct the transvers beam profile including both the beam core and beam halo can be reconstructed. Namely any other correction is not necessary to join together all measured plots. In this scheme, it is possible to expand the dynamic range by using the higher sensitivity beam loss monitors.

ISBN 978-3-95450-176-2

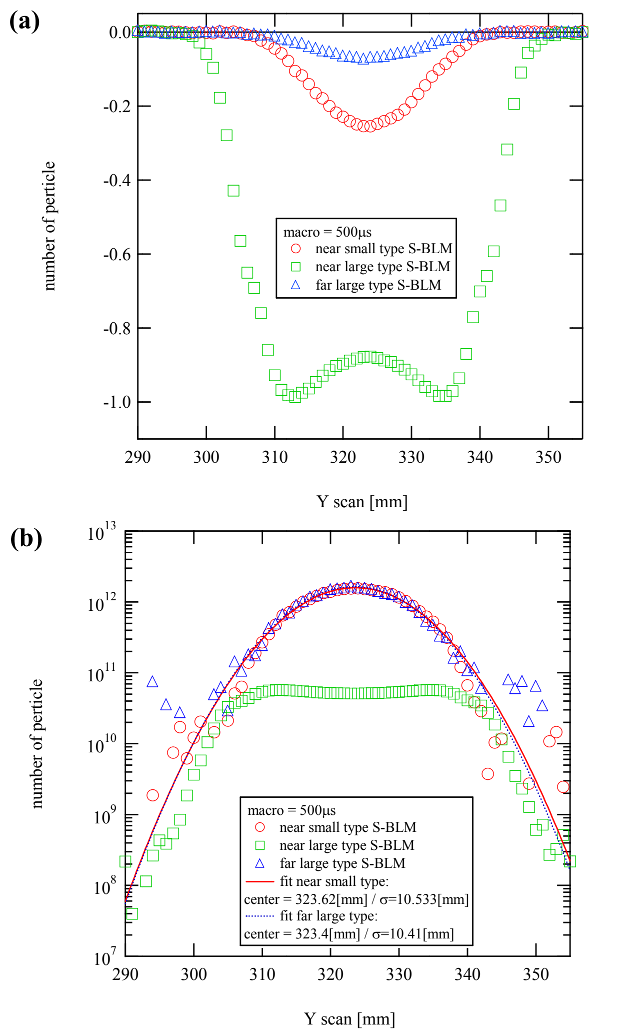

Figure 6: Demonstration of the transverse beam profile reconstruction with the output beam power of 320kW equivalent. (a) : Each S-BLM signal plots. (b) : Conversion data plots by using each sensitivity calibration curve formula.

NEW BLM DEVELOPMENT FOR THE INTRA-BUNCH BEAM HALO MEASUREMENT

Distortion of the Bunch Signal from the Plastic Scintillator BLM

We verified that the RCS Beam Halo Monitor has the ultra-wide dynamic range and can reconstruct the transverse beam profile including both the beam core and halo. But our final goal of this halo monitor is to measure the intra-bunch beam halo of extracted two bunches from the RCS. Then we reconstructed the two-dimensional profiles (bunch length vs beam size) from the two BLMs with low-sensitivity; Near-Small plastic scintillator and Far-Large plastic scintillator. Fig. 7 shows the comparison between two plastic scintillators. Uppers show the two-dimensional profile from the Near-Small type, and lowers show the one from the Small-Large type. These transverse distributions were consistent, but the time distributions were markedly different.

In order to investigate these differences in the time distribution, the raw signals from the two BLMs where the wire scanner inserted at the beam centre were compered as shown in Fig. 8. After the subtraction the background signal from the whole signal, pure beam loss signal at the wire scanner can be obtained. The tail component of the bunch signal from the Far-Large type increases more than one from the Near-Small type. The plastic scintillator BLMs detected not only the radiation from the wire but also reflected one from other devices and wall. This indelible tail component was caused the reflected radiation. Thus the bunch signal from the plastic scintillators was distorted as far from the wire scanner.

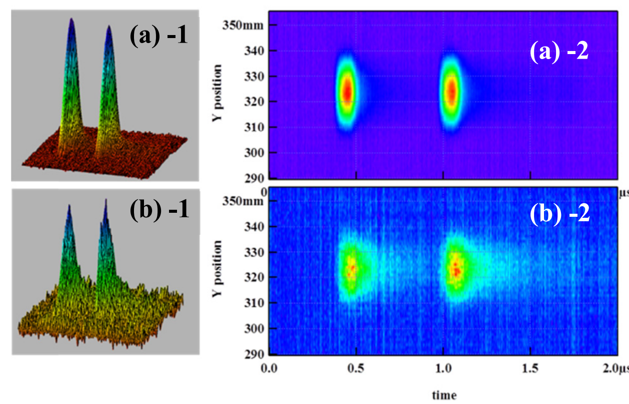

Figure 7: Reconstructed 2D-profile. (a): Near-Small type, (b): Far-Large type.

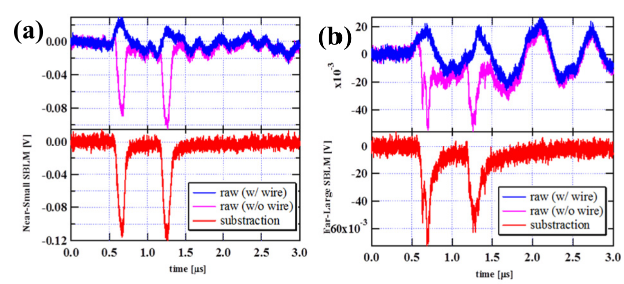

Figure 8: Typical result of the noise reduction of the S-BLM signal. (a): Near-Small type, (b): Far-Large type.

Upper plots show the comparison of the raw S-BLM signals between inserted and retracted the wire scanner. Lower plot shows pure beam loss signal at the wire scanner after the background noise reduction.

New-type BLM

To obtain the bunched beam structure from the BLM clearly, it is necessary to suppress these reflected radiations. The energy of the radiation decreases after the reflection generally. Therefore new-type BLM is required

ISBN 978-3-95450-176-2

to have a high sensitivity toward the faster radiation particles. Then we develop new-type BLMs, which are scintillation-type BLM of lead glass and Cherenkov-type BLM of quartz or UV acrylic as shown in Fig. 9. The lead glass scintillator has a long bar structure and then it has the higher sensitivity toward the faster gamma-ray which approaches from the top of the long bar. On the other one, quartz and UV acrylic are short disk structure and then it has the higher sensitivity toward the faster electron to generate the Cherenkov light.

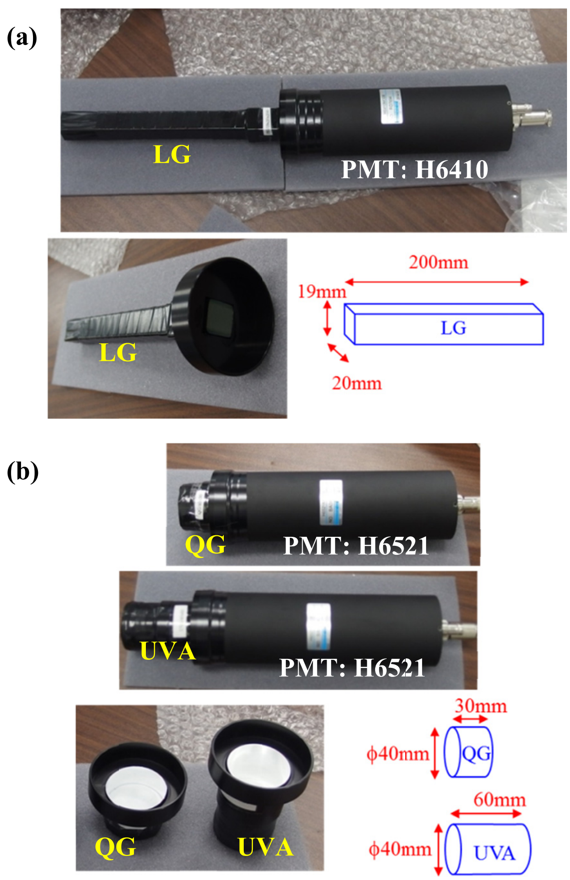

Figure 9: Photograph of the new-type BLMs. (a): scintillation-type BLM of the lead glass. (b): Cherenkov-type BLM of the quartz or UV acrylic.

Trial Beam Test

In order to see if the new-type BLMs work as they were expected to, they were installed near the wire scanner and trial beam tests were carried out. The beam destination for the extracted beam from the 3GeV-RCS switched from the MLF-target (MLF-TGT) to 3NBT-beam dump (3NBT-BD) because the effect of the reflected radiation can enhance dynamically.

At first, the ultra-low intensity beam was used to prevent the saturation of the BLM. The wire was fixed on the beam centre, and the beam destination switched between the MLF-TGT and 3NBT-BD. Fig. 10 shows the raw signals from the every BLM. The single intermediate bunched beam was injected into the RCS. Therefore the only one bunched beam was extracted. The plastic scintillator detected the reflected radiation from the 3NBT-BD as a result the bunch signal was distorted as shown in Fig.10 (a). On the other hand, all new-type BLMs can suppress the reflected radiation drastically. Offcuts these suppressions were not perfect until now and then they have to more progress to achieve the intra-bunch beam halo measurement. But we can probe the availability of the new-type BLMs.

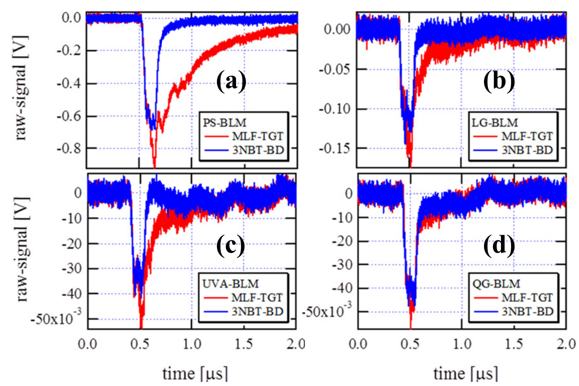

Figure 10: Raw signals of the BLMs compared between the MLF-TGT and the 3NBT-BD operation mode. (a): plastic scintillator, (b): lead glass, (c) UV acrylic, (d) quartz glass.

Next, the high intensity beam was used for the high power beam commissioning. In this time, the beam destination is fixed to the 3NBT-BD and the wire position changed between on centre of the beam and far from the beam. Fig. 11 shows the raw signals compared between two wire positions and the subtracted signal from the every BLM. Plastic scintillator signal was saturated due to the reflected radiation and subtracted signal was distorted. But all bunch signals measured by new-type BLM were almost not distorted. From these results, the transverse beam profile can be measured in the 3NBT-BD operation mode by using these new-type BLMs.

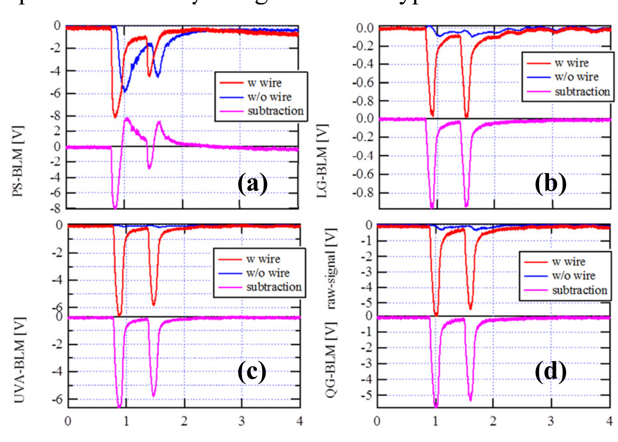

Figure 11: Raw signals of the BLMs compared between the inserted and retracted the wire. (a): plastic scintillator, (b): lead glass, (c) UV acrylic, (d) quartz glass.

ISBN 978-3-95450-176-2

Then the beam profile measurements with various beam intensity were carried out in the 3NBT-BD operation mode. Fig. 12 shows the scanning result from every BLM. In the case of the plastic scintillator, the transverse profile was distorted as shown in the Fig. 12 (a), because the raw signals were saturated due to the reflected radiation from the 3NBT-BD. On the other hand, the new-type BLMs can measure the beam profiles. So we analysed and calculated the calibration formula for each new-BLM roughly, and tried to reconstruct the transverse beam profile as shown in Fig. 13.

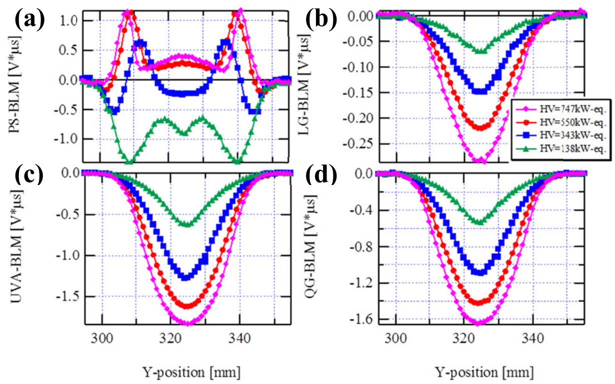

Figure 12: Scanning plot of the BLMs with various beam intensity. (a): plastic scintillator, (b): lead glass, (c) UV acrylic, (d) quartz.

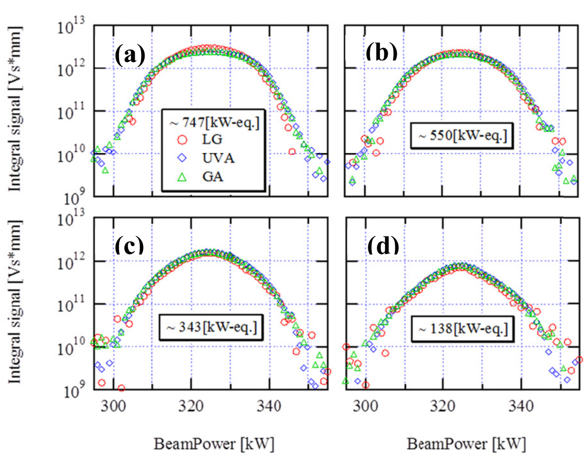

Figure 13: Demonstration of the transverse beam profile reconstruction from the new-type BLM. (a) : 747kW-eq.. (b) : 550kW-eq., (c) 343kW-eq., (d) 138kW-eq.

SUMMARY

In the J-PARC RCS, new beam halo monitor, which is combined a wire scanner and some beam loss monitors, was developed to measure the transverse profile of the extraction beam. This new halo monitor aims to achieve the ultra-wide dynamic range. By using several beam loss monitors of plastic scintillator type with different sensitivities, the transverse beam profile including the beam core and halo elements can be reconstructed.

The transverse beam profile including both the beam core and beam halo can be reconstructed by using the several BLMs with the various sensitivities. Only by using sensitivity calibration formula for the each BLM, transverse profile including both the beam core and beam halo can be reconstructed directly.

In this scheme, it is possible to expand the dynamic range by using the higher sensitivity BLMs. The time structure of the bunch signal measured by the plastic scintillator was distorted, because of the reflected the radiation. The new-type BLMs, which are scintillation-type BLM of lead glass and Cherenkov-type BLM of quartz or UV acrylic, can be reduced the reflected radiation drastically. In order to achieve the intra-bunch beam halo measurement, the new-type BLMs have to progress.

REFERENCES

[1] High-intensity Proton Accelerator Project Team, JAERI Report No. JAERI-Tech 2003-044 and KEK Report No. 2002-13.

[2] S. Meigo, et. al., “BEAM FLATTENING SYSTEM BASED ON NON-LINEAR OPTICS FOR HIGH POWER SPALLATION NEUTRON TARGET AT J-PARC”, Proc. IPAC2014, Dresden, Germany (2014), MOPRI116.

[3] H. Hotchi, “1-MW Beam Operation Scenario of the J-PARC d-GeV Rapid Cycling Synchrotron”, JPS Conf. Proc. 8, 012013 (2015).

[4] M. Yoshimoto, et. al., “DEVELOPMENT OF THE BEAM HALO MONITOR IN THE J-PARC 3-GEV RCS”, Proc. IPAC2012, NewOrlins, USA (2012), WEOAA03.

ISBN 978-3-95450-176-2

POSITION RESOLUTION OF OPTICAL FIBRE-BASED BEAM LOSS MONITORS USING LONG ELECTRON PULSES

E. Nebot del Busto, M. Kastriotou, CERN, Geneva, Switzerland & University of Liverpool, UK
M.J. Boland, ASCo, Clayton & The University of Melbourne, Australia
R.P. Rasool, The University of Melbourne, Australia
W. Farabolini, CERN, Geneva, Switzerland & CEA/DSM/IRFU, Saclay, France
S. Doerbert, E. Effinger, E. B. Holzer, F.S. Domingues, W. Viganò, CERN, Geneva, Switzerland
C.P. Welsch Cockcroft Institute, Warrington; University of Liverpool, UK

Abstract

Beam loss monitoring systems based on optical fibres (oBLM), have been under consideration for future colliders for several years. To distinguish losses between consecutive quadrupoles, the position resolution of detected losses is required to be less than 1 m. A resolution of better than 0.5 m has been achieved in machines with single, short pulses of the order of a nanosecond. In the case of longer beam pulses with 150 ns duration, as they would be in the Compact LInear Collider (CLIC), the longitudinal length of signals in the fibre is close to the duration of the beam pulse which makes loss reconstruction very challenging. In this contribution results from experiments into the position resolution of an oBLM system based on long beam pulses are presented. These measurements have been performed at the CLIC Test Facility (CTF3) at CERN and the Australian Synchrotron Light Source (ASLS). In the former, controlled beam losses were created in a 22.5 m long decelerating Test Beam Line (TBL) LINAC. In the latter, loss localization was studied by comparing that from single bunches with those from longer bunch trains. In both cases the losses were detected using a 200 µm core pure silica fibre coupled to a Silicon Photomultiplier (SiPM) photon detector.

INTRODUCTION

The operation of particle accelerators would not be possible without the use of instruments and diagnostics systems that allow the main properties of the beam to be characterized. Beam Loss Monitors (BLM), particle detectors installed outside of the vacuum chamber to detect beam induced showers, are a powerful tool for the optimization of the performance of a machine as well as for protecting it against damage. Over the past ten years, optical fibre based BLM (oBLM) systems have been studied and implemented in several accelerator facilities [1] due to the various advantages that they bring with respect to standard BLM techniques. The prompt nature of the Cherenkov light generated in the fibre by the crossing of a high energy charged particle provides a very fast detection technique, with the main limitation coming from dispersive effects in the fibre core. Moreover, only photons with energies above the electron-positron generation threshold would (indirectly) generate light. This is particularly interesting in synchrotron light sources where the large number of low energy photons can limit the sensitivity of BLM systems. From a machine protection perspective, an optical fibre may provide coverage of a full beam line preventing any potentially dangerous beam losses from going undetected. In this contribution, the determination of the original location of beam losses via the time of flight of photons in the fibre core of oBLM systems is discussed. Several experiments conducted at the Australian Synchrotron Light Source (ASLS) and the CLIC Test Facility at CERN (CTF3) with single electron bunches and long multi-bunch pulses are presented.

THE MACHINES

This section describes the most important features of the two facilities where the presented studies were conducted.

The Australian Synchrotron Light Source

The Australian Synchrotron [2] can be schematically seen on the right side of Figure 1. A thermionic gun injects electrons into a 14 m LINAC equipped with two 3 GHz normal conducting RF cavities that accelerate electrons up to 100 MeV. The particle energies are increased up to 3 GeV in a 130 m Booster ring equipped with 500 MHz RF cavities. Electrons are finally injected into a 216 m storage ring, also equipped with 500 MHz normal conducting cavities. The storage ring is subdivided into 14 sectors, each one of them containing a double bend achromat cell and a straight section. In Vacuum Undulators (IVU) are installed in the straight sections of sectors 3, 5 and 13, and the RF cavities in sectors 6 and 7. Sector 11 is equipped with beam scrapers to protect the insertion devices by concentrating beam losses at this location. The machine provides a flexibility to tune the beam conditions used for these experiments. The bunch charge can be varied from $10^{+5} – 10^{+9}$ [4], the bucket in which a single bunch will be injected can be chosen and injection of up to 75 bunches is possible.

The Test Beam Line at CTF3

CTF3 was designed and constructed to verify the feasibility of the novel two-beam acceleration concept of the Compact LInear Collider (CLIC) [3]. A thermionic gun and a bunching system provide an electron pulse with a peak current of 3.0 A and a length that can vary from 0.1 to 1.4 µm. Four normal conducting RF structures boost the electron energies up to 120 MeV. Particles are then driven towards a small delay loop and a storage ring that may be used for

ISBN 978-3-95450-176-2

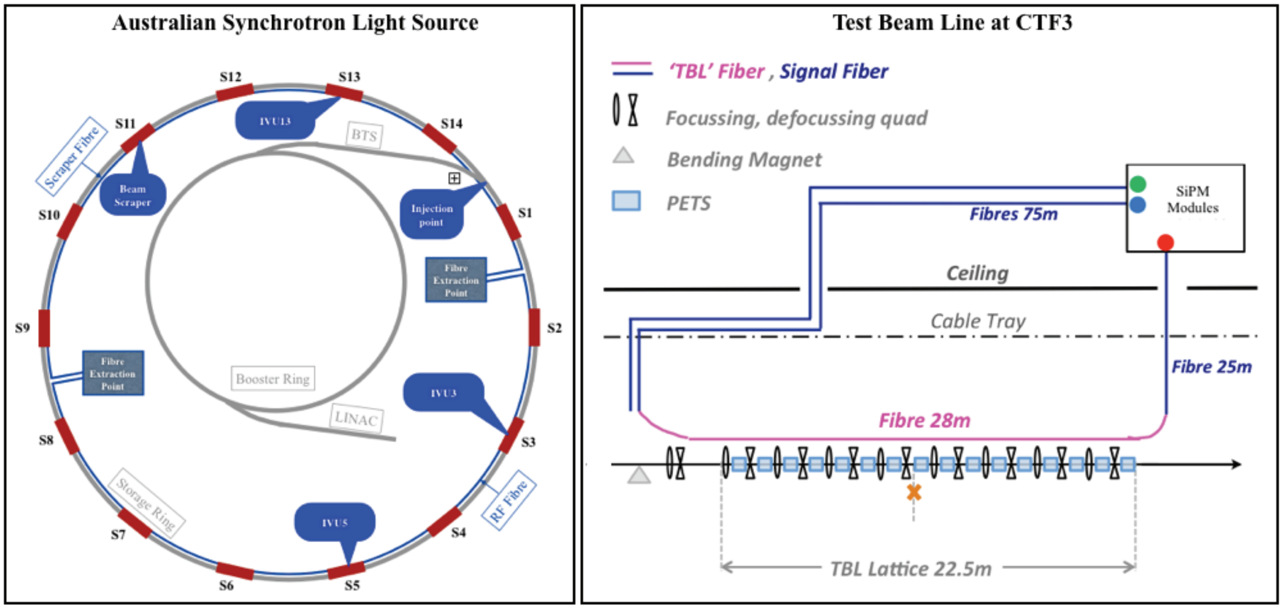

Figure 1: Simplified sketch of ASLS, the TBL and the respective optical fibre instalations.

shortening the injected beam pulse and increasing the peak current. These pulses are then directed to the experimental hall where the TBL, shown on the left side of Figure 1, is located. The TBL [5] is a 22.5 meter long decelerating LINAC that is composed of eight 2.8 meter long FODO cells that feature two quadrupoles, two Beam Position Monitors (BPM) and two Power Extraction and Transfer Structures (PETS). The BPMs at the TBL [6] provide the only beam current measurement device along the line with an accuracy of around 10 %.

OPTICAL FIBRE BLM SYSTEM

The prototype oBLM system used for the experiments described in this document is composed of three main parts, namely: the active detector (fibre), the front-end electronics and the back-end electronics. The optical fibres have a pure silica 200 (245) µm core (cladding) and a 345 µm acrylate coating. A dark nylon jacket then encloses the cable and protects the fibre from ambient light, humidity and mechanical breakage. The longitudinal dimensions are different in the case of the two facilities to meet their specific requirements.

At the ASLS, two 125 m cables cover the full storage ring with some margin to extract the generated light out of the accelerator tunnel, to where the electronics is located. In the following sections we will refer to the ASLS fibres as the RF fibre and scraper fibre according to the device they are protecting. The two light extraction points were located in sectors 2 and 9. The fibres were located in the horizontal plane on the inner side of the rectangular beam vacuum chamber, approximately 5.5 cm from the beam. At the TBL, a 28 m long signal fibre is located on top of the beam vacuum chamber, some 28 cm from the beam. The light is directed out of the tunnel via a 25 m and 75 m extraction fibres at the downstream and upstream ends respectively. Two identical optical fibres are installed parallel to these extraction fibres to subtract any potential background light not generated in the TBL itself. A sketch of the fibre installation is also illustrated in Figure 1.

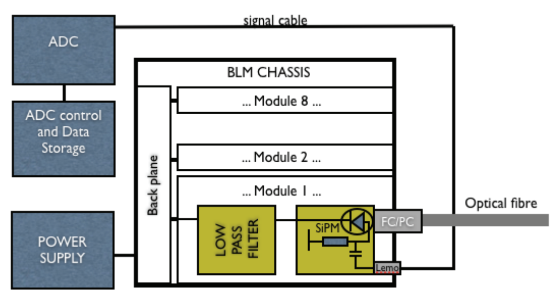

Figure 2: Schematic view of the oBLM read out.

The front-end electronics, shown schematically in Figure 2, features custom made Silicon Photomultiplier (SiPM) readout cards connected to a backplane that distributes the bias voltage for the sensors, the voltage for amplification and provides the grounding. A detailed description of the individual modules, that include low pass filters in the bias voltage input and an AC coupled signal readout can be found in [7]. The SiPMs are Hamamatsu s12572-015C detectors selected for their fast response and wide dynamic range. The back-end electronics consists of analog to digital converters (ADC). In the case of the TBL system, the signals were read out via 8 channel SIS3320 cards with 250 MHz bandwidth, up to 1.25 GS/s sampling rate and 10 bit resolution controlled via VME crate. Two different digitizers, Acqiris cards U1071a and DC282, were used at ASLS. The specifications in terms of sampling rate, bandwidth and resolution were 1 GHz, 2GS/s and 8 bit for the former and 2 GHz, 2GS/s

ISBN 978-3-95450-176-2

and 10 bit for the latter. Both digitizers were connected to PCs that provided the processing power and data storage.

SINGLE BUNCH MEASUREMENTS

Two sets of single bunch measurements were performed at the ASLS storage ring as a reference for the studies presented in this contribution.

Understanding of Beam Losses

One single bunch was injected into an empty machine and the beam losses during the first turn were investigated. Figure 3 presents a multi-peak structure due to losses occurring at various locations in the scraper (top) and RF (bottom) fibres respectively. Note that due to the better position resolution achievable with photons traveling upstream the fibre [8], only this output is studied throughout this contribution.

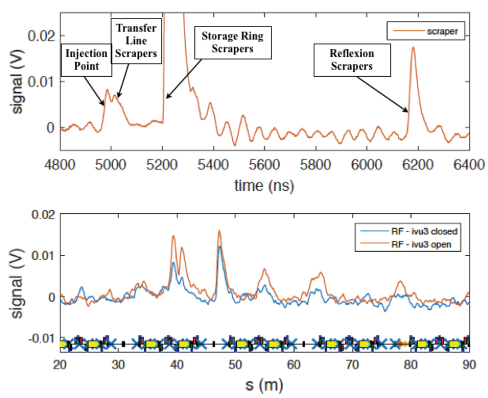

Figure 3: First turn losses observed in the scraper (top) and RF (bottom) fibres.

A sketch of development of signals in the scraper fibre during the first turn is shown in Figure 4. Electrons are kicked horizontally from the transfer lines into the storage ring, generating losses around the injection point (x_1). This produces a photon pulse in the scraper fibre that travels towards the upstream end with velocity $v_Q = c/n_Q$, with $n_Q = 1.47$ representing the (average) refractive index of quartz in the wavelength range of interest (200-900 nm) and c is the speed of light. The first detected light pulse in the scraper fibre shows a double peak behaviour, with the second peak attributed to showers generated in the beam scrapers of the transfer lines. Thereafter, the beam travels for a sector and exits the fraction of the storage ring covered by the scraper fibre. Once the beam reaches sector 9 it runs again parallel to the scraper fibre and in sector 11, it hits the beam scraper generating more showers (at position x_2). This process is illustrated in Figure 4. The arrival time of photons generated at x_1 and x_2 at the SiPM can be calculated as:

$$t_1 = t_0 + x_2/v_Q \tag{1}$$

and

$$t_2 = t_0 + L/c + x_1/v_Q \tag{2}$$

where t_0 represents the time at injection and L is the distance between the two loss points measured in the direction of the beam. Subtracting the two equations above and using the relation $\Delta x = x_1 - x_2 = L_{RING} - L$, with $L_{RING} = 216$ m, we can calculate the distance between the two points as:

$$\Delta x = \frac{L_{RING} - c\Delta t}{1 + n_Q} \tag{3}$$

For a measured temporal distance between the peaks x_1 and x_2 of $\Delta t = 220$ ns a distance of $\Delta x = 60.7$ m is calculated, which corresponds to the distance between the injection point and the beam scrapers. A third peak at $t \sim 6.2$ µs is also observed. This is attributed to the large number of photons generated at the beam scrapers that travel to the downstream end of the fibre and partly reflected to the upstream end.

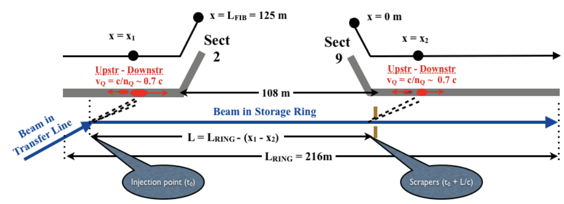

Figure 4: Sketch of the development of signals in the scraper fibre during the first turn.

In the case of the RF fibre the interpretation of the signals is much simpler as the beam travels, without interruption, parallel to the fibre. Thus, the distance between two loss points can be calculates as:

$$\Delta x = \frac{c\Delta t}{1 + n_Q} \tag{4}$$

Figure 3 shows, for the RF fibre, a multi-peak structure that is attributed to a modulation of the transverse beam size. A mockup of the double bend achromat lattice overlaid on Figure 3 shows that the peaks correspond to the quadrupole position. The effect of an opened and closed IVU3 located at approximately 30 m after the injection point, is also shown in the graphic. When closed during the first turn it limits losses downstream, while when open more downstream losses are observed. Note that in the bottom figure, the x axis has been scaled to position via Eq. (4).

Intrinsic Time Resolution

In order to understand the intrinsic time resolution of the system the raising edge of the signals generated at the beam scrapers, as a well defined loss location, were studied . An individual bunch was injected with the RF bucket in which it was injected incremented on every injection. The leading edge of 1000 pulses is presented in Figure 5 with a different color for each bucket. Note that, the oBLM system is clearly capable of disentangling signals separated by 2 ns on a shot by shot basis.

To probe the response of the system to signals separated by shorter time periods the RF phase of the Booster was shifted by 180° with respect to that of the storage ring. The arrival

ISBN 978-3-95450-176-2

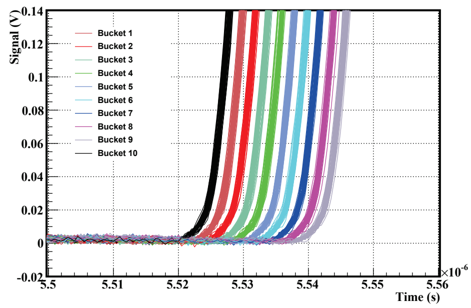

Figure 5: Leading edge of signals generated at the scrapers by single bunches injected into buckets 1 to 10.

time of the photons to the upstream end of the fibre was calculated as the temporal value for which the oBLM signal reached $V_{thr} = 100$ mV. To accomplish that, the sample value closer to V_{thr} was taken as a central value for an exponential fit ($V = a \cdot e^{b \cdot t}$) that included two samples (acquired at a 2 GS/s rate) on each side.

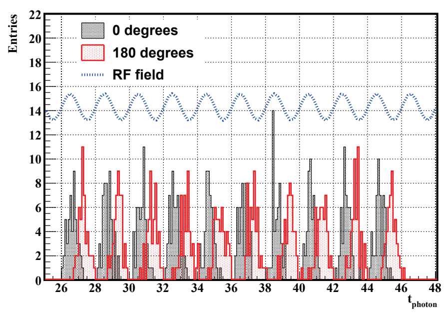

Figure 6: Photon arrival time at the upstream end of the fibre.

Figure 6 shows the distribution of photon arrival time for 0 (black) and 180° (red) phase shift as well as the modulation of the 500 MHz RF field. A slight overlap of the distributions tails for both RF phase shifts is observed. The distance between the mean values of the single bucket distribution is lower than the expected 1 nanosecond. This effect is not understood and is still under investigation. The overall time resolution of the system is calculated based on the quantity $\Delta t = t_{photon} - t_{mean}$, where t_{photon} is the arrival time as described above and $t_{mean} = t_{off} + n \cdot T_{RF}$ is the central value of the n^{th} bucket. For the Δt distributions shown in Figure 7, t_{off} is chosen as the mean value of the gaussian corresponding to the fifth bucket. It can be seen that the one sigma resolution obtained for both phases are compatible with each other and less than 300 ps.

MULTI BUNCH MEASUREMENTS

Multi bunch measurements conducted at both ASLS and CTF3 were performed to understand the behaviour of the oBLM system with longer pulses.

Multi Bunch Losses at ASLS

First turn losses were again investigated at the storage ring of the synchrotron but this time the length of the injected pulse was modified. Signals in the oBLM system were studied with trains of 15, 25, 50 and 75 bunches which corresponds to 30, 50, 100 and 150 ns pulse length. As expected, for losses sufficiently separated in position, loss structure is still observable (Figure 8). In the scraper fibre the two peaks corresponding to the injection point and the beam scrapers are still observable with the time difference between the raising edge of the observed peaks matching the distance calculated in the single bunch case.

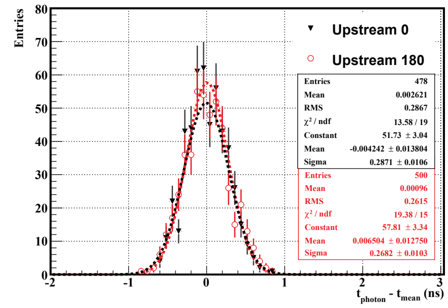

Figure 7: Δt distribution and gaussian fit for 0 and 180 degree phase shift between booster and storage ring RF.

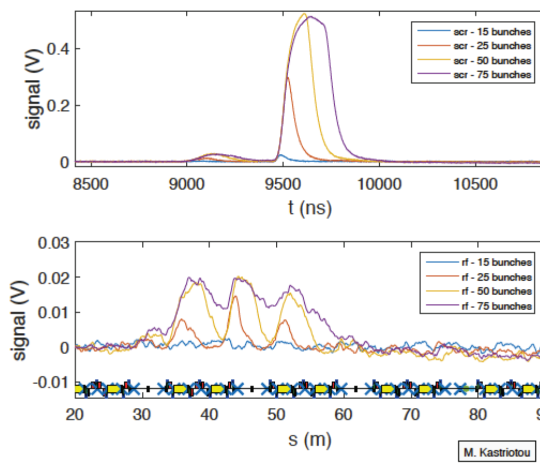

Figure 8: Multi bunch generated signals in the upstream scraper (RF) fibre at the top (bottom).

However, determining the location of beam losses signals close in time is more challenging. This is illustrated in the RF plot of Figure 8, where losses are produced at quadrupoles separated in some cases by less than 2 metres. Without any further processing, the peak structure of the oBLM signals is more and more spread out as the pulse length is increased. This limitation may be overcame de convoluting the signals by taking into account the non flat intensity profile in a bunch train. Measuring the bunch by bunch charge in a full train with the wall current monitor located after the gun, it is observed that the first few bunches carry very low charge. The intensity increases along the train and it becomes constant after the 15th bunch has been injected.

ISBN 978-3-95450-176-2

Long Electron Pulses

A final test with a 1 µs long beam pulse was conducted at the TBL in CTF3. The bunch spacing was defined by the 3GHz RF frequency and the measured peak current was 3 A. Beam losses during standard operation, i.e. with nominal quadrupoles settings, were measured and compared to those generated when turning off various magnets. The signals induced by shower generated at the TBL were computed by subtracting the signals observed in the background fibre to those measured in the TBL fibre. This is illustrated in Figure 9 for the case of nominal beam transmission, where it is shown that both the signal and background fibres carry an almost identical amount of light in the first (~150) nanoseconds. The very low signal level is attributed to observing only a very small fraction of beam loss and to attenuation in the 75 meter long extraction fibre at the upstream end.

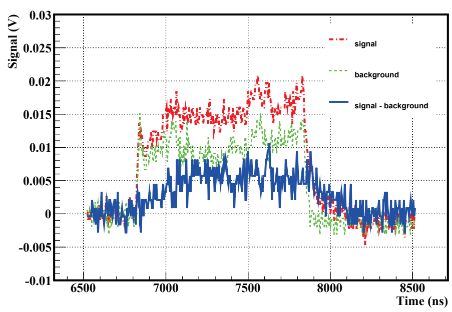

Figure 9: BLM signals observed during nominal beam transmission at the TBL.

During this experiment, the location of beam losses was determined by looking at the oBLM signals and comparing it to the intensity signal of the BPMs (1-16) along the TBL, as shown in Figure 10. A the top of the graph, the x axis indicates relative position in the line as demonstrated by the 1.4 meter distance between consecutive points. In the nominal case, there are no beam losses observed to within the accuracy of the devices. This is consistent with the low signals observed in the oBLMs (5 mV peak) for these quadrupole settings. When successively switching off specific quadrupoles, the first measured beam loss is observed with the BPM located immediately downstream of the next quadrupole.

The top of Figure 10 shows the leading edge of the (background subtracted) oBLM signal. Each trace is the average of 100 shots acquired for each quadrupole setting, with background subtraction performed on a shot-by-shot basis. At the top of the graph, the axis represents the relative position along the line as calculated by Eq. (4). It can be seen that there is very good agreement between the loss location calculated from the oBLM rising edge and that given by the BPM signals, with localisation down to below 2m easily achieved.

CONCLUSION

An oBLM system with SiPM based optical readout has been installed in the storage ring of the Australian Synchrotron and at the TBL of CTF3 at CERN. The former system has been used to perform single bunch studies that have shown the system to have an intrinsic time resolution for the system better than three hundred picoseconds and set the ground for multi bunch studies. The latter has been used to experimentally demonstrate, for the first time to the best of our knowledge, that reconstructing the original location of a beam loss is also possible with longer electron pulses.

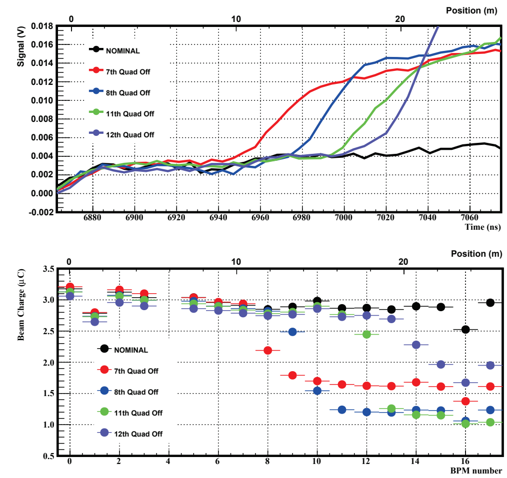

Figure 10: Leading edge of the BLM signals (top) and current measured by the BPMs (bottom) at the TBL.

ACKNOWLEDGMENT

The authors of this paper would like to thank the operators of CTF3 and the ASLS for their invaluable help on the execution of the experiments necessary for obtaining these results. This work has been partly funded by the Royal Society via the Intentional Exchange Scheme project PPR10353.

REFERENCES

[1] T. Obina, “Optical fibre based Beam Loss Monitoring for electron storage rings”, IBIC13, Oxford, September 2013.

[2] J. Boldeman et al., “The physics design of the Australian synchrotron storage ring”, Nucl. Instr. and Meth., A 521, 2004.

[3] CLIC Collaboration, “A multi-TeV linear collider based on CLIC technology”, CLIC Conceptual Design Report. Volume 1 Technical Report. CERN, Geneva 2012.

[4] E. Nebot et al., “Measurement of beam losses at the Australian synchrotron”, IBIC14, Monterrey, September 2014.

[5] R. Lillestrol et al., “Experimental results from the Test Beam Line in the CLIC Test Facility 3”, IPAC13, Shangai, 2013.

[6] J. J. Garcia-Garrigos et al., “Design and Construction of an inductive pick-up for beam position monitoring in the test beam line of CTF3”, EPAC2008.

[7] E. Nebot et al., “Studies of SiPM nonlinearities and transients at short light pulse detection”, LA3NET, Mallorca, March 2015.

[8] J. van Hoorne, “Cherenkov fibers for Beam Loss Monitoring at the CLIC Two Beam Module”, CERN-THESIS-2012-112.

COMMISSIONING OF THE NEW ONLINE-RADIATION-MONITORING-SYSTEM AT THE NEW EUROPEAN XFEL INJECTOR WITH FIRST TESTS OF THE HIGH-SENSITIVITY-MODE FOR INTRA-TUNNEL RACK SURVEILLANCE

Frank Schmidt-Foehre, Lars Fröhlich, Dirk Noelle, Rainer Susen, Kay Wittenburg, DESY, Hamburg, Germany

Abstract

The new Embedded Online-Radiation-Monitoring-System, developed for the 17.5 GeV superconducting European XFEL (E-XFEL) that is currently being built between the DESY campus at Hamburg and Schenefeld at Schleswig-Holstein [1,2], has been commissioned in a first system test setup at the E-XFEL Injector. As most of the electronic systems for machine control, diagnostics and safety of the E-XFEL will be located in cabinets inside the accelerator tunnel, the test setup incorporates all system parts like cabinet-internal and -external monitor electronics, infrastructure interface boards, firmware, software, cabling and sensors. Hence the commissioning system setup gives the possibility for first operation of the complete online radiation monitoring system under realistic environmental conditions in terms of irradiation, electro-magnetic interference (EMI) inside the injector tunnel, as well as operational and control system aspects. Commissioning results and measurements based on different internal and external sensor channels will be presented here, together with recent measurements done at different radiation sources using the high-sensibility mode for intra-rack radiation monitoring.

INTRODUCTION

The European XFEL that is currently being built between the DESY campus at Hamburg and Schenefeld at Schleswig-Holstein [1,2], will provide high duty cycle, ultra short X-Ray beams at wavelength about 0.5 Å with extreme brilliance. 27000 pulses per second are possible due to the super conducting 17.5 GeV linac, providing an electron beam with the corresponding time structure. The beam can be distributed into 3 undulator sections of about 200 m length, each consisting of about 30 undulators. Due to the overall length of the facility of about 3.4 km located in the city area of Hamburg, the installation of all parts including the electronics was chosen to be inside of a single tunnel system.

Due to the environmental conditions of the installation in a single tunnel, the control of beam losses and radiation damage is essential. Hence a new Embedded Radiation-Monitor-System (DosiMon) has been developed. The DosiMon system has been designed for measurement of γ-radiation at various appropriate electronics-internal and rack-external measurement points and dose levels. For future extension, the system design already incorporates provisions for measurement of Neutron-radiation in similar measurement point setups.

Most of the electronic systems cabinets for machine control, diagnostics and safety of the E-XFEL located in the accelerator tunnel are shielded, based on pre-estimated radiation levels and the expected damage threshold for standard non radiation hard electronics [3]. The current expansion state of the DosiMon system provides an online γ-radiation dose measurement inside those cabinets for this task.

External radiation detection sensors will also be used in addition to monitor e. g. the dose rates in the SASE undulator regions. Lifecycle estimates for the electronics and the sensitive undulators will trigger alarms, before significant radiation damage occurs. Furthermore, the online data from the dosimetry network allow correlating dose rates with machine settings, and thus to detect and to avoid dangerous operation modes.

A complete new modular system architecture has been designed for the DosiMon as shown in Fig. 1 and Fig. 2. The basic readout principle is similar to the reader design developed for undulator radiation measurements at the Fermi accelerator at Elettra-Sincrotrone Trieste(Italy) [4]. Corresponding orienting tests at the DESY Linac II [5] have demonstrated operation with zero-biased RadFets at DosiMon-comparable prototype testboards for a high dynamic range of ~1 Gy to >1000 Gy (e. g. for lifetime surveillance of the undulators in the XFEL SASE sections) at reduced sensitivity. Further calibration measurements have been taken at Fermi at Elettra [6] in a similar dose range, which can be used for start of commissioning at the XFEL. In addition to the zero-bias mode for enhanced dynamic range at a reduced sensitivity, the system also enables a high-sensitivity +18V bias-mode of the RadFet sensors, working in a reduced dynamic range.

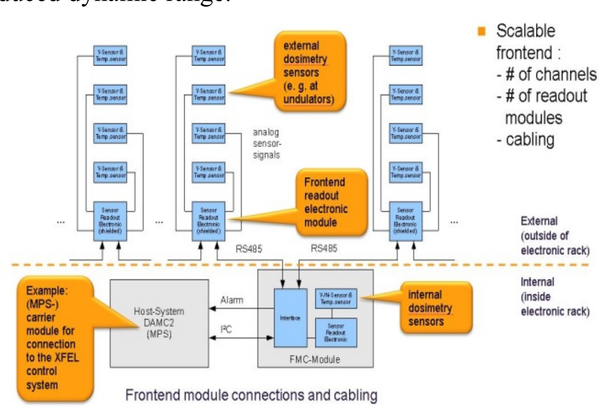

Figure 1: XFEL DosiMon basic system architecture.

ISBN 978-3-95450-176-2

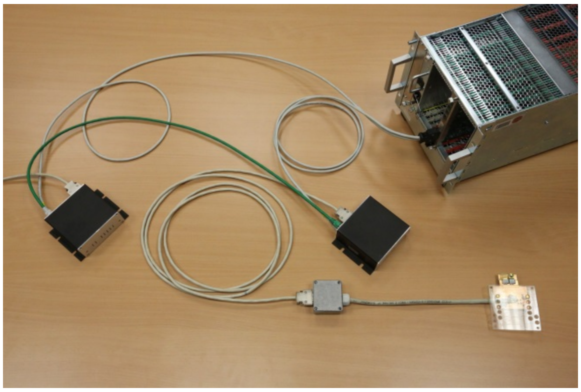

Figure 2: XFEL DosiMon system components.

A fingertip-sized, online-readable RadFet-type [7] RFT-300-CC10G1 sensor from REM Oxford Ltd. [8] has been successfully used throughout all tests and measurements and has consequently been selected as an appropriate γ-radiation sensor for series production. The sensor principle and key parameters are described in [4,7].

TEST SETUPS FOR COMMISSIONING

Since April 2015 various distinct system properties of the new XFEL radiation-monitoring system and several different test setups have been implemented and tested in operation at different accelerators and facilities at DESY. These test setups will be described in the following section, together with their goals and results:

1. full pre-series system test setup at XFEL Injector
2. calibration measurement with a Cs-137 calibration source at DESY's D3 personal radiation safety group
3. full series system test setup at the Flash RF-Gun
4. system test setup at the DESY 2 booster synchrotron
5. EMI test at functional Undulator setup.

SYSTEM TEST AT THE XFEL INJECTOR

After the first operation of XFEL gun with beam in the beginning of 2015, a complete pre-series system has been installed at the XFEL injector for commissioning test. The system was configured with internal and external measurement points both at +18V bias-mode for measurement of γ-radiation from em-showers induced by losses and dark current of the XFEL Gun. Due to delays in the completion and the restart of the XFEL injector, the commissioning test with beam had to be postponed, so that only the technical commissioning without beam could be successfully tested so far. Fig. 3 shows the external readout module and the sensor at the XFEL Injector. The installed pre-series system contains the FMC mezzanine board [9] with an internal sensor on it, sitting on a DAMC2 AMC carrier card for the XFEL machine-protection-system inside a MTCA.4 for physics standard crate [10]. Two external radiation monitor readout-electronic modules are connected together two the FMC-card in a ring-topology. One readout electronics is located below the XFEL gun (see Fig. 3). The other was positioned near the injector dump.

Successful readout of all sensors connected to both external readout-modules proved for the system operability as prepared for XFEL Injector operation, is currently delivering only noise without beam.

Figure 3: external readout module and sensor at the XFEL Injector.

COMMISIONING AT THE FLASH GUN

Another full pre-system test setup has been installed during the summer 2015 at the injector of the FLASH accelerator at DESY to enable commissioning of the DosiMon system with beam. The FLASH accelerator, served as a test facility for XFEL and provides similar electrical and operational conditions up to 2400 bunches with 20pC to 2nC at arbitrary bunch patterns and a maximum RF-pulse length of 800us at up to 1.25GeV. The test setup contains a FMC mezzanine-card with an internal RadFet-sensor and a corresponding TLD close to the RadFet as a reference. Connected to the FMC, an external sensor-readout-module is located inside the rack-shielding.

Figure 4: full system setup at Flash RF-gun rack.

Two external sensor boards are connected to the readout-module, one located between the rack-roof and

ISBN 978-3-95450-176-2

the acceleration module ACC#1 and the other located downstream at the lower edge of the rack in direct vicinity of an online personal-safety-dosimeter (Pandora).

The installed XFEL DosiMon system uses identical pre-series components like the ones located in the XFEL Injector. All RadFet sensors are operated in +18V-bias-mode for high sensitivity. The energy range at the FLASH system test setup position is up to 130MeV and the bunch timing of FLASH is similar to the XFEL system. All additional measurements and results with beam presented here where taken from the test setup at FLASH as shown in Fig. 4 as a reference for XFEL operation.

Fig. 5 shows the corresponding dose progress diagram of the personal-safety-dosimeter beside the downstream sensor. The RadFet readout voltage diagram shown in Fig. 6 depicts the uncorrected voltage over time of both dose-correlated RadFet channels at the downstream sensor.

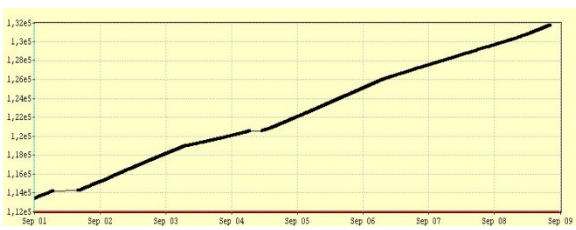

Figure 5: dose level [µSv] vs time (Pandora)

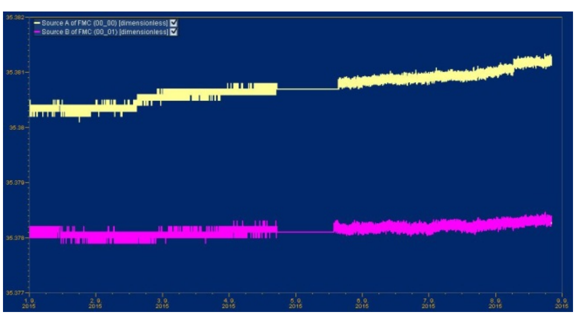

Figure 6: uncorrected RadFet threshold voltages vs time (interrupted signal due to archive development work).

While the temperature at the measurement point remains in a small regime around an average (not shown here), the uncorrected threshold voltages of the RadFet show an increasing signal, correlated with dose level as shown in the reference dosimeter diagram. Detailed dose calculation is underway, based on the first calibration of the +18V-bias-mode presented here. The FMC-internal RadFet inside the rack (Fig. 4) also shows a slight reaction, corresponding to the uncorrected dose of approximately below 11 mSv that was seen by the reference TLD100 nearby the RadFet.

CS-137 CALIBRATION MEASUREMENT

The new DosiMon radiation-monitoring system for XFEL enables a +18V-bias-mode for the RadFet sensors, intended for measurements at low dose rates and dose levels down to approximately 10 mGy, as will be used for operation inside shielded electronic cabinets in the XFEL. This mode is also called rack-surveillance mode, because a RadFet-/TLD-sensor-pair is mounted on a FMC board, typically located inside an electronic rack. After orienting pre-tests at the Linac II at DESY had shown the principle functionality of the high sensitivity mode [5], a RadFet connected to a testboard with readout electronics similar to the DosiMon pre-series has recently been tested in a Cs-137 calibration test setup as shown in Fig. 7. The RadFet, located on a sensor-holder pcb, positioned in the figure on the left side of the radiation semicircle was positioned in a distance of 30cm in front of a common standard Cs-137 source (pellet at radiation semicircle center position). For reference, 2 further TLD100 where placed nearby the RadFet and a set of additional 4(-6) TLD100 were located in the same distance to the source on the opposite side of the 30cm radius semicircle (right).

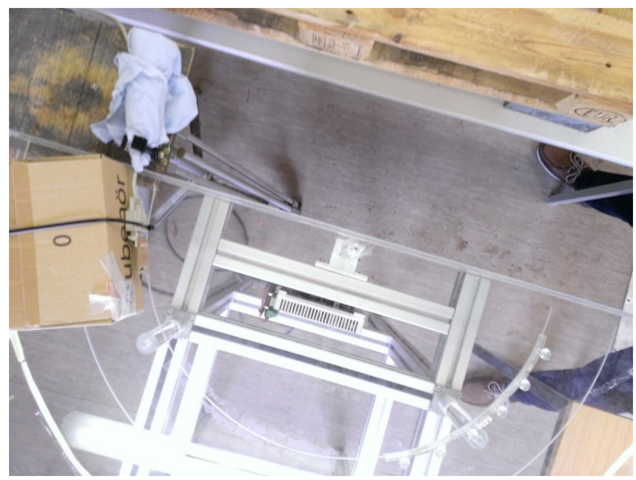

Figure 7: Cs-137 calibration setup (top view).

The radiation test setup was located inside a metallic standard container and had a strong room temperature-dependence from the outer environmental air temperature. The RadFet ambient room temperature as shown in Fig. 8 was logged by the Pt1000 temperature sensor located on the sensor-holder nearby the RadFet.

The RadFet was irradiated in two subsequent phases with approximately 1 week of duration each together with the reference sensors (13.7 days in total). Over both phases, the irradiation with constant dose rate by the Cs-137 source was only interrupted by very short breaks of 18 minutes in total for exchange of the TLD100 reference sensors. Hence, the relative error below 0.1% has been neglected in the further discussion.

ISBN 978-3-95450-176-2

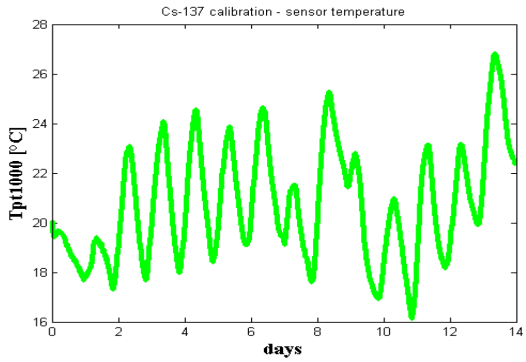

Figure 8: ambient temperature of the RadFet during Cs-137 irradiation.

The overall dose deposited on the RadFet sensor over this time was ~105 mSv (the TLD100 reference sensors that were used for cross-calibration measure dose equivalent). The threshold voltages of the 2 RadFet channels on the chip were monitored by the new readout system together with the room temperature and other internal parameters.

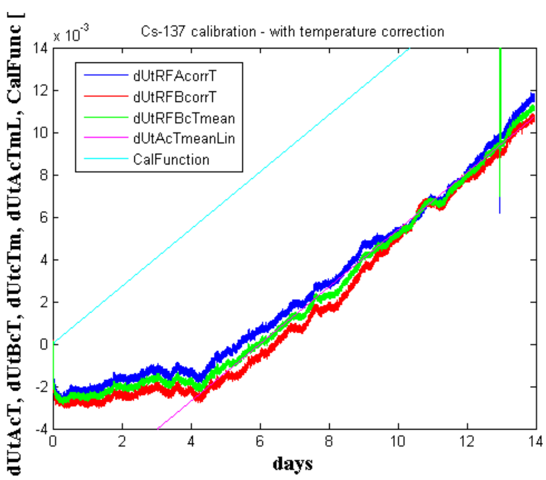

Figure 9: temperature-corrected threshold voltages [V] vs time of an un-irradiated RadFet at Cs-137 irradiation.

Figure 9 shows the mean (green curve) of the temperature corrected theshold voltages of both RadFet channels (red, blue) over the whole irradiation phase. The short peak after 13 days is probably an artefact from a short period of a transient external EMI-event to the electronics. In general, a recent orienting test measurement has shown that the pre-series electronics is sufficiently insensitive against typical EMI-disturbances induced by the strong drives of a XFEL undulator. The data correction at the Cs-137 calibration measurement includes systematic electronic errors and temperature dependence of both RadFet sensors. As this measurement has only been done with a single RadFet up to now, no statistical errors could be investigated yet. It can be seen from the green curve (mean of both RadFet channels), that the measured signal is overlayed by a short-term decreasing initial charge balance current and another, probably temperature-dependent effect over the first four days, that is not yet fully understood. As an initially linear response from a fresh RadFet is physically expected for very low dose levels until well above 100 mGy, the mean RadFet threshold voltage (green curve) shown in the diagram has been estimated by a linear fit (magenta) in the linear range of the curve. For correction of these overlayed effects, the fit was shifted to zero offset (cyan curve). Further measurements are needed, if these overlayed effects have to be corrected or vanish by statistics.

In combination with the linearly increasing dose level (up to ~105 mSv), this linearly fitted function results in a 'linear threshold voltage to dose'-calibration function for the lower dynamic range. As expected, the result in a range of 5.639 Sv/V falls in between the measurements done at former times at Fermi at Elettra for +9V- and +25V-positive bias mode [6].

TEST SETUP AT DESY2 BOOSTER RING

For the test of the high-sensitivity bias-mode, 2 RadFets with bias-voltage of +9V and +18V have been irradiated over a period of 5 months in an electronics room close to the Desy2 booster synchrotron. The RadFet readout was done by a system testboard with readout electronics similar to the DosiMon pre-series electronics. Radiation level reference measurement points were taken periodically every 2 weeks by consecutive high precision TLD100 measurements. The reference measurements were supplemented by an online γ- and neutron-sensitive radiation monitoring system for personal safety [11] at the same location. This measurement was intended to show measurement performance at high energies up to 6 GeV at high bunch duty-rates of 1 MBunches/s. As a long-term test, this measurement is intended to show fading (annealing) influence with the +18V-bias-mode used for XFEL.

As expected from the Pandora measurements showing a significant amount of neutron radiation at the measurement location, all TLD100 reference measurements showed clear influence from the presence of neutrons, leading to a significant overestimation of γ-dose levels from the unshielded TLD100s. Detailed investigations for quantification of the neutron impact on the TLD measurements were conducted, using differently shielded TLD100 sensors, to enable neutron-correction of the TLD100 total dose results and gain pure γ-reference results. In addition, the pre-estimation of the +9V-biased RadFet readings showed only small response over the first 2 weeks of permanent accelerator operation and significant dose build-up, as seen by the reference sensors.

A first estimate of the expectable dynamic range for the DosiMon series system yielded to an adequate sensitivity at the low dose range (startup-region) and a clearly sufficient dynamic range well above the goal of 10Gy for a +18V-biased RadFet. Hence a second +18V biased RadFet was introduced in the measurement run and showed analogue results over the measurement period. Analysis of the data taken from the DESY 2 run is highly

ISBN 978-3-95450-176-2

dependent on the results from the TLD100 and Pandora references correlated to the operation phases of the DESY 2 accelerator. Hence data analysis is ongoing, based on the Cs-137 calibration data presented above.

After first operational long-term measurements of the +18V bias-mode RadFet at the DESY2 accelerator, +18V bias-operation was chosen for the default high-sensitivity radiation monitoring mode for intra-rack surveillance inside the XFEL.

CONCLUSION

Different test setups have been successfully implemented and commissioned at different accelerators at DESY for the test of distinct system properties of the new radiation-monitoring system for XFEL.

An additional calibration measurement based on +18V-biased RadFet sensors has been successfully done with a CS-137 calibration source as a first calibration run of the systems high-sensitivity rack-surveillance mode.

All tests and measurements mentioned above have shown, that the new radiation-monitoring-system for the European XFEL works for all included zero- and positive-biased external and all positive-biased internal measuring points within all internal and external electronic system components (sensor measuring points).

OUTLOOK

The following list shows further steps, that are planned for commissioning and further development:

- Commissioning of the DosiMon system at the XFEL injector with beam (Nov. 2015)
- Measurements for the estimation of impact from the readout timing on RadFet response
- Release of the pre-series design for series production of components
- Advanced calibration measurements for the external and the high-sensitive internal mode (removal of statistical errors, clarification of the overlaying effects at the startup range of the high-sensitivity mode)
- Advanced measurements for the estimation of fading influence on the measured dose values in external sensor- and high-sensitivity internal sensor-mode
- Measurements for the estimation of neutron impact on RadFet response
- Measurements for the estimation of energy impact on RadFet response
- Calibration measurements in high-sensibility mode at Co-60 source for improved calibration up to 1.2MeV energy range.

ACKNOWLEDGEMENTS

We thank J. Pflüger and the WP71 team (all XFEL GmbH), F. Hellberg and A. Hedqvist (all Stockholm University, Sweden), A. Holmes-Siedle (REM Oxford Ltd.), M. Salmani and A. Leuschner (both Desy D3) for fruitful discussions, W. Decking and L. Fröhlich for valuable hints and discussions, J. Jaeger and S. Karstensen for firmware and software support and the whole DESY/XFEL WP17 team for its substantial support.

REFERENCES

[1] M. Altarelli et al., “The European X-Ray Free-Electron Laser”, Technical design report, http://www.xfel.eu/en/documents/, (2007).

[2] R. Brinkmann, “The European XFEL Project”, FEL´06, Berlin, MOBAU03, p. 24, (2006), http://www.JACoW.org

[3] Franz Czempik et. al., “Rack-Shielding for XFEL”, Version 0.06 draft, DESY Internal Technical Report, December 6, 2011, (2011).

[4] L. Fröhlich et al., “Online monitoring of absorbed dose in undulator magnets with RADFET dosimeters at FERMI@Elettra.”, Nucl. Instr. and Meth. A 703, pp. 70–79, (2012).

[5] F. Schmidt-Föhre et. al., „A New Embedded Radiation Monitor System for Dosimetry at the European XFEL”, Proceedings of IPAC11, San Sebastian, Spain, p. 2364 (2011).

[6] L. Fröhlich, S. Grulja, and F. Löhl, DOSFET-L02, “An advanced online dosimetry system for RADFET sensors“, Proc. IBIC'13, pp. 481–484, Oxford, UK, September 2013, (2013).

[7] Ravotti et. al., “Development and Characterisation of Radiation Monitoring Sensors for the High Energy Physics Experiments of the CERN LHC Accelerator”,CERN-THESIS-2007-013,Genf (2007).

[8] REM Oxford Ltd., “data sheet RFTDAT-CC10(REV B)”, component data sheet rft0888CC10dat0B.doc, Sept 2009, (2009).

[9] VMEbus International Trade Association, American National Standards Institute, Inc., “American National Standard for FPGA Mezzanine Card (FMC) Standard”, ANSI Standard ANSI/VITA 57.1-2008, (2008), http://www.vita.com/

[10] PICMG®, “PICMG® Specification MicroTCA.4 Rev. 1.0, Enhancements for rear I/O and Precision Timing”, August 22, 2011, (2011).

[11] A. Leuschner et. al., „Die Strahlungsüberwachungsanlage PANDORA“, DESY, Internal Technical Seminar M., March 2, (2012).

ISBN 978-3-95450-176-2

HTc-SQUID BEAM CURRENT MONITOR AT THE RIBF*

T. Watanabe†, N. Fukunishi, M. Kase, RIKEN, Wako, Japan
S. Inamori, K. Kon, TEP CorporationI, Katsushika, Japan

Abstract

For the purpose of measuring the DC current of heavy-ion beams non-destructively at high resolution, we have developed a high critical temperature (HTc) superconducting quantum interference device (SQUID) beam current monitor for use in the radioactive isotope beam factory (RIBF) at RIKEN in Japan. Because of its low vibration, a pulse-tube refrigerator cools the HTc fabrications that include the SQUID in such a way that the size and the operational costs of the system are reduced. Last year,we significantly reinforced the magnetic shielding system. The new strong magnetic shielding system can attenuate the external AC magnetic noise by 10^{-10}. With the aim of practical use in acceleration operation, we disassembled the prototype high-Tc SQUID current monitor (SQUID monitor), installed improved parts, and re-assembled it. Beginning this year, we have installed the SQUID monitor in the beam transport line in the RIBF. Here we describe the present details of the developed SQUID monitor system and the results of beam measurements.

INTRODUCTION

The reason for using a superconducting quantum interference device (SQUID) as a beam current monitor is that it has a very high magnetic sensitivity. For example, SQUIDs are used in studies of the neural activity inside brains and to diagnosis heart conditions in clinical environments. The magnetic fields induced by the brain and heart are very faint in the range of from 10^{-10} to 10^{-14} T. This extreme sensitivity allows a SQUID to measure a beam current nondestructively. Furthermore, we aim to downsize the system and reduce running costs by using high critical temperature (HTc) materials including the SQUIDs. Schematic drawings of the SQUID monitor and the cryostat inside the SQUID monitor are shown in Fig. 1. Both the HTc magnetic shield and the HTc current sensor were fabricated by dip-coating a thin Bi_2-Sr_2-Ca_2-Cu_3-O_x (Bi-2223) layer on a 99.7% MgO ceramic substrate [1]. The Bi-2223 layer is approximately 500 μm thick. When a charged particle (ion or electron) beam passes along the axis of the HTc current sensor, a shielding current produced by the Meissner effect flows in the opposite direction along the wall of the HTc current sensor. The shielding current acts so as to eliminate the magnetic field produced by the beam. Since the outer surface of the HTc current sensor is designed to have a bridge circuit [1], the current generated by the charged particle beam is concentrated in the bridge circuit and forms an azimuthal magnetic field around it. The HTc SQUID is set close to the bridge circuit and can detect the azimuthal magnetic field with a high S/N ratio. The beam current can be precisely obtained by previously calibrating the HTc SQUID output voltage with a known reference current. As shown in Fig. 1-(b), the HTc SQUID monitor consists of two vacuum chambers completely separate from each other. One chamber contains a cryostat in which the HTc SQUID, HTc magnetic shield, and HTc current sensor are cooled. The other is the chamber through which the beam passes. All the fabricated HTc devices are cooled to around 70 K by a low-vibration pulse-tube refrigerator with a refrigeration power of 11 W at a temperature of 77 K. Eight vibration rubbers dampen the vibration caused by the pulse-tube refrigerator. Figure 2 shows a bird’s-eye view schematic of the RIBF facility indicating the positions of the SQUID monitor. The research activities of the RIBF project make extensive use of the heavy-ion accelerator complex, which consists of two linacs and five ring cyclotrons, i.e., two RIKEN heavy-ion linacs (RILAC I, II), the AVF cyclotron, the RIKEN ring cyclotron (RRC), the fixed-frequency ring cyclotron (fRC), the intermediate-stage ring cyclotron (IRC), and the superconducting ring cyclotron (SRC). Energetic heavy-ion beams are converted into intense RI beams via the projectile fragmentation of stable ions or the in-flight fission of uranium ions by using the superconducting isotope separator BigRIPS.

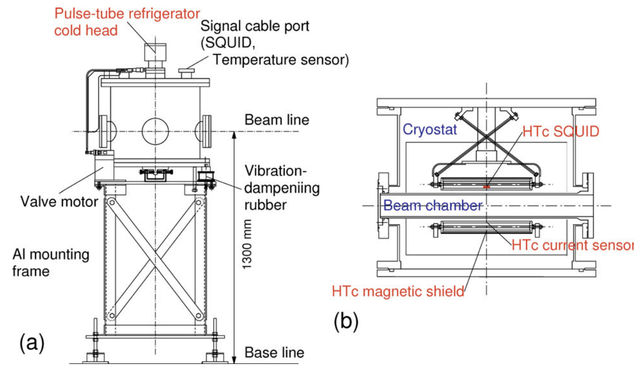

Figure 1: Schematic drawing of the (a) high-Tc SQUID current monitor (SQUID monitor) and (b) the cryostat inside the SQUID monitor.

Beginning this year, we have installed the SQUID monitor in the beam transport line in the RIBF (Fig. 2). We are presently using the SQUID monitor in practice for measurement of the current of beams of heavy-ions such as uranium.

* Work supported by JSPS KAKENHI (Grants-in-Aid for Scientific Research) Grant Number 15K04749

† wtamaki@riken.jp

ISBN 978-3-95450-176-2

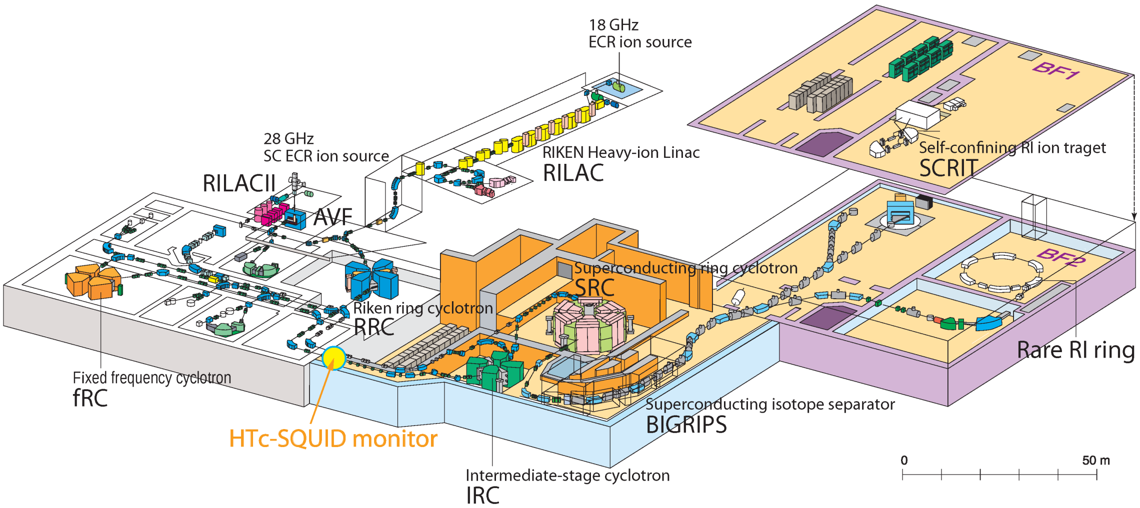

Figure 2: Bird's-eye view schematic of the RIBF facility showing the position of the HTc SQUID monitor.

PROTOTYPE DEVELOPMENT

HTc Current Sensor and SQUID

With the aim of increasing the beam current resolution of the SQUID monitor, we investigated improvement of the coupling efficiency between the magnetic field that is generated at the bridge circuit and the input coil of the HTc SQUID [1]. We developed a new HTc SQUID [2] with a high-permeability core that was installed in the two input coils of the HTc SQUID (Fig. 3). Furthermore, to increase the magnetic field produced by the bridge circuit, we successfully fabricated an HTc current sensor with two coils by using a newly developed spraying machine [3]. Although the conventional hand-coating method required professional skill to apply the Bi2223 layer onto the MgO substrate, the spray machine can perform the operation automatically and uniformly. As a result, the problem of Bi-2223 material peeling off during the sinter process was resolved and experience with coatings and the sinter process was gained.

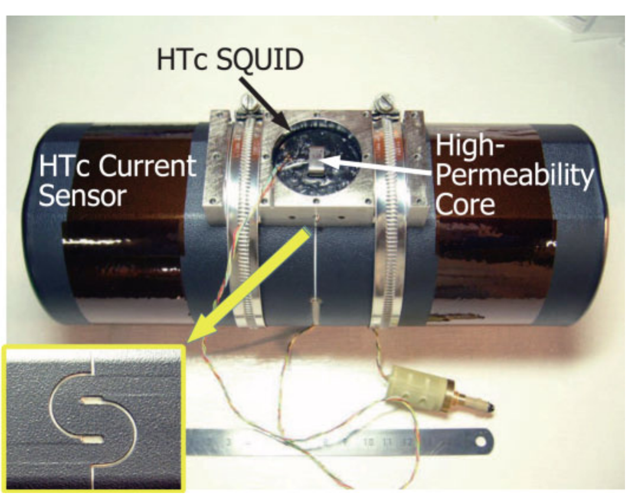

Figure 3: New HTc SQUID [2] with a high-permeability core that was installed in the two input coils of the HTc SQUID and HTc current sensor with two coils.

Prior to coating the MgO substrate with Bi-2223 material by using the spraying machine, we analyzed the critical temperature (Tc), critical current density (Jc), and X-ray diffraction patterns. Using three test pieces of MgO substrates (5 W ~ 50 D ~ 5 H [mm]) coated with Bi-2223 material, we confirmed the critical temperature of 105 K and critical current density of 3250 A/cm^2. From the X-ray diffraction patterns, it was clear that major peaks appear in the Bi-2223 phase.

Reinforcement of the Magnetic Shield

In general, the performance of monitors such as the SQUID monitor is determined by the S/N ratio. To improve the measurement resolution, it is important to attenuate external magnetic noise, which is mainly generated by distribution and transmission lines from the high current power supplies in the RIBF. Therefore, we developed a hybrid magnetic shielding method based on the properties of perfect diamagnetic materials (superconductors) and ferromagnetic materials [4]. The HTc current sensor also works as a superconducting shield by the Meissner effect (perfect diamagnetism). To design a hybrid magnetic shielding system, the attenuated magnetic field was calculated by using the electromagnetic field simulation program Opera-3d [5]. Since Opera-3d cannot deal with superconductivity, the value of 1×10^{-12} was used for the relative permeability of the HTc current sensor in the approximate calculation. The calculation shows that the hybrid magnetic shielding system can achieve a magnetic attenuation factor of 10^{-4}.

Since there exist 50 Hz and higher-order AC magnetic noises in the acceleration facility, that are much stronger than terrestrial magnetism, a noise canceller system (78200DAMC [6]) was designed and introduced to the SQUID monitor. This system is comprised of a magnetic field control unit, 3-axis AC/DC magnetic field sensors, and

ISBN 978-3-95450-176-2

compensation coils. The compensation coils consist of three pairs of coils that are arranged perpendicular to each other. Each of these pairs forms a so-called Helmholtz-Coil-Pair, which is able to produce a homogenous magnetic field in between them. Each pair controls one direction (i.e., along the x-, y-, or z- axis).

To evaluate the performance of the hybrid magnetic shielding system and the noise canceller system, the output signals of the HTc SQUID were analyzed in the time- and frequency domains. Based on these findings, we consider that the combination of the hybrid magnetic shielding system and the noise canceller system can attenuate the external magnetic noise of the 50 Hz component by 10^{-10}.

INSTALLATION IN THE RIBF

Characteristic Frequency and Current Calibration

Because the prototype SQUID monitor was intend for practical use in accelerator operation, we disassemble it and installed improved parts, namely the HTc current sensor with two coils, the HTc SQUID with a high-permeability core, and the hybrid magnetic shield. During the reassembly operation, we improved the attainment temperature of the SQUID from 71 K to 67 K, by renewing the super insulation and applying Apiezon grease between the HTc SQUID and the SQUID holder. We then measured the characteristic frequency and calibrated the SQUID output voltage with a simulated beam current. The output voltage of the high-Tc SQUID controller as a function of the simulated beam current is plotted in Fig. 4. From these measurement results, we obtained the following calibration equation:

$$\begin{aligned} V_s &= S_{co} \times I_b \times G/500 \\ &= 49.28 \times I_b \times G/500, \end{aligned}$$

where S_{co}, I_b, V_s, and G are the coupling efficiency (mV/μA), beam current (μA), output voltage of the SQUID controller (mV), and gain of the SQUID controller, respectively. Furthermore, the characteristic frequency of the

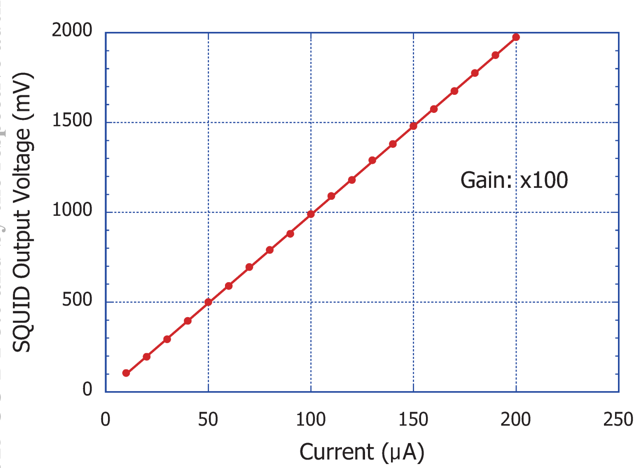

Figure 4: Output voltage of the HTc SQUID controller as a function of simulated beam current.

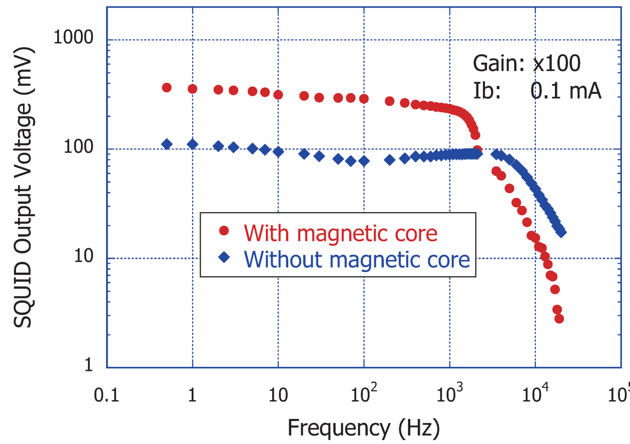

Figure 5: Characteristic frequency of the SQUID monitor measured by FFT in the frequency domain.

SQUID monitor was measured by performing a fast Fourier transform (FFT) in the frequency domain (Fig. 5). Although the frequency range with the magnetic core is several kHz narrower than without the core, the output voltage is higher with the core. Figure 6 shows the SQUID monitor equipped with the noise cancellation system, which was installed in the transport line between the fRC and IRC (Fig. 2).

Data Acquisition and Control System

A block diagram of the data acquisition and control system of the SQUID monitor is shown in Fig. 7. The PXI controller (NI PXI-8106 [7]) controls the HTc-SQUID controller (iMC-303 [8]), signal acquisition module (USB-4431 [7]), noise canceller controller and power supply (78200DAMC [6]), and temperature controller (Model 34 [9]). The analogue output signal from the HTc SQUID controller is acquired with the signal acquisition module and converted into a mea-

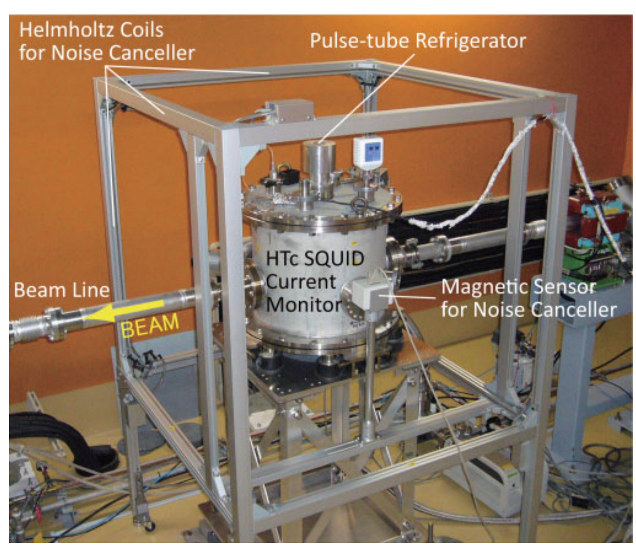

Figure 6: SQUID monitor equipped with the noise canceller system, which was installed in the transport line between the fRC and the IRC (Fig. 2).

ISBN 978-3-95450-176-2

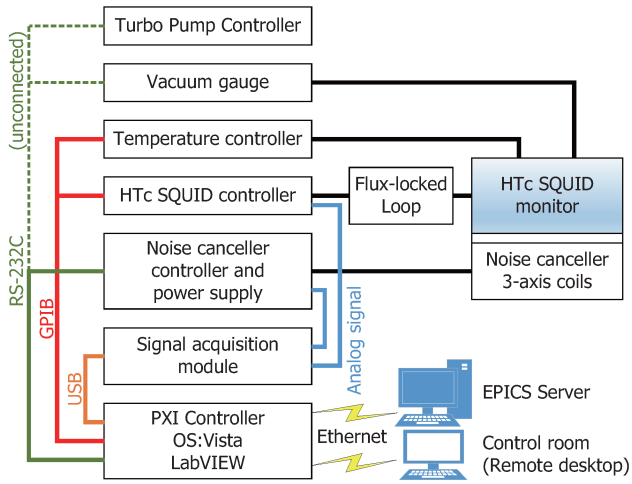

Figure 7: Block diagram of the data acquisition and control system of the SQUID monitor.

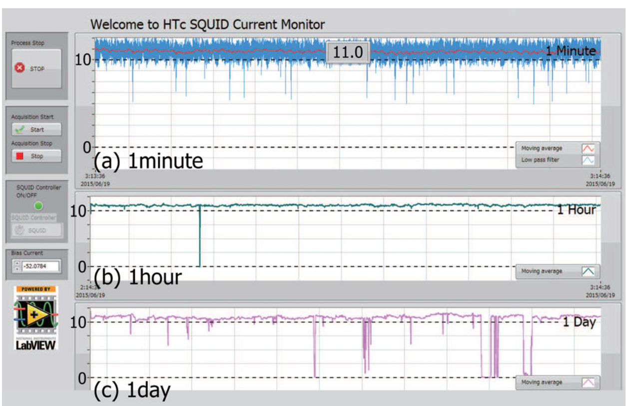

Figure 8: The 11 μA ^{78}Kr^{36+} intensity of the beam (50 MeV/u) was successfully measured with 500 nA resolution.

surement of the beam current. Similarly, the output signals of the 3-axis AC and DC magnetic fields measured with the noise canceller are also AD converted by the signal acquisition module. The feedback gains of the noise canceller are set via RS-232c and the bias current, modulation voltage, and skew voltage that concern the SQUID controller are set via GPIB. The programs for the data acquisition, control, and results display are written in LabVIEW [7]. The PXI controller is connected to a laptop in the main control room located 100 m from IRC hall via Ethernet and a remote desktop connection. The driving control and status monitoring of the beam chopper are controlled by the EPICS system.

MEASUREMENT OF BEAM CURRENT

Flux Trapping Removal

After we started to accelerate the heavy-ion beam and started the RIBF experiment, external magnetic flux passed through the HTc SQUID sensor and some unexpected flux was trapped inside it during its superconducting state. This flux trapping caused noise in the highly sensitive SQUID chip. The HTc SQUID is operated in a null detection mode where a flux-locked loop provides a negative feedback to maintain linear operation. The noise generated by the flux trapping gradually increased with time. Eventually, the flux-locked loop could no longer maintain the negative feedback because the noise level exceeded the amount of negative feedback. To purge any magnetic flux trapped in the sensor, a heater made of a small resister was mounted close to the SQUID chip in the sensor package. By raising the temperature of the HTc SQUID above its critical temperature Tc for 30 s, the SQUID noise was greatly reduced and the problem was resolved.

Experimental Results

We successfully measured the intensity of an 11 μA beam of ^{78}Kr^{36+} (50 MeV/u) with 500 nA resolution (Fig. 8), where the 11 μA beam produced a magnetic flux of 0.236 Φ_0 (a magnetic flux quantum phi zero of 2.07×10^{-15} weber) at the input coil of the high-Tc SQUID. Prolonged 1 min, 1 h, and 1 day recordings of the Kr beam current extracted from the fRC were achieved (Fig. 8). In these recordings, several dips in beam intensity due to ECR ion source discharge can be observed. The different beam current signals were analyzed by performing FFTs in the frequency domain (Fig. 9). The amplitude of the ripples in the modulated beam current increased with the beam current. The sampling time for data acquisition was 500 μs, and 2000 data points were averaged to improve the S/N ratio. Because the zero current point drifted due to temperature change, it was calibrated every hour by firing the beam chopper; this should be resolved in the near future.

CONCLUSIONS AND OUTLOOK

To measure the DC current of heavy-ion beams non-destructively at high resolution, we have developed a SQUID monitor for use in the RIBF at RIKEN in Japan. In the previous year, we strongly reinforced the magnetic shielding system. Since the prototype SQUID monitor was intended for practical use in acceleration operation, we disassembled

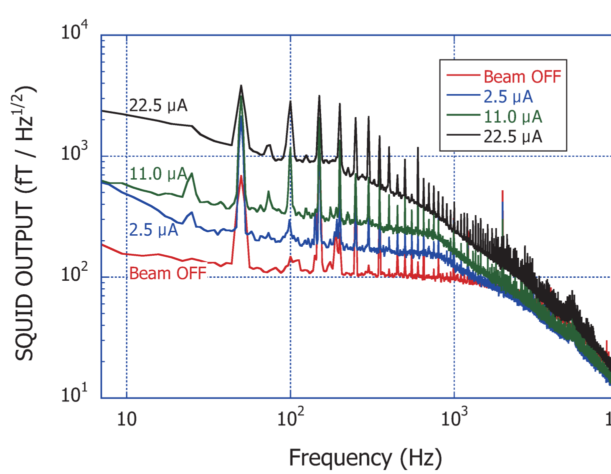

Figure 9: The results of analyses of different beam current signals by FFTs in the frequency domain.

ISBN 978-3-95450-176-2

it, installed improved parts, and re-assembled it. At the Beginning of this year, we installed the SQUID monitor in the beam transport line in the RIBF and we have been using the SQUID monitor for current measurement of heavy-ions beams.

Although we can measure the intensity of a sub-μA beam, a minimum current resolution of more than two orders of magnitude lower is required at the RIBF. We can use MgO ceramic tubes for the substrates in the SQUID monitor, but it is difficult to make the required complex shape. Therefore, we are now investigating the possibility of coating a thin layer (70 μm) of Bi_2-Sr_2-Ca_1-Cu_2-O_x (Bi-2212) on a silver (Ag) substrate capable of corresponding to the complex shape. Although we tried to fabricate an HTc current sensor coated by Bi-2212 [10], it did not work as a superconductor because its critical temperature (Tc) was under 70 K. Figure 10 shows a comparison between the surfaces of Bi-2223 and Bi-2212 under a scanning electron microscope. It is clear that the surface of Bi-2212 is smoother than that of the Bi-2223. We coated both HTc materials on MgO substrates and confirmed that the Tc of each was higher than the temperature of liquid nitrogen.

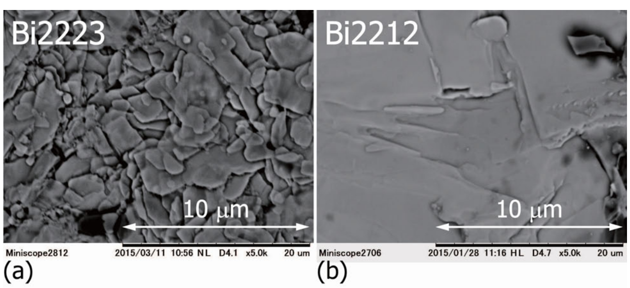

Figure 10: Comparison of the surfaces of (a) Bi-2223 and (b) Bi-2212 (b) as observed by a scanning electron microscope.

ACKNOWLEDGMENT

The authors are grateful to M. I. Faley of Forschungszentrum Juelich GmbH for valuable discussions about the high-Tc SQUID; E. Nemoto of JEOL DATUM, Ltd., for cooperation regarding the noise cancellation system; A. Kamoshida cooperation regarding the LabVIEW programing; and operators of SHI Accelerator Service Ltd. for their assistance. This work was supported by JSPS KAKENHI Grant Number 15K04749.

REFERENCES

[1] T. Watanabe et al., "DEVELOPMENT OF BEAM CURRENT MONITOR WITH HIGH-Tc SQUID AT RIBF", Proc. 2010 Beam Instrumentation Workshop (BIW10), Santa Fe, New Mexico, U.S.A pp. 523-532 (2010).

[2] M. I. Faley, "Epitaxial Oxide Heterostructures for Ultimate High-Tc Quantum Interferometers", Applications of High-Tc Superconductivity, Dr. Adir Luiz (Ed.), pp. 148-176 (2011), ISBN: 978-953-307-308-8, InTech.

[3] T. Watanabe et al., "Beam Current Monitor with a High-Tc Current Sensor and SQUID at the RIBF", J Supercond Nov Magn, Vol.**26**, Issue 4, pp. 1297-1300 (2013), doi:10.1007/s10948-012-1943-0.

[4] T. Watanabe et al., "Improvements of a Beam Current Monitor by using a High Tc Current Sensor and SQUID at the RIBF", 11th European Conference on Applied Superconductivity (EUCAS2013), IOP Publishing Journal of Physics: Conference Series **50** (2014) 042047, doi:10.1088/1742-6596/507/4/042047

[5] COBHAM, http://www.cobham.com/home.aspx

[6] JEOL Ltd., http://www.jeol.co.jp/en/

[7] National Instruments, http://www.ni.com/.

[8] Tristan Technologies, http://www.tristantech.com/.

[9] Cryogenic Control Systems Inc. (Cryo-con), http://www.cryocon.com/.

[10] T. Watanabe et al., "Development of new HTS-SQUID and HTS current sensor for HTS-SQUID beam current monitor", 8th European Conference on Applied Superconductivity (EUCAS2007), IOP Publishing Journal of Physics: Conference Series **97** (2008) 012248, doi:10.1088/1742-6596/97/1/012248.

ISBN 978-3-95450-176-2

WIDEBAND VERTICAL INTRA-BUNCH FEEDBACK AT THE SPS – TECHNOLOGY DEVELOPMENT, RECENT ACCELERATOR MEASUREMENTS AND NEXT STEPS*

J. Fox, J. Dusatko, C. Rivetta, O. Turgut
Stanford Linear Accelerator Center Stanford, CA, USA
H. Bartosik, W. Hofle, B. Salvant, U. Wehrle, CERN, Geneva, Switzerland
S. De Santis, LBL Berkeley, CA, USA

Abstract

A wideband vertical intra-bunch feedback system is in development at the CERN SPS for use to control potential Ecloud and TMCI instabilities. The work is motivated by planned intensity increases from the LIU and HL-LHC upgrade programs. System technical features include pickups, upgraded kickers and related RF power amplifiers, 1 GHz bandwidth analog processing used in conjunction with a 4 GS/sec reconfigurable digital signal processing system. Recent results include driven beam experiments and beam simulation methods to verify the damping provided by the wideband system, and validate reduced MIMO models and model-based controllers. Noise effects and uncertainties in the model are evaluated via SPS measurements to predict the limits of control techniques applied to stabilize the intrabunch dynamics. We present data showing the excitation and damping of unstable modes. The plans for the next year, including experimental measurements, hardware upgrades and future control developments are described.

INTRODUCTION - CONTROL OF INTRA-BUNCH INSTABILITIES

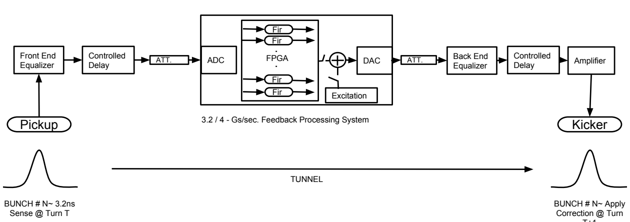

Figure 1: System diagram for the demonstration intra-bunch signal processing

Instability control via feedback at light sources and accelerators requires techniques to sense beam motion, compute correction signals and apply these corrections to the beam. This intra-bunch feedback system follows the same principles, but acts on modes of beam motion within a single bunch as well as coupled bunch modes between bunches. The basic formalism uses digital processing techniques to remove noise and DC orbit offsets from the bunch signals, apply gain at the oscillation frequency with a tailored phase shift to apply a net damping signal at a kicker structure. An intra-bunch feedback system using digital processing formalism has been demonstrated at JPARC [1, 2] for 150 ns long bunches and at the CERN PS for 60 ns bunches [3]. The challenge in our work directed at the CERN SPS is the necessary bandwidth, as the SPS bunch 4σ is roughly 1.7 ns, so our systems sample at 3.2 or 4 GS/sec (Fig. 2). The kicker and pickup elements then require roughly a GHz of bandwidth, and all the processing elements within the loop require careful attention to deviations from linear phase response to allow high closed loop gain without causing oscillations or instabilities.

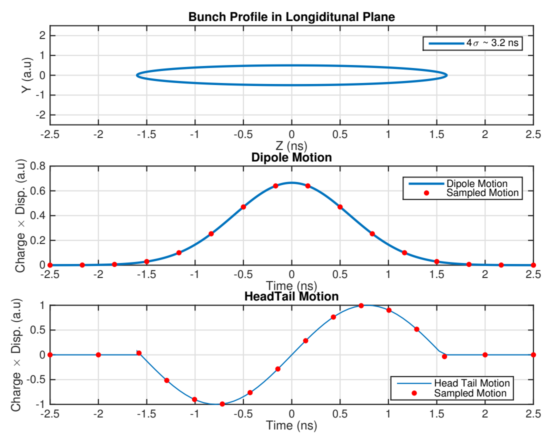

Figure 2: The intra-bunch system samples 16 vertical coodinates across each bunch, and computes correction signals in a processing filter to be applied on later turns.

The high-current operation of the SPS for HL-LHC injection will require mitigation of possible Ecloud and TMCI effects [4]. These intensity-limiting instabilities can be controlled through several measures, including special coatings of the vacuum chamber, tailored machine optics [5] or wideband feedback techniques [6]. A single-bunch wideband digital feedback system was initially tested at the CERN SPS in November 2012 [7, 8]. The project is part of a larger LHC injector upgrade [6]. In 2014, during the shutdown interval this system has been expanded with installation of wideband kickers and associated RF amplifiers [9]. While the original bandwidth-limited system achieved control of mode 0 and mode 1 unstable beams, we must explore the new wideband kicker performance, and understand necessary capabilities to control beams anticipated in the HL operating scenario.

* Work supported by the U.S. Department of Energy under contract # DE-AC02-76SF00515 and the US LHC Accelerator Research Program (LARP).

ISBN 978-3-95450-176-2

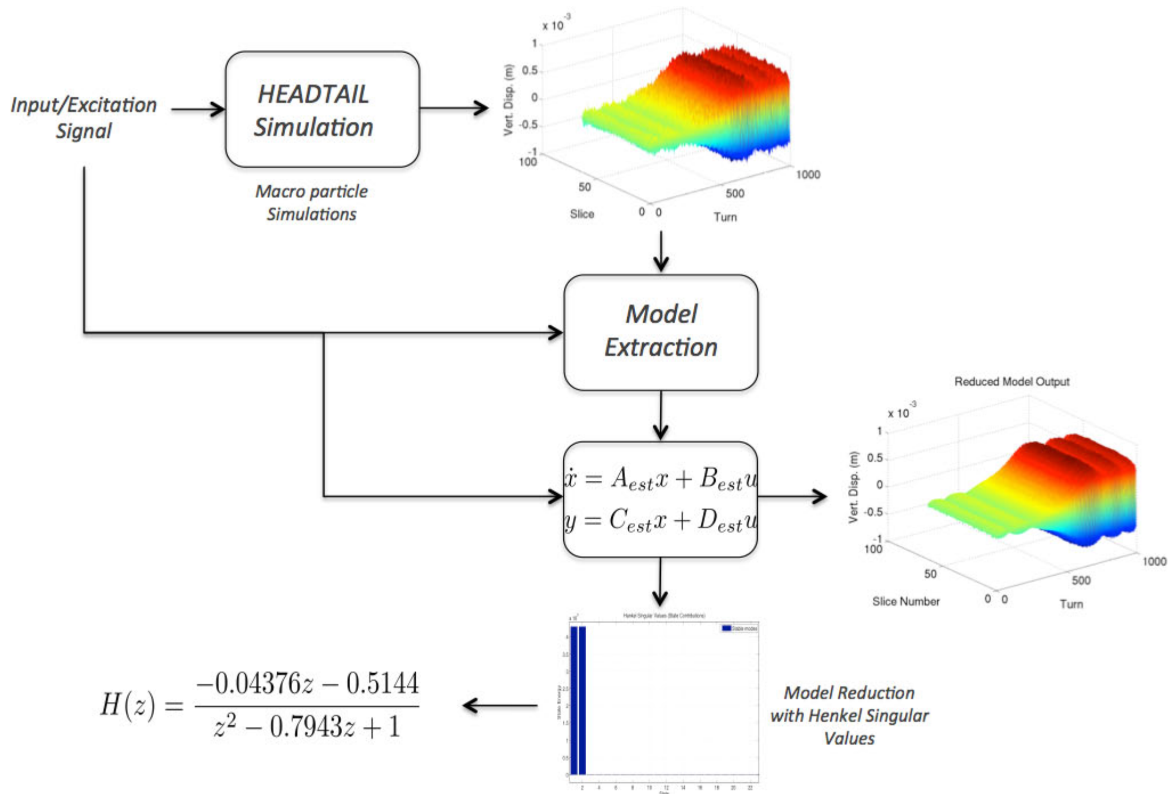

Figure 3: The reduced model parameters are generated by fitting the model response to physical data from machine measurements, or from numerical simulations such as Head-Tail or CMAD. The order or complexity of the reduced model is chosen to capture the most essential dynamics in the data set. This example shows open-loop motion of mode 0, excited by an external driving excitation

We cannot expect the limited-function Demonstration System to have the capability of the final system, instead we want to confidently predict the behavior and margins of a more complex full-featured system. To do this, we need methods to simulate realistic future beam conditions interacting with possible feeback systems, and methods to compare the behavior of the Demonstration system and beam against simulations. In the near term we must study the system under a sub-set of HL beam conditions, and validate that our models of the feedback and beam are faithfully duplicating the real-world measured performance. Our goal in testing the demonstration system is to validate the performance as achieved, and through simulation tools to predict the behavior for high-current and HL upgraded injector conditions. These tests are also very significant technical demonstrations of the functioning of the 4 GS/sec digital signal processing hardware and build confidence that the proposed full-function architecture can be developed and commissioned as planned.

SYSTEM DEVELOPMENT AND UPGRADES

The modular architecture and basic FPGA platform of the Demonstration Processor allows the expansion of new control filters and the additon of new control features. During the LS1 interval the analog signal processing of the system was carefully upgraded, with special attention to the input pickup processing and the behavior of the wideband equalizers and 3.2 GS/sec ADC stages. This improvement increased rejection of spurious signals and nonlinear behavior of the analog processing which had been visible in the original implementation data. With these improvements and development of a more robust grounding and shielding scheme, the analog front end systems now have a full 54 dB dynamic range and the noise floor is now flat over the operating frequencies. A new timing and synchronization system was incorporated which keeps the high-speed 3.2 or 4 GS/sec. output DAC stream phase aligned with the SPS RF system, so that timing consistency and operational robustness was improved. A new scrubbing fill feedback processing mode was added, so that two adjecent buckets with 5 ns separation can be indivually controlled, each with 16 samples of intra-bunch control. The single-bunch control filter has been extended to process and generate signals for a 64 bunch train. CERN completed the fabrication of two stripline kicker modules [10], which were installed on the SPS beam line with associated cabling and infrastructure to allow control and monitoring of new wideband RF amplifiers. The analog equalizer functions, needed to maintain linear phase response over the 1 GHz system bandwidth, were upgraded to include the responses of the new kicker cable plant [11]. An extensive evaluation of 11 commercial wideband RF amplifiers resulted in the development of a

ISBN 978-3-95450-176-2

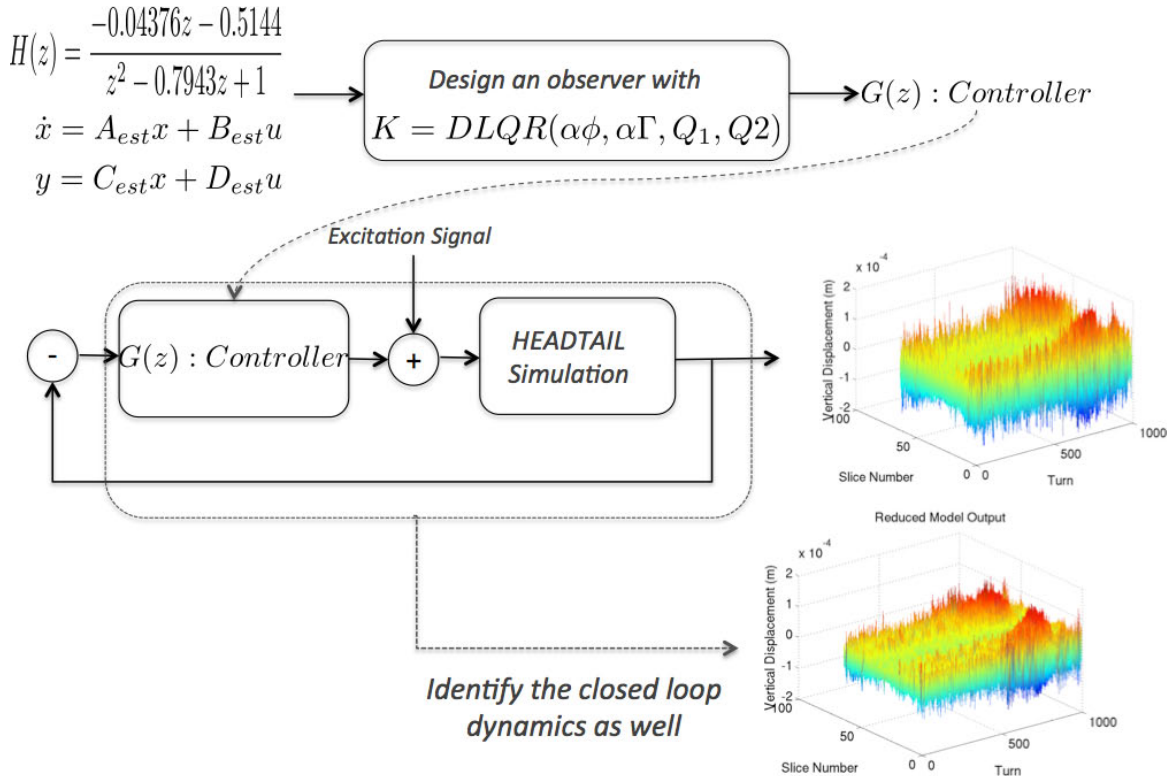

Figure 4: The reduced model behavior under the action of a feedback controller can be directly compared to the behavior of the nonlinear simulation with that controller, or against with machine studies of the beam under the action of that controller through the Demonstration system.

new variant of a commercial 5 - 1000 MHz amplifier with excellent time response to 100% AM modulated signals. Two of these 250W amplifiers, with associated remote control functions, have been installed and commissioned in the SPS tunnel. Two more are expected to be installed on the second stripline kicker in winter 2015/2016.

REDUCED MODEL DEVELOPMENT AND APPLICATION

This feedback task is challenging as the beam dynamics and instability physics is inherently nonlinear. Nonlinear particle tracking codes such as Head-Tail can simulate complex dynamics and can faithfully replicate physical beam dynamics if there is good knowledge of machine impedances, a high order model of the machine lattice, and realistic estimates of electron-cloud densities, etc. It is possible to include a simplified feedback processing model into this type of simulation [12]. But this simulation produces time-domain trajectories over finite time intervals, and produces no insight into stability magins and the impact of small changes in parameters on stability. This type of time-domain nonlinear tool also does not have a direct formal method to design feedback controllers. We need reduced system models to design our feedback controllers using modern control methods. This design approach gives us analytic methods to specify the control filter, directly estimate the stability margins of the closed loop system and identify the necessary system bandwidth and gain as a function of reduced model parameters.

The reduced model represents the dominant dynamics in the physical system with a discrete-time linear MIMO model of coupled harmonic oscillators [13, 14] and we design feedback controllers using these linear models [15, 16]. As seen in Figure 3, the model is fit to either machine measurement data or numeric simulation data. The reduced model is analytic and linear, and allows design of control filters using optimal and modern control techniques. After the optimization of a control filter with the linear model, as seen in Figure 4 we then study system performance using the head-tail simulation code with an incorporated feedback model [13, 17]. The use of any of these codes only has value if the results can be compared in a quantified way with actual physical measurements. One very important value of the reduced model is to validate the fidelity of numeric simulations against physical beam measurements. If the two reduced models, independently derived from simulations and machine studies have good agreement, then the numeric simulation parameters are faithfully reproducing the actual physics seen in the measurements. With this understanding we can make confident predictions for the performance of yet-unbuilt expanded feedback capabilities, the behavior of systems under higher intensity beam conditions or for new optics, etc.

ISBN 978-3-95450-176-2

EVALUATING THE UPGRADED SYSTEM PERFORMANCE

We use two core methods to evaluate the behavior of both simulation studies and physical beam measurements. Both methods utilize the feedback system processing to excite the beam from data files, and record the beam responses digitally within the feedback processing. One technique uses frequency-domain tests by applying swept excitations, a complementary method uses time domain studies where the feedback gain is varied in time while the beam motion is recorded (grow-damp studies).

The frequency domain studies use swept excitation chirps driving the beam-feedback system across a frequency span that includes oscillation modes of interest, and measuring the beam response using a spectrogram technique. These quasi-steady state excitations originate from data samples stored within the feedback processing system (effectively arbitrary waveforms which can be applied to 16 samples across the bunch for thousands of turns) [18]. These excitations can be modulated in frequency, and in spatial pattern, to allow careful excitation of particular intra-bunch modes.

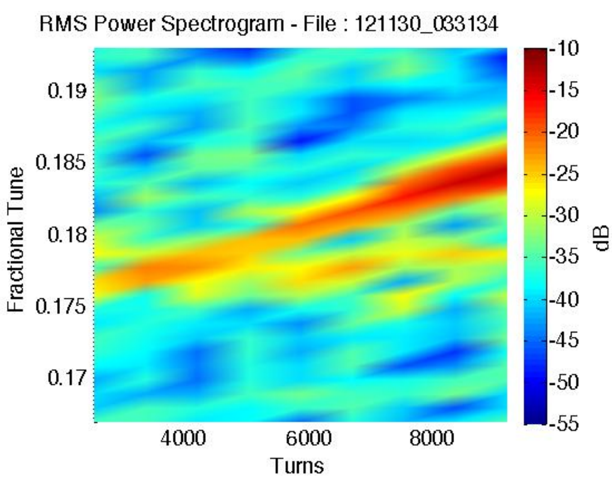

Figure 5: Open-loop vertical beam response chirp spectrogram measurement (no feedback). A 16 sample modulated excitation is driven by the kicker onto the SPS beam for 10,000 turns. The chirp excitation passes through the mode zero tune of 0.177 at turn 4000, and then the mode 1 upper synchrotron sideband at turn 8000 (Q20 lattice). The color code shows the amplitude of the motion for the detected signal.

These excitation studies can be done without feedback, or with feedback in various forms. We can also drive either the nonlinear head-tail numeric simulation, or the reduced model linear simulation with the identical chirp, and study the simulation result using the same spectral techniques.

An example of comparing physical measurements with measurements of a reduced feedback model is shown in Figures 5 and 6. The only real significant difference is the presence of external noise in the physical beam measurement, the reduced model has only numeric noise. But we see excellent agreement with the frequencies excited in the beam in both cases, and excellent respresentation of the mode 0 and mode 1 amplitudes. This suggests that the reduced model can be used with good fidelity to predict the beam responses, and can be used in the design of feedback controllers with confidence that the analytic results faithfully replicate the physical system [13].

Time-domain studies are the second method we use to analyze the performance of the combined beam-feedback system. Figure 7 shows an open-loop (no feedback) time recording of the bunch motion where the beam is unstable in mode 0. The time domain shows the growth of beam motion, and then, as charge is lost from the bunch, stability of the system. Figure 8 shows the spectrogram representation of this transient, we see the prominent excitation of mode 0, plus modes 1,2 from chromatic effects, as well as the clear tune shift as charge is lost at turn 3000. A similar beam condition, but with the feedback system active, is shown in Figures 9 (time domain) and 10 (spectrogram). Under the action of the feedback, the beam motion is controlled and the large charge loss does not occur.

To validate the damping rates achieved, studies such as shown in Figures 11 and 12 the polarity of the feedback is switched during the fill so that the beam is first excited, then damped by the feedback system. Damping rates are shown for two feedback gains. The measurements are taken from the SPS (low chromaticity Q26 lattice and bunch intensity of 1.1×10^{11}). The factor of 4 gain increase and the measurements of the damping rates are used to validate the expected damping rate based on knowledge of the system gain, kicker strength, and other system parameters.

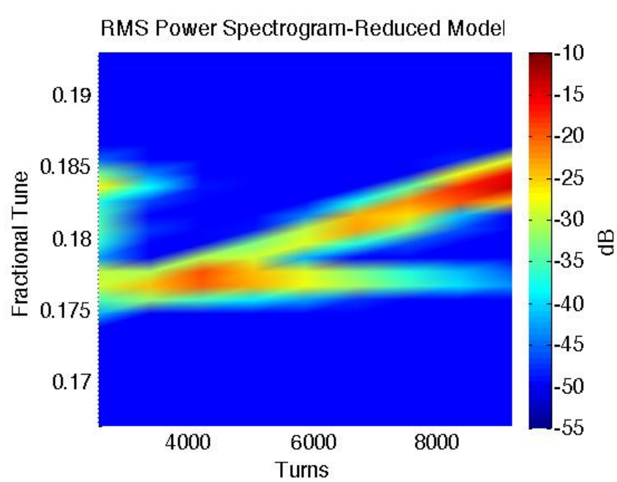

Figure 6: Beam motion spectogram response for the reduced beam model (same excitation as Figure 1). Comparing with the physical measurement we see very close agreement between the oscillation frequencies and the amplitudes of the excited motion.

ISBN 978-3-95450-176-2

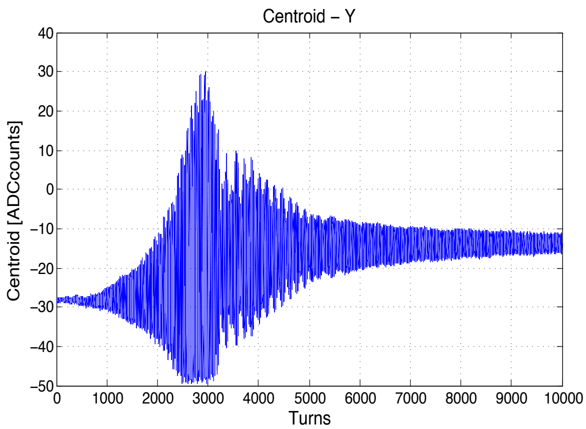

Figure 7: Open-Loop (no feedback) time-domain recording of bunch motion, Q26 lattice, vertical centroid via bunch samples. Unstable bunch motion grows from injection, with charge loss, then stability at roughly turn 3000.

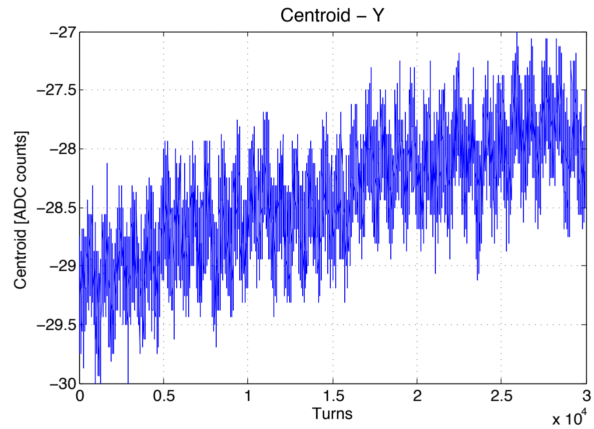

Figure 9: Closed-Loop (feedback on) time-domain recording of bunch motion, bunch samples averaged to show the vertical centroid. The same beam conditions as Figure 7 (mode 0 instability) but motion is controlled by the feedback system. Vertical sensitivity is roughly 14 µm/count.

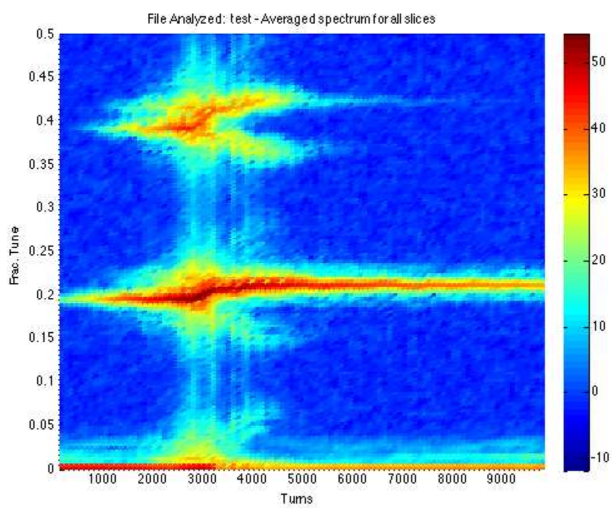

Figure 8: Open-Loop (no feedback) spectrogram of same transient as Figure 7. The beam is unstable in these conditions, $\nu_y = 0.185$ $\nu_s = 0.006$. At turn 2000 chromatic effects show sidebands of the mode zero motion, and with charge loss these end at turn 4500. Significant intensity-dependent tune shifts are seen as charge is lost in the transient.

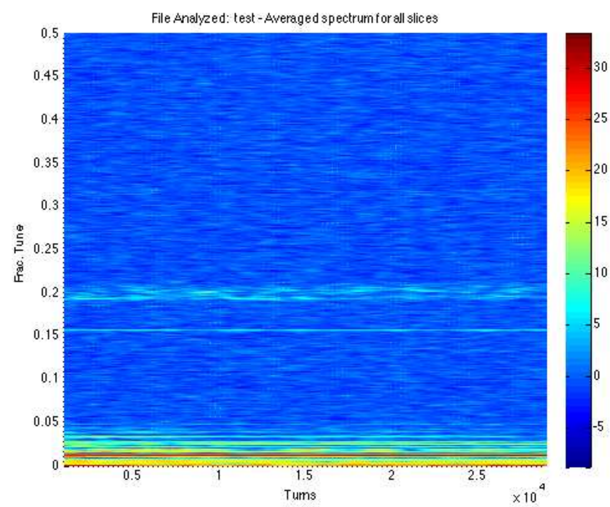

Figure 10: Closed-Loop (feedback on) spectrogram of Figure 7 transient. The beam is unstable in these conditions, Q26 lattice, $\nu_y = 0.185$ $\nu_s = 0.006$. A small amount of motion at mode zero is seen, this driven motion is reduced by the feedback gain. The feedback control keeps the mode 1 and 2 sidebands at the noise floor of the feedback receiver, or roughly 6 microns.

ESTIMATING THE IMPACTS OF SYSTEM NOISE AND LIMITATIONS

This type of steady state controlled beam study does not help quantify the gain margin, or stability margins of the system (this requires multiple studies at fixed gains, or the grow-damp method with time-varying gain). However, the steady state recording does have important information about the noise floor in the feedback detector and the processing filter. We see small motion of the beam at mode zero, which is a combination of driven motion, attenuated by the feedback action, plus the noise in the feedback receiver path. However, we see almost no detected signal at mode 2, which shows that the unstable motion is damped to the effective noise floor. This is seen in the time domain signal (Figure 9) as the fluctuating centroid controlled to less than 1 count of ADC resolution (roughly 6 microns rms vertical motion). These studies are very helpful in understanding the impact of noise within the feedback channel, and choosing an optimal gain for the range of operating conditions.

SUMMARY AND PLANS FOR NEXT MD STUDIES

The immediate tasks at hand are the validation of the kicker and amplifer performance. Another important task is exploration of control methods for several candidate ma-

ISBN 978-3-95450-176-2

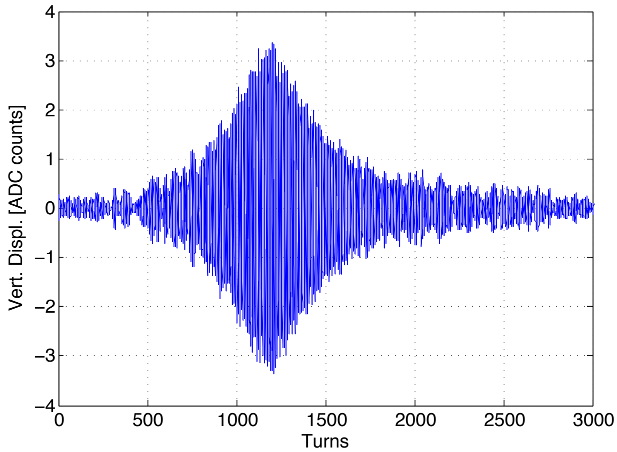

Figure 11: Time domain grow-damp study, SPS beam with excitation of mode 0, followed by damping through the feedback system with gain x4

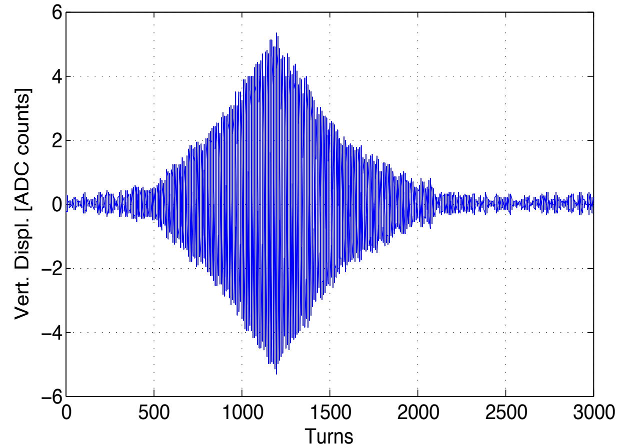

Figure 12: Time domain grow damp study, same beam conditions as Figure 11 but with damping gain x16

chine optics. While we have shown good control with FIR based filters for the Q26 optics, control of the machine with Q20 or other proposed optics needs more study. An early IIR filter design for the Q20 optics has been studied in simulations, we must study and validate the performance in the physical machine, particularly with regard to the dynamic range required in the processing and possible sensitivity to out of band noise signals [15, 16].

The goal of developing a full-function instability control system for the SPS is envisaged to span two generations of hardware. The Slotline wideband kicker design is still in mechanical design and we anticipate this new kicker will be fabricated and installed in 2016 [10], with commissioning in 2017. During this interval before LS2 we want to explore a second hardware platform as shown in Figure 13, based on a higher sampling rate A/D and D/A processing system, with associated higher-capacity FPGA processing functions [9]. This increased processing capacity may be needed to support architectures with multiple pickups, or possible two-channel processing streams which use both the Δ signal (beam motion) and the Σ signal (bunch charge) as part of the computation of a correction signal. These studies and technology development will be used to propose in 2017 the full-function system design for use in the SPS as the HL LHC injector.

ACKNOWLEDGEMENTS

We thank S. Uemura, A. Bullitt, J. Cesaratto, J. Platt, K. Pollock, S. Verdu, G. Kotzian, D. Valuch, M. Wendt, D. Aguilera, E. Montesinos, D. Teytelman, Sei Mizue and the R & K Company LTD for their technical contributions, and the SLAC Controls I&C-EE and ARD, CERN ABP group, the US LHC Accelerator Research Program and the US-Japan Cooperative Program in High Energy Physics for support.

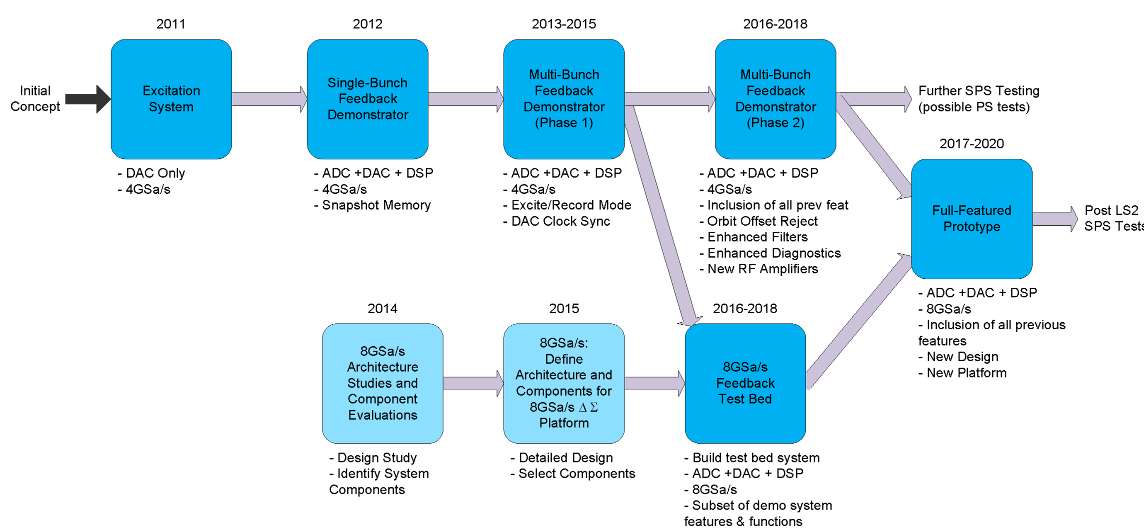

Figure 13: The development plan for the LARP Wideband Feedback effort, showing a possible path of expansion of the Demonstration system, and a parallel technology path with a higher sampling rate. We anticipate that the operational experience from the demonstrator system will guide the features to be implemented in the full-featured system.

ISBN 978-3-95450-176-2

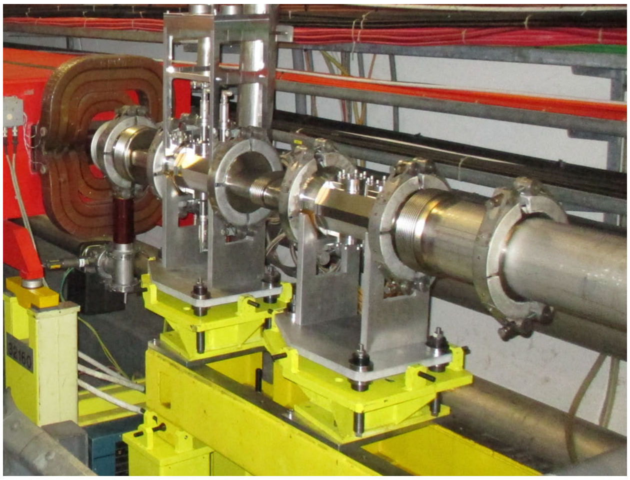

Figure 14: Two stripline vertical kickers on the SPS beamline, developed for the 1 GHz bandwidth wideband intra-bunch feedback.

Figure 15: Two wideband 5 - 1000 MHz amplifiers installed in the SPS tunnel as part of the upgrade to use 1 GHz bandwidth vertical kicker striplines. Two more additonal amplifiers will be installed in 2016 to power the second stripline.

REFERENCES

[1] Y. H. Chin *et al.*, "Performance of Transverse Intra-Bunch Feedback System at J-PARC MR", THO3AB01, Proceedings of HB'14, East-Lansing, MI, USA, 2014.

[2] K. Nakamura *et al.*, "Transverse Intra-bunch Feedback in the J-PARC MR", THOAA03, Proceedings of IPAC'14, Dresden, Germany, 2014.

[3] A. Blas *et al.*, "Beam Tests and Plans for the CERN PS Transverse Damper System", WEPME011, Proceedings of IPAC'13, Shanghai, China, 2013.

[4] E. Shaposhnikova, "Intensity Upgrade Plans for CERN-LHC Injectors", 42nd ICFA Advanced Beam Dynamics Workshop, Nashville, TN, USA, CERN-AB-2008-065, 2008.

[5] H. Bartosik, "Beam Dynamics and Optics Studies for the LHC injectors Upgrade", CERN-THESIS-2013-257 2013

[6] H. Damerau *et al.*, "LHC Injectors Upgrade, Technical Design Report, Vol. I: Protons", CERN-ACC-2014-0337

[7] J. Fox *et al.*, "First Results and Analysis of the Performance of a 4 GS/s Intra-Bunch Vertical Feedback System at the SPS", WEPME060, Proceedings of IPAC'13, Shanghai, China, 2013.

[8] J. Fox *et al.*, "Development of a 4 GS/s Intra-bunch Instability Control System for the SPS – Next Steps", TUPRI085, Proceedings of IPAC'14, Dresden, Germany, 2014.

[9] J. Dusatko *et al.*, "Upgrade and Operation of the Demonstration 4 GS/Sec. Intra-Bunch Instability Control System for the SPS", MOPWI037, Proceedings of IPAC'15, Richmond, VA, USA, 2015.

[10] J. M. Cesaratto *et al.*, "SPS Wideband Transverse Feedback Kicker: Design Report", SLAC-R-1037.

[11] K. Pollock *et al.*, "Signal Equalizer for SPS Ecloud/TMCI Instability Feedback Control System", TUPA32, Proceedings of IBIC'12, Tsukuba, Japan, 2012.

[12] M. Pivi *et al.*, "Simulation Code Implementation to Include Models of a Novel Single-bunch Instability Feedback System and Intra-beam Scattering", WEPPR091, Proceedings of IPAC'12, New Orleans, LA, USA, 2012.

[13] O. Turgut *et al.*, "Identification of Intra-bunch Transverse Dynamics for Feedback Control Purposes at CERN Super Proton Synchrotron", MOPAB24, Proceedings of HB'14, East-Lansing, MI, USA, 2014.

[14] C. Rivetta *et al.*, "Reduced Mathematical Model of Transverse Intra-bunch Dynamics", WEPPP080, Proceedings of IPAC'12, New Orleans, LA, USA, 2012.

[15] C. Rivetta *et al.*, "Feedback System Design Techniques for Control of Intra-bunch Instabilities at the SPS", TUPRI086, Proceedings of IPAC'14, Dresden, Germany, 2014.

[16] C. Rivetta *et al.*, "Modeling and Feedback Design Techniques for Controlling Intra-Bunch Instabilities at CERN SPS Ring", THO3AB04, Proceedings of HB'14, East-Lansing, MI, USA, 2014.

[17] K. Li *et al.*, "Modelling and Studies for a Wideband Feedback System for Mitigation of Transverse Single Bunch Instabilities", WEPME042, Proceedings of IPAC'13, Shanghai, China, 2013.

[18] J. Fox *et al.*, "A 4.2 GS/s Synchronized Vertical Excitation System for SPS Studies – Steps Toward Wideband Feedback", WEPPR090, Proceedings of IPAC'12, New Orleans, LA, USA, 2012.

ISBN 978-3-95450-176-2

FIRST RESULTS OF SOLARIS SYNCHROTRON COMMISSIONING*

A.I. Wawrzyniak#, C.J. Bocchetta, P. Borowiec, P. Bulira, P.P. Goryl, A. Kisiel, M. Kopeć, A. Marendziak, M.J. Stankiewicz, M. Zając, Ł. Żytniak, Solaris NSRC, Krakow, Poland
R. Nietubyć, Solaris NSRC, Krakow and NCNR, Otwock, Poland

Abstract

Solaris is a third generation light source recently constructed at the Jagiellonian University in Krakow. The installation of the 600 MeV S-band linear accelerator with thermionic RF gun and transfer line as well as the 1.5 GeV storage ring is now complete. In November 2014 subsystem tests and conditioning of the Solaris linac were started. A 300 MeV electron beam at the end of the linac was observed for the first time in February 2015 after which the machine was shut down for 2.5 months to complete transfer line and storage ring installation. In May the commissioning of the linac together with the transfer line and storage ring began. The beam was soon observed on the YAG screen monitor, installed at the injection straight in the storage ring. The beam current measured with the fast current transformer in the transfer line was 8 mA over 180 ns, at 360 MeV. The commissioning of the machine is still in progress and preliminary results of Solaris are presented.

INTRODUCTION

Solaris is a third generation light source constructed at the Jagiellonian University (JU) in Krakow, Poland. The project was started in 2010 with a unique cooperation between JU and Lund University/MAX-Lab in Lund, Sweden. Within this framework two twin 1.5 GeV storage rings were designed and built.

The installation of the Solaris accelerators started on May 2014 and was completed one year later. In November 2014 subsystem tests and conditioning of the linac started and by the end of February 2015 a 300 MeV electron beam at the end of the linac was observed for the first time. After this achievement the machine was shut down for 2.5 months to complete the transfer line and storage ring installation. In May 2015 the commissioning of the linac together with the transfer line and storage ring began. In June first turns were observed and then beam was accumulated and stored with the single kicker and RF system. On the 19th of June a 7 µA current was stored at 360 MeV and the first synchrotron light from the dipole was detected at the fluorescent screen in the front end of the PEEM beamline. In August the machine was shut down for a month to allow installation of an aluminium vacuum chamber and an elliptically polarized undulator (EPU) in the 5th straight section of the storage ring.

MACHINE DESCRIPTION

The Solaris injector is designed to efficiently fill the storage ring. Since the RF linac structures and waveguides are not completely conditioned yet, injection into the storage ring takes place at the energy of 490 MeV. After accumulation of the electron beam, the energy will be ramped in the storage ring to 1.5 GeV and RF power is provided by two 100 MHz RF cavities fed by two 60 kW solid state amplifiers.

Injector

The Solaris injector consists of a 0.6 GeV S-band linac with a thermionic RF gun and a vertical dog-leg beam transfer line (TL) [1,2]. The electron source is a thermionic RF gun with a BaO cathode that has been chosen for simplicity of operation. This gun was designed and manufactured at MAX IV Laboratory. The energy of the electron beam exiting the gun is 2.8 MeV and the average current of the bunch train right after the gun is 200 mA. To focus the bunches two solenoid magnets are installed after the gun. The beam is transported through the chopper section and an energy filter in order to compress and clean the beam.

Storage Ring

The Solaris 1.5 GeV storage ring is composed of twelve double bend achromat (DBA) cells [3-5]. Most of the magnets in the DBA are multifunction:

- Bending magnets with defocusing gradient and pole face strips;
- Focusing quadrupoles with focusing sextupole content;
- Defocusing sextupoles with trim coils for skew quads;
- Correction sextupoles magnets with additional coils of steering magnets.

All the magnets within one DBA cell are shaped in one Armco block. This innovative approach allows the mutual alignment of magnets within the DBA cell to be within a 25 µm tolerance range and makes the cell short - 4.2 m. This implementation however comes at a cost of challenging manufacturing of magnets and vacuum chambers and their assembly.

*Work supported by the European Regional Development Fund within the frame of the Innovative Economy Operational Program: POIG.02.01.00-12-213/09
#adriana.wawrzyniak@uj.edu.pl

Table 1: The storage ring design parameters

Energy [GeV]	1.5
Current [mA]	500
Circumference [m]	96
RF frequency [MHz]	99.931
Harmonic number	32
Radiation losses [keV]	114.1
Betatron tunes (H/V)	11.22/3.15
Nat. chromaticities (H /V)	-22.98/-17.14
Corrected chromaticities (H/V)	+2/+2 or +1/+1
Momentum compaction factor	$3.055 \cdot 10^{-3}$
Damping partition numer Jx	1.46348

There are twelve 3.5 m long straight sections in the storage ring. Two of them are completely occupied with diagnostic instruments, a vertical pinger, the injection septum magnet (1st straight), two 100MHz RF cavities and two Landau cavities (12th straight). Additionally, in the 3rd straight section the dipole injection kicker magnet is installed. All the other straight sections are fully dedicated for insertion devices (IDs).

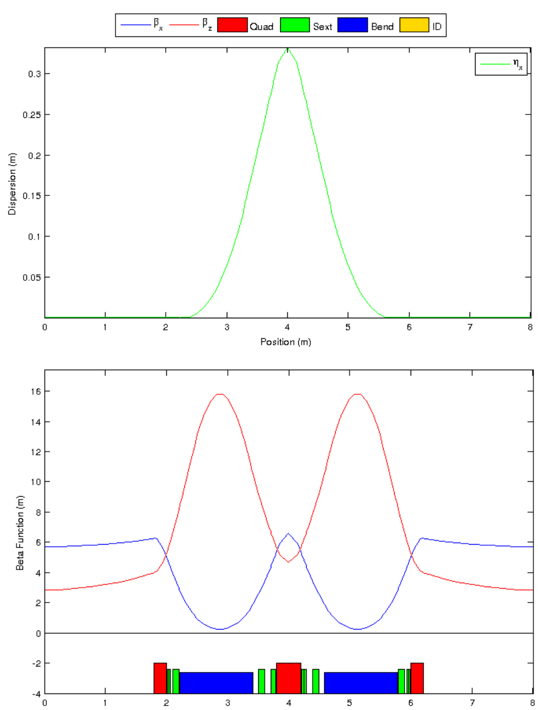

Figure 1: The optical functions for single DBA cell.

The optical functions for the achromat are shown in Fig. 1. As one can see, the beta functions and dispersion have low values, reducing the need for large vacuum chamber apertures. The cross section of the vacuum chambers has inner dimensions of 40/20 mm (horizontal/vertical), however at the center of the double-bend achromat the aperture is increased to 56/28mm.

Beam injection into the storage ring is done by a single pulsed dipole magnet installed in the 3rd straight section. The detailed studies of the injection to the 1.5 GeV storage ring at 0.55 GeV and ramping are presented in [6,7].

INSTRUMENTATION

In the linac injector seven current transformers (CTs) from the company FCC are installed in different places for beam current measurements. The bandwidth of the CT is 100 MHz. The data is acquired by Rohde & Schwarz RTO1004 oscilloscopes. For the beam position measurements eight quarter wave directional stripline beam position monitors (BPMs) with Libera Single Pass electronics from Instrumentation Technologies are used. Additionally, YAG screens are installed in a few places along the linac and the transfer line and injection section. The YAG crystal is inserted in the beam path by either a pneumatic actuator or by a stepper motor. The YAG screens are equipped with CCD Basler cameras using Tokina and Computar 100mm and 50 mm focal lenses.

In the storage ring the in flange "New Parametric Current Transformer" (NPCT) probe from Bergoz is connected to a Keithley 3706A DMM (7.5 digits) readout device. One method for the tune measurement uses a stripline kicker followed by spectrum analysis of button pick-ups. The second method uses the vertical (pinger) and horizontal (kicker) pulsed magnets to excite the beam and a fast Fourier transform (FFT) of BPM signals. In the injection section straight vertical and horizontal scrapers are installed. The vertical scraper will give information on the average pressure in the machine and as a result - on elastic and inelastic and Touschek lifetime. Furthermore, with knowledge of the vertical beta function, the vertical acceptance of the ring can be determined. The horizontal scraper will reveal the dynamic energy acceptance and/or the RF energy acceptance.

The Solaris storage ring uses 36 button pickups in a diagonal architecture for the beam position monitors. These BPMs are connected to commercial electronics from Instrumentation Technologies – Libera Brilliance+. The electronics, in addition to 'turn-by-turn' mode, can operate also in 'first turn' mode to help with commissioning. A slow orbit correction is possible at 10 Hz. Additionally, the Libera electronics is equipped with GDX modules for fast orbit feedback at 1kHz (input). However this option will be used in the future.

SOLARIS COMMISSIONING

The beam current in the pre-injector was measured with current transformers connected to oscilloscopes. The average current of the beam right after the gun body is about 200mA over 1.1 µs. When the beam is transported through the 500 MHz chopper and the limiting aperture about three-quarters of the current is lost. After passing

ISBN 978-3-95450-176-2

the energy filter where the beam is compressed and cleaned of low energy electrons, the current of the beam entering the linac is 12mA over 200 ns. Figure 2 shows the current data from the oscilloscope.

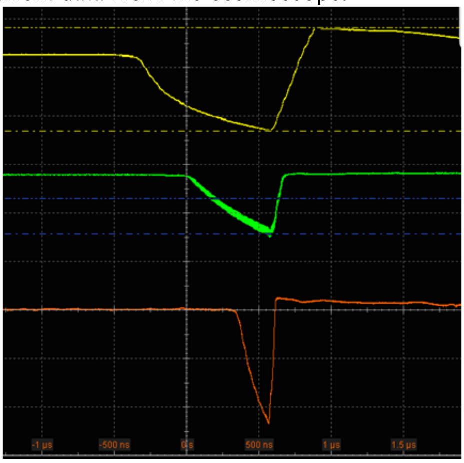

Figure 2: The beam current measured at 3 different locations in the pre-injector. Yellow: current of the electron beam after the gun body (200 mA), green: before energy filter (EF) (50mA) whereas the orange: after energy filter before entering the first linac section (12mA).

In the linac the beam is accelerated up to 490 MeV. The energy was measured in the transfer line using the 17° dipole magnet as a spectrometer. The beam current was measured at the exit of the transfer line and this value was used to estimate the injection efficiency. The average charge of the beam is 1.4 nC, which is injected into the storage ring at a 1 Hz repetition rate. The current is measured with the NPCT in the storage ring. An example plot of 13.4 mA current accumulation is presented in the Fig. 3.

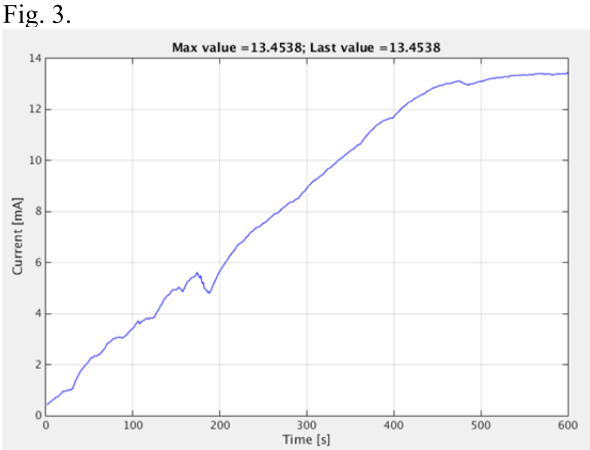

Figure 3: Accumulated current in the storage ring.

The transport of the charge from gun to the storage ring is less than 1% and its improvement is underway. The main location of losses is at the septum magnet.

It has to be noted that so far injection to the storage ring as well as accumulation takes place without any correction of the closed orbit. The alignment of the magnet, which act as their own girders, is very good and the rms values of the closed orbit without orbit correction are 2.28mm horizontally and 0.7 mm vertically. The closed orbit is shown in the Fig. 4.

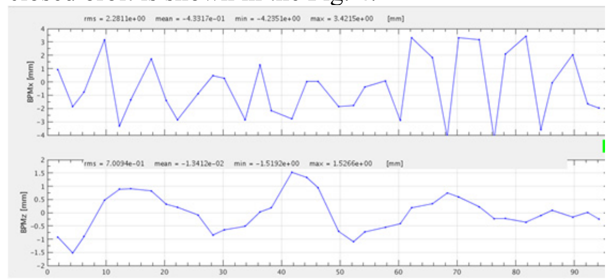

Figure 4: the closed orbit of stored beam without any correction.

The tune measurements were done by exciting the beam with the vertical pinger and the horizontal kicker magnet and a button BPM signal was processed using Libera Brilliance + turn-by-turn data. The fractional tune was plotted using MATLAB software and is presented in the Fig. 5. The tune of the machine is 10.78 and 3.601, which is different from the design values presented in Table 1. However the optics was found to be more stable and the injection more efficient. Due the some temporary problems with the pole face strips, that are used to change the gradient, it was not possible to operate at the design optics.

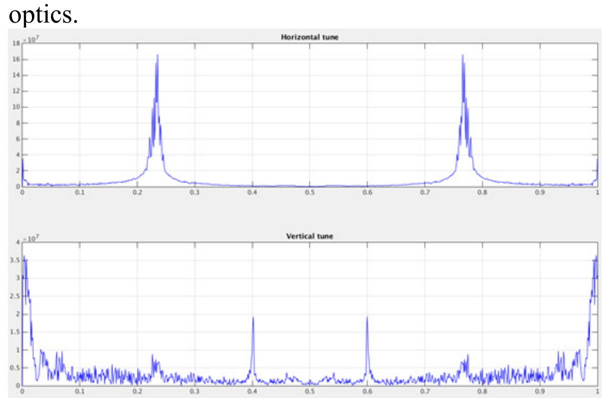

Figure 5: The fractional tune measurement.

Ramping of the stored beam in the storage ring was tested during the last few days before shut-down. The beam was ramped up to 743MeV before the total stored current was lost due to a fault on power supply controllers. Further tests of the ramping software to 1.5 GeV will be conducted after the summer shutdown and no issues are expected.

The vacuum system in the storage ring uses 61 ion getter pumps and 12 titanium sublimation pumps from Gamma Vacuum and also 24 non-evaporable getter strips from SAES. The mean pressure without beam depends on maintenance work and is usually around $3.5 \cdot 10^{-10}$ mbar. The pressure level in the storage ring without a beam is presented in the Fig.6. During accumulation of the current in the storage ring up to the level of 13.4 mA (Fig. 3) the mean pressure in the storage ring was $5.1 \cdot 10^{-9}$ mbar (Fig. 7).

ISBN 978-3-95450-176-2

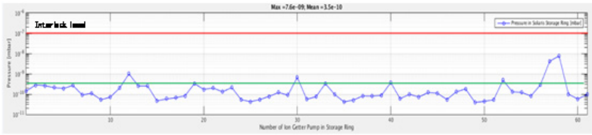

Figure 6: Pressure level inside the storage ring without the beam. Green line represents mean level of the pressure and red line interlock level.

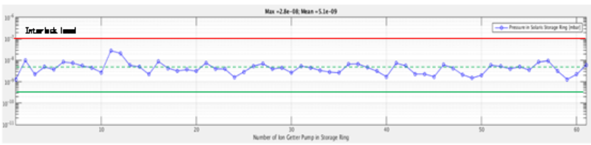

Figure 7: Pressure level inside the storage ring with the beam. Solid green line represents mean level of the pressure without the beam, dashed green line with the beam and red line represents interlock level.

So far the vacuum interlock level in the storage ring has never been triggered.

The total beam lifetime at 13.4 mA is around 5 min and increases with decreasing the current reaching 32 min at 1.5 mA. At this stage the lifetime is dominated by the gas scattering.

SUMMARY

Commissioning of the Solaris light source is on-going. The linac and storage ring RF systems have not yet reached their full performance and are still being conditioned. Therefore, injection to the storage ring is done at 490 MeV with a repetition rate of 2 Hz maximum. The injection efficiency is low and is being optimised. The ramping to full energy is under going tests and the linear optics at intermediate energies between 490 MeV and 1.5 GeV has to be corrected and proper snapshots need to be prepared in order to ramp the beam without losses. For the present the storage ring does not operate at its nominal optics but is expected to do so as commissioning progresses with full characterisation of the optics and closed orbit correction.

ACKNOWLEDGMENTS

The authors would like to thank the MAXIV team for help during the design, installation and the commissioning phase.

Special thanks to Guenther Rehm from Diamond for the support and discussions during first days of storage ring commissioning.

REFERENCES

[1] A.I. Wawrzyniak et al, “Injector layout and beam injection into Solaris”, IPAC’11, San Sebastian, Sept. 2011, THPC123, p. 3173; http://www.JACoW.org

[2] M.R. Bartosik et al.,“Solaris—National Synchrotron Radiation Centre, project progress, May2012”, to be published in Radiat. Phys. Chem. (2013)

[3] MAXIV Detailed Design Report, https://www.maxlab.lu.se/node/113

[4] S.C. Leemann, “Updates to the MAX IV 1.5 GeV Storage Ring Lattice,” MAX-lab Internal Note 20120313, April, 2012

[5] S.C. Leemann, ”Recent Progress on the MAX IV 1.5 GeV Storage Ring Lattice and Optics”, IPAC’12, New Orleans, May 2012, TUPPP024, p. 1662 (2012); http://www.JACoW.org

[6] A. I. Wawrzyniak, R. Nietubyc et al.,“ Ramping of the Solaris Storage Ring Achromats”, IPAC’13, Shanghai, MOPEA047, within these proceedings, (2013);

[7] S.C. Leemann, “Injection with a single dipole kicker into the MAX IV storage rings”, Nuclear Instruments and Methods in Physics Research A 693 (2012) 117–129

ISBN 978-3-95450-176-2

HIGH FREQUENCY ELECTRO-OPTIC BEAM POSITION MONITORS FOR INTRA-BUNCH DIAGNOSTICS AT THE LHC

S. M. Gibson*, A. Arteche, G. E. Boorman, A. Bosco, Royal Holloway, University of London, UK
P. Y. Darmedru, T. Lefèvre, T. Levens, CERN, Geneva, Switzerland

Abstract

At the HL-LHC, proton bunches will be rotated by crab-cavities close to the interaction regions to maximize the luminosity. A method to rapidly monitor the transverse position of particles within each 1 ns bunch is required. A novel, compact beam diagnostic to measure the bunch rotation is under development, based on electro-optic crystals, which have sufficient time resolution (< 50ps) to monitor intra-bunch perturbations. The electro-optic beam position monitor uses two pairs of crystals, mounted on opposite sides of the beam pipe, whose birefringence is modified by the electric field of the passing charged particle beam. The change of birefringence depends on the electric field which itself depends on the beam position, and is measured using polarized laser beams. The electro-optic response of the crystal to the passing bunch has been simulated for HL-LHC bunch scenarios. An electro-optical test stand including a high voltage modulator has been developed to characterize $LiTaO_3$ and $LiNiO_3$ crystals. Tests to validate the different optical configurations will be reviewed. The opto-mechanical design of an electro-optic prototype that will be installed in the CERN SPS will be presented.

MOTIVATION

HL-LHC Crab-Cavity Bunch Rotation

An ambitious High Luminosity upgrade of the Large Hadron Collider will increase the luminosity by a factor of ten. The proton bunches will be rotated by crab-cavities placed before and after the interaction regions, so that the bunches collide head-on to reduce the overlap area and maximize the luminosity. Optimising the performance of the crab-cavities at the HL-LHC requires new instrumentation that can perform intra-bunch measurements of the transverse position of particles within a 1 ns bunch. Conventional electrostatic stripline BPMs are fundamentally limited to a few GHz bandwidth and take up valuable space close to the interaction region. A novel, compact beam diagnostic to measure the bunch rotation is under development, based on electro-optic crystals, which have sufficient time resolution (<50 ps) to monitor intra-bunch perturbations.

Head-tail Instability Monitors

A high-frequency monitor is also necessary to detect intra-bunch instabilities on a turn by turn basis. At the SPS and LHC, *head-tail* (HT) monitors are the main instruments to visualise and study beam instabilities as they occur [1]. The present HT monitors are based on stripline beam position monitors and fast sampling oscilloscopes [2]. Recent measurements reveal low order modes as shown in Figure 1. However the HT monitors only offer a bandwidth up to few GHz limited by the pick-up, cables and acquisition system. Novel pick-ups based on electro-optical crystals and laser pulses [3, 4] have already demonstrated response times in the picosecond range [5], making this technique a promising candidate to achieve higher resolutions to improve the HT monitors capacity to solve bunch shapes and instabilities.

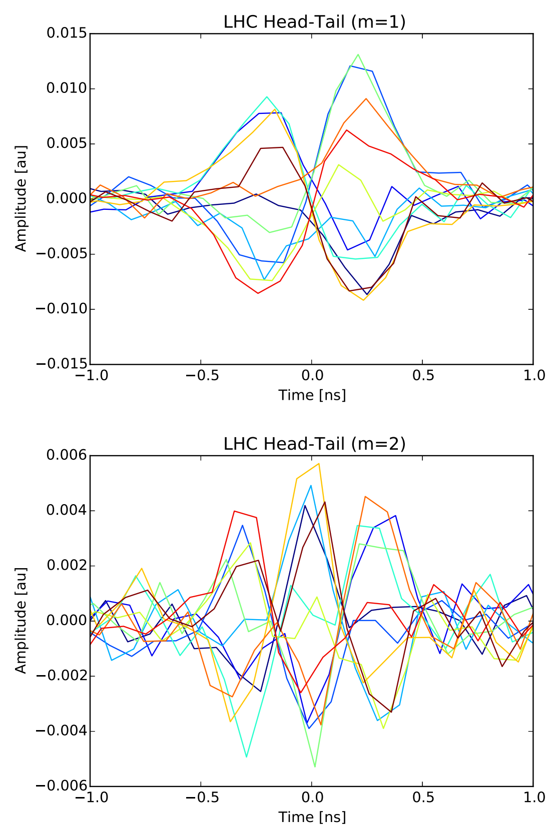

Figure 1: Mode 1 and 2 bunch instabilities recorded with a stripline BPM HT monitor in August 2015 at the LHC.

EO-BPM Project Aims

The above considerations have stimulated a collaboration between the CERN Beam Instrumentation group and Royal Holloway, University of London (RHUL) to develop novel beam diagnostics based on electro-optical crystals, which have sufficient time resolution to monitor intra-bunch perturbations. The aim is to develop a prototype electro-optic Beam Position Monitor (EO-BPM) that will be initially tested to monitor intra-bunch instabilities in the CERN SPS. Success would validate their use as a future diagnostic tool for the HL-LHC to monitor crab rotation of the bunches.

* stephen.gibson@rhul.ac.uk

ISBN 978-3-95450-176-2

EO-BPM CONCEPT AND DESIGN

Electro-Optic Beam Position Monitor Concept

The concept of using electro-optic crystals to monitor beam position has been previously proposed [3–7]. The general technique is to exploit the Pockels electro-optic effect, which has a linear dependence on the applied electric field. An electro-optic beam position monitor (EO-BPM) is essentially a conventional button-BPM, in which the pick-ups have been replaced with electro-optic crystals. Each axis of the EO-BPM uses a pair of crystals, mounted on opposite sides of the beam pipe, whose birefringence is modified by the electric field of the passing charged particle bunch. The change of birefringence depends on the electric field which itself depends on the bunch position, and can be measured using polarized laser beams.

Design and Optical Configuration

In designing the EO-BPM for the SPS/LHC, several configurations of the crystal type, cut, the light propagation direction, polarizer/analyser orientation and electric field were considered. The challenge is to tune these parameters to ensure the best time and positional resolution is achieved for the LHC bunch. Two configurations were selected for experimental investigation as shown in Figure 2. Both options are fibre-coupled so that the laser and detection system can be housed in a remote counting room, 160 m from the accelerator tunnel.

(a) Polarizer-analyser per pick-up Light from a laser in the counting room is conveyed via optical fibre to a vacuum feedthrough in the BPM flange, where the divergent beam is collimated by a GRIN lens. The light passes through a polarizer, reflects into an electro-optic crystal and emerges through an analyser, before being coupled back into fibre and the signal is recorded by a remote photodetector. As the particle beam passes, the electric field across the crystal induces a rotation in the polarization, which creates an intensity change at the detector. The light travels parallel to the particle beam to aid phase matching with the electric field of the relativistic bunch. The pick-ups are independently readout and the difference and sum signals are determined by electronic signal processing, like a conventional BPM. This layout has the advantage of a simple robust design, however, the full signal due to the charge of the passing bunch must be covered by operational range of the photodetector.

(b) Interferometric design An alternative arrangement proposed here is based on a fibre-coupled interferometer that uses electro-optic phase modulation to monitor the bunch position. Coherent light is exploited to optically suppress the common mode signal, such that the detector directly measures the difference signal between the two pick-ups. The potential advantage of this layout is to improve the positional resolution by using the full dynamic range of the detector to record the optically generated difference signal. A free-space interferometric design was originally considered in

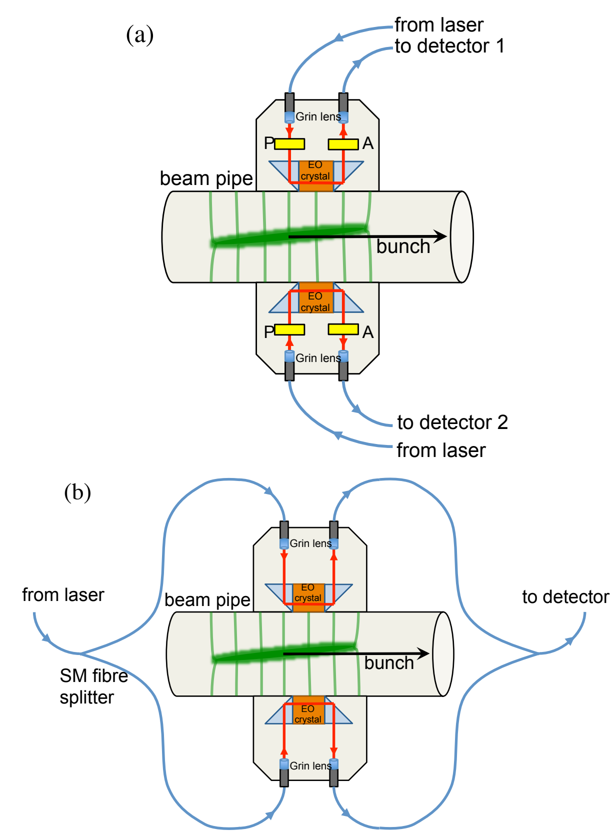

Figure 2: Two optical configurations are investigated for a fibre-coupled electro-optic beam position monitor: (a) a polarizer-analyser per pick-up; (b) a phase-modulated interferometric design.

earlier studies, but was ruled out due to the thermal stability and alignment requirements across the mechanical BPM body [8]. However, the stability tolerance may be improved by using short and equal lengths of optical fibre between the fibre-splitters and BPM, with similar routing, such that common thermal fluctuations cancel in the difference signal. The fibres should also be of equal length, so that the arrival time of the light at both pick-up is synchronized to interact with the same time-slice of the charged particle field.

Detection and Acquisition Scheme

The signals generated by the two configurations have been simulated, as detailed in the next section. In both cases, Metal-Semiconductor-Metal (MSM) photodetectors are envisaged, owing to their <30 ps rise time and the polarity independent biasing facility [8]. One option is to directly acquire the MSM signal with a high speed digitizer. At the required analogue bandwidth of 6-12 GHz, however, the effective number of bits is at best ∼6, which limits the transverse positional resolution, especially in the P-A configuration. A related development is the multiband-instability-monitor (MIM) [9] that uses frequency domain analogue pre-processing to achieve higher resolutions than direct sampling. The MIM would benefit from the additional frequency range that the eo-pick-up has over traditional striplines [10].

ISBN 978-3-95450-176-2

SIMULATION OF EO-BPM SIGNALS FOR LHC BUNCH PARAMETERS

A computer model has been developed to study the optical response of the electro-optic pick-up to a transversely perturbed relativistic bunch. The input parameters to the simulations are summarised in Table 1 and the simulations involve three main steps:

1. The time profile of the transverse electric field generated at the radial position of each eo-crystal is calculated for the relativistic perturbed bunch.

2. The electro-optic response to the electric field is calculated using the crystal parameters and wavelength, for each optical configuration.

3. A simple difference signal is calculated for the polarizer-analyser setup, or the interference signal is calculated.

A transverse offset is first applied along the particle bunch according to the shape of the instability mode as in Figure 3a. The contributions from slices of the relativistic Gaussian charge distribution are then summed to calcualte the electric field at each pick-up, as in Figures 3b and 3c. The difference signals generated in a model of the crystal response for the polariser-analyzer and interferometric configurations are plotted in Figures 3d and 3e respectively.

Both optical configurations are sensitive to the instability modes. In the P-A setup, however, the photodetector must capture the full Gaussian signal of the passing bunch charge distribution, whereas the interferometer is directly sensitive to the difference signal. For the maximum crystal length of 20 mm taken in these simulations, this results in some non-linearity at large amplitudes (see e.g. mode-0) in the P-A setup, because the polarization change exceeds the linear region of the sinusoidal intensity variation. This non-linearity can be reduced by selecting a shorter crystal, albeit with a corresponding reduction in the sensitivity. In contrast, the interferometer signal exhibits no non-linearity at these amplitudes, because it is sensitive to the phase difference between the two crystals.

The P-A setup measures both pick-ups independently, so it is possible to compute a difference over sum normalization. The interferometer setup can be improved by adding a fur-

Table 1: Input Parameters to the EO-BPM Simulation

LHC bunch intensity	1.15×10^{11}	protons per bunch
Bunch length 4σ	1.0	ns
SPS beam energy	450	GeV
Instability modes	0, 1, 2 & 6	
Instability amplitude	0 to 2.5	mm
Pick-up radius	40	mm
Laser wavelength	632.8	nm
Crystal type	$LiNiO_3$	[also $LiTaO_3$]
Crystal length	1, 5, 10, **20**	mm

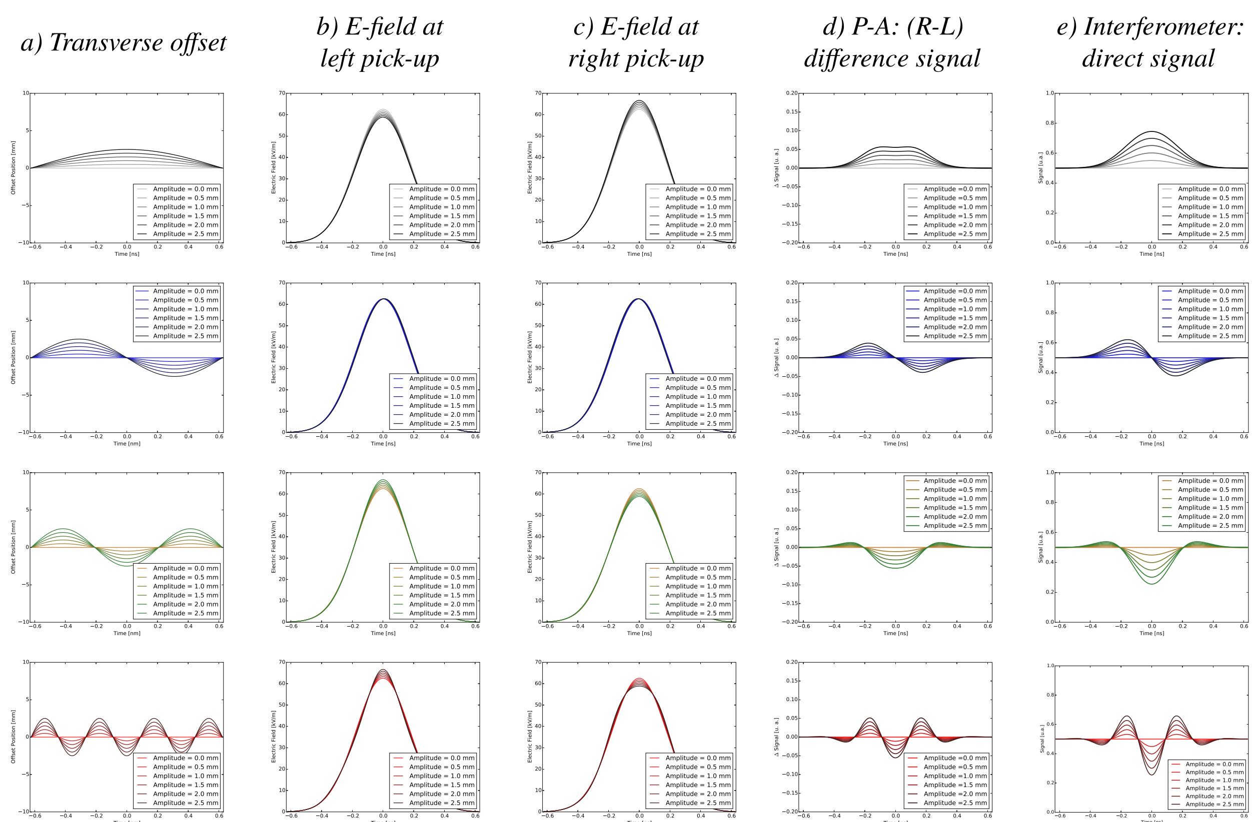

Figure 3: Simulation of EO-BPM response to bunch instability modes 0, 1, 2, and 6.

ISBN 978-3-95450-176-2

ther fibre-splitter after each crystal, before the combiner, to enable the phase modulation of each crystal to be measured independently, as well as the optically generated difference signal. Both configurations will be evaluated experimentally as described in the next sections.

CRYSTAL CHARACTERISATION EXPERIMENTAL RESULTS

Electro-Optic Theory and Crystal Choice

The eo-crystals investigated are $LiNbO_3$ and $LiTaO_3$, which are uniaxial crystals with excellent electro-optic coefficients and are related to Al_2O_3, known to be fairly radiation tolerant[1]. In a z-cut $LiNbO_3$ [or $LiTaO_3$] crystal, with light propagating in the x-direction the principle refractive indices under an applied electric field along z are

$$n'_y = n_o - \frac{1}{2} n_o^3 r_{13} E_{az} \tag{1}$$

$$n'_z = n_e - \frac{1}{2} n_e^3 r_{33} E_{az}, \tag{2}$$

where the ordinary and extraordinary refractive indices are $n_o = 2.29[2.19]$ and $n_e = 2.21[2.18]$ (at 633 nm), and the dieletric tensor elements are $r_{33} = 30.9[30.5]$ pm/V and $r_{13} = 9.6[8.4]$ pm/V. The eo-crystal response is characterised by the half-wave voltage,

$$V_\pi = \frac{\lambda}{r_{33} n_e^3 - r_{13} n_0^3} \frac{d}{L}, \tag{3}$$

where the wavelength λ, crystal height d and length L, are free parameters to be selected. $LiTaO_3$ is less prevalent than $LiNiO_3$, but has a slightly better V_π for equivalent crystal dimensions and is more robust, with a higher density, melting point and damage threshold.

Experimental Validation

Samples of $LiNbO_3$ and $LiTaO_3$ crystals have been characterized with a high voltage (HV) modulator and optical test stand at Royal Holloway, as shown in Figure 4. The setup allows linearly polarized light to be directed onto the crystal face, while HV is applied across the crystal, and the throughput light intensity is recorded after an analyser. The polarizer and analyser have their orientations controlled by automated rotation stages, enabling the polarization state at any voltage to be assessed.

Tests were initially conducted at $\lambda = 532$ nm, to reproduce earlier tests at CERN [7], in which the wavelength was selected from considerations of the sensitivity and dispersion. An intensity modulation with HV was achievable, however, it was found that the photorefractive effect dominates at this wavelength, even when a MgO doped $LiNiO_3$ was used. To avoid this region, tests were performed with a HeNe laser, $\lambda = 632.8$ nm, at which the refractive index still implies a good sensitivity. An example HV scan at 632.8 nm is shown in Figure 5 and the fitted $V_\pi = 1410 \pm 19$ V is in good agreement with the predicted value of $V_\pi = 1398.2$ V.

[1] the radiation tolerance of the selected crystal will be assessed.

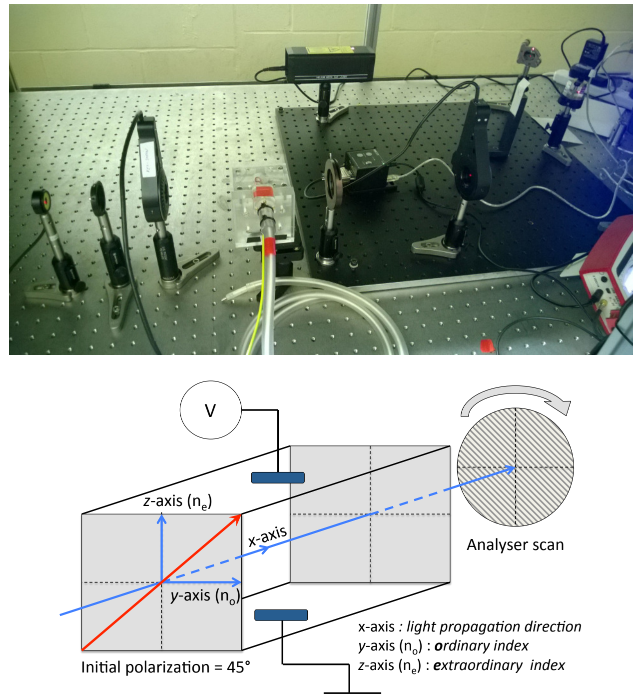

Figure 4: Crystal characterisation test stand and configuration of the e-o crystal. Linearly polarised light incident at 45° on the crystal is rotated when high-voltage is applied.

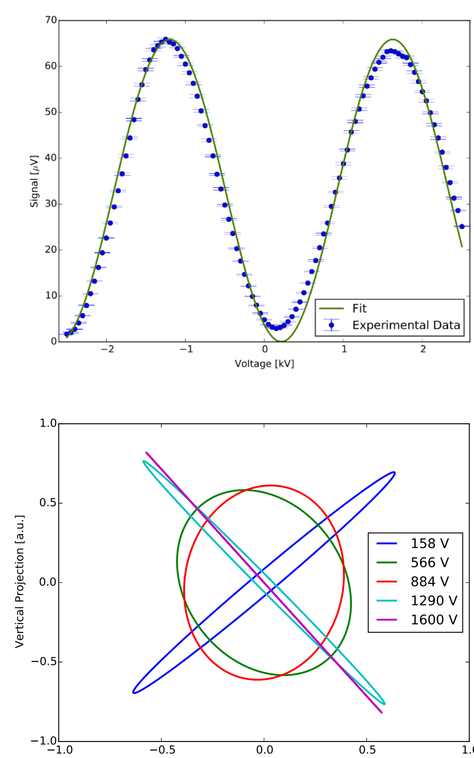

Figure 5: HV scan of a z=5 mm, x=10 mm, MgO:$LiNiO_3$ crystal. The polarization state at key voltages is analysed.

ISBN 978-3-95450-176-2

A PROTOTYPE EO-BPM FOR CERN SPS

A beam test of a prototype EO-BPM is planned in the CERN SPS, with the dual aim of validating the electro-optic pick-up with the LHC bunch parameters and monitoring SPS bunch instabilities. Space has been reserved for the EO-BPM prototype at SPS point 4, close to the existing head-tail monitor stripline BPM, so it can be used for cross-checks. The opto-mechanical layout of the EO-BPM has been designed [11] and is shown in Figure 6.

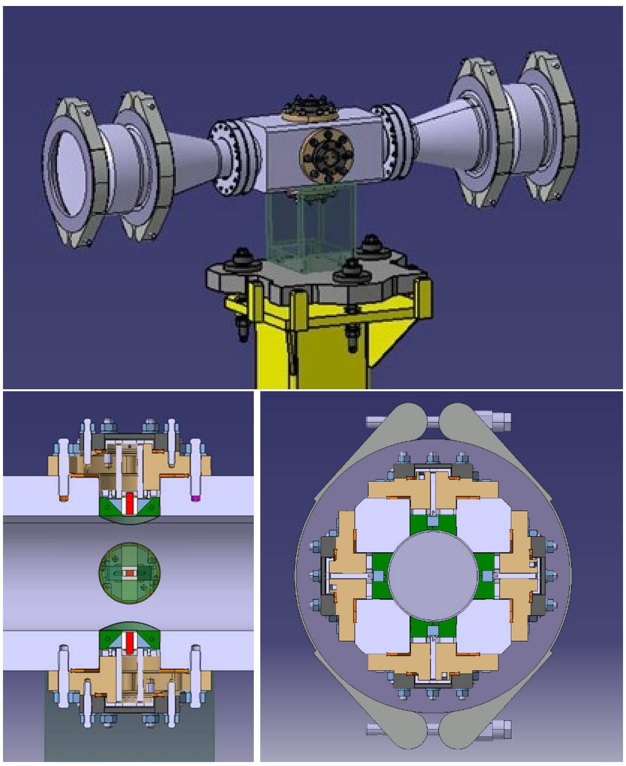

Figure 6: Preliminary opto-mechanical design of a prototype EO-BPM, planned for installation the SPS at CERN.

The design is based on a CERN standard BPM body that is compatible with the LHC aperture. A taper brings the SPS aperture to the 80 mm diameter, which ensures the pick-ups are tested at the appropriate radius. The two configuration concepts described earlier will be tested in orthogonal planes.

In these first tests it is planned that the opposing pair of pick-ups in the horizontal plane will be illuminated and read-out via an anti-reflection coated viewport to offer maximum flexibility for possible reconfiguration. In the design, incoming linearly polarized light is reflected from a 45° prism towards the eo-crystal, highlighted in red, and the outgoing beam is then reflected by a second prism. In the vertical plane, a pair of fibre-coupled pick-ups is envisaged, with the aim of checking the compact fibre optic configuration and evaluating the sensitivity of the interferometric method. It is expected that the BPM body will be installed in the Christmas shutdown and SPS beam tests with the EO-BPM prototype will commence in 2016.

CONCLUSIONS AND FUTURE

An Electro-Optic Beam Position Monitor is under development, aimed at high-frequency bunch instability monitoring at the CERN SPS and intra-bunch diagnostics at the HL-LHC. The electro-optical response has been simulated and indicates good sensitivity to high order bunch instability modes for electro-optic crystal lengths of 10 to 20 mm. The e-o crystal response has been validated in laser laboratory bench tests, using the polarizer-analyser configuration. An interferometric setup has been proposed with the potential for enhanced sensitivity. The opto-mechanical layout of an EO-BPM has been designed, in preparation for installation of a prototype in the CERN SPS in early 2016.

ACKNOWLEDGEMENTS

We thank Ralph Steinhagen for useful discussions and the initial studies by his student, James Doherty, at CERN. We thank Steve Jamison and David Walsh for their expert guidance on electro-optics and Rhodri Jones, Laurie Nevay, Alexey Lyapin and Stewart Boogert for helpful discussions. Work supported by CERN, STFC JAI & Royal Holloway.

REFERENCES

[1] B. Salvant et al, “Transverse Mode-coupling Instability in the CERN SPS/ Comparing HEADTAIL simulations with Beam Measurement”, Proceedings of Hadron Beam conference, Nashville, Tennessee, USA, 2008, 45.

[2] R. Jones et al, “Recent advances in the Measurement of Chromaticity via Head-tail Phase shift analysis”, Proceedings of DIPAC, Mainz, Germany, 2003, 107.

[3] M.A. Brubaker et al, “Electro-Optic Beam Position and Pulsed Power Monitors for the Second Axis of DARHT”, Proceedings of PAC, Chicago, USA 2001, 534.

[4] Adam Joseph Iverson, “Electro-optic Pockels cell voltage sensors for accelerator diagnostics”, Masters thesis in Electrical Engineering, Montana State University, 2004.

[5] Y. Okayasu et al, “The First Electron Bunch Measurement by Means of Organic EO Crystals”, Proceedings of IBIC, Tsukuba, Japan, 2012.

[6] D.H. Dowell et al., “An Electro-Optic Beam Position Monitor with Sub-Picosecond Resolution”, Workshop on Laser Issues for Electron RF Photoinjectors, SLAC, October, 2002.

[7] J. Doherty and R.J. Steinhagen, “The Electro-Optic Beam Position Monitor”, CERN student report, October 2013.

[8] R. J. Steinhagen et al, “Application of metal-semiconductor-metal (MSM) photodetectors for transverse and longitudinal intra-bunch beam diagnostics”, MOP20, Proceedings of IBIC2013, Oxford, UK.

[9] R. J. Steinhagen et al, “A multiband-instability-monitor for high-frequency intra-bunch beam diagnostics”, MOP20, Proceedings of IBIC2013, Oxford, UK.

[10] R. Jones, “Challenges in beam instrumentation and diagnostics for large ring colliders - based on the LHC experience” SUT1B2, Proceedings of HF2014, Beijing, China.

[11] P.-Y. Darmedru “Conception mécanique d’un instrument de mesure de position d’un faisceau de particules”, CERN EN report, Groupe 2A04, 2015.

ISBN 978-3-95450-176-2

BEAM PROFILE MONITOR AT THE 1 MW SPALLATION NEUTRON SOURCE

Shin-ichiro Meigo*, Motoki Ooi, Kiyomi Ikezaki, Tomoyuki Kawasaki, Hidetaka Kinoshita,
Atsushi Akutsu, Masaaki Nishikawa and Shinpei Fukuta, J-PARC center, JAEA, 319-1195, Japan
Hiroshi Fujimori, J-PARC center, KEK, 305-0801, Japan

Abstract

Since 2008, the Japanese Spallation Neutron Source (JSNS) of J-PARC has produced a high-power proton beam of 300 kW. In order to operate with high intensity beam such as 1 MW, a reliable profile monitor system is required. Beam profile monitor system was developed by using SiC sensor wires. Since pitting erosion was found at the vessel of the spallation neutron target at other facility of SNS, the beam current density at the target should be kept as low as possible. In order to decrease the beam density, a beam flattering system based on a non-linear optics with octupole magnets was developed. It was found that the beam profile at the target obtained with the Multi Wire Profile Monitor (MWPM) showed flat distribution and showed good agreement with the design calculation. Furthermore, the present status of the development of the profile monitor is also described.

INTRODUCTION

In the Japan Proton Accelerator Research Complex (J-PARC) [1], a MW-class pulsed neutron source, the Japan Spallation Neutron Source (JSNS) [2], and the Muon Science facility (MUSE) [3] will be installed in the Materials and Life Science Experimental Facility (MLF) shown in Fig. 1. Since 2008, this source has produced a high-power proton beam of 300 kW. In 2015, we successfully ramped up beam power to 500 kW and delivered the 1-MW beam to the targets. To produce a neutron source, a 3 GeV proton beam collides with a mercury target, and to produce a muon source, the 3 GeV proton beam collides with a 2-cm-thick carbon graphite target. To efficiently use the proton beam for particle production, both targets are aligned in a cascade scheme, with the graphite target placed 33 m upstream of the neutron target. For both sources, the 3 GeV proton beam is delivered from a rapid cycling synchrotron (RCS) to the targets by the 3NBT (3 GeV RCS to Neutron facility Beam Transport) [4–6]. Before injection into the RCS, the proton beam is accelerated up to 0.4 GeV by a LINAC. The beam is accumulated in two short bunches and accelerated up to 3 GeV in the RCS. The extracted 3 GeV proton beam, with a 150 ns bunch width and a spacing of 600 ns, is transferred to the muon production target and the spallation neutron source.

Recently, pitting damage became evident in the mercury target container [7], and the extent of the damage is proportional to the fourth power of the peak current density of the proton beam. After operating the beam at high power, significant pitting damage was observed at the spent mercury target vessel at JSNS and at the Spallation Neutron Source in Oak Ridge National Laboratory [8, 9]. Using linear optics (i.e., quadrupole magnets) for beam transport, the peak current density can be reduced by expanding the beam at the target. However, beam expansion increases heat in the vicinity of the target, where shielding and the neutron reflector are located. Therefore, the peak current density is limited by the heat induced in the vicinity of the target. At the JSNS, the minimum peak current density is expected to be 9 μA/cm^2, which gives a thermal energy density at the target of 14 J/cm^3/pulse [10]. Because the pitting damage goes as the fourth power of the peak density, scanning the beam with a deflecting magnetic field will not mitigate the pitting damage.

Beam profile monitoring plays an important role in comprehending the damage to the target. Therefore it is very important to watch continuously the status of the beam at the target at the JSNS especially for the peak current density. We have developed a reliable beam profile monitor for the target by using Multi Wire Profile Monitor (MWPM). In order to watch the two dimensional profile on the target, we have also developed the profile monitor based on the imaging of radiation of the target vessel after beam irradiation. In this paper, the present status of the beam monitor at the spallation neutron source is described.

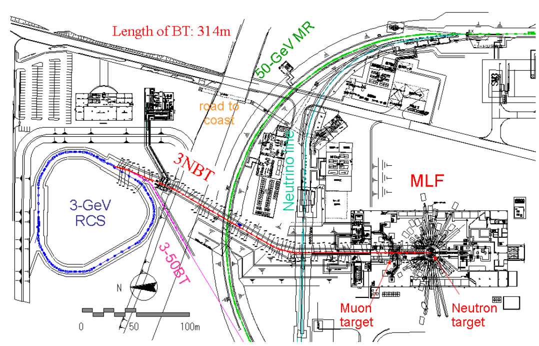

Figure 1: Plan of rapid cycling synchrotron (RCS) at the Materials and Life Science Experimental Facility (MLF) at J-PARC.

BEAM MONITOR SYSTEM AT THE BEAM TRANSPORT TO THE TARGET

Silicon Carbide Sensor Wire

In order to obtain the characteristics of the proton beam, diagnostic system based on a Multi Wire Profile Monitor

* meigo.shinichiro@jaea.go.jp

ISBN 978-3-95450-176-2

(MWPM) was developed. Principle of the MWPM is simple to observe the amount of the electron emission by the interaction of the beam at the wire. As a material of sensitive wire, usually tungsten wire is selected due to large emission amount of the electron and having high temperature melting point. In the present system, silicon carbide (SiC) was chosen due to the high resistance of the radiation [11], which can survive for 80 DPA. Due to the interaction, the beam loss is caused, which is one of issues of the high intensity proton accelerator and the optimization of the beam loss is important. The angular differential cross section of Rutherford scattering is proportional to square of atomic number of wire material. Therefore wire material with low atomic number has advantage for beam loss. Here, we compare property between tungsten and SiC. Since the average atomic number of SiC is 10, the differential cross section of SiC becomes 1/55 times of the cross section of tungsten. In order to obtain the angular distribution after scattered by the wire is calculated with revised DECAY-TURTLE [12] by Paul Scherrer Institute (PSI) [13]. It was recognized that SiC wire than tungsten gives less influence on the beam. In order to estimate of the lifetime of monitor wire, the displacement cross section of DPA is calculated with NMTC/JAM [14]. By the calculation, it is found that the DPA cross section of SiC and tungsten for 3-GeV proton is 278 and 7997 b respectably, which shows that DPA of the tungsten is about 29 times larger than SiC. SiC was chosen as wire of as a standard model of the profile monitor at the 3NBT.

Multi Wire Profile Monitor

The view of MWPM is shown in Fig. 2. Along the beam transport line, 15 sets of movable MWPMs are placed to measure the beam profile. The MWPM frame has 31 wires of SiC with the spacing pitch of 6 mm for each horizontal and vertical direction. We employed the SiC wire having diameter of 0.1 mm, which has a tungsten core of 0.01 mm and is coated with 1 μm of pyrolytic carbon. The wire frame made of aluminum oxide with purity more than 95 % is selected due to the high radiation resistance. In order to sustain with the fixed tension, wires are kept by the holder with spring, which gives the unique tension of 0.6 N to the wire. The frame of wires is placed in the vacuum chamber made of titanium, which is selected by the following reason, good vacuum characteristics and low activation. In order to avoid unnecessary irradiation of the wires, the frame can retract and moves like the pendulum motion. During the profile measurement, the beam loss due to the scattering at wires was observed by the beam loss monitor. For the practical aspect, beam loss cased at the MWPM can be utilized to calibrate the beam loss monitors.

For the actual high intensity beam tuning, it is important to know the beam parameter. The intrinsic parameters of the beam transport was confirmed by observing response of beam position for the kick angle of the steering magnet. By the observation of the beam width by the MWPMs, the Twiss parameter and the beam emittance can be acquired.

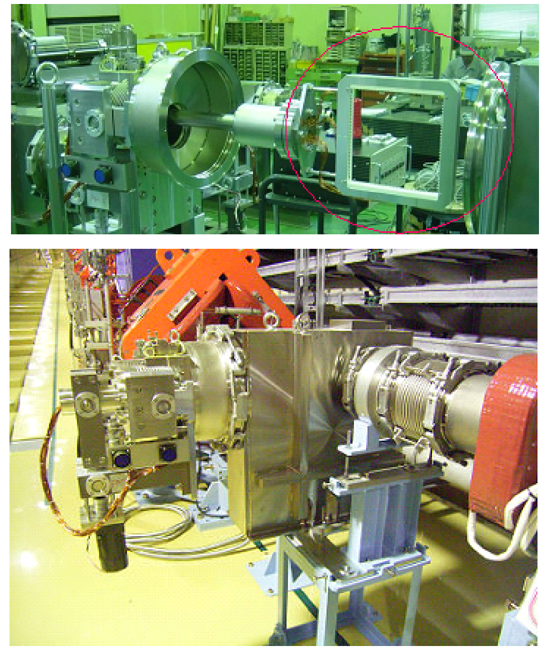

Figure 2: Movable MWPM placed at the beam transport line. (top: MWPM and frame inside the vacuum chamber. bottom: MWPM and chamber placed in the beam transport line).

Monitors Placed at Proton Beam Window

Continuously observing the characteristics of the proton beam introduced to the spallation target is very important. Due to the high activations caused by the neutron produced at the target, remote handling technique is necessary to exchange the beam monitor for the target. In order to decrease the radiation produced at the spallation neutron target, shielding above the monitor was required. To decrease the difficulties of the exchange work and decrease of the shielding, we combined the beam monitors with a Proton Beam Window (PBW) for separation between the vacuum region of the accelerator and the helium region around the neutron target. The PBW is better to be placed closer to the target where distance between the target and the PBW is 1.8 m, which gives reliable profile at the target. In Fig. 3, the MWPM placed at the center of vacuum chamber of the PBW is shown. In order to avoid exceed heat at target vicinities, beam halo monitors are placed as well. The chamber of the PBW has inflatable vacuum seal called pillow seal. Due to the pillow seal, the monitors can be changed by the remote handling. Io calibrate sensitivity of each wire, the signal was observed by the scanning the position with narrow width beam. It was found that the difference of individual sensitivity was 6 % at most.

In an actual beam operation, the heat at the target vicinities such as shielding, which mainly does not have water cooling channel, is important for reduction the peak density. Beam halo monitors attached at the PBW to observe the heat deposition at the target vicinities such as reflector and shielding, which is not allowed to exceed 1 W/cm^3. A view of the

ISBN 978-3-95450-176-2

beam halo monitor is shown in Fig. 4. We placed two types of beam halo monitors to obtain the thermal information by thermocouple and the emission of electron by electrode. Since the emission of electron indicates relative intensity of the beam halo, the beam halo relative intensity, which can be normalized by the following thermal observation, can be obtained by several shots of the beam. To observe the absolute intensity of the halo, the thermocouple type was implemented, which consists of copper strips coupled with the thermocouple. With 5 minutes of 25 Hz beam operation, the absolute intensity of the beam halo can be determined by the differential of temperature by time. These procedure was normally performed in actual beam operation.

Since wires at the MWPM placed at the PBW are fixed type and continuously irradiated to the beam, long lifetime wire is required. The profile monitor at the PBW is important so that a redundant system using SiC and tungsten wires was applied. In summer of 2013, some spots were observed at the surface of helium side of the PBW, which were thought to be produced by the erosion of nitric acid produced by the radiolysis around the target. We decided to change the 1st PBW already received the integration beam power of 2000 MWh to the new one. Until 2000 MWh, the wires still gave normal signals and after irradiation they were not found serious damage by inspection.

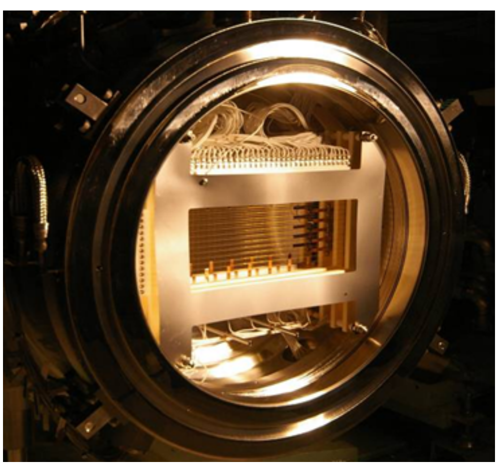

Figure 3: MWPM and beam halo monitors placed at the Proton Beam Window (PBW).

All signals of MWPM is transfer to the local control room by twisted pare cables with high radiation harding. As for the MWPM of the PBW, Mineral Insulator Cables (MICs) are applied because the cables receives quite high radiation does more than 1 MGy. The signal is fed to the inverter amp (Technoland N-GK 160 32ch Inverter AMP) and fed to the charge collective ADC (Technoland C-TS 301B) with the integration time range of 3 μs, which has integration charge range of -3000 pC in total and is driven by the CAMAC bus. The signals on the CAMAC bus are read out via crate controller of Toyo CC/NET. All signals is controlled by the EPICS [15] and is data base server based on PSQL server.

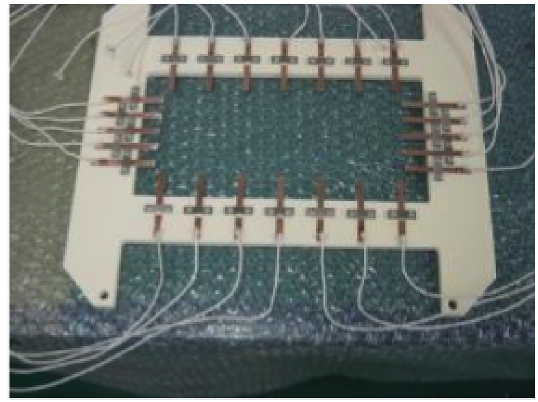

Figure 4: Thermocouple type of beam halo monitors placed at the Proton Beam Window (PBW).

In Fig. 5, the beam profile at the PBW obtained by the present system is shown. Each result is fitted by the Gaussian and base distribution for every second. Result of the center position and the width is utilized to watch the status of beam injected to the target.

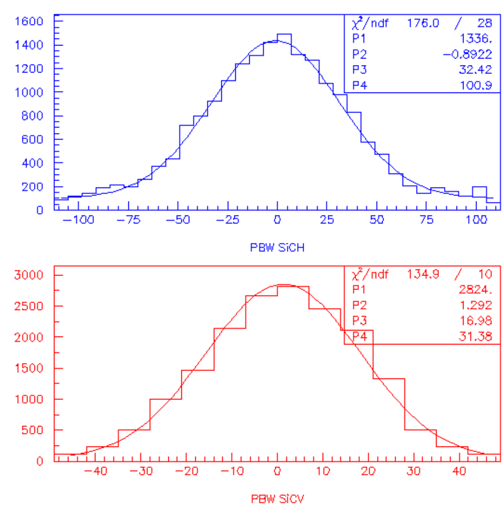

Figure 5: Beam profile obtained by the MWPM located at the proton beam window for 0.3 MW beam. Top and bottom graph shows the result for horizontal and vertical direction, respectively.

PROFILE MONITOR BY IMAGING PLATE

Imaging Plate Attached to Target After Beam Irradiation

For achievement good performance at the neutron source, enough gap is not remaining between the target and the vicinities to place any devices for the beam profile measurement. During the first beam commissioning, the beam profile was obtained by the activation technique with 0.3 mm thickness aluminum foil placed at the target vessel. After extraction the foil from the target, an imaging plate (IP: Fuji

ISBN 978-3-95450-176-2

Firm BAS-SR 2040) attached to the foil to read the distribution. The observed beam shape was clear gaussian and no skew. After the first beam commissioning, the target was already activated and the radiation around the target was extremely high such as several tenth Sv/h so that a remote handling technique was required to obtain the beam profile. We have developed an activation technique by utilizing the IP instead of using the foil. The IP is attached to the mercury target vessel by the remote handling as shown in Fig. 6. The radiation at the entrance of the hot cell was several tenth of μSv/h so that human can access at the entrance. The IP contained the holder was attached to the crane at the hot cell in the MLF by human access. By the crane, the IP approached to the target and contacted with the target by help of the master slave manipulator as shown in Fig. 6. After about 10 min exposure and the extraction of the IP, the image of radiation was observed by the IP reader . Since the exposed dose of the IP exceeded the acceptance of the reader, which is several micro Sv, the IP was irradiated by the UV room right for several minutes to reduce the recorded does. After this procedure, the image of the IP can be measured by the IP reader without any saturation. We already obtained the profile result of 500 kW beam with short duration such as several days after the beam stopped, the profile for 1 MW can be observed with long cooling duration of the radiation.

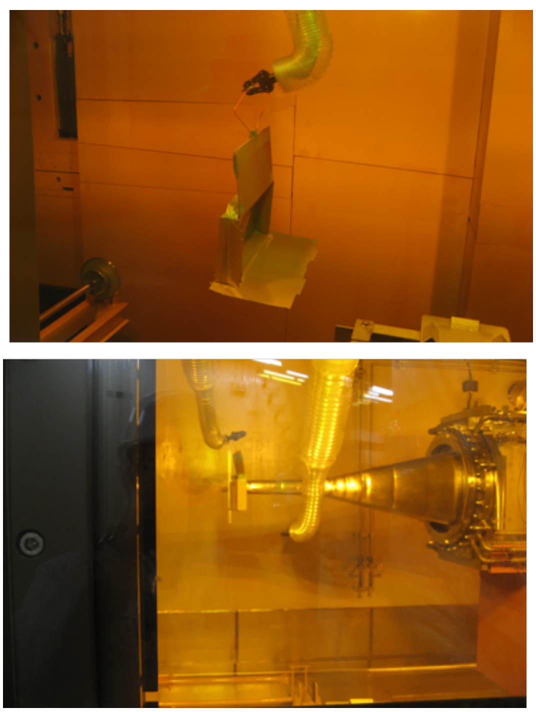

Figure 6: Activation technique using Imaging Plate (IP) located on the target vessel performed after irradiation at hot cell of the MLF. (top) IP holder placed at crane (bottom) IP attached by the master slave manipulator.

Figure 7 shows the beam profile obtained by the activation technique with the IP after 120 kW beam operation. In the distribution, it is shown that a clear Gaussian peak exists

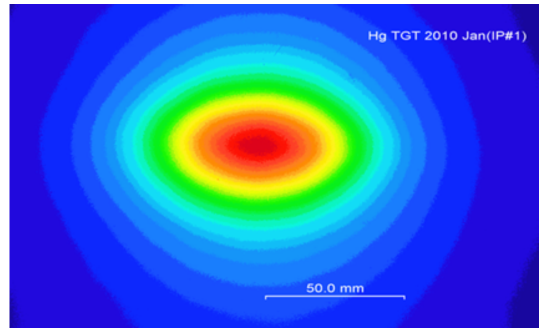

Figure 7: 2Dl beam profile obtained by the IP attached to the mercury target vessel.

without skew of the beam, which was also presented by foil activation technique.

The beam profile in horizontal distribution obtained by the IP is shown in Fig. 8. The distribution can be well described by the combinations of two Gaussian functions having small and large widths. The smaller one was thought to be the initial protons. The larger width was thought to be the secondary particles mainly neutrons or some background radiation. By using the shorter width, the primary beam width at the target can be obtained.

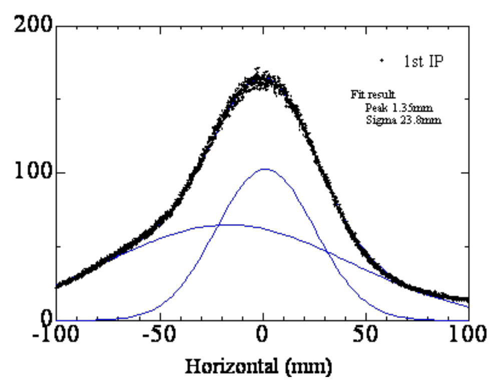

Figure 8: Beam profile in horizontal direction obtained by the IP with fitting of two Gaussian curves.

During beam commissioning using 300 kW, beam width was gradually expanded as each beam run. After each run, the beam width at the target was measured by the IP as well as observed by the MWPM. The beam width obtained by the IP considerably showed good agreement with result obtained by the MWPM including collection of the position by taking account of the beam gradient, which implies that reliable width can be obtained by the present profile monitor system. By using the MWPM, the present beam width can be obtained each beam pulse.

Machine Protection System

The beam monitoring at the target became quite important after target anomaly occurred at hadron experimental hall in J-PARC, which was caused by the malfunction of the slow extraction device and will not happen at the spallation

ISBN 978-3-95450-176-2

neutron source. For the safety, if any anomaly of the beam was found such as offset of the beam position, the beam should be immediately. The machine protect system (MPS) was developed, which cut out the beam immediately if either the beam position exceeded 5 mm offset or the beam peak density exceeded the threshold giving the peak heat density of 14 J/cm^3/pulse at the mercury target. Due to the MPS, high power beam operation such as 1 MW can be performed with high confident. Data of the beam profile for every shots are watched by the control system driven by the EPICS and are stored in data base.

DEVELOPMENT OF BEAM FLATTERING SYSTEM USING NON-LINEAR BEAM OPTICS

Distribution of the beam extracted from the RCS can be described well by a simple Gaussian [6]. With an ordinary beam optics, which is linear optics, the beam shape becomes a Gaussian at all place. By using non-linear optics, the beam particles located at the edge is bent to the center so that the distribution can become flat. In order to obtain flat shape for each horizontal and vertical direction, two octupole magnets is required. These octupole magnets can be placed at anywhere upstream of the target except the place where the phase advance between the magnet and the mercury target is an integer multiple of π. Since the targets had been irradiated by the beam for 5 years, the radiation dose around the targets is too high to place magnet. Therefore, two octupole magnets (OCT1, OCT2) are placed at upstream of the muon target as shown in Fig. 9.

In briefly, the fundamental of the beam flattering is based on the edge folding by the high order magnet of octupole magnet. By choosing appropriate octupole magnetic field, a flat beam distribution can be obtained as shown in Fig. 10.

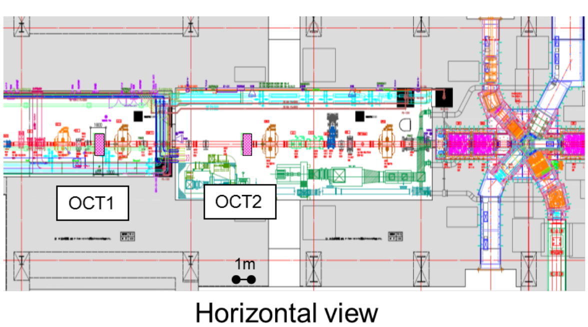

Figure 9: Plan of octupole magnets for beam flattening system, which is to be placed upstream of muon production target shown in right side.

Beam Optics for Flattering System

In order to achieve flat distribution, the required octupole field is proportional to the inverse square of the beta functions at the octupole magnet. Due to the relative high momentum of the present beam, achievement of a large octupole

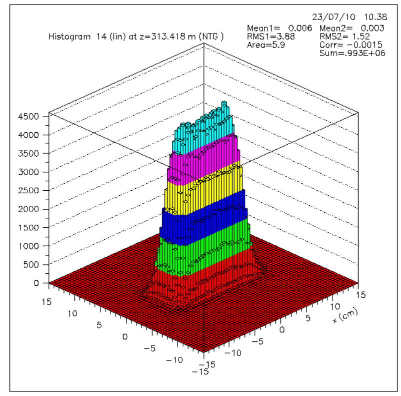

Figure 10: Flat beam distribution at the mercury target by using two set of octupole magnets.

field of the K is difficult. To obtain the flat shape with the realistic K of the octupole, we expand the beam at the octupole magnet to have large β function. Around the octupole magnet, since physical aperture of quadrupole magnets was fixed to 300 mm, we determined the aperture of the octupole magnet to 300 mm. In the linear beam optics, the admittance of the beam is designed to have 324 π mm mrad, which is given by the beam collimator placed at the RCS . A study of the RCS [16] showed that the transverse emittance will be as small as 250 π mm mrad. The beam admittance at the octupole was determined to 250 π mm mrad and the beta function at the octupole magnets was chosen to 200 m.

Octupole Magnets

Based on the optics design, two pieces of the octupole magnet shown in Fig. 11 were fabricated. The designed field gradient is 800 T/m^3 with a bore diameter of 0.3 m and 0.6 m in length of pole and the current of 700 A. Using a hall prove, the field gradient was measured. It was confirmed that the magnetic field were in good agreement with the design calculation. In an actual beam operation, the beam centering at the octupole is important to avoid peak at the edge. To perform centering, beam position monitor was installed in each octupole magnet.

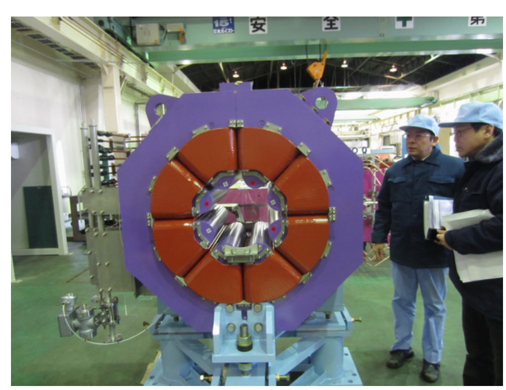

Figure 11: Fabricated octupole magnet with magnetic field gradient of 800 T/m^3.

ISBN 978-3-95450-176-2

Beam Profile with Non-linear Optics

In order to obtain the beam profile at the neutron source, SAD code is utilized, which provide beam information by fitting the result given by the MWPM placed at upstream of the octupole magnet. Also revised DECAY-TURTLE [12] by Paul Scherrer Institute (PSI) [13] is utilized to simulate multiple scattering at the muon target. Figure 12 shows results of beam profile for 800 kW beam with and without excitation of the octupole magnets. The beam profile shown in Fig. 12 was observed by the MWPM placed at the PBW. It can be found that considerable flat distribution can be obtained by the non-linear optics. The calculation results with and without excitation are also shown in Fig 12. The calculation results show good agree with the experiment ones with and without octupole magnetic field. It is also confirmed that the calculated beam profile by using the muon target showed good agreement with the experiment for both cases with and without octupole magnetic field. By the calculation result, the peak density can be thought to be reduced by 30% compared with the linear optics.

DEVELOPMENT NEW PROFILE MONITOR

Lifetime Estimation of the PBW

The MWPM placed at the PBW so that the lifetime estimation of the PBW is important. When the water was leaked from the PBW, enormous efforts and time will be necessary for restoring. If water leaked from the PBW to the vacuum side, the baking procedure will be necessary to reduce the outgas inside vacuum. We chose aluminum alloy as the material of the PBW, because SINQ at PSI had a good result for lifetime as a safety hull material of the target, At SINQ, the post irradiation examination (PIE) was already performed and material property was studied preciously. The lifetime can be thought to be determined by the embrittlement due to the helium caused by the spallation reaction. Therefore, helium gas production rate is important to estimation of the lifetime. Due to the difference of the proton energy, calculation should be made for gas production rate for the proton energy, whereas the SINQ is utilized 590-MeV protons. Since no experimental data exist for 3-GeV proton so that the validation of calculation can not be possible. In order to obtain gas production rate, we are planning to measure tritium production using thin aluminum foil placed at the beam dump. By using Q-mass analyzer, the hydrogen and helium gas production rate will be obtained. After measurement of the gas production rate for 3-GeV proton, more reliable lifetime can be obtained.

Development of New Profile Monitor

Until now the monitor wire survived up to 2000 MWh, which was at attached the first PBW, however, there is no evidence that the MWPM will survive for long duration of 1 MW beam. The lifetime of the PBW is expected as 2 years for 1 MW beam [17], which has proton fluence 2 × 10^{21} /cm^{-2} and the integral beam power of 10000 MWh. In order to observe 2D profile, a on-line type profile monitor is desired because the present 2D beam profile by IP can be obtained after the irradiation. Therefore we begun to develop a new beam profile monitors.

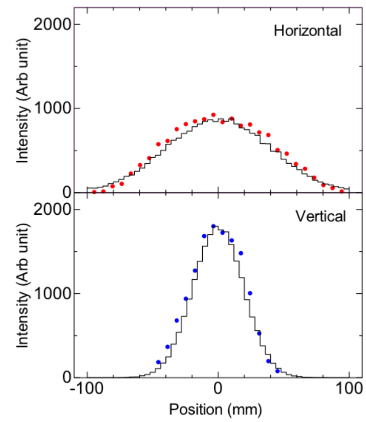

(a) OCT 0A

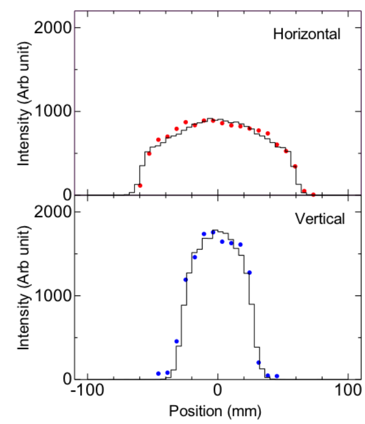

(b) OCT 698A

Figure 12: Beam profile obtained with calculations (line) compared with result by the MWPM (dots) supplying current of (a) 0 A and (b) 698 A to octupole magnet . Upper and bottom figure represents for horizontal and vertical directions, respectively.

By observation of the thermal distribution at the target, the beam profile can be obtained. We developed an infrared camera system with bundled hollow-core fibers having length of 1 m. The hollow-core fibers were made of the quartz capillary-tube coated by polyimide. Since beam monitor is placed at the PBW, the radiation hardening of the monitor is required obviously. The capillary tube is made of inorganic material and the camera can be placed far away from the radiation source so that the infrared system can be thought to have enough high radiation hardening. As an examination of the system, the thermal distribution on the ceramic heater was observed by the infrared system. The result of the thermal image is shown in Fig. 13. A clear image of the ceramic

ISBN 978-3-95450-176-2

heater was found. In the present system, capillary tube has only 12 × 12 channels, which may not be sufficient for the beam profile system. Although further R&D is required especially for increase the number of pixels, this infrared camera system is probably to be utilized as profile monitor in future.

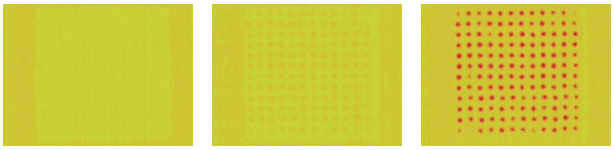

(a) 50 °C (b) 100 °C (c) 250 °C

Figure 13: Images obtained by the infrared system for various temperature of ceramic heater.

Also we developed a profile monitor based on the bundled optical fibers with high radiation hardening (Fujikura FISR-20) having 20000 pixels and length of 5 m. By painting fluorescence material such as alumina at the target vessel, the beam profile can be observed with fluorescence, which already utilized at the SNS. In future, we will place the present fiber system at the PBW.

To observe anomaly target status exceeded heated, the image of fibers was obtained with the near infrared filter to cut the visible light. Figure 14 shows the direct image of the near infrared from the ceramic heater. The present near infrared system may be utilized for diagnostic system of the muon production target. Since the muon production target was the rotating target cooled by the radiation heat having any cooling channel, if the rotation stopped by certain cause then the temperature will arise rapidly eventually introduce break of the target. Due to the rotation target, observation of the temperature by the thermocouple was difficult. Normally the temperature of the target exceeded 1000 °C so that By the near infrared system, the anomaly of the target can be easily detected.

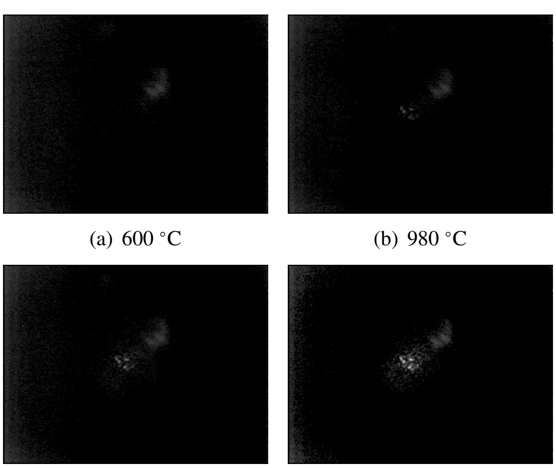

(a) 600 °C (b) 980 °C

(c) 11150 °C (d) 1300 °C

Figure 14: Images obtained by the near infrared system for various temperature of ceramic heater.

CONCLUSION

For reliable beam operation at the JSNS in J-PARC, beam monitor system with the MWPM and the halo monitor was developed. By using the MWPM, beam parameter such as the emittance and Twiss parameter can be obtained by several shots of the beam. To obtain two dimensional beam profile at the mercury target, a technique based on the activation technique with the IP was developed. Under the present system, high power beam operation such as 1 MW can be performed with high confident.

In order to reduce peak density of the beam current at the target, a non-linear beam optics with the octupole magnets was developed. By the present system, it was found that the flat shape can be obtained. The calculation simulation shows good agreement with the result obtained with the present profile monitor, which implies that the beam flattening can be achieved by the design of optics having large β function at the octupole magnet and an appropriate phase advance between the octupole and the mercury target. By the calculation including with the beam scattering on the muon production target, it is shown that the peak current density can be reduced about 30 % of the peak density without the non-linear beam optics.

ACKNOWLEDGMENT

This work is partly supported by the Ministry of Education, Culture, Sports, Science and Technology (MEXT) KAKENHI Grant-in-Aid for Scientific Research (C) Grant no. 26390114.

REFERENCES

[1] The Joint Project Team of JAERI and KEK, JAERI-Tech 99-56, 1999.

[2] Y. Ikeda, Nucl. Instrum. Meth. **A600**, (2009) 1.

[3] Y. Miyake, et al., Physica B **404** (2009) 957.

[4] S. Meigo, et al., Nucl. Instrum. Meth. **A562**, (2006) 569.

[5] S. Sakamoto, et al., Nucl. Instrum. Meth. **A562**, (2006) 638.

[6] S. Meigo, et al., Nucl. Instrum. Meth. **A600**, (2009) 41.

[7] M. Futakawa, et al., J. Nucl. Sci. Technol. **40** (2004) 895.

[8] T. Naoe, et al., J. Nucl. Mater. **450** (2014) 123.

[9] D. A. McClintock, et al., J. Nucl. Mater., **431** (2012) 147.

[10] S. Meigo, et al., MOPEB066, IPAC10 (2010).

[11] G. E. Youngbllood, et al., J. Nucl. Matler. , **258 - 263**, 1551 (1998).

[12] K.L. Brown, Ch. Iselin and D.C. Carey: Decay Turtle, CERN 74-2 (1974).

[13] PSI Graphic Turtle Framework by U. Rohrer based on a CERN-SLAC-FERMILAB version.

[14] K. Niita, et al., JAERI-Data/Code 2001-007 (2001).

[15] M. Ooi, et al., PO1.024-1, ICALEPCS10 (2005).

[16] H. Hotchi, et al., THPPP080, IPAC12 (2012).

[17] S. Meigo, et al., J. Nucl. Matler. , **450**, 141 (2014).

ISBN 978-3-95450-176-2

BEAM POSITION MEASUREMENT SYSTEM DESIGN

H. Schmickler, CERN, Geneva, Switzerland

Abstract

For newcomers, but also with interesting details for oldies, all components of a modern beam position measurement system are reviewed and explained. From specifications, sensor types, analogue and digital electronics over calibration methods the whole field will be covered.

INTRODUCTION

The Beam Position Monitor (BPM) can be found in every accelerator. Its role is to provide information on the position of the beam in the vacuum chamber at the monitor location. For linacs and transfer lines the BPMs are used to measure and correct beam trajectories, while for synchrotrons such monitors are distributed around the ring and used to calculate the closed orbit. In circular machines, their location is usually chosen close to the main quadrupole magnets where the β-functions are largest and so any orbit distortion a maximum. For 90° lattices a typical layout involves placing horizontal monitors near the focusing quadrupoles (where the horizontal β-function is large) and the vertical monitors near the defocusing quadrupoles (where the vertical β-function is large). Apart from closed orbit measurements, the BPMs are also used for trajectory measurements (the first turn trajectory is particularly important for closing the orbit on itself) and for accelerator physics experiments, where turn-by-turn data, and even bunch-to-bunch data is often required.

In the early days a BPM monitoring system simply consisted of an oscilloscope linked directly to the pick-up signals. Since then, enormous advances in the acquisition and processing electronics have been made, turning beam position monitors into very complex systems. Modern BPMs are capable of digitising individual bunches separated by a few nanoseconds, with a spatial resolution of a micrometre or less, while the resulting orbit or trajectory collected from several hundred pick-ups can be displayed in a fraction of a second.

In the next chapter the mostly used sensors will be described (Pick-ups), followed by a detailed description on the acquisition electronics. Other important aspects, like calibration, timing and synchronization, large scale maintenance and component obsolescence are not treated.

PICK-UPS

The measurement of beam position relies on processing the information from pick-up electrodes located in the beam pipe. Here we treat the three most commonly employed:

- Electrostatic – including so-called 'button' and 'shoe-box' pick-ups
- Electromagnetic – stripline couplers
- Resonant cavity – especially suited for high frequency linacs

An excellent in depth analysis of most of these pick-ups is presented in Ref. [1]. Here we will briefly describe the three most commonly used, namely the electrostatic, electromagnetic and cavity pick-up.

Electrostatic (Capacitive)

The electrostatic or capacitive pick-up is the most widely used in circular accelerators. It consists of metallic electrodes situated on opposite sides of the vacuum chamber at the location where the beam is to be measured. As the beam passes through, electric charges are induced on the electrodes, with more induced on the side which is closer to the beam than the one furthest from the beam. By measuring the difference in the charge induced, the position can be calculated.

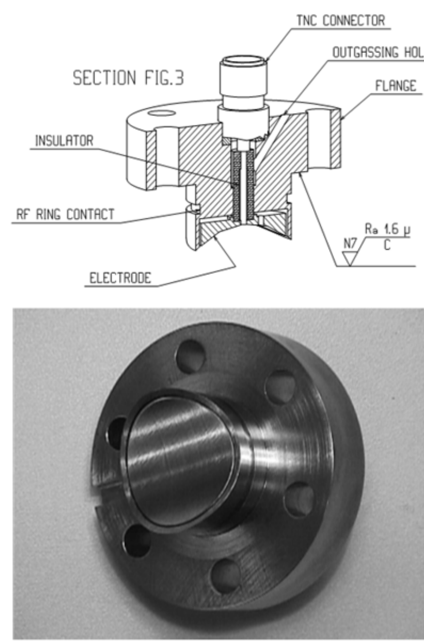

Figure 1: Cross-section and photo of an LHC button.

ISBN 978-3-95450-176-2

electrode.

Let us analyse the properties of button pick-ups (see Fig. 1) since they are the most popular due to their low cost and ease of construction.

The image current associated with the beam will induce a charge on the button which is proportional to the beam intensity and inversely proportional to the position of the beam from the electrode.

The figure of merit for any electrode is its transfer impedance (the ratio of the pick-up output voltage, V, to the beam current, IB). For a capacitive pick-up the signal is proportional to the rate of change of beam current at low frequencies, while for high frequencies the capacitance 'integrates' the signal and the transfer impedance tends to its maximum.

Impedance transformation can be used to improve the low frequency response at the expense of that at high frequency. Figure 2(a) shows the frequency response of an 8pF button electrode for the matched 50Ω impedance case (1:1) and after two different impedance transformations. The time response of the button for different bunch lengths can be seen in Fig. 2(b).

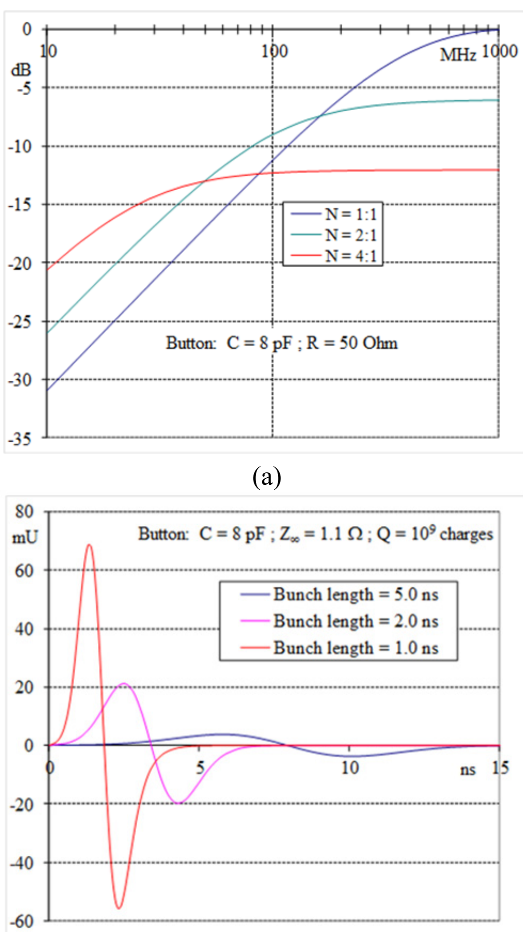

(a)

(b)

Figure 2: (a) Frequency response and (b) time response of a button electrode.

When designing such pick-ups care must be taken to limit the impedance variations when the transmission line used for signal extraction passes from the vacuum to a feedthrough or cable dielectric (such as ceramic, glass or air). Any such mismatch will produce unwanted reflections, often at high frequency, which could perturb the processing electronics. For this reason most processing chains introduce a low-pass filter on the button output. Special care must also be taken to pair the electrodes on opposite sides of the chamber to minimise offsets in the position reading. This pairing can be made less sensitive to capacitance variations if the high frequency cut-off for the processing electronics sits on the linear part of the button response, with the disadvantage that the overall signal amplitude is reduced.

Electromagnetic (stripline)

The electromagnetic pick-up is a transmission line (stripline) which couples to the transverse electromagnetic (TEM) field of the beam. The transmission line is formed between the stripline and the wall of the vacuum chamber and is excited by the beam only at the gaps on either end of the stripline where a longitudinal field occurs. Figure 3 shows the layout of such an electromagnetic stripline electrode.

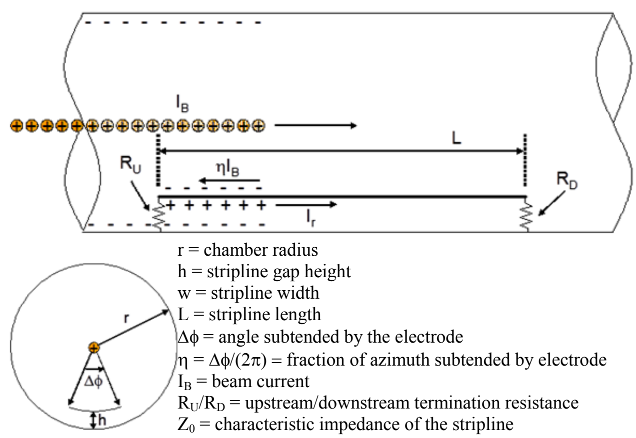

Figure 3: Schematic and photo of an electromagnetic stripline pick-up.

Consider a bunch travelling from left to right (upstream to downstream). While it is over the upstream port there is a voltage V_r across R_U, causing a voltage wave of that amplitude to be launched to the right. The stripline forms a transmission line with the wall of the vacuum chamber of characteristic impedance Z_0. The voltage wave is therefore accompanied by a right travelling current wave of amplitude $I_r = V_r / Z_0$. This current flows along the bottom surface of the electrode whilst an equal and opposite current flows along the chamber wall. In addition an image current of amplitude ηI_B travels along the top surface of the electrode. The voltage V_r across R_U can therefore be expressed as;

ISBN 978-3-95450-176-2

$$V_r = (-I_r + \eta I_B) R_U = \eta I_B \frac{R_U Z_0}{R_U + Z_0} \quad \Rightarrow \quad V_r = \tfrac{1}{2} \eta I_B Z_0$$

for a matched stripline ($R_U = Z_0$)

When the beam is over the downstream port it produces a voltage $-V_r = -\frac{1}{2} \eta I_B Z_0$ across R_D in the same way as it produced a voltage $+V_r$ across R_U. This launches a left-travelling wave of the same magnitude, but different sign to the right-travelling wave, which propagates along the transmission line formed by the stripline and the chamber wall and will produce an inverted signal upon arrival at the upstream port a time L/c later. The final signal observed at the upstream port will therefore be a bipolar pulse with the maxima separated by 2L/c (see Fig. 4(a)).

When the RF wavelength of the beam is equal to multiples of 2L, the reflection and the signal from next bunch will cancel and there will be no net signal from the stripline. A maximum in the frequency response will be observed when L is a quarter of an RF period, and hence the stripline pick-up length is usually chosen accordingly. The full frequency response of a 60cm long stripline is shown in Fig. 4(b) and has a lobe structure, with the minima located at multiples of c/(2L).

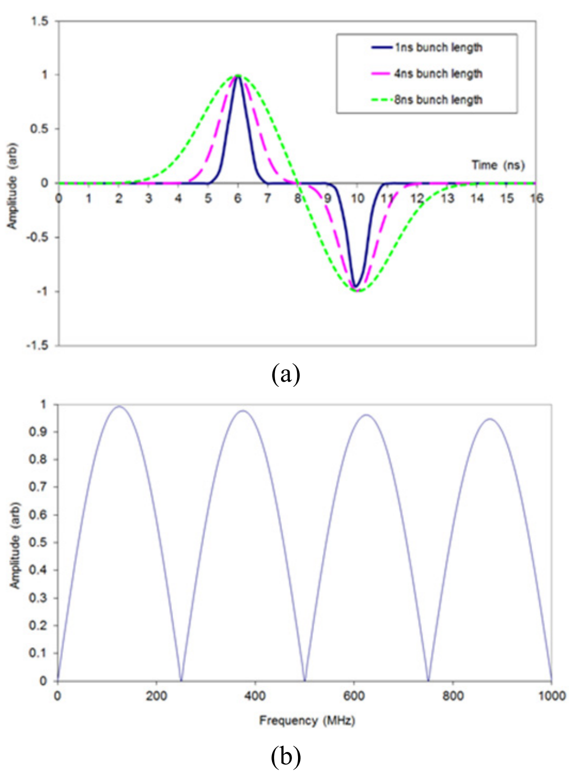

Figure 4: (a) Time response and (b) frequency response of a 60cm long electromagnetic stripline pick-up.

For a relativistic beam the voltage due to the beam passing the downstream port is produced at the same time as the right-travelling wave propagating between the stripline and the wall arrives at the downstream port. The two equal and opposite voltages therefore cancel producing no net signal at the downstream port. The electromagnetic stripline pick-up is therefore said to be "directional", i.e. a signal is only observed on the upstream port with respect to the beam direction. These pick-ups are therefore used in all locations where there are two counter rotating beams in the same vacuum chamber. Due to imperfections in the stripline and feedthrough impedance matching, the best directivity one can hope to obtain for a real stripline is generally around 25-30dB.

Resonant Cavity

Resonant structures, e.g. "pill-box" or rectangular cavities, coaxial resonators and more complex waveguide-loaded resonators, have become very popular to fulfil the high resolution, single-pass beam position monitoring demands of next generation, high energy, linear accelerators [1,2], or for driving a SASE-FEL beam-line [3].

These are constructed to exploit the fact that an off-centre beam excites a dipole mode (TM_{110}) in the cavity, with the amplitude of excitation almost linearly dependent on the off-axis displacement of the beam (Fig. 5). This dipole mode has a slightly different frequency from the main monopole mode (TM_{010}) of the cavity, which allows the processing electronics to select only the frequency of interest (dipole TM_{110}) and so suppress much of the large, unwanted, intensity related signal (monopole TM_{010}).

Nevertheless, even with this frequency difference, the presence of the fundamental TM_{010} monopole mode still adds a strong common mode component to the dipole-mode position signal, limiting the performance of the cavity BPM. Rather than picking off the signal from the cavity using four symmetrically arranged pin antennas it is therefore preferable to couple to the cavity using waveguides. Selecting the width of the waveguides such that they have a cut-off frequency above the TM_{010} monopole mode results in a very efficient, internal high-pass filter and makes the cavity BPM quasi "common-mode free". Such waveguide-loaded rectangular resonators (Fig. 6) have demonstrated a world record resolution of 8.7 nm at the ATF2 final focus test beam-line [4]

ISBN 978-3-95450-176-2

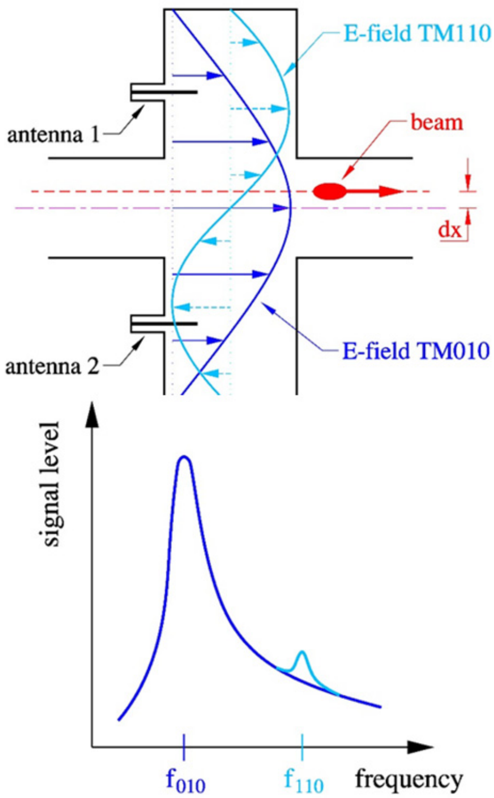

Figure 5: Principle and frequency response of a cavity BPM.

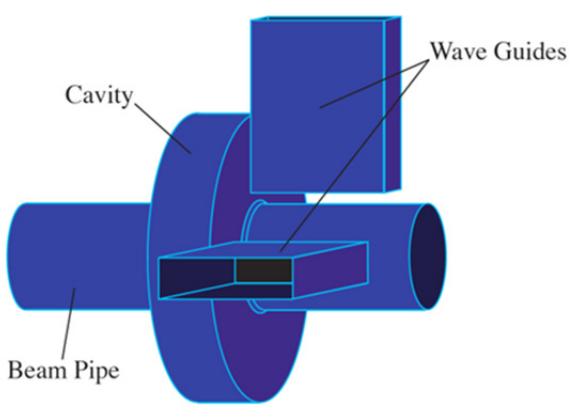

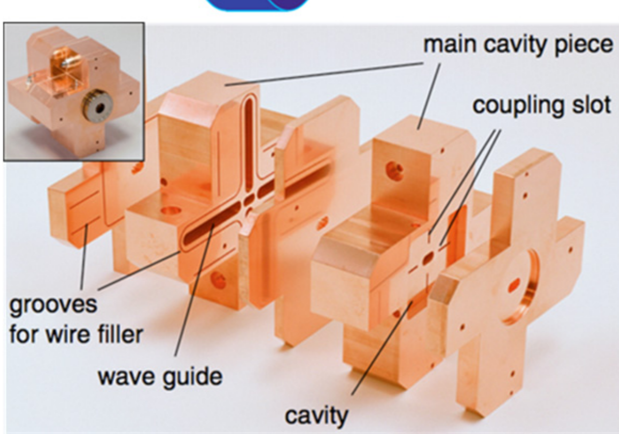

Figure 6: Principle and example of a waveguide coupled cavity pick-up (ATF2, KEK, Japan).

BEAM POSITION ACQUISITION SYSTEMS

Once the signals from the opposite electrodes of a pick-up have been obtained, the next step is to convert these signals into a meaningful beam position. The first thing to do is to normalise the position, i.e. to make it independent of the signal amplitude (i.e. beam intensity). This is generally done using one of three algorithms, whose response curves can be seen in Fig. 7.

- **Difference over sum (Δ/Σ) -** The sum and difference can be obtained either directly from a cavity BPM, or for the other pick-up types using a 0°/180° passive hybrid, a differential amplifier or calculated by software (after digitising), to give:

$$Normalised\ \ Position = \frac{A-B}{A+B}$$

The transfer function of this algorithm can be seen to be highly linear.

- **Logarithmic ratio -** The two input signals are converted into their logarithmic counterparts and subtracted. In practice this is done using logarithmic amplifiers followed by a differential amplifier. This gives:

$$Normalised\ Position =$$

$$Log(A) - Log(B)\left(= Log\left[\frac{A}{B}\right]\right)$$

whose response curve is seen to be an reversed S-shape, which becomes highly non-linear when exceeding 70% of the normalised aperture.

- **Amplitude to Phase -** The two input signals are converted by a 90° passive hybrid into signals of equal amplitude but varying phase, with the position dependence of this phase given by:

$$Normalised\ Position = \phi = 2 \times ArcTan(A/B)$$

Here the transfer function again deviates from the linear in an S form, but does not diverge for large excursions. In addition, the gradient is larger around zero, making it more sensitive towards the middle of the pick-up. A variation on the amplitude to phase algorithm is amplitude to time conversion, the technique used for the beam position system of the LHC [5].

ISBN 978-3-95450-176-2

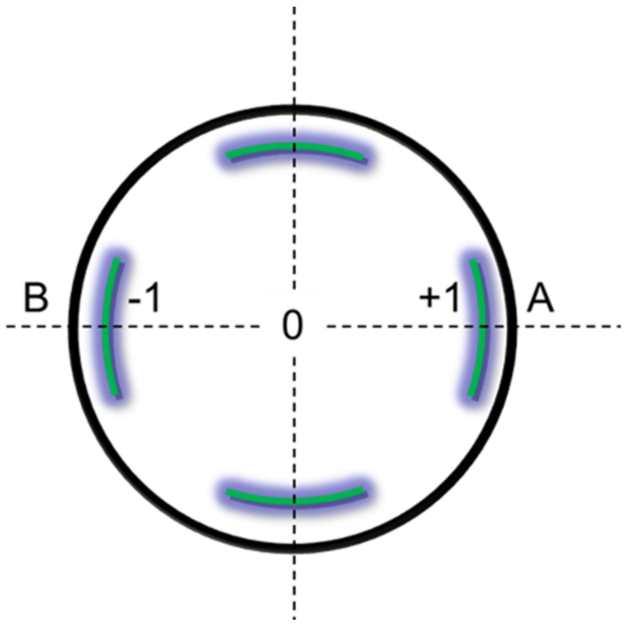

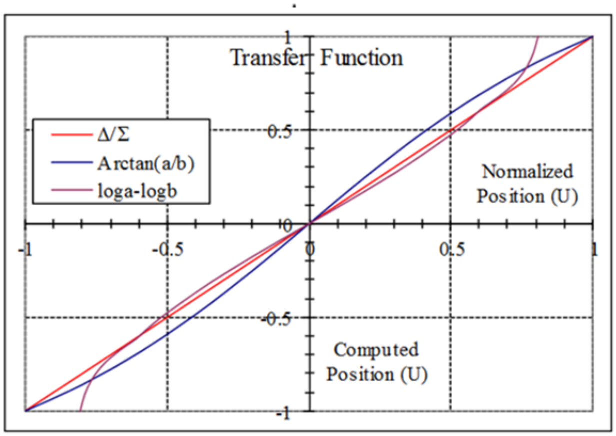

Figure 7: Transfer functions for three commonly used position normalisation algorithms.

The type of algorithm to be used will depend on the choice of processing electronics. In all cases the non-linearity is taken into account by calibration circuits and correction algorithms. A summary of commonly used beam position acquisition systems is given in Fig. 8. Here we will only briefly mention the various families in passing, but detailed descriptions along with the advantages and disadvantages of each system can be found in [7].

MPX (multiplexed) – each of the BPM electrodes is multiplexed in turn onto the same, single electronics acquisition chain. This eliminates channel to channel variations, but since the switching is generally quite slow such an acquisition only tends to be used in circulating machines where the average orbit is of main importance.

Hybrid (Sigma & Delta) – here a 0°/180° passive hybrid is usually used to obtain the sum (Σ) and difference (Δ) signal from the two electrodes. The position (or ratio of the sum and difference signals) can then be obtained in many ways including: direct digitisation, homodyne detection (mixing the sum and delta signals with the sum signal itself) or heterodyne detection (mixing sum and delta signals with an external reference).

Individual Treatment – in this case each electrode is treated separately, but in parallel. The acquisition can either consist of directly digitising each signal or using logarithmic amplifiers as outlined above. The disadvantage of this method is that it requires two (or four depending on the pick-up orientation) very well matched chains of electronics, since the combination of the signals to obtain a position is performed at the very end of the chain.

Passive Normalisation – here the amplitude difference (i.e. position information) in the input signals is directly converted into a phase or time difference. Intensity information is lost in this procedure, but the result is a varying phase or time which is directly proportional to the position.

Read-out Electronics

The read-out system interfaces the BPM pickup to the accelerator data acquisition (control) system. This requires signal conditioning, normalisation and linearisation of the BPM signals with conversion to a digital format somewhere along this chain in order to ultimately provide a time-stamped beam position.

Modern BPM read-out electronics are typically based on the individual treatment of the electrode signals using frequency domain signal processing techniques [ ]. These techniques were developed for the telecommunications market and make use of the high frequency and high resolution analogue to digital converters (ADCs) that are now readily available. In such schemes, bandpass filters in the analogue section convert the BPM signals into sinewave-like signal bursts for waveform sampling and processing in the following digital electronics. Microwave and RF analogue components, 12-16 bit pipeline ADCs, Field Programmable Gate Arrays (FPGAs) and clock distribution chips with sub-picosecond jitter are some of the key hardware elements. Figure 10 illustrates a typical electronics arrangement for a broad-band BPM pickup with only 1 of the 4 channels shown. For cavity BPMs the schematic is similar.

The analogue chain, consisting of bandpass filters, amplifiers and typically a frequency down-conversion stage prepare the electrode signal for sampling by an ADC. In order to reconstruct the input sine wave the ADC is either clocked at some sub-harmonic of the accelerator radio frequency or with an external clock (NCO – numerically controlled oscillator). This clock is typically chosen to give a sampling at 4 times the frequency of the input sine wave or to under-sample the input sine wave by a multiple of 4. This allows I/Q demodulation to be carried out in the digital domain. In-phase / Quadrature (I/Q) demodulation is nothing more than sampling at some 4th multiple or sub-harmonic of the input frequency. The knowledge that the sampled points are then all 90° apart on the sine wave allows for easy computation in the

ISBN 978-3-95450-176-2

digital domain without the need for sine and cosine lookup tables. If the frequency is correct, and the phase is locked, then all the quadrature samples are zero and only the in-phase samples need to be considered, giving directly the amplitude of the sine wave. These data can then be treated either in their raw form for bunch to bunch measurements, in a wide-band form for turn by turn measurements or in narrow-band for orbit measurements.

The narrow band orbit data is typically always available on-line from such systems, with the wideband and raw data available on request for a limited number of turns or bunches respectively. By producing the sum and difference of the amplitudes from opposite electrodes and applying calibration and linearization factors this data can then be converted into a meaningful beam position.

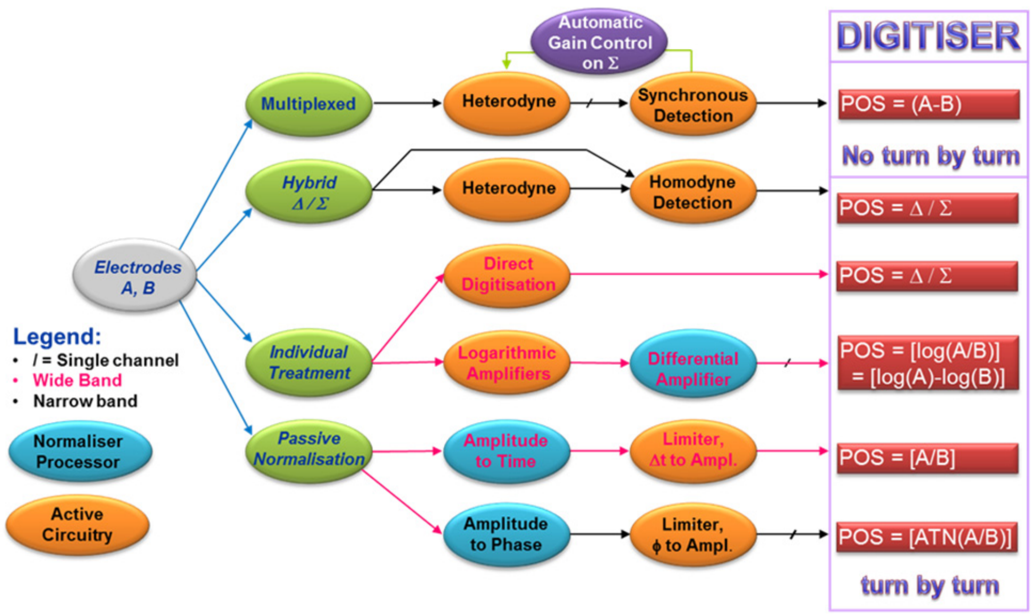

Figure 8: Schematic representation of the various beam position processing families.

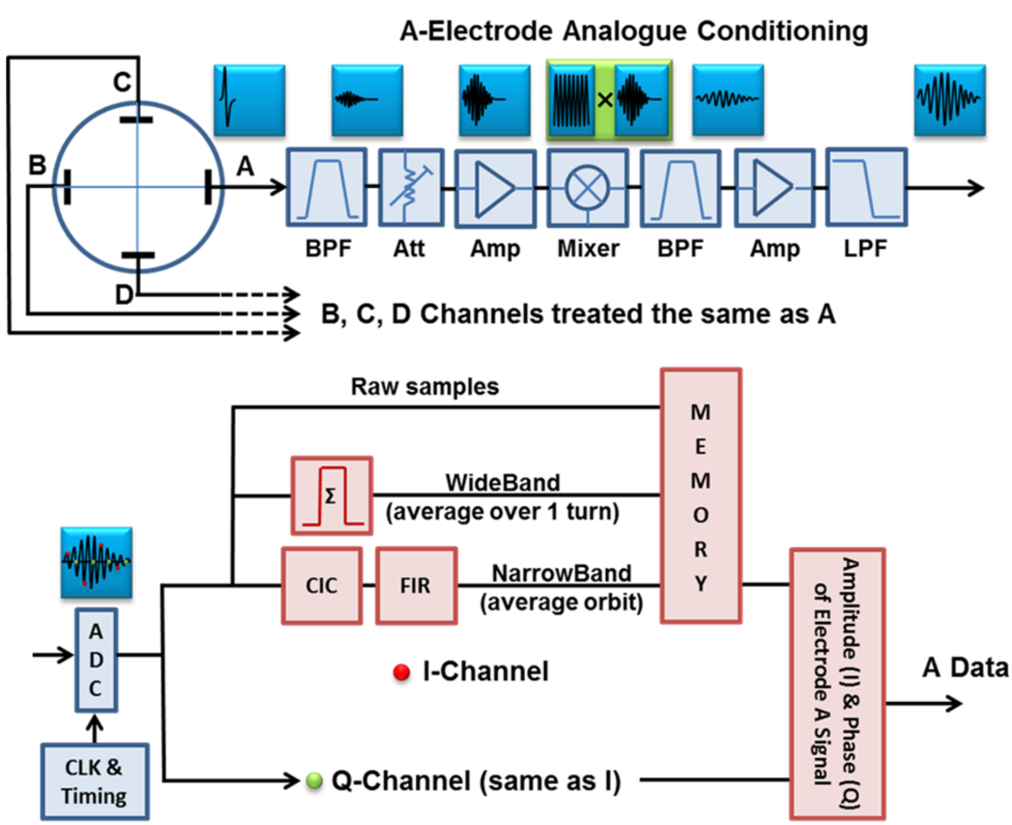

Figure 9: Key elements of modern BPM read-out electronics.

ISBN 978-3-95450-176-2

REFERENCES

[1] D.A. Goldberg, G.R. Lambertson, "Dynamic devices : a primer on pickups and kickers ", US Part. Acc. School, 1991. AIP Conf. Proc., 249,1992.
[2] S. Walson, et.al., "Performance of a High Resolution Cavity Beam Position Monitor System," NIM-A, 578 (2007), pp. 1-22.
[3] S. T. Boogert, et.al., "Cavity Beam Position Monitor System for ATF2," IPAC'10, Kyoto, Japan, May 2010, MOPE070, pp. 1140-42 (2010).
[4] S. Smith, et.al., "LCLS Cavity Beam Position Monitors," DIPAC'09, Basel, Switzerland, May 2009, TUOC03, pp. 285-287 (2009).
[5] T. Nakamura, et.al., "High Resolution Cavity BPM for ILC Final Focus System (IP-BPM)," LCWS/ILC 2007, Hamburg, Germany, May/June 2007, arXiv:0709.2254v1, eConf C0705302.
[6] D. Cocq, "The Wide Band Normaliser : a New Circuit to Measure Transverse Bunch Position in Accelerators and Colliders", Nucl. Instrum. Methods Phys. Res., A 416 (1998) 1.
[7] G. Vismara, "Signal Processing for Beam Position Monitors", 9th Beam Instrumentation Workshop, BIW 2000, Cambridge, MA, USA , May 2000, AIP Conf. Proc. 546, pp36-60.
[8] V. Schlott, et.al., "First Operational Experience with the Digital Beam Position Monitoring System for the Swiss Light Source," EPAC'00, Vienna, Austria, June 2000, pp. 1809-11.

ISBN 978-3-95450-176-2

CHARACTERIZATION OF NSLS2 STORAGE RING BEAM ORBIT STABILITY*

Weixing Cheng#, Kiman Ha, Joe Mead, Boris Podobedov, Om Singh, Yuke Tian, Li-hua Yu
NSLS-II, Brookhaven National Laboratory, Upton, NY 11973

Abstract

Similar to other advanced third generation light sources, NSLS2 storage ring has stringent requirements on beam orbit stability. NSLS2 BPMs can be synchronously triggered to record turn by turn or fast acquisition 10kHz data. Spectrum of these data reveals various beam motion frequencies and it has been characterized at various machine conditions. Compared to the ground motion and utility system vibration spectra, beam motion introduced by the vibrations can be identified. An algorithm to locate possible noise sources from the measured spectrum has been developed. Preliminary results of locating orbit sources will be discussed in this paper as well.

INTRODUCTION

NSLS2 is an advanced third generation light source recently constructed at Brookhaven National Laboratory. The 3GeV storage ring generates ultra-low emittance of less than 1nm.rad horizontally and 8pm.rad vertically. Machine commissioning has been finished with six beamlines early this year and it's open for user experiments. With one super-conducting cavity, average beam current of 300mA has been achieved. Typical user operation current has been increased in steps, now it operates at 150mA and refills at every three hours. Top off operation will start soon.

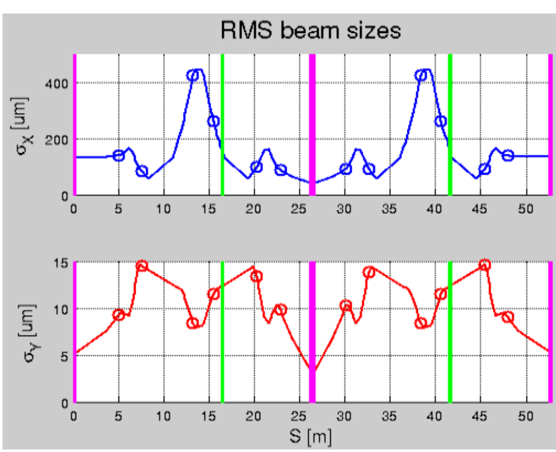

Figure 1: Horizontal and vertical RMS beam sizes in one super cell, calculated using emittance of $\varepsilon_x/\varepsilon_y$ = 0.9/0.008 nm.rad and energy spread of 0.09%.

NSLS2 storage ring has 30 DBA cells. 15 high beta (long) and 15 low beta (short) straight sections are available for insertion devices. Three damping wigglers are installed at long straight sections in C08,C18 and C28. These damping wigglers decrease the bare lattice horizontal emittance of 2nm.rad down to 0.9nm.rad. Figure 1 plots the RMS beam sizes in one super cell (high beta cell + low beta cell). Beam sizes at various beamline source points are marked with vertical lines. Smallest beam sizes of 3 μm are found to be at the center of short straight sections. With 10% beam stability requirement, the orbit needs to be controlled within 300nm at these source points. There are 6 BPMs in each cell to monitor the beam trajectory/orbit. BPM locations are marked as circles in Fig. 1. These BPM readings are used for orbit correction and fast orbit feedback control. There are 6 slow correctors and 3 fast correctors per cell to maintain the beam in desired reference orbit. In addition to the normal BPMs in the cell, there are 2 (or 3 for canted ID straights) ID BPMs on both end of the insertion devices. These BPMs are typically mounted on high stability stands and configured to have better vertical sensitivity. ID BPMs are used to monitor the orbit at the insertion devices. This information is used to ensure that the beam stays within the pre-defined active interlock envelope, as required for machine protection. More information of the NSLS2 button BPM design and performance can be found at [1,2].

In-house developed BPM electronics are used in NSLS2 complex, including the LINAC, transport lines, Booster and Storage ring. Button signals feed to the pilot tone combiner (PTC) box inside the tunnel, where beam signal is filtered. PTC includes a coupler to allow the pilot tone signal be injected into the signal processing chain. This pilot tone signal was designed to dynamically calibrate the BPM electronics drift. It turned out that this kind of dynamic pilot tone calibration is not needed as BPM electronics reside in temperature stabilized racks (+/- 0.1 degC). BPM processing electronics are assembled in a 1-U chassis, analog front end (AFE) first conditions the button signal with band pass filter, variable attenuators and amplifiers. Button signal is sampled by 16-bit ADC sampling rate of 117MHz. Sampled data is then processed in the digital front end (DFE) board, in which ADC/TbT/FA/SA data are available. NSLS2 storage ring BPMs can provide to the user in 4 switchable modes, ADC, TbT (Turn-by-Turn, up to 1M samples, on-demand), FA (Fast Acquisition, 10 kHz, up to 1M samples, on-demand) , and SA (Slow Acquisition, 10 Hz, continuous). 10kHz FA data is shared around the ring through SDI fiber link network, these data are used for fast orbit feedback and active interlock system. Details of the BPM electronics development are reported in previous conferences [3-6]. We report the measured beam orbit stability using these advanced BPMs.

*Work supported by DOE contract No: DE-AC02-98CH10886
#chengwx@bnl.gov

ISBN 978-3-95450-176-2

BPM ELECTRONICS PERFORMANCE

To characterize the beam orbit stability, it's important to know the measurement resolution and accuracy. BPM electronics resolution is mainly determined by the beam current, electronics gain and measurement bandwidth. BPM resolution has been measured with beam at three different fills: single bunch, 20-bunches short train and ~1000 multi-bunch train. Total beam current was increased in steps till BPM electronics saturate. BPM ADC, TbT and FA waveform data was recorded to calculate the resolution of different types of data. During maintenance when there was no beam, pilot tone signal with the same frequency as of RF was injected to the electronics to characterize the BPM resolution in fine steps. BPM attenuator was varied to simulate different signal strength. Measured results are shown in Fig. 2. The figure plots the measured resolution at different averaged ADC counts, which is basically BPM SUM signal. At high current (>10mA) with long bunch train, BPM resolution in TbT mode is better than 1µm when ADC counts is more than 4000. FA data had about 200nm resolution at these current. It's also noticed that with single bunch measurement, at 0.7 mA bunch current, beam was unstable due to TMCI instability, that's the reason there is one point didn't follow the curve in the TbT resolution plot. During 20 bunch fill, horizontal measured resolution with beam was slightly higher compared to the pilot tone results, which could be due to some orbit instabilities.

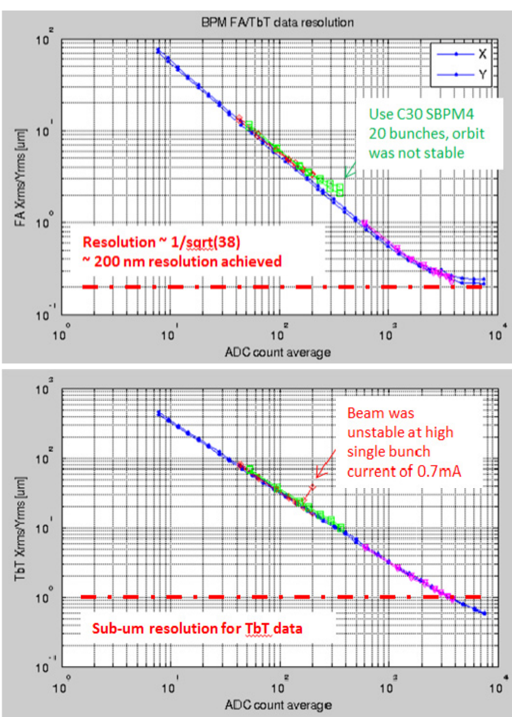

Figure 2: BPM TbT and 10kHz FA data resolution measured using pilot tone beam. Blue dots – test with pilot tone while varying the attenuators. Red diamonds – single bunch beam; Green square – 20 bunches beam; Magenta triangle – 1000 bunches beam. BPM attenuators were fixed at 0dB for beam test.

When the front end BPM attenuators are changing, the four channels electronic gains may not change by exactly the same amount. This will cause artificial position jumps when the RF attenuator is varied. While this is not expected to be an issue during the planned top-off operations, when the beam current and fill pattern variations will be tightly constrained thus eliminating the need for attenuator change, this effect needs to be addressed for various machine physics studies as well initial user operations without top-off. This is why static gain calibration coefficients have been implemented to compensate this effect. Assuming the beam orbit didn't move during some short period of time (~30 minutes), beam based static gain calibration look up table was created at different attenuator settings. Fig. 3 shows one BPM's position drift before and after the calibration. While attenuators scanned from 0 to 20dB in 1dB steps, most of the BPMs saw position drift of several tens of microns, some BPMs had drifted more than 100 microns. With the new beam based calibration coefficients, all BPMs have position drifts less than +/-10µm in the same RF attenuator scan. Note that these coefficients were generated at fill of 20 bunches with total current ~1.2mA in Nov. 2014 and they are still working fine now, many months later, with different beam current and fill patterns. Notice the X/Y position scales are same in Fig. 3 which is 100µm full range. Absolute position readings are different because these two sets of data are separate by more than 6 months and reference orbits could be very different.

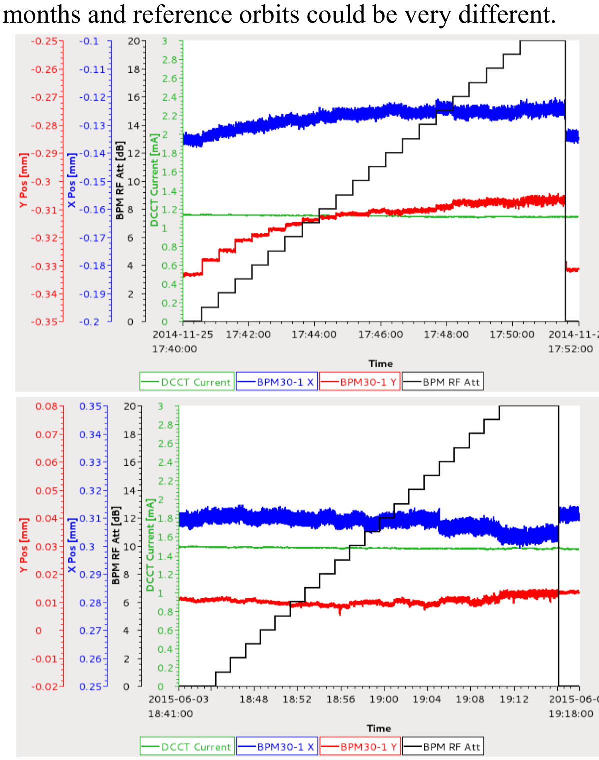

Figure 3: BPM RF attenuator dependency, C30 BPM1 horizontal/vertical position drift while attenuator scanned from 0 to 20dB in 1dB steps. Upper plot shows the position drifts before calibration, this particular BPM had vertical position drift about 30um; Lower plot gives the same scan with calibrated LUT.

ISBN 978-3-95450-176-2

To further check the BPMs current and fill pattern dependency, three consecutive fills were tried with 100 bunches, 200 bunches and 350 bunches, total beam current of all three fills were kept at 10mA. There was little difference on the BPM reported position readings. During the initial fill, especially when total beam current is low (<0.2mA, typically happened during single bunch studies), BPMs near RF cavity area saw large position drifts. This was investigated and found to be due to interference from RF system. Once beam signal is dominant (Ib > 0.2mA), BPM reported current dependency is negligible.

BPM ORBIT SPECTRUM

BPM 10kHz FA data are shared around ring through fiber network, there is one cell controller in each cell who communicate to the BPMs and power supplies in the cell. 30 cells in the ring are connected together with SDI interface. These synchronized 10kHz data are used for fast orbit feedback and active interlock. As the beam orbit motion typically appears in frequency range of several Hz to hundreds of Hz, 10kHz sampling rate FA data is well suitable to analyze the beam motion spectrum.

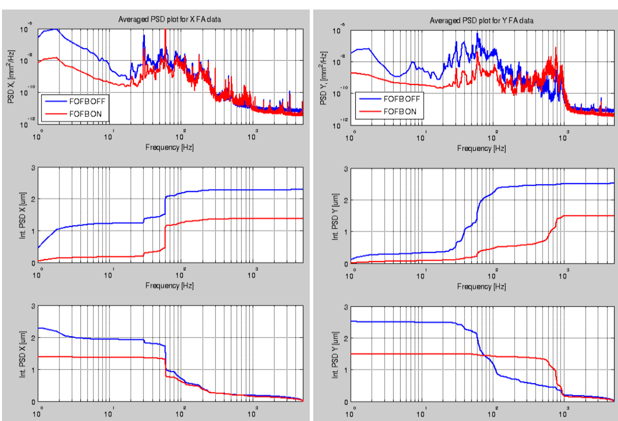

Figure 4: BPM 10kHz FA data spectrum and integrated RMS motions (from low to high frequency and vice versa), compared with FOFB ON and OFF.

Figure 4 gives an example of beam spectrum measured with FOFB ON and OFF. 10 seconds of synchronized data was acquired from all 180 BPMs, 16384 points of FFT spectrum was calculated with blocks of FA data. BPM at different locations will see different motion levels, the spectrum shown here is averaged from all non-dispersive BPMs in the ring. Blue lines are results without FOFB, most of the beam motions are in frequency range between 10Hz to 100Hz. There is a clear 60Hz peak coming from the AC line. A majority of this 60Hz noises is coming from pulse magnets. Around 30-40Hz peaks are believed to be utility system related. Mechanical motions of the girder and BPM chamber have been measured during operation. Girder motion is similar to what have been reported in [7], BPM chamber vibration spectrum saw peaks between 30-40Hz, which are likely induced by cooling water on the multipole vacuum chamber. Red lines are the PSD spectrum and integrated RMS motions with FOFB ON. Below 200Hz motions were able to be suppressed significantly in vertical plane. Horizontal FOFB is able to reduce the motions below several tens of Hz, which can be further optimized.

From the above mentioned PSD spectrum, RMS motions at each BPM can be calculated in some pre-defined frequency ranges. Figure 5 gives the 12 BPMs in C02 and C03 RMS motion integrated between 1-500Hz. Blue circles and red stars represent the RMS motions without and with FOFB. 1% of horizontal beam sizes and 10% of vertical beam sizes along the cells were plotted as dashed lines, to have a comparison of beam motions to the beam sizes. As can been seen, due to large horizontal beam sizes, X RMS motions is around 1% of the beam sizes which is well within the requirement. Vertical motions are typically ~ 20% of beam sizes without FOFB and they were able to be suppressed to ~ 5% of the beam sizes. In the middle waist locates C03 IVU, which supplies x-ray for the HXN (Hard X-ray Nano probe) beamline. This particular beamline has the tightest requirement on orbit stability. From two BPM readings on both ends of the insertion device, position and angle at the IVU center can be calculated. This virtual BPM position and angle spectrum were calculated and integrated motions in the same frequency range are 0.216 μm and 0.136 μrad, both meet the requirements of 10% beam sizes and 10% of beam divergence.

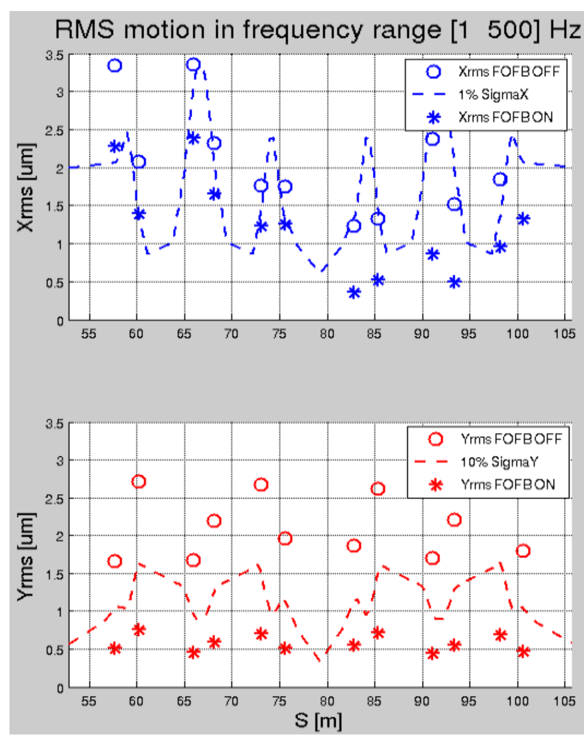

Figure 5: Integrated RMS motion in frequency range 1-500Hz, plotted for 12 BPMs in one super-cell (C02 and C03). C03 IVU locates in the center where beam sizes are smallest in both x/y planes.

In the HXN beamline, there is a photon BPM (xBPM) locates ~16 m from the source point. Using a similar digitizer, this photon BPM is capable to acquire long

ISBN 978-3-95450-176-2

buffer of 10 kHz data. X/Y position spectrums at the photon BPM location have been compared from direct measurement of xBPM and calculated from two ID BPMs in the straight section. The directly measured and calculated spectrums agree well, as shown in Fig. 6. Photon BPM directly measured spectrum better performance above 1kHz which indicated less electronics noises. For lower frequency range, beam motion is dominant.

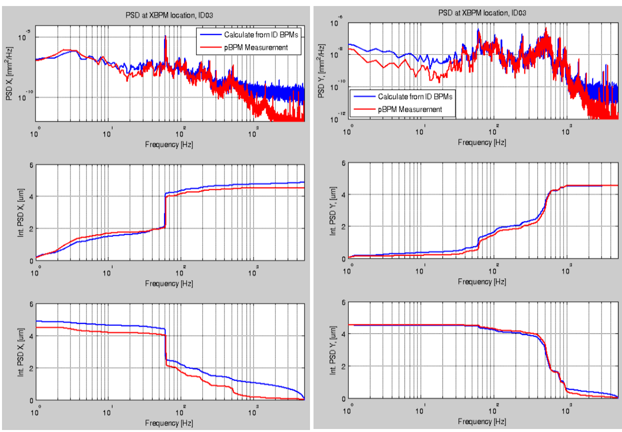

Figure 6: Photon beam spectrum at C03 xBPM location. Blue lines are the calculated spectrum and integrated RMS motions from two ID BPMs; Red lines are directly measurement spectrum from xBPM.

LONG TERM STABILITY

To check the long term stability of BPM electronics and beam orbit, 10Hz slow acquisition data was used. All BPMs 10Hz data was archived. There is a dedicated BPM pickup used to test the electronics noises, four buttons signal were combined together then splitting in to four digitizer channels. This configuration is to measure the electronics noises instead of beam motions.

NSLS2 user operation beam current has been increased in steps, at present user operation beam is initial filled to 150mA and refilled every three hours. Typical beam current is around 110mA at refills. BPM electronics long term stability has been checked during the 150mA operation, for ~8 hours period, BPM electronics drift has 450 nm peak to peak variations, RMS drift during the time is ~ 80nm. NSLS2 BPM electronics are housed in well regulated environment, experiment hall temperatures are controlled within +/- 1 degC; tunnel and rack temperatures are within +/- 0.1 degC.

With fast orbit feedback in operation, typical beam orbit drift measured at short ID center are within 0.5 μm vertically. Angle stability is the insertion device is within 0.2 μrad for the 8-hour period, see Fig. 7, which shows the data from July 04 0:00 to 8:00. The position and angle are calculated from synchronized 10Hz data of two ID BPMs on both ends of the insertion device. Horizontal plane has slightly worse long term stability performance and usually it's not a concern.

C03 photon BPM long term stability has been checked during the same period of time. Using the calculated ID center position/angle from ID BPMs (as shown in Fig. 7), photon beam positions can be calculated similar to 10kHz FA data. Calculated 8-hour positions from ID BPMs have been compared with the direct measurement results from photon BPM, the results agree within the same 8-hour period of Fig. 7. At the xBPM location, photon beam drifted within +/- 10 μm horizontally and +/-2 μm vertically. This photon beam drift was mainly determined by the electron beam angular stability at ID source point.

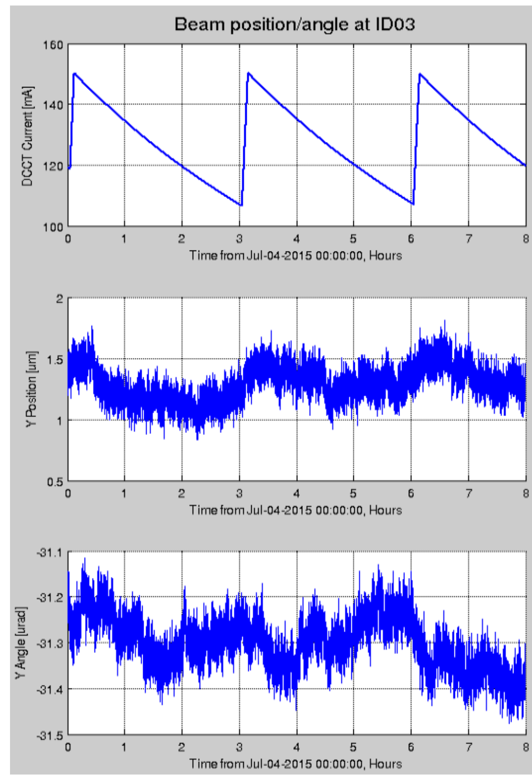

Figure 7: BPM long term stability at ID03 center. Position and angle at the location were calculated from two ID BPMs.

NSLS2 storage ring is measuring the betatron tunes using a pilot single bunch. It was first noticed that horizontal tune had a daily drift pattern when slow orbit feedback was operating. Once fast orbit feedback was commissioning and left ON for user operations, it's interesting to find out that the tune shift pattern disappeared but there is daily orbit drifts on dispersive BPMs, which are not included in the horizontal plan FOFB loop. With further investigation, it is believed that the tidal effect causes ring circumference change and energy mis-match. Plot in Fig. 8 are the six BPMs X/Y position histories in C30. During the two days period, beam was operated at 150mA for the first day and decayed from 150mA to ~20mA due to injector power supply failure. Positions are offset by 50 μm in between BPMs to have a better view of the drift. First two BPMs (red and blue) and last two BPMs (cyan and black) in the cell don't see much drifts, these BPMs are in the non-dispersion sections. However dispersive BPMs (green and magenta) have a clear daily drift pattern on the X position

ISBN 978-3-95450-176-2

readings. The position valleys are checked to appear at high tides of nearby harbors. It's not obvious though, only one valley was observed on the BPM position drifts while there should have two high tides daily, further investigation is needed.

One can see at the larger dispersive BPM (BPM #3 in the figure), X position drifted more than 50 µm. As the lattice has been well characterized and corrected, dispersive at the BPM should be close to the model of 0.424 m, which gives energy drift of $\Delta E/E$ = 1.18e-4. Assume the momentum compaction factor is known, we calculate the ring circumference changed by 34 µm. RF frequency should be adjusted by 21Hz to compensate this energy mis-match. Considering NSLS2 site is close to the ocean and the ring size is relatively big (~792m circumference), it's not surprise to observe these tidal effects on the beam orbit. RF frequency dynamic adjustment could be added to correct this effect, even though it doesn't have a direct effect on the orbit stability at the ID source points.

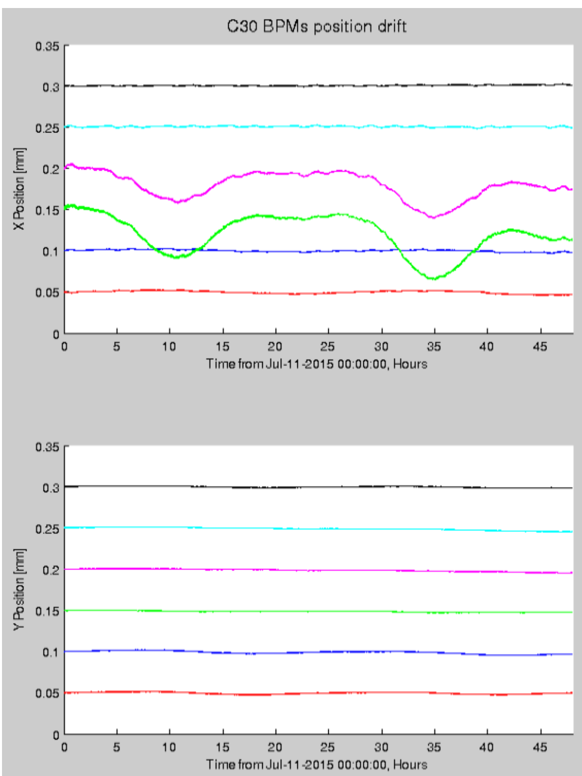

Figure 8: C30 six BPMs X/Y position drift during two days of period. BPM positions are offset by 50 µm. BPM #3, #4 (Blue, Magenta) located at dispersive section see the daily horizontal position drift pattern.

SUMMARY

NSLS2 BPMs system are designed, constructed and commissioned. BPM pickups sensitivity and nonlinear have been thoroughly investigated. Special ID BPMs are installed for better sensitivity and mechanical stability. Using the most advanced FPGA and digital processing technology, the in-hour developed BPM electronics are capable of suppling synchronized TbT/FA/SA data. Storage ring BPMs measurement resolution as well as attenuator dependency, current and fill pattern dependency have been characterized.

Long term and short term beam orbit stability has been measured with FOFB ON/OFF. With FOFB, RMS motions between 1-500Hz are well within the specification of 10% of beam sizes and divergences. Photon beam stability has been measured at one particular beamline using a dedicated photon BPM. Compare to the calculated values from two ID BPMs on both ends of the insertion devices, direct measured and calculated spectrum agree well. Even though the orbit stability meets the specification, tighter requirement may come up with particular beamlines. FOFB loop can be further optimized to improve the orbit stability in the future.

Long term stability was able to be analyzed with the archived 10Hz data. For a typical 8 hour period during 150mA user operation, position/angle stability has been checked to be within 0.5µm/0.2µrad at short ID straight center. A daily drift pattern has been observed on dispersive BPMs, this is likely due to the tidal effect. RF frequency feedback is under evaluation and can be implemented to compensate the energy mis-match due to ring circumference change.

Diagnostic group personnel gave various technical supports on the construction and operation of BPM system. Discussion with members from physics group, coordination group, control group, ID group and beamline groups are useful. Thanks for operation group for a reliable beam delivery during studies and operations. Special thanks to Ferdinand Willeke, Timur Shaftan and NSLS2 management for their continuous support.

REFERENCES

[1] W. Cheng et al., "NSLS2 Beam Position Calibration", BIW'2012
[2] W. Cheng et al., "Performance of NSLS2 Button BPMs", IBIC'2013
[3] K. Vetter et al., "NSLS-II RF Beam Position Monitor", PAC'2011
[4] K. Vetter et al., "NSLS-II RF Beam Position Monitor Update", BIW'2012
[5] O. Singh et al., "NSLS-II BPM and Fast Orbit Feedback System", IBIC'2013
[6] J. Mead "NSLS-II RF Beam Position Monitor Commissioning Update", IBIC'2014
[7] W. Cheng et al., "Vibration Measurement and Its Effect on Beam Stability at NSLS2", IBIC'2013

ISBN 978-3-95450-176-2

SUMMARY OF THE 2014 BEAM-HALO MONITORING WORKSHOP*

Alan S. Fisher#, SLAC National Accelerator Laboratory, Menlo Park, California 94025, USA

Abstract

Understanding and controlling beam halo is important for high-intensity hadron accelerators, for high-brightness electron linacs, and for low-emittance light sources. This can only be achieved by developing suitable diagnostics. The main challenge faced by such instrumentation is the high dynamic range needed to observe the halo in the presence of an intense core. In addition, measurements must often be made non-invasively.

This talk summarizes the one-day workshop on Beam-Halo Monitoring that was held at SLAC on September 19 last year, immediately following IBIC 2014 in Monterey. Workshop presentations described invasive techniques using wires, screens, or crystal collimators, and non-invasive measurements with gas or scattered electrons. Talks on optical methods showed the close links between observing halo and astronomical problems like observing the solar corona or directly observing a planet orbiting another star.

INTRODUCTION

There were 39 participants [1] in the workshop on beam-halo monitoring [2]. This paper summarizes the 11 talks and draws from the slides, which are posted on-line [3], without additional reference numbers. Each contributor's name appears in **boldface** when first cited below, and appears again in figure captions.

The subject of beam halo was introduced by **Kay Wittenburg** (DESY). Although a broad definition is difficult, "halo is low density and therefore difficult to measure." Charge near the core of a bunched beam, with a density of 10^{-1} to 10^{-4} of the peak, is commonly considered a "tail". Halo has even lower densities and is often further from the core, although there are no clear boundaries (Figure 1). The dynamic range required for measurement can span 5 to perhaps 8 orders of magnitude, depending on the number of poorly bunched, high-energy particles needed to damage the machine.

Halo has a variety of sources, including space-charge or beam-beam forces; poorly matched, misaligned or non-linear accelerator optics; instabilities and resonances; RF noise; scattering (intra-beam, residual gas, macroparticles, photons, obstacles, stripping foil, screens, etc.); electron clouds; beam-energy tails from uncaptured particles; or transverse-longitudinal coupling in the RF field.

Quantifying halo is made more difficult by varying definitions. Also, oscillations in phase space may cause measurements using projections into real space to vary with position along the machine. The techniques fall into three broad groupings: invasive measurements (wire

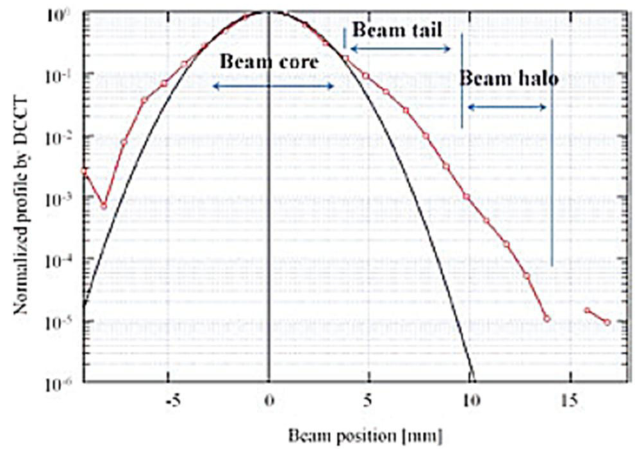

Figure 1: A beam profile showing core, tail, and halo (log scale). (K. Wittenburg, from M. Yoshimoto [4])

scanners, scrapers); non-invasive, non-optical methods (gas jets, electrons); and optical measurements. Workshop talks presented many of these approaches.

INVASIVE TECHNIQUES

Wire Scanners

Pavel Evtushenko (Jefferson Lab) stressed the need to protect electron linacs with continuous RF and MW beams from damage due to beam loss from tails and halos. Even in idealized Parmela simulations, the JLab FEL injector forms a tail at the level of 3×10^{-3}. Images using optical transition radiation (OTR) and YAG:Ce

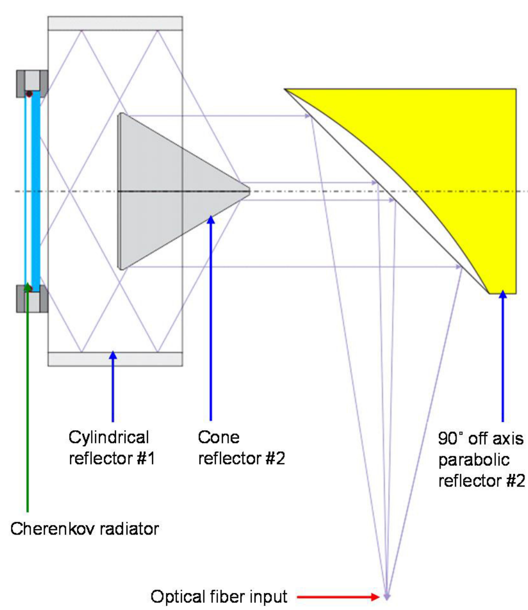

Figure 2: A loss shower emits light in a Cherenkov radiator. The light couples to an optical fibre leading to a PMT outside the tunnel. (P. Evtushenko)

*SLAC is supported by the U.S. Department of Energy under Contract DE-AC02-76SF00515.
#afisher@slac.stanford.edu

ISBN 978-3-95450-176-2

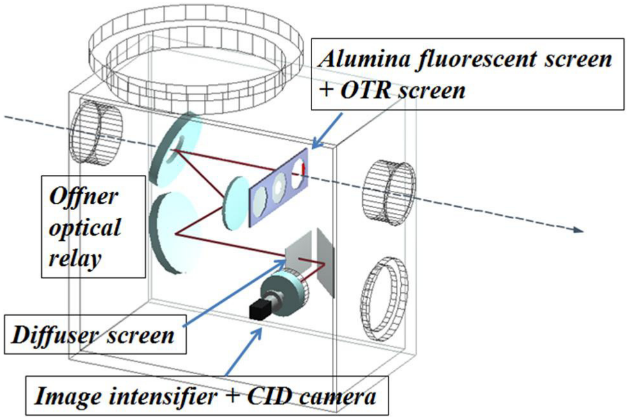

Figure 3: Two OTR screens and a fluorescent screen, with an optical relay, to image the core, tail, and halo of the J-PARC proton beam. (T. Mitsuhashi)

screens along the machine show that this tail has different Twiss parameters from those of the core.

In a wire scanner, the loss shower caused by moving a wire through a beam is detected by a scintillator or by Cherenkov radiation in a radiator or optical fibre. A photomultiplier (PMT) detects the emitted light. Since some PMTs have dark currents as low as a few nA, they can provide a high dynamic range when combined with appropriate electronics.

Pulse counting is feasible for beams with high repetition rates, such as in CEBAF. Paired measurements in coincidence can further reduce background. At lower rates, a gated analogue integrator can provide a wide dynamic range. Using two integrators with sensitivities differing by a factor of 100 can further extend the range to 10^6. Logarithmic current-to-voltage converters with a dynamic range of 10^8 to 10^{10} are being evaluated as an alternative, although the noise behaviour and bandwidth are more complex.

A Cherenkov radiator with efficient reflective optics coupling its light into a fibre was also described (Figure 2). The fibre brings the light to a PMT placed outside the tunnel to reduce background.

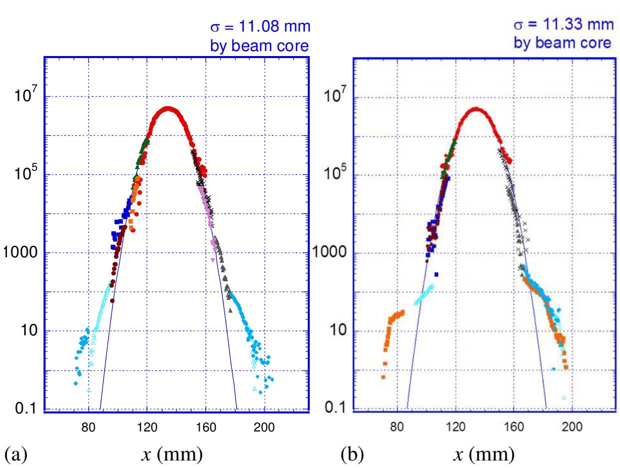

Figure 4: Horizontal profiles (log scale) of the J-PARC proton beam, combined from three types of screen; (a) without and (b) with collimation. (T. Mitsuhashi)

OTR and Fluorescent Screens

Toshiyuki Mitsuhashi (KEK) described the use of three targets to image the 3.5-GeV proton beam in J-PARC: an OTR screen to capture light from the core, an OTR with a central hole for the tail, and four fluorescent screens at large $|x|$ and $|y|$ to obtain more sensitivity for the halo. An OTR image using a foil at 45° to the beam would be blurred by the short depth of field resulting from the beam's wide OTR angular distribution. Instead, forward emission at normal incidence is collected by a mirror with a central hole, the first stage of an Offner optical relay (Figure 3).

The intensity scales of the three measurements can be matched over portions of the beam profile covered by two images, to get the combined horizontal profiles of Figure 4. The collimators are removed in 4a but inserted in 4b. We see the importance of making halo measurements while collimating: here its effect is to increase the halo.

Bent Crystals

Uli Wienands (SLAC) pointed out that although crystal collimation of protons has shown some promise, it has not been thought suitable for electrons due to a lower channelling efficiency and enhanced scattering. However, a recent test at SLAC (T-513) shows that a related process, volume reflection (Figure 5a), can efficiently deflect electrons (5b) in a mosaic Si crystal with a slight bend of 0.4 mrad, reducing the tail by a factor of 10.

NON-INVASIVE, NON-OPTICAL TECHNIQUES

Gas Jets

Adam Jeff (CERN and University of Liverpool) compared two ways to make an ionization profile monitor with a gas jet. In one, a thin gas sheet crosses a proton beam at angle (typically 45°). An electric field draws the ions transversely to a microchannel plate and phosphor screen. The space charge created by the sheet can distort the image. Alternatively, he proposed a thin "pencil" jet

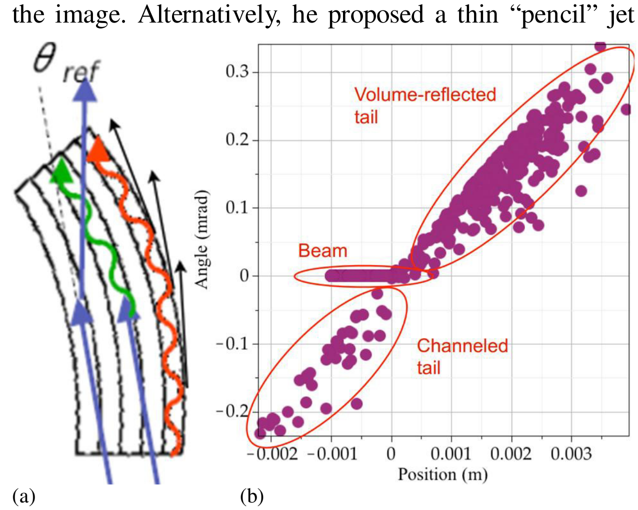

Figure 5: (a) Volume reflection (left) and channelling (centre and right) in a bent crystal. (b) Channelled and reflected electrons in T-513 at SLAC. (U. Wienands)

ISBN 978-3-95450-176-2

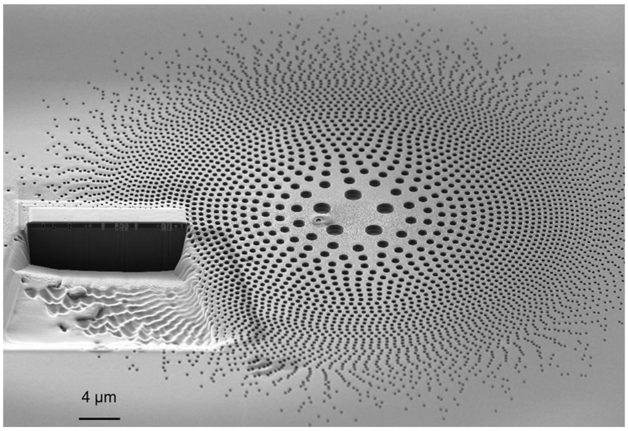

Figure 6: An atomic sieve to focus a thin gas jet. (A. Jeff)

of gas that scans across the beam, quickly though the core and slowly through the tail and halo.

Such a thin jet could be made with the matter-wave analogue of a Fresnel zone plate. This has been demonstrated [5] with room-temperature helium, which has a deBroglie wavelength of 0.05 nm. With a monoenergetic source, the focal size would be comparable to the 100-nm width of the outer zone. However, zone-pate focusing is strongly chromatic and so gave a still impressive resolution of 2 µm FWHM.

A "photon sieve" [6] for x-ray imaging replaces the rings with a pattern of holes that give a sharper focus and easier fabrication. At the time of the workshop, the corresponding structure for matter waves, an "atomic sieve" (Figure 6) for a gas jet, was being fabricated.

Beam-Gas Vertex Detector

Rhodri Jones (CERN) described beam-gas measurements of the distributions of the two proton beams near the IP of the LHCb detector. The vertex locator (VELO), a series of radial and azimuthal silicon-strip sensors, records the charged-particle tracks. Reconstructing the vertices of these events gives the proton distributions (Figure 7a), from which the luminosity overlap integral can be computed. Pulsed gas injection has been used to speed data accumulation. Beam-gas has measured the relative charges in the individual bunches, comparing well with the fast bunch-current transformer, and has measured unbunched ("ghost") charge.

A new instrument, BGV, is being developed using gas injection into a chamber with differential pumping (Figure 7b). It may have capabilities for measuring halo at 4 to 6 sigmas from the core, although the beam-gas rate will be orders of magnitude smaller. It may be possible to find the average halo in the beams. A large increase in pressure, perhaps with a gas sheet or jet, could be helpful.

Scattered Electrons

Peter Thieberger (BNL) presented a tool for co-aligning two electron lenses with the RHIC beams, with a tolerance of 30 µm. In an electron lens, the electro-magnetic field of a low-energy electron beam (~5 keV) focuses the high-energy (100 GeV/amu) protons or ions

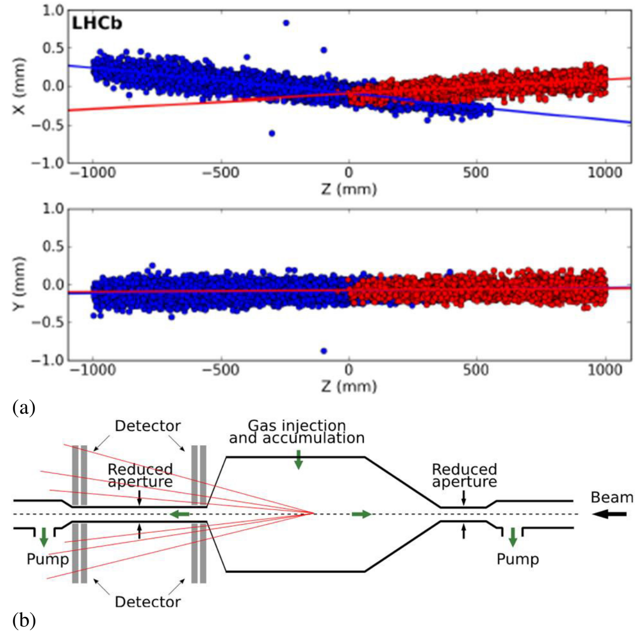

Figure 7: (a) Proton distributions in the LHC determined from beam-gas vertices. (b) A design sketch of the BGV. (R. Jones)

travelling in the opposite direction. Electrons back-scattered from the beam produce an alignment-dependent signal in a scintillator and PMT. Scattering of electrons in residual gas contributes to background and so necessitates excellent vacuum.

A hollow electron beam (a cylindrical shell) could probe beam halo by backscattering. Figure 8 shows a conceptual design.

OPTICAL TECHNIQUES

Any discussion about optical techniques for observing a dim halo in the vicinity of a bright core begins with a related problem from astronomy: viewing the solar corona. A million times dimmer than the sun's disc, the corona is normally visible only during an eclipse, when the moon blocks the sun's light. Many unsuccessful attempts were made to image the corona on a more convenient schedule by inserting a similar stop at an intermediate image plane inside a telescope. The problem was finally solved in 1934 by Bernard Lyot [7], who noted that the Airy diffraction rings from a telescope's entrance aperture or first optic overlap the image of the

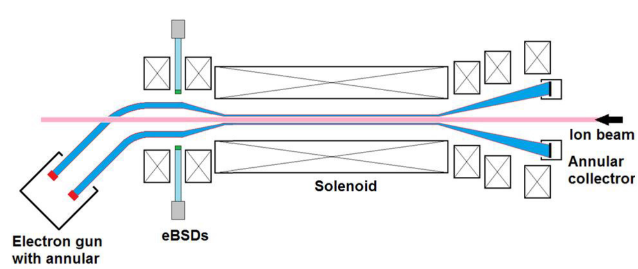

Figure 8: A hollow electron lens with electron back-scattering detectors (eBSDs) for measuring beam halo. (P. Thieberger)

ISBN 978-3-95450-176-2

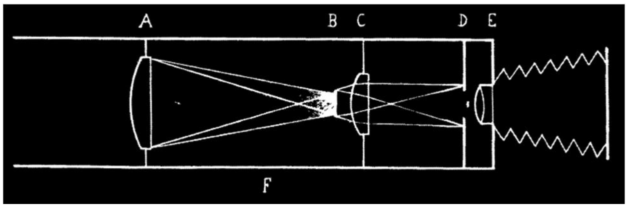

Figure 9: Lyot's coronagraph [7]. The image of the sun formed by lens A is blocked by stop B, which passes light from the corona. Lens A is imaged by lens C onto aperture D—the "Lyot stop"—but D blocks the image of A's edge, removing the Airy diffraction rings. The corona is imaged by lens E onto the film. See [8].

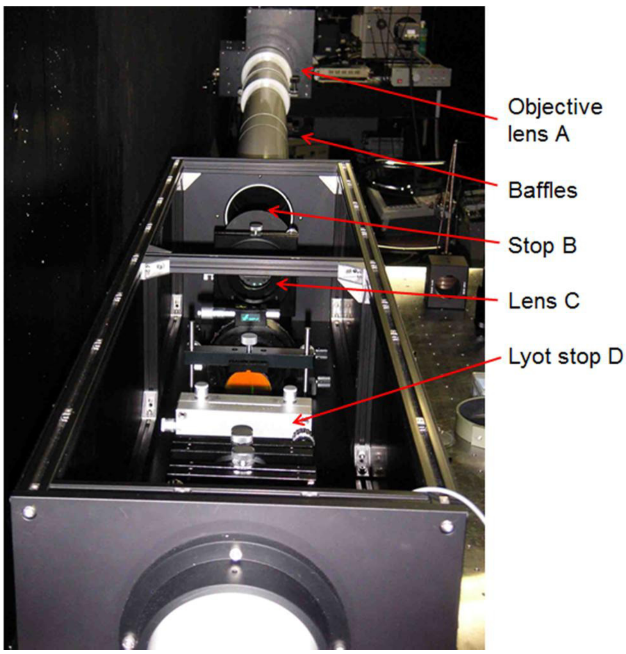

Figure 10: Coronagraph at the Photon Factory. (T. Mitsuhashi)

corona and are much brighter. He blocked them with a second stop (Figure 9). In contrast, a telescope viewing a solar eclipse is entirely within the large umbra of the moon and so can see the corona without competition from diffraction rings.

A Coronagraph for Beam Halo

Toshiyuki Mitsuhashi (KEK) explained the principle of the coronagraph and described one he built to observe beam halo in the Photon Factory (Figure 10). He emphasized design issues such as scattering from defects and dust on the surface of the objective lens or relay mirrors, and background from reflections inside the instrument. Light from the beam is split into two paths, providing simultaneous images of the core and halo (Figure 11).

Digital Micro-Mirror Arrays

Digital micro-mirror arrays (DMAs) are commonly used in computer projectors. **Jeff Corbett** (SLAC) described measurements with a DMA having a grid of 1024 × 768, 13.7-µm-square mirrors. When powered,

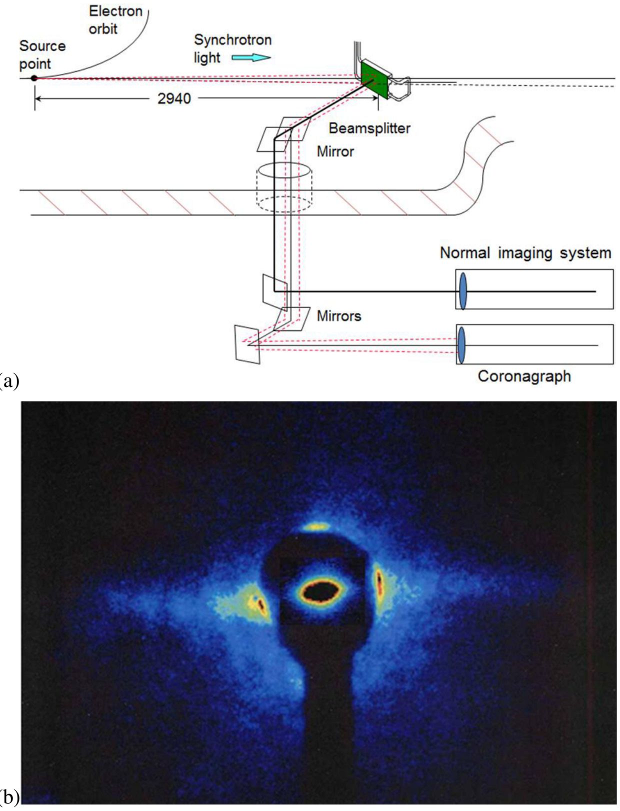

(a)

(b)

Figure 11: (a) The dual optical transport line for synchrotron light at the Photon Factory sends light to both a standard imaging system and the coronagraph. (b) Superimposed images of the beam's core and halo. (T. Mitsuhashi)

each mirror tilts to one of two positions, rotating about one diagonal by ±12° under programmed control (Figure 12). In studies on the SPEAR3 ring at SLAC, a synchrotron-light image of a beam was separated into core and halo by reflecting the light from these regions in two directions.

A fast gated camera with a Peltier-cooled detector was set for a constant 2-ms exposure. With the full DMA reflecting the light to the camera, and with a neutral-density (spectrally flat) optical filter attenuating by 10^5, the camera showed only the core. Mirror segments were then toggled to remove light from regions of the image

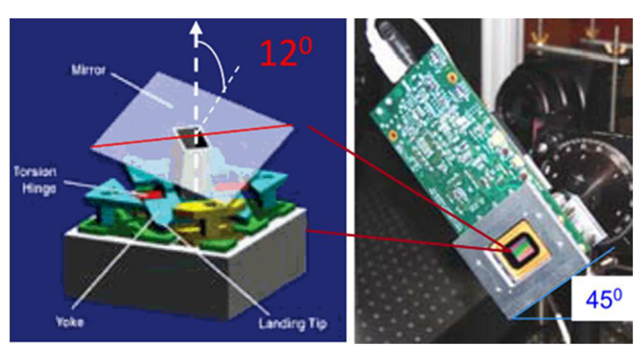

Figure 12: One micro-mirror (left) and the full DMA (right). The test board was mounted at 45° so that the two reflections remained on the horizontal plane. (J. Corbett)

ISBN 978-3-95450-176-2

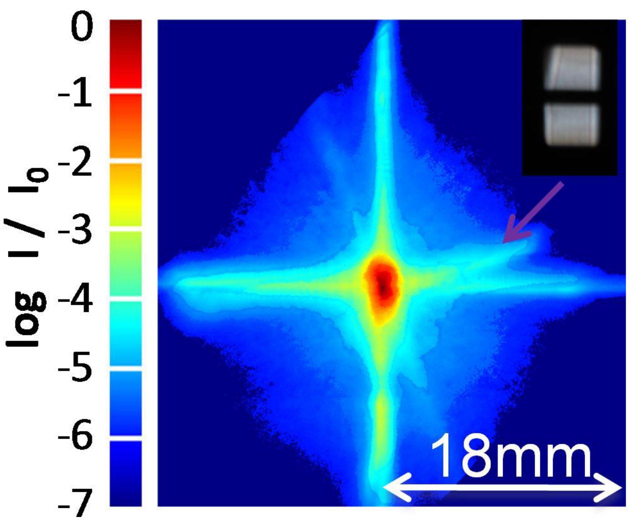

Figure 13: This composite beam image (log scale showing 7 orders of magnitude) was created in 6 steps. The brightest 90% of the previous image was removed by toggling the DMA mirrors while reducing the optical attenuation by 10. The inset shows incoming light from the transport line. The central black bar is the shadow of a cooled mask on the midplane that blocks synchrotron x rays. (J. Corbett)

with intensities greater than 10% of maximum, the optical attenuation was reduced by 10, and a new image was taken. This continued in steps of 10 until no filter was used. The brightest regions in the final image were five orders of magnitude below the peak of the core, and the dynamic range of the camera went two or more orders below this. Figure 13 shows a composite image of the intensity on a logarithmic scale.

Amplitude Apodizers

The diffraction rings removed in Lyot's coronagraph originate in the Fourier transform of the entrance aperture. Making this sharp-edged "pupil function" more gradual lessens the severity of the diffraction. Mitsuhashi addressed this briefly at the end of his coronagraph talk.

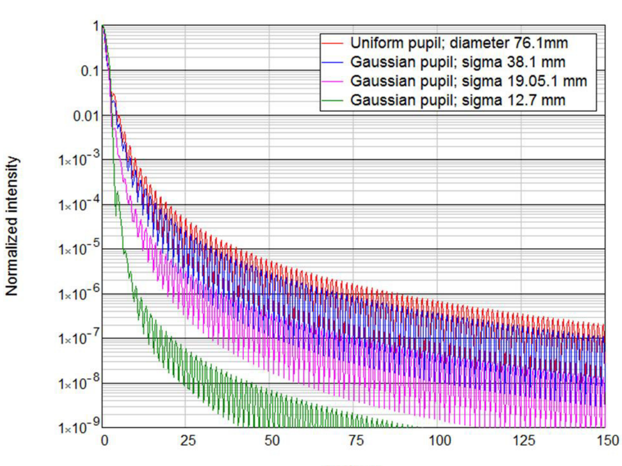

Figure 14: Point-spread functions of a hard edge and of various Gaussian apodizers. (P. Evtushenko)

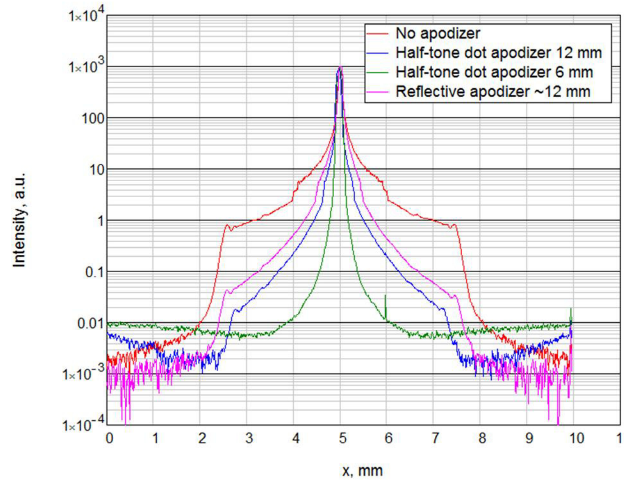

Figure 15: Line-outs (log scale) across the centre of images of a pinhole, with various apodizers at the lens. (P. Evtushenko)

Pavel Evtushenko (Jefferson Lab) returned to this theme, showing the image of a point source on the transform plane (the "point-spread function") after the aperture is replaced by Gaussian "apodizers" of various widths (Figure 14). Although narrowing an aperture generally worsens the diffractive resolution limit, the effect of softening the edge dominates in this range. A similar improvement results when these point-spread functions are convolved with a Gaussian beam.

A Gaussian transmission function can be approximated by a carefully designed pattern of black dots on a transparent base—a "half-tone dot apodizer". If the dots are small enough, their high spatial frequencies do not affect the image. In Figure 15, a pinhole source is imaged onto a CCD camera. The central line is compared for: no apodizer, a continuous reflective Gaussian apodizer, and two Gaussian dot apodizers of different widths. We see that the narrow dot apodizer has the best performance.

Astronomical Techniques

The concluding workshop talk returned fully to astronomy. **Sandrine Thomas** (NASA Ames Research Centre and University of California Santa Cruz) discussed optics descended from Lyot's that are being prepared for the direct observation of planets orbiting nearby stars. This objective, seeing a dim exoplanet close to a bright star, is comparable to observing beam halo optically, but even more demanding.

Nearly 1000 confirmed exoplanets, plus almost 3000 candidates, have been found to date, but most detection used either the dimming of the light as the planet's orbit briefly transits between the star and the Earth, or gravitational effects: the star's wobble, shifting its position and Doppler shifting its light, or gravitational microlensing as the planet changes the apparent position of a distant star in line with it. Direct detection of an Earth-like planet would enable spectroscopy of the planetary atmosphere. However, seeing the planet requires a dynamic range of 10 orders of magnitude. Thomas compared the task to

ISBN 978-3-95450-176-2

"searching for a firefly next to a lighthouse in San Francisco from Boston". Two approaches are in development: advanced coronagraphs and a "starshade".

Lyot's design can be improved with the micro-dot apodizer discussed previously, as well as with adaptive optics—deformable mirrors and wavefront sensors in feedback—to control static and dynamic aberrations. The gains can be seen in the simulations of Figures 16 to 18.

The starshade returns to the more favourable optics of a solar eclipse, by blocking the starlight with a large stop far from the telescope. An "occulter", a 32-m-diameter with a sunflower-shaped edge to approximate an apodizer, would sit at the Sun-Earth L_2 Lagrange point, 40,000 km from a space telescope, and allow the telescope to see a planetary system around a star in direct line with the starshade. The distant location of the occulter makes this scheme less suitable for viewing beam halo than the coronagraph.

CONCLUSIONS

Any device to measure beam halo is challenged by the need to span a dynamic range of 10^6 and to determine that these measurements are not influenced by background.

With careful design, two of the invasive techniques presented, the wire scanner and the combined OTR and fluorescent screens, have shown this capability, but invasive measurements are not suitable for many purposes. The other non-optical methods are at this time more speculative for halo monitoring.

Optical methods with high dynamic range have been demonstrated, including the DMA and others not presented here [9]: a charge-injection device (CID) camera and a small, masked, moving PMT. The composite image from the DMA (Figure 13) has a wide dynamic range. However, any optical method is subject to background light from sources other than halo, such as diffraction of light from the core or from the micro-mirrors themselves, scattering from imperfections in upstream optics, or reflection from the chamber walls. The DMA, CID, and scanned PMT can give a measure of the point-spread function of the optics (while folding in the bunch size), but further work is needed to determine that the halo dominates over the background.

NASA Ames has a laboratory with both the detection optics a careful simulation of the sources. Optical halo techniques should be developed in a similar setting, with light sources widely adjustable in size, position and intensity, to represent the core and halo. After an optical system is installed in a beamline, interference from wall reflections and imperfections in viewports can be probed by seeing whether any halo image is affected by moving collimators, changing background pressure, or otherwise influencing the halo distribution.

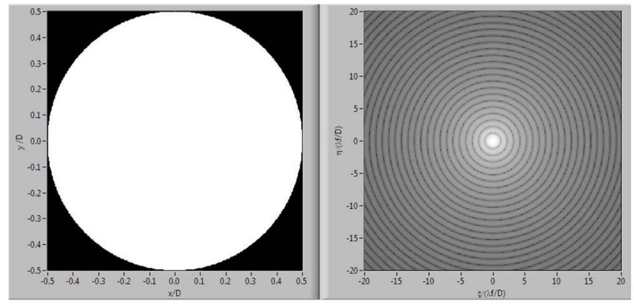

(a) (b)

Figure 16: In this series of simulations, (a) a uniformly illuminated lens with a hard-edged entrance aperture has (b) diffraction rings one focal length away that are too bright to detect a planet. (S. Thomas)

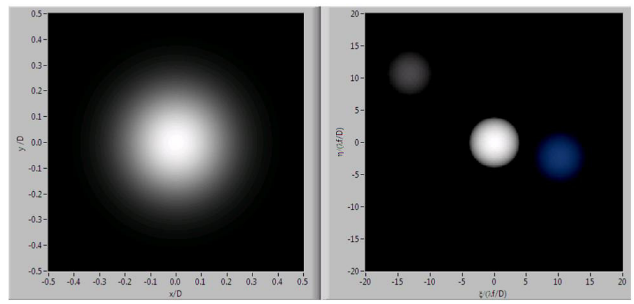

(a) (b)

Figure 17: (a) Inserting an apodizer at the lens of Figure 16 sharpens the image, removes the rings, and brings two planets into view. (S. Thomas)

ACKNOWLEDGMENT

I thank my accelerator colleagues who stayed on after IBIC 2014 to attend the workshop and to present and discuss the work on beam-halo measurements. I also want to thank Sandrine Thomas for presenting related efforts in astronomy to a meeting of accelerator physicists. She and her colleagues at NASA Ames took time to show me their lab and to discuss their approach to our common optical problems. We have much to gain from collaboration.

I thank all the speakers for allowing SLAC to post their contributions on-line [3].

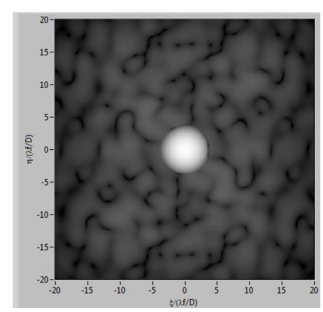

Figure 18: But if the lens has aberrations, the planets in Figure 17 cannot be seen. (S. Thomas)

REFERENCES

[1] https://portal.slac.stanford.edu/sites/conf_public/bhm_2014/Lists/registration/Public_view.aspx
[2] https://portal.slac.stanford.edu/sites/conf_public/bhm_2014/Pages/default.aspx
[3] https://portal.slac.stanford.edu/sites/conf_public/bhm_2014/Presentations/Forms/AllItems.aspx
[4] M. Yoshimoto, "Development of the Beam-Halo Monitor in the J-PARC 3-GeV RCS", Proc. IPAC 2012, WEOAA03, New Orleans, LA, USA.
[5] T. Reisinger, S. Eder, M.M. Greve, H.I. Smith, B. Holst, "Free-Standing Silicon-Nitride Zone Plates for

ISBN 978-3-95450-176-2

Neutral-Helium Microscopy", Microelectronic Engi–neering 87 (2010) 1011.
[6] L. Kipp, M. Skibowski, R.L. Johnson, R. Berndt, R. Adelung, S. Harm and R. Seemann, "Sharper Images by Focusing Soft X-Rays with Photon Sieves", Nature 414 (2001) 184.
[7] M.B. Lyot, "A Study of the Solar Corona and Prominences without Eclipses", Monthly Notices of the Royal Astronomical Society 99 (1939) 580.
[8] A. Sivaramakrishnan, C.D. Koresko, R.B. Makidon, T. Berkefeld and M.J. Kuchner, "Ground-Based Coronography with High-Order Adaptive Optics", Astrophys. J. 552 (2001) 397.
[9] C.P. Welsch, E. Bravin, B. Burel, T. Lefèvre, T. Chapman and M.J. Pilon, "Alternative Techniques for Beam Halo Measurements", Meas. Sci. Technol. 17 (2006) 2035.

ISBN 978-3-95450-176-2

IBIC 2014 SCIENTIFIC HIGHLIGHTS

Stephen R. Smith, SLAC National Accelerator Lab, Menlo Park, CA 94025, USA

Abstract

The SLAC National Accelerator Lab hosted the 3rd International Beam Instrumentation Conference (IBIC 2014) at the Portola Hotel in Monterey, California September 14-18, 2014. The four day scientific program consisted of tutorials, invited talks, contributed talks, poster sessions and industrial sponsor exhibits.

PARTICIPANTS

Conference attendance included 181 participants. Notably less than one third of the participants were from the host continent. Two-thirds of the participants travelled from Asia, South America, and Europe which alone was responsible for half of the attendees. This likely reflects the vibrancy of the European accelerator scene with projects such as the European XFEL, the European Spallation Source, FAIR, and LHC underway.

Table 1: Participation

Country	People	Continent
Japan	13	Asia 23
People's Republic of China	1	
Republic of Korea	8	
Taiwan	1	
Armenia	1	Europe 96
Belgium	1	
France	8	
Germany	37	
Italy	8	
Poland	1	
Slovenia	2	
Spain	4	
Sweden	3	
Switzerland	16	
United Kingdom	15	
United States	57	North America 57
Brazil	2	South America 3
Columbia	1	
Total	181	

PROGRAM

Tutorials

Both tutorials were very well received. Mike Gruchalla's (Los Alamos National Labs) tutorial "Managing Electromagnetic Interference in Large Instrumentation Environments"[1] provides very useful advice on understanding EMI with many subtle (and not so subtle) examples. He emphasized starting by understanding exactly what you are trying to measure, and then understanding what is not to be included in that measurement and understanding the coupling of both, with a frequent refrain of "draw a picture."

Thomas H. Lee of Stanford University presented "Dark (and Bright) Secrets of RF Design"[2] including some ancient history of RF technology and its ties to accelerators. He says "RF design is a mystery to many engineers" and that "… arcane incantations are needed to make oscillators oscillate and amplifiers amplify (and not vice-versa). Part of the mystery has to do with the many ways that ever-present parasitics undergo surprising impedance transformations, as well as the sometimes counterintuitive ways that nonlinear and time-varying processes can affect noise in amplifiers, oscillators and mixers." Lee starts with a short list of why RF design is hard: parasitics, limited device power gain, tough noise and nonlinearity requirements, and poor device models. A nice overview of relevant topics such as amplifier matching, noise sources, and some odd effects were explained, and many examples followed.

Superconducting Detector Technology

Kent Irwin[3] (SLAC and Stanford University) presented an exciting talk on arrays of superconducting detectors spanning their applications from X-ray beamlines to the recent announcement of detection of evidence for gravitational waves in the early universe. The detectors are arrays of superconducting transition-edge sensors (TES), sensitive to anything which can deposit energy. The signal is amplified by superconducting quantum-interference devices (SQUID), potentially with frequency-division multiplexing based on superconducting resonators whose frequency is shifted by the energy deposited in the TES. These technologies may well be more broadly useful to our community.

Lab Talks and Posters

LHC Beam Instrumentation was presented by Rhodri Jones (CERN). He pointed out the great challenges due to relative inaccessibility and high stored energies in the machine[4]. Weixing Cheng (Brookhaven National Lab) presented "NSLS2 Diagnostic Systems Commissioning

ISBN 978-3-95450-176-2

and Measurements" [5] wherein he discussed the start of commissioning. DESY projects were represented with Nicoleta Baboi presenting "Commissioning of the FLASH2 Electron Beam Diagnostics in Respect to its use at the European XFEL"[6] and Dirk Noelle presenting Status of the Standard Diagnostic Systems of the European XFEL"[7].

Henrik Loos (SLAC) presented "LCLS Beam Diagnostics" emphasizing what worked, what did not, and what is new and improved since LCLS turned on in 2009[8]. We heard about commissioning of beam diagnostics for the KEK Compact ERL from Ryota Takai[9].

Rasmus Ischebeck (PSI) in "Overview of Beam Instrumentation Activities for SwissFEL" presented how that project is addressing the gamut of FEL diagnostics, beam charge, position, arrival time, transverse and longitudinal profiles, compression, and loss monitors.[10]

Papers by Topic

The proceedings feature many talks on beam position, profiles, and longitudinal profile measurements as shown in Table 2.

Table 2: Papers by Topic

Classification	**Papers**
Charge Monitor	9
Loss Monitor	6
Profile	36
Position & Stability	36
Feedbacks	7
General Diagnostics	20
Overview & Commissioning	11
Time Resolved & Synchronization	20
Xray	3
Total	148

REFERENCES

[1] M. Gruchalla, "Managing Electromagnetic Interference in Large Instrumentation Environments", IBIC'14, Monterey, Sept. 2014, p. 224; http://www.JACoW.org

[2] T.H. Lee, "Dark Secrets of RF Design", IBIC'14, Monterey, Sept. 2014, WETUB1 slides, http://www.JACoW.org

[3] K.D. Irwin, "Superconducting Detectors for X-ray Beamline Applications and Cosmology", IBIC'14, Monterey, Sept. 2014, MOIXB3 slides, http://www.JACoW.org

[4] O. R. Jones, The Beam Instrumentation and Diagnostic Challenges for LHC Operation at High Energy", IBIC'14, Monterey, Sept. 2014, p. 216; http://www.JACoW.org

[5] W.X. Cheng, "NSLS2 Diagnostic Systems Commissioning and Measurements", IBIC'14, Monterey, Sept. 2014, p. 16; http://www.JACoW.org

[6] N. Baboi, "Commissioning of the FLASH2 Electron Beam Diagnostics in Respect to its use at the European XFEL", IBIC'14, Monterey, Sept. 2014, p. 712; http://www.JACoW.org

[7] D. Noelle, "Status of the Standard Diagnostic Systems of the European XFEL", IBIC'14, Monterey, Sept. 2014, p. 569; http://www.JACoW.org

[8] H. Loos, "LCLS Beam Diagnostics", IBIC'14, Monterey, Sept. 2014, p. 475; http://www.JACoW.org

[9] Ryota Takai, "Design and Initial Commissioning of Beam Diagnostics for the KEK Compact ERL", IBIC'14, Monterey, Sept. 2014, p. 7; http://www.JACoW.org

[10] R. Ischebeck, "Overview of Beam Instrumentation Activities for SwissFEL", IBIC'14, Monterey, Sept. 2014, p. 119; http://www.JACoW.org

ISBN 978-3-95450-176-2

List of Authors

Bold papercodes indicate primary authors

ISBN 978-3-95450-176-2

ISBN 978-3-95450-176-2

ISBN 978-3-95450-176-2

ISBN 978-3-95450-176-2

ISBN 978-3-95450-176-2

— Z —

ISBN 978-3-95450-176-2

Institutes List

ALBA-CELLS Synchrotron
Cerdanyola del Vallès, Spain
- Colldelram, C.
- Crisol, A.
- Iriso, U.
- Moldes, J.
- Nosych, A.A.
- Olmos, A.
- Pérez, F.
- Torino, L.

ANSTO
Menai, New South Wales, Australia
- Button, D.T.
- Garton, D.B.
- Mann, M.C.

ARPANSA
Yallambie, Australia
- Webb, D.

ASCo
Clayton, Victoria, Australia
- Boland, M.J.
- Clarken, R.
- Cunningham, S.
- Michalczyk, A.
- Starritt, A. C.

BME
Murnau, Germany
- Bergmann, T.

BNL
Upton, Long Island, New York, USA
- Bacha, B.
- Blaskiewicz, M.
- Blednykh, A.
- Cheng, W.X.
- Fedotov, A.V.
- Fedurin, M.G.
- Gassner, D.M.
- Ha, K.
- Hu, Y.
- Kayran, D.
- Kewisch, J.
- Li, Y.
- Mead, J.
- Miller, T.A.
- Minty, M.G.
- Pinayev, I.
- Podobedov, B.
- Pogorelsky, I.
- Shaftan, T.V.
- Singh, O.
- Thieberger, P.
- Tian, Y.
- Tuozzolo, J.E.
- Wang, G.M.
- Yu, L.

CEA/DSM/IRFU
CEA/DSM/IRFU, France
- Farabolini, W.

CEA/IRFU
Gif-sur-Yvette, France
- Bolzon, B.
- Chauvin, N.
- Chel, S.
- Gobin, R.
- Senée, F.
- Valette, M.

CERN
Geneva, Switzerland
- Alexopoulos, A.
- Andersson, A.
- Andreazza, W.
- Angoletta, M.E.
- Antoniou, F.
- Artoos, K.
- Bartosik, H.
- Bartosik, M.R.
- Bergamaschi, M.
- Bodart, D.
- Bravin, E.
- Buzio, M.C.L.
- Caiazza, D.
- Catalán Lasheras, N.
- Cherif, A.
- Chritin, N.
- Corsini, R.
- Darmedru, P.Y.
- Dehning, B.
- Döbert, S.
- Domingues Sousa, F.S.
- Doytchinov, I.P.
- Effinger, E.
- Emery, J.
- Farabolini, W.
- Fernandes, M.F.
- Fuchs, J.-F.
- Gaddi, A.
- Galindo Munoz, N.
- Gayde, J.
- Gudkov, D.
- Guerrero, A.
- Herranz, J.
- Hofmann, T.
- Holzer, E.B.
- Höfle, W.

ISBN 978-3-95450-176-2

- Jeff, A.
- Jones, O.R.
- Kain, V.
- Kastriotou, M.
- Kieffer, R.
- Kotzian, G.
- Kuhn, M.
- Langner, A.
- Lefèvre, T.
- Levasseur, S.
- Levens, T.E.
- Ludwig, M.
- Magagnin, P.
- Mainaud Durand, H.
- Marco-Hernandez, R.
- Mazzoni, S.
- Modena, M.
- Molendijk, J.C.
- Nebot Del Busto, E.
- Novotny, P.
- Pacholek, P.
- Papaphilippou, Y.
- Pedersen, F.
- Pereira, C.
- Piselli, E.
- Raich, U.
- Rakai, A.
- Roberts, J.
- Roncarolo, F.
- Ruffieux, R.
- Russenschuck, S.
- Salvant, B.
- Samuelsson, S.
- Sanchez-Quesada, J.
- Sanz, C.
- Sapinski, M.
- Schmickler, H.
- Schneider, G.
- Severino, G.
- Sirvent Blasco, J.L.
- Skowroński, P.K.
- Søby, L.
- Solomon, K.W.
- Steyart, D.
- Storey, J.W.
- Tan, J.
- Tomás, R.
- Towler, J.R.
- Trad, G.
- Tshilumba, D.
- Valuch, D.
- Veness, R.
- Viganò, W.
- Vlachakis, V.
- Wehrle, U.
- Wendt, M.
- Zorzetti, S.

CIVIDEC Instrumentation
Wien, Austria

- Griesmayer, E.

Cockcroft Institute
Warrington, Cheshire, United Kingdom

- Alexandrova, A.S.
- Fernandes, M.F.
- Jeff, A.
- Kastriotou, M.
- Tzoganis, V.
- Welsch, C.P.
- Zhang, H.D.

Cornell University (CLASSE), Cornell Laboratory for Accelerator-Based Sciences and Education
Ithaca, New York, USA

- Billing, M.G.
- Conway, J.V.
- Shanks, J.P.

D-Pace
Nelson, British Columbia, Canada

- Dehnel, M.P.

DCOM-iTEAM-UPV
Valencia, Spain

- Boria, V.E.

DESY
Hamburg, Germany

- Baboi, N.
- Bajt, S.
- Duhme, H.T.
- Flöttmann, K.
- Fröhlich, L.
- Gharibyan, V.
- Golz, T.
- Kube, G.
- Lorbeer, B.
- Nölle, D.
- Schlarb, H.
- Schmidt-Föhre, F.
- Stojanovic, N.
- Susen, R.
- Sydlo, C.
- Wittenburg, K.

DLS
Oxfordshire, United Kingdom

- Abbott, M.G.
- Bobb, L.M.
- Morgan, A.F.D.
- Rehm, G.
- Uzun, I.S.

East China University of Science and Technology
Shanghai, People's Republic of China

- Li, C.L.

ISBN 978-3-95450-176-2

ESS
Lund, Sweden
- Danared, H.
- Hassanzadegan, H.

Fermilab
Batavia, Illinois, USA
- Alvarez, M.L.
- Fellenz, B.J.
- Fitzgerald, J.
- Lundberg, C.E.
- Prieto, P.S.
- Roberts, M.
- Thurman-Keup, R.M.
- Zagel, J.R.

FHI
Berlin, Germany
- Kampfrath, T.

Forschungszentrum Jülich, Peter Gruenberg Institut
Jülich, Germany
- Krause, H.-J.

FRIB
East Lansing, Michigan, USA
- Cogan, S.
- Constan-Wahl, D.
- Crisp, J.L.
- He, Z.Q.
- Ikegami, M.
- Li, Z.
- Lidia, S.M.
- Liu, Z.
- Marti, F.
- Nesterenko, I.N.
- Pozdeyev, G.
- Russo, T.
- Shane, R.
- Webber, R.C.
- Zhang, Y.
- Zhao, Q.
- Zheng, Z.

FSU Jena
Jena, Germany
- Neubert, R.
- Seidel, P.

FZJ
Jülich, Germany
- Bai, M.
- Böhme, C.
- Gebel, R.
- Halama, A.J.
- Hinder, F.
- Kamerdzhiev, V.
- Klehr, F.
- Prasuhn, D.
- Reimers, K.
- Soltner, H.
- Srinivasan, S.
- Temme, D.
- Trinkel, F.
- Tölle, R.

GSI
Darmstadt, Germany
- Forck, P.
- Kowina, P.
- Kurian, F.
- Reeg, H.
- Reiter, A.
- Schwickert, M.
- Sieber, T.
- Singh, R.
- Steinhagen, R.J.
- Stöhlker, T.

HIJ
Jena, Germany
- Geithner, R.
- Kessler, A.
- Stöhlker, T.

HUST
Wuhan, People's Republic of China
- Huang, J.
- Liu, K.F.
- Yang, J.
- Zhang, L.G.
- Zuo, C.

HZB
Berlin, Germany
- Jankowiak, A.
- Kamps, T.
- Panofski, E.

HZDR
Dresden, Germany
- Gensch, M.
- Green, B.W.
- Justus, M.
- Kovalev, S.
- Kuntzsch, M.
- Lehnert, U.
- Lu, P.N.
- Michel, P.
- Schurig, R.
- Steinbrück, R.
- Teichert, J.

ISBN 978-3-95450-176-2

IFIC
Valencia, Spain
- Faus-Golfe, A.

IFMIF/EVEDA
Rokkasho, Japan
- Knaster, J.
- Okumura, Y.

IHEP
Beijing, People's Republic of China
- Cao, J.S.
- Deng, Q.Y.
- He, J.
- Hu, J.
- Li, P.
- Ma, H.Z.
- Sui, Y.F.
- Wang, L.
- Wei, S.J.
- Xu, T.G.
- Ye, Q.
- Yue, J.H.
- Zhao, Y.

IKP
Mainz, Germany
- Lauth, W.

ILSF
Tehran, Iran
- Jafarzadeh, M.
- Rahighi, J.
- Shafiee, M.Sh.

Imperial College of Science and Technology, Department of Physics
London, United Kingdom
- Kurup, A.
- Pozimski, J.K.
- Savage, P.

Indian Institute of Technology
New Delhi, India
- Malik, H.K.

INFN/LNF
Frascati (Roma), Italy
- Cioeta, F.
- Falone, A.
- Ghigo, A.
- Marcellini, F.
- Serio, M.
- Stella, A.

IOFFE
St. Petersburg, Russia
- Eremin, V.
- Verbitskaya, E.

IOQ
Jena, Germany
- Geithner, R.
- Stöhlker, T.

iThemba LABS
Somerset West, South Africa
- Conradie, J.L.
- Crombie, M.A.
- Mostert, H.W.

IUAC
New Delhi, India
- Hariwal, R.V.
- Kedia, S.
- Mehta, R.

J-PARC, KEK & JAEA
Ibaraki-ken, Japan
- Maruta, T.
- Toyama, T.

JAEA/J-PARC
Tokai-Mura, Naka-Gun, Ibaraki-Ken, Japan
- Akutsu, A.
- Harada, H.
- Hayashi, N.
- Ikezaki, K.
- Kato, S.
- Kinsho, M.
- Meigo, S.I.
- Miura, A.
- Nishikawa, M.
- Okabe, K.
- Ooi, M.
- Satou, K.
- Shobuda, Y.
- Yamamoto, K.
- Yoshimoto, M.

JAEA
Aomori, Japan
- Ichimiya, R.

JAI
Oxford, United Kingdom
- Bett, D.R.
- Blaskovic Kraljevic, N.
- Boogert, S.T.
- Bromwich, T.
- Burrows, P.
- Christian, G.B.
- Davis, M.R.

ISBN 978-3-95450-176-2

- Gibson, S.M.
- Kruchinin, K.O.
- Lyapin, A.
- Perry, C.
- Roberts, J.

Japan Atomic Energy Agency (JAEA), International Fusion Energy Research Center (IFERC)
Rokkasho, Kamikita, Aomori, Japan
- Shinto, K.

JASRI/SPring-8
Hyogo-ken, Japan
- Dewa, H.
- Fujita, T.
- Masaki, M.
- Matsubara, S.
- Sasaki, S.
- Takano, S.

JLab
Newport News, Virginia, USA
- Evtushenko, P.E.
- Gubeli, J.

Kanto Information Service (KIS), Accelerator Group
Ibaraki, Japan
- Saotome, H.S.

KEK/JAEA
Ibaraki-Ken, Japan
- Fukuta, S.F.
- Liu, Y.

KEK
Ibaraki, Japan
- Chin, Y.H.
- Flanagan, J.W.
- Furukawa, K.
- Ikeda, H.
- Koseki, T.
- Kuboki, H.
- Mitsuhashi, T.M.
- Miyahara, F.
- Miyao, T.
- Naito, T.
- Obina, T.
- Okada, M.
- Satoh, M.
- Seimiya, Y.
- Suwada, T.
- Tejima, M.
- Terunuma, N.
- Tobiyama, M.

King Faisal Specialist Hospital and Research Centre
Riyadh 11211, Kingdom of Saudi Arabia
- Alghaith, A.
- Alrumayan, F.M.
- Hendy, A.

KIRAMS/KHIMA
Seoul, Republic of Korea
- Chang, S.D.
- Hwang, J.G.
- Kim, C.H.
- Noh, S.Y.
- Park, C.W.

KIRAMS
Seoul, Republic of Korea
- An, D.H.
- Hahn, G.
- Yang, T.K.
- Yim, H.

KIT
Karlsruhe, Germany
- Borysenko, A.
- Hiller, N.
- Hofherr, M.
- Ilin, K.S.
- Müller, A.-S.
- Raasch, J.
- Scheuring, A.
- Schönfeldt, P.
- Siegel, M.
- Steinmann, J.L.
- Thoma, P.
- Wuensch, S.

Kyoto University
Kyoto, Japan
- Nakamura, K.G.
- Zen, H.

LANL
Los Alamos, New Mexico, USA
- Martinez, D.
- McCrady, R.C.
- Nguyen, J.D.
- Sedillo, J.D.
- Watkins, H.A.

LBNL
Berkeley, California, USA
- De Santis, S.

LHEP
Bern, Switzerland
- Auger, M.

- Braccini, S.
- Carzaniga, T.S.
- Ereditato, A.
- Nesteruk, K.P.
- Scampoli, P.

LNLS
Campinas, Brazil
- Duarte, H.O.C.
- Marques, S.R.

LPI
Moscow, Russia
- Artyukov, I.A.

Nagoya University
Nagoya, Japan
- Hosaka, M.
- Takashima, Y.
- Yamamoto, N.

Naples University Federico II
Napoli, Italy
- Scampoli, P.

NFRI
Daejon, Republic of Korea
- Choo, W.I.
- Jang, S.O.
- You, H.J.

NIRS
Chiba-shi, Japan
- Furukawa, T.
- Hara, Y.
- Mizushima, K.
- Noda, K.
- Saotome, N. S.
- Saraya, Y.
- Shirai, T.
- Tansho, R.

NI
Macquarie Park, New South Wales, Australia
- Yan, S.

NSRRC
Hsinchu, Taiwan
- Chen, J.
- Cheng, Y.-S.
- Chiu, P.C.
- Chou, M.C.
- Hsu, K.T.
- Hsu, S.Y.
- Hsueh, H.P.
- Hu, K.H.
- Huang, C. H.
- Huang, N.Y.
- Hwang, J.-Y.
- Kuan, C.K.
- Kuo, C.H.
- Lau, W.K.
- Lee, A.P.
- Lee, D.
- Liang, C.C.
- Liao, C.Y.
- Tsou, M.T.
- Wu, C.Y.

NTHU
Hsinchu, Taiwan
- Wang, P.

ORNL
Oak Ridge, Tennessee, USA
- Aleksandrov, A.V.
- Blokland, W.

Oxford University, Physics Department
Oxford, Oxon, United Kingdom
- Burrows, P.
- Perry, C.

PAL
Pohang, Kyungbuk, Republic of Korea
- Choi, H. J.
- Han, J.H.
- Hong, J.H.
- Kang, H.-S.
- Kim, C.
- Kim, S.H.
- Park, B.R.
- Park, S.J.

PhLAM/CERCLA
Villeneuve d'Ascq Cedex, France
- Bielawski, S.
- Roussel, E.

PhLAM/CERLA
Villeneuve d'Ascq, France
- Bielawski, S.
- Evain, C.
- Roussel, E.
- Szwaj, C.

Proactive Research and Development
Barcelona, Spain
- Herranz, J.

ISBN 978-3-95450-176-2

PSI
Villigen PSI, Switzerland
- Baldinger, R.
- Dehler, M.M.
- Ditter, R.
- Engeler, D.
- Frei, F.
- Gloor, M.
- Ischebeck, R.
- Keil, B.
- Koprek, W.
- Kramert, R.
- Llorente Sancho, D.
- Malatesta, A.
- Marcellini, F.
- Marinkovic, G.
- Ozkan Loch, C.
- Pollet, P.
- Roggli, M.
- Rohrer, M.
- Schlott, V.
- Stadler, M.
- Treyer, D.M.

RadiaBeam
Santa Monica, California, USA
- Agustsson, R.B.
- Campese, T.J.
- Harrison, M.A.
- Jacobson, B.T.
- Murokh, A.Y.
- Ovodenko, A.G.
- Ruelas, M.
- To, H.L.

Research School of Physics and Engineering, Australian National University
Canberra, Australian Capitol Territory, Australia
- Linardakis, P.
- Lobanov, N.R.
- Tsifakis, D.

RIKEN Nishina Center
Wako, Japan
- Fukunishi, N.
- Kase, M.
- Tzoganis, V.
- Watanabe, T.

RIKEN SPring-8 Center
Sayo-cho, Sayo-gun, Hyogo, Japan
- Asaka, T.
- Maesaka, H.
- Ohshima, T.
- Otake, Y.
- Tanaka, H.

RIKEN
Saitama, Japan
- Tzoganis, V.

Rome University La Sapienza
Roma, Italy
- Mostacci, A.

Royal Holloway, University of London
Surrey, United Kingdom
- Arteche, A.
- Aumeyr, T.
- Boorman, G.E.
- Bosco, A.
- Gibson, S.M.
- Karataev, P.
- Kruchinin, K.O.
- Rajaeifar, N.

SESAME
Allan, Jordan
- Al-Mohammad, H.
- Manukyan, K.

SES
Hyogo-pref., Japan
- Sumitomo, H.

Shahid Beheshti University
Tehran, Iran
- Feghhi, A.H.

SINAP
Shanghai, People's Republic of China
- Zhao, Z.T.

SLAC
Menlo Park, California, USA
- Campell, M.L.
- Clarke, C.I.
- Corbett, W.J.
- D'Ewart, J.M.
- Dusatko, J.E.
- Fisher, A.S.
- Fox, J.D.
- Frisch, J.C.
- Green, S.Z.
- Hast, C.
- Hogan, M.J.
- Krejcik, P.
- Lipkowitz, N.
- Loos, H.
- Luchini, K.
- Rivetta, C.H.
- Smith, S.R.
- Turgut, O.

- White, G.R.
- Wootton, K.P.
- Yakimenko, V.
- Yocky, G.
- Young, A.

SLRI
Nakhon Ratchasima, Thailand
- Hoyes, G.G.
- Klysubun, P.
- Kongtawong, S.
- Krainara, S.
- Sudmuang, P.
- Suradet, N.
- Teawphet, S.

SLSA
Clayton, Australia
- Basten, N.J.
- Boland, M.J.
- Cornall, T.D.
- Joseph Vettoor, E.
- Starritt, A. C.
- Tan, Y.E.

Sokendai
Ibaraki, Japan
- Mulyani, E.

Solaris National Synchrotron Radiation Centre, Jagiellonian University
Kraków, Poland
- Marendziak, A.M.
- Stankiewicz, M.J.
- Zając, M.

Solaris
Kraków, Poland
- Bocchetta, C.J.
- Borowiec, P.B.
- Bulira, P.
- Goryl, P.P.
- Kisiel, A.
- Kopec, M.P.
- Nietubyć, R.
- Wawrzyniak, A.I.
- Å»ytniak, Ł.

SOLEIL
Gif-sur-Yvette, France
- Abiven, Y.-M.
- Cassinari, L.
- Chapuis, L.
- Dohou, F.
- El Ajjouri, M.E.
- Hubert, N.
- Loulergue, A.
- Marcouillé, O.
- Monteiro, P.
- Nadolski, L.S.
- Pédeau, D.
- Rommeluère, P.

SSRF
Shanghai, People's Republic of China
- Chen, H.J.
- Chen, J.
- Chen, Z.C.
- Lai, L.W.
- Leng, Y.B.
- Yan, Y.B.
- Yang, Y.
- Yu, L.Y.
- Yuan, R.X.
- Zhou, W.M.

STFC/RAL/ISIS
Chilton, Didcot, Oxon, United Kingdom
- Lawrie, S.R.
- Letchford, A.P.

STFC/RAL
Chilton, Didcot, Oxon, United Kingdom
- Letchford, A.P.
- Pozimski, J.K.

Stockholm University, Department of Physics
Stockholm, Sweden
- Thomas, R.D.

Stockholm University
Stockholm, Sweden
- Björkhage, M.
- Blom, M.
- Cederquist, H.
- Eklund, G.
- Källberg, A.
- Liljeby, L.
- Löfgren, P.
- Paal, A.
- Reinhed, P.
- Rosén, S.
- Schmidt, H.T.
- Silverstein, S.B.
- Simonsson, A.

TEP Corporation
Tokyo, Japan
- Inamori, S.I.
- Kon, K.

The University of Liverpool
Liverpool, United Kingdom
- Alexandrova, A.S.
- Fernandes, M.F.

ISBN 978-3-95450-176-2

- Jeff, A.
- Kastriotou, M.
- Nebot Del Busto, E.
- Tzoganis, V.
- Welsch, C.P.

The University of Melbourne
Melbourne, Victoria, Australia
- Boland, M.J.
- Giansiracusa, P.J.
- Lucas, T.G.
- Peake, D.J.
- Rassool, R.P.
- Taylor, G.

TPU
Tomsk, Russia
- Potylitsyn, A.
- Sukhikh, L.G.
- Vukolov, A.V.

TRIUMF, Canada's National Laboratory for Particle and Nuclear Physics
Vancouver, Canada
- Verzilov, V.A.

TUB
Beijing, People's Republic of China
- Jiang, H.

UAB
Barcelona, Spain
- Olle, J.

UB
Barcelona, Spain
- Dieguez, A.

UCLA
Los Angeles, California, USA
- Curry, E.J.
- Musumeci, P.

UCL
London, United Kingdom
- Jolly, S.

Universitat Politécnica de Catalunya
Barcelona, Spain
- Barjau, A.
- Herranz, J.

University of Sussex
Brighton, United Kingdom
- Gale, J.D.

University of Tsukuba, Graduate School of Pure and Applied Sciences,
Tsukuba, Ibaraki, Japan
- Fukuoka, S.

Università di Pisa
Pisa, Italy
- Fanucci, L.

Universität Bern, Institute of Applied Physics
Bern, Switzerland
- Fabianska, J.
- Feurer, T.
- Hayati, M.

UVSOR
Okazaki, Japan
- Adachi, M.
- Katoh, M.
- Kimura, S.I.
- Konomi, T.

Warsaw University of Technology, Institute of Electronic Systems
Warsaw, Poland
- Jabłoński, S.

ISBN 978-3-95450-176-2